SPONSE

SIXTH INTERNATIONAL WORKSHOP
ON SEISMIC PERFORMANCE OF
NON-STRUCTURAL ELEMENTS

Proceedings of

Sixth International Workshop on Seismic Performance of Non-Structural Elements (SPONSE 2026)



MRRC

Institute of
SCIENCE TOKYO

Local Organizing Committee

Shoichi Kishiki (Chair, SPONSE 2026, Science Tokyo, Japan)
Shojiro Motoyui (Science Tokyo, Japan)
Tadashi Ishihara (Science Tokyo, Japan)
Daiki Sato (Science Tokyo, Japan)
Koshiro Nishimura (Science Tokyo, Japan)
Yoshihiro Yamazaki (Science Tokyo, Japan)
Sujan Pradhan (Science Tokyo, Japan)
Miku Kurosawa (Science Tokyo, Japan)
Yinli Chen (Science Tokyo, Japan)
Trevor Zhiqing Yeow (Science Tokyo, Japan)
Ichiro Hirano (Science Tokyo, Japan)
Motoko Okubo (Science Tokyo, Japan)
Eiko Nagami (Science Tokyo, Japan)
Misae Takano (Science Tokyo, Japan)
Shegay Alex (The University of Auckland, New Zealand)
Masahiro Kurata (Kyoto University, Japan)
Shinya Matsumoto (Kindai University, Japan)
Tetsuo Yamashita (Kogakuin University, Japan)
Tsuyoshi Seike (The University of Tokyo, Japan)
Satoshi Yamada (The University of Tokyo, Japan)
Kunio Mizutani (Tokyo Polytechnic University, Japan)
Takuya Nagae (Nagoya University, Japan)
Kazuhiro Matsuda (Meijo University, Japan)
Yoshio Wakiyama (National Institute for Land and Infrastructure Management, Japan)
Yusuke Oki (Building Research Institute, Japan)
Shotaro Yagi (Building Research Institute, Japan)
Shinichi Honda (Okuju corporation, Japan)
Yasuaki Sato (Takenaka corporation, Japan)

Reviewer List

The reviewers are listed in alphabetical order by family name.

Erideng Aoqier (Shizuoka Institute of Science and Technology, Japan)
Tatsuya Asai (The University of Tokyo, Japan)
Ting-wei Chang (Feng Chia University, Taiwan)
Yinli Chen (Institute of Science Tokyo, Japan)
Junwu Dai (China Earthquake Administration, China)
Rajesh Dhakal (University of Canterbury, New Zealand)
Peter Grzesik (Hilti AG, Liechtenstein)
Keisuke Himoto (Institute of Science Tokyo, Japan)
Ichiro Hirano (Institute of Science Tokyo, Japan)
Tadashi Ishihara (Institute of Science Tokyo, Japan)
Huanjun Jiang (Tongji University, China)
Yu Jiao (Tokyo City University, Japan)
Kensaku Kaneko (Osaka Metropolitan University, Japan)
Shoichi Kishiki (Institute of Science Tokyo, Japan)
Susumu Kono (Institute of Science Tokyo, Japan)
Miku Kurosawa (Institute of Science Tokyo, Japan)
Gennaro Magliulo (Università degli Studi di Napoli Federico II, Italy)
Kazuhiro Matsuda (Meijo University, Japan)
Yoriyuki Matsuda (Kogakuin University, Japan)
Ryota Matsui (Hokkaido University, Japan)
Shinya Matsumoto (Kindai University, Japan)
Kazuya Mitsui (Institute of Science Tokyo, Japan)
Shohei Miyata (The University of Tokyo, Japan)
Kunio Mizutani (Tokyo Polytechnic University, Japan)
Gilberto Mosqueda (University of California San Diego, United States)
Shojiro Motoyui (Tokyo Instiute of Technology, Japan)
Takuya Nagae (Nagoya University, Japan)
Takaharu Nakano (Institute of Science Tokyo, Japan)
Koshiro Nishimura (Institute of Science Tokyo, Japan)
Yusuke Oki (Building Research Institute, Japan)
Dave Montellano Osabel (Chonnam National University, Korea)
Sujan Pradhan (Institute of Science Tokyo, Japan)
Rodrigo Retamales (Seismic Intelligence SpA, Chile)

Keri Ryan (University of Nevada, Reno, United States)
Natsuhiko Sakiyama (Tokyo University of Science, Japan)
Daiki Sato (Institute of Science Tokyo, Japan)
Yasuaki Sato (Takenaka Corporation, Japan)
Alex Shegay (University of Auckland, New Zealand)
Yuki Terazawa (Institute of Science Tokyo, Japan)
Yoshio Wakiyama (National Institute for Land and Infrastructure Management, Japan)
Satoshi Yamada (The University of Tokyo, Japan)
Tetsuo Yamashita (Kogakuin University, Japan)
Yoshihiro Yamazaki (Institute of Science Tokyo, Japan)
Taro Yaoyama (The University of Tokyo, Japan)
Trevor Zhiqing Yeow (Institute of Science Tokyo, Japan)

Table of Contents

Conference Program ····· **i~xiv**

Technical Session 1A: RESPONSE, DAMAGE – 1 ····· **1~36**

Paper ID: 26007
Pages: 1~11
Presenting Author: Martin Kusz
Co-authors: Martin Kusz, Jason Swart, Jack Schwarz
Title: Dynamic design of non-structural elements

Paper ID: 26010
Pages: 12~19
Presenting Author: Dustin Cook
Co-authors: Dustin Cook, Jitendra Bhatta, Amanpreet Singh, Mohammed M. Eladly, Adam Zsarnóczay, Siamak Sattar, Ben Schafer, and Matthew Speicher
Title: An open-source nonstructural element database to streamline tech transfer between nonstructural research and building design

Paper ID: 26012
Pages: 20~30
Presenting Author: Didier COMBESCURE
Co-authors: D. Combescure, C. Benouaret, M. Ruiz, V. Dominguez, F. Rueda, C. Melendez, G. Theunis, N. Jobert, C. Houivet
Title: Generation of seismic motion for seismic qualification of active component

Paper ID: 26020
Pages: 31~36
Presenting Author: Chia-Ming Chang
Co-authors: Chia-Ming Chang and Wei-Kai Chen
Title: Preliminary investigation of isolation bearings with discontinuous inerters for seismic protection of essential equipment and components

Technical Session 1B: WALL, PANEL - 1 ····· **37~67**

Paper ID: 26030
Pages: 37~46
Presenting Author: Sora Hagiwara

Co-authors: Sora Hagiwara, Daiki Sato, Sono Yanagiya, Yinli Chen, Alex Shegay, Shoichi Kishiki, Tadashi Ishihara, Shojiro Motoyui, Yuzi Huang
Title: System identification of natural frequency and damping ratio of partition wall from earthquake observation records

Paper ID: 26051
Pages: 47~57
Presenting Author: Luigi Fiorino
Co-authors: Vito D'Addesa, Alessandro Prota, Luigi Fiorino, Marco Garofalo, Ghislain Rivron, Dominik Herfurth and Raffaele Landolfo
Title: Screw connections between gypsum panels and cfs profiles: experimental evaluation of shear response

Paper ID: 26094
Pages: 58~67
Presenting Author: Marco Donà
Co-authors: Ahmed Mabrouk, Marco Donà, Luca Tosolini, Marco Gaspri, and Francesca da Porto
Title: Seismic assessment of thin masonry-infilled RC frames via a coupled in-plane/out-of-plane macro-model

Technical Session 2A: CEILING - 1 ····· 68~99

Paper ID: 26026
Pages: 68~78
Presenting Author: Cameron Flude
Co-authors: Cameron Flude, David Lau, Jeffrey Erochko and Saranja Siventhirarajah
Title: Shake table testing of suspended ceilings

Paper ID: 26031
Pages: 79~87
Presenting Author: Eun-Rim Baek
Co-authors: Eun-Rim Baek, Jae-Bong Kim, Ju-Chan Kim, Sang-Hoon Oh, and Sang-Ho Lee
Title: Shake table test on suspended nonstructural components in a large-scale ceiling system

Paper ID: 26038
Pages: 88~99
Presenting Author: Igor Lanese

Co-authors: Igor Lanese, Miriam Bazzini, Paolo Dubini, and Emanuele Brunesi
Title: Code-based methodologies for the seismic qualification of non-structural elements: integrating experimental testing and numerical modelling

Technical Session 2B: BUILDING EQUIPMENT, SHELF - 1 ····· 100~139

Paper ID: 26002
Pages: 100~110
Presenting Author: Tara C. Hutchinson
Co-authors: Xianzhao Zhang, Jiachen Zhang, and Tara C. Hutchinson
Title: Shake table testing of rooftop mechanical equipment with different attachment strategies on a full-scale ten-story building

Paper ID: 26011
Pages: 111~117
Presenting Author: George C. Yao
Co-authors: George C. Yao, and Yu-Jyun Fang
Title: A study on library bookshelf safety and book falling in earthquakes

Paper ID: 26021
Pages: 118~128
Presenting Author: Min-Chi KO
Co-authors: Min-Chi Ko, Fan-Ru Lin, Juin-Fu Chai, Keng-Chang Kuo, Wei-Hung Hsu, Bai-Yi Huang, Wei-Chung Chen
Title: A study on bookshelves overturning evaluation based on reconnaissance in the 2024 HuaLien earthquake

Paper ID: 26033
Pages: 129~139
Presenting Author: Gilberto Mosqueda
Co-authors: S. Kavei, G. Mosqueda, and J. Park
Title: Seismic protection systems for safety-related equipment cabinets

Technical Session 3A: VIBRATION, CONTROL ····· 140~172

Paper ID: 26005
Pages: 140~150
Presenting Author: Tara Hutchinson
Co-authors: Sorosh S., Zhang J., Kovac A., Smith K., Schafer B.W., and Hutchinson T.C.
Title: Influence of stair system flexibility on building vibration period: insights from full-scale building shake table tests at low-amplitude excitation

Paper ID: 26013
Pages: 151~161
Presenting Author: Min Ho Chey
Co-authors: Khine Thazin P. Kyaw, Mehta Vikas, Sung Hyun Jang and Min Ho Chey
Title: Enhanced seismic stability for the freestanding contents in base-isolated buildings

Paper ID: 26058
Pages: 162~172
Presenting Author: Kazuhiro Matsuda
Co-authors: Kazuhiro Matsuda, Eisaku Asatsuma
Title: Seismic performance enhancement of suspended cable tray systems using steel wires

Technical Session 3B: RESPONSE, DAMAGE - 2 ····· 173~201

Paper ID: 26074
Pages: 173~179
Presenting Author: Yasuaki Sato
Co-authors: Yasuaki Sato , Alex Shegay, Fumihiko Sakuraba and Shojiro Motoyui
Title: Validation of analytical method for axial force- bending interaction of gypsum boards

Paper ID: 26076
Pages: 180~190
Presenting Author: Roberto Nascimbene
Co-authors: Muhammad Yousaf Anwar, Davide Bellotti, Emanuele Brunesi, and Roberto Nascimbene
Title: Derivation of floor response spectra in masonry infilled precast concrete buildings

Paper ID: 26081
Pages: 191~201
Presenting Author: Jitendra Bhatta
Co-authors: Jitendra Bhatta, Andrew Baird, Catalina Miranda, Jitendra Bothara, Lucas Hogan, Andrew Stolte, Chungwook Sim, Sutat Leelataviwat, and Amorn Pimanmas
Title: Myanmar earthquake reconnaissance: damage to non-structural elements in high-rise buildings in Bangkok

Technical Session 4A: CONNECTION PART, DESIGN, LOAD ····· 202~234

Paper ID: 26047

Pages: 202~212
Presenting Author: Kosuke Fujita
Co-authors: Kosuke Fujita, Shoichi Kishiki, and Takayuki Iijima
Title: Failure mechanisms and pull-out strength of the screw-type fastening post-installed anchors

Paper ID: 26001
Pages: 213~223
Presenting Author: Vladimir Vukobratović
Co-authors: Vladimir Vukobratović and Peter Fajfar
Title: Floor response spectra in the new generation of Eurocode 8: an overview and example of application

Paper ID: 26034
Pages: 224~234
Presenting Author: Davide Bellotti
Co-authors: Davide Bellotti, Francesco Cavalieri, Emanuele Brunesi, and Roberto Nascimbene
Title: Seismic demand evaluation for the design of non-structural elements in precast concrete buildings

Technical Session 4B: WALL, PANEL - 2 ····· 235~277

Paper ID: 26091
Pages: 235~245
Presenting Author: Marco Preti
Co-authors: Van Sang Doan, Simone Pelucco, and Marco Preti
Title: Seismic design of reinforced concrete frames with sliding joint ductile infills

Paper ID: 26093
Pages: 246~255
Presenting Author: Marco Gaspari
Co-authors: Gaspari M., Donà M., and da Porto F.
Title: Out-of-plane seismic assessment of URM infill walls through parametric analysis

Paper ID: 26096
Pages: 256~266
Presenting Author: Fumihiko Sakuraba
Co-authors: Fumihiko SAKURABA, Shota MIZUNO, Alex SHEGAY, Yasuaki

SATO and Shojiro MOTOYUI
Title: Influence of screw connection on out-of-plane behavior of LGS walls

Paper ID: 26102
Pages: 267~277
Presenting Author: Hao Wu
Co-authors: Hao Wu, Xiaoying Zhu and Zuochen Zhang
Title: Experimental investigation on the seismic performance of self-centering concrete wall structures with low damage infill walls

Technical Session 5A: FIRE RESISTIVE……278~319

Paper ID: 26062
Pages: 278~287
Presenting Author: Serdar Selamet
Co-authors: Serdar Selamet and Masahiro Kurata
Title: Drift-based functional fragility framework for fire-rated doors in post-earthquake fires

Paper ID: 26075
Pages: 288~298
Presenting Author: Francesco Monte
Co-authors: Monte F., Tartaglia R., De Angelis A., Del Vecchio C., and Maddaloni G.
Title: Influence of tee joint capacity on the seismic behaviour of a fire suppression system

Paper ID: 26089
Pages: 299~308
Presenting Author: Gianni Blasi
Co-authors: Gianni Blasi, Daniele Perrone, Marianovella Leone, Maria Antonietta Aiello
Title: Probabilistic seismic demand assessment of rising pipe lines in fire-protection systems

Paper ID: 26202
Pages: 309~319
Presenting Author: Francesco Micelli
Co-authors: Francesco Micelli, Daniele Perrone, Giammaria Gabbianelli, Chiara Miglietta, Bryan Chalarca, Emanuele Brunesi, Mariano Ciucci
Title: Experimental seismic response assessment of piping networks in industrial

facilities: the mitplant project
Technical Session 5B: BUILDING EQUIPMENT, SHELF - 2 ·····320~363
Paper ID: 26003
Pages: 320~330
Presenting Author: Jitendra Bhatta
Co-authors: Jitendra Bhatta, Prashanna Mishra, Dustin T. Cook, Siamak Sattar, John W. van de Lindt, and Andre R. Barbosa
Title: Seismic performance of a full-scale code-compliant fire sprinkler piping system in a six-storey building

Paper ID: 26046
Pages: 331~341
Presenting Author: Ichiro Hirano
Co-authors: Ichiro Hirano and Shoichi Kishiki
Title: Strength evaluation of inserts hardware for building equipment under deck composite slab

Paper ID: 26086
Pages: 342~352
Presenting Author: Marco Donà
Co-authors: Marco Donà, Alberto Zonta, Marco Ceresara, and Francesca da Porto
Title: Seismic fragility assessment of industrial pallet racks in Italy

Paper ID: 26203
Pages: 353~363
Presenting Author: Alessandro Zona
Co-authors: Alessandro Zona, Fabio Micozzi, Laura Gioiella, Fabrizio Scozzese, Michele Mirra, Michele Morici, Francesco Allegrezza, Graziano Leoni and Andrea Dall'Asta
Title: Design and testing of school furniture as life-saving non-structural building components: a case study
Technical Session 6A: WALL, PANEL - 3·····364~405
Paper ID: 26057
Pages: 364~372
Presenting Author: Yusuke Oki
Co-authors: Yusuke Oki, Shoichi Kishiki and Tadashi Ishihara
Title: Damage behavior of light gauge steel partition wall under in-plane and out-of-plane external forces

Paper ID: 26082
Pages: 373~383
Presenting Author: Igor Lanese
Co-authors: Riccardo R. Milanesi, Maithree Kurukulasuriya, Igor Lanese, Guido Magenes, Paolo Morandi
Title: Influence of in-plane damage on the out-of-plane seismic response of weak clay masonry infills through shaking table dynamic tests

Paper ID: 26084
Pages: 384~394
Presenting Author: Keri L. Ryan
Co-authors: Keri L. Ryan, Tara C. Hutchinson, Shokrullah Sorosh, William Roser, Yi-En Ji, Sir Lathan Wynn
Title: NHERI TallWood project part 1: overview and nonstructural subassembly details

Paper ID: 26085
Pages: 395~405
Presenting Author: Keri L. Ryan
Co-authors: Keri L. Ryan, Tara C. Hutchinson, Shokrullah Sorosh, William Roser, Yi-En Ji, Sir Lathan Wynn
Title: NHERI TallWood project part 2: performance of building and nonstructural subassemblies

Technical Session 6B: RESPONSE, DAMAGE - 3……406~451

Paper ID: 26025
Pages: 406~414
Presenting Author: Angela Poposka
Co-authors: Angela Poposka, Aleksandra Bogdanovic, Filip Manojlovski, Antonio Shoklarovski, Lidija Krstevska
Title: Experimental shake table evaluation of non-structural elements in accordance with AC-156

Paper ID: 26027
Pages: 415~425
Presenting Author: Fan-Ru Lin
Co-authors: Fan-Ru Lin, Bai-Yi Huang, Wei-Hung Hsu, Min-Chi Ko, Wei-Chung Chen, Wen-Hsuan Huang and Juin-Fu Chai
Title: A study on non-structural seismic damage of critical facilities in 0403 HuaLien

earthquake in Taiwan

Paper ID: 26032
Pages: 426~439
Presenting Author: Shuoguo Qiu
Co-authors: Shuoguo Qiu and Quincy Ma
Title: Seismic resilience assessment of hospitals using dynamic bayesian network

Paper ID: 26036
Pages: 440~451
Presenting Author: Scott Menegon
Co-authors: Alex Shegay, Mojtaba Hosseini, Jitendra Bhatta, Rajesh Dhakal, Paul Kim, Scott Menegon, Glen Pring, Wei-Chung Chen, Min-Chi Ko and Santiago Pujol
Title: Performance of non-structural components in a 5-storey shake-table test

Technical Session 7A: RESPONSE, DAMAGE - 4……452~493

Paper ID: 26049
Pages: 452~461
Presenting Author: Gerard J. O'Reilly
Co-authors: Gerard J. O'Reilly, and Masayoshi Nakashima
Title: Issues in the fragility analysis of non-structural elements and the role of structural health monitoring

Paper ID: 26050
Pages: 462~472
Presenting Author: Rola Assi
Co-authors: Majid Mehrjoo, Rola Assi
Title: Proposed ductility-based force factors for acceleration-sensitive light non-structural components

Paper ID: 26065
Pages: 473~483
Presenting Author: Rajesh Dhakal
Co-authors: Rajesh P. Dhakal, Jitendra Bhatta, Rajesh Shrestha, Aasish Tiwari, Ping Xiang, Zhenduo Yan, Yu'ao Lin, Sixian Cao, Jiajun Yu, Yiqing Liu, Gregory A. MacRae, Geoffrey Rodgers, Shahab Ramhormozian, G. Charles Clifton, Liang-Jiu Jia and Xianzhong Zhao
Title: Shake-table tests on full-scale non-structural elements in a low-damage 3-story steel building: key results from the ROBUST project

Paper ID: 26008
Pages: 484~493
Presenting Author: Marko M. Marinković
Co-authors: Marko M. Marinković and Christoph H. Butenweg
Title: The benefits and advantages of using RC frames with isolated or decoupled infills in practice: INODIS connection

Technical Session 7B: CEILING - 2·····494~536

Paper ID: 26052
Pages: 494~503
Presenting Author: Alessandro Prota
Co-authors: Alessandro Prota, Vito D'Addesa, Luigi Fiorino, Ghislain Rivron, Marco Garofalo, Dominik Herfurth, and Raffaele Landolfo
Title: Seismic assessment of concealed grid suspended ceilings: design of a large-scale experimental setup for shaking-table testing

Paper ID: 26054
Pages: 504~514
Presenting Author: Huanjun Jiang
Co-authors: Huanjun Jiang, Youlu Huang, and Xinyi He
Title: Experimental study on pounding response of suspended ceiling system with mineral wool board

Paper ID: 26060
Pages: 515~525
Presenting Author: Peizhi Zhao
Co-authors: Peizhi Zhao, Rokhyun Yoon, and Yasushi Sanada
Title: Numerical simulation of the structural test on a 2.5- story model frame representing lower stories of existing high-rise RC buildings with non- structural flat walls

Paper ID: 26063
Pages: 526~536
Presenting Author: Haruki Yamaguchi
Co-authors: Haruki Yamaguchi, Tadashi Ishihara, and Yusuke Oki
Title: Shaking table test of seismic-resistant ceiling systems with asymmetric mass or stiffness distribution

Technical Session 8: RESPONSE, DAMAGE - 5·····537~555

Paper ID: 26072

Pages: 537~545
Presenting Author: Gennaro Magliulo
Co-authors: G. Magliulo, C. R. Addeo, D. D'Angela, M. De Stefano, C. Di Salvatore and F. Tuozzo
Title: Preliminary observations on the effects of 2024-2025 bradyseism earthquakes on nonstructural elements in Campi Flegrei

Paper ID: 26071
Pages: 546~555
Presenting Author: Ricardo Monteiro
Co-authors: Besim Yukselen, Gianrocco Mucedero, and Ricardo Monteiro
Title: Optimising seismic retrofit design to reduce non-structural element losses using multiple objectives

Technical Session 9: EARLY CAREER BEST PAPER AWARD SESSION – 1……556~611

Paper ID: 26006
Pages: 556~566
Presenting Author: Amanpreet Singh
Co-authors: Amanpreet Singh, Fidence Cyizere Rukundo, Jason R. Ameen, Saeed Fathali, Jordan Jaramillo, Bob Torbin, Jereme Huntress, Geza Szakats, Dustin T. Cook, Matthew S. Speicher, Siamak Sattar, Tara C. Hutchinson, and Benjamin W. Schafer
Title: Interaction of suspended ceilings and pressurized piping in a full-scale 10-story cold-formed steel building shake table test program

Paper ID: 26009
Pages: 567~577
Presenting Author: Minhui Li
Co-authors: Minhui. LI, Daiki. SATO, and Shojiro. MOTOYUI
Title: Study on the horizontal stiffness of single and double-layer CHN-US style ceiling

Paper ID: 26004
Pages: 578~588
Presenting Author: Roberto J. Merino
Co-authors: Roberto J. Merino, Roberto Gentile, and Carmine Galasso
Title: Estimation of floor response spectra for risk- targeted seismic design of non-structural elements

Paper ID: 26053

Pages: 589~600
Presenting Author: Chang-Jun Bae
Co-authors: Chang-Jun Bae, Cheol-Ho Lee, and Su-Chan Jun
Title: Evaluation of component amplification factor considering structure-NSC interaction and NSC-clustering

Paper ID: 26019
Pages: 601~611
Presenting Author: Wei-Chung Chen
Co-authors: W.C. Chen, M.C. Ko, W.H. Huang, J.F. Chai, and F.R. Lin
Title: Experimental and field investigations of suspended air handling units

Technical Session 10: EARLY CAREER BEST PAPER AWARD SESSION – 2 ···· 612~662

Paper ID: 26101
Pages: 612~622
Presenting Author: Ahmed Awad
Co-authors: Ahmed Awad, Marco Simoncelli, and Claudio Bernuzzi
Title: Innovative seismic isolation strategies for equipment and non-structural components: experimental investigation and analytical modeling of systems isolated with spring-viscoelastic mounts

Paper ID: 26056
Pages: 623~633
Presenting Author: Simona Bianchi
Co-authors: Simona Bianchi, Guido Lori, Jonathan Ciurlanti, Giovanni Milan, Nebojša Buljan
Title: Low-carbon resilient curtain walls: experimental study of timber-glass unitized systems

Paper ID: 26059
Pages: 634~643
Presenting Author: Zeyu SUN
Co-authors: Zeyu SUN, Miku KUROSAWA, Shoichi KISHIKI, Yusuke OKI, Shinichi HONDA, and Takayuki SATOU
Title: In-plane loading experiments on seismic damage and functional retention performance of LGS partition walls with opening

Paper ID: 26067
Pages: 644~653

Presenting Author: Danilo D'Angela
Co-authors: D. D'Angela, A. Bonati, O. Coppola, and G. Magliulo
Title: Hysteretic behavior stiffness degradation and energy dissipation in screw connections of cold- formed steel framed plasterboard partitions

Paper ID: 26078
Pages: 654~662
Presenting Author: Ghislain Rivron
Co-authors: Catalina M. Nigro and Ghislain Rivron
Title: Experimental analysis of the seismic in-plane performance of cold-formed steel gypsum drywall systems: glued vs. screwed connections

EARLY CAREER BEST PAPER AWARD ····· **663**

Institute of SCIENCE TOKYO

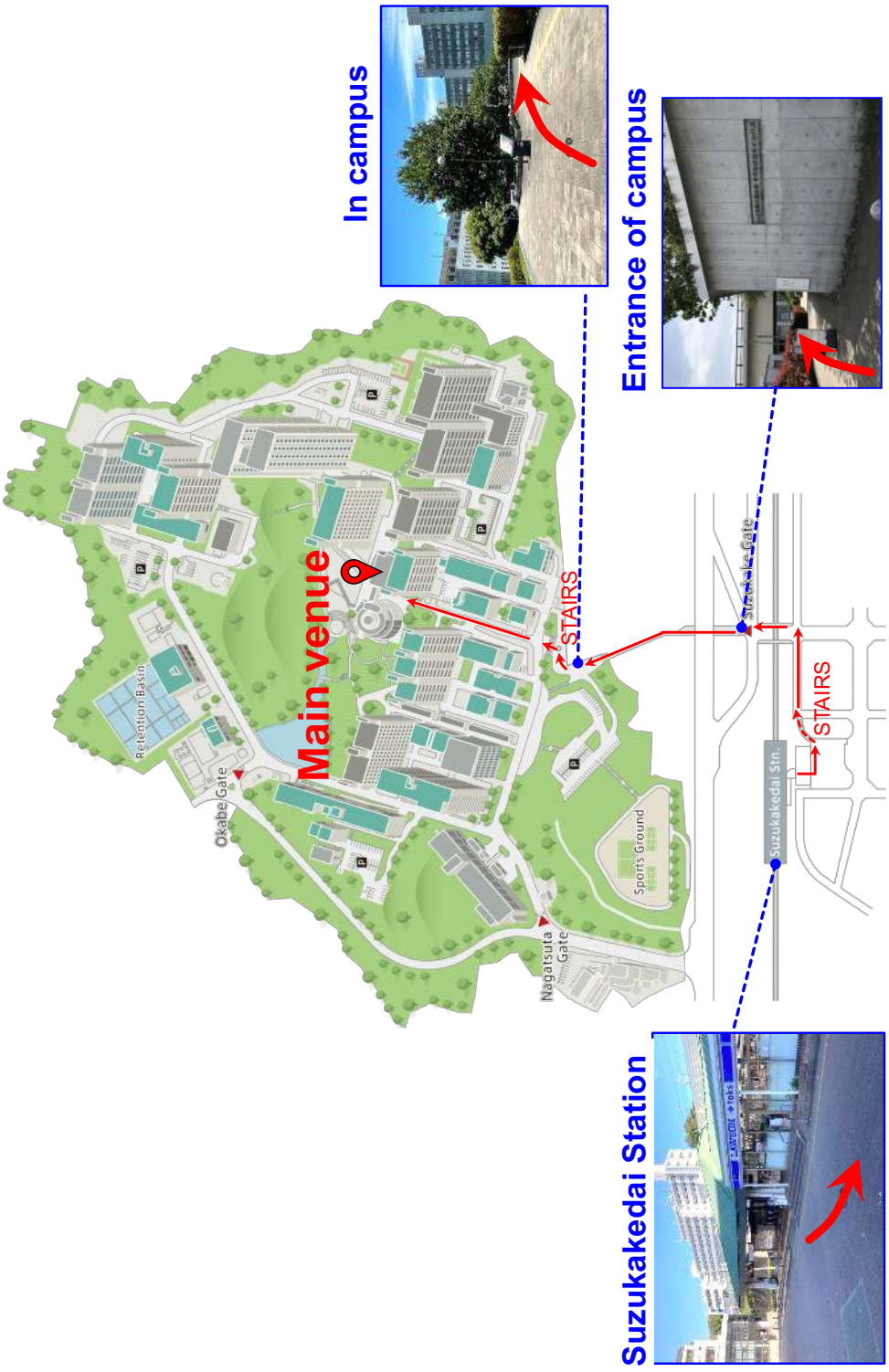
MRRC

SPONSE

SIXTH INTERNATIONAL WORKSHOP ON SEISMIC PERFORMANCE OF NON-STRUCTURAL ELEMENTS

March 10-13, 2026
Yokohama, Kanagawa, JAPAN

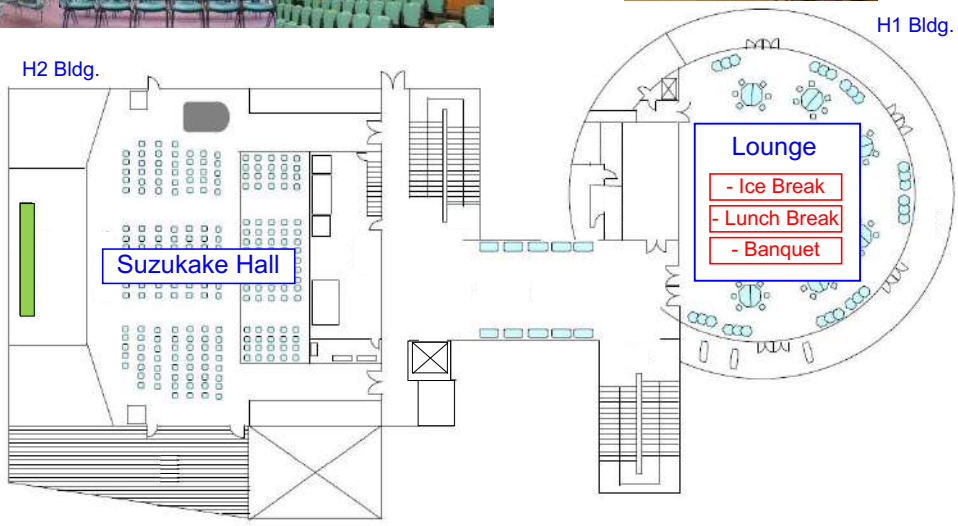
Note: Papers with titles shown in strike through indicate those that were registered but not presented.


In campus
Entrance of campus
Main venue
STAIRS
Okabe Gate
Retention Basin
Sports Ground
Nagatsuta Gate
Suzukakedai Stn.
STAIRS
Suzukakedai Station

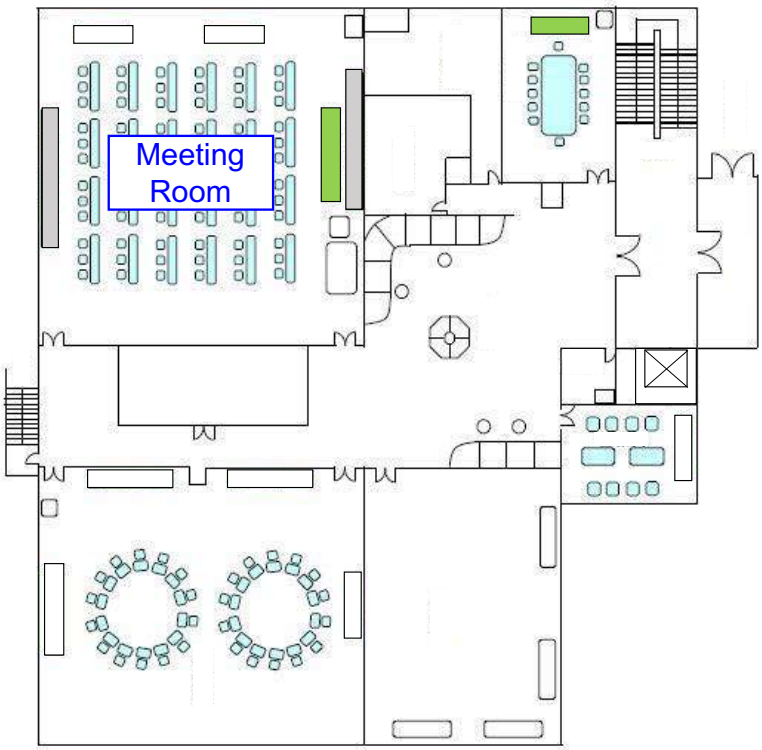
3F, H1 & H2 Bldgs.





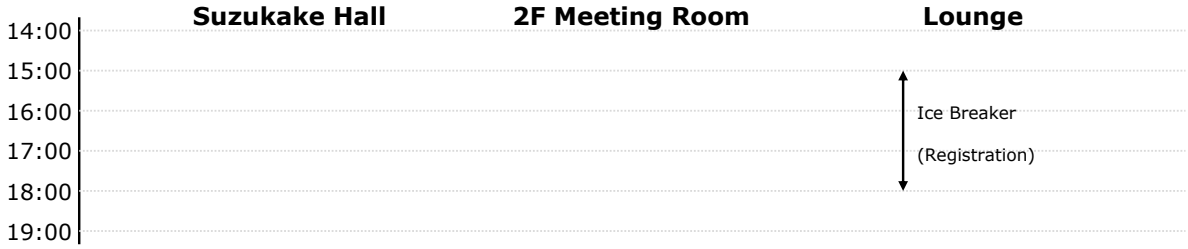


2F, H2 Bldg.

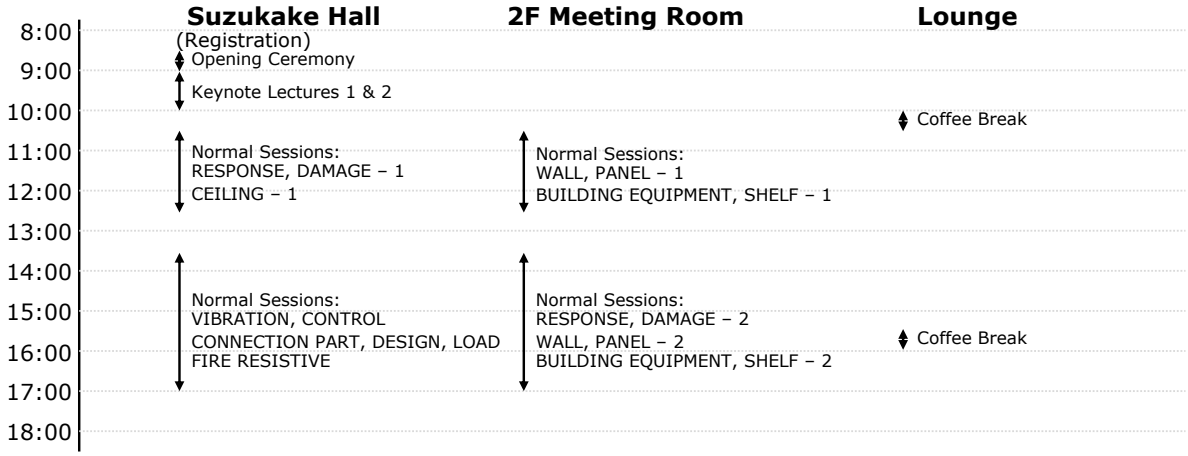


Overview of SPONSE 2026

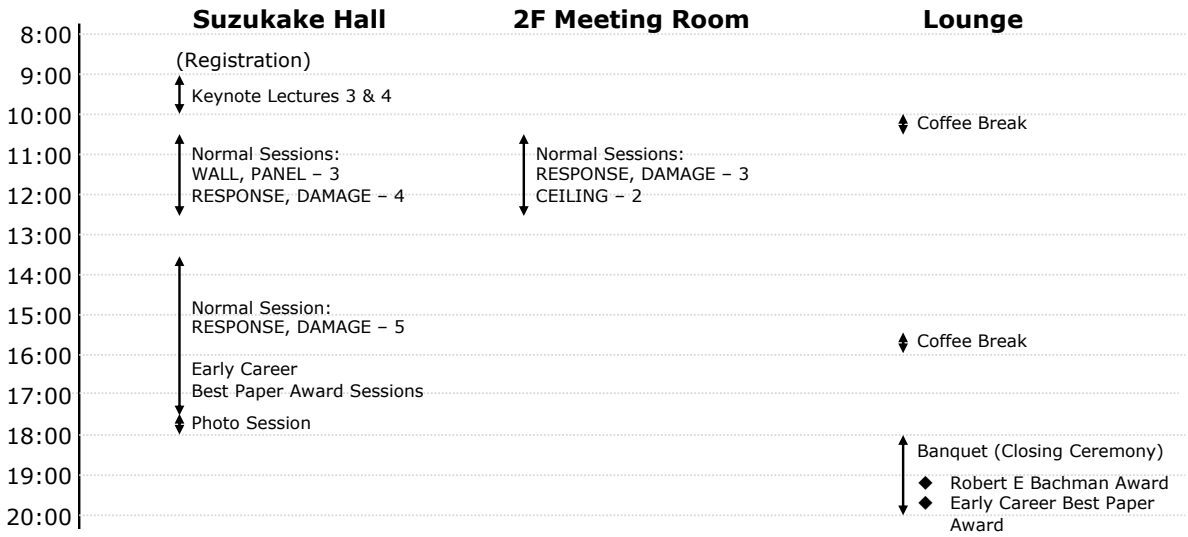
March 10, 2026 (Tuesday)



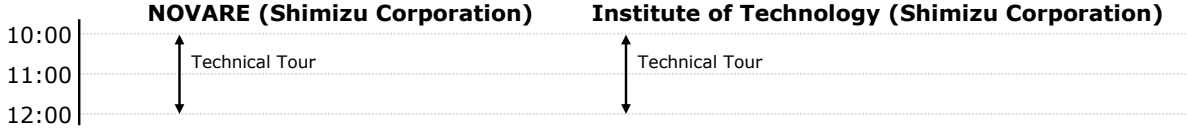
March 11, 2026 (Wednesday)



March 12, 2026 (Thursday)



March 13, 2026 (Friday)



Final Full Papers

The final full papers can be accessed via the QR code above from March 10 to March 13, 2026.
The access passcode will be provided at the registration desk.

Guidelines for Presentation

- Presentations shall be delivered in English.
- Each presentation will be given total of 15 minutes for:
  - Presentation = 10 min (1st bell = 8-min mark, 2nd bell = end of presentation)
  - Discussion = 5 min (3rd bell = end of discussion)
- Presenters must conduct *equipment check* before the start of the session.
- Types of ports available for projectors are (a) standard HDMI and (b) VGA.
- Laser pointers are available for use.

DETAILED PROGRAM

Tuesday, March 10, 2026

15:00-17:00 **REGISTRATION (Lounge)**

15:00-18:00 **ICE BREAKER (Lounge)**

Wednesday, March 11, 2026

8:00-8:30 **REGISTRATION (Suzukake Hall)**

8:30-9:00 **OPENING CEREMONY (Suzukake Hall)**
Institute of Science Tokyo - *S. Kishiki*
SPONSE Committee - *R. Dhakal*

9:00-9:30 **KEYNOTE LECTURE 1 (Suzukake Hall)**
A nonstructural element simulator based on substructural shake table testing
Speaker: *Zhe QU(Institute of Engineering Mechanics, China)*
Chair: S. Kishiki

9:30-10:00 **KEYNOTE LECTURE 2 (Suzukake Hall)**
JSCA's proposal to ensure the safety of non-structural components
Speaker: *Hirokuni TSUCHIYA (Nihon Sekkei Co., Ltd, Japan)*
Chair: D. Sato

10:00-10:30 **COFFEE BREAK (Lounge)**

10:30-11:30 **PARALLEL SESSIONS:**

SESSION 1A - RESPONSE, DAMAGE - 1 (Suzukake Hall)
CO-CHAIRS: I. Lanese — E. Baek

1. "Dynamic design of suspended services" - Paper ID: 26007
   Presenting Author: Martin Kusz
2. "An open-source nonstructural element database to streamline tech transfer between nonstructural research and building design" - Paper ID: 26010
   Presenting Author: Dustin Cook
3. "~~Generation of seismic motion for seismic qualification of active component~~" - Paper ID: 26012
   Presenting Author: Didier COMBESCURE
4. "Preliminary investigation of isolation bearings with discontinuous inerters for seismic protection of essential equipment and components" - Paper ID: 26020
   Presenting Author: Chia-Ming Chang

SESSION 1B - WALL, PANEL - 1 (2F Meeting Room)
CO-CHAIRS: M. Ko — T. Hutchinson

1. "System identification of natural frequency and damping ratio of partition wall from earthquake observation records" - Paper ID: 26030
   Presenting Author: Sora Hagiwara
2. "Screw connections between gypsum panels and cfs profiles: experimental evaluation of shear response" - Paper ID: 26051
   Presenting Author: Luigi Fiorino
3. "Seismic assessment of thin masonry-infilled RC frames via a coupled in-plane/out-of-plane macro-model" - Paper ID: 26094
   Presenting Author: Marco Donà

11:30-12:30 PARALLEL SESSIONS:

SESSION 2A - CEILING - 1 (Suzukake Hall)
CO-CHAIRS: D. Cook — D. Combescure

1. "Shake table testing of suspended ceilings" - Paper ID: 26026
   Presenting Author: Cameron Flude
2. "Shake table test on suspended nonstructural components in a large-scale ceiling system" - Paper ID: 26031
   Presenting Author: Eun-Rim Baek
3. "Code-based methodologies for the seismic qualification of non-structural elements: integrating experimental testing and numerical modelling" - Paper ID: 26038
   Presenting Author: Igor Lanese

SESSION 2B - BUILDING EQUIPMENT, SHELF - 1 (2F Meeting Room)
CO-CHAIRS: M. Donà — L. Fiorino

1. "Shake table testing of rooftop mechanical equipment with different attachment strategies on a full-scale ten-story building" - Paper ID: 26002
   Presenting Author: Tara C. Hutchinson
2. "A study on library bookshelf safety and book falling in earthquakes" - Paper ID: 26011
   Presenting Author: George C. Yao
3. "A study on bookshelves overturning evaluation based on reconnaissance in the 2024 HuaLien earthquake" - Paper ID: 26021
   Presenting Author: Min-Chi KO
4. "Seismic protection systems for safety-related equipment cabinets" - Paper ID: 26033
   Presenting Author: Gilberto Mosqueda

12:30-13:30 LUNCH BREAK (Lounge)

13:30-14:30 PARALLEL SESSIONS:

SESSION 3A - VIBRATION, CONTROL (Suzukake Hall)
CO-CHAIRS: V. Vukobratović — D. Bellotti

1. "Influence of stair system flexibility on building vibration period: insights from full-scale building shake table tests at low-amplitude excitation" - Paper ID: 26005
   Presenting Author: Tara Hutchinson
2. "~~Enhanced seismic stability for the freestanding contents in base-isolated buildings~~" - Paper ID: 26013
   Presenting Author: Min Ho Chey
3. "Seismic performance enhancement of suspended cable tray systems using steel wires" - Paper ID: 26058
   Presenting Author: Kazuhiro Matsuda

SESSION 3B - RESPONSE, DAMAGE - 2 (2F Meeting Room)
CO-CHAIRS: M. Donà — J. Bhatta

1. "Validation of analytical method for axial force- bending interaction of gypsum boards" - Paper ID: 26074
   Presenting Author: Yasuaki Sato
2. "Derivation of floor response spectra in masonry infilled precast concrete buildings" - Paper ID: 26076
   Presenting Author: Roberto Nascimbene
3. "Myanmar earthquake reconnaissance: damage to non-structural elements in high-rise buildings in Bangkok" - Paper ID: 26081
   Presenting Author: Jitendra Bhatta

14:30-15:30 PARALLEL SESSIONS:

SESSION 4A - CONNECTION PART, DESIGN, LOAD (Suzukake Hall)
CO-CHAIRS: G. Blasi — F. Micelli

1. "Failure mechanisms and pull-out strength of the screw-type fastening post-installed anchors" - Paper ID: 26047
   Presenting Author: Kosuke FUJITA
2. "Floor response spectra in the new generation of Eurocode 8: an overview and example of application" - Paper ID: 26001
   Presenting Author: Vladimir Vukobratović
3. "Seismic demand evaluation for the design of non-structural elements in precast concrete buildings" - Paper ID: 26034
   Presenting Author: Davide Bellotti

SESSION 4B - WALL, PANEL - 2 (2F Meeting Room)
CO-CHAIRS: Y. Sato — J. Bhatta

1. "Seismic design of reinforced concrete frames with sliding joint ductile infills" - Paper ID: 26091
   Presenting Author: Marco Preti
2. "Out-of-plane seismic assessment of URM infill walls through parametric analysis" - Paper ID: 26093
   Presenting Author: Marco Gaspari
3. "Influence of screw connection on out-of-plane behavior of LGS walls" - Paper ID: 26096
   Presenting Author: Fumihiko SAKURABA
4. "Experimental investigation on the seismic performance of self-centering concrete wall structures with low damage infill walls" - Paper ID: 26102
   Presenting Author: Hao Wu

15:30-16:00 COFFEE BREAK (Lounge)

16:00-17:00 PARALLEL SESSIONS:

SESSION 5A - FIRE RESISTIVE (Suzukake Hall)
CO-CHAIRS: T. Hutchinson — K. Matsuda

1. "Drift-based functional fragility framework for fire-rated doors in post-earthquake fires" - Paper ID: 26062
   Presenting Author: Serdar Selamet
2. "Influence of tee joint capacity on the seismic behaviour of a fire suppression system" - Paper ID: 26075
   Presenting Author: Francesco Monte
3. "Probabilistic seismic demand assessment of rising pipe lines in fire-protection systems" - Paper ID: 26089
   Presenting Author: Gianni Blasi
4. "Experimental seismic response assessment of piping networks in industrial facilities: the mitplant project" - Paper ID: 26202
   Presenting Author: Francesco Micelli

SESSION 5B - BUILDING EQUIPMENT, SHELF - 2 (2F Meeting Room)
CO-CHAIRS: H. Wu — M. Gaspari

1. "Seismic performance of a full-scale code-compliant fire sprinkler piping system in a six-storey building " - Paper ID: 26003
   Presenting Author: Jitendra Bhatta
2. "Strength evaluation of inserts hardware for building equipment under deck composite slab" - Paper ID: 26046
   Presenting Author: Ichiro Hirano
3. "Seismic fragility assessment of industrial pallet racks in Italy" - Paper ID: 26086
   Presenting Author: Marco Donà
4. "~~Design and testing of school furniture as life-saving non-structural building components: a case study~~" - Paper ID: 26203
   Presenting Author: Alessandro Zona

Thursday, March 12, 2026

8:30-9:00 **REGISTRATION (Suzukake Hall)**

9:00-9:30 **KEYNOTE LECTURE 3 (Suzukake Hall)**
Development of a NSE code of practice
Speaker: *Andrew BAIRD (Beca)*
Chair: R. Dhakal

9:30-10:00 **KEYNOTE LECTURE 4 (Suzukake Hall)**
Seismic damage to building equipment
Speaker: *Kunio MIZUTANI (Tokyo Polytechnic University, Japan)*
Chair: S. Motoyui

10:00-10:30 **COFFEE BREAK (Lounge)**

10:30-11:30 **PARALLEL SESSIONS:**

SESSION 6A - WALL, PANEL - 3 (Suzukake Hall)
CO-CHAIRS: G. O'reilly — R. Assi

1. "Damage behavior of light gauge steel partition wall under in-plane and out-of-plane external forces" - Paper ID: 26057
   Presenting Author: Yusuke Oki
2. "Influence of in-plane damage on the out-of-plane seismic response of weak clay masonry infills through shaking table dynamic tests" - Paper ID: 26082
   Presenting Author: Igor Lanese
3. "NHERI TallWood project part 1: overview and nonstructural subassembly details" - Paper ID: 26084
   Presenting Author: Keri L. Ryan
4. "NHERI TallWood project part 2: performance of building and nonstructural subassemblies" - Paper ID: 26085
   Presenting Author: Keri L. Ryan

SESSION 6B - RESPONSE, DAMAGE - 3 (2F Meeting Room)
CO-CHAIRS: P. Zhao — H. Jiang

1. "Experimental shake table evaluation of non-structural elements in accordance with AC-156" - Paper ID: 26025
   Presenting Author: Angela Poposka
2. "A study on non-structural seismic damage of critical facilities in 0403 HuaLien earthquake in Taiwan" - Paper ID: 26027
   Presenting Author: Fan-Ru Lin
3. "Seismic resilience assessment of hospitals using dynamic bayesian network" - Paper ID: 26032
   Presenting Author: Shuoguo Qiu
4. "Performance of non-structural components in a 5-storey shake-table test" - Paper ID: 26036
   Presenting Author: Scott Menegon

11:30-12:30 PARALLEL SESSIONS:

SESSION 7A - RESPONSE, DAMAGE - 4 (Suzukake Hall)
CO-CHAIRS: K. Ryan — I. Lanese

1. "Issues in the fragility analysis of non-structural elements and the role of structural health monitoring" - Paper ID: 26049
   Presenting Author: Gerard J. O'Reilly
2. "Proposed ductility-based force factors for acceleration-sensitive light non-structural components" - Paper ID: 26050
   Presenting Author: Rola Assi
3. "Shake-table tests on full-scale non-structural elements in a low-damage 3-story steel building: key results from the ROBUST project" - Paper ID: 26065
   Presenting Author: Rajesh Dhakal
4. "The benefits and advantages of using RC frames with isolated or decoupled infills in practice: INODIS connection" - Paper ID: 26008
   Presenting Author: Marko M. Marinković

SESSION 7B - CEILING - 2 (2F Meeting Room)
CO-CHAIRS: S. Qiu — F. Lin

1. "Seismic assessment of concealed grid suspended ceilings: design of a large-scale experimental setup for shaking-table testing" - Paper ID: 26052
   Presenting Author: Alessandro Prota
2. "Experimental study on pounding response of suspended ceiling system with mineral wool board" - Paper ID: 26054
   Presenting Author: Huanjun Jiang
3. "Numerical simulation of the structural test on a 2.5- story model frame representing lower stories of existing high-rise RC buildings with non- structural flat walls" - Paper ID: 26060
   Presenting Author: Peizhi Zhao
4. "Shaking table test of seismic-resistant ceiling systems with asymmetric mass or stiffness distribution" - Paper ID: 26063
   Presenting Author: Haruki Yamaguchi

12:30-13:30 LUNCH BREAK (Lounge)

13:30-14:00 NORMAL SESSION:

SESSION 8 - RESPONSE, DAMAGE - 5 (Suzukake Hall)
CO-CHAIRS: G. Mosqueda — G. Rivron

1. "Preliminary observations on the effects of 2024-2025 bradyseism earthquakes on nonstructural elements in Campi Flegrei" - Paper ID: 26072
   Presenting Author: Gennaro Magliulo
2. "Optimising seismic retrofit design to reduce non- structural element losses using multiple objectives" - Paper ID: 26071
   Presenting Author: Ricardo Monteiro

14:00-15:15 EARLY CAREER BEST PAPER AWARD SESSION:

SESSION 9 - EARLY CAREER BEST PAPER AWARD SESSION - 1 (Suzukake Hall)
CHAIR: Y. Sato

1. "Interaction of suspended ceilings and pressurized piping in a full-scale 10-story cold-formed steel building shake table test program" - Paper ID: 26006
   Presenting Author: Amanpreet Singh (Proxy Presenting Author: Tara Hutchinson)
2. "Study on the horizontal stiffness of single and double-layer CHN-US style ceiling" - Paper ID: 26009
   Presenting Author: Minhui LI
3. "Estimation of floor response spectra for risk- targeted seismic design of non-structural elements" - Paper ID: 26004
   Presenting Author: Roberto J. Merino
4. "Evaluation of component amplification factor considering structure-NSC interaction and NSC-clustering" - Paper ID: 26053
   Presenting Author: Chang-Jun Bae
5. "Experimental and field investigations of suspended air handling units" - Paper ID: 26019
   Presenting Author: Wei-Chung Chen

15:15-16:15 COFFEE BREAK (Lounge)

16:15-17:30 EARLY CAREER BEST PAPER AWARD SESSION:

SESSION 10 - EARLY CAREER BEST PAPER AWARD SESSION - 2 (Suzukake Hall)
CHAIR: Y. Oki

1. "Innovative seismic isolation strategies for equipment and non-structural components: experimental investigation and analytical modeling of systems isolated with spring-viscoelastic mounts" - Paper ID: 26101
   Presenting Author: Ahmed Awad
2. "Low-carbon resilient curtain walls: experimental study of timber-glass unitized systems" - Paper ID: 26056
   Presenting Author: Simona Bianchi
3. "In-plane loading experiments on seismic damage and functional retention performance of LGS partition walls with opening" - Paper ID: 26059
   Presenting Author: Zeyu SUN
4. "Hysteretic behavior, stiffness degradation, and energy dissipation in screw connections of cold- formed steel framed plasterboard partitions" - Paper ID: 26067
   Presenting Author: Danilo D'Angela
5. "Experimental analysis of the seismic in-plane performance of cold-formed steel gypsum drywall systems: glued vs. screwed connections" - Paper ID: 26078
   Presenting Author: Ghislain Rivron

18:00-20:00 **BANQUET / CLOSING CEREMONY (Lounge)**
Speaker: Gennaro Magliulo (SPONSE Committee)

ROBERT E BACHMAN AWARD (Lounge)

EARLY CAREER BEST PAPER AWARD (Lounge)

Friday, March 13, 2026

10:00-12:00 **TECHNICAL TOUR**

Exhibitors

Exhibitor	Exhibition Details
Gypsum Board Association of Japan	General introduction to the gypsum board manufacturers association and other information
Japan Steel Furring Industry Association	Improving the seismic performance of non-structural components and reducing CO_2 emissions
INTEX INTERNATIONAL	Showcasing Qbit360 / Backdrop Bumen / Sample of product
Hilti Corporation	Hilti plans to introduce their seismic resistance initiatives for fastening and joining products through posters and videos, and also intends to display some actual products.

Collaborators

Dynamic Design of Non-structural Elements (SPONSE 2026)

Martin Kusz[1], Jason Swart[2], Jack Schwarz[2]

[1] KUSCH
Mount Beauty, VIC, Australia
e-mail: martin@kusch.com.au
[2] KUSCH
Brisbane, QLD, Australia
e-mail: jason.swart@kusch.com.au, jack.schwarz@kusch.com.au

Abstract. Although extensive research into dynamic seismic design methods for non-structural elements (NSEs) has been carried out over the past several decades, these approaches remain under-utilised in engineering practice. Most designers rely on prescriptive rules and simplified equivalent-static force-based methods that do not evaluate component displacement, despite displacement being the primary driver of NSE damage during an earthquake. While dynamic methods can predict the dynamic response of NSEs to earthquake actions, difficulties prevail in establishing their dynamic properties (natural period and damping ratios), given that construction details are varied and inconsistent throughout industry.

This study explores the practical application and benefits of dynamic methods for the seismic design of suspended NSEs. Field measurement tools were developed to accurately determine the natural periods and damping ratios of real-world suspended systems, providing essential input for spectral and analytical models. Research into Floor Response Spectra (FRS) is reviewed, and spectral analyses, time-history simulations, and shake-table experiments are used to assess and compare different approaches.

A practical seismic design workflow incorporating dynamic principles is presented, which can be adopted by design practitioners. This workflow improves visibility of seismic design displacement demands and supports better alignment with intended performance objectives, while also presenting opportunities for economical 'unbraced' design options for scenarios with relatively low seismic demand.

Keywords: dynamic, NSE, displacement, non-structural, services, isolation

1. Introduction

Non-structural elements (NSEs) such as building services, ceilings and partitions, play a critical role in the overall seismic performance of modern buildings. Studies have shown that NSE damage accounts for most earthquake-related losses and often exceeds structural damage in both cost and disruption [Applied Technology Council, 2018; Dhakal et al., 2011; Federal Emergency Management Agency, 2012; Taghavi & Miranda, 2003].

In Australia, seismic design of NSEs is governed by AS1170.4, which provides equivalent static force-based design loads in a similar form to most earthquake design load standards throughout the world. While these provisions are simple and practical, they offer no guidance on how to design NSEs to meet performance objectives. As a result, engineers rely heavily on international industry design guides that specify restraint details and maximum brace spacings, most of which are empirically derived from past earthquake observations. These methods do not explicitly address the displacement behaviour of NSEs under seismic loads, even though displacement is the primary driver of NSE damage.

Clause 8.1.2(a) of AS1170.4 permits the use of "established principles of structural dynamics" for the seismic design of NSEs. This paper explores the use of field vibration testing, analytical modelling, shake-table testing and Floor Response Spectra (FRS) to determine the dynamic behaviour and peak displacement demand of unbraced and braced suspended building services under seismic loads. It presents practical workflows that can be used by designers to improve their understanding of NSE seismic behaviour, identify performance deficiencies with existing simplified methods, and also identify opportunities for economical unbraced 'flexible' design concepts for regions and scenarios with relatively low seismic demands.

2. Background and Literature Review

2.1 Evolution and Limitations of Current NSE Design Methods

Formal seismic design provisions for NSEs emerged following damaging earthquakes in California during the 1970s, which led to government regulations and the Uniform Building Code introducing NSE earthquake load requirements. Official standards provided equivalent static force-based seismic loads, and an empirically derived list of design exclusions. However, it was the U.S. industry association SMACNA that developed the first seismic design manual (building on OSHPD's guidelines for hospitals in California) that translated seismic load provisions into prescriptive restraint rules, nominal brace spacings and standard seismic brace details.

While these prescriptive approaches have improved the seismic resilience of suspended NSEs, they are primarily empirical in origin and offer limited insight into the actual seismic performance of these systems. For example, the standardised 9m maximum lateral brace spacing limit that is now adopted in many regions of the world does not consider the stiffness or capacity of a particular service at that support distance. New Zealand's NZS4219 does reduce restraint spacings for small pipe, which appears to maintain elastic behaviour under SLS loading, but doesn't vary restraint spacings for other services.

While official standards and seismic design guides often consider the structural demand and capacity of a seismic brace, they typically don't specify brace displacement limits or consider the impact of boundary conditions like connections at penetrations through structural elements. These design documents often include minimum clearance tables intended to prevent collisions between elements, but the displacement performance objectives for services aren't defined and clearance tables can yield both conservative and inadequate results. Performance objectives regarding NSE damage are rarely specified, and standard

restraint details frequently overlook key load-path limitations, such as the friction capacity of pipe clamps, or the effect of eccentricities between an NSE's centre of mass and its restraint connection.

Although seismic design requirements for NSEs have been included in codes and design guides for more than 30 years, their implementation has progressed slowly. Consequently, real-world examples of how these empirical rules and force-based methods perform under true design-level shaking are limited. For instance, NSEs designed using these methods appeared to perform reasonably well in hospitals affected by the Napa (2014) and Kaikōura (2016) earthquakes; however, the recorded peak ground accelerations in both events were only about half of the design-level values.

It is well established that displacement governs NSE damage during earthquakes, whether through collisions, overstress, or connection failures. Force-based design methods, which focus primarily on inertial forces and give little attention to displacement, therefore risk failing to meet the intended performance objectives. In critical facilities such as hospitals, this gap means that current force-based approaches may not ensure post-disaster functionality. Explicitly considering NSE displacement is essential, both to identify deficiencies in simplified methods and, where appropriate, to validate their adequacy.

2.2 Floor Response Spectra and Displacement-Based Design Methods

Response spectra describe the peak accelerations and displacements of idealised single-degree-of-freedom (SDOF) oscillators subjected to ground motion and are used to approximate the dynamic behaviour of real buildings in most code-based seismic design procedures. More recent advances have extended this concept to multi-degree-of-freedom (MDOF) floor response spectra (FRS), enabling the prediction of acceleration and displacement demands on components attached to specific building floors. Filiatrault et al. [2021] proposed a direct displacement-based design (DDBD) method that uses floor-level displacement spectra to determine the stiffness and strength required to meet defined displacement objectives for suspended NSEs.

Subsequent studies have refined this concept from two directions. Haymes et al. [2020] developed a mechanistic, modal-superposition formulation that expresses floor spectra in closed form using dynamic amplification factors and damping adjustments, offering a physically transparent, design-level tool. In contrast, Liu et al. [2025] derived empirical design floor spectra from more than twenty-six thousand time-history simulations, providing statistically calibrated amplification factors for different building types and site conditions. All these approaches demonstrate that when displacement behaviour is explicitly considered, rather than ignored in favour of empirical restraint rules, designers can achieve more accurate, efficient, and performance-consistent seismic design outcomes for non-structural elements.

While displacement-based frameworks offer improved accuracy over traditional force-based rules, they depend on reliable estimates of damping and consistent characterisation of NSE hysteretic behaviour, which can be challenging to obtain. A practical implementation of this approach is described in Section 4.

2.3 Computation of Floor Response Spectra and Peak Displacements

The method proposed by Filiatrault et al. [2021] derives floor response spectra (FRS) directly from a building's ground response by treating the structure as a dynamic filter between the ground motion and the attached NSE. The procedure begins with the peak acceleration from the ground response spectrum at the building's natural period, then applies period and damping-dependent amplification factors that account for the interaction between the NSE period and damping, the building period, and the building's effective inelastic behaviour.

This formulation produces a floor acceleration spectrum that rises as the NSE period approaches the building period, plateaus, and then gradually decays. Because the decay region may under-predict demands, the authors recommend capping the spectrum at the corner period to maintain conservative values. Relative

floor displacements are obtained from the same spectrum using the standard pseudo-spectral acceleration–displacement relationship.

Overall, this method provides a direct and practical means of estimating floor-level accelerations and displacements for NSEs using code-based design spectra, linking analytical spectral procedures to measurable floor motions and forming the basis for the dynamic validation undertaken in this study.

2.4 TIME-HISTORY ANALYSIS FOR VALIDATION OF RESPONSE SPECTRA

Time-history analysis is widely used to evaluate how response-spectrum predictions compare with actual building behaviour. In regions with limited recorded earthquake data, such as Australia, ground motions from other sites are commonly scaled to match the target design spectrum, ensuring analyses remain consistent with the local seismic hazard [AS 1170.4 Commentary, 2021; Somerville et al., n.d.]. Spectrum-compatible synthetic accelerograms provide an alternative, guaranteeing conformity with the design spectrum while maintaining realistic temporal characteristics [Brewick et al., 2018; Rizzo et al., 1975]. Databases such as the PEER Simulated Ground Motion Database (SGMD) offer large suites of such simulated motions [McCallen et al., 2025].

Seismic input is often interpreted through single-degree-of-freedom (SDOF) oscillator models, which link input motions to dynamic properties but capture only first-mode behaviour. Multi-degree-of-freedom (MDOF) analyses are required when higher-mode effects become significant, particularly when secondary mode periods align with peaks in the design spectrum or with the natural period of NSEs. Recent research has shown that these higher-mode interactions can introduce additional peaks in floor-response spectra [Liu et al., 2025].

3.Methods

The purpose of this investigation is to evaluate the feasibility of incorporating dynamic principles into NSE seismic design practice. Four complimentary methods were explored, including field measurement of real NSEs, modal analysis of analytical models, time-history simulations, and shake-table testing. The primary purpose was to develop efficient means of establishing real-world NSE dynamic properties, and to test if analytical methods can accurately predict dynamic behaviour and be incorporated into NSE seismic design workflows.

3.1 FIELD MEASUREMENT OF DYNAMIC PROPERTIES



a) b) c)

Figure 1: Photos showing the accelerometer circled in red for a) pipe system 1, b) pipe system 2, c) duct system

The natural periods and effective damping ratios of the suspended systems in Figure 1 were measured using a wireless accelerometer. Each service was manually excited in the direction of maximum response, inducing free vibration. The recorded decay curves were fitted to a viscous-damped single-degree-of-freedom model, with results averaged across five repeated tests.

Although this approach represents frictional and hysteretic energy loss using an equivalent viscous damping value, it aligns with the assumptions used in the displacement-based model of Filiatrault et al. [2021]. Because viscous damping is proportional to velocity, it dominates system behaviour at higher energy levels—precisely where seismic peak-displacement demands occur. Any limitations at low energy input have minimal influence on peak-response predictions.

These field measurements provide design-relevant dynamic properties that are typically unknown but essential for displacement-based assessment.

3.2 FINITE-ELEMENT MODAL ANALYSIS OF NSE SYSTEMS

Finite-element modal analysis was performed in SpaceGass on the configuration shown in Figure 1a to estimate natural periods and mode shapes. Beam elements, lumped masses, and observed support conditions were modelled based on observations and measurements obtained from inspection.

It is understood that modal properties can be sensitive to assumptions regarding connection stiffness, mass distribution, and boundary conditions. The results from this analysis will be compared with the measured properties obtained from field tests, in part to assess the accuracy of these assumptions and to consider how appropriate it may be to represent NSEs with such models.

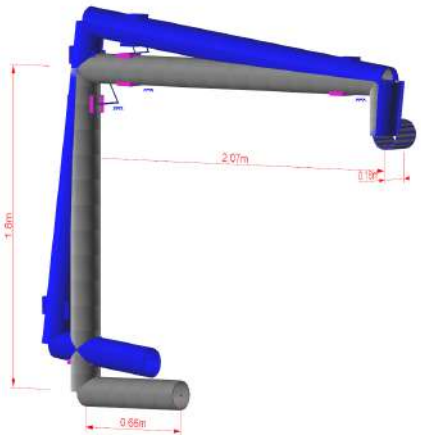


Figure 2: SpaceGass model & mode shape

3.3 TIME HISTORY SIMULATION

Shake-table tests will be used to further compare analytical predictions with experimental observations, and to do this will require the development of input motions that are representative of realistic floor-level displacements. To achieve this, approximately 200 ground motions from the PEER Simulated Ground Motion Database were scaled to be broadly consistent with the AS1170.4 design spectrum for the selected site parameters ($Z = 0.08$, $k_p = 1.3$, Subsoil Class E). These motions were applied to 500 SDOF oscillators spanning periods from 0.01 s to 5.0s with 5% damping to produce a ground response spectrum (GRS).

A representative oscillator with a natural period of 1.0s was then arbitrarily selected. Its displacement history—representing an idealised building floor motion—was used as the base-displacement input to the shake table. The same building motion was applied to secondary oscillators to generate Floor Response Spectra (FRS) that capture in-structure amplification effects for NSEs with various natural periods and damping values.

The SDOF oscillators followed the standard base-excited equation of motion:

$$-\ddot{u}(t) = \omega_n^2 y(t) + 2\zeta\omega_n \dot{y}(t) + \ddot{y}\,(t)$$

These simulations allowed direct comparison between spectrum-based analytical predictions and experimentally recorded responses.

3.4 SHAKE TABLE TESTING & EXPERIMENTAL PROGRAM

An inverted single-axis shake table was used to subject a suspended NSE to the simulated building-floor motions that were generated in Section 3.3. The table consists of a steel frame driven by a servomotor and ball-screw mechanism to reproduce precise base-displacement histories.

Tests were carried out on a 1.5 m long, 200 mm diameter steel pipe suspended from two 1.3 m long M12 threaded rods. Displacements were recorded at the suspension points and along the pipe to compare the measured response with analytical predictions and validate the dynamic modelling approach.

4.Results and Validation

4.1 FIELD MEASUREMENTS OF NATURAL PERIOD AND DAMPING

Free-vibration tests of the NSEs shown in Figure 2 confirmed that these behave as damped oscillators. The test samples possessed periods ranging from 0.13–0.49s, with damping ratios between 0.5% and 1.5% (Table 1). While suspended NSEs can readily display much longer periods and much higher damping ratios, the samples were considered appropriate for the objective of comparing measured dynamic responses with modelled results. Figure 3 illustrates the viscous damped oscillator model fit to the recorded acceleration decay. As can be seen, the model accurately captures the system decay at high energy levels which represent peak displacements. The model overpredicts energy dissipation at low energy levels, but this is inconsequential as NSE damage is not expected under small vibrations. Results are summarised in Table 1, and the measured period and viscous damping values are used as inputs for displacement-based analysis in Section 4.3.

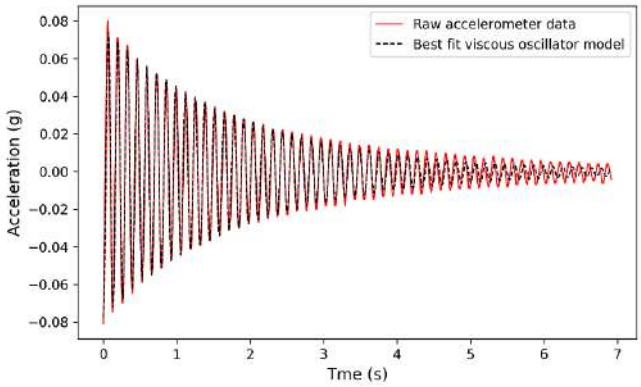


Figure 3. Example of generation of best fit viscous damped oscillator model to raw accelerometer data

Table 1. Measured periods and damping ratios for installed NSEs

NSE	T_n (s)	Damping Ratio (%)
Pipe 1	0.13	1.13
Pipe 2	0.18	0.53
Duct	0.49	1.52

4.2 MODAL ANALYSIS

Carrying out modal analysis of the section of pipework shown in Figure 1a, the analysis reported a natural period of 0.15 seconds for the fundamental mode, which corresponded to a lateral sway motion of the supported pipe. Higher modes, involving localised bending of the pipe span and vertical oscillations of the suspension rods, were also identified but at significantly shorter periods and with reduced participation in overall response.

This predicted value of 0.15s is within 13% of the measured natural period of 0.13s (Pipe 1, Table 1). This level of accuracy could readily be accommodated in a design process using a typical uncertainty factor. This particular system is relatively simple, and model accuracy would be expected to decrease with system complexity. Practitioners should therefore adopt appropriate uncertainty factors when using modal analysis to predict peak displacements and regularly validate models with testing to ensure appropriate assumptions are being made.

4.3 NUMERICAL TIME HISTORY SIMULATION

Figure shows the displacement time history of the record adopted PEER ground motion and the corresponding response of a single-degree-of-freedom oscillator with a natural period of 1.0s. The comparison illustrates how building-level motions filter and amplify the ground excitation.

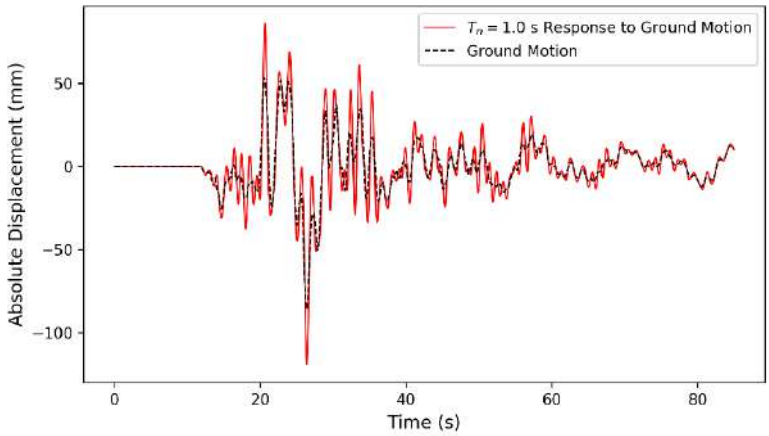


Figure 4: Time history simulation showing the ground motion and the corresponding SDOF model response

Figure 5 summarises the spectral characteristics of the full record set. Figure 5a presents the ground response spectra, including individual spectra, their average, the selected record, and the AS1170.4 design spectrum. Figure 5b shows the corresponding floor response spectra (FRS) generated using the 1.0 s building response, with the predictive formulation of Filiatrault et al. included for comparison. The selected record is highlighted to demonstrate its representativeness within the dataset.

For this motion, the time-history simulation produced a peak NSE displacement of 433 mm and an equivalent pseudo-spectral acceleration of 0.54 g. These values form the basis for comparison with the shake-table experiment in Section 4.4, which applied the same building-level displacement history.

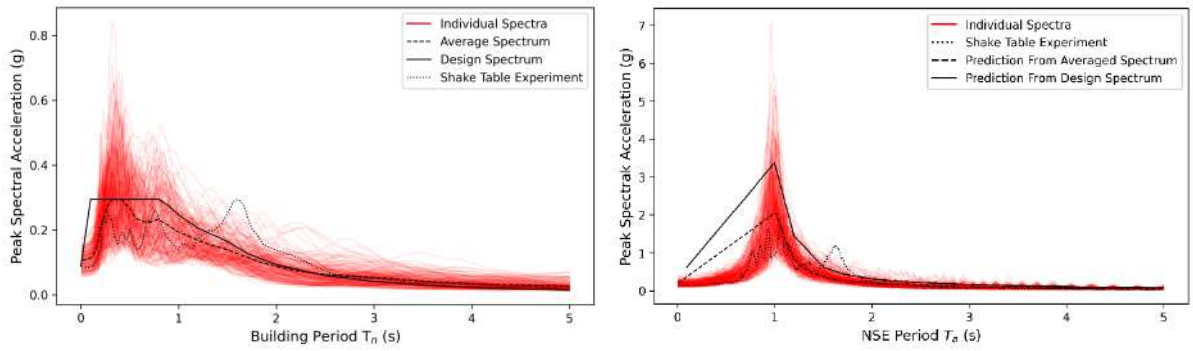
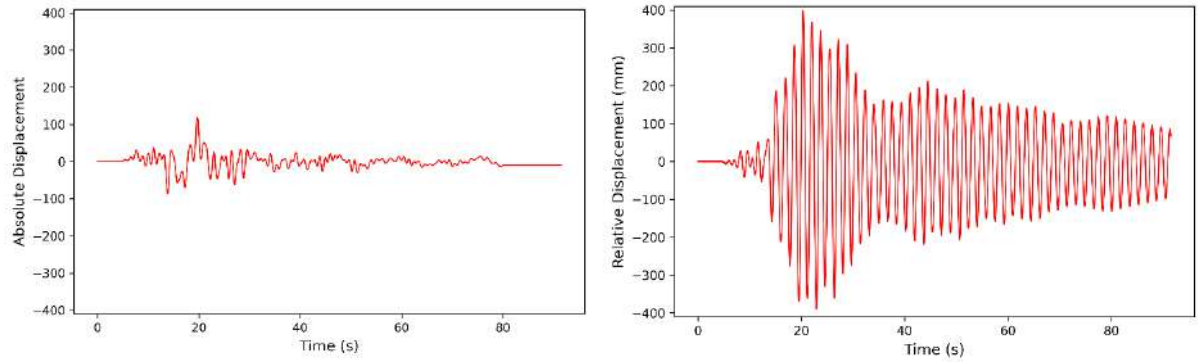


Figure 5: a) Ground response spectra, b) Floor response spectra for an oscillator of 1.0s, compared to Filiatrault et al.

4.4 SHAKE TABLE EXPERIMENTS

Figure illustrates the absolute displacement history of the shake table test, when run with the same imposed motions that were used in the time-history-analysis of section 4.3. The shake test generated displacements of 400mm in the test specimen. While these results are relatively large from a seismic design perspective, the purpose of the test is to compare predictive methods with measured results, and in this instance the results were within 10% of each other (400mm vs 433mm). Again, the use of uncertainty factors would be appropriate when assessing the seismic response of NSEs using analytical means, and further research comparing results in more complex systems would be warranted to ensure adopted uncertainty factors are appropriate more broadly.



a) b)

Figure 6. a) Absolute displacement of the shake table representing the top floor of a building with $T_n = 1.0s$ b) relative displacement of the pipe in the shake table experiment when subjected to building motion.

5. Discussion And Design Implications

The analytical and experimental results show that dynamic analysis provides a robust and practical basis for estimating seismic displacement demands of suspended non-structural elements (NSEs), particularly when real-world natural periods and damping ratios are available. Free-vibration testing confirmed that suspended services behave as viscous-damped single-degree-of-freedom systems, while comparisons with modal analysis highlighted the sensitivity of predicted periods to boundary conditions and connection stiffness. These findings underscore the importance of direct measurement for establishing reliable system properties and validating modelling assumptions.

Numerical time-history simulations and shake-table experiments demonstrated that dynamic analysis can accurately reproduce the behaviour of suspended services under design-level excitation. Floor-response spectra generated from the simulations closely matched both analytical formulations and experimentally observed displacements when design-spectrum-compatible motions were used. This alignment confirms that spectral-based dynamic procedures can reliably predict NSE displacement demands when appropriate dynamic properties are defined.

Dynamic analysis also addresses key limitations of empirical or rule-based restraint methods. Conventional force-based procedures and standard brace-spacing rules offer simplified solutions but cannot verify whether critical performance objectives—such as limiting collisions, overstress, or connection failures—are achieved. By explicitly linking seismic demand to measured or predicted system response, dynamic methods support the development of both braced and unbraced solutions that satisfy displacement and ductility

requirements. For facilities that must remain operational after earthquakes, this provides a level of performance assurance not possible through simplified static approaches.

6. Practical Application of Dynamic Design Methods

Although Floor Response Spectra (FRS) provide a theoretical basis for determining the seismic displacement demands of suspended NSEs, predicting the real-world response of a particular system before it has been constructed remains challenging. The methods, products and configurations commonly used to support suspended services can vary greatly and have a strong influence on a system's natural period, damping, and displacement demand. These properties can be accurately measured, but only after a system has been constructed, and well after a seismic design has typically been completed. However, typical seismic design workflows can be modified to incorporate dynamic testing and methods, providing design practitioners with valuable insight into a systems dynamic behaviour under earthquake loads.

The following dynamic design workflow represents a performance-based alternative to common force-based methods:

1. Establish project-specific seismic design parameters and Ground Response Spectrum.

2. Conduct in-situ vibration testing on suspended NSEs to determine natural period and damping. This is achieved by applying low-amplitude excitation (typically by hand at resonance) and recording the free-vibration decay using simple instrumentation.

3. Calculate the Floor Response Spectrum and determine design displacement demand from the using the measured dynamic properties.

4. Note: Testing systems that have been braced using current force-based methods will help designers identify any performance gaps or trends, while testing unbraced systems, particularly in low seismic regions, may reveal opportunities for unbraced, flexible seismic design solutions.

5. Assess the implications of the expected displacements, including potential collisions, internal stresses, support reactions, and interactions with rigid elements, supported by additional structural analysis where required.

6. Specify seismic restraints only where required to achieve the intended performance objectives, using simplified force-based provisions (or displacement-based (DDBD) methods as proposed by Filiatrault et al [2021]).

7. Verify performance through follow-up site testing where appropriate, confirming that the installed system satisfies the displacement and performance criteria.

It is important to note that the following test procedure is valid for the direction that the vibration test (step 2) was done in. It would be necessary to conduct the test in orthogonal directions for the entire design process. For example, a section of pipework must be tested in the longitudinal and transverse directions, as these directions will have different stiffnesses, and thus different dynamic responses.

The above workflow brings the dynamic behaviour of suspended NSEs into clear view, enabling designers to identify situations where force-based rules or minimum brace-spacing requirements fail to meet the intended performance objectives, often due to excessive displacements and collisions or differential

movement between elements. Equally, it enables identification of scenarios where additional restraint is unnecessary, even when prescriptive methods might require it, such as when calculated displacements are low and surrounding systems can comfortably accommodate these seismic design movements.

The proposed methodology currently applies to systems that can be excited manually; however, experience shows that even relatively heavy installations can be mobilised when excited near their natural frequency, which is easily identified through a simple frequency sweep. Future work may explore complementary excitation methods, such as impact hammer testing, for very large or stiff systems that cannot be excited by hand.

In summary, dynamic analysis, modelling, and testing offers a practical, evidence-based means of assessing the actual seismic performance of suspended NSEs. It represents a key step toward performance-based design for both braced and unbraced systems and provides clearer visibility of displacement demands, leading to more reliable and more economical design outcomes.

7.Conclusion

This study demonstrates that dynamic design methods provide a practical and accurate basis for designing suspended non-structural elements for seismic actions. Field measurements confirmed that real-world services behave as damped oscillators with repeatable natural periods and damping ratios, enabling these properties to be incorporated directly into analytical and spectral assessments. Comparisons between time-history simulations, floor response spectra, and inverted shake-table tests showed close agreement, validating the reliability of displacement-based approaches for suspended systems.

By making the dynamic behaviour of NSEs visible to the design engineer, dynamic methods help ensure that critical performance objectives are met, objectives that are often overlooked when relying solely on prescriptive or force-based restraint rules. These methods also reveal opportunities for more economical designs where displacement demands are low and additional restraint provides no performance benefit. For such scenarios, the findings offer a pathway to more rational and flexible solutions that leverage the inherent isolation, flexibility, and damping of suspended NSEs, something that's expressly permitted in the dynamic design clause of AS1170.4 (Clause 8.1.2(a)).

A practical workflow was proposed to enable the adoption of dynamic principles within typical design practice, supported by field testing, spectral analysis, and simplified assessment methods. Future work should extend this approach to multi-degree-of-freedom systems, investigate testing methods for heavier and more complex NSE installations, and develop streamlined design tools to facilitate broader implementation.

REFERENCES

Applied Technology Council. (2018). Recommendations for improved seismic performance of nonstructural components (No. NIST GCR 18-917-43; p. NIST GCR 18-917-43). National Institute of Standards and Technology. https://doi.org/10.6028/NIST.GCR.18-917-43

Australian Earthquake Engineering Society, Scott, M., Wilson, J., & Lam, N. (Eds.). (2021). AS 1170.4–2007 Commentary, Second Edition. Australian Earthquake Engineering Society. https://aees.org.au/product/as-1170-4-commentary-2021/

Brewick, P. T., Hernandez-Garcia, M., Masri, S. F., & Smyth, A. W. (2018). A Data-based Probabilistic Approach for the Generation of Spectra-Compatible Time-History Records. Journal of Earthquake Engineering, 22(8), 1365–1391. https://doi.org/10.1080/13632469.2017.1286618

Dhakal, R. P., MacRae, G. A., & Hogg, K. (2011). Performance of ceilings in the February 2011 Christchurch earthquake. Bulletin of the New Zealand Society for Earthquake Engineering, 44(4), 377–387. https://doi.org/10.5459/bnzsee.44.4.377-387

Federal Emergency Management Agency. (2012). Reducing the Risks of Non-Structural Earthquake Damage. https://www.fema.gov/node/reducing-risks-non-structural-earthquake-damage

Filiatrault, A., Perrone, D., Merino, R. J., & Calvi, G. M. (2021). Performance-Based Seismic Design of Nonstructural Building Elements. Journal of Earthquake Engineering, 25(2), 237–269. https://doi.org/10.1080/13632469.2018.1512910

Haymes, K., Sullivan, T., & Chandramohan, R. (2020). A simple method to predict floor response spectral demands on nonstructural components. https://hdl.handle.net/10092/101230

Liu, R., Bai, W., Dai, J., Shao, Z., Jiang, T., & Zhao, B. (2025). Research on the design floor response spectrum of buildings by dynamic analysis. Earthquake Engineering and Engineering Vibration, 24(2), 413–436. https://doi.org/10.1007/s11803-025-2317-5

McCallen, D., Pitarka, A., Tang, H., Nakata, R., Mosalam, K. M., Petrone, F., Günay, S., & Perez, C. (2025). An open-access simulated earthquake ground-motion database for an M7 Hayward Fault earthquake in the San Francisco Bay Region. Earthquake Spectra, 41(3), 2560–2597. https://doi.org/10.1177/87552930251340960

Rizzo, P. C., Shaw, D. E., & Jarecki, S. J. (1975). Development of real/synthetic time histories to match smooth design spectra. Nuclear Engineering and Design, 32(1), 148–155. https://doi.org/10.1016/0029-5493(75)90096-5

Somerville, M., McCue, K., & Sinadinovski, C. (n.d.). RESPONSE SPECTRA RECOMMENDED FOR AUSTRALIA.

Taghavi, S., & Miranda, E. (2003). Response Assessment of Nonstructural Building Elements (No. PEER Report 2003/05). Pacific Earthquake Engineering Research Center, College of Engineering, University of California Berkeley.

An Open-Source Nonstructural Element Database to Streamline Tech Transfer Between Nonstructural Research and Building Design

Dustin Cook[1], Jitendra Bhatta[2], Amanpreet Singh[3], Mohammed M. Eladly[3], Adam Zsarnóczay[4,3], Siamak Sattar[1], Ben Schafer[3], and Matthew Speicher[1]

[1] National Institute of Standards and Technology
100 Bureau Dr., Gaithersburg, MD 20899
e-mail: dustin.cook@nist.gov
[2] University of Canterbury
20 Kirkwood Ave., Upper Riccarton, Christchurch 8041, New Zealand
[3] Johns Hopkins University
3400 N Charles St., Baltimore, MD 21218
[4] Stanford University
450 Jane Stanford Way, Stanford, CA 94305

Abstract. Observations since the 2011 Christchurch, New Zealand earthquake, and subsequent earthquakes around the globe have revealed two important findings that are shaping structural engineering research and design: (1) there is a pressing need for functional recovery design solutions to support long-term community resilience, and (2) damage to nonstructural components is often the leading cause of loss of building function after earthquakes. However, the readily available nonstructural fragility data most often used by engineers and researchers to inform decisions about the influence of nonstructural elements on building performance is fragmented and outdated.

To address this critical data collection and dissemination gap, the U.S. National Institute of Standards and Technology (NIST) developed the Nonstructural Element Database (NED), a public repository that organizes nonstructural experimental test data and seismic fragilities into a robust SQL database. Through an extensive literature review, we collected over 2000 experimental test records and explicitly related experimental records to seismic fragility models. The relational and open-source architecture of the database promotes data transparency, reuse, and scalability, where observations of nonstructural damage can be continuously uploaded to an online repository and directly queried by engineers and researchers for use in seismic risk assessment and design. By providing a centralized and public repository of nonstructural element data, NED can facilitate a better understanding of how nonstructural elements perform during earthquakes and support better decision-making to reduce the impact of earthquakes on communities.

Keywords: Nonstructural Elements, Performance-based seismic design, Seismic fragility models, Functional recovery, Database development, Tech transfer

1. INTRODUCTION

The seismic performance of nonstructural building elements is a critical aspect of earthquake engineering, as nonstructural elements make up approximately 75 % to 85 % of the construction cost of a building (excluding tenant contents; FEMA, 2011). Damage to nonstructural elements often accounts for the majority of direct property losses due to earthquakes (ATC, 2008), and their seismic performance typically dictates the post-earthquake building functionality and building recovery (Filiatrault et al., 2001; Fischer, 2014). However, nonstructural elements have historically received less attention than structural elements, leading to a knowledge gap in understanding their behavior under seismic loading.

Many studies have sought to address this gap by investigating, either through experimentation or post-earthquake reconnaissance, the seismic performance of various nonstructural elements, including ceiling systems, infill walls, and many others. The Federal Emergency Management Agency (FEMA) P-58 project (FEMA, 2012) undertook a substantial effort to collect, document, and publish nonstructural element seismic fragility and consequence models for use in building seismic risk assessments.

Despite these efforts, a substantial knowledge gap remains in (a) understanding the extent of experimental, reconnaissance, and analytical work that has been performed on nonstructural elements to date and (b) identifying where more data is needed to improve our understanding of how nonstructural component performance contributes to seismic risk. For instance, the FEMA P-58 fragility model for fire sprinkler piping is based solely on expert opinion (Bachman, 2012). Since the publication of the FEMA P-58 fragility database, several notable experimental programs (e.g., Pantoli et al., 2013; Ryan et al., 2016; Bhatta et al., 2025; etc.) have tested many configurations of fire sprinkler piping, bracing, and sprinkler heads. However, the FEMA P-58 database has not been updated to reflect this data, and practitioners continue to use the judgment-based fragilities from FEMA P-58 to make decisions about the performance and design of their buildings.

This paper introduces the Nonstructural Element Database (NED), developed by the National Institute of Standards and Technology in the U.S., to address existing knowledge gaps and provide a robust repository of experimental tests and seismic fragility models for nonstructural building elements. Structured as a relational database, NED facilitates an organized understanding of the state of the art in nonstructural experimental test data, with test records explicitly related to available seismic fragility models. By providing a centralized and public repository of nonstructural element data, NED can streamline the technology transfer gap between experimental investigation and practice, promoting data transparency, reuse, scalability, and facilitating better understanding and decision-making regarding the seismic performance of nonstructural elements.

2. THE FEMA P-58 FRAGILITY DATABASE

The FEMA P-58 performance assessment methodology is a comprehensive framework for evaluating the seismic performance of buildings. It provides a structured approach to quantify the potential impacts of earthquakes on buildings, including casualties, repair and replacement costs, and repair time (FEMA, 2012). A critical aspect of the methodology is the use of fragility functions for various building elements, including nonstructural elements. Nonstructural elements, such as MEP (mechanical, electrical, and plumbing) equipment, distribution systems, elevators, and architectural elements like glazing and suspended ceilings, are incorporated into the FEMA P-58 assessment methodology as seismic fragility models, quantifying the likelihood of various element-level damage states conditioned on deformation or accelerations experienced by the elements.

One of the foundational contributions of the FEMA P-58 effort is the development of the FEMA P-58 fragility database, which provides a collection of structural and nonstructural element fragility and consequence models necessary for estimating the seismic performance of buildings. The database contains fragility functions for over 700 structural and nonstructural building elements, including MEP equipment and distribution systems, elevators, curtain walls, suspended ceilings, storage racks, stairs, masonry chimneys, and other critical nonstructural elements under various installation conditions.

While the FEMA P-58 fragility database represents a significant advancement in the collection of nonstructural fragility models, the database is not without its limitations. The source of the data forming the basis for each component fragility model varies significantly. Some models are based on experimental testing, some on earthquake experience data (i.e., post-earthquake field observations), and others on expert opinion. Table 1 lists the types of nonstructural components provided in the database, ordered according to the data source forming the basis of the fragility model and the number of component performance observations available for each. While many of the architectural components are derived from experimental data, many MEP components are based on limited data sources, especially distributed MEP components, whose basis of fragility is formed entirely from expert opinion. Furthermore, the most current experimental findings are not reflected in the FEMA P-58 database, as most of the fragility models have not been updated in the 15-plus years since they were first created. While FEMA P-58 provides general background documentation for each fragility model (or group of fragility models), the experiment observations used to develop the fragilities are not always clear, and the finalized data in the fragility database do not always match the recommended parameters in the background documentation. As more research on nonstructural element performance is conducted, the FEMA P-58 fragility database becomes increasingly obsolete. However, because most design projects lack the budget to develop up-to-date fragility functions for the many nonstructural components within a building, practitioners need a tool like the FEMA P-58 database to realistically quantify the impact of nonstructural damage.

Table 1. Summary of nonstructural fragility models available in the FEMA P-58 database.

Component Type	Basis of Fragility	Total Number of Observations	Last Updated
Glazing	Experimental	44	2011
Tile Roofing	Experimental	24	2009
Interior Partitions	Experimental	74	2016
Suspended Ceilings and Recessed Lighting	Experimental	13	2016
Pendant lighting	Experimental	18	2009
Stairs	Experimental	9	2011
Elevators	Earthquake reconnaissance	206*	2009
MEP Equipment	Earthquake reconnaissance	2859*	2009
Cladding (precast)	Expert opinion	N/A	2009
Domestic and Sanitary Piping	Expert opinion	N/A	2012
Distributed HVAC	Expert opinion	N/A	2012
Fire Suppression	Expert opinion	N/A	2012

**Most of the data points forming the basis for the fragility curves are observations of non-damage from non-instrumented buildings.*

3. THE NONSTRUCTURAL ELEMENT DATABASE (NED)

3.1 NED INFRASTRUCTURE AND ARCHITECTURE

The Nonstructural Element Database is a relational database that collects and organizes experimental test data and seismic fragility models of nonstructural building elements into an open-source, public repository, accessible on GitHub under the NIST profile (Cook, 2025).

By using a web-hosted SQL database and Git repository, NED provides a next-generation evolution of the FEMA P-58 database. In NED, nonstructural element data is organized in a scalable and easily accessible fashion, facilitating data transparency and reuse. The open-source nature of the database allows researchers to upload data from experimental tests, query and discover other experimental programs, and actively create new seismic fragility models, thereby narrowing the technology transfer gap between experimental research and building performance evaluations. The SQL format ensures data integrity and consistency, thus reducing the risk of data corruption, while the Git repository provides a version control and tracking system, allowing researchers to monitor changes to the database and code over time.

Nonstructural element data in NED is organized into distinct tables (model classes) for tracking outcomes from experimental tests, seismic fragility models, and damage consequence functions. Primary and foreign keys establish explicit relationships between instances within each table, resulting in a robust and transparent data schema. For example, a user can easily filter the database to find the exact experimental test records that form the basis of a particular fragility model, or quickly list the references for a set of fragility models or experimental studies.

Figure 1 provides an overview of the current data tables and relationships in NED, as well as links to external datasets and future developments. NED categorizes nonstructural element test specimens and fragility models by "Component Type" using the NISTIR taxonomy (Charett and Marshall, 1999) as the classification system. The “Experimental Test” data table includes damage and response observations from nonstructural test specimens under various loading conditions, along with many specimen attributes describing the details of the specimen, testing configuration, and testing outcomes. Specimen damage is classified by the "Damage State (DS) Class" attribute, consisting of three mutually exclusive classifications: No damage, Inconsequential Damage, and Consequential Damage. This attribute helps fragility developers rapidly separate observations of consequential damage from inconsequential damage when developing new “Fragility Models”. “Fragility Models” represents a collection of “Fragility Curves” (i.e., functions that describe the likelihood of individual damage state exceedance) characterizing the overall vulnerability of nonstructural elements based on observations from experimental tests or earthquake reconnaissance. The "Experiment-to-Fragility Model Bridge" table establishes a many-to-many relationship between experiments and fragility models, enabling users to link experimental test data to corresponding fragility models (see Figure 1).

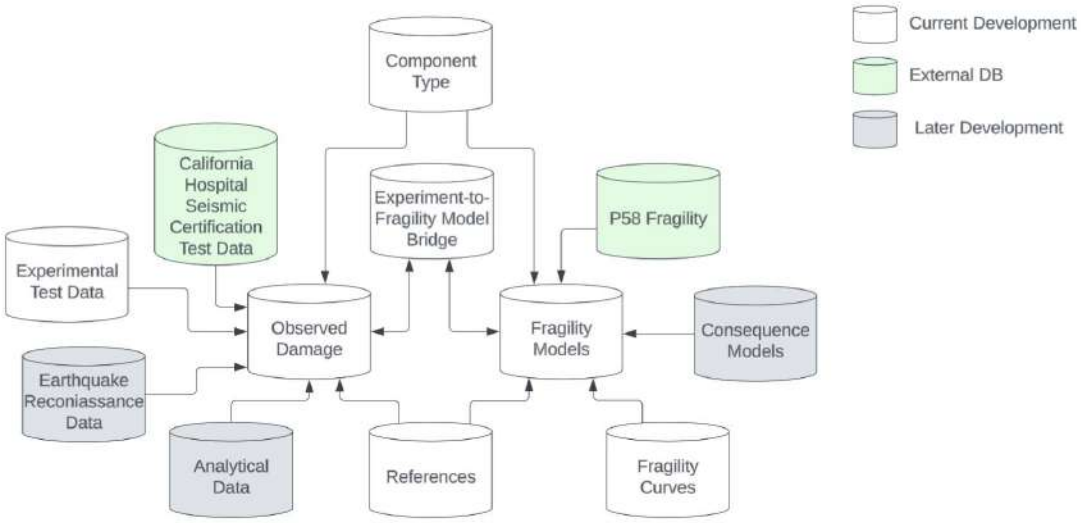


Figure 1 - Overview of the Nonstructural Element Database (NED) architecture.

To seed the database with nonstructural element experimental test data and fragility models, a substantial literature review was conducted, and test data were extracted from over 60 experimental studies conducted over the last 20 years. The data extracted included individual component test studies and full-building test programs outfitted with nonstructural elements, such as the Building Nonstructural Components and Systems (BNCS) project conducted at UC San Diego (Pantoli et al, 2016) and the NEES Nonstructural Grand Challenge testing conducted at the E-Defense test facility (Guzman and Ryan, 2015). All fragility models in the FEMA P-58 fragility database, as well as all experimental studies referenced in the FEMA P-58 background documents, were included, resulting in over 2,000 experimental test records. Figure 2 illustrates how those records break down among the various nonstructural element types.

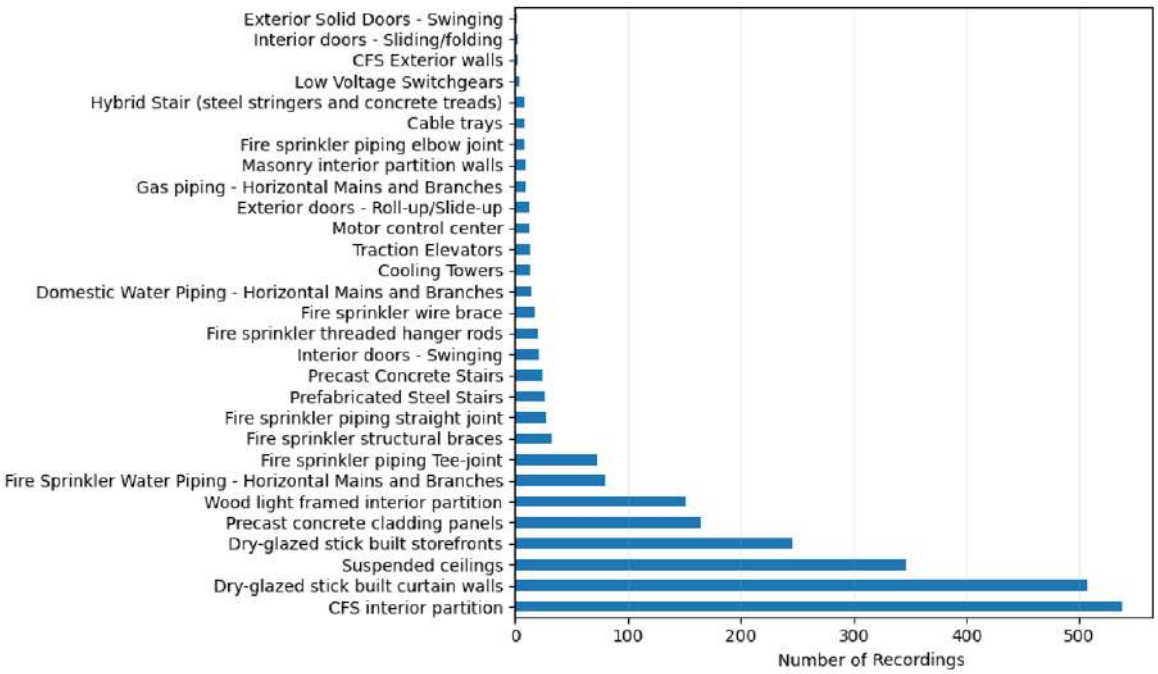


Figure 2 - The number of experimental test records collected within NED for various types of nonstructural elements.

3.2 USING NED TO SHORTEN THE TECH TRANSFER GAP

NED is designed to be a scalable repository of nonstructural building element data. The data is structured to support the addition of new experimental records and fragility models, enabling it to expand and adapt to the needs of researchers and practitioners. This flexibility enables researchers to continuously improve the available seismic fragility models by reusing existing data alongside new nonstructural performance observations.

For example, a recent study by Bhatta et al. (n.d.) compiled a dataset of experimental damage data from multiple full-scale experiments on fire sprinkler piping systems available within NED alongside observations from a new full-scale experimental program (Bhatta et al., 2025). The authors categorized the damage observed in the experimental tests into three damage states: Superficial, Minor Repair, and Critical. Figure 3 illustrates the breakdown of fire sprinkler experimental test data from the existing NED records and the new experimental testing records added from Bhatta et al., 2025. Using the compiled dataset from Figure 3, the authors developed a new fragility curve for the Minor Repair damage state for seismically braced fire sprinkler systems. Additionally, the authors used statistical inference to show disagreements between the existing FEMA P-58 fragility functions and the experimental evidence. New adjusted fragility curves for minor and major leak damage states were proposed, resulting in a new recommended fragility model shown in Figure 4.

The additional data within NED enabled the authors to develop a more comprehensive understanding of the seismic performance of fire sprinkler piping systems and replace the judgment-based fragility models from FEMA P-58 with a robust set of fragilities founded on experimental evidence. These new fragility models were then uploaded into NED for practitioners to use in seismic risk assessments and building design. The new fragility models in NED were then explicitly linked back to the records of the experimental observations in NED on which the models are based, providing robust data provenance.

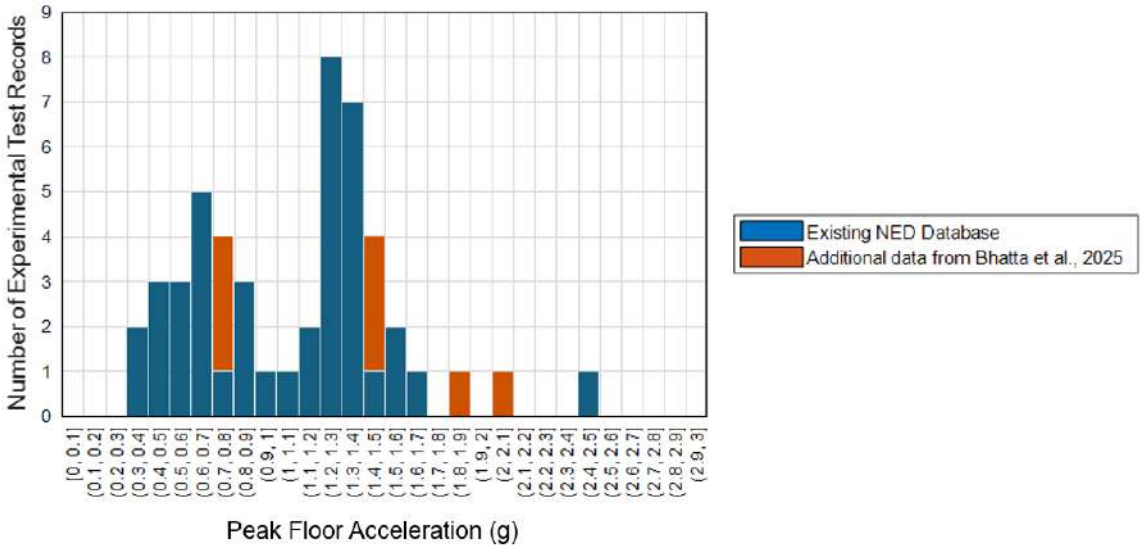


Figure 3 - Experimental test records used in Bhatta et al (n.d.) to develop new seismic fragility functions for braced fire sprinkler fragilities in terms of Peak Floor Acceleration.

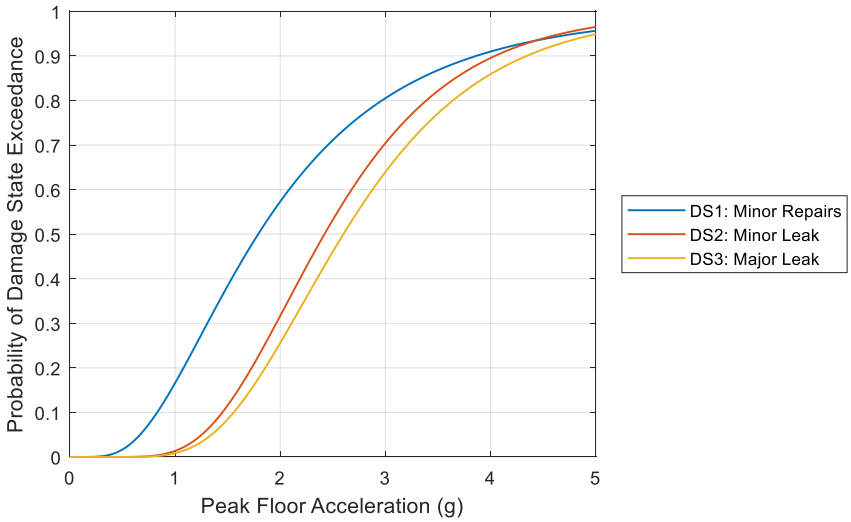


Figure 4 - New seismic fragility model for braced fire sprinkler piping – horizontal mains and branches designed to ASCE 7 Seismic Design Category D, E, or F, proposed by Bhatta et al., n.d., based on data collected in NED.

4. CONCLUSIONS

The NED data repository was developed by the National Institute of Standards and Technology to provide a centralized, open-source, and public repository of nonstructural element data; improve the data transparency, reuse, and technology transfer to engineering practice; and inform functional recovery design solutions that mitigate the impact of earthquakes on communities. NED directly contributes to two pressing issues outlined in the NIST GCR 17-917-44 report (NIST, 2017) on the seismic analysis, design, and installation of nonstructural components and systems. Specifically, it addresses recommendation 9.3.5, "Create a Plan for Post-Earthquake Reconnaissance and Data Collection," by providing a platform for the collection of earthquake response data on nonstructural components, and recommendation 9.3.6, "Conduct Component Testing," by serving as a repository for component test data.

Future researchers can contribute to NED by adding new test data and fragility models or by validating existing fragility models against new test data. In the online repository (Cook, 2025), the database is accompanied by a set of guidelines and tools to facilitate contribution, including a guide that outlines the steps for setting up a local development environment, installing required packages, and adding data to the database. The general applicability and robustness of NED will expand as the database continues to grow with the addition of new data and models. Future research could expand the scope of the database to include multi-hazard fragilities, additional consequence models, structural fragility and test data, and data for non-building structures such as bridge and lifeline components, thereby enhancing its utility for risk assessments and building design. If adopted by researchers and practitioners, NED will play a critical role in facilitating rapid technology transfer from research to practice, while fostering transparent and reproducible research for performance-based earthquake engineering.

6. REFERENCES

ATC (2008). Reducing the Risks of Nonstructural Earthquake Damage: State-of-the-Art and Practice Report (ATC-69 Report). Prepared for the U.S. Department of Homeland Security, Federal Emergency Management Agency.

Bachman, R. (2012). Development of Seismic Fragilities for MEP Distribution Systems for the ATC-58 Project. Prepared for the Federal Emergency Management Agency. FEMA P-58/BD-3.9.11.

Bhatta, J., Mishra, P., Cook, D., Sattar, S., Barbosa, A. R., & van de Lindt, J. (2025). Seismic Response of Pressurized Full-Scale Fire Sprinkler Piping System in Six-Story Building. Journal of Earthquake Engineering, 1–27. https://doi.org/10.1080/13632469.2025.2470335

Bhatta, J., Cook, D., and Sattar, S. (n.d.). Development of full-scale experiment-based seismic fragility functions for code-compliant fire sprinkler piping systems. Submitted to Earthquake Spectra. *In review.*

Charette, R. and Marshall, H. (1999), UNIFORMAT II Elemental Classification for Building Specifications, Cost Estimating and Cost Analysis, NIST Interagency/Internal Report (NISTIR), National Institute of Standards and Technology, Gaithersburg, MD.

Cook, D. (2025). Nonstructural Element Database v1.0. Released on July 17, 2025. Accessed via https://github.com/usnistgov/NED

FEMA (2012). Seismic Performance Assessment of Buildings, Volume 1 – Methodology, First Edition. FEMA P-58-1.

FEMA E-74 (2011) Reducing the Risks of Nonstructural Earthquake Damage – A Practical Guide. Federal Emergency Management Agency.

Filiatrault, A., Uang, C.-M., Folz, B., and Chrstopoulos, C., 2001. Reconnaissance report of the February 28, 2001 Nisqually (Seattle-Olympia) Earthquake (No. Report No. SSRP–2001/02). University of California, San Diego.

Fischer, E., 2014. Learning from Earthquakes: 2014 Napa Valley Earthquake Reconnaissance Report. Lyles School of Civil Engineering Graduate Student Reports. Paper 1.

Guzman, J.C. and Ryan, K.L., 2015a, "Data from the Network for Earthquake Engineering Simulation/E-Defense collaborative test program on innovative isolation systems and nonstructural components," *Earthquake Spectra*, Vol. 31, No. 2, pp. 1195-1209, DOI: 10.1193/083113EQS241.

NIST (2017). NIST GCR 17-917-44: Seismic Analysis, Design, and Installation of Nonstructural Components and Systems – Background and Recommendations for Future Work. Prepared by the Applied Technology Council for the National Institute of Standards and Technology, Gaithersburg, Maryland.

Pantoli, E., Chen, M. C., Astroza, R., Hutchinson, T. C., Restrepo, J. I., Bachman, R. E., Englekirk, R., Faghihi, M., Ebrahimian, H., Conte, J. P., Hoehler, M. S., Marin, C., Walsh, K. D., & Wang, X. (2016). Full-Scale Structural and Nonstructural Building System Performance during Earthquakes: Part II – NCS Damage States. Earthquake Spectra, 32(2), 771–794.

Ryan KL, Soroushian S, Maragakis E, Sato E, Sasaki T and Okazaki T (2016) Seismic simulation of an integrated ceiling-partition wall-piping system at E-Defense. I: Three-dimensional structural response and base isolation. *Journal of Structural Engineering* 142(2): 04015130.

Generation of seismic motion for seismic qualification of active component

D. Combescure[1], C. Benouaret[2], M. Ruiz[3], V. Dominguez[4], F. Rueda[5], C. Melendez[6],

G. Theunis[7], N. Jobert[8], C. Houivet[9]

[1] Dr Ing., Technical Officer, FUTED, Fusion for Energy, Barcelona, Spain (didier.combescure@f4e.europa.eu)
2 Ing., Technical Officer, FUTED, Fusion for Energy, Barcelona, Spain (celia.benouaret@f4e.europa.eu)
3 M., Trainee, FUTED, Fusion for Energy, Barcelona, Spain (currently IFMIF-DONES PhD student, Grenada, Spain)
4 Ing., Esteyco, Madrid, Spain (victor.dominguez@esteyco.com)
5 Ing., Esteyco, Madrid, Spain (Fernando.rueda@esteyco.com)
6 Ing., Esteyco, Madrid, Spain (carlos.melendez@esteyco.com)
7 Ing. Tractebel Engineering, Marseille, France (gilles.theunis@tractebel.engie.com)
8 Ing. Alma Consulting, Arcueil, France (nicolas.jobert@alma-consulting.eu)
9 ORANO, La Hague, France (clement.houivet1@orano.group)ss

Abstract. The seismic qualification of active components requires an important input data which is the definition of the seismic motion. The required response spectrum (RRS) shall be deduced from the seismic ground spectra or the spectra transferred to the civil works interface, taking into account the potential local amplifications due to the support of the equipment as well as the multiple positions of the equipment in the facility. This paper will focus on two fundamental needs that are, on one side, the determination of the potential amplification due to the local support and, on the other side, the possibility to re-use easily the tests already done for the qualification of other similar components and/or configurations. The interest of in-situ experimental tests for the determination or the check of the RRS will also be discussed.

Keywords: Active component, Seismic motion, Required Input Motion, Floor Response Spectrum

1. INTRODUCTION

The seismic qualification of active components requires an important input data which is the definition of the seismic motion. Active mechanical or electrical components are characterized by the presence of actuators or moveable parts that make difficult or impossible the demonstration by analysis of their functionality after or during a seismic avent. A qualification by seismic tests is very often needed. The required response spectrum (RRS) possibly completed with the relative displacement between supports is generally used for the qualification by test. The RRS shall be deduced from the seismic ground spectra or the spectra transferred to the civil works interface, taking into account the potential local amplifications due to the support of the equipment as well as the multiple positions of the equipment in the facility. The different types of uncertainties (uncertainty from modelling, potential design change in supports, etc.) must also be well considered. Previous papers presented in several SMiRT conferences have shown several examples of transfer using simplified formulas or more precise numerical methods (time integration, direct method in the frequency domain in Ezeberry et al., 2015 and Combescure et al., 2022). A method to simplify the calculated spectra and facilitate the propagation of this important input data for the qualification of materials has been applied to the ITER Tokamak buildings in Combescure et al., 2022.

Two fundamental needs are, on one side, the determination of the potential amplification due to the local support and, on the other side, the possibility to re-use easily the tests already done for the qualification of other similar components and/or configurations. The work presented in this paper is aimed at proposing pragmatic solution for fulfilling these two needs. A direct method in the frequency domain has been used to transfer the seismic motion from ground to floor (Floor Response Spectrum) or from floor to component (Component Response Spectrum). An effort to simplify and identify the driving parameters has allowed to propose a limited number of standardized RRS curves. The interest of in-situ experimental tests for the determination or the check of the RRS will also be discussed in the last part of the paper.

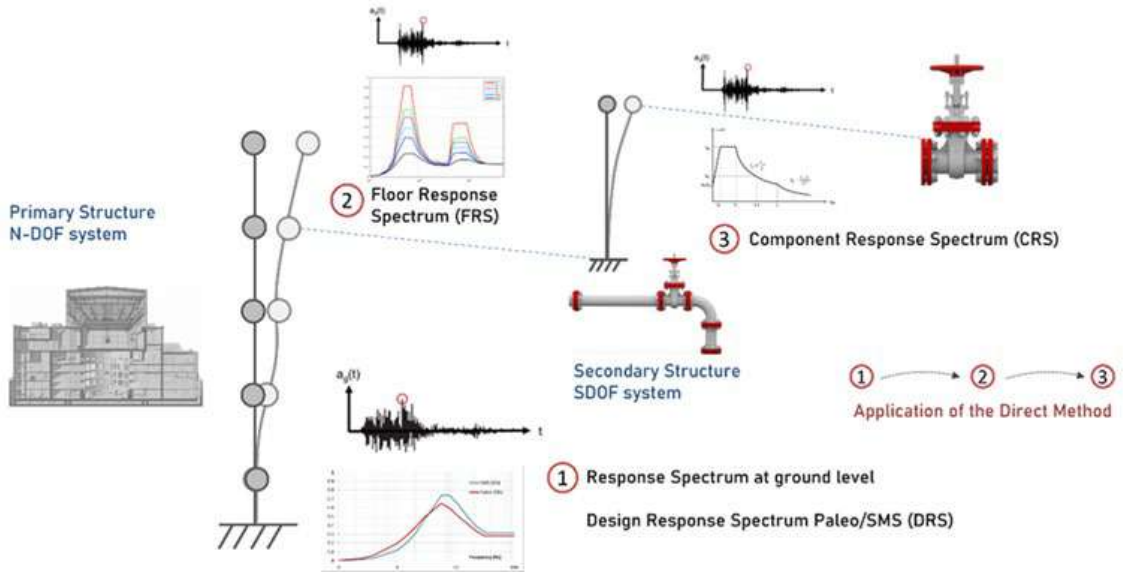


Figure 1. Transfer of seismic motion in the Tokamak building and secondary structures

2.TRANSFERRING THE SEISMIC MOTION IN THE FREQUENCY DOMAIN

The oscillator spectrum or seismic response spectrum (SRO) and the power spectral density (PSD) are two representations of seismic motion in the frequency domain. The power spectral density (Figure 2a) is less commonly used than the oscillator spectrum (Figure 2b), but it does help to understand that the vibrational energy of seismic motion is limited in the frequency domain. The maximum vibrational energy corresponds to the beginning of the plateau of the oscillator spectrum. Beyond the cut-off frequency, this energy should be negligeable, and the spectral density is virtually zero. This corresponds to the high-frequency asymptote of the oscillator spectrum and the maximum ground acceleration or zero period acceleration (ZPA). The oscillator spectrum is generally calculated by computing the time response of a large number of oscillators, conserving the maximum relative displacement of each oscillator and deducing the spectral acceleration (Figure 3a).

The oscillator spectrum from the power spectral density of a seismic signal (ground motion or transferred motion) can be determined by calculating the spectral density of the corresponding spectral quantity (relative displacement, velocity, acceleration, pseudo-acceleration or pseudo-velocity) for a large number of oscillators (Figures 3b and 3c). Let's take the example of an acceleration spectrum. The transfer function between the ground acceleration and the acceleration of the one-degree-of-freedom system has 3 parts: a unit constant function at low frequency, a resonance peak at the oscillator frequency and filtering at high frequencies. At low and medium frequencies, the oscillator will strongly amplify the input spectral density (Figure 3b). At high frequencies, since the vibratory energy is zero, the response will be dominated by the low-frequency content, which is transmitted without amplification by the one-degree-of-freedom system (Figure 3c). This reasoning is also valid for a multi-frequency system (Figure 4).

The determination of the maxima of the physical quantity of the system with one degree of freedom (displacement, velocity or acceleration) requires the recall of two important equations of the theory of random vibrations:

- The integral of the power density function G(ω) of a zero-mean time signal is equal to the variance of the signal, σ^2.

$$\sigma^2 = \int_0^\infty G(\omega) d\omega \tag{1}$$

- The maximum response of the physical quantity and the standard deviation are linked by the peak factor $r_{s,p}$ (ω_n,s) which depends on the frequency content of the signal, which may be broadband (e.g. ground motion) or narrowband (quasi-sinusoidal transferred motion).

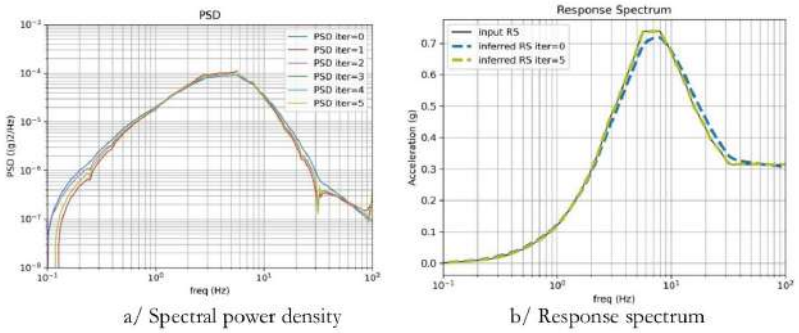
$$S_{as,p}(\omega_n, s) = r_{s,p}(\omega_n, s)\ \sigma_{SDOF,a}(\omega_n, s) \tag{2}$$

With: $S_{as,p}(\omega_n,s)$: the pseudo acceleration at the pulse ω_n and s the duration of the signal

$\sigma_{SDOF,a}(\omega_n,s)$: standard deviation of the pseudo-acceleration of the SDOF

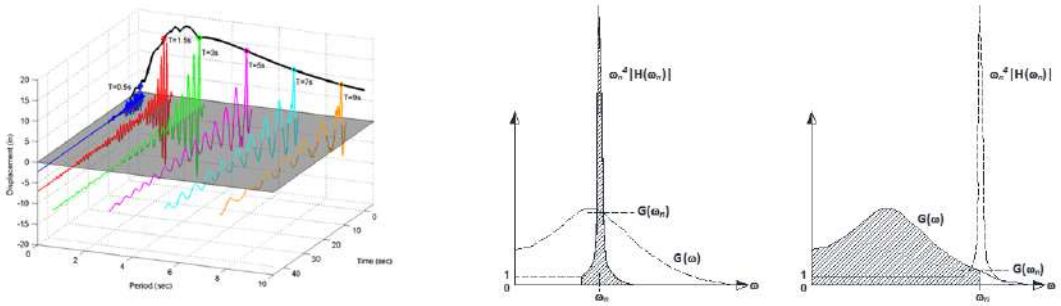
$r_{s,p}(\omega_n,s)$): peak factor

An illustration of the values of the peak factor for two different signals (sinusoidal and seismic signals) is given in Figure 4. The peak factor is determined on the basis of Vanmarcke [1976]



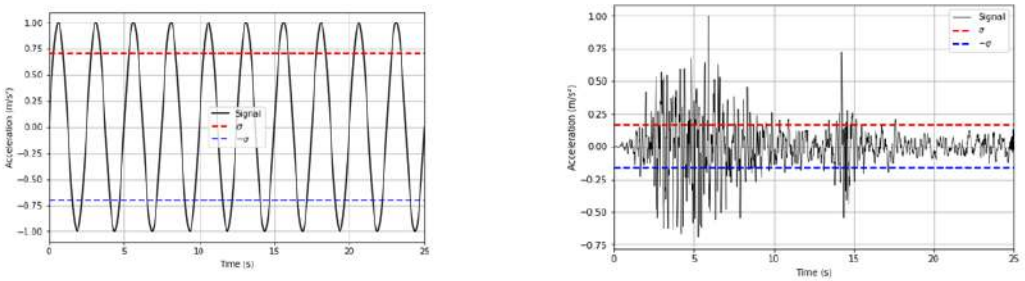
a/ Spectral power density b/ Response spectrum

Figure 2. Equivalence between Power Spectral Density and Response Spectrum



a/ Calculation of a spectrum using the time method b/ Response for a resonant case c/ Response for a rigid case

Figure 3. Calculation of the response of a one-degree-of-freedom structure using the time method (a) and the Power Spectral Density (b) (c)



Sinusoidal signal at 0.8 Hz (scaled to 1)

σ = 0.707

Peak Factor = 1.414

Seismic signal Rock 1 (scaled to 1)

σ = 0.164

Peak Factor = 6.098

Figure 4. Comparison between maximum value and standard variation (left: sinusoidal signal, right: seismic signal)

Once the power spectral density of the input motion has been established (on the ground or at the floor level), the power spectral density of the transferred motion is determined by a simple frequency-domain calculation (convolution of the input motion with the transfer function). The transfer function of the building or support can be calculated on a physical or modal basis. It can also be determined experimentally using in-situ measurement. Figure 6 shows the successive steps to generate the floor response spectrum from the ground response spectrum.

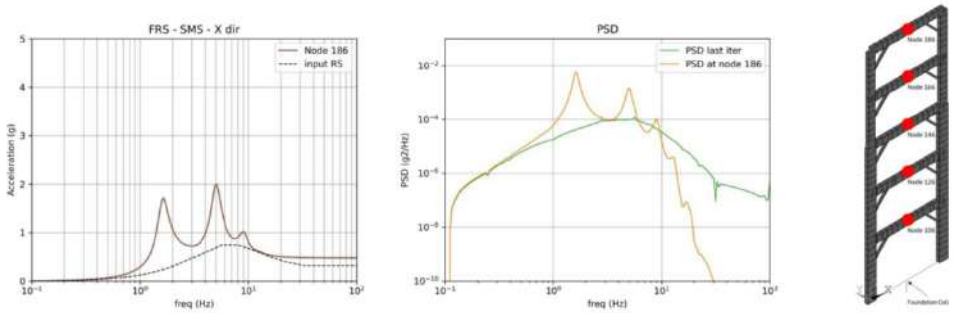


Figure 5. Comparison of seismic ground motion and transferred motion for the portal structure of the AFPS (2013) ICPE Structures support guide (main modes: 1.57Hz and 4.85Hz)

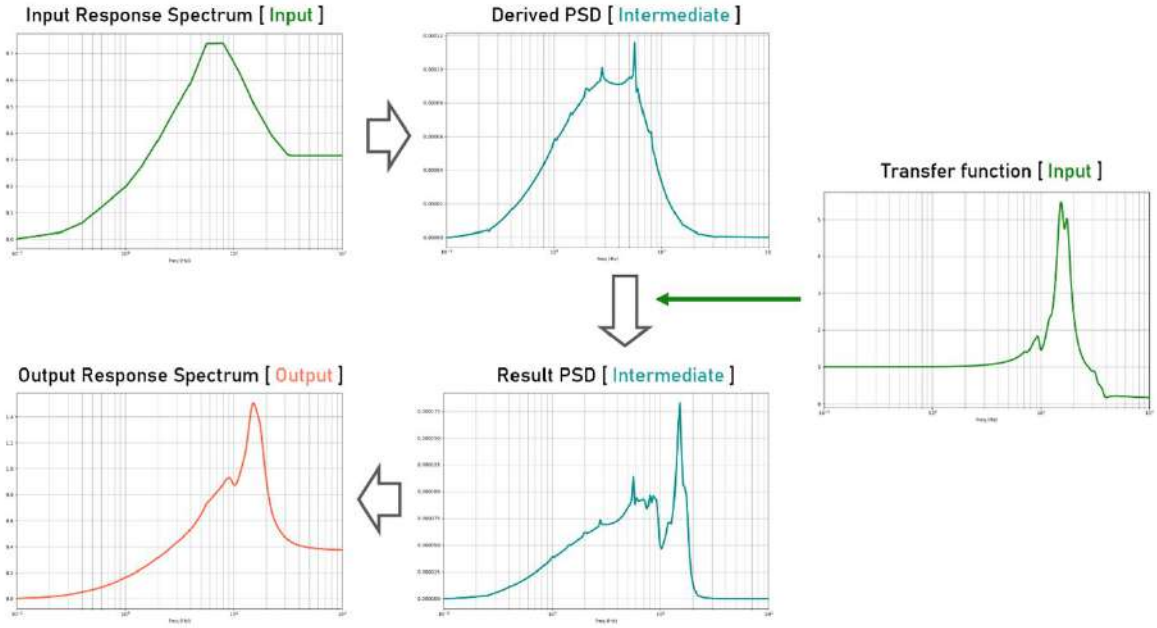


Figure 6. Response spectra and power spectral densities for a structure

3.SIMPLIFYING THE SEISMIC MOTION TO STANDARDIZE THE INPUT DATA FOR SEISMIC QUALIFICATIONS

The experimental seismic qualification of Safety Important active Components requires the determination of the RRS (Required Response Spectrum). The propagation of this input data for the qualification should be properly controlled and the information well stored in the qualification database. A seismic FRS (Floor Response Spectrum) or CRS (Component Response Spectrum) is a curve, and so a complex mathematical object. It is important to characterize the seismic input for the seismic qualification through, if possible, few physical parameters. An easy and practical way to consider the potential flexibility of the support is also a key-element for reducing the cost and limit of risk of underestimation of the seismic input for qualification.

3.1 REDUCING CURVES INTO A LIMITED NUMBER OF PARAMETERS

The idea is to simplify the RRS curves into a set of parameters in order to ease their propagation to the experimental facilities in charge of the seismic qualification in a similar way than the RRS proposed by the

French standard RCC-E. In Combescure et al. (2022), a method has been proposed to identify the main physical parameters of the FRSs and calculate easily envelops. Because of the seismic isolation in ITER, the horizontal FRSs have a specific shape with two peaks and low values of ZPA but high values of spectral displacement. The automatic generation of the simplified RRS is based on the determination of local maximum values of spectral quantities and values of frequency such as the cut-off frequency or the limits of the plateau. statistical studies were carried out on the floor spectra of the ITER Tokamak building.

Statistical studies have been performed to determine the key parameters identified the following properties:

- Below 2Hz, the spectra are very similar for all points and a single envelope curve can be taken for each direction (enveloping the first peak for horizontal spectra and close to ground motion for vertical spectra).

- The maximum acceleration (ZPA) and spectral acceleration (Sa) of the second peak of the horizontal spectra do not show a clear correlation and pairs of values (ZPA, Sa) have been proposed for the standardised spectra.

- The maximum acceleration and spectral acceleration of the vertical spectra show a clear correlation and a relationship has been proposed to conservatively deduce the spectral acceleration from the ZPA for standardised spectra (factor 7 for 5% damping).

- Conservative frequency values were easily determined for the pseudo-acceleration plateaux (0.48Hz-0.71Hz for the first horizontal peak, 4Hz-21Hz for the plateau of the second horizontal peak and 4Hz-14H for the plateau of the vertical spectrum).

Table 1, Figures 7a and 7b show the proposed standardised spectra and a comparison between the standardised spectra and the floor spectra. In the ITER Tokamak building, maps giving the class to be considered for the horizontal and vertical FRS are available and ease the determination of the input RRS for the systems directly fixed onto the building or on a rigid support.

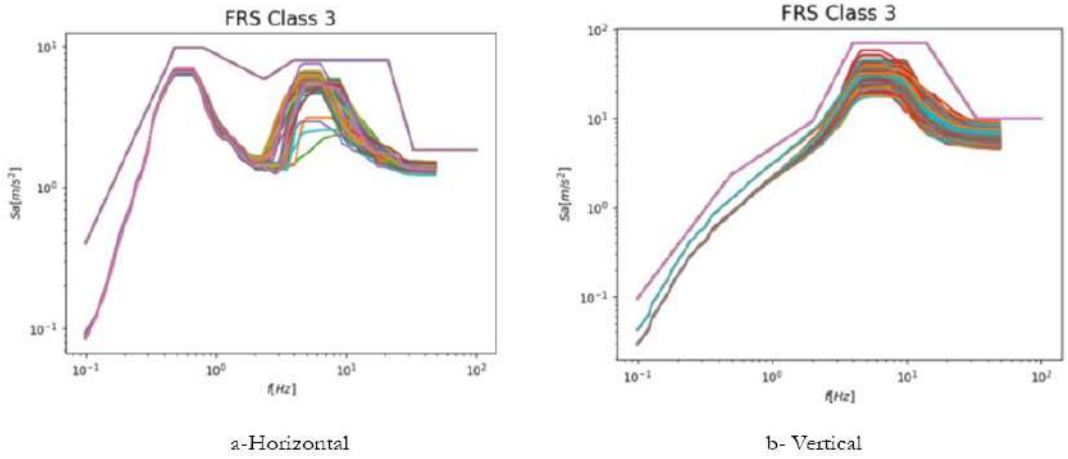


Figure 7. Proposal of standardised required response spectra in the ITER Tokamak building

3.2 CONSIDERING THE POTENTIAL EFFECT OF THE SUPPORTS

Let now discuss the issue of the potential amplification of the component support. The direct method presented in the first section was applied to a large number of floor response spectra (1118 points) in the ITER Tokamak building for typical support structures with frequencies between 2.5Hz and 30Hz (V. Domingue, 2023). In this study, each support was considered as a SDOF. One of the objectives was to

estimate the amplification of non-perfectly rigid supports (f<33Hz). Figure 8 shows comparisons between the input spectra and the spectra transferred by these supports. From 12.5 Hz, amplification is reduced and almost non-existent for 20Hz. In this case, the only effect is often to widen only the plateau of the input spectrum. Very flexible and very stiff supports ensure that the seismic movement is not amplified. Figure 9 shows the maximum acceleration and spectral acceleration amplifications for two values of support frequency. (5Hz and 30Hz). It is interesting to remark that, for the non-rigid or resonant support (5Hz), the amplification of the spectral acceleration is higher than the amplification of ZPA. This property comes from the narrow band nature of the transferred signal. The ratio between spectral acceleration and ZPA is higher for a sinusoidal signal (narrow band signal) than for a random noise (broadband signal).

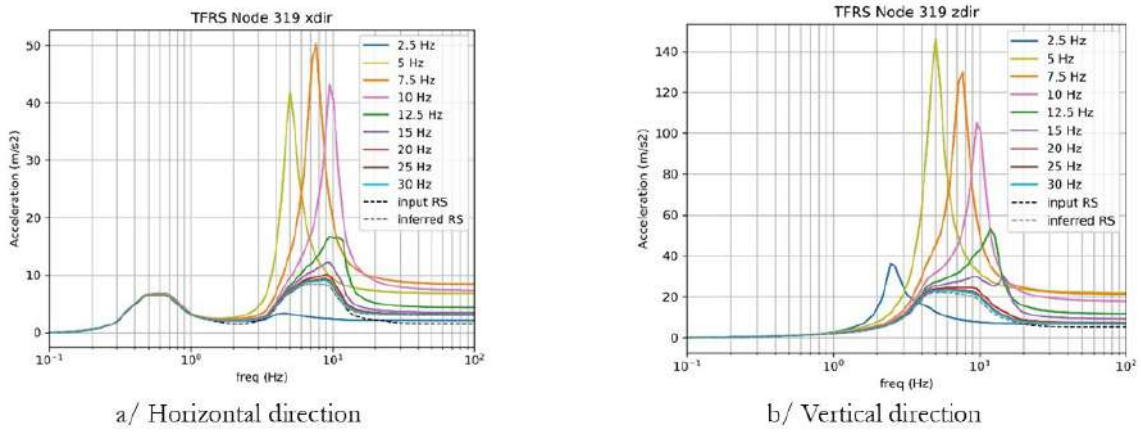


Figure 8. Modification of the seismic motion by the support structure

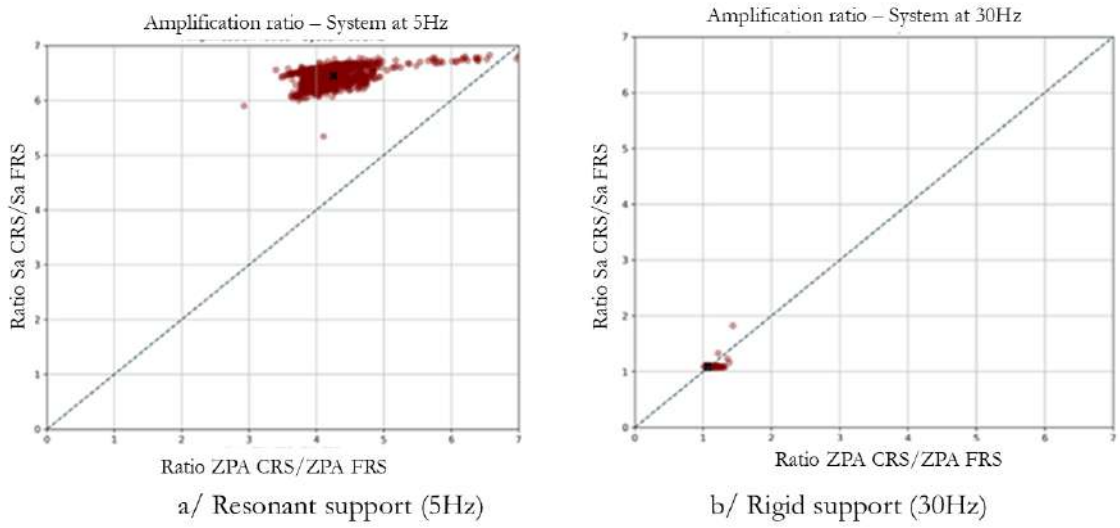
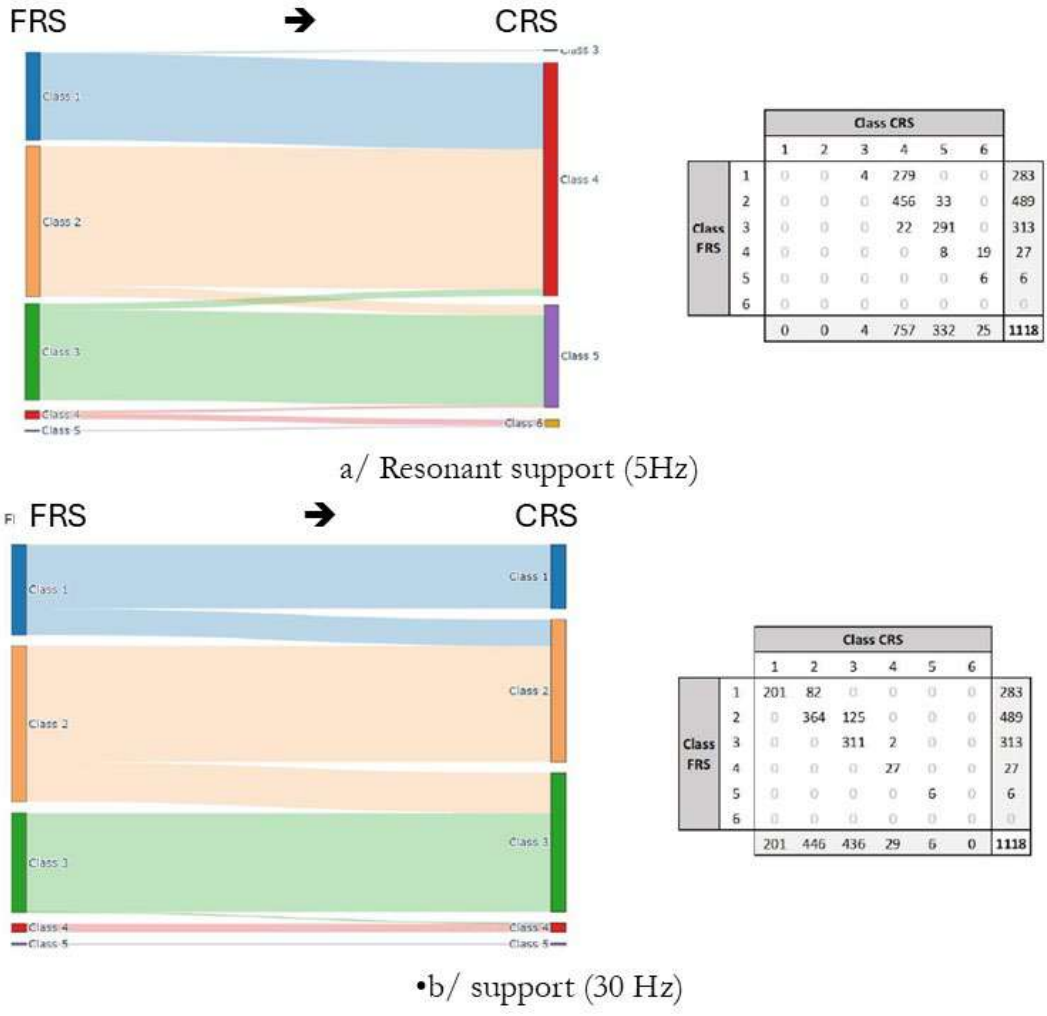


Figure 9. Amplification of ZPA and Spectral acceleration (5% damping) in the ITER Tokamak Complex

When the input data for the qualification of a component is needed, it is interesting to translate the potential amplification factor of a support into an upgrade of class for horizontal or vertical RRS. Figure 10 gives such an indication. For rigid or semi-rigid supports, the upgrade of classes between FRS and CRS is very limited and at maximum by one class. The flexible support has much more impact and an upgrade by 2 or

3 classes should be considered. This result is valid for SDOF support. Real supports are very often more complex with several eigenmodes and coupling between directions (vertical excitation may induce horizontal response and vice-versa). To allow the use of the strategy based on classes, a tool for the engineers in charge of the determination of the RRS for qualification is under development. The tools is aimed at giving access to the input FRSs in the ITER Tokamak complex and other buildings of ITER Facility or other facilties, allowing the possibility to introduce the transfer functions of the component support based on the calculated eigenmodes or the experimental transfer function and providing the numerical tools to simplify the Component Response Spectrum and determine the class of each RRS.



Class FRS \ Class CRS	1	2	3	4	5	6	
1	0	0	4	279	0	0	283
2	0	0	0	456	33	0	489
3	0	0	0	22	291	0	313
4	0	0	0	0	8	19	27
5	0	0	0	0	0	6	6
6	0	0	0	0	0	0	0
	0	0	4	757	332	25	1118

Class FRS \ Class CRS	1	2	3	4	5	6	
1	201	82	0	0	0	0	283
2	0	364	125	0	0	0	489
3	0	0	311	2	0	0	313
4	0	0	0	27	0	0	27
5	0	0	0	0	6	0	6
6	0	0	0	0	0	0	0
	201	446	436	29	6	0	1118

Figure 10. Influence of the support onto the class of RSS to be considered for qualification (FRS: interface with building structure, CRS: interface with supporting structure)

4.EXAMPLES OF QUALIFICATION USING RRS CLASSES

ITER nuclear fusion facility shall qualify many components related to vacuum technology. For instance, Non-Evaporable Getter (NEG) pumps are high vacuum and ultra-high vacuum pumps able to effectively capture the so-called active gases present in vacuum systems. The getter pump consists of two fundamental

parts: the mounting flange and the pump cartridge. The mounting flange consists of a high vacuum "ConFlat" base flange of size DN100 with a glass feedthrough to power the built-in heater of the pump cartridge. The cartridge incorporates the ZAO (Zr, V, Ti and Al) sintered disks that perform the chemical processes. The power supply and control of the getter pumps is done by means of a controller connected to the mounting flange connector with cables. These pumps require high temperatures for activation of the pump cartridge in order to perform the physical processes that allow the capture of gases. The pump underwent thus seismic tests while being heated at 550°C.

Figure 11 gives a view of the environment of a getter pump of the ITER Leak Detection System and a picture of the specimen of getter pump that has been seismically qualified.

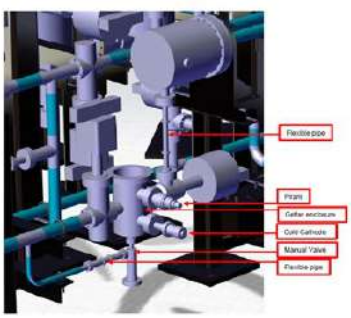
The RRS considered for the seismic qualification are characterized by their ZPA and a shape in agreement with the KTA German standard. The values of ZPA and the eigenmodes of the piping system have been calculated through a set of response spectrum analysis with FEA models of the process piping system and are reported in the flexibility reports. From the existing ITER seismic classes (see Table 1) an enveloping RRS is chosen to envelope the ZPA and shape defined by KTA.

5.ABOUT THE USE OF IN-SITU EXPERIMENTAL TESTS

A procedure to determine the transfer function has been developed. It is based on the measurement of the input motion (at the interface with the building structure) and the output motion (at the component location). The experimental measurement is used to estimate the cross-spectral power density matrix for the inputs (GXX) as well as the outputs-inputs (GYX). An estimator ($H=GYX.GXX^{-1}$) based on these measurements is used to obtain the experimental transfer function both in the presence or absence of noise (extraneous noise should be quantified, using the magnitude-squared coherence). Figure 12 shows an application of the experimental method for the determination of the transfer function of a benchmark case (simple frame structure).

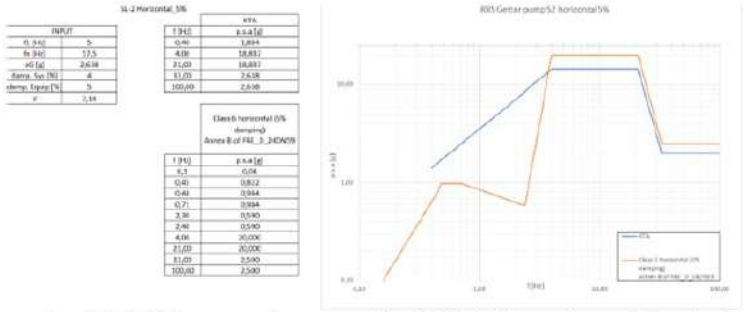
While this procedure in itself is straightforward, it is essential to bear in mind a number of practical limitations, which are absolutely critical with respect to the quality of the results:

- the procedures aim at capturing the motion transfer function for base motion and the structure should not be excited by other sources (wind, fluid circulations, human activity);
- instrumentation should be practically noiseless for the input sensors, since the numerical procedure works under the assumption that they are noise-free. This in turn requires that at least the input signals should be collected using stringent quality control, and sensors installed, protected, and monitored by sufficiently experienced staff
- in most situations the signal/noise ratio will worsen at very low frequencies (around 1Hz) and the input motions cannot be assumed to be uniform in the high frequency range. This imposes a limited frequency range for which the transfer function can be determined experimentally.





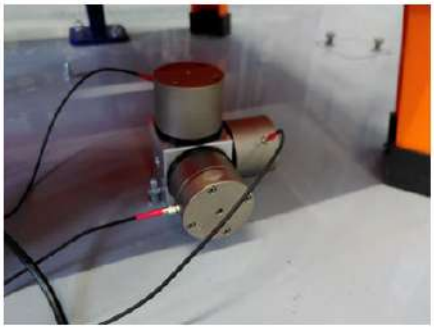
a- Drawings showing the getter pump environment b- View of a specimen seismically qualified



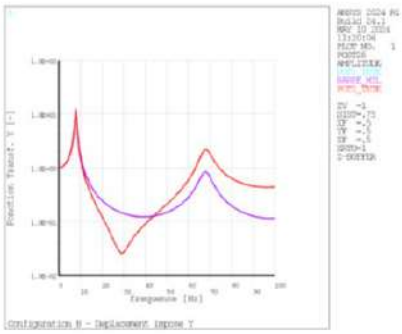
c- Example of RRS (blue curve) compared to FRS (red curve) used for the Qualification

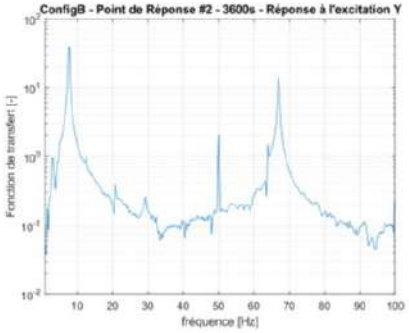
Figure 11: View of a getter pump and the RRS





a/ General view of the frame with additional mass b/ View of a triaxial accelerometer





c/ Comparison between numerical (left) and experimental (right) transfer functions

Figure 12. Application of the experimental method for the determination of the transfer function of a benchmark case

5.CONCLUSIONS

This paper has focused on two fundamental needs for the seismic qualification of components that are, on one side, the determination of the potential amplification of the seismic motion due to the local support and, on the other side, the possibility to re-use easily the seismic tests already done for the qualification of other similar components and/or configurations. The author is convinced by the importance of proposing practical rules and tools to reduce the cost and secure the seismic qualification of components not only for a single project but also for the reuse of existing qualification for other projects or in other fields.

Table 1. Classes proposed for the RRS for qualification of ITER Components (vertical direction)

Freq (Hz)	Damping	*0.1*	*0.5*	*2*	*4*	*14*	*33*	*100*
Sa-Class 1 (m/s2)	5%	0.1	2.28	9.3	28	28	4	4
	4%	0.11	2.55	10.40	31.30	31.30	4	4
Sa-Class 2 (m/s2)	5%	0.1	2.28	9.3	35	35	5	5
	4%	0.11	2.55	10.40	39.13	39.13	5	5
Sa-Class 3 (m/s2)	5%	0.1	2.28	9.3	70	70	10	10
	4%	0.11	2.55	10.40	78.26	78.26	10	10
Sa-Class 4 (m/s2)	5%	0.1	2.28	9.3	140	140	20	20
	4%	0.11	2.55	10.40	156.52	156.52	20	20
Sa-Class 5 (m/s2)	5%	0.1	2.28	9.3	350	350	50	50
	4%	0.11	2.55	10.40	391.31	391.31	50	50

REFERENCES

AFPS (2013). Guidelines for the seismic design of the supporting structure, ICPE industrial facility, AFPS.

Combescure D., Kaldas S., Mujica J. (2022), Generating motion for seismic qualification of components on semi-rigid supports. Application to the ITER leak detection system, SMiRT-, Berlin, Germany.

Dominguez V. (2023), Propagation of FRS by the direct method - Theoretical background and examples of application for specific ITER equipment, Report F4E_D_3278X6.

Dominguez V. (2023), Derivation of seismic loading for components mounted on SDOF systems in the TKC with the Direct Method, Report F4E_D_32ENQA.

Ezeberry J. and Combescure D. (2015), A direct method for determining floor response spectra at the ITER Tokamak Complex, SMiRT-23, Manchester, United Kingdom.

F4E (2023), Guidelines for seismic design, analysis and qualification of complex industrial and nuclear facilities against seismic hazard. Report F4E_D_26R65J v3.1.

KTA (2012). KTA 2201.4 Design of Nuclear Power Plants against Seismic Events; Part 4: Components, KTA, Germany.

Melendez C., M. Ruiz (2025), E-Direct RS - A tool for the implementation of the direct method for the transfer of response spectra - User's guide, Reports F4E_D_326FE8 and F4E_D_39LWJN.

Vanmarcke E.H. (1976). Structural response to earthquakes, in Developments in Geotechnical Engineering (Eds.: Lomnitz and Rosenblueth), pp. 287-337, Elsevier.

Preliminary Investigation of Isolation Bearings with Discontinuous Inerters for Seismic Protection of Essential Equipment and Components

Chia-Ming Chang[1] and Wei-Kai Chen[2]

[1] Department of Civil Engineering, National Taiwan University
No 1, Sec 4, Roosevelt Rd, Taipei 10617, Taiwan
e-mail: changcm@ntu.edu.tw
[2] Department of Civil Engineering, National Taiwan University
No 1, Sec 4, Roosevelt Rd, Taipei 10617, Taiwan
e-mail: r11521243@ntu.edu.tw

Abstract. Earthquakes not only impact buildings but also influence essential equipment and components, such as high-precision manufacturing machines in high-tech facilities. Meanwhile, excessive earthquakes can cause enormous economic losses for the equipment and components. To prevent damage from these earthquakes, seismic isolation underneath these equipment and components is commonly applied to enhance seismic performance. In recent years, researchers found that additional inerters, along with seismic isolation, can yield better performance in reducing isolation responses. However, this combination further reduces accelerations while increasing displacements in the isolation layer. Therefore, this study aims to develop and experimentally verify seismic isolation bearings with discontinuous inerters. In this study, the mathematical model of the proposed system is established. In the phase transition, the conservation of momentum is employed. Then, this model is evaluated using the harmonic balance method to obtain the frequency response with respect to an input intensity. This frequency response provides an understanding of the effect of discontinuity compared to the isolation bearings alone and the isolation bearings fully attached with inerters. Finally, this frequency response is experimentally verified using shake table testing. In addition, historical earthquake inputs are also exploited in the experiment to evaluate the performance of the proposed isolation system. The experimental results show that the proposed isolation system can generate better performance as the input intensity increases.

Keywords: Seismic Isolation, Discontinuous Inerters, Shake Table Testing, Harmonic Balance Method, Proof-of-Concept Experiment.

1. INTRODUCTION

Inerters generate force proportional to relative acceleration and can modify system dynamics without increasing seismic mass. Previous studies (Ikago et al., 2013; Chen et al., 2014; Abdeddaim et al., 2018; Zhang et al., 2020) demonstrated that inerters can enhance damping and control performance, especially under abrupt momentum changes. This research introduces a seismic isolation system equipped with discontinuous inerters to protect sensitive equipment in high-tech facilities. The inerters, comprising flywheels and steering wheels, are engaged via friction only near equilibrium, offering seismic resistance with reduced displacement demands.

2. SINGLE-CURVATURE ISOLATION SYSTEM WITH DISCONTINUOUS INERTERS

This prototype isolation system consists of a platform with four wheels on single-curvature tracks, and the inertance is derived from steering wheels driving flywheels through the friction plates. To realize the discontinuous effect, the friction plates are only placed near the equilibrium position of the isolation system. After a certain effective region, the friction plates no longer contact the steering wheels. Moreover, to examine the length of the effective region, the friction plates are segmented into several short pieces and can produce a number of combinations. Because the steering wheels rely on static friction, additional normal force is added by pre-tensioning rubber bands. Eventually, this prototype isolation system can further reduce isolation accelerations with effective inerters, while the increased natural frequency without the aid of inerters limits more isolation displacements to achieve.

For the proposed isolation system, the equation of motion can be expressed by

$$m_{\mathrm{iso}}(1+\beta)\ddot{x} + c_{\mathrm{iso}}\dot{x} + k_{\mathrm{iso}}x = -m_{\mathrm{iso}}\ddot{x}_{\mathrm{g}} \tag{1}$$

where

$$\begin{gathered} \dot{x}^{+} = \frac{1}{1+\beta}\left(\dot{x}^{-} + \beta r_{\mathrm{s}}\dot{\theta}^{-}\right) \text{ if } |x| \le d_{\mathrm{limit}} \\ \dot{\theta}^{+} = \frac{1}{r_{\mathrm{s}}}\dot{x}^{-} \text{ if } |x| > d_{\mathrm{limit}} \\ \beta = \frac{1}{2}\frac{m_{\mathrm{w}}}{m_{\mathrm{iso}}}\frac{r_{\mathrm{w}}^2}{r_{\mathrm{s}}^2} \text{ if } |x| \le d_{\mathrm{limit}};\ \beta = 0 \text{ if } |x| > d_{\mathrm{limit}} \\ k_{\mathrm{iso}} = \frac{m_{\mathrm{iso}}g}{R_{\mathrm{iso}}},\ c_{\mathrm{iso}} = \alpha m_{\mathrm{iso}} \end{gathered} \tag{2}$$

m_{iso}, c_{iso}, and k_{iso} are the isolation mass (i.e., including all the movable mass, such as wheels and wheel axles), damping coefficient, and linearized stiffness. β and m_{w} are the effective inertance ratio and flywheels mass, where the mass of steering wheels and flywheel rods is neglected. x, $\dot{x}$, and $\ddot{x}$ are the relative displacement, velocity, and acceleration to the ground. d_{limit} indicates the effective inertance region. $\dot{\theta}$ is the angular velocity of the steering wheels and flywheels, and both types of wheels share the same angular velocity. r_{w}, r_s, and R_{iso} are the flywheel radius, steering wheel radius, and radius of gyration of the single-curvature tracks. The superscripts + and – indicate the instant before and after contact. g and $\ddot{x}_{\mathrm{g}}$ are the gravitational and ground accelerations. Note that the damping coefficient in this system is quite small. To avoid any numerical instability, a small level of damping is still assumed. The linearized stiffness is derived with respect to the radius of gyration of the single-curvature tracks and with the small-angle assumption.

Also, when the steering wheels leave the effective region, the effective ineratnace ratio becomes zero. Meanwhile, the flywheels maintain the constant angular velocity. After the steering wheels reengage to the isolation system, the conservative momentum is satisfied and expressed by Eq. (2).

In addition, the harmonic balance method can be employed to estimate the steady-state amplitude of a nonlinear system. In the proposed isolation system, the isolation platform with the single-curvature tracks can be assumed to be linear; however, the discontinuous inerters are actually nonlinear. Thus, the harmonic balance method is applied to Eq. (1), and the displacement and acceleration amplitudes with respect to different frequencies are estimated by

$$B^2 = (-A\Omega\alpha)^2 + \left(-A\Omega^2 + \frac{gA}{R_{\text{iso}}} - A\Omega^2\beta\left(\frac{z_1}{\pi}\right)\right)^2 \tag{3}$$

where

$$z_1 = 2\phi_0 - \sin(2\phi_0),\ \phi_0 = \sin^{-1}\left(\frac{d_{\text{limit}}}{A}\right) \text{ if } A > d_{\text{limit}}$$

$$z_1 = \pi \text{ if } A \le d_{\text{limit}}$$

$$\ddot{x}_{\text{g}} = B\sin(\Omega t)$$

A is the displacement amplitude of the proposed isolation system under harmonic excitation. As for the isolation accelerations, the steady-state amplitude can be determined by

$$A_{\text{accel}}^2 = \left(-A\Omega^2 + B\cos(\varphi)\right)^2 + \left(B\sin(\varphi)\right)^2 \tag{4}$$

where

$$\varphi = tan^{-1}\left(\frac{-\Omega\alpha}{-\Omega^2 + \frac{g}{R_{\text{iso}}} - \Omega^2\beta\left(\frac{z_1}{\pi}\right)}\right) \in [0, \pi]$$

By Eqs. (3-4), the frequency displacement and acceleration responses can be calculated and compared with the conventional isolation system and the isolation system with continuous inerters.

3. NUMERICAL STUDY OF PROPOSED ISOLATION SYSTEM

In this numerical study, the proposed isolation system with discontinuous inerters is compared to the conventional isolation system (i.e., without any inerters) and the one with continuous inerters. The parameters used in this study is listed in **Table 1**.

The steady-state displacement and acceleration amplitudes under harmonic excitation are investigated. **Figure 1** shows the frequency response of displacements against different levels of inputs. As can be seen, the frequency responses of the proposed system align with the conventional system. If the displacement is less than the upper limit of the effective inertance region, the curve will be changed to the system with continuous inerters. If the input excitation has a low amplitude, the switching between the conventional system and the one with continuous inerters will be at a low frequency. Also, a high inertance introduces

the switching at a higher frequency. To sum up, the performance of the proposed system will be similar to the one with continuous inverters because the dominant frequency of far-field earthquakes is roughly located around high frequencies, of which the range is considered in this investigation.

Table 1. Parameters used in the numerical study

Symbol	Value	Symbol	Value
m_{iso}	100 kg	β	0.05-0.5
α	0.0042	d_{limit}	0.05 m
R_{iso}	2.2364 m		

(a) (b)

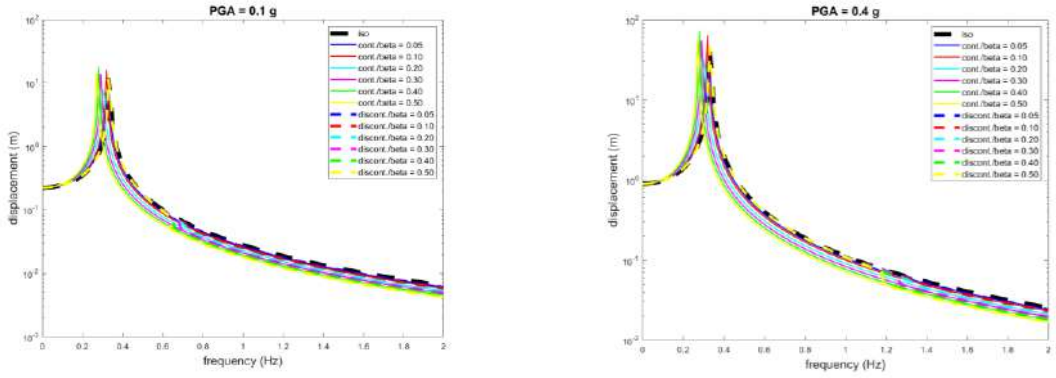


Figure 1. Frequency responses of displacements subjected to harmonic excitation with the level: (a) 0.1g and (b) 0.4g

Figure 2 exhibits the frequency response of accelerations under different levels of harmonic inputs. As can be seen, the proposed system will maintain the mode with inerters when the input level is low. When the input becomes large, the switching will move to high frequencies, and the effective isolation band (i.e., the concaves in curves) can be extended. To compare with the conventional isolation system, the effective isolation band can be maintained if the inertance ratio is sufficiently small (i.e., around 0.2 for this ratio), and further acceleration reductions can be found. Note that **Figures 1** and **2** do not consider the momentum conservation in Eqs. (3-4). The true switching effect (e.g., suddenly increasing acceleration) can not be included in these plots. Although the frequency response investigation is toward the better capability of the proposed system, the claimed performance may be a little bit over expectation.

(a) (b)

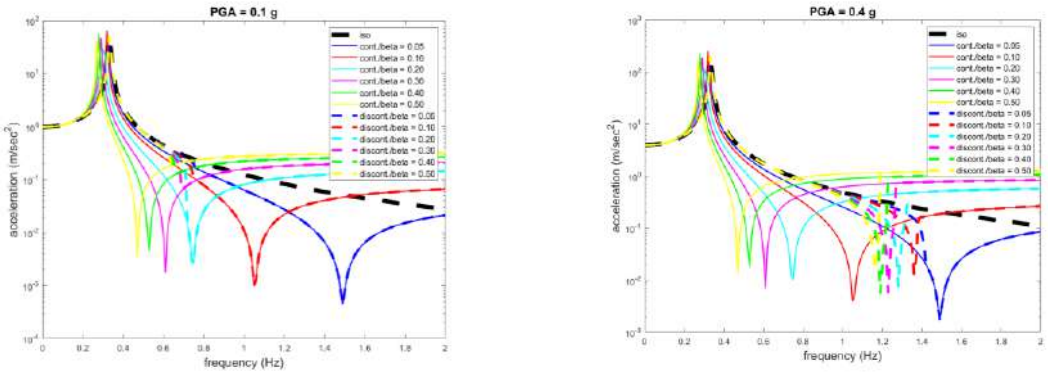


Figure 2. Frequency responses of accelerations subjected to harmonic excitation with the level: (a) 0.1g and (b) 0.4g

4. EXPERIMENTAL VERIFICATION OF PROPOSED ISOLATION SYSTEM

In the experimental verification, a prototype isolation system with discontinuous inerters is evaluated using shake table testing. The movable mass, i.e., the cart, wheels, and friction plates, is 18.11 kg. The radius of gyration of the single-curvature track is 1.2 m, which is equivalent to 0.455 Hz. The allowable horizontal displacement for this isolation system is 0.3 m. Moreover, the flywheel per disk has a diameter and mass of 0.12 m and 0.6 kg, while the steering wheel has a diameter and mass of 0.02 m and 0.025 kg. Although the flywheels in this prototype system can be stacked to a bigger mass moment of inertia, only one at a side (i.e., a pair) is employed in the test. The resulting inertance ratio is 0.25. In this experimental verification, the only variable used is the effective inertance length for the discontinuous inerters.

Peak and RMS responses of isolation displacements and accelerations of the proposed system are investigated and compared to the conventional system without and with continuous inerters. **Figure 3** shows the results when earthquake input varies from 0.05g to 0.3g. Note that the horizontal axis represents the achieved peak ground acceleration on the shake table. The effective inertance length considered is 0.06 m in this case. As found in the results, both isolation systems with inerters have low isolation displacements when the input earthquake has a small amplitude. As the earthquake intensity increases, the isolation accelerations can have more reductions compared to the conventional system. In addition, because the effective inertance length is 0.06 m, the performance of the isolation systems with continuous and discontinuous inerters is identical if the displacements do not exceed this limit. When the earthquake input becomes large, the one with discontinuous inerters performs better that with continuous inerters, particularly for the peak accelerations. To sum up, the proposed system with discontinuous inerters has the advantage of reducing isolation displacement better than the conventional system, while the proposed system can further reduce the isolation acceleration as compared to the one with continuous inerters when the seismic input is large.

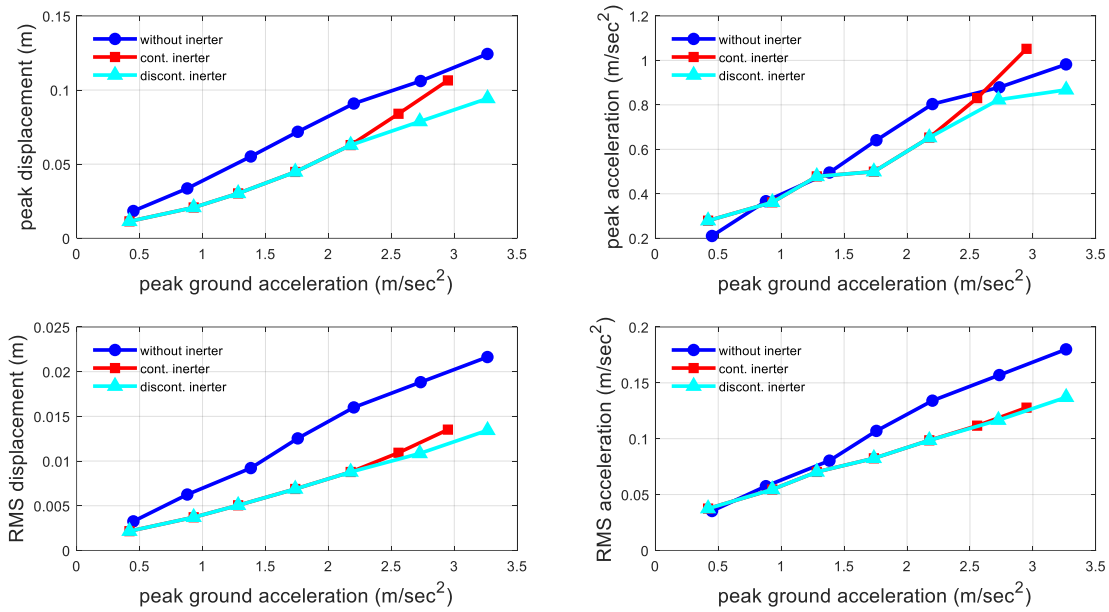


Figure 3. Peak and RMS displacement and acceleration responses under seismic excitation

5. CONCLUSIONS

An isolation system with discontinuous inerters was developed and experimentally verified for seismic protection of essential equipment and components. In the mathematical model, the proposed system can reduce isolation accelerations better around the equilibrium and further decrease isolation displacements when inputs are large. As seen in frequency responses, inertance was only effective for a specific region of frequencies per input level. In the experimental results, the proposed system was capable of further reducing responses as compared to the conventional isolation system.

REFERENCES

Ikago, K., Saito, K., Inoue, N. [2012] "Seismic control of single-degree-of-freedom structure using tuned viscous mass damper," *Earthquake Engineering & Structural Dynamics*, Vol. 41, No. 3, pp. 453-474.

Chen, M.Z., Hu, Y., Huang, L., Chen, G. [2014] "Influence of inerter on natural frequencies of vibration systems," *Journal of Sound and Vibration*, Vol. 333, No. 7, pp. 1874-1887.

Abdeddaim, M., Kasar, A.A., Djedoui, N. [2018] "Seismic vibration control using a novel inerto-elastic damper," *Proceedings of MATEC Web of Conferences*, Vol. 211, p. 14003.

Zhang, R., Zhao, Z., Pan, C., Ikago, K., Xue, S. [2020] "Damping enhancement principle of inerter system," *Structural Control and Health Monitoring*, Vol. 27, No. 5, e2523.

System Identification of Natural Frequency and Damping Ratio of Partition Wall from Earthquake Observation Records

Sora Hagiwara[1], Daiki Sato[2], Sono Yanagiya[3], Yinli Chen[2], Alex Shegay[4], Shoichi Kishiki[2], Tadashi Ishihara[2], Shojiro Motoyui[3], Yuzi Huang[5]

[1] School of Environment and Society, Institute of Science Tokyo,
Nagatsuta 4259, Midori-ku, Yokohama, Kanagawa 226-8501, Japan
e-mail: hagiwara.s.ah@m.titech.ac.jp
[2] Institute of Integrated Research, Institute of Science Tokyo,
Nagatsuta 4259, Midori-ku, Yokohama, Kanagawa 226-8501, Japan
[3] Formerly at Tokyo Institute of Technology,
Nagatsuta 4259, Midori-ku, Yokohama, Kanagawa 226-8501, Japan
[4] The University of Auckland,
22 Princes Street Auckland CBD Auckland 1010, New Zealand
[5] School of Environment and Society, Institute of Science Tokyo,
Nagatsuta 4259, Midori-ku, Yokohama, Kanagawa 226-8501, Japan

Abstract. Natural frequency and damping ratio are two essential factors to analyze the damage of partition walls subjected to earthquakes. However, the behaviors of a partition wall are also affected by the surrounding members, which are complicated to be observed by conducting experiments. Therefore, system identification of the partition walls installed in a real building by the recorded data from structural health monitoring is a feasible method to obtain their actual behaviors. In this study, the seismic responses of a partition wall from an actual building are utilized to estimate natural frequency and damping ratio in out-of-plane direction by calculating its transfer function and singular value. The analysis results reveal that, the out-of-plane response of the partition wall is significantly stronger than that of floor when subjected to low level of seismic excitation, while it is align with that of floor under high level of seismic excitation. Moreover, the natural frequency of the partition wall remains approximately constant regardless of the floor's maximum acceleration, whereas the damping ratio is positively correlated with the floor's maximum acceleration.

Keywords: System Identification, Partition Wall, Structural Health Monitoring, Observation Record, Seismic Response, Natural Frequency, Damping ratio.

1.INTRODUCTION

In recent years, it has been reported casualties because of the damage of non-structural components. In these cases, even though structural components such as columns and beams haven't been damaged by large-scale earthquakes, the collapse of non-structural components caused direct harm to human and property, as well as the secondary disasters due to the obstruction of evacuation routes. On the other hand, evaluating the natural frequency and damping ratio of partition walls, which affect their responses during earthquakes, is functional for evaluating their damage. For this purpose, several experiments focusing partition walls have been conducted. Luigi, F. et al. [2019] reported the results of dynamic shake table tests performed on prototypes made of indoor partition walls, outdoor facade walls and suspended continuous ceilings, Gennaro, M. et al. [2014] evaluated the seismic performance of partition walls via shake table tests with increasing intensity. However, the seismic behavior of partition walls is expected to be influenced by surrounding structural elements. Therefore, it's a useable approach to conduct system identification with the structural health monitoring on the partition walls in an actual building, which has been relatively limited to be mentioned.

In this study, based on the observation records of the response acceleration of the partition wall installed in an actual building, we analyze the dynamic characteristics of partition walls and evaluate their natural frequencies and damping ratios. The results shown in this paper can contribute for constructing a numerical model for estimating the allowable acceleration of partition walls.

2.OVERVIEW OF TARGET BUILDINGS AND OBSERVED EARTHQUAKES

This study takes the partition wall installed in J2-3 building as the research target [Kikuchi et al., 2014]. J2-3 building is a high-rise base-isolated building situated on the Suzukakedai Campus of Institute of Science Tokyo (Figure 1). The location of isolation layer is located between the 1st and 2nd floor of J2-3 building. The observation data utilized in this study is recorded from the floor and partition walls on the 7th floor of J3 building. The partition wall has a C65-type @303 base with two layers of boards,12.5 mm reinforced gypsum board and 9.5 mm hard gypsum board on both sides. Figure 2 illustrates the locations of the accelerometers, whose on-site photos are shown in Figure 3. Accelerometer P0 is installed on the floor, while accelerometers P1 and P2 are installed on a partition wall, which are 1960 mm and 1280 mm above the floor, respectively. Besides, P0 is approximately 5 m apart from P1 and P2 in the horizontal plane. As shown in Figure 3, the X-direction represents the out-of-plane direction of the partition wall, and the Y-direction is the in-plane direction. The sampling frequency of the accelerometers is 100 Hz, and its cut-off frequency is 31.25 Hz.

Table 1 shows the list of 14 earthquakes analyzed in this paper with the maximum acceleration measured on the floor of the seismic isolation layer [Matsuda et al., 2012] and the 7th floor, where the X and Y directions are the same as shown in Figure 3.



Figure 1. Exterior view of J2-3 building

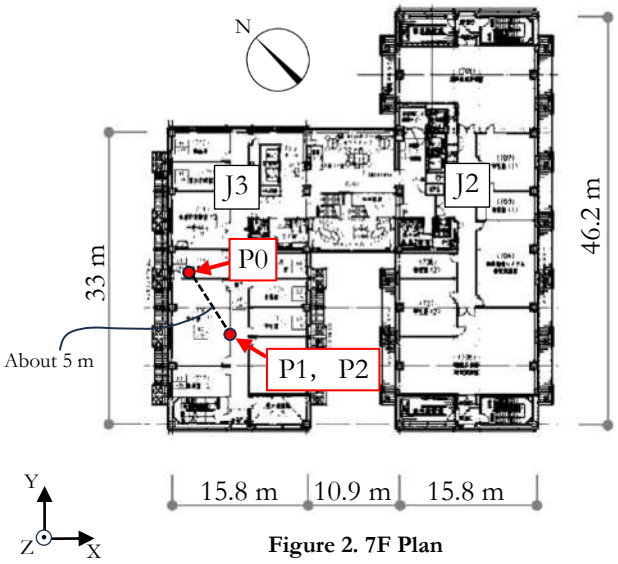


Figure 2. 7F Plan

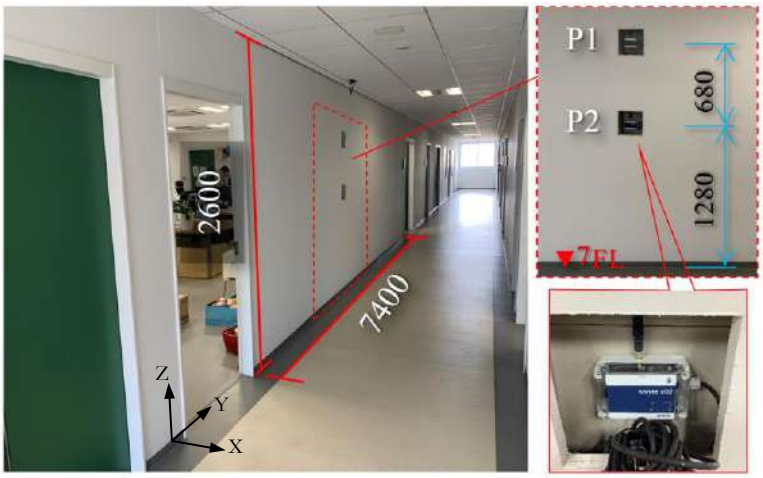


Figure 3. Observation status photo (unit: mm)

Table 1. Observed earthquake

Earthquake Name	Time of earthquake	Acceleration of Isolation [cm/s²]		Acceleration of 7th floor[cm/s²]	
		X	Y	X	Y
E1	2022/03/16 23:36	13.87	10.85	13.67	16.23
E2	2022/07/09 19:10	4.62	3.19	1.04	2.19
E3	2022/09/03 11:54	1.82	1.10	1.04	1.66
E4	2022/09/23 09:53	1.91	1.68	1.18	1.98
E5	2022/09/30 14:58	1.49	1.48	1.27	1.41
E6	2022/11/09 17:40	1.45	1.70	1.11	1.90
E7	2022/11/14 17:08	2.48	2.74	2.31	2.52
E8	2022/12/16 09:25	1.28	1.19	1.24	1.55
E9	2022/12/27 09:09	2.31	1.31	1.11	1.37
E10	2023/01/29 21:19	1.63	1.19	1.38	1.35
E11	2023/05/10 11:20	2.62	2.40	1.37	1.51
E12	2023/05/11 04:16	5.45	4.41	3.52	3.30
E13	2023/05/26 19:03	2.41	2.82	2.37	4.04
E14	2024/01/01 16:10	3.21	5.27	6.31	12.82

3.ANALYSIS OF RESPONSE CHARACTERISTICS

The acceleration time history observed by accelerometer P1 and P0 of the earthquake E1 are shown in Figure 4 as an example. The acceleration amplification factor, A_{acc}, is defined as the ratio of the peak acceleration of the partition wall to the peak floor acceleration, as expressed by the following equation:

$$A_{acc} = \frac{|a_{wall,max}|}{|a_{floor,max}|} \quad (1)$$

where $a_{wall,max}$: the maximum acceleration of the partition wall,
$a_{floor,max}$: the maximum acceleration of the floor.

Figure 5 summerizes the A_{acc} results of all earthquakes in Table 1. From Figure 5, it can be observed that in the in-plane direction, the A_{acc} remains approximately 1 regardless of peak floor acceleration. In contrast, in the out-of-plane direction, the A_{acc} decreases as the peak floor acceleration increases for both P1 and P2. Furthermore, there was no difference in the amplification rate between accelerometers P1 and P2 in both the in-plane and out-of-plane directions.

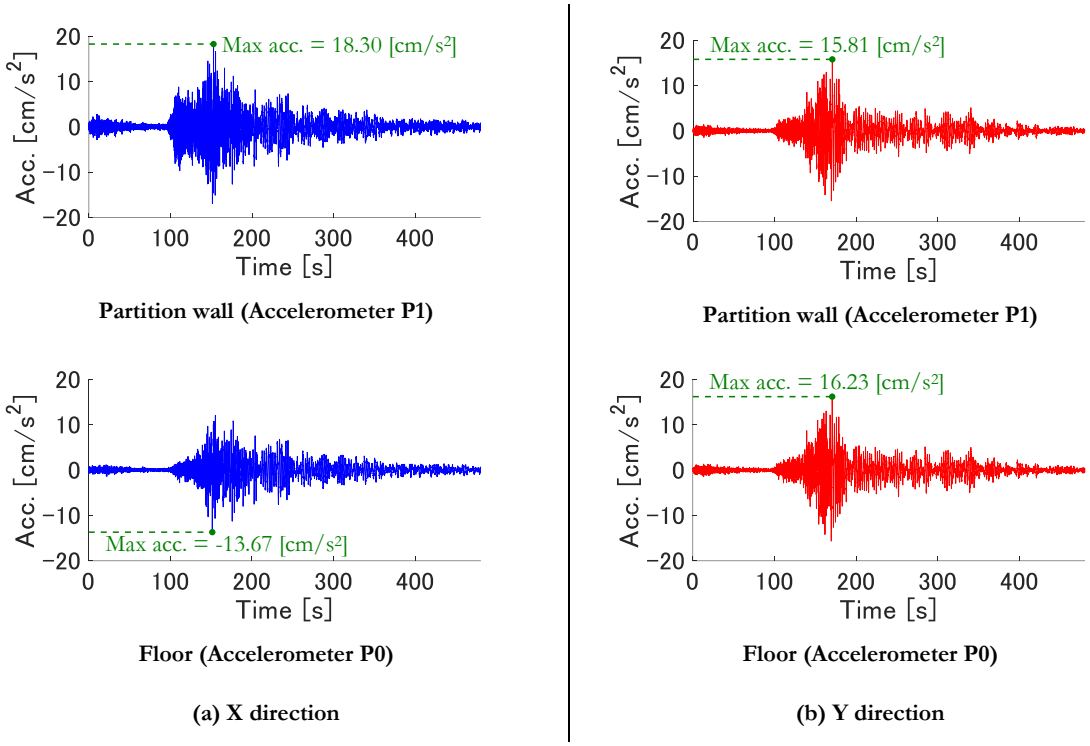


Figure 4. Acceleration time history (Earthquake E1)

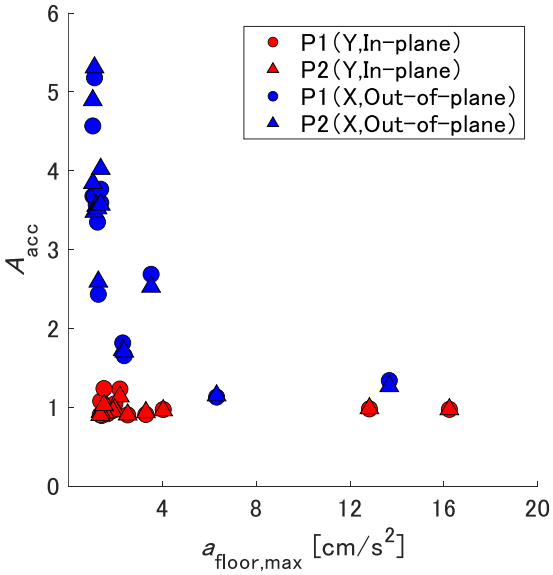


Figure 5. Relationship between maximum floor acceleration and acceleration amplification

4.SYSTEM IDENTIFICATION BY CURVE FITTING METHOD

This section shows the calculation method and the system identification results of the partition wall in the out-of-plane direction.

4.1 TRANSFER FUNCTION BASED ON OBSERVATION RECORDS

The transfer function obtained from the observation records is shown in Equation (2).

$$|H_{\mathrm{obs}}|=\frac{|F_{\mathrm{P}i}|}{|F_{\mathrm{P0}}|} \tag{2}$$

$|F_{\mathrm{P}i}|$: Fourier amplitude spectrum of accelerometer P1 or P2, where i represetnts the number of the accelerometer

$|F_{\mathrm{P0}}|$: Fourier amplitude spectrum of accelerometer P0

Figure 6 shows an example of the transfer function calculated from the records of earthquake E1 by accelerometer P1 and P0. There is a clear peak in the transfer function curve of the out-of-plane direction, while there is no large peak in that of the in-plane direction. Since similar results are obtained from other earthquakes, only the transfer function of the out-of-plane direction is discussed in the following chapters.

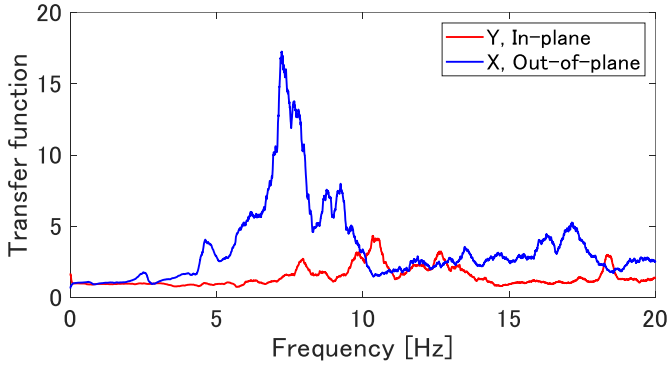


Figure 6. Transfer function based on observation records (Earthquake E1, P1)

4.2 SYSTEM IDENTIFICATION METHOD

The natural frequency and damping ratio of the partition wall are calculated by curve fitting for the transfer function, which was given below:

$$|H_{\mathrm{est}}|=\left|\sum_{s=1}^{3} b_s\left(\frac{1+2h_s\left(\frac{p}{f_s}\right)i}{1-\left(\frac{p}{f_s}\right)^2+2h_s\left(\frac{p}{f_s}\right)i}\right)+\left(1-\sum_{s=1}^{3} b_s\right)\right| \tag{3}$$

where b_s : s -th mode participation factor, h_s : s -th mode damping ratio, f_s : s-th mode natural frequency, p : frequency

Note that the transfer function shown in (3) consists of nine unknowns. These unknowns are determined by minimizing the sum of squared residuals S by the following equation from 0 Hz to 30 Hz.

$$S=\int_0^{30}(|H_{\mathrm{obs}}|-|H_{\mathrm{est}}|)^2\,dp \tag{4}$$

4.3 SYSTEM IDENTIFICATION RESULTS

After conducting curve fitting, the estimated transfer function captures the characteristics of the observed one transfer function and matches it well, as shown Figure 7.

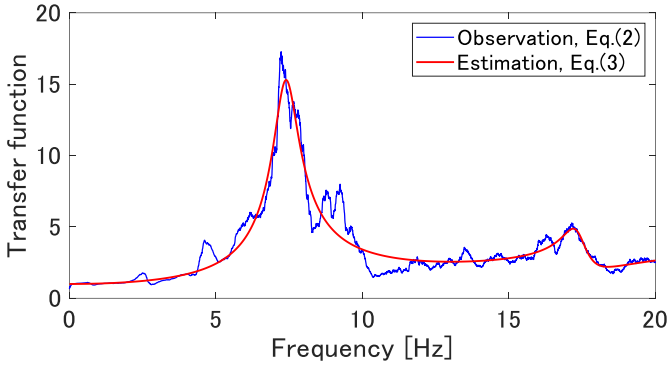
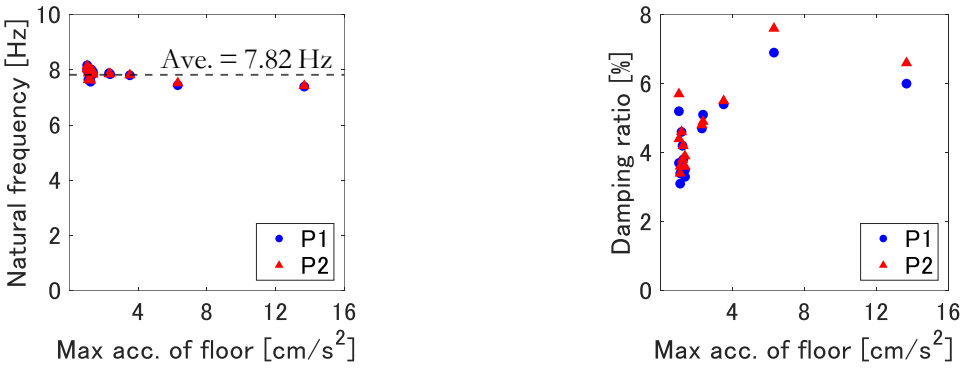


Figure 7. Curve fitting result of transfer function (Earthquake E1, P1)

Figure 8 summarizes the 1st mode natural frequency and damping ratio in relationship with the maximum out-of-plane acceleration of the floor, respectively. From Figure 8 (a), it can be observed that the natural frequency stays stable in range of 7.5 to 8.0 Hz regardless of the out-of-plane maximum acceleration, with an average value of 7.82 Hz. Moreover, the results calculated from the observed records of accelerometer P1 shows little difference with that of P2. Meanwhile, in Figure 8 (b), although the damping ratio performs variability in low out-of-plane maximum acceleration of the floor, which represents low level of earthquake, there is still a tendency that the damping ratio increases as the out-of-plane maximum acceleration of the floor increases.



(a)Natural frequency **(b)Damping ratio**

Figure 8. System identification results by curve fitting

5.IDENTIFICATION OF NATURAL FREQUENCY AND DAMPING RATIO USING FDD METHOD

This section shows system identification results using FDD method.

5.1 SYSTEM IDENTIFICATION METHOD

FDD is an output-only method proposed by Brincker et al. [Brincker et al., 2000]. In a specific system, if the power special density (PSD) matrices of the input and output are denoted as $G_{xx}(j\omega)$ and $G_{yy}(j\omega)$, respectively, the following equation holds:

$$G_{yy}(j\omega)=\overline{H}(j\omega)G_{xx}(j\omega)H^{\mathrm{T}}(j\omega) \tag{5}$$

Where, j is the imaginary unit, ω is the circular natural frequency, $H(j\omega)$ represents the frequency response function (FRF) matrix, and $\overline{H}(j\omega)$ and $H^{\mathrm{T}}(j\omega)$ represent the conjugate and transpose of $H(j\omega)$, respectively. After some mathematical operations, (5) can be expressed as the equation below:

$$G_{yy}(j\omega_i)=U_iS_iU_i^{\mathrm{H}} \tag{6}$$

Where, $U_i = [u_{i1}, u_{i2}, \ldots, u_{im}]$ is a unitary matrix with the singular vector u_{ij}, S_i is a diagonal matrix that stores the singular value (SV) sij, and H represents the conjugate transpose of the matrix. Next, a boundary pass filter (BPF) is applied to the first peak of the SV curve, and the inverse Fourier transform result, so called the impulse response function (IRF), is considered as the free vibration time history of a SDOF system. Using the least squares method, the circular natural frequency ω and damping ratio b are identified from this IRF and the free vibration time history curve of the SDOF by (7), and the natural frequency f is obtained from ω.

$$y=Ce^{-b\omega t}\sin(\sqrt{1-b^2}\omega t+\theta) \tag{7}$$

The observation records are collected between 0:00:00 and 0:08:00 a.m. of nine days shown in Table 2. Then, the record of every 8 minutes (480 seconds) is divided into 40 ensembles, and the SV is obtained by the average of these 40 ensembles. These measurements are performed under non-load and non-seismic conditions.

Table 2. Date and time of observation records using FDD method

year	month	day	time
2025	1	10, 20, 30	0:00:00~0:08:00
	2	10, 20, 28	
	3	10, 20, 30	
	4	10, 20, 30	

5.2 SYSTEM IDENTIFICATION RESULTS

Figure 9 shows the SV obtained from the observation records on January 10 as an example, with a BPF applied to the first peak. After the system identification process mentioned in Chapter 5.1, the estimated natural frequency of this record is 8.16 Hz and damping ratio is 3.93 %. Figure 10 shows a comparison between the time history obtained by IFFT to the SV curve and the free vibration of SDOF system with a natural frequency of 8.16 Hz and damping ratio of 3.93 %.

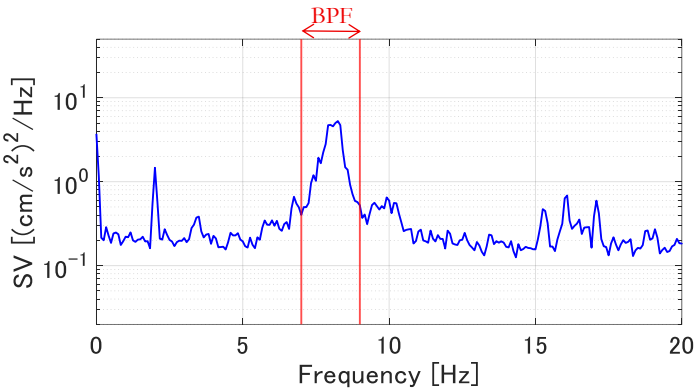


Figure 9. An Example of a Singular Values

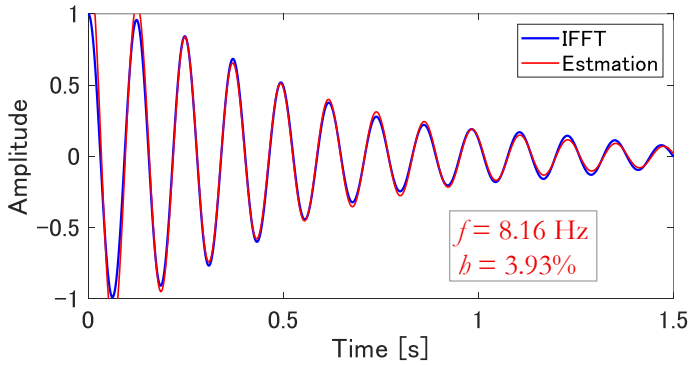
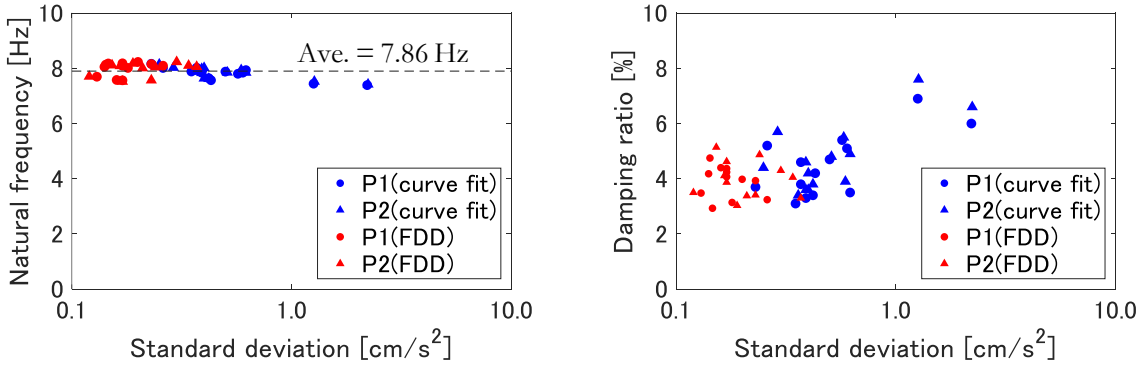


Figure 10. Comparison of free vibration waveforms

The system identification results of all observation records are summarized in Figure 11,whose horizontal axis represents the standard deviation of the acceleration of the partition wall. In Figure 11(a), the natural frequencies obtained by the curve fitting method and the FDD method are almost identical, with an average value of 7.86 Hz. While as shown in Figure 11(b), the damping ratios calculated by FDD method are between 3% and 5%, with a small standard deviation. However, the curve fitting method, which obtains a large standard deviation, resulted in larger damping ratio.



(a)Natural frequency **(b)Damping ratio**

Figure 11. System identification results by FDD

6.CONCLUSION

In this study, we analyze the response acceleration records of a partition wall installed in J2-3 building and conduct system identification to these records by two different methods, curve fitting and FDD. The findings are shown below.

i. In the in-plane direction, the acceleration amplification of a partition wall is approximately equal to 1 regardless of the earthquake, while in the out-of-plane direction, the acceleration amplification decreases as the floor acceleration increases. Furthermore, there is no difference between the acceleration amplification calculated from the records of accelerometers P1 and P2 in both the in-plane and out-of-plane directions.

ii. By curve fitting method, the system identification results of the natural frequencies in the out-of-plane direction of the partition wall are almost constant regardless of the maximum acceleration of the floor. On the other hand, damping ratio tend to increase as the maximum acceleration of the floor increases.

iii. When comparing the system identification results obtained by curve fitting method and FDD method, the estimated natural frequencies are almost the same. However, damping ratio obtained by FDD method are within the range of 3% to 5%, while those obtained by the curve fitting method vary widely.

REFERENCES

Brincker, R., Zhang, L., Andersen, P. [2000] *Output-only modal analysis by frequency domain decomposition*, Proceedings of the ISMA25 Noise and Vibration Engineering, 717-723

Gennaro, M., Crescenzo, P., Vittorio, C., Giuseppe, M., Pauline, L., Gaetano, M., [2014] *Seismic performance evaluation of plasterboard partitions via shake table tests*, Bulletin of Earthquake Engineering, Volume 12, 1657–1677

Kikuchi, T., Fujimori, S., Takeuchi, T., Wada, A. [2014] *Design of Seismic Isolated Tall Building with High Aspect-Ratio*, International Journal of High-Rise Buildings, Vol 3, No 1, 1-8

Luigi, F., Bianca, B., Raffaele, L. [2019] *Evaluation of seismic dynamic behaviour of drywall partitions, façades and ceilings through shake table testing*, Engineering Structures, Volume 180, 103-123

Matsuda, K., Kasai, K., Yamagiwa, H., Sato, D. [2012] *Responses of Base-Isolated Buildings in Tokyo during the 2011 Great East Japan Earthquake*, 15th World Conference on Earthquake Engineering, No. 5024

Screw Connections Between Gypsum Panels and CFS Profiles: Experimental Evaluation of Shear Response

Vito D'Addesa[1], Alessandro Prota[1], Luigi Fiorino[1], Marco Garofalo[2], Ghislain Rivron[3], Dominik Herfurth[3] and Raffaele Landolfo[1]

[1] Department of Structures for Engineering and Architecture, University of Naples "Federico II"
Via Forno Vecchio 36, 80134, Naples, Italy
e-mail: {vito.daddesa,alessandro.prota,lfiorino,landolfo}@unina.it
[2] Knauf di Knauf S.r.l S.a.s, Via Livornese 20, 56040, Castellina Marittima (PI), Italy
e-mail: marco.garofalo@knauf.com
[3] Knauf Gips KG, Am Bahnhof 7, 97346 Iphofen, Germany
e-mail: {ghislain.rivron, dominik.herfurth}@knauf.com

Abstract. Drywall partitions can be significantly affected by earthquake-induced lateral loads, although they are typically not designed to resist seismic actions. Under such conditions, the mechanical behaviour of screw connections between cold-formed steel (CFS) profiles and gypsum panels plays a crucial role in the overall response of partition walls. This study presents an experimental investigation on the shear behaviour of these connections, including both monotonic and cyclic shear tests. The focus is on the most common configuration, in which screws are inserted perpendicular to the interface between panels and profiles. Shear tests were performed on connections with one gypsum panel per side, as well as configurations with two panels per side, under both monotonic and cyclic loading conditions. A comparative analysis was carried out to evaluate the influence of panel arrangement. In parallel, material tests were conducted to characterize the mechanical properties of the individual components, including tensile and bending tests on screws, and interaction tests such as gypsum embedment and screw head pull-through. The aim of this work is to provide a comprehensive understanding of connection behaviour under shear loading, thereby supporting the development of more accurate models and design approaches for drywall systems.

Keywords: Cold-formed steel, Gypsum panels, Lightweight steel, Screw connections, Shear tests.

Classified as Internal and General Business

1. INTRODUCTION

Non-structural architectural elements are often susceptible to considerable damage during seismic events. This has led to a growing need for non-structural components that are specifically certified to withstand seismic forces. The primary goal is to minimize the risk to human life associated with the partial or total failure of these elements. Economic factors are also significant, as non-structural components represent a substantial portion of a building's total construction cost. According to Whittaker and Soong [2003], post-earthquake repair costs for finishes and fixtures in non-structural elements frequently exceed those for the structural system. Within this framework, assessing the seismic performance of drywall partitions, among the most critical non-structural elements, becomes particularly important.

This research focuses on an experimental study of the shear behaviour of screw connections between gypsum panels and cold-formed steel (CFS) profiles, which strongly influence the in-plane performance of drywall partitions. Both monotonic and cyclic loading tests were performed, with the focus on the most common configuration, in which screws are placed perpendicular to the interface between panels and profiles. Shear tests were performed on connections with one gypsum panel per side, as well as configurations with two panels per side, under both monotonic and cyclic loading conditions. Additionally, component-level tests were carried out to identify the key parameters affecting the connection's shear response. The results will enable either the development of an analytical model for predicting the shear behaviour of gypsum-to-CFS connections or the verification of existing analytical approaches.

2. SHEAR BEHAVIOUR OF THE CONNECTION BETWEEN GYPSUM PANEL AND CFS PROFILE

Drywall partitions are typically built using cold-formed steel (CFS) studs and tracks that form a frame, generally sheathed with gypsum panels on both faces. The studs usually have a C-shaped cross-section and are equally spaced with a spacing between 300 mm and 600 mm, with their ends connected to U-shaped track profiles. Standard gypsum panels used for these systems are about 12.5 mm thick and are fixed to the steel frame with self-tapping screws, typically up to 3.5 mm in diameter. Figure 1 illustrates a representative drywall partition layout.

As non-structural components, these partitions must possess sufficient ductility to accommodate lateral movements imposed by the surrounding structure. The current edition of the second-generation Eurocode 8 [CEN prEN1998-1-2, 2024] specifies allowable storey drift limits at Damage Limitation Limit State: 0.35% for buildings with brittle ancillary elements attached, and 1.00% for buildings with ductile ancillary elements, or where such elements are installed so as not to interfere with structural deformations, or in buildings without non-structural elements. Within this framework, drywall partitions can be considered ductile elements [Pali et al., 2018].

From a seismic performance perspective, the in-plane behaviour of drywall partitions is usually governed by the shear performance of the gypsum panel-to-CFS profile screw connections. While the current edition of the second-generation Eurocode 5 [CEN prEN 1995-1-1, 2024] provides equations for evaluating the shear capacity of wood panel-to-steel plate connections, no analytical formulation is presently available in European standards for gypsum panel-to-steel plate connections. When a gypsum panel-to-CFS profile screw connection is subjected to shear loading, different failure mechanisms may occur, potentially involving the screw, the panel, and the CFS profile. These include screw tilting, screw bending, screw head pull-through, screw pull-out, edge tearing of the panel, and embedment of the CFS profile. Any analytical

approach aimed at predicting such behaviour must account for all these possible modes, making component-level testing, alongside full connection shear tests.

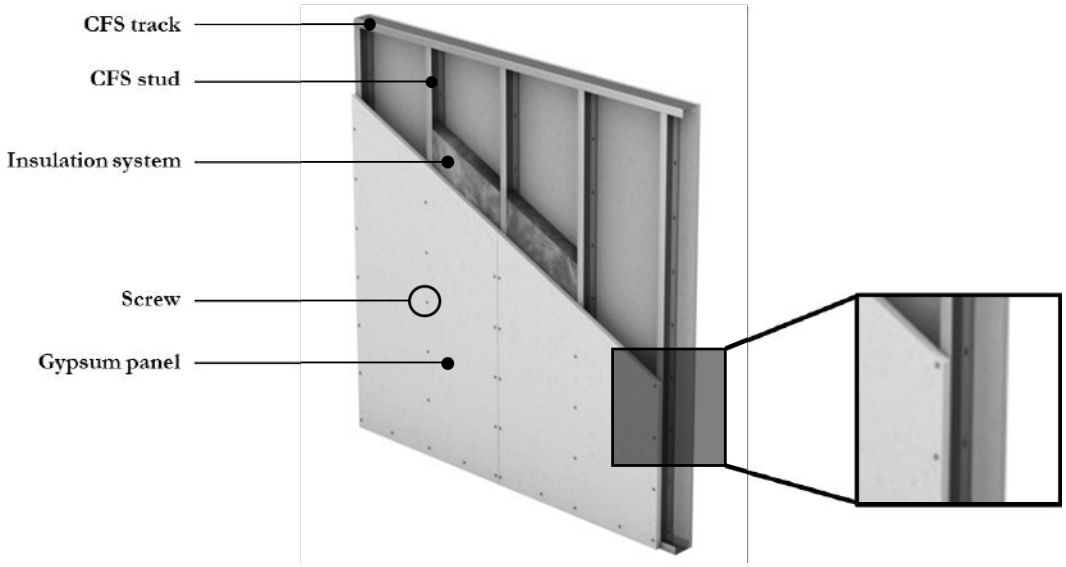


Figure 1. Typical drywall partition configuration

3. EXPERIMENTAL PROGRAM

The experimental program consisted of shear tests on screw connections between gypsum panels and CFS profiles, aimed at experimentally characterizing these connections within typical drywall partitions. Component-level tests were also carried out to determine the overall shear behaviour of the gypsum panel-to-CFS profile screw connections.

3.1 COMPONENT-LEVEL TESTS

Since the overall shear behaviour of connections between gypsum panels and CFS profiles results from the interaction of different resisting mechanisms, component-level tests were carried out to support the development of an analytical assessment method.. The testing program included material tests (screw tensile tests and screw bending tests) as well as interaction tests (gypsum embedment tests and screw head pull-through tests). Table 1 presents the number of nominally identical tests performed for each test type, along with the corresponding reference standards applied. In Figure 2, a schematic representation of the assembly of each type of test is reported. The screws involved in the tests were self-tapping screws with a nominal diameter equal to 3.5 mm and an 8 mm countersunk flat head. The gypsum panels were 12.5 mm thick and the CFS profiles were 0.60 mm thick.

Table 1. Component-level tests program

Test typology	Number of nominally identical tests	Reference standard
Screw tensile test	4	ISO 898-1:2013 [2013]
Screw bending test	6	ASTM F1575/F1575M-21 [2021]
Gypsum embedment test	4	EN 383:2007 [2007] (1)
Screw head pull-through test	4	EN 1383:2016 [2016] (1)

(1) Standard for wood panels.

Figure 3 shows the curves representing the main component-level tests performed. Figure 3a represents the stress-strain curve from screw tensile tests, with the stress defined as the applied load divided by the cross-section associated to the minor diameter equal to 2.2 mm. The average value of the maximum stress reached is equal to 1457 MPa, with a coefficient of variation equal to 0.02. Figure 3b represents the load-displacement curves from the screw bending tests. The average value of the maximum load reached is equal to 532 N, with a coefficient of variation equal to 0.05. Figure 3c represents the stress-displacement curve from gypsum embedment tests, with the stress defined as the applied load divided by the contact area, that is, the product of the screw nominal diameter and the gypsum panel thickness. The average value of the maximum stress reached up to a displacement equal to 5 mm (embedment strength as per EN 383:2007 [2007]) is equal to 7.31 MPa, with a coefficient of variation equal to 0.04, and the average value of the foundation modulus is equal to 270 N/mm, with a coefficient of variation equal to 0.20. Figure 3d represents the load-displacement curve from screw head pull-through tests. The average value of the maximum load reached is equal to 454 N, with a coefficient of variation equal to 0.05.

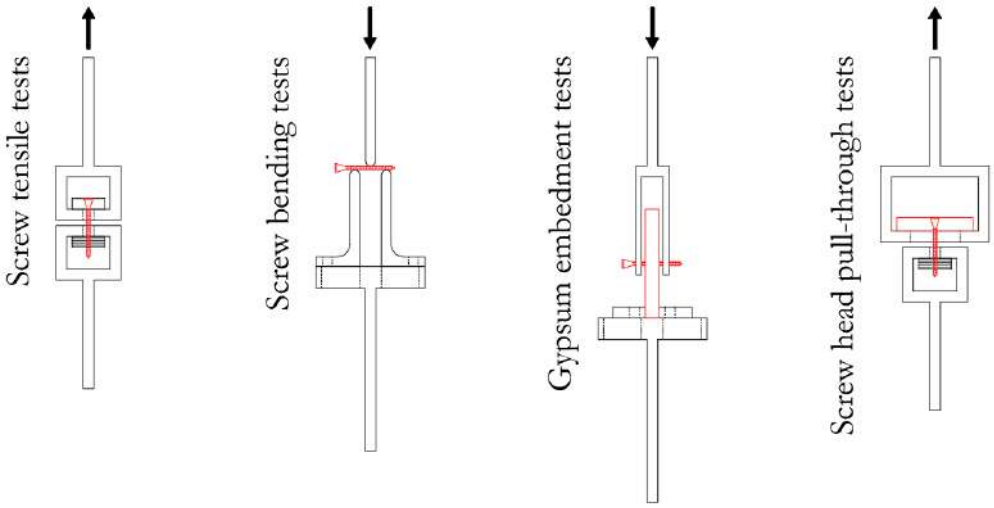
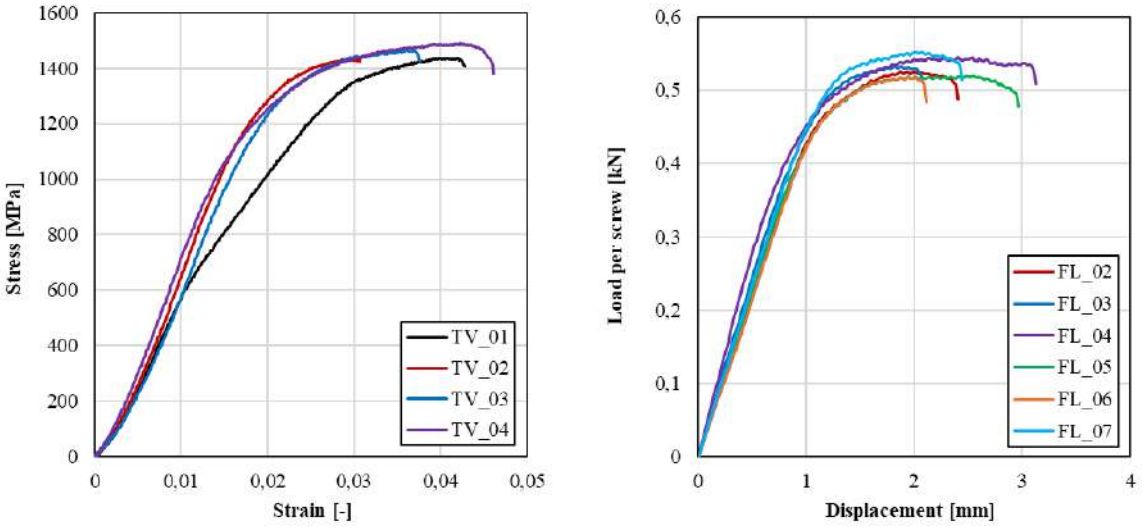
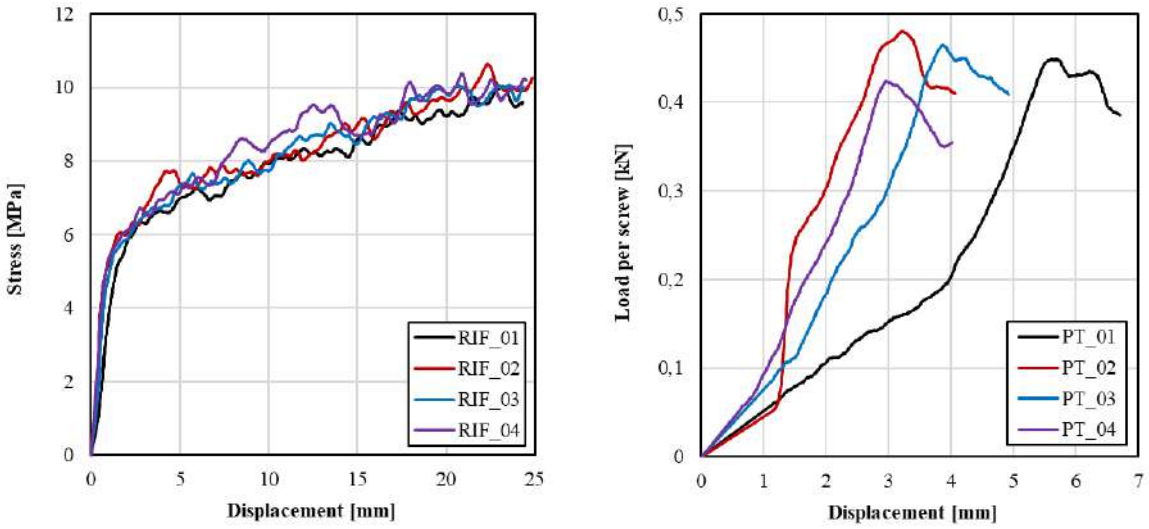


Figure 2. Component-level tests assembly



a) Screw tensile tests **b) Screw bending tests**

Figure 3. Component-level tests (1/2)



c) Gypsum embedment tests **d) Screw head pull-through tests**

Figure 3. Component-level tests (2/2)

3.2 SHEAR TESTS ON CONNECTIONS

3.2.1 Experimental program, specimen typologies, loading protocol and instrumentation

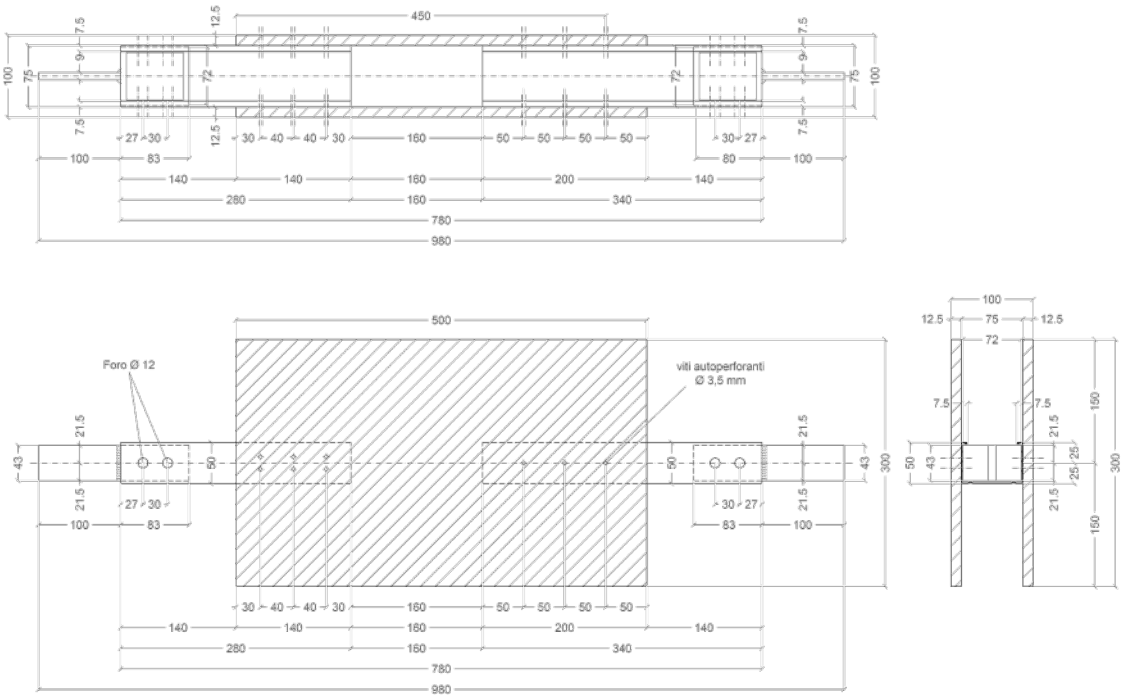
A total of 8 shear tests (4 monotonic and 4 cyclic) were carried out on 8 nominally identical specimens with one panel per side, while a total of 6 shear tests (3 monotonic and 3 cyclic) were carried out on 6 nominally identical specimens with two panels per side. The tests were performed in accordance with the EN 520:2009 [2009] standard, originally intended for connections between wooden elements and gypsum panels, adapted to the specific case addressed in this study.

Figure 4 illustrates the assembly of the gypsum panel-to-CFS profile screw connections specimens. Each specimen consisted of two CFS profiles sheathed on both flanges with either one or two 12.5 mm thick gypsum-based panels per side. The fasteners used were 3.5 mm diameter self-tapping screws, with an 8 mm countersunk flat head. The profiles, representative of partition stud sections, were lipped channel stud sections measuring 75 × 50 × 6 × 0.6 mm (web depth × flange size × lip size × thickness) and were spaced 160 mm apart. The profile at the top of the specimen measured 340 mm in length, while the one at the bottom measured 280 mm. The upper side of the panel was fixed to the flange of the profile with three screws (connections under test) having spacing and edge distance parallel to the loading direction equal to 50 mm. The lower side was fixed with six screws (overstrength connections) arranged in two rows, 30 mm from the edge parallel to the loading direction, 40 mm apart in the parallel direction, and 15 mm apart in the perpendicular direction. The total specimen length was 980 mm.

Monotonic tests were performed by subjecting the connection specimens to progressive displacements up to failure. The displacement-controlled test procedure involved displacements at a rate of 0.15 mm/s and the data were recorded with a sampling frequency of 10 Hz. Cyclic tests were carried out by adopting a loading protocol known as "CUREE ordinary ground motions reversed cyclic load protocol" developed for wood-frame structures by Krawinkler et al. [2001]. The cyclic loading test protocol consists of a series of stepwise increasing deformation cycles (see Figure 5). The displacement amplitudes of each cycle are defined starting from a reference deformation $\Delta = \gamma\Delta_m$, where the values of Δ_m are calculated on the basis of the monotonic test results, as the average conventional ultimate displacement (d_u) corresponding to a load equal to 80% of the maximum load on the post-peak branch of the response curve and γ is assumed equal to 0.60.

In particular, Δ was set equal to 7.30 mm for cyclic tests on specimens with one gypsum panel per side and to 13.30 mm for cyclic tests on specimens with two gypsum panels per side. The cyclic tests were performed with a constant frequency equal to 0.25 Hz and the data were recorded with a sampling frequency of 25 Hz.

Two linear variable differential transducers (LVDTs) with a maximum displacement of 50 mm were used for measuring the relative displacements between panels and steel profiles at the specimen top sides.



a) Geometrical dimensions of the specimen with one panel per side

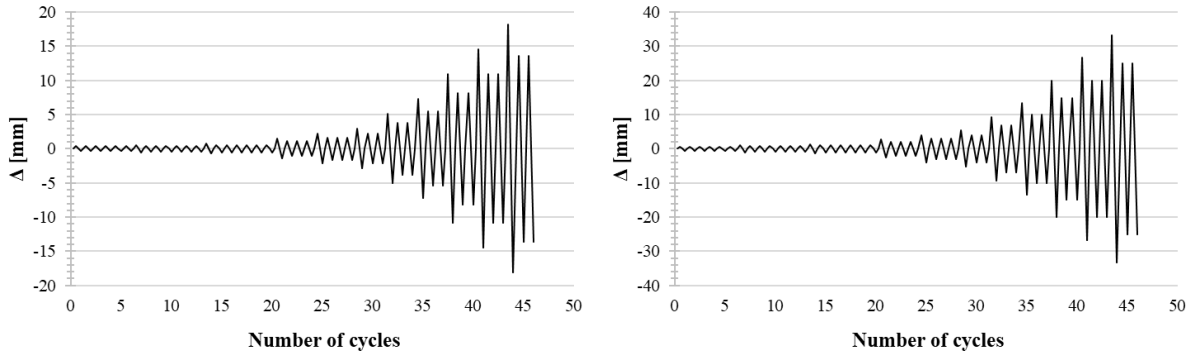


b) Specimen with one panel per side



c) Specimen with two panels per side

Figure 4. Shear tests assembly



a) Specimen with one panel per side **b) Specimen with two panels per side**

Figure 5. Cyclic loading protocol

3.2.2 Test results

The analysis of the test results was conducted by referring to the load resisted by a single screw, obtained by dividing the total measured load by six (i.e., total number of tested screws per specimen), and thus deriving an average unit load. Figure 6 illustrates the load–displacement curves obtained from monotonic tests on connections with one or two panels per side, whereas Figure 7 presents the typical response under cyclic loading, which exhibits a fully nonlinear and pinched hysteretic behaviour. The backbone curves derived from all cyclic tests are reported in Figure 8.

In all cases, failure of the connection was governed by screw tilting in combination with screw head pull-through.

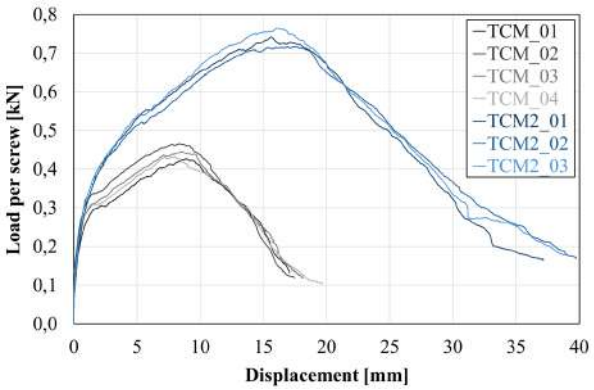


Figure 6. Monotonic shear tests on connections with one and two panels per side (the resistance of connections with two panels per side is 68% higher compared to that of connections with one panel per side)

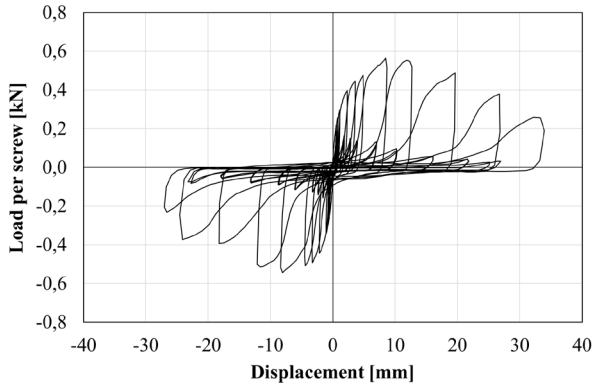


Figure 7. Typical load-displacement curve from a cyclic test on connections

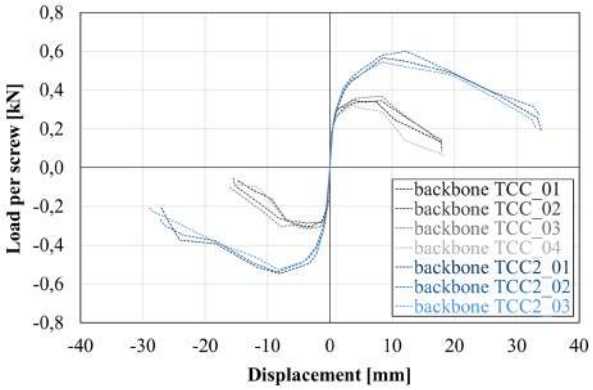


Figure 8. Backbone curves from cyclic shear tests on connections with one and two panels per side (the resistance of connections with two panels per side is 70% higher compared to that of connections with one panel per side)

Parameters used to describe the experimental behaviour of a monotonic test are: maximum load (F_p); displacement corresponding to F_p (d_p); conventional elastic limit load (F_e) equal to $0.40F_p$; displacement corresponding to F_e on the pre-peak branch of the response curve (d_e); conventional elastic stiffness (k_e) equal to F_e/d_e; conventional ultimate load (F_u) equal to $0.80F_p$; conventional ultimate displacement (d_u) corresponding to F_u on the post-peak branch of the response curve; maximum ductility (μ) equal to d_u/d_e; dissipated energy (E) defined as the area under the response curve for displacements not more than d_u. Table 2 shows the results from monotonic tests with one panel per side, while Table 3 shows the results from monotonic tests with two panels per side. The same set of parameters was adopted to describe the behaviour of cyclic tests, which were evaluated on both positive and negative backbone curves and expressed as the average between positive and negative curves. Table 4 shows the results from cyclic tests with one panel per side, while Table 5 shows the results from cyclic tests with two panels per side. In addition to the average parameters evaluated on the backbone curves, Table 4 and Table 5 also report the dissipated cyclic energy E_c, defined as the sum of area inside each cycle.

Based on the results, the average value of the maximum load is equal to 0.44 and 0.74 kN for the monotonic tests, and equal to 0.32 and 0.55 kN for the cyclic tests, in case of one panel per side and two panels per side, respectively. These results indicate that increasing from one to two panels per side leads to a comparable increasing in resistance, equal to about 68% in monotonic tests and 70% in cyclic tests. In both configurations, however, the resistance measured under cyclic loading is approximately 25% lower than that obtained in the corresponding monotonic tests. This result can be justified by the negative effect due to cyclical reversal of the screw tilting.

For the elastic stiffness, the average value is 0.73 and 0.36 kN/mm for the monotonic tests, and equal to 0.77 and 0.40 kN/mm for the cyclic tests, in case of one panel per side and two panels per side, respectively. These results show that increasing from one to two panels per side produces a comparable reduction in elastic stiffness, equal to about 50% in monotonic tests and 48% in cyclic tests. In both configurations, however, the elastic stiffness recorded under cyclic loading is slightly higher, by approximately 10%, than that obtained in the corresponding monotonic tests.

For the dissipated energy, the average value is 4.49 and 13.35 kNmm for the monotonic tests, and equal to 2.78 and 8.85 kNmm for the cyclic tests, in case of one panel per side and two panels per side, respectively. These results show that increasing from one to two panels per side produces a significant increase in dissipated energy, equal to about 198% in monotonic tests and 218% in cyclic tests. In both configurations,

however, the dissipated energy measured under cyclic loading is approximately 35% lower than that obtained in the corresponding monotonic tests.

With regard to the dissipated cyclic energy, the average value is 20.30 and 47.25 kNmm, in case of one panel per side and two panels per side, respectively. These results show that increasing from one to two panels per side produces a significant increase in dissipated cyclic energy equal to about 133%.

Table 2. Monotonic tests on connections with one panel per side

LABEL	F_e [kN]	d_e [mm]	k_e [kN/mm]	F_p [kN]	d_p [mm]	F_u [kN]	d_u [mm]	μ [-]	E [kNmm]
TCM_01	0.17	0.28	0.61	0.43	8.86	0.34	12.30	43.93	4.35
TCM_02	0.19	0.21	0.89	0.47	8.39	0.37	11.52	54.86	4.58
TCM_03	0.18	0.23	0.77	0.44	8.61	0.36	12.11	52.65	4.53
TCM_04	0.17	0.27	0.64	0.43	7.75	0.34	12.37	45.81	4.49
min	0.17	0.21	0.61	0.43	7.75	0.34	11.52	43.93	4.35
max	0.19	0.28	0.89	0.47	8.86	0.37	12.37	54.86	4.58
average	0.18	0.25	0.73	0.44	8.40	0.35	12.08	49.31	4.49
st.dev.	0.007	0.033	0.129	0.018	0.475	0.014	0.386	5.264	0.101
av.–st.dev.	**0.17**	**0.21**	**0.60**	**0.42**	**7.93**	**0.34**	**11.69**	**44.05**	**4.39**
av.+st.dev.	**0.18**	**0.28**	**0.86**	**0.46**	**8.88**	**0.37**	**12.46**	**54.58**	**4.59**
c.o.v.	0.040	0.133	0.177	0.040	0.057	0.040	0.032	0.107	0.023

Table 3. Monotonic tests on connections with two panels per side

LABEL	F_e [kN]	d_e [mm]	k_e [kN/mm]	F_p [kN]	d_p [mm]	F_u [kN]	d_u [mm]	μ [-]	E [kNmm]
TCM2_01	0.30	0.93	0.32	0.74	15.60	0.59	21.84	23.48	13.14
TCM2_02	0.29	0.69	0.42	0.72	17.65	0.57	23.16	33.57	13.71
TCM2_03	0.31	0.86	0.36	0.76	16.20	0.61	21.50	25.00	13.21
min	0.29	0.69	0.32	0.72	15.60	0.57	21.50	23.48	13.14
max	0.31	0.93	0.42	0.76	17.65	0.61	23.16	33.57	13.71
average	0.30	0.83	0.36	0.74	16.48	0.59	22.17	27.35	13.35
st.dev.	0.009	0.123	0.049	0.024	1.054	0.019	0.877	5.436	0.308
av.–st.dev.	**0.29**	**0.70**	**0.31**	**0.72**	**15.43**	**0.57**	**21.29**	**21.91**	**13.05**
av.+st.dev.	**0.31**	**0.95**	**0.41**	**0.76**	**17.54**	**0.61**	**23.04**	**32.79**	**13.66**
c.o.v.	0.032	0.149	0.134	0.032	0.064	0.032	0.040	0.199	0.023

Table 4. Cyclic tests on connections with one panel per side

LABEL	F_e [kN]	d_e [mm]	k_e [kN/mm]	F_p [kN]	d_p [mm]	F_u [kN]	d_u [mm]	μ [-]	E [kNmm]	E_c [kNmm]
TCC_01	0.13	0.17	0.81	0.32	5.89	0.26	8.56	52.83	2.49	17.18
TCC_02	0.13	0.15	0.86	0.32	3.71	0.25	10.30	69.15	3.03	21.29
TCC_03	0.14	0.19	0.73	0.34	5.94	0.27	10.42	55.97	3.23	23.08
TCC_04	0.13	0.18	0.69	0.32	3.49	0.25	8.39	45.58	2.38	19.66
min	0.13	0.15	0.69	0.32	3.49	0.25	8.39	45.58	2.38	17.18
max	0.14	0.19	0.86	0.34	5.94	0.27	10.42	69.15	3.23	23.08
average	0.13	0.17	0.77	0.32	4.76	0.26	9.42	55.88	2.78	20.30
st.dev.	0.004	0.017	0.074	0.010	1.340	0.008	1.094	9.858	0.409	2.507
av.–st.dev.	**0.13**	**0.15**	**0.70**	**0.31**	**3.42**	**0.25**	**8.32**	**46.03**	**2.37**	**17.79**
av.+st.dev.	**0.13**	**0.19**	**0.85**	**0.34**	**6.09**	**0.27**	**10.51**	**65.74**	**3.19**	**22.81**
c.o.v.	0.032	0.101	0.096	0.032	0.282	0.032	0.116	0.176	0.147	0.123

Table 5. Cyclic tests on connections with two panels per side

LABEL	F_e [kN]	d_e [mm]	k_e [kN/mm]	F_p [kN]	d_p [mm]	F_u [kN]	d_u [mm]	μ [-]	E [kNmm]	E_c [kNmm]
TCC2_01	0.22	0.58	0.38	0.55	8.28	0.44	18.96	32.43	9.12	47.83
TCC2_02	0.23	0.58	0.39	0.57	10.35	0.46	17.86	30.55	8.75	48.66
TCC2_03	0.21	0.50	0.43	0.54	8.23	0.43	18.68	37.29	8.67	45.26
min	0.21	0.50	0.38	0.54	8.23	0.43	17.86	30.55	8.67	45.26
max	0.23	0.58	0.43	0.57	10.35	0.46	18.96	37.29	9.12	48.66
average	0.22	0.55	0.40	0.55	8.95	0.44	18.50	33.43	8.85	47.25
st.dev.	0.007	0.049	0.026	0.018	1.211	0.014	0.568	3.475	0.240	1.775
av.–st.dev.	**0.21**	**0.51**	**0.38**	**0.54**	**7.74**	**0.43**	**17.93**	**29.95**	**8.61**	**45.47**
av.+st.dev.	**0.23**	**0.60**	**0.43**	**0.57**	**10.16**	**0.46**	**19.07**	**36.90**	**9.09**	**49.02**
c.o.v.	0.032	0.088	0.064	0.032	0.135	0.032	0.031	0.104	0.027	0.038

4.CONCLUSIONS

The research found that:

- the in-plane lateral performance of drywall partitions is largely controlled by the shear behaviour of gypsum panel-to-CFS stud connections, which can be determined through experimental testing;
- current European standards do not provide a procedure for calculating the shear strength of such joints, highlighting the need for a dedicated analytical method;

- the development and validation of such a method require both shear tests on full connections and component-level tests to capture the contribution of individual failure mechanisms;

- test results indicate that replacing monotonic loading with cyclic loading decreases the resistance of gypsum panel-to-CFS profile screw connections by about 25%, increases the elastic stiffness by about 10%, and decreases the dissipated energy by about 35%;

- results also show that switching from a connection with one panel per side to a connection with two panels per side leads to an increase of 68% and 70% in terms of resistance, a decrease of 50% and 48% in terms of elastic stiffness, and an increase of 198% and 218% in terms of dissipated energy, under monotonic and cyclic loading, respectively. Furthermore, moving from a connection with one panel per side to a connection with two panels per side leads to an increase of 133% in terms of dissipated cyclic energy.

REFERENCES

ASTM F1575/F1575M [2021] *Standard Test Method for Determining Bending Yield Moment of Nails*, ASTM International, West Conshohocken, Pennsylvania.

CEN EN 383 [2007] *Timber structures - Test methods - Determination of embedding strength and foundation values for dowel type fasteners*, European Committee for Standardization, Brussels.

CEN EN 520 [2009] *Gypsum plasterboards - Definitions, requirements and test methods*, European Committee for Standardization, Brussels.

CEN EN 1383 [2016] *Timber structures - Test methods - Pull-through resistance of timber fasteners*, European Committee for Standardization, Brussels.

CEN prEN 1995-1-1 [2024] *Eurocode 5: Design of timber structures Part 1-1: general - General rules and rules for buildings*, European Committee for Standardization. Brussels.

CEN prEN 1998-1-2 [2024] *Eurocode 8: Design of structures for earthquake resistance Part 1-2: Rules for new buildings*, European Committee for Standardization. Brussels.

ISO 898-1 [2013] *Mechanical properties of fasteners made of carbon steel and alloy steel - Part 1: Bolts, screws and studs with specified property classes - Coarse thread and fine pitch thread*, International Organization for Standardization, Vernier.

Krawinkler, H., Parisi, F., Ibarra, L., Ayoub, A., Medina, R., [2001] "Development of a Testing Protocol for Woodframe Structures," *Report W-02*, CUREE/Caltech woodframe project. Richmond, California.

Pali, T., Macillo, V., Terracciano, M.T., Bucciero, B., Fiorino, L., Landolfo, R. [2018] "In-plane quasi-static cyclic tests of nonstructural lightweight steel drywall partitions for seis-mic performance evaluation," *Earthquake Engineering & Structural Dynamics*, 47(6), 1566-1588.

Whittaker, A.S., Soong, T.T. [2003] "An overview of nonstructural component research at three U.S. earthquake engineering research centers," *Proceedings of seminar on seismic design, performance, and retrofit of nonstructural components in critical facilities*. Redwood City, California.

Seismic Assessment of Thin Masonry-Infilled RC Frames via a Coupled In-Plane/Out-of-Plane Macro-Model

Ahmed Mabrouk[1], Marco Donà[1,2,3], Luca Tosolini[1], Marco Gaspri[1], and Francesca da Porto[1]

[1] Department of Geosciences
University of Padova, Via Gradenigo 6, 35131, Padova, Italy
e-mail: ahmedhishamahmedsabryhassanein.mabrouk@phf.unipd.it
[2] Department of Cultural Heritage
University of Padova, Piazza Capitaniato 7, 35139 Padova, Italy
[3] Department of Information Engineering
University of Padova, Via Gradenigo 6/b, 35131 Padova, Italy
e-mail: luca.tosolini@phd.unpid.it , marco.gaspari.2@phd.unipd.it ,{marco.dona.1, francesca.daporto}@unipd.it

Abstract. Thin clay masonry infills are commonly employed in reinforced concrete (RC) frame buildings across the globe. Despite their widespread use, these elements exhibit a brittle response and engage in complex in-plane (IP) and out-of-plane (OOP) interaction under seismic loading—often leading to a significant increase in the structural vulnerability of infilled frames. Accurately representing this coupled behaviour remains a key challenge for seismic assessment and design. To address this, a new macro-modelling strategy is developed and implemented within the OpenSees-STKO framework. The proposed model aims to simulate the seismic response of infill panels by explicitly accounting for the interplay between IP and OOP actions. The infill is represented by four diagonal struts—two per diagonal—combined with a pair of lumped masses placed at the centre of the panel to reproduce inertial OOP demands. Each strut is divided into two beam-column elements, with a mid-span plastic hinge that governs the nonlinear coupling effects through a fibre-based section formulation. Model calibration and validation are carried out using a comprehensive set of experimental results on both unreinforced and retrofitted thin clay masonry panels. Once validated, the model is applied in a series of nonlinear time-history analyses as part of a parametric investigation involving different infill typologies and strengthening strategies. The outcomes highlight the model's capability to replicate critical IP/OOP interaction mechanisms, while also demonstrating the effectiveness of retrofitting solutions in mitigating adverse seismic effects.

Keywords: Clay masonry infill walls, thin infill walls, strengthened infill walls, combined IP/OOP interaction behaviour, Experimental calibration.

1. Introduction

Clay masonry infill walls are often used in reinforced concrete (RC) frame structures across many countries, including highly seismic regions such as Italy. Their use became increasingly common after World War II, with a marked rise in construction after 1961 and especially after 1981, driven by their ease of installation and thermal–acoustic advantages (Istat, 2011; INSYSME, 2014). Despite their prevalence, infill walls are typically treated as non-structural components and are often excluded from design considerations (Di Ludovico et al., 2016; Dolce & Goretti, 2015). This neglect has contributed to the seismic vulnerability of many RC buildings, as infill panels exhibit brittle behaviour and can suffer severe damage even under low-to-moderate earthquake intensities due to coupled in-plane (IP) and out-of-plane (OOP) interactions. Over the years, experimental and post-earthquake studies have repeatedly underscored the significant influence of infills on overall structural response (Masi et al., 2017; Verderame et al., 2014). Thin clay masonry panels are particularly susceptible to OOP collapse following prior IP cracking (Furtado et al., 2021; Ricci et al., 2018). To mitigate this, various strengthening solutions—such as FRP, TRM, and steel-based systems—have been developed to improve OOP capacity (Silva et al., 2016). However, deterioration induced by prior IP deformations remains a persistent issue, and current design codes provide limited guidance for modelling IP/OOP coupling. To bridge this gap, recent research has advanced macro-modelling approaches that integrate OOP mass effects, nonlinear degradation mechanisms, and simplified truss or beam models requiring stepwise updates of material properties to reproduce IP–OOP interaction. These models achieve a practical balance between computational efficiency and accuracy, making them viable for large-scale simulations. Within this framework, the present study builds upon the fiber-based macro-model proposed by Donà et al. (2021), implementing and recalibrating it in the STKO–OpenSees environment. The model is validated using experimental data from thin clay masonry panels, both unreinforced and strengthened with TRM and FRM systems. Subsequently, nonlinear time-history (TH) analyses are performed on a representative RC frame in three configurations: (1) bare, (2) infilled, and (3) strengthened. The investigation focuses on thin masonry panels ($\leq$ 20 cm thick), which continue to characterize a significant portion of the European building stock despite the gradual transition toward more robust façade systems.

2. Modelling approach of infill wall and RC frame

The masonry infill walls are simulated using the macro-model developed by Donà et al. (2021), specifically formulated to capture the coupled IP and OOP behaviour of infill panels within RC frames. The model employs a multi-strut configuration, where each panel is represented by four diagonal struts—two along each diagonal—connected to the surrounding RC frame through pinned joints. Each strut is composed of two Beam With Hinges (BWH) elements, creating a central nonlinear hinge region where damage localizes. The hinges use fiber sections oriented along the OOP axis to reproduce the IP–OOP interaction. The fiber sections incorporate a compression-only trilinear hysteretic material, which reflects the brittle characteristics of clay masonry and allows simulation of stiffness degradation, strength deterioration, and residual resistance under cyclic and bidirectional loading. The OOP inertial mass of the panel is lumped at the midpoint of the struts, and EqualDOF constraints are imposed to synchronize nodal displacements, ensuring realistic dynamic coupling between the infill and frame. The geometric placement of the struts is determined based on the effective contact length between the infill and the surrounding frame, estimated from the relative stiffness of the masonry and adjacent RC members (Donà et al., 2021). Analytical formulations are used to derive the elastic properties of the struts, including the equivalent axial area A_{eq}, moment of inertia I_{eq}, and the diagonal modulus of elasticity $E_{m\theta}$. These parameters are initially obtained through mechanics-based assumptions and subsequently refined through calibration against experimental data. A schematic representation of the macro-model configuration is provided in Figure 2-1.

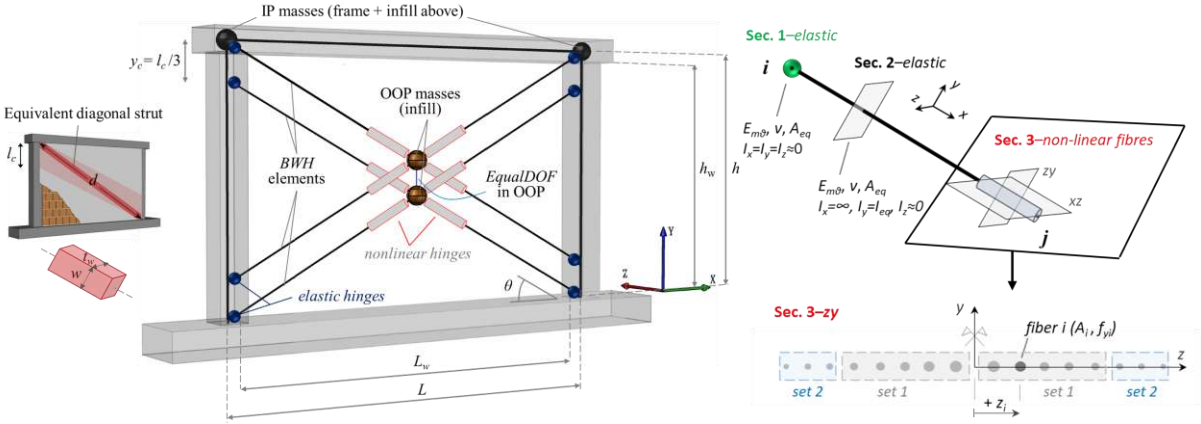


Figure 2-1: Donà et al, (2021) Macro-model of infill panel: a) general presentation and b) detail of the BWH element

The RC frame itself is modelled using force-based beam–column (FB–BC) elements with nonlinear fiber sections, capable of capturing the distributed plasticity and the moment–curvature response under seismic excitation. Each member is subdivided to represent the actual detailing of confined and unconfined concrete regions, particularly around beam–column joints. Concrete fibers adopt the Concrete02 material model, which incorporates strength and stiffness degradation, tension stiffening, and distinct confined–unconfined behaviour (Kent & Park, 1971; Mander et al., 1988). Steel reinforcement is represented using Steel02, which accounts for kinematic hardening and Bauschinger effects to realistically model cyclic degradation. A Gauss–Lobatto integration scheme with five integration points per element is applied, offering a balance between computational efficiency and accurate nonlinear response representation.

3. Infill macro-model calibration

The calibration process draws upon experimental data from two benchmark studies that investigated the coupled IP and OOP response of infilled RC frames. The first, conducted by Calvi and Bolognini (2001), tested unreinforced masonry (URM) panels subjected to cyclic IP loading followed by monotonic OOP loading, highlighting the pronounced reduction in OOP strength induced by prior IP damage. The second, by Minotto et al. (2021), examined strengthened panels incorporating three TRM/FRM systems—F, FB, and RBB—under a similar sequential loading protocol. In both studies, OOP tests were performed after three predefined IP drift levels: 0%, 0.5%, and 1.2%. The macro-model was calibrated for all panel configurations (URM, F, FB, and RBB); however, only the URM and F panels are discussed here, as they directly correspond to the configurations analyzed in the subsequent dynamic analyses.

The reimplementation and calibration of the Donà et al. (2021) model were carried out within the STKO–OpenSees environment to maintain consistent modelling assumptions and ensure smooth integration with the time-history analyses. The calibrated model effectively reproduced the distinctive responses of both URM and F panels, particularly the enhanced IP and OOP strength provided by the strengthening system (Figure 3-1). For the F configuration, the added plaster layer contributed to improved resistance, which the model successfully captured across varying levels of prior IP deformation. Based on the calibration outcomes, a set of displacement interaction domains was developed (Table 3-1), establishing the relationship between OOP capacity and IP drift for each panel type. These domains serve as the foundation for defining infill performance limit states, enabling the simulation of progressive OOP strength degradation under seismic loading. Overall, the calibration validated the model's ability to replicate realistic infill behaviour, confirming its suitability for the nonlinear dynamic analyses presented in the following chapter.

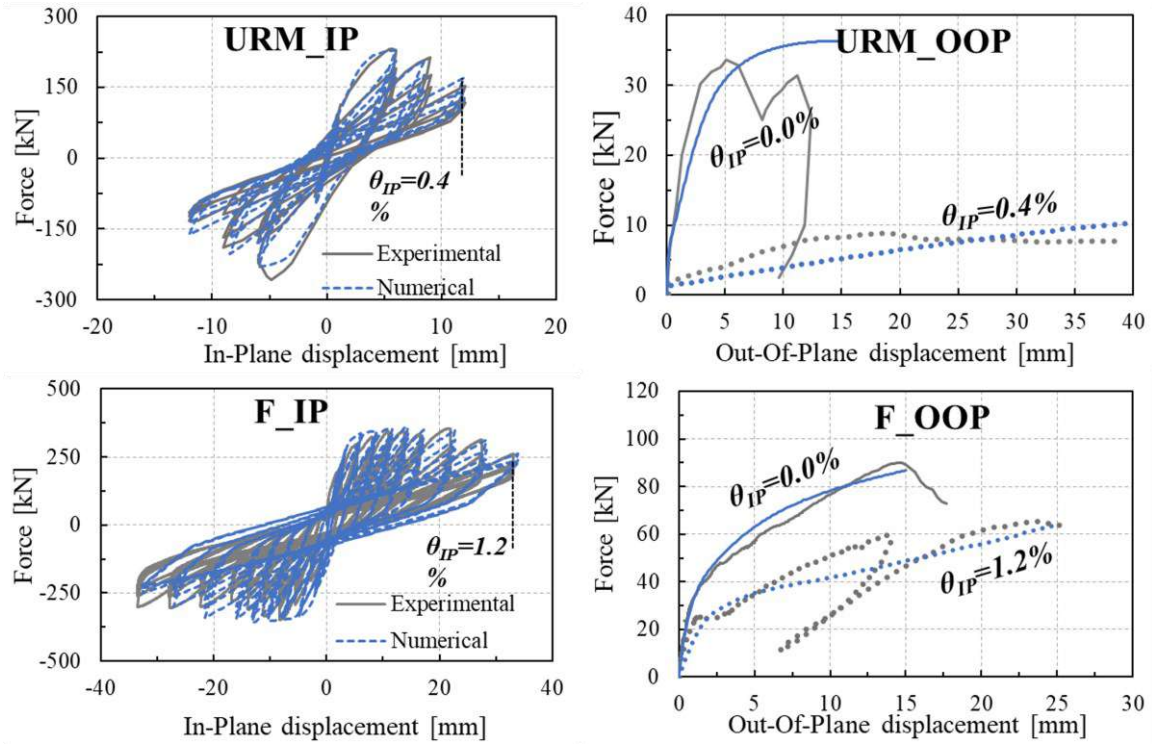


Figure 3-1: Experimental and numerical results: cyclic IP (left), and monotonic OOP (right) response

Table 3-1: IP drift values at limit states, and OOP displacements as a function of IP drift at OOP limit states

		URM	F
IP drift (θ_{IP}) [%]	(DLS, ULS_L, ULS_U)	0.3%, 0.5%, 1.0%	0.3%, 0.5%, 1.5%
	DLS	5.10	14.60
OOP disp. [mm]	ULS_L	$16.00\theta_{IP} + 6.4$	$6.25\theta_{IP} + 16.00$
	ULS_U	$30.00\theta_{IP} + 8.0$	$7.08\theta_{IP} + 17.5$

4. Assessment of infill macro-model through non-linear TH analysis

4.1 PRESENTATION OF CASE STUDY FRAME

The case study examines the seismic performance of a two-dimensional reinforced concrete (RC) frame model (Figure 4-1-a) representative of residential buildings constructed in Italy between the 1960s and 1980s, typically designed for gravity loads only. The structure consists of an eight-storey, three-bay RC frame with regular geometry in both plan and elevation. Detailed cross-sectional information can be found in Minotto (2019). Three configurations are analyzed: BF – bare frame without infills, URM – frame infilled with unreinforced masonry (hollow clay units), and F – frame infilled with panels strengthened using a fiber-reinforced plaster (F) system. Beams and columns are modeled using the force-based fiber section formulation described in Section 2. All frame variants share identical geometry, boundary conditions, and gravity loads, ensuring that any variation in response arises solely from the presence and characteristics of

the infill panels. The infills are assigned the calibrated properties derived in Section 3 and are present across all storeys and bays. For the nonlinear time-history (TH) analysis, seven bidirectional ground motion records were selected from the SIMBAD database. These records were scaled to achieve average compatibility with the Type 1 elastic response spectrum of Eurocode 8 (EC8), assuming a bedrock acceleration $ag = 0.25g$ and soil type B, corresponding to a peak ground acceleration of 0.3 g. The main characteristics of the selected accelerograms are summarized in Table 4-1, while their (mean) acceleration spectra are presented in Figure 4-1-b alongside the EC8 reference spectrum.

Table 4-1: Selected bidirectional natural records

ID	Earthquake	Date	M_w	Epicentral Distance [km]	Scale Factor X	Scale Factor Y
Acc. 1	Eastern Fukushima Prefecture	2011/04/11	6.5	26.24	1.30	1.38
Acc. 2	Imperial Valley	1979/10/15	6.5	24.68	1.59	1.48
Acc. 3	S. Suruga Bay	2009/08/10	6.2	25.38	0.60	0.97
Acc. 4	Friuli 1st shock	1976/05/06	6.4	21.72	0.79	0.72
Acc. 5	Eastern Fukushima Prefecture	2011/04/11	6.6	27.56	2.33	1.41
Acc. 6	Irpinia	1980/11/23	6.9	21.79	1.34	1.93
Acc. 7	Irpinia	1980/11/23	6.9	18.85	1.43	1.58

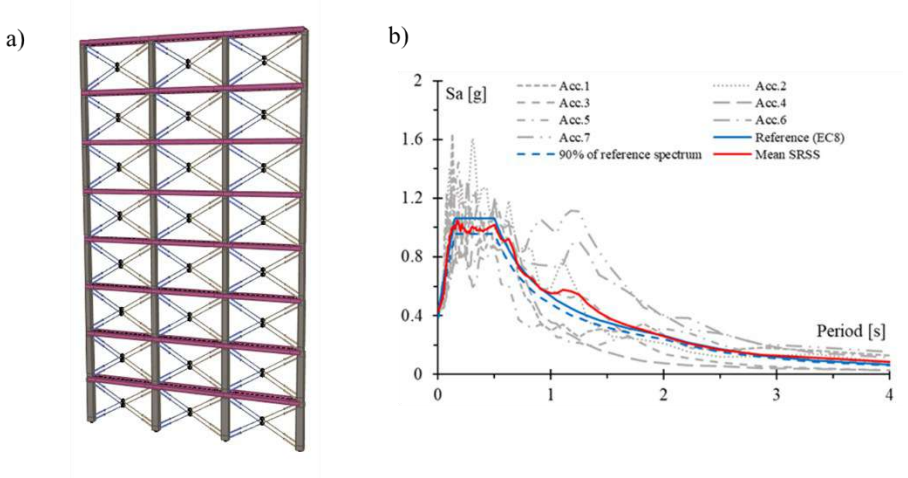


Figure 4-1: a) RC frame building configuration b) acceleration response spectra of the selected records and EC8 reference spectrum

4.2 DEFINITION OF PERFORMANCE LEVELS

Performance levels (PL) are defined separately for infill panels and RC frame elements to allow comprehensive evaluation of structural and nonstructural behaviour during dynamic loading. Infill panels are assessed using three combined IP drift–OOP displacement domains derived from experimental calibration: infDLS – Damage Limit State (first cracking or peak strength), infULS – Ultimate LS (in the range between 20% strength degradation (lower limit, ULS_L) and the theoretical point of zero resistance in the degrading branch (upper limit, ULS_U). These domains define thresholds for infill performance as a function of combined deformation, acknowledging that different combinations of IP and OOP demand can trigger failure. The domain boundaries, summarized in Table 3-1 are used in dynamic analysis to evaluate infill performance in real-time and identify limit exceedance. RC frame performance is assessed through standard deformation- and force-based criteria. Two global performance levels are defined frDLS – Damage Limit State: first column yielding (colYM) or 0.5% interstorey drift, frULS – Ultimate Limit State: any of the following: Exceedance of ultimate curvature (colUM, beamUM), Shear failure (colSF, beamSF), Nodal failure (NF) due to excessive plastic rotation. To evaluate curvature limits, a moment–curvature (M–χ)

analysis is performed for key beam and column sections under varying axial loads. The resulting yield and ultimate curvatures are expressed as polynomial functions of axial load, which are monitored during the TH analysis. Shear and chord rotation checks follow Sezen & Moehle (2004) and Circ. 7/2019, respectively. This performance-based framework supports detailed evaluation of both structural and nonstructural components throughout the seismic analysis.

4.3 TIME-HISTORY ANALYSIS, AND POST-PROCESSING

The seismic performance of the three frame configurations—bare (BF), URM-infilled, and F-infilled—is evaluated through nonlinear time-history analyses in OpenSees using a custom STKO implementation. Each frame is subjected to seven natural ground motions, scaled to five PGA levels (0.1g–0.5g). The calibrated macro-model features a displacement-based removal scheme that monitors combined IP drift and OOP displacement for each infill panel. When deformation exceeds the upper ultimate limit ($infULS_U$), the corresponding struts are removed to simulate collapse. This mechanism is automated through a TCL control script integrated into the analysis loop. At each timestep, the analysis performs: (i) infill checks against infDLS, $infULS_L$, and $infULS_U$ domains; (ii) RC element checks for curvature, shear (Sezen & Moehle, 2004), and chord rotation (Circ. 7/2019); and (iii) global drift checks at 0.5% (DLS) and 2.0% (ULS), per EC8 and DM 2018. These criteria are embedded within the time integration routine, enabling continuous damage tracking. Post-analysis, results are automatically organized by PGA level and ground motion, including maximum drifts, force–displacement curves, and limit-state exceedances for both frame and infill components. This structured post-processing enables direct comparison between infill strategies and forms the basis of the results discussed in the following section.

4.4 RESULTS

Figure 4-2 shows the average infill performance level (PL) ratios across increasing PGA levels for the URM- and F-infilled configurations, highlighting the influence of strengthening on infill response. In the URM frame, out-of-plane (OOP) collapse (OOP ULS_U) occurs at PGA = 0.3 g following the exceedance of the in-plane (IP) ULS_L limit. Consequently, results for higher PGAs (0.4 g and 0.5 g) are excluded, as the corresponding infill struts are removed from the model upon collapse, rendering further IP assessment meaningless. In contrast, the F-infilled configuration exceeds only the IP ULS_L limit at PGA = 0.5 g, demonstrating the enhanced IP and OOP capacity provided by the strengthening system.

Figure 4-3 presents the average frame PL ratios versus PGA for all three configurations: bare (BF), URM-infilled, and F-infilled. In the BF model, PL ratios increase steadily with seismic intensity, with column curvature emerging as the primary damage mechanism. Results for PGA = 0.5 g are omitted due to convergence issues in several records, which would otherwise bias the averaged response. Both infilled configurations display improved performance relative to the bare frame, primarily due to the initial stiffening effect of the masonry panels, which reduces drift and curvature demands. However, this advantage diminishes with increasing damage, particularly for the URM model, where the failure mode transitions toward column shear. The F-infilled frame, by contrast, delays the onset of drift- and flexure-related limit states up to PGA = 0.5 g, confirming the beneficial influence of strengthening. Overall, the results emphasize the dual role of masonry infills while unreinforced panels enhance initial stiffness but are prone to early OOP collapse, strengthened infills significantly improve both structural and nonstructural performance. These outcomes validate the model's capacity to capture infill–frame interaction, progressive degradation, and failure mechanisms under varying seismic intensities, reinforcing the importance of infill strengthening in the seismic retrofit of gravity-designed RC buildings.

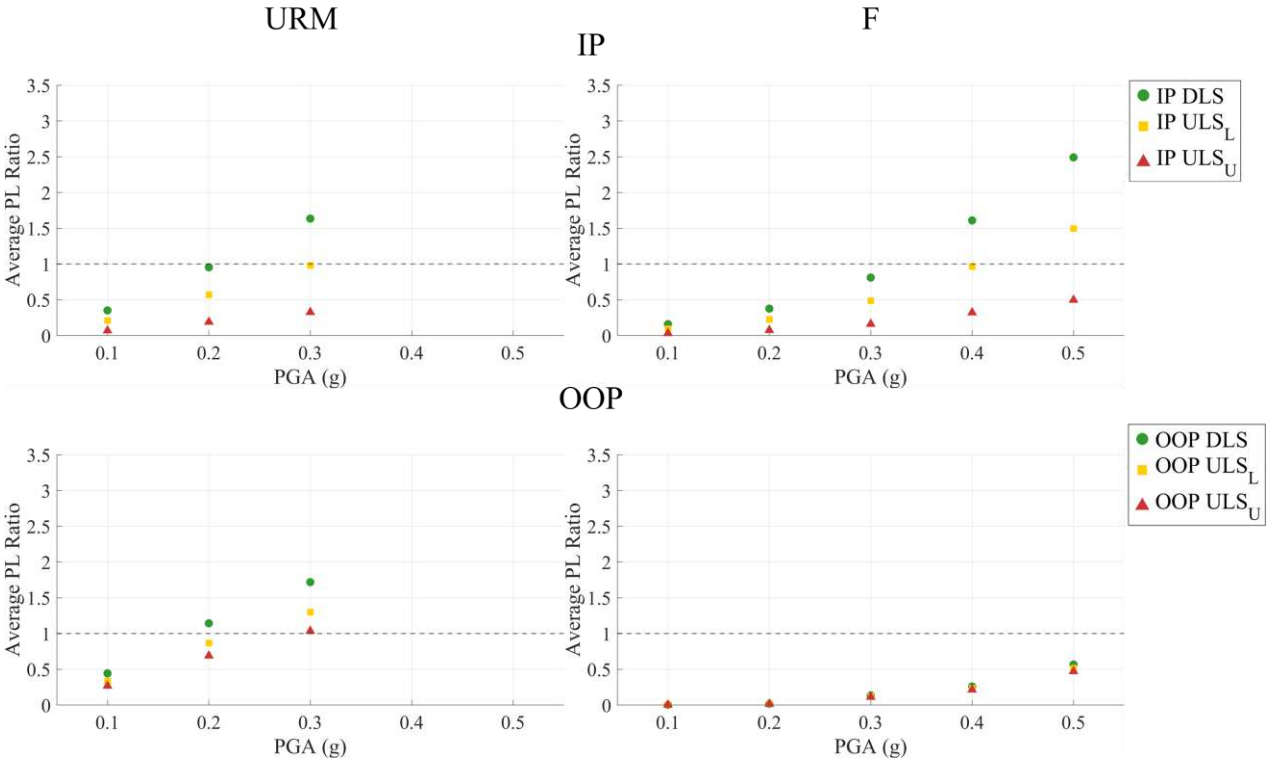


Figure 4-2: Average infill performance level ratios, for infilled frame configurations

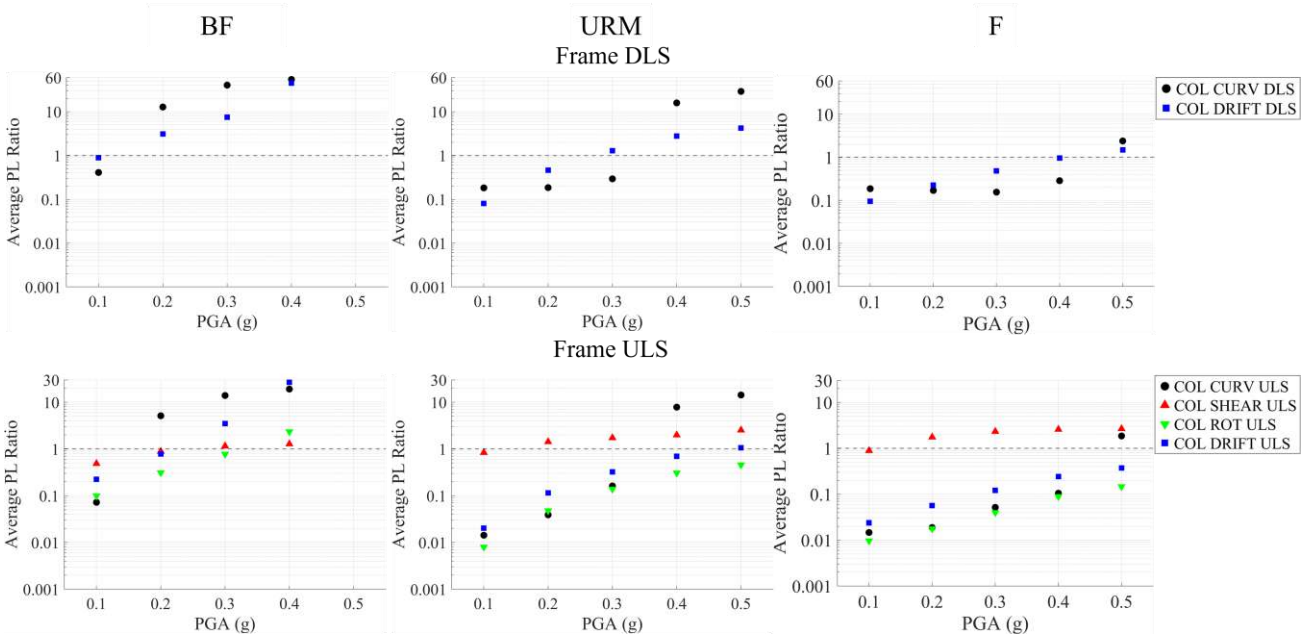


Figure 4-3: Average frame performance level ratios, for all frame configurations

5. Conclusions

This study explored the seismic behaviour of reinforced concrete (RC) frames with clay masonry infill walls using a calibrated macro-model capable of capturing the coupled in-plane (IP) and out-of-plane (OOP) interaction of infill panels. A central contribution lies in the re-implementation and re-calibration of the infill macro-model by Donà et al. (2021) within the STKO–OpenSees environment. The model was validated against experimental data for both unreinforced (URM) and strengthened panels, accurately reproducing their cyclic IP and OOP response across various damage states. The calibrated parameters were applied in nonlinear time-history analyses of a three-bay, eight-storey RC frame subjected to multiple natural ground motions and varying PGA levels. Results showed that URM infills, while initially stiffening the frame, are highly susceptible to OOP collapse once damaged in-plane behaviour realistically reproduced through displacement-based panel removal logic. Strengthened panels (F type) demonstrated superior seismic performance, with no collapse observed up to 0.5g, delaying frame limit states and reducing flexural and drift demands. In contrast, the bare frame experienced early flexural and drift damage, underscoring the vulnerability of traditional RC systems without infill contribution. Overall, the findings highlight the critical role of infill walls not only in modifying stiffness but also in influencing the progression of structural damage. The proposed modelling strategy enables detailed damage tracking and realistic failure simulation, offering a robust tool for parametric and retrofit analyses. Future developments will extend this framework to include diverse infill typologies and three-dimensional frame configurations, supporting the formulation of assessment guidelines for RC infilled frames, with emphasis on IP–OOP interaction effects.

REFERENCES

Asdea, (2023). ASDEA software technology, scientific ToolKit for OpenSees, STKO. Pescara, Italy.

CEN (European Committee for Standardization), 2004. Design of structures for earthquake resistance, Part 1: General rules, seismic actions and rules for buildings. Eurocode 8, EN 1998-1, Brussels, Belgium: CEN.

CEN (European Committee for Standardization), 2005. Design of masonry structures, Part 1-1: General rules for reinforced and unreinforced masonry structures. Eurocode 6, EN 1996-1-1, Brussels, Belgium: CEN.

da Porto F, Donà M, Verlato N, Guidi G. Experimental testing and numerical modelling of robust unreinforced and reinforced clay masonry infill walls, with and without openings. Front Built Environ 2020. https://doi.org/10.3389/fbuil.2020.591985.

Dolce M, Goretti A. Building damage assessment after the 2009 Abruzzi earthquake. Bull Earthq Eng 2015;13(8):2241–64. https://doi.org/10.1007/s10518-015-9723-4.

Donà M, Minotto M, Saler E, Tecchio G, da Porto F. Combined in-plane and out-of-plane seismic effects on masonry infills in RC frames. Ingegneria Sismica 2017;34:157–73. https://doi.org/10.1061/(ASCE)CC.1943-5614.0001067.

Donà, M., Minotto, M., Verlato, N., & Da Porto, F. (2021). A new macro-model to analyse the combined in-plane/out-of-plane behaviour of unreinforced and strengthened infill walls. Engineering Structures, 250, 113487. https://doi.org/10.1016/j.engstruct.2021.113487

FEMA, 2000. Prestandard and commentary for the seismic rehabilitation of buildings. Federal Emergency Management Agency (FEMA), 356. Washington, D.C.

Hak S, Morandi P, Magenes G, Sullivan TJ. Damage Control for Clay Masonry Infills in the Design of RC Frame Structures. J Earthquake Eng 2012;16(sup1):1–35. https://doi.org/10.1080/13632469.2012.670575.

I. Iervolino, C. Galasso & E. Cosenza, REXEL: computer aided record selection for code-based seismic structural analysis. Bulletin of Earthquake Engineering 8: 339-362, doi: 10.1007/s10518-009-9146-1, 2009.

INSYSME (2014). Report on types of structural frames, related enclosure wall systems, and requirements for the construction systems INSYSME Project D3.1. Padova, Italy: INSYSME.

ISTAT (Italian National Institute of Statistics) (2011). Website and data warehouse: https://www.istat.it/it/censimenti-permanenti/censimenti-precedenti/popolazione-e-abitazioni.

Kadysiewski, S., and Mosalam, K.M. (2009). Modeling of Unreinforced Masonry Infill Walls Considering In-Plane and Out-of-Plane Interaction. Report PEER 2008/102, Pacific Earthquake Engineering Research Center (PEER), University of California, Berkeley, CA.

Kent DC, Park R. Flexural members with confined concrete. J Struct Eng 1971;97 (ST7):1969–90.

Mander JB, Priestley MJN, Park R. Theoretical Stress-Strain Model for Confined Concrete. J Struct Eng 1988;114(8):1804–26.

Masi A, Chiauzzi L, Santarsiero G, Manfredi V, Biondi S, Spacone E, et al. Seismic response of RC buildings during the Mw 6.0 August 24, 2016, Central Italy earthquake: the Amatrice case study. Bull Earthq Eng 2017;17(10):5631–54. https://doi.org/10.1007/s10518-017-0277-5.

McKenna, F., Fenves, G., Scott, M., and Jeremic, B., 2000. Open System for Earthquake Engineering Simulation (OpenSees). University of California, Berkeley, CA.

Milanesi RR, Morandi P, Hak S, Magenes G. Experiment-based out-of-plane resistance of strong masonry infills for codified applications. Eng Struct 2021;242:112525. https://doi.org/10.1016/j.engstruct.2021.112525.

Minotto M, Verlato N, Donà M, da Porto F. Strengthening of in-plane and out-of-plane capacity of thin clay masonry infills using textile-and fibre-reinforced mortar. J Compos Constr 2020;24(6):1–22. https://doi.org/10.1061/(ASCE)CC.1943-5614.0001067.

Minotto, M., 2019. Experimentation and development of numerical models to assess the seismic performance of new strengthening technologies for masonry infill walls in existing RC frames. Ph.D. Thesis, XXXII cycle (triennium 2017-2019), University of Brescia.

MIT (Italian Ministry of Infrastructure and Transport), 2018. Update of the "Technical Standards for Constructions". DM 2018/01/17, "S.O. No. 8 alla G.U. del 20 Febbraio 2018, No. 32", Rome, Italy (in Italian).

MIT (Italian Ministry of Infrastructure and Transport), 2019. Instructions for the application of the «Update of the "Technical Standards for Constructions"». Circ. 2019/01/21 no. 7, "S.O. No. 5 alla G.U. del 11 Febbraio 2019, No. 35", Rome, Italy (in Italian).

Morandi, P., Hak, S., and Magenes, G., 2013. Simplified out-of-plane resistance verification for slender clay masonry infills in RC frames. Proceedings of the XV ANIDIS - L'Ingegneria Sismica in Italia, Padova, Italy.

Mosalam KM, Günay S. Progressive collapse analysis of reinforced concrete frames with unreinforced masonry infill walls considering in-plane/out-of-plane interaction. Earthquake Spectra 2015;31(2):921–94. https://doi.org/10.1193/2F062113EQS165M.

Papia, M., Cavaleri, L., and Fossetti, M., 2003. Infilled frames: developments in the evaluation of the stiffening effect of infills. Struct Eng Mech 16(6), 675–693. https://doi.org/10.12989/sem.2003.16.6.675.

Ricci P, Di Domenico M, Verderame GM. Experimental investigation of the influence of slenderness ratio and of the in-plane/out-of-plane interaction on the out-of-plane strength of URM infill walls. Constr Build Mater 2018;191:507–22. https://doi.org/10.1016/j.conbuildmat.2018.10.011.

Ricci, P., Di Domenico, M., Verderame, G.M., 2020. Effects of the In-Plane/Out-of-Plane Interaction in URM Infills on the Seismic Performance of RC Buildings Designed to Eurocodes. J Earthquake Eng, DOI: 10.1080/13632469.2020.1733137.

Rossi A, Morandi P, Magenes G. A novel approach for the evaluation of the economical losses due to seismic actions on RC buildings with masonry infills. Soil Dyn Earthquake Eng 2021;145:106722. https://doi.org/10.1016/j.soildyn.2021.106722.

Sezen, H., & Moehle, J. P. (2004). Shear strength model for lightly reinforced concrete columns. *Journal of Structural Engineering*, *130*(11), 1692-1703. https://doi.org/10.1061/(asce)0733-9445(2004)130:11(1692)

Silva, L.M., Vasconcelos, G., Lourenço, P.B., and Akhoundi, F. (2016). Experimental evaluation of a constructive system for earthquake-resisting masonry enclosure walls. Proceedings of the 16th International Brick and Block Masonry Conference, Padova, Italy.

Verderame GM, Ricci P, De Luca F, Del Gaudio C, De Risi MT. Damage scenarios for RC buildings during the 2012 Emilia (Italy) earthquake. Soil Dyn Earthquake Eng 2014;66:385–400. https://doi.org/10.1016/j.soildyn.2014.06.034.

Shake Table Testing of Suspended Ceilings

Cameron Flude[1], David Lau[2], Jeffrey Erochko[3] and Saranja Siventhirarajah[4]

[1] Department of Civil Engineering, Carleton University
Ottawa, ON, Canada
e-mail: cameronflude@cmail.carleton.ca
[2] Department of Civil Engineering, Carleton University
Ottawa, ON, Canada
e-mail: davidlau@cunet.carleton.ca
[3] Department of Civil Engineering, Carleton University
Ottawa, ON, Canada
e-mail: jeffreyerochko@cunet.carleton.ca
[1] Department of Civil Engineering, Carleton University
Ottawa, ON, Canada
e-mail: saranjasiventhiraraj@cmail.carleton.ca

Abstract. Seismic performance of non-structural components, also referred to as operational and functional components, in buildings has received increasing attention in the earthquake engineering community as part of the global effort to improve seismic safety and reduce earthquake losses. This paper presents an on-going research program on suspended ceiling systems which includes shake table testing of suspended ceilings. While there have been previous shake table tests on suspended ceilings, most of these tests considered only horizontal motions, and only limited studies included the vertical component of floor motions. In the present shake table investigation, one of the goals is to understand and quantify in a comprehensive manner the influence of the vertical and rotational components of building floor motions on the performance of suspended ceilings. Building properties, such as height and stiffness, impact the building vibration response and behaviour during earthquakes. Super-tall buildings are more flexible and deflect more as part of their structural system characteristics, which their design strategy relies upon to dissipate seismic energy during earthquakes. As a result, especially at high floor levels, the floor vibration response includes more pronounced vertical and rotational components. The behaviour and performance of suspended ceilings in buildings of different heights, including super-tall buildings, are investigated by varying the ratio of the magnitude of the horizontal, vertical, and rotational components of the test motions to determine their relative influence on failure mechanisms associated with each component and the performance of the suspended ceiling system. Shake table tests are carried out to obtain insights and improve understanding of the seismic performance and vulnerabilities of ceilings.

Keywords: Suspended Ceiling, Non-structural Component, Shake Table, Floor Motion, Tall Buildings.

1. Introduction

Over the past decades there have been significant advancements in earthquake engineering in building design, resulting in stronger, more resilient, and safer structures. However, over the same period the improvements in building safety related to performance of non-structural components during earthquakes are much more limited. A modern structure designed in accordance with current building codes can be expected to survive a significant earthquake remaining intact even though it may suffer a controlled amount of damage. In contrast, experiences from recent major earthquakes, such as the 1994 Northridge [Norton et al., 1994], 2011 Christchurch [Dhakal et al., 2011], 2011 Tohoku [Motosaka & Mitsuji, 2012], and 2018 Anchorage earthquakes [Rodgers et al., 2021], have clearly demonstrated that non-structural components are susceptible to suffer significant damage which affect the operation and functional performance of their hosting structures. For example, Norton et al. [1994] observed that of the commercial buildings within the epicentral area of the 1994 Northridge earthquake, only 2% experienced structural damage whereas 15% suffered non-structural damage significant enough to deem the building unoccupiable. Similarly, during the 2011 Christchurch earthquake severe non-structural damage was observed in low-medium rise buildings despite only minor structural damage [Dhakal et al., 2011]. In a survey study, Taghavi and Miranda [2003] pointed out that non-structural components represent significant asset value which can account for 65% to 85% of the total cost of commercial buildings. Filiatrault and Sullivan [2014] noted that earthquake losses from damage to non-structural components has been shown to exceed losses from structural damage, resulting in billions of direct (damage) and indirect (business disruption and downtime) economic losses.

Suspended ceilings are among the many types of non-structural components commonly used in commercial, office and institutional buildings such as schools and some medical facilities. Ceiling failure poses a major life safety hazard as falling ceilings are a serious threat to building occupants and can cause significant damage to other collocated components like electrical wiring or gas lines, resulting in loss of building function or possibly starting fires in the building. Furthermore, fallen ceilings create additional hazards as they can severely impede evacuation of the building and subsequent emergency search and rescue response. Damage to suspended ceilings has been reported as one of the most commonly observed types of damage to non-structural components even in moderate earthquakes that have higher probability of occurrence [Phan & Taylor, 1996]. Examples of ceiling failure causing detrimental business disruption include the shutdown of the San Francisco International Airport during the 1989 Loma Prieta earthquake [Yao, 2000] and school closures after the 2018 Anchorage earthquake [Rodgers et al., 2021]. Despite their observed poor performance and the impact of failure on life safety, there is a lack of thorough investigation on understanding the behaviour and failure mechanisms of suspended ceilings during earthquakes.

A suspended ceiling is typically attached to the underside of a floor slab in a building. The acceleration motion imparted to the suspended ceiling is influenced by the building's dynamic vibration characteristics and its response to the earthquake ground motions at its foundations. Consequently, the location of the ceiling in relation to the height of the building and the stiffness of the ceiling systems relative to the building can significantly influence the performance of the ceilings during earthquakes. Earthquake ground motions are three dimensional, but typically in earthquake engineering design practice, only the effects of the usually dominant horizontal ground motion components are considered. This ignores the potential significance of the vertical ground motion component. However, recent near-fault earthquakes have recorded vertical ground shaking components that are greater than the horizontal ground motion components [Chang et al., 1995]. Recent studies on seismic performance of suspended ceilings show that the vertical component of earthquake shaking may have a significant effect on the behaviour of suspended ceilings [Gilani et al., 2010a; Soroushian et al., 2016; Ryu & Reinhorn, 2019]. The extent and severity of dislodgement of ceiling panels from the supporting grid may be influenced by the direct vertical motion of the building. As the ceiling panels are critical in maintaining the in-plane rigidity of the suspended ceiling system, the loss of ceiling panels can lead to failure of the ceiling grid and complete collapse of the entire suspended ceiling system.

Because of advances in design and construction technologies in recent years, a new generation of super-tall buildings are being constructed in major cities around the world. Because most of these super-tall buildings have not been subjected to any major earthquakes [Lu & Guan, 2021], there is limited information regarding the performance of suspended ceilings in super-tall buildings. These super-tall buildings are more flexible and deflect more as part of their design strategy to dissipate seismic energy during earthquakes. When the top of the building experiences substantial lateral deflection, the floors begin to tilt with respect to the horizontal axis. As a result, especially at high floor levels, the floor vibration response includes more pronounced rotational components. Consequently, this rotational floor motion component together with the vertical motion component may have a significant impact on the performance of suspended ceilings in super-tall buildings making them more vulnerable to seismic damage and failure.

This paper describes the development of a new testing program to investigate the failure mechanisms and seismic performance of suspended ceilings. This includes the development of appropriate floor response motions from a typical super-tall building to determine the influence of the vertical and rotational components of building floor motions. The research is part of a joint research project with Institute of Science Tokyo and Tongji University which includes larger scale bi-directional suspended ceiling tests performed at Tongji University [Jiang et al., 2021; Wang et al., 2023]. The goal of the present research is to further advance the knowledge of seismic performance of suspended ceilings, including the understanding of the effects of rotational motions, which has not been included in any previous studies. This is particularly important for determining the resilience of suspended ceilings in super-tall buildings that experience significant rotation on the high floors during earthquakes.

2. Seismic performance of suspended ceilings

Suspended ceilings are any ceilings that are hung from the structure above, typically from a floor or roof slab. Two common types are suspended drywall ceilings or suspended lay-in tile ceiling systems, but other more specialized types exist as well. In the context of this paper, the term suspended ceiling will typically refer to suspended lay-in tile ceiling systems which are commonly known as T-bar ceilings. These systems consist of a light gauge metal grid system suspended from the structure with hanger wires and lightweight ceiling panels which are laid into the grid system typically without any physical connection. They are typically supported at the perimeter by a light gauge metal angle fastened to the partition walls. It is common in areas of moderate or high seismicity to have more robust or stringent seismic requirements at the perimeter connections and/or lateral braces for the ceiling grids. The lateral braces typically consist of a compression post (such as a light gauge steel stud) and four 45° splay wire braces.

Failures of suspended ceilings have been observed in many past earthquakes and are often identified as the most common type of damage to non-structural components. The types and severity of the damage observed have varied between earthquakes and the types of buildings the ceilings were located in. The full extent of the damage and a detailed description of all of the ceiling damage can be difficult to capture following an earthquake. Seike et al. [2012] noted during their field review after the 2011 Tohoku earthquake that it was difficult to gain access to many buildings, and they found that damaged non-structural elements had been removed from many buildings before their review could take place. Because of these limitations and the vastness of non-structural damage, many of the reconnaissance reports of non-structural damage are not complete or do not have detailed information on the failure mechanisms. It has been observed after several earthquakes including the 1994 Northridge earthquake [Norton et al., 1994], 1998 earthquake in southern Taiwan [Yao, 2000], and the 2011 Christchurch earthquake [Dhakal et al., 2011], that damage is often initiated by failure at the perimeter connection. Suspended ceiling earthquake damage has also been attributed to strong vertical accelerations of the supporting structure. Significant ceiling damage was observed during the 2011 Tohoku earthquake. Motosaka and Mitsuji [2011] observed the loss of ceiling

boards in large span structures. They investigated the vibration characteristics of one of these structures and found that significant vertical motions were induced in the roof structure from horizontal input motions. They noted that based on the observed damage it appeared that the ceiling design did not account for the vertical motions experienced. Seike et al. [2012] observed suspended ceiling damage in large space buildings, such as auditoriums or gymnasiums, office buildings, and low-rise commercial buildings. Hisada et al. [2012] reviewed the damage in high-rise buildings in Tokyo during the Tohoku earthquake and found that ceiling damage occurred on the middle to upper floors, despite a relatively low severity of ground shaking.

Various studies including experimental testing of the seismic performance of suspended ceilings have been performed throughout the years. The studies have included a range of ceiling types, sizes, configurations, and input motions. While the studies explore many different aspects of seismic performance of suspended ceilings, they have tended to focus on the effectiveness of lateral braces and have produced conflicting results regarding their effectiveness. Yao [2000] found that lateral braces did not increase the seismic performance of the suspended ceilings, but the installation of transverse supports at the perimeter of the ceiling that prevented the lateral spread of the grid system did. Gilani et al. [2010a] observed the dislodgement of ceiling panels at the center of their test specimen and almost no damage at the perimeter. The observed damage was largely attributed to the flexibility of the test frame which resulted in amplification of the vertical input motions and unexpected large vertical accelerations at the center of the test frame. During tests performed with a full-scale five-storey building, Soroushian et al. [2016] observed that when subjected to vertical accelerations greater than 1g, the lateral braces, originally intended to enhance the seismic performance of the suspended ceiling, actually had a negative opposite effect on ceiling performance. This was observed because the lateral braces provide a rigid connection between the floor structure and the ceiling grid. When the floor structure acceleration is greater than 1g downwards, the floor and ceiling grid move together but the unconnected ceiling panels only experience acceleration due to gravity and become separated from the grid system. When acting together with acceleration motions in the horizontal direction, this results in the ceiling panels becoming easily dislodged. In contrast, Ryu and Reinhorn [2019] found that the use of lateral restraints improved the performance of the suspended ceiling in their large-scale ceiling tests but noted that the effects of the vertical amplification of the supporting structure was not assessed due to the relatively high stiffness of the test frame in the vertical direction.

The observations of ceiling performance from past earthquakes and previous experimental seismic testing of suspended ceilings have indicated that the perimeter connections are a vulnerable component of the suspended ceiling system. They have also shown that vibration characteristics of the supporting structure can result in large vertical accelerations that have a significant impact on the performance of the suspended ceiling. This emphasizes the importance of the proper determination of the floor motion responses which ceilings could be subjected to, including the potential significant influence of the vertical motion component imparted to the ceiling system from the supporting structure as well as the importance of proper test setup and equipment that can realistically and accurately replicate the proper floor response motions. While previous studies have included the effects of vertical accelerations, a more systemic approach to evaluate the significance of the vertical component of impart motion in relation to the horizontal motion has not been investigated. In the present study, the effect of the vertical component in terms of the ratio of horizontal to vertical motions is investigated. In addition, there have been no studies previously that also included the effects of rotations which may have an impact on exacerbating the effect of vertical component of motion on the ceilings.

3. Floor motion response of super-tall buildings

In order to properly simulate earthquake motions experienced by suspended ceilings it is essential to consider also the dynamic properties of the building and floor structure which support the ceiling.

As mentioned previously, there has not been any field experience of super-tall buildings subjected to major earthquakes (Lu & Guan, 2021) and, therefore, there is limited information regarding the response of super-tall buildings to actual seismic events. In a previous study by the researchers, two prototype building models were used to produce simulated floor response motions [Flude et al., 2024]. The first is a model of the 128-storey Shanghai Tower, one of the tallest buildings in the world. The second is a model of a ten-storey building located on the Carleton University campus in Ottawa, Ontario, Canada to draw comparison with the first model. The buildings were chosen as representatives of a typical super-tall and a mid-rise building, respectively. The intention of these two models is to observe the different characteristics in floor responses between mid-rise and super-tall buildings in order to determine the impact of the influence of the characteristics of super-tall buildings on the seismic performance of suspended ceilings. It was observed that the floor motions from the super-tall building could have a large vertical component as well as a small, but possibly significant, rotational component.

4. Experimental seismic testing of suspended ceilings

Several different methods have been used in experimental seismic testing of suspended ceilings. Some tests have used acceleration time histories based on a building design spectrum [Yao, 2000], others have used acceleration time histories generated from the recommended required response spectrum (RRS) in ICC-ES AC156 [Gilani et al, 2010a; Ryu & Reinhorn, 2019], and some tests have been performed on full-scale buildings subjected to ground motions [Soroushian, 2016]. Testing non-structural components using direct ground motions or a building design spectrum is less realistic because the amplification or filtering effect due to the dynamic response of the building structure are not taken into account. Testing with full building models will most closely replicate the loading conditions of suspended ceilings in the field but is prohibitively expensive and impractical for large buildings. A viable alternative approach is to use floor response motions determined from computer models of buildings as the input excitations to the suspended ceilings in shake table tests of the non-structural components. The influence of different buildings characteristics and parameters on the response behaviour of suspended ceilings can be investigated by a rigorous testing program using floor response motions of different building types and characteristics obtained by computer simulation of building models.

The AC156 [ICC, 2010] testing procedure has been used by ceiling manufacturers for testing suspended ceilings [Gilani et al., 2010b] and was also used to develop the fragility curves in FEMA P-58 [Bachman, 2011]. AC156 is a testing standard procedure for seismic certification of non-structural components, which is referenced in ASCE 7-22 [ASCE, 2021] as a possible alternative to the force design procedures. The AC156 procedure involves development of a required response spectrum (RRS) for generating spectrum compatible excitations to be used as the input motions for shake table tests. The RRS is constructed using the horizontal spectral acceleration values for flexible components and rigid components specified in AC156. The equations for these factors are based on the horizontal force equation for the design of non-structural components in ASCE 7-16 [ASCE, 2017]. This equation has factors that account for the component response, the seismicity of the area and the relative height of the component with the building but there are no factors that account for the seismic response of the building. As a result, the design force for a component will be the same whether it is attached to the roof of a single-storey shear wall structure or the roof of a 50-storey moment frame structure. As a result, the AC156 test motions and procedure can be used in qualification tests of ceilings in all building types for compliance with ASCE 7-16 seismic design requirements of ceilings without consideration of the effect of building dynamic response behaviour to earthquake ground motions. The equation for the vertical force applied to non-structural components in ASCE 7-16 [ASCE, 2017] simply accounts for the weight of the components and the seismicity of the area the building is located. There are no factors to account for the building type and the location of the component within the building, or even the component type. Therefore, the vertical force on a non-

structural component will be the same for any component located anywhere within any building with the same seismicity. This equation is also equal to two-thirds of the minimum value that can be taken for the horizontal force in ASCE 7-16 and as a result, the vertical response spectrum in the AC156 procedure will always be more conservative than the ASCE 7-16 vertical force equations.

The use of the AC156 procedure for shake table testing of suspended ceilings has been found to produce results that do not match the typical failures observed in the field [Gilani et al., 2010b]. Since the procedure uses the ASCE 7-16 force equation to develop the RRS, no properties of the supporting structure are considered when developing the input motions. The requirement for the vertical RRS to be two-thirds of the horizontal RRS for the base level of the building also results in higher vertical components than is considered by code. However, as discussed, the vertical force component on non-structural components is not well understood and will not be the same for all buildings. Since it has been shown that suspended ceilings are susceptible to vertical accelerations further investigation is required to determine if these testing procedures actually replicate the range of possible input motions for suspended ceilings and other non-structural components.

5.New test program

A rigorous seismic testing program has been developed to investigate the seismic performance of suspended ceilings subjected to floor motions from different types of buildings including super-tall buildings. Testing is performed using a newly developed shake table system consisting of four independent mobile shake tables by MTS Systems Corporation and their subsidiary E2M Technologies B.V. capable of duplicating motions in six degrees-of-freedom. For the suspended ceiling tests being performed, the four independent tables are positioned in a square layout to support a 5.4m x 5.4m steel test frame from which the ceiling specimen is suspended. The test frame, specially designed for testing non-structural components [Davidson, 2021] is shown in Figure 1. The test frame was designed with the intention to reduce the amplification of the input excitations in both the vertical and horizontal directions and as such the bare frame's fundamental frequency in the horizontal and vertical directions was designed to be greater than 20 Hz. The relatively high stiffness of the frame will reduce amplification and therefore allow desired floor motion responses to be inputted directly and give greater control of the response motion to the researchers.



Figure 1: Test frame setup

5.1 TEST MOTIONS

The input motions used in the testing program include random white noise (for system identification), random excitation records and recorded floor motions from instrumented buildings or simulated floor motions from computer models of buildings. RRS compatible AC156 floor motions are also used in the tests for comparison purposes as these have been commonly used in previous major shake table

investigations on suspended ceilings. However, the ratio of magnitude of the horizontal to vertical components of the motion is varied between tests to investigate the influence of the vertical component.

System identification tests are performed using a random white noise record generated using the MTS STEX Pro software with a frequency range of 0.5 Hz to 30 Hz and an input magnitude of 0.05g. Because these motions were input to the tables directly without the iterative process, the motions that were produced were amplified by the frame properties and had accelerations at the top of the test frame of about 0.3g in the X and Y directions and 0.1g in the Z direction. These low magnitude motions are used to measure the ceiling properties before the test and repeat through the testing program after each increase of intensity level of the test motions to ascertain and quantify any damage in the ceiling from the test by capturing any changes in the ceiling dynamic properties.

The first phase of the tests use random acceleration records generated using the MTS STEX Pro software which meet the required response spectra specified in AC156 but with the ratio of the magnitude of the horizontal to vertical input motions as well as the duration of the strong motion varied between the tests. The intention of these tests is to determine the effects of the vertical component of the floor motion as well as effects of the duration of the strong motion. The test uses the horizontal to vertical magnitude ratio prescribed in AC156. This test serves as a baseline for comparison with previous test results by other researchers. The magnitude of the response spectrum is defined by the maximum considered earthquake spectral response acceleration parameter at short periods (S_s) as defined in ASCE 7-16. The magnitudes of the motions range from an S_s value of 0.50 up to 3.50. The response spectrums of the achieved motions matched very well to the RRS up to a magnitude of S_s equal to 2.25. Above this value, the desired motions had to be filtered to avoid exceeding the velocity capacity of the tables. The required and achieved 5% damped response spectrums for S_s equal to 2.25 and 3.50 are shown in Figure 2.

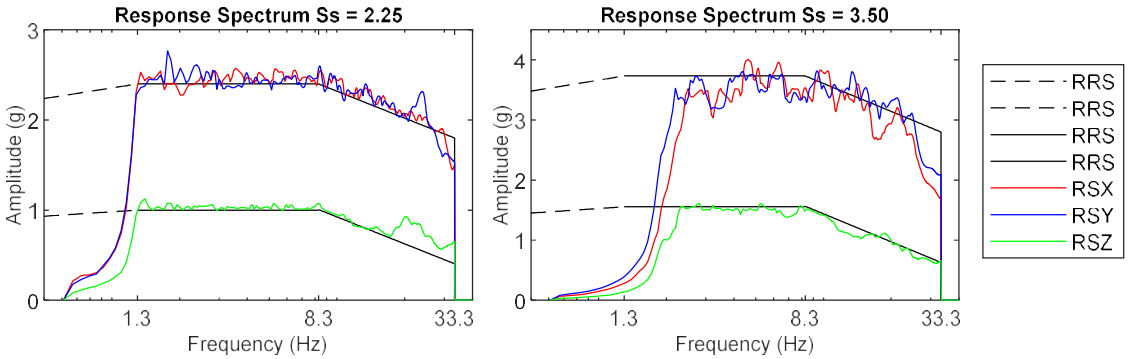


Figure 2: Response spectrum of achieved test motions

The second phase of tests use floor motions developed from computer models of buildings and floor motions recorded from instrumented buildings subjected to real earthquakes. The models include buildings with heights of 10 storeys and 128 storeys. For comparison, ceiling test results obtained from floor motions at top of building with or without floor rotation component are conducted to evaluate the effect of floor rotation on the seismic performance of suspended ceilings.

5.2 TEST SPECIMEN

The goal of the present investigation is to evaluate the effects of different types of floor motions on the seismic performance of suspended ceilings. In order to maximize the variations in the parameters of the input test motions, the test program considers only one type of ceiling specimen of the same square shape dimensions. The properties of the test specimen are selected as representative of ceilings in buildings located in regions of higher seismicity. The ceiling test specimens are designed to meet the requirements of ATSM E580 [ASTM, 2020] for a suspended ceiling in a building with a seismic category D/E/F according to ASCE

7. The ceiling specimen is in a square layout measuring 5156mm x 5156mm. The ceiling grid members are spaced at 610mm in both directions to support nominal 610mm x 610mm square ceiling tiles. The ceiling grid has a suspension height of approximately 800mm. To meet the requirements of ASTM E580 the perimeter connections are attached along two adjacent sides and unattached at opposite sides. The reference ceiling specimen layout has two lateral seismic braces which consist of a vertical compression post and four diagonal splay wires. The ceiling specimen layout and the installed specimen are shown in Figure 3.

The suspended ceiling specimen are instrumented with loads cells, accelerometers, displacement measurement devices and strain gauges to measure the ceiling response. In collaboration with research team from Queen's University, Canada, a novel fibre optic strain measuring system is used with fibre optic cables installed along the top and bottom of the main runners of the ceiling grid to measure the deformation of ceiling grid members along their entire length. In a first time ever application of the fibre optic strain measurement technique in suspended ceiling experiment, these strain results provide detailed strain distribution information of the ceiling during dynamic response that allow insights to be gained on the deformation pattern of the entire ceiling in unprecedented level of details and coverage area of the ceiling. The fibre optic strain measurements are also used to calculate the bending behaviour in the grid members over the entire ceiling area, which help to give a better understanding on the failure mechanisms of the test ceilings. In addition to the instrumentation discussed above in another collaboration with researchers from National Taipei University of Technology, Taiwan, a new digital image correlation (DIC) platform consisting of 12 cameras is used to measure the deformation profile of the ceiling grid and the test frame. Details of this innovative DIC system is presented in a separate reference [Seyfu & Yang, 2025].

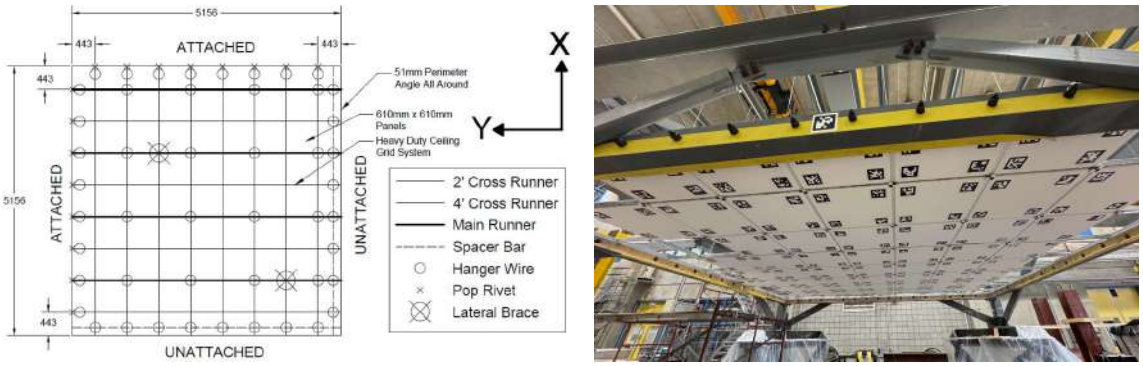


Figure 3: Reflected ceiling plan (left) and ceiling specimen (right)

6. Results

Preliminary ceiling test results of the system identification of the ceiling and the AC156 input motions at the intensity level of Ss = 0.75 are discussed here.

6.1 System Identification

System identification tests are performed for the ceiling test specimen using the white noise motions described above. Accelerometer readings on the supporting test frame and the ceiling specimen are used to calculate the frequency response function (FRF) of the ceiling specimen to identify the natural frequency response of the ceiling. The FRF's in the x, y, and z direction (refer to Figure 3 for ceiling orientation) are shown in Figure 4. The natural frequency of the ceiling is identified as approximately 8.75 Hz. The FRF calculated before the first test and after the AC156 test motions appear to have not changed, confirming that no change in condition of the ceiling specimen from the tests runs that have been performed.

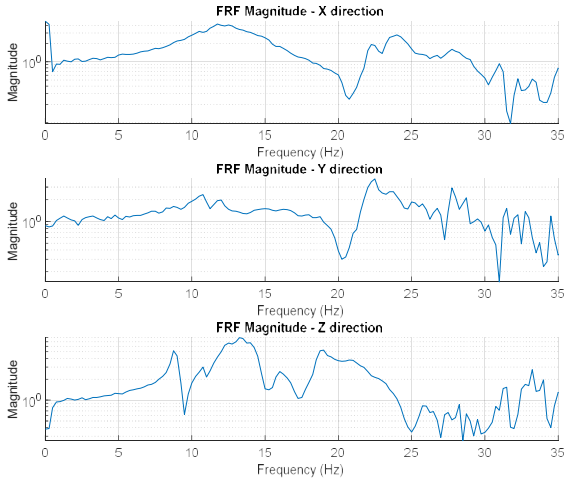


Figure 4: FRF of ceiling specimen prior to test sequence

6.2 AC-156 TEST PROTOCOL

Shake table test of the ceiling has been carried out using AC-156 motions up to the intensity level of Ss = 0.75. The acceleration time history recoded on accelerometers attached to the center of the test frame and accelerometers attached to the ceiling grid near the center of the ceiling specimen are shown in Figure 5. The orientation of the ceiling grid is shown in Figure 3. Even at these low test motion magnitudes, signification amplification of the input motions are seen on the ceiling specimen. Testing will continue at higher magnitudes until collapse of the test specimen.

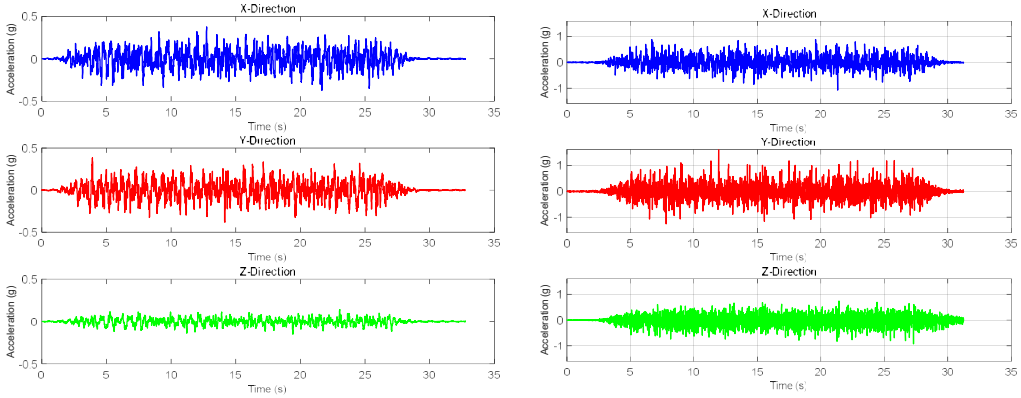


Figure 5: Recorded accelerations on test frame (left) and ceiling specimen (right)

7. Conclusions

Previous earthquake experience has shown that earthquake damage to non-structural components, and especially suspended ceilings, can be a significant hazard to life and the continuing function of the building. Damage to suspended ceilings has commonly been the most reported type of damage to non-structural components and has resulted in large economic losses due to property damage and often more significantly the extended closure of business. Suspended ceiling performance in previous earthquakes and in

experimental testing has shown that ceilings are susceptible to damage at their perimeter connections and that vertical acceleration of the supporting structure has a significant impact on the ceiling's performance.

A seismic testing system has been designed specifically for experimental testing of the seismic performance of non-structural components including suspended ceilings. The system consists of six degree-of-freedom mobile shake tables supporting a rigid steel frame which can be used to accurately simulate the floor response of super-tall buildings including the rotational components of the motion. Testing is performed using the AC156 test protocol. Preliminary test results show significant amplification of the input motions to the suspended ceilings even a low input magnitudes but no significant damage to the ceiling specimen.

8. Acknowledgements

The authors would like to acknowledge the earlier research carried out by Geoffrey Davidson as a part of the research team, and the technical assistance of providing the numerical model of the Shanghai Tower by Xilin Lu, Huanjun Jiang and Y. Wang of Tongji University, China and the assistance provided by S. Motoyui, K. Kasai and M. Li ofInstitute of Science Tokyo, Japan for this research. The authors also acknowledge the funding support from CFI for the new shake table test facilities, which are essential for this research.

9. References

American Society of Civil Engineers [2017] *ASCE/SEI 7-16 Minimum Design Loads and Associated Criteria for Buildings and Other Structures*, American Society of Civil Engineers, USA.

American Society of Civil Engineers [2021] *ASCE/SEI 7-22 Minimum Design Loads and Associated Criteria for Buildings and Other Structures*, American Society of Civil Engineers, USA.

ASTM International [2020] *ASTM E580-20 Standard Practice for Installation of Ceiling Suspension Systems for Acoustical Tile and Lay-in Panels in Areas Subject to Earthquake Ground Motions*, ASTM International, USA.

Chang, S., Bray, J., Seed, R. [1995] "Ground motions from the Northridge Earthquake," Proceedings of Third International Conference on Recent Advances in Geotechnical Earthquake Engineering and Soil Dynamics, St. Louis, Missouri.

Davidson, G. [2021] "Development of testing facilities and procedures for seismic performance of suspended ceilings," Thesis, Carleton University, Canada.

Dhakal, R., MacRae, G., Hogg, K. [2011] "Performance of ceilings in the February 2011 Christchurch earthquake," *Bulletin of the New Zealand Society for Earthquake Engineering*, Vol. 44, No. 4, pp. 379–389.

Filiatrault, A., Sullivan, T. [2014] "Performance-based seismic design of nonstructural building components: The next frontier of earthquake engineering," *Earthquake Engineering and Engineering Vibration*, Vol. 13, Suppl. 1, pp. 17–46.

Flude, C., Lau, D., Erochko, J. [2024] "Experimental Seismic Testing of Suspended Ceilings Using Floor Motions of Super-Tall Buildings," Proceedings of 18th World Conference on Earthquake Engineering, Milan, Italy.

Gilani, A., Reinhorn, A., Glasgow, B., Lavan, O., Miyamoto, H.K. [2010] "Earthquake simulator testing and seismic evaluation of suspended ceilings," *Journal of Architectural Engineering*, Vol. 16, No. 2, pp. 63–73.

Gilani, A., Takhirov, S., Reinhorn, A., Mahin, S. [2010] "Seismic qualification testing of suspended ceilings: Lessons learned and the requirements for a new test standard and qualification procedure," pp. 2555–2566.

Hisada, Y., Yamashita, T., Murakami, M., Kubo, T., Arata, T., Shindo, J., Aizawa, K. [2012] "Seismic Response and Damage of High-Rise Buildings in Tokyo, Japan, during the 2011 Tohoku Earthquake," Proceedings of 15th World Conference on Earthquake Engineering, Lisbon, Portugal.

ICC Evaluation Service [2010] *AC-156 Acceptance criteria for seismic certification by shake-table testing of nonstructural components*, ICC Evaluation Service, USA.

Jiang, H., Wang, Y., He, L. [2021] "Study of Seismic Performance of Chinese-Style Single-Layer Suspended Ceiling System by Shaking Table Tests," *Advances in Civil Engineering*, Article ID 9861722.

Lu, X., Guan, H. [2021] *Earthquake Disaster Simulation of Civil Infrastructures*, Springer, Singapore.

Motosaka, M., Mitsuji, K. [2012] "Building damage during the 2011 off the Pacific coast of Tohoku Earthquake," *Soils and Foundations*, Vol. 52, No. 5, pp. 929–944.

Norton, J., King, A., Bull, D., Chapman, H., McVerry, G., Larkin, T., Spring, K. [1994] "Northridge earthquake reconnaissance report," *Bulletin of the New Zealand Society for Earthquake Engineering*, Vol. 27, No. 4, pp. 235–344.

Phan, L., Taylor, A. [1996] *State of the art report on seismic design requirements for nonstructural building components*, U.S. Department of Commerce, National Institute of Standards and Technology, USA.

Rodgers, J., Hassan, W., Motter, C., Thornley, J. [2021] "Impacts of the 2018 M7.1 Anchorage earthquake on schools," *Earthquake Spectra*, Vol. 37, No. 3, pp. 1849–1874.

Ryu, K.P., Reinhorn, A.M. [2019] "Experimental study of large area suspended ceilings," *Journal of Earthquake Engineering*, Vol. 23, No. 6, pp. 1001–1032.

Seike, T., Natori, A., Kumagai, R., Eguchi, T. [2012] "Preliminary Reconnaissance Report of the 2011 Tohoku-Chiho Taiheiyo-Oki Earthquake, Chapter 9, Damage to Non-structural Elements," Springer, Japan.

Seyfu, M.K., Yang, Y.-S. [2025] "A Stereo Synchronization Method for Consumer-Grade Video Cameras to Measure Multi-Target 3D Displacement Using Image Processing in Shake Table Experiments," *Sensors*, Vol. 25, No. 17, Article 5535.

Soroushian, S., Maragakis, E.M., Ryan, K.L., Sato, E., Sasaki, T., Okazaki, T., Mosqueda, G. [2016] "Seismic simulation of an integrated ceiling-partition wall-piping system at E-Defense. II: Evaluation of nonstructural damage and fragilities," *Journal of Structural Engineering*, Vol. 142, No. 2.

Taghavi, S., Miranda, E. [2003] *Response assessment of non-structural building elements (PEER Report 2003/05)*, Pacific Earthquake Engineering Research Centre, USA.

Wang, Y., Jiang, H., Motoyui, S., Kasai, K., Qin, Z., Huang, Y. [2023] "Study on seismic performance of suspended ceiling system with semi-free boundary condition," *Engineering Structures*, Vol. 275, Article 115208.

Yao, G.C. [2000] "Seismic performance of direct hung suspended ceiling systems," *Journal of Architectural Engineering*, Vol. 6, No. 1, pp. 6–11.

Shake Table Test on Suspended Nonstructural Components in a Large-Scale Ceiling System

Eun-Rim Baek[1], Jae-Bong Kim[2], Ju-Chan Kim[3], Sang-Hoon Oh[4], and Sang-Ho Lee[5]

[1] Seismic Research and Test Center, Pusan National University
49 Busandaehak-ro Mulgeum-eup Yangsan Gyeongsangnam-do, Republic of Korea
e-mail: ufo35@pusan.ac.kr
[2] Seismic Research and Test Center, Pusan National University
49 Busandaehak-ro Mulgeum-eup Yangsan Gyeongsangnam-do, Republic of Korea
e-mail: kjb@pusan.ac.kr
[3] Seismic Research and Test Center, Pusan National University
49 Busandaehak-ro Mulgeum-eup Yangsan Gyeongsangnam-do, Republic of Korea
e-mail: juchan@pusan.ac.kr
[4] Department of Architectural Engineering, Pusan National University
63 beon-gil Busandaehak-ro Busan, Republic of Korea
e-mail: osh@pusan.ac.kr
[5] Department of Architectural Engineering, Pusan National University
63 beon-gil Busandaehak-ro Busan, Republic of Korea
e-mail: sangho@pusan.ac.kr

Abstract. Suspended non-structural components such as ceilings, sprinkler piping, and mechanical equipment exhibit different dynamic behavior during earthquakes due to interaction effects, which may lead to functional failure or economic loss. In this study, the dynamic behavior of suspended non-structural components was evaluated through a large-area, full-scale shaking table test that realistically reflected actual installation conditions. The test specimen consisted of a T-bar metal ceiling, a sprinkler piping system, and a heavy Pre-conditioned Air Unit (PAU), all installed on a rigid steel test frame with a floor area of 121 m², simulating an actual ceiling space. The experiment aimed to evaluate, under various levels of ground motion intensity, the behavior of a ceiling and vibration-isolated equipment supported by isolation springs, as well as the interaction among components and the effectiveness of seismic reinforcement details. The results showed that the ceiling system with high-stiffness frame experienced almost no structural damage even under strong excitation, whereas the heavy PAU produced large horizontal displacements, causing local damage to adjacent supports. Furthermore, the vibration-isolated PAU experienced collapse failure under beyond-design-level earthquakes, even when seismic reinforcement was applied. This study highlights the importance of integrated seismic design considering interaction among multiple suspended non-structural components, and it reveals the limitations of current seismic details for vibration-isolated equipment.

Keywords: Non-structural components, ceiling system, sprinkler piping, PAU, shaking table test, seismic performance, component interaction.

1. INTRODUCTION

Recent earthquake damage cases have demonstrated that failures of non-structural components (NSCs) not only cause direct economic losses but also lead to serious functional disruptions of buildings [FEMA, 2011]. Consequently, numerous studies have been conducted to evaluate and enhance the seismic performance of NSCs. Most NSCs are assembled products composed of multiple components that exhibit nonlinear contact behavior. Therefore, even when designed according to seismic provisions, discrepancies may exist between the designed performance and the actual performance of the installed product. Experimental verification is thus essential to confirm whether the intended performance is fully achieved.

In addition, many non-structural components such as ceiling systems, piping, and HVAC equipment are suspended from slabs and are installed in complex configurations. These components are significantly affected by interaction effects during earthquakes. Although various shaking table tests on individual non-structural components have been performed worldwide, the interaction behavior among multiple suspended components in combined systems has not yet been sufficiently clarified.

Therefore, this study experimentally investigates the integrated dynamic behavior of multiple suspended non-structural components, including a ceiling system, a pre-conditioned air unit (PAU), sprinkler piping, and air-conditioning units. The main objectives of this study are to evaluate the interaction characteristics between the ceiling system and the attached non-structural components, to examine the seismic behavior of a ceiling system that forms a high-stiffness diaphragm-type, to compare the dynamic response of branch pipes with different stiffnesses of sway bracing devices, and to assess the seismic performance of vibration-isolated PAU with varying reinforcement details. This paper primarily discusses the observed damage to the specmen.

2. DAMAGE OF NONSTRUCTURAL COMPONENTS IN PAST EARTHQUAKES

Extensive damage to suspended NSCs has been reported in the past earthquakes. The 2011 Great East Japan Earthquake provided one of the most comprehensive lessons on the vulnerability of NSCs [JABMEE, 2013]. Numerous cases were reported of suspended ceilings collapsing in large spaces, sprinkler systems discharging unintentionally, and piping networks sustaining ruptures due to excessive displacement. In many instances, expansion-type post-installed anchors failed because of inadequate quality control, resulting in partial or total pullout during shaking. Large ducts also experienced flange rupture and disconnections, further emphasizing the limitations of existing support systems.

Similarly, during the 2024 Hualien Earthquake in Taiwan, NSC damage was documented in schools and hospitals by NCREE [2024]. Suspended equipment supported by spring hangers exhibited excessive vibration, which in some cases caused sprinkler pipes to rupture and led to indoor flooding. These cases once again highlighted recurring weaknesses in hangers, anchors, and flexible joints.

The commonality across different events is that NSC damage often originates from insufficient anchorage capacity, poor installation quality, lack of transverse bracing, and limited ability of joints to accommodate multidirectional displacements. These recurring failure patterns underline the need for experimental research under controlled conditions to validate design details and develop mitigation strategies.

3. LARGE-SCALE SHAKING TABLE EXPERIMENTS

3.1 SPECIMENS

The specimen consisted of the suspended ceiling of 121m² with three air-conditioning indoor units, sprinkler piping and the isolated heavy mechanical equipment. Figure 1 shows the whole specimen configuration. The ceiling system was an indirectly suspended T-bar metal panel ceiling, as shown in Figure 2.

In an indirect suspension system, the ceiling frame composed of T-bars is first connected to the carrying channels, and the hangers are attached to the carrying channels—not directly to the T-bars. These hangers, consisting of 3/8-inch threaded rods, suspend the entire T-frame from the slab, allowing the ceiling mass and suspension forces to be transferred through the carrying channels before reaching the slab. The continuous grid was formed by assembling the cross T-bars at 610 mm intervals onto the main T-bars, which were also spaced at 610 mm. Unlike conventional products, the T-bars used in this study had a folded-flange cross-section, which provides better out-of-plane stiffness. At the joints between the main T-bars and cross T-bars, cross-joint caps provided an additional mechanical engagement, further increasing the connection rigidity, and the carrying channels were also interconnected using carrying-joint caps. These mechanical connections, combined with the folded-flange T-bars and the integrated carrying-channel system, significantly increased the overall frame stiffness and enabled the ceiling to behave as a high-stiffness diaphragm. The suspension height was 1.5m.

To replicate the boundary conditions of ceilings installed in actual buildings, the perimeter of the ceiling surface was constrained using a simulated edge-support configuration. Four perimeter boundaries were constructed with 10-mm-thick wooden panels, on which aluminum moldings were installed. The ceiling components were then connected to these moldings. The ceiling frame was mechanically engaged with the aluminum moldings on two adjacent sides, while the remaining two sides were placed freely supported by resting the T-bars and carrying channels on top of the moldings. In this configuration, the clearance between the moldings and the ceiling members at the free edges was kept within 2 mm, which corresponds to typical installation tolerances.

Three air-conditioning units were installed together with the ceiling panels. Each unit weighed approximately 67 kg, and was suspended by four 3/8-inch threaded rods. The three units were installed at distances of 0.8 m, 2.5 m, and 5.3 m from the western boundary of the ceiling frame, respectively. Figure 3 shows the details of ceiling specimen.

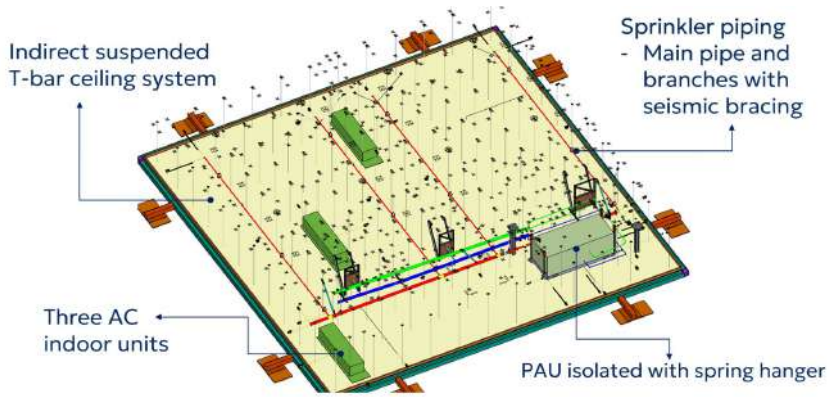


Figure 1. Layout of the test specimens

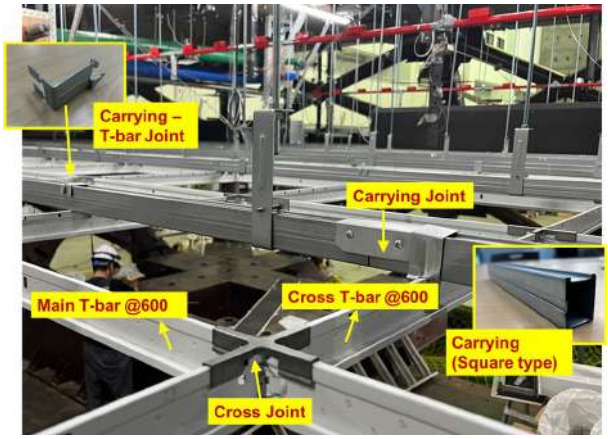


Figure 2. Configuration of the indirect suspended T-bar ceiling specimen

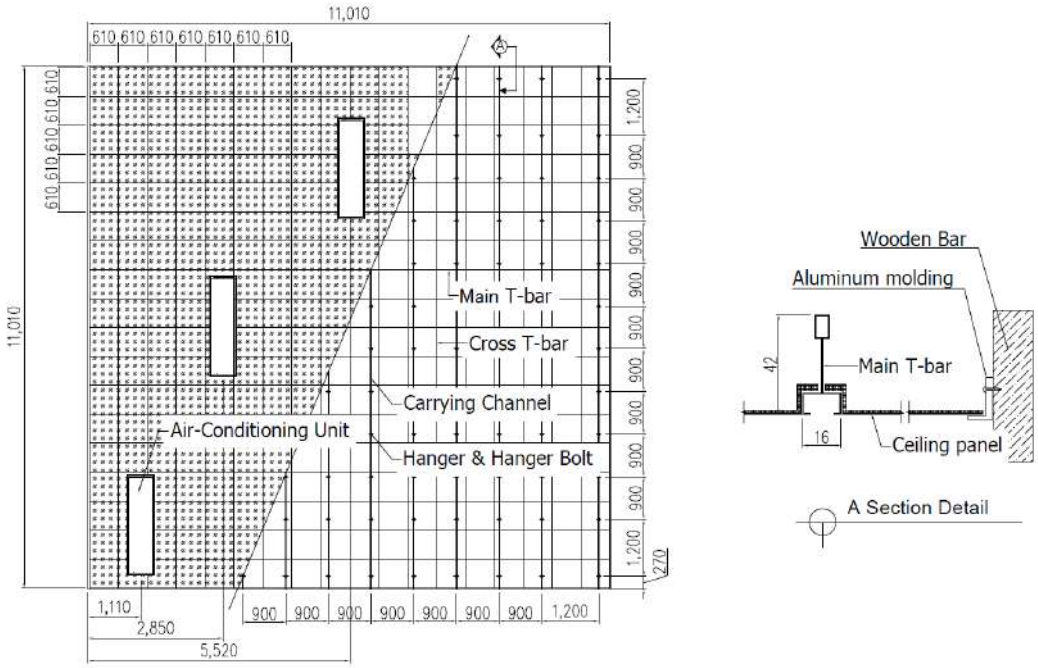


Figure 3. Drawings of the Ceiling specimen and boundary connection

The sprinkler piping system consisted of one main pipe whose diameter reduced from 3 inches to 1.5 inches, with four 1-inch branch pipes connected to it. The total length of the main pipe was 9.7 m, and each branch pipe was 7.4 m long. The hangers were made of 3/8-inch threaded rods and installed at intervals of 2.5 to 3.5 m. In accordance with Korean seismic requirements, the sprinkler system was equipped with seismic braces. A longitudinal brace was installed at the midspan of the main pipe, while lateral braces were installed at both ends. All braces were pipe-type braces set at 45° angles. Among the four branch pipes, three were equipped with different types of sway bracing devices: (1) a one-direction cable brace, (2) a one-direction ½-inch threaded rod brace, and (3) a two-direction ½-inch threaded rod brace. The remaining branch pipe was left unbraced for comparison purposes. The suspension height of the piping was 0.75m.

The heavy mechanical equipment used in the test was a Pre-conditioned Air Unit (PAU) weighing approximately 230 kg and the suspension height was 1,1m. It was suspended by four 3/8-inch threaded rods, with vibration-isolation spring mounts installed on the near-slab side. The PAU was connected to inlet and outlet pipes directly, without flexible joints. To enhance seismic performance, cable braces were installed

at approximately 45° angles to the top steel plate of the test frame. However, due to interference with adjacent piping, two of the braces were connected to an H-shaped cantilever support fixed to the top plate. While the target installation angle was 45°, some braces were installed at around 50°, and those attached to the column were relatively short. The hanger rods were also strengthened with steel angle, as shown in figure 3. These reinforcement details followed the ASHRAE guide [2012], representing a realistic on-site installation condition. Figure 4 and 5 show the overall layout of the piping and PAU specimens.

The lateral resistance mechanism of the vibration-isolated PAU consisted of four cable-type seismic braces installed in an X-shaped configuration around the unit. These braces were connected to the upper steel frame (or the adjacent steel column where interference occurred) at approximately 45° to provide bidirectional lateral restraint. Since the PAU was supported by vertical coil springs with negligible horizontal stiffness, the cable braces served as the primary source of lateral stiffness by developing tensile forces during horizontal motion. However, excessive preset tension in the cable braces may interfere with the isolation function of the springs by restricting relative horizontal and vertical displacements. Therefore, the cable braces were installed with minimal initial tension and were intended to act primarily as displacement-limiting devices rather than as rigid lateral restraints.

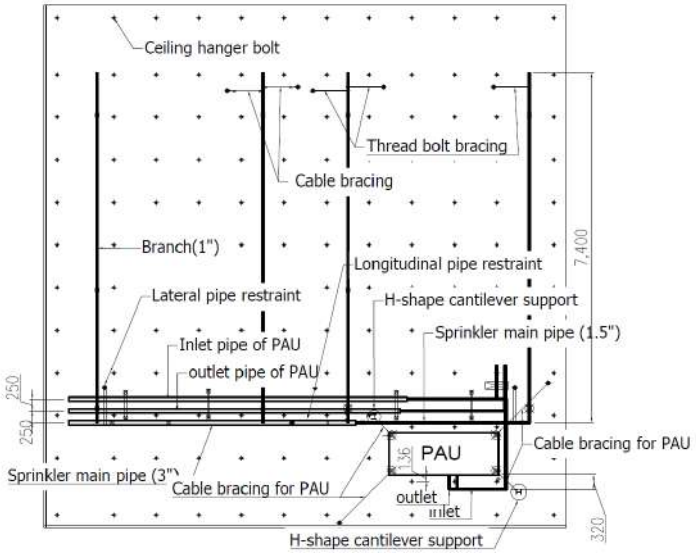


Figure 4. Configuration of the piping system and PAU

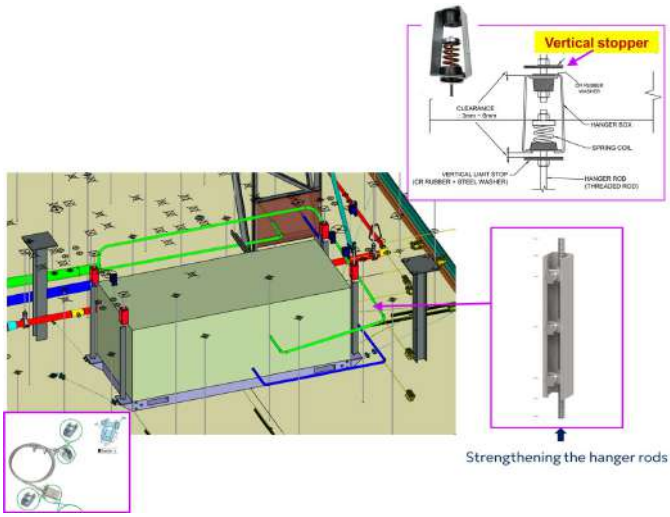


Figure 5. Strengthening of isolated PAU with spring mount

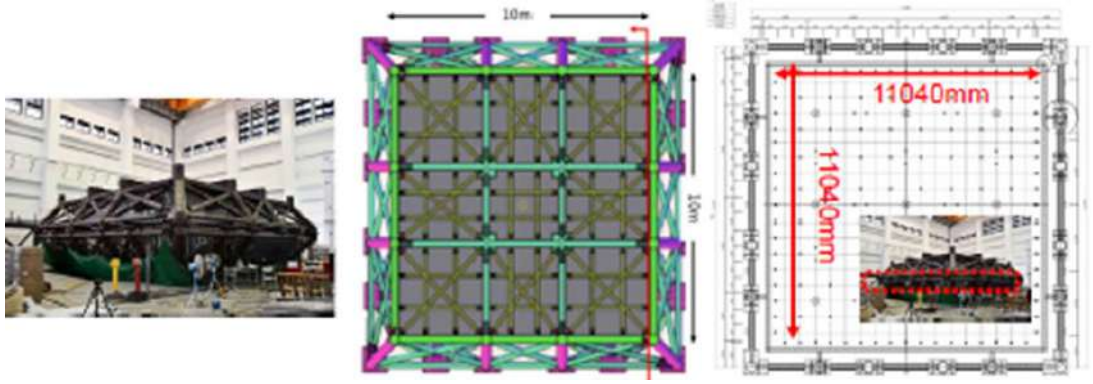
3.2 TEST SETUP

The shaking table test was conducted at the National Center for Research on Earthquake Engineering (NCREE) in Taiwan. The suspended non-structural components were installed on a large, rigid steel test frame, as shown in Figure 6. The test frame provided an installation area of approximately 121 m². It was designed so that its natural frequencies exceeded the amplification range of the Required Response Spectrum (RRS) specified in the AC156 standard [2025], thereby minimizing the influence of the supporting frame on the test response. The designed natural frequencies of the test frame were 18 Hz in the horizontal direction and 13 Hz in the vertical direction.

All test specimens were suspended from a 10 mm thick steel plate attached to the top of the test frame. The ceiling hangers were connected using welded anchor nuts, and the reinforcing braces were fixed by machined holes and bolted connections to simulate realistic installation conditions.

The shaking table was operated in six degrees of freedom, and the input motion was applied simultaneously in two horizontal directions and one vertical direction. The input ground motions were generated based on the AC156 Required Response Spectrum (RRS), with parameters of S_{DS} = 1.2 g and z/h = 1.0. An artificial ground motion (KPH) was synthesized using scaled and combined the ground acceleration records from the 1995 Kobe earthquake (Japan), the 2017 Pohang earthquake (Korea), and the 2024 Hualien earthquake (Taiwan), to capture representative spectral and duration characteristics of each event. AC156 is a widely adopted seismic qualification standard for nonstructural components and represents the floor acceleration demand filtered through the building response, rather than free-field ground motions. Therefore, scaling the seed records to the AC156 RRS ensures that the input motion reflects building-filtered acceleration levels that suspended nonstructural components are expected to experience during an earthquake.

Three intensity levels of the KPH input—25%, 50%, and 95%—were applied sequentially. For reference, the design earthquake level in Korea corresponds to approximately S_{DS} = 0.55 g, which is roughly equivalent to the 50% KPH input level in this study. Figure 7 shows the input motion.



(a) overall view **(b) top view** **(c) mid-height plan view**

Figure 6. Test frame for specimen installation

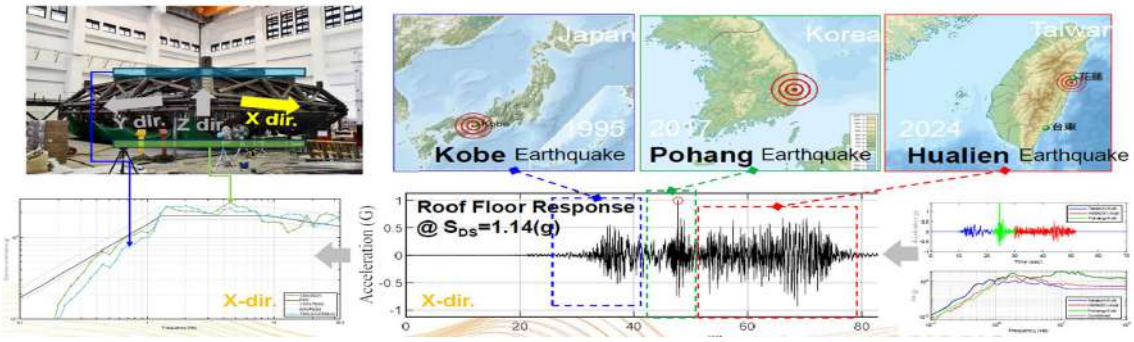


Figure 7. Input motion (KPH) generated according to AC156 RRS

4. EXPERIMENTAL RESULTS

4.1 CEILINGS

The ceiling system exhibited minimal movement owing to its high-stiffnes. Slight oscillation of ceiling panels was observed near the section connected to the air-conditioning unit, and one panel became detached; however, no other significant damage occurred. After the 50% KPH input, deformation was observed in the adjacent ceiling hanger rods and the carrying channel due to the impact motion of the PAU, which occurred because the clearance between the PAU and the ceiling components was only about 100 mm. Although the carrying channels deformed slightly, they did not detach from the ceiling frame, and no panel fall or T-bar frame failure occurred. Figure 8 shows the observed damage to the ceiling.

4.2 PIPINGS

After the 95% KPH excitation, the anchor of the axial sway brace loosened, leading to detachment of the bracing connection. The loosening was likely caused by repeated shaking during multiple test runs. In addition, fracture occurred at one of the T-joint connections of a branch pipe, accompanied by water leakage from the damaged section. Figure 9 shows the damage of the piping

4.3 ISOLATED PAU

Under the non-seismic (unbraced) condition, the PAU experienced very large horizontal motion but did not fall. The spring mounts effectively prevented the springs from popping out by acting as stoppers. However, the unit collided with the ceiling hangers due to excessive lateral sway. In the seismic-strengthened condition, local plastic deformation was observed in the unreinforced hanger bars, and minor relaxation of the cable braces occurred at the 50% KPH input level. The upper part of the PAU showed significant rocking motion, resulting in repeated collisions with the ceiling members and causing concentrated plastic deformation in the unreinforced hangers. At 95% KPH, both the vibration amplitude and nonlinear response increased significantly, eventually leading to fracture at the embedded portion of the threaded rod anchors, as shown in Figure 10.



(a) Detachment of the panel (b) Deformation of the carrying channel and hanger

Figure 8. Damage of the ceiling



(a) Fracture of tee joint (b) longitudinal brace

Figure 9. Damage of the piping

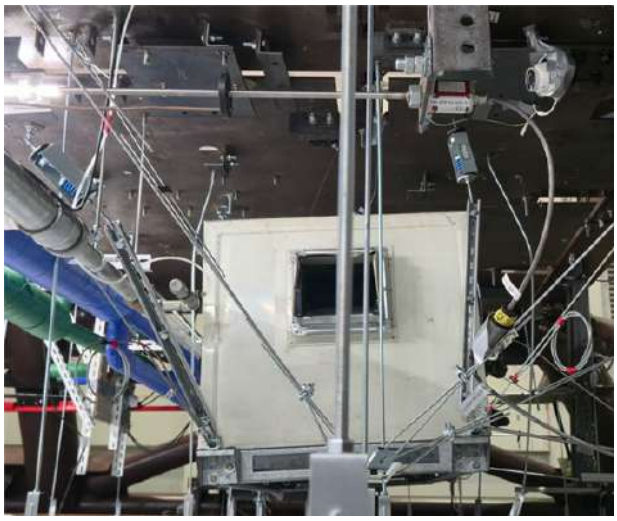


Figure 10. Damage of the isolated PAU

5. DISCUSSION

In this study, a large-scale shaking table test was conducted using a 121 m² steel test frame to simulate real installation conditions of suspended non-structural components, including the ceiling system, air-conditioning units, sprinkler piping, and a pre-conditioned air unit (PAU). The dynamic responses and damage mechanisms of these components were evaluated under earthquake excitations.

The ceiling system with a high-stiffness configuration demonstrated stable behavior and sustained almost no damage, even under strong input motions. No panel collapse or T-bar failure was observed. These results suggest that the high in-plane stiffness of the ceiling system may have contributed to distributing inertial forces across the ceiling plane, although this interpretation is based solely on the observations from the present test. In particular, specimens with properly fixed ceiling edges and well-connected air-conditioning units tended to exhibit reduced local deformation compared with more flexible edge conditions.

The sprinkler piping system maintained its functional integrity when seismic details were applied according to the design standard. However, the heavy PAU suspended by vibration-isolation springs generated large horizontal displacements, causing local damage to adjacent ceiling supports. While cable bracing and hanger reinforcements were introduced to mitigate such movements, the test results showed that depending on the installation conditions, these reinforcements could induce nonlinear behavior and even lead to greater localized damage

These findings emphasize the importance of integrated seismic design that considers the interaction among multiple suspended non-structural components, particularly when combining flexible and vibration-isolated systems within the same ceiling space.

REFERENCES

ASHRAE [2012] *Practical Guide to Seismic Restraint*, American Society of Healing, Refrigerating and Air-Conditioning Engineering, USA.

FEMA [2011] *Reducing the Risks of Nonstructural Earthquake Damage – A Practical Guide*, Applied Technology Council, USA.

ICC [2025] *AC156 Seismic Certification by Shake-Table Testing of Nonstructural Components*, International Code Council, USA.

JABMEE [2013] *Report on Equipment Damage and Seismic Countermeasures from the Great East Japan Earthquake*, Japan Association of Building Mechanical and Electrical Engineers, Japan.

NCREE [2024] *Reconnaissance Report of Seismic Damages Caused by the 3 April 2024 Earthquake*, National Center for Research on Earthquaek Enginnring, Taiwan.

Code-based methodologies for the seismic qualification of non-structural elements: Integrating experimental testing and numerical modelling

Igor Lanese[1], Miriam Bazzini[1], Paolo Dubini[1], and Emanuele Brunesi[1]

[1] European Centre for Training and Research in Earthquake Engineering (EUCENTRE)
Via Ferrata 1, 27100 Pavia, Italy
e-mail: {igor.lanese, miriam.bazzini, paolo.dubini, emanuele.brunesi}@eucentre.it

Abstract. While the general awareness of seismic requirements and qualification needs of non-structural (NS) components is continuously increasing among manufacturers and design engineers, there are still some parts of the process that certainly need further improvements. First, most of the manufacturers typically does not have a strong structural and earthquake engineering background, resulting in products designed to withstand gravity loads and vibrations due to transport and functioning. In many cases, field experience and costs optimization led the design, and in many cases adaptations alien to good earthquake engineering practice are adopted. Another relevant and recursive aspect in the qualification process of a whole production line is the way to extend the results of a specific NS element qualification, which could be jeopardized by the wide variety of possible configurations a NS component may have. As such, this paper presents a case study, involving numerical modelling for the integration of shake-table test results meant to qualify the item, and share some thoughts coming from experience and a number of experimental qualification tests on NS elements carried out at the EUCENTRE accredited laboratories of Pavia, Italy.

Keywords: Seismic qualification testing, Shake-table testing, Mechanical and electrical equipment, Numerical modelling, Seismic performance assessment.

1. INTRODUCTION

Even moderate seismic events occurred in urban regions of countries with well-established seismic design codes have repeatedly demonstrated the importance and vulnerabilities of non-structural elements (NSEs) [Filiatrault et al., 2001; Gupta and McDonald, 2008; Ricci et al., 2011; Belleri et al., 2015; Perrone et al., 2019], thus triggering significant interest in seismic demand/design and performance-related issues [Filiatrault and Sullivan, 2014; Merino et al., 2018; Merino et al., 2019; Gabbianelli et al., 2020; Rodriguez et al., 2021; Perrone et al., 2022; Gabbianelli et al., 2022; Peloso et al., 2023; Merino et al., 2024; Anwar et al., 2025]. Special relevance has been gained in recent years due to recent advancements in performance-based earthquake engineering and the economic losses attributed to NSEs, which is ascribed both to the higher vulnerability of NSEs at lower seismic intensities in comparison with the vast majority of structural systems as well as to the much higher investment associated with NSEs, with respect to the total structural cost counterpart. The above issues become even clearer when attention is focussed on critical structures (e.g. hospitals, schools, and barracks) or production facilities, and several research studies (e.g. [Achour et al., 2011; Baird et al., 2014; Masi et al., 2014; Gabbianelli et al., 2020; Merino et al., 2018; Merino et al., 2019]) can clearly be brought to readers' attention for potential seismic vulnerabilities associated with NSEs housed in critical facilities such as hospitals or industrial plants.

On the other hand, or by the same token, to put it from a proper perspective, codification efforts have been made in the last four decades, leading authorities and regulators to conceive and release several national and international codes and standards or guidelines for seismic qualification of NSEs by either testing or analysis or both (see e.g. [ICC-ES, 2020; ISO, 2013; IEC/IEEE, 2018; IEC/IEEE, 2020; IEC, 2022]). Product-specific standards for a few types of NSEs (e.g. [IEEE, 2018]) accompany less specific ones (e.g. [ICC-ES. 2020]) or ones that are meant to set principles and philosophies for proper qualification (e.g. [ISO, 2013]), all standing alongside a variety of national seismic design standards/codes intended to set performance criteria, stability and functionality mostly, for the design of NSEs (see e.g. [NTC, 2018; ASCE, 2022; NZS, 1995; FEMA, 2007; FEMA, 2008]. Such a scenario is nowadays obvious to researchers and regulators and stems from the fact that NSEs include architectural elements, building utility systems as well as building contents. In addition to such a wide typological classification, another involves behaviour, given that acceleration sensitive, and displacement sensitive and acceleration-and-displacement sensitive NSEs do exist, complicating the context further. As an example, window wall, curtain wall and storefront systems are regulated for what concerns earthquake-induced actions for instance by the Americal Architectural Manufacturer Association (AAMA), whilst ventilated façades are not covered, not even at the EAD (European Assessment Document) level (Peloso et al., 2022).

Major issues and gaps emerging from daily routine/experience include, but are not limited to: i) knowledge gap, which aspect involves different actors/players such as designers, manufacturers, installers and directors of works, and ii) stock gap, which aspect involves the economic feasibility of testing, for instance by shaking table, an entire stock of products (each of which with its own dimensions, weight, and internal configuration details). For what concerns point i), it is noteworthy that NSEs are very often not designed to be part of the load-bearing system of a building structure in spite of being subjected to the same dynamic environment as the supporting structure during a seismic event. As a matter of fact, the design is usually experience-driven and based on load conditions other than earthquakes (e.g. gravity loads, transportation, and vibration during service). Again as a matter of fact, point ii) brings in a genuinely remarkable aspect or downside, that is, no matter how wide a given stock of products is, testing each and every configuration of each and every product is certainly not feasible, from both logistic and economic standpoints. Testing facilities are not very many, in comparison with possible testing demand and needs, and manufacturers and installers seek for flexibility and versatility during installation and a design concept that adapt the purposes of as many installation cases and circumstances as possible.

As such, rationale code-based methodologies are needed for the seismic qualification of NSEs that integrate experimental testing and numerical modelling, as a robust tool that allow extension of obtained results for a case/unit to other similar ones, sharing similar/comparable features in a systematic manner. That would, in turn, permit the efficient and effective seismic qualification of groups/classes of NSEs by a joint effort involving shake-table testing and numerical modelling/analysis, as well as the availability to treat and to take into account issues related to equipment inherently too complex to be modelled and simulated (e.g. electrical and/or mechanical parts/components/items a NSE may be equipped with). Accordingly, this paper would be a contribution towards this direction, discussing first some common challenges in seismic design of NSEs as well as qualification and code-compliancy, and then proposing a procedure for qualification by similarity that should meet the criteria of an integrated approach merging testing with – as easy as possible, not easier – numerical model and related analysis. Its application to a few case studies, owing to issues of space/page limits, closes the paper along with a critical discussion on the validation of developed numerical models.

2.CODE-COMPLIANCY AND QUALIFICATION

Most modern seismic codes require the verification of non-structural elements (NSEs) in line with the performance objectives prescribed for the primary structural system (e.g., [NTC, 2018], [CEN, 2004]). This requirement ensures that both structure and related NSEs achieve uniform performance across the relevant limit states. While this principle is now well recognized within the research community, manufacturers of NSEs are often unprepared when clients or project managers request seismic qualification evidence. Traditionally, the design of NSEs such as electrical equipment, HVACR systems, IT components, etc. has been primarily guided by experience, cost optimization, resistance to self-weight, transportation and operational vibrations. In some cases, base anchorage is not explicitly designed, relying solely on friction, or it is not adequately detailed. It is recalled here that a properly designed anchorage system is mandatory to ensure a reliable base connection, and replicable during shake table testing. In some cases, the interaction between the testing laboratory and manufacturers reveals these deficiencies, prompting late-stage modifications to address weak or missing aspects. The nuclear industry played a pioneering role in seismic qualification as early as the 1960s–70s, when building codes did not yet provide explicit requirements for NSEs. Very strict standards were developed to ensure the full functionality of emergency cooling and safety systems under seismic conditions [EPRI, 1991]. Since then, several national and international standards and guidelines have emerged. Some are general in scope, not tied to a specific NSE typology, such as [ISO, 2013; ICC-ES, 2020]. Other standards target specific sectors, with detailed requirements for pre- and post-test measurements and verifications such as [IEC, 2019a; IEEE, 2018; IEC-IEEE, 2020]. Despite their differences, all these documents recognize shake table testing as the most reliable and effective qualification method, being physical proof of the dynamic response of the NSE against the required seismic intensity, and as it allows for the equipment functional verification after loading. Given the inherent complexity of most NSEs - including chassis, internal components, and connections - experimental testing remains the primary option. Some standards (e.g., [IEEE, 2018]) describe alternative methods, such as quasi-static testing or numerical modelling, depending on the equipment's typology and role. In certain cases, specific NSEs are even deemed "inherently qualified," provided that their anchorage is verified analytically.

3.QUALIFICATION BY SIMILARITY: INTEGRATED APPROACH

Key references for seismic qualification, such as [ICC-ES, 2020] and [IEC, 2019a], are focused and do provide detailed testing procedures only; however, the practical challenges in terms of costs and logistic of testing every component variation within a product line is recognised. [ICC-ES, 2020], for instance, allows the selection of test specimens that adequately represent an entire product line. The rationale for specimen selection must be based on i) structural features, ii)mounting features, i.e. selecting smallest size and/or

number of tie-down bolts or weld, iii) subassemblies, iv) mass distribution, v) component variation. Similarly, [IEC, 2019a] restricts its scope to testing but recognizes that combined test-analysis approaches may be acceptable. [IEEE, 2018] also prioritizes shake table testing, but explicitly permits alternative methodologies depending on equipment type, voltage rating and complexity. Some equipment is considered "inherently acceptable" based on ruggedness and seismic performance history, requiring only anchorage verification by calculation. [IEEE, 2018] also permits numerical analyses - static coefficient, static, and dynamic methods (including response spectrum and time-history analyses) - and allows the so-called "qualification by group," where the most vulnerable unit is tested or analysed, and results are extended to similar configurations with supporting documentation. In practice, all major references implicitly or explicitly allow qualification by similarity or group. [IEEE, 2018], for example, specifies requirements for group definition and worst-case identification, including i) Mass and stiffness of the equipment; ii) Geometry (e.g. general configuration, height, location of the centre of mass); iii) Use of identical or very similar components; iv) Dynamic response of the equipment; v) Magnitude of conductor load effects; vi) Strength of load-carrying elements; vii) Differences that may influence functionality; viii) Support structure; ix) Anchorage details. Given this extensive and not exhaustive set of criteria, a rigorous process for extrapolating experimental results through calibrated numerical models is far from straightforward. A balanced approach is needed, weighing equipment complexity, functional role, performance requirements, and – not last – the number of configurations targeted for extension. In the following an integrated qualification framework is described; such approach combines targeted shake table testing with advanced numerical modelling to extend results on a robust basis across a product line. The process is structured as follows:

Step 0: Product Grouping and Worst Case(s) Identification: A detailed analysis, jointly developed with the manufacturer, identifies which product configurations can be grouped together, their differences, and the worst case or bounding configurations. Expert judgment, supported by code provisions [ICC-ES, 2020; IEC, 2019a; IEEE, 2018], guides this process.

Step 1: Shake-Table Testing of Representative Case(s): While this phase might be similar to a typical NSE qualification through shake table testing, some relevant differences to make it suitable for the following steps need to be considered. The testing campaign must be conceived to provide all relevant data needed for the numerical model calibration, i.e. more than what is required by the standards and guidelines above mentioned. To this end, a specific instrumentation layout must be defined to gather all relevant quantities to be compared afterwards. Modal quantities – considering higher modes too if possible – and damping are needed, requiring an adequate number of accelerometers in proper locations. Additionally, acceleration and displacement tracking in the identified control points serve to characterize the dynamic response under seismic loading. Finally, strain measurement in critical locations need to be considered as well. On the testing protocol side, in addition to low intensity random and/or sine-sweep excitation and actual seismic tests, it is found very important to apply seismic loading intensity sufficient to trigger the damage mechanism(s) of the unit. This in fact reveals the non-linear threshold to consider to limit or properly tune the numerical model. Additionally, this defines whether the numerical model is able to represent such mechanism or not, thus providing important limitations or the need to consider such limit state through parallel analytical methods.

Step 2: Numerical Model Development, Calibration, and Validation: As mentioned in Step 1, the numerical model must rely on a good matching of modal characteristics, damping, acceleration and displacement of the selected control point, strains and damage mechanism.

A detailed discussion on the Step 2 is not presented here; in this paper, the main focus to this end is rather to underline some relevant points related to the pathway to achieve a reliable numerical model for results extrapolation. First, a huge variety of NSEs on which experimental results extrapolation would be desirable exist, and the wide majority of them typically show a higher modelling complexity when compared to many

structural systems. There are cases for instance in which NSE subcomponents are not effectively interconnected, but they can be separated and independently sliding and/or hitting against each other (e.g. false ceiling tiles clipped into guides), unreliable poor mechanical connections such as very few (2-3) threads of bolt connections on thin metal sheets, or again different element in contact with each other but simply laid or plugged with unknown frictional resistance. Also, some equipment typically features internal component serving their functioning, but having as a side effect structural relevance with unproper conception (e.g. massive copper busbars of UPS systems). Moreover, the number of internal elements of an electrical/electronic equipment might pose some serious modelling challenges. Lastly, all components related to the functioning of the unit must be verified in terms of i) same components of the tested configuration and ii) lower or equal seismic action suffered, meaning that all, or at least the highest acceleration experimented must be identified and recorded. In the next chapter, two case studies part of the recent seismic qualification experience of EUCENTRE accredited laboratories of Pavia, Italy, are described, highlighting many of the aspects above discussed.

4. CASE STUDIES

4.1 A FAN WALL UNIT

In this context, the first case study presented concerns a Fan Wall unit, a cooling system that delivers uniform, large-volume airflow, designed for thermal management of data centre; a 3D rendering of the specimen is shown in Figure 1(a). The analysed equipment has dimensions 3600×1600×3500 mm and operating weight of 2310 kg. The evaluation is carried out through both numerical and analytical analyses, aimed at identifying any potential structural vulnerability, then through experimental test in order to confirm the result obtained by modelling. The unit consists of an external aluminium frame, equipped with enclosure panels and front filter doors. Inside, large fans are arranged between galvanized steel sheets and uprights, which are riveted to a steel base frame. At the rear of the unit, coil batteries are installed above a condensate collection tray. The connection between the two stacked units of the fan wall specifically involves the use of three pairs of steel connecting plates located on three sides of the unit (Figure 2). The absence of connecting plates on the fourth side is due to limited accessibility during and after wall installation.



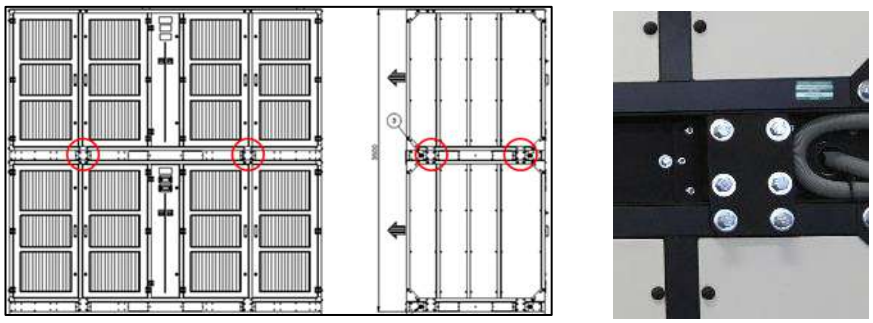
(a) (b)

Figure 1. (a) 3D rendering of the analysed equipment and (b) detail of a connection

4.1.1 Critical review based on expert judgment

From the inspection of the actual unit, it is observed that the four corner uprights terminate with a quadrangular nylon element, into which the two horizontal crossbeams are inserted with a socket-type (cup-shaped) connection. These same uprights are connected to the short-side crossbeam of the unit, both at the top and bottom, by means of a steel bracket fastened with two bolts, one on the crossbeam and one on the upright, as reported in Figure 1(b). Based on technical review and preliminary assessment of potential

structural deficiencies, the manufacturer revised the bracket design by adding an additional bolt. The remaining uprights feature a single-bolt connection at both the top and bottom ends. These aspects are more challenging to model accurately in the absence of a specific characterization of the individual element, highlighting the importance of expert engineering judgment.

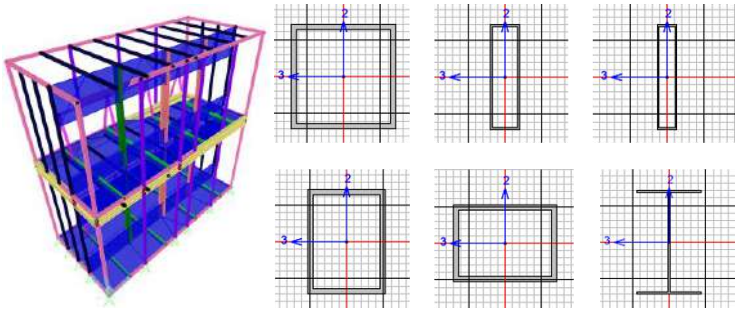


(a) (b)

Figure 2. (a) Location of connection plates between the two stacked units and (b) actual connection plate

4.1.2 Description of numerical model

The finite element model was developed using the commercial software SAP2000 (CSI). A 3D view of the model, with structural elements identified with different colours, is presented in Figure 3(a).



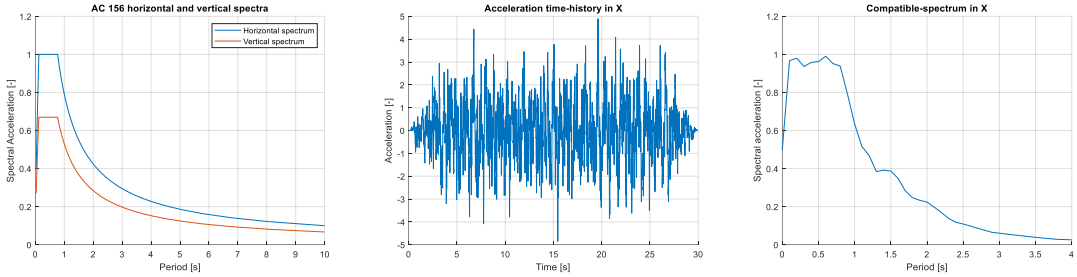
(a) (b)

Figure 3. (a) Model of the specimen and (b) sections of frame elements

Regarding the materials, the structure consists of an external frame made of raw and painted extruded aluminium alloy EN AW 6060-T6, and internal reinforcing elements made of galvanized steel. The modulus of elasticity is 69000 MPa for the aluminium alloy and 210000 MPa for the galvanized steel. As for the uprights and crossbeams, these were modelled using linear frame elements, in accordance with the actual geometric characteristics of the equipment. In addition to the aforementioned profiles, two C-shaped beams located beneath the base of the elevated unit were also explicitly modelled. The cross-sectional profiles used in the model are reported in Figure 3(b). The unit's base panel and the internal sheets supporting the fans were modelled using two-dimensional shell elements, based on a thin-shell formulation, reproducing the actual geometry of the equipment, with a thickness of 40 mm. Lumped masses were introduced to simulate the batteries housed within the unit, allowing their mass to be applied at the correct centre of mass location. These masses are connected at the base by eight rigid elements. Boundary conditions were defined based on these connection details: a fully restrained (fixed-end) connection was assumed for the corner uprights, and for the remaining uprights, an internal hinged connection was considered a more proper idealisation, reflecting the single-bolt fastening configuration.

4.1.3 Numerical analyses

In addition to a critical review of the structural configuration based on the available/provided documentation, linear dynamic analyses were conducted. In the absence of a site-specific seismic hazard assessment, design spectra from the [ICC-ES, 2020] guideline were considered, as illustrated in Figure 4(a). The spectral level reported in the paper has been normalised. Due to the asymmetric behaviour of the connection between the two stacked units of the fan wall, a nonlinear model was also required. Under compression, contact occurs along the entire perimeter of the units, whereas in tension, the reaction system relies on the steel plates only. To model this connection, nonlinear Gap/Hook links were employed. Six hook elements were defined at the positions corresponding to the connecting plates between the two units, with stiffness equal to the axial stiffness of the steel brackets. At the remaining nodes along the interface between the two stacked units, gap elements were assigned with axial stiffness approximately two orders of magnitude greater than the stiffness assigned to the Hook-type links. Because the models include nonlinear structural elements, nonlinear time-history analyses were carried out by defining a set of three components, phase independent, acting along the main directions. These time-histories were generated from the response spectra adopted in the linear dynamic analyses, thus spectrum-compatible, as illustrated in Figure 4.



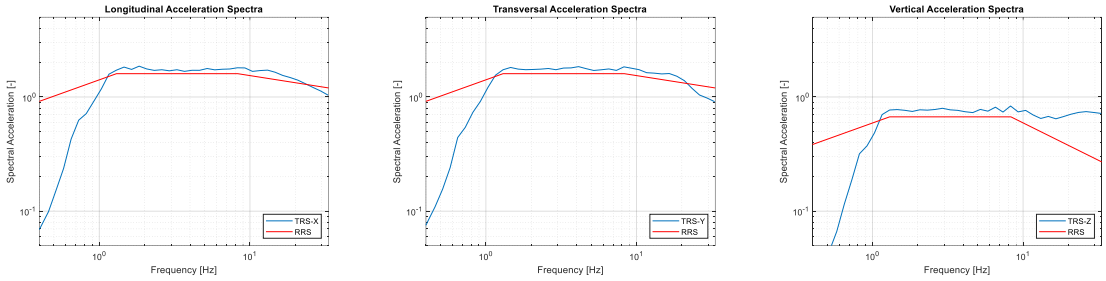
(a) (b) (c)

Figure 4. (a) ICC-ES AC 156 horizontal and vertical RRS, (b) time history in acceleration in X and (c) time history in X actual response spectrum

The results of the analysis were used to verify the main structural elements of the item. Specifically, all checks were performed with reference to the Italian Building Code (NTC, 2018), assessing instability mechanisms such as compression buckling, as well as shear and combined axial-bending effects (including both members in tension and compression). The most critical verification was found to be the combined axial-bending, as a greater number of elements exhibited lower collapse load multipliers - i.e. the ratio between capacity and demand -. In particular, the most critical elements were identified as the external vertical uprights located at the corner positions of the lower unit. Overall, the unit was found to be quite flexible, with a fundamental period of about 0.77s. The only stiffening and lateral-force resisting - although not specifically designed for this purpose - are the internal support walls for the fans, together with the external enclosure panels and doors, which did play a role in the response of this NSE. This notwithstanding, the latter components may be very prone to instability and/or damage at their connections to the external frame, as they are very thin and have a sandwich structure. Such a failure mechanism – involving connections – should be further evaluated through dedicated laboratory testing on individual components rather than on the entire unit. The lack of the connection between the two stacked units of the fan wall on one side was found to be non-critical, as it exhibits a significant safety factor against tensile yielding.

4.1.4 Experimental shake table testing for seismic qualification

Subsequently, shake table tests were performed on the aforementioned unit. Each input signal was generated in accordance with the [ICC-ES, 2020], meeting specific requirements such as the spectra to match (Figure 5), minimum total duration, duration of the strong-motion phase, etc.



(a) (b) (c)

Figure 5. (a) Comparison of TRS and RRS for test in X direction, (b) Y direction and (c) Z direction

Each component had a total duration of 30 seconds. A comparison between the Test Response Spectra (TRS) and the Required Response Spectra (RRS) – identical to those used in the modelling analyses, but plotted against frequency – is presented for the three principal directions in Figure 5. After the test, the specimen exhibited significant structural damage and noticeable deformations. The following issues were observed: the nylon edgeboard of the bottom module in the lower corner slipped in the transversal direction, as shown in Figure 6 and the door panel opened, due to a damage to the door upper lock.



Figure 6. Slipped of nylon edgeboard

The criticality of the nylon edgeboard elements was primarily identified through critical review, while this might be not duly considered directly focusing on "basic" numerical models. Furthermore, a reliable model of such connection is difficult to achieve in absence of specific mechanical characterization. Post-test evidence have confirmed their critical influence, emphasizing the need for both thorough characterization and explicit modelling. Nonetheless, such detailed procedures are seldom incorporated into typical professional practice, which tends to favour simplified numerical models. This further underlines the essential role of experimental testing, in supporting and validating the analytical process.

4.2 AN UNINTERRUPTIBLE POWER SUPPLY (UPS) UNIT

The second case study presented in this paper refers to an Uninterruptible Power Supply (UPS) unit. A 3D rendering of the specimen, along with a partial internal view highlighting typical components, is shown in Figure 7(a,b).



(a) (b) (c)

Figure 7. (a) 3D rendering of the analysed equipment, (b) partial internal view of the specimen and (c) UPS *FEM*

The structure consists of a galvanized sheet metal frame with closure panels, reinforced at the lower base and upper corners with C-shaped stiffeners. The unit is composed of three modules connected to each other through bolted connections and top plates bolted as well. Each of these modules is made up of sheet metal panels, uprights, and crossbeams in galvanized steel sheet; the dimensions and total mass of the unit are 2990x1022x2000mm and 2260 kg. The structure features a front and a rear crossbeam, both anchored to the floor and to the uprights with bolts and a backing plate with steel brackets.

4.2.1 Numerical model

The finite element model was developed using the commercial software SAP2000. Linear dynamic analyses with response spectrum were performed. The model includes the internal structural frame, drawers, disconnectors, and various internal components. Many of these elements are interconnected; some are in contact with others but are not rigidly connected, relying instead on frictional contact - for example, the copper bars with insulating components. Regarding the materials, the structure consists of a galvanized sheet metal frame and internal reinforcing stainless steel bolted connections. The modulus of elasticity is 200000 MPa for the galvanized sheet metal and 210000 MPa for the stainless steel. Of particular interest is the fact that the structural frame is composed of C-shaped profiles of 29 different types and dimensions - identified with different colours in Figure 7(c) - which hampers easiness of modelling endeavours for analysts. This required a detailed survey of the actual geometric properties of each element to ensure proper representation in the model, both in terms of geometry and in the correct orientation of the members. Special attention was given to the alignment of local axes of each element as per their real-world placement. These aspects significantly increased the time-effort required for the modelling process. Regarding the drawers present within some units, they were modelled using two-dimensional linear shell elements, based on a thin-shell formulation, reflecting the geometric characteristics and stiffness of the actual components. A material density value was assigned to the drawers such that their weight matched that of the real components, a necessary step to properly define their mass. The bolted connection system was modelled using "body" type constraints. Regarding the internal constraints between the various frame elements, two limiting cases were considered for the analyses and verifications: a first case with fully fixed internal connections, and a second case with internal hinged connections, which serve the purposes of upper and lower bound demand estimates (considering the duality of force and displacement for seismic demand assessment). Components not explicitly modelled were represented as lumped masses, distributed across the nodes so as to accurately reproduce the actual position of the centre of mass. For each of the three modules, the contribution of the internal components to be included in the model was determined starting from the total weight provided in the technical drawings. This was achieved by subtracting the weight of the modelled structural elements from the total weight.

4.2.2 Likeliest local failure mechanisms

Linear dynamic analyses were performed using response spectra based on [ICC-ES, 2020], with a horizontal spectral plateau of 1.0g (Sds = 1.0g, z/H = 0), and were used to carry out checks meant to determine the

likelihood of a certain mechanism to take place during shake-table testing. For this specific NSE, the following mechanisms were deemed significant and were thus checked: i) buckling, ii) shear and iii) combined axial-bending, all of them in accordance with [NTC, 2018] for what concerns calculation of capacity. The most critical verification was found to be the one related to buckling and combined axial-bending, as a greater number of elements exhibited lower collapse load multipliers. In particular, the most critical ones were identified as the external vertical uprights located in the modules housing the drawers.. Additionally, other offline checks were undertaken because local failure mechanisms were identified as potentially critical. These behaviours would require a different modelling approach, both in terms of scale and numerical formulation, for an explicit representation. At this stage shake table tests have not been yet executed, therefore, no direct comparison between numerical results and experimental data is currently available.

5.CLOSING REMARKS

Seismic qualification of NSEs is vital, and numerical modelling may be or become instrumental under some circumstances, especially when analysis efforts merge and integrate with more standard experimental testing endeavours. In light of this, a methodology for qualification by similarity has been proposed and presented in this paper, which showcased it by means of two illustrative examples, namely a fan wall unit and an UPS one. Merging testing and modelling implies taking pros of each and eliminating downsides of both; modelling alone would be meaningless for particular situations and case-specific aspects (e.g. functionality of electrical and/or mechanical parts/equipment), whereas the testing of an entire stock of products - regardless of which minor change(s) in geometry each NSE of that stock/portfolio would feature - is certainly cumbersome, to the limit of unfeasibility from both logistic and economic standpoints.

In closing, it is worth noting that the above is certainly acknowledged by current codes and standards for seismic qualification, each with its specific features or peculiarities, although further efforts could be envisaged towards this direction and towards harmonisation. For instance, the definition of clearer boundaries for field or ranges of applicability is certainly a noteworthy aspect, not an open issue clearly and admittedly but at the same time not a choice a manufacturer has to make or should be in a position to make, sometimes blindly based on monetary reasons, but rather a decision that shall be guided by experienced third parties supported by code-compliancy and more quantitative indications for specific cases of interest.

REFERENCES

Achour, N., Miyajima, M., Kitaura, M., Price, A. [2011] "Earthquake-induced structural and nonstructural damage in hospitals," *Earthquake Spectra*, Vol. 27, No. 3, pp. 617–634. https://doi.org/10.1193/1.3604815.

Anwar, M.Y., Peloso, S., Brunesi, E., [2025] "Test-informed in-plane/out-of-plane capacity domain-driven seismic fragility models for masonry infills in reinforced concrete frames," *Structures*, Vol. 76, 109014.

ASCE [2022] ASCE/SEI 7-22 Minimum Design Loads and Associated Criteria for Buildings and Other Structures, American Society of Civil Engineers.

Baird, A., Tasligedik, A.S., Palermo, A., Pampanin, S. [2014] "Seismic performance of vertical nonstructural components in the 22 February 2011 Christchurch Earthquake," *Earthquake Spectra*, Vol. 30, No. 1, pp. 401–425. https://doi.org/10.1193/031013EQS067M.

Belleri, A., Brunesi, E., Nascimbene, R., Pagani, M., Riva, P. [2015] "Seismic performance of precast industrial facilities following major earthquakes in the Italian territory," *Journal of Performance of Constructed Facilities*, Vol. 29, No. 5, 04014135.

CEN [2004] Eurocode 8: Design of Structures for Earthquake Resistance, European Committee for Standardization.

EPRI [1991] Guidelines for Nuclear Plant Seismic Margin Analysis, Electric Power Research Institute.

FEMA461 [2007] *Interim testing protocols for determining the seismic performance characteristics of structural and nonstructural components*, Federal Emergency Management Agency (FEMA), Washington, DC, USA.

FEMA [2008] FEMA E-74: Reducing the Risks of Nonstructural Earthquake Damage, Federal Emergency Management Agency.

Filiatrault, A., Uang, C.M., Folz, B., Christopoulos, C., Gatto, K. [2001] *Reconnaissance report of the February 28, 2001 Nisqually (Seattle-Olympia) earthquake*, Structural Systems Research Project Report No. SSRP-2000/15, Department of Structural Engineering, University of California, San Diego, La Jolla, CA, USA.

Filiatrault, A., Sullivan, T.J. [2014] "Performance-based seismic design of nonstructural building components: The next frontier of earthquake engineering," *Earthquake Engineering and Engineering Vibration*, Vol. 13, No. 1, pp. 17-46.

Gabbianelli, G., Perrone, D., Brunesi, E., Monteiro, R. [2020] "Seismic acceleration and displacement demand profiles of non-structural elements in hospital buildings," *Buildings*, Vol. 10, No. 243. https://doi.org/10.3390/buildings10120243.

Gabbianelli, G., Perrone, D., Brunesi, E., Monteiro, R. [2022] "Seismic acceleration demand and fragility assessment of storage tanks installed in industrial steel moment-resisting frame structures," *Soil Dynamics and Earthquake Engineering*, Vol. 152, 107016.

Gupta, A., McDonald, B.M. [2008] "Performance of building structures during the October 15, 2006 Hawaii earthquake," *Proceedings of the 14th World Conference on Earthquake Engineering*, Beijing, China.

ICC-ES [2020] AC156: Acceptance Criteria for Seismic Certification by Shake-Table Testing of Nonstructural Components, International Code Council Evaluation Service.

IEC [2019a] IEC EN 60068-3-3: Environmental Testing – Part 3-3: Supporting Documentation and Guidance – Seismic Test Methods for Equipment, International Electrotechnical Commission.

IEC [2022] IEC 60780-323: Nuclear power plants – Electrical equipment – Type test methods for earthquake protection, International Electrotechnical Commission.

IEC-IEEE [2020] IEC/IEEE 60980-344: Standard for Seismic Qualification of Equipment for Nuclear Power Generating Stations, International Electrotechnical Commission and Institute of Electrical and Electronics Engineers.

IEEE [2018] IEEE 693-2018: Recommended Practice for Seismic Design of Substations, Institute of Electrical and Electronics Engineers.

ISO [2013] ISO 13033: Bases for Design of Structures — Seismic Actions on Nonstructural Components for Building Applications, International Organization for Standardization.

Masi, A., Santarsiero, G., Gallipoli, M.R., Mucciarelli, M., Manfredi, V., Dusi, A., Stabile, T.A. [2014] "Performance of the health facilities during the 2012 Emilia (Italy) earthquake and analysis of the Mirandola hospital case study," *Bulletin of Earthquake Engineering*, Vol. 12, No. 5, pp. 2419–2443. https://doi.org/10.1007/s10518-013-9518-4.

Merino Vela, R.J., Brunesi, E., Nascimbene, R. [2018] "Derivation of floor acceleration spectra for an industrial liquid tank supporting structure with braced frame systems," *Engineering Structures*, Vol. 171, pp. 105-122. https://doi.org/10.1016/j.engstruct.2018.05.053.

Merino Vela, R.J., Brunesi, E., Nascimbene, R. [2019] "Seismic assessment of an industrial frame-tank system: development of fragility functions," *Bulletin of Earthquake Engineering*, Vol. 17, No. 5, pp. 2569-2602. https://doi.org/10.1007/s10518-018-00548-2.

Merino, R.J., Rodriguez, D., Peloso, S., Brunesi, E., Perrone, D., Filiatrault, A., Nascimbene, R. [2024] "Experimentally Calibrated Numerical Modeling for Performance-Based Seismic Design of Low-Frequency Rocking Electrical Cabinets," *Journal of Earthquake Engineering*. https://doi.org/10.1080/13632469.2024.2390090.

NTC [2018] Norme Tecniche per le Costruzioni, Italian Ministry of Infrastructure.

NZS [1995] NZS 4219: Code of Practice for the Seismic Design of Engineering Systems for Buildings, Standards New Zealand.

Peloso, S., Brunesi, E., Rizzo Parisi, E. [2022] "Component-test-informed seismic design methodology for façade systems," *Proceedings of the Fifth International Workshop on the Seismic Performance of Non-Structural Elements (SPONSE)*, Palo Alto, CA, USA.

Peloso, S., Brunesi, E., Perrone, D., Moroni, C. [2023] "In-plane seismic fragility models for clay masonry infills in reinforced concrete frames," *Structures*, Vol. 56, 105043.

Perrone, D., Calvi, P.M., Nascimbene, R., Fischer, E. C., Magliulo, G. [2019] "Seismic performance of non-structural elements during the 2016 Central Italy earthquake," *Bulletin of Earthquake Engineering*, Vol. 17, No. 10, pp. 5655-5677.

Perrone, D., Rodriguez, D., Filiatrault, A., Brunesi, E., Beiter, C., Piccinin, R. [2022] "A Framework for the Quantification of Non-Structural Seismic Performance Factors," *Journal of Earthquake Engineering*, Vol. 26, No.16, pp. 8468–8494.

Ricci, P., De Luca, F., Verderame, G.M. [2011] "6th April 2009 L'Aquila earthquake, Italy: Reinforced concrete building performance," *Bulletin of Earthquake Engineering*, Vol. 9, No. 1, pp. 285-305.

Rodriguez, D., Perrone, D., Filiatrault, A., Brunesi, E. [2021] "A probabilistic strong floor motion duration model for seismic performance assessment of non-structural building elements," *Earthquake Engineering and Structural Dynamics*, Vol. 50, No. 15, pp. 4161-4179.

Shake Table Testing of Rooftop Mechanical Equipment with Different Attachment Strategies on A Full-Scale Ten-Story Building

Xianzhao Zhang[1], Jiachen Zhang[1], and Tara C. Hutchinson[1]

[1] Department of Structural Engineering, University of California San Diego
La Jolla, CA 92093, USA
e-mail: xiz217@ucsd.edu, j-charlie-zhang@ucsd.edu, tahutchinson@ucsd.edu

Abstract. The seismic performance of acceleration-sensitive mechanical equipment is a major area of interest within the field of nonstructural components and systems (NCSs). To save indoor space, conserve energy, or meet functional requirements, such equipment is often installed on building rooftops, where higher acceleration demands during earthquakes make rooftop-mounted units more susceptible to damage. Floor-mounted mechanical equipment is typically supported by vibration and noise isolation devices to reduce the transmission of unwanted motion to the supporting structure. However, limited attention has been given to understanding under what conditions, and to what extent, vibration and acoustical design strategies may enhance, or potentially compromise, the seismic performance of lightweight NCSs. To investigate this issue, five lightweight air-conditioning condenser units, each weighing no more than 1,500 N, including three with a slender aspect ratio of 3.7 and two with a squat aspect ratio of 1.1, were installed on the rooftop of a full-scale, ten-story cold-formed steel (CFS) building tested on a six-degree-of-freedom outdoor shake table. Different base attachment strategies were employed. All three slender units were screw-mounted at four manufacturer-provided feet to the CFS studs. Two of the units had a modified base boundary condition, with neoprene pads and spring isolators respectively added under the base feet. Both squat units were screw-mounted using four steel angles connected to the CFS studs, with one additionally supported by neoprene pads placed beneath the equipment. This paper presents the first release of preliminary results from the recently completed experimental program, focusing on rooftop mechanical equipment responses under service-level, design-level, and maximum-considered earthquake motions. Results presented include measured floor acceleration amplification factors, peak component accelerations, and component amplification factors. These findings are compared with code-based provisions to evaluate the adequacy of current design coefficients in capturing the acceleration demands on lightweight components.

Keywords: Attachment design, HVAC equipment, Nonstructural components, Seismic performance, Shake table test

1. INTRODUCTION

The safety and functionality of nonstructural components and systems (NCSs) during both frequent and rare earthquake events are essential for maintaining operational continuity of buildings and other infrastructure. Buildings that serve to provide emergency shelter, food, medical care, information, and other indispensable services must also remain functional as they serve as a cornerstone of community resilience.

For buildings engineered to withstand earthquakes, nonstructural damage often accounts for a substantial share of economic losses, particularly in acceleration-sensitive components such as mechanical and electrical equipment [Papadopoulos *et al.*, 2019]. For such equipment, the attachment condition significantly affects its performance during an earthquake. Feinstein and Moehle [2022] tested different attachments using yielding steel angles with varying stiffness and strength, demonstrating their influence on the dynamic response of floor-mounted NCSs connected to a reinforced concrete slab. Similarly, Elkady *et al.* [2025] studied the efficacy of sacrificial steel yielding elements as an attachment method to limit acceleration demands in sliding-motion-governed NCSs. In their work, a steel carriage supporting interchangeable mass plates was used to experimentally mimic the sliding components.

These and other experimental investigations of real mechanical or electrical equipment face two major challenges. First, the high capital cost of testing makes it difficult for academic institutions to pursue such research without direct collaboration with manufacturers. In practice, manufacturer-sponsored shake table tests conducted for seismic certification are primarily intended to quality the equipment for use in earthquake-prone applications, using either synthetic earthquake motions or prescribed test protocols (e.g., AC156 [ICC 2012]). These tests have limited focus on comparing attachment methods or advancing fundamental understanding. Second, the inherent complexity of mechanical and electrical equipment, characterized by irregular geometries, uneven mass distribution, and designs developed outside the structural engineering domain without consideration of seismic performance, poses difficulties for deriving generalized rules of behaviour that hold scientific value.

Vibration-isolated heavy mechanical equipment has attracted particular research interest. Fathali and Filiatrault [2008] investigated a vibration-isolated centrifugal liquid chiller weighing 117,655 N, tested on a six-degree-of-freedom (6-DOF) shake table using synthetic ground motions derived from AC156 [ICC 2012]. Their study focused on evaluating the influence of snubber gap size on the dynamic response of the chiller. Astroza *et al.* [2015] conducted shake table tests on a rooftop-mounted cooling tower weighing 279,000 N (when filled with water), installed on a full-scale, five-story reinforced concrete building subjected to unidirectional shaking. Their findings showed that component amplification factors could substantially exceed those prescribed in standards, particularly when the equipment period was close to the predominant period of the supporting structure.

A shake table testing campaign of a full-scale, ten-story cold-formed steel (CFS) building was recently conducted at the Large High-Performance Outdoor Shake Table (LHPOST6) at University of California San Diego. This program provides a unique opportunity to investigate the seismic performance of both the structural system and a select suite of NCSs. On the building rooftop, three identical slender air-conditioning condenser units, each weighing 1,434 N with a resulting maximum aspect ratio of 3.7, and two identical squat condenser units, each weighing 1,339 N with a resulting aspect ratio of 1.1, were installed. Various attachment strategies were implemented, including direct anchorage, neoprene pads, and spring isolators, with the objective of comparing and understanding the influence of vibration and acoustical design practices on the seismic performance of lightweight mechanical equipment under real earthquake excitations. This paper first outlines the shake table test program and earthquake protocol, followed by a discussion of attachment designs implemented and equipment instrumentation. Subsequently, experimental findings related to the mechanical equipment are presented, including floor acceleration amplifications, peak component accelerations (PCAs), and component amplification factors.

2.EXPERIMENTAL PROGRAM

2.1 BUILDING SPECIMEN

The test specimen was a full-scale, 10-story CFS-framed building (Figure 1). The building measured 11.6 m by 6.9 m in plan, with a uniform story height of 3.05 m across all 10 stories, in addition to a CFS parapet at the roof level measuring 1.1 m in height. The lateral force-resisting system consisted of symmetric steel-sheet-sheathed shear walls along both the longitudinal (east−west) and transverse (north−south) directions. Further details about the structural system and its design considerations can be found in Hutchinson *et al.* [2026]. The building was of high fidelity, including nonstructural features such as prefabricated steel stairs, windows and doors, suspended ceilings, fire sprinkler systems, and rooftop mechanical equipment.

As shown in Figure 1(c–d), five roof curbs of two different geometries but with the same height of 172 mm were rigidly connected to either CFS floor joists or CFS blocking through the roof cementitious panel using CFS support clips. The roof curbs were constructed of CFS studs and cementitious floor panel material, similar to that used throughout the building floor diaphragm. The attachment of the roof curbs and roof diaphragm were designed to remain fixed, with no relative displacement assumed. Five supplemental weights, simulated by cementitious floor panels, were also anchored to the roof. In addition, a diaphragm opening of 1,219 mm by 1,219 mm was constructed to accommodate a roof access hatch near the southwest corner of the roof.

2.2 EARTHQUAKE TEST PROTOCOL

A total of 18 seismic tests, including 15 service-level earthquakes (SLE), one design earthquake (DE), and two risk-targeted maximum considered earthquakes (MCE_R), were conducted to cover a wide range of amplitudes, durations, and directionalities, with the three hazard levels progressively increasing the seismic demand on both the structure and the NCSs. Table 1 [Zhang *et al.*, 2026] summarizes the earthquake motions used in the CFS building tests, and Figure 2 presents the achieved peak input accelerations (PIA), recorded at the shake table platen using accelerometers located at its centre of mass (CoM).

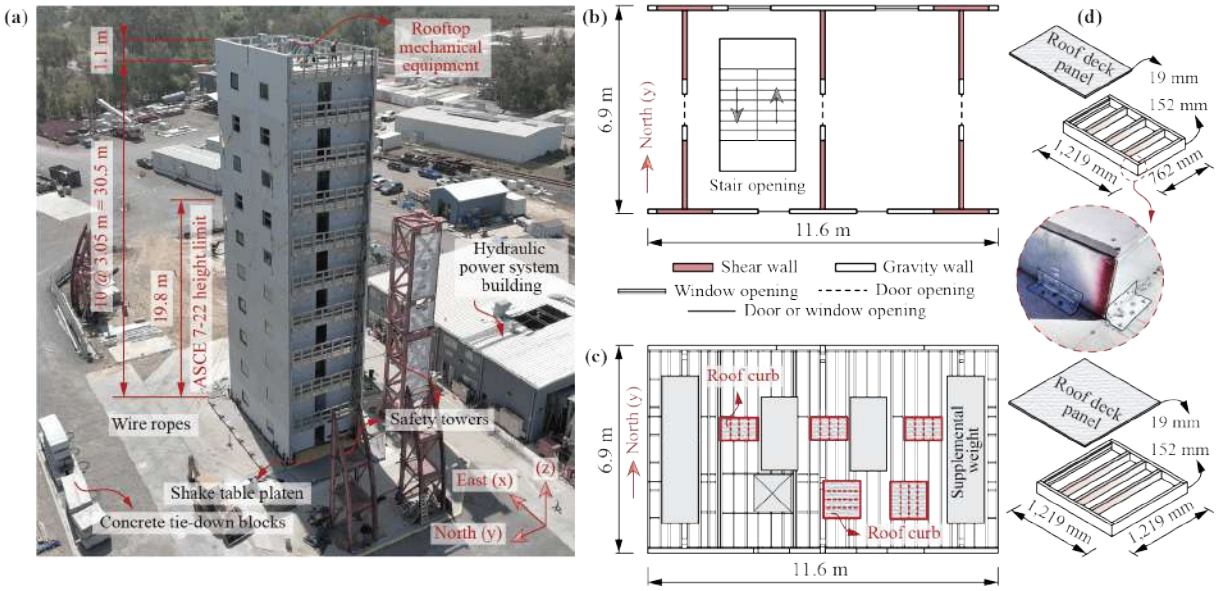


Figure 1. CFS building specimen: (a) aerial perspective view of the completed building from the northwest corner, (b) typical floor plan, (c) roof panel plan view, and (d) roof curb design

Table 1. Ground motion records and target hazard scales selected for shake table testing

Hazard level	MID	Earthquake event				Components		Input DOF	$D_{5\text{-}95}$ [sec]
		Name	Year	M_w	Station	x	y		
SLE	1	Loma Prieta, California	1989	6.9	Gilroy Array #3	90°	0°	xyz	11.4
	2					90°	0°	xyz	11.4
	3					90°	–	x	11.4
	4					–	0°	y	6.4
	5	Northridge, California	1994	6.7	LA City Terrace	90°	180°	xyz	11.9
	6					180°	90°	xyz	11.9
	7					180°	–	x	11.9
	8					–	90°	y	11.6
	9	Cape Mendocino, California	1992	7.0	Rio Dell Overpass	270°	360°	xyz	15.3
	10					360°	270°	xyz	15.3
	11[a]	Kahramanmaras, Türkiye	2023	7.8	4611	E	N	xyz	43.4
	12					E	N	xyz	43.4
	13	Elbistan, Türkiye	2023	7.5	4611	E	N	xyz	35.1
	14	Maule, Chile	2010	8.8	Curico Hospital	EW	NS	xy	45.2
	15	Kahramanmaras, Türkiye	2023	7.8	4611	E	N	xyz	43.4
DE	16	Loma Prieta, California	1989	6.9	Gilroy Array #3	90°	0°	xy	11.4
MCE_R	17	Loma Prieta, California	1989	6.9	Gilroy Array #3	90°	0°	xy	11.4
	18[b]	Cape Mendocino, California	1992	7.0	Rio Dell Overpass	360°	270°	xy	11.4

[a] MID11 target was 75% SLE.

[b] MID18 target was 90% of MCE_R.

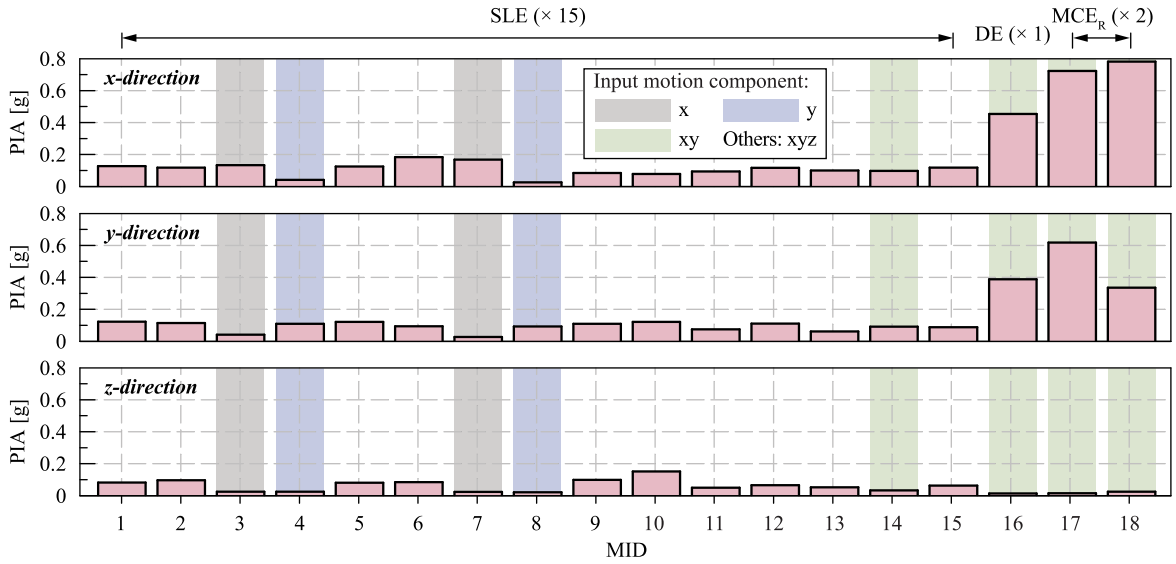


Figure 2. Achieved peak input acceleration at the shake table platen

2.3 ROOFTOP MECHANICAL EQUIPMENT

As shown in Figure 3(a), five lightweight air-conditioning condenser units, consisting of two different models, were installed on the roof curbs of the building. For brevity, SL-DA denotes the slender unit with direct attachment, SL-NP the slender unit with neoprene pads, SL-SI the slender unit with spring isolators, SQ-DA the squat unit with direct attachment, and SQ-NP the squat unit with neoprene pads. The slender unit measured 1,000 mm by 368 mm in plan and 1,365 mm in height, with a resulting maximum aspect ratio of 3.7 (Figure 3(b)), while the squat unit measured 902 mm by 902 mm in plan and 972 mm in height, resulting in an aspect ratio of 1.1 (Figure 3(c)). The slender unit was supported by two manufacturer-prefabricated steel tracks with four feet attached to its bottom face, whereas the squat units had no such installation aids. Because all five condenser units were pre-owned, the amount of refrigerant in each unit was uncertain. Loss of refrigerant charge reduces the unit weight, leading to small variations among the equipment. However, the contribution of refrigerant to the total weight was estimated to be less than 5%, so this variation was considered negligible. To obtain conservative seismic force estimates, the equipment weights were determined assuming each unit contained the full refrigerant charge, which corresponds to the maximum weight condition. The estimated weights of the slender and squat units were 1,434 N and 1,339 N, respectively.

Different base attachment strategies were employed for each rooftop mechanical equipment unit. As a benchmark configuration without vibration or acoustical mitigation measures (Figure 3(d)), a slender unit was directly screw-mounted at its four manufacturer-provided feet to the CFS studs of the roof curb. A 6.4 mm × 25.4 mm × 1.6 mm (inner diameter × outer diameter × thickness) fender washer was placed under the head of each self-drilling screw, which had a thread length of 76.2 mm and a nominal shank major diameter of 6.2 mm. To modify the base boundary conditions, two alternative attachment strategies were applied to slender units. In the first case (Figure 3(e)), four neoprene pads, each measuring 101.6 mm × 101.6 mm × 19 mm (length × width × thickness) were placed beneath shim plates. The shim plates distributed the load into the pads and directly supported the equipment feet. In the second case (Figure 3(f)), four spring isolators were used, each rated for a maximum vertical load of 500 N and a maximum horizontal load of 1,600 N. Both squat units were installed using four steel angle support clips (Figure 3(g–h)). One of the units was additionally supported by four neoprene pads placed beneath the equipment (Figure 3(i)). Each clip was fastened on the equipment housing side with three shorter self-drilling screws (thread length of 19 mm and nominal shank major diameter of 6.2 mm) and on the CFS stud side with two self-drilling screws identical to those used for the slender units. Although both squat units were oriented in the same direction, the placement of the CFS studs in the roof curb required different attachment layouts (Figure 1(c)). For the SQ-DA, the support clips were installed on the west and east sides of the equipment, while for the SQ-NP, they were installed on the north and south sides.

2.4 INSTRUMENTATION

For the seismic tests, more than 800 analogue sensors were strategically installed throughout the building to monitor the response of both the structure and the NCSs. Specifically for the rooftop mechanical equipment, a total of 36 analogue channels were used, consisting of 16 accelerometers and 20 linear potentiometers installed at selected locations. Figure 4 illustrates the instrumentation scheme of accelerometers and displacement transducers used for the rooftop equipment. Two uniaxial y-direction accelerometers were mounted at the northwest and southeast top corners of the slender unit to capture potential torsional response, since the mass of the slender condenser was offset toward the west side opposite the fan. In addition, one uniaxial x-direction accelerometer and one uniaxial z-direction accelerometer were installed at the centre of the top face of the slender unit. For the squat unit, one uniaxial accelerometer in each of the x- and y-directions was installed at the centre of the top face. Since the shake table test program for the DE and MCE_R ground motions did not include z-direction input and the squat unit was expected to generate negligible z-direction acceleration under these conditions, no z-direction accelerometers were installed on the squat units.

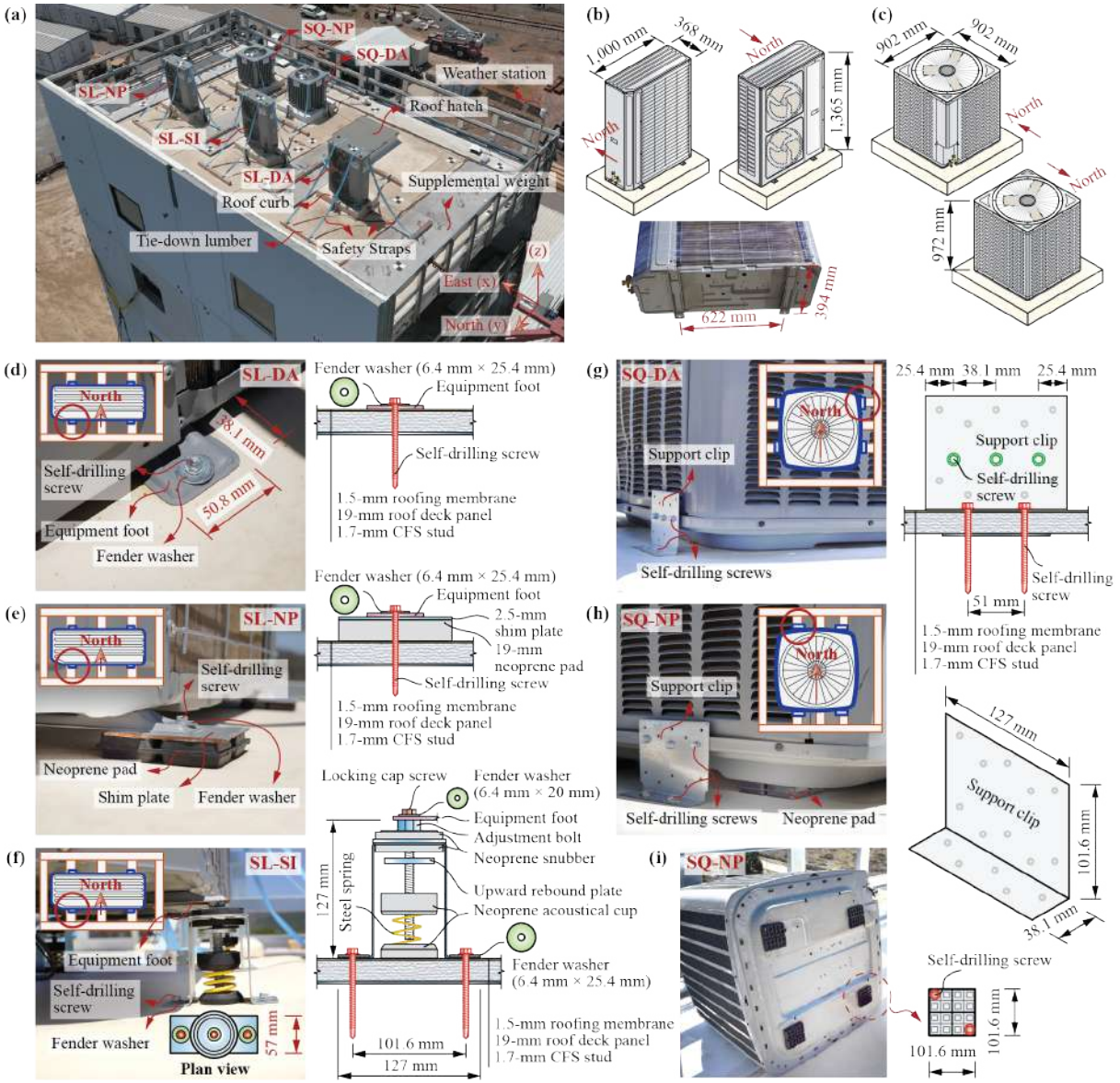


Figure 3. Overview of rooftop mechanical equipment: (a) aerial perspective view of the equipment layout from the northwest corner, (b) slender and (c) squat unit geometry, and attachment designs of (d) SL-DA, (e) SL-NP, (f) SL-SI, (g) SQ-DA, (h) SQ-NP, and (i) bottom view of SQ-NP

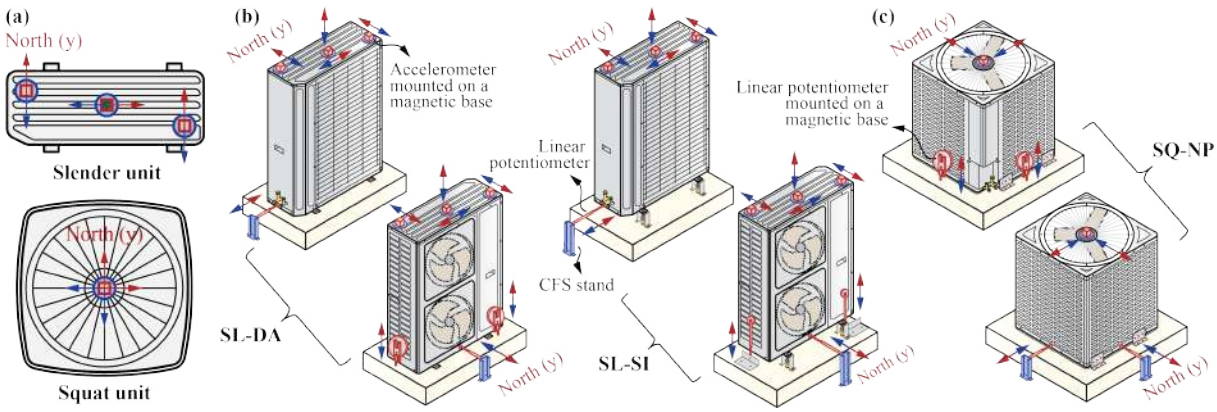


Figure 4. Instrumentation of rooftop mechanical equipment: (a) top view of accelerometer layout, representative configurations of accelerometers and displacement transducers for (b) slender and (c) squat units

The displacement transducer layout for the slender and squat units followed a similar approach (Figure 4(b-c)). One x-direction and one y-direction linear potentiometer were installed at the base of the equipment to measure displacements relative to the roof diaphragm, while two z-direction potentiometers were installed on adjacent sides near the base to record uplift. All recorded acceleration and displacement signals of the mechanical equipment were baseline-corrected and filtered using a fourth order bandpass Butterworth filter with cutoff frequencies of 0.2 Hz and 35 Hz, to remove signal noise while retaining the true response.

3.EXPERIMENTAL RESULTS

3.1 RESPONSE OF BUILDING SPECIMEN

Floor accelerations and the corresponding acceleration amplification factors are among the most critical structural response parameters affecting acceleration-sensitive NCSs. All accelerometers supplied by the LHPOST6 facility were used to generate the PFA/PIA profile. Note that only the motions actively exciting each orthogonal direction are considered. Figure 5 presents the peak floor acceleration (PFA), normalized by the achieved PIA, for both the x- and y-directions under 13 SLEs, one DE, and two MCE_R scaled tests. To capture the translational acceleration response of the building, one uniaxial accelerometer in the x-direction and one in the y-direction, provided by the LHPOST6 facility, were installed at the calculated CoM, as well as at the northwest and southeast corners of each floor. On the roof level, additional accelerometers were deployed on the eastern side of the CoM, at a distance of 2,185 mm, and at the northeast and southwest corners of the roof to provide a denser instrumentation array. In Figure 5, the variability of recorded accelerations among sensors on the same floor is depicted by a shaded light grey region, which spans the mean ± standard deviation, while the arithmetic mean response is highlighted by the red.

In the x-direction, the maximum average PFA/PIA ratios were 2.39 (SLE), 2.05 (DE), and 2.24 (MCE_R). In the y-direction, the corresponding averages were 2.67, 2.08, and 2.23. These maxima consistently occurred at the roof, where the building's whipping action led to greater acceleration amplification. Compared with the SLE and MCE_R cases, the DE case exhibited smaller roof-level amplification. However, this result may not be statistically robust, as it is based on only one DE ground motion. ASCE/SEI 7-22 [ASCE, 2022] Chapter 13 provides two alternative equations for calculating acceleration amplification factors along the height of a building. The fundamental-period-independent method, Equation (13.3-5), assumes a linear amplification profile ranging from 1.0 at the ground level to 3.5 at the roof level. The fundamental-period-dependent method, Equation (13.3-4), introduced in the latest edition, aims to improve prediction accuracy by incorporating the building's fundamental period. For the tested building specimen, the fundamental periods used in Equation (13.3-4), were determined from white-noise excitation data, prior to earthquake tests, as 0.77 sec in the x-direction and 0.73 sec in the y-direction.

As shown in Figure 5, the differences between the code-based acceleration amplification factors and the mean PFA/PIA ratios were calculated and compared at each floor. Under SLEs, both Equations (13.3-4) and (13.3-5) did not consistently yield conservative predictions of acceleration amplification, as shown in the shaded light red region, when the PFA/PIA ratios were computed from individual accelerometer recordings. Considering that the acceleration demand under SLE ground motions is relatively small, this lack of conservatism is unlikely to pose a safety concern. Overall, median box-plot values at each floor indicate that both code-based equations consistently provide reliable, conservative, acceleration amplification predictions, with the most conservative results consistently occurring at the ninth floor across both directions and all hazard levels.

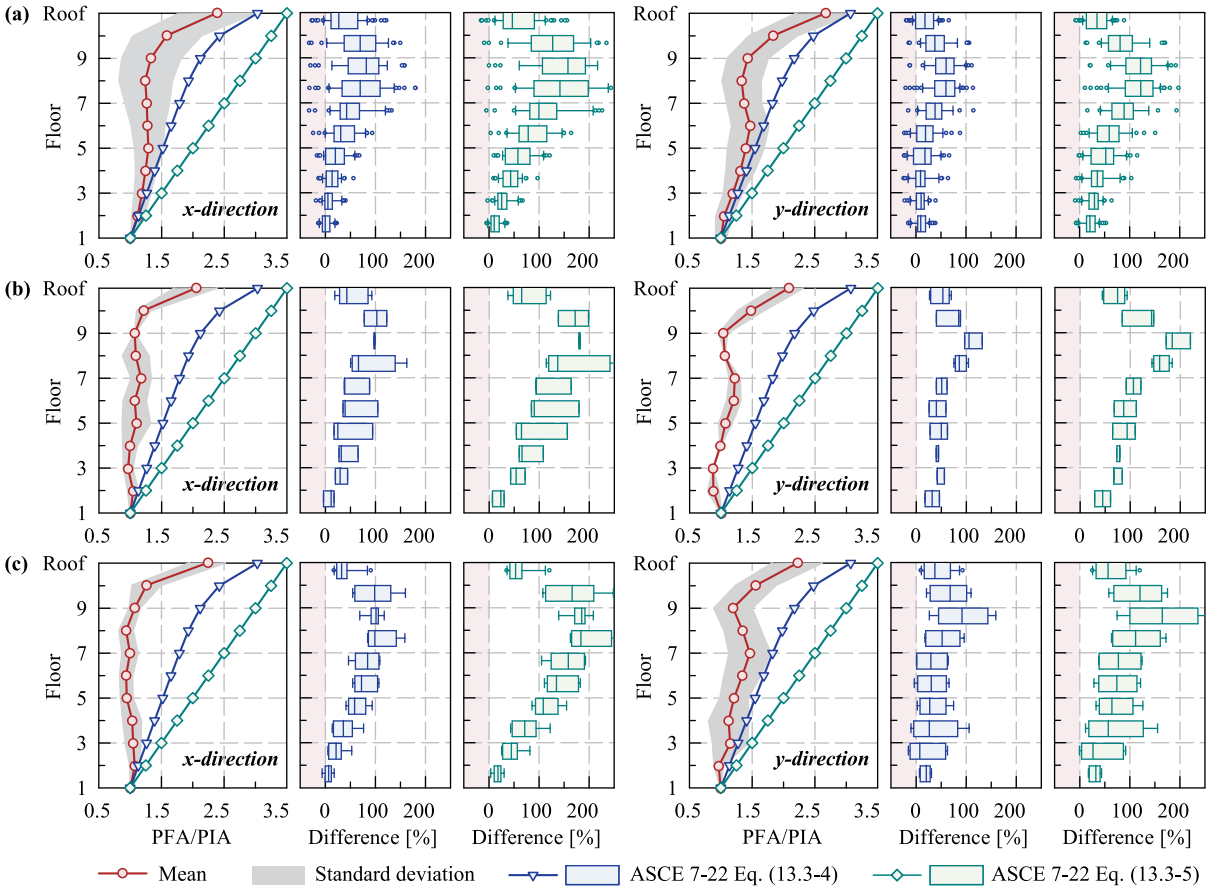


Figure 5. Acceleration amplification factors under: (a) SLE, (b) DE, and (c) MCE_R

3.2 Response of Rooftop Mechanical Equipment

The peak component acceleration serves as a key parameter to compute the seismic design forces of acceleration-sensitive NCSs. In this study, PCA is defined as the maximum acceleration recorded by the accelerometers mounted at the top of each equipment unit. It should be noted that the actual CoM of the equipment is below the accelerometer locations, i.e., along the equipment's height. Therefore, the reported PCA values are expected to be larger than the accelerations corresponding to the true CoM. Figure 6 shows the PCAs induced by SLE, DE, and MCE_R ground motions. For DE and MCE_R cases, the z-direction PCAs are also included. In a qualitative sense, compared with SL-DA, the slender units with flexible base supports (SL-SI and SL-NP) tended to record larger PCAs under SLE tests in the y-direction, corresponding to the rocking-prone weak axis. Under DE and MCER tests, however, larger PCAs were recorded in the x-direction.

Due to the relatively large torsional mode of the building, the recorded accelerations varied across different roof locations. For the SLE cases, the coefficient of variation (CV) of peak roof accelerations (PRAs) ranged from 10.8% to 31.2% in the x-direction and 5.4% to 32.2% in the y-direction. For the DE case, the CVs were 16.7% and 11.3% in the x- and y-directions, respectively. For the MCE_R cases, the CV in the x-direction reached up to 15.2%. Figure 7(a–b) presents representative contour plots of PRAs in the x- and y-directions under four SLEs, one DE, and two MCER ground motions. These results indicate that locations sharing the same x-coordinate generally exhibited similar y-direction accelerations, while locations sharing the same y-coordinate exhibited similar x-direction accelerations. These observations are consistent with the findings of Ruggieri and Vukobratović [2024], who numerically evaluated floor acceleration demands of low-rise RC buildings considering in-plane torsional effects.

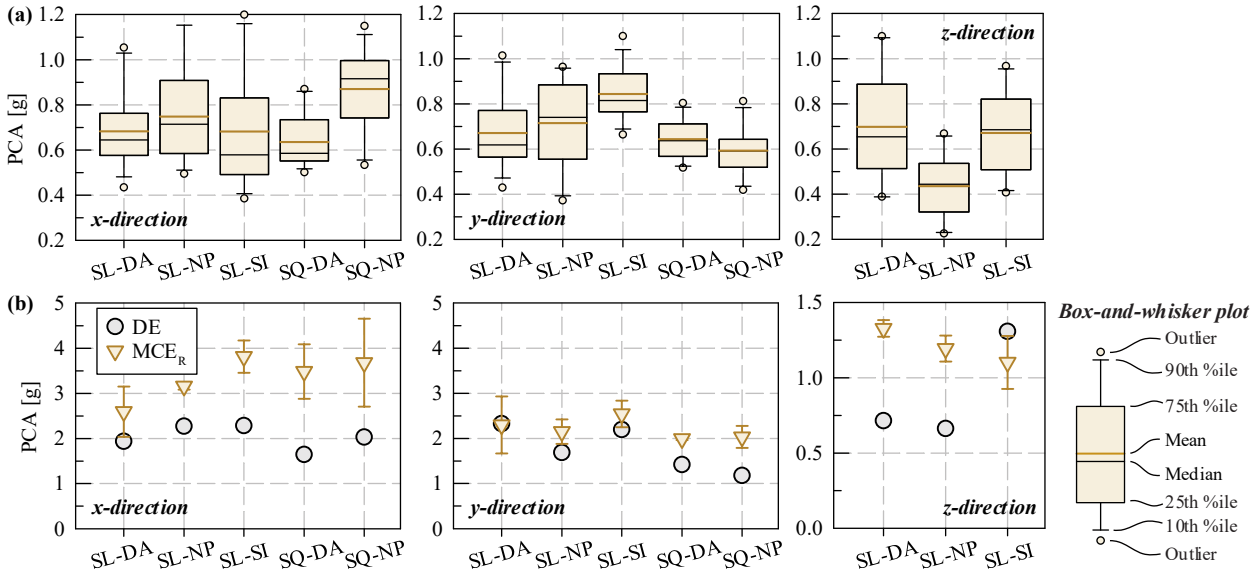


Figure 6. Peak component accelerations under: (a) SLE and (b) DE and MCE$_R$ tests

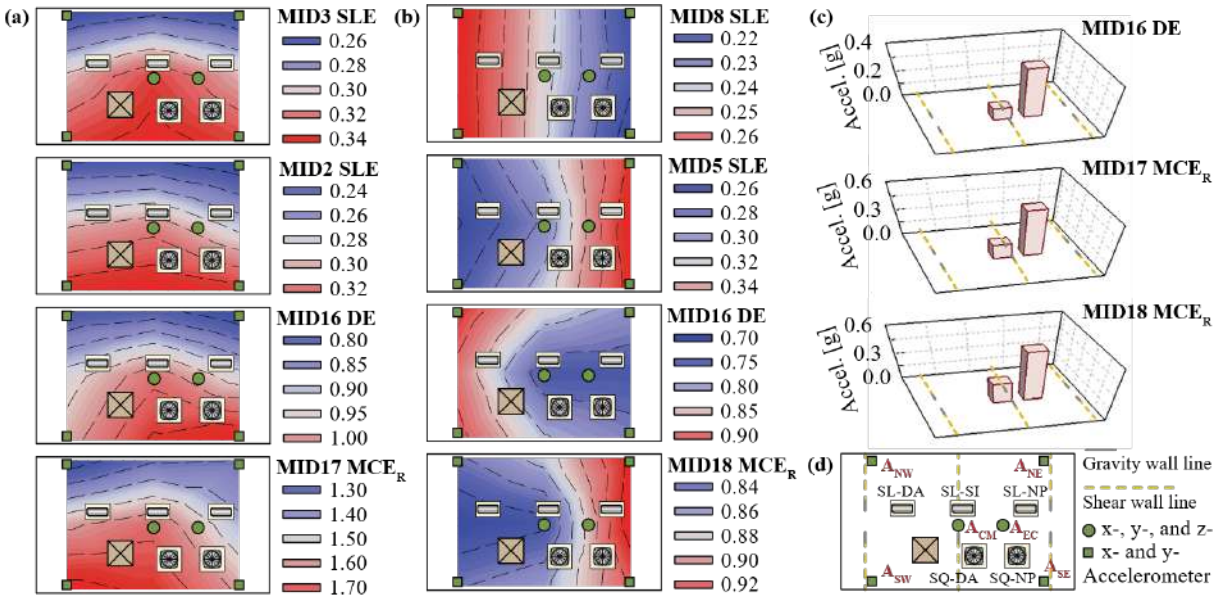


Figure 7. Peak roof acceleration distributions: contour plots of roof accelerations in the (a) x-direction and (b) y-direction, (c) bar graph representation of z-direction accelerations, and (d) layout of accelerometers on the roof diaphragm

In the z-direction, PRAs were governed by the vertical boundary conditions, as shown in Figure 7(c–d). Notably, the PRA recorded by the accelerometer at the calculated CoM (A_{CM}) was 63.7%, 67.7%, and 71.3% lower than that measured by the accelerometer (A_{EC}) positioned between the two shear wall lines, for MID16 (DE), MID17 (MCE$_R$), and MID18 (MCE$_R$), respectively. Component acceleration amplification factor, defined as PCA/PRA, was evaluated using the contour plots of PRAs (e.g., Figure 7). For the x- and y-directions, PRAs recorded at the geometric centre of the planar projection of each unit were directly used to calculate PCA/PRA. For the z-direction, PCA/PRA was evaluated using accelerometers located nearest to each unit. As illustrated in Figure 7(d), A_{CM} was used for SL-SI and A_{EC} was used for SL-NP. For the SL-DA, where no z-direction accelerometer was available in proximity, the sensor, A_{EC} adjacent to the calculated CoM was selected, based on the symmetry in the shear wall layout.

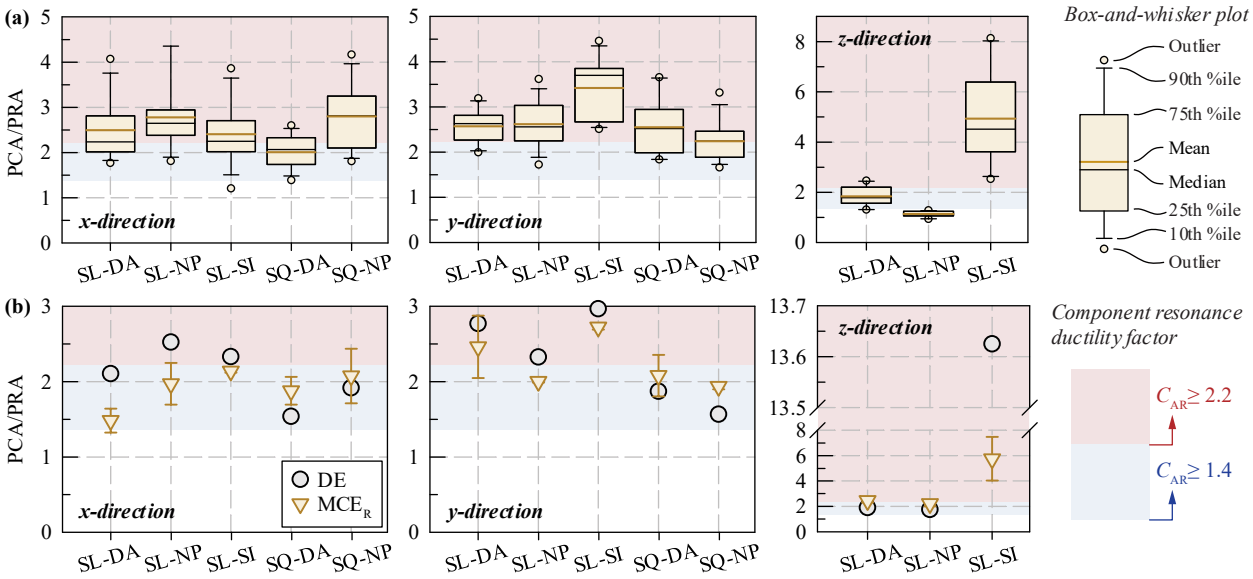


Figure 8. Component acceleration amplification factors under: (a) SLE and (b) DE and MCE$_R$ tests

Figure 8 presents the component acceleration amplification factors for all five equipment units under SLE, DE, and MCE$_R$ tests. For comparison, the code-based resonance ductility factor, C_{AR} specified in ASCE/SEI 7-22 [ASCE, 2022], 1.4 for non-vibration-isolated air-conditioning units and 2.2 for vibration-isolated components, are also plotted. Under SLE tests, comparison of the mean and median PCA/PRA values from the box plots indicates that the code-based coefficients generally underestimate the amplification demands for both non-isolated and vibration-isolated equipment. At higher hazard levels (DE and MCE$_R$), the code coefficients still do not consistently provide conservative envelope values above the calculated PCA/PRA scatter diagram. In particular, the spring-isolated slender unit (SL-SI) experienced significantly larger amplification in the z-direction than predicted by the code coefficient, owing to the inherent flexibility of its spring supports.

Two main factors likely explain these discrepancies. First, the PCAs reported in this study were measured at the top of each equipment unit, which are expected to be higher than CoM-associated PCAs. Second, the C_{AR} proposed in ASCE/SEI 7-22 [ASCE, 2022] may be more appropriate for heavier NCSs, whereas the mechanical equipment units evaluated here are exempt from seismic design calculations under the current code, since each unit weighs less than 1,779 N and has a CoM located no more than 1.22 m above the adjacent floor level.

4.CONCLUSIONS

This paper presents preliminary findings on the acceleration response of a full-scale, ten-story CFS building and its rooftop mechanical equipment from a shake table testing campaign. Five different equipment were installed, with varying attachment strategies implemented. It should be noted that piping connected to equipment that undergoes considerable movement must be sufficiently flexible to prevent damage at rigid interfaces. In this study, piping is not included. Its influence is isolated by assuming flexible connections, and only the equipment is evaluated experimentally. The results provide insight into the adequacy of current design provisions in capturing the acceleration demands on lightweight NCSs, while also offering an important benchmark dataset upon which numerical models can be evaluated. Modal properties and displacement responses of the equipment will be examined in future work.

ACKNOWLEDGEMENTS

This project was executed with support of the National Science Foundation under Grants CMMI-1663569 and CMMI-1663348, together with numerous other federal, state, and industry partners. Specific to the rooftop mechanical equipment discussed herein, additional support was provided by Mason West, Inc., Mason Industries, Inc., and Wells Plumbing and Heating Supplies, Inc. A complete list of sponsors and partners is available at: cfs10.ucsd.edu/sponsors-partners. The authors gratefully acknowledge all undergraduate and graduate students and visiting scholars (cfs10.ucsd.edu/people), as well as the LHPOST6 facility staff (esec.ucsd.edu/about/personnel), for their contributions to the project. Any opinions, findings, conclusions, or recommendations expressed in this paper are those of the authors and do not necessarily reflect the views of the sponsoring organizations.

REFERENCES

ASCE [2022] *Minimum Design Loads and Associated Criteria for Buildings and Other Structures*, American Society of Civil Engineers, Reston, Virginia, USA.

Astroza, R., Pantoli, E., Selva, F., Restrepo, J.I., Hutchinson, T.C., Conte, J.P. [2015] "Experimental evaluation of the seismic response of a rooftop-mounted cooling tower," *Earthquake Spectra*, Vol. 31, No. 3, pp. 1567-1589.

Elkady, A., Kazantzi, A.K., Dietz, M., Dihoru, L., De Risi, R., Vamvatsikos, D., Lignos, D.G., Miranda, E., Mylonakis, G. [2025] "Shake table tests on nonlinear steel fuses for the acceleration-control of nonstructural components," *Earthquake Spectra.* (Online First)

Fathali, S., Filiatrault, A. [2008] "Effect of elastomeric snubber properties on seismic response of vibration-isolated mechanical equipment: An experimental study," *Earthquake spectra*, Vol. 24, No. 2, pp. 387-403.

Feinstein, T., Moehle, J.P. [2022] "Seismic response of floor-anchored nonstructural components fastened with yielding elements," *Earthquake Engineering & Structural Dynamics*, Vol. 51, No. 1, pp. 3-21.

ICC [2004] *Acceptance Criteria for Seismic Qualification by Shake-Table Testing of Nonstructural Components and Systems*, International Code Council, Whittier, California, USA.

Papadopoulos, A.N., Vamvatsikos, D., Kazantzi, A.K. [2019] "Development and application of FEMA P-58 compatible story loss functions," *Earthquake Spectra*, Vol. 35, No. 1, pp. 95-112.

Ruggieri, S., Vukobratović, V. [2024] "The influence of torsion on acceleration demands in low-rise RC buildings," *Bulletin of Earthquake Engineering*, Vol. 22, No. 5, pp. 2433-2468.

Hutchinson, T.C., Eladly, M., Ji, R., Rivera, D., Rukundo, F.C., Singh, A., Sorosh, S., Zhang, J., Zhang, X., Padgett, L., Jones, H., Karns, J., Schafer, B.W. [2026] "Advancing use of cold-formed steel framing systems for mid-rise residential construction in seismic zones via full-scale shake table testing," *Proceedings of the 8th Residential Building Design & Construction Conference*, State College, Pennsylvania.

Zhang, J., Sorosh, S., Ji, R., Lotfizadeh, K.H., Schafer, B.W., Hutchinson, T.C. [2026] "Full-scale 10-story cold-formed steel building shake table test: Protocol development and shake table performance," *Proceedings of the 13th National Conference on Earthquake Engineering*, Portland, Oregon, 2026. In review.

A Study on Library Bookshelf Safety and Book Falling in Earthquakes

George C. Yao[1], and Yu-Jyun Fang [2]

[1] Dept. of Architecture, NCKU, Taiwan
#1 University Rd., Tainan, Taiwan
e-mail: gcyaoncku@gmail.com
[2] Dept. of Architecture, NCKU, Taiwan
#1 University Rd., Tainan, Taiwan
e-mail: xxx6857@gmail.com

Abstract. In recent years, seismic measures have effectively prevented the collapse of bookshelves in libraries. However, the issue of mass book falls remains a significant problem. This study, based on Taiwan's CNS standards, selects commonly used library bookshelves to conduct shake table tests. First, the fundamental frequency of the bookshelf is identified using a system identification method to understand its dynamic characteristics. Then, real earthquake scenarios are simulated with the bookshelf used inside a library, and the resulting book-fall behavior is observed. The input ground motion is the rooftop response waveform recorded during the 1995 JMA Kobe Earthquake on a ten-story steel frame building. The experimental results indicate that when the bookshelf is fully loaded with books, an acceleration exceeding 772 gal will significantly increases the risk of book falls. However, the addition of anti-fall components markedly reduces this risk. Finally, this paper provides recommendations for the seismic design of bookshelves and book storage systems to reduce earthquake-induced damage and ensure that libraries can resume operations promptly after an earthquake.

Keywords: Library Safety, Earthquake, Bookshelf Seismic Resistance

1. INTRODUCTION

In recent years, multiple large-scale earthquakes have caused bookshelf collapses and book falls, resulting in severe internal damage to library spaces. For library administrators, post-disaster reconstruction is extremely difficult and restoring normal operations takes a significant amount of time. Therefore, improving the seismic resistance of bookshelves and books is crucial for maintaining library functionality. For library users, the ability to safely find shelter during an earthquake without being injured by falling books or shelves is also an important concern of this study.

Chao-Jen Wang (2003), in his master's thesis at the Graduate Institute of Architecture, National Cheng Kung University, titled 'Seismic Reinforcement Characteristics of Library Bookshelves and Bookends in Taiwan,' explored the effects of different types of bookends in preventing book falls. His study conducted shake table tests to evaluate the seismic performance of various bookends and analyzed their effectiveness in reducing book falls during earthquakes. The results indicated that most bookends began to fail when the top-shelf acceleration reached 1.043G, causing mass book falls. Among them, the panel-type bookend performed best, with major falls only occurring at an acceleration of 1.99G. This superior performance was attributed to the larger contact area between the bookend and books, which provided more gripping points and better stability. However, its drawback was reduced usability, making books harder to move. These findings provide important insights into enhancing the anti-fall performance of library bookshelves.

This study aims to approach the problem from the perspectives of both library users and administrators. It seeks to ensure that users are not harmed by falling books during an earthquake, and to reduce the recovery burden on administrators, thereby minimizing the damage to valuable library resources. The research simulates an anti-fall steel cable system similar to that used at National Dong Hwa University and employs real earthquake waves to replicate seismic conditions within a library. The study observes the behavior of bookshelves and books under such conditions.

2. EXPERIMENTAL PLAN

2.1 DESCRIPTION OF TEST SPECIMEN

In this study, a commonly used double-sided supported bookshelf was selected as the test specimen, based on the Taiwan national standard CNS 14308 (Figure 1). The double-sided support type is widely adopted in most libraries in Taiwan. A shaking table test was conducted on this bookshelf type to evaluate its seismic performance.

The specifications of the test specimen are as follows:

Material and dimensions of upright columns: 70 × 30 mm rectangular steel tubes (SPHC 2.0T), welded
Bookshelf height: 1950 mm, 6 shelves of books
Self-weight of bookshelf: approximately 90 kg
Fully loaded bookshelf weight: approximately 455 kg
.

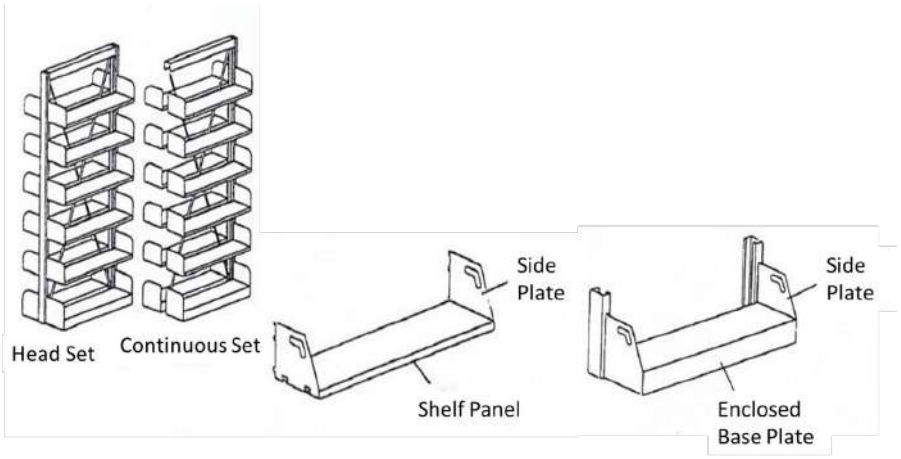


Fig. 1. A double-sided book shelf and Side-Plate

2.2 EXPERIMENTAL METHOD

This experiment was conducted using the long-stroke shaking table at the National Center for Research on Earthquake Engineering (NCREE) in Tainan. A full-scale library bookshelf was mounted on the table, and seismic waves representative of building responses were input to observe its dynamic behavior.

To prevent relative sliding between the bookshelf and the shaking table during testing, the bookshelf was securely anchored to the table using bolts. An accelerometer was installed at the top of the bookshelf to measure its dynamic response.

As shown in Figure 2, the experimental setup was configured accordingly. For consistency in subsequent discussions, the X-direction is defined as the transverse direction, and the Y-direction as the longitudinal direction of the bookshelf.



Fig. 2. Test Setup

2.3 INSTALLATION METHOD OF ANTI-FALL CABLES

As illustrated in Fig. 3, the anti-fall cable installation in this experiment involved drilling holes on both side plate of each bookshelf level, approximately 10 cm above the shelf panels. Steel cables were threaded

through these holes and secured in place using cable clamps at designated positions, following the applicable usage specifications. The chosen height of 10 cm above the shelf panel surface was primarily intended to balance functionality and user accessibility. This placement encures ease of access for library users retrieving books while also considering that some books are relatively small – setting the cable too high could diminish its blocking effectiveness.



Fig. 3. Photo of cable installation

3. EXPERIMENTAL RESULTS AND ANALYSIS

3.1 SYSTEM IDENTIFICATION OF THE BOOKSHELF SYSTEM

The bookshelf was placed freely on the shaking table (i.e., without anchoring it to the table surface first). A white noise excitation ranging from 0.1 Hz to 40 Hz with an amplitude of 100 gal was applied. The acceleration measured at the top of the bookshelf and that measured on the table surface were analyzed using a transfer function to determine the predominant frequency of the bookshelf.

(1) Empty Bookshelf (Figure 4)

When no books were placed on it, the bookshelf had a total weight of approximately 90 kg. From the transfer function analysis conducted with the bookshelf standing freely on the floor, the longitudinal (Y-direction) natural frequency was found to be approximately 3.9 Hz, and the transverse (X-direction) natural frequency was also approximately 3.9 Hz.

(2) Fully Loaded Bookshelf (Figure 5)

When the bookshelf was fully loaded with books, the total weight was approximately 455 kg. From the transfer function analysis conducted with the bookshelf standing freely on the floor, the longitudinal (Y-direction) natural frequency was found to be approximately 2.1 Hz, and the transverse (X-direction) natural frequency was approximately 2.7 Hz.

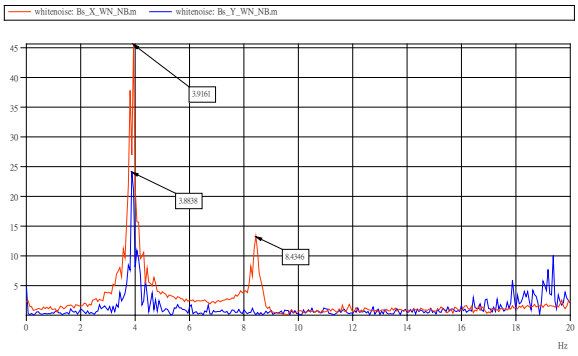


Fig. 4. Transfer function of empty shelf

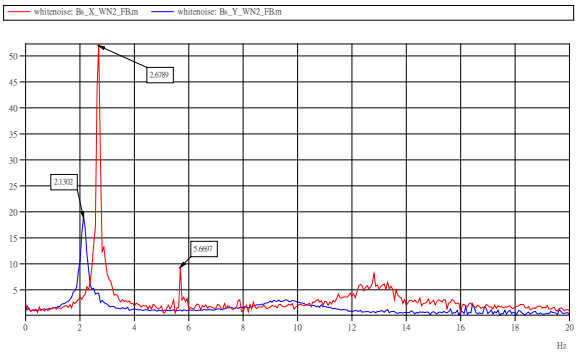


Fig. 5. Transfer function of full shelf

3.2 EXPERIMENT WITHOUT ANTI-FALL CABLES

In this study, vibration tests were conducted on base-fixed bookshelf specimens without anti-fall cables, using unitdirectional and bidirectional seismic wave inputs corresponding to 25% and 10% intensity levels of the Kobe earthquake. The test result is shown in Table 1.

In the longitudinal direction (Y-axis) test, a significant number of books began to fall when the top-shelf acceleration exceeded 772 gal. In the transverse direction (X-axis) test, book-falling incidents increased markedly when the top-shelf acceleration exceeded 764 gal. Further test results indicated the following:

- Transverse direction (X-axis): When the top-shelf acceleration reached 2418gal, approximately 62.5% of the books fell from the bookshelf.
- Longitudinal direction (Y-axis): When the top-shelf acceleration reached 3621 gal, approximately 8.5% of the books fell.

The test results, as shown in Figure 6, demonstrate that bookshelves without anti-fall cables experience a significantly elevated risk of bookfall during seismic events. This is especially pronounced under high acceleration conditions, potentially leading to extensive book loss and posing threats to library operations and user safety.

Table 1. Data from No Anti-fall cable tests

	Unidirectional in X Kobe10X	Unidirectional in Y Kobe10Y	Bidirectional in XY Kobe10XY	Unidirectional in X Kobe25X	Unidirectional in Y Kobe25Y
Peak Table Acceleration	X：251 gal	Y：243 gal	X：258gal Y：236gal	X：615 gal	Y：718 gal
Peak Bookshelf top Acceleration	X：764 gal	Y：772 gal	X：728 gal Y：879 gal	X：2418 gal	Y：3621 gal
Book Fall rate	0	0	8.5%	62.5%	8.5%

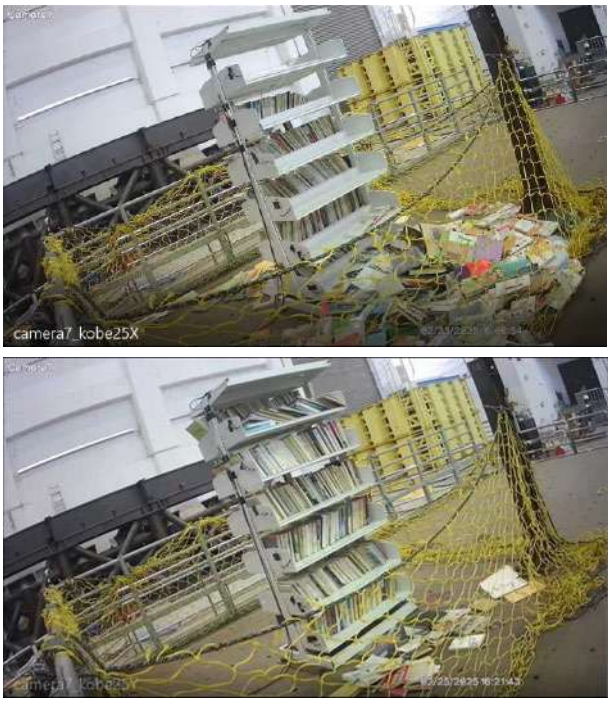


Fig.6. Bookfall photo in Kobe25%(Top in X dir, Bottom in Y dir)

3.3 EXPERIMENT WITH ANTI-FALL CABLES

For base-fixed bookshelf specimens equipped with anti-fall cables, this study conducted unidirectional and bidirectional shaking table tests using 25% and 50% intensity levels of the Kobe earthquake. The test results in Table 2 demonstrated that, under identical seismic input conditions, the presence of anti-fall cables significantly reduced the likelihood of books falling.

In the unidirection longitudinal direction (Y-axis) test, when the top-shelf acceleration reached 4022 gal, the books remained stable with no falling incidents. Similarly, in the transverse direction (X-axis) test, even when the top-shelf acceleration reached 1687 gal, no books fell. However, under bidirectional input testing, approximately 10% of the books fell.

To expedite the reset process between test runs during the Kobe 50% test, books on the top three shelves were removed, and only the lower three shelves were retained for the experiment. The results were as follows:

Longitudinal direction (Y-axis): When the top-shelf acceleration reached 4029 gal, no book fell.

Transverse direction (X-axis): When the top-shelf acceleration reached 1695 gal, no book fell. When the top-shelf acceleration reached 3831 gal in Y direction and X direction reached 2251 gal, approximately 10% of the books fell.

As shown in Figures 7, comparison of pre- and post-test conditions confirms that the installation of anti-fall cables effectively reduces the risk of bookfall and enhances the seismic safety of library bookshelves.

Table 2. Data from Anti-fall cable tests

	Unidirectional in X Kobe25X	Unidirectional in Y Kobe25Y	Bidirectional in XY Kobe25XY
Peak Table Acceleration	X：615 gal	Y：722 gal	X：656 gal Y：696 gal
Peak Bookshelf top Acceleration	X：1695 gal	Y：4029 gal	X：2251 gal Y：3831 gal
Book Fall rate	0	0	10%

4. CONCLUSIONS AND RECOMMENDATIONS

This study utilized shaking table tests to verify the effectiveness of anti-fall cables in reducing bookfall from library bookshelves during seismic events. Experimental results indicated that for unprotected bookshelf, when the transverse (X-axis) top-shelf acceleration exceeded 764 gal, the probability of books falling began to rise. However, after installing anti-fall cables, the critical acceleration at which bookfall occurred increased to 1687 gal, indicating a substantial reduction in risk. Similarly, in the longitudinal direction (Y-axis), books were highly prone to falling when the top-shelf acceleration exceeded 772 gal for unprotected bookshelf, whereas with anti-fall cables installed, the critical acceleration rose to 3855 gal, confirming the significant effectiveness of the anti-fall system.

Furthermore, the results highlighted that the installation quality of the cables plays a critical role in their seismic performance. If the cables become loose due to installation errors or long-term use, their effectiveness in preventing bookfall will be greatly diminished. Therefore, in practical applications, it is essential to maintain proper cable tension to ensure optimal protection.

The study also found that during earthquakes, books are prone to sliding motion due to seismic vibrations. When subjected to high acceleration, even though anti-fall cables can effectively prevent books from falling off the shelf, rocking behavior within the bookshelf may still occur, causing displacement or rotation of books. Nevertheless, compared to books scattering on the floor, this phenomenon significantly reduces the post-earthquake recovery time for library administrators and minimizes the risk of injury to users walking between shelves during an earthquake.

In summary, the use of anti-fall cables effectively enhances the seismic safety of library bookshelves, reducing both the damage to collections and the recovery time after an earthquake. It is hoped that this study will also inspire bookshelf manufacturers to explore more simple and economically feasible anti-fall components, thereby improving the safety of non-structural elements in libraries during seismic events.

REFERENCES

CNS 14308 (1999). *"CNS 14308 –Steel Bookshelves for Libraries."* Republic of China National Standard, Taiwan

Wang, C.-J. (2003). "*Seismic Retrofitting Characteristics of Library Bookshelves and Bookstoppers in Taiwan."* Master's Thesis, Department of Architecture, National Cheng Kung University, Tainan, Taiwan.

A Study on Bookshelves Overturning Evaluation Based on Reconnaissance in the 2024 Hualien Earthquake

Min-Chi Ko [1], Fan-Ru Lin[2], Juin-Fu Chai[2], Keng-Chang Kuo[3], Wei-Hung Hsu[2], Bai-Yi Huang[4], Wei-Chung Chen[4]

[1] National Center for Research on Earthquake Engineering, National Institutes of Applied Research
No. 2001, Sec. 1, Zhongzheng S. Rd., Guiren Dist., Tainan City 711015, Taiwan (R.O.C.)
e-mail: mcko@niar.org.tw

[2] National Center for Research on Earthquake Engineering, National Institutes of Applied Research
No. 200, Sec. 3, Xinhai Rd., Da'an Dist., Taipei City 106219, Taiwan (R.O.C.)
e-mail: {frlin, chai, mikehsu}@niar.org.tw

[3]National Kaohsiung University of Science and Technology
No.1, University Rd., Yanchao Dist., Kaohsiung City 82445, Taiwan (R.O.C.)
e-mail: kkuo@nkust.edu.tw

[4]National Center for Research on Earthquake Engineering, National Institutes of Applied Research
No. 2001, Sec. 1, Zhongzheng S. Rd., Guiren Dist., Tainan City 711015, Taiwan (R.O.C.)
e-mail: {byhuang, chenwc}@niar.org.tw

Abstract. A magnitude 7.2 earthquake occurred Hualien on April 3, 2024. Post-earthquake reconnaissance of a case library revealed extensive damage: bookshelves and CD racks were overturned, and a large number of books and CDs were dropped. Many shelving units were deformed or structural function failed, rendering them unusable for an extended period and necessitating significant financial and manpower resources for recovery. This paper investigates the structural forms and types of load-bearing racks (including bookshelves and CD racks) in the library. It presents an overturning analysis of free-standing load-bearing racks across different floors. The analytical results are compared with observed damage to assess the applicability of the rigid body overturning assessment method for library shelves. In order to improve the seismic performance of existing bookshelves, this study also proposes preliminary retrofit suggestions based on a review of FEMA E-74.

Keywords: 2024 Hualien Earthquake, Bookshelves, Overturning Evaluation, Overturning Response Spectrum

1. Background

On April 3, 2024, a moment magnitude (Mw) 7.2 earthquake struck Hualien, Taiwan (hereafter referred to as the 0403 Earthquake), and was strongly felt throughout the island. A post-earthquake reconnaissance of a university library revealed severe damage, a large number of fallen books and CDs, as well as the overturning of bookshelves and CD racks. The overturning led to deformation and structural failure of these shelves. Due to the damage, the library was rendered unusable in the short term and required significant manpower and financial resources for repair and recovery.

This study adopts the overturning theory of Ishiyama (1982), and the asymmetric rigid-body overturning response spectrum method proposed by Wang (2019), which modifies Housner's (1963) classical overturning theory. Considering the seismic response conditions observed in the library, overturning assessments were carried out on bookshelves and CD racks. Based on actual field observations of overturned racks, the applicability of current evaluation methods was further examined. Finally, this study proposes a systematic procedure for evaluating the overturning of existing shelves. Retrofitting and improvement strategies are also suggested with reference to FEMA E-74 guidelines.

2. Damaged Shelves Introduction And Observation

This study focused on the damaged double-sided steel bookshelves (Figure 1) and the CD racks (Figure 2). These units sustained severe seismic damage in the case-study library and serve as the primary subjects for subsequent investigation. The structural components of the steel bookshelves are identified in Figure 3.



Figure 1 Double-sided steel bookshelves.



Figure 2 Damaged CD racks.



Figure 3 The structural components of the steel bookshelves.

Falling books, CDs and overturning shelves were the main damages in the library. Ineffective shelf brackets caused falling books, which became more severe on higher floors. Rocking also led to books being crushed (Figure 4). In higher floor, cables wires were installed on the higher layers of bookshelves as anti-falling devices, but loose tension and long anchoring spans (455 cm) limited the effectiveness. However, they still showed some function on the lower layers of the shelves (Figure 5). Severe overturning occurred in the 2nd-floor CD racks (Figure 6) and 5th-floor bookshelves (Figure 7). Overturning, deformation of longitudinal ties, and shear failure occurred due to insufficient connector strength on the connection (Figure 8, Figure 9). However, longitudinal ties were a good retrofit strategy for bookshelves, free-standing and uneven loading were another reason for overturning.



Figure 4 Falling books and book crushing



Figure 5 Different efficacy of cables installed on upper and lower layers



Figure 6 Overturned CD racks (Already up-righted)



Figure 7 Overturned bookshelves and bended longitudinal ties



Figure 8 Deformed and failed longitudinal tie of CD rack



Figure 9 Deformed connections of bookshelf longitudinal ties

3.Overturning Analysis of Shelves

Based on the reconnaissance results of damaged shelves in the library during the earthquake, this chapter investigates the applicability of rigid-body overturning evaluation theory. By integrating system identification from the 0403 Hualien Earthquake and Ambient Vibration Measurements (AVM), floor amplification estimation, and overturning analysis, these analyses are used to examine the applicability of overturning evaluation methods. Furthermore, the calculated minimum number of interconnected shelves required to resist overturning is compared with the actual overturning observed during the earthquake.

3.1 Analysis for 0403 Hualien Earthquake and Library

For the overturning analysis of shelves, acceleration time histories recorded by the Taiwan P-ALERT system at the free field (D002) and the library's 2nd floor (D003) were used (Figure 10). D002T and D003T represent the reoriented time histories adjusted to match the library coordinate system (Figure 11~Figure 15). Figure 16 and Figure 17 are the plot of Fast Fourier Transform (FFT) and Frequency Response Function (FRF) by transfer function. Based on the FRF method of the structure's frequency, the library's natural frequencies would be more clearly revealed. Compared with the FFT and FRF analysis results, the library's frequency in the X-direction was 2.0 Hz, and 2.1 Hz in the Y-direction. A natural frequency of 2.4 Hz was identified from FFT (Figure 18) and Power Spectral Density (PSD, Figure 19) obtained from AVM.

Since overturning occurred during the earthquake, strong-motion frequencies of X-dir. 2.0 Hz and Y-dir. 2.1 Hz were adopted (Table 1). Velocity time histories from $D002^T$ and $D003^T$ were obtained (Figure 20, Figure 21). Assuming that the amplification between the free field and the 1st floor (with a height difference of 1.6 m) is negligible, the 5th-floor accelerations were estimated as 464 gal (X) and 367 gal (Y). As overturning occurred along the X direction, the corresponding velocity was 91.7 cm/s (Table 2).



Figure 10 D002 and D003 monitoring station in P-ALERT System

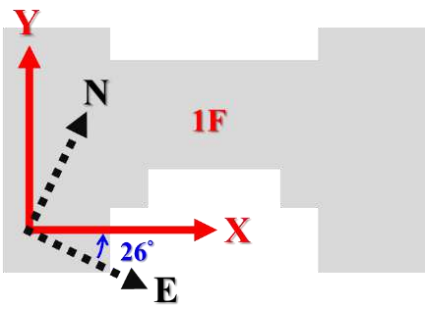


Figure 11 Coordinate transformation for global and library orientation

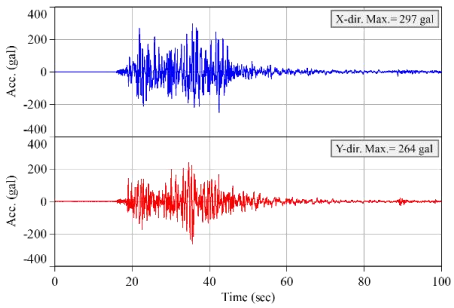


Figure 12 $D002^T$ acceleration time history

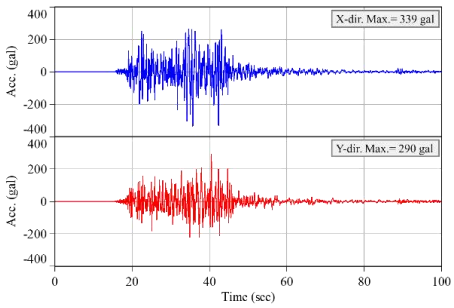


Figure 13 $D003^T$ acceleration time history

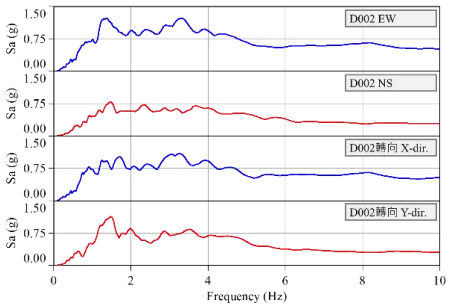


Figure 14 D002^{T} response spectrum

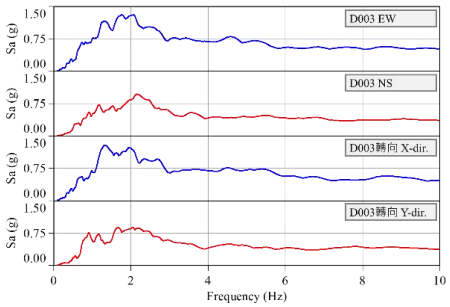


Figure 15 D003^{T} response spectrum

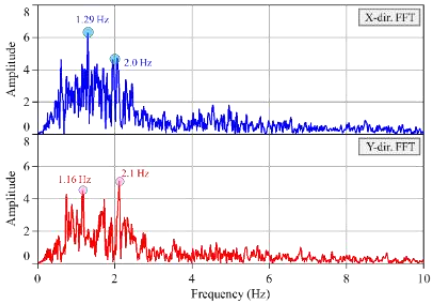


Figure 16 FFT spectrum of D003^{T}

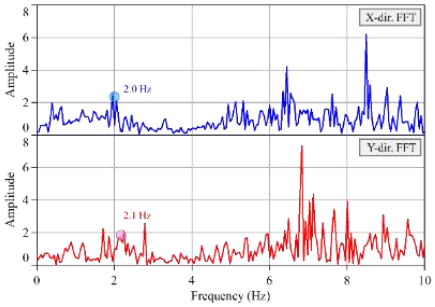


Figure 17 FRF spectrum of D003^{T}

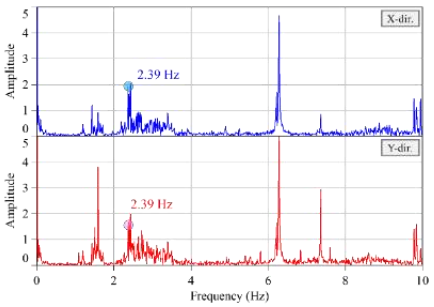


Figure 18 Acceleration FFT spectrum of AMV

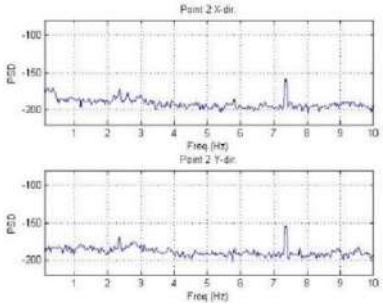


Figure 19 Velocity PSD spectrum of AMV

(Provided By Keng-Chang Kuo)

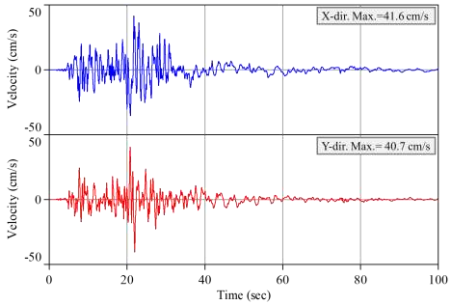


Figure 20 D002^{T} Velocity time history

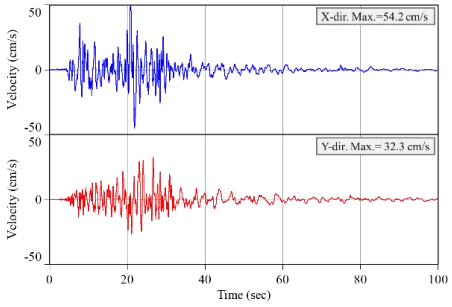


Figure 21 D003^{T} Velocity time history

Table 1. System identification table

Dir.	Acc. AVM FFT	Vel. AVM FFT	D003^{T} FFT	D003^{T} FRF
X-Dir.	2.39 Hz	2.40 Hz	2.0 Hz	2.0 Hz
Y-Dir.	2.39 Hz	2.40 Hz	2.1 Hz	2.1 Hz

Table 2. Library's linear estimated peak acceleration and velocity by D002^{T} and D003^{T}

Floor	P-ALERT NO. & Ground Level (m)		PA (gal)		PV (cm/s)
	NO.	GL	X-Dir.	Y-Dir.	X-Dir.
RF		33.1	591	446	129.8
6F		24.1	507	394	104.6
5F		19.5	464	367	91.7
4F		15.1	423	342	79.4
3F		10.6	381	316	66.8
2F	46 (D003)	6.1	339	290	54.2
1F		1.6	297	264	41.6
Ground	40 (D002)	0	297	264	41.6

3.2 SHELVES OVERTURNING ANALYSIS

Ishiyama's rigid body and criteria overturning equations were used to calculate the minimum rocking acceleration Equation (1):

$$a = \frac{B}{H} \cdot g \tag{1}$$

and overturning velocity Equation (2):

$$v = \frac{B}{\sqrt{H}} \cdot 10 \tag{2}$$

by the body width (B) and height (H).

Wang (2020) further proposed an Excel-based overturning response spectrum for asymmetric rigid bodies considering centroid height (G), radius of gyration (R, R′), and overturning angles (α, α') (Figure 22). However, post-earthquake could not confirm whether shelves created symmetric conditions or whether support-foot joints were intact (Figure 23). Therefore, six cases combining different centroid heights and joint conditions were assumed for analysis.

A row of modular CD rack was composed of 11 units (91×52×210 cm, total 1001 cm) and overturning direction matched the library Y-axis (Figure 24, Figure 25). The modular bookshelf was composed of 7 units (91×54×233 cm; total 647 cm) and overturned along the X-axis (Figure 26, Figure 27). Table 3 showed the CD rack had rocking acceleration (242.82 cm/s²) is less than floor acceleration (290 gal). Overturning velocity (35.88 cm/s) is greater than floor velocity (32.3 cm/s). It means that rocking without overturning. For the bookshelves, both rocking acceleration (227.26 cm/s²) and velocity (35.38 cm/s) were far below estimated floor values (464 gal, 91.7 cm/s), confirming rocking and overturning. The overturning spectrum (Figure 28, Figure 29) indicate that intact joints can prevent overturning, whereas failed joints or elevated centroids lead to collapse. Table 4 summarizes that CD racks should not overturn unless failed joints, yet all collapsed in reality; bookshelves should remain stable at lower centroid heights, but still overturned.

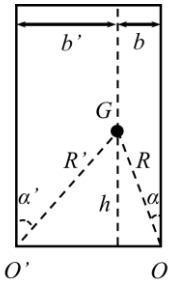


Figure 22 Asymmetric rigid body and centroid height relation

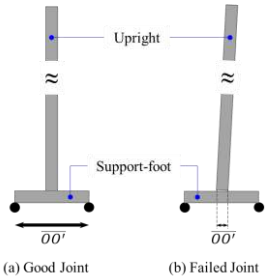


Figure 23 The joint interaction between support-foot and upright

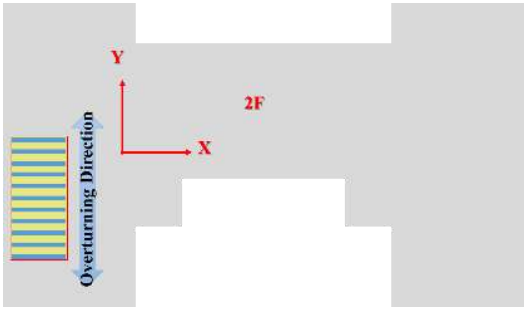


Figure 24 Overturning direction of CD racks and structural orientation

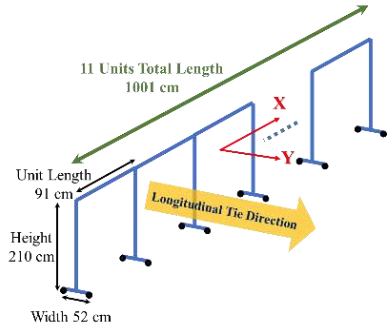


Figure 25 Modular CD rack orientation and specification

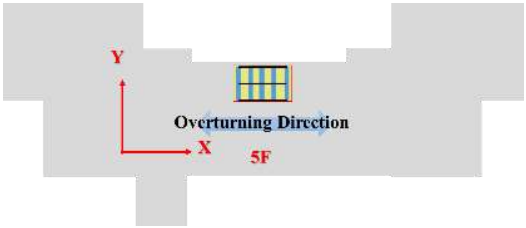


Figure 26 Overturning direction of bookshelves and structural orientation

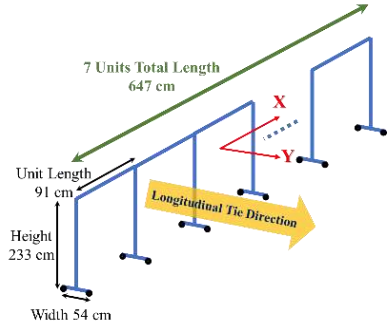


Figure 27 Modular bookshelf orientation and specification

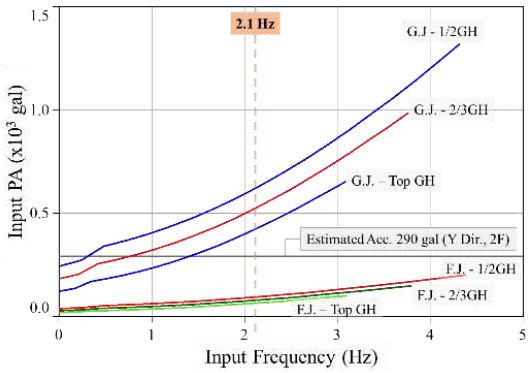


Figure 28 Overturning response spectrum for CD racks

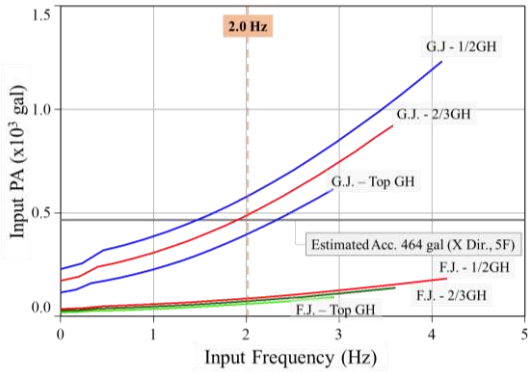


Figure 29 Overturning response spectrum for bookshelves

Table 3 Comparation for Library Estimated Response and Ishiyama Formula Calculation Results

Floor	Library Estimated Response				Formula Calculation Results	
	PA (gal)		PV (cm/s)		Rocking Acceleration (cm/s^2)	Overturning Velocity (cm/s)
	X-Dir.	Y-Dir.	X-Dir.	Y-Dir.	Lateral	Lateral
5F (Bookshelves)	**464**	367	**91.7**	-	227.26	35.38
2F (CD Racks)	297	**290**	54.2	**32.3**	242.82	35.38

Table 4 Summary of CD Racks and Bookshelves Overturning Analysis Results

Subject	ISHIYAMA Formula Calculation	Overturning Response Spectrum
CD Racks	Rocking. But No Overturning	Overturning Under Failed Joint
Bookshelves	Rocking and Overturning	Overturning Under Failed Joint

Although longitudinal ties connected each bookshelf and CD rack, severe overturning still occurred during the earthquake. Shown as Table 5, according to Ishiyama's rigid-body overturning formula, no overturning would be expected if the shelves acted as a single rigid system, suggesting that longitudinal ties could be effective if properly integrated.

Table 5 Comparison of Overturning Capacity

	Library Current Situation		Ishiyama Calculation Results		Estimated Floor Response	
Subject	Number of Connected Shelves	Actual Width	Rocking Acc.	Overturning Vel.	Floor Acc.	Floor Vel.
CD Racks	11	1772 cm	8277.8 cm/s2	1222.8 cm/s	290 gal	32.3 cm/s
Bookshelves	5	750 cm	3157.7 cm/s2	491.3 cm/s	464 gal	91.7 cm/s

The minimum number of anti-overturning shelves connected by longitudinal ties was calculated, assuming the spacing between 2 bookshelves was 120 cm and the same estimated floor response. The calculated minimum width was 139.97 cm, which means it should be connected at least 2 bookshelves units. However, 5 units overturned in the earthquake, indicating that simply increasing the number of serial connections may not be sufficient. Effective structural anchorage, displacement restraint, and retrofitted connection of shelf frame system are essential measures for practical mitigation.

4. Evaluation of Shelves Overturning

As shown in Table 4, theoretical overturning evaluation indicates that overturning during the 0403 earthquake would not occur unless the gravity center of the shelf was located at the top, and adopting longitudinal ties strategies could effectively prevent overturning. However, severe overturning was observed in the library shelves, implying that the shelves did not behave as a rigid body. Significant unexpected responses, deformations, and failures occurred, leading to overturning. Therefore, strengthening the structural system, joint strength, and stiffness of the shelves themselves should be the primary mitigation strategy. Figure 26 illustrates a proposed process for improving the stability of free-standing shelves with

longitudinal ties, though the seismic performance of the ties and connections should be further verified by professionals. The process consists of 2 stages:

i. Overturning Evaluation: overturning capacity is assessed using Ishiyama's theory and the overturning response spectrum, with known geometry and mass parameters. If overturning is not expected but failed joints exist, reference can be made to FEMA E74 (2012) §6.5.2. Longitudinal ties with additional 45° bracing, and improved joint connections (e.g., changing bolts to welds, or strengthening connections) are suggested from FEMA E-74.

ii. Structural Analysis

a. If overturning is expected with good joints: Modify shelf usage (removal, reduced storage height, or floor relocation), add floor anchorage, or connect to wall and ceiling (Fig. 27). Bracing between suspended ceiling/secondary components and the floor or shelves, along with anchoring shelf bases to the slab, can further improve performance (Fig. 28).

b. If overturning is expected with failed joints: Retrofit the frame, replace components, or change bolted connections to welded joints. Alternatively, replace with compact moveable shelves or reduce storage load and adjust floor usage to lower overturning risk.

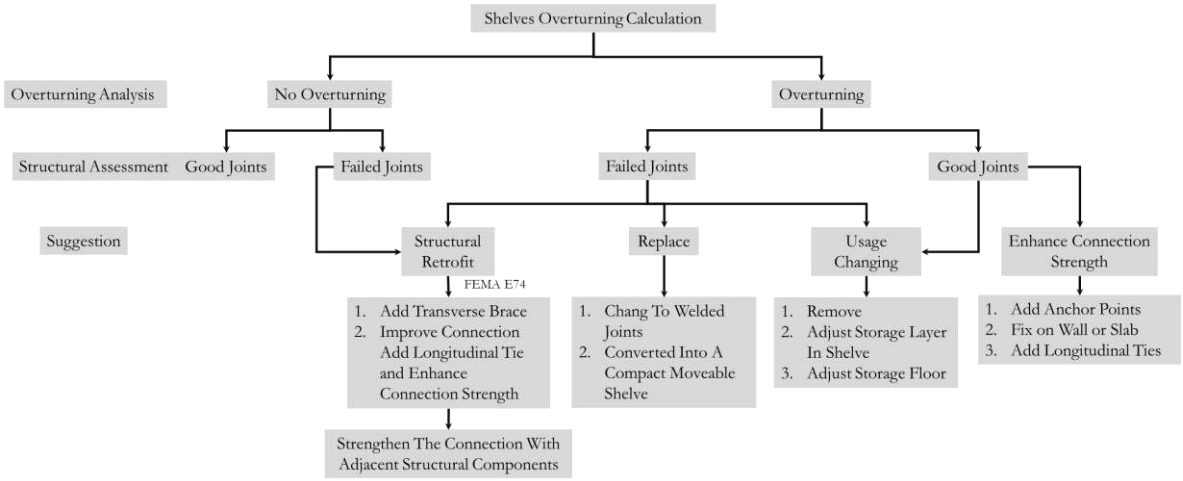
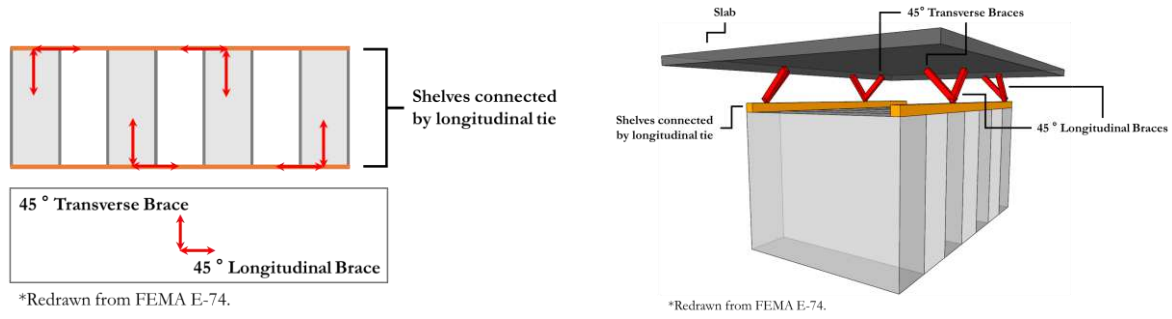


Figure 30 Stability improvement process for existing free-standing shelves



(a) Plan view **(b) Perspective view**

Figure 31 Retrofitted shelves by 45° braces and longitudinal ties

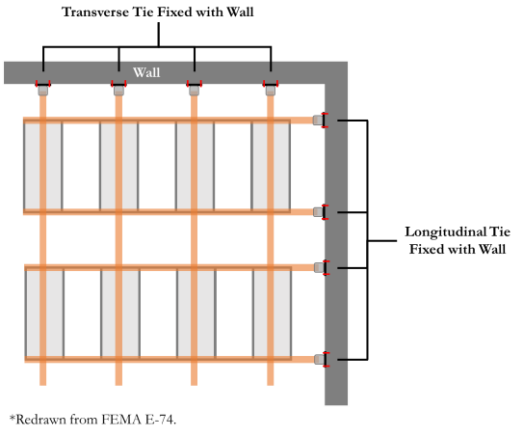


Figure 32 Longitudinal and transverse tie fixed on wall

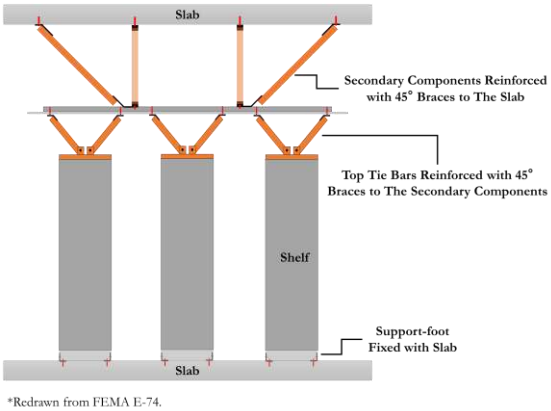


Figure 33 Elevation of 45° braces between shelves, secondary components, and slabs

5. Conclusions and Recommendations

During the 0403 Hualien earthquake, severe overturning of standard free-standing bookshelves and CD racks with longitudinal ties, falling books and CDs were observed in library. Although longitudinal ties were intended to improve seismic performance, the connections between longitudinal tie and shelf only used only 1 to 2 screws, which were insufficient to resist seismic forces. Overturning, joint failure, and deformation of longitudinal ties and connections occurred during earthquake. Even after repositioning, deformed shelves could not remain stable. The severe earthquake damage required substantial time, financial resources, and manpower for post-earthquake recovery.

This study aims to analyze the overturning behavior of the library's bookshelves and CD racks by Ishiyama overturning formulas and overturning response spectrum. The analysis results shows that while extreme cases are more prone to overturning during earthquake, and the rigid-body assumptions do not reflect the actual shelves behavior. To enhance the stability of existing shelf systems, feasible mitigation strategies are proposed based on observed damage, structural assessment, and FEMA E-74. Including:

i. Structural improvement: adding transverse braces, strengthening connections, and increasing capacity of longitudinal ties.

ii. Component replacement or retrofitting: changing to welding connections, replacing shelves with compact moveable shelves.

iii. Usage adjustment: reducing storage layers, relocating shelves, or removing damaged shelves.

iv. Anchorage: fixing shelves and longitudinal/transverse ties to adjacent structures to improve connectivity.

These strategies provide a reference for industry and institutions for evaluating shelves overturning and improving seismic performance in similar free-standing shelving systems.

REFERENCES

George C., Yao, C.Y., Tu, Y.K. Wang (2020). A Study on Overturning Limit of One-Sine Pulse Type Excitation to Free-standing Rigid Bodies. Journal of Architecture, (114), 21-40.

K.L., Chen (2003). Earthquake-Resistance in Compact Shelving. Bulletin of the Taipei Public Library, 20(3), 45-54.

S.H., Huang, etc. (2000). The Study on the Recovery and Reconstruction After 9-21 Earthquake Disaster of the Public Libraries of Taiwan in 1999. The Study Group on the Recovery and Reconstruction of Public Libraries After the 921 Earthquake, Council for Cultural Affairs (CCA).

P-Alert Strong Motion Network (2013). P-Alert Strong Motion Network. https://palert.earth.sinica.edu.tw/

Ishiyama, Y. (1982). Motions of rigid bodies and criteria for overturning by earthquake excitations. Earthquake Engineering & Structural Dynamics, 10(5), 635-650.

Housner, G. (1963). The behavior of inverted pendulum structures during earthquakes. Bulletin of the Seismological Society of America, 53(2), 403-417.

Federal Emergency Management Agency (2012). FEMA E-74: Reducing the Risk of Nonstructural Earthquake Damage-A Practical Guide. Washington D.C., USA.

National Information Standards Organization (2012). ANSI/NISO Z39.73-1994 (R2012): Single-Tier Steel Bracket Library Shelving. National Information Standards Organization Baltimore, Maryland, U.S.A.

Seismic Protection Systems for Safety-Related Equipment Cabinets

S. Kavei[1], G. Mosqueda[2], and J. Park[3]

[1] Department of Structural Engineering, University of California San Diego, La Jolla, California, USA
skavei@ucsd.edu
[2] Department of Structural Engineering, University of California San Diego, La Jolla, California, USA
gmosqueda@ucsd.edu
[3] Structural and Seismic Safety Research Division, Korea Atomic Energy Research Institute, S.Korea
jhpark78@kaeri.re.kr

Abstract. Ensuring the reliable operation and safe shutdown of Power Plants is critical for safety and continuous electricity supply. Earthquakes pose a major threat by damaging structural and nonstructural components, particularly electrical cabinets housing essential control and distribution systems. Cabinets and their content must remain functional during and after a Design Basis Safe Shutdown Earthquake. Conventional seismic qualification using shake-table testing and experimental generation of in-cabinet response spectra is costly, time-consuming, and limited in capturing failure modes beyond design thresholds. Detailed Finite Element (FE) models with nonlinear behavior in ABAQUS can evaluate cabinet seismic performance across a broader design space. While effective for localized failures, FE models are computationally intensive. In this study, a reduced-order, yet detailed OpenSees model is proposed and validated by comparison to a high-fidelity ABAQUS model and experimental results. Static pushover and modal properties are first verified, then the model is subjected to floor motions derived from a Power Plant model under ground motions compatible with a Uniform Hazard Spectrum (UHS). The model is then applied to examine the effectiveness of seismic base isolators and tuned mass dampers (TMDs) to enhance cabinet performance under high-frequency floor excitations. Results show seismic isolation and TMDs can reduce in-cabinet response spectra (ICRS) by approximately 70% and 54%, respectively, significantly improving seismic resilience.

Keywords: Electrical cabinets, Base isolation, Tuned mass damper Nonstructural component, OpenSees modeling,

1. INTRODUCTION

Power plants must maintain functionality during seismic events to ensure a safe shut down as necessary. Failures in safety-related components, especially electrical cabinets, can threaten operational continuity and public safety. High-frequency seismic motions pose particular risks to such equipment. The 2016 Gyeongju (M5.8) and 2017 Pohang (M5.4) earthquakes revealed significant vulnerabilities, with reports of cabinet overturning, damage, and economic loss [Naik et al., 2020]. These incidents highlight the need for improved seismic protection of critical systems. Seismic qualification of electrical cabinets has evolved from fragility-based risk assessments outlined in early Electric Power Research Institute (EPRI) guidance to broader methods such as anchorage checks, adequacy evaluations, and experience-based qualification, thereby reducing reliance on costly shake-table tests. Despite these advancements, protecting cabinets remains a key challenge due to their critical safety role and complex dynamic response. Their high natural frequencies, sensitive components, and need for uninterrupted operation complicate protection efforts.

Failure modes of electrical cabinets are generally classified as global or local. Global failures involve rigid body motions such as sliding, rocking, twisting, and overturning, which can compromise structural integrity. Fragility curves, based on engineering demand parameters (EDPs) are commonly used to assess global performance by linking EDPs to damage states through intensity-scaled testing. Key global metrics include top acceleration, drift ratios, deformation profiles, and top displacement. OpenSees enables efficient modeling of this behavior through nonlinear time-history analysis, incorporating material and geometric nonlinearities. In contrast, local performance focuses on internal components and is typically evaluated using In-Cabinet Response Spectra (ICRS), which characterizes seismic input at equipment mounting points through a response spectrum. The ICRS shape depends on cabinet dynamics, damping, nonlinearities, equipment layout, and input motion characteristics.

A model for seismic analysis should effectively capture the key dynamic behaviors influencing the ICRS. This study proposed a reduced-order OpenSees model, validated against ABAQUS simulations and shake table tests, to evaluate cabinet response. The computationally efficient model can be used for detailed parametric assessment and is used here to examine the effectiveness of protective systems. Base isolators (BI) and tuned mass dampers (TMD) illustrated in Figure 1 can be effective strategies for reducing seismic demands and mitigating global and local failures. The performance of cabinets with BI and TMD systems are compared with conventional anchorage systems.

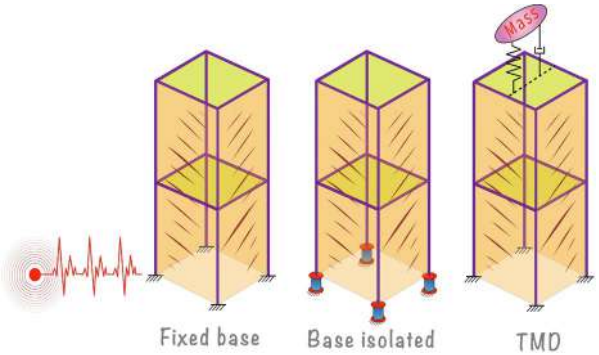


Figure 1. Fixed Base, Base-Isolated, and TMD-Equipped Cabinet

2. PROTECTIVE SYSTEMS

Base isolation techniques employ an isolation plane or flexible supports to decouple cabinets from floor motion. Typical devices include rubber bearings, friction pendulum bearings, and steel wire rope isolators,

each offering energy dissipation capabilities. Kim et al. [2021] reported a 70% reduction in acceleration and elimination of failure modes such as panel detachment by using a friction pendulum system in experimental tests. Similarly, Lee et al. [2024] reported a 42.6% reduction in top acceleration across multiple seismic inputs. These findings highlight the efficacy of friction-based isolators for cabinet protection. Demetriades et al. [1993] demonstrated that wire rope isolators can reduce cabinet displacements by over 90% while maintaining acceleration levels comparable to fixed-base systems, highlighting their effectiveness in providing seismic protection through multi-directional flexibility.

TMDs composed of a mass, spring, and damper, are tuned to the structure's natural frequency to absorb seismic energy. In equipment, TMDs help reduce cabinet vibrations, supporting continuous equipment functionality during earthquakes. The main parameters for TMD design including mass, stiffness, and damping are defined in (1) to (3):

$$m_{TMD} = \mu \cdot M \tag{1}$$

$$K_{TMD} = \omega_0^2 \cdot f^2 \cdot m_{TMD} \tag{2}$$

$$C_{TMD} = 2 \cdot \zeta \cdot \omega_0 \cdot f \cdot m_{TMD} \tag{3}$$

where, μ is the mass ratio, M the structural mass, f the frequency ratio of the fundamental frequency of TMD to that of the structure, ω_0 the natural frequency, ζ the damping ratio, and β the base structure damping. Optimal frequency and damping ratios have been proposed by Den Hartog [1956], Warburton [1982], Sadek et al. [1997] as summarized in Table 1.

Table 1**. Optimal Frequency and Damping Ratios for Tuned Mass Dampers Based on Various Formulations**

Model	Optimal Frequency Ratio	Optimal Damping Ratio
Den Hartog	$f_{opt} = \frac{1}{1+\mu}$	$\xi_{opt} = \sqrt{\frac{3\mu}{8(1+\mu)}}$
Warburton	$f_{opt} = \frac{1}{1+\mu}\sqrt{1-\frac{\mu}{2}}$	$\xi_{opt} = \sqrt{\frac{\mu(1-\mu/4)}{4(1+\mu)(1-\mu/2)}}$
Sadek	$f_{opt} = \frac{1}{1+\mu}\left(1-\beta\sqrt{\frac{\mu}{1+\mu}}\right)$	$\xi_{opt} = \frac{\beta}{1+\mu} + \sqrt{\frac{\mu}{1+\mu}}$

Chang et al. [2019] modeled an electrical cabinet with a TMD in SAP2000 using Warburton's tuning, reporting a 10–30% reduction in top accelerations under sine sweep and earthquake inputs. Cho et al. [2020] conducted shake table tests and simulations using formulas from Den Hartog, Warburton, and Sadek, achieving 44.7–62.9% spectral reductions. All models performed similarly, though the Sadek design yielded slightly higher accelerations. Moussallam et al. [2019] experimentally validated TMDs on cabinets, observing up to 50% reduction in ICRS. Go et al. [2024] observed a 14–31% reduction in spectral acceleration in their experiment using a TMD tuned to 85% of the cabinet's natural frequency.

3. EXPERIMENTAL STUDY AND FINITE ELEMENT MODELING

Jeon et al. [2021] investigated the seismic behavior of single-door electrical cabinets (800 × 800 × 2350 mm, 500 kg) through shake table tests and numerical modeling, focusing on high-frequency dynamics. The steel-framed cabinet (Figure 2.a) was rigidly bolted to the table to reflect typical installation. Resonance searches

before and after shaking identified two dominant modes at 16 Hz in side-to-side (SS) and 24 Hz in front-to-back (FB) direction. These results are used in this study to validate the proposed OpenSees model.

They developed a high-fidelity finite element model of the cabinet in ABAQUS, including three main assemblies: enclosure panels, internal frame, and shelving system (Figure 2.b). Enclosure panels consist of top, header, door, and side panels, all made from 3 mm folded sheet metal. The door panel, shown in Figure 2.c, features corrugated reinforcement and connected with hinges and a mid-height lock. Figure 2.d illustrates the internal frame sections. Solid elements used for the frame (C3D8R) and shell elements for panels (S4R). Detailed fastener modeling replicated actual assembly, and elastic–plastic material behavior with isotropic hardening was applied under rigid anchorage conditions. The model accurately reproduced the first two global modes (16.1 Hz and 23.9 Hz), matching experiments within 1%. It also captured key responses, including global shear, panel buckling, and internal stress distribution, serving as a benchmark for the model developed here.

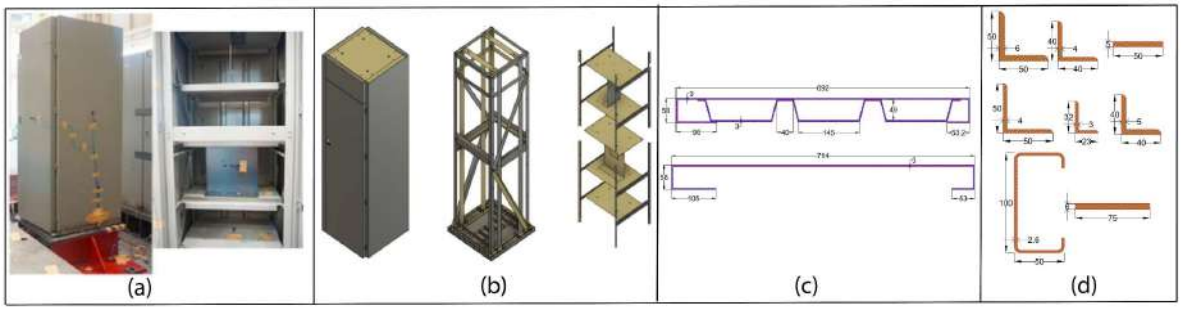


Figure 2. Configurations and structural details of the single-door electrical cabinet analyzed by Jeon et al. [2021]: (a) General view of the tested cabinet; (b) Separation into three subassemblies: enclosure panel, internal frame, and shelving system (left to right); (c) cross-section of the door and side panels; (d) Cross-sections of internal frame

4. SIMPLIFIED OPENSEES MODEL

While shake table tests and high-fidelity ABAQUS models offer valuable insight into cabinet seismic behavior, they are costly and computationally intensive. Efficient reduced-order models are needed to enable broader parametric studies probabilistic seismic analysis. Moreover, a direct comparison between BI and TMD for cabinet protection remains lacking. This study addresses these gaps by developing a reduced order OpenSees model, derived and validated from the ABAQUS model. The model is used to assess the effectiveness of BI and TMD relative to conventional anchorage systems.

4.1 INTERNAL FRAME

The cabinet's internal frame was modeled in OpenSees using a force-based distributed plasticity approach (forceBeamColumn element), which accurately captures axial–bending interaction, critical for cabinet elements. Compared to displacement-based methods, the force-based formulation better represents nonlinear behavior under combined loading. Fiber sections were used for all members to simulate material nonlinearity and plastic deformations efficiently, while capturing both geometric and material effects. The frame configuration and section assignments are shown in Figure 3.a. Material behavior was defined using the Steel02 model in OpenSees. This model captures cyclic steel behavior, including Bauschinger effects and nonlinear hardening. Connections between all beams and diagonal elements to exterior columns were modeled as pinned using ZeroLength elements, assigning soft rotational and rigid translational stiffness, to simulate free rotation with translational continuity. All other joints were modeled as rigid.

4.2 DOOR AND SIDE PANELS

Four strategies were explored for modeling cabinet door and side panels: (1) flexible beams with connectors, (2) single diagonal, (3) distributed diagonals, and (4) flexible shells with connectors. Connectors, representing fasteners, were included only in methods (1) and (4). The flexible beam method, inspired by cold-formed steel shear wall modeling, connects screw locations with deformable elements to simulate panel deformation. Approaches (2) and (3) use tension-only diagonal elements to represent in-plane stiffness, similar to the strip model for steel plate shear walls [Sabelli and Bruneau, 2007]. The distinction between the second and third approaches is the number and angle of the diagonal elements. In the flexible shell approach, panels were discretized using shell elements and connected to the frame at anchor points. Figure 3.b summarizes all panel modeling strategies. After evaluating all four methods, the distributed diagonal element model was selected based on its ability to provide reliable results with computational efficiency. Further details on these modeling strategies can be found in the report by Lin et al. [2024].

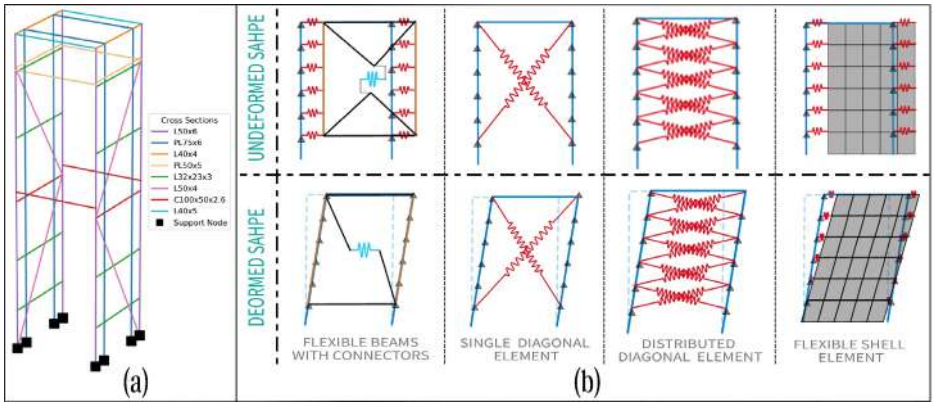


Figure 3. Overall Configuration, Section Assignments, and Modeling Strategies for Enclosure Panels

The cabinet's thin side panels behave like infill plates in steel plate shear walls (SPSWs), resisting lateral loads through in-plane shear and post-buckling tension fields. SPSWs are typically modeled using membrane or strip models [Sabelli and Bruneau, 2007], as shown in Figure 4.a. While membrane models provide detail, strip models offer faster and sufficiently accurate results for tension-dominated thin plates. Accordingly, this study adopted the distributed diagonal element approach, equivalent to strip modeling.

While strips mainly resist tensile forces, they can tolerate limited compression before buckling. To simulate the side panels' tension-dominated behavior and post-buckling degradation under seismic loads, the material model must capture both tensile response and compressive degradation. Common OpenSees models like Steel01, Steel02, and Elastic–Perfectly Plastic do not fully capture cyclic degradation in thin steel plates. To improve this, Choi–Park [2010] and Purba–Bruneau [2015] proposed specialized models, though with some limitations in simulating in-cycle deterioration. Jalali et al. [2016] addressed these limitations by developing the SPSW02 model in OpenSees, which includes in-cycle softening and energy-based degradation. Figure 4.b compares SPSW02 with earlier models, showing differences in degradation. SPSW02 was adopted in this study for the side panel strips to ensure accurate seismic response simulation.

In strip models, the inclination angle (α) of the tensile field (Figure 4.a) strongly influences wall stiffness and shear capacity. According to AISC Design Guide 20 [Sabelli and Bruneau, 2007], the tensile field angle α in SPSW systems typically ranges from 30° to 55°. While a default value of 45° is allowed for design simplicity, more accurate estimation is encouraged. AISC Design Guide 20 (Equation 4) provides a stiffness-based method to compute α considering the panel and frame properties.

$$tan^4\,\alpha = \frac{1+\frac{t_w L}{2A_c}}{1+t_w h\left(\frac{1}{A_b}+\frac{h^3}{360 I_c L}\right)} \tag{4}$$

Where, h is the centerline distance between horizontal boundaries, $A_b$and $A_c$are the cross-sectional areas of horizontal and vertical boundary elements, and I_c is the vertical element's moment of inertia about the axis perpendicular to the web. For cabinet side panels, the resulting angle (α) was approximately 11°, much lower than typical SPSW values due to low stiffness and aspect ratio.

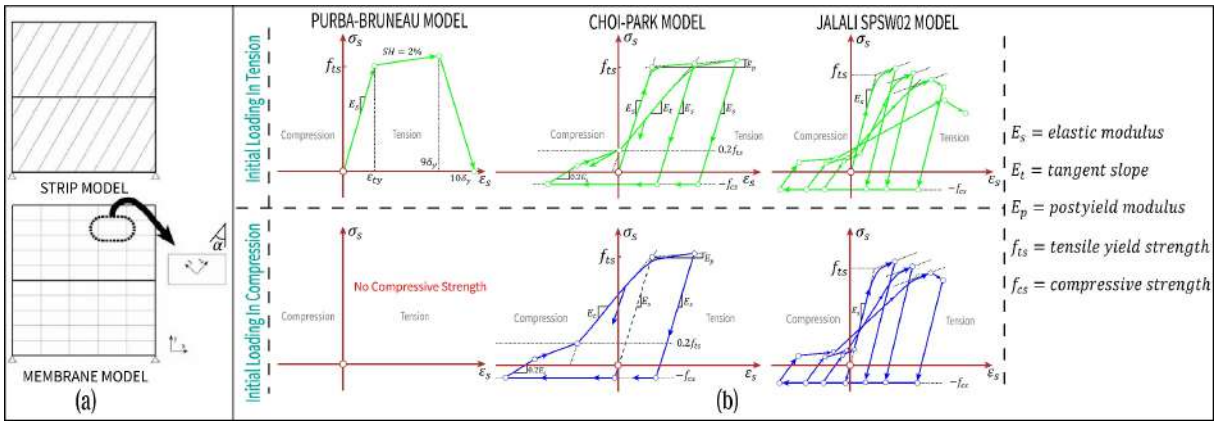


Figure 4. Comparison of Membrane and Strip Modeling Approaches, Material Behavior of Different Models

The door panel consists of a corrugated steel sheet attached to a side plate, connected to the cabinet by four hinges on one edge and a mid-height lock on the other, with no additional restraints. To capture in-plane stiffness, the door was modeled using four diagonal truss elements extending from the lock to each hinge. These elements used the Steel02 material in OpenSees to represent nonlinear hysteresis. A scaling factor was applied to the truss area to fully match the cabinet's side-to-side stiffness, frequency, and dynamic response with experimental data. Figure 5.a shows 3D, side-to-side, and front-to-back views of the model.

4.3 BASEPLATE

The cabinet baseplate contributes notable flexibility, particularly at unanchored edges prone to uplift during dynamic loading, as shown in modal analysis (Figure 5.b). This behavior aligns with previous studies on cabinet mounting flexibility [Chang and Cho, 2019; Cho et al., 2020; Moussallam et al., 2019], which reported uplift and rocking around anchor lines. As illustrated in Figure 6.b, cabinet columns are linked to baseplate stiffeners via coupling constraints that allow rotation about bolt axes while restraining other motions. Stiffeners and the baseplate are tied, and anchor locations are explicitly modeled to match observed boundary conditions. Three baseplate modeling approaches were evaluated in OpenSees (Figure 5.c): (i) Rigid baseplate with a central spring system, (ii) Equivalent vertical and rotational springs beneath each column, and (iii) Equivalent beam-column elements.

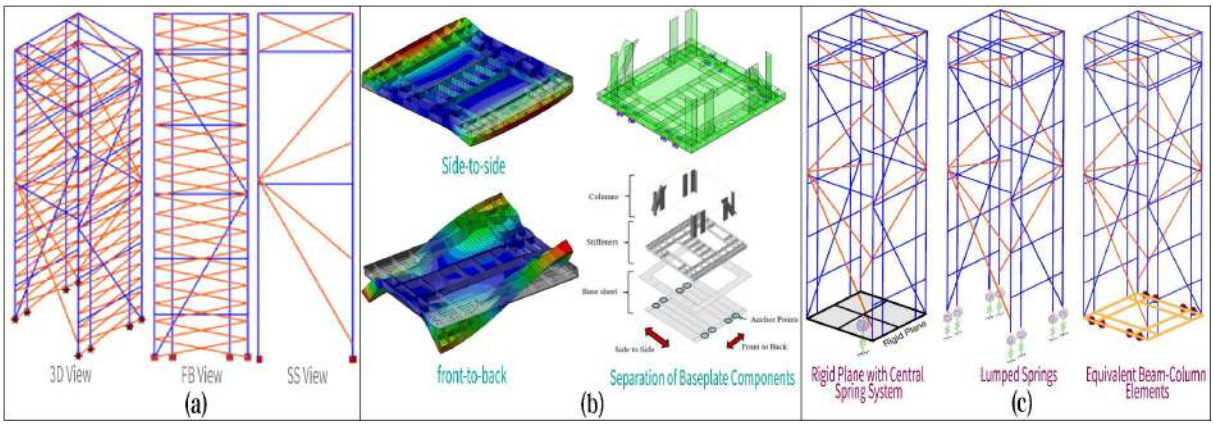


Figure 5. Views of Side and Door Panels Model and Flexible Baseplate Modeling Approaches

In the first method, a rigid diaphragm was assumed at the cabinet base, with vertical and rotational springs placed at center. While simple, this approach was difficult to calibrate and failed to capture the distributed deformation of the baseplate, which significantly influences cabinet dynamics. In the second approach, vertical and rotational springs modeled with *twoNodeLink* elements were placed under each column and calibrated to match modal and pushover responses from the ABAQUS model. However, since the longitudinal springs beneath corner columns contribute to both SS and FB behavior, matching frequencies and lateral stiffness in both directions was challenging. The third approach modeled baseplate flexibility using equivalent beam-column elements. The baseplate was segmented along principal directions, with each segment assigned a calibrated element to replicate ABAQUS-derived force–displacement behavior, improving accuracy. Due to its superior accuracy, easier calibration, and ability to match dynamics in both directions, this method was adopted in the study. Further details provided in the report by Lin et al. [2024].

4.4 MODEL VALIDATION

The OpenSees cabinet model was validated through pushover and modal analyses compared to high-fidelity ABAQUS results. Pushover analysis evaluated nonlinear force–deformation behavior under 50 mm lateral displacement in both FB and SS directions, while modal analysis confirmed accurate natural frequencies and mode shapes. As shown in Figure 6.a, the OpenSees pushover curves closely matched ABAQUS results, demonstrating that the simplified model effectively captures the cabinet's nonlinear seismic response. Lateral elastic stiffness values, extracted from the initial slope of the force–displacement curves in SS and FB directions, are summarized in Table 2. Differences between the OpenSees and ABAQUS models remained within 6%, confirming strong agreement.

Table 2. Comparison of Frequency and Lateral Elastic Stiffness

	Side-to-Side Direction				Front-to-Back Direction			
Model	frequency [Hz]	difference [%]	stiffness [N/mm]	difference [%]	frequency [Hz]	difference [%]	stiffness [N/mm]	difference [%]
OpenSees	14.7	8.1	1590	5.4	25.2	5.0	4600	3.4
ABAQUS	16.1	0.6	1680	0.0	23.9	0.4	4450	0.0
Experiment	16.0	0.0	-	-	24.0	0.0	-	-

First natural frequencies in the SS and FB directions are summarized in Table 2, with differences under 8%, confirming model validity. Mode shape comparisons in Figure 6.b further demonstrate consistency between the OpenSees and ABAQUS models in capturing cabinet dynamic behavior.

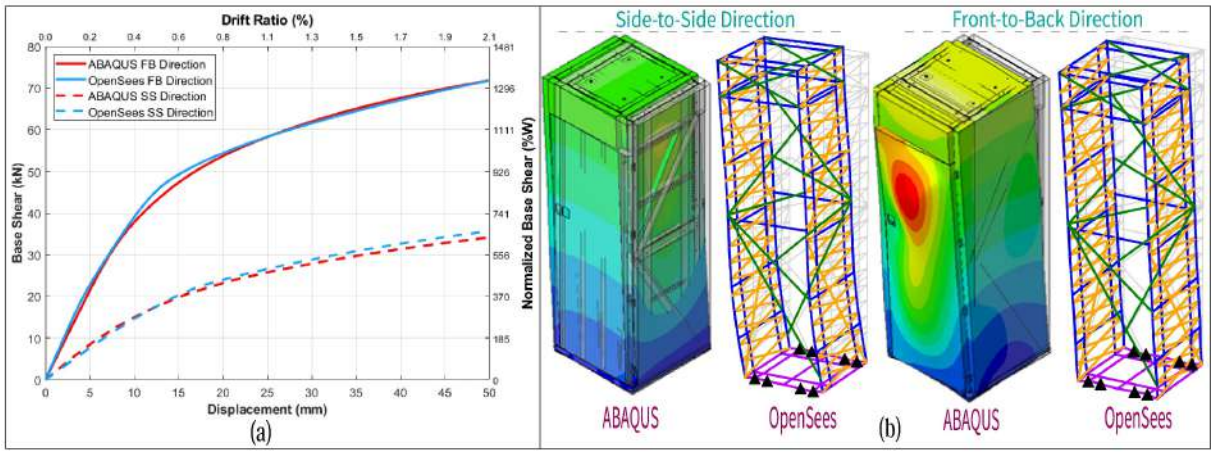


Figure 6. Comparison of Pushover Curves and Predominant Mode Shapes between ABAQUS and OpenSees Models

5. NONLINEAR DYNAMIC ANALYSIS

Thirty floor motions compatible with a Uniform Hazard Spectrum (UHS) were used, scaled to represent seismic hazard at a South Korean NPP site. The UHS accounted for horizontal and vertical excitations and was used to assess floor spectral amplification, damping, and ductility demands. Motions were provided at two key elevations, 100.5 ft and 165 ft within a NPP. Figure 7.a shows the acceleration spectra of the records.

5.1 TUNED MASS DAMPER

To enhance seismic performance, a TMD was installed at the cabinet top. In OpenSees, it was modeled using two nodes, one node represents the TMD mass and one attached to the cabinet, connected by Truss or TwoNodeLink elements. An elastic material is assigned to one element to simulate stiffness, while a uniaxial viscous material is assigned to the second element to represent damping (Figure 7.b). This setup allows independent tuning of stiffness and damping in both SS and FB directions, enabling accurate dynamic response control. TMD design parameters, mass, stiffness, and damping, were computed using Equations (1) to (3). Considering the cabinet's total weight of 500 kg, TMD mass ratios of 3%, 5%, 7%, and 9% corresponding to 15, 25, 35, and 45 kg were evaluated to assess their influence on seismic response. Formulas by Sadek [1997], Den Hartog [1956], and Warburton [1982] were compared. While Sadek's yields higher damping and Warburton's more conservative values, Den Hartog's method was adopted for subsequent analyses due to its balanced results and more widespread use.

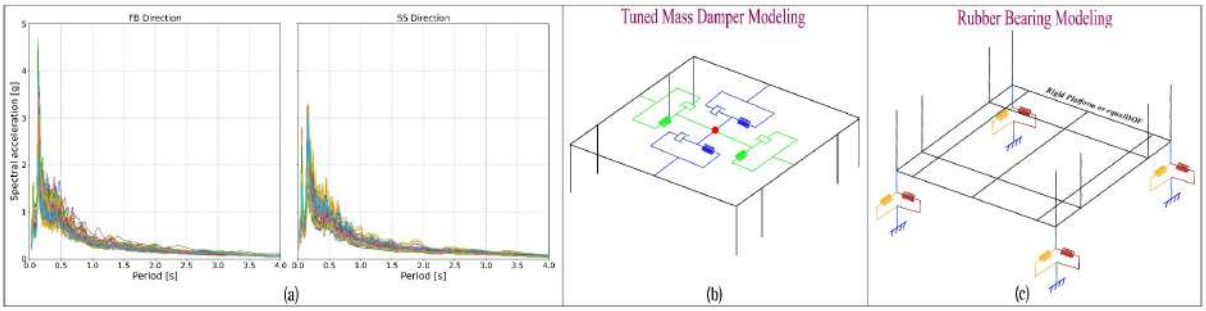


Figure 7. Spectral Acceleration of Scaled Floor Motions and Implementation of TMD and Rubber Bearing in OpenSees

Figure 9 shows the average ICRS, computed from 30 floor motions, for TMD cases. TMD implementation significantly reduced peak spectral accelerations by 40–47% in the FB and 55–74% in the SS direction at the top level, indicating improved effectiveness with higher mass ratios. Peak ICRS values were higher in the SS direction due to the cabinet's lower stiffness and longer period. Without a TMD, ICRS peaks aligned with the first-mode frequencies, confirming first-mode dominance. With a TMD, however, the response split into two peaks, above and below the first mode frequency. This split is a hallmark of TMD behavior, where energy is redistributed away from the primary resonance, effectively mitigating vibrations. TMD effects on peak rack drift ratio were also assessed. Reductions were greater in the SS direction, reflecting lower cabinet stiffness. Notably, a 3% mass ratio slightly outperformed 9% ratio in drift reduction, indicating that higher mass ratios, while more effective for acceleration control, may offer a less pronounced impact on drift reduction. This trade-off should be considered in TMD design for cabinet protection.

5.2 RUBBER BEARING

Base isolators enhance cabinet seismic performance by limiting force transmission along the height. Effective operation requires a rigid base to ensure uniform lateral displacement, achieved by assigning rigid baseplate properties or coupling lateral DOFs using EqualDOF constraints. Four elastomeric bearings were modeled beneath the corner columns using the Elastomeric Bearing (Plasticity) element (Figure 7.c). This element uses a coupled yielding surface for shear and retains high axial, flexural, and rotational stiffness. Figure 8.a illustrates its bilinear hysteresis behavior. The isolated system's effective period, calculated using

Equation (5), depends on effective stiffness and cabinet weight (W). A typical assumption of one-seventh of the initial stiffness was used for effective stiffness, though it depends on the maximum displacement.

$$T_{eff} = \sqrt{\frac{4\pi^2 W}{g K_{eff}}} \tag{5}$$

Isolator characteristic strength typically ranges from 5% to 15% of the supported weight, with effective periods between 1–3 seconds. To evaluate their impact, this study considered two strength levels (5%W, 15%W) and two periods (1s, 3s), representing typical design bounds for parametric seismic analysis. Figure 8.b shows the first mode shapes of the isolated cabinet, corresponding to frequencies of 2.81 Hz and 0.94 Hz for effective periods of 1s and 3s, respectively. These frequencies were computed using the initial stiffness, not effective stiffness. The results confirm that the isolators enable rigid-body horizontal motion with minimal relative displacement along the cabinet height, indicating effective isolation behavior.

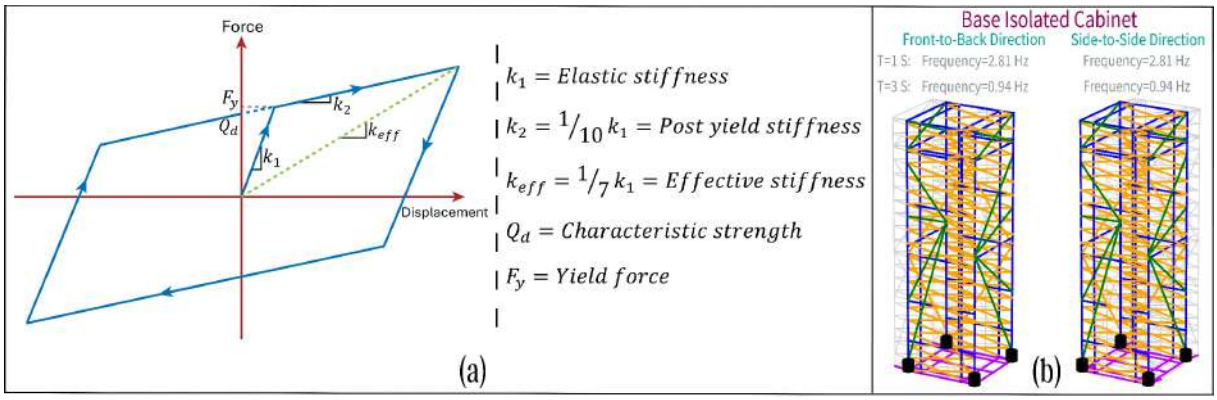


Figure 8. Bilinear Hysteresis of Isolator and First Mode Shape of Base-Isolated Cabinet in FB and SS Direction

Figure 9 shows the average ICRS from 30 floor motions. Compared to the fixed-base case, base-isolated configurations significantly reduce ICRS in both directions. While all isolator setups exhibit similar overall behavior, detailed analysis reveals trends related to characteristic strength and effective period. Increasing the effective period results in greater ICRS reduction, and lower characteristic strength also leads to lower ICRS. As the effective period increases, the ICRS difference between high and low characteristic strength isolators becomes less pronounced. This is due to the response spectrum shape of the input floor motions; at 3s, the system shifts to the flatter region of the spectral acceleration curve, where the excitation demand is lower, the system response becomes less sensitive to variations in characteristic strength, resulting in smaller differences between isolator configurations. Overall, differences between isolator configurations, defined by characteristic strength and effective period, are minor and likely negligible in practice.

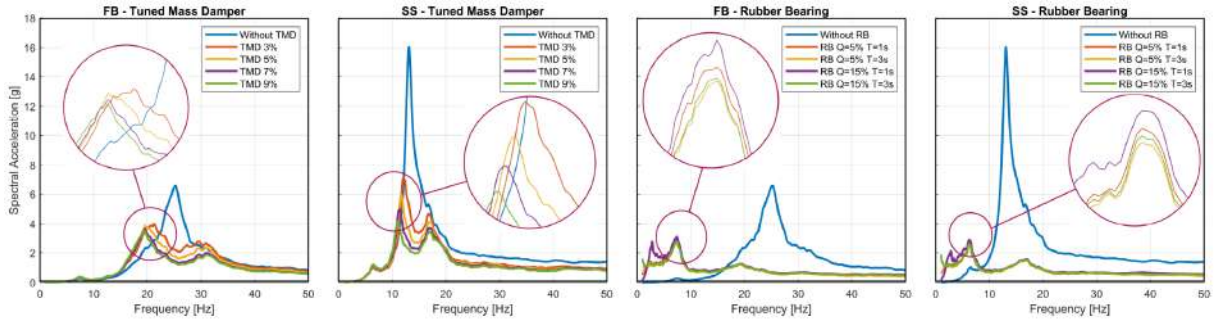


Figure 9. Comparison of ICRS at the Top Level for Main Cabinet, TMD, and Rubber Bearing Models

ICRS plots typically display a peak aligned with dominant input motion frequencies. At 15% characteristic strength, a second peak appears near the isolated cabinet's first natural frequency (2.81 Hz for 1s, 0.94 Hz

for 3s periods). This results from the nonlinear force–displacement behavior of elastomeric isolators, which exhibit bilinear hysteresis with distinct pre- and post-yield stiffness. At low characteristic strength, isolators yield early and operate mainly in the post-yield regime, decoupling the cabinet from high-frequency input and suppressing resonance. At higher strength, yielding is delayed, keeping the system in the stiff pre-yield regime longer, behaving more like a linear oscillator and amplifying response near the cabinet's first mode, producing a secondary ICRS peak. Additionally, ICRS values remain nearly uniform along the base-isolated cabinet height, unlike cabinets with TMDs, confirming effective rigid-body motion that reduces relative displacement, limits base rocking, and improves internal component stability.

Peak displacement is a key factor in assessing clearance requirements for base isolation. In this study, maximum lateral displacements ranged from 37 mm to 88 mm across isolator configurations, which are relatively small and manageable from a design perspective. Table 3 compares peak ICRS values for TMD and base isolator configurations against the fixed-base cabinet. Base isolators consistently achieved greater reductions, with average peak ICRS reductions of 70%, compared to 54% for TMDs across both FB and SS directions, highlighting their superior seismic mitigation performance.

Table 3. Comparison of Peak In-Cabinet Responses Spectra and Reduction Percentages

Model	FB Direction [g]	SS Direction [g]	Reduction in FB [%]	Reduction in SS [%]
Main	6.58	16.06	-	-
TMD 3% (15Kg)	3.97	7.11	39.7	55.7
TMD 5% (25Kg)	3.86	5.97	41.3	62.8
TMD 7% (35Kg)	3.65	5.00	44.5	68.9
TMD 9% (45Kg)	3.49	4.16	47.0	74.1
RB Q=5% T=1S	2.85	2.68	56.7	83.3
RB Q=5% T=3S	2.72	2.52	58.7	84.3
RB Q=15% T=1S	3.10	2.89	52.9	82.0
RB Q=15% T=3S	2.76	2.60	58.1	83.8

6. CONCLUSION

In this study, a simplified OpenSees model was developed to evaluate the effectiveness of BI and TMD compared to conventional anchorage systems in electrical cabinets.

- The internal frame can be modeled using a force-based distributed plasticity approach (*forceBeamColumn* element) with fiber sections to capture nonlinear behavior. The simplified model accurately captures both the dynamic characteristics (mode shapes and natural frequencies) and the nonlinear force–deformation behavior under lateral loading.

- The door and side panels can be efficiently modeled using diagonally distributed spring elements with SPSW02 material to simulate in-plane shear response.

- The most reliable approach for modeling the baseplate is using equivalent beam-column elements, as they accurately capture the bi-directional flexibility.

- Base isolators demonstrate superior effectiveness in mitigating seismic demands compared to TMDs. They achieved an average 70% reduction in peak ICRS, while TMDs achieved 54%.

REFERENCES

Chang, S., Cho, S.G. [2019] "Mitigation effect of seismic acceleration of nuclear power plant electric cabinet using tuned mass damper under earthquakes," Individual Study, Preprints 2019, 2019090261.

Cho, S.G., Chang, S., Sung, D. [2020] "Application of tuned mass damper to mitigation of the seismic responses of electrical equipment in nuclear power plants," Energies, Vol. 13, No. 2, p. 427.

Choi, I.R., Park, H.G. [2010] "Hysteresis model of thin infill plate for cyclic nonlinear analysis of steel plate shear walls," *Journal of Structural Engineering*, Vol. 136, No. 11, pp. 1423–1434.

Demetriades, G.F., Constantinou, M.C., Reinhorn, A.M. [1993] "Study of wire rope systems for seismic protection of equipment in buildings," *Engineering Structures*, Vol. 15, No. 5, pp. 321–334.

Den Hartog, J.P. [1956] *Mechanical Vibrations*, 3rd Edition, McGraw-Hill Book Company, New York and London.

Go, C., Kwag, S., Kwak, J., Oh, J., Lee, S., Ju, B.-S. [2024] "Experimental and numerical study on the seismic response reduction effect of TMD on nuclear cabinets using shaking table test," *Case Studies in Construction Materials*, Vol.21.

Jalali, S.A., Banazadeh, M. [2016] "Development of a new deteriorating hysteresis model for seismic collapse assessment of thin steel plate shear walls," *Thin-Walled Structures*, Vol. 106, pp. 244–257.

Jeon, B.-G., Son, H.-Y., Eem, S.-H., Choi, I.-K., Ju, B.-S. [2021] "Dynamic characteristics of single door electrical cabinet under rocking: Source reconciliation of experimental and numerical findings," *Nuclear Engineering and Technology*, Vol. 53, No. 7, pp. 2387–2395.

Kim, S.-W., Jeon, B.-G., Yun, D.-W., Jung, W.-Y., Ju, B.-S. [2021] "Seismic experimental assessment of remote terminal unit system with friction pendulum under triaxial shake table tests," *Metals*, Vol. 11, No. 9, pp. 1428-1453.

Lee, S., Jeon, B., Kim, S., Yun, D., Jung, W. [2024] "Evaluating the applicability of seismic retrofit of an electric cabinet in a power plant," *Proceedings of the Institution of Civil Engineers–Structures and Buildings*, Vol. 177, No. 7, pp. 589–605.

Lin, L., Kavei, S., Mosqueda, G., Park, J. [2024] "Improved Seismic Performance of Safety Related Equipment in Nuclear Power Plants," *Report*, Department of Structural Engineering, University of California, San Diego, USA.

Moussallam, N., Geiss, M., Buck, M., Tschukarov, H. [2019] "Optimized tuned mass damper for the seismic protection of electrical cabinets," *Proceedings of the 25th Conference on Structural Mechanics in Reactor Technology*, Charlotte, USA.

Naik, S.P., Lee, K., Lee, H., Kim, J., Lee, J., Choi, H., et al. [2020] "Intensity reassessment of the 2017 Pohang earthquake Mw = 5.4 (South Korea) using ESI-07 scale," *Geosciences*, Vol. 10, No. 11, pp. 471-484.

Purba, R., Bruneau, M. [2015] "Seismic performance of steel plate shear walls considering two different design philosophies of infill plates. I: Deterioration model development," *Journal of Structural Engineering*, Vol. 141, No.6.

Sadek, F., Mohraz, B., Taylor, A.W., Chung, R.M. [1997] "A method of estimating the parameters of tuned mass dampers for seismic applications," *Earthquake Engineering & Structural Dynamics*, Vol. 26, No. 6, pp. 617–635.

Sabelli, R., Bruneau, M. [2007] *Steel Plate Shear Walls (AISC Design Guide*), American Institute of Steel Construction,USA.

Warburton, G.B. [1982] "Optimum absorber parameters for various combinations of response and excitation parameters," *Earthquake Engineering & Structural Dynamics*, Vol. 10, No. 3, pp. 381–401.

Influence of Stair System Flexibility on Building Vibration Period: Insights from Full-Scale Building Shake Table Tests at Low-Amplitude Excitation

Sorosh S.[1], Zhang J.[1], Kovac A.[2], Smith K.[3], Schafer B.W.[4], and Hutchinson T.C[1].

[1] Structural Engineering Department, University of California San Diego, CA, USA
e-mail: {ssorosh,j-charlie-zhang,tara}@ucsd.edu
[2] Construction Specialties, Inc., Muncy, Pennsylvania, USA
e-mail: AKovac@c-sgroup.com
[3] Synergi, Inc., Elkridge, Maryland, USA
e-mail: kevin.smith@synergillc.com
[4] Department of Civil and Systems Engineering, Johns Hopkins University, MD, USA
e-mail: schafer@jhu.edu

Abstract. Stair systems, which provide the primary means of egress in and out of a building during and after an earthquake, play a critical role in seismic resiliency. Often, these systems are detailed with fixed flight-to-landing connections. However, previous experimental studies and field reconnaissance have shown that such configurations are prone to severe damage. To mitigate this damage to both the stair systems and the supporting structural members, as well as to avoid the ensuing potential to stiffen the lateral force resisting system of the building, stair connections are often detailed to release drift demands. Referred to as drift-release, these approaches generally focus on releasing inter-story drift at the flight-to-landing connections. Findings from a recent shake table test of a 10-story prefabricated stair system within a mass timber building showed that stair systems with drift-release connections result in a seismically resilient egress solution. However, due to the free movement of stair flights, handrail connections received damage at multiple levels. In a complementary follow-on study, a 9-story stair system with refined connection details was integrated into a 10-story cold-formed steel (CFS10) building recently tested at NHERI@UC San Diego. Numerical analyses have indicated that stair systems with fixed flight-to-landing connections can influence the dynamic characteristics of the supporting structure due to strut action. As such, stairs in the CFS10 building system were designed to allow for easy modification between fixed and drift-release connections by installing or removing locking bolts at the flight to mid-landing interfaces. In the CFS10 building, white noise tests were conducted in each orthogonal direction under two configurations: first, with the stair connections fixed, and then with the locking bolts removed. This study aims to determine the impact of stair connection detailing on the modal characteristics of the building. In addition, complementary numerical simulations were carried out for both fixed and drift-release stair configurations. Based on both experimental and numerical studies, it is found that, under low-amplitude excitation, the impact of stair flexibility on the building vibration period is not significant because the drift-release connection is not appreciably engaged under small lateral loading. However, the impact of stair strut action under large-amplitude excitation still needs to be investigated.

Keywords: Modal analysis, System identification, Stairs, Dynamic characteristics, Shake table test.

1. INTRODUCTION

Stairs are among the most critical nonstructural systems, serving as the primary means of egress during and after an earthquake. Ensuring their functionality is crucial for occupant safety and building usability after an event. Past earthquakes [Li and Mosalam, 2013; Bull, 2011] and experimental studies [Higgins, 2009; Wang et al., 2015] have reported significant damage to stairs, particularly those with rigid flight-to-landing connections (see also [Hutchinson et al., 2025]). To mitigate the damage to stairs and supporting structural members and to avoid the bracing effects of stairs, recent editions of ASCE [ASCE 7-16, 2016, and ASCE 7-22, 2022] require stairs which are not designed as part of the lateral force resisting system to be detailed such that they accommodate the seismic-induced interstory drift. In alignment with this requirement, Black et al. [2017, 2020] proposed and tested several drift-release connections at the story level (i.e., subsystem level). Subsequent system-level tests by Sorosh et al. [2025] considered the performance of three types of drift-release connections as part of a 10-story mass timber building [Pei et al., 2024]. This study found that drift-release connections effectively reduce damage to the stair system even under risk-targeted maximum considered earthquake (MCE_R) motions with peak interstory drift ratios exceeding 2%. However, they observed that the free movement of stair flights can lead to minor damage in the form of handrail detachment and fracture. To further refine the design of drift-release connections and to test drift-compatible handrail attachments, a 9-story prefabricated steel stair was integrated into a 10-story cold-formed steel (CFS) building, tested on the 6-DOF Large High-Performance Outdoor Shake Table (LHPOST6) at UC San Diego. This paper provides a brief discussion of this test program with an emphasis on the impact of stair flexibility on the vibration periods of the building.

In building design practice, typically, stair systems are often ignored in the structural model. However, numerical simulations of building-stair systems have shown that incorporating the stairs into a building's finite element model (FEM) can increase story stiffness and reduce both floor relative displacements and the building's vibration period, especially in stair systems with fixed flight-to-landing connections. For instance, Tegos et al. [2013] used SAP2000 to perform multi-modal response spectrum analysis on a reinforced concrete building with various stair configurations. They found that including stairs in the building's FEM increased the building's stiffness and reduced floor displacements. Similarly, Noorifard and Tabeshpoor [2018] investigated the interaction between stair systems and a supporting five-story reinforced concrete building. This study found that including stairs in the buildings' FEM not only increased stiffness and reduced the fundamental period but also altered the internal force distribution in structural members. More recently, Wen et al. [2022] conducted a numerical investigation on frame structures with beam-type staircases. Their study found that including stairs as part of a building's FEM, whether with fixed or sliding connections, significantly influenced both the staircase and overall building response. Notably, they found that sliding connections, as compared to fixed connections, reduced seismic demands on both the stair components and the supporting structural system. However, none of these results have yet to be experimentally confirmed - though they elevate the need to experimentally investigate the impact of stair stiffness on the modal characteristics of the supporting structure. In this regard, to evaluate the impact of stair stiffness on vibration periods of the supporting structure, the stair systems in the CFS10 building were designed to allow for reconfiguration between fixed and drift-release connections. This was achieved by installing or removing bolts at the flight-to-mid-landing connections. White noise tests were conducted in each orthogonal direction under two configurations, namely 1) with the stair connections fixed, and subsequently, 2) with the locking bolts removed to allow the stair flights at their mid-landings to move freely. This paper discusses the impact of stair stiffness on the modal characteristics of the supporting structure numerically and experimentally, as elicited from these unique test configurations.

2. SHAKE TABLE TEST PROGRAM

2.1 TEST SPECIMEN

2.1.1 CFS10 Building

The CFS-NHERI project is a multi-university-industry collaborative project that aims to advance the understanding of the seismic performance of mid-rise CFS buildings beyond the current height limitation of 19.8 m set by ASCE 7-22 [2022]. As part of this project, a capstone 10-story CFS-framed test building, coined CFS10, with a total height of 30.5 m and a floor plan of 6.86 m × 11.58 m, shown in Figures 1A and 1B, was built and tested on top of the 6-DOF Large High-Performance Outdoor Shake Table (LHPOST6) at UC San Diego. The primary lateral force resisting system of this building consists of steel sheet sheathed shear walls, along with, in one direction, chord studs detailed with both a continuous tie-rod system and outer CFS compression packs, and in the other direction, a mix of CFS compression packs and hollow structural sections (HSSs) to resist high overturning moments of such a tall building. Hutchinson et al. [2026] provides a detailed discussion of the test program, design narratives, and preliminary seismic response results of the CFS10 test building. Specifics of the design details are also provided in greater detail in the compilation by Singh et al. [2022, with extensions to the design in 2024]. Various nonstructural components and systems, including a 9-story stair system with various drift-release connections, windows, fire sprinklers and risers, and gas pipes, were incorporated into this building.

2.1.2 9-story Stair System

A 9-story stair tower, shown in Figure 1C, was integrated into the CFS10 building. The scissor-style prefabricated steel stair system was oriented such that its strong (longitudinal) axis aligned with the building's Y-axis, while its weak (transverse) axis aligned with the X-axis of the building. This shake table test program featured a modular stair system (MSS), in which stair units were preassembled off-site and installed as complete story-level units. Each story unit was designed to carry the gravity load of the entire stair tower, while lateral loads were transferred to the floor diaphragm through shear straps installed at each level. The use of a modular design in the stair system offers advantages such as reduced construction time and improved control over stair-to-diaphragm construction tolerances (Rivera et al., 2026).

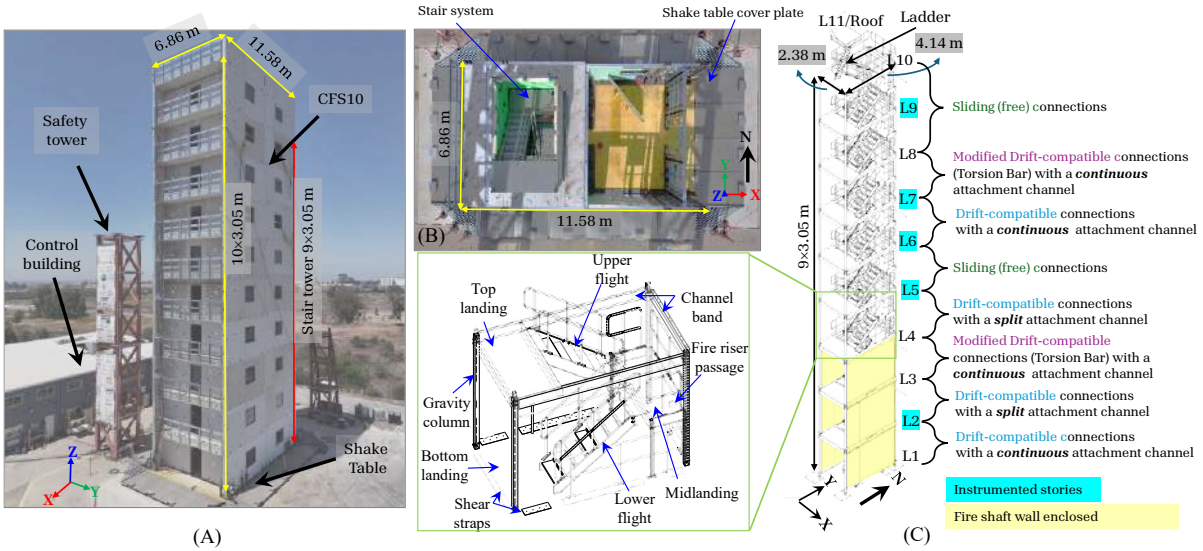


Figure 1. (A) CFS10 building isometric view, (B) CFS10 building plan view, and (C) stair tower isometric view (various connection types are color-coded)

As shown in Figure 1C, stairs with various configurations and midlanding connection details were incorporated in the CFS10 building. Three types of drift-release connections that were integrated into this building (1) sliding or free connections (Figure 2A) with two translational degrees of freedom (DOFs) (Δ_X, Δ_Y) along with a rotational DOF about Z axis (θ_Z), and (2) drift-compatible connections (Figure 2B) with two translational DOFs (Δ_X, Δ_Y), one rotational DOF (θ_X), and a nominal vertical DOF (Δ_Z), and (3) a modified drift-compatible connection (Figure 2C) with two translational DOFs (Δ_X, Δ_Y) and two rotational DOF (θ_X, θ_Z). Figure 2 presents details of these connections, where translational and rotational DOFs are indicated by green arrows. Notably, in the modified drift-compatible connection (Figure 2C), the rotational DOF about the Z-axis (θ_Z) is coupled with translational motion, as shown by the blue arrow at the connection interface. In stair systems with a free connection, as depicted in Figure 2A, both lower flight (LF) and upper flight (UF) stairs are resting on the gravity support at midlaning (ML). As shown in Figure 2D, in stair systems with drift-compatible connections, two attachment strategies are used: (1) at levels 2 and 4, each stair flight is attached to an attachment channel, and the movement of each flight is isolated from the others; however, (2) at levels 1 and 6, both stair flights are connected to the drift-compatible connection using a single attachment channel. Likewise, stair systems with modified drift-compatible connections utilize a continuous or single attachment channel. Note that despite the variation in details, all connection configurations comply with the requirements of ASCE 7-22 [2022]. Sorosh et al. [2025b] provide a thorough discussion of the design details of these stair systems. To lock the drift-release connections, temporary locking bolts were integrated at the midlanding levels, as shown in Figure 2. These locking bolts were installed during the first phase of the shake table test program to study the impact of stairs with fixed connections on the dynamic response of the building.

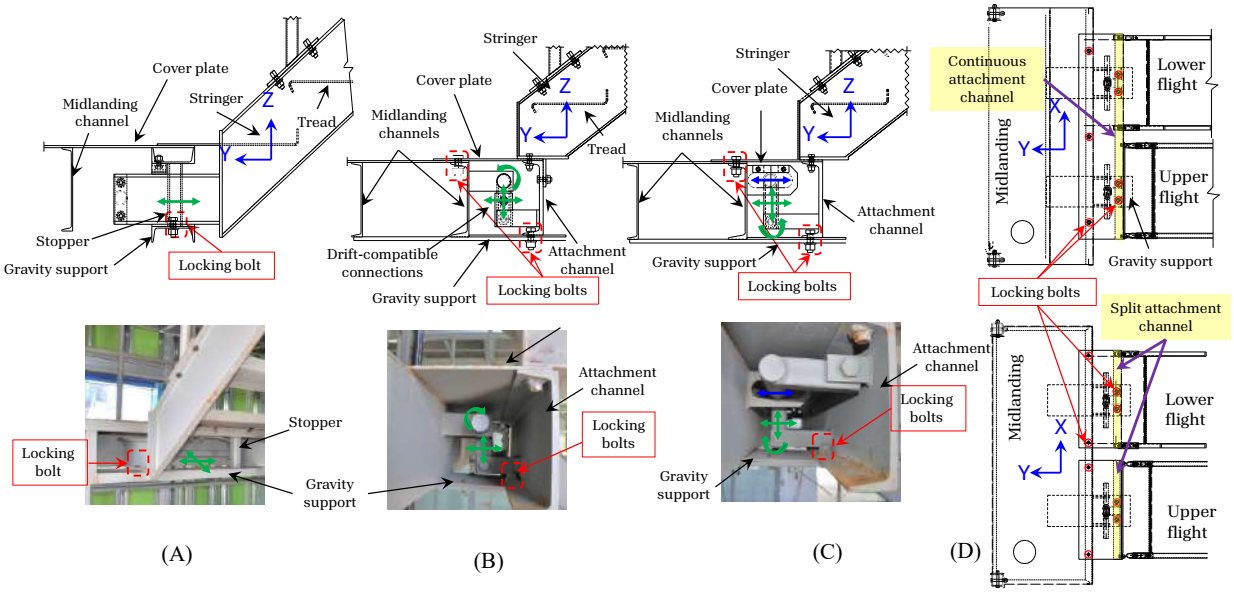


Figure 2. Stair flight to midlanding connection details and configurations (A) sliding (free) connection, (B) drift-compatible connection, (C) modified drift-compatible connection, and (D) continuous and split attachment channel details (note: DOFs are highlighted in green and blue arrows)

2.2 TEST MATRIX

The CFS10 building was tested under 18 simulated earthquake motions scaled to three distinct targeted seismic hazard levels, namely, 15 service-level earthquakes (SLE), one design earthquake (DE), and two risk-targeted maximum considered earthquakes (MCE_R). To monitor the dynamic characteristics of the building, low-amplitude unidirectional white noise tests in each orthogonal direction were conducted after earthquake motions. It is worth noting that at the beginning of each locked and unlocked stairs phase, to tune the shake table with the presence of the building, one white noise test in each orthogonal direction with a target root mean square (RMS) of 4%g and duration of 160 seconds was conducted. All other WN tests, except WN3

and WN4, were conducted with a target RMS of 4%g and a duration of 64 seconds. WN3 and WN4 were intentionally conducted with a target RMS of 3%g and a duration of 64 seconds to investigate the frequency response function of the building at smaller amplitude excitation. It is expected that larger amplitude WN tests will result in larger periods of the building at a given state. Table 1 lists the subset of tests discussed in this paper. The vibration period of the building under WN1 through WN12, with two configurations of stairs locked and unlocked, will be discussed. In addition, briefly, the response of the stairs and CFS10 building under MID1 and MID2 will be included.

Table 1. Subset of tests discussed in this paper (Note: for brevity, MID3 and MID4 are excluded from this paper. RMS: root mean square, WN: white noise, and SLE: service level earthquake).

Test Day, *Configuration*	Test	Description
Test Day 1, ***Stairs Locked***	WN1	WN_X 4.0%g RMS for a duration of 160 sec
	WN2	WN_Y 4.0%g RMS for a duration of 160 sec
	WN3	WN_Z 10.0%g RMS for a duration of 160 sec
Test Day 2, ***Stairs Locked***	WN4	WN_X 3.0%g RMS for a duration of 64 sec
	WN5	WN_Y 3.0%g RMS for a duration of 64 sec
	MID1	1989 Loma Prieta XYZ SLE (station: Gilroy Array #3)
	WN6	WN_X 4.0%g RMS for a duration of 64 sec
Stairs were unlocked after WN7	WN7	WN_Y4.0%g RMS for a duration of 64 sec
Test Day 3, ***Stairs Unlocked***	WN8	WN_X 4.0%g RMS for a duration of 160 sec
	WN9	WN_Y 4.0%g RMS for a duration of 160 sec
	WN10	WN_Z 10.0%g RMS for a duration of 160 sec
	MID2	1989 Loma Prieta XYZ SLE (station: Gilroy Array #3)
	MID3	1989 Loma Prieta X SLE (station: Gilroy Array #3)
	MID4	1989 Loma Prieta Y SLE (station: Gilroy Array #3)
	WN11	WN_X 4.0%g RMS for a duration of 64 sec
	WN12	WN_Y 4.0%g RMS for a duration of 64 sec

3.EXPERIMENTAL RESULTS

3.1 STAIR SYSTEM DISPLACEMENT RESPONSE

The response of the CFS10 building and its nonstuctural components and systems during the shake table test program was monitored using more than 1000 analog sensors. Pertinent to the analyses herein, the accelerations at each level of the building and stair components were measured using accelerometers. In addition, relative displacements across stair flights to story-level landings and midlanding interfaces were measured using linear potentiometers. Note that not all levels were instrumented; refer to Figure 1C for those stories with detailed stair instrumentation. Figure 3 shows the displacements of the stair flight with respect to the midlanding in both X and Y directions under MID1 (locked phase) and MID2 (unlocked phase) at Levels 2.5 and 5.5 (midlanding locations). Locking the stair connection, which was achieved by bolting the connection, was efficient, and small displacements across the joints were recorded during MID1. MID2 was conducted with all stair midlandings unlocked, and despite this being a service-level earthquake, small relative movements across the stair's drift-release connections were measured. As seen in Figure 3, these movements across drift-compatible connections at L2.2 and free connections at L5.5 were in the range of 0.1 to 1 mm.

3.2 BUILDING ACCELERATION RESPONSE

Figure 4 shows the acceleration time histories and corresponding 2% damped spectral acceleration recorded at the estimated center of mass (CoM) locations at levels 1, 5, and 10 in both X and Y directions. It is seen that at certain periods, for instance, at a period closer to the first flexural modes in each orthogonal direction, the power in spectral acceleration during MID1 is larger than that during MID2. This is more pronounced

in the responses in the Y direction, which is anticipated as this is the strong axis of the stairs. In addition, from the acceleration response histories, it is seen that during MID1, the acceleration demand is higher than that during MID2. This may be attributed to the fixity of the stair system during MID1, as the bracing effect of the stair system during the locked phase is expected to result in larger floor accelerations. However, it is worth noting that this subtle change in acceleration demand could also be due to a change in the building's dynamic characteristics due to five white noise tests conducted between MID1 and MID2.

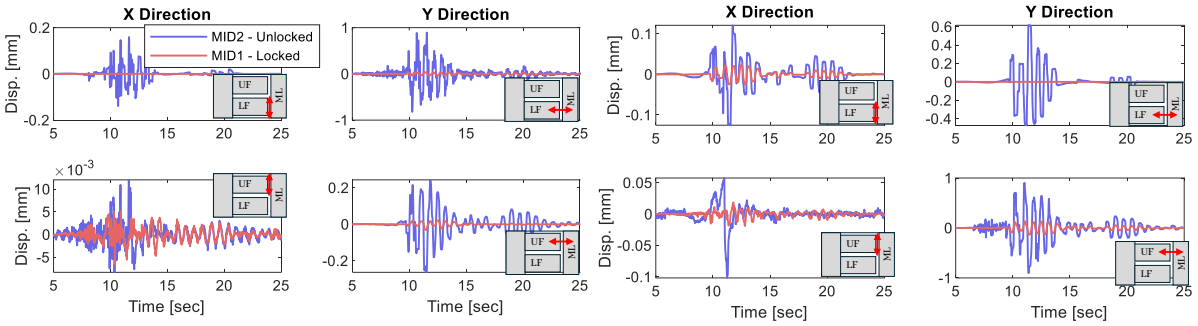


Figure 3. Stair connection displacement response during MID1 (stairs locked) vs MID2 (stairs unlocked) at (A) L2.5, and (B) L5.5

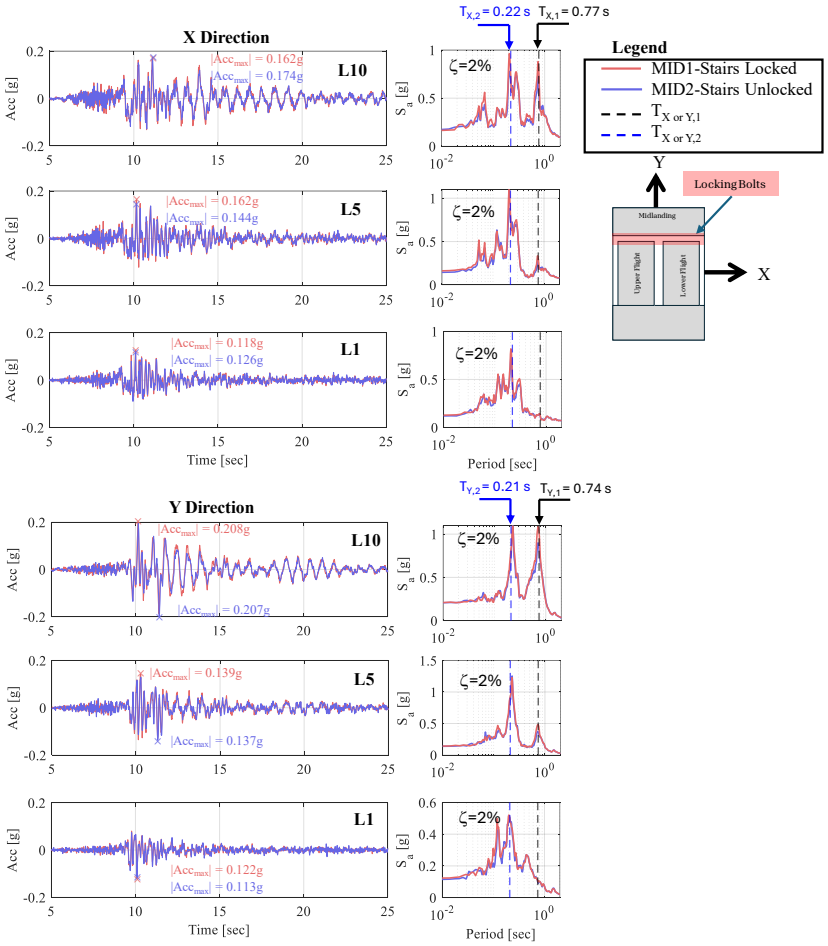


Figure 4. Acceleration time histories and corresponding 2% damped elastic spectral acceleration at Levels 1,5, and 10 during MID1 and MID2 in each of the X and Y directions

3.3 BUILDING VIBRATION PERIOD

Modal characteristics of the first three fundamental vibration modes were determined using both input-output and output-only system identification (SID) techniques. In the input-output SID, the frequency response function (FRF) of the building during the WN tests conducted in each orthogonal direction was used. In the output-only SID method, the Stochastic Subspace Identification (SSID) technique, first described by Van Overschee and De Moor (1996), was employed. All acceleration data used in the SID analysis are initially filtered using a 4th order Butterworth bandpass filter [Matlab, 2022] with cut-off frequencies of [0.075 50] Hz and then baseline corrected using the mean of the first 256 data points, i.e., the first second of data.

3.3.1 Frequency Response Function

Frequency response functions define how different parts of the building amplify specific frequency components of the excitation at the base. Since white noise (WN) tests are low-amplitude broadband excitation, they excite the building modes with approximately equal energy. This characteristic of the WN test enables the estimation of modal characteristics without any significant nonlinear response of the building. In this study, the FRFs were calculated based on one acceleration either at the estimated CoM location on the shake table platen or the north-west corner of the shake table platen as the input, and the acceleration at the CoM or north-west corner at each of the other levels in the building served as the output. Considering two input signal locations, 20 output signal locations in each orthogonal direction, results in a total of 4 input and 40 output signals used in these analyses. Figure 5 shows the average FRF in the X and Y directions during WN tests listed in Table 1.

Two modal characteristic extraction methods were employed to estimate the vibration periods of the building using FRFs. In the first method, the conventional peak picking (PP) method was used to extract the vibration frequency associated with the first two flexural vibration modes and the first torsional mode based on the peaks of the FRF around these vibration modes. In addition, using FRFs, the vibration frequencies were extracted using the Least Squares Rational Function (LSRF) curve fitting algorithm with a modal order of 100 [Matlab, 2022]. Figure 6 shows the periods associated with the first three vibration modes using the methods discussed here. In general, the predicted periods using the PP and LSRF methods are in good agreement.

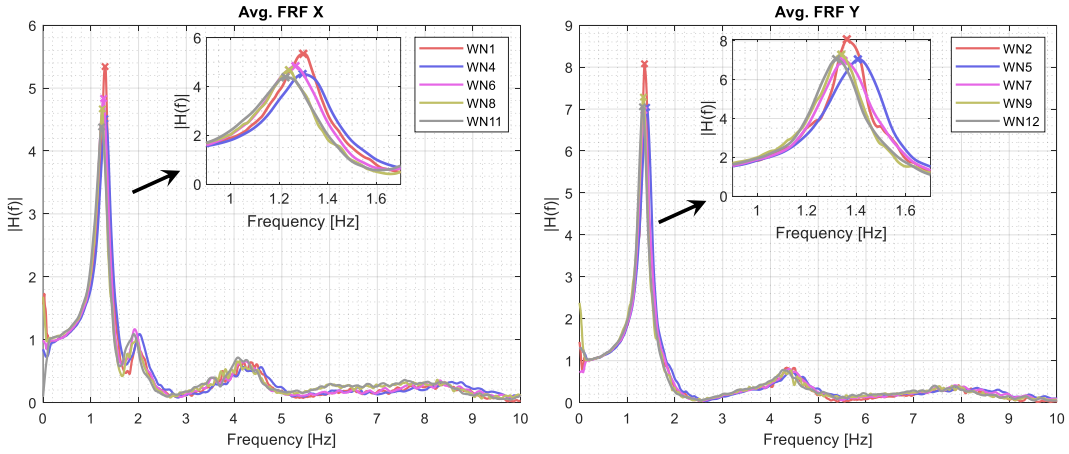


Figure 5. Averaged frequency response function

3.3.2 Stochastic Subspace Identification

Using WN test data, in addition to the two input-output methods of system identification, this study uses a time-domain output-only system identification (SID) method. In output-only SID analysis, a data-driven

stochastic subspace identification (SSID) method [Van Overschee and De Moor, 1996] is used to extract the modal characteristics of the CFS10 building. SSID is a promising method for the current effort to characterize such a complex building with closely spaced modes. In this analysis, the data from 44 accelerometer channels, consisting of two accelerometer channels each at the estimated CoM on the shake table platen and the north-west corner at L1, and 40 accelerometers at the estimated CoM and north-west corner at levels 2 to L11, were used. In this analysis, the output block Hankel matrix is constructed using 100 block rows with 22 rows per block. Figure 6 and Table 2 compare the predicted period using the various SID techniques discussed in this section. The key observations from this figure are as follows:

- The predicted vibration periods based on various SID techniques match reasonably well. In general, the SSID method predicts slightly higher periods than either input-output method.
- Based on the mean of the vibration periods estimated with each method, the change in building periods corresponding to the first two flexural modes after MID1 is smaller than 2.2%. This change after MID2, MID3, and MID4 is smaller than 1.7%. However, the change in period based on the individual SID technique is as high as 3-4%.
- Observing the mean of the period estimated based on WN tests before and after unlocking the stairs, there is about 1.3% and 0.9% change in the periods corresponding to the first flexural mode in the X and Y directions, respectively. This change, based on the individual SID method, is reported as high as 2.1% and 1.8% in the periods corresponding to the first flexural mode in X and Y directions, respectively. However, it is worth noting that, as was listed in Table 1, WN8 and WN9 are 160 seconds long while WN6 and WN7 are 64 seconds long. In addition, it is noted that under such small excitation levels, the drift-release connections of stair systems are not significantly engaged, and therefore, there is a small difference between drift-release and fixed connections at low levels of shaking. However, under stronger excitation, the gap between the vibration period of a building with fixed stairs and that of a building with stairs having drift-release connections is expected to increase.

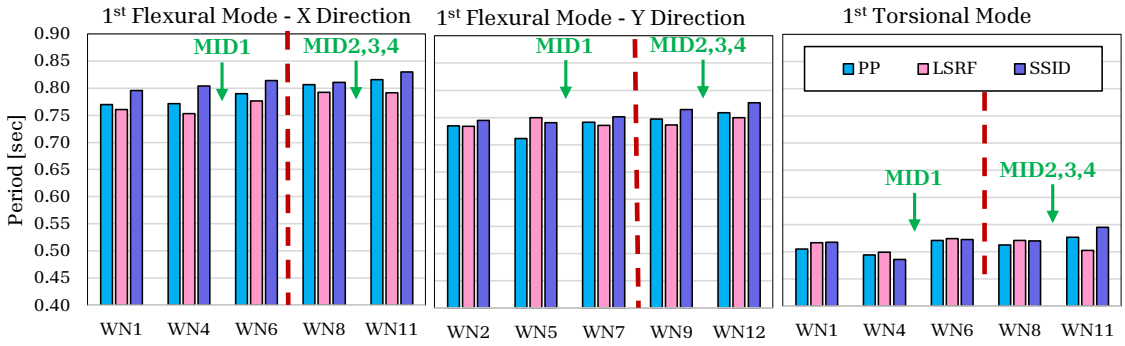


Figure 6. Building vibration periods corresponding to the first flexural modes in each orthogonal direction and the first torsional mode based on peak picking (PP), least squares rational function (LSRF), and stochastic subspace identification (SSID) methods. Note: the red vertical dashed line shows the instant of unlocking the stairs

4.NUMERICAL SIMULATION

A general-purpose finite element software [ETABS, 2018] was used to develop a simplified finite element model of individual stories of the stairs with various drift-release and fixed connections. A detailed discussion of this modeling effort is provided in Sorosh et al. [2025b]. Using these finite element models, displacement-based linear pushover analyses were conducted to estimate the story stiffness of the stairs, and these stiffnesses were incorporated into a model of the CFS10 building. Stair story stiffnesses were defined

with zero-length shear springs that represent the stair tower as part of the building's finite element model previously developed by Zhang et al. [2024]. This building–stair system level simulation was used to complement the experimental modal analysis presented in the current paper. Table 3 summarizes the building vibration periods corresponding to the first three fundamental modes from eigenvalue analysis and compares them with the experimental results discussed in Section 3. Although the building model included only the minimum DOF essential to predict the building's dynamic response with low computational cost, periods from eigenvalue analysis match the experimental results reasonably well. It is seen that locking stair connections does not significantly affect the vibration periods of the building. However, based on eigenvalue analysis, excluding stairs from the building model results in a relatively larger increase in the building period, particularly in the direction parallel to the stair run (Y direction).

Table 2. Building vibration period corresponding to the first three fundamental modes (note: green lines define the instance of subjecting the building to a service-level earthquake, red dashed line is the instance of unlocking the stairs)

Mode	SID Method	Period [sec]					Period Change[1] [%]				
		WN1	*WN4*	*WN6*	*WN8*	*WN11*	*WN1*	*WN4*	*WN6*	*WN8*	*WN11*
1st Flexural Mode in the X Direction	PP	0.77	0.77	0.79	0.81	0.82	0.00	0.23	2.31	2.11	1.20
	LSRF	0.76	0.75	0.78	0.79	0.79	0.00	-1.02	3.09	2.05	-0.09
	SSID	0.80	0.80	0.81	0.81	0.83	0.00	1.03	1.15	-0.30	2.38
	Average	0.78	0.78	0.79	0.80	0.81	0.00	0.08	2.19	1.29	1.16
1st Flexural Mode in the Y Direction		*WN2*	*WN5*	*WN7*	*WN9*	*WN12*	*WN2*	*WN5*	*WN7*	*WN9*	*WN12*
	Peak Picking	0.73	0.71	0.74	0.75	0.76	0.00	-3.18	4.31	0.69	1.56
	LSRF	0.73	0.75	0.74	0.74	0.75	0.00	2.17	-1.90	0.09	1.84
	SSID	0.74	0.74	0.75	0.76	0.78	0.00	-0.53	1.45	1.81	1.64
	Average	0.74	0.73	0.74	0.75	0.76	0.00	-0.51	1.29	0.87	1.68
1st Torsional Mode		*WN1*	*WN4*	*WN6*	*WN8*	*WN11*	*WN1*	*WN4*	*WN6*	*WN8*	*WN11*
	Peak Picking	0.51	0.49	0.52	0.51	0.53	0.00	-2.13	5.26	-1.59	2.79
	LSRF	0.52	0.50	0.52	0.52	0.50	0.00	-3.44	4.96	-0.65	-3.43
	SSID	0.52	0.49	0.52	0.52	0.54	0.00	-6.26	7.24	-0.25	4.69
	Average	0.51	0.49	0.52	0.52	0.52	0.00	-3.94	5.82	-0.83	1.35

PP: Peak picking
LSRF: Least square rational function
SSID: Stochastic subspace identification
[1]Period change refers to the difference in period during a WN test compared to the previous test in the same direction.

Table 3. Building vibration period corresponding to the first three fundamental modes based on experiment and eigenvalue analysis

Mode	Experiment[1]		Numerical simulation[2]		
	Stairs Locked	*Stairs Unlocked*	*Stairs Locked*	*Stairs Unlocked*	*No stair*
1st Flexural Mode in the X Direction	0.78	0.80	0.69	0.69	0.70
1st Flexural Mode in the Y Direction	0.74	0.75	0.61	0.62	0.66
1st Torsional Mode	0.51	0.52	0.54	0.55	0.56

[1]These periods are based on the average of the 3 different methods summarized in Table 2
[2]These results are per Sorosh et al. (2025b)

5.CONCLUDING REMARKS

Previous earthquake events and tests of stair systems have confirmed that stairs are prone to severe damage under lateral loads, particularly for stairs with fixed flight-to-landing connections. In addition, numerical simulations have shown that stairs with fixed connections act as braces and significantly reduce the vibration period of supporting buildings. However, in practice, stairs are usually not incorporated into the finite element model of the supporting building. To experimentally investigate the impact of stair flexibility on the vibration period of a building, a nine-story stair tower featuring various drift-release connections was

recently tested as part of a full-scale ten-story CFS building. The drift-release connections in these stairs were detailed to also facilitate a fixed connection using bolted connections. Select test results from this program are discussed in the current paper, with particular attention to the impact of stair flexibility on the vibration period of the building. Three different system identification techniques were used to extract the vibration period of the building using acceleration data recorded during white noise tests. The results from all SID techniques agree well with each other, though the output-only SSID method is generally consistently higher than the traditional input-output methods considered. It was found that locking the stair connections did not significantly change the vibration period of the building. The observed minimal change in the period of the building when comparing the locked and unlocked stairs cases was due to the small-level excitation imposed. Under small-level excitations, the drift-release connections are not fully released, and therefore, the gap between the vibration period of the building with fixed stairs and that of the building with stairs having drift-release connections is not significantly large. Nonetheless, using the experimental data herein, future numerical studies should consider larger earthquake excitations with the stairs locked and unlocked to elicit their impact on building systems under more severe hazard scenarios.

ACKNOWLEDGMENTS

The CFS10 project was funded through the National Science Foundation (NSF) grants CMMI 1663569 and CMMI 1663348, project entitled: Collaborative Research: Seismic Resiliency of Repetitively Framed Mid-Rise Cold-Formed Steel Buildings, and numerous other federal/state and industry partners. A complete list of sponsors/partners to the CFS10 program may be found at: https://cfs10.ucsd.edu/sponsors-partners. Materials and in-kind support for the stair system are provided by Construction Specialties. The authors appreciate the aforementioned support. The efforts of all undergraduate and graduate students and visiting scholars listed at https://cfs10.ucsd.edu/people/ are greatly appreciated. The opinions and findings of this study are those of the authors and do not necessarily reflect those of the sponsors.

REFERENCES

ASCE [2016] *Minimum Design Loads and Associated Criteria for Buildings and Other Structures*, Standard ASCE/SEI 7-16, Structural Engineering Institute of American Society of Civil Engineers, Reston, VA, USA.

ASCE [2022] *Minimum Design Loads and Associated Criteria for Buildings and Other Structures*, Standard ASCE/SEI 7-22, Structural Engineering Institute of American Society of Civil Engineers, Reston, VA, USA.

Black, C., Aiken, I., Smith, K., Belvin, R., Peachey, A. [2017] "Seismically-resilient stair systems for buildings," *Proceedings of Structural Engineers Association of California Annual Convention (SEAOC 2017)*, San Diego, CA.

Black, C., Aiken, I., Smith, K., Belvin, R., Peachey, A. [2020] "Shake table testing of seismically resilient stair systems for buildings," *Proceedings of 17th World Conference on Earthquake Engineering*, Sendai, Japan.

Bull, D.K. [2011] *Stair and access ramps between floors in multi-storey buildings*, Report for the Canterbury Earthquake Royal Commission, Christchurch, New Zealand.

Computers and Structures Inc. (CSI) [2018] ETABS, Version 18.1.1, Berkeley, CA.

Higgins, C. [2009] "Prefabricated steel stair performance under combined seismic and gravity loads," *ASCE Journal of Structural Engineering*, Vol. 135, No. 2, pp. 122–129. https://doi.org/10.1061/(ASCE)0733-9445(2009)135:2(122)

Hutchinson, T.C., Sorosh, S., Bull, D., Kovac, A., Lizundia, B., Ryan, K., Sari, A., Smith, K., Wang, X., Zhou, Y. [2025] "Seismic behavior, observed performance, and design of stair systems: State-of-the-art," *Journal of Earthquake Engineering*, pp. 1–37. https://doi.org/10.1080/13632469.2025.2523783

Hutchinson, T.C., Eladly, M., Ji, R., Rivera, D., Rukundo, F.C., Singh, A., Sorosh, S., Zhang, J., Zhang, X., Padgett, L., Jones, H., Karns, J., Schafer, B.W. [2026] "Advancing use of cold-formed steel framing systems for mid-rise residential construction in seismic zones via full-scale shake table testing," *Proceedings of the 8th Residential Building Design and Construction Conference, State College*, PA, March 18–19.

Li, B., Mosalam, K.M. [2013] "Seismic performance of reinforced concrete stairways during the 2008 Wenchuan earthquake," *ASCE Journal of Performance of Constructed Facilities*, Vol. 27, No. 6, pp. 721–730. https://doi.org/10.1061/(ASCE)CF.1943-5509.0000382

MathWorks [2022] MATLAB Documentation (R2022), The MathWorks, Inc. https://www.mathworks.com/help/matlab/

Pei, S., Ryan, K.L., Berman, J.W., van de Lindt, J.W., Pryor, S., Huang, D., Dolan, J. [2024] "Shake-table testing of a full-scale 10-story resilient mass timber building," *ASCE Journal of Structural Engineering*, Vol. 150, No. 12, 04024183. https://doi.org/10.1061/JSENDH.STENG-13752

Rivera, D., Zhang, J., Singh, A., Ji, R., Sorosh, S., Eladly, M., Cyizere Rukundo, F., Rivera, D., Ellis, M., Padgett, L., Jones, H., Karns, J., Stewart, D., Schafer, B.W., Hutchinson, T.C. [2026] "Investigating construction methods in a landmark 10-story cold-formed steel residential building specimen shake table test program," *Proceedings of the 8th Residential Building Design andConstruction Conference*, Pennsylvania Housing Research Center, State College, PA, March 18–19.

Sorosh, S., Hutchinson, T.C., Ryan, K.L., Smith, K.W., Kovac, A., Zabet, S., Pei, S. [2025a] "Experimental characterization of a full-scale stair system detailed to achieve seismic resiliency," *Earthquake Engineering and Structural Dynamics*. https://doi.org/10.1002/eqe.4376

Sorosh, S., Zhang, J., Kovac, A., Smith, K., Hutchinson, T.C. [2025b] "Design strategies and modelling verification for steel stairs with drift-compatible connections," *Proceedings of the 2025 Structural Engineers Association of California (SEAOC) Convention*, San Diego, CA.

Singh, A., Hutchinson, T.C., Torabian, S., Schafer, B.W., Peterman, K.D., Padgett, L., Jones, H. [2022] "Structural design narrative of the CFS-NHERI 10-story test building for multi-dimensional shake table testing," *Proceedings of the Cold-Formed Steel Research Consortium Colloquium 2022*, Baltimore, MD.

Singh, A., Zhang, J., Rivera, D., Eladly, M., Jones, H., Kovac, A., Padgett, L., Rivera, D., Smith, K., Torabian, S., Peterman, K.D., Schafer, B.W., Hutchinson, T.C. [2024] "CFS-NHERI 10-story building shake table test specimen: Design updates," *Proceedings of the 18th World Conference on Earthquake Engineering (WCEE2024)*, Milan, Italy.

Overschee, P.V., De Moor, B.L. [1996] Subspace Identification for Linear Systems: Theory–Implementation–Applications, Kluwer Academic Publishers, Norwell, MA.

Wang, X., Astroza, R., Hutchinson, T.C., Conte, J.P., Restrepo, J.I. [2015] "Dynamic characteristics and seismic behavior of prefabricated steel stairs in a full-scale five-story building shake table test program," *Earthquake Engineering and Structural Dynamic*s, Vol. 44, No. 14, pp. 2507–2527. https://doi.org/10.1002/eqe.2595

Zhang, J., Singh, A., Eladly, M., Schafer, B.W., Hutchinson, T.C. [2024] "Pre-test numerical modeling of the CFS-NHERI 10-story capstone building," *Proceedings of the 18th World Conference on Earthquake Engineering (WCEE2024)*, Milan, Italy.

Enhanced Seismic Stability for the Freestanding Contents in Base-Isolated Buildings (SPONSE 2026)

Khine Thazin P. Kyaw[1], Mehta Vikas[2], Sung Hyun Jang[2] and Min Ho Chey[2]

[1] Dept. of Civil Engineering and Management, University of Manchester
Oxford Rd., Manchester, M13 9PL, United Kingdom
e-mail: khinethazin173@gmail.com
[2] Dept. of Civil Engineering, Keimyung University
1096 Dalgubeol-daero, Daegu City, Republic of Korea
e-mail: mchey@kmu.ac.kr

Abstract. This study investigates the seismic rocking and overturning behavior of freestanding contents (FSCs) in buildings, focusing on the impact of base isolation systems. Under 30 SAC Phase II earthquake records, the analysis evaluated floor demands by peak floor acceleration (PFA) and peak floor velocity (PFV). The study also examined three structural configurations—fixed-base, base-isolated, and hybrid (base isolation with viscous dampers). Results highlight that base isolation effectively reduces PFA, thereby lowering the overturning potential of FSCs. However, it can introduce higher PFV due to the longer period of building sway, potentially causing sustained rocking. Adding damping devices to the isolation system significantly mitigates this velocity amplification, offering better control of both rocking and overturning. This combined approach provides a robust strategy for protecting FSCs during earthquakes. Key insights emphasize that seismic demand on FSCs depends heavily on floor-level response, which varies by building type and ground motion intensity. By focusing on both PFA and PFV, engineers can better predict the risk of overturning and design appropriate mitigation measures. This emphasizes the need to incorporate base isolation and supplemental damping into performance-based seismic design, thereby increasing the stability and resilience of non-structural elements.

Keywords: NSE, Freestanding, Rocking, Overturning, Base-Isolation

1. INTRODUCTION

The risk and damage of non-structural elements due to the seismic impact on the structural components have become a critical issue for the safety of valuable contents and the lives of occupants. In many cases, the damage of nonstructural elements is greater than structural damage, and it leads to property loss and death and injuries to the people inside [Zito et al., 2022; Gabbianelli et al., 2020]. Among nonstructural elements, the free-standing contents (FSC) are sensitive to the acceleration response of floors, and the motions of FSC on each floor are difficult to predict under multi-level earthquake excitations, and the floor responses influence the motion of contents, such as sliding, rocking, and overturning.

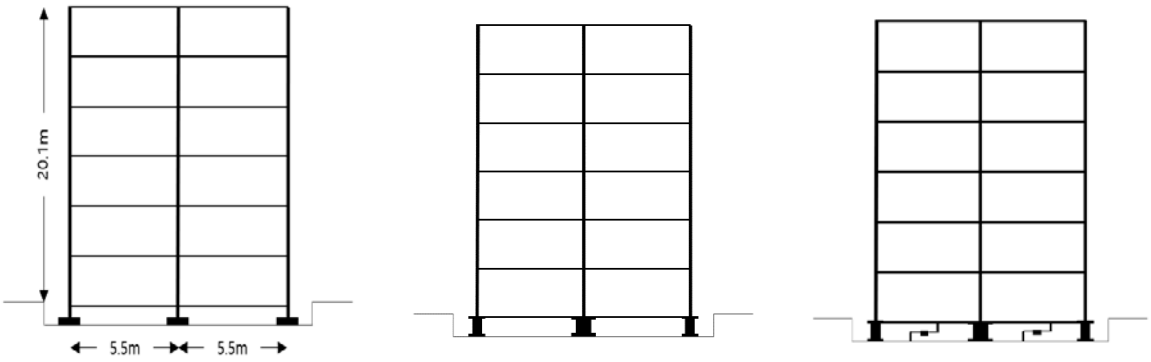
The efficacy of LRB can be seen in decreasing structural responses as acceleration, base shear and relative story displacements compared to a fixed structure, which is due to the increased structural periods by base isolation [D'Amato et al., 2019; Sugihardjo et al., 2018]. On the other hand, the utilization of viscous fluid dampers is to reduce the ductility, displacement, and drifts of a structure, and the larger the damping incremental value dissipates the more energy released from earthquake vibrations [Lamprea et al., 2019].

This study presents the overturning of 3 different slenderness FSCs related to rocking, which are located inside three comparative buildings. To evaluate the multi-level hazard assessment, acceleration records categorized as low, medium and high suites are utilized. Consequently, the modified overturning criterion to assess the overturning of the contents on every floor of three buildings.

2. METHODOLOGY

2.1 DESCRIPTION OF COMPARATIVE MODELS

For assessing the rocking and overturning of freestanding contents, the comparative target structures are considered as 6-story two-bay reinforced concrete frame having base-fixed (model 1), base isolation using lead rubber bearings (model 2) and hybrid system with the combination of base isolation and passive fluid viscous dampers (model 3). The layout of target structures is described in Figure 1. The span and inter-story height of the structure are 5.5m and 3.35m, respectively. The original design of the structure was developed by Jury [Jury, 1978] based on New Zealand Loading Code, and it has been the benchmark model in Ruaumoko [Chey, et al., 2009].



Model 1 (Base Fixed) Model 2 (Base Isolated) Model 3 (Hybrid)

Figure 1. Modeling of 6-story Framed Structure (Models 1, 2 and 3)

Due to the provision of LRB at the base, the structural periods of models 2 and 3 increased from 0.798 sec to 1.37 sec, as shown in Tables 2 and 3. Rayleigh damping & Tangent stiffness is exploited in model 1 to assign 5% damping in the 1st and 6th modes of the analysis. User-specified model damping is chosen for models 2 and 3 to designate 0% damping at the 1st mode, which is known as the isolation mode, and 0.5% for the structural modes.

2.2 DESIGN OF LEAD RUBBER BEARING AND VISCOUS DAMPER (MODELS 2 AND 3)

In this study, lead rubber bearings are installed at the base of models 2 and 3 to minimize the floor response accelerations, which impacts the rate of rocking and overturning of FSCs. The compressive vertical loads exerted on the external and internal columns are computed to estimate the appropriate sizes of LRB for each column. The mechanical properties of LRB are based on the standard of ISO 22762-3:2010 [ISO, 2010].

The initial lateral stiffness (K_i) concerning the post-yield stiffness (K_d) of bilinear LRB is calculated as below and α_i has the typical reference value of 5-10.

$$K_i = \alpha_i K_d \quad (1) \qquad K_d = C_r(\gamma).K_r + C_p(\gamma).K_p \quad (2)$$

The correction factors for shear stiffness of the isolator (C_r) and stiffness of the lead plug (C_p) at 100% shear strain are taken as 1. The shear stiffness of the elastomeric isolator (K_r) using shear modulus at design shear strain (G) and the shear stiffness of lead plug (K_p) using apparent shear modulus (α)are defined. The effective areas of laminated rubber (A) and lead plug (A_p) are computed as the sizes of outer diameter (d_0) and inner diameter (d_i).

$$K_r = \mathrm{G}\frac{A}{T_r} \quad (3) \qquad K_p = \alpha\frac{A_p}{T_r} \quad (4) \qquad \mathrm{A} = \frac{\pi}{4}({d_o}^2 - {d_i}^2) \quad (5) \qquad A_p = \frac{\pi}{4}{d_i}^2 \quad (6)$$

The equivalent shear stiffness or effective stiffness (K_h) is computed based on characteristic strength (Q_d) and post-yield stiffness (K_d). The compressive stiffness (K_v) and the apparent Young's Modulus for compressibility (E_c) can be written.

$$K_{\mathrm{h}} = \frac{Q_d}{\gamma T_r} + K_d \quad (7) \qquad Q_d = \tau_p A_p \quad (8) \qquad K_v = \frac{A E_c}{T_r} \quad (9) \qquad E_c = \left[\frac{1}{E_{ap}} + \frac{1}{E_\infty}\right]^{-1} \quad (10)$$

$$E_{ap} = E_0(1 + 2\kappa {S_1}^2) \quad (11)$$

Table 1. Properties of Lead Rubber Bearing for External and Internal Columns

Properties of LRB	External Column	Internal Column
Compressive load, $\boldsymbol{P}$ (KN)	913	1496
Outer diameter, $\boldsymbol{d_0}$ (mm)	410	540
Inner diameter, $\boldsymbol{d_i}$ (mm)	80	120

Thickness of rubber, t_r (mm)	4	5
Number of layers, n	44	44
Effective Area, A (mm^2)	126.9 x 10^3	217.7 x 10^3
Area of lead plug, A_p (mm^2)	5.02 x 10^3	11.309 x 10^3
Shear stiffness of rubber, K_r (kN/m)	280	383.96
Stiffness of lead plug, K_p (kN/m)	16.77	30.23
Post-yield stiffness of bilinear LRB, K_d (kN/m)	296.77	414.19
Initial stiffness of bilinear LRB, K_i (kN/m)	2,967.7	4,141.9
First shape factor, S_1	25.63	27
Compressive stiffness, K_v (kN/m)	637.718 x 10^3	924.771 x 10^3
Characteristic strength, Q_d (kN)	41.82	94.2
Equivalent shear stiffness, K_h (kN/m)	534.38	842.37
Yield strength of isolator, F_y (kN)	46.47	104.67
Maximum design isolator displacement, D_{max} (m)	0.176	0.22
Energy dissipated by cycle, W_d (kN-m)	26.82	73.37
Equivalent damping ratio of LRB, h_{eq} (%)	25.8	28.6
Damping coefficient of LRB, c (kN-s/m)	115.06	205
Damping coefficient of viscous damper, c (kN-s/m)	390	

where E_{ap} is the apparent Young's Modulus, E_0 is the Young's modulus, E_∞ is the Bulk modulus, K is the correction factor and S_1 is the first shape factor of $\frac{d_o}{4t_r}$.

The yield strength of the isolator (F_y) depending on the characteristic strength (Q_d) and yield displacement (D_y) is expressed as:

$$F_y = Q_d + K_d \, . D_y \qquad (12) \qquad Q_d = \tau_p \, A_p \qquad (13) \qquad D_y = \frac{F_y}{K_i} \qquad (14)$$

The equivalent damping ratio of LRB (h_{eq}) and energy dissipated in a cycle of bilinear hysteresis (W_d) are evaluated as below, where D_{max} is the maximum design isolator displacement at maximum shear strain.

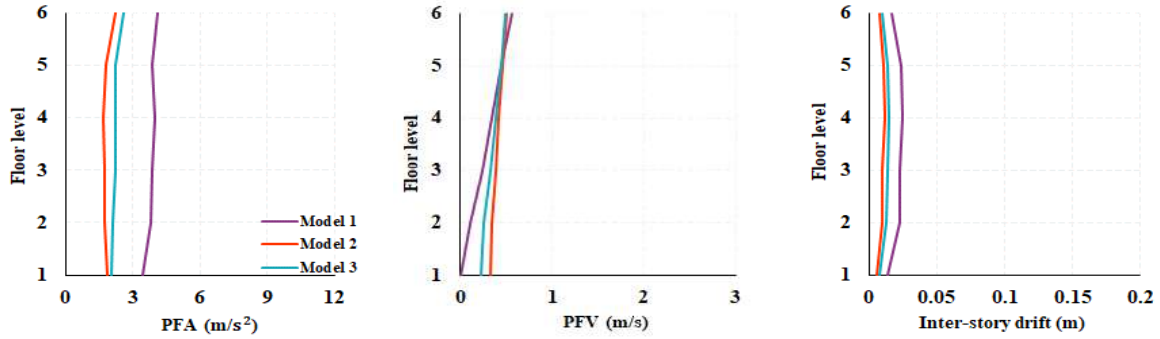
$$\mathrm{h}_{eq} = \frac{1}{2\pi} \cdot \frac{W_d}{K_\mathrm{h} \ (\gamma T_r)^2} \qquad (15) \qquad W_d = 4 \, Q_d (D_{max} - D_y) \qquad (16) \qquad D_{max} = \gamma T_r \qquad (17)$$

2.3 CHARACTERISTICS OF EARTHQUAKE RECORDS AND LOG-NORMAL DISTRIBUTION METHOD

The responses of FSC as rocking and overturning can vary according to the intensity of earthquake excitations. The excitation frequency, magnitude, distance from the source to the station and peak ground acceleration of the records influence the seismic behavior of FSC. In this study, 30 acceleration records of Los Angeles from SAC Phase II steel projects [Somerville, et al., 1997] are considered. Records are categorized as low, medium, and high suites according to the probabilities of exceedance, such as 50%, 10% and 2% in 50 years. Each suite comprised ten acceleration records, and floor responses obtained from the suite are transformed into a target median response spectrum employing the exponential log-normal distribution method.

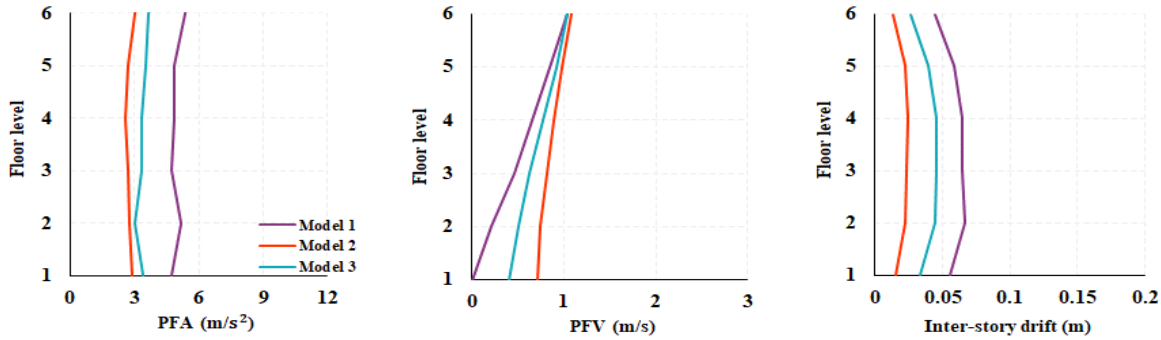
3. SEISMIC DEMANDS OF MODEL

Based on the assessment results (Figures 2-4), the absolute peak floor accelerations (PFAs) obtained from model 2 show the smallest values among the three models under all suites. Compared to the original fixed structure (model 1), the PFA values of model 2 are reduced by 50% under low suite and by around 40% under medium and high suite excitations. Regarding model 3, the PFAs are reduced by 40% under the low suite and by 30% under the medium suite. For the high suite, around a 30% to 40% reduction is observed on the lower floors. The PFAs of model 3 are slightly larger than that obtained from model 2, but they are still smaller than that of model 1 under all suites.



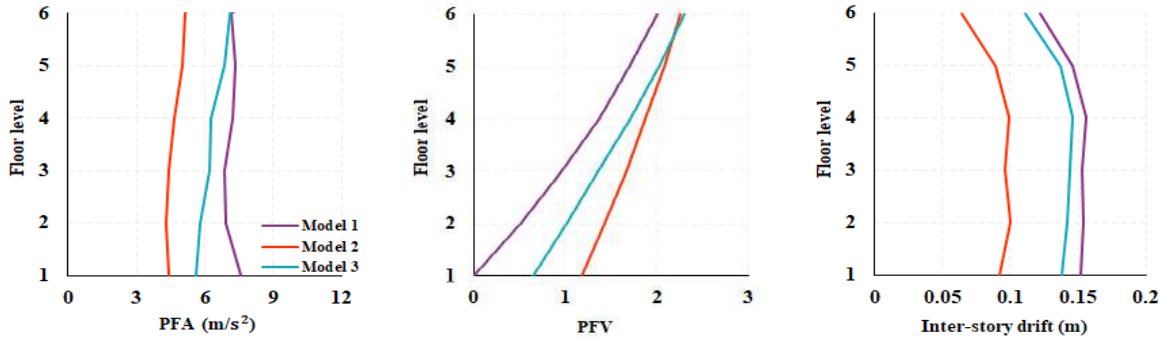
(a) Peak Floor Acceleration (b) Peak Floor Velocity (c) Inter-storey drift

Figure 2. Floor Responses under Low Suite



(a) Peak Floor Acceleration (b) Peak Floor Velocity (c) Inter-storey drift

Figure 3. Floor Responses under Medium Suite



(a) Peak Floor Acceleration (b) Peak Floor Velocity (c) Inter-storey drift

Figure 4. Floor Responses under High Suite

Same as PFAs, the inter-story drifts of model 2 turned out as the most effective, and then model 3 and model 1 are in order. According to the results of model 1, the inter-story drifts of model 2 show a 50% to 60% decrease in the low suite, a 60% to 70% decrease in the medium suite and a 40% decrease in the high suite, respectively. Correspondingly, the inter-story drifts of model 3 are dropped by 40% under the low suite, by 30% under the medium suite and by 10% under the high suite.

As opposed to the results of PFAs and drifts, the relative PFVs of model 1 on the 1st floor are observed as 0 for all suites since model 1 is the ordinary fixed structure at the base, and the motion of the superstructure motion is flexible with larger inter-story drifts along the floors. In contrast, the PFVs of model 2 are 0.32 m/s, 0.71 m./s and 1.18 m/s under low, medium and high suites. To reduce the larger velocity responses from model 2, fluid viscous dampers are provided at the base of model 3, and the velocity sensitiveness (PFVs) are reduced to 0.23 m/s, 0.21 m/s and 0.65 m/s under low, medium and high suites respectively. Unlike PFAs, the PFVs increase gradually as the floors are higher and show an insignificant difference on the 6th floor.

4. STABILITY CRITERIA OF NONSTRUCTURAL ELEMENTS

4.1 MODIFIED OVERTURNING CRITERION

To define the overturning state of freestanding contents, the lower limit of maximum acceleration to measure the initial rocking state was introduced by Milne [1881].

$$a_i = \frac{B}{H}\ g \tag{18}$$

As in Figure 5, B and H describe the horizontal and vertical distances from the center of gravity to the pivot (rotating) point of content and g is the acceleration due to gravity. There have been many experimental and analytical assessments to investigate the overturning of FSC. The study by Berto et al. [Berto, et al., 2018] has stated the Ishiyama criterion [Ishiyama, 1984] as the most effective criterion among Lam-Gad, Kinematic linear and nonlinear methods through experimental and analytical results. However, the Ishiyama criterion showed the unreasonable relationship between rocking and overturning of contents under low and medium suite excitations. Therefore, the modified criterion was developed based on the previous studies and proved as the reliable overturning criterion according to the rocking of FSC. Consequently, in this study, modified criterion was utilized to evaluate the effectiveness of base isolation and damping devices for FSC. The lowest maximum velocity to define the overturning of rectangular contents can be defined as below:

$$v_i = \alpha \sqrt{\frac{4gR}{3}} \tag{19}$$

4.2 SELECTED FREESTANDING CONTENTS

According to the different geometric parameters of FSC, different seismic capacities can be obtained using B, H, R and the ratios of B/H (slenderness ratios). Depending on the type of structure, location of FSC, the intensity of earthquake excitation, and the location and the size of FSC influence the intensities of rocking and overturning. In this study, 3 different sizes of FSC are considered as targeted contents to compute the seismic capacities, which are necessary to compare with seismic demands. The geometric parameters of selected FSC and the reference bookshelves can be seen in Figure 5-6.

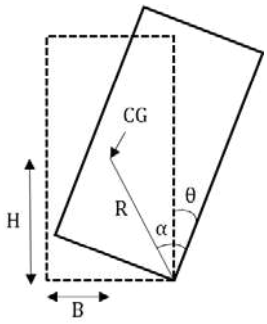
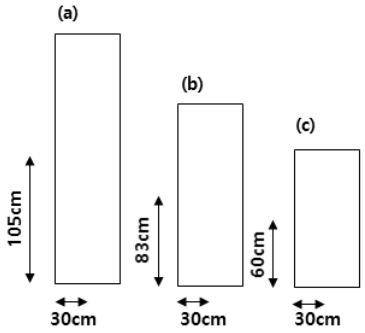


Figure 5. Schematic Diagram of a Rectangular Content



(a) B/H=0.286 (b) B/H=0.361 (c) B/H=0.500

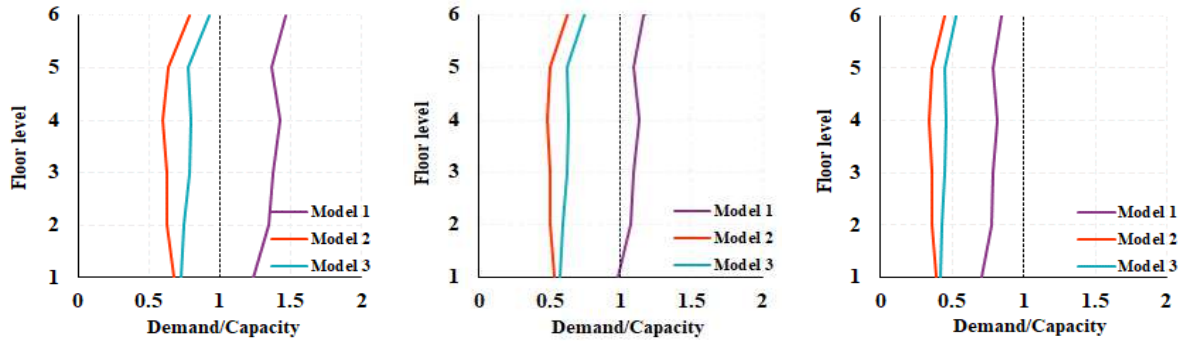
Figure 6. Selected Freestanding Contents

5. PERFORMANCE RESULTS OF THE CONTENTS ELEMENTS

The ratios of demand (PFA or PFV) by capacity are utilized to simply define the rocking and overturning states of FSC. If the ratio is smaller than 1, it states that the seismic demand arising at the particular floor is smaller than the seismic capacity of FSC; therefore, the content does not show rocking or overturning. On the contrary, when the demand is the same or greater than capacity, the seismic demand reaches or exceeds the minimum seismic capacity which can trigger instability such as rocking or overturning after rocking.

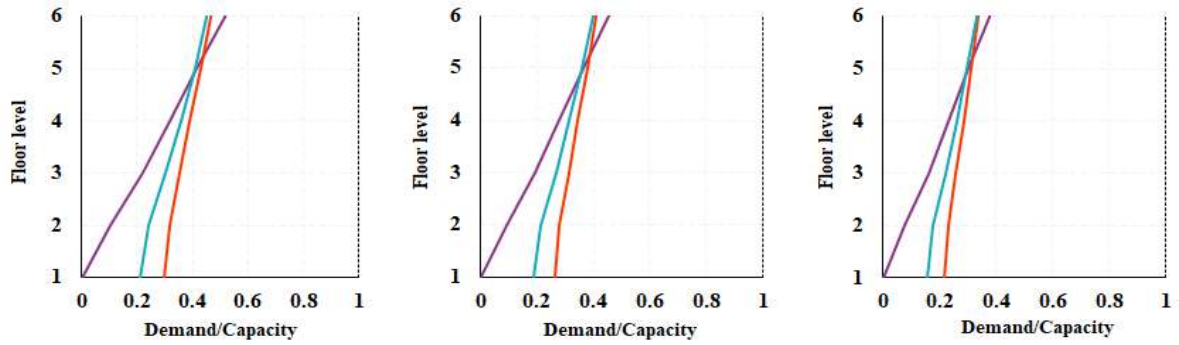
5.1 Assessment Results (Low Suite)

As stated in Figures 7-8, model 1 indicates the highest risk of rocking, while model 2 turned out as the lowest risk since the PFAs of model 2 are smaller than that of model 1 for all suites. The ratios representing the rocking of models 2 and 3 are 50% and 40% less than model 1, respectively. For 0.268 and 0.361 contents, the ratios of demand by the capacity of models 2 and 3 do not exceed 1; that is, the contents inside models 2 and 3 do not rock on all floors under low suite excitation. On the other hand, the same contents inside model 1 rock on all floors. The smallest 0.500 contents show stability without rocking on all floors of models 1, 2 and 3. Model 1 shows the lowest risk of overturning while the highest risk is observed in model 2, and it is due to the largest PFV values of model 2, expressed in section 3. Since the viscous dampers reduce the velocity sensitiveness of model 2, the ratio for model 3 is decreased by 30% on the 1st floor compared to model 2; however, the risk is still higher than that of model 1. To conclude, all the contents inside models 1, 2 and 3 do not overturn under low suite earthquakes.



(a) B/H=0.286 (b) B/H=0.361 (c) B/H=0.500

Figure 7. Rocking Assessment of Contents inside Three Models (Low Suite)

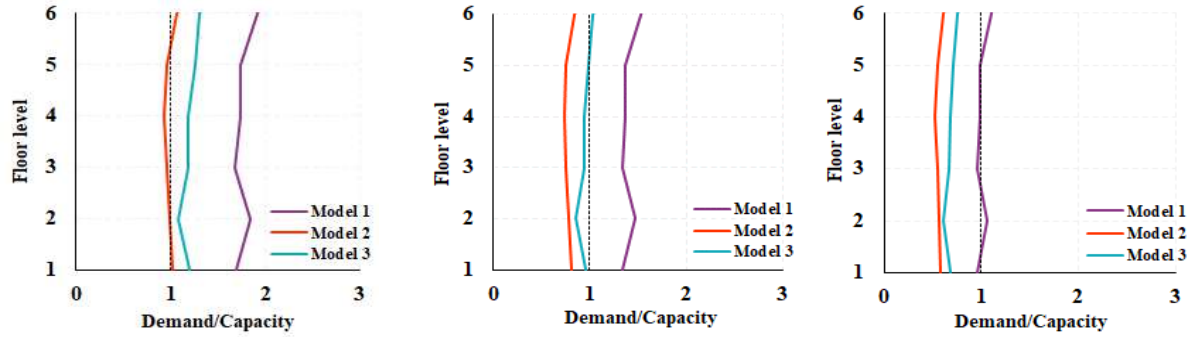


(a) B/H=0.286 (b) B/H=0.361 (c) B/H=0.500

Figure 8. Overturning Assessment of Contents inside Three Models (Low Suite)

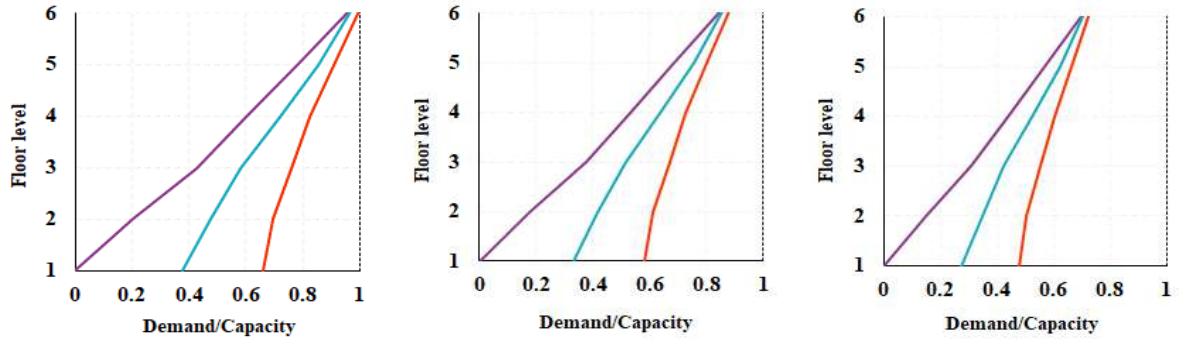
5.2 Assessment Results (Medium Suite)

Similar to the low suite, the lowest rocking ratios can be seen in model 2 and then followed by models 3 and 1, as in Figures 9-10. The ratios of rocking for models 2 and 3 are reduced by around 40% and 30%. For 0.286, contents inside model 2 rock on the 1st, 2nd and 6th floors, while contents inside models 1 and 3 show rocking on all floors. The 0.361 contents inside model 2 do not rock, though they rock on the upper floors of model 3 and the entire floors of model 1. For the smallest contents (0.500), no rocking occurs inside models 2 and 3, while contents inside model 1 rock on some floors.



(a) B/H=0.286 (b) B/H=0.361 (c) B/H=0.500

Figure 9. Rocking Assessment of Contents inside Three Models (Medium Suite)



(a) B/H=0.286 (b) B/H=0.361 (c) B/H=0.500

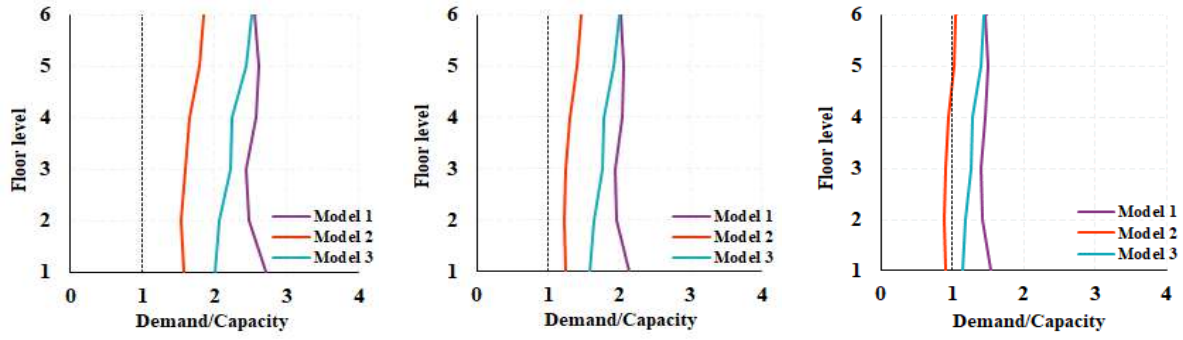
Figure 10. Overturning Assessment of Contents inside Three Models (Medium Suite)

Regarding the overturning charts, model 2 expresses the highest ratios among the three models. The 0.286 contents inside model 2 overturn on the 6th floor; however, no overturning occurs inside models 1 and 3. For 0.361 and 0.500 contents, the overturning instability of contents inside the three models does not occur for all floors.

5.3 Assessment Results (High Suite)

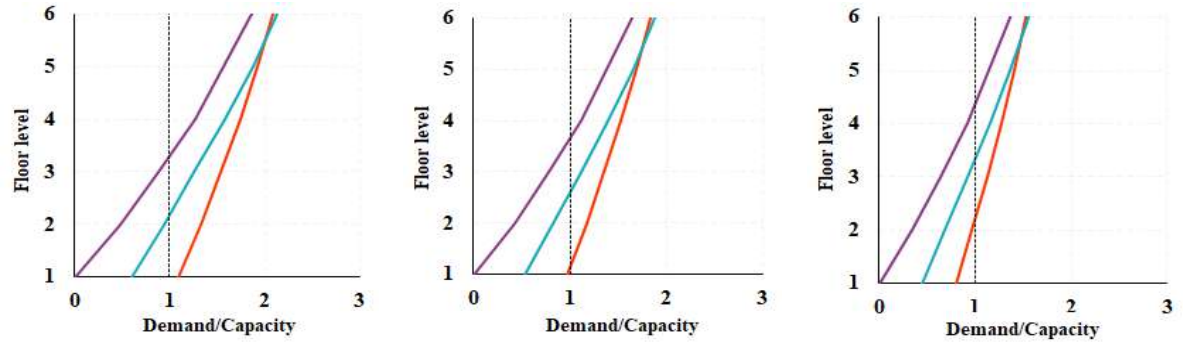
Like low and medium suites, the ratios in the rocking of contents inside model 2 show the lowest, but for overturning, it indicated the highest than models 1 and 3. The 0.286 and 0.361 contents rock on all floors inside models 1, 2 and 3. In comparison, 0.500 contents rock inside the entire floors of models 1 and 3 but rock only on the 5th and 6th floors of model 2. Investigating the overturning assessment, 0.286 contents inside model 2 start overturning on the 1st floor, although contents inside models 3 and 1 initiate overturning on the 2nd and 4th floors, respectively. Similarly, the higher overturning instability of 0.361 and 0.50 contents is discovered in model 2 as in Figures 11-12. In case of 0.500 content, the direct overturning of FSC is observed on the 3rd and 4th floors inside model 2 since the sliding motion of base isolated structure arouses the overturning without rocking which is unlikely to occur in ordinary fixed structure.

To conclude, model 2 decreases the acceleration responses of floors more than models 1 and 3; thus, the risk of rocking is the highest in model 2. In contrast, the velocity sensitiveness is the highest in model 2, which stimulates the risk of the overturning of contents inside model 2 than in 1 and 3.



(a) B/H=0.286 (b) B/H=0.361 (c) B/H=0.500

Figure 11. Rocking Assessment of Contents inside Three Models (High Suite)



(a) B/H=0.286 (b) B/H=0.361 (c) B/H=0.500

Figure 12. Overturning Assessment of Contents inside Three Models (High Suite)

6. CONCLUSION

In the previous study, a modified overturning criterion has been developed to achieve a reliable overturning assessment related to the rocking motion. In this study, ordinary base fixed structure (model 1), base-isolated structure (model 2) and hybrid structure combination of base isolation and fluid viscous dampers (model 3) were considered to assess the better seismic performance of contents on all floors under low, medium and high suite excitations and the conclusions regarding rocking and overturning assessments are as below:

Model 2 can effectively decrease the peak floor accelerations due to the rigid motion of the structure at 1st mode and increase the structural period into the velocity sensitiveness utilizing lead rubber bearings at the base. Like model 2, model 3 reduces the acceleration responses though they are slightly larger than model 2 due to the energy dissipation by fluid viscous dampers.

Therefore, the lowest risk of rocking is observed in model 2 among models 1 and 3. (model 1 > model 3 > model 2).

On the contrary, the peak floor velocities are the highest in model 2, slightly decreased in model 3 but still larger than in model 1.

Hence, model 2 presents the highest overturning ratios than models 1 and 3 (model 2 > model 3 > model 1); however, it can still be safe without overturning under low and medium suites until high suite excitations.

Special consideration and detailed LRB design are required to achieve the appropriate structural period that can reduce both acceleration and velocity sensitivity of the structure and overcome the overturning failure of FSC, especially under high suite excitation. The future study will discuss the solution of overturning contents for all suites.

Acknowledgement

This research was supported by the National Research Foundation of Korea (NRF) (grant No. 2019R1F1A1062711).

REFERENCES

Berto, L.; Rocca, I.; Saetta, A. [2018] "Vulnerability Assessment Methods for Rocking and Overturning of Free Standing Elements," *Soil Dynamics and Earthquake Engineering*, 110, 121–136.

Chey, M.-H.; Chase, J.G.; Mander, J.B.; Carr, A.J. [2009] "Semi-Active Tuned Mass Damper Building Systems: Application," *Earthquake Engineering & Structural Dynamics*, 39(1), n/a-n/a.

D'Amato, M.; Gigliotti, R.; Laguardia, R. [2019] "Seismic Isolation for Protecting Historical Buildings: A Case Study," *Frontiers in Built Environment*, 5.

Gabbianelli, G.; Perrone, D.; Brunesi, E.; Monteiro, R. [2020] "Seismic Acceleration and Displacement Demand Profiles of Non-Structural Elements in Hospital Buildings," *Buildings*, 10, 243.

Ishiyama, Y. [1984] "Motions of Rigid Bodies and Criteria for Overturning by Earthquake Excitations," *Bulletin of the New Zealand Society for Earthquake Engineering*, 17, 24–37.

ISO 22762-3 [2010] "Elastomeric seismic protection isolators, Part 3: Applications for Buildings - Specification"

Jury, R.D. [1978] "Seismic Load Demands on Columns of Reinforced Concrete Multistorey Frames," A Report Submitted in Partial Fulfilment of the Requirements for the Degree of Master of Engineering at the University of Canterbury, Christchurch, New Zealand. PhD diss., University of Canterbury.

Lamprea Pineda, A.C.; Garzón Amortegui, L.F.; Chesi, C. [2019] "Use of Viscous Fluid Dampers for the Improvement of the Seismic Response of RC Structures," *Vibroengineering PROCEDIA*, 23, 87–92.

Milne, J. [1881] "Experiments in observational seismology," *Trans. Seismol. Soc. Jpn.*, 3, 12-64.

Somerville, P.; Smith, N.; Punyamurthula, S.; Sun, Joseph. [1997] "Development of ground motion time histories for phase 2 of the FEMA/S AC steel project 1997," *SAC/BD-97/04*; SAC Joint Venture.

Sugihardjo, H.; Tavio; Manalu, I.; Lesmana, Y. [2018] "Seismic Study of Application of Lead Rubber Bearings in Kutai Kartanegara Steel Arch Bridge," *International Journal on Advanced Science, Engineering and Information Technology*, 8, 540.

Zito, M.; Nascimbene, R.; Dubini, P.; D'Angela, D.; Magliulo, G. [2022] "Experimental Seismic Assessment of Nonstructural Elements: Testing Protocols and Novel Perspectives," *Buildings*, 12, 1871. https://doi.org/10.3390/buildings12111871.

Seismic Performance Enhancement of Suspended Cable Tray Systems Using Steel Wires

Kazuhiro Matsuda[1], Eisaku Asatsuma[2]

[1] Department of Architecture, Faculty of Science and Technology, Meijo University
1-501 Shiogamaguchi, Tempaku-ku, Nagoya, Aichi 468-8502, Japan
e-mail: matsuda@meijo-u.ac.jp
[2] Research Department, Negurosu Denko Co., Ltd.
2-5-1 Shinonome, Koto-ku, Tokyo 135-0062, Japan
e-mail: e.asatsuma@negurosu.co.jp

Abstract. Cable tray systems are widely used to support and distribute electrical cables inside buildings. In large facilities, the cables they carry can weigh up to 1 kN/m, and damage or collapse of cable tray systems may cause serious accidents or injuries. Previous studies have clarified that during earthquakes, damage in suspended cable tray systems typically initiates in the cable tray itself (the horizontal components). To address this vulnerability, we propose a novel reinforcement method using a distinctive arrangement of wires. Unlike simple diagonal reinforcement, the proposed method considers the deformation pattern of cable trays during earthquakes and is characterized by wiring each wire so that it simultaneously carries tensile forces across all regions. After outlining previous shaking table tests, this paper presents the proposed reinforcement method for horizontal components. The load-bearing capacity of the reinforced components and the seismic performance of suspended cable tray systems reinforced with steel wires are investigated through static loading tests and vibration exciter tests. Through these tests, the effectiveness of the proposed method is demonstrated.

Keywords: Cable Tray, Full-Scale Tests, Steel Wire Reinforcement, Vibration Exciter

1. INTRODUCTION

Cable tray systems that support numerous power and transmission cables (Fig. 1) are acceleration-sensitive nonstructural components. The mass of cables required in large buildings can be as high as 1 kN/m, and as shown in Fig. 2, cable tray systems can even cause serious injuries or fatalities if they collapse. Moreover, severe damage can interrupt a building's electrical power system. Minimizing damage to these critical systems is crucial for rapid recovery after seismic events or other disasters. Notably, non-structural components in many buildings were severely damaged in the 2011 Great East Japan Earthquake [Kasai *et al.*, 2013]. Among electrical equipment, 30% of the reported damage occurred in cable trays, which was the second-largest proportion after lighting equipment [SHASE, 2011]. Thus, cable tray systems are critical in terms of resilience. However, relatively limited research has been conducted on this topic, and most existing studies have focused on systems in nuclear power plants. The authors have previously investigated the application of energy-dissipative devices to improve the seismic performance of cable tray systems in general-use buildings [Matsuda *et al.*, 2018, 2020]. The seismic behavior of cable tray systems has been investigated through shaking table tests. Based on these findings, it was clarified that in cable tray systems, damage initiates in the horizontal components, that is, in the cable tray itself.

The objective of this study is to propose an efficient seismic reinforcement method for horizontal components and to verify its effectiveness. After describing the outline of previous shaking table tests in Chapter 2, we propose a novel and unique method to reinforce horizontal components in Chapter 3. In Chapter 4, the load-bearing capacity of the reinforced horizontal components is examined through static tests, and in Chapter 5, their dynamic characteristics after reinforcement are investigated by means of vibration exciter tests.



Figure 1. Suspended cable tray system



Figure 2. Cable tray collapse during Tohoku Pacific Ocean Earthquake

2. OUTLINE OF SHAKE TABLE TEST

2.1 OUTLINE OF SHAKE TABLE TEST

The cable tray system was suspended from a rigid platform with a plan dimension of 11.64 m × 12.84 m and a natural frequency of approximately 9 Hz constructed on the shaking table. Three cable tray lines were installed, each incorporating different seismic elements (Fig. 3), which are defined by Japanese seismic design standards [BCJ, 2021]. The configurations of the cable tray system are shown in Fig. 4. Two seismic elements were installed on each line. According to Japanese seismic design standards [BCJ, 2021], seismic elements must be installed at intervals of at least 8 or 6 m. Accordingly, the length of each cable tray specimen should

have been 16 or 12 m to accommodate two seismic elements per line. To compensate, 2-m cable tray weights were attached at both ends of the Type-B and Type-A specimens, and 1-m cable tray weights were attached at both ends of the Type-S_A specimen.

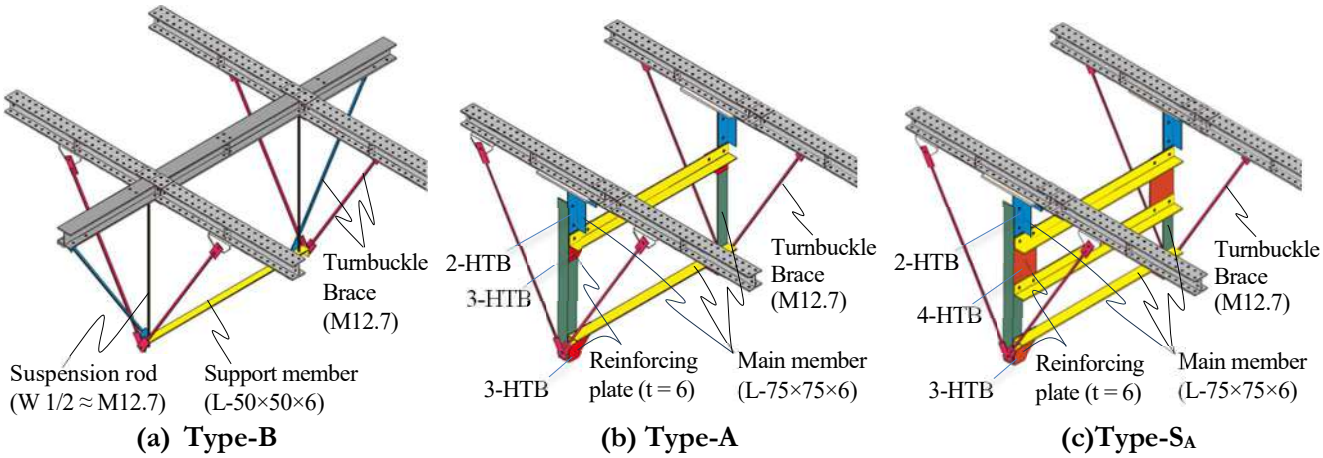


Figure 3. Three types of seismic resistant element [BCJ, 2021]

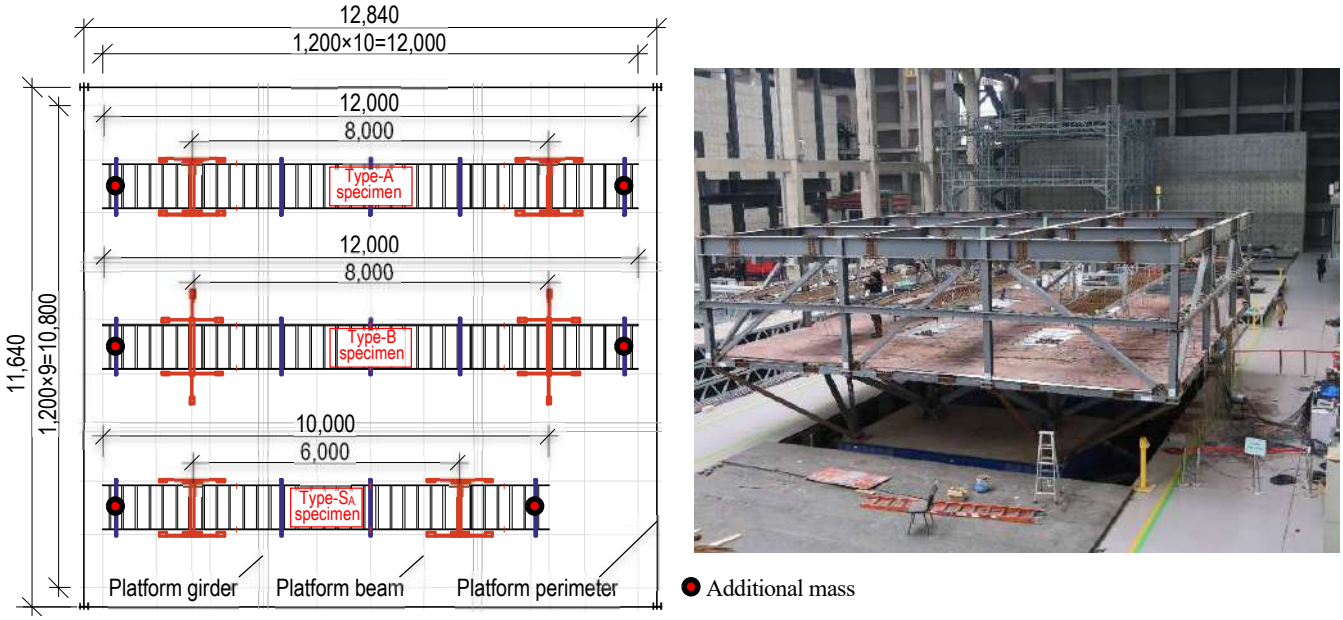


Figure 4. Cable tray configuration in shaking table tests

Instead of actual cables, ϕ16 steel rebar was installed in the cable trays to simulate mass. The total distributed mass including the cable tray was 106.2 kg/m. To avoid constraining the behavior of the cable tray, bars were cut at 2-m intervals. Both ends of each 2-m segment were fastened to the sub-beams with nylon bands in accordance with actual practice. In addition, rubber sheets of the same type as cable sheathing were placed between the bars and the cable tray to replicate cable slippage on the tray. To capture the global behavior of the specimen, relative displacements and absolute accelerations were measured at the seismic supports. In principle, the displacement transducers were fixed to the perimeter of the platform. In addition, absolute acceleration was measured at multiple corner locations on both the shaking table and the platform to provide information on dynamic loading.

Sweep waves with constant acceleration amplitude were generated as the primary input motions. The initial acceleration was 50 cm/s², which was increased in increments of 50 cm/s², and the tests were continued until the specimens experienced severe damage. An example of a sweep wave input with an acceleration of 100 cm/s² is shown in Fig. 5. The frequency of the sweep waves varied from a high of 6.0 Hz to a low of 0.8 Hz at a rate of two octaves per minute, with a total duration of 100 s.

Before and after each sweep wave excitation, a wave of white noise with a peak acceleration of 50 cm/s² was applied to evaluate the dynamic properties of each specimen, such as their natural frequency and damping ratio. The natural frequencies and damping ratios were calculated by assuming a steady-state response and fitting an idealized transfer function to the empirical transfer function estimated from acceleration data. The amplitude of the empirical transfer function was defined as the ratio of Fourier spectrum amplitudes between the center of each seismic element and the top of the platform.

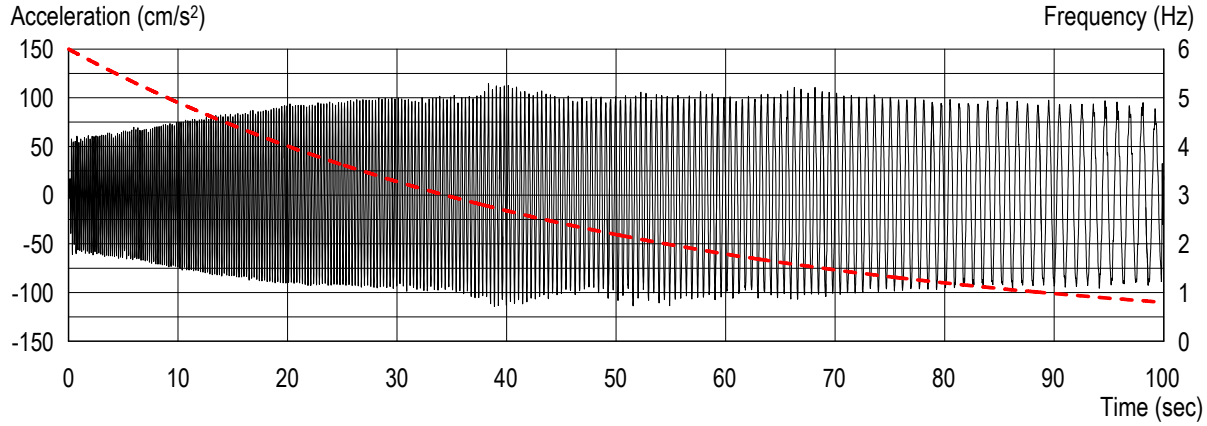
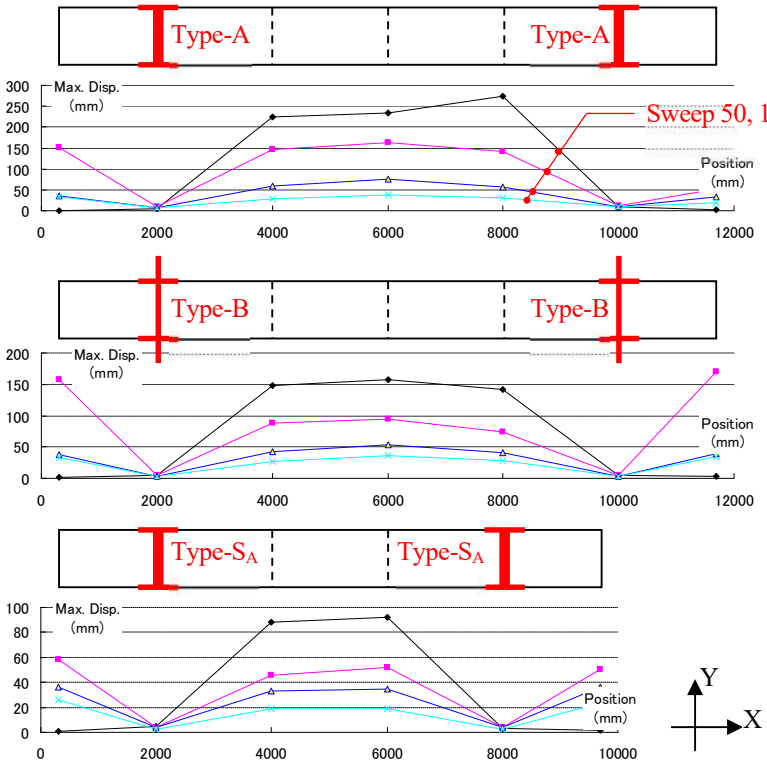


Figure 5. Example of sweep wave (100 cm/s²)

2.2 RESULTS OF SHAKE TABLE TEST

Fig. 6 shows the maximum response of each specimen subjected to the sweep-wave excitation. The table in the figure summarizes the observed maximum displacement at the center of the seismic elements at the level of the cable tray as well as the natural frequencies and damping ratios

The maximum displacement was observed in Type-A, whereas the minimum displacement occurred in Type-S_A. Because the deformations were concentrated in the cable trays, it is considered that the effects of span length were more significant than those of the type of seismic element examined. The initial natural frequencies obtained from white noise excitation also reflected the impact of the length of the span, with approximately 2.2 Hz for the 8-m span and 2.9 Hz for the 6-m span in both phases. As deformations increased, the natural frequency decreased owing to a reduction in stiffness. The initial damping ratio was approximately 4% for all specimens. The damping ratio gradually increased with increasing deformation during excitation; however, this was attributed to the progression of damage rather than improved damping performance. Although not shown, the response accelerations during sweep excitation were larger at the mid-span, where displacements were greatest, and smaller at the seismic support and joint regions. The maximum response acceleration reached approximately 1.2 G in Phase 1 at 200 cm/s² and 1.5 G in Phase 2 at 200 cm/s² in both directions.



Name	X	Y	Type-A center	Type-B center	Type-SA center
	cm/s^2				
WN	50	50	2.15Hz, 3.5%	2.23Hz, 4.4%	2.94Hz, 4.3%
Sweep	0	50	38.1mm	36.8mm	18.9mm
WN	50	50	2.12Hz, 3.3%	2.17Hz, 4.8%	2.91Hz, 4.7%
Sweep	0	100	75.2mm	53.0mm	33.4mm
WN	50	50	1.88Hz, 6.2%	2.04Hz, 4.7%	2.76Hz, 4.8%
Sweep	0	150	163.1mm	94.8mm	45.4mm
WN	50	50	1.57Hz, 10.8%	1.80Hz, 9.2%	2.73Hz, 5.1%
Sweep	0	200	234.7mm	157.7mm	88.3mm
WN	50	50	1.18Hz, 11.2%	1.43Hz, 16.9%	2.07Hz, 10.7%

WN: White noise

Figure 6. Maximum displacement, natural frequency, and damping ratio

3. PROPOSAL OF REINFORCEMENT METHOD

Previous studies have reported that the deformation of cable trays is governed mainly by shear deformation owing to elasto-plastic rotations at the joints between the main-beams and sub-beams, whereas flexural deformation remains relatively small [Matsuda *et al.*, 2018]. Therefore, brace-type reinforcement is considered effective in reducing transverse deformation in cable trays. However, rigid reinforcement using angle members or similar elements is inefficient because cable trays are non-structural components. Therefore, we considered a simple reinforcement method using steel wires.

With steel wires arranged only in the diagonal direction, slippage occurs at the turning points as the cable tray deforms under the load, and the wires cannot provide sufficient resistance (Fig. 7a). To overcome this, a single steel wire is arranged alternately in diagonal and transverse directions in the proposed method to reinforce the cable tray more efficiently (Fig. 7b). Considering the deformation pattern of the cable tray, the wiring system is altered at the positions of seismic-resistant elements and at the midpoints between them.

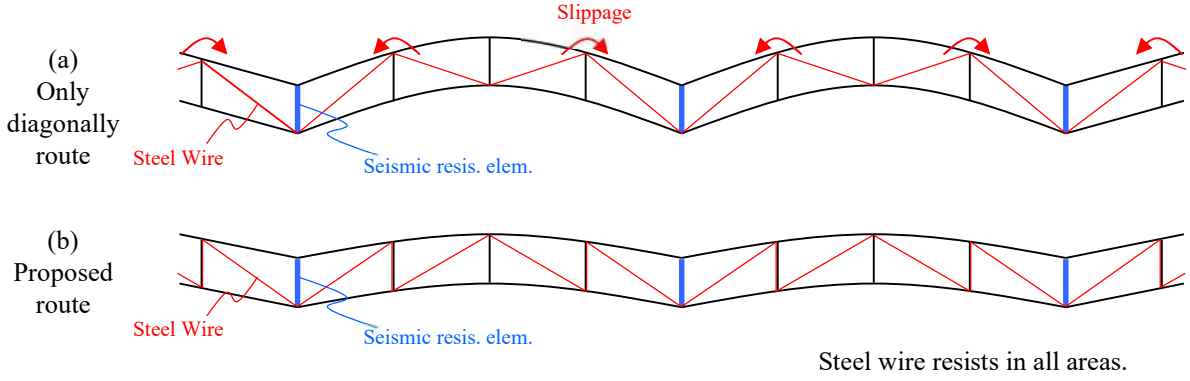


Figure 7. Proposed steel wire reinforcement

4. STATIC OF CABLE TRAY

4.1 OUTLINE OF CABLE TRAY TEST

Three-point loading tests were conducted using a cable tray. Specimens is shown in Fig. 8a; they were 7.5 m long. Three types of specimens were prepared, including one unreinforced specimen (designated as No) and two reinforced specimens (B2, B3 and B4), which differed in the diameter of the wire and the joint fittings used. The wires were bent at each support member (Fig. 8b). At the ends of the wire, a tensile force of 0.2 kN was applied: the ϕ2 steel wire of B2 was fixed using a one-way clutch joint fitting (Fig. 8c), while the ϕ3 and ϕ4 steel wire of B3 and B4 was clamped with a steel tube (Fig. 8d). The supports were spaced 1.5 m apart due to space limitations in the laboratory, and the outermost 0.75-m segments on both sides were reinforced with steel plates to prevent deformation. The test setup is illustrated in Fig. 9. The roller reaction had a span of 6.5 m, and monotonic loading was applied at the center, which was designed as a seismic-resistant element. To prevent out-of-plane deformation, the horizontally placed specimen was vertically supported with eight steels angles equipped with low-friction Teflon sheets.

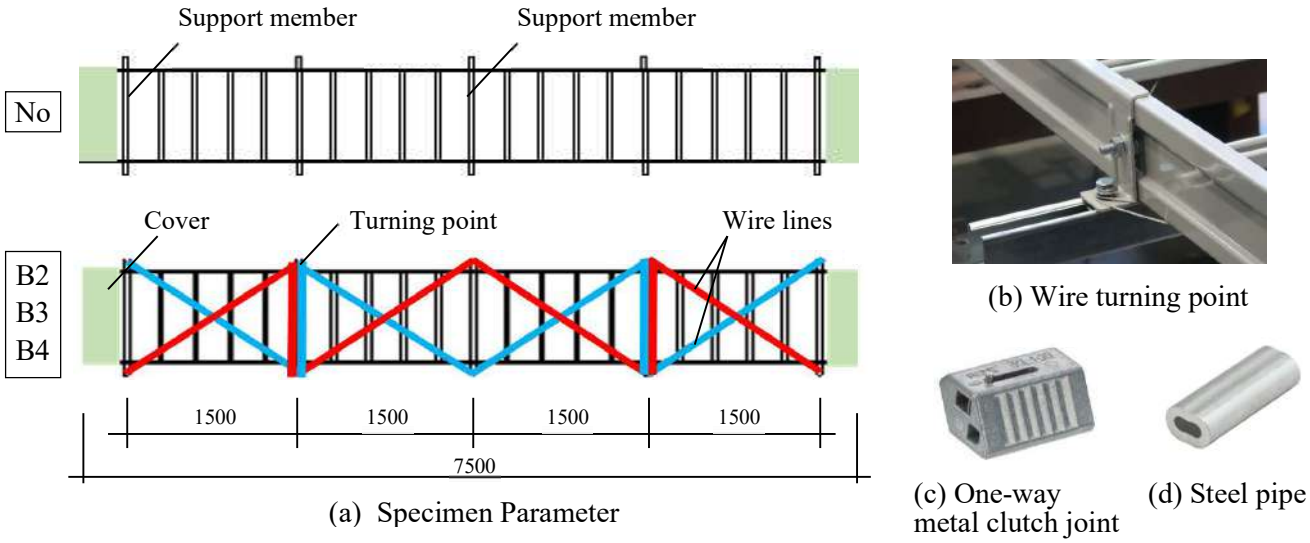


Figure 8. Specimen & parameter of cable tray static tests

The measurement scheme is illustrated in Fig. 10. The applied load (ch.0) was measured using a tension-type load cell. The absolute displacements representing the overall behavior of the cable tray were measured at ch.1–ch.7, ch.14, and ch.15. Displacements were also measured at the reaction points (ch.1, ch.2), at the positions of support members (ch.3–ch.7), in the longitudinal direction of the main-beam (ch.8–ch.11), and at fixed plates (ch.12, ch.13). Almost no displacements were recorded at the reaction points (ch.1, ch.2) or at the fixed plates (ch.12, ch.13). The bending deformation of the cable tray was considered negligible given that the displacements measured from ch.8 to ch.11 were very small.

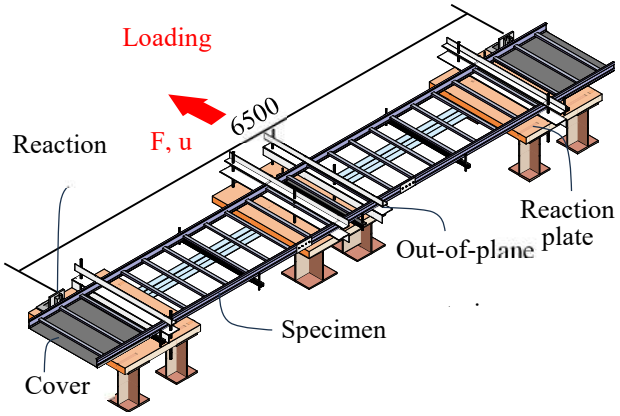


Figure 9. Setup of cable tray static tests

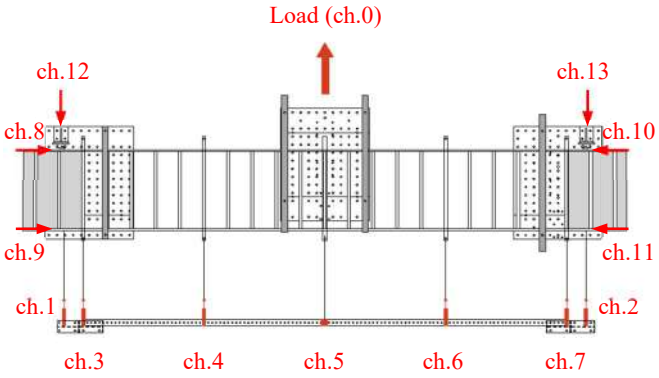


Figure 10. Measurement of cable tray static tests

4.2 Results of Cable Tray Test

4.2.1 Relationship between center load and deformation

The relationship between the applied center load and deformation is shown in Fig. 11, and the distribution of measured displacement values is shown in Fig. 12. The results confirmed that shear deformation was predominant because the cable tray deformed in a nearly linear manner. For specimen No, the maximum load was 3.9 kN, and deformation progressed as the joints between the main- and sub-beams rotated. In contrast, the reinforced specimens with steel wires exhibited a higher initial stiffness than specimen No. Among them, specimen B3, which had wires with a larger diameter, showed a greater initial stiffness than B2. In B2, the wires ruptured at 6.0 kN, and in B3, rupture occurred at 11.3 kN. Subsequently, the load–deformation relationships were similar to that of specimen No. The design strengths of the Type-A and Type-S_A seismic elements were 4.7 kN and 5.9 kN, respectively [BCJ, 2021], both of which were significantly exceeded by specimen B3 and B4. Therefore, we would expect wire reinforcement to be effective in preventing premature damage to cable trays observed in the shaking table tests.

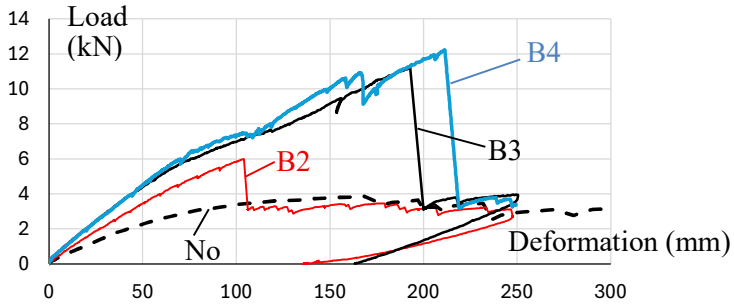
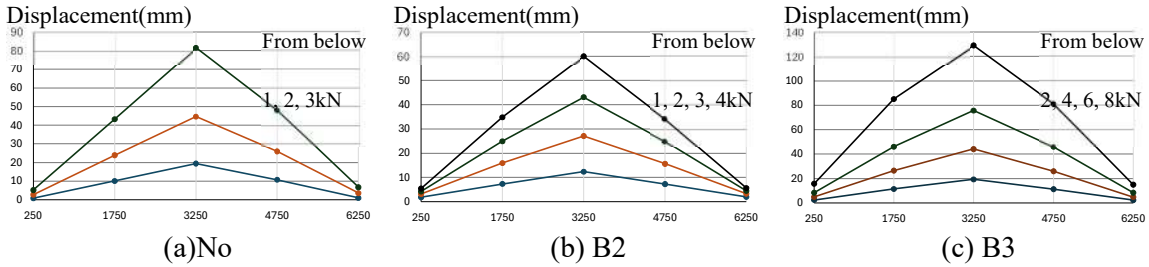


Figure 11. Relationship between center load and deformation



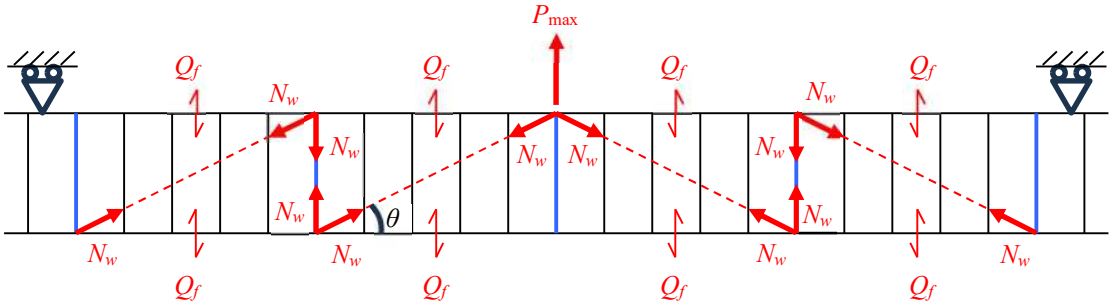
(a)No (b) B2 (c) B3

Figure 12. Relationship between center load and deformation (except B4)

4.2.2 Discussion of wire axial force

The axial forces acting on the wires in the specimens B2, B3 and B4 were evaluated. The distributions of forces at the maximum load of each specimen are shown in Fig. 13. The shear force of the main-beams Q_f at the maximum load Pmax of each specimen was calculated from the load of specimen No at the same deformation level. Assuming an equal axial force distribution in the wires, the load carried by the wires Q_w at Pmax was obtained using the relationship expressed below.

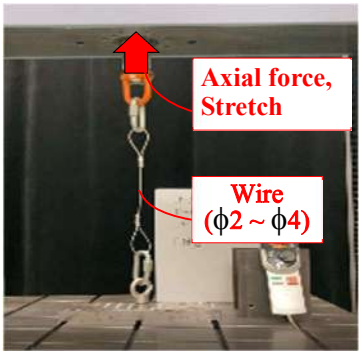
$$N_w = \frac{P_{\max} - 4Q_f}{2\sin\theta}. \quad (1)$$



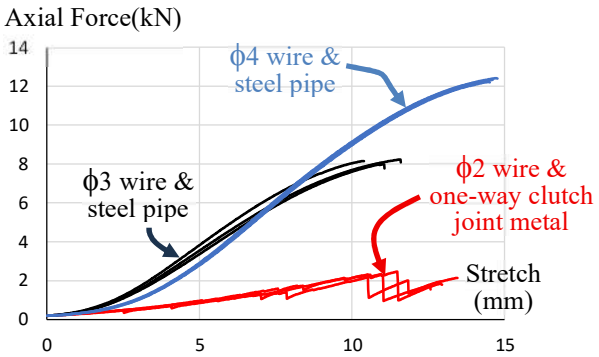
Q_f is obtained from specimen "No" at the same deformation

Figure 13. Mechanical model of reinforced cable tray

The wire axial force Nw at maximum load was determined as 2.2 kN for B2, 6.4 kN for B3 and 7.5 kN for B4. The results of separate single-wire tensile tests (Fig. 14) showed that the ϕ2, ϕ3 and ϕ4 wires exhibited ultimate strengths of approximately 2.4 kN, 8.1 kN and 12.3 kN, respectively. Although the values of Nw were slightly lower than the values obtained from the tensile test, this was likely due to damage to the wires caused by friction at the turning points during the test. The development of smoother wiring methods at turning points remains as a subject for future research.



(a) Single-wire tests



(b) Results of single-wire tests

Figure 14. Tensile test of single wires

5. VIBRATION EXCITER TESTS OF CABLE TRAY SYSTEM

5.1 OUTLINE OF VIBRATION EXCITER TESTS

The specimens are shown in Fig. 15, and the test parameters are listed in Table 1. Each specimen had a total length of 19.5 m, a suspension length of 1 m, and a vertical support span of 2 m. The specimens were suspended from a sufficiently rigid frame and loaded with cables weighing 100 kg/m. The test parameters consisted of two categories: the presence or absence of ϕ4.0 wire reinforcement (denoted as B4 and N, respectively), and the span of Type-A seismic supports (8 m or 12 m, denoted as S8 and S12, respectively). By combining these parameters, four specimen types were prepared. The wires were arranged continuously as far as possible. The tests were conducted sequentially from the top of Table 1, and since little damage was expected from excitation, the same cable trays were reused.

The excitation and measurement locations are shown in Fig. 16. For each specimen, two types of excitation were conducted in the direction perpendicular to the rack axis. First, sweep excitation was applied using a vibration exciter to evaluate the natural frequency. Subsequently, human-induced excitation was performed at the natural frequency identified from the sweep excitation, and the natural frequency and damping ratio were evaluated from the resulting free-vibration responses. During human-induced excitation, the exciter was removed from the specimen. Excitation was applied at the mid-span between seismic resistant elements, with two locations for specimens NS8 and B4S8, and one location for specimens NS12 and B4S12.

As shown in Fig. 17, the exciter (SSV-125, SANES) was placed on top of the cables, and a steel fixture spanning three sub-beams was installed beneath the rack. The exciter base was then fastened to the fixture with threaded bolts. Measurements were conducted in the vertical direction of Fig. 16, recording absolute displacement and acceleration at each vertical support position, as well as the displacement and acceleration of the exciter. The sampling frequency was set at 200 Hz.

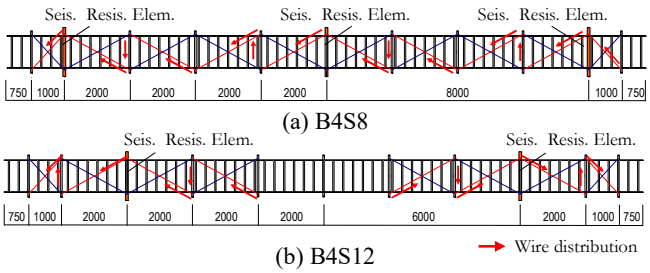


Figure 15. Specimen of vib. exciter tests

Table 3. Specimen parameter of vib. exciter tests

Test No.	Name	Wire reinforcement	Seis. resis. elem. interval
1	NS8	No	8m
2	B4S8	B4	
3	NS12	No	12m
4	B4S12	B4	

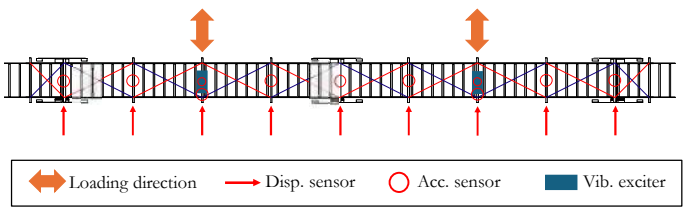


Figure 36. Measurement scheme of vib. exciter tests



Figure 37. Vibration exciter

5.2 RESULTS OF VIBRATION EXCITER TESTS

As a result of the sweep excitation, examples of Fourier spectra obtained from the accelerometer installed at the exciter location are shown in Fig. 18. Since the excitation duration, frequency range, and sweep rate were varied for each specimen, the amplitude levels differ accordingly. The curves for B4S12 and NS12 exhibit slight irregularities at the peak frequencies, which may have been influenced by the repeated use of the specimens. The peak frequencies were approximately 3.0 Hz, 2.4 Hz, 2.3 Hz, and 1.8 Hz for B4S8, NS8,

B4S12, and NS12, respectively. A comparison at the same seismic support span shows that the specimens reinforced with wires had higher natural frequencies, confirming that the reinforcement increased stiffness. The ratio of natural frequencies between B4S8 and NS8 was slightly over 1.2, and given that their masses were identical, the equivalent stiffness of the system is estimated to differ by about 1.5 times. The natural frequencies of NS8 and B4S12 were nearly identical, suggesting that the 12 m-span system with 8 m of wire reinforcement possessed stiffness comparable to that of the unreinforced 8 m-span system.

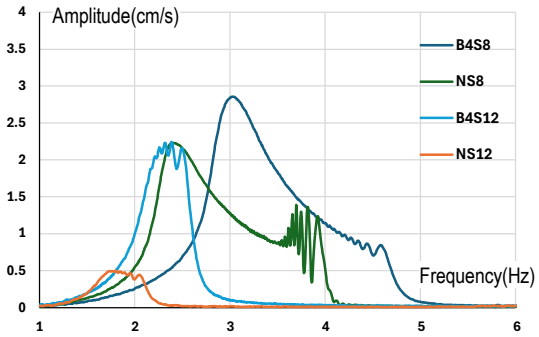


Figure 18. Fourier spectrum

Fig. 19 shows the relationship between natural frequency and drift angle evaluated from human-induced excitations, and Fig. 20 presents the variation of the damping ratio. For each specimen, three to four human-induced excitations were conducted, and the accelerometer values at the loading location were used for the evaluation. The natural frequency was determined from the zero-crossing time, while the damping ratio h was calculated using the amplitude ratio d of the maximum amplitude X_n according to the following equation.

$$h = \left(\frac{\ln d}{2\pi}\right) / \sqrt{1 + \left(\frac{\ln}{2\pi}\right)^2} \quad , \qquad d = X_n / X_{n+1} \tag{2a, b}$$

From Fig. 19, it can be seen that the natural frequency was higher in the wire-reinforced specimens and tended to increase as the drift angle decreased. The horizontal axis of Fig. 20 represents the number of evaluations of the damping ratio obtained from free vibration, and regression lines were drawn to clarify the overall trend. Regarding the damping ratio, the values decreased with smaller deformations in the wire-reinforced specimens, whereas in the unreinforced specimens they remained nearly constant regardless of deformation.

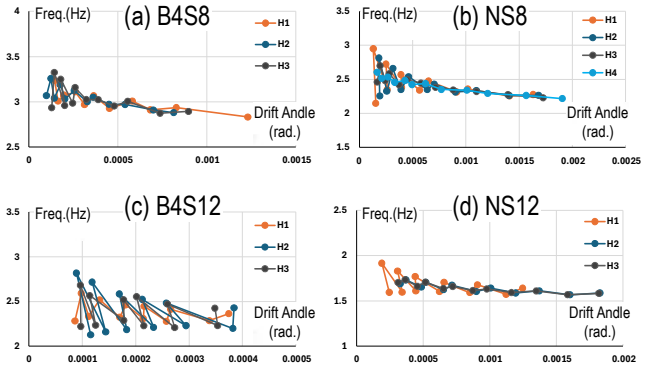


Figure 49. Variation in natural frequency

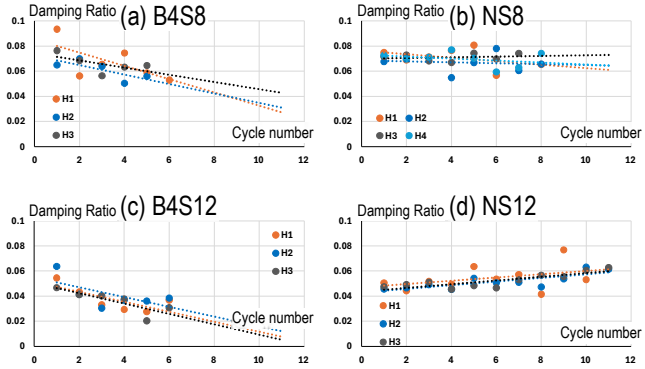


Figure 20. Variation in damping ratio

6. CONCLUSIONS

In this study, we proposed a unique reinforcement method for horizontal components, which tend to sustain damage at lower wave intensity during earthquakes compared to seismic elements, and we verified the effectiveness of the proposed approach through static tests and vibration exciter tests. Our main findings are summarized below along with some considerations for future research.

1) We have proposed a novel reinforcement method using a distinctive arrangement of wires. Instead of simple diagonal wire reinforcement, the proposed method takes into account the deformation pattern of cable trays during earthquakes and is characterized by wiring each wire so that it simultaneously carries tensile forces across all regions.

2) We carried out static loading tests of cable trays to evaluate shear stiffness and shear strength. Increasing the diameters of the wires enhanced the load-carrying capacity of the cable tray, although the tensile resistance did not reach the strength levels obtained in single-wire tensile tests. Our results show that the reinforced cable trays with $\phi 3$ and $\phi 4$ wires exhibited strengths significantly higher than the design strength of the seismic-resistant elements.

3) We carried out vibration exciter tests of cable tray system to evaluate dynamic properties. It was confirmed that wire reinforcement increased the stiffness of the horizontal components and raised their natural frequency. Even in the specimens with a seismic support span of 12 m, the natural frequency became comparable to that of specimens with an 8 m seismic support span when wire reinforcement was applied.

ACKNOWLEDGEMENT

The static tests of the cable trays were assisted by undergraduate students from the Department of Architecture, Meijo University: Mr. Tatsuya Yamashita, Ms. Yuika Yamada, and Mr. Taisuke Naruse. The vibration exciter tests of the cable tray system were supported by Mr. Toshiaki Suzuki and Mr. Ryo Sakamoto from the Research Department, Negurosu Denko. Their kind assistance is gratefully acknowledged.

REFERENCES

Building Center of Japan (BCJ)[2021] "Guidelines for Seismic Design and Construction of Building Equipment 2014 Edition Main Text translated in English (Draft)" (English translation of the 2014 Guidelines)

Kasai K., Mita A., Kitamura H., Matsuda K., Morgan T., Taylor A. [2013] "Performance of seismic protection technologies during the 2011 Tohoku-Oki Earthquake" *Earthquake Spectra Special Issue on the 2011 Tohoku-Oki Earthquake and Tsunami*: 265–294.

Matsuda K., Kasai K., Nakamura T. [2018] "Study on the mechanical behavior and passive control mechanism of suspended cable rack system for electric wiring" *AIJ Journal of Technology and Design* 2018;24(56):63–68. (in Japanese)

Matsuda K., Kasai K., Mizutani K., Asatsuma E., Sato Y. [2020] "Experimental Study on Dynamic Behavior of Cable Tray System Using Large Shaking Table" *Proceedings of the 17th World Conference on Earthquake Engineering (17WCEE)*, Sendai, Japan

Society of Heating, Air-Conditioning and Sanitary Engineers of Japan (SHASE) [2011] "*Report on the survey of building equipment damage caused by the 2011 Tohoku Pacific Ocean Earthquake*" Tokyo: (in Japanese).

Validation of Analytical Method for Axial Force-Bending Interaction of Gypsum Boards

Yasuaki Sato [1], Alex Shegay[2], Fumihiko Sakuraba[3] and Shojiro Motoyui[4]

[1] Researcher, Research&Development, Takenaka Corporation
1-5-1 Ohtsuka, Inzai-shi,Chiba 270-1395, Japan
satou.yasuaki@takenaka.co.jp
[2] Assistant Professor, University of Auckland, Auckland, New Zealand
alex.shegay@auckland.ac.nz
[3] Corporate Officer, Someno Construction Materials Co., Ltd.
648 Shishiko-cho, Ushiku-shi, Ibaraki 300-1231, Japan
sakuraba@someno.co.jp
[4] Professor Emeritus, Tokyo Institute of Technology, Japan
smotoyui@gmail.com

Abstract. During earthquakes, gypsum boards attached to light gauge steel (LGS) walls are subjected to simultaneous axial force and bending moment. The objective of this study is to investigate the axial force-bending moment interaction diagram of gypsum boards under such loading conditions. The out-of-plane bending behavior of gypsum boards can be reproduced by cross-sectional analysis using a fiber model with stress-strain relationships of gypsum and base paper obtained from uniaxial loading tests. The N-M interaction diagram of gypsum boards is predicted using this analytical method. Eccentric compression and tension tests are conducted on gypsum board specimens, and the experimental results are compared with the analytical predictions to verify the consistency between both approaches.

Keywords: Gypsum board, N-M interaction diagram, Eccentric loading test, Fiber model.

1. INTRODUCTION

Since the Tohoku Pacific Ocean Earthquake, there have been many reports of severe damage to inner walls made of the light gauge steel members (Figure 1). In Japan, while the earthquake resistance of major structures has improved since the Great Hanshin-Awaji Earthquake, there are still issues with the earthquake resistance of non-structural components such as inner walls.



Figure 1. Example of damage of non-structural elements in Kumamoto earthquake in S. Kishiki [2018]

It is generally believed that gypsum board attached to LGS is subjected to an in-plane axial force N and a bending moment M simultaneously due to the composite beam effect (Figure 2). Therefore, when examining the seismic resistance of LGS walls, it is possible to use the N-M correlation curve of the gypsum board. Japanese standards for the material properties of gypsum board that makes up the walls and ceilings of LGS only require that the breaking load be confirmed through a bending test in JIS A 6901 [2013], and do not require a stress-strain curve for the gypsum board.

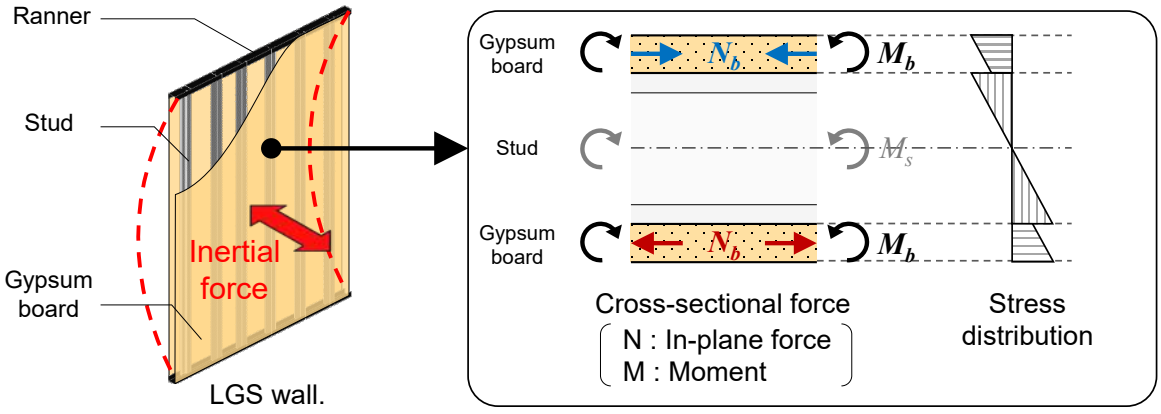


Figure 2. Concept of axial force and bending moment acting on gypsum board

We have previously shown that the material properties of gypsum board under axial force and bending moment can be quantitatively evaluated by numerical analysis using the fiber model of F. Sakuraba [2022]. In previous research by Y. Sato [2024], the N-M correlation curve of gypsum board was obtained using numerical analysis, but the behavior of gypsum board in the direction parallel to the fibers of the gypsum board's base paper was only examined. In this study, we used the numerical analysis to predict the N-M correlation curve of gypsum board orthogonal to the fibers of the base paper, and verified the validity of the analytical results by comparing them with experiments.

2.UNIFORM LOADING TEST

Using the approach presented in Y. Sato [2024], the material properties of gypsum board (Composite), gypsum (Gypsum), and base paper (Paper) orthogonal to the fiber direction of the base paper will be confirmed through uniaxial loading tests.

2.1 TENSILE PROPERTY

Figure 3 shows the relationship between the paper fiber direction on the surface of the gypsum board and the material axis direction of the test pieces. The test pieces were cut using a band saw and laser cutter so that the material axis direction was orthogonal to the paper fiber direction. The strain of the test pieces was measured using digital image correlation (DIC analysis), so the random pattern was painted on the test piece. The load F applied to the test piece and the displacement δ of the gripping jig were measured using sensors built into the tensile testing machine.

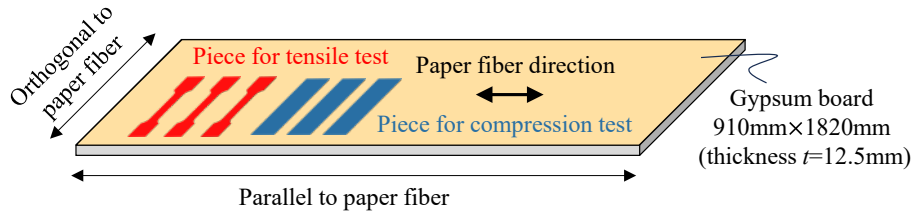
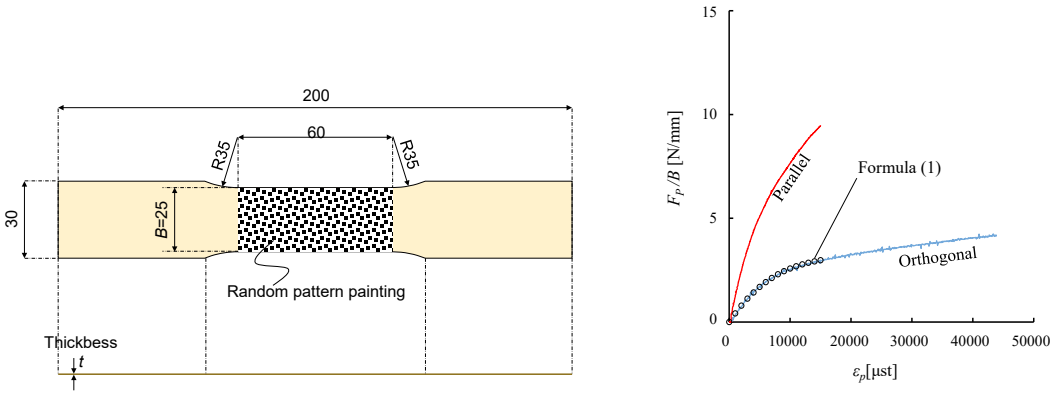


Figure 3. Sampling the test pieces.

Figure 4 shows the stress-strain relationship obtained from the test. The horizontal axis is the average tensile strain obtained from DIC analysis, and the vertical axis is the load F_P divided by the width B of the test piece. The results obtained in Y. Sato [2024] for the test piece parallel to the paper fibers (red line) show that the results orthogonal to the paper fibers (blue line) clearly have lower stiffness and yield strength. This result suggests that the paper has anisotropic material properties depending on the fiber direction. The curves in Figure 4 are approximated by the following cubic function for the later numerical analysis.

$$\left(\frac{F_P}{B}\right)_{Orth(\varepsilon_P)} = 0.42 \times 10^{-12}{\varepsilon_P}^3 - 2.24 \times 10^{-8}{\varepsilon_P}^2 + 0.44 \times 10^{-3}\varepsilon_P \quad (1)$$

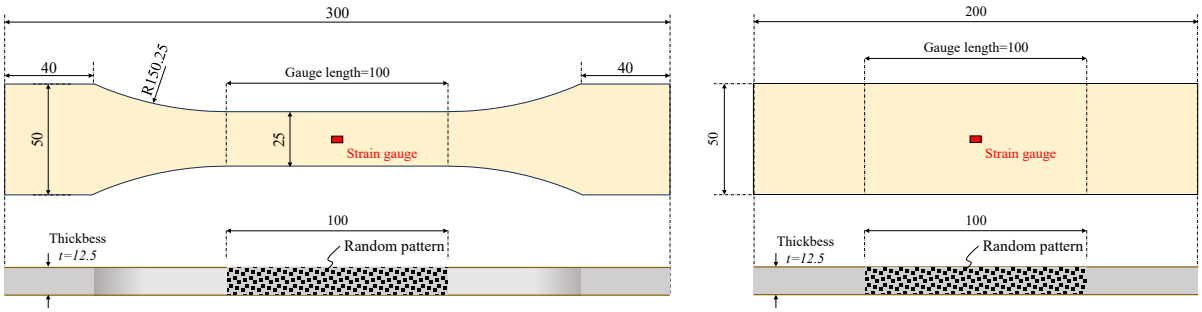
Here, the tensile strain ε_P of the base paper is the range of $0 \leqq \varepsilon_P \leqq 15000\mu st$.



a) Dimensions of test piece. **b) Relationship between F/B and εp.**

Figure 4. The tensile test of paper.

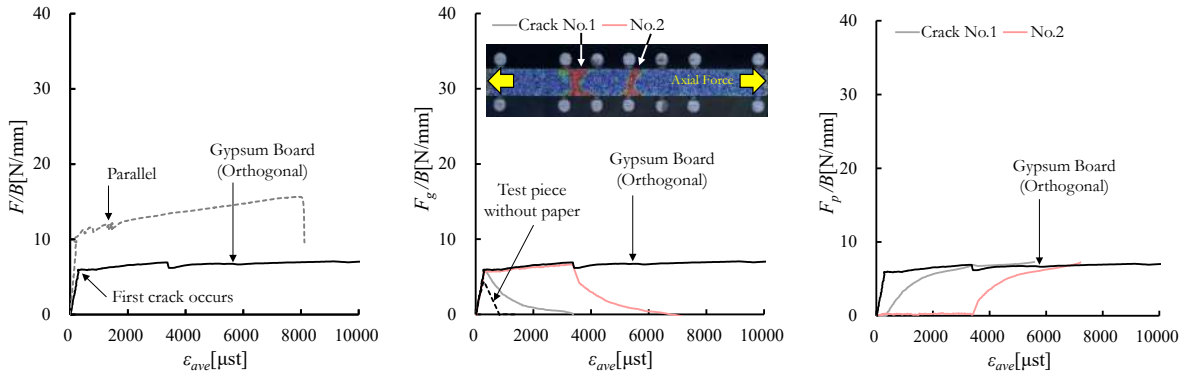
Next, the test pieces for compression and tension tests of gypsum board are shown in Figure 5. The tensile test pieces of gypsum board orthogonal to the fibers of the base paper were expected to have low stiffness and strength, same to the base paper, so the dumbbell-shaped test piece was designed with a gradual change in the transition section. The compression test pieces were the same as those in Y. Sato [2024].



(a) Tensile test piece. **(b) Compression test piece.**

Figure 5. Dimensions of test piece.

Figure 6 shows the strain distributions of the gypsum board, gypsum, and base paper orthogonal to the paper fibers. Two cracks appeared during the tensile test of the gypsum board. The local strains ε_{p1} and ε_{p2} in the cracked area were obtained using the method same to that used in Y. Sato [2024], and the tensile force F_p/B generated in the base paper was obtained by substituting their average value for εp in equation (1). Furthermore, the force F_g of the gypsum was obtained by subtracting the force F_p of the base paper from the load F acting on the gypsum board. Figure 6(b)(c) shows that when the gypsum begins to crack, the tensile forces (F_p/B and F_g/B) acting on the gypsum and the base papers are switched. Using the method same to that used by Y. Sato [2024], the tensile test was conducted on test piece in which notches were made at 5 mm intervals in the base papers alone, and the results is shown by the black dotted line in Figure 6(b). The test pieces without the base paper (black dotted line in Figure 6(b)) exhibited brittle behavior, with the lower maximum strength than the test pieces with the base paper (black solid line). Furthermore, the gypsum test piece (both Crack No.1 and 2) showed a gradual decrease in strength after reaching the maximum strength, suggesting the tension stiffening effect similar to that observed in Y. Sato [2024]. Compared to the result of test piece parallel to the base paper fibers (gray dotted line in Figure 6(a)) shown in Y. Sato [2024], the test piece orthogonal to the base paper fiber direction (black solid line in Figure 6(a)) has a lower muximum strength and a smaller increase in strength after crack. This difference is thought to be due to the anisotropy of the base paper fibers.

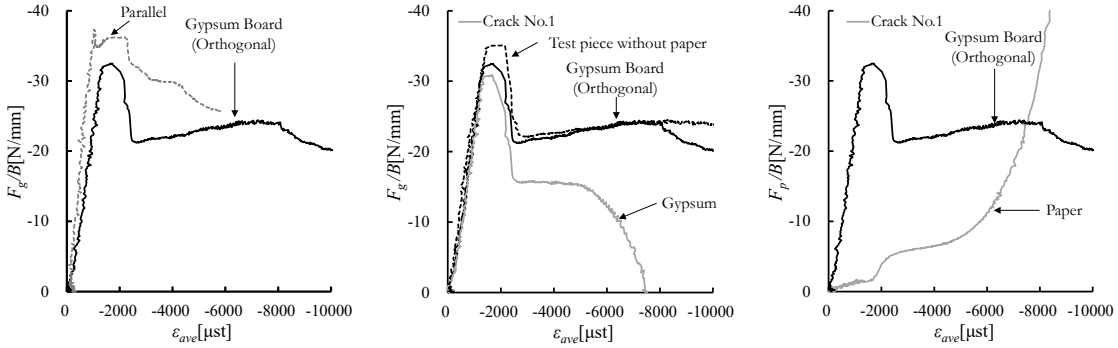


(a)Gypsum board. **(b)Gypsum.** **(c)Paper.**

Figure 6. F/B-ε relationship of gypsum board subjected to tensile force.

2.2 COMPRESSIVE PROPERTY

The compression test was also conducted in the same manner as the tensile test, and the resulting F/B-ε relationship diagram is shown in Figure 7. In the compression test, cracks appeared in only one location, and in Figure 7(a), the effect of the anisotropy of the base paper becomes apparent after the maximum strength at which cracks appeared. The test piece in which the base paper was cut (black dotted line in Figure 7(b)) does not show a significant difference from a normal test piece in which the base paper was not cut (black solid line in Figure 7(b)). Because the base paper has low axial rigidity, the compressive force of bace paper is small up to the maximum load, as shown in Figure 7(c). Furthermore, after the maximum load, the base paper buckles as the gypsum cracks. For these reasons, it is thought that the effect of the base paper on the compressive property of gypsum board is small.

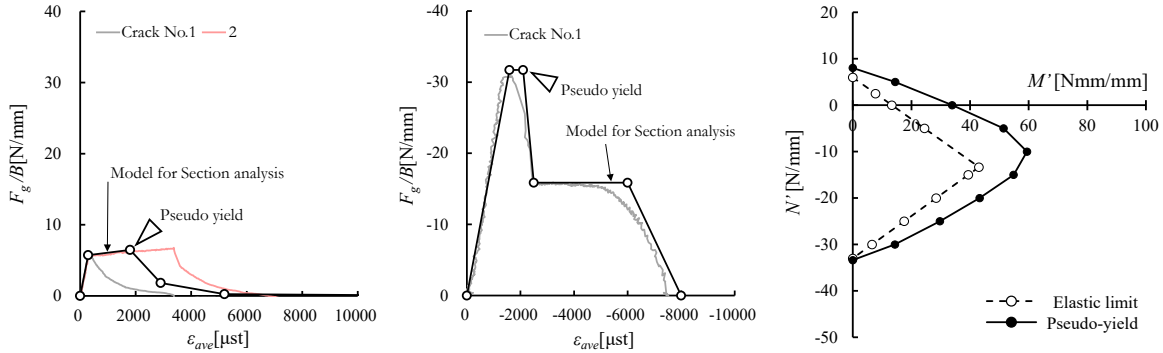


(a)Gypsum board. **(b)Gypsum.** **(c)Paper.**

Figure 7. F/B-ε relationship of gypsum board subjected to compression force.

3. N-M INTERACTION CURVE OF GYPSUM BOARD

Using the results of the uniaxial loading tests presented above, the N-M interaction curve of the gypsum board orthogonal to the base paper fiber direction is predicted using the cross-sectional analysis of the fiber model same to Y. Sato [2024]. The gypsum material properties used in this analysis are a skeleton curve that traces the test results, as shown in Figures 8(a) and (b). The tensile and compressive properties of the base paper are approximated by the cubic function in Equation (1). As shown in Chapter 2, the compressive property of the base paper has little effect on the gypsum board, so they can be considered equal to the tensile property. Furthermore, in the model of the compressive and tensile properties of the gypsum board, the point at which strength declines is defined as the "quasi-yield point" (Figure 8). The *N-M* curve obtained from the cross-sectional analysis is shown in Figure 8(c). The vertical axis represents the axial force per unit width (*N'*), and the horizontal axis represents the moment per unit width (*M'*). The elastic limit is indicated by the dotted line, and the quasi-yield point is indicated by the solid line.



(a) Tensile property. **(b) Compression property.** **(c) N'-M' interaction curve.**

Figure 8. Estimate N-M interaction curve by Analysis.

Next, to confirme the validity of Figure 8(c), an eccentric compression-tension test was conducted (Figure 9). The test pieces were three and had a 12.5 mm thick normal gypsum board, with their longitudinal direction orthogonal to the fiber direction of the base paper. The true eccentricity e was obtained by adding the initial eccentricity e_0 and the out-of-plane displacement Δe at the center of the test piece measured by DIC analysis. The axial force N was measured using the test machine, and the bending moment M was calculated by multiplying N and e. Two strain gauge was attached to the center of the test piece, and the strain measured with this was used as the reference value for elastic strain. The compressive loading test was conducted assuming e_0 = 5 mm, where the moment is maximized at the elastic limit, as well as tension and compression loading tests with e_0 = 3 mm. Note that e_0 in Figure 9 is exaggerated for illustration compared to the actual distance given in the experiment.

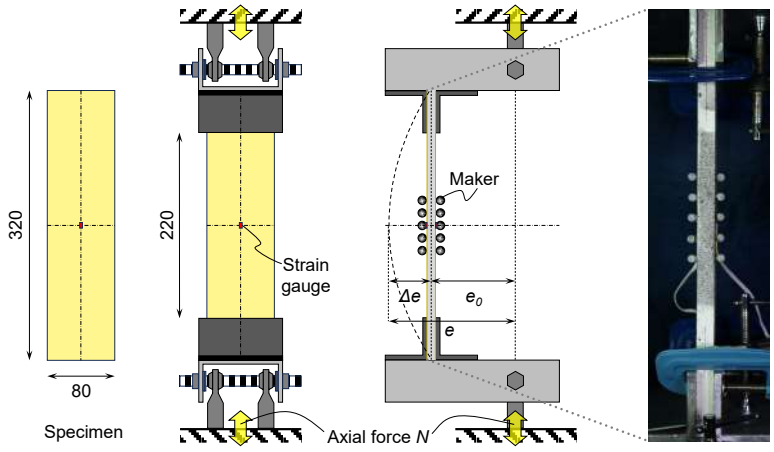
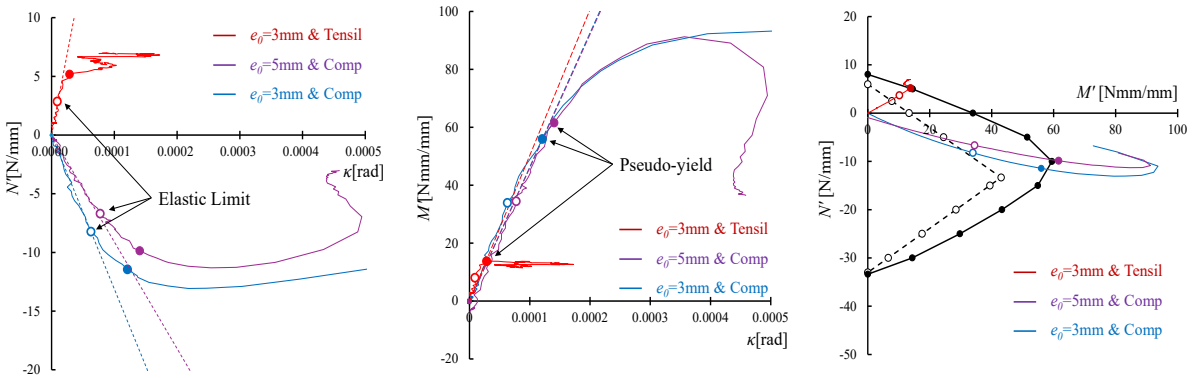


Figure 9. Set up and dimensions of the eccentric compression and tensile test of the gypsum board.

The test results are shown in Figure 10. In Figure 10, the white points indicate the elastic limit and filled points indicate the pseudo-yield point. The dotted lines in Figures 10(a) and (b) indicate the initial gradient from the test results. The N'-M' interaction curves obtained by the test and numerical analysis are compared in Figure 10(c). The white point where N' deviates from the initial gradient were located approximately at the elastic limit of Figure 10(c), and the filled point where M' deviates from the initial gradient were located approximately at the pseudo-yield point of Figure 10(c). In each the elastic limit and pseudo-yield points, it was confirmed that the test and numerical analysis of curves are roughly consistent. The validity of the N-M interaction curve evaluated by the proposed numerical analysis was also confirmed for the test pieces orthogonal to the fiber direction of the base paper.



(a) N'-$\varkappa$ curve. **(b) M'-$\varkappa$ curve.** **(c) N'-M' interaction curve.**

Figure 10. Comparison of test results and analysis results

4. CONCLUSION

In this study, we investigated the N-M curve of gypsum board orthogonal to the base paper fiber direction using cross-sectional analysis with a fiber model. The results obtained in this study are as follows:

1) Including the results of Y. Sato [2024], the proposed cross-sectional analysis using the fiber model can evaluate the N-M correlation curve of gypsum board parallel and orthogonal to the base paper fibers.

2) The point where N' deviates from the initial gradient is located approximately at the elastic limit, and the point where M' deviates from the initial gradient is located approximately at the pseudo-yield point.

3) Including the results of Y. Sato [2024], DIC analysis is effective for material testing of gypsum board.

In practice, since gypsum board strength and stiffness are likely to vary, this study needs to be supplemented with statistical analysis using a larger sample size. Detailed investigation is a future topic.

REFERENCES

[1] S. Kishiki, T. Seike, S. Motoyui, N. Koshiishi : Development of Reduction Method for Seismic Damage to LGS Partition Wall Part 1 research background and purpose of research, Summaries of Technical papers of annual meeting Architectural Institute of Japan, pp. 1073-1074, 2018

[2] JIS A 6901 (2013). Japanese Industrial Standards, Japanese Industrial Standards Committee, Japan.

[3] F. Sakuraba, A. Shegay, Y. Sato and S. Motoyui : Numerical analysis of gypsum board subjected to bending moment using fiber model, Proceedings of the 5th international Workshop on Seismic Performance of Non-structural Elements, California, USA, 2022.

[4] Y. Sato, A. Shegay, F. Sakuraba and S. Motoyui : Study on mechanical properties of gypsum boards subjected to in-plane forces and bending, Proceedings of 18th world conference on earthquake engineering, Milano, Italy, 2024.

Derivation of floor response spectra in masonry infilled precast concrete buildings

Muhammad Yousaf Anwar[1,2], Davide Bellotti[1], Emanuele Brunesi[1], and Roberto Nascimbene[1,2]

[1] European Centre for Training and Research in Earthquake Engineering (EUCENTRE)
Via Ferrata 1, 27100 Pavia, Italy
e-mail: yousaf.anwar@eucentre.it; davide.bellotti@eucentre.it; emanuele.brunesi@eucentre.it; roberto.nascimbene@eucentre.it

[2] University School for Advanced Studies (IUSS)
Palazzo del Broletto, Piazza della Vittoria 15, 27100 Pavia, Italy
e-mail: roberto.nascimbene@iusspavia.it

Abstract. The evaluation of seismic demand acting upon non-structural elements (NSEs) and equipment is of utmost importance when assessing or designing a complex structural system, which will be inevitably exposed to seismic hazard during its lifetime. As such, this paper is chiefly concerned with the derivation of absolute acceleration and relative displacement floor response spectra (FRS) for reinforced precast concrete buildings subjected to frequent, or serviceability-level earthquakes. Thus, two single-storey precast structures representative of the Italian construction period of the '70s were selected and designed according to the code provisions enforced at the construction time. The first structure is assumed to be located in Naples and features beam-to-column frictional connections, consistently with the classification of Naples as a non-seismic site, and the second one is located in L'Aquila and features dowels in beam-to-column connections following design for seismic loads. Nonlinear time-history analyses were performed to derive FRS for the design of NSEs housed therein, also providing a quantification of the effect of masonry infills, the latter being generally neglected both in the design and in the evaluation of FRS, which could lead to un-conservative design of NSEs.

Keywords: Precast industrial buildings, Absolute acceleration floor response spectra, Relative displacement floor response spectra, Masonry infills, Beam-column connections.

1. INTRODUCTION

Historically, the tilt towards precast concrete structures in Italy caught pace during the post-war reconstruction phase ((Bellotti et al., 2025; Matteini et al., 2024). Most of the first precast structures were meant to serve industrial functions e.g., warehouses, industrial and manufacturing plants whereas their application in roads and bridges followed suit. As such, from a classification point of view, with substantial diversity noticeable in many of their characteristics, yet functional and technological similarities mean most industrial precast buildings in Italy have some identical features i.e., overall structural dimensions, arrangement of different structural elements etc. (Casotto et al., 2015; Deyanova et al., 2023).

In addition to addressing functional and infrastructural demands, precast concrete as well catered to special structural needs with improved seismic performance being one of them. Innovations and extensive research during the last half century made possible the advent of precast concrete structures that are tailor-made to withstand high seismic hazard (see for instance Crisafulli et al., 2002; Ameli, 2015; Kurama et al., 2018 among others). Within the context of Italian precast building stock, several authors have carried out empirical seismic vulnerability studies (e.g., Toniolo and Colombo, 2012; Bournas et al., 2014; Belleri et al., 2014; Savoia et al., 2017) whereas others have reported results of analytical seismic fragility analysis of the same (refer to Casotto et al., 2015; Babic and Dolsek, 2016; Beilic et al., 2017; Cavalieri et al., 2023 among several others). Current literature also documented suitable modelling approaches for seismic performance evaluation of low-rise single storey precast buildings (Bressanelli et al., 2021; Bosio et al., 2023) as well as the effect of corrosion (Biondini et al., 2011), P-Δ effects (Ercolino et al., 2018) and cladding panels (Biondini et al, 2013; Belleri et al., 2016; Ercolino et al., 2018) on seismic performance of the precast structures. Experimental campaigns were also undertaken to investigate cyclic response of seismic-resisting precast structures with more than one storey (Brunesi et al. 2015) as well as the seismic response of precast wall connections (Brunesi et al., 2020).

In case of Italy, there exists a noticeable abundance of literature on performance of industrial precast structures during the Emilia earthquakes in Northern Italy, providing details regarding the actual on-ground damage extent to such buildings (see e.g., Bournas et al., 2014; Magliulo et al., 2014; Ercolino et al., 2016; Minghini et al., 2016; Batalha et al., 2019). Conversely, the number of analytical studies on this topic is much lower than their empirical counterparts (refer to Bovo et al., 2018; Magliulo et al., 2018; Bosio et al., 2020; Brunesi et al., 2017, among others).

Nevertheless, despite abundant presence of different type infills in industrial precast buildings, research studies covering floor-wise seismic response of precast concrete structures with masonry infills remain scant with the very few recent examples addressing the issue from a non-structural elements point of view. This paper tends to obtain floor response spectra following a multi-stripe analysis on two archetypes selected after a rigorous selection procedure grounded in classification schemes presented by researchers including author(s) of this study. Furthermore, bare and infill models of the two archetypes are also compared to comment on seismic demand acting upon NSEs.

Following the selection of suitable archetypes, 3D finite element models of the same are built using OpenSees (2006) with special attention given to the modelling of beam-to-column connections for the different types of jointures observed in the selected archetypes. Thereon, a set of ground motion records – pertinent to the soil type and geographical location of the respective structure – is assembled comprising of 20 records per each earthquake return period considered. A multi-stripe analysis (MSA) – under bidirectional records as ground-acceleration inputs for nonlinear time history analysis (NLTHA) – is carried out to obtain displacement and acceleration data recorded in the two horizontal directions. Post-processing of the data at hand then results in floor response spectra for the two archetypes and each of their bare and infill counterparts. Statistical parameters such as median and median ± one standard deviation are also plotted along the individual plots in order to better visualize the results obtained therein.

2. ARCHETYPE DETAILS

The structures investigated within the scope of this work are single-story RC precast structures, intended and designed to serve mostly industrial functions e.g., warehouses, production facilities etc. Selection of different archetypes, representative of Italian precast structures of the aforementioned typology, is made based on conclusions derived from classification studies and databases present in current literature. In line with the classification schemes and databases compiled heretofore, including those by the author(s), two different archeyptes were selected representing single-storey non-residental precast buildings. The first of the two archetypes is assumed to lack regulatory design, built in line with building practices of the time and in the absence of documented regulations. The counterpart archetype is a design-compliant single storey precast structure designed according to concurrent Italian building codes, where explicit design specifications/limits for precast structures were present in documented form. The primary differentiating factor between the two is signified by the presence (or absence thereof) of dedicated beam-column connections with the former relying solely on friction between the structural elements whereas the latter is equipped with steel dowel-connections. The detailed geometric configuration and material properties of the two structures are provided in the following paragraphs.

2.1 ARCHETYPE 1 – NAPOLI, 1970S

Of the two structures considered herein, the former is an archetypical single-storey assembly representative of non-residential precast structures built in Naples during the 1970s. Designed to resist gravity loads only, the structure comprises of 20 meters long main prestressed beams along the transverse direction, supporting multiple secondary beams of 6 meters length along the longitudinal axis. The I-section main beams having variable depth are doubly-sloped with 10% inclination whereas the secondary beams bear a T-shaped cross section. The aforesaid assembly rests on 0.35 × 0.35 meters square columns with a height of 6 meters, having concrete filled foundations at the base and neoprene pads at top for beam placement. With no auxiliary device or mechanism augmenting the connection between the main beam and the column top, it can be characterized as a 'friction-only' connection as opposed to the presence of dedicated connection devices – steel dowels protruding from column heads – reinforcing the connection between the girders (secondary beams) and the column tops. Double-tee prestressed elements rigidly connected to the main beams constitute the roof of the structure where additional anchorage between the roof elements and main beams is facilitated through additional steel bars with a concrete slab casted above the assembly. A twin of this archetype with external masonry infill panels lined along the entire parameter of the building furnishes the 'infill counterpart' to be compared with the otherwise 'bare' configuration of this archetype (**Figure 1**).

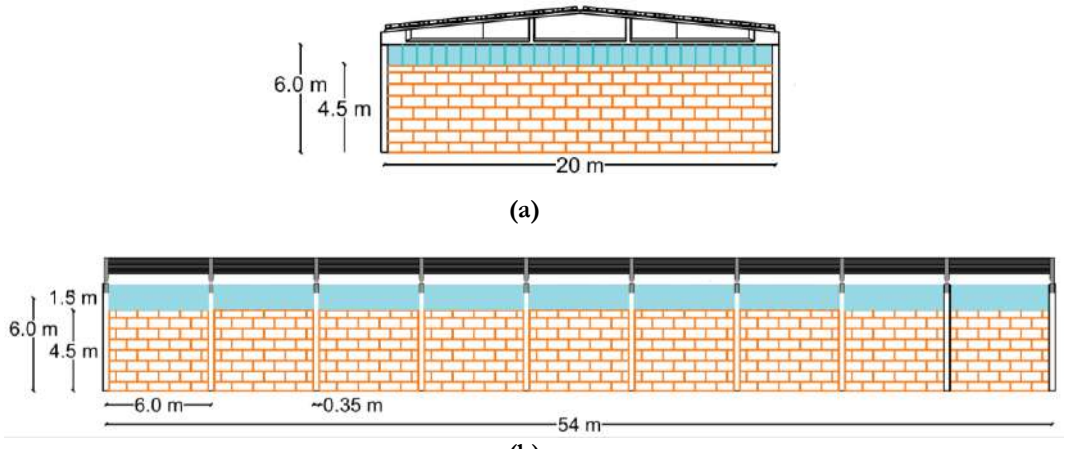


Figure 1: External view of the Napoli archetype in **(a)** transverse x-direction and **(b)** longitudinal z-direction (Bosio et al. 2023)

2.2 ARCHETYPE 2 – L'AQUILA, 1970S

The second archetype, meant to include the design and construction practices of the 1970s, is located in L'Aquila with a floor plan of 20×54 m² and 6 m tall square columns bearing 0.55×0.55 m² cross-sectional area. Prestressed main beams of 20 m length and variable I-shaped cross-section span the transverse direction with a 10% double-sloped inclination whereas 6 m long T-shaped sections extend along the longitudinal direction. Column tops of this archetypical structure feature steel dowels to secure a distinct beam-to-column connection with both the main and secondary beams, thus rendering a firmer jointure as compared to friction-only beam-column unions. The roof assembly of the structure along with the 5 cm thick cast-in-situ slab can be considered rigid according to EC8 (CEN 2004) due to the bolted steel-plate connections firmly anchoring the precast double-tee roof elements to the main beams. The corresponding infill counterpart of the second archetype features 20 cm thick vertical precast RC panels encompassing all sides of the building. These enclosure panels are fastened to the beams through hammer-head strap connections, leaving a narrow gap between the panel and the beam.

3. NUMERICAL MODELLING AND MSA

The archetypes detailed in the preceding section are converted into numerical models for simulation of the same under the selected ground motion records. The numerical modelling and details of the analysis are enunciated as follows.

3.1 NUMERICAL MODELLING

3D finite element models of the considered archetypes are built using OpenSees (2006), an open-source platform presenting the authors with a vast library of material models incorporating nonlinearity. A lumped plasticity approach is adopted for all the models wherein a plastic hinge, introduced in the column element, functions to capture the global structural nonlinearity. The material response of this plastic hinge is modelled using the Modified Ibarra-Medina-Krawinkler Deterioration Model with Peak-Oriented Hysteretic Response (ModIMKPeakOriented) material, implemented in OpenSees (2006), making use of mechanical parameters' values documented by Bosio et al. (2023). The beam elements of the archetype are modelled using elastic elements of the OpenSees library.

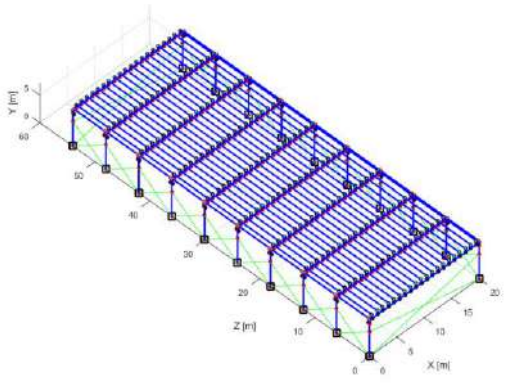


Figure 2: OpenSees infilled model of the Napoli archetype

Regarding the beam-column joints of the first archetype, the aforenamed 'friction-only' connections (between main beams and columns) are modelled using the flatSliderBearing element of OpenSees while for the dowel assisted girder-column connections, pinned joints (i.e., pure hinges) were introduced. The flatSliderBearing element used herein allows bidirectional translation under the corresponding frictional force computed through the Coulomb model for which the relevant friction coefficient is evaluated in line

with Magliulo et al. (2011). On the other hand, a relatively more elaborate modelling approach was implemented to simulate the dowel connections between the main beams and columns of the second archetype. In doing so, the two nodes (bearing the same coordinates) representing the generic beam-to-column joint are connected through two parallelly aligned elements i.e., a flatSliderBearing element and a zeroLength element with each serving to simulate its corresponding joint mechanism. Of the two elements, the former reflects the shear friction resistance between the contact surfaces of the corresponding beam and column whereas the latter simulates the dowel connection and is characterized by a bilinear behaviour along the two horizontal directions. Material-wise, appropriate inclusion of plastic hardening and post-peak degradation merits the assignment of ModIMKPeakOriented material to the zeroLength element simulating the dowel connection. Finally, the girder-to-column dowel connections of the second archetype were modelled using pinned connections. Given the presence of rigid cast-in-situ concrete slabs as well as bolted steel plate connections, the roof system for both archetypes was, justifiably, assumed as a rigid diaphragm. With respect to the modelling of masonry infills, two diagonal compression-only struts were placed between successive columns (see **Figure 2**) where the backbone curve for the struts was obtained following the procedure detailed by Bosio et al. (2023).

3.2 GROUND MOTION RECORD SELECTION AND MULTI-STRIPE ANALYSIS

The selection of ground motion for multi-stripe analysis (MSA) was made in line with the outcomes of the RINTC project (Iervolino et al. 2018). Keeping in mind the soil profiles of the two cities considered in this study (i.e., Napoli and L'Aquila), soil type C, corresponding to $V_{s,30}$ values in the 180-360 m/s range, was agreed upon. Following the Conditional Spectrum method (Jayaram, Lin, and Baker 2011), 20 records per each of the ten intensity levels, associated with 10 different earthquake return periods, were extracted from Italian accelerometric archive (Luzi et al. 2008) and the NGAwest2 database (Ancheta et al. 2014). Compliant with bidirectional nonlinear time history analysis, two orthogonal acceleration records (in x and z directions) were finalized for each of the ground motion considered. Subsequently, under the selected records, each of the structures modelled herein was subjected to two MSAs i.e., one per each bare and infill iteration of the parent archetype. Ultimately, floor response spectra were calculated using data from the acceleration recorders placed at top of column elements in each OpenSees model.

4. RESULTS AND DISCUSSION

As discussed in earlier sections of the text, the results of the NLTHAs are presented in this section in terms of absolute acceleration-displacement floor response spectra for bare and infill counterparts of each of the two archetypes considered herein. In the graphics to follow, individual acceleration-displacement floor response spectra, computed for all of the ground motion records, are plotted in grey whereas the solid (non-grey) coloured lines mark the median of those floor spectra with dotted lines of the same colour representing the corresponding median ± one standard deviation. In the comparison plots, however, only the median floor spectra along with median ± one standard deviation plots are illustrated to avoid over-congested graphics. Starting with the archetype for Napoli, **Figure 3a** and **3b** depict the acceleration-displacement floor response spectra (FRS) for the bare configuration of this archetype in x-direction for SLS and ULS, respectively. The individual spectrum plots herein (grey lines in the respective figures) reveal the acceleration demand to be governing the SLS limit state with majority of the plotted spectra falling behind the 0.03 m mark on the displacement axis (**Figure 3a**). Conversely, for the ULS limit state, both acceleration and displacement seem to be imposing a substantial demand on the NSEs housed in the precast structure, made evident by a cluster of plots either reaching or extending beyond 0.1 m and 10 m/s2 on the displacement and acceleration axes of **Figure 3b**, respectively. A scaled-up comparison plot of the median and median ± one standard deviation for both the SLS and ULS, shown in **Figure 3c**, serves to confirm the foregoing interpretation.

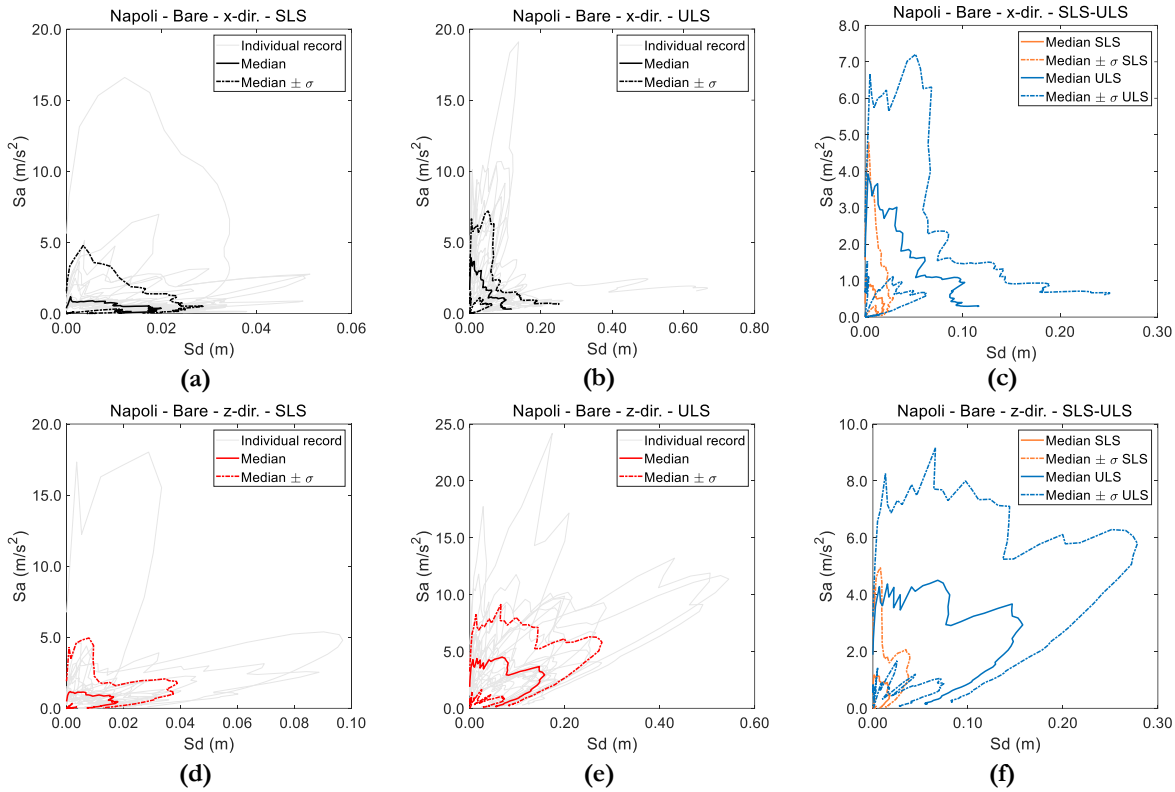


Figure 3: Floor response spectra for Napoli archetype associated with its **(a)** x-dir for SLS, **(b)** x-dir for ULS, **(c)** x-dir SLS-ULS comparison, **(d)** z-dir for SLS, **(e)** z-dir for ULS, **(f)** z-dir SLS-ULS comparison

A similar trend of dominant acceleration demand is observed when reading the z-direction spectra associated with SLS where (in **Figure 3d**) the majority of the individual plots as well as the median floor response spectra corresponds to an abscissa range of 0.03-0.04 m against a 3-4 m/s2 capping along the ordinate for most of the plots. As for the ULS case in z-direction, there is a coupling of imposed demands defined by higher displacement as well as acceleration demands on NSEs (see **Figure 3e**) when compared with the same for SLS. The plots in **Figure 3f** corroborate this fact wherein the median floor response spectrum for the ULS scenario is evidently more spread out along both axes, accompanied by the higher standard deviation from the median signifying greater dispersion of acceleration and displacement demands.

The foremost bare-vs-infill comparison of the floor spectra – in term of median and median ± 1 standard deviation plots – of the Napoli archetype is illustrated in **Figures 4a-4d**. In this regard, the x-direction median floor spectra (i.e., **Figure 4a** and **4b**), for the bare and infill configurations exhibit noticeable similarity in their trajectories for both limit states; especially in the case of ULS (see **Figure 4b**), the paths of the bare and infill spectra are in near unison. As for z-direction, there exists a sizeable difference between the bare and infill cases marked by higher floor spectral accelerations in the infilled precast structures against distinctively greater displacement demands for the bare counterparts (see **Figure 4c** and **4d**). This can be justifiably attributed to the changed dynamic characteristics of the infilled models impacted by addition of panels between columns of the otherwise bare frames. Moreover, higher mass participating ratios in the first mode also amplifies the floor spectral accelerations as compared to those of their bare counterparts.

Similar trends (for floor spectra in x-direction) are observed for the L'Aquila archetype visible, albeit vaguely, from **Figures 5a** and **5b** and more explicitly from **Figure 5c**. The steeper climb of the median floor spectrum for SLS case (in **Figure 5c**) points towards a narrower (and relatively lower) range of floor spectral displacements as opposed to the wider dispersion of the statistical plots for ULS case. Individual as well as statistical plots in **Figure 5d-5f** imply that the same trends hold for z-direction as well.

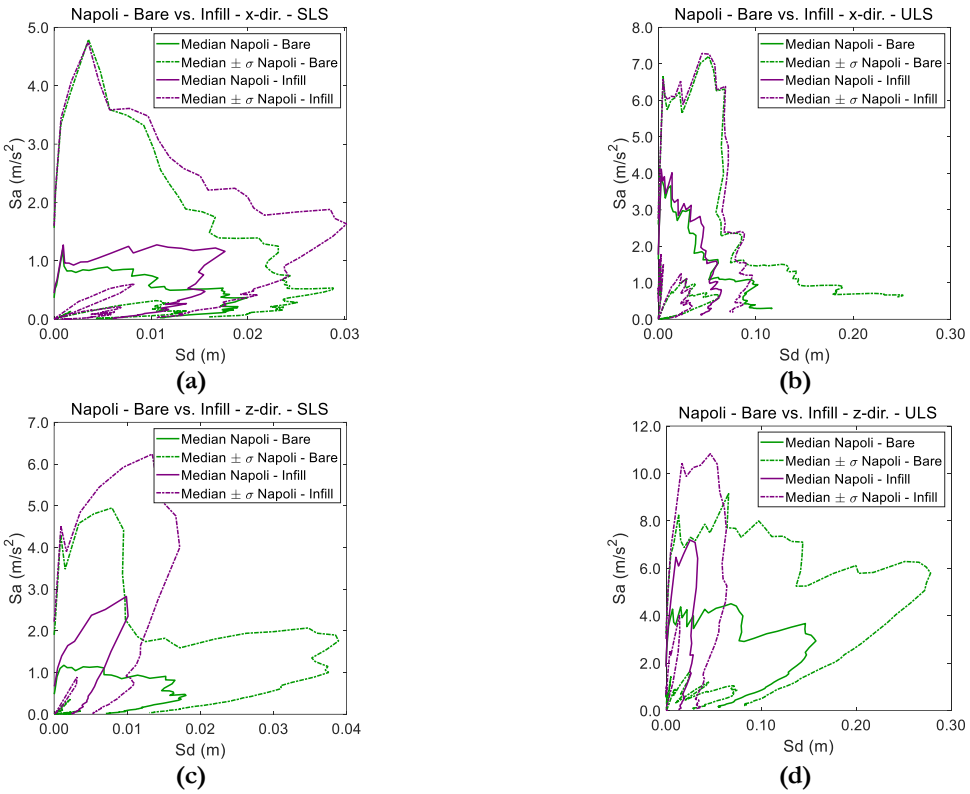


Figure 4: Bare vs Infill floor response spectra associated with Napoli archetype's **(a)** x-dir for SLS, **(b)** x-dir for ULS, **(c)** z-dir for SLS, **(d)** z-dir for ULS

Concerning the bare-vs-infill comparison for the L'Aquila archetype, the bare and infilled median floor response spectra follow a near identical course until a spectral acceleration peak is reached (see **Figure 6a** and **6b**), indicative of comparable peak spectral acceleration demands for the bare and infilled models along the x-direction. The post-peak descent of the graphs, however, exhibits notable divergence, thus signalling to higher dispersal of both spectral acceleration and displacement between the two counterparts.

Due to scaling issues, the otherwise unviewable floor response spectra for the infilled iteration of the L'Aquila archetype are made visible as enhanced version of the corresponding part of the plots in **Figure 6c** and **6d**, associated with spectra for z-direction. Comparing the infilled and bare models in terms of their respective floor spectra (in z-direction) clearly points to very low spectral floor accelerations and displacements in the infilled model when pitched against its bare counterpart. This could possibly be associated with the addition of multiple infill panels in series which in turn absorbs much of the acceleration and displacement demand along the longitudinal z-direction.

Whereas an erstwhile deficient literature on floor-wise seismic response of masonry infilled precast concrete structures hampers a direct validation of the results compiled herein, nevertheless a comparison with prior experimental studies by the authors derivationally corroborates well the acceptability of the numerical model. Case in point, first instances of failures in the numerical model are associated with shearing of beam-column and girder-column connections, in line with findings reported by Brunesi et al. (2015, 2020) and Brunesi & Nascimbene (2017). Similarly, comparison plots in **Figure 4** and **6** are evidently consistent with the variability known to be inherent in the seismic behaviour of precast structures with frictional connections.

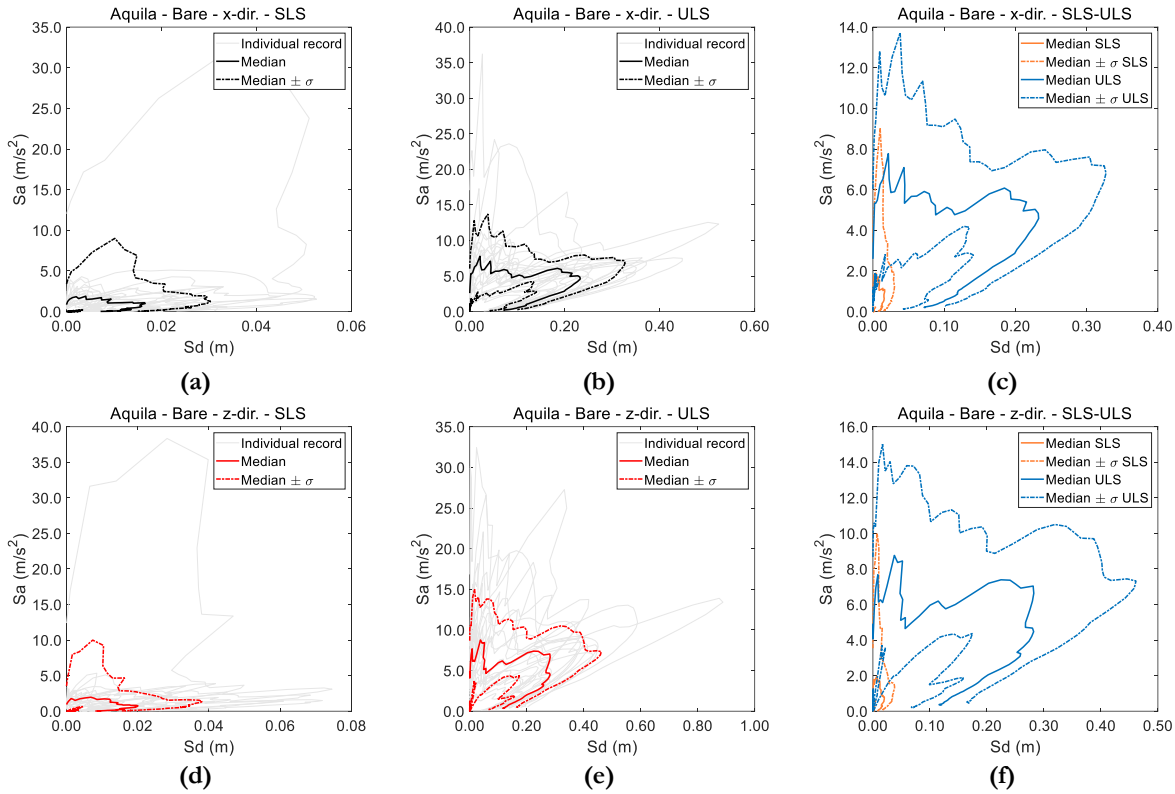


Figure 5: Floor response spectra for L'Aquila archetype associated with its **(a)** x-dir for SLS, **(b)** x-dir for ULS, **(c)** x-dir SLS-ULS comparison, **(d**) z-dir for SLS, **(e)** z-dir for ULS, **(f)** z-dir SLS-ULS comparison

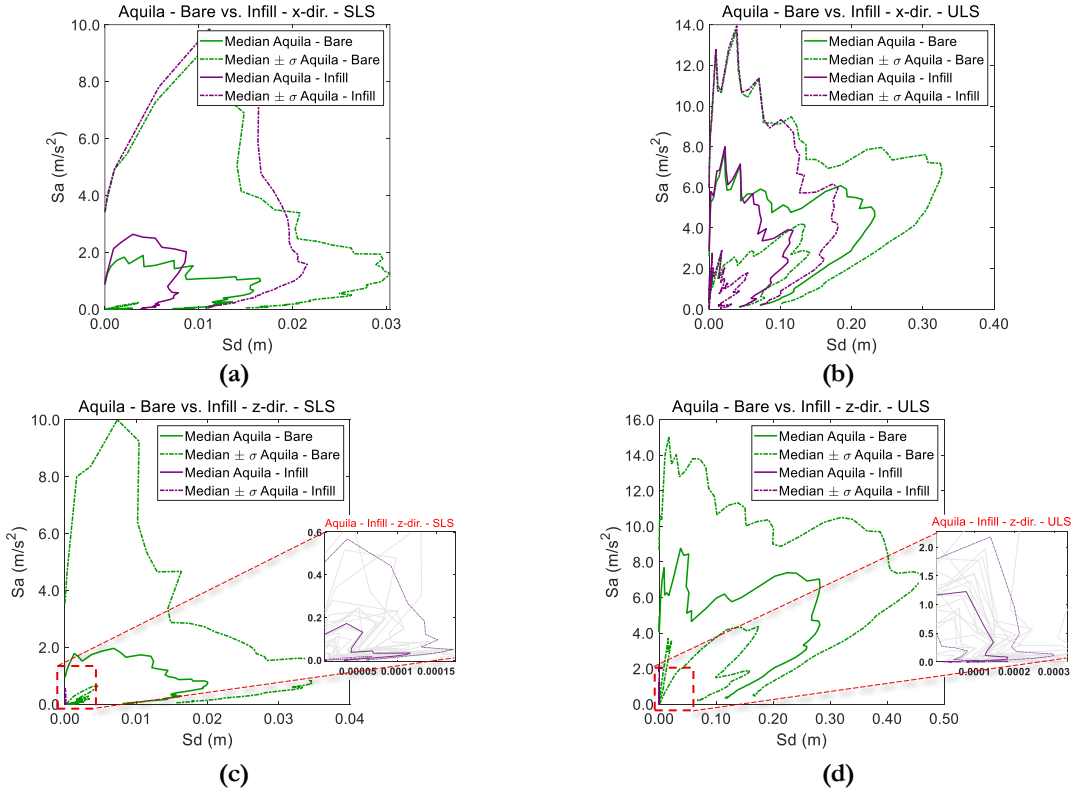


Figure 6: Bare vs Infill floor response spectra associated with L'Aquila archetype's **(a)** x-dir for SLS, **(b)** x-dir for ULS, **(c)** z-dir for SLS, **(d)** z-dir for ULS

5. CONCLUSIONS

In line with the derived floor response spectra for masonry infilled precast buildings and the discussion on the results obtained therein, the following conclusions can be made:

1. For bare configuration of both archetypes considered herein, a limit state transition from SLS to ULS is marked by increased displacement demand on the NSEs installed along both transverse and longitudinal directions.
2. The spectral displacements, along x and z directions, tend to exhibit higher dispersion for the ULS state in both archetypes.
3. Comparison of bare and infill counterparts for both archetypes yield comparable floor responses for the two, along the transverse (x) direction whereas for the longitudinal (z) direction the trajectories vary significantly.
4. Notably higher dispersion of spectral displacements (as well as higher displacement demand) along the longitudinal (z) direction exists for the bare configuration of the Napoli archetype when compared with its infilled twin the median floor response spectrum of which demonstrates higher spectral acceleration peaks as compared to the bare structure.
5. Significantly lower spectral acceleration and displacement values for the infilled iteration of the L'Aquila archetype is observed along the longitudinal z-direction for both SLS and ULS limit states.

REFERENCES

[1] Ameli, M. J., Parks, J. E., Brown, D. N., & Pantelides, C. P. (2015). Seismic evaluation of grouted splice sleeve connections for reinforced precast concrete column–to–cap beam joints in accelerated bridge construction. PCI Journal, 60(2), 80–103. https://doi.org/10.15554/pcij.03012015.80.103

[2] Ancheta, T. D., Darragh, R. B., Stewart, J. P., Seyhan, E., Silva, W. J., Chiou, B. S. J., Wooddell, K. E., Graves, R. W., Kottke, A. R., Boore, D. M., et al. (2014). NGA-West2 database. Earthquake Spectra 30 (3):989–1005. https://doi.org/10.1193/070913EQS197M

[2] Babič, A., & Dolšek, M. (2016). Seismic fragility functions of industrial precast building classes. Engineering Structures, 118, 357–370. https://doi.org/10.1016/j.engstruct.2016.03.069

[3] Batalha, N., Rodrigues, H., & Varum, H. (2019). Seismic performance of RC precast industrial buildings—learning with the past earthquakes. Innovative Infrastructure Solutions, 4(1), 4. https://doi.org/10.1007/s41062-018-0191-y

[4] Beilic, D., Casotto, C., Nascimbene, R., Cicola, D., & Rodrigues, D. (2017). Seismic fragility curves of single storey RC precast structures by comparing different Italian codes. Earthquakes and Structures, 12(3), 359–374. https://doi.org/10.12989/eas.2017.12.3.359

[5] Belleri, A., Brunesi, E., Nascimbene, R., Pagani, M., & Riva, P. (2015). Seismic Performance of Precast Industrial Facilities Following Major Earthquakes in the Italian Territory. Journal of Performance of Constructed Facilities, 29(5). https://doi.org/10.1061/(ASCE)CF.1943-5509.0000617

[6] Belleri, A., Torquati, M., Marini, A., & Riva, P. (2016). Horizontal cladding panels: in-plane seismic performance in precast concrete buildings. Bulletin of Earthquake Engineering, 14(4), 1103–1129. https://doi.org/10.1007/s10518-015-9861-8

[7] Bellotti, D., Cavalieri, F., & Nascimbene, R. (2025). Classification of Italian precast concrete structures. Journal of Building Engineering, 108, 112787. https://doi.org/10.1016/j.jobe.2025.112787

[8] Biondini, F., Dal Lago, B., & Toniolo, G. (2013). Role of wall panel connections on the seismic performance of precast structures. Bulletin of Earthquake Engineering, 11(4), 1061–1081. https://doi.org/10.1007/s10518-012-9418-z

[9] Biondini, F., Palermo, A., & Toniolo, G. (2011). Seismic performance of concrete structures exposed to corrosion: case studies of low-rise precast buildings. Structure and Infrastructure Engineering, 7(1–2), 109–119. https://doi.org/10.1080/15732471003588437

[10] Blandón, J. J., & Rodríguez, M. E. (2005). Behavior of Connections and Floor Diaphragms in Seismic-Resisting Precast Concrete Buildings. PCI Journal, 50(2), 56–75. https://doi.org/10.15554/pcij.03012005.56.75

[11] Bosio, M., Belleri, A., Riva, P., & Marini, A. (2020). Displacement-Based Simplified Seismic Loss Assessment of Italian Precast Buildings. Journal of Earthquake Engineering, 24(sup1), 60–81. https://doi.org/10.1080/13632469.2020.1724215

[12] Bosio, M., di Salvatore, C., Bellotti, D., Capacci, L., Belleri, A., Piccolo, V., Cavalieri, F., Lago, B. D., Riva, P., Magliulo, G., Nascimbene, R., & Biondini, F. (2023). Modelling and Seismic Response Analysis of Non-residential Single-storey Existing Precast Buildings in Italy. Journal of Earthquake Engineering, 27(4), 1047–1068. https://doi.org/10.1080/13632469.2022.2033364

[13] Bournas, D. A., Negro, P., & Taucer, F. F. (2014). Performance of industrial buildings during the Emilia earthquakes in Northern Italy and recommendations for their strengthening. Bulletin of Earthquake Engineering, 12(5), 2383–2404. https://doi.org/10.1007/s10518-013-9466-z

[14] Bovo, M., & Savoia, M. (2018). Numerical Simulation of Seismic-Induced Failure of a Precast Structure during the Emilia Earthquake. Journal of Performance of Constructed Facilities, 32(1). https://doi.org/10.1061/(ASCE)CF.1943-5509.0001086

[15] Bressanelli, M. E., Bellotti, D., Belleri, A., Cavalieri, F., Riva, P., & Nascimbene, R. (2021). Influence of Modelling Assumptions on the Seismic Risk of Industrial Precast Concrete Structures. Frontiers in Built Environment, 7. https://doi.org/10.3389/fbuil.2021.629956

[16] Brunesi, E., & Nascimbene, R. (2017). Experimental and numerical investigation of the seismic response of precast wall connections. Bulletin of Earthquake Engineering, 15(12), 5511–5550. https://doi.org/10.1007/s10518-017-0166-y

[17] Brunesi, E., Nascimbene, R., Bolognini, D., & Bellotti, D. (2015). Experimental investigation of the cyclic response of reinforced precast concrete framed structures. PCI Journal, 60(2), 57–79. https://doi.org/10.15554/pcij.03012015.57.79

[18] Brunesi, E., Nascimbene, R., & Peloso, S. (2020). Evaluation of the Seismic Response of Precast Wall Connections: Experimental Observations and Numerical Modeling. Journal of Earthquake Engineering, 24(7), 1057–1082. https://doi.org/10.1080/13632469.2018.1469440

[19] Casotto, C., Silva, V., Crowley, H., Nascimbene, R., & Pinho, R. (2015). Seismic fragility of Italian RC precast industrial structures. Engineering Structures, 94, 122–136. https://doi.org/10.1016/j.engstruct.2015.02.034

[20] Cavalieri, F., Bellotti, D., & Nascimbene, R. (2023). Seismic vulnerability of existing precast buildings with frictional beam-to-column connections, including treatment of epistemic uncertainty. Bulletin of Earthquake Engineering, 21(2), 1117–1138. https://doi.org/10.1007/s10518-022-01574-x

[21] Crisafulli, F. J., Restrepo, J. I., & Park, R. (2002). Seismic Design of Lightly Reinforced Precast Concrete Rectangular Wall Panels. PCI Journal, 47(4), 104–121. https://doi.org/10.15554/pcij.07012002.104.121

[22] Deyanova, M., Bellotti, D., Nascimbene, R., & Pampanin, S. (2023). Performance-based assessment of slender reinforced concrete columns typical of precast industrial buildings. Bulletin of Earthquake Engineering, 21(1), 433–471. https://doi.org/10.1007/s10518-022-01542-5

[23] Ercolino, M., Bellotti, D., Magliulo, G., & Nascimbene, R. (2018). Vulnerability analysis of industrial RC precast buildings designed according to modern seismic codes. Engineering Structures, 158, 67–78. https://doi.org/10.1016/j.engstruct.2017.12.005

[24] Ercolino, M., Magliulo, G., & Manfredi, G. (2016). Failure of a precast RC building due to Emilia-Romagna earthquakes. Engineering Structures, 118, 262–273. https://doi.org/10.1016/j.engstruct.2016.03.054

[25] Ercolino, M., Magliulo, G., & Manfredi, G. (2018). Seismic Performance of Single-Story Precast Buildings: Effect of Cladding Panels. Journal of Structural Engineering, 144(9). https://doi.org/10.1061/(ASCE)ST.1943-541X.0002114

[26] Ercolino, M., Petrone, C., Magliulo, G., & Manfredi, G. (2018). Seismic Design of Single-Story Precast Structures for P -Δ Effects. ACI Structural Journal, 115(4). https://doi.org/10.14359/51701915

[27] Iervolino, I., A. Spillatura, and P. Bazzurro. (2018). Seismic reliability of code-conforming Italian buildings. Journal of Earthquake Engineering 22 (sup2): 5–27. https://doi.org/10.1080/13632469.2018.1540372

[28] Jayaram, N., Lin, T., Baker, J.W. (2011). A computationally efficient ground-motion selection algorithm for matching a target response spectrum mean and variance. Earthquake Spectra, 27(3): 797-815. https://doi.org/10.1193/1.3608002

[29] Kurama, Y. C., Sritharan, S., Fleischman, R. B., Restrepo, J. I., Henry, R. S., Cleland, N. M., Ghosh, S. K., & Bonelli, P. (2018). Seismic-Resistant Precast Concrete Structures: State of the Art. Journal of Structural Engineering, 144(4). https://doi.org/10.1061/(ASCE)ST.1943-541X.0001972

[30] Luzi, L., S. Hailemikael, D. Bindi, F. Pacor, F. Mele, and F. Sabetta. (2008). ITACA (Italian AC celerometric archive): A web portal for the dissemination of Italian strong-motion data. Seismological Research Letters 79 (5):716–22. https://doi.org/10.1785/gssrl.79.5.716

[31] Magliulo, G., Capozzi, V. , Fabbrocino, G., and Manfredi, G. (2011). Neoprene–concrete friction relationships for seismic assessment of existing precast buildings. Engineering Structures 33 (2): 532–38. https://doi.org/10.1016/j.engstruct.2010.11.011

[32] Magliulo, G., Bellotti, D., Cimmino, M., & Nascimbene, R. (2018). Modeling and Seismic Response Analysis of RC Precast Italian Code-Conforming Buildings. Journal of Earthquake Engineering, 22(sup2), 140–167. https://doi.org/10.1080/13632469.2018.1531093

[33] Magliulo, G., Ercolino, M., Petrone, C., Coppola, O., & Manfredi, G. (2014). The Emilia Earthquake: Seismic Performance of Precast Reinforced Concrete Buildings. Earthquake Spectra, 30(2), 891–912. https://doi.org/10.1193/091012EQS285M

[34] Matteini, I., Coccimiglio, S., Scussolini, L., Ceravolo, R., Chiorino, M. A., & Ferro, G. A. (2024). An historical research on the development and application of prestressed concrete in Italy. Procedia Structural Integrity, 62, 738–746. https://doi.org/10.1016/j.prostr.2024.09.101

[35] Minghini, F., Ongaretto, E., Ligabue, V., Savoia, M., & Tullini, N. (2016). Observational failure analysis of precast buildings after the 2012 Emilia earthquakes. Earthquakes and Structures, 11(2), 327–346. https://doi.org/10.12989/eas.2016.11.2.327

[36] Mazzoni, S., McKenna, F., Scott, M.H., Fenves, G.L. (2006) OpenSees Command Language Manual, Pacific Earthquake Engineering Research (PEER) Center, Berkeley, California, USA; 2006.

[37] Rossetto, T., Verrucci, E., Alexander, D., Ioannou, I., Borg, R., Melo, J., Cahill, B., & Kongar, I. (2012). The 20th May 2012 Emilia-Romagna earthquake - EPICentre field observation report.

[38] Savoia, M., Buratti, N., & Vincenzi, L. (2017). Damage and collapses in industrial precast buildings after the 2012 Emilia earthquake. Engineering Structures, 137, 162–180. https://doi.org/10.1016/j.engstruct.2017.01.059

[39] Toniolo, G., & Colombo, A. (2012). Precast concrete structures: the lessons learned from the L'Aquila earthquake. Structural Concrete, 13(2), 73–83. https://doi.org/10.1002/suco.201100052

Myanmar Earthquake Reconnaissance: Damage to Non-Structural Elements in High-rise Buildings in Bangkok

Jitendra Bhatta[1], Andrew Baird[2], Catalina Miranda[3], Jitendra Bothara[4], Lucas Hogan[5], Andrew Stolte[6], Chungwook Sim[7], Sutat Leelataviwat[8], and Amorn Pimanmas[9]

[1] Postdoctoral Fellow, University of Canterbury, New Zealand, jitendra.bhatta@canterbury.ac.nz
[2] Associate Engineer, Beca Ltd, New Zealand, andrew.baird@beca.com
[3] Lecturer, Joint Center for Disaster Research, Massey University, New Zealand, c.miranda1@massey.ac.nz
[4]Director, Resipro International Engineering Ltd, jitendra.bothara@gmail.com
[5,6]Lecturer, University of Auckland, New Zealand, {andrew.stolte, lucas.hogan}@auckland.ac.nz
[7]Associate Professor, Konkuk University, Korea, csim@konkuk.ac.kr
[8]Professor, King Mongkut's University of Technology Thonburi, Thailand, sutat.lee@kmutt.ac.th
[9]Professor, Kasetsart University, Thailand, amorn.pi@ku.ac.th

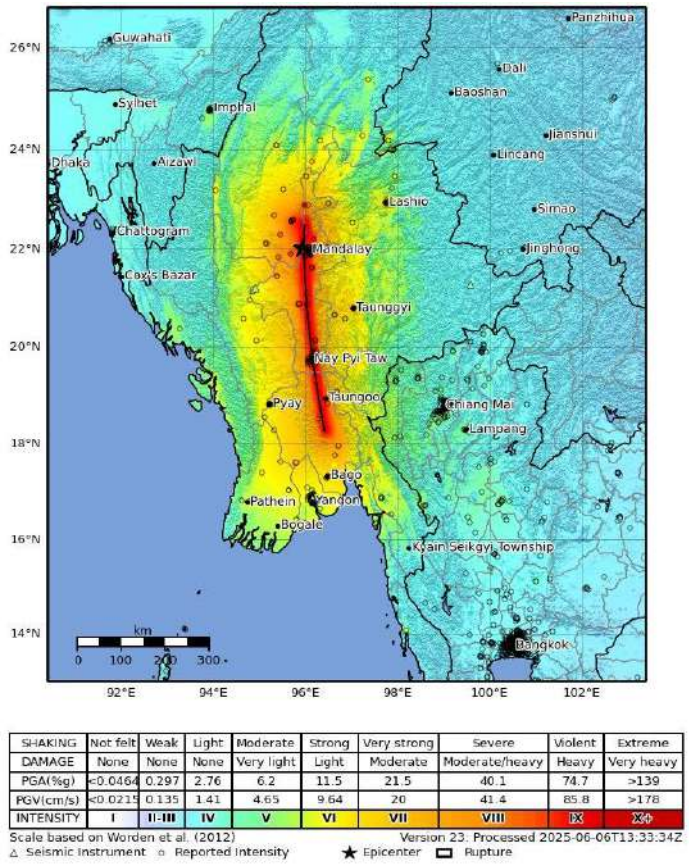
Abstract

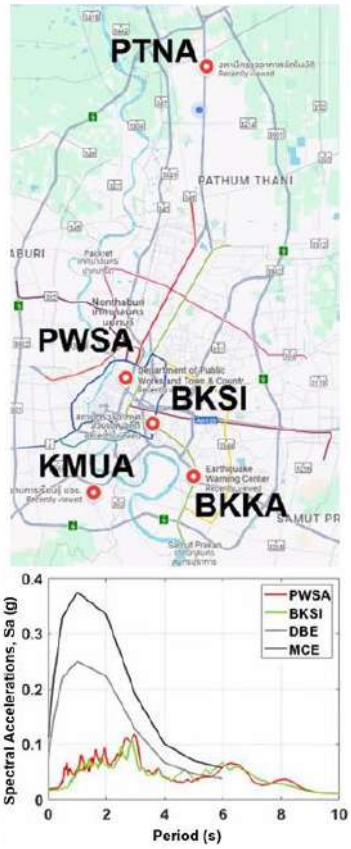
This paper investigates the performance of non-structural elements (NSEs) in high-rise buildings in Bangkok following the 28 March 2025 Mandalay earthquake, Myanmar. Widespread NSE damage was observed during a post-earthquake reconnaissance of 10 buildings, conducted approximately 2.5 months after the event. The reconnaissance included high-rise buildings of various occupancy types, including residential, commercial, and hospital. While damage to structural systems was generally minor, damage to infill walls, ceilings, tiles, glazing, and building services was observed. Most of the non-structural damage was drift-related, with damage to masonry infill partitions featuring prominently. Based on the recorded spectrum and period elongation, the estimated code-based inter-story drifts for the inspected high-rises (25-79 stories) ranged from 0.24% to 0.48%. Damage to other architectural elements such as ceilings and floor tiles was also observed. Building services were less disrupted, with most systems remaining functional immediately following the earthquake. Key findings reveal that 70% of surveyed buildings experienced elevator malfunctions, while recurring NSE damage patterns were observed at mid-height stories (typically between the 8th and 20th stories) likely due to increased inter-storey drifts. Localized concentrations of damage were observed in buildings with structural irregularities such as vertical setbacks or water tanks. These observations demonstrate that even in low seismic regions like Bangkok, NSE vulnerability is evident. This highlights opportunities to enhance design and construction method, particularly by addressing drift-induced vulnerabilities to enhance building resilience and recovery times.

Keywords: Mandalay Earthquake, Bangkok Earthquake Reconnaissance, Seismic Performance, Non-structural Elements, High-rise Buildings

1.INTRODUCTION

On March 28, 2025, a powerful 7.7 Mw earthquake struck Myanmar, with its epicenter near Mandalay along the Sagaing Fault (USGS, 2025), as shown in Figure 1a. Due to its shallow depth of around 10 km (6.2 miles), intense ground shaking resulted in significant destruction and loss of life in the affected region (Laosunthara et al., 2025). Although the epicenter was roughly 1,000 km northwest of Bangkok (capital city of Thailand), the city still experienced long-period ground motion, likely amplified by underlying soft soil conditions. Consequently, even at low peak ground accelerations (~0.02 g), buildings with natural periods exceeding 5 seconds (equivalent to roughly 50 stories or taller) experienced spectral accelerations surpassing the design response spectra derived from (DPT, 2019) for the Design Basis Earthquake (DBE) (and in some cases, even the Maximum Considered Earthquake (MCE)) at both 5% and 2.5% damping ratios as shown in Figure 1b (Warnitchai et al., 2025). Although Thailand is not located near a major tectonic boundary, it has experienced destructive earthquakes in the past, such as the 2014 Mae Lao Earthquake (6.2 Mw) in Chiang Rai Province. (Ornthammarath & Warnitchai, 2016).





a) Map showing location of epicenter and intensity of the 2025 Myanmar Earthquake (USGS, 2025)

b) DBE and MCE design vs. actual response spectrum from the recording stations shown in the map (Warnitchai et al., 2025)

Figure 1. Location, intensity and response spectrum of 2025 Myanmar Earthquake in Bangkok, Thailand

In Bangkok, most high-rise structures (such as condominiums, apartments, and office towers) are built using reinforced concrete (RC) frame and shear (or core) wall systems with post-stressed slabs. Thailand has a national building code which includes design provisions for seismic hazards (DPT, 2019; Poovarodom et al., 2018). Following the 28th of March 2025 Mandalay Earthquake, the Department of Public Works and

Town and Country Planning (DPT) initiated a nationwide inspection of public buildings, assessing their structural safety and usability. Buildings were classified into three damage categories: Green (safe for use), Yellow (moderate damage, usable with restrictions), and Red (severe structural damage, unsafe for occupancy) (Bangkok Post, 2025b). Despite Bangkok's distance from the epicenter, one under-construction building intended for State Audit Office collapsed, (Bangkok Post, 2025a), some high-rise buildings suffered damage to structural components (e.g., columns, shear walls) and non-structural elements (NSEs) (Laosunthara et al., 2025). This aligned with observations from the 2014 Mae Lao Earthquake, where extensive non-structural damage to glazing, ceilings, infill walls, and building contents was observed in Chiang Rai Province (Ornthammarath & Warnitchai, 2016; Ornthammarath & Puavaranukroh, 2018). NSEs, such as suspended ceilings, cladding and glazing systems, internal partitions/infill walls, doors, windows, chimneys, parapets, equipment, furnishings, sprinkler piping systems, and other building services, are vital for building functionality and contribute significantly to construction costs (ATC-69, 2009; FEMA74-FM, 2005; Taghavi & Miranda, 2003). Past earthquakes, worldwide, have shown that NSE damage often leads to higher financial losses than structural damage, due to repair expenses and operational disruptions (Bachman, 2004; Filiatrault, 2002; Ornthammarath & Puavaranukroh, 2018).

In response to the earthquake's impact on Bangkok's high-rise buildings, a multidisciplinary reconnaissance team from New Zealand was deployed with three key objectives (i) Site-specific ground motion analysis using broadband seismometers to enhance future seismic hazard assessments, (ii) Functional recovery surveys to evaluate the operational status and recovery timelines of critical building systems, and (iii) Systematic damage inspection and documentation of both structural and non-structural damage. This study presents preliminary findings from the reconnaissance mission conducted 2.5 months post-earthquake (June 11-17), specifically examining the extent and patterns of NSE damage in Bangkok's high-rise buildings. The timing allowed for assessment of both immediate impacts and early-stage recovery efforts, while providing deeper technical insights into NSE vulnerabilities.

2.METHODOLOGY

The reconnaissance study focused on high-rise buildings in central Bangkok and its surrounding areas. In collaboration with Thai partners (including academics, structural engineers and graduate students), the team investigated 10 buildings that included four buildings that were known to have structural damage (see Table 1). The investigated buildings include commercial, residential, hospital, and mixed-use structures. All inspected structures were constructed using reinforced concrete frame systems other than one building, consistent with typical construction practices in the region. All buildings had shear walls as primary lateral resisting structural system. The reconnaissance team conducted systematic visual inspections to document earthquake-induced damage to both structural and NSEs. All observed damage was photographically recorded for detailed analysis. The assessment also included well-performing buildings to identify effective seismic-resistant design features and construction practices that contributed to their resilience.

3.STRUCTURAL AND NON-STRUCTURAL ELEMENTS TYPOLOGIES IN INSPECTED BUILDINGS

3.1 FEATURES OF STRUCTURAL SYSTEMS OF INVESTIGATED BUILDINGS

Several features of the structural system of the investigated buildings (Table 1). RC core wall systems dominate (80 % of cases), particularly in commercial (C1, C2, C3) and older residential (R2, 1993) buildings, while newer constructions (post-2020) adopt hybrid systems, such as steel-concrete composites (C4). Similarly, hospitals seem to prioritize buildings with 11 to 25 stories with mixed systems; residential buildings

span the oldest (1993) and newest (2025) builds, ranging between 30 to 45 stories; and commercial towers escalate in height (up to 61 stories), with one steel-concrete hybrid (building C4). The increased use of high-strength concrete since the early 2000s may have allowed for slimmer structural sections, leading to more flexible buildings compared to pre-2000 structures. Additionally, the widespread adoption of structural analysis software from the mid-2000s may have facilitated the design of more refined structural systems. This shift also suggests possible variations in code requirements and construction standards over time, though core walls remain prevalent for lateral stability in high-rise buildings.

Table 1. List of inspected buildings

Building ID*	Usage/occupancy Type	Primary Structural system	Year of Construction	Number of Storeys
H1	Hospital	Reinforced Concrete (RC) Frame with post-tensioned flat slab and RC walls on four corners	2019	25
H2	Hospital	RC, core walls on the four corners	Under construction	11
R1	Residential	RC walls with post-tensioned (PT) flat slab	2025	45
R2	Residential	RC, core walls (with vertical setbacks)	1993	45
R3	Residential	RC, flat slab with band beams, core walls	2006	30
R4	Mixed Use - Residential, Hotel, Convention	RC, shear core with outrigger and PT slab	2011	79
C1	Commercial	RC, core walls	2024	47
C2	Commercial	RC, core walls	1995	32
C3	Commercial	RC, core walls	2023	61
C4	Commercial	RC+Steel (Concrete Filled Tubes)	2020	30

*Building names have been anonymised to conceal their identity.

3.2 NON-STRUCTURAL ELEMENTS

This section describes the non-structural elements typology in the inspected buildings.

3.2.1 Infill Wall Types

Aerated and hollow concrete blocks, typically 75 mm thick with cement-sand plaster on both faces, are the predominant infill materials in buildings constructed post-2000 (e.g., buildings H1, H2, R3, C3), while clay bricks are more commonly found in buildings-built pre-2000 (e.g., buildings R2 and C2). The most recently constructed residential building, R1 (2025), incorporates wire-mesh reinforced plaster of masonry infills, suggesting improved seismic detailing. Likewise, building C4 features modern drywall construction with cold-formed steel framing lined with plasterboards, a system commonly used in commercial buildings in countries like the United States and New Zealand. Figure 2 shows photos of infill walls constructed in buildings H1 and H2.

3.2.2 Ceiling Systems

The concealed plasterboard ceilings are nearly ubiquitous (80 % of the inspected buildings), particularly in residential and hospital buildings, whereas grid-and-tile ceilings appear in wet areas (such as in building H1 washrooms) and acoustically sensitive spaces (building C3).



Figure 2. Photo of 75 mm thick hollow brick and masonry infill walls in buildings H1 and H2 (typical)



Figure 3. Photo of installed mechanical services without bracing in building H2 (typical)

3.2.3 Mechanical Services

Although detailed mechanical service installations were only explicitly documented in buildings H1 and H2, field observations and local practice indicate that suspended mechanical systems in most Bangkok high-rise buildings typically employ simple hangers or trapeze supports without seismic bracing. This conventional installation approach might reflect Thailand's historical perception of low seismic risk. Representative examples of these unbraced mechanical service installations in buildings H1 and H2 are shown in Figure 3.

3.2.4 Cladding systems

The cladding systems in all inspected commercial buildings (C1, C2, C3, and C4) and the mixed-use building R4 primarily consisted of glazing systems (curtain walls). Additionally, Building C4 featured precast concrete cladding panels with 'rocking' details with similar concept as tested by Bhatta et al. (2022, 2023a, 2023b) alongside the glazing system.

4.OBSERVED DAMAGE TO NON-STRUCTURAL ELEMENTS

This section documents the observed damage to non-structural elements across the surveyed buildings.

4.1 INFILL WALLS (MOST VULNERABLE NSE COMPONENT)

The infill walls emerged as the most vulnerable NSE component across all buildings. Severe cracking consistently occurred at interfaces with structural elements, particularly around door openings and at slab connections, as seen in buildings R1 (8^{th} and 9^{th} stories) and C2 (10^{th} and 20^{th} stories). The damage patterns revealed height-dependent vulnerability, with mid-height stories (8^{th} to 15^{th} stories in building R3, above 57^{th} storey in building R4) showing concentrated damage. Material performance varied significantly where traditional clay brick infills (in building R2) exhibited brittle failure at building setbacks, while modern cold-formed steel infills (in building C4) demonstrated superior performance with only minor cracking at the interface of structural walls and infills. However, newer buildings using lighter but brittle materials (e.g., aerated blocks) still suffered cracking, suggesting the need for improved seismic detailing. The vertical setback at the 14^{th} floor of building R2 created a stiffness discontinuity that exacerbated exterior wall damage, highlighting how architectural features can amplify seismic vulnerability. Overall, damage was especially prominent at the interface between infill walls and structural elements, indicating deformation incompatibility, stress concentrations and insufficient detailing at these junctions. Typical damage to infill walls is shown in Figure 4.



a) Minor damage to masonry wall, building H1



b) Severe damage to concrete block masonry external infill wall, building R2



c) Severe damage to concrete block masonry infill wall, building C2

Figure 4. Photos showing typical damage observed in infill walls

4.2 CEILING AND INTERIOR FINISHES DAMAGE

Plasterboard ceiling (prevalent in 80% of buildings) showed consistent damage at perimeters (at wall interfaces) (for e.g. in buildings H1, R2, and C2) whereas grid-and-tile ceilings were less commonly reported as damaged (only tile displacement was observed in building H1). The damage severity correlated with building height, with mid-height stories experiencing more pronounced cracking, perhaps due to greater drift demands. The wall-to-ceiling interfaces are observed to be recurring weak points, possibly indicating inadequate edge detailing. Typical damage to ceilings is shown in Figure 5.



a) Dislodgement of ceiling tiles in a grid-and-tile ceiling system, building H1



b) Minor damage to plasterboard ceiling, building C2



c) Moderate damage to plasterboard ceiling, building R2

Figure 5. Photos showing typical damage observed in ceilings

4.3 MECHANICAL AND PLUMBING SERVICES

Mechanical services revealed almost no damage and most of them remained functional. Sprinkler pipe interactions caused wall damage in building R1. Water pipework damage led to rebar corrosion and the shutdown of water supply to affected taps in building R3 (in 5th and 6th stories). Although, ejection of sprinkler escutcheons (in building H1) is considered as minor damage it indicates possible interaction between sprinkler heads and adjacent ceiling. There was swimming pool surge tank leakage in building R3 and water tank damage in building R4. Typical damage to mechanical and plumbing services is shown in Figure 6.



a) Falling of sprinkler escutcheons, building H1



b) Water supply shutdown to the tap due to pipe damage, building R3



c) Location of water leakage from surge tanks of swimming pools due to joint cracks, building R3

Figure 6. Photos showing typical damage observed to mechanical and plumbing services

4.4 FLOOR AND WALL TILES

Minor to moderate cracking of ceramic tiles was reported in multiple buildings (e.g., building H1, R3, C3), affecting both floors and wall finishes. Ceramic and granite tiles showed uplift and detachment (e.g., buildings R2 at 39th floor and C3). The upper floors demonstrated greater tile damage, likely due, local deformation or differential movement between structural elements and finishes. In buildings C2 and C3, granite tiles detached and fell, posing potential safety hazards. It is a possible indication of poor anchorage or bonding of the tiles to the substrate. Typical damage to floor and wall tiles is shown in Figure 7.

4.5 CLADDING AND GLAZING SYSTEM DAMAGE

Cladding and glazing systems were damaged in several buildings (e.g., in buildings C2, C3), where the damage was mostly concentrated at the interfaces between cladding and structure. In building H1, windows were seen with dislodged gaskets while broken cladding seals had led to water leakage in building R3. In contrast rocking concrete cladding system and modern unitized systems (in building C4) performed better. As such, cladding performance varied significantly between buildings. Typical damage to windows is shown in Figure 8.



a) Minor damage to floor tiles, building H1



b) Minor damage to floor tiles, building R3



b) Fallen tiles from walls, building C2

Figure 7. Photos showing typical damage observed to floor and wall tiles

4.6 ACCESS ISSUES

Jammed doors (in building R1) and damaged glass door (in building C3) lateral deformation in buildings. Moreover, 70% of the 10 inspected buildings, spanning residential, commercial, and hospital occupancies, experienced at least one elevator becoming non-operational following the earthquake. This recurring issue suggests that elevator systems may be particularly vulnerable to seismic shaking, even in cases where structural damage was minimal. Typical damage to door frames and glass doors is shown in Figure 9.



Figure 8. Dislodgement of window gasket, building H1



a) Severe damage to door frame, building R1



b) Damaged glass door, building C3

Figure 9. Photos showing typical damage to doors

4.7 DAMAGE PATTERN ACROSS BUILDING HEIGHTS AND VERTICAL IRREGULARITIES

The damage distribution revealed possible vertical trends, with mid-height stories (8^{th} to 20^{th}) showing the most extensive NSE damage across multiple buildings (R1, R3, C2). These stories, perhaps, correspond with peak inter-storey drift ratios in many high-rise buildings, where flexible modes of vibration result in larger relative displacements between floors. Vertical irregularities, like building R2's 14^{th} floor setback, created localized damage concentrations, suggesting that geometric and stiffness discontinuities cause higher deformation incompatibilities resulting in local overstress in NSEs. Building R3 also showed significant damage around the 5^{th} and 6^{th} stories, which housed plumbing, water systems, and a swimming pool surge tank. It indicates that mechanical rooms, typically located in podiums or mid-height, can suffer secondary damage due to system failure or water leakage. These patterns also confirm that seismic demands can vary significantly along building height, which can be further exacerbated by mass and geometric irregularities both vertically and in plan. Moreover, preliminary observations suggest that inspected buildings with a higher wall-to-floor area ratio sustained lesser damage as compared with buildings having lower higher wall-to-floor area ratio.

5.CODE-BASED BUILDING DRIFT ESTIMATION

A simplified methodology was employed based on recorded spectrum and established building dynamics to calculate a rough estimate of inter-story drifts for the inspected tall buildings in Bangkok. The initial period (T) for a building is defined by the Thailand code (DPT, 2019) as T=0.02H, where, H is the height of the building. Accounting for inelastic behavior during seismic events, this period is elongated by a factor of 1.3,

leading to an effective period of (T_e) =1.3T. The roof drift was then approximated as 1.5 times the spectral displacement (S_d) corresponding to this effective period T_e, i.e., $\delta_{roof} = 1.5S_d/H=1.5S_{amax}(T_e/(2\pi))^2/H$, where S_{amax} is the maximum spectral acceleration from the recorded spectrum (see Figure 1b), irrespective of the location of the building. Finally, the inter-story drift (δ_{max}) was estimated to be 1.5 times the calculated roof drift i.e., $\delta_{max} = 1.5\delta_{roof}$. Applying this procedure yielded an estimated range of inter-story drifts from 0.24% to 0.48% for buildings ranging from 25 to 79 stories tall (100 to 316 m tall, assuming 4 m storey height), as shown in Figure 10.

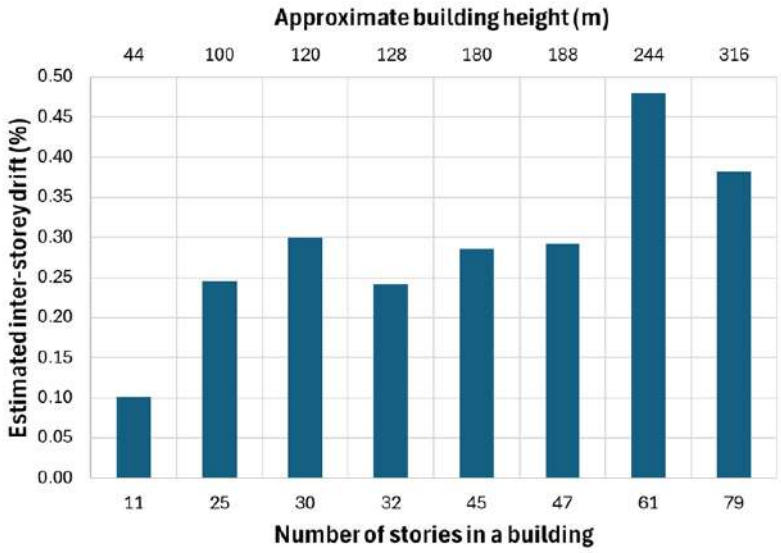


Figure 10. Estimated inter-storey drifts in the inspected buildings

6.CONCLUSIONS

The post-earthquake reconnaissance of high-rise buildings in Bangkok following the 2025 Mandalay earthquake suggest that while structural systems generally performed well, non-structural elements experienced widespread and diverse damage, primarily due to building drifts, despite low regional seismicity. The estimated code-based inter-story drifts for the inspected high-rise buildings (ranging from 25 to 79 stories), derived from recorded spectrum also considering for period elongation, were between 0.24% and 0.48%. The most prevalent damage occurred in infill walls and architectural finishes, with recurring failure patterns observed at component interfaces and mid-height building levels (typically between 8th to 20th storey). Additional damage to some ceiling systems, water plumbing services and cracking/dislodgement of tiles were also observed. Furthermore, damage was more prevalant near structural irregularities such as vertical setbacks or at levels with complex structural systems, e.g. those housing mechanical systems, pools or water tanks (with larger mass), suggesting that these zones may be susceptible to both drift and acceleration effects. Notably, 70% of inspected buildings experienced elevator malfunctions, underscoring the operational consequences of non-structural damage.

The widespread non-structural damage across all building types and ages, suggests that non-structural performance may not yet a core focus in design and construction in a low seismicity context like in Bangkok. However, the findings point to potential opportunities to enhance design and construction methods of non-structural elements in Thailand's buildings. Some constructive steps might include, though not exhaustive, (i) considering drift-compatible connections between infill walls (and partitions) with structure, (ii) developing ways for ceilings and finishes to accommodate seismic demands on buildings, (iii) implementing

performance-based criteria for functional recovery of critical buildings, and (iv) lowering inter-storey drift allowances for high-risk buildings with infills. The good performance of some modern systems with seismic-compatible detailing, such as rocking cladding panels, showed promising performance compared to conventional methods, offering useful insights for future design enhancements. This event serves as a crucial wake-up call for Thailand and other low-seismicity regions to upgrade building codes and construction practices for high-rises against similar seismic events.

ACKNOWLEDGEMENTS

We extend our sincere gratitude to the many engineers, academics, and students in Bangkok who generously hosted our reconnaissance mission and provided access to critical sites. This work was made possible through the support of the Natural Hazards Commission - Toka Tū Ake, QuakeCoRE, and the New Zealand Society for Earthquake Engineering. This project was partially supported by QuakeCoRE, a New Zealand Tertiary Education Commission-funded Centre. This is QuakeCoRE publication number 1088. Thanks for continuing to support learning from earthquake missions.

REFERENCES

ATC-69. (2009). Reducing the risks of nonstructural earthquake damage, state-of-the-art, and practice report. Applied Technology Council for the Federal Emergency Management Agency in Cooperation with the National Earthquake Hazard Reduction Program,

Bachman, R. E. (2004). The ATC-58 project plan for nonstructural components. Paper presented at the Performance-Based Seismic Design: Concepts and Implementation, Proceedings of the International Workshop, Bled, Slovenia, 28 June–1 July 2004,

Bangkok Post. (2025a, 28 March). Dozens of workers trapped in collapsed Bangkok high-rise. https://www.bangkokpost.com/thailand/general/2989962/dozens-of-workers-trapped-in-collapsed-bangkok-high-rise

Bangkok Post. (2025b, 2 April). National checks find 34 buildings badly damaged. Bangkok Post https://www.bangkokpost.com/thailand/general/2993976/national-checks-find-34-buildings-badly-damaged

Bhatta, J., Dhakal, R. P., & Sullivan, T. J. (2023a). Cyclic Behaviour of two-story low-damage rocking precast concrete cladding panel system. Journal of Earthquake Engineering, 27(6), 1414–1439.

Bhatta, J., Dhakal, R. P., & Sullivan, T. J. (2023b). Seismic performance of a rocking precast concrete cladding panel system under lateral cyclic displacement demands. Journal of Earthquake Engineering, 27(4), 929–958.

Bhatta, J., Dhakal, R. P., Sullivan, T. J., & Lanyon, M. (2022). Low-damage rocking precast concrete cladding panels: Design approach and experimental validation. Journal of Earthquake Engineering, 26(9), 4387–4420.

DPT. (2019). Seismic Resistant Design of Buildings and Structures, DPT 1301/1302-61 (in Thai). Department of Public Works and Town & Country Planning.

FEMA74-FM. (2005). Earthquake Hazard Mitigation for Nonstructural Elements- Field Manual. https://mitigation.eeri.org/files/FEMA74_FieldManual.pdf

Filiatrault, A. (2002). Guidelines, specifications, and seismic performance characterization of nonstructural building components and equipment. Pacific Earthquake Engineering Research Center.

Laosunthara, A., Krutphong, K., Leelawat, N., Wararuksajja, W., Sukulthanasorn, N., Suppasri, A., Thongthip, R., & Chintanapakdee, C. (2025). Initial Observations and Immediate Lessons Learned from Thailand's Response to the 2025 Mandalay Earthquake. International Journal of Disaster Risk Reduction, 105675.

Ornthammarath, T., & Puavaranukroh, T. (2018). Observed hospital damages following the 2014 Mae Lao (Northern Thailand) earthquake: A survey report. Journal of Disaster Research, 13(4), 804–812.

Ornthammarath, T., & Warnitchai, P. (2016). 5 May 2014 MW 6.1 Mae Lao (Northern Thailand) earthquake: Interpretations of recorded ground motion and structural damage. Earthquake Spectra, 32(2), 1209–1238.

Poovarodom, N., Warnitchai, P., Ornthammarath, T., Leelataviwat, S., Panyakapo, P., Pimanmas, A., Chintanapakdee, C., & Lukkunaprasit, P. (2018). A new earthquake resistant design standard for buildings in Thailand.

Taghavi, S., & Miranda, M. M. (2003). Response assessment of nonstructural building elements. Pacific Earthquake Engineering Research Center.

USGS. (2025). M 7.7 - 2025 Mandalay, Burma (Myanmar) Earthquake ShakeMap. United States Geological Survey.

Warnitchai, P., Ornthammarath, T., & Miranda, E. (2025). Observations from the 2025 M7.7 Myanmar Earthquake: Impacts in Thailand and Engineering Implications. Paper presented at the https://www.eeri.org/what-we-offer/webinars/26458-observations-from-the-2025-m7-7-myanmar-earthquake-webinar-series

Failure Mechanisms and Pull-Out Strength of the Screw-Type Fastening Post-Installed Anchors

Kosuke Fujita [1], Shoichi Kishiki [2], and Takayuki Iijima [3]

[1] School of Environment and Society, Institute of Science Tokyo.
4259 Nagatsuta-cho, Midori-ku, Yokohama, Kanagawa, Japan
e-mail: fujita.k.9d4f@m.isct.ac.jp
[2] IIR, Institute of Science Tokyo.
4259 Nagatsuta-cho, Midori-ku, Yokohama, Kanagawa, Japan
e-mail: kishiki.s.02d9@m.isct.ac.jp
[3] Department of Development & Marketing, Japan Power Fastening Co.
20-7 Nihonbashi Hakozaki-cho, Chuo-ku, Tokyo, Japan
e-mail: t-iijima@jpf-net.co.jp

Abstract. Post-installed anchors are used in a wide range of applications, from connections of seismic retrofit for existing buildings to anchoring building equipment. Currently, post-installed anchors are classified into three types according to the anchoring method: (1) adhesive anchors, (2) mechanical anchors, and (3) other anchors. The screw-type fastening post-installed anchors are categorized as other anchors and mainly consist of an equipment mounting screw and an embedded screw. The height of these anchors can be easily adjusted, and they can be removed when no longer needed. In this study, pull-out experiments have been conducted on the screw-type fastening post-installed anchors to investigate effects of various parameters on the pull-out strength and to establish a method for strength evaluation. The experimental results indicate that the pull-out strength of the screw-type fastening post-installed anchors is determined by the engagement resistance between the embedded screw and concrete. An evaluation method for the pull-out strength was proposed by combining the bond strength and the cone-type strength, based on the observed failure mechanisms. The lower portion of the embedded threads exhibited bond-type failure, while the upper portion showed cone-type failure of the surrounding concrete.

Keywords: Post-Installed Anchor , Failure Mechanism , Pull-Out Strength , Cone Failure , Bond Failure.

1. INTRODUCTION

Post-installed anchors are commonly used for anchoring equipment and devices. "Mechanical anchors" may cause cracking or incomplete installation when the edge distance or anchor pitch is insufficient. In contrast, the screw-type fastening post-installed anchors, classified as "other anchors", are orderly installed by drilling a hole, removing debris, and threading the embedded screw into a smaller-diameter pre-drilled hole using a power tool. Then, equipment is connected by using mounting screws (Figure 1). In this study, pull-out experiments are conducted on the screw-type fastening post-installed anchors to investigate the effects of various parameters and propose an evaluation method for pull-out strength.

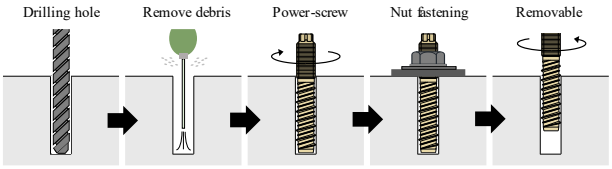


Figure 1. Installation procedure

2. EXPERIMENTAL PROGRAM

2.1 TEST PARAMETERS

In this chapter, the experimental plan is presented to investigate the effects of fundamental parameters on the pull-out strength of the screw-type fastening post-installed anchors. First, details of the test parameters and loading protocol are provided below. An overview of the test specimens with test parameters is shown in Figure 2. Each test specimen consisted of a single screw-type fastening post-installed anchor installed in a concrete block. Three types of anchors with outer thread diameters of 6.5 mm, 8.5 mm, and 10.5 mm were prepared. Since these correspond to the nominal sizes of M6, M8, and M10 equipment mounting screws, the specimens are hereafter referred to by their nominal screw size. For each nominal screw size, the diameter L of a circle inscribed around the anchor and the three reaction supports placed on the concrete surface was defined as the reaction support diameter, which was adopted as one of the experimental parameters. In addition, the embedment depth, l, measured from the concrete surface to the tip of the anchor, and the pre-drilled hole diameter, d, were varied from 15 to 75 mm and from 5.4 to 9.5 mm, respectively. The test specimens were classified into two types according to embedment depth: a standard type and a long type (Figure 3). Although the dimensions of the threaded portion of the embedded screw were the same in both types, the long type included an additional smooth section without threads between the equipment mounting screw and the embedded screw. As shown in Figure 3, the applicable embedment depth, l, was set to 15~45 mm for the standard

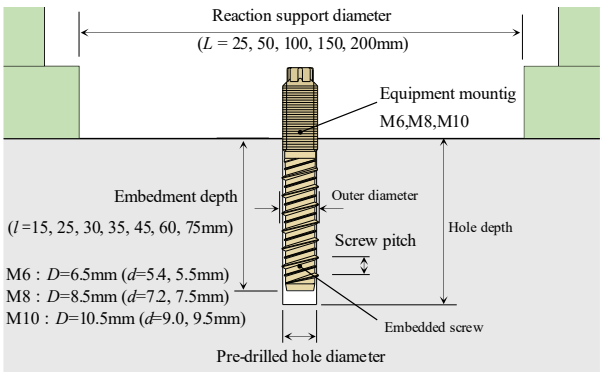


Figure 2. Overview of the Test Specimens and Parameters

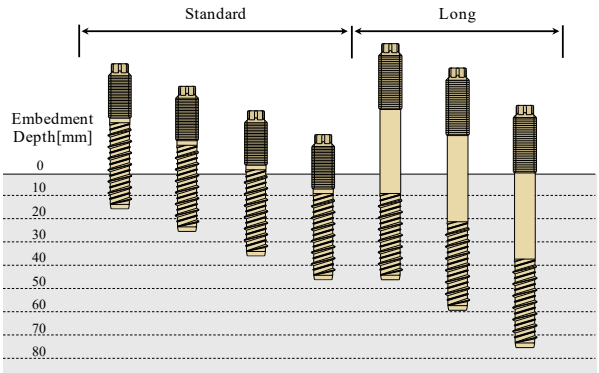


Figure 3. Relationship between the Anchors and the Embedment Depth

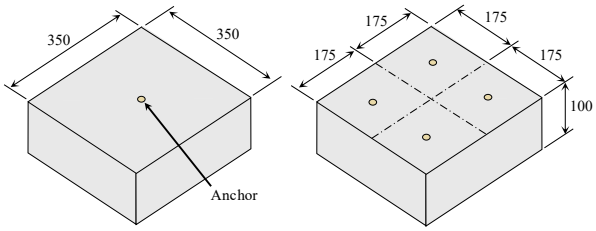


Figure 4. Installation Positions of Anchors in the Concrete Block

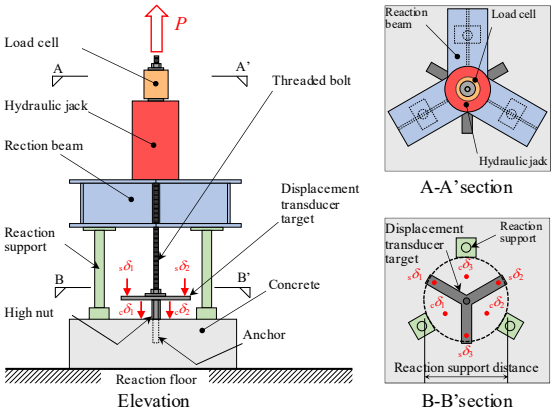


Figure 5. Setup and Measurement Plan

type and 45~75 mm for the long type. An overview of the concrete blocks used to install the anchors and the anchor installation positions is shown in Figure 4. Each concrete block was an unreinforced concrete prism with a height of 100 mm and a plan dimension of 350 × 350 mm. The anchors were installed either at the center of the block or at the centers of quartered areas, with multiple anchors placed on both sides of the block. The edge distance between anchors was ensured to be at least 87.5 mm, and anchors were not installed at the same position on both sides.

2.2 LOADING PROTOCOL

The experimental setup and measurement plan are shown in Figure 5. In the experiment, a threaded bolt was connected to the screw-type fastening post-installed anchor through a high nut, and a monotonic tensile load was applied using a hydraulic jack. The hydraulic jack was placed on a reaction beam supported by three reaction supports arranged on the concrete block, forming a self-balanced loading system. During the experiment, the applied load P was measured by a load cell installed at the top of the hydraulic jack. The deformation was measured as the relative displacement between displacement transducers placed directly above the high nut and reference points on the concrete surface, with three measurements taken from the reaction floor. For data analysis, the deformation, δ, was defined as the difference between the average values obtained from the three displacement transducers above the high nut and those on the concrete surface. Loading was continued until the maximum strength was reached and a sufficient reduction in load-carrying capacity was observed.

3. RESULTS AND DISCUSSION OF FUNDAMENTAL PARAMETERS

3.1 OVERVIEW OF THE LOAD-DEFORMATION RELATIONSHIP

This chapter presents the test results and discusses the influence of basic parameters on the maximum strength. Typical load–displacement relationships are shown in Fig. 6, where the vertical axis is the measured load, P, and the horizontal axis is the deformation, δ. The effects of (a) reaction support diameter, (b) embedment depth, and (c) pre-drilled hole diameter are compared. In the figures, the initial stiffness, K, obtained by least-squares fitting of the initial linear range is shown by a red line, while the elastic limit strength, P_e, and the maximum strength, P_{max}, are indicated by solid symbols. The elastic limit strength, P_e, is defined as the load at which the secant stiffness decreases to 90% of the initial stiffness K. In all cases, the response is initially stiff, then softening starts at around, P_e, and the load eventually reaches, P_{max}, followed by a sudden drop. At or just before/after, P_{max}, cone-shaped cracking patterns are

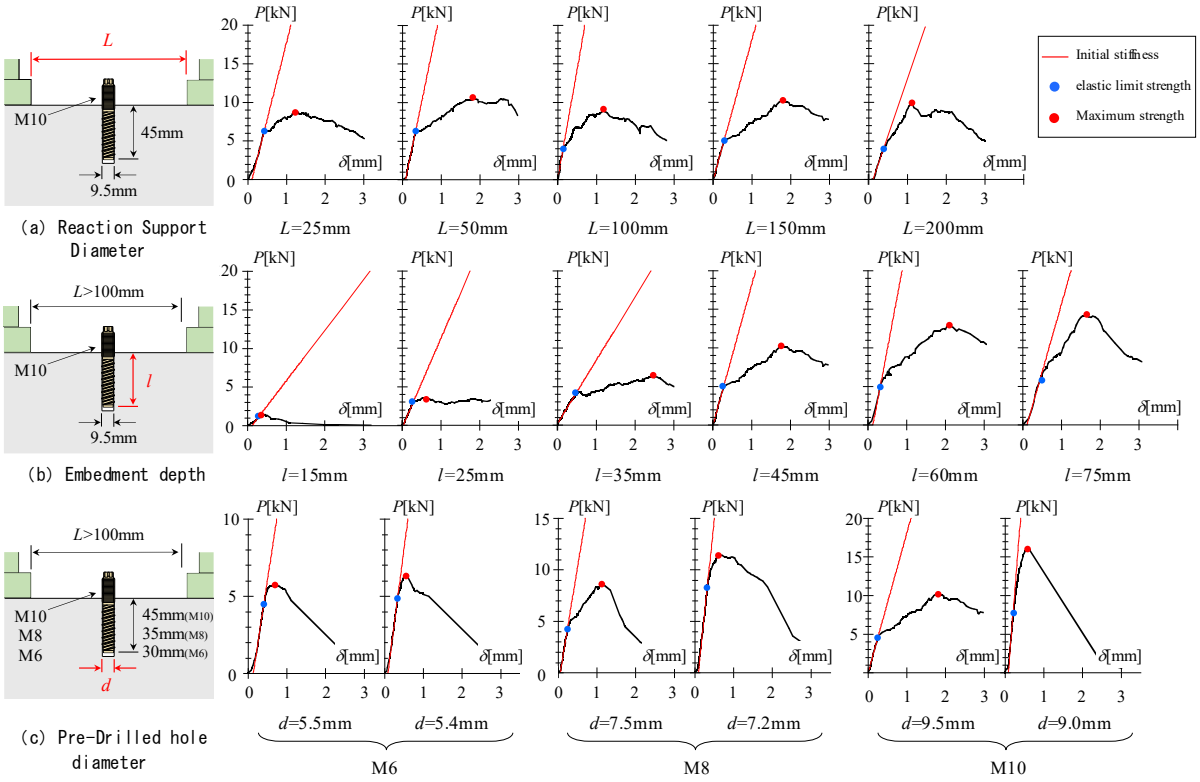


Figure 6. Load-Deformation Relationship

observed at the concrete surface around most anchors, as described later. The effect of reaction support diameter, L, (Fig. 6(a)) is very small: the initial stiffness, elastic limit strength and maximum strength are all almost insensitive to L in the tested range. In contrast, the embedment depth, l, (Fig. 6(b)) has a clear effect: larger l leads to higher K, P_e, and P_{max}. The pre-drilled hole diameter, d, (Fig. 6(c)) shows a similar trend: smaller d, meaning a larger engagement between the embedded threaded part and the concrete, results in higher K, P_e, and P_{max} for all machine screw sizes. These trends were observed consistently for other test configurations as well.

3.2 FAILURE MODE AT MAXIMUM STRENGTH

The failure conditions after reaching the maximum strength are shown in Photo 1. Based on the cracking patterns around the anchor bolts, the failure modes were classified into four types: "bond + cone failure," "bond + cone splitting failure," "splitting failure," and "bond failure." In many specimens, circular cracks centered on the anchor were observed (Photo 1(a)). After loading, the lower portion of the embedded threads retained locally attached concrete, while cone-shaped failure occurred in the upper region—defined as "bond + cone failure." When radial cracks also appeared in addition to this pattern (Photo 1(b)), the mode was defined as "bond + cone splitting failure." Cases showing only radial cracks and no cone-shaped failure (Photo 1(c)) were classified as "splitting failure." In contrast, when the anchor was pulled out without visible surface cracks (Photo 1(d)), this was regarded as "bond failure." Figure 7 shows the proportion of failure modes for each embedment depth. For embedment depths of 15~45 mm, "bond + cone failure" occurred in 50~80% of specimens. Because no clear difference in maximum strength was found between "bond + cone failure" and "bond + cone splitting failure," they are treated as the same failure mechanism. Thus, for the standard type, maximum strength is governed by both bond and cone actions. For embedment depths of 60 and 75 mm, "bond failure" was observed in 70~80% of specimens, with no meaningful difference from "splitting failure." Therefore, for the long type anchors (embedment ≥ 60 mm), the governing mechanism of maximum

strength is bond failure.

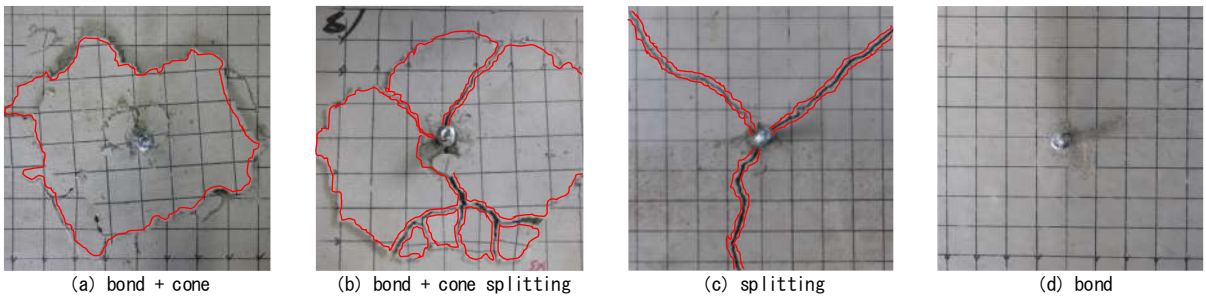


Photo 1. Failure Mode at Maximum Strength

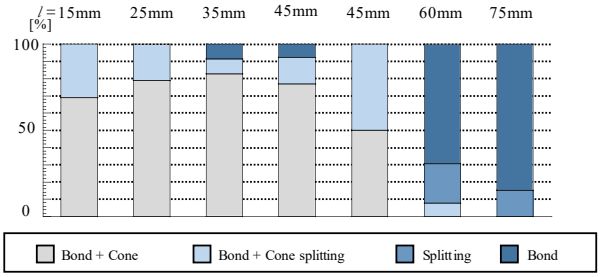


Figure 7. Failure Mode at Maximum Strength

3.3 CONE FAILURE STRENGTH

The pull-out strength governed by cone failure, hereafter denoted as P_{cone}, can be expressed, neglecting reduction factors, in terms of the effective projected area, A_c, and the concrete compressive strength ${}_c\sigma_b$ as given in Eq. (1).

$$p_1 = 0.31\sqrt{{}_c\sigma_b} \cdot A_c \tag{1}$$

In Eq. (1), the effective projected area, A_c, is approximately equal to the area of a circle whose diameter is the sum of the anchor diameter and twice the effective embedment depth. It corresponds to the projection of a failure surface assumed to extend at 45° from the anchor tip. Although Eq. (1) is empirical, derived from the correlation between P_{cone} and A_c, it is convenient because the effects of edge distance and group interaction can be accounted for simply by subtracting or overlapping the projected areas.

3.4 EFFECT OF REACTION SUPPORT DIAMETER

The effect of reaction support diameter, L, is examined in Fig. 8, which shows the relationship between P_{max} and L for M10 anchors with l = 45 mm and d = 9.5 mm. In conventional pull-out tests, L is usually taken larger than the diameter of the projected area (90 mm in this case). However, the present results show that P_{max} is almost constant regardless of L. Thus, the maximum strength is essentially independent of the reaction support diameter at least down to L = 25 mm.

3.5 EFFECT OF EMBEDMENT DEPTH

Figure 9 shows the relationship between P_{max} and embedment depth, l, for M10 anchors with d = 9.5

mm. The solid lines indicate the cone strength calculated from Eq. (1). The maximum strength increases approximately in proportion to *l* for all cases. For embedment depths up to about 45 mm, the calculated cone strength agrees well with the test results, but for larger embedment depths the experimental values deviate from Eq. (1). This indicates that the maximum strength of the screw-type fastening post-installed anchors cannot be explained solely by cone failure; the contribution of bond action must also be considered.

3.6 EFFECT OF PRE-DRILLED HOLE DIAMETER

The influence of pre-drilled hole diameter, *d*, is examined for each machine screw size in Fig. 10, which shows the relationship between P_{max} and *d*. The vertical axis is P_{max}, and the horizontal axis is *d*; the shade of the plot symbols indicates the machine screw size. In the current product specification, the standard pre-drilled hole diameter is 1.0 mm smaller than the outer diameter *D* of the embedded threaded part. In the figure, the standard pre-drilled hole diameter is plotted as ■, and pre-drilled holes 0.1~0.5 mm smaller than the standard are plotted as △. In all cases, smaller pre-drilled hole diameters lead to higher maximum strengths. The increase is more pronounced for larger machine screw sizes, where the difference from the standard pre-drilled hole diameter is larger. This increase in strength due to a 0.1~0.5 mm reduction in *d* cannot be explained by cone strength alone and is attributed to enhanced engagement between the embedded threaded part and the concrete.

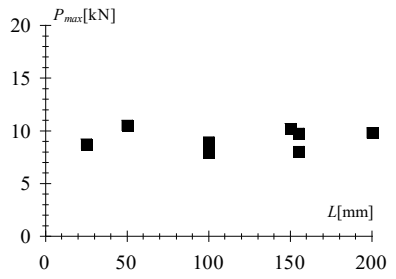


Figure 8. Effect of Reaction Support Diameter on the Maximum Strength

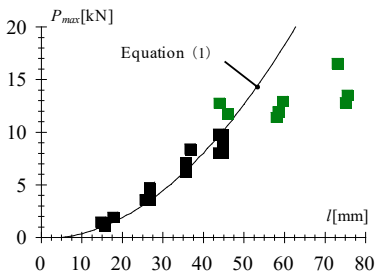


Figure 9. Effect of Embedment Depth on the Maximum Strength

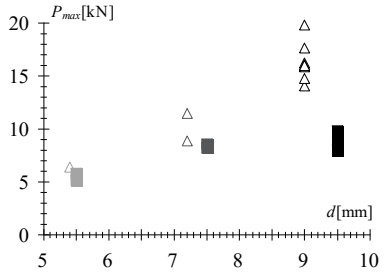


Figure 10. Effect of Pre-drilled hole diameter on the Maximum Strength

3.7 EVALUATION OF MAXIMUM STRENGTH

3.7.1 Depth of Cone Failure

The maximum strength of the screw-type fastening post-installed anchors is now evaluated separately for the standard and long types based on their respective failure mechanisms. As described in Section 3.2, both cone and bond failure are observed for the standard type (embedment depth 15~45 mm). To quantify their contributions, the post-test condition of the embedded threads is examined in detail. A

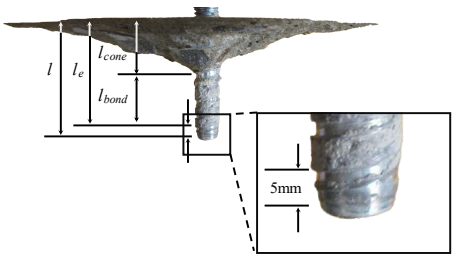


Photo 2. Condition of Anchors after Tensile Loading

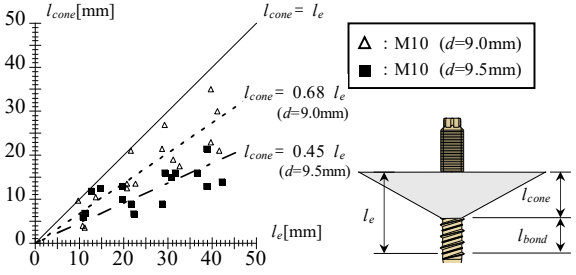


Figure 11. Relationship between Cone Depth and Effective Embedment Depth

representative example is shown in Photo 2. The lower 5 mm of the embedded screw has no threads; therefore, no concrete adhered at the tip, confirming that the effective embedment depth can be taken as l - 5 mm.

Next, the depth of cone failure, hereafter denoted as l_{cone}, is evaluated. The length of the embedded region where concrete remains attached to the threads after testing, defined as the bond length l_{bond}, is measured, and l_{cone} is obtained by subtracting l_{bond} from l_e. The relationship between l_{cone} and l_e for M10 anchors is plotted in Fig. 11, where ■ denotes the standard pre-drilled hole diameter (d = 9.5 mm) and △ denotes a smaller pre-drilled hole (d = 9.0 mm). Least-squares regression lines passing through the origin are also shown. The ratio $\alpha = l_{cone} / l_e$ is 0.45 for the standard pre-drilled hole and 0.68 for the smaller pre -drilled hole, indicating about a 1.5-fold difference. Therefore, the effective projected area for the cone resistance of screw-type fastening post-installed anchors can be expressed using the ratio a as in Eq. (2).

$$A_c = \pi \cdot \alpha l_e (\alpha l_e + d) \tag{2}$$

3.7.2 Definition of Engagement Area and Bond Strength

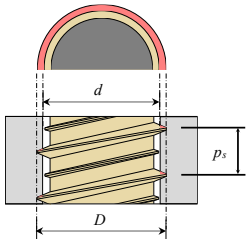


Figure 12. Overview of the Engagement Area

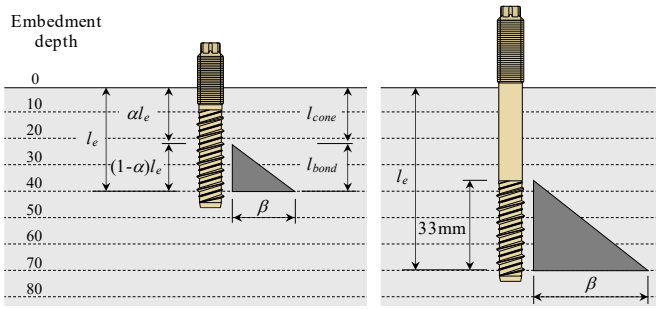


Figure 13. Overview of the Bond Strength

The test results show that P_{max} is independent of reaction support diameter, increases approximately in proportion to embedment depth, and is strongly influenced by the pre-drilled hole diameter through the degree of engagement. As l increases, the engagement between the embedded threaded part and the concrete also increases. In this study, the area of this engagemented region is defined as the engagement area and used to evaluate the bond contribution. The engagement area is illustrated in Fig. 12; the red shaded region represents the engagement area where the concrete "bites" into the thread. The engagement area per one thread pitch A_0 can be expressed in terms of the outer diameter, D, of the embedded threaded part and the pre-drilled hole diameter, d, as follows:

$$A_0 = \frac{\pi(D^2 - d^2)}{4} \tag{3}$$

The total engagement area A_n of the embedded threads is obtained by considering the entire bond length. First, the bond length, l_{bond}, can be expressed using the ratio α of cone depth to effective embedment depth as well as the effective embedment depth, l_e, as follows:

$$l_{bond} = (1 - \alpha) \cdot l_e \tag{4}$$

Accordingly, the total engagement area, A_n, of the embedded threads can be expressed using the thread pitch, p_s, as follows:

$$A_n = A_0 \cdot \frac{l_{bond}}{p_s} \tag{5}$$

The bond strength distribution along the embedment depth is schematically shown in Fig. 13. The local bond stress is assumed to increase with depth and reach a maximum value at the bottom of the bond region, forming a triangular distribution. Denoting the maximum bond stress by a coefficient β multiplied by $\sqrt{}_c\sigma_b$, the bond pull-out strength P_{bond} is obtained using β and A_n, as expressed in Eq. (6).

$$P_{bond} = \frac{1}{2}\beta\sqrt{}_c\sigma_b \cdot A_n \tag{6}$$

3.7.3 Combination of Cone Failure Strength and Bond Failure Strength

Finally, the cone and bond components are combined. For the standard type anchors, both cone and bond failures are observed, and it is assumed that the maximum strength is reached when both resistance mechanisms act simultaneously. Thus, the ultimate strength P_{u1} is expressed as the sum of the cone component from Eq. (1) and the bond component from Eq. (6), giving Eq. (7).

$$P_{u1} = 0.31\sqrt{}_c\sigma_b \cdot A_c + \frac{1}{2}\beta\sqrt{}_c\sigma_b \cdot A_n \tag{7}$$

Substituting Eqs. (2)–(5) into Eq. (6) and rearranging Eq. (7) yields the quadratic expression shown in Eq. (8).

$$P_{u1} = \sqrt{}_c\sigma_b \cdot \pi \cdot l_e \left\{ \alpha^2 (0.31 l_e) + \alpha \left[(0.31d) - \frac{\beta(D^2 - d^2)}{8 p_s} \right] + \frac{\beta(D^2 - d^2)}{8 p_s} \right\} \tag{8}$$

Differentiating Eq. (8) with respect to a yields Eq. (9).

$$\frac{\partial P_{u1}}{\partial \alpha} = \sqrt{}_c\sigma_b \cdot \pi \cdot l_e \left\{ 2\alpha(0.31 l_e) + (0.31d - \frac{\beta(D^2 - d^2)}{8 p_s}) \right\} \tag{9}$$

The ultimate strength is taken as the minimum value of the sum of the cone and bond resistances, that is, the condition where Eq. (9) becomes zero. By substituting the experimentally obtained value of a into Eq. (9), the coefficient b representing the bond strength can be obtained as in Eq. (10).

$$\beta = \frac{2.48 p_s}{(D^2 - d^2)} \cdot (2\alpha l_e + d) \tag{10}$$

For the long type anchors, in which the maximum strength is governed primarily by bond failure at embedment depths of 60 mm or greater, the ultimate strength Pu_2 can be expressed by Eq. (11).

$$P_{u2} = \frac{1}{2}\beta\sqrt{{}_c\sigma_b}\cdot A_n \tag{11}$$

Since the length of the embedded threaded part is constant for all long type anchors, the bond length l_{bond} is taken as 33 mm.

3.8 COMPARISON BETWEEN EXPERIMENTAL AND CALCULATED VALUES

3.8.1 Calculated and Experimental Values Corresponding to Embedment Depth

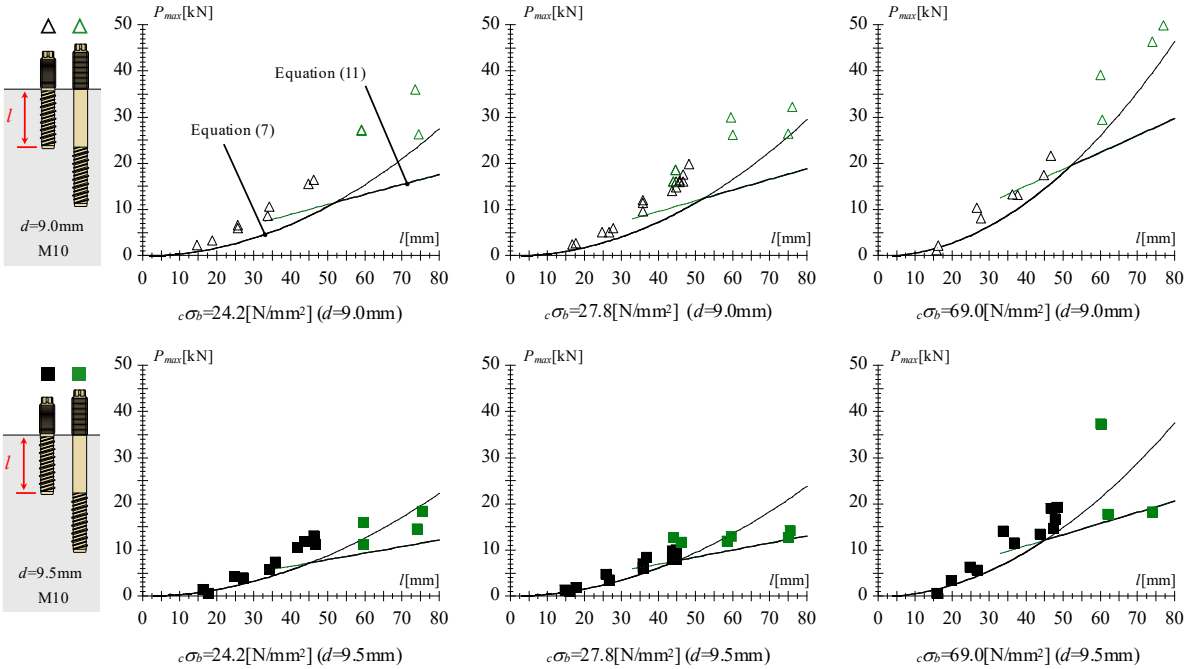


Figure 14. Relationship between Maximum Strength and Embedment Depth

Figure 14 compares the test results and the calculated ultimate strengths for M10 anchors. The figure shows the relationship between P_{max} and embedment depth for three concrete compressive strengths (${}_c\sigma_b$ = 24.2, 27.8, 69.0 N/mm²). For each concrete strength, the upper plot corresponds to a smaller pre-drilled hole (d = 9.0 mm) and the lower plot to the standard pre-drilled hole (d = 9.5 mm). Triangles represent the smaller pre-drilled hole and squares the standard pre-drilled hole. Standard and long types are distinguished by the color of the symbols. The calculated ultimate strengths for "bond + cone failure" (Eq. (7)) and "bond failure" (Eq. (11)) are shown by black and green solid lines, respectively. For the smaller pre-drilled hole, the calculated strengths slightly underestimate the test results, while for the standard pre-drilled hole the agreement is generally good. In all cases, however, the calculated curves capture well the increase and decrease of P_{max} with embedment depth for both standard and long types.

3.8.2 Calculation of Allowable Strength

In this subsection, in addition to the maximum strength obtained from the experiments, the elastic limit strength, P_e, corresponding to allowable stress design, is also examined. Figure 15 shows the definition of the elastic limit strength, P_e, in the load–deformation relationship and the relationship between the maximum strength and the elastic limit strength. Although some scatter is observed, the average ratio of elastic limit strength to maximum strength is approximately 0.5. Therefore, the elastic limit strength can be expressed as:

$$P_e = 0.5P_u \tag{12}$$

where the elastic limit strength is taken as 0.5 times the ultimate strength.

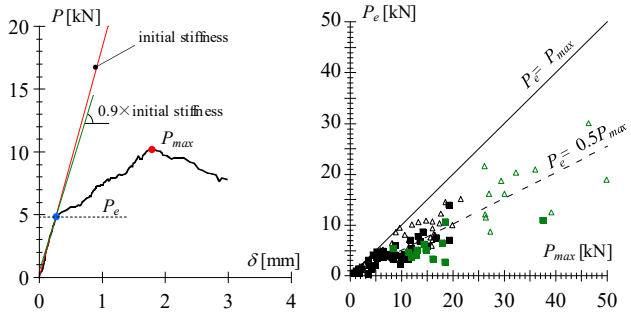


Figure 15. Definition of Elastic limit Strength and the Relationship Between Maximum Strength and Elastic limit

3.8.3 Accuracy of the Evaluation Equations

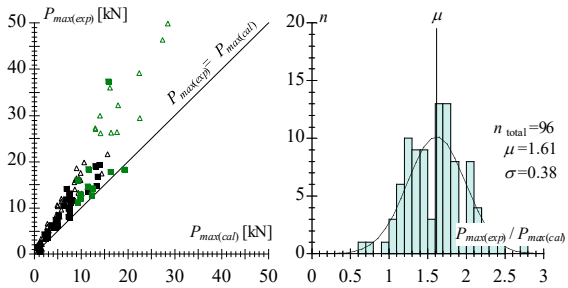


Figure 16. Accuracy of the Evaluation Equation for Ultimate Strength

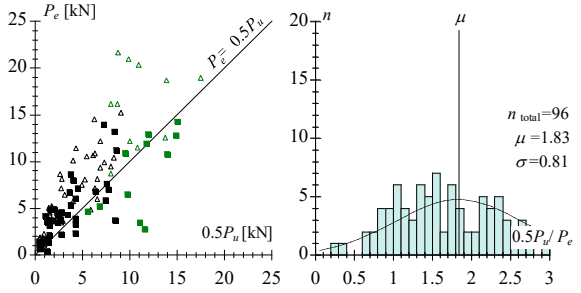


Figure 17. Accuracy of the Evaluation Equation for Elastic limit Strength

Figures 16 and 17 compare the experimental and calculated strengths based on the ultimate strength equations for the maximum strength and the elastic limit strength, respectively. In each figure, the left-side plot shows the relationship between the experimental and calculated values, while the right-side plot presents the histogram of the ratio of experimental to calculated values together with the normal distribution curve derived from the mean value μ and standard deviation σ. For the maximum strength (Figure 16), the calculated ultimate strengths provide conservative estimates for approximately 97% of all specimens. The distribution of ratios is well represented by the normal distribution curve, with μ = 1.61 and σ = 0.37. For the elastic limit strength (Figure 17), a larger number of cases exceed the calculated values compared with the maximum strength; however, approximately 85% of all specimens are still conservatively evaluated. The histogram follows an approximately normal distribution, with μ = 1.83 and σ = 0.81. Based on these results, the allowable tensile strength for use in allowable stress design can be expressed as

$$P_a = \phi \cdot P_u \tag{13}$$

where ϕ is a reduction factor (0.5 for short-term loading and 0.1 for long-term loading). For short-term loading, ϕ is selected to ensure a safety margin of 1.7 times the maximum strength, considering the relatively small scatter of the calculated maximum strengths ϕ=2.0×(1.61−2×0.38).

For long-term loading, ϕ is determined so that the allowable strength remains below the elastic limit strength even when considering the observed scatter ϕ=0.5×(1.83−2×0.81).

4. CONCLUSIONS

In this study, the screw-type fastening post-installed anchors, classified as "other anchors," were examined. The effects of fundamental parameters—including reaction support diameter, embedment depth, pre-drilled hole diameter, and concrete compressive strength—on the pull-out strength were investigated, and an evaluation method based on the failure mechanisms governing the maximum strength was developed.

[1] The reaction support diameter, which was an experimental condition, had only a minor influence on the maximum strength even when reduced to approximately 25 mm. In contrast, the embedment depth, pre-drilled hole diameter, and concrete compressive strength affected the maximum strength, with the pre-drilled hole diameter having the greatest influence. Therefore, the pull-out strength of the screw-type fastening post-installed anchors is considered to be governed by the engagement resistance between the embedded threads and the concrete.

[2] Regarding the failure conditions after reaching the maximum strength, the standard-type anchors—composed only of the embedded threaded portion—exhibited bond failure in the lower region and cone-shaped failure emanating from the anchor bolt in the upper region. In contrast, the long-type anchors, which include an unthreaded portion in the embedded region and have embedment depths of 60 mm or greater, exhibited only bond failure.

[3] Based on the measured ranges in which bond failure and cone failure occurred, the bond strength was identified, and an evaluation equation for the ultimate strength was derived by summing the strengths associated with the two failure mechanisms. The elastic limit strength evaluated from the experimental results was shown to be approximately half of the maximum strength on average. Furthermore, after confirming that the proposed evaluation equations provided conservative predictions relative to the experimental results, allowable tensile strengths corresponding to the current allowable stress design were proposed together with the reduction factor ϕ.

REFERENCES

AIJ [2023] *AIJ Recommendation for Design of Composite Construction, Architectural Institute of Japan*, Tokyo, Japan. (in Japanese)

Hosokawa, Y., Aoyama, H., Kotani, S., Niwa, R., and Yoshida, T. [1987] "Experimental Study on Placement in Concrete and Pull-Out Strength of Adhesive Drilled Anchors (Part 2: Evaluation of Pull-Out Strength)," *Summaries of Technical Papers of Annual Meeting*, Architectural Institute of Japan, pp. 593–594. (in Japanese)

Matsuzaki, H., Nakano, Y., and Sato, T. [2004] "Experimental Study on Pull-Out Behavior of Expansion Anchors under Cyclic Loading," *Journal of Structural and Construction Engineering*, AIJ, No. 567, pp. 115–122. (in Japanese)

Shimizu, Y. [1995] "Pull-Out Strength of Metallic Expansion Post-Installed Anchors," *Journal of Structural and Construction Engineering*, AIJ, No. 471, pp. 97–100. (in Japanese)

Floor Response Spectra in the New Generation of Eurocode 8: An Overview and Example of Application

Vladimir Vukobratović[1] and Peter Fajfar[2]

[1] Faculty of Technical Sciences, University of Novi Sad
Trg Dositeja Obradovića 6, 21000 Novi Sad, Serbia
e-mail: vladavuk@uns.ac.rs
[2] Faculty of Civil and Geodetic Engineering, University of Ljubljana
Jamova cesta 2, 1000 Ljubljana, Slovenia
e-mail: peter.fajfar@fgg.uni-lj.si

Abstract. The preparation of the new generation of Eurocode 8 is in the final phase. Its implementation in practice is a demanding and complex process, primarily based on the timely familiarization of the professional public with all relevant details. The main goal of this paper is to provide information about the floor response (acceleration) spectra (FRS) in the part 1-2 of the new Eurocode 8, used for the seismic design of non-structural elements (NSEs) sensitive to accelerations. The approach for the FRS determination provided in the standard is based on the method for the direct FRS determination previously developed and proposed by the authors. An overview of formulas for the FRS calculation is provided in a step-by-step manner, along with the appropriate theoretical and background explanations. Afterwards, their practical application is demonstrated on a case study building containing both linear elastic and nonlinear NSEs.

Keywords: Floor Response Spectra, Eurocode 8, Non-Structural Elements.

1. INTRODUCTION

Floor response (acceleration) spectra (FRS) are commonly used for the seismic design and evaluation of acceleration-sensitive non-structural elements (NSEs, termed ancillary elements in Eurocode 8). The FRS concept is based on uncoupled analysis of the structure and NSEs, i.e., the dynamic interaction between them is neglected, making it sufficiently accurate in cases of NSEs whose mass is significantly smaller than the structural mass. FRS can be "accurately" determined by performing a response history analysis, which is time-consuming, and is therefore used only in exceptional circumstances. For common design practice, an approximate approach is widely used, in which FRS are determined directly from the ground motion spectra, by using appropriate direct method(s).

The approach for the direct FRS determination given in the normative Annex C of the new Eurocode 8, part 1-2 [CEN, 2025] is based on the method for the direct FRS determination previously developed and proposed by the authors of this paper. Thus, an overview of Eurocode 8 formulas for the FRS calculation is provided herein in a step-by-step manner, along with the appropriate theoretical and background explanations. Afterwards, their practical application is demonstrated on a case study building containing different linear elastic and nonlinear NSEs.

2. BACKGROUND OF THE DIRECT FRS APPROACH

Direct method for the FRS determination, which served as a basis for the new Eurocode 8 FRS approach, has been developed through an extensive research conducted at the Faculty of Civil and Geodetic Engineering, University of Ljubljana, Slovenia. It all started in the early 90s, and the first achievements have been reported in two papers [Novak and Fajfar, 1994; Fajfar and Novak, 1995]. Starting from the previously made observations, and following the method of Yasui et al. [1993], after more than a decade, the research has been continued by the authors of this paper, within the PhD studies of the first author, as discussed below.

As noted, Yasui et al. [1993] method played an important role in the direct FRS method proposed by the authors, primarily due to the fact that it is based on the theory of structural dynamics. The equation for direct FRS determination was derived analytically, by using the Duhamel integral for the response calculation. Since the derivation conducted by Yasui et al. [1993] was not presented in their paper in detail, an independent derivation can be found in the PhD thesis of the first author [Vukobratović, 2015]. The original formula has been extended and modified over time, and has been made applicable for both linear elastic and nonlinear single-degree-of-freedom (SDOF) and multi-degree-of-freedom (MDOF) structures and SDOF NSEs.

To be able to properly assess the accuracy of the Yasui et al. [1993] method, the authors performed a parametric study in which 5760 FRS were calculated, for linear elastic and nonlinear structures and linear elastic NSEs, represented by SDOF systems in all cases. Since considerable inaccuracy of the Yasui et al. [1993] method was observed in the resonance region, the amplification factors (*AMP*s), based on the results obtained in the parametric study, were used for the FRS limitation in our approach. Simultaneously, for nonlinear structures the application of inelastic acceleration spectrum, according to Vidic et al [1994], was introduced. All findings were reported in two conference papers [Vukobratović and Fajfar, 2012; Vukobratović and Fajfar, 2013], and were wrapped up in a journal paper [Vukobratović and Fajfar, 2015].

The next step was the expansion of the formulas to linear elastic and nonlinear MDOF structures, while considering NSEs as linear elastic. Parametric study was conducted, considering stiff and flexible frame and wall structures, and the results served as a basis for the assessment of newly proposed formulas. For

nonlinear structures, the method was coupled with the pushover-based N2 method [Fajfar, 1999; Fajfar, 2000]. When it comes to the *AMP*s, originally defined in a comprehensive manner, a simple definition by Sullivan et al. [2013] was offered as a partial alternative. Finally, a proposal of the approach for a proper combination of FRS obtained for individual modes was provided. The final outcomes of this research phase were reported in a journal paper [Vukobratović and Fajfar, 2016].

Shortly after, another journal paper was published [Vukobratović and Fajfar, 2017], with a main goal to provide a simplified code-oriented version of the method, which involved: (1) neglecting the natural period lengthening (the effective natural period determined from the N2 method is used regardless of the hysteretic behavior); (2) the use of the above mentioned Sullivan et al. [2013] definition of *AMP* was incorporated in the *AMP* formulas; and (3) a simple variant of the modal combination approach was provided. In addition, an option for approximately taking into account the nonlinear NSE response was added. Namely, it was found that the beneficial effect of NSE nonlinearity to FRS values can be taken into account by increasing the NSE damping. The option was also mentioned in the conference paper by Fajfar and Vukobratović [2022], in which the conceptual differences between a previous draft of the new Eurocode 8, part 1-2 and ASCE 7-22 [ASCE, 2021] were also shown.

The above mentioned increased damping option was used to consider nonlinear NSE response in a test example prepared by Fajfar and Vukobratović [2023], and a sufficient accuracy of the approach was demonstrated. An additional check of the increased damping application was performed by Vukobratović and Fajfar [2024a], again confirming the approach applicability. In the same journal paper, however, driven by the idea to take into account both the NSE and structural nonlinearity in a consistent manner, the authors further extended the direct FRS method. Based on the results of the new parametric study, the authors proposed a strength reduction factor for NSEs, and updated the main FRS determination formula accordingly. In addition, the *AMP* definition was also updated, covering a range of NSEs with the ductility ratios between 1 and 4. In the paper, both SDOF and MDOF structures were considered within the validation of the extended direct FRS method, which was also presented in a condensed form in a conference paper [Vukobratović and Fajfar, 2024b]. Lastly and most importantly, the method, validated by comparing its results with the results of response-history analyses, found its way to the normative Annex C of the new Eurocode 8, part 1-2 [CEN, 2025]. It should be noted that the development of the new generation of Eurocode 8 took several years. The treatment of FRS in the standard changed over time until, very recently, it reached its final formulation. In previous papers, the authors always referred to the working versions of the standard valid at the time of writing.

3. CALCULATION OF FRS IN THE NEW EUROCODE 8

In the new Eurocode 8, FRS are addressed in Part 1-2 (Buildings) [CEN, 2025] and in Part 4 (Industrial Facilities) [CEN, 2024]. Part 1-2 provides two methods for the calculation of FRS. The general method is codified in Annex C, and is the primary focus of this paper. A simplified method, applicable only to rigid NSEs, is given in Section 7.2. The corresponding formula represents a simplified special case of the general formula in Annex C.

Part 4, Section 9, offers three alternative methods. The first method refers to the procedure described in Part 1-2, Annex C, but involves a more conservative approach for determining the building behavior factor related to deformation capacity and energy dissipation capacity, typically limiting it to 1.0 if no overstrength verification is performed. The second method should be used when the properties of the NSE are not known. This approach is similar to the simplified method in Part 1-2, Section 7.2, but conservatively assumes that the NSE is tuned to the vibration period of the supporting structure. In both the first and second methods, the NSE and its anchorage system must be designed with sufficient strength to remain linear

elastic under seismic loading. Therefore, both approaches are classified as "non-dissipative". The third method is a "dissipative" design approach. As in the second method, it assumes limited knowledge of the NSE properties. However, it allows certain components of the anchorage system to yield in a ductile manner for energy dissipation. A detailed description of the FRS calculation methods in Part 4 was provided by Kazantzi et al. [2024].

4. OVERVIEW OF THE FRS CALCULATION ACCORDING TO THE NEW EUROCODE 8, PART 1-2, ANNEX C

Formulas for the FRS calculation are provided in the normative Annex C of the new Eurocode 8, part 1-2 [CEN, 2025], and their overview is given in this section. The calculation follows the most recent version of the authors' approach defined by Vukobratović and Fajfar [2024a], with two very minor modifications described at the end of this section.

In the direction under consideration, the FRS value for mode *i* and floor *j* should be determined from Equations (1) to (4).

$$S_{\mathrm{ap,ij}} = \frac{\Gamma_{\mathrm{i}}\phi_{\mathrm{ij}}}{\left|\left(T_{\mathrm{ap}} / T_{\mathrm{p,i}}\right)^2 - 1\right|}\sqrt{\left(\frac{S_{\mathrm{ep,i}}}{q'_{\mathrm{D}}}\right)^2 + \left[\left(T_{\mathrm{ap}} / T_{\mathrm{p,i}}\right)^2 \frac{S_{\mathrm{eap}}}{q'_{\mathrm{ap,D,i}}}\right]^2} \tag{1}$$

$$\left|S_{\mathrm{ap,ij}}\right| \le AMP_{\mathrm{i}} \times \left|PFA_{\mathrm{ij}}\right| \tag{2}$$

$$AMP_{\mathrm{i}} = \begin{cases} 2.5\sqrt{10/\left(5+\xi_{\mathrm{ap}}\right)}, & \text{if } T_{\mathrm{p,i}} / T_{\mathrm{C}} = 0 \\ \text{linear between } AMP_{\mathrm{i}}\left(\dfrac{T_{\mathrm{p,i}}}{T_{\mathrm{C}}} = 0\right) \text{ and } AMP_{\mathrm{i}}\left(\dfrac{T_{\mathrm{p,i}}}{T_{\mathrm{C}}} = 0.2\right), & \text{if } 0 \le T_{\mathrm{p,i}} / T_{\mathrm{C}} \le 0.2 \\ c / \xi_{\mathrm{ap}}^{\mathrm{k}} \ge 1, & \text{if } T_{\mathrm{p,i}} / T_{\mathrm{C}} \ge 0.2 \end{cases} \tag{3}$$

$$PFA_{\mathrm{ij}} = \Gamma_{\mathrm{i}}\phi_{\mathrm{ij}}\frac{S_{\mathrm{ep,i}}}{q'_{\mathrm{D}}} \tag{4}$$

The indices 'p' and 'ap' correspond to the primary (building) structure and the NSE (i.e., ancillary element), respectively. $S_{\mathrm{ep,i}} = S_{\mathrm{e}}(T_{\mathrm{p,i}}, \xi_{\mathrm{p,i}})$ is the value in the elastic response spectrum which applies to the i^{th} mode of the primary structure, and $S_{\mathrm{eap}} = S_{\mathrm{e}}(T_{\mathrm{ap}}, \xi_{\mathrm{ap}})$ is the value in the elastic response spectrum which applies to the NSE. $T_{\mathrm{p,i}}$ and $\xi_{\mathrm{p,i}}$ are the natural period and the critical damping ratio (in %) of the i^{th} mode of the primary structure, respectively. According to the standard, the latter is equal to 5%. T_{ap} and ξ_{ap} are the natural period and the critical damping ratio of the SDOF NSE, respectively. Unless greater values are demonstrated, ξ_{ap} may be taken equal to 2%. T_{C} denotes the upper corner period of the constant spectral acceleration range in the elastic response spectrum. Γ_{i} and ϕ_{ij} are the modal participation factor for the i^{th} mode and the i^{th} mode shape component at the j^{th} floor, respectively. If a planar model with concentrated masses is used, a simple formula (not listed here) is provided for Γ_{i}. As for the ϕ_{ij}, in the case of lateral force analysis, the displacement shape of the first mode used for the determination of lateral forces may be used, whereas in the case of pushover analysis, the inelastic deformation shape (corresponding to the design seismic action at the limit state under consideration) should be used instead. *AMP* denotes amplification factor, whereas *PFA* denotes peak floor acceleration.

Structural nonlinearity is taken into account through the period-dependent behavior factor q'_D, which is defined as:

$$q'_D = \begin{cases} 1, & \text{if } T_1 \le T_A \\ \text{linear between 1 and } q_D, & \text{if } T_A \le T_1 \le T_C \\ q_D, & \text{if } T_1 \ge T_C \end{cases} \quad (5)$$

where T_1 is the fundamental period of the building in the considered direction, q_D is the building behavior factor component accounting for deformation capacity and energy dissipation capacity provided in the relevant parts of Eurocode 8, and T_A is the short-period cut-off associated to the zero-period acceleration. In the absence of specific studies, T_A may be taken equal to 0.02 s.

NSE nonlinearity is considered through the behavior factor component $q'_{ap,D,i}$, which accounts for the deformation capacity and energy dissipation capacity of the NSE for mode i of the primary structure, and is defined as:

$$q'_{ap,D,i} = \begin{cases} \left(T_{ap} / T_{p,i}\right)\left(q_{ap,D} - 1\right) + 1, & \text{if } T_{ap} < T_{p,i} \\ q_{ap,D}, & \text{if } T_{ap} \ge T_{p,i} \end{cases} \quad (6)$$

For various NSEs, the values of $q_{ap,D}$, equal to 1 or 2, are provided in the Table C.2 of Annex C. These limiting values should be used unless (1) $q_{ap,D}$ is obtained experimentally, (2) $q_{ap,D}$ is provided in the relevant parts of Eurocode 8, or (3) the behavior of the element is documented as the rigid-plastic.

Constants c and k, needed for the determination of AMP in the third line of Equation (3), are provided in Table 1, for six $q_{ap,D}$ values. For convenience, unlike in the Annex C, the AMP values are also provided, considering different values of the NSE damping.

Table 1. Values of c and k with corresponding AMPs for different $q_{ap,D}$ and ξ_{ap}

$q_{ap,D}$	c	k	$AMP = c / \xi_{ap}^k$					
1	10	0.5	10	7.1	5.8	4.5	3.8	3.2
1.25	5	0.25	5.0	4.2	3.8	3.3	3.1	2.8
1.5	3.5	0.15	3.5	3.2	3.0	2.7	2.6	2.5
2	2.3	0.1	2.3	2.1	2.1	2.0	1.9	1.8
3	1.6	0.07	1.6	1.5	1.5	1.4	1.4	1.4
4	1.3	0.03	1.3	1.3	1.3	1.2	1.2	1.2
		ξ_{ap} =	**1%**	**2%**	**3%**	**5%**	**7%**	**10%**

Finally, at every floor, the FRS, determined separately for all modes of vibration contributing significantly to the global response, should be combined in order to obtain the resulting FRS. For this purpose, the well-known square root of sum of squares (SRSS) or complete quadratic combination (CQC) rules, may be applied.

The resulting FRS should not have values lower than the ground motion acceleration spectrum corresponding to the damping and ductility of the NSE, determined as $S_{eap}/q'_{ap,D}$, where $q'_{ap,D}$ is defined as:

$$q'_{\mathrm{ap,D}} = \begin{cases} \left(T_{\mathrm{ap}} / T_{\mathrm{C}}\right)\left(q_{\mathrm{ap,D}} - 1\right) + 1, & \text{if } T_{\mathrm{ap}} < T_{\mathrm{C}} \\ q_{\mathrm{ap,D}}, & \text{if } T_{\mathrm{ap}} \geq T_{\mathrm{C}} \end{cases} \tag{7}$$

Note that Equation (7) is not explicitly provided in the Annex C, i.e., it yields from the text of the clause C.3(5).

4.1 DIFFERENCES BETWEEN THE AUTHORS' METHOD AND ANNEX C

As said, the approach for the FRS determination provided in the new Eurocode 8, part 1-2, Annex C, is based on the method for the direct FRS determination previously developed and proposed by the authors. However, two slight differences should be outlined:

i. In the method proposed by Vukobratović and Fajfar [2024], the SRSS or CQC modal combination rules are used up to and including the end of the plateau of the first mode resonance region. Afterwards, the algebraic sum (ALGSUM) is used, in which the relevant signs of individual modes are taken into account. ALGSUM is not incorporated in the new Eurocode 8 approach;

ii. According to the new Eurocode 8, the lower limit should be applied at all floors, whereas in Vukobratović and Fajfar [2024] it is stated that the lower limit should be applied along the bottom third (1/3) of the building height. However, some conservatism of the new Eurocode 8 approach is reasonable considering the uncertainties involved in the FRS.

The above differences are not significant, and are not expected to cause a noticeable difference between the results of the two approaches.

5. CASE STUDY EXAMPLE

The application of the new Eurocode 8 FRS method is shown considering a three-story reinforced concrete frame structure named "SPEAR building". More precisely, its variant termed EC8 H, re-designed according to the first generation of Eurocode 8, part 1 [CEN, 2004], by Rozman and Fajfar [2009]. The most important structural properties, mathematical model, and its analysis were provided by Vukobratović and Fajfar [2017]. As for NSEs, both linear elastic and nonlinear elements (with $q_{\mathrm{ap,D}} = 2$) are considered, in both cases with 2% damping.

Seismic input is defined according to the part 1-1 of the new Eurocode 8 [CEN, 2023], considering a moderate seismicity level with $S_{\alpha,475} = 0.25$ g ($S_{\beta,475} = f_{\mathrm{h}} S_{\alpha,475} = 0.075$ g, $f_{\mathrm{h}} = 0.3$ for moderate seismicity level) and site belonging to category C (no amplification due to topography, i.e., $F_{\mathrm{T}} = 1$, site amplification factors for short and intermediate periods are $F_{\alpha} = 1.52$ and $F_{\beta} = 2.25$, respectively), along with the consequence class CC2 and the SD limit state (i.e., the corresponding return period is 475 years, $\gamma_{\mathrm{SD,CC2}} = 1$). Elastic pseudo-acceleration spectra obtained for 5% (default value, correction factor $\eta = 1$) and 2% damping (correction factor η ranging from 1 to 1.20), which correspond to the building and NSEs, respectively, are shown in Figure 1a. Note that the spectral values at the plateaus and at $T = 1$ s, S_{α} and S_{β}, which are the two main parameters that define the new Eurocode 8 elastic spectra, are obtained as $F_{\alpha} F_{\mathrm{T}} \gamma_{\mathrm{SD,CC2}} S_{\alpha,475}$ and $F_{\beta} F_{\mathrm{T}} \gamma_{\mathrm{SD,CC2}} S_{\beta,475}$, respectively.

For the considered SPEAR building, it turned out that for the applied seismic input its response is linear elastic due to the low seismic input, as shown in Figure 1b. For convenience, the input data for the FRS calculation related to the building structure are provided in Table 2, whereas the data related to the NSEs, are given in Table 3.

The obtained FRS are shown in Figure 2. For convenience, layout and vertical cross-section of the structure are shown, along with the corresponding dimensions. At the first floor, floor spectrum obtained for the linear elastic NSEs has three resonance regions, meaning that all three structural modes significantly influence spectral values. However, the influence of the third mode becomes irrelevant for nonlinear NSEs. More importantly, the beneficial influence of the NSE nonlinearity, in terms of the reduction of spectral values, can be clearly observed. When it comes to lower limits, for linear elastic NSEs the limit is applicable in the region before the third mode peak, and between first and second mode peaks. For nonlinear NSEs, the need for the lower limit use can be observed only in the short period region before the third mode. In all cases, the correction due to the consideration of the lower limit is very small.

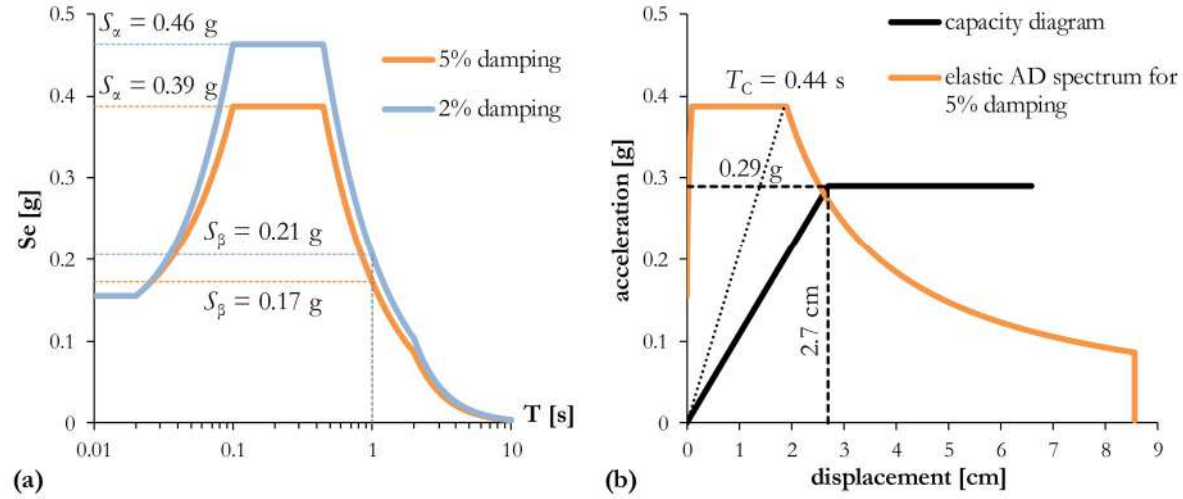


Figure 1. (a) Seismic input in terms of ground motion acceleration spectra used for the building and NSEs (5% and 2% damping, respectively), and (b) comparison of the structural capacity diagram (adapted from Fig. 3b in Vukobratović and Fajfar [2017]) and elastic 5% damping spectrum in acceleration-displacement (AD) format

Table 2. Input data for the FRS calculation (building structure)

Structure (linear elastic, $q'_D = 1$)	**Mode (i)**	**1**	**2**	**3**
	$T_{p,i}$ **[s]**	**0.56**	**0.19**	**0.12**
	$S_{ep,i}$ **[g]**	**0.31**	**0.39**	**0.39**
Floor	Γ_i	1.28	–0.34	0.08
1	ϕ_{i1}	0.33	–1.16	2.83
2	ϕ_{i2}	0.69	–0.86	–2.55
3 (roof)	ϕ_{i3}	1.00	1.00	1.00

Table 3. Input data for the FRS calculation (NSEs)

NSEs	**Damping ξ_{ap} = 2%**	
	Linear elastic	**Nonlinear**
	$q_{ap,D} = 1$	$q_{ap,D} = 2$
c	10	2.3
k	0.5	0.1

FRS obtained at the roof level are shown in the upper part of Figure 2. As expected, spectral values are significantly larger than the ones at the first floor. The benefit of nonlinear NSE response becomes even more pronounced, especially in the resonance region related to the first structural mode. A small influence of the third mode can be seen in the case of linear elastic NSEs, while for nonlinear ones it is practically negligible. At the roof level, there is no need to apply lower limits since they are below the obtained FRS.

In order to illustrate the benefit of nonlinear structural behavior in terms of the FRS reduction, it is assumed that the seismic capacity of the structure equals ½ of the previously used one. The building behavior factor component accounting for the deformation capacity and energy dissipation capacity $q_D = 2$ is adopted; the period of the fundamental mode, determined from the N2 method, equals 0.61 s; while the corresponding pseudo-acceleration from the input spectrum amounts to 0.28 g. All other parameters are the same as above. Only FRS at the roof level are determined and presented in Figure 3, along with the results from Figure 2 for the purpose of comparison. The colors of the latter are the same in both figures.

Comparing the results obtained for linear elastic NSEs (blue graphs), there is an obvious reduction of FRS values when structural behavior is nonlinear, in the period range up to the end of the first mode plateau. Afterwards, the reduction is negligible. The same observation applies to the FRS obtained for nonlinear NSEs (red graphs). Considering two limit cases, i.e., linear elastic structure and NSEs, and their nonlinear variants, linear elastic case produces acceleration values at the first mode plateau that are more than 6 times larger than in the nonlinear case. Therefore, even a fairly low ductility demand of 2 considered for the structure and NSEs leads to the tremendously reduced NSE seismic demands.

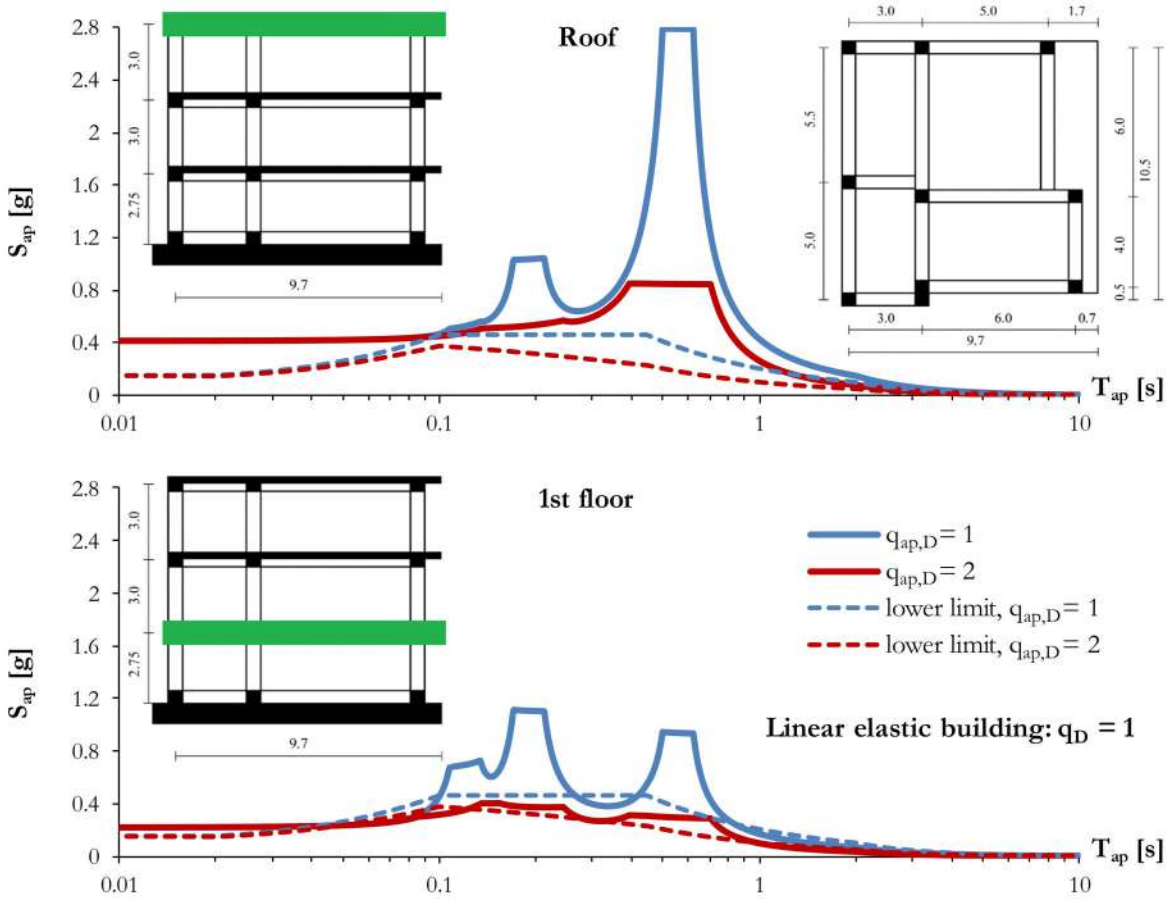


Figure 2. FRS obtained for linear elastic building by using the provisions of new Eurocode 8

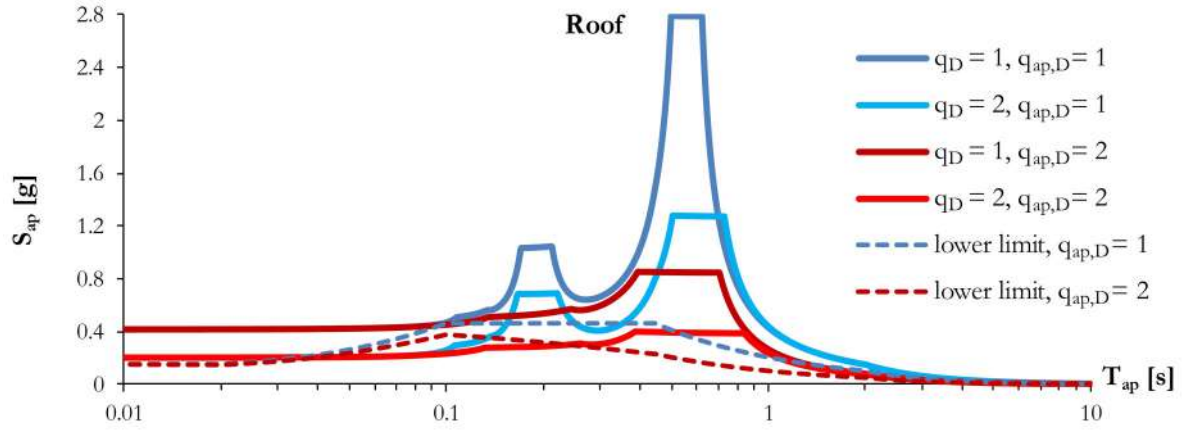


Figure 3. FRS obtained at the roof level considering both linear elastic and nonlinear building structure and NSEs

6. CONCLUSIONS

The intention of this paper is to stimulate and facilitate the application of the direct FRS determination, as implemented in the new generation of Eurocode 8. The approach is largely based on structural dynamics theory, supplemented by empirical data and well-established approaches for accounting for nonlinear effects. In previous years, the results of the proposed method have been widely checked with the results of the response history analysis, and a reasonable correlation between the two has been obtained. The closed-form FRS equation is applicable to various structural systems and NSEs, and aligns with the preferences of advanced designers seeking physically grounded design approaches. In practical terms, the method is applied by using the input ground motion spectra, and the dynamic properties of the supporting structure and the NSE. The obtained FRS value is then used to determine the seismic force acting on the NSE. The method is comprehensive and generally applicable, making it attractive for everyday use. However, it requires sufficiently accurate input regarding the NSE properties, which is an aspect that may not always be satisfied at present. Given the growing attention to the topic of NSEs, it is reasonable to expect that knowledge of NSE properties will improve significantly in the near future.

ACKNOWLEDGMENT

The research of the first author has been supported by the Ministry of Science, Technological Development and Innovation (Contract No. 451-03-137/2025-03/200156) and the Faculty of Technical Sciences, University of Novi Sad through project "Scientific and Artistic Research Work of Researchers in Teaching and Associate Positions at the Faculty of Technical Sciences, University of Novi Sad 2025" (No. 01-50/295).

REFERENCES

ASCE [2021] Minimum Design Loads and Associated Criteria for Buildings and Other Structures, ASCE/SEI 7-22, Structural Engineering Institute of American Society of Civil Engineers, Reston, VA, USA.

CEN [2004] EN 1998–1:2004: Eurocode 8: Design of structures for earthquake resistance. Part 1: General rules, seismic actions and rules for buildings., CEN, Brussels.

CEN [2023] FprEN 1998–1–1:2024: Eurocode 8: Design of structures for earthquake resistance. Part 1-1: General rules and seismic action, CEN, Brussels. 12.9.2023

CEN [2024] FprEN 1998–4:2025: Eurocode 8: Design of structures for earthquake resistance. Part 4: Silos, tanks and pipelines, towers, masts and chimneys, CEN, Brussels. 14.9.2024

CEN [2025] FprEN 1998–1–2:2025 Eurocode 8: Design of structures for earthquake resistance. Part 1-2: Buildings, CEN, Brussels. 21.3.2025

Fajfar, P. [1999] "Capacity spectrum method based on inelastic demand spectra", *Earthquake Engineering and Structural Dynamics*, Vol. 28, No. 9, pp. 979-993. https://doi.org/10.1002/(SICI)1096-9845(199909)28:9<979::AID-EQE850>3.0.CO;2-1

Fajfar, P. [2000] "A nonlinear analysis method for performance based seismic design", *Earthquake Spectra*, Vol. 16, No. 3, pp. 573-592. https://doi.org/10.1193/1.1586128

Fajfar, P., Novak, D. [1995] "Floor response spectra for inelastic structures", *Transactions of the 13th International Conference on Structural Mechanics in Reactor Technology (SMiRT 13)*, Porto Alegre, Brazil, paper no. K044/1, pp. 259-264.

Fajfar, P., Vukobratović, V. [2022] "Floor Acceleration Spectra: From Research to Seismic Code Provisions", *Proceedings of the Fifth International Workshop on the Seismic Performance of Non-Structural Elements (SPONSE)*, Palo Alto, CA, USA, pp 2-14–2-26.

Fajfar, P., Vukobratović, V. [2023] "Floor Acceleration Spectra Based on Structural Dynamics", *Proceedings of the Anniversary Workshop in Commemoration of the 1999 Chi-Chi and 2022 Chihshang Earthquakes*, Taipei, Taiwan, pp 182-185.

Kazantzi, A.K., Karaferis, N.D., Melissianos, V.E., Vamvatsikos, D. [2024] "Seismic reliability of acceleration-sensitive ancillary elements in the new generation of Eurocode", *Proceedings of the 18th World Conference on Earthquake Engineering*, Milan, Italy, paper no. 727.

Novak, D., Fajfar, P. [1994] "Nelinearni etažni spektri odziva za racionalno aseizmično projektiranje opreme", *Zbornik 16. zborovanja gradbenih konstruktorjev Slovenije*, Bled, Slovenia, pp. 95-102 (in Slovenian).

Rozman, M., Fajfar, P. [2009] "Seismic response of a RC frame building designed according to old and modern practices", *Bulletin of Earthquake Engineering*, Vol. 7, No. 3, pp. 779-799. https://doi.org/10.1007/s10518-009-9119-4

Sullivan, T.J., Calvi, P.M., Nascimbene, R. [2013] "Towards improved floor spectra estimates for seismic design", *Earthquakes and Structures*, Vol. 4, No. 1, pp. 109-132. https://doi.org/10.12989/eas.2013.4.1.109

Vidic, T., Fajfar, P., Fischinger, M. [1994] "Consistent inelastic design spectra: Strength and displacement", *Earthquake Engineering and Structural Dynamics*, Vol. 23, No. 5, pp. 507-521. https://doi.org/10.1002/eqe.4290230504

Vukobratović, V. [2015] "The influence of nonlinear seismic response of structures on the floor acceleration spectra", *Doctoral dissertation*, University of Ljubljana, Slovenia. http://drugg.fgg.uni-lj.si/5153/

Vukobratović, V., Fajfar, P. [2012] "A method for direct determination of inelastic floor response spectra", *Proceedings of the 15th World Conference on Earthquake Engineering*, Lisbon, Portugal, paper no. 727.

Vukobratović, V., Fajfar, P. [2013] "A method for direct generation of floor acceleration spectra for inelastic structures", *Transactions of the 22nd International Conference on Structural Mechanics in Reactor Technology (SMiRT 22)*, San Francisco, CA, USA, paper no. 215.

Vukobratović, V., Fajfar, P. [2015] "A method for the direct determination of approximate floor response spectra for SDOF inelastic structures", *Bulletin of Earthquake Engineering*, Vol. 13, No. 5, pp. 1405-1424. https://doi.org/10.1007/s10518-014-9667-0

Vukobratović, V., Fajfar, P. [2016] "A method for the direct estimation of floor acceleration spectra for elastic and inelastic MDOF structures", *Earthquake Engineering and Structural Dynamics*, Vol. 45, No. 15, pp. 2495-2511. https://doi.org/10.1002/eqe.2779

Vukobratović, V., Fajfar, P. [2017] "Code-oriented floor acceleration spectra for building structures", *Bulletin of Earthquake Engineering*, Vol. 15, No. 7, pp. 3013-3026. https://doi.org/10.1007/s10518-016-0076-4

Vukobratović, V., Fajfar, P. [2024a] "Direct floor response spectra for nonlinear nonstructural components", *Bulletin of Earthquake Engineering*, Vol. 22, No. 3, pp. 1033-1053. https://doi.org/10.1007/s10518-023-01818-4

Vukobratović, V., Fajfar, P. [2024b] "Floor response spectra for nonlinear SDOF nonstructural components", *Transactions of the 27th International Conference on Structural Mechanics in Reactor Technology (SMiRT 27)*, Yokohama, Japan.

Yasui, Y., Yoshihara, J., Takeda, T., Miyamoto, A. [1993] "Direct generation method for floor response spectra", *Transactions of the 12th International Conference on Structural Mechanics in Reactor Technology (SMiRT 12)*, Stuttgart, Germany, paper no. K13/4, pp. 367-372.

Seismic demand evaluation for the design of non-structural elements in precast concrete buildings

Davide Bellotti[1], Francesco Cavalieri[1], Emanuele Brunesi[1], and Roberto Nascimbene[1,2]

[1] European Centre for Training and Research in Earthquake Engineering (EUCENTRE)
Via Ferrata 1, 27100 Pavia, Italy
e-mail: {davide.bellotti,francesco.cavalieri,emanuele.brunesi,roberto.nascimbene}@eucentre.it
[2] University School for Advanced Studies (IUSS)
Palazzo del Broletto, Piazza della Vittoria 15, 27100 Pavia, Italy
e-mail: roberto.nascimbene@iusspavia.it

Abstract. During recent earthquakes, reinforced concrete precast buildings have exhibited major seismic vulnerabilities, and in several cases have experienced severe damage, not only to structural members, but also to non-structural elements (NSEs). This work proposes a methodology for the evaluation of the seismic demand that is needed for the design of NSEs typically present in precast industrial buildings. The considered case study structure, representative of the Italian construction period of the '90s and located in L'Aquila, features dowel-based beam-to-column connections and precast cladding panels. Two three-dimensional models, with implicit or explicit modelling of the cladding system, were created in OpenSees following an indirect analysis approach, in which NSEs are thus not modelled. Within nonlinear dynamic analyses carried out with ground motions scaled at two selected return periods, the structural response was recorded in terms of acceleration time-histories along both the main horizontal directions in several key nodes of the roof, the latter being assumed rigid in its plane. Finally, floor response spectra in acceleration-displacement space, which can be readily used for the design of NSEs, were generated considering three possible periods and two limit states, highlighting the influence of the cladding system modelling assumptions.

Keywords: Precast industrial buildings, Cladding panels, Floor response spectra, Acceleration-displacement space, Seismic design.

1. INTRODUCTION

A relevant portion of the non-residential facilities built all over the world in the last six decades is composed of reinforced concrete (RC) precast buildings, which have experienced heavy damage following recent seismic sequences. The lessons learned coming from field surveys suggest that analyses should focus not only on the main (or supporting) structure, but also on the design and vulnerability assessment of elements other than skeletal ones. For a precast industrial building, these elements include precast concrete cladding panels, steel racks adjacent or directly restrained to the panels, and roof elements, among others, and some of them can be classified as supported non-structural elements (NSEs) depending on if overall structural stiffness is affected or not. For example, during the 2012 Emilia-Romagna earthquake sequence in Northern Italy, the panel-to-beam connections often suffered extensive damage, causing the panel collapse due to overturning. In other cases, such collapse occurred due to the seismic interaction with adjacent steel racks [Bellotti *et al.*, 2024]. Concerning the roof, Bournas *et al.* [2014] reported that 25% of the analysed damaged buildings presented a partial or total collapse of the roof elements, mainly due to loss of support of the main beams. Similarly, Liberatore *et al.* [2013] observed the unseating of shed beams (used as roofing elements) in almost 30% of the 30 surveyed buildings [Savoia *et al.*, 2017]. Observed damage to NSEs following the 2016 Central Italy earthquake sequence was reported by Perrone *et al.* [2019].

In general, two are the viable methods to account for the interaction between the supporting structure and the supported elements, namely the *indirect approach* and the *direct approach*. According to the former, NSEs are not modelled together with the structure, and use is made of acceleration or displacement floor spectra. An example is the method adopted in FEMA P-58 [FEMA, 2018] and similar ones, which do not explicitly model the NSEs and use instead peak floor acceleration (PFA) directly as the engineering demand parameter (EDP), rather than the element's response itself. For the prediction of floor spectra, a number of building codes provide analytical or semi-analytical rules [e.g. ASCE 7-10, 2010; EC8, CEN, 2004], which tend to produce highly inaccurate results in some cases/conditions. In short, code compliant formulations tend to disregard damping levels for both the structure and the supported elements, resonance with higher modes of the structure, and the inelastic structural response. In the light of these shortcomings, it is commonly believed that deriving acceleration floor spectra analytically is a more robust option for the purpose of evaluating the seismic demand needed for designing NSEs [e.g. Merino *et al.*, 2018; 2019]: a number of analytical approaches have been actually proposed to derive floor spectra [e.g. Sullivan *et al.*, 2013; Calvi and Sullivan, 2014; Petrone *et al.*, 2015; Vukobratović and Fajfar, 2015; 2016; 2017; Lucchini *et al.*, 2016; 2017; Merino *et al.*, 2020; Rodriguez *et al.*, 2023]. Other researchers evaluated the seismic demand on NSEs in terms of acceleration and displacement floor spectra derived numerically, that is, by using the conventional procedure based on dynamic response history analysis undertaken on a nonlinear numerical model. Recent examples of these studies include those by Mohsenian *et al.* [2019], concerning five- and ten-storey steel frame structures, Gabbianelli *et al.* [2020], focussing on RC hospitals, Ruggieri and Vukobratović [2023], investigating RC school buildings, and Challagulla *et al.* [2023], related to five-storey RC buildings.

On the other hand, the direct approach envisages the modelling and analysis of both structural and non-structural elements altogether within the same numerical model [e.g. Wanitkorkul and Filiatrault, 2008; Merino *et al.*, 2018; 2019; Gabbianelli *et al.*, 2022]. This method, although computationally more expensive than the use of floor spectra, fully describes the dynamic interaction between structural and non-structural elements over time, and can therefore be considered as the reference option for use when it comes to accounting for NSEs [Merino *et al.*, 2019].

Few studies are available to date that specifically focus on the seismic demand evaluation for the design of non-structural elements in precast concrete buildings. One example is the work by Zhou *et al.* [2012], who evaluated the seismic demand of non-structural elements sensitive to accelerations in self-centring (SC) precast concrete wall structures. Another example is represented by the recent work of Blasi *et al.* [2025], in which the non-structural seismic demand is assessed using two different modelling approaches (flexible and

rigid diaphragm) for the roof, and carrying out linear dynamic analyses on two elastic models in SAP2000 [CSI, 2025]. Clearly, the seismic demand evaluation for non-structural elements in single-storey precast concrete buildings is not fully investigated yet: this lack prompted the current research, whose main goals are (i) to illustrate a methodology for the evaluation of the seismic demand that is needed for the design of non-structural elements typically present in precast industrial structures, and (ii) to highlight the influence of the cladding system modelling assumptions. A case study building representative of the Italian construction period of the '90s was modelled in OpenSees [McKenna *et al.*, 2000] following an indirect analysis approach. Two 3D numerical models were created, with explicit or implicit modelling of the cladding system, and subjected to nonlinear static and dynamic analyses. Starting from the roof's acceleration response, floor response spectra (FRS) in acceleration-displacement space [see e.g. Merino *et al.*, 2024] were generated for two limit states and both building directions with reference to three possible non-structural periods for demand identification and discussion: these FRS, indeed, can be readily used for the design of NSEs, such as roof elements and their connections to main beams.

2. CASE STUDY BUILDING

The definition of the case study was carried out by selecting one of the most common typologies of single-storey precast concrete structures used for industrial buildings in Italy in the last decades. Such a typology, indicated as Type 1 in Bellotti *et al.* [2025], consists of a series of single-storey basic portal frames arranged along the transverse direction. The investigated building (see Figure 1), located in L'Aquila, with the closure made of precast concrete lightened cladding panels, represents the Italian construction period of the '90s.

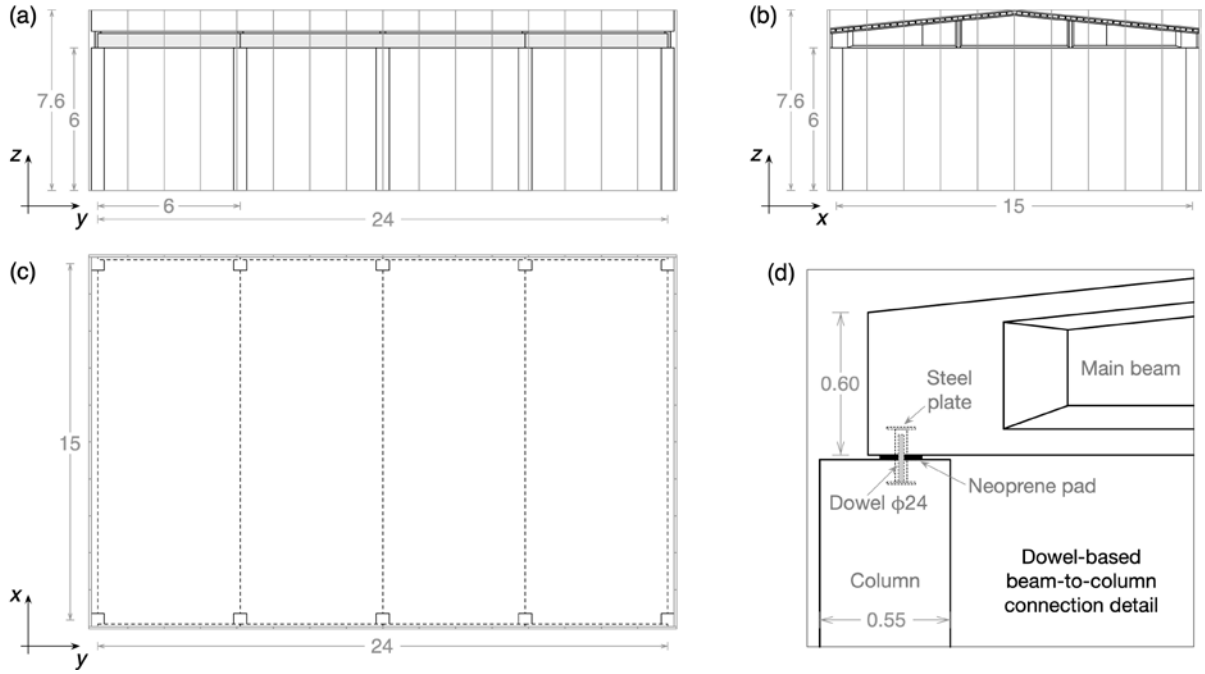


Figure 1. (a) Side, (b) frontal and (c) top view of the case study building, with (d) detail of the dowel-based beam-to-column connection (Units: m)

It is characterised by a rectangular plan with a total size of 15 × 24 m², with columns featuring a 0.55 × 0.55 m² cross-sectional area and a 6 m height. The prestressed main beams in the transverse (*x*) direction have a span of 15 m and a double slope (10% inclination) with an I-section variable in both height and thickness. The secondary beams, or girders, oriented along the longer side in plan (i.e. *y*-direction), are 6 m long and feature a tee cross-section. This building features dowel-based beam-to-column connections for both the

main and secondary beams. The roof system is constituted of precast double-tee elements, covered by a 5 cm thick cast-in-situ slab and connected to the main beams with bolted steel plates: for these reasons, and according to EC8 [CEN, 2004], the roof may be considered rigid in its plane. The external closure is composed of vertical RC expanded polystyrene (EPS)-lightened precast panels, 7.6 m high, 1.5 m wide and 20 cm thick. Such panels are attached to the beams through hammer-head strap connections, which allow the presence of a gap between the panel and the beam.

3. MODELLING ASSUMPTIONS

As already said in the Introduction, two 3D numerical models of the case study building were created in OpenSees, with explicit (M1) or implicit (M2) modelling of the cladding system. In both of them, a concentrated plasticity approach with a plastic hinge at the base of the columns was used to describe the global structural nonlinear behaviour: the stiffness of the entire element is obtained by connecting in series the stiffness of the rotational spring and the one of the column element. The plastic hinge model was defined using the "Modified Ibarra-Medina-Krawinkler Deterioration Model with Peak-Oriented Hysteretic Response" (*ModIMKPeakOriented*) material, as implemented in OpenSees, whose mechanical parameter values (the same for the two horizontal directions) were assigned according to Bosio *et al.* [2023].

The dowel-based beam-to-column connections for the main beams were modelled explicitly. Two elements were introduced (in parallel) between the two nodes (sharing the same position) representing the generic beam-to-column joint, namely a *Flat Slider bearing* element and a *zeroLength* element. The former, simulating the shear friction resisting mechanism acting together with the dowel, allows the translation in both the main horizontal directions at the attainment of the friction force computed following the Coulomb model; the friction coefficient was evaluated according to the model proposed by Magliulo *et al.* [2011] for neoprene–concrete friction, as a function of the normal stress acting on the sliding surface. The *zeroLength* element represents the dowel and features a bilinear behaviour along the two main horizontal directions: the latter behaviour, which includes post-yielding hardening and post-capping degradation, was modelled by means of the *ModIMKPeakOriented* material. A simulated design of the dowel was carried out in accordance with non-mandatory (i.e. in the form of *instructions*) prescriptions provided by the Italian National Research Council (CNR), namely CNR 10025/84 [1984], resulting in one ϕ24 mm steel bar for each joint. The parameters of the force-displacement relationship characterising the dowel, and assigned within the *ModIMKPeakOriented* material, were evaluated following Bressanelli *et al.* [2021], where the connection's stiffness is derived according to Ferreira and El Debs [2000]. The dowel-based beam-to-column connections for the girders were modelled through pinned connections. The properties of the roof system, as described in Section 2, justify the adopted assumption of rigid diaphragm for the roof in both models. In particular, the roof elements and the cast-in-situ slab were only considered as loads, a master node was introduced in the roof centroid and linked to the other nodes of the plane by a *RigidDiaphragm* constraint of OpenSees.

For the model with explicit modelling of the cladding system (M1), a strategy similar to the one proposed by Magliulo *et al.* [2015] for vertical panels was implemented. Specifically, the generic vertical panel was explicitly modelled as two elastic elements with high stiffness, each embedding a half of the panel's mass, which is lumped in the elements' upper node (at the level of connection to the beam). The elements are restrained at the base through a fixed connection in the direction parallel to the plane of the panel and a pinned connection (i.e. a hinge) in the out-of-plane direction, whilst another hinge at the node of attachment to the beam ensures that the panel behaves as a pendulum in the out-of-plane direction. In this way, the influence of the vertical panels on the response of the precast structure only depends on the in-plane properties of the anchors of connection to the beam, in the upper part of the panels. The anchors typically adopted to connect vertical panels to beams are hammer-head strap connections, which allow the presence of a gap, of size d_{gap}, between the panel and the beam. Such connections are characterised by a hysteretic

response, for which the force-displacement relationship proposed in the study by Zoubek *et al.* [2016] was herein taken as reference and modified. The aim was to reproduce the backbone curve, characterised by four points, proposed by Babič and Dolšek [2016] for the type of anchors of interest herein (called "Fastening A" in that study). Figure 2 shows the obtained cyclic response of the implemented model, the latter being assigned to a *zeroLength* element representing the connection. It has to be remarked that the first backbone point represents the attainment of the friction force in the connection, a condition causing the hammer-head strap to freely (i.e. with zero stiffness) slide in the panel's slot up to d_{gap} (i.e. to point #2). More details can be found in Bellotti *et al.* [2024].

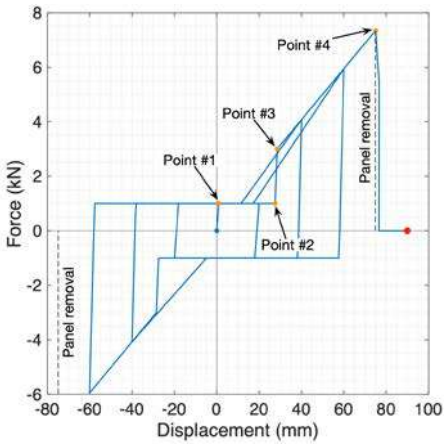


Figure 2. Force-displacement relationship of the *zeroLength* element employed to model the panel's connection

To model the in-plane failure of the panel-beam connection and the consequent removal of the generic vertical panel, the (static and dynamic) analyses in OpenSees were carried out on a step-by-step basis, monitoring at each step the force that is transmitted by the connection. When the force demand equals (in absolute value) the capacity, corresponding to the force value (i.e. 7.35 kN) of point #4 in the backbone, the *zeroLength* element modelling the connection is deleted by invoking the *remove element* command, the panel's mass in the connection nodes is removed as well, and the analysis is then resumed.

The model with implicit modelling of the cladding system (M2) only differs from the one described above for the absence of elastic elements representing vertical panels; however, the panels' masses are still present and lumped in the nodes belonging to beams or girders and located in correspondence of the previously modelled elastic vertical elements. The fundamental periods of the two models with explicit or implicit modelling of the cladding system resulted to be 1.07 s and 1.56 s, respectively.

4. STATIC AND DYNAMIC ANALYSES

Both OpenSees structural models were firstly subjected to nonlinear static (pushover) analyses in both the main directions (see Figure 3). The model with panels introduced as masses only (i.e. M2) is formally a bare frame model, whose behaviour is governed by the plastic hinges at the base of the columns, with the base shear never reaching the dowel's yielding or capacity. The model exhibits the same pushover (dashed purple) curves in the two directions, owing to the symmetric attribution of the plastic hinge parameter values. In both directions, the pushover curve (in green) of the model with panels explicitly modelled (i.e. M1) shows an increased initial stiffness with respect to the bare frame; it is noted that this increase is considerably lower than what expected if the panels were inserted within the structural frames, a behaviour also observed in the experimental tests carried out by Brunesi *et al.* [2015]. It is evident how the panel-to-beam connections along the *y*-direction collapse soon after the yield point of columns, for a displacement of 0.075 m, corresponding to a column drift of 1.25%: such a value is quite similar to the value experimentally observed

by Brunesi *et al.* [2015]. The panel removal is simulated as described in Section 3, with all panels being still present in the model, but without their masses and actually no longer following the deformed shape of the structure. Owing to the panel removal, the curve shows a sharp reduction of base shear, after which it then follows the curve of the bare frame model, as expected. The shape of the green curves in Figure 3, with increased initial stiffness and sharp base shear reduction, reflects the mechanical behaviour of the *zeroLength* element employed to model the panel-to-beam connections, displayed in Figure 2.

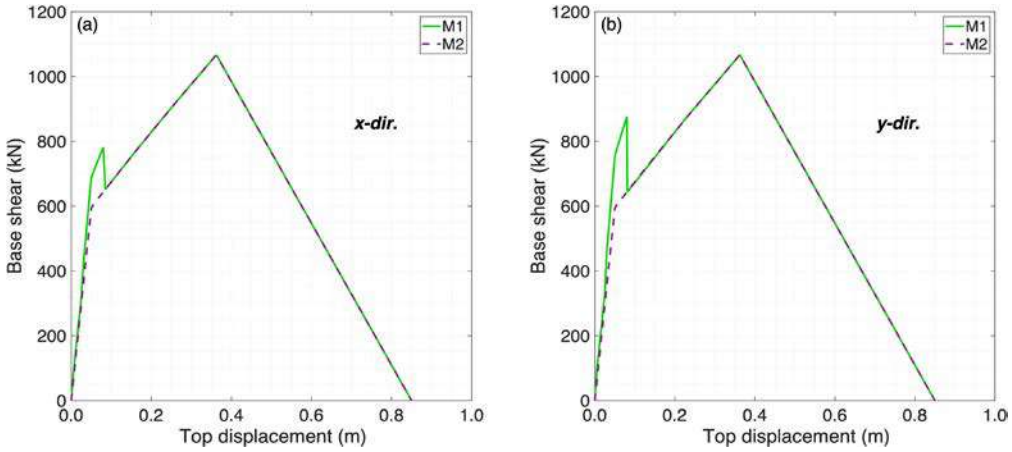


Figure 3. Pushover curves for both models along (a) the *x*-direction and (b) the *y*-direction

Both OpenSees models were also subjected to nonlinear dynamic analyses (NDAs) along the two horizontal directions. Two levels of intensity (or stripes) of a selected conditioning intensity measure (IM) were considered, at return periods of 50 and 500 years. The latter approximately characterise two limit states indicated in the current Italian seismic code provisions [D.M. 17/01/2018, also called NTC18], namely serviceability limit state (SLS), with reference probability of exceedance P_R = 81% in 50 yr, and ultimate limit state (ULS), with P_R = 10% in 50 yr (this is actually a life safety, no-collapse limit state). Soil type C was assumed, representing an averagely dense soil with a time-averaged shear wave velocity in the upper 30 m, $V_{S,30}$, ranging between 180 and 360 m/s, according to EC8 [CEN, 2004]. The Conditional Spectrum method [Jayaram *et al.*, 2011] was adopted to select, separately at each stripe, 20 natural spectrum-compatible recordings, extracted from the Italian accelerometric archive [Luzi *et al.*, 2008] and the NGAwest2 database [Ancheta *et al.*, 2014] within the Italian RINTC project [2015-2021]. The selected ground motions were scaled to two values (at the two return periods) of the conditioning IM, chosen to be the spectral acceleration at the fundamental period, $S_a(T_1)$: based on the periods of the two structural models, reported above, two different sets of recordings were selected, scaled at $S_a(1.0)$ and $S_a(1.5)$ respectively.

Within the dynamic analyses, the acceleration response time-histories were recorded along both the main horizontal directions in five nodes of the roof, namely the master (centroid) node of the rigid diaphragm and the four corner nodes of the building. Firstly, it was observed how the responses in the five nodes are identical along the same direction, in both models. This can be justified (i) by recalling the presence of a rigid diaphragm, and (ii) by noting that the models are characterised by the first two modes being purely translational along the *x*- and *y*-direction, owing to mass and stiffness regularity in plan; this allows obtaining independent behaviour along the two directions and the absence of a torsional response. Consequently, the acceleration responses in the master node only were post-processed, to derive the FRS in acceleration-displacement space (ADRS). For illustrative purposes, Figure 4 displays the FRS of individual records obtained along the *x*-direction for M1 at both limit states, with the superposition of the median curves and median ± 1 standard deviation (σ) curves, as a sort of statistical curves. Each point of the curves provides the spectral acceleration, S_a, and spectral displacement, S_d, both at a certain period, representing the seismic demand needed for the design of NSEs, the latter being acceleration- or displacement- or acceleration-displacement sensitive.

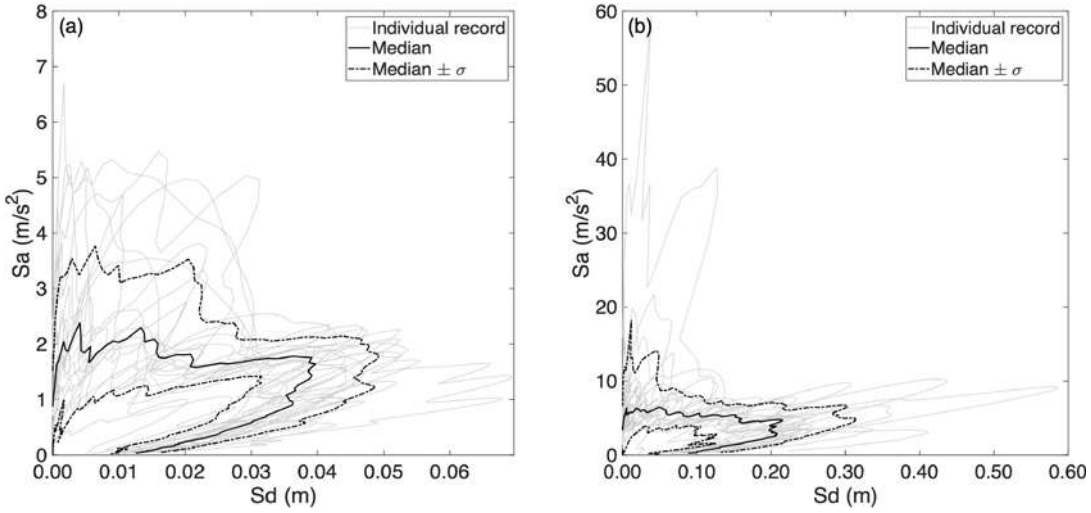


Figure 4. FRS obtained from the NDAs along the *x*-direction for M1, at (a) SLS and (b) ULS limit states, with the superposition of the median curves and median ± σ curves

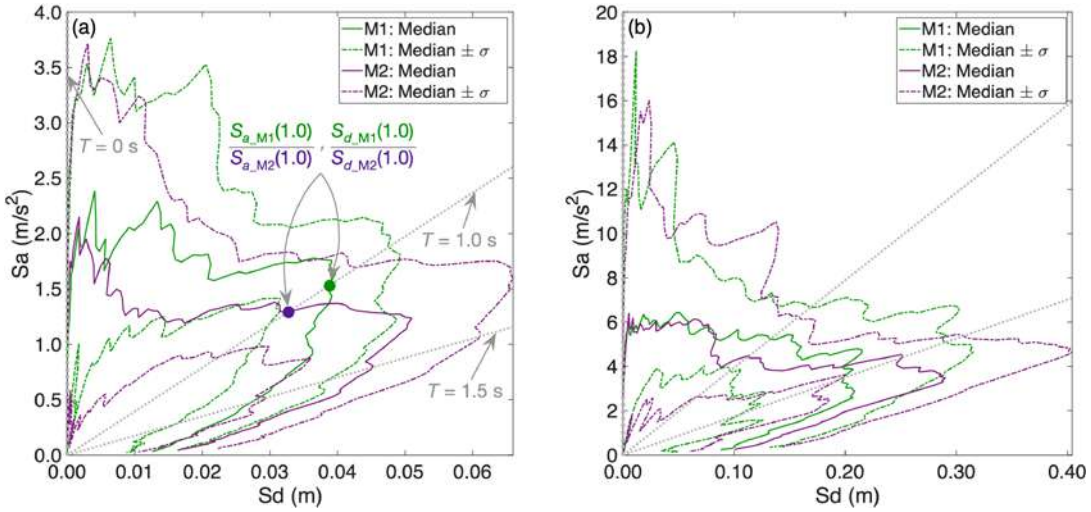


Figure 5. FRS median curves and median ± σ curves for both M1 and M2 along the *x*-direction, at (a) SLS and (b) ULS limit states. Grey dotted constant period lines are also displayed

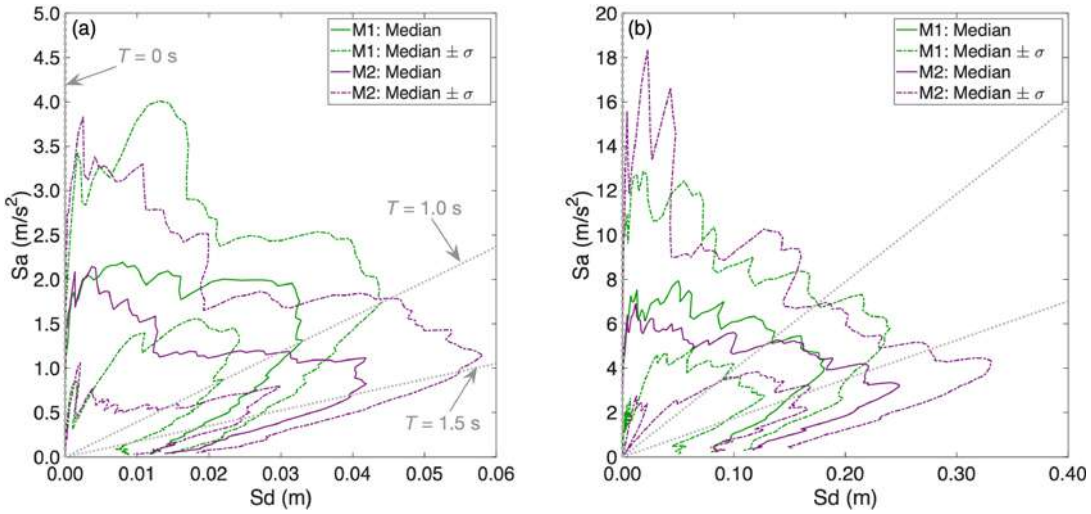


Figure 6. FRS median curves and median ± σ curves for both M1 and M2 along the *y*-direction, at (a) SLS and (b) ULS limit states. Grey dotted constant period lines are also displayed

Figure 5 and Figure 6, focussing on the comparison of the response of the two models, also display three (grey dotted) constant period lines, related to T = 0 s and hence rigid NSEs (vertical line superimposed to the y-axis), as well as two commonly found periods of NSEs, namely T = 1.0 s and T = 1.5 s. Firstly, in the plots it is possible to qualitatively distinguish the periods based on the distance between the three couples of statistical curves related to M1 (green) and M2 (purple), as well as the consistency or not of the (order of magnitude of) distance between such curves. To allow for a quantitative comparison of the response of the two models, the ratios of spectral accelerations and displacements at the three considered periods were computed on the three couples of statistical curves, as shown in Figure 5a with reference to the median curves (solid green and purple lines) at their intersection with the T = 1.0 s line. Table 1 reports such ratios for T = 0 s and T = 1.0 s only, for the two limit states and both directions, computed on the median FRS and the median + σ curves. For the case of T = 0 s, only the ratios in terms of spectral accelerations can be naturally obtained, whilst at T = 1.0 s the ratios in terms of S_a and S_d yield similar values for the different combinations. At T = 0 s the divergence between SLS and ULS appears obvious. At SLS the panels in M1 are still in place, leading to the same total mass but increased stiffness and lower S_a demands of M1 with respect to M2. On the other hand, at ULS the panels in M1 are detached, leading to the same stiffness but reduced total mass and higher S_a demands of M1 with respect to M2: the largest ratios are reached along the x-direction (values reported in bold in Table 1), indicating an increase of up to 44% of the demand corresponding to M1. Most of the ratios in the table are larger than unity, suggesting that the more refined model M1 generally leads to higher demands and thus a conservative design of NSEs, for the two periods considered in Table 1: the opposite situation happens for the case of T = 1.5 s (not reported here due to space constraints), where all ratios resulted to be lower than unity, even lower than 0.5 for some combinations (demands predicted by M1 are less than half those by M2). This observation confirms that the suitability of certain modelling assumptions strongly depends on the period of the NSE of interest.

Table 1. Ratios of spectral accelerations and displacements for two different periods, the two limit states and both directions, computed on the median FRS and the median + σ curves

		T = 0 s				T = 1.0 s			
		SLS		ULS		SLS		ULS	
		x-dir.	y-dir.	x-dir.	y-dir.	x-dir.	y-dir.	x-dir.	y-dir.
Median	S_{a_M1}/S_{a_M2}	0.825	0.932	**1.442**	1.279	1.196	1.117	1.171	1.062
	S_{d_M1}/S_{d_M2}	-	-	-	-	1.194	1.115	1.176	1.061
Median + σ	S_{a_M1}/S_{a_M2}	0.929	0.924	**1.337**	1.101	1.114	0.979	1.061	1.013
	S_{d_M1}/S_{d_M2}	-	-	-	-	1.113	0.979	1.065	1.023

5. CONCLUSIONS

The main goals of this work are (i) to illustrate a methodology for the evaluation of the seismic demand that is needed for the design of NSEs typically present in RC precast industrial structures, and (ii) to highlight the influence of the cladding system modelling assumptions. Two 3D numerical models of a case study building representative of the Italian construction period of the '90s were created in OpenSees, featuring explicit (M1) or implicit (M2) modelling of the cladding system. The models were subjected to nonlinear static and dynamic analyses. Starting from the roof's acceleration response, FRS in ADRS space were generated for three possible periods of NSEs, two limit states and both directions. Using the M1 vs M2 ratios of spectral accelerations and displacements to quantitatively compare the two models, markedly different trends for the three considered periods were observed. This confirms that the suitability of certain modelling assumptions towards conservative design of NSEs strongly depends on the period of the NSE of interest. The influence of the cladding system modelling is particularly evident in the case of rigid NSEs.

REFERENCES

Ancheta, T. D., Darragh, R. B., Stewart, J. P., Seyhan, E., Silva, W. J., Chiou, B. S.-J., Wooddell, K. E., Graves, R. W., Kottke, A. R., Boore, D. M., Kishida, T., Donahue, J. L. [2014] "NGA-West2 database," *Earthquake Spectra*, Vol. 30, No. 3, pp. 989-1005.

ASCE/SEI 7-10 [2010] "Minimum design loads for buildings and other structures," American Society of Civil Engineers (ASCE), Reston.

Babič, A., Dolšek, M. [2016] "Seismic fragility functions of industrial precast building classes," *Engineering Structures*, Vol. 118, pp. 357-370.

Bellotti, D., Cavalieri, F., Nascimbene, R. [2024] "Influence of closure external panels modelling on the seismic response of non-residential precast buildings," *Journal of Earthquake Engineering*, Vol. 28, No. 1, 288-304.

Bellotti, D., Cavalieri, F., Nascimbene, R. [2025] "Classification of Italian precast concrete structures," *Journal of Building Engineering*, Vol. 108, 112787.

Blasi, G., Ruggieri, S., Perrone, D., Vukobratović, V. [2025] "Quantification of non-structural seismic demands in buildings with flexible diaphragms through different modelling approaches," *Proceedings of COMPDYN 2025 - 10th International Conference on Computational Methods in Structural Dynamics and Earthquake Engineering*, 15-18 June 2025, Rhodes Island, Greece.

Bosio, M., Di Salvatore, C., Bellotti, D., Capacci, L., Belleri, A., Piccolo, V., Cavalieri, F., Dal Lago, B., Riva, P., Magliulo, G., Nascimbene, R., Biondini, F. [2023] "Modelling and seismic response analysis of non-residential single-storey existing precast buildings in Italy," *Journal of Earthquake Engineering*, Vol. 27, No. 4, pp. 1047-1068.

Bournas, D. A., Negro, P., Taucer, F. F. [2014] "Performance of industrial buildings during the Emilia earthquakes in Northern Italy and recommendations for their strengthening," *Bulletin of Earthquake Engineering*, Vol. 12, pp. 2383-2404.

Bressanelli, M. E., Bellotti, D., Belleri, A., Cavalieri, F., Riva, P., Nascimbene, R. [2021] "Influence of modelling assumptions on the seismic risk of industrial precast concrete structures," *Frontiers in Built Environment*, Vol. 7, 629956.

Brunesi, E., Nascimbene, R., Bolognini, D., Bellotti, D. [2015] "Experimental investigation of the cyclic response of reinforced precast concrete framed structures," *PCI Journal*, Vol. 60, No. 2, pp. 57-79.

Calvi, P. M., Sullivan, T. J. [2014] "Estimating floor spectra in multiple degree of freedom systems," *Earthquakes and Structures*, Vol .7, No. 1, 17-38.

CEN [2004] "EN 1998-1:2004. Eurocode 8: Design of structures for earthquake resistance - Part 1: General rules, seismic actions and rules for buildings," European Committee for Standardization.

Challagulla, S. P., Kontoni, D. P. N., Suluguru, A. K., Hossain, I., Ramakrishna, U., Jameel, M. [2023] "Assessing the seismic demands on non-structural components attached to reinforced concrete frames," *Applied Sciences*, Vol. 13, No. 3, 1817.

Consiglio Nazionale delle Ricerche (CNR) 10025/84 [1984] "Istruzioni per il progetto, l'esecuzione e il controllo delle strutture prefabbricate in conglomerate cementizio e per le strutture costruite con sistemi industrializzati," Bollettino Ufficiale del CNR (in Italian).

CSI [2025] "SAP2000 Integrated Software for Structural Analysis and Design," Computers & Structures, Inc., Berkeley, California, USA.

Decreto Ministeriale (D.M.) 17/01/2018 [2018] "Aggiornamento delle Norme tecniche per le costruzioni," In Suppl. ord. n. 8 alla G.U. Serie Generale n. 42 del 20/02/2018. Ministero delle Infrastrutture e dei Trasporti: Rome, Italy (in Italian).

FEMA [2018] "Seismic Performance Assessment of Buildings, Volume 1 – Methodology, Second Edition, FEMA P-58-1," prepared by the Applied Technology Council for the Federal Emergency Management Agency, Washington, D.C.

Ferreira, A., El Debs, M. K. [2000] "Deformability of beam-column connection with elastomeric cushion and dowel bar to beam axial force," *Proceedings of 2nd International Symposium on Prefabrication "Knowledge, Technology and the Future"*, 17-19 May, Helsinki, Finland.

Gabbianelli, G., Perrone, D., Brunesi, E., Monteiro, R. [2020] "Seismic acceleration and displacement demand profiles of non-structural elements in hospital buildings," *Buildings*, Vol. 10, No. 12, 243.

Gabbianelli, G., Perrone, D., Brunesi, E., Monteiro, R. [2022] "Seismic acceleration demand and fragility assessment of storage tanks installed in industrial steel moment-resisting frame structures," *Soil Dynamics and Earthquake Engineering*, Vol. 152, 107016.

Jayaram, N., Lin, T., Baker, J. W. [2011] "A computationally efficient ground-motion selection algorithm for matching a target response spectrum mean and variance," *Earthquake spectra*, Vol. 27, No. 3, pp. 797-815.

Liberatore, L., Sorrentino, L., Liberatore, D., Decanini, L. D. [2013] "Failure of industrial structures induced by the Emilia (Italy) 2012 earthquakes," *Engineering Failure Analysis*, Vol. 34, pp. 629-647.

Lucchini, A., Franchin, P., Mollaioli, F. [2016] "Probabilistic seismic demand model for nonstructural components," *Earthquake Engineering & Structural Dynamics*, Vol. 45, No. 4, pp. 599-617.

Lucchini, A., Franchin, P., Mollaioli, F. (2017). "Uniform hazard floor acceleration spectra for linear structures," *Earthquake Engineering & Structural Dynamics*, Vol. 46, No. 7, pp. 1121-1140.

Luzi, L., Hailemikael, S., Bindi, D., Pacor, F., Mele, F., Sabetta, F. [2008] "ITACA (ITalian ACcelerometric Archive): a web portal for the dissemination of Italian strong-motion data," *Seismol Res Lett*, Vol. 79, No. 5, pp. 716-722.

Magliulo, G., Capozzi, V., Fabbrocino, G., Manfredi, G. [2011] "Neoprene–concrete friction relationships for seismic assessment of existing precast buildings," *Engineering Structures*, Vol. 33, No. 2, pp. 532-538.

Magliulo, G., Ercolino, M., Manfredi, G. [2015] "Influence of cladding panels on the first period of one-story precast buildings," *Bulletin of Earthquake Engineering*, Vol. 13, No. 5, pp. 1531-1555.

McKenna, F., Fenves, G. L., Scott, M. H. (2000) "OpenSees: Open System for Earthquake Engineering Simulation," Software; University of California, Berkeley, CA, USA. Available online: http://opensees.berkeley.edu.

Merino, R. J., Brunesi, E., Nascimbene, R. [2018] "Derivation of floor acceleration spectra for an industrial liquid tank supporting structure with braced frame systems," *Engineering Structures*, Vol. 171, pp. 105-122.

Merino, R. J., Brunesi, E., Nascimbene, R. [2019] "Seismic assessment of an industrial frame-tank system: development of fragility functions," *Bulletin of Earthquake Engineering*, Vol. 17, pp. 2569-2602.

Merino, R. J., Mucedero, G., Perrone, D., Monteiro, R., Aiello, M. A., Nascimbene, R. [2024] "Estimation of consistent absolute acceleration and relative displacement floor response spectra in existing masonry-infilled reinforced concrete buildings," *Bulletin of Earthquake Engineering*, Vol. 22, pp. 5083-5118.

Merino, R. J., Perrone, D., Filiatrault, A. [2020] "Consistent floor response spectra for performance-based seismic design of nonstructural elements," *Earthquake Engineering & Structural Dynamics*, Vol. 49, No. 3, pp. 261-284.

Mohsenian, V., Gharaei-Moghaddam, N., Hajirasouliha, I. [2019] "Multilevel seismic demand prediction for acceleration-sensitive non-structural components," *Engineering Structures*, Vol. 200, 109713.

Perrone, D., Calvi, P. M., Nascimbene, R., Fischer, E. C., Magliulo, G. [2019] "Seismic performance of non-structural elements during the 2016 Central Italy earthquake," *Bulletin of Earthquake Engineering*, Vol. 17, pp. 5655-5677.

Petrone, C., Magliulo, G., Manfredi, G. [2015] "Seismic demand on light acceleration-sensitive nonstructural components in European reinforced concrete buildings," *Earthquake Engineering & Structural Dynamics*, Vol. 44, No. 8, pp. 1203-1217.

RINTC [2015-2021] "Implicit seismic risk of code-conforming structures in Italy," Joint ReLUIS-EUCENTRE project, funded by the Italian Department of Civil Protection (DPC).

Rodriguez, D., Perrone, D., Filiatrault, A. [2023] "Seismic demand on non-structural elements for quantifying seismic performance factors," *Earthquake Engineering & Structural Dynamics*, Vol. 52, No. 4, pp. 1016-1039.

Ruggieri, S., Vukobratović, V. [2023] "Acceleration demands in single-storey RC buildings with flexible diaphragms," *Engineering Structures*, Vol. 275, 115276.

Savoia, M., Buratti, N., Vincenzi, L. [2017] "Damage and collapses in industrial precast buildings after the 2012 Emilia earthquake," *Engineering Structures*, Vol. 137, pp. 162-180.

Sullivan, T. J., Calvi, P. M., Nascimbene, R. [2013] "Towards improved floor spectra estimates for seismic design," *Earthquakes and Structures*, Vol. 4, No. 1, pp. 109-132.

Vukobratović, V., Fajfar, P. [2015] "A method for the direct determination of approximate floor response spectra for SDOF inelastic structures," *Bulletin of Earthquake Engineering*, Vol. 13, pp. 1405-1424.

Vukobratović, V., Fajfar, P. [2016] "A method for the direct estimation of floor acceleration spectra for elastic and inelastic MDOF structures," *Earthquake Engineering & Structural Dynamics*, Vol. 45, No. 15, pp. 2495-2511.

Vukobratović, V., Fajfar, P. [2017] "Code-oriented floor acceleration spectra for building structures," *Bulletin of Earthquake Engineering*, Vol. 15, pp. 3013-3026.

Wanitkorkul, A., Filiatrault, A. [2008] "Influence of passive supplemental damping systems on structural and nonstructural seismic fragilities of a steel building," *Engineering Structures*, Vol. 30, No. 3, pp. 675-682.

Zhou, Y., Zhu, X., Wu, H., Djerrad, A., Ke, X. [2022] "Seismic demands of structural and non-structural components in self-centering precast concrete wall buildings," *Soil Dynamics and Earthquake Engineering*, Vol. 152, 107056.

Zoubek, B., Fischinger, M., Isaković, T. [2016] "Cyclic response of hammer-head strap cladding-to-structure connections used in RC precast building," *Engineering Structures*, Vol. 119, pp. 135-148.

Seismic Design of Reinforced Concrete Frames with Sliding Joint Ductile Infills

Van Sang Doan[1], Simone Pelucco[1], and Marco Preti[1]

[1] Department of Civil, Environmental, Architectural, Engineering and Mathematics, University of Brescia, via Branze, 43, Brescia, 25123, Italy
e-mail: v.doan@unibs.it
s.pelucco@unibs.it
marco.preti@unibs.it

Abstract. The paper describes some key results of a comprehensive study on the seismic performance of reinforced concrete (RC) frames infilled with deformable masonry panels incorporating horizontal sliding joints. These innovative infill systems are designed to address the seismic vulnerabilities typically observed in traditional RC structures with rigid infills, where the interaction between the frame and infill often leads to undesirable and well-known brittle failure mechanisms. The study analyses the response of three RC building models with three, five, and seven storeys, by varying the infill properties and design ductility classes. Structural responses are assessed through linear, nonlinear static, and nonlinear dynamic analyses, and are discussed across different seismic performance limit states. The focus is placed on the reliability of the different methods of analysis, on the ductility verification and the type of collapse mechanisms. Comparative results reveal how the presence of deformable infills, under varying design parameters and different modelling strategies, influences the global seismic response. These findings provide support to the development of design guidelines. Overall, the study confirms the potential of sliding-joint infills in improving seismic performance and support their possible integration into performance-based design methodologies. It also highlights the potential capability of Response Spectrum Analysis and Pushover analysis to capture seismic demands in infilled frames when the infill contribution to the structural response is considered.

Keywords: Ductile masonry infill, Sliding joint, Seismic resistant frame, Earthquake damage mitigation, Soft storey.

1. INTRODUCTION

Reinforced concrete (RC) frames with traditional masonry infills have repeatedly shown seismic vulnerability during past earthquakes [Fikri et al., 2019], mainly due to the interaction between the infill and the frame. To overcome these limitations, inspired by the idea of Langenbach [2007], a family of deformable infills has been proposed. These are typically achieved either by subdividing the masonry wall into sliding sub-panels [Preti et al., 2012] or by decoupling the panel from the frame with deformable joints placed along its perimeter [Ju et al., 2012]. The distinctive feature of these systems is to both reduce the high shear action demand on the columns and the significant in-plane damage of the traditional interacting masonry infills, keeping the advantage of the use of masonry panels for acoustic and thermal performances. Research programs have focused on the role of infills in the structural frames during earthquakes, and design codes [Draft Eurocode 8] are progressively placing more emphasis on their proper design and the associated safety checks. Among the seismic-resilient solutions, ductile infills with sliding joints have emerged as a promising option, designed to mitigate the detrimental effects of frame–infill interaction, reduce post-earthquake damage, and enable a more rational prediction of building response. Experimental [Morandi et al., 2018] and numerical [Bolis et al., 2017] studies have confirmed their potential; however, practical design guidelines are still lacking. In particular, clearer recommendations are needed on overstrength detailing, behaviour factor selection, and the applicability of simplified analysis methods for infilled frame structures.

This paper presents a synthesis of the results from a parametric analysis aimed at supporting the development of such design guidelines. The study investigates three RC building case studies of different heights, designed in accordance with Eurocodes and the Italian building code. In line with common practice, the infills are not explicitly included in the initial design model; instead, their influence is assessed through a detailed evaluation of the seismic response. This approach reflects the non-structural role of infills, whose composition and arrangement may change during the building's service life due to architectural renovations or functional modifications. Nevertheless, their contribution is explicitly considered in safety checks, particularly in relation to soft-storey mechanisms.

Three types of seismic analyses are performed and compared: linear dynamic response spectrum analysis (RSA), nonlinear static (pushover) analysis (PO), and nonlinear dynamic time-history analysis (NLTH). The study also investigates different levels of ductility and infill strength, and evaluates the capacity behaviour factor, thereby quantifying the influence of ductile sliding-joint infills on the seismic response of RC frames.

2. CASE STUDIES

The case studies examine three RC moment-resisting frame structures with different heights (three, five, and seven storeys) specifically selected to capture the influence of building height on seismic response. All buildings are representative of residential structures and are located in the Municipality of Cosenza (CS), a high-seismicity area in Italy, with site conditions defined by soil type "C" and topography category "T1." Each structure has five spans in the longitudinal direction and three spans in the transverse direction (Figure 1), founded on a rigid box underground structure. The design complies with the Italian building code and the European seismic standard, and the construction materials used are C35/45 concrete and B450C steel. The design gravity loads are reported in Table 1. Infills are placed along the perimeter and in two internal frames adjacent to the stairwell. These infilled frames are treated as primary structural elements, while the remaining frames are designed as secondary, resisting gravity loads only. The case study analysis focuses on one of the two external frames aligned along the shorter building dimension.

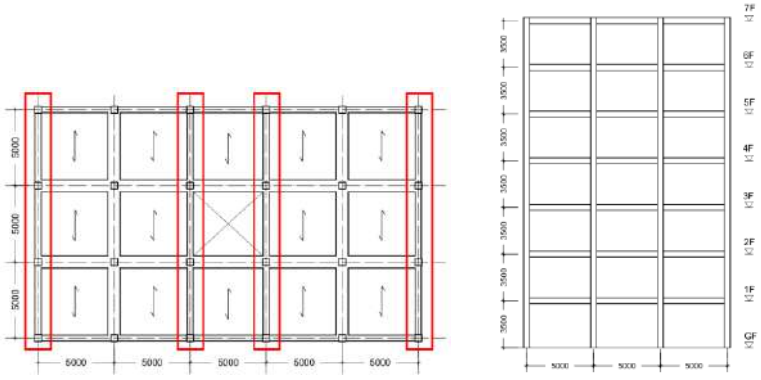


Figure 1. The case study structure in plan and elevation focusing on the seismic resistant frame in the minor direction (dimensions in [mm])

Table 1. Design gravity load

Floor type	G1 (kN/m²)	G2 (kN/m²)	Q (kN/m²)
Floors	3.55	3.60	2.00
Roof	3.55	3.30	0.50
Line loads			
Infills load (kN/m)	7.56		

Seismic design is carried out using response spectrum analysis (RSA), with the elastic site spectra shown in Figure 2.

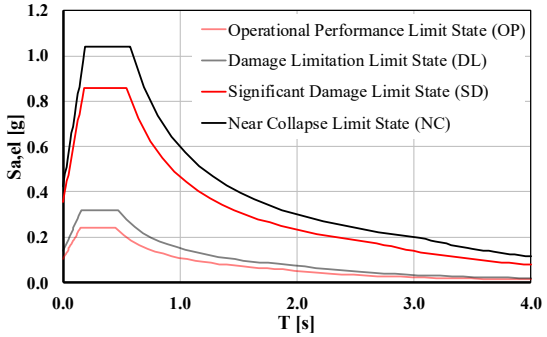


Figure 2. Design horizontal acceleration elastic spectra

Consistent with current design practice, the primary frame is designed without explicitly modelling the contribution of infills. Precautions against the detrimental effect of the infilled frame interaction is taken according to the prescription included in the Eurocode 8 [2004] and the Italian NTC [2018]. The case study bare frame is modelled using a bidimensional design, and this simplification is allowed by code as long as the bending strength of the columns is fictitiously reduced to 70% in the safety checks [Eurocode 8, 2004]. This is to ensure the compliance with capacity design and hierarchy of strength principles in the three-dimensional response, including bidirectional horizontal seismic excitation. To account for concrete cracking, a uniform stiffness reduction factor of 0.5 is applied to all members during the design. At the Serviceability Limit States (SLS), the interstorey drift limits specified for ductile infill walls are considered, with values set as follows: δ_{DL} = 1.0 % and δ_{OP} = 2/3 δ_{DL}. Three ductility classes are investigated (high (DCH), medium (DCM), and low (DCL)), resulting in three frames for each case study with different flexibility levels. The design behaviour factors of each frame are reported in Table 2. The behaviour factors in the DCH design for the 5-storey and 7-storey case studies, as well as in the DCM design for the 7-storey case study, are reduced with respect to the maximum allowable values. This adjustment is necessary because, at the fundamental period of the structures, the response spectrum ordinates fall below the minimum spectral acceleration of $0.2a_g$ prescribed by the Italian NTC (§3.2.3.5) and the Eurocode (§3.2.2.5). For the

DCL class, the behaviour factor is set to 2.7 for the 3- and 5-storey case studies, and to 2.5 for the 7-storey case study, in order to limit plasticization at both the serviceability and ultimate limit states. Size and reinforcement of the structural element are optimized to match the minimum required design flexural strength in the plastic hinge sections of the assumed collapse mechanism, with a target 10% maximum nominal overstrength of the design resisting bending moment compared to the corresponding demand (effect of actions).

The dynamic properties of the frames, including fundamental periods for both uncracked and cracked sections, are summarized in Table 2. As expected, flexibility increases with ductility level due to reduced cross-sections.

Table 2. Selected behaviour factors and fundamental periods of the different frame models: Uncracked sections with full elastic stiffness ("Uncracked"), cracked section with assumed 50% reduced stiffness for beams and columns ("Design"), and cracked section with assumed 30% and 50% reduced stiffness for beams and columns, respectively, for comparison to non-linear analysis types ("Comparison").

Case study	Ductility class	α_I/α_u	q_0	q	T_1 (s) Uncracked	T_1 (s) Design	T_1 (s) Comparisons
3-storey	DCH	1.3	5.85	5.85	0.80	1.13	1.28
	DCM	1.3	3.9	3.9	0.73	1.04	1.19
	DCL	N.A	N.A	2.7	0.58	0.83	0.95
5-storey	DCH	1.3	5.85	5.85 → 4.9	1.27	1.79	2.09
	DCM	1.3	3.9	3.9	1.03	1.46	1.70
	DCL	N.A	N.A	2.7	0.79	1.11	1.29
7-storey	DCH	1.3	5.85	5.85 → 4.2	1.43	2.00	2.35
	DCM	1.3	3.9	3.9 → 3.5	1.30	1.75	2.15
	DCL	N.A	N.A	2.5	0.99	1.39	1.62

Beams, in particular, exhibit significant stiffness reduction under cracking, especially where axial loads are low [Paulay & Priestley, 1992], with effective stiffness falling to less than half the uncracked value. To ensure consistency and reliability when comparing seismic demands from RSA and nonlinear analysis results, a stiffness reduction factor of 0.3 is adopted for the beams in the RSA analysis [Pelucco, 2024]. Each frame is examined in different configurations: bare, traditional and ductile infills (with three different infill thicknesses 200, 250, and 300 mm). The mechanical and geometrical properties of the infills required for their modelling follow Preti et al. [2015] and Di Trapani et al. [2020].

3.METHOD OF ANALYSIS

The seismic behaviour of the case-study building is investigated through three analysis approaches: linear dynamic response spectrum analysis (RSA), nonlinear static pushover analysis (PO), and nonlinear dynamic time-history analysis (NLTH). Masonry infills are represented using concentric equivalent diagonal strut macro-models according to Preti et al. [2019] and Di Trapani et al. [2020], calibrated to reproduce the bay-sway mechanism through an axial constitutive law. The column shear overload induced by the trust of the infill on the columns is quantified a posteriori.

For ductile infill, the RSA linear strut is calibrated with an equivalent secant stiffness at 1% interstorey drift, according to Bolis et al. [2017]. For the PO and NLTH, the infill macro-model accounts for a multilinear cyclic response as a result of the combination of three parallel non-linear axial springs, calibrated on the analytical prediction of the infill response validated against experimental tests [Pelucco, 2024].

In the PO and NLTH simulations, the RC members are represented using a fibre modelling strategy [Spacone et al., 1996]. Beams and columns adopt a refined discretization strategy to capture inelastic behaviour and varying confinement effects. Columns are subdivided into three regions: confined end zones that accommodate inelastic strains and a central elastic region with unconfined concrete. Plastic hinge formation is captured using Lobatto integration with two Gauss points at each end, in line with the method proposed by Ghannoum, & Moehle, [2012], while the central region is modelled with five integration points. The yield penetration of reinforcement in the foundation and in the column joint is taken into account by non-linear zero-length element calibrated to simulate rebar extension into adjoining members. A similar strategy is applied to beams, where the central region is modelled as elastic with a reduced moment of inertia by a factor of 0.35 to account for cracking, following Paulay & Priestley, [1992]. Beam-column joints are modelled implicitly by extending beam and column elements into the joint region. On the beam side, an elastic extension with reduced stiffness (representing cracked sections) is used, while no stiffness reduction is applied on the column side. Geometric nonlinearity is considered in the structural model through the inclusion of P-Delta effects, ensuring accurate representation of second-order moments under lateral seismic loading. The complete modelling scheme is summarised schematically in Figure 3.

The structural capacity at different limit states is assessed both globally and locally. For the Near Collapse (NC) limit state, local collapse is considered to occur when either the confined concrete reaches its ultimate compressive strain or the reinforcing steel attains a tensile strain of 4.0%, as captured by the fibre-based model. Shear failure is not explicitly assessed, based on previous findings [Pelucco, 2024] which showed that adequate stirrup detailing can cover the shear demands introduced by infills. At the global level, NC is identified by either a 15% drop in lateral resistance or exceeding a 4.0% interstorey drift, consistent with NIST GCR 17-917-46v3 guidelines and supported by experimental evidence from Preti et al. [2015] and Morandi et al. [2018]. The Significant Damage Limit State (SD) is defined by limiting material strains to 75% of those at NC and by adopting 1.5% and 2.5% interstorey drift thresholds for traditional and ductile masonry infills respectively. The value for ductile infill is based on the same experimental studies, which showed infill systems maintaining integrity up to 3.0% drift. At this limit, limited crushing of the sub-panels corners is expected together with plaster cracking at the sliding joint planes. Further cracking was experimentally observed in infill specimens with the opening but without any significant strength degradation. For lower damage states, interstorey drift limits of 0.5% for the Operational Performance Limit State (OP) and 1.25% for the Damage Limitation Limit State (DL) are adopted for ductile infills, where only horizontal cracks at sliding joint are expected in plaster. These values are reduced to 0.2% and 0.5% respectively for traditional infills.

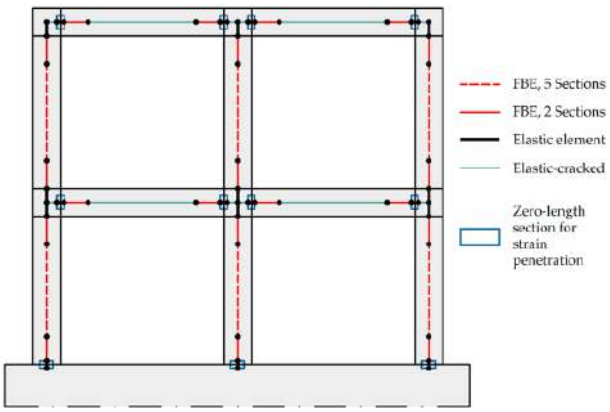


Figure 3. Modelling scheme represented for a two-bay and two-storey frame ("FBE" = Force based element, "5 Sections" = 5 integration sections assumed for the element, "2 Sections" = 2 integration sections assumed for the element, "Elastic-cracked" = Elastic element characterised by sectional stiffness reduced to 35% of the uncracked section) [Pelucco, 2024]

The design demand for the four limit state is quantified using the N2 method Fajfar & Gašperšič, [1996] for the PO, while seven spectrum-compatible accelerograms are adopted for NLTH, as detailed in Table 3.

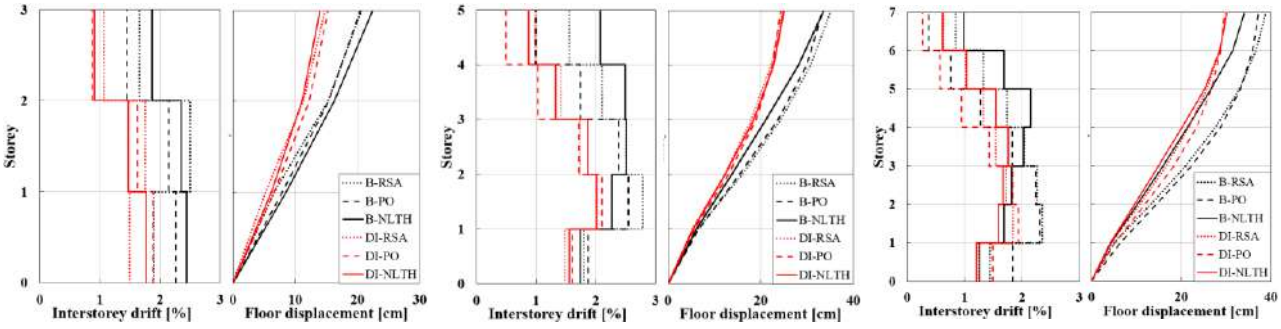
Table 3. Selected ground motions for SD

Code	Recorder ID	ID ITACA	Scale factor
SD1	IT.NOR.00.HG.EMSC-20161026_0000077	EMSC-20161026_0000077	E: 2.210
SD2	IT.MTR.00.HG.EMSC-20160824_0000006	EMSC-20160824_0000006	E: 4.395
SD3	IT.SAN0.00.HN.IT-2012-0011	IT-2012-0011	N: 1.605
SD4	IT.MRN.00.HN.IT-2012-0008	IT-2012-0008	E: 1.352
SD5	IT.SAN0.00.HN.IT-2012-0011	IT-2012-0011	E: 2.035
SD6	IT.NOR.00.HG.EMSC-20161026_0000095	EMSC-20161026_0000095	N: 2.939
SD7	IV.T0819..HN.IT-2012-0010	IT-2012-0010	E: 1.374

4.NUMERICAL RESULTS

This section presents key findings from the parametric analysis of the three case studies, focusing on the seismic performance of bare and infilled frame configurations designed for high ductility. The results, obtained from RSA, modal PO, and NLTH analyses (Figure 4), show that RSA and modal PO are generally in good agreement with each other and with NLTH, although discrepancies emerge at the upper floors. The match is noticeably better in infilled frames than in bare ones, for both interstorey drift and displacement. Moreover, RSA provides a safe estimate of maximum interstorey drift and top displacement in most cases.

To further evaluate the accuracy of linear and nonlinear analyses, Figure 5 compares maximum interstorey drift demands across all case studies at the SD limit state, highlighting deviations of RSA and PO from NLTH for different infill thicknesses at high ductility level. RSA results are closely aligned with PO and also with NLTH, with discrepancies generally below 10%. In particular, RSA predictions for the bare frame closely match those of NLTH. Overall, both RSA and modal PO demonstrate a good ability to approximate NLTH demands.



a) 3-storey **b) 5-storey** **c) 7-storey**

Figure 4. Interstorey drift and displacement demand at the SD limit state from PO, RSA, and NLTH analyses for bare (B) and ductile-infilled (DI) frames (200 mm infill) at DCH level in the three case studies

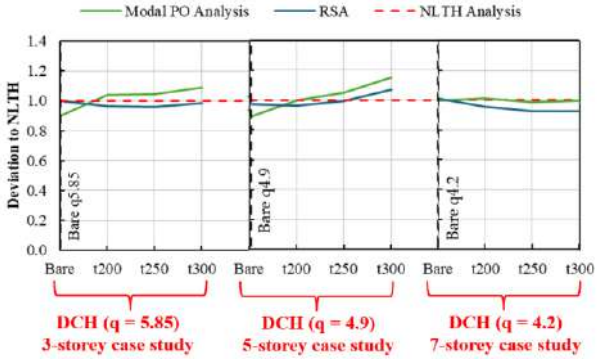


Figure 5. Relative deviation of interstorey drift demands at the SD limit state from modal PO and RSA analyses for bare and ductile-infilled frames (200, 250, 300 mm infill) compared to NLTH results at DCH level in the three case studies

Figure 6 compares capacity and demand in the force-displacement response for bare and infilled high-ductility frames across the three case studies, as quantified by the PO assuming a distribution of acceleration at the floor levels consistent with the frame in the 1st mode of vibration (modal PO). For comparison, the same frame with non-ductile infills ("traditional," i.e., having the same masonry properties as the ductile one but with a continuous running bond layout across the entire bay span and no sliding joints) is also included. The results show that in all cases, the bare and ductile infilled frames show a similar hardening response trend, but the ductile infilled frame exhibits higher initial stiffness and overall lateral strength. The traditional infilled frame shows the highest initial stiffness and peak strength, but followed by a degradation of more than 15% at low deformation levels. Demands are always far below the structural capacity for ductile infilled frame, while traditional infilled frame show vulnerability at the ultimate limit state with demand in excess of the capacity in all case studies. The corresponding nonlinear frame deformation mechanisms at the NC limit state for the 7-storey case study are shown in Figure 7. The presence of ductile infills does not significantly alter the mechanism at the NC limit state from the bare to ductile infilled case. In the traditional infilled frame, a soft-storey mechanism develops at the 1st and 2nd storeys, which is not observed in either the bare or ductile infilled frames.

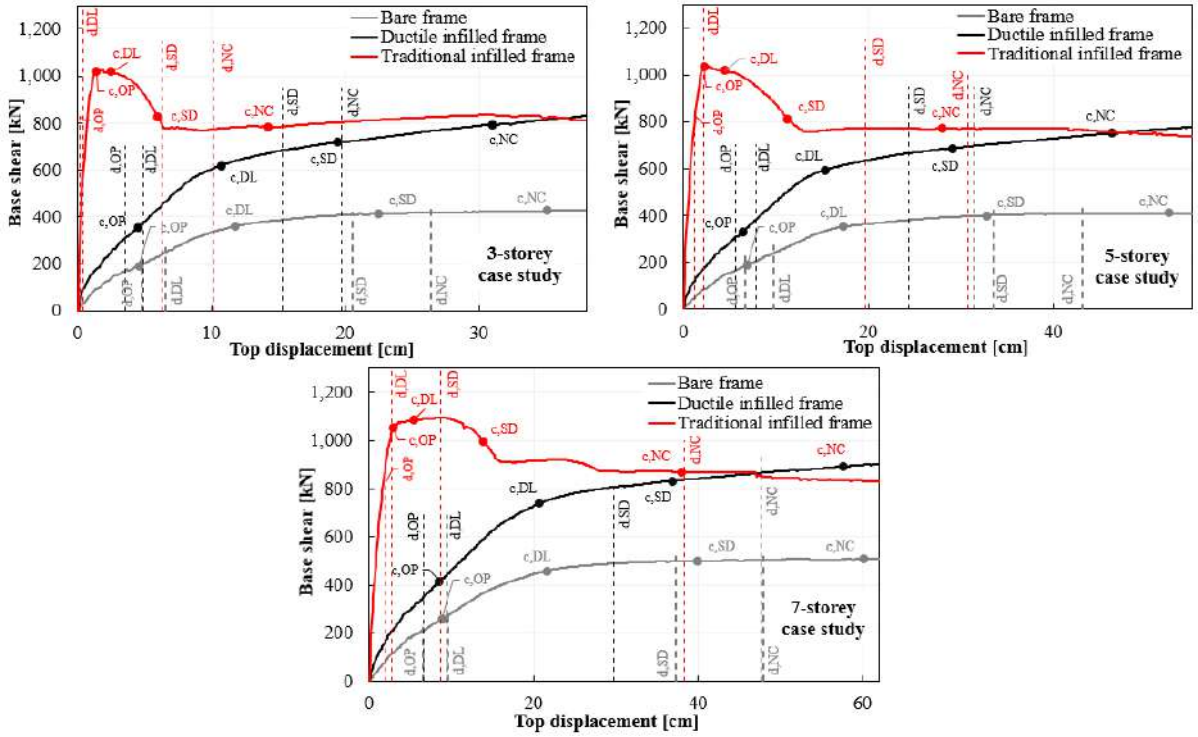
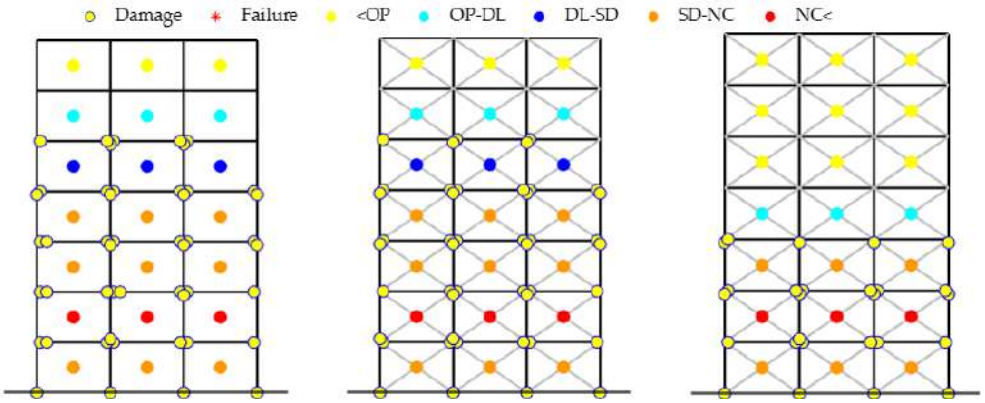


Figure 6. Capacity curves with the demand ("d") and capacity ("c") from modal PO analysis for bare, traditional and ductile infilled frames (200 mm infill) at DCH level in the three case studies



a) Bare frame **b) Ductile infilled frame** **c) Traditional infilled frame**

Figure 7. Mechanisms at the NC limit state capacity for (a) bare, (b) ductile, and (c) traditional infilled frames (200 mm infill) under modal PO analysis at DCH level of the 7-storey case study. For the beam, two control sections are considered: one at the beam-column interface, and another at a distance equal to the critical length from the same beam end section

Extending the investigation, the influence of sliding joint infills on the seismic response of structures is quantified through the evaluation of the capacity behaviour factor. The behaviour factor is evaluated by considering three components, as outlined in the Draft of Eurocode 8, namely the deformation and energy dissipation capacity (q_D), the overstrength due to the redistribution of seismic action effects in redundant structures (q_R), and the overstrength from other sources (q_S). For a more detailed examination of the behaviour factor evaluation, it can be referred to Ferraioli [2021], Morandi et al., [2022], and Ricci et al., [2023]. To compare the behaviour factor derived from the multi degree of freedom (MDOF) system with that from the equivalent single degree of freedom system, the modal participation factor (Γ) is used to relate the responses of the two systems.

To include the effect of ductile infills, the factor $q_{S,inf}$ was specifically introduced here as part of the definition of the capacity behaviour factor starting from the work of Pelucco [2024], in order to quantify the actual effects resulting from the inclusion of ductile infills in frame structures. The capacity behaviour factor is thus calculated as the product of the following factors.

Overstrength factor, infill $$q_{S,inf} = \frac{F_{y,d,infilled}}{F_{y,d,bare}} \quad (1)$$

Overstrength factor, I $$q_{S,I} = \frac{F_{y,m}}{F_{y,d}} \quad (2)$$

Redundancy factor $$q_R = \frac{F_{y,eq}}{F_{y,m}} \quad (3)$$

Ductility factor $$q_D = \frac{d_u}{d_{y,eq}} \quad (4)$$

Capacity behaviour factor $$q_c = q_{S,inf} \cdot q_{S,I} \cdot q_R \cdot q_D \quad (5)$$

Figure 8 illustrates the meaning of the key quantities of equations 1 to 5 referring to the capacity curves of the 3-storey "DCH" frame case study, considering both the bare and 200 mm ductile infilled configurations. Bilinearization of the curves is obtained targeting the significant damage displacement, d_u. Subscripts "m" and "d" refer to the median and design values of the material mechanical properties, respectively.

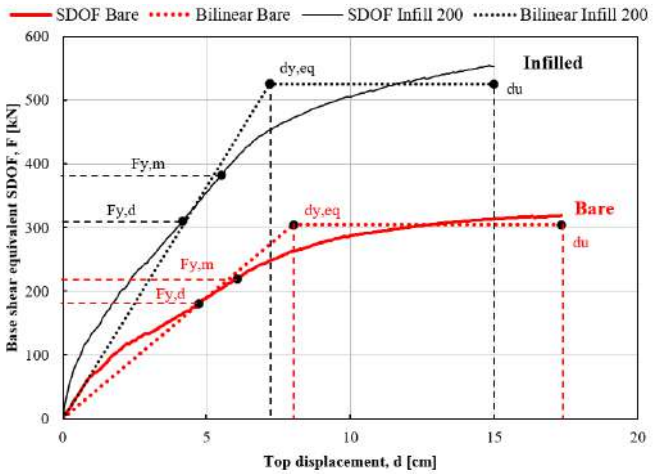


Figure 8. Example representation of key points on the equivalent SDOF systems for the bare DCH frame and the corresponding infilled configuration with 200 mm infill in the 3-storey case study

Figure 9 illustrates the trend of variation of the capacity behaviour factor at the SD limit state for the three case studies under consideration, varying the building height and the infill thicknesses. The behaviour factor is quantified with and without inclusion of infill overstrength factor, $q_{S,inf}$. When the infill overstrength factor is considered, the capacity behaviour factor increases with the infill thickness and is always greater or equal to the behaviour factor adopted in the design of the frame structure. This agrees with the safety checks, which show that capacity consistently exceeds demand. Conversely, neglecting the infill overstrength factor leads to a significant underestimation of the capacity behaviour factor, which results significantly smaller than the one adopted in the design. The capacity behaviour factor is essentially insensitive to building height. The adoption of $q_{S,inf}$ enables a more accurate comparison of the seismic performance between the bare and infilled structures. The infill acts as a supplementary seismic-resistant system, delaying the plasticization of the frame. This effect is captured with the inclusion of the $q_{S,inf}$ factor.

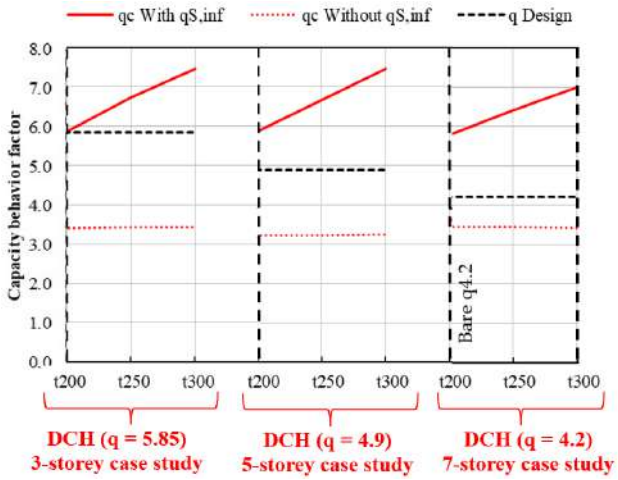


Figure 9. The capacity behaviour factor (with drift limit) at the SD limit state and DCH level in the three case studies, evaluated by considering "q_c With $q_{S,inf}$" or not "q_c Without $q_{S,inf}$" the contribution of the overstrength factor $q_{S,inf}$

5. CONCLUSIONS

A parametric analysis across 3 case studies focusing on the effect of ductile infills of a reinforced concrete frame is presented in the paper. Some initial results are reported here and suggest the following trend:

- Simplified analyses such as linear dynamic analysis or non-linear static analysis seem to well capture the response obtained by means of more refined non-linear time history analyses;
- The ductile infills seem not to alter the non-linear response of RC frames designed for ductility. No concentration of the infill damage and deformation at a single storey is observed, which is otherwise observed in traditionally infilled frames (induced soft story mechanism);
- The study also used nonlinear static analyses to examine the impact of infills on the behaviour factor capacity. Those results revealed that the presence of ductile infills increased the system's lateral strength and delayed the plasticization on its mechanism, highlighting that conventional evaluations of the behaviour factor should incorporate this additional overstrength. Importantly, the overall behaviour factor capacity does not decline when infills were introduced.

Those results are promising in reducing the post-earthquake damage and simplifying the seismic design of infilled RC structures. However, further analyses are still needed to confirm the findings.

ACKNOWLEDGEMENTS

The study presented in this work has been supported within the framework of DPC/ReLUIS project 2022-2024, WP10.

REFERENCES

Applied Technology Council. (2017). Guidelines for nonlinear structural analysis and design of buildings. Part IIb—Reinforced concrete moment frames (No. NIST GCR 17-917-46v3; p. NIST GCR 17-917-46v3). National Institute of Standards and Technology. https://doi.org/10.6028/NIST.GCR.17-917-46v3

Bolis, V., Stavridis, A., & Preti, M. (2017). Numerical Investigation of the In-Plane Performance of Masonry-Infilled RC Frames with Sliding Subpanels. Journal of Structural Engineering, 143(2), 04016168. https://doi.org/10.1061/(ASCE)ST.1943-541X.0001651

Di Trapani, F., Bolis, V., Basone, F., & Preti, M. (2020). Seismic reliability and loss assessment of RC frame structures with traditional and innovative masonry infills. Engineering Structures, 208, 110306. https://doi.org/10.1016/j.engstruct.2020.110306

DM 17 gennaio 2018— NTC. Ministry Decree, Norme tecniche per le costruzioni (Technical codes for construction) [in Italian]; 2018.

Eurocode 8: Design of structures for earthquake resistance - Part 1: general rules, seismic actions and rules for buildings. European Committee for Standardization, Brussels; 2004.

Fajfar, P., & Gašperšič, P. (1996). THE N2 METHOD FOR THE SEISMIC DAMAGE ANALYSIS OF RC BUILDINGS. Earthquake Engineering & Structural Dynamics, 25(1), 31–46. https://doi.org/10.1002/(SICI)1096-9845(199601)25:1<31::AID-EQE534>3.0.CO;2-V

Ferraioli, M. (2021). Behaviour Factor of Ductile Code-Designed Reinforced Concrete Frames. Advances in Civil Engineering, 2021(1), 6666687. https://doi.org/10.1155/2021/6666687

Fikri, R., Dizhur, D., Walsh, K., & Ingham, J. (2019). Seismic performance of Reinforced Concrete Frame with Masonry Infill buildings in the 2010/2011 Canterbury, New Zealand earthquakes. Bulletin of Earthquake Engineering, 17(2), 737–757. https://doi.org/10.1007/s10518-018-0476-8

Final Draft EN1998–1–2 NEN SC8 PT2 2019b–11–08 Draft Eurocode 8: Design of structures for earthquake resistance—Part 1–2: Rules for new buildings. 2019. (n.d.).

Ghannoum, & Moehle. (2012). Dynamic Collapse Analysis of a Concrete Frame Sustaining Column Axial Failures. Aci Structural Journal, 109(3), 403–412. https://doi.org/10.14359/51683754

Ju, R.-S., Lee, H.-J., Chen, C.-C., & Tao, C.-C. (2012). Experimental study on separating reinforced concrete infill walls from steel moment frames. Journal of Constructional Steel Research, 71, 119–128. https://doi.org/10.1016/j.jcsr.2011.10.004

Langenbach, R. (2007). From "Opus Craticium" to the "Chicago Frame": Earthquake-Resistant Traditional Construction∗. International Journal of Architectural Heritage, 1(1), 29–59. https://doi.org/10.1080/15583050601125998

Morandi, P., Butenweg, C., Breis, K., Beyer, K., & Magenes, G. (2022). Latest findings on the behaviour factor q for the seismic design of URM buildings. 20, 5797–5848. https://doi.org/10.1007/s10518-022-01419-7

Morandi, P., Milanesi, R. R., & Magenes, G. (2018). Innovative solution for seismic-resistant masonry infills with sliding joints: In-plane experimental performance. Engineering Structures, 176, 719–733. https://doi.org/10.1016/j.engstruct.2018.09.018

Paulay, & Priestley. (1992). Seismic Design of Reinforced Concrete and Masonry Buildings.

Pelucco, S. (2024). Seismic performance and modelling of reinforced concrete frames infilled with horizontal sliding joint deformable infills [PhD thesis]. Università degli Studi di Brescia.

Preti, M., Bettini ,N., & and Plizzari, G. (2012). Infill Walls with Sliding Joints to Limit Infill-Frame Seismic Interaction: Large-Scale Experimental Test. Journal of Earthquake Engineering, 16(1), 125–141. https://doi.org/10.1080/13632469.2011.579815

Preti, M., Bolis ,V., & and Stavridis, A. (2019). Seismic infill–frame interaction of masonry walls partitioned with horizontal sliding joints: Analysis and simplified modeling. Journal of Earthquake Engineering, 23(10), 1651–1677. https://doi.org/10.1080/13632469.2017.1387195

Preti, M., Migliorati, L., & Giuriani, E. P. (2015). Experimental testing of engineered masonry infill walls for post-earthquake structural damage control. https://doi.org/10.1007/s10518-014-9701-2

Ricci, P., Di Domenico, M., & Verderame, G. M. (2023). Behaviour factor and seismic safety of reinforced concrete structures designed according to Eurocodes. Structures, 55, 677–689. https://doi.org/10.1016/j.istruc.2023.06.060

Spacone, E., Filippou, F. C., & Taucer, F. F. (1996). Fibre Beam–Column Model for Non-Linear Analysis of R/C Frames: Part I. Formulation. Earthquake Engineering & Structural Dynamics, 25(7), 711–725. https://doi.org/10.1002/(SICI)1096-9845(199607)25:7<711::AID-EQE576>3.0.CO;2-9

Out-of-Plane Seismic Assessment of URM Infill Walls through Parametric Analysis

Gaspari M.[1], Donà M.[2], and da Porto F.[2]

[1] University of Padova, Padova, Italy
e-mail: marco.gaspari.2@phd.unipd.it
[2] University of Padova, Padova, Italy,
e-mail: marco.dona.1,francesca.daporto@unipd.it

Abstract. Out-of-plane (OOP) collapse of unreinforced masonry (URM) infill walls is a critical vulnerability in reinforced concrete (RC) buildings during seismic events. Although often overlooked in seismic design due to their classification as non-structural components, these infills can significantly affect building performance because of their geometric slenderness and brittle failure modes. This study builds upon a analytical model based on plate behaviour to perform an extensive parametric investigation. The influence of key parameters—such as aspect ratio (L_p/H_p), slenderness (H_p/t_p), masonry strength, and perforation direction—is systematically evaluated. The results are summarised into simplified design charts that offer practical tools for preliminary assessment, seismic verification, and prioritisation of retrofit interventions. The proposed framework aims to enhance the integration of OOP performance criteria in the seismic assessment of non-structural elements.

Keywords: Masonrry Infill walls, Out-of-Plane capacity, Analytical model, Arch mechanisms, Parametric Study.

1. Introduction

The use of masonry infill walls within reinforced concrete (RC) frames is a widely adopted construction practice worldwide. While these infill walls are often classified as non-structural elements in many design codes, their influence on the overall structural behaviour of buildings is significant and cannot be overlooked. They can alter the seismic response of RC frames, affecting both strength and stiffness, and their fragility often leads to damage that compromises building functionality and incurs substantial economic losses, even during minor to moderate seismic events [Del Gaudio et al., 2020].

Over the past decades, extensive experimental campaigns have been conducted to understand better the In-plane (IP) and Out-of-Plane (OOP) behaviour of masonry infill walls [Calvi and Bolognini, 2001; da Porto et al., 2020; De Risi et al., 2020; Furtado et al., 2016; Minotto et al., 2020; Morandi et al., 2022; Ricci et al., 2018]. However, the outcomes of these studies often differ due to a variety of factors, such as differences in test scales, the types of RC frames used, the mechanical properties and configuration of the masonry units (e.g., compressive strength and hole orientation), the slenderness and aspect ratio of the infill walls, and the nature of the applied loading. This variability makes it challenging to interpret the results comprehensively and has hindered the development of widely accepted formulations for evaluating the OOP capacity of different infill walls.

In this work, an analytical plate-based model [Gaspari, 2025] is employed to investigate the OOP response of masonry infill walls through a broad parametric study. The analysis systematically explores the role of geometric and mechanical properties - such as aspect ratio, slenderness, masonry strength, and perforation direction - on the collapse capacity. The results of the investigation are synthesised into simplified design charts, providing practical tools for preliminary assessment, seismic verification, and the prioritisation of retrofit strategies, with the broader goal of promoting the inclusion of OOP performance considerations in seismic evaluation procedures.".

2. Presentation of the Analytical Model

The analytical model is designed to evaluate the out-of-plane (OOP) capacity of masonry infill walls within reinforced concrete (RC) frames, accounting for both unreinforced and reinforced masonry configurations. The model has been developed and implemented in a MATLAB environment to facilitate the iterative resolution of equilibrium conditions.

The failure mechanism of the infill wall, illustrated in Figure 1, is based on a plate-like behaviour and can be assessed through the arching mechanism in both the vertical and horizontal directions. These mechanisms are analysed separately and then combined to determine the overall response. Depending on the section under analysis, the aspect ratio of the panel, and the failure angle - calculated as a function of the masonry unit geometry following the approach by Vaculik and Griffith [2017] -, the panel is divided into two or three rigid segments for both arching mechanisms.

Each segment rotates rigidly, Figure 2, around the frame supports (i.e., beams or columns), linking the displacement at the centre of the infill panel to a specific rotation angle, as shown in Figure 1. The model also considers the deformation of the elastic supports due to the rotation of the segments, which affects the geometric configuration of the system and the internal forces (tension and compression) within the sections.

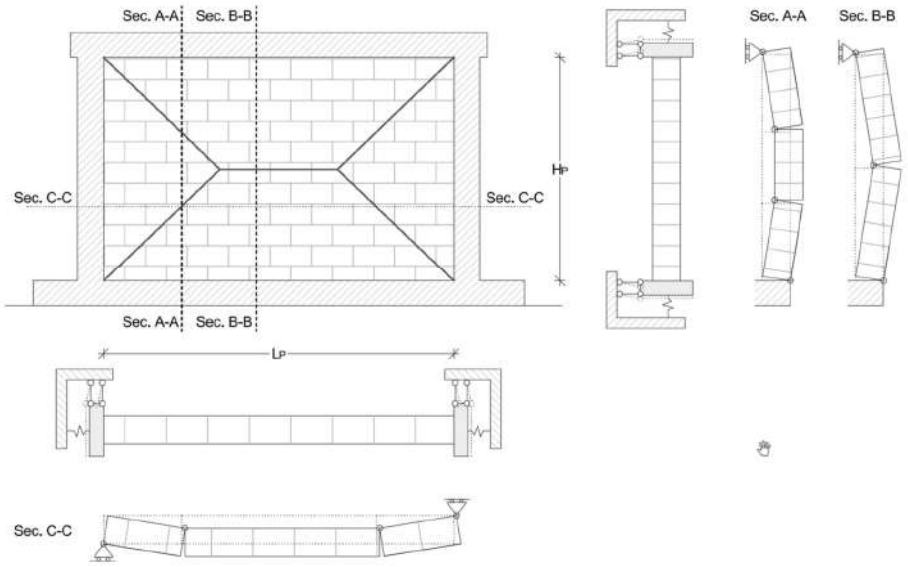


Figure 1. Schematic representation of the assumed plate-like failure mechanism and typical crack patterns (black thick line) in fully confined panels.

The deformation of the perimeter constraints is defined as a function of their flexural stiffness in a double-clamped configuration, as illustrated in Figure 2. The maximum deformation occurs at mid-span sections, characterized by two segments, and decreases near the beam-column joint, where the deformation is assumed to be zero. The compressive behaviour of the masonry and plaster is represented using an elastoplastic stress-strain relationship with a softening branch, Figure 3, while the tensile behaviour of reinforce, when these are applied to the infill wall, is modelled as elastic with brittle fracture.

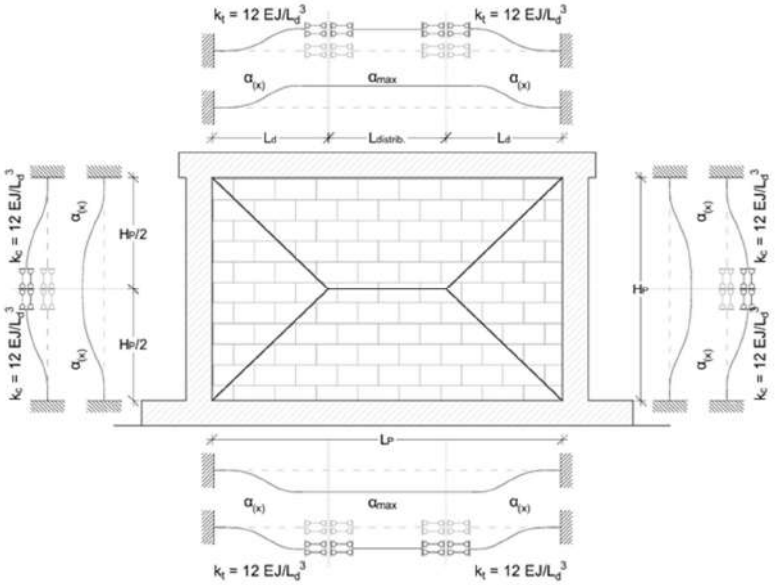


Figure 2. Deformation of the perimeter constraints and the resulting rigid-body rotations (α) of infill segments.

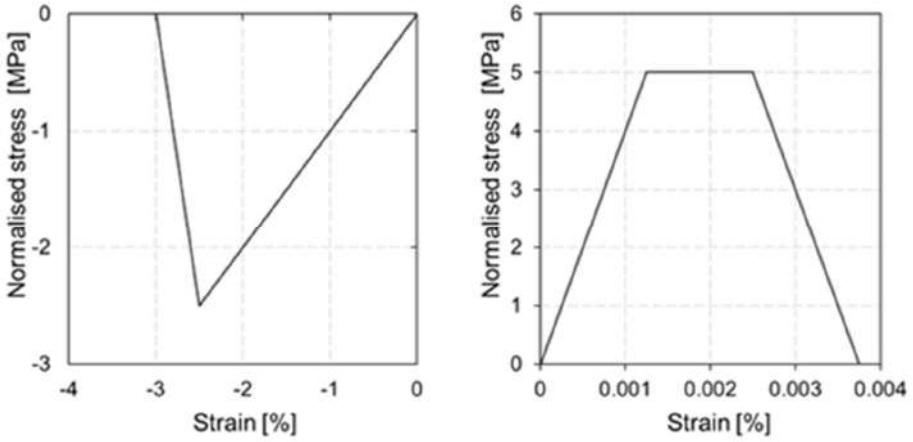


Figure 3. Stress-strain law of masonry and plaster in compression (right), stress-strain, law of tensile reinforce (left).

The OOP resistance of the infill walls is determined through an iterative computational process that establishes the rotational equilibrium of the masonry segments under external OOP loads and the reaction forces from the confining frame. The algorithm starts by assigning an initial displacement and computing the corresponding rigid rotation of the segments, along with the induced deformations of the bounding frame. The interaction between masonry and confining elements is resolved iteratively by updating displacement and force equilibrium until convergence is reached. Once the deformation state is determined, stabilizing moments are computed at cross-sections, and finally the external load responsible for the imposed OOP displacement. The process continues iteratively until the post-peak resistance drops to 60% of the maximum capacity or a predefined displacement threshold is reached. This approach is applied separately to both vertical and horizontal arching mechanisms, considering the specific mechanical properties governing each direction.

For additional insights into the validation of the analytical model, readers are referred to the work of Gaspari, [2025], where its validation is also presented through different experimental campaigns conducted on various infill walls [Angel et al., 1994; Calvi and Bolognini, 2001; Ricci et al., 2018; De Risi et al., 2020; Furtado et al., 2016; Koutas and Bournas, 2019; Akhoundi et al., 2020; Morandi et al., 2022]. An excerpt of this validation is reported in Figure 4, which shows the ratio between the predicted maximum OOP capacity and the corresponding experimental value. In the figure, H_p and t_p denote the height and thickness of the infill panel, respectively The left-hand plot illustrates the results obtained using the simplified formulation of Eurocode 6 (EC6) [CEN, 2020] while the right-hand plot presents the outcomes of the proposed plate-based model. As can be observed, the analytical model achieves a closer agreement with the experimental results, significantly reducing the scatter and providing a more accurate estimation of the infill capacity across different test campaigns.

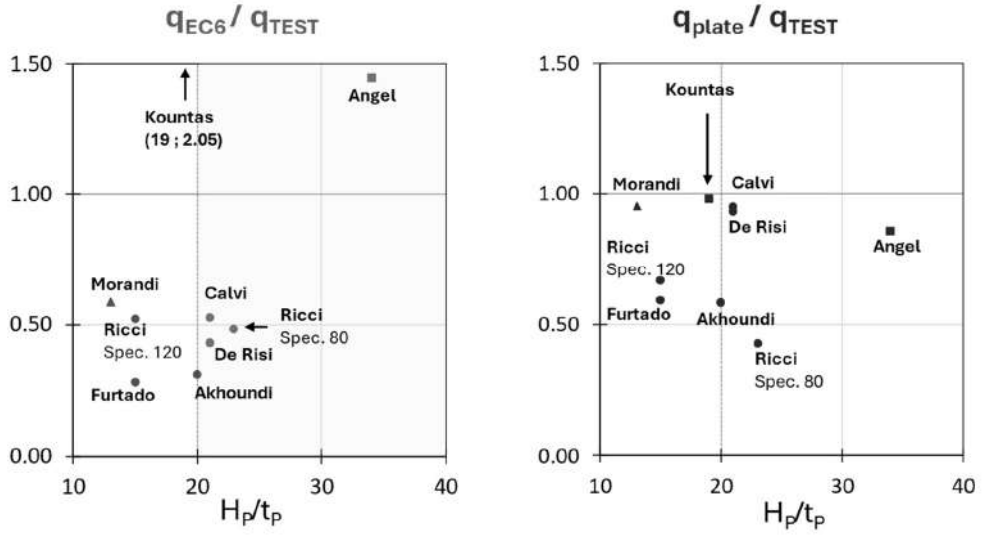


Figure 4. Predicted-to-experimental capacity ratios from: (left) EC6-based approach; (right) proposed plate-like model. (Markers: ■ solid clay bricks ▲ vertically perforated blocks ● horizontally perforated blocks).

3. Parametric Analysis of OOP Capacity and Discussion of the Results

This study presents a parametric analysis aimed at evaluating the Out-of-Plane (*OOP*) resistance of unreinforced clay unit masonry infill walls. The capacity, expressed as a uniform pressure on the panel (in kPa), is analysed through two distinct parametric investigations. The first analysis examines the influence of the aspect ratio (L_p/H_p), expressed as the ratio between the panel length and its height, and the compressive strength of the masonry (f_k) on the OOP resistance. The second analysis explores the relationship between the OOP resistance and the slenderness ratio (H_p/t_p) of the infill walls.

3.1 Effect of the Aspect Ratio on the OOP Capacity

The analysis varied the aspect ratio by maintaining a constant panel height of 3.5 m, selected to reflect realistic dimensions commonly used in RC frames, while incrementally increasing the panel width. The aspect ratio (L_p/H_p) ranged from 0.67 to 2.5. The compressive strength of the masonry (f_k) was analyzed for three values: 2 N/mm², 4 N/mm² and 6 N/mm², measured parallel to the perforations of the clay units (i.e. along the longitudinal hollow cores of the blocks). In the direction perpendicular to the perforations (i.e., across the webs of the units), the compressive strength was assumed to be one quarter of the parallel value, reflecting the well-known anisotropic behaviour of hollow clay masonry. In the following, horizontal perforation refers to blocks laid with the hollow cores running horizontally, whereas vertical perforation refers to blocks with hollow cores oriented vertically within the panel.

The wall thickness was fixed at 180 mm. This configuration resulted in a slenderness ratio (H_p/t_p) of 19.44. For all the analyses performed, the failure angle (θ) of the panel was set to 45°.

The RC frame was defined with a rectangular cross-section for both the columns and the top beam, adopting dimensions and reinforcement details representative of construction practices in seismic zones. The columns had a cross-section of 30×30cm, with 3% longitudinal reinforcement relative to the cross-sectional area. The transverse reinforcement consisted of 10 mm diameter stirrups spaced at 50 cm in the critical zones and 8 mm diameter stirrups spaced at 130 cm in the central zones. The beam had a cross-section of 50×25cm, with 2% longitudinal reinforcement relative to the cross-sectional area. Its transverse

reinforcement included 8 mm diameter stirrups spaced at 60 cm in the critical zones and 8 mm diameter stirrups spaced at 130 cm in the central zones.

The results of this parametric analysis are illustrated in Figure 5, which shows the OOP resistance (Q) of the infill walls as a function of the aspect ratio (L_p/H_p) for varying values of masonry compressive strength (f_k). The graph highlights that infill walls with low aspect ratios ($L_p/H_p < 1$) and horizontal perforation exhibit higher resistance values. This is because the contribution of the horizontal arching mechanism increases significantly in this range. Additionally, since the horizontal arch acts along the direction parallel to the perforation of the clay blocks, where the compressive strength is higher, this further enhances the resistance of the panel. Beyond an aspect ratio of 1, the contribution of the horizontal arching mechanism stabilizes, as the size of the rotating segments resisting the OOP load no longer increases. Consequently, as L_p/H_p increases further, the behaviour of the panel stabilizes and transitions toward being dominated by the vertical arching mechanism.

The influence of masonry compressive strength (f_k) is also evident in the graph, with higher f_k values consistently leading to greater resistance across all aspect ratios. The trends observed align with the expected mechanical behaviour of infill walls, confirming the analytical model's ability to capture the key parameters governing OOP resistance.

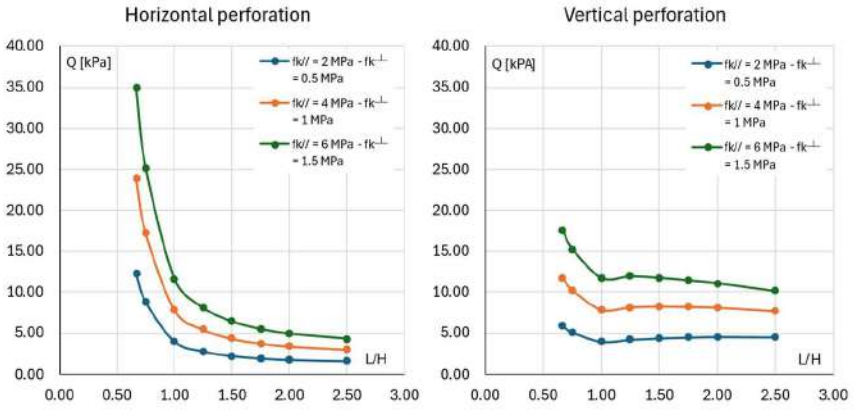


Figure 5. Out-of-plane capacity (Q) of the infill walls as a function of the aspect ratio (L_P/H_P) for different values of masonry compressive strength (f_k), for horizontal and vertical perforation.

3.2 Effect of the Slenderness Ratio on the OOP Capacity

The second parametric analysis focused on the slenderness ratio (H_p/t_p) of the infill walls, defined as the ratio between the panel height (H_p) and its thickness (t). In this analysis, three aspect ratios (L_p/H_p) were investigated: 0.67, 1, and 1.5, while the masonry compressive strength (f_k) was fixed at 4 MPa. The out-of-plane capacity (Q) was evaluated as a function of the slenderness ratio by varying the panel thickness (t_p) from a minimum of 8 cm to a maximum of 40 cm. The panel height was kept constant at 3.5 m to reflect realistic dimensions. The failure angle (θ) of the panel and the frame characteristics were the same as those used in the previous parametric analysis.

The results of this parametric analysis are illustrated in Figure 6. The orange line represents the OOP capacity trend for infill walls with vertical perforation, while the blue corresponds to infill walls with horizontal perforation.

The relationship between perforation orientation and aspect ratio (L_p/H_p) plays a critical role in determining the out-of-plane (OOP) behaviour of masonry infill walls. For $L_p/H_p > 1$, infill walls with vertical

perforation exhibit significantly higher OOP capacities compared to those with horizontal perforation, highlighting the dominant contribution of vertical arching mechanisms. This suggests that vertical perforation orientation should be preferred over horizontal orientation in such configurations to enhance structural performance. Conversely, for L_p/H_p = 1, the OOP capacities of both orientations are nearly identical, indicating that aspect ratio serves as a pivotal parameter in assessing the influence of perforations orientation on panel behaviour.

Regardless of the aspect ratio, increasing the slenderness ratio (H_p/t_p) leads to a marked reduction in OOP capacity. This effect becomes especially pronounced beyond the EC6 slenderness limit (H_p/t_p > 15), where the decline is sharper, underscoring the importance of panel thickness in ensuring structural performance under OOP loads.

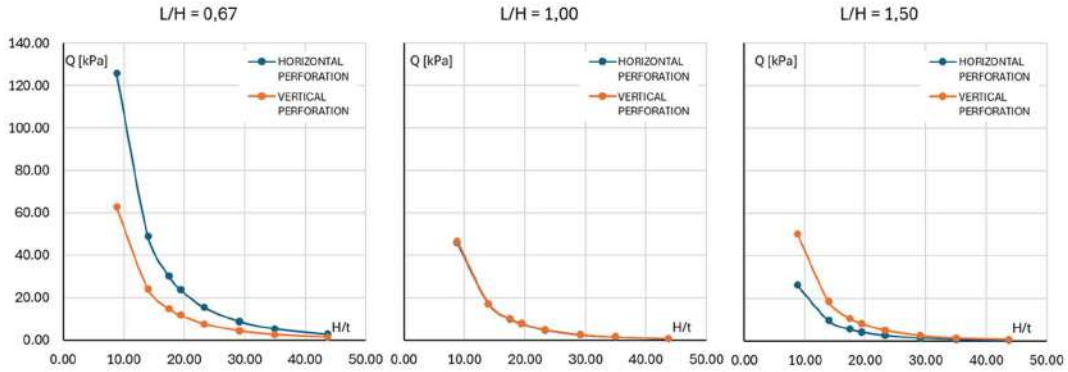


Figure 6. OOP capacity of infill walls depending upon the slenderness ratio (H_p/t_p) and aspect ratio (L_p/H_p).

3.3 SIMPLIFIED CAPACITY CHARTS FOR DESIGN-ORIENTED APPLICATIONS

To translate the outcomes of the parametric analyses into practical tools for preliminary assessment, the results were synthesised into simplified capacity charts. Starting from the two independent investigations - aspect ratio (L_p/H_p) versus masonry strength, and slenderness ratio (H_p/t_p) versus aspect ratio - the full parametric space was expanded to generate continuous capacity surfaces. For clarity of interpretation, only the surfaces corresponding to a masonry compressive strength of 4 MPa are presented here, both for horizontal and vertical perforation, Figure 7.

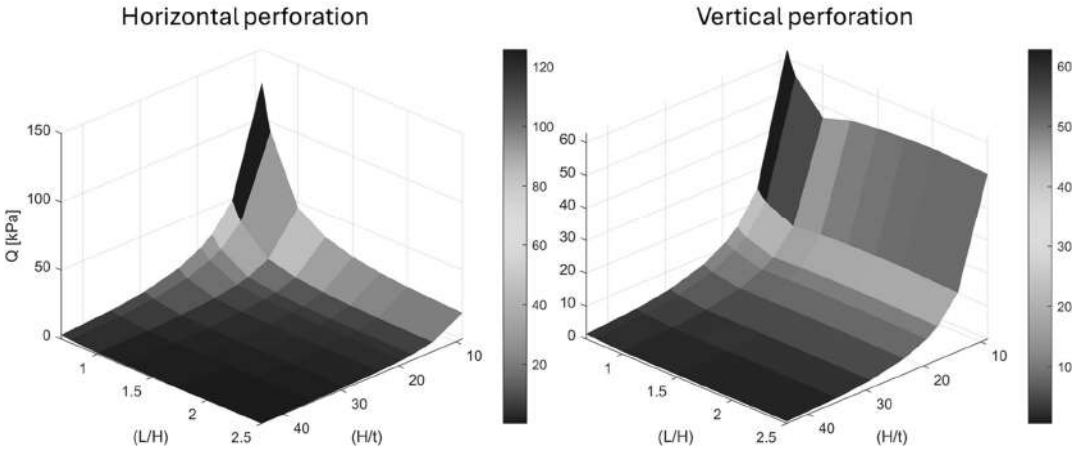


Figure 7. Capacity surfaces obtained from the parametric analyses for masonry compressive strength fk = 4 MPa, shown for both horizontal (left) and vertical perforation orientations (right).

From these capacity surfaces, simplified charts were derived to provide a direct correlation between the geometric parameters $(H/t)$and L_p/H_p and the resulting OOP resistance. In Figures 8 and 9, the horizontal axis represents the slenderness ratio H/t, while the vertical axis reports the aspect ratio L/H. The out-of-plane direction of the charts corresponds to the predicted OOP capacity Q, which is plotted as a surface over the (H_p/t_p and L_p/H_p) plane. Figure 8 is extracted from the capacity surface corresponding to horizontally perforated units (Figure 7, left), whereas Figure 9 is derived from the surface associated with vertically perforated units (Figure 7, right).

To improve readability, each chart is presented separately for panels with L_p/H_p <1 (left) and L_p/H_p >1 (right), reflecting the distinct behaviours previously discussed. For L_p/H_p <1, the capacity surface exhibits a steeper gradient as the slenderness ratio decreases (i.e., for thicker panels), highlighting the dominant contribution of the horizontal arching mechanism. Conversely, for L_p/H_p >1, the surface becomes smoother, and the response is increasingly governed by the vertical arching mechanism, making the effect of perforation orientation more evident.

Overall, Figures 8 and 9 provide a compact yet comprehensive visualisation of the parametric results, enabling the OOP capacity of infill walls to be estimated directly as a function of $H/t$and L_p/H_p, thereby bridging the gap between detailed analytical modelling and practical application in seismic verification and retrofit prioritisation.

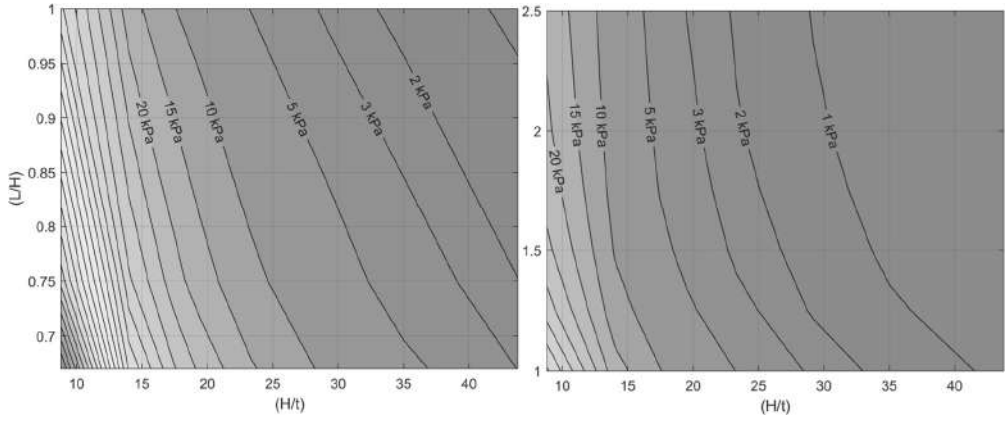


Figure 8. Simplified capacity charts derived from the Horizontal Perforation surfaces (Figure 7-left). Separately reported for panels with L_p/H_p < 1 (left) and L_p/H_p > 1 (right).

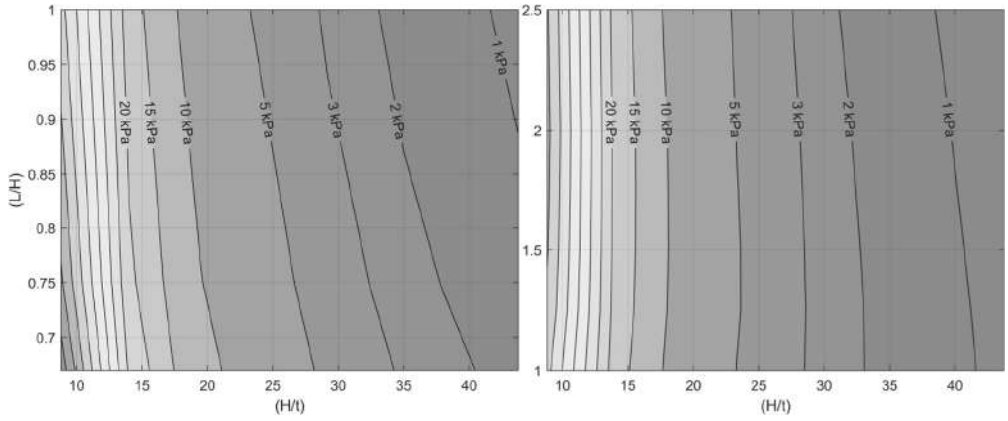


Figure 9. Simplified capacity charts derived from the Vertical Perforation surfaces (Figure 7-right). Separately reported for panels with L_p/H_p < 1 (left) and L_p/H_p > 1 (right).

4. Conclusion

This study presented an analytical framework for evaluating the out-of-plane (OOP) resistance of unreinforced masonry (URM) infill walls, based on a plate mechanism that combines vertical and horizontal arching actions while accounting for the deformability of the surrounding RC frame. The model was first validated against experimental data, demonstrating improved predictive accuracy compared to the simplified Eurocode 6 approach.

Two parametric analyses were conducted to investigate the influence of the aspect ratio (L_p/H_p), slenderness ratio (H_p/t_p), and perforation orientation of hollow clay units on the OOP capacity of infill walls. The results confirmed the strong dependence of OOP resistance on the geometric configuration of the panel. For narrow walls ($L_p/H_p < 1$), the horizontal arching mechanism governs the response, and horizontally perforated units (i.e., blocks with their hollow cores running along the horizontal direction), exhibit higher capacities because compression develops parallel to the stronger material direction. Conversely, for wider panels ($L_p/H_p > 1$), the vertical arching mechanism becomes dominant, and vertically perforated units provide superior performance as the compressive stresses align with the vertical orientation of the hollow cores. This confirms that the inherent anisotropy of hollow clay masonry has a decisive influence on the activated arching mechanism and thus on the resulting OOP capacity.

Increasing the slenderness ratio (H_p/t_p) consistently reduced the OOP capacity across all configurations, with a more pronounced decline beyond the EC6 slenderness limit. This highlights the critical role of panel thickness in preventing OOP collapse and reinforces the need to consider slenderness explicitly in seismic assessment procedures.

The parametric results were then synthesised into simplified capacity charts, offering practical tools to estimate OOP resistance as a function of basic geometric parameters. These charts are intended to support preliminary seismic assessment, design verification, and the prioritisation of retrofit interventions.

Future developments will focus on extending the model to account for additional variables, such as boundary conditions, in-plane damage interaction, and the effect of retrofitting techniques, with the aim of broadening its applicability in performance-based seismic assessment of RC buildings.

Acknowledgments

Special thanks are due to the Italian Department of Civil Protection and ReLUIS, which funded this study in the framework of the ReLUIS-DPC Project 2024-2026 – Work Package 10 Task 3: "Non-structural masonry".

REFERENCES

Akhoundi, F., Vasconcelos, G., Lourenço, P. [2020] *"Experimental Out-Of-Plane Behavior of Brick Masonry Infilled Frames."* Int. J. Archit. Herit. 14, 221–237. https://doi.org/10.1080/15583058.2018.1529207

Angel, R., Abrams, D.P., Shapiro, D., Uzarski, J., Webster, M. [1994] *"Behavior of Reinforced Concrete Frames with Masonry Infills."* Civ. Eng. Stud. SRS-589.

Calvi, G.M., Bolognini, D. [2001] *"Seismic Response of Reinforced Concrete Frames Infilled with Weakly Reinforced Masonry Panels."* J. Earthq. Eng. 5, 153–185. https://doi.org/10.1080/13632460109350390

CEN [2020] *"Eurocode 6 - Design of masonry structures - Part 1-1: General rules for reinforced and unreinforced masonry structures"*.

da Porto, F., Donà, M., Verlato, N., Guidi, G. [2020] *"Experimental Testing and Numerical Modeling of Robust Unreinforced and Reinforced Clay Masonry Infill Walls, With and Without Openings."* Front. Built Environ. 6. https://doi.org/10.3389/fbuil.2020.591985

De Risi, M.T., Furtado, A., Rodrigues, H., Melo, J., Verderame, G.M., António, A., Varum, H., Manfredi, G. [2020] *"Experimental analysis of strengthening solutions for the out-of-plane collapse of masonry infills in RC structures through textile reinforced mortars."* Eng. Struct. 207, 110203. https://doi.org/10.1016/j.engstruct.2020.110203

Del Gaudio, C., Di Ludovico, M., Polese, M., Manfredi, G., Prota, A., Ricci, P., Verderame, G.M. [2020] *"Seismic fragility for Italian RC buildings based on damage data of the last 50 years."* Bull. Earthq. Eng. 18, 2023–2059. https://doi.org/10.1007/s10518-019-00762-6

Furtado, A., Rodrigues, H., Arêde, A., Varum, H. [2016] *"Experimental evaluation of out-of-plane capacity of masonry infill walls."* Eng. Struct. 111, 48–63. https://doi.org/10.1016/j.engstruct.2015.12.013

Gaspari, M. [2025] *"Towards Scalable and Rapid Seismic Vulnerability and Deterioration Assessment of Heterogeneous Building Stocks: Simplified Methodologies and Innovative Tools"*. Universty of Padova.

Koutas, L.N., Bournas, D.A. [2019] *"Out-of-Plane Strengthening of Masonry-Infilled RC Frames with Textile-Reinforced Mortar Jackets."* J. Compos. Constr. 23, 04018079. https://doi.org/10.1061/(ASCE)CC.1943-5614.0000911

Minotto, M., Verlato, N., Donà, M., da Porto, F. [2020] *"Strengthening of In-Plane and Out-of-Plane Capacity of Thin Clay Masonry Infills Using Textile- and Fiber-Reinforced Mortar."* J. Compos. Constr. 24, 04020059. https://doi.org/10.1061/(ASCE)CC.1943-5614.0001067

Morandi, P., Hak, S., Milanesi, R.R., Magenes, G. [2022] *"In-plane/out-of-plane interaction of strong masonry infills: From cyclic tests to out-of-plane verifications."* Earthq. Eng. Struct. Dyn. 51, 648–672. https://doi.org/10.1002/eqe.3584

Ricci, P., Di Domenico, M., Verderame, G.M. [2018] *"Experimental assessment of the in-plane/out-of-plane interaction in unreinforced masonry infill walls."* Eng. Struct. 173, 960–978. https://doi.org/10.1016/j.engstruct.2018.07.033

Vaculik, J., Griffith, M.C. [2017] *"Out-of-plane load–displacement model for two-way spanning masonry walls."* Eng. Struct. 141, 328–343. https://doi.org/10.1016/j.engstruct.2017.03.024

INFLUENCE OF SCREW CONNECTION ON OUT-OF-PLANE BEHAVIOR OF LGS WALLS

Fumihiko SAKURABA[1], Shota MIZUNO[2], Alex SHEGAY[3], Yasuaki SATO[4]

and Shojiro MOTOYUI[5]

[1] Corporate Officer, Someno Construction Materials Co., Ltd.
648 Shishiko-cho, Ushiku-shi, Ibaraki 300-1231, Japan
sakuraba@someno.co.jp
[2] Structural Engineer, Toyota T&S Construction CO.LTD.
3-23 Gokisodori, Showa-ku, Nagoya-shi, Aichi 466-0015, Japan
mspg368@gmail.com
[3] Assistant Professor, University of Auckland, Auckland, New Zealand
alex.shegay@auckland.ac.nz
[4] Researcher, Research & Development, Takenaka Corporation
1-5-1 Ohtsuka, Inzai-shi,Chiba 270-1395, Japan
satou.yasuaki@takenaka.co.jp
[5] Emeritus Professor. School of Environment and Society, Tokyo Institute of Technology
4259 Nagatsuta, Midori-ku, Yokohama, Kanagawa 226-8502, Japan
smotoyui@gmail.com

Abstract. In this report, we proposed a method to extract the mechanical properties of screw connections from bending test results and understand the behavior of screw connections in LGS walls subjected to actual out-of-plane bending. The main objective was to clarify the effect of screw connections on the out-of-plane bending behavior (particularly initial stiffness) of LGS walls. We also proposed a to method to calculate the bending rigidity of LGS walls using composite beam theory using the initial slip stiffness of screw connections obtained through 3 points bending test of LGS walls. We demonstrated the validity of this calculation method for the bending rigidity of LGS wall by comparing it with the results of bending tests with different screw spacing.

Keywords: LGS wall, Out of plane bending behavior, Screw connection, Incomplete composite beam.

1. INTRUDUCTION

The dry partition wall construction method, shown in Figure 1, involves assembling lightweight steel members called studs and facing materials such as gypsum board on-site (hereinafter referred to as LGS walls). This construction method offers superior workability compared to wet finishing methods. For this reason, it is widely used around the world; however, damage has been reported to these components in several recent earthquakes. The reason why earthquake damage to nonstructural elements, including LGS walls, is generally considered a problem is the fact that there have been cases where severe damage has occurred to nonstructural elements despite earthquake motions of a magnitude that caused little damage to the structure. While the improvements in seismic design methods for building structures have improved their seismic performance, controlling and mitigating damage, there has been a relative lack of seismic performance improvement to nonstructural elements. Therefore, to reduce earthquake damage to nonstructural elements, it is essential to develop methods for objectively designing nonstructural elements so that their seismic performance can match that of the structure.

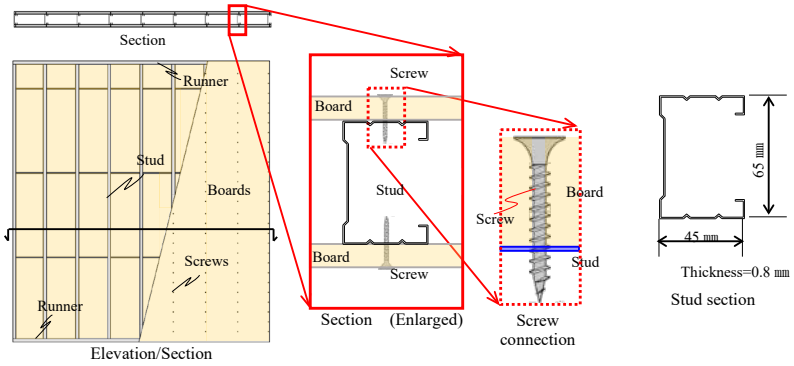


Figure 1. Composition of LGS wall and its components

During an earthquake, LGS walls are subjected to both out-of-plane inertial forces and in-plane displacements. This paper focuses on the out-of-plane bending behavior of LGS walls, with the goal of mitigating damage. The effects of special boundary conditions due to runners at the top and bottom edges of LGS walls are ignored. Factors that determine the out-of-plane bending characteristics of LGS walls include the mechanical properties of the studs and boards that make up the wall and the mechanical properties of the screw connections between the studs and gypsum board (hereinafter referred to as screw connections). For this reason, a great deal of research has been conducted on each of these characteristics. In particular, many papers have been published focusing on screw connections (e.g., Herfurth, 2024). We have also conducted element tests using extracted screw connections, as shown in Figure 2 [Minatogawa et al., 2014].

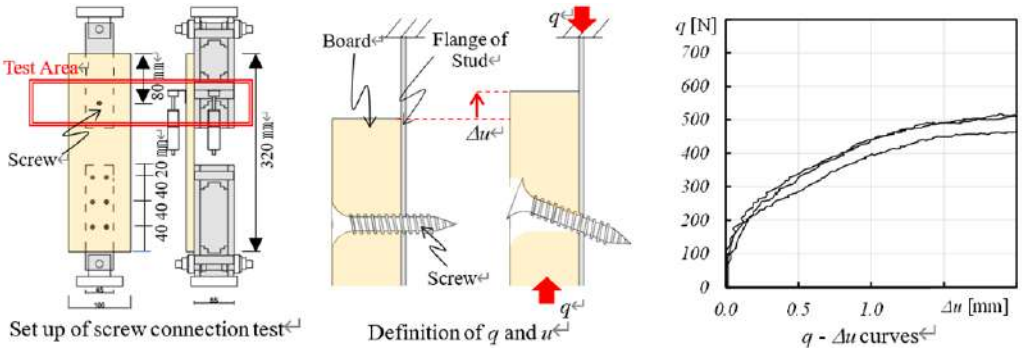


Figure 2. Past test results for slip behavior of screw connection

Strictly speaking, when an LGS wall is subjected to out-of-plane bending, the gypsum board is simultaneously subjected to in-plane forces acting as a composite beam, as well as local stresses such as bearing pressure near the screw connections. Such stress conditions are significantly different from the stress conditions in element tests. This fact suggests that element tests that simply isolate only the screw connections are insufficient; however, to the authors' knowledge, there is no research that has examined the validity of element tests on screw connections.

In this study, to clarify the effect of screw connections on the out-of-plane bending deformation of LGS walls, we consider a three-point bending condition on the LGS wall shown in Figure 3. The parameters in this test are board arrangement (both stud sides lined, **LGS-B**oth and only single side lined on compression side or tension side; **LGS-C**omp or **LGS-T**ens), board thickness (12.5 mm, 21 mm), and screw spacing (36 mm, 110 mm, 330 mm). The most notable feature of this test is that each side had only one piece of gypsum board was attached to the stud, and that gypsum board was intentionally made shorter than the stud. The reason for using a single piece of gypsum board is to eliminate the impact of the joints between the boards that would occur if multiple sheets of gypsum board are attached. The reason for making the gypsum board shorter than the stud is to avoid potential restraint from the supporting beams on the slip shear response between the stud and board. Both considerations are intended to reproduce the conditions assumed in Newmark's incomplete composite beam theory. In addition, because the stud cross section is an asymmetric open cross section, there is a risk of torsional-bending deformation when a transverse force is applied. Therefore, the two studs are fastened to an independent piece of gypsum board near the supporting points to act as a stiffener (labeled "Board" in Figure 3) to restrain this torsional-bending deformation.

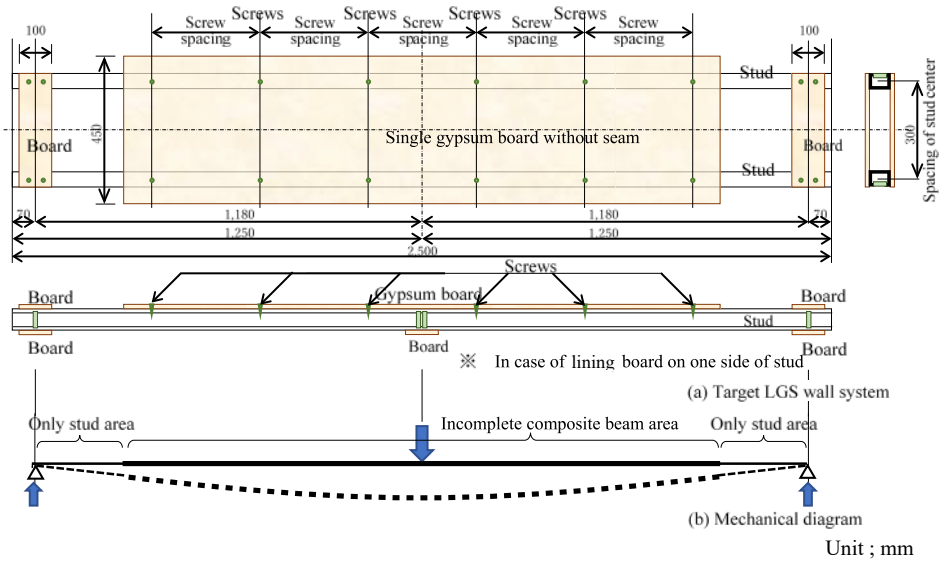


Figure 3. Feature of present target LGS wall system

2. INCOMPLETE COMPOSITE BEAM THEORY BY NEWMARK

2.1 OVERVIEW OF NEWMARK THEORY

We apply Newmark's incomplete composite beam theory (hereafter referred to as Newmark theory), which is commonly used to analyze composite beams, to objectively understand the effect of the slip stiffness of screw connections on the out-of-plane bending rigidity of LGS walls. Since Newmark theory has been widely described in the literature, we will omit the detailed formulation here and only describe assumptions applied in Newmark theory. The theory makes the following assumptions:

1: The problem is two-dimensional in the x-z plane.

2: The screws are uniformly and continuously distributed in the axial (x-) direction, and their restraining effect on the "slip" between the studs and the board is continuous.
3: The force q_T, q_B generated by the screws (hereafter referred to as "slip shear force") is proportional to the amount of "slip displacement" Δu_T, Δu_B (see Figure 4).
4: The studs and gypsum boards are continuous and uniform in the axial direction.
5: The assumptions of plane and normality hold true within each stud and gypsum board component.
6: The out-of-plane displacement, rate of change, and curvature of each component of the studs and gypsum board are equal.

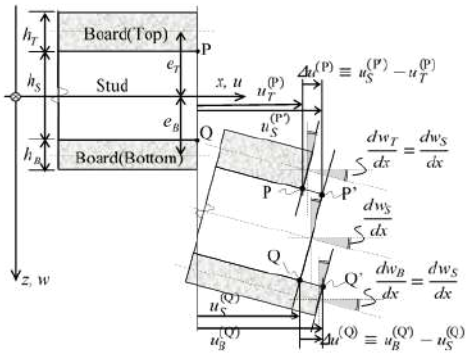


Figure 4(a). Incomplete composite beam with three layers

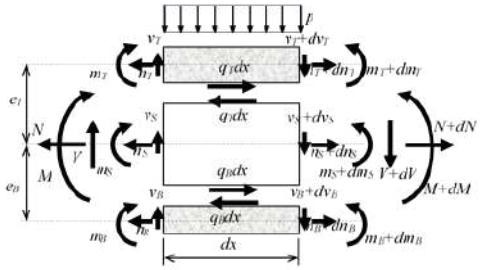
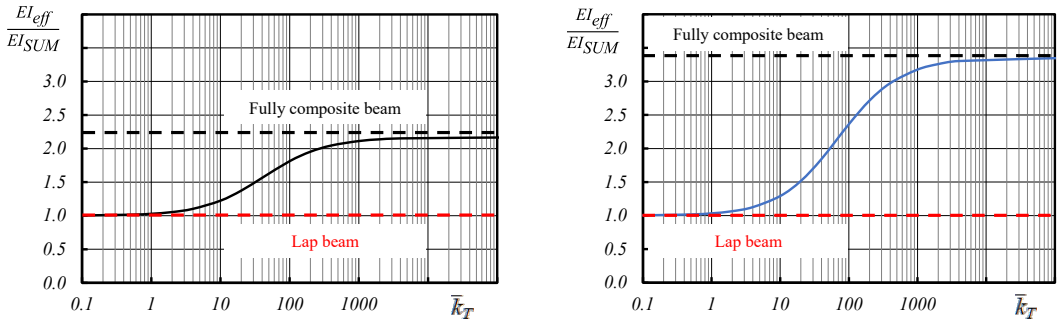


Figure 4(b): Resultant stress on each layer

Figure 5 shows the relationship between the effective bending rigidity of the LGS wall and the slip resistance of screw connections, calculated using an equation derived from Newmark theory for the test specimen shown in Figure 3. The slip resistance $\bar{k}_T$ [N/mm²] is the slip stiffness for one screw k [N/mm] divided by the screw spacing s. The figures show results for two board thicknesses: 12.5 mm (Figure 5(a)) and 21 mm (Figure 5(b)). The vertical axes of the graph represent the non-dimensional effective bending rigidity EI_{eff}/EI_{SUM} obtained by dividing the effective bending rigidity EI_{eff} by the bending rigidity of the lap beam EI_{SUM} (the sum of the bending rigidity of the stud and the board). As the slip resistance decreases, the effective bending rigidity asymptotically approaches the bending rigidity of the lap beam, shown by the red dashed line. Conversely, as the slip resistance increases, the effective bending rigidity asymptotically approaches the bending rigidity of the fully composite beam, shown by the black dashed line. However, these figures also show that an extremely large slip resistance of more than $\bar{k}_T$ = 1000 (e.g., k = 300,000 N/mm when the screw spacing is 300 mm) is required to ensure the effective bending rigidity of a fully composite beam.

Once the slip stiffness for one screw can be determined, it is possible to determine the effective bending rigidity for an LGS wall with the same geometric and stress boundary conditions. This will be explained again in Section 4.2.



(a) Board thickness=12.5mm **(b) Board thickness=21mm**

Figure 5. Influence of slip resistance on effective bending rigidity

2.2 APPLICABILITY TO DISCRETE SCREW CONNECTIONS

Newmark theory assumes that the slip resistance between the studs and boards is continuous (Assumption 2). Whereas, in actual LGS walls, the boards are intermittently fastened by screws, so this assumption is not necessarily true. While this assumption of continuous slip resistance is likely appropriate when the screw spacing is sufficiently small, its scope of applicability is unclear. Therefore, when using the theoretical solution, it is necessary to clarify the impact that the differences between the continuous and discrete models have on the behavior of LGS walls. Here, we compare the numerical analysis results using the discrete model with the theoretical solution to verify the validity of using the theoretical solution, which assumes continuous slip resistance, in the discrete model, and also discuss points to note when using the theoretical solution. Figure 6 shows the numerical analysis model. All components are modeled using beam elements. The boards are fastened to the studs with screws at spacings s. The boards extend from the outermost screw, including an extra length of 85 mm (on both ends), and the studs extend an additional 75 mm from the end of the board. Fig. 7 compares the theoretical solution (continuous model) and the numerical analysis results (discrete model) for the distribution of deflection, deflection angle, board axial force, and slip shear force for an example with a relatively small screw spacing (s = 36 mm) and a relatively large screw spacing (s = 330 mm).

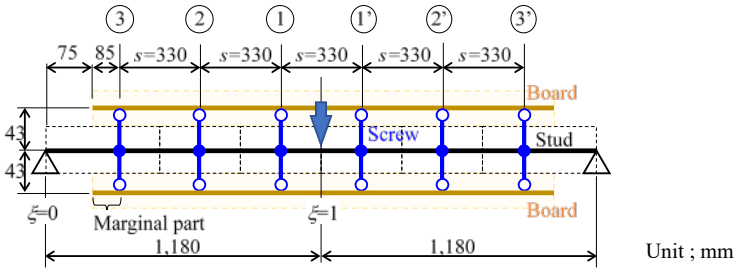
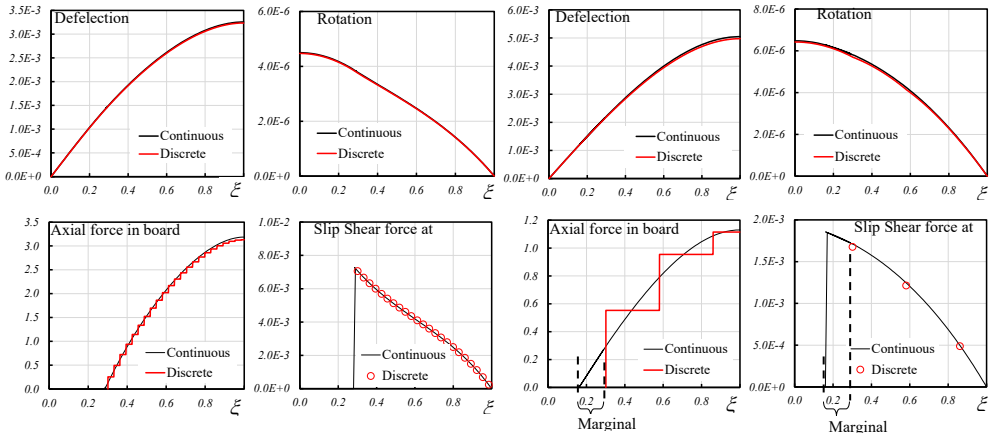


Figure 6. Numerical (Discrete) model for target LGS wall

When comparing the discrete and continuous models, care must be taken in the handling of the board marginal length (i.e., the board length extending from the end screw ③ in Figure 6). To satisfy the assumption of uniform slip resistance in Newmark theory, this length of the board must be half the uniform screw spacing (s). In other words, even if the actual marginal part in the numerical model is 85 mm, the value used in the theoretical solution must be calculated as $s/2$ = 165 mm. The theoretical solution taking account of the above precaution and numerical analysis results obtained from the continuous model correspond well, even for relatively large screw spacing.

From the above, it is clear that Newmark theory can be used to estimate elastic behavior, even for large screw spacings such as those considered in this study, although some caution is required.



Screw spacing=36 mm **Screw spacing=330 mm**

Figure 7. Comparison of theoretical (continuous) and numerical (discrete) results

3. OUT OF PLANE BENDING TEST

3.1 OUTLINE OF EXPERIMENT

A schematic of specimen and the experimental set-up is shown in Figure 8. The loading method was a centrally concentrated load, and the force was applied using a single oil jack. As shown in Figure 8, a slider that moves freely only in the vertical direction was used to restrain the lateral displacement at the center of the two studs, while also ensuring that the vertical displacement occurs as evenly as possible. In addition, metal parts called "spacers" were attached to the stud openings at the loading point and three locations where the concentrated force of both supports acts, in order to maintain the cross-section shape of the studs under loading. Photograph 1 shows an overall view of the experiment.

Japan Industrial Standards allow for relatively large tolerances for extremely thin steel plates. In the case of studs, the plate thickness is 0.8 mm, with a tolerance of 0.09 mm or less. While this tolerance value is sufficiently small in absolute terms, it represents a difference of over 10% relative to the nominal plate thickness, and its impact on cross-sectional performance cannot be ignored. Taking this into consideration, an additional bending test was also conducted on an Only-stud specimen to accurately evaluate the bending rigidity of the stud itself, which is used as the basis for evaluating the composite beam effect. Furthermore, with asymmetric open cross sections such as studs, depending on the position of the loading point, eccentric loading with respect to the shear center can occur, resulting in torsional-bending deformation and thus a reduction in the apparent bending rigidity. Therefore, to investigate the effect of the loading point position, bending tests are conducted on Only-stud specimens for two different loading points, as shown in Figure 9.

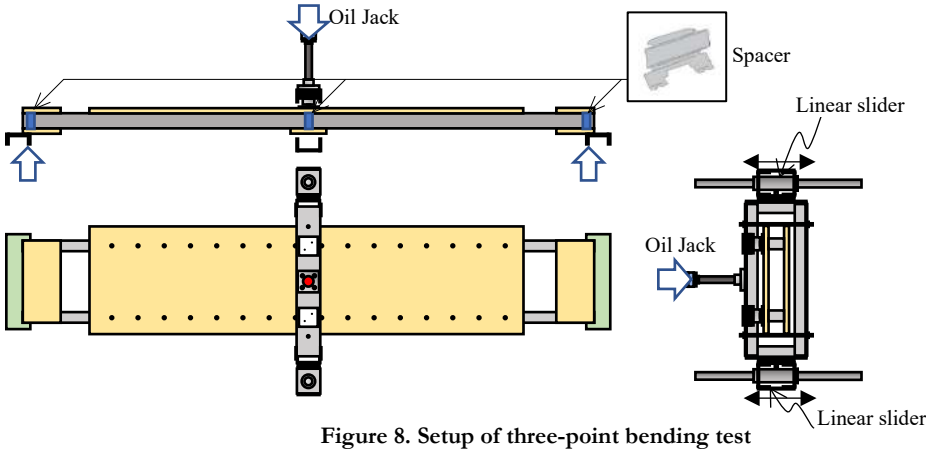
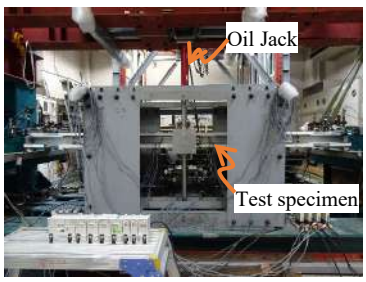
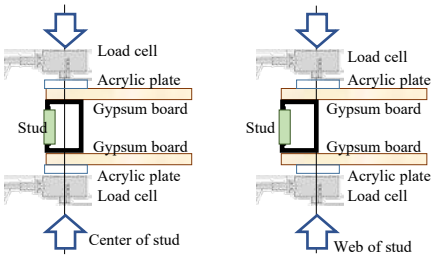


Figure 8. Setup of three-point bending test



Photograph 1. Overall view of bending test



(a) Position C **(b) Position W**

Figure 9. Loading/supporting position

3.2 MEASUREMENT

For the central vertical load, the load value at the loading point for each stud (positions shown in Figure 9) was measured using a load cell, and the sum of both load values was taken as the central vertical load. For the vertical displacement at the center of the specimen, the vertical displacement at the loading point and the corresponding displacement at the support positions at both ends were measured to determine the net vertical displacement due to the specimen's deflection. For the LGS-C and LGS-T specimens, strain gauges were attached to both surfaces of the board at the positions shown in Figure 10(a) in order to calculate the in-plane force of the board, and displacement transducers were used to measure the slip displacement between the stud flange and board at the screw connection. For the Only-stud specimens, strains were measured at two locations each on the top and bottom flanges of the stud near the center (see Figure 10(b)) to confirm the degree of torsional-bending deformation.

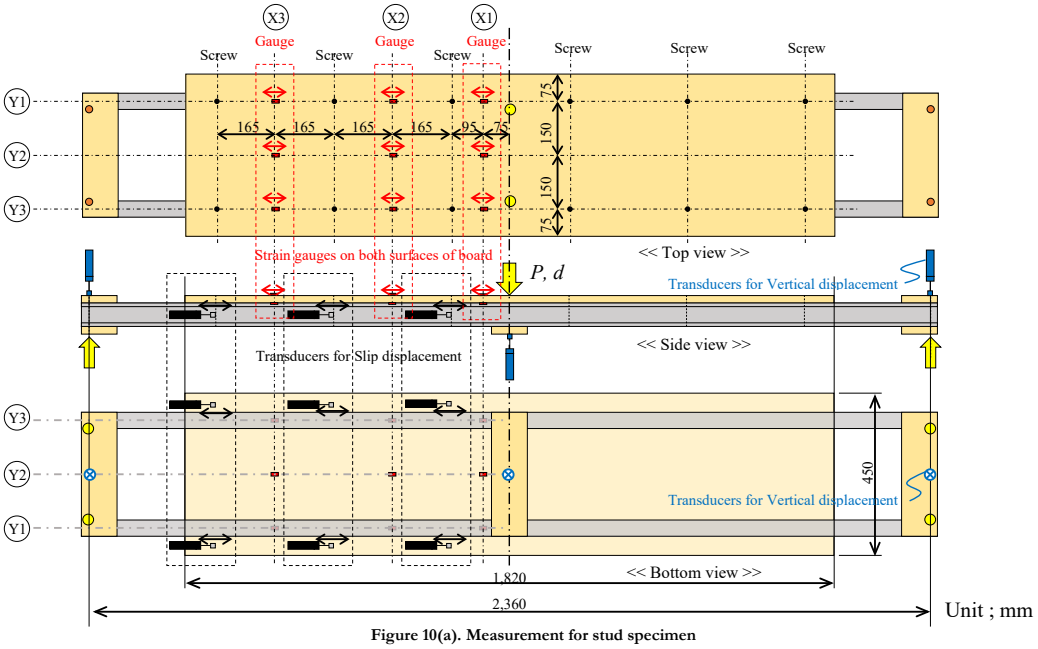


Figure 10(a). Measurement for stud specimen

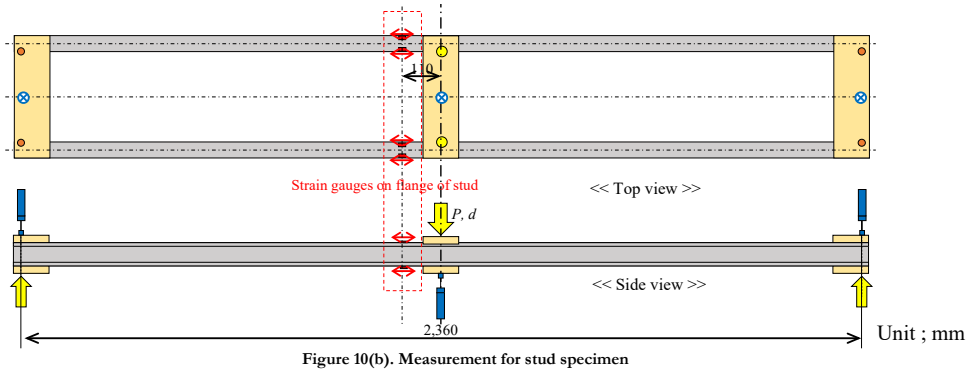


Figure 10(b). Measurement for stud specimen

Figure 10. Measurement of LGS wall specimen and Only-stud specimen

3.4 TEST RESULTS

First, we show the results of the Only-stud specimen. Figure 11 shows the relationship between load and displacement at the loading point, and the right-hand figure shows an enlarged view of the small displacement region. The red line shows the results when the loading and support points are located at the center of the stud cross section, while the black line shows the results when these points are located at the web of the stud cross section. Figure 12 shows the strain distribution at the load levels (P1, P2, P3) shown

in Figure 11. In the Only-stud specimens, the gypsum board is fastened with screws as lateral stiffeners at the loading and support points. This likely suppresses bending-torsional deformation due to eccentricity at the loading point, and the difference in the load-displacement relationship between the two positions in Figure 11 is small. When the loading point is located at the center of the stud in Figure 12(a), large differences in strain within the same flange are observed (areas inside the red square), whereas such differences are not observed in Figure 12(b). This is thought to be because in the latter case, where the eccentricity from the shear center is small, the effect of the transverse stiffeners sufficiently suppresses torsional-bending deformation. Therefore, the moment of inertia of the stud is calculated based on the initial gradient (gray dashed-dotted line in the figure) when the web position, where purer bending deformation occurs, is used as the loading point. The result obtained with a Young's modulus of 205 GPa was 95,000 mm^4. This value is small, about 90% of the value based on the nominal dimensions (10,500 mm^4), but is considered reasonable considering the aforementioned steel plate thickness tolerance. The cross-sectional area is also reduced by the same ratio (144 mm^2 → 130 mm^2). Below, these values will be used as the actual values for the cross-sectional performance of the stud.

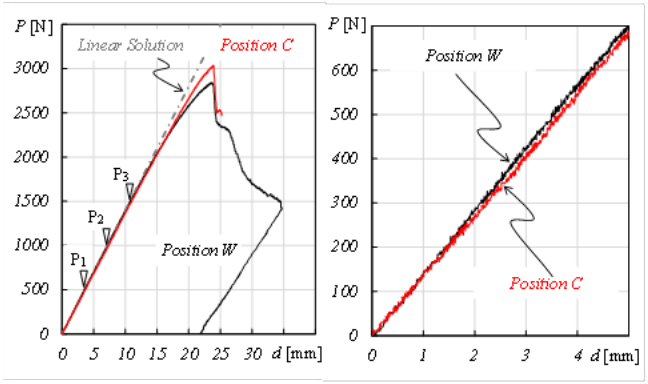
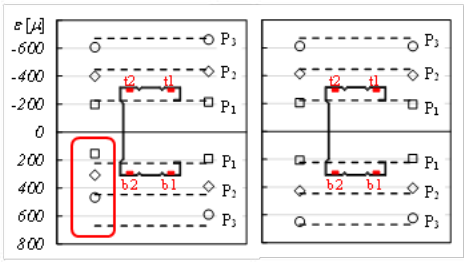


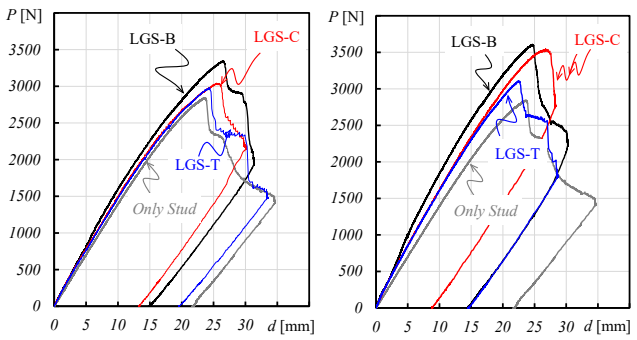
Figure 11. Load-displacement for Only-stud specimen



(a) Position C (b) Position W

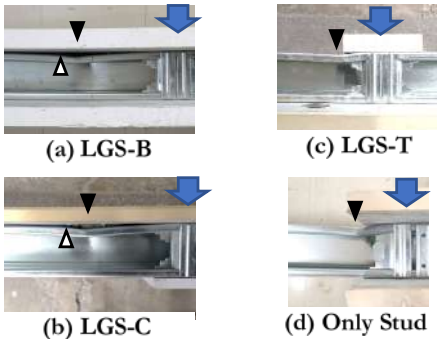
Figure 12. Strain distribution on top and bottom flange of stud

Next, we will discuss the overall qualitative characteristics of the LGS wall specimens. The screw spacing for all specimens shown here is 330 mm. Figure 13 shows the load-displacement relationships obtained for specimens with boards attached to both sides (LGS-B, black line), one compression side (LGS-C, red line), and one tension side (LGS-T, blue line). For comparison, the results for the stud-only specimen (Only-stud) are shown with a gray line.



(a) with board of 12.5 mm (b) with board of 21 mm

Figure 13. Load-displacement curve for LGS specimen



(a) LGS-B (c) LGS-T (b) LGS-C (d) Only Stud

▼ and △ show buckling points and position of screws

Photograph 5. Collapse modes.

The order of initial stiffness magnitude was Only-stud < LGS-T = LGS-C < LGS-B, (i.e., no difference was observed between LGS-C and LGS-T). This result is consistent with Newmark theory. The maximum strength showed a different trend from the initial stiffness. For the 21 mm board thickness, the magnitude order was Only-stud < LGS-T < LGS-C = LGS-B. Meanwhile, for the 12.5 mm board thickness, the maximum strength of LGS-C was clearly lower than that of LGS-B and only slightly higher than that of

LGS-T. As is clear from the graph, the composite beam effect of the board is small for the 12.5 mm board thickness, making it susceptible to variation, which is thought to be the reason for this result.

Photo 3 shows the final deformation of each specimen. The ▼ in the figure indicates the maximum buckling deformation point, and the △ indicates the screw location. For the LGS-T and stud-only specimens, which have no board on the compression side, local buckling was observed near the center, where bending was greatest. For the LGS-B and LGS-C specimens, which have a board on the compression side, local buckling waveforms were observed near the innermost screw. This difference in the location of local buckling is thought to be due to the composite beam effect, where the board bears the compressive force.

4. INFLUENCE OF SCREW CONNECTION ON BENDING BEHAVIOR OF LGS WALL SYSTEM

4.1 EXTRACTION OF SCREW CONNECTION MECHANICAL CHARACTERISTICS

The relationship between slip shear force and slip displacement at the screw connection will be extracted from the experimental results for LGS-C and LGS-T shown in the previous section. Figure 14 illustrates this extraction method. As shown in this figure, the slip shear force acting on the screw connection causes a change in the in-plane force of the board. That is,

$$q_3 = \frac{1}{2}n_3, \quad q_2 = \frac{1}{2}(n_2 - n_3), \quad q_1 = \frac{1}{2}(n_1 - n_2) \tag{1}$$

where 1/2 comes from the fact that there are two screws per cross section. In this experiment, strain gauges were attached at positions X3, X2, and X1 in order to estimate the in-plane force (n_1, n_2, n_3) of the board (see Figure 10). Multiplying the strains by the axial stiffness of the board obtained in advance through material testing, yields the in-plane force of the board. Substituting the obtained in-plane force of the board into Equation (1) yields the slip shear force at the screw connection. Using this and the slip displacement between the stud and board measured separately with a displacement gauge, the relationship between slip shear force and slip displacement can be extracted. Figure 15 shows the results.

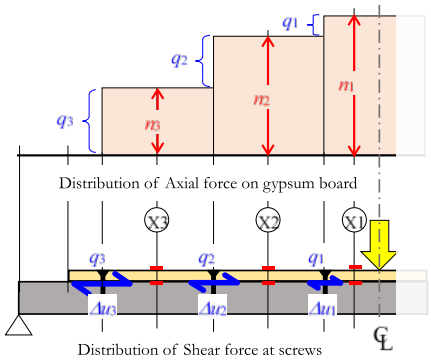


Figure 14. Extraction method of slip behavior from bending test results

Figure 15 shows the slip shear force-slip displacement relationships ((q_3-Δu_3) red, (q_2-Δu_2) blue, and (q_1-Δu_1) black) for screw connections ①, ②, and ③ extracted from the bending test results, along with the results of the past element tests (in gray). Figures 15(a) and (b) show the results extracted from LGS-C and LGS-T with 12.5 mm boards, while (c) and (d) show the results extracted from LGS-C and LGS-T with 21 mm boards.

The slip shear force-slip displacement relationship extracted from the bending test results closely match the relationship obtained from the element tests, in the early loading stages. Visually judging the initial gradient from these graphs, we obtain values of 1,300 N/mm for the board thickness of 12.5 mm and 2,500 N/mm for the board thickness of 21 mm. These values are shown by the dashed-dotted lines in Figure 15. In both graphs, the initial gradients indicated by the dashed-dotted lines closely reflect the experimental results. Subsequently, as the slip displacement progresses, the extracted slip shear force tends to be larger than the element test results when the board is in compression and smaller when the board is in tension. Furthermore, it is quite interesting to note that as the slip shear force capacity increases, the maximum strength of the LGS wall also tends to increase (however, this does not necessarily apply to LGS-C_12mm). This indicates that as the slip shear force of the screw connection increases, the in-plane force of the board increases, improving the composite beam effect, which is thought to increase the maximum strength of the LGS wall system. Unfortunately, due to the small sample size, it is difficult to immediately conclude that the element tests are insufficient. However, it is deemed meaningful to consider a method of extracting screw connection characteristics from bending tests.

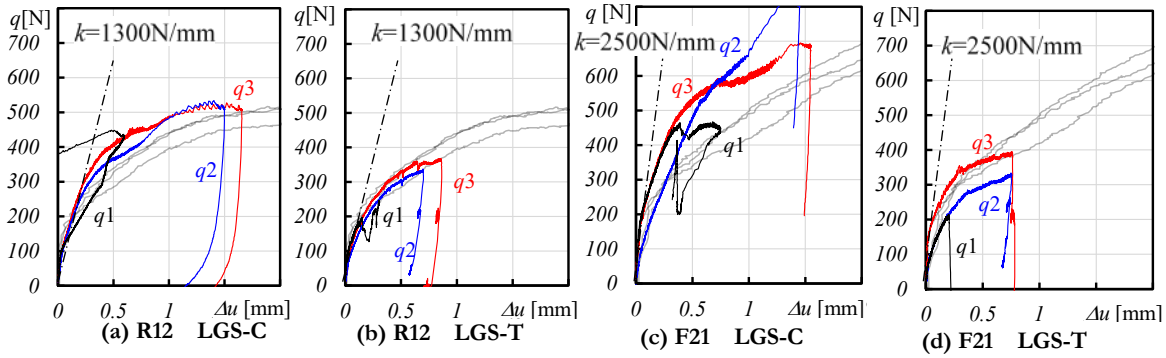


Figure 15. Comparison of extracted and parts test results

4.2 BENDING RIGIDITY OF LGS WALL

In this section, we verify the validity of the effective bending rigidity calculated by applying the initial slip stiffness of screw connections obtained in the previous section to Newmark's incomplete composite beam theory.

The effective bending rigidity can be calculated as follows:
Note that because there are two screws in one board cross section, the slip stiffness at one board cross section, K, used here is twice the slip stiffness for one screw, k [2,500 N/mm/screw], found in the previous section. Thus, the continuous slip resistance $\bar{k}_T$ can be calculated as K/s, resulting in values of 139 N/mm², 45 N/mm², 15 N/mm² for cases of screw spacing, s of 36 mm, 110 mm and 330 mm, respectively. Using the values of these $\bar{k}_T$, the non-dimensional effective bending rigidity can be obtained from the effective bending rigidity-continuous shear resistance relationship diagram (around 2.5, 2.0, 1.5, respectively from Figure 16). Note that the above values in parentheses indicate values for a board thickness of 21 mm.

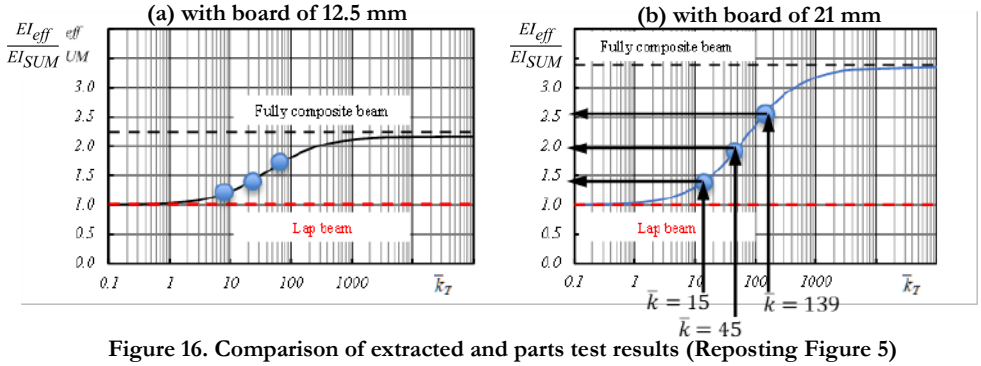


Figure 16. Comparison of extracted and parts test results (Reposting Figure 5)

Figure 17 compares the linear solution for three-point bending calculated based on the effective bending rigidity obtained from the initial slip stiffness of the screw connection with the experimental results at the initial stage. The focus here is on the LGS-B series, in which the composite beam effect is particularly evident in the initial stages of loading. To observe the influence of slip stiffness per unit length, three experimental results were used with screw spacings of 36 mm, 110 mm, and 330 mm. As can be seen from this figure, the theoretical solution agrees with the experimental results for all results, regardless of board thickness or screw spacing.

This agreement validates the method for extracting the slip stiffness for one screw and calculating the effective bending stiffness of LGS wall derived in the previous section.

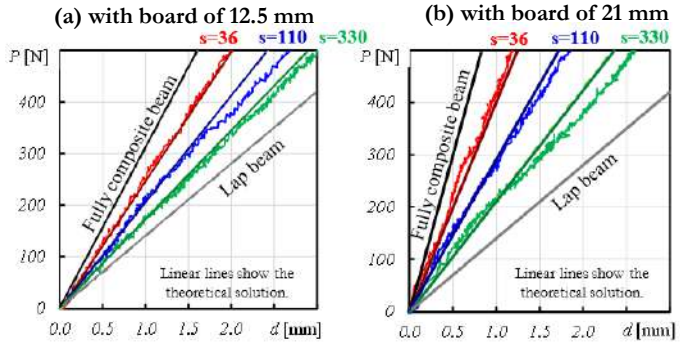


Figure 17. Comparison of extracted and parts test results (Reposting Figure 5)

5 CONCLUSION

In this report, we proposed a method to extract the mechanical properties of screw connections from bending test results and understand the behavior of screw connections in LGS walls subjected to actual out-of-plane bending. This result enables the quantification of the effect of screw connections on the out-of-plane bending behavior of LGS walls, particularly on the initial stiffness. Noteably, we proposed a method to calculate the bending rigidity of LGS walls through composite beam theory using the initial slip stiffness of screw connections. We demonstrated the validity of this calculation method for the bending rigidity of LGS wall by comparing it with the results of bending tests with different screw spacings. Due to an insufficient sample size, it was unclear whether the results of screw connections extracted from the bending tests in this study represented statistical variation or intrinsic behavior. We plan to address this issue by increasing the amount of data in the future.

REFERENCE

Newmark, N.M., Siess, C.P., Viest, I.M. [1951] "Tests and analysis of composite beams with incomplete interaction", Proceeding of the Society of Experimental Analysis, Vol. 9, No. 1.

Herfurth, D [2024] Mechanische Verbundeigenschaften zusammengesetzter Querschnitte aus trockenbauüblichen, dünnwandigen Stahlprofilen und mineralisch basierten Plattenwerkstoffen unter statischen und seismischen Beanspruchungen, Doctoral Dissertation, The Technical University of Darmstadt.

MINATOGAWA, R., MOTOYUI S., et al. [2014] "Mechanical characteristics of components in nonstructural members, part2 study on shear slip and pull out strength", Summaries of technical papers of annual meeting, AIJ (in Japanese).

Experimental investigation on the seismic performance of self-centering concrete wall structures with low damage infill walls

Hao Wu [1,2], Xiaoying Zhu [2] and Zuochen Zhang [2]

[1] State Key Laboratory of Disaster Reduction in Civil Engineering, Tongji University, 1239 Siping Rd., Shanghai 200092, China.
e-mail: 2009wuhao_tom@tongji.edu.cn
[2] Department of Disaster Mitigation for Structures, College of Civil Engineering, Tongji University, 1239 Siping Rd., Shanghai 200092, China.
e-mail: { Xiaoying Zhu, Zuochen Zhang} xiaoying01@tongji.edu.cn, tjzzc@tongji.edu.cn

Abstract. Self-centering wall structure is a typical seismic resilient structural system that demonstrates enhanced deformation capacity, reduced residual displacements, and low-damage characteristics under seismic loading. Previous research on self-centering (SC) concrete walls has mainly concentrated on the structural level, while the interaction mechanisms with non-structural components have not been sufficiently explored. This paper investigates the cooperative mechanism between SC walls and different types of infill walls through quasi-static tests. The proposed low-damage infill walls were designed to connect the lateral force-resistant element (SC wall) and the gravity force-resistant element (column) through flexible connections, aiming to coordinate the deformation between the structural skeleton and infill walls, while isolating infill walls from the main structure to achieve low-damage performance. In addition, U-shaped steel dampers and viscoelastic dampers were integrated into the infill walls to enhance the overall energy dissipation capacity of the system. Experimental results demonstrate that SC walls and infill walls exhibit favorable deformation compatibility and low-damage behavior, while the incorporation of dampers significantly improves the energy dissipation capacity of the structure.

Keywords: Experimental investigation, Self-centering wall, Low damage, Infill wall, Seismic performance.

1.INTRODUCTION

With the increasing demand for structures that achieve both cost-effectiveness and high seismic performance, damage-control technologies have emerged. In recent years, a series of effective solutions have been developed to enable low-damage performance in concrete structures [Grigorian et al., 2019]. The PRESSS (Precast Seismic Structural System) research program, for example, investigated unbonded post-tensioned precast concrete walls that allow self-centering behavior at the joints [Priestley et al., 1999]. However, recent seismic events have highlighted the considerable economic losses associated with non-structural component damage, thereby increasing the demand for reducing post-earthquake damage to these elements [Filiatrault and Sullivan, 2014]. Among the various types of non-structural components, infill walls are of particular importance, as they can significantly alter the mechanical properties of adjacent structural members [Huang et al., 2021]. Traditional infill walls, such as masonry-infilled frame systems, are widely used in buildings worldwide. Nevertheless, many researchers have reported that conventional infill walls are prone to seismic damage [Fiore et al., 2016; Hermanns et al., 2014]. Such damage arises from strong interactions with the surrounding frame, even under low earthquake intensities, or from the brittle nature of the infill itself. Therefore, achieving seismic compatibility between structural and non-structural components remains a significant challenge, and relevant studies are still relatively limited.

To address this issue, two main strategies have been proposed: First, the seismic performance of the infill wall itself can be enhanced by strengthening measures or surface coating treatments to improve its strength and deformation capacity [Furtado et al., 2020; Sharbatdar and Tajari, 2021]. However, such approaches tend to intensify the interaction between the infill wall and the primary structural system, which may, in turn, reduce the overall performance of the structural system. Second, the interaction between the structural frame and the infill wall can be intentionally weakened by incorporating sliding joints or separation layers to reduce constraint forces and thereby control infill wall damage [Zhou et al., 2023; Zhang et al., 2022; Lu et al., 2024]. Depending on the design requirements, sliding joints may be arranged either horizontally or vertically [Li et al., 2023]. Extensive experimental and numerical studies have shown that sliding-joint infill walls exhibit significantly improved seismic resilience compared with traditional configurations [Zhu et al., 2024]. In particular, vertical sliding joints have been shown to effectively reduce shear transfer from the infill to the surrounding frame columns [Tasligedik et al., 2015; Tasligedik and Pampanin, 2017] and their applicability in self-centering wall systems has been confirmed in relevant studies [Guo et al., 2018; Wang et al., 2025].

In response to the severe post-earthquake damage observed in traditional infill walls, several flexible connection systems and energy dissipation measures have been proposed. However, their deformation capacity remains limited, and the effectiveness of the energy-dissipating layers requires further improvement. To date, no infill wall configuration has successfully combined both high deformation capacity and significant energy dissipation. Therefore, it is necessary to develop a new type of infill wall that can simultaneously achieve low damage and effective energy dissipation, while allowing easy replacement of energy-dissipating components after earthquakes to ensure the post-earthquake recoverability of the infill wall system.To address this gap, this study proposes five innovative infill wall configurations for self-centering systems, designed to operate independently from the structural skeleton. In addition, a traditional infill wall configuration is designed for comparison. The first three innovative configurations adopt infill wall panels, while the latter two, along with the traditional type, employ masonry blocks. To further investigate and validate the seismic performance of SCW structures incorporating infill walls, an extensive cyclic loading test program was conducted. This program included five specimens: one self-centering wall structure without infill walls, and four specimens incorporating different infill wall types proposed in this study. This paper first introduces the design principles and construction techniques of five innovative and one traditional infill wall configurations, followed by an explanation of the experimental design and loading procedures. Subsequently, the experimental results of the five specimens are analyzed to reveal the seismic performance and resilience characteristics of SCW structures with different infill wall configurations.

2.Test program

2.1 CONFIGURATION OF LOW DAMAGE INFILL WALL

Five innovative construction techniques for infill walls are used in the study, each tailored to address specific structural considerations. The first technique concentrated on isolated infill wall panels, strategically designed to alleviate constraints between the structural framework and the infill panels. As depicted in Figure 1(a), the infill wall panels are vertically oriented, and specialized steel connections featuring slots are employed on both sides to establish a linkage between the infill wall panel and the structural framework. These connections serve the dual purpose of relaxing vertical constraints while facilitating the transfer of horizontal forces and displacements. At the base of the wall panel, a connection to the foundation is established through the use of mortar. This innovative approach permits controlled relative deformation between the structural framework and the infill wall panel, thus mitigating damage to the infill wall panel resulting from incongruous deformations.

The second and third variations of infill wall panels (IWP) extend and enhance the foundational approach introduced in the first form by the incorporation of supplementary dampers. Illustrated in Figure 1(b), these variants introduce metallic dampers between the infill wall panels. The activation of these dampers is contingent upon the occurrence of horizontal actions and deformations within the structure, which, in turn, trigger vertical relative displacements between the infill wall panels. Conversely, Figure 1(c) shows the incorporation of viscoelastic dampers within the infill wall panels as an alternative to U-shaped steel dampers. This modification enables a comparative investigation of the distinct structural effects of these damping elements.

In a departure from the preceding forms, the fourth approach adopts aerated lightweight concrete (ALC) blocks as the core material for the infill wall components. Deliberate spacing is introduced between the infill wall and its surrounding structures. Furthermore, to optimize the performance of the ALC blocks, an engineered cementitious composite (ECC), a cement-based composite material, is applied to the surface of the blocks. The infill wall configuration is divided into three horizontally arranged wall panels, as delineated in Figure 1(d).

The fifth method utilizes ordinary clay bricks as infill material. Illustrated in Figure 1(e), rubber strips are placed between the main structure and the infill wall to release the restraint effect in this system.T he horizontal system is composed of four components, while the vertical system includes three components. In both subsystems, rubber strips are bonded to the frame and masonry through a thin layer of cement mortar. The thickness of the vertical strips is determined by the interstory drift demand, serving to accommodate in-plane deformation of the frame. At the top of the infill wall, identical rubber strips are installed, with a sliding surface placed between adjacent strips to enable smooth movement of the slotted beam and reduce frictional shear transfer to the masonry. Furthermore, steel angles are anchored at the wall ends to enhance out-of-plane stability. This design approach is capable of resisting both in-plane drift and out-of-plane loads, with the thickness of the rubber strips and the dimensions of the steel angles adjusted according to different seismic demands. Such a conceptual design is applicable to all types of masonry units, offering low cost and requiring no additional measures.

The last method represents a traditional infill wall construction technique, using the same masonry material as in the fifth approach. In this system, the connection is achieved by enhancing the restraint between the main structure and the infill wall. As shown in Figure 1(f), a rigid connection is established through a combination of bonded rebars and external carbon fiber reinforced polymer (CFRP) sheets. On the gravity-column side, two 6-mm-diameter tie bars are provided at a vertical spacing of 500–600 mm and anchored 700 mm into the infill wall. On the self-centering wall side, however, the reinforcement layout is dense within the bottom 1 m region, making it impractical to install additional dowels. Therefore, externally

bonded CFRP sheets are adopted as an alternative, thereby simulating the tensile mechanism of reinforcement.

2.2 EXPERIMENTAL DESIGN

The main structure consists of a parallel system composed of self-centering walls and gravity frames connected through slotted beams. The self-centering wall has a width of 1600 mm and a thickness of 200 mm, while the gravity columns have cross-sectional dimensions of 350 mm × 350 mm, and the slotted beams measure 200 mm × 300 mm in cross-section. Based on the above structural configuration, six specimens were designed, but only four have been constructed so far, each incorporating a different type of infill wall detailing. Figure 2 provides a visual representation of the design outcomes for the experimental structure and the lower section of the SC wall.

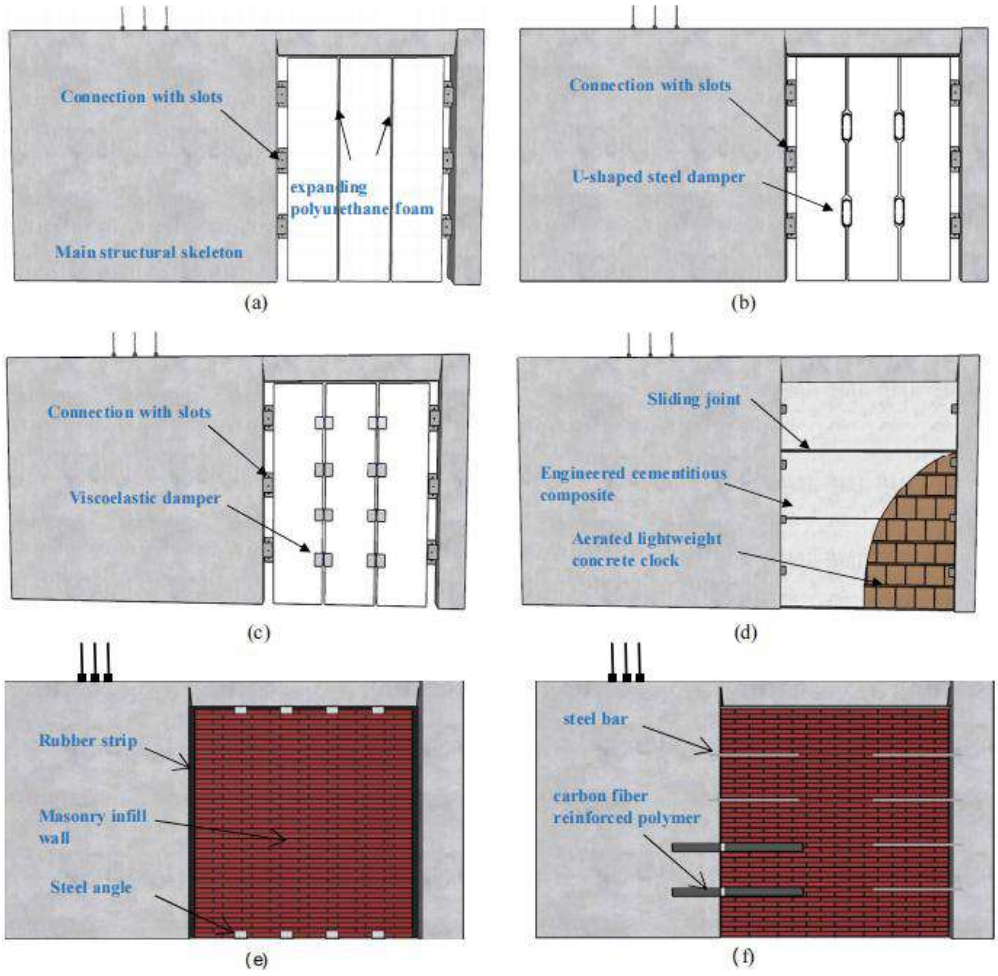


Figure 1. Different configurations of Infill walls

The mechanical properties of concrete, steel, and two distinct damper types were determined through laboratory testing. In the construction of the test specimens, C40 (as in Chinese code, the standard cubic strength for the concrete is 40 MPa) concrete was utilized for the SC walls and gravity frames, while C30 (as in Chinese code, the standard cubic strength for the concrete is 30 MPa) concrete was deployed for the foundation. Due to constraints imposed by the laboratory environment, autoclaved lightweight concrete could not be employed for the formation of infill wall panels; consequently, C20 (as in Chinese code, the standard cubic strength for the concrete is 20 MPa) concrete with lower strength characteristics was used as a substitute.

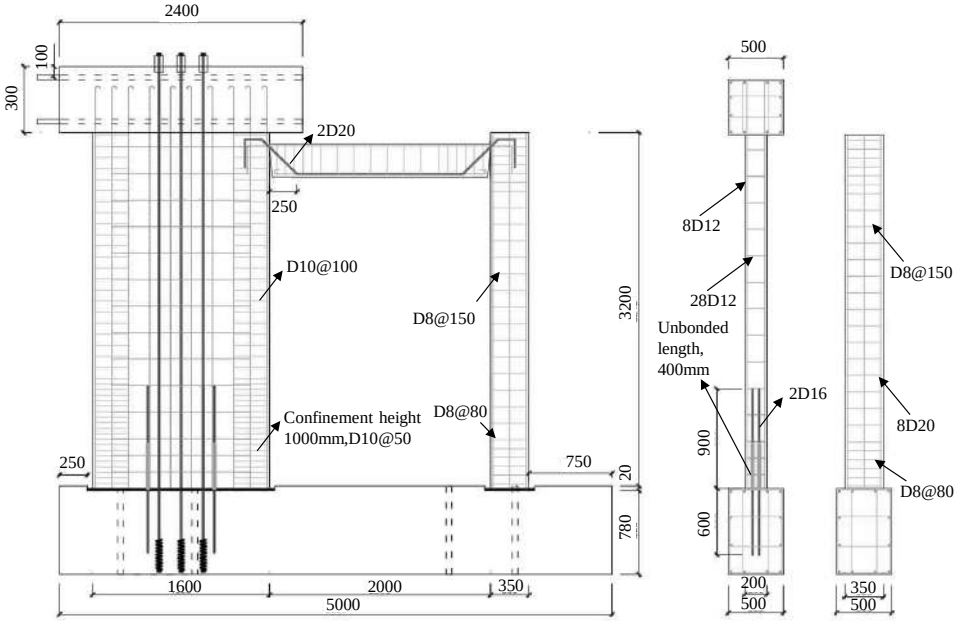


Figure 2. Design results of the test specimen

2.3 LOADING PROTOCOL

The experiment was conducted on the Jiading Campus of Tongji University. Figure 3 shows the layout of the test setup. The horizontal loading actuator used for the specimens had a maximum capacity of 1000 kN and a maximum displacement of 300 mm, which fully satisfied the test requirements. The vertical load was applied using a 1000 kN modular loading system composed of two through-hole servo jacks, a main crossbeam, two tie rods, and two loading bases. Each tie rod passed through the through-hole actuators and the main crossbeam, with one end anchored to the top of the actuator and the other hinged to the loading base. During the test, when the combined force of the two through-hole actuators was below the target value, the actuators elongated synchronously to increase the vertical load on the specimen. The overall loading error was controlled within approximately 0.2%. Compared with the previously used roller-type jacks, this system provided significantly improved vertical load stability and met the precision requirements for vertical loading in the experiment.

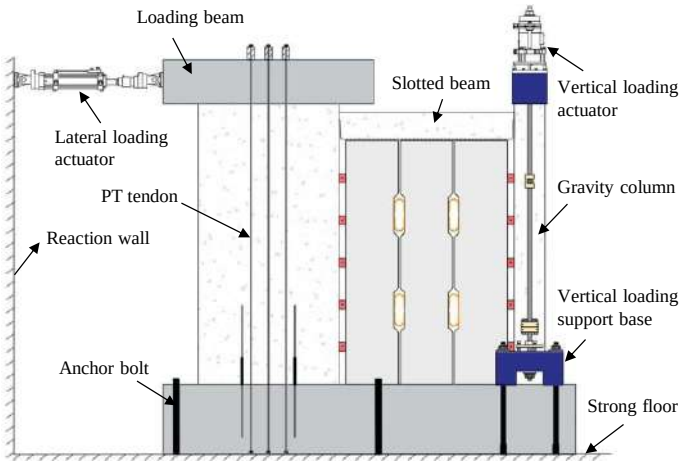


Figure 3. Layout of test setup

A displacement-controlled loading protocol was adopted to systematically investigate the mechanical performance of the specimens under cyclic loading. A constant vertical load was applied to the top of the gravity columns, while horizontal loading was introduced through a hydraulic actuator system. As delineated in Figure 4, the loading protocol consisted of three stages: prestress application, vertical load application, and horizontal displacement loading. The interstory drift ratio was incrementally increased from 0.05% to 4.0%, with a loading rate of 1 mm/s and three cycles at each drift level. The test was terminated when the lateral load capacity decreased to 85% of the peak strength. For Specimen 2, designed with replaceable energy-dissipating reinforcement, the test was stopped at a drift ratio of 2.5%; the remaining specimens were tested up to 4.0% drift. The loading process exhibited four distinct stages: (Ⅰ) elastic behavior, (Ⅱ) uplift at the bottom joint, (Ⅲ) crack propagation, and (Ⅳ) ultimate failure. During the tests, particular attention was paid to critical displacement thresholds specified in the Chinese seismic code, including 1/800 (elastic limit of frame–shear wall structures), 1/550 (elastic limit of frames), 1/100 (elastoplastic limit of frame–shear wall structures), and 1/50 (elastoplastic limit of frames).

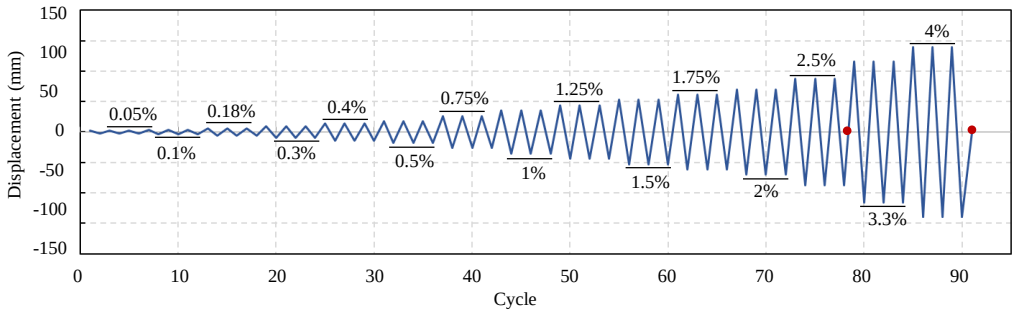


Figure 4. Loading protocol

3.Experimental results and discussion

3.1 DAMAGE EVOLUTION

3.1.1 Specimen SCW

The experimental study began by subjecting a structural skeleton (SCW) consisting of an SC wall and a parallel gravity frame to tests. The specimen showed minimal deformation and no visible cracks on the concrete surface during prestressing and vertical load application. The study can be divided into four phases:

- In the 0.05% - 0.3% stage, no cracks or structural anomalies were observed, except for slight grout layer loosening at the SC wall corner (Figure 5(a)).
- During the 0.4% - 1% phase, minor cracks appeared in the slotted beams and the gravity column. Cracking began at a 0.4% drift ratio, primarily in the slotted beams (Figure 5(b)), with tiny cracks near the center of the base of the SC wall at a 0.75% drift ratio.
- In the 1.25% - 2% stage, the SC wall exhibited uplift and cracks at a 1.5% drift ratio, continuing as the drift ratio reached 2% (Figure 5(d)).
- At a 2.5% drift ratio, one mild steel bar (as shown in Figure 2 for the 2D16 rebar) fractured during unloading. The test was terminated after three loading cycles. Overall, the SC wall, gravity column, and slotted beams endured 39 cycles across 13 loading conditions, with minimal damage and superficial cracks.



Figure 5. Damage evolution of the specimen SCW

3.1.2 Specimen SCW-IWP

Building upon specimen SCW, this study introduces isolated connections in the infill wall panels, where both sides of the infill wall panels are linked to the structural skeleton using steel connections featuring slots. Preceding the test, polyurethane foam is used to fill the gaps between the infill wall panels and between the infill wall and the slotted beam. The experimental observations can be divided into four distinct phases:

- In the initial phase (0.05% - 0.3%), the force-displacement relationship is primarily linear, with a minor crack appearing at the slotted beam at a 0.3% drift ratio.
- In the 0.4% - 1% phase, the steel connections start to slide with metallic sounds, but no damage to the SC wall or infill wall panels is noted.
- The phase from 1.25% to 2% sees cracks in the SC walls and signs of foam insulation loosening, with minimal damage and cracks within the specified target displacement.
- The 2.5% - 4% stage witnesses varying degrees of damage, with all mild steel bars fracturing and an ultimate reduction in loading capacity. As the last mild steel bar is pulled apart, the loading capacity of the specimen diminishes, accompanied by concrete crushing observed in the corner section of the left infill wall panel, as depicted in Figure 6.

3.1.3 Specimen SCW-IWPUS

Incorporating U-shaped dampers in specimen SCW-IWP, this study focuses on energy dissipation during vertical infill wall panel deformation, which is observed in four phases:

- Initial stage (0.05% - 0.3%): Linear force-displacement relationship with no notable observations. SCW-IWPU is stiffer than SCW-IWP.
- 0.4% - 1%: Cracks in slotted beam, damper yielding, and energy dissipation. Accelerated damper deformation at 1%.
- 1.25% - 2%: SC wall cracks, slight infill wall panel damage, and damper deformation. Limited structural and panel damage.
- 2.5% - 4%: Ultimate failure, with all mild steel bars fracturing and obstructed steel connections with slots. Wedged steel connection at 3.3%. Foam agents loosen at 4%, with damper residual deformation. Fracture of all mild steel bars during reverse loading.

3.1.4 Specimen SCW-IWPVE

Adding viscoelastic dampers in specimen SCW-IWP to dissipate energy during vertical infill wall panel deformation in four phases:

- Initial stage (0.05% - 0.3%): Linear force-displacement, tiny crack in slotted beam, minor loosening in SC wall corner. SCW-IWPE is less stiff than SCW-IWPU due to viscoelastic damping.
- 0.4% - 1%: Corner of SC wall lifts, damper dissipates energy, cracks in grout layer, and gaps between infill wall panels and grout indicating rocking.
- 1.25% - 2%: SC wall cracks, slight infill wall panel damage, damper surface deformation, and a crack at the back of the damper connection.
- 2.5% - 4%: Steel connections with slots obstruct, three mild steel bars fracture.

3.1.5 Specimen SCW-MIW

This study uses Autoclaved Lightweight Concrete (ALC) blocks with an exterior layer of Engineered Cementitious Composite (ECC) for infill walls, divided into three panels. Observations are as follows:

- In the 0.05% - 0.3% phase, a linear force-displacement relationship is seen, with a slotted beam crack at a 0.3% drift ratio.
- At 0.4% - 1%, cracks develop in the lower infill wall panel, while the SC wall remains intact.
- During 1.25% - 2%, more slotted beam cracks occur with no damage in the SC wall.
- In the 2.5% - 4% phase, the first SC wall crack is seen, and three mild steel bars fracture, primarily affecting the lower infill wall. Upper panels remain undamaged. The final condition of the specimens is depicted in Figure 6.

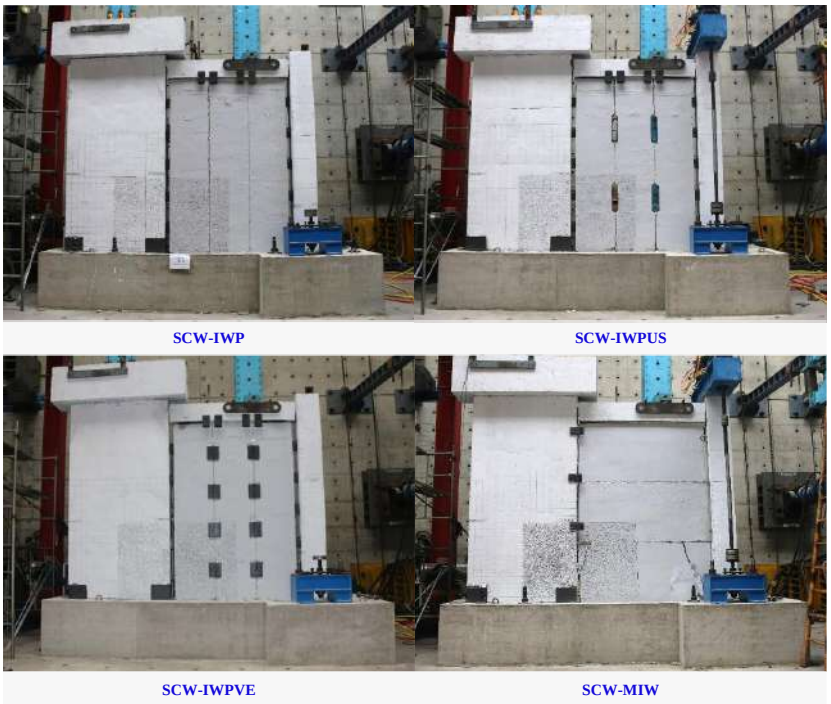


Figure 6. Damage evolution of the specimen SCW-IWP, SCW-IWPUS, SCW-IWPVE and SCW-MIW

3.2 COMPARISON OF PRELIMINARY RESULTS

Based on the overall testing process, both the infill wall panels and the structural skeleton exhibited low levels of damage under lateral loading. For specimens SCW-IWPUS and SCW-IWPVE, the introduction of dampers led to increased damage in the slotted beams and infill wall panels. In addition, SCW-IWPUS showed larger residual deformation than SCW-IWPVE, reflecting differences in the deformation recovery capabilities of the two types of dampers. It is important to note that the observed damage primarily consisted of surface cracks or localized concrete spalling, all of which are easy to repair. In contrast, the performance

of specimen SCW-MIW was not satisfactory, likely due to excessive adhesive restricting the intended sliding between wall panels, indicating the need for further improvement of this configuration.

Figure 7(a) compares the hysteretic responses of specimens with isolated infill wall connections (SCW-IWP, SCW-MIW) to the structural skeleton (SCW). Both infilled specimens have negligible influence on lateral performance, although SCW-IWP better accommodates the deformation mode, sustaining noticeable damage at 4% drift. Figure 7(b) compares specimens with dampers (SCW-IWPUS, SCW-IWPVE) to SCW-IWP. The addition of dampers enhances force capacity and stiffness, with the viscoelastic damper showing limited improvement in initial stiffness compared with the U-shaped steel damper. At larger drifts, however, the viscoelastic damper exhibits a rapid stiffness increase and superior recovery performance. Figure 7(c) presents residual displacement results, showing gradual increases with drift in smooth, continuous curves. At 2.5% drift, the residual drift ratios of the five specimens are 0.29%, 0.25%, 0.39%, 0.36%, and 0.42%, respectively, indicating repairable damage at the design limit state. Notably, SCW-IWPVE shows larger residual drift at small displacements, while SCW-IWPUS exhibits the highest residual drift at the end of loading, reflecting the distinct deformation and energy dissipation characteristics of viscoelastic and metallic dampers. Figure 7(d) shows the energy dissipation capacity of five specimens in the first cycle of each loading condition. At small displacements (less than 18 mm), all specimens exhibit similar performance. With increasing displacement, SCW-IWPUS and SCW-IWPVE dissipate significantly more energy due to the contribution of dampers, with SCW-IWPVE eventually surpassing SCW-IWPUS. In contrast, SCW, SCW-IWP, and SCW-MIW display comparable patterns throughout. Notably, SCW ceases energy dissipation at 2.5% drift, while SCW-IWP shows a sharp reduction at 4% drift due to mild steel bar fracture and the resulting loss of capacity, consistent with the force–displacement results.

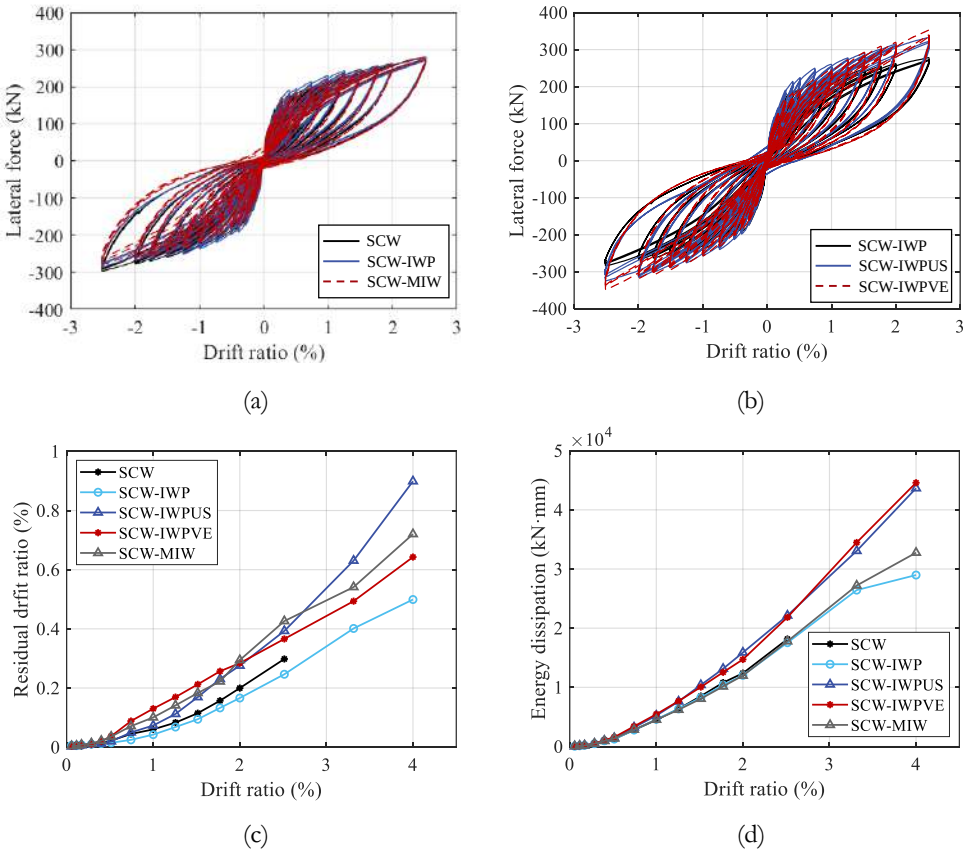


Figure 7. Damag Comparison of data results: (a) hysteretic curves of specimen SCW, SCW-IWP, and SCW-MIW; (b) hysteretic curves of specimen SCW-IWP, SCW-IWPUS, and SCW-IWPVE; (c) residual drift ratio; (d) energy dissipation capacity.

4.Conclusion

This study proposes several innovative infill wall configurations based on sliding mechanisms and energy dissipation characteristics, aiming to meet the requirements of low-damage seismic resilience, particularly for self-centering wall systems. A comprehensive cyclic lateral loading test program was designed and carried out on five distinct specimens, with detailed experimental observations recorded and systematically compared. The results indicate that the deformation behavior of the infill wall panels is well coordinated with the structural skeleton, and both maintained low-damage characteristics under 4% interstory drift. Although the incorporation of dampers led to slightly higher damage levels in the slotted beams and infill panels, such damage remained within acceptable limits under strong seismic loading and was readily repairable. Notably, specimens equipped with U-shaped steel dampers exhibited larger residual deformations compared with those using viscoelastic dampers, due to the inherent material properties. However, specimens with ALC block infill walls showed inferior performance, suggesting that this scheme requires further optimization.

Acknowledgments

This work is financially supported by the National Natural Science Foundation of China (Grant No. 52378528). The aforementioned sources of financial support are gratefully acknowledged.

REFERENCE

1. Filiatrault A, Sullivan T. [2014] "Performance-based seismic design of non-structural building components: The next frontier of earthquake engineering," *Earthquake Engineering and Engineering Vibration*, Vol. 13, No. 1, pp. 17-46.

2. Fiore A, Spagnoletti G, Greco R. [2016] "On the prediction of shear brittle collapse mechanisms due to the infill-frame interaction in RC buildings under pushover analysis," *Engineering Structures*, Vol. 121, pp. 147-159.

3. Furtado A, Rodrigues H, Arêde A, et al. [2020] "Experimental tests on strengthening strategies for masonry infill walls: A literature review," *Construction and Building Materials*, Vol. 263, No. 2, pp. 120520.

4. Grigorian M, Moghadam A S, Mohammadi H, et al. [2019] "Methodology for developing earthquake-resilient structures," *The Structural Design of Tall and Special Buildings*, Vol. 28, No. 2, pp. e1571.

5. Guo T, Wang L, Xu Z, et al. [2017] "Experimental and numerical investigation of jointed self-centering concrete walls with friction connectors," *Engineering Structures*, Vol. 161, No. 0, pp 192-206.

6. Hermanns L, Fraile A, Alarcón E, et al. [2014] "Performance of buildings with masonry infill walls during the 2011 Lorca earthquake," *Bulletin of Earthquake Engineering*, Vol. 12, No. 5, pp. 1977-1997.

7. Huang L, Zhou Z, Zhang Z, et al. [2021] "Seismic performance and fragility analyses of self-centering prestressed concrete frames with infill walls," *Journal of Earthquake Engineering*, Vol. 25, No. 3, pp. 535-565.

8. Li Y, Gao C, Li X, et al. [2023] "Experimental study on the seismic performance of steel frames with infill ALC wall panels," *Journal of Building Engineering*, Vol. 65, pp. 105739.

9. Lu Y, Lv Q, Liu Y. [2024] "Hysteresis performance and damage mode of self-centering frame with masonry infill wall: Experimental study assisted with DIC technique," *Engineering Structures*, Vol. 318, pp. 118797.

10. Priestley MJN, Sritharan SS, Conley JR, Pampanin S. [1999] "Preliminary results and conclusions from the PRESSS five-story precast concrete test building," PCI Journal, Vol. 44, No. 6, pp. 42-67.

11. Sharbatdar M K, Tajari A. [2021] "Experimental in-plane seismic strengthening of masonry infilled reinforced concrete frames by engineered cementitious composites (ECC)," *Construction and Building Materials*, Vol. 293, pp. 123529.

12. Tasligedik A S, Pampanin S. [2017] "Rocking cantilever clay brick infill wall panels: a novel low damage infill wall system," *Journal of Earthquake Engineering*, Vol. 21, No. 7, pp. 1023-1049.

13. Tasligedik A S, Pampanin S, Palermo A. [2015] "Low damage seismic solutions for non-structural drywall partitions," *Bulletin of Earthquake Engineering*, Vol. 13, No. 4, pp. 1029-1050.

14. Zhou Y, Chen Z, Zhong G. [2023] "Investigation on the seismic performance of the masonry infill wall with damping layer joint," *Engineering Structures*, Vol. 285, pp. 115979.

15. Zhu R, Guo T, Xie L L, et al. [2024] "Seismic risk assessment of self-centering prestressed concrete frames with sliding and masonry infill walls: experimental and numerical models," *Bulletin of Earthquake Engineering*, Vol. 22, No. 8, pp. 4115-4141.

16. Zhang C, Ling B, Huang W, et al. [2022] "Cyclic behavior of semi-rigid steel frame infilled with damping wall panels," *Journal of Building Engineering*, Vol. 51, pp. 104238.

Drift-Based Functional Fragility Framework for Fire-Rated Doors in Post-Earthquake Fires

Serdar Selamet[1] and Masahiro Kurata[2]

[1] Exponent Inc.
149 Commonwealth Dr. Menlo Park, CA 94025 USA
e-mail: sselamet@exponent.com
[2] Disaster Prevention Research Institute, Kyoto University
Kyoto, Japan
e-mail: kurata@dpri.kyoto-u.ac.jp

Abstract. This study evaluates the expected post-earthquake fire performance of fire-rated door assemblies by integrating structural drift demands from full-scale seismic testing with fire door fragility characterization. A fragility curve for 90-minute-rated fire doors is first developed based on the experiments of Calayir et al. [2022], in which doors were subjected to quasi-static cyclic loading followed by standard fire resistance tests. The resulting curve relates inter-story drift ratio (IDR) to the probability of fire rating loss, indicating reductions of approximately 70% at drift levels around 2%. The fragility curve is then applied to the partition walls in a steel-moment-resisting frame specimen reported by Huang et al. [2022], where a full-scale, four-story steel moment-resisting frame was subjected to increasing ground motions. Recorded IDRs reached approximately 1.45% at the second story. By mapping these drift demands to the fragility curve, the likely degradation in fire performance of hypothetical fire door sets is inferred for each story. This approach constitutes the first quantitative method to express the functional degradation of fire doors as a function of seismic deformation, enabling integration of fire compartmentation reliability into multi-hazard fragility assessments and informing code provisions for seismic qualification and post-earthquake inspection of fire-rated doors. Results suggest that, within the tested door configuration, drift levels of 1% and 2% caused approximately 30% and 40% reductions in fire-resistance rating, respectively, based on the integrated fragility model.

Keywords: fire-rated doors, post-earthquake fire, functional loss, fragility curves, non-structural components.

1. INTRODUCTION

Modern building performance under multi-hazard scenarios, particularly earthquakes followed by fire, has become a major focus in structural and fire safety engineering. Past earthquakes have shown that even when the primary structure remains stable, nonstructural damage can severely compromise compartmentation and fire containment. Following the 1995 Kobe (Hanshin-Awaji) earthquake, post-event inspections reported that approximately 30 % of fire-rated door sets were damaged, threatening the integrity of fire compartments [Nishino, 2023]. Fire doors are critical passive fire-protection elements; when distorted or misaligned by seismic drift, their ability to restrict smoke and flame spread diminishes sharply creating pathways for post-earthquake fires (PEFs).

Recent work has begun to quantify the seismic fragility of fire-rated assemblies and other passive fire-protection systems. Calayir et. al [2022] conducted the first full-scale study on fire-door performance under in-plane cyclic drift, demonstrating that even moderate inter-story drifts cause door-frame rotation, hinge distress, and seal degradation. When doors were subsequently tested to EN 1634-1 under the ISO 834 standard curve, fire-resistance durations decreased by as much as 70 % once inter-story drift ratios (IDR) approached 2.0–2.3 %, primarily due to 8 mm door–frame gaps and crushed or dislodged intumescent seals. Similar experimental observations were reported by Collier [2005] and Bartlett [2022] for racked wall-door assemblies, where small separations reduced rated fire resistance by 50 % or more. Mulligan et al. [2020] also found that plasterboard partitions with door openings experienced early cracking and detachment at only 0.8–1.0 % drift, reinforcing that ordinary office partitions cannot sustain design-level deformation without affecting attached fire doors.

Complementary research has addressed the system-level implications of such local failures. Dashti et al. [2025] highlighted that compartmentation loss in passive fire-protection components remains one of the least-quantified uncertainties in PEF modeling. Covi et al. [2024] developed fragility functions for fires-following-earthquakes (FFE), showing that even minor drift-induced misalignments in doors, windows, and partitions can drastically increase predicted fire-spread probabilities. Nishino [2023] proposed a probabilistic framework linking seismic damage states of passive systems—door frames and gypsum wall assemblies—to their expected reduction in fire endurance. These studies converge on the conclusion that door and partition fragilities dominate early fire-spread pathways in multistory buildings subjected to design-level earthquakes.

This paper reports the expected post-earthquake fire performance of fire-rated door assemblies, evaluated by integrating structural drift demands from full-scale seismic testing with fire door fragility characterization. A fragility curve for 90-minute-rated fire doors is first developed based on previously reported experiment dataset, in which doors were subjected to quasi-static cyclic loading followed by standard fire resistance tests. The resulting curve relates inter-story drift ratio (IDR) to the probability of fire rating loss, indicating reductions of approximately70% at drift levels around 2%. The fragility curve is then applied to the partition walls in a full-scale shaking table test. By mapping the drift demands to the fragility curve, the likely degradation in fire performance of hypothetical fire door sets is inferred for each story.

2. POST-EARTHQUAKE FIRE-DOOR EXPERIMENTS

The first author and colleagues from Turkey investigated the post-earthquake performance of fire-rated steel door assemblies [Calayir et. al., 2022]. The objective was to quantify how in-plane cyclic deformation influences the fire-resistance rating (FRR) of a compartmentation element. The test specimens were standard single-leaf steel fire door sets (as seen in Figure 1) rated for 90 minutes of fire endurance (insulation

criterion) and 120 minutes integrity. According to EN 1634-1 [CEN, 2014], fire integrity *E* failure occurs when excessive deformation or clearance between the door leaf and frame allows sustained flaming or hot gases to pass to the unexposed side. It is characterized by visible cracks or fissures, continuous flaming for more than 10 s, or ignition of a cotton pad placed on the unexposed surface. Fire insulation (I_2) failure, on the other hand, is defined by excessive heat transfer through the door: when thermocouples positioned at least 100 mm from the edges record a temperature rise exceeding 180 °C at any point, 360 °C at the frame, or an average increase of 140 °C across the central area, indicating that the door no longer provides adequate thermal protection.

2.1 EXPERIMENTAL PROGRAM

Each door frame was mounted in a stiff timber loading frame and cyclic lateral displacements were applied at the top of the door frame to impose racking deformations. The loading protocols followed standardized approaches to incrementally increase drift demands up to a target level around 2.3% IDR, representing a design-level earthquake for a tall building. Three identical door sets (Door 2–4) were each loaded to this drift level, while a fourth door set (Door 1) was tested quasi-statically up to 3% drift to examine ultimate failure modes. After the lateral loading, the damaged door specimens were subjected to standard fire resistance tests to determine their remaining fire endurance.

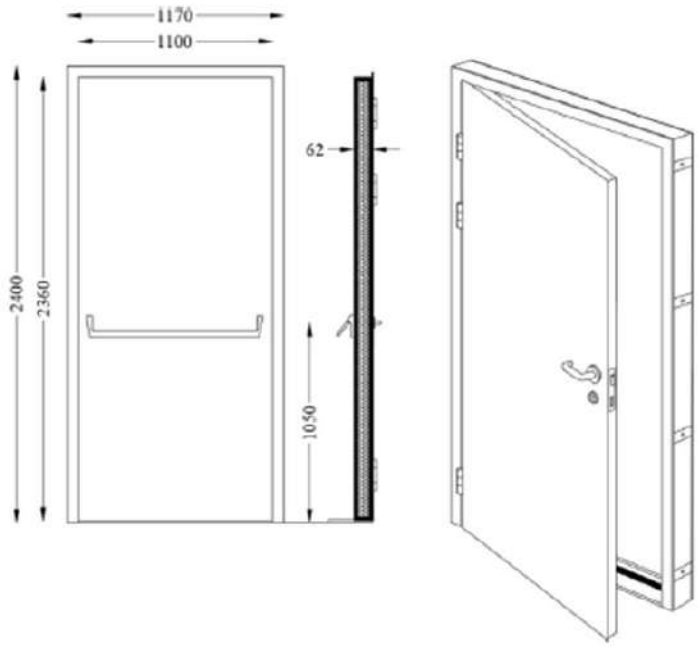


Figure 1. Construction details and dimensions (mm) of the tested fire door set [Calayir et. al. 2022]

2.2 DAMAGE OBSERVATIONS

During the cyclic drift tests, the fire door sets sustained progressively worsening damage with increasing story drift. Initial drifts (~0.5%) caused minor visible gaps and distortions. As drifts exceeded ~1%, the steel door frames bent and separated notably from the door panels at the top corners. By around 2% IDR, all tested door sets had developed large permanent set, the door frames were visibly racked (parallelogram-shaped) and the door panels jammed in place due to frame narrowing at one corner. Figure 2 a–c [Calayir et al. 2022] shows the distorted shape of three door specimens at their peak drift: each exhibits a significant gap opening at the upper latch-side corner, along with localized tearing or cracking of the frame steel near the lock area. The doors at this point could not be operated (they were stuck in the deformed frame) and had residual offsets. Additional damage included loosened hinge attachments and compressed/crushed

intumescent seals along the edges (especially where the door edge bore against the frame). One specimen showed a crack through the frame corner weld at 1.9% drift, and another had tearing around the latch bolt by 2.3% drift.

Table 1. Summary of quasi-statically loaded fire door test results [Calayir et al., 2022]

Door Specimen	Peak Cyclic Drift (IDR)	Notable Seismic Damage	Residual Fire Resistance (min)	Fire Rating Loss
Door Set No.2	2.3%	Frame tearing at lock; large top gap (~8mm)	36 min	69%
Door Set No.3	1.9%	Frame cracked at top corner; door jammed	38 min	67%
Door Set No.4	2.3%	Severe frame distortion; hinges loosened	37 min	68%

The fire exposure tests revealed drastic reductions in fire endurance for the earthquake-damaged doors. All three door sets that underwent seismic loading failed to achieve even half of the original 90-minute rating. Table 1 and Figure 3 summarize the outcomes. While an undamaged control door easily survived the full 90-min (and indeed had no integrity or insulation failure even at 2 hours, demonstrating some safety margin), the drifted specimens failed between about 30 and 40 minutes under the same fire test. The mode of fire failure for the damaged doors was integrity failure: due to the quake-induced gaps, hot gases and flames penetrated the door-frame interface well before 90 minutes. In Calayir et al. [2022] tests, flaming was observed around the warped frame edges after roughly 30–40 minutes of fire exposure, leading to the cotton pad ignition criterion being met (i.e. fire breaching). Additionally, thermocouples on the frame registered rapid temperature rise – one door exceeded the 360 °C frame temperature limit at around 40 min. All damaged doors thus failed the integrity criterion by 40 min, versus the control door which maintained integrity past 120 min. The insulation criterion (average door temperature rise) was satisfied for the damaged doors up to their failure time, meaning the door panels themselves did not overheat; it was the through-gap hot gas leakage that caused failure. This highlights that gaps and distortions, not panel burn-through, were the critical weakness in the post-quake fire performance. With only three data points, Calayir et al. [2022] did not demonstrate fitting a specific probability distribution; however, the implication is that the fragility function for fire door failure (loss of rating) is steep – likely a lognormal curve. The authors succinctly stated: "The fire performance of 90-min rated door sets reduced approximately70% in terms of insulation and integrity failure." They recommend that post-earthquake inspections measure door frame gaps, and if gaps exceed ~8 mm (which corresponded to ~2% IDR in their tests), the door should be considered compromised.

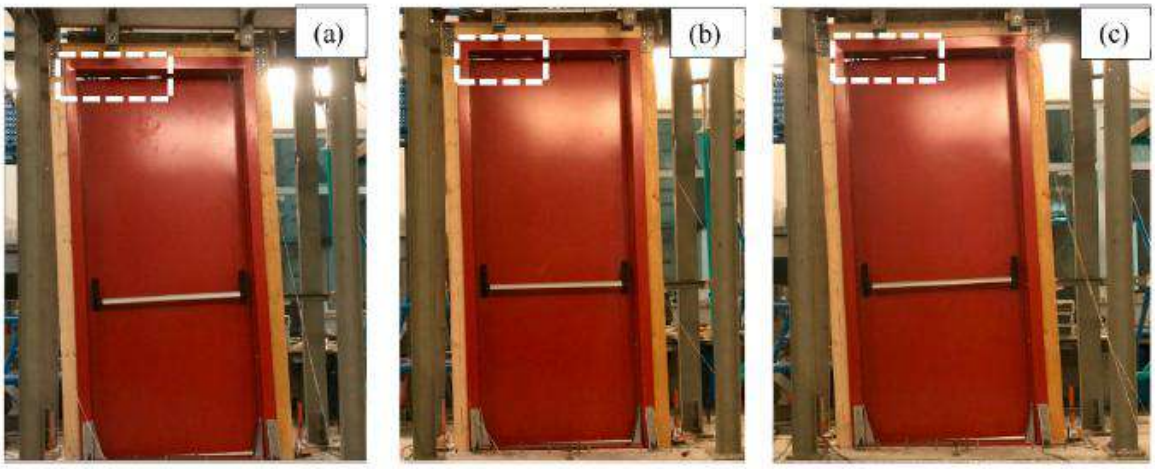


Figure 2. Observed damage to fire door sets under lateral drift [Calayir et al., 2022]: (a–c) Permanent distortion of three 90-min fire door specimens at their failure inter-story drifts (~1.9–2.3% IDR) – note large gap openings at top corners and tearing near the locks

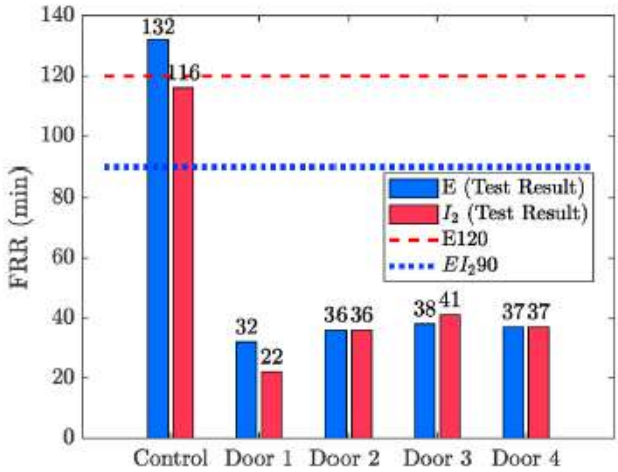


Figure 3. Residual fire resistance of 90-min rated fire doors versus inter-story drift ratio, based on data from Calayir et al. [2022]. Higher seismic drifts lead to drastic reductions in fire endurance (approximately 70% loss at 2.3 % IDR)

3.PARTITION WALL FRAGILITY

To investigate realistic drift demands on non-structural walls and door frames, the second author and colleagues from Japan conducted full-scale shake-table tests on a four-story steel moment-resisting frame with non-structural components and medical equipment. The experiment took place at the E-Defense facility in Japan. Huang et al. [2022] reported the summary for cold-formed steel (CFS) gypsum partition wall behaviours, highlighting the influence of the vertical boundary conditions on the wall damages.

3.1 EXPERIMENTAL CONFIGURATION

The steel frame building measured 4 stories tall (approximately 3.8 m per story, 15.2 m total height) and was designed to modern code standards. A total of sixteen non-structural drywall partition panels were installed on each floor, in typical office layout configurations, including some with door openings and others spanning between columns. Some partition walls included door frame segments though the doors themselves were not installed, the framing and opening were present. This means that these test results can

shed light on door frame deformations. The frame was subjected to a sequence of six earthquake input cases of increasing intensity. These included scaled versions of the 1995 Kobe (JMA Kobe) ground motion and a long-duration long-period design ground motion (the Nankai Trough earthquake of Mw 9.0 scenario) at Osaka soft-soil site, applied in both horizontal directions to simulate a variety of seismic demands. Throughout these tests, extensive instrumentation measured structural and non-structural responses, including inter-story drift ratios (via string potentiometers) at each floor and detailed observation of partition wall damage progression.

After each test, the partition walls were inspected and damage was catalogued in detail (cracks, gaps, screw failures, etc.). Huang et al. [2022] reported that all partition walls containing door frames suffered damage type of panel detachment at door-frame connections and type of board cracking by the end of the tests. This indicates that the presence of a door opening created a weak point where seismic drift concentrated damage, consistent with expectations.

The maximum IDR recorded was approximately 1.5% at the second floor. The first story and third story experienced slightly lower peak drifts, and the top story was the most rigid. The second floor with ~1.45% IDR, and the first/third floors with ~1.0–1.2% IDR exceed the drift at which Calayir et al. [2022] observed major fire door damage (~1–2% IDR). In other words, a realistic design-level earthquake caused drifts in this mid-rise building that likely would compromise 90-min fire doors.

3.2 DAMAGE OBSERVATIONS

The damage observed for representing partition walls without door frames are summarized in Table 2. The GA and GB configurations represent strong-strong boundary condition and weak-weak/strong boundary condition, , respectively and -N represents walls without door. The walls exhibited median story drift ratios of 0.5 %, 0.7 %, and 1.6 % for DS1–DS3, respectively. Here, DS1–DS3 correspond to superficial, minor and severe damage, respectively. Although actual door leaves were not present in the test, it can be inferred that if a fire door had been installed within those frames, it would have experienced similar in-plane racking to that observed in the quasi-static fire door experiments by Calayir et al. [2022].

The observed partition wall damage around the boundary frame indicates that the surrounding frame members likely deformed several millimeters out of square under drift demands of approximately 1–2%. Huang et al. [2022] did not directly measure door gap widening (as no door leaf was installed), but visible cracking and separations of 5–10 mm around the panel boundaries suggest that a hypothetical fire door would have experienced comparable corner misalignments. This is consistent with Calayir et al. [2022], where an 8 mm top gap corresponded to a 2% drift ratio. Therefore, for second-story drift levels near 1.4–1.5%, a door installed within the same boundary condition could be expected to exhibit 5–6 mm corner gaps.

Table 2. Summary of partition wall test results [Huang et al., 2022]

Boundary Type	Specimens	Boundary Description	Median IDR (DS1 / DS 2 /DS 3) [%]	Seismic Damage
GA-N / GB-D	P1, P2, P8, P10, P13, P14, P4, P6, P7, P11, P15	Strong–strong external boundaries, no door frame	0.5 / 0.7 / 1.6	Edge crumpling and screw failures near both vertical boundaries; diagonal cracking; plaster spalling concentrated at corners,
		At least one weak (panel or stud) external boundary, no door frame		Cracking and crushing along weak boundary; localized panel separation; limited overall deformation

Huang's fragility framework explicitly quantifies the influence of boundary stiffness on the seismic vulnerability of non-structural walls. The GA-D configuration representing a door frame embedded between two stiff vertical supports serves as a direct analogue to the boundary condition of a fire-rated door assembly, forming the structural basis for the functional fragility relationships developed in the next section. The fragility function in Huang et al. [2002] follows a lognormal cumulative distribution where m_i is the median drift, $\beta = 0.25$ is the logarithmic standard deviation [FEMA P-58, 2018], and Φ is the standard normal cumulative distribution.

$$P(DS \geq i \mid IDR) = \Phi((\ln(IDR) - \ln(m_i))/\beta) \quad (1)$$

4. INTEGRATION OF SEISMIC DAMAGE AND FIRE FUNCTIONALITY FRAGILITIES

To evaluate post-earthquake fire performance of door assemblies, the drift-based fragility framework established by Huang et al. [2022] was adapted to represent fire-resistance loss. The inter-story drift ratio (IDR) was used as the engineering demand parameter (EDP) for both datasets, where IDR = Δ/h describes the relative story deformation imposed on the door–frame system. Three functional loss states (LS1–LS3) were defined to characterize the degradation of fire-resistance rating (FRR).

Table 3. Functional limit states for fire-rated doors

Limit state	Representative FRR loss	Median IDR (m_i)	Source	Physical interpretation
LS1 (DS1)	20 %	0.5 %	Huang [2022]	Onset of distortion; minor seal separation
LS2 (DS2)	50 %	0.7 %	Huang [2022]	≈ 5 mm gap; partial loss of seal continuity
LS3 (DS3)	70 %	2.3 %	Calayir et. al. [2022]	≈ 8 mm gap; loss of fire integrity and insulation

The first two median drifts were adopted from the GA-D configuration in Huang et al. [2022], representing strong–strong boundaries with a door frame, which most closely resemble the boundary conditions of a fire-rated door assembly installed within a rigid structural frame. The third median, 2.3 %, corresponds to the measured approximately 70 % reduction in FRR observed in the Calayir et al. [2022] door experiments, where full integrity failure occurred between 2.0–2.3 % drift. Relative to the 132-minute integrity performance of the control door, the drifted specimens achieved only 32, 36, 38, and 37 minutes of fire endurance, corresponding to reductions of 76%, 73%, 71%, and 72%, respectively. Because LS3 is based on only three fire-tested specimens of identical construction, its statistical basis is limited. The LS3 parameters should therefore be interpreted as an engineering estimate anchored to the observed failure mechanism rather than a statistically robust distribution. Each limit state was modeled as a lognormal fragility function, consistent with Huang et al. [2022] and FEMA P-58 conventions:

$$P(LS \geq i \mid IDR) = \Phi((\ln(IDR) - \ln(m_i))/\beta) \quad (2)$$

where m_i is the median drift, $\beta = 0.4$ is the logarithmic standard deviation [Miranda et al. 2003] for interior doors), and Φ is the standard normal cumulative distribution.

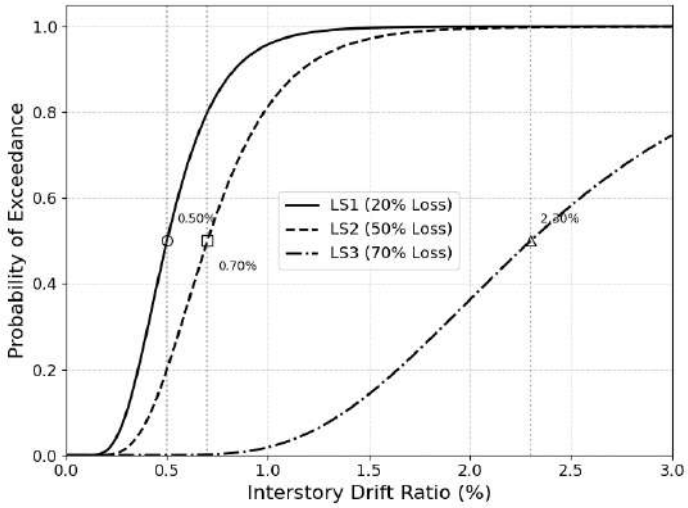


Figure 4. Drift-based fragility curves for fire-rated door assemblies showing probability of exceedance for three functional loss states (LS1–LS3) as a function of interstory drift ratio.

The three fragility curves describe the probability of exceeding each loss state as a function of drift (Figure 4). To relate these exceedance probabilities to residual fire performance, an expected functionality curve was derived as seen in Figure 5, expressing the mean retained FRR at each drift level:

$$E[L(IDR)] = L_1^*(F_1 - F_2) + L_2^*(F_2 - F_3) + L_3^* F_3 \quad (3)$$

where $F_i = P(LS \geq i)$ and L_i^* are representative loss values for each interval as $L_1^* = 0.10$, $L_2^* = 0.35$, $L_3^* = 0.60$. The expected retained functionality is then:

$$E[R_f(IDR)] = 1 - E[L(IDR)] \quad (4)$$

This curve transitions from E [R_f] = 1.0 and E [R_f] = 0.3 at 2.0-2.5 % IDR reflecting the progressive degradation of fire-door performance with increasing seismic deformation.

The combined model bridges the structural fragility of partition walls and the functional degradation of fire-rated doors:

- Huang [2022] data define the early deformation thresholds (0.5–0.7 % IDR) where gaps initiate and seals begin to fail.
- Calayir et al. [2022] results establish the severe-damage threshold (≈ 2.3 % IDR) corresponding to full seal failure and a 70 % FRR loss.
- The adopted dispersion β=0.4 captures installation variability typical of interior door systems and provides a conservative envelope compared with Huang's β ≈ 0.25–0.30 for laboratory partitions.

The resulting functionality model quantitatively connects earthquake-induced drift to loss of fire compartmentation, enabling integration of fire-safety metrics within seismic fragility analyses.

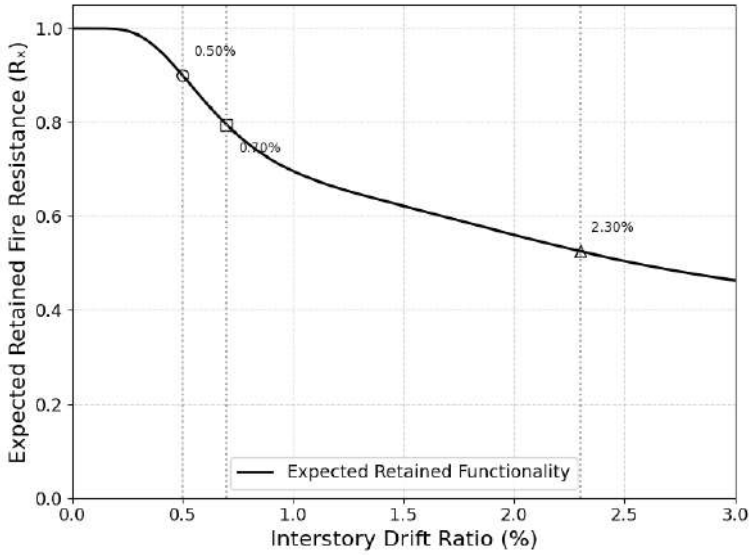


Figure 5. Functional loss curve of the fire-rated door showing retained FRR with increasing drift

5.CONCLUSIONS

This study evaluates the post-earthquake performance of fire-rated door assemblies by integrating the authors' prior experimental fragility data [Calayir et al., 2022] with full-scale structural response measurements from Huang et al. [2022]. Calayir et al. [2022] demonstrated that drift-induced distortion can significantly impair the performance of fire-rated doors. Quasi-static testing of 90-minute fire-rated steel door assemblies showed that moderate interstory drifts (1–2%) cause significant frame distortion, hinge loosening, and seal damage. Under subsequent standard fire exposure, the fire-resistance rating decreased by approximately ~70%, with integrity failure observed after 30 minutes instead of the nominal 90 minutes. The results confirm that drift ratio is a reliable predictor of fire performance loss. In the four-story steel moment frame tested by Huang et al. [2022], peak story drifts during design-level shaking reached ~1.0–1.5%. Partition walls with door openings on the most drifted floor exhibited severe boundary damage.

The main findings are as follows:

- Applying the fire-door fragility model to the measured story drifts in the four-story steel moment frame indicated that the probability of door failure (FRR < 90 min) was approximately 50–60% on the maximum observed IDR.

- While based on a limited case study, the analysis indicates that compartmentation for fire safety can be substantially impaired following a design-level earthquake. A fire igniting on a story with drift-damaged doors could spread beyond the room of origin due to premature leakage or flame passage through frame gaps. A practical post-earthquake inspection criterion is the door-frame gap width: observed separations of >6–8 mm should be considered indicative of compromised fire resistance.

- The expected retained fire resistance decreases from nearly 100% at low drift to about 80% at 0.7 % IDR and 60% at 1.5% IDR, the latter corresponding to design-level story drifts observed in Huang et al. [2022]. The functional loss curve thus provides the first quantitative method to relate seismic drift directly to fire-door performance degradation, enabling consistent assessment of compartmentation reliability in multi-hazard design.

In summary, this work identifies a critical linkage between seismic deformation and fire-safety performance. Fire doors designed to provide 90 minutes of protection may offer only 55 minutes of resistance following moderate structural drift. Quantifying this reduction enables realistic assessment of fire spread potential after earthquakes. The findings support consideration of seismic qualification and post-event inspection provisions for fire-rated doors in future editions of ASCE 7 and NFPA 80, ensuring that both structural and compartmentation systems retain functionality under multi-hazard conditions.

6.REFERENCES

Bartlett, J. [2022] "Vulnerabilities of fire-rated, non-load-bearing wall systems under seismic actions," *Proceedings of the Australian Earthquake Engineering Society Conference (AEES)*, Hobart, Australia.

Calayir, M., Selamet, S., and Wang, Y.C. [2022] "Post-earthquake fire performance of fire door sets," *Fire Safety Journal*, Vol. 130, Article 103589.

CEN [2014] *EN 1634-1: Fire resistance and smoke control tests for door and shutter assemblies, openable windows and elements of building hardware – Part 1: Fire resistance test for door and shutter assemblies and openable windows*, European Committee for Standardization, Brussels, Belgium.

Collier, P. [2005] "Post-earthquake performance of passive fire protection systems," *BRANZ Study Report SR 147*, Building Research Association of New Zealand, Porirua, New Zealand.

Covi, E., Boschini, F., and Moser, M. [2024] "Fires following earthquake fragility functions for non-structural components," *Fire Technology*, Vol. 60, pp. 2143-2162.

Dashti, S., Yuan, M., and McAllister, T. [2025] "Post-earthquake fire resistance in structures: a review of current research and future directions," *Applied Sciences*, Vol. 15, No. 6, Article 3311.

FEMA [2018] *Seismic Performance Assessment of Buildings, Volume 1–Methodology and Volume 2–Implementation Guide (FEMA P-58, 2nd Edition)*, Federal Emergency Management Agency, Washington, D.C., USA

Huang, J., Kurata, M., Kawamata, Y., Kanao, I., Qi, L., and Takaoka, M. [2022] "In-plane damage of partition walls with various boundaries during earthquakes," *Earthquake Engineering & Structural Dynamics*, Vol. 52, No. 4, pp. 1-19.

Mulligan, J., Sullivan, T., and Dhakal, R. [2020] "Experimental study of the seismic performance of plasterboard partition walls with seismic gaps," *Bulletin of the New Zealand Society for Earthquake Engineering*, Vol. 53, No. 4, pp. 175-188.

Miranda, E., and Taghavi, S. [2003] "Response assessment of nonstructural building elements," *Pacific Earthquake Engineering Research Center (PEER) Report 2003/05*, University of California, Berkeley, 253 pp.

Miranda, E., and Taghavi, S. [2006] "Approximate floor acceleration demands in multi-story buildings," *Earthquake Engineering and Structural Dynamics*, Vol. 35, No. 4, pp. 419–442.

Nishino, T. [2023] "Derivation of damage models for post-earthquake fire risk assessment," *Journal of Asian Architecture and Building Engineering*, Vol. 22, No. 3, pp. 329-341.

Influence of tee joint capacity on the seismic behaviour of a fire suppression system

Monte F.[1], Tartaglia R.[2], De Angelis A.[3], Del Vecchio C.[3], and Maddaloni G.[3]

[1] University of Sannio
Piazza Roma 21, 82100, Benevento, Italy
e-mail: fmonte@unisannio.it
[2] University of Sannio
Piazza Roma 21, 82100, Benevento, Italy
e-mail: rotartaglia@unisannio.it
[3] University of Sannio
Piazza Roma 21, 82100, Benevento, Italy
e-mail: {adeangelis, cdelvecchio, maddaloni}@ unisannio.it

Abstract. The vulnerability of non-structural elements may significantly influence the operability of facilities during and in the aftermath of seismic events. The inadequate seismic performance of suspended piping systems has been documented after recent seismic events in urban regions. This has resulted in the disruption of the continuous operation of several buildings and facilities. Consequently, there is a need to extend the knowledge on the seismic response of these non-structural elements in order to improve their performance. In this direction this paper presents the results of a numerical investigation conducted within the ENRICH research project, with the purpose of examining the influence of tee joint capacity and of the relative connections on the seismic capacity of a fire suppression system. The moment-rotation curve and equivalent plastic deformation (PEEQ) distribution demonstrate that, increasing the capacity of the tee joint has a significant influence on the response of the entire system, while the connection adopted between the joint and the pipes assumes significant importance when the joint shows a bending capacity higher than the plastic resistance of the connected pipes.

Keywords: Non-structural elements, pipe system, seismic performance, moment-rotation response, numerical analyses.

1. Introduction

Hospital and healthcare facilities are essential components of the society; nevertheless, their operability during and following seismic events is frequently compromised by the vulnerabilities exhibited by non-structural elements. It is evident that a wide range of non-structural elements have demonstrated inadequate seismic performance following recent seismic events. This has resulted in interruption of the functionality of buildings and facilities, as documented by [Miranda et al., 2012; OSHPD, 1995]. Furthermore, a multitude of loss estimation studies conducted on extant buildings have emphasised that losses pertaining to non-structural elements are, in general, greater than those associated with the structural elements [Del Vecchio et al., 2020; O'Reilly et al., 2018; Sousa et al., 2018]. Consequently, the seismic performance of non-structural elements has become a fundamental aspect of the performance-based earthquake engineering framework, as demonstrated by [Deierlein et al., 2003].

Starting from these considerations, several experimental and numerical studies in the literature have been carried out with the aim of improving the knowledge on the non-structural elements' behaviour during an earthquake [Bonati et al., 2025; Coppola et al., 2024; D'Angela et al., 2024; De Angelis et al., 2025a, 2025b; Magliulo et al., 2024; Zidarich et al., 2023; Zidarich et al., 2025; Zito et al., 2022]. In particular, a significant number of studies have concentrated on the influence of hanger-rods or trapezes designed for gravity loads, as well as transverse and longitudinal sway-braced trapezes or rods, on the seismic behaviour of suspended piping systems [Perrone et al., 2020a, 2020b; Perrone et al., 2022; Rodriguez et al., 2025; Wood et al., 2013]. Furthermore, the rotational capacity at first leakage of pressurised tee joints of different diameters, materials and connection typologies under monotonic and cyclic loads were experimentally and numerically investigated by [Tian et al., 2014; Tian et al., 2015]. Finally, the effect of vertical floor accelerations on the seismic performance of suspended piping systems was analysed by [Blasi et al., 2023; and Tatarsky et al.,2018]. In this particular instance, it was determined that the vertical accelerations exerted a negligible influence on the damage sustained by suspended piping systems.

Within the framework of the PRIN 2020 ENRICH project, this paper presents the results of a parametric analysis investigating the influence of tee joint resistance on the seismic performance of a suspended piping system. The results indicated that the capacity of this node element has a substantial impact on the seismic response of the entire system. Furthermore, two tee joint configurations were investigated in the analyses conducted by changing the connection between the node element and the principal pipe: i) in the first configuration, the ends of the tee joint and the end of the pipe were threaded and connected by a threaded collar; and ii) in the second configuration, the joint element and the pipe were flanged together. Changing the connection type revealed that the flanged connection provides a better system response to seismic action under service conditions, with plastic deformation developing at a higher rotation rate. However, this type of connection resulted in greater damage concentration in the connected pipes.

2.Case Study

To investigate the seismic performance of suspended piping systems, a full-scale fire suppression system was designed and installed at the Civil Engineering Laboratory (LInC) at the University of Sannio. Designed in accordance with the most recent European codes (UNI 10779:2021 and UNI EN 12845:2020), the system was divided into two parts:

- The principal line, which used S280 GD steel pipes with an 80 mm nominal diameter.
- The secondary line, which used steel pipes with a nominal diameter of 24 mm.

All the pipes were anchored to the structure using 10 mm diameter circular-section hangers.

The tee joints examined in this study were part of the main line of the fire suppression system, as depicted in Figure 1. In order to examine the influence of the connection between the joint element and the connected pipes on the seismic response of the entire system, two configurations were considered and numerically investigated:

- Conf. 1: The tee joint was connected to the side pipes by means of a flanged connection, while a threaded collar was adopted for the connection with the central pipe (Figure 1.b).
- Conf. 2: All the pipes were connected to the joint element through the utilisation of a flanged connection (Figure 1.c).

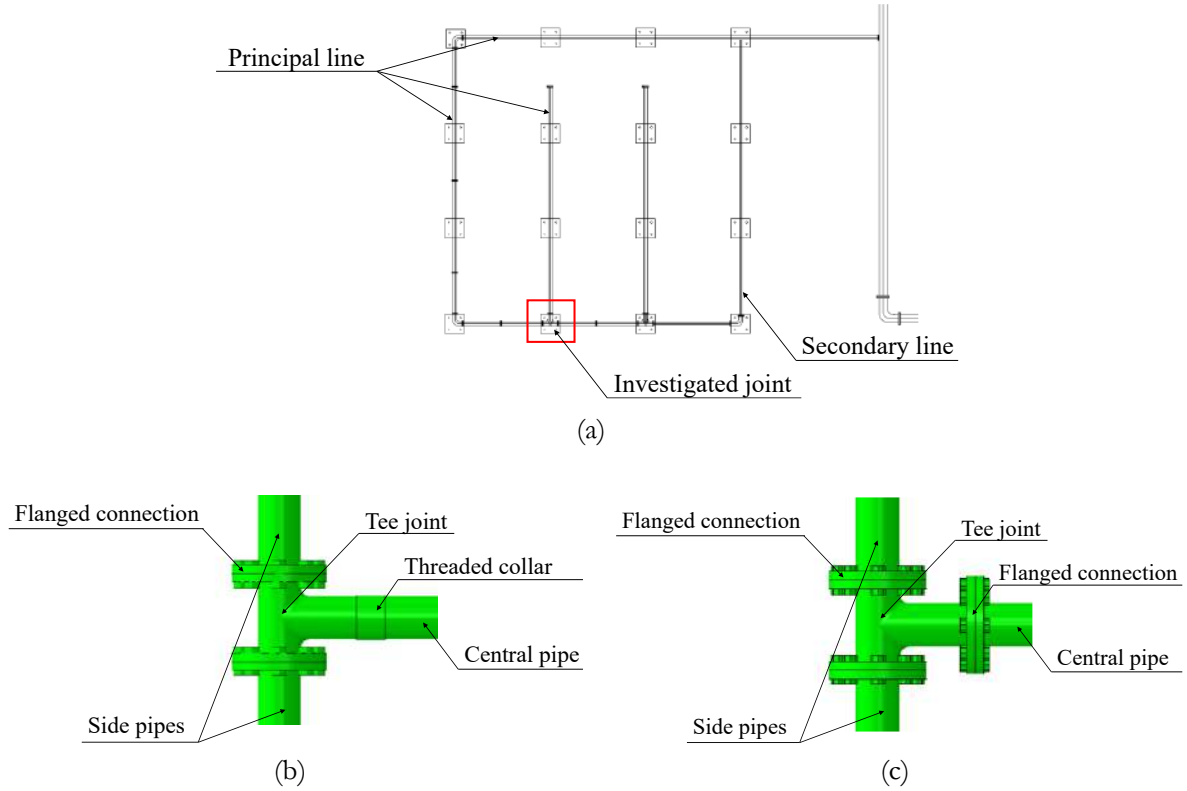
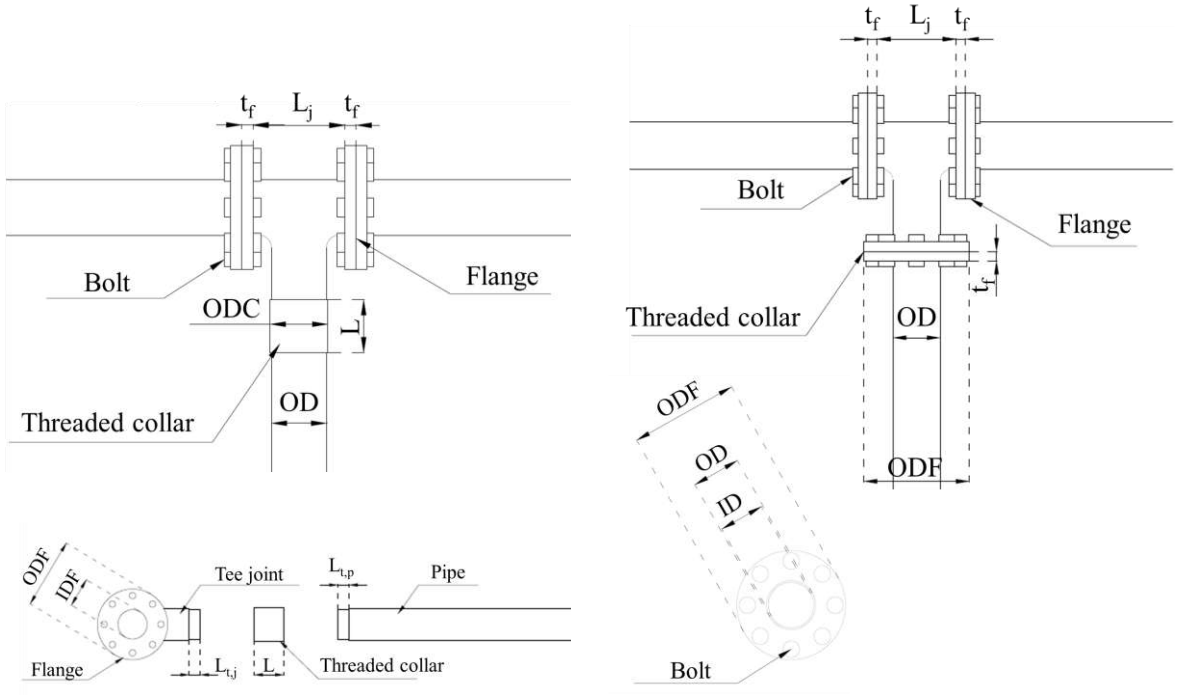


Figure 1. Sketch of the experimental mock-up: a) Location of the investigated joint in the full-scale system; b) tee joint in the Conf. 1; c) tee joint in the Conf. 2.

The main geometrical features of the investigated joints are reported in Table 1 and depicted in Figure 2.

Table 1. Geometrical features of investigated joints

Configuration	Pipe DN80		Tee Joint	Threaded portion		Threaded collar			Flanged connection			
	OD [mm]	ID [mm]	Lj [mm]	Tee Joint $L_{t,j}$ [mm]	Pipe $L_{t,p}$ [mm]	L [mm]	ODC [mm]	t_c [mm]	ODF [mm]	IDF [mm]	t_f [mm]	Bolt diameter [mm]
Conf. 1	88.9	82.5	148	30	30	75	103	9	198	84	18	16
Conf. 2			148	-	-	-	-	-	198	84	18	16



(a) (b)

Figure 2. Geometrical features of investigated joints: a) Conf. 1; b) Conf. 2

3.Numerical Models

The behaviour of the investigated tee joints was numerically analysed by means of finite elements (FE) models developed in Abaqus (Figure 3). A total of eight numerical models were developed, four for each tee joint configuration under investigation, by changing the tee joint material. In particular, the S235, S275 and S355 steel materials were considered for the tee joints in the different models. Furthermore, a perfectly elastic steel material was adopted to simulate the case of utilising an over-resistant joint. The length of the

connected DN80 S280GD steel pipes was defined in the context of the investigation of the joints from the full-scale fire suppression system, which was designed and tested by the University of Sannio (Italy).
The flanges utilised for the connections between the pipes and the tee joint were fabricated from S355 steel, and M16 8.8 high-resistant bolts were employed. For the threaded collar of each model developed for configuration 1, the same material as the corresponding tee joint was adopted. All steel materials considered in the models were modelled according to the Von Mises criterion for yielding, assuming the nominal yield capacity.
The combined Kinematic and Isotropic hardening law available in Abaqus was assumed for plastic hardening, using the data provided by [Dutta et al., 2010]. The bolts were modelled as dumbbell shape elements and their non-linear behaviour was defined as indicated by [D'aniello et al., 2016; D'Aniello et al., 2017].
In the developed numerical models, the interactions between adjacent elements were modelled using the surface-to-surface interaction available in Abaqus, with "Hard" Contact and a Coulomb friction coefficient of 0.3, as indicated for regular steel-to-steel interfaces. Contrariwise, Tie Constraints were adopted to model the interactions between welded elements. The definition of Reference Points and Rigid Body constraints was implemented to facilitate the assignment of the boundary conditions, as showed in Figure 3.a.
The mesh of the pipes, the connection flanges and the bolts in all the models were made by C3D8R (8-node linear brick, reduced integration) elements with the aim of reducing the computational time, while the tee joint was discretised by means of C3D10 (10-node quadratic tetrahedron) elements. In accordance with the findings of the sensitivity analysis conducted within this study, an approximate size of 10mm was assigned to all elements of the pipes, flanges and bolts. Conversely, an approximate size of 7.5mm was assumed for the elements of the tee joint.

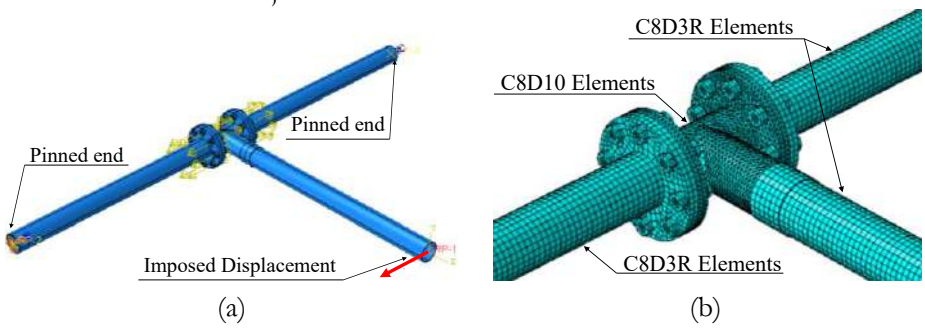


Figure 3. Numerical model: a) Sub-structuration and Boundary conditions; b) Mesh

A two-step Dynamic Implicit Quasi-Static analysis was conducted. In the initial step, the clamping of the bolts was implemented through the utilisation of the "Bolt Load" command available in Abaqus, while the displacement was applied at the free end of the connected principal pipe in the subsequent step.
The results of the numerical analyses carried out on the developed numerical models have been discussed in the following in terms of moment-rotation response curve and equivalent plastic strain (PEEQ) distribution.

4.Numerical Results

In Figure 4, the comparison between the moment response curve obtained for the two investigated tee joint configurations (i.e., Conf. 1 and Conf. 2) by changing the material was illustrated. In these graphs, the moment *M* was evaluated as the product of the reaction force obtained in Abaqus at the free end of the central pipe (i.e., where the displacement was imposed) for the distance between this point and the tee joint. Instead, the rotation at each time step was calculated as the ratio between the imposed displacement and the same free end-to-tee joint distance. Furthermore, the plastic capacity of the connected pipe (i.e.,

$M_{pl,DN80}$), obtained as the plastic section modulus for the yielding capacity of the pipe steel material, was introduced to verify in which cases the investigated tee joints have a considerable influence on the seismic response of the pipe system. As it can be observed, in both the examined cases, the ratio between the capacity of the joint element and the plastic capacity of the connected pipes has a significant influence on the ultimate capacity of the entire pipe system. Indeed, it was determined that the bending capacity of the tee joint limits the system's capacity for all the steel materials under consideration, until this component is less resistant to the connected pipes.

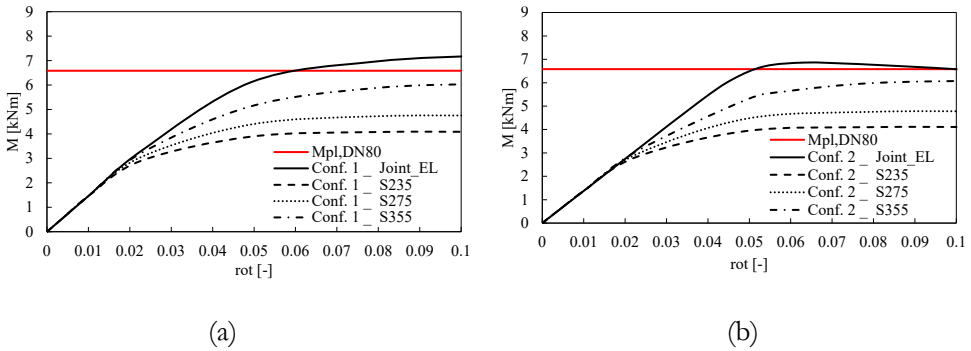


Figure 4. Moment-Rotation response curve varying the tee joint material: a) Conf. 1; b) Conf. 2.

The comparison between the moment-rotation curves obtained for the two investigated configurations considering the same material were depicted in Figure 5. In this case, it can be observed that for both configurations analysed, the type of connection between the pipe and the joint element had a negligible effect on the performance of the piping system until the bending capacity of the tee joint is lower than that of the connected pipes. Instead, when the capacity of the pipe system was limited by the capacity of the pipes (i.e. Joint_EL models), it was observed that the presence of the flanged connection in the configuration 2 leads to have a different PEEQ distribution and damage in the connected pipe (see Figure 6) than that shown by the system with the configuration 1, and an higher capacity degradation for higher rotation levels.

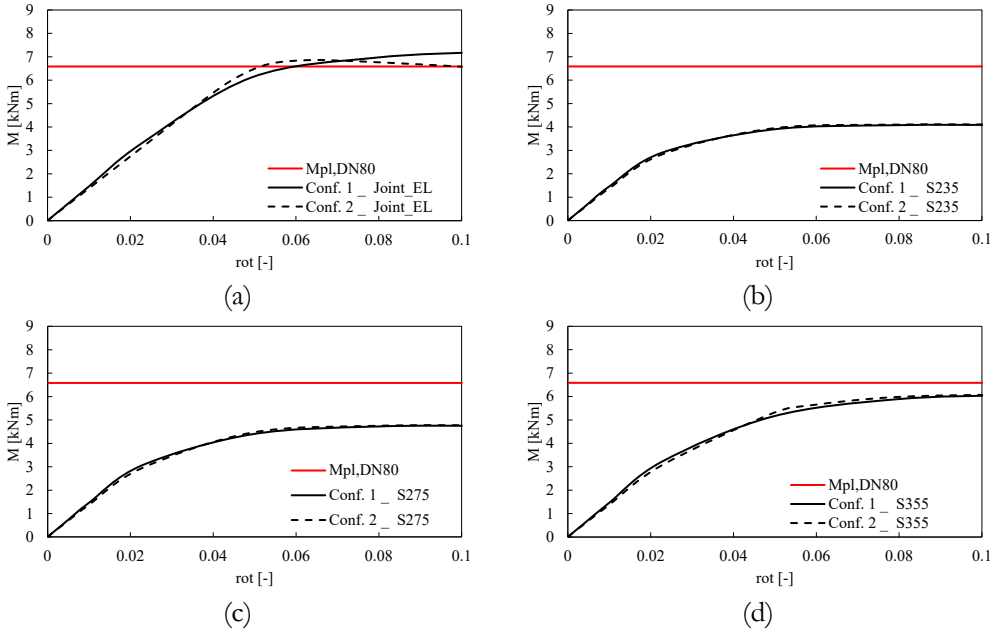
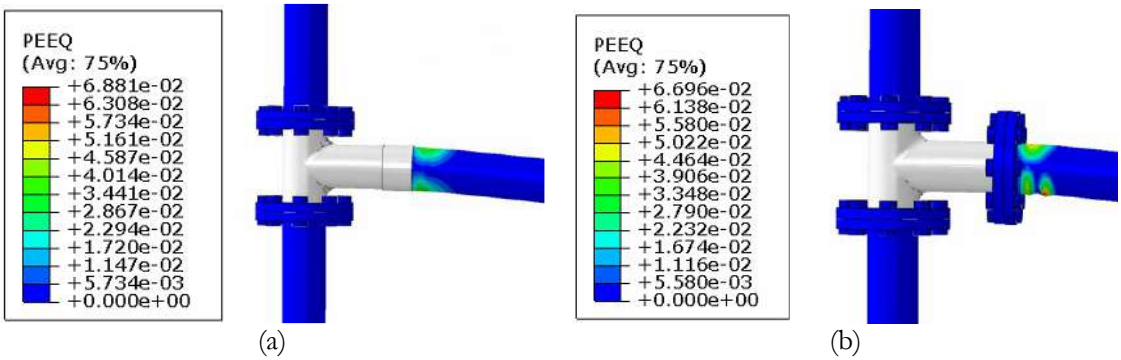


Figure 5. Comparison between the moment-rotation curve obtained for the two configurations investigated for the same tee joint material: a) Joint_EL; b) S235; c) S275; d) S355.



(a) (b)

Figure 6. Equivalent plastic deformation (PEEQ) distribution at high rotation level (i.e. 10%): a) Conf. 1_Joint_EL; b) Conf. 2_Joint_EL.

In the context of performance-based design for hospital and healthcare facilities, it is essential that non-structural elements, such as piping systems, exhibit negligible plastic deformations and that post-seismic operations are not hindered. Therefore, in this study, it is noteworthy that for both investigated configurations, the initial plasticization of the system occurs for a rotation of approximately 2%.
As depicted in Figure 7, for this particular rotation level, at this rotation level, plastic deformations are primarily localised in the tee joint.

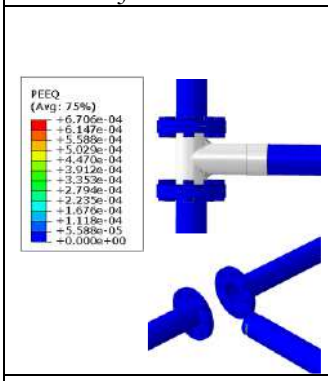
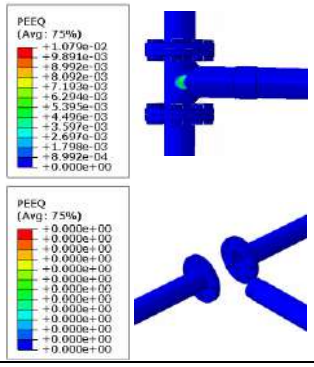
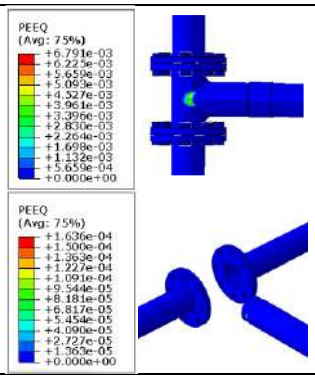
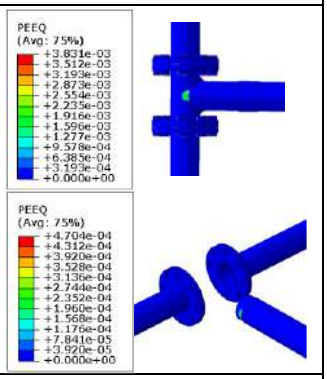
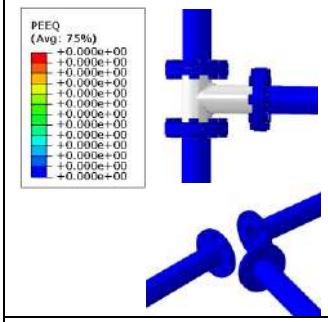
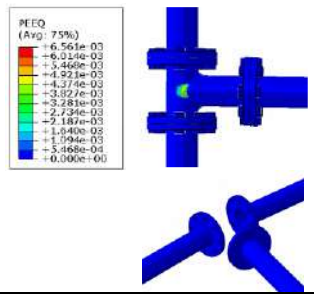
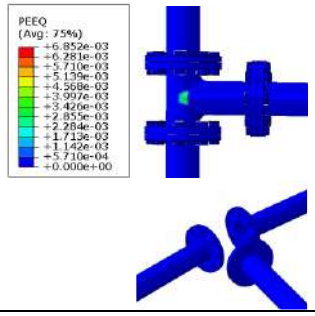
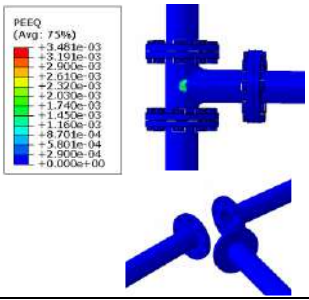
Configuration 1			
Joint-EL	S235	S275	S355
			
(a)	(b)	(c)	(d)
Configuration 2			
Joint-EL	S235	S275	S355
			
(e)	(f)	(g)	(h)

Figure 7. Equivalent plastic deformation (PEEQ) distribution for 2% rotation level

The type of connection between the pipe and the joint has a negligible effect on the PEEQ value when the same joint material was considered. However, it can be observed that in the configuration 1, plasticization also occurs in the threaded part of the connected pipe, where a higher PEEQ value was registered as the resistance of the tee joint increases.
Instead, for the configuration 2 no plastic deformations were observed on the pipes. In fact, as shown in Figure 7.a, Figure 7.e and Figure 5.a, for a rotation level equal to 2% some plastic deformations are showed by the numerical models of the Conf. 1_Joint_EL, with the PEEQ concentrated only in the threaded part of the connected pipe, while for the Conf 2_Joint_EL model exhibited no plastic deformations at rotation levels below 5%, at which point the pipe system's ultimate capacity was achieved.

5.Conclusions

The present study investigates the influence of the resistance of the tee joint on the global behaviour of a fire suppression system. To this end, numerical models developed in Abaqus were utilised. The following conclusions can be drawn from the results obtained:

- The capacity of the system is, in all instances, limited by the capacity of the tee joint. Indeed, an increase of the capacity of this element results in an increase in the capacity of the entire system.
- In all the cases under investigation, the pipe system demonstrated evidence of plastic deformation for a rotational level of approximately 2%, with the concentration of plastic deformations occurring at the centre point of the tee joint.
- The connection between the joint and the pipes has been shown to exert a negligible influence on the behaviour of the system when the capacity of the tee joint is lower than the plastic moment of the connected pipe. Indeed, the findings of the models with an elastic joint suggest that the utilisation of a flanged connection eliminates the necessity for threaded parts on the pipes, thereby preventing any significant plastic deformation until the system's bearing capacity is reached.
- The type of the connection between pipe and joint is of significant importance when considering large rotations, particularly when an over-strength tee joint has been adopted. Indeed, it was determined that configuration 1, which incorporates a threaded collar, exhibits superior ductility in comparison to configuration 2, which has flanged connection. As demonstrated by the numerical analyses conducted, the flanged connection exhibits elevated strength and stiffness. This results in a greater PEEQ concentration within the connected pipe at high rotation rates, leading to increased damage and strength degradation.

The results presented in this study are directly related to a specific fire suppression piping system described in the paper; however, they can be extended to a general piping system or similar non-structural networks, when similar bolted steel connections are adopted.

Acknowledgement

This study has been developed in the framework of the PRIN ENRICH- “ENhancing the Resilience of Italian healthCare and Hospital facilities”. A part of the work has been developed in the framework of the 2024–2026 ReLUIS-DPC research program funded by the Italian Civil Protection Department, as a contribution of the UniSannio research units to WP 17 “Elementi non strutturali”.

REFERENCES

Blasi, G., Perrone, D., Aiello, M.A. [2023] "Parametric investigation on the response of suspended piping systems to tri-directional seismic excitation," Engineering Structures, Vol. 293:116713. https://doi.org/10.1016/j.engstruct.2023.116713.

Bonati, A., Caterino, N., Cimmino, M., Coppola, O., De Angelis, A., Maddaloni, G., et al. [2025] "Assessment of Seismic Capacity of Building Envelope Nonstructural Components," *Journal of Earthquake Engineering*, pp.1–36. https://doi.org/10.1080/13632469.2025.2470328.

Coppola, O., Nironi, L., De Luca, A., Franco, A., Bonati, A. [2024] "Internal partition kits: toward a harmonized approach for the assessment of the seismic capacity by experimental tests," *Proceedings of the 18th World Conference on Earthquake Engineering*, Milano, Italy.

D'Angela, D., Magliulo, G., Di Salvatore, C., Zito, M. [2024] "Seismic assessment and qualification of acceleration-sensitive nonstructural elements through shake table testing: reliability of testing protocols and reliability-targeted safety factors," *Engineering Structures,* 117271. https://doi.org/10.1016/j.engstruct.2023.117271.

D'Aniello, M., Cassiano, D., Landolfo, R. [2016] "Monotonic and cyclic inelastic tensile response of European preloadable GR10.9 bolt assemblies," *Journal of Constructional Steel Research*, Vol. 124, pp. 77–90.

D'Aniello, M., Cassiano, D., Landolfo, R. [2017] "Simplified criteria for finite element modelling of European preloadable bolts," *Steel Compos Struct, Int J*; Vol. 24, No. 6, pp. 643–58.

De Angelis, A., Rillo, V., Pengue, S., Maddaloni, G. [2025a] "Dynamic identification of masonry partition walls by ambient vibration data," *Proceedings of the 10th ECCOMAS Thematic Conference on Computational Methods in Structural Dynamics and Earthquake Engineering*, Rhodes Island, Greece.

De Angelis, A., Tartaglia, R., Rillo, V., Maddaloni, G. [2025b] "In-situ experimental tests of piping systems in hospitals and health facilities," *Proceedings of the 10th ECCOMAS Thematic Conference on Computational Methods in Structural Dynamics and Earthquake Engineering*, Rhodes Island, Greece.

Deierlein, G.G., Krawinkler, H., Cornell, C.A. [2003] "A framework for performance-based earthquake engineering," *Proceedings of Pacific Conference on Earthquake Engineering,* Christchurch, New Zealand.

Del Vecchio C., Di Ludovico M., Prota A. [2020] "Repair costs of reinforced concrete building components: From actual data analysis to calibrated consequence functions". Earthquake Spectra, Vol. 36 (1), pp. 353–377

Dutta, A., Dhar, S., Acharyya, S.K. [2010] "Material characterization of SS 316 in low cycle fatigue loading," *Journal of Materials Science*, Vol. 45, pp. 1782–9.

Magliulo, G., D'Angela, D. [2024] "Seismic response and capacity of inelastic acceleration-sensitive nonstructural elements subjected to building floor motions" *Earthquake Engineering & Structural Dynamics* eqe.4080. https://doi.org/10.1002/eqe.4080.

Miranda, E., Mosqueda, G., Retamales, R., Pekcan, G. [2012] "Performance of nonstructural components during the 27 February 2010 Chile earthquake," *Earthquake Spectra*, Vol 28, pp. 453-471. https://doi.org/10.1193/1.4000032.

O'Reilly, G.J., Perrone, D., Fox, M., Monteiro, R., Filiatrault, A. [2018] "Seismic assessment and loss estimation of existing school buildings in Italy," *Engineering Structures,* Vol 168, pp. 142–62. https://doi.org/10.1016/j.engstruct.2018.04.056.

OSHPD. [1995] "The Northridge earthquake: a report to the hospital building safety board on the performance of hospitals," *Official of Statewide Health Planning and Development, Facilities Development Division*, Sacramento, CA, U.S.

Perrone, D., Filiatrault, A., Peloso, S., Brunesi, E., Beiter, C., Piccinin, R. [2020a] "Experimental seismic response evaluation of suspended piping restraint installations," *Bulletin of Earthquake Engineering*; Vol. 18, pp. 1499–524. https://doi.org/10.1007/s10518-019-00755-5.

Perrone, D., Brunesi, E., Filiatrault, A., Peloso, S., Nascimbene, R., Beiter, C., et al.[2020b] "Seismic numerical modelling of suspended piping trapeze restraint installations based on component testing," *Bulletin of Earthquake Engineering*; Vol. 18, pp. 3247–83. https://doi.org/10.1007/ s10518-020-00832-0.

Perrone, D., Rodriguez, D., Filiatrault, A., Brunesi, E., Beiter, C., Piccinin, R. [2022] "A framework for the quantification of non-structural seismic performance factors," *Journal of Earthquake Engineering*, Vol. 26, pp. 8468–94. https://doi.org/10.1080/13632469.2021.1991516.

Rodriguez, D., Perrone, D., Filiatrault, A. [2025] "Influence of gravity load trapezes in the seismic performance of suspended piping systems," *Engineering Structures*, Vol. 333, 120188. https://doi.org/10.1016/j.engstruct.2025.120188.

Sousa, L., Monteiro, R. [2018] "Seismic retrofit options for non-structural building partition walls: impact on loss estimation and cost-benefit analysis," *Engineering Structures,* Vol 161, pp. 8–27. https://doi.org/10.1016/j.engstruct.2018.01.028.

Tatarsky, M., Filiatrault, A. [2018] "Seismic response of viscously damped thin-wall piping system: a proof-of-concept case study," *Bulletin of Earthquake Engineering. https://doi.org/10.1007/s10518-018-0447-0.*

Tian, Y., Filiatrault, A., Mosqueda, G. [2014] 2Experimental seismic fragility of pressurized fire suppression sprinkler piping joints," *Earthquake Spectra*, Vol. 30, pp.1733–48. https://doi. org/10.1193/111011EQS278M.

Tian, Y., Filiatrault, A., Mosqueda, G. [2015] "Seismic response of pressurized fire sprinkler piping systems II: numerical study," *Journal of Earthquake Engineering*; Vol. 19, pp. 674–99. https://doi.org/ 10.1080/13632469.2014.994148.

Wood, R., Hutchinson, T., Hoehler, M., Kreidl, B. [2013] "Numerical Model Development and Experimental Validation of Trapeze Assemblies Utilizing Modular Channel Systems," *Individual Study*. San Diego La Jolla: Department of Structural Engineering, University of California; 2013.

Zidarich, S., Sestito, M., Crescimbene, M., Musacchio, G., Reitano, D., Perrone, D., et al. [2023] "Seismic risk perception in Italian hospitals: the role of non-structural elements" *Proceedings of the 42° National Conference GNGTS*, Ferrara, Italy.

Zidarich, S., Sestito, M., Crescimbene, M., Musacchio, G., Reitano, D., Perrone, D., et al. [2025] "Seismic risk perception of non-structural elements in Italian hospitals: pilot studies," *Bollettino di Geofisica Teorica ed Applicata (BGO).* https://doi.org/10.4430/bgo00481.

Zito, M., D'Angela, D., Maddaloni, G., Magliulo, G. [2022] "A shake table protocol for seismic assessment and qualification of acceleration-sensitive nonstructural elements," *Computer Aided Civil Engineering.* https://doi.org/10.1111/mice.12951.

Probabilistic seismic demand assessment of rising pipe lines in fire-protection systems

Gianni Blasi[1], Daniele Perrone[1], Marianovella Leone[1], Maria Antonietta Aiello[1]

[1]Department of Engineering for Innovation, University of Salento, Italy.

e-mail {gianni.blasi, daniele.perrone, marianovella.leone, antonietta.aiello}@unisalento.it

Abstract. The seismic demand of piping systems is often of difficult evaluation, due to several uncertainties in the definition of their dynamic response. Additionally, the high variability of the geometrical and mechanical properties of structural systems evidences the need of conducting parametric analyses to comprehensively address the seismic demand scenarios on such non-structural components. This work presents a probabilistic assessment of the seismic demand on a rising main line in a fire-protection piping system running along the height of a multi-storey building. The presence of firestops at the crossing point of the main line at each floor was considered to define the seismic loads transferred from the structure to the piping system. The properties of the building were defined based on a real case study hospital facility, assuming both regular and irregular configuration in elevation to assess its influence on the non-structural seismic demand. The seismic response of the piping system is evaluated defining the operational loss performance level based on mechanical damage on pipe joints. Furthermore, performance evolution over time were analysed, assuming mechanical degradation of the piping system due to material aging.

Keywords: Non-structural components, piping systems, firestops, rising pipe line, non-linear modelling.

1 INTRODUCTION

Despite the seismic vulnerability assessment of non-structural components (NSCs) has been increasingly addressed in modern seismic design codes (FEMA 412 2002; FEMA E-74 2012; NTC-2018 2018), significant improvements are still required due to the great uncertainty on the parameters ruling non-structural seismic behaviour. Recent methods proposed for the evaluation of the seismic demand on NSCs evidenced the need of accounting for several parameters of difficult computation (Merino et al. 2020; Vukobratović and Fajfar 2024). Hence, major hardships arise in the definition of simplified design/assessment approaches for NSCs, particularly in case of elements characterized by complex configuration.

Additionally, specific performance requirements should be defined for critical NSCs from either (or both) a life safety or economical standpoint (Miranda et al. 2012; Perrone et al. 2018). To this regard, fire-protection systems (FP) in strategic facilities (e.g. Hospitals) are an emblematic example. A specific evaluation of the seismic demand for FP is required, as their operation is fundamental in case of emergency. Past studies conducted from the authors of this manuscript (Blasi et al. 2023) evidenced the need of analysing the response of FP referred to a structural seismic demand beyond the traditional operational limit performance level (EN 1998-1 2004). This approach allows assessing the damage on such systems even in case of post-elastic behaviour of the structure, which causes large displacement demands on the piping system. Additionally, accurate modelling of the non-linear response of both pipe joints and connections to the structure is required, to account for all the main failure modes.

Extensive physical testing and numerical modelling of critical components in piping network from a seismic vulnerability perspective (Tian et al. 2015; Blasi et al. 2018; Perrone et al. 2020) allowed the definition of accurate non-linear models for global seismic analyses. Most of the previous studies analysed horizontal suspended piping networks, aiming to evaluate seismic fragility based on pipe joints and pipe restraints damage (Blasi et al. 2021; Merino et al. 2022). Such systems are classified as acceleration-sensitive components, as they are generally affected by dynamic interaction with the structure rather than the imposed displacements.

On the other hand, vertical rising lines crossing the floors of the building are displacement-sensitive NSCs which require further investigation, as different performance parameters should be considered compared to suspended piping networks. This study aims to address such issue, focusing on a rising main line of a FP piping system. The system is assumed to be installed in an archetype hospital building, defined based on a real case study. The presence of firestops at the floor-crossing point of the rising pipe is considered, as such elements have major influence on the displacement and acceleration demand transferred from the structure.

The seismic response assessment of the piping systems was conducted by mean of Non-Linear Time-History (NLTH) analysis. The numerical model of the structural system and of the pipe line were modelled together. Each floor of the structural system was rigidly connected to the vertical line at the floor crossing point. A surrogate elastic model of the building was used to reduce computational time, as the comprehensive seismic response characterization of the structural system is outside the scope of this paper. The operational-loss limit state of the pipe line was defined considering pipe joints leakage related to mechanical damage. A simplified evaluation of the effect of the ageing of the piping system on its seismic performance was also conducted. Particularly, degradation of the flexural response of pipe joints over time was assumed due to steel corrosion.

2 DESCRIPTION OF THE METHODS

The FP rising line analysed in this study is composed of steel pipes with diameter equal to 114.30 mm (4"), crossing all the floors of a 7-storey hospital building. A threaded carbon steel tee-joint connection between the rising line and a suspended horizontal branching line is assumed at the top of each floor of the building. The branching lines were characterized by 60.3 mm (2") steel pipes, which were directly connected to the slab of the building, through gravity and seismic piping restraint installations, characterized by simple cables and trapezes with longitudinal and transverse braces, respectively. Firestops are installed at each floor-crossing point, for fire compartmentation purpose.

The properties of the building were defined based on a real case study located in Lecce (Italy). The structural system is characterized by reinforced concrete (RC) moment resisting frames (MRF), designed only for gravity loads. This configuration is representative of most of Italian building constructed between 1970 and 2000. The building features seven floors and an irregular distribution of the mass and the stiffness along the height, related to floor setbacks. However, due to the need of obtaining more generalized results, the case study building was only considered as a benchmark to define an archetype structural system. Particularly, the inter-storey height, the floor surface, the dead and live loads, and the columns' cross section of the real case study were considered in the archetype definition. Such properties are listed in Table 1.

Table 1. Geometry and gravity loads assumed for the archetype building.

DESCRIPTION	SYMBOL	VALUE
Inter-storey height [m]	h	3.40
Floor Dead loads [kN/m²]	G_k	4.50
Floor Live loads [kN/m²]	Q_k	5.00
Floor surface [m²]	A_{floor}	750.00
Column's cross section [mm²]	A_{col}	400x400

The archetype building was assumed to be realized in a high seismic hazard zone in Italy (L'Aquila). Aiming to consider the case of seismic detailing of the RC frames, an overstrength ratio, Ω_{col}, equal to 1.69 was assumed for the columns, consistently with the capacity design provisions of Italian seismic code (NTC-2018 2018). Such value of Ω_{col} allowed assuming a pre-yielding response of the structure also for a seismic demand corresponding to LS performance level. Hence, a linear elastic model with cracked stiffness could reasonably simulate the structural behaviour at this stage. The reinforcement details of beams and columns are not discussed herein, as they are outside the scope of this paper.

2.1 Modelling approach

The numerical models of the piping system and the building (Figure 1) were developed in STKO (Petracca and Camata 2022). Herein, the horizontal lines of the FP system are not explicitly modelled and are only considered in terms of tributary mass, which was lumped at each pipe joint. Linear elastic beam elements were used to simulate the vertical pipes, while the non-linear response of tee-joint connections was simulated using zero length flexural springs characterized by Pinching4 uniaxial material (Lowes et al. 2003). The M-θ hysteretic behaviour of 4" and 2" pipe joints (i.e. for pipe connection along the rising line and to the branching lines, respectively) is depicted in Figure 2**a** and **b**, respectively (please note that different scales are used for the Y-axis for a better visualization).

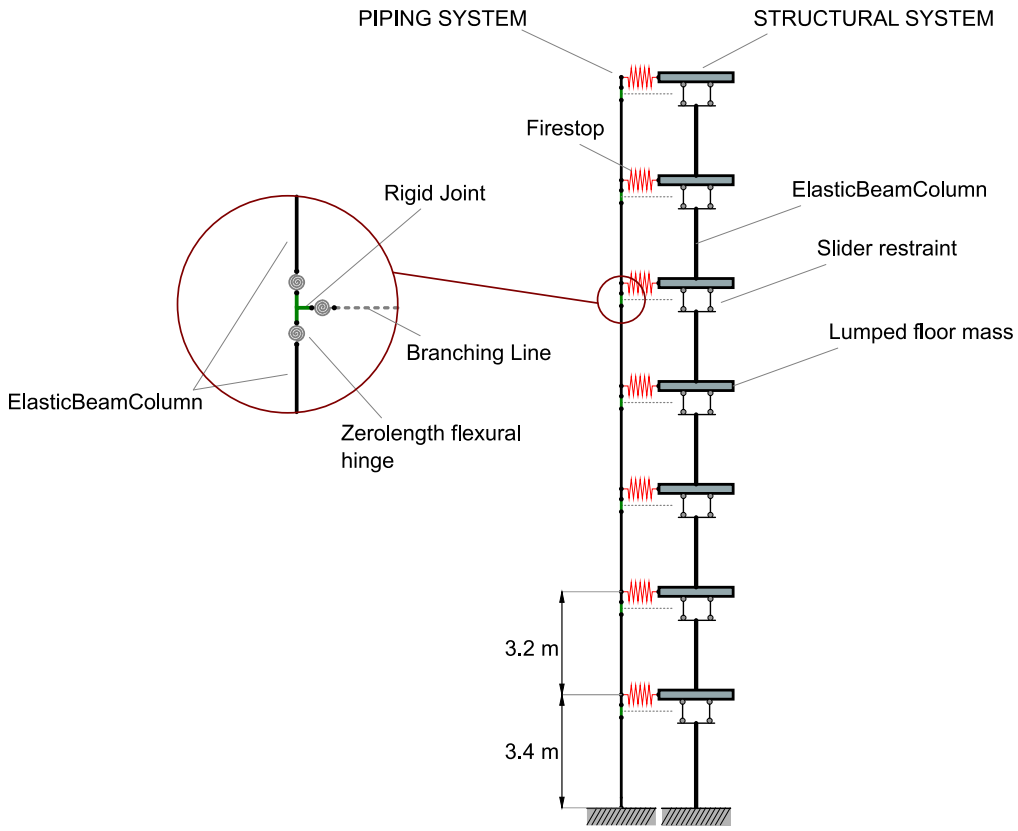
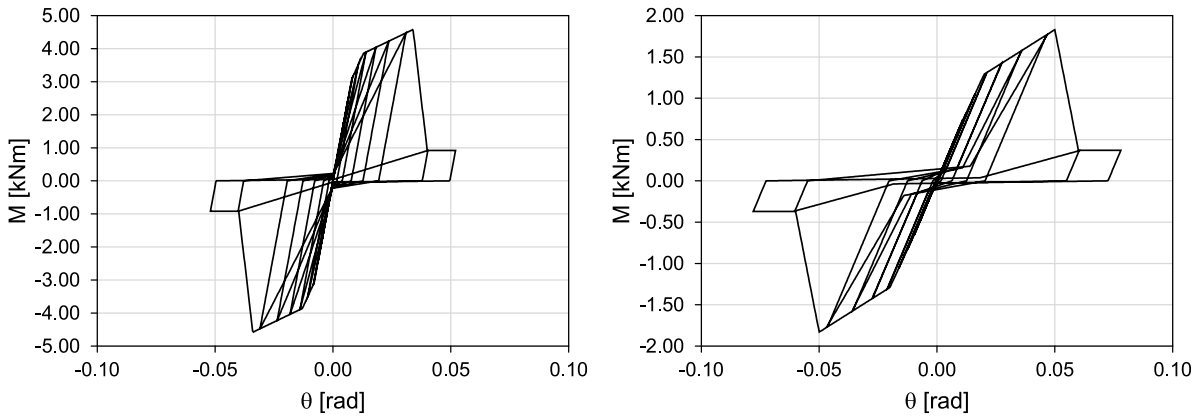


Figure 1. Numerical model developed

The hysteretic parameters were calibrated based on previous laboratory tests and micro-models (Blasi et al. 2018, 2021). Because of the presence of firestops, a semi-rigid connection between the rising line and the floor of the building was assumed at each crossing point. Future studies will investigate the effects of the stiffness of the firestop on the interaction between the FP system and the structure.



(a) **(b)**

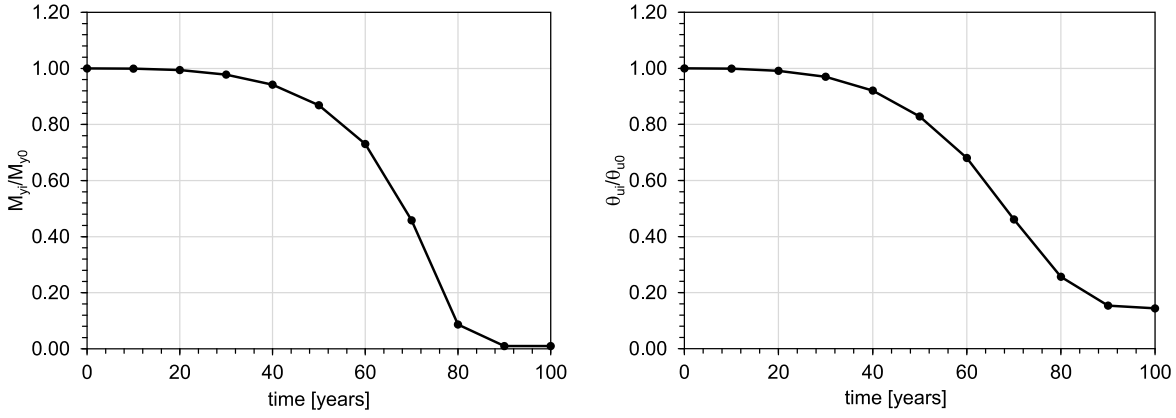
Figure 2. Hysteretic M-θ behaviour in numerical model for (a) 4" and (b) 2" pipe joints.

A surrogate elastic model was developed to simulate the structural system of the hospital building, to significantly reduce the computational time, allowing for a parametric investigation. The surrogate model consists of seven equivalent beam elements connected in series, where each element represents the total lateral and axial response of all the columns at a given floor. The floor mass is lumped at the top node of the corresponding beam element. Hence, as floor masses were aligned with the longitudinal axis of the equivalent beam elements, no eccentricity between the centre of mass and the centre of stiffness was obtained at each floor using such surrogate model. Consequently, in-plan irregularity was not addressed in this study. On the other hand, both regular and irregular configurations in-elevation were considered. In the regular configuration, a constant lateral stiffness of the equivalent elements along the height was set. In the irregular configuration, the lateral stiffness was kept constant up to the third floor, and was progressively reduced by 40% at each floor from the fourth to the seventh floor.

2.2 Mechanical performance decay over service life

Aiming to account for the effect of material degradation on the non-structural seismic vulnerability, the analyses of the FP were conducted every ten years over a 100-years service life of the building. The effect of ageing was considered by modifying the non-linear flexural response of the threaded tee-joints. Particularly, the elastic limit strength, the maximum strength and the ultimate rotation were progressively reduced according to existing degradation models for steel elements.

It is worth mentioning the lack of literature studies specifically addressing degradation of steel pipe joints. Hence, consolidated formulations usually adopted for steel rebars corrosion were used herein (Imperatore et al. 2017). A further analysis of such phenomenon will be conducted in the following, based on micro modelling of the tee-joints. The degradation models for elastic limit bending moment and ultimate rotation are depicted in Figure 3.



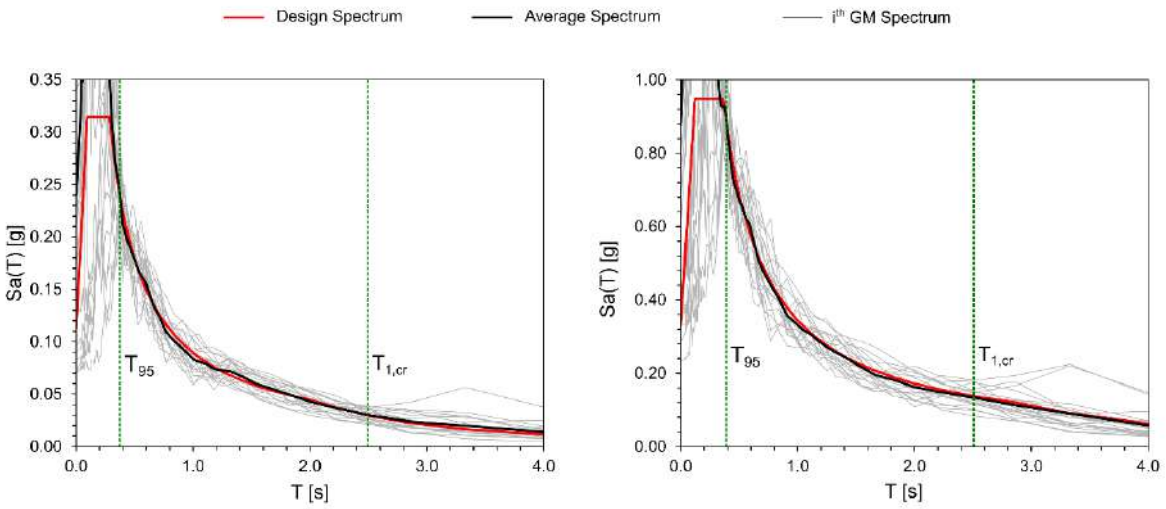
(a) **(b)**

Figure 3. Evolution of (a) elastic limit flexural strength and (b) ultimate rotation of pipe joints over time due to steel corrosion.

3 NON-LINEAR TIME HISTORY ANALYSIS

The NLTH analysis was performed by subjecting the system (FP line + surrogate structural model) to ground motion excitation along the two horizontal directions. Three sets composed of 20 spectrum-compatible ground motions were selected from the European strong-motion database (Ambraseys et al.

2002). Each ground motion set was defined considering a specific return period (Tr), namely 60, 101, and 949 years, corresponding to the operational limit (OL), the damage limitation (DL), and the life safety (LS) performance level, respectively. The least squared error estimation method was used to calibrate scaling factors for the records in each set, to match the design spectrum within the range [T_{95}:$T_{1,cr}$]. The lower boundary of such range (T_{95}) is the period of the mode associated with a 95% cumulative participating mass ratio of the building, while the upper boundary ($T_{1,cr}$) is the fundamental period referred to cracked stiffness of the building. The design spectrum was defined considering a soil type A and a nominal life of the building equal to 100 years. The 5% damped elastic spectra of the selected ground motions at OL and LS performance level, along with the design spectra, are provided in **Figure 4**. It is worth noting that the analysis at LS performance level is useful for the damage assessment of the piping system in case of post-elastic response of the structure.



(a) **(b)**

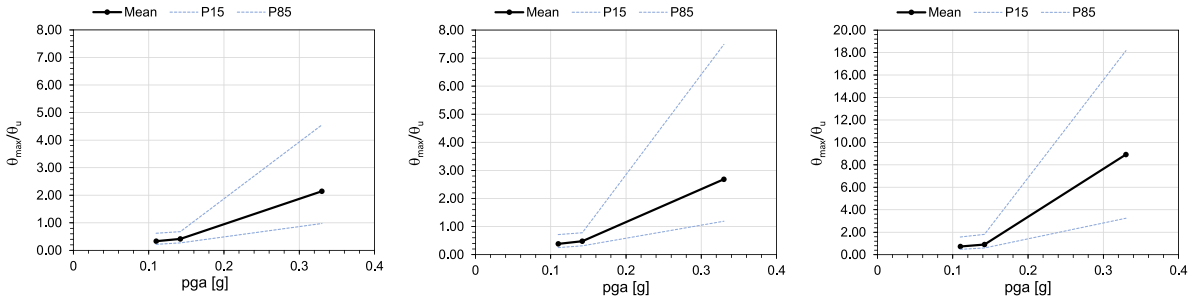
Figure 4. Horizontal response spectra of the selected ground motions at (a) OL and (b) LS performance level.

4 RESULTS AND DISCUSSION

The seismic performance parameter considered herein for the FP system is represented by the maximum damage of pipe joints. Such parameter was computed as the ratio between the maximum rotation recorded in the NLTH analysis and the ultimate rotation of the joint (θ_{max}/θ_u). The highest value of θ_{max}/θ_u among all the pipe joints was evaluated for each analysis, and its mean and the P15-P85 (15^{th}-85^{th} percentile) range of variation over the 20 ground motions was analysed. The results obtained for the regular configuration of the structure as function of the peak ground acceleration (pga) are depicted in Figure 5, considering the variation of the response over the 100-year service life of the building. A different scale of the Y-axis is considered for Figure 5-c for a clearer visualization.

The three dots of the mean curve are referred to the ground motions sets selected for OL, DL and LS, respectively. At construction stage (i.e. for an age of the facility t = 0 years), failure of tee joints (i.e. θ_{max}/θ_u >1) was obtained only at LS performance level, as expected for displacement-sensitive NSCs in seismically designed buildings. However, a significant increase of the maximum damage is detected as t increases, due to corrosion-induced mechanical degradation of the pipe joints. The results provided in Figure 5-b are referred to t = 50 years, at which the onset of flexural performance decay was obtained. In Figure 5-c the

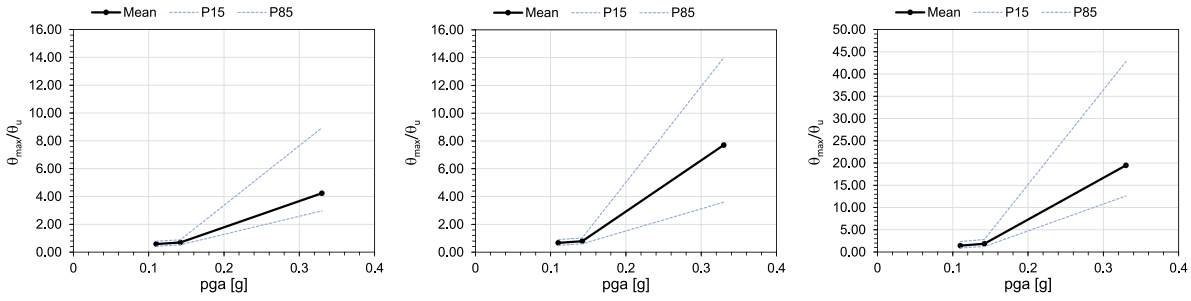
results obtained at 70 years-age are provided, after which a major reduction of the flexural performance was observed, leading to joint failure even in case of OL and DL.



(a) **(b)** **(c)**

Figure 5. Mean value and P15-P85 variation range of θ_{max}/θ_u as function of the pga at (a) time 0, (b) time = 50 years and (c) time = 70 years in case of regular building

The results obtained for the irregular configuration of the building are provided in Figure 6. Higher damage was observed in this case compared to the regular configuration (please note that Figure 5 and Figure 6 feature different Y-axis scales) mainly because of the greater displacements of upper floors and the uneven distribution of the seismic loads along the height. Additionally, failure of the pipe joints in case of OL and DL performance level was obtained at earlier age of the facility, as θ_{max}/θ_u is higher than 1.0 at t = 70 years. The results show a greater record-to-record variability at LS performance level, because of the non-linear response of the pipe joints obtained for greater seismic excitation.



(a) **(b)** **(c)**

Figure 6. Mean value and P15-P85 variation range of θ_{max}/θ_u as function of the pga at (a) time 0, (b) time = 50 years and (c) time = 70 years in case of irregular building

The variation of the pipe joints damage along the height of the building is showed in Figure 7 and Figure 8, referring to t = 0 and 70 years, respectively. At t = 0, the damage to pipe joints in case of regular building (Figure 7-a) is greater at lowest floors, characterized by higher inter-storey drift. A different fashion is observed for irregular building. In fact, θ_{max}/θ_u is inversely proportional to the floor level up to floor 3, while a progressive increase is detected from floor 4 to floor 7, accordingly with the reduction of the lateral stiffness of the columns. A similar trend is obtained for t = 70 years, as shown in Figure 8, although greater pipe joint damage is observed at this stage.

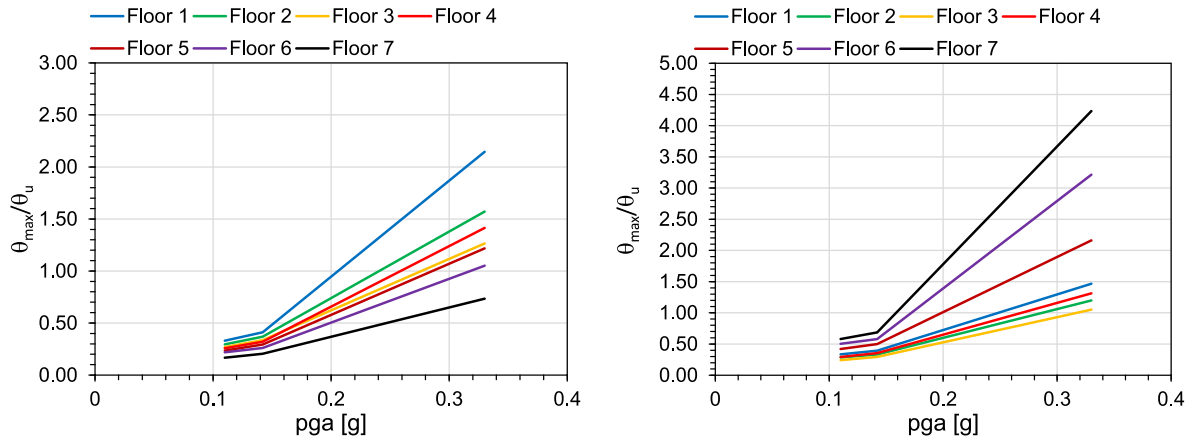


Figure 7. Mean value of θ_{max}/θ_u at different floor levels as function of the pga in case of (a) regular building and (b) irregular building at time 0.

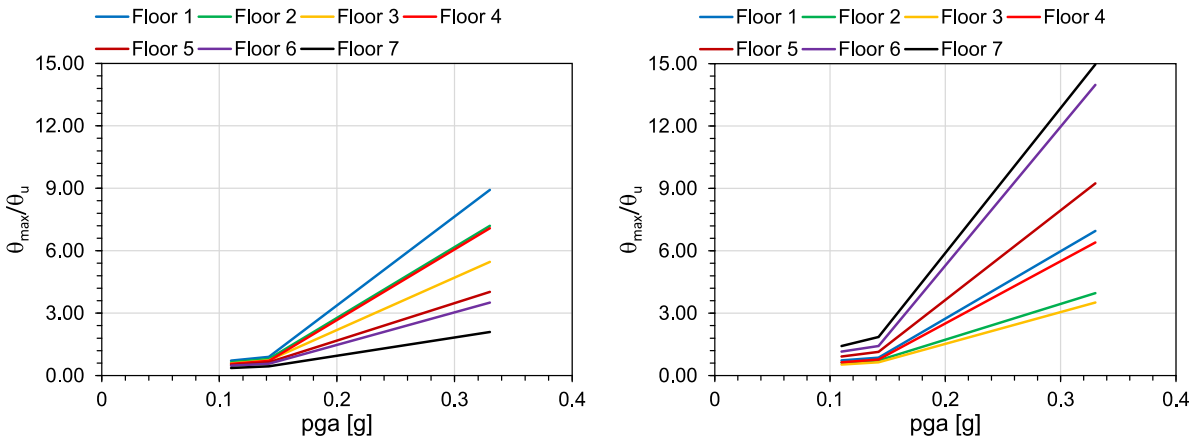


Figure 8. Mean value of θ_{max}/θ_u at different floor levels as function of the pga in case of (a) regular building and (b) irregular building at time = 70 years.

5 CONCLUSIONS

The analysis performed in this study was aimed at evaluating different aspects related to the seismic vulnerability of vertical rising lines of fire-protection piping systems in hospital buildings. The effect of rigid connections between the pipe line and the building, due to the need of firestop installation, was investigated. Aging of the pipe joints material was also considered, to evaluate the variation of the non-linear flexural response of the pipe line over the service life. Additionally, the case of regular and irregular configuration of the building was addressed.

The seismic response of the piping system was evaluated considering different return periods of the seismic demand, to assess the performance levels in case of both near-elastic and post-elastic behaviour of the building. Such aspect is fundamental when dealing with fire-protection system, whose functionality should be guaranteed also for a seismic demand beyond the damage-limitation performance level.

The results obtained showed a major influence of the building regularity on the seismic damage to the fire-protection system, as well as the need of accounting for mechanical performance degradation due to material aging. Failure of the piping system at the tee-joint connections was obtained in almost all considered cases when assuming a seismic demand corresponding to the life-safety performance level.

As two configurations of the building (regular and irregular) and a single configuration of the rising pipe line were considered, the outcome of this study is only representative of a limited scenario. Moreover, the effect of seismic hazard was not investigated, as a single site condition was assumed. Additional aspects which require a further investigation were neglected in this study, as the accurate modelling of the post-elastic response of the building, its in-plan irregularity and the stiffness of the firestop. Future studies will address such aspects with more complex modelling approaches, also including the interaction between the vertical pipe line and the horizontal branching line.

ACKNOWLEDGEMENTS

The authors gratefully acknowledge the support of the PNRR project "Multi-Risk sciEnce for resilienT commUnities undeR a changiNg climate (RETURN)" - CUP H93C22000610002 (Cascade call – ERCULES project)

REFERENCES

Ambraseys NN, Smit P, Douglas J, et al (2002) Internet site for European strong-motion data. In: Eur. Comm. Res. Gen. Environ. Clim. Program. http://www.isesd.hi.is/ESD_Local/frameset.htm

Blasi G, Aiello MA, Maddaloni G, Pecce MR (2018) Seismic response evaluation of medical gas and fire-protection pipelines' Tee-Joints. Eng Struct 173:1039–1053. https://doi.org/https://doi.org/10.1016/j.engstruct.2018.07.045

Blasi G, Perrone D, Aiello MA (2023) Parametric investigation on the response of suspended piping systems to tri-directional seismic excitation. Eng Struct 293:116713. https://doi.org/10.1016/j.engstruct.2023.116713

Blasi G, Perrone D, Aiello MA, Pecce MR (2021) Seismic performance assessment of piping systems in bare and infilled RC buildings. Soil Dyn Earthq Eng 149:. https://doi.org/10.1016/j.soildyn.2021.106897

EN 1998-1 (2004) Eurocode 8 - Design of structures for earthquake resistance - Part 1: General rules, seismic actions and rules for buildings. European Standard

FEMA 412 (2002) Seismic restraints for mechanical equipment. Federal Emergency Menagement Agency

FEMA E-74 (2012) Reducing the risks of nonstructural earthquake damage – A practical guide

Imperatore S, Rinaldi Z, Drago C (2017) Degradation relationships for the mechanical properties of corroded steel rebars. Constr Build Mater 148:219–230. https://doi.org/10.1016/j.conbuildmat.2017.04.209

Lowes LN, Mitra N, Altoontash A (2003) A Beam-Column Joint Model for Simulating the Earthquake Response of Reinforced Concrete Frames. University of California, Berkeley

Merino RJ, Perrone D, Filiatrault A (2020) Consistent floor response spectra for performance-based seismic design of nonstructural elements. Earthq Eng Struct Dyn 49:261–284. https://doi.org/10.1002/eqe.3236

Merino RJ, Perrone D, Filiatrault A (2022) Appraisal of seismic design methodologies for suspended non-structural elements in Europe. Springer Netherlands

Miranda E, Mosqueda G, Retamales R, Pekcan G (2012) Performance of Nonstructural Components during the 27 February 2010 Chile Earthquake. Earthq Spectra 28:453–471. https://doi.org/10.1193/1.4000032

NTC-2018 (2018) Aggiornamento delle «Norme tecniche per le costruzioni». D.M. 17/01/2018, Italy

Perrone D, Brunesi E, Filiatrault A, et al (2020) Seismic numerical modelling of suspended piping trapeze restraint installations based on component testing. Springer Netherlands

Perrone D, Calvi PM, Nascimbene R, et al (2018) Seismic performance of non-structural elements during the 2016 Central Italy earthquake. Bull Earthq Eng 1–23. https://doi.org/10.1007/s10518-018-0361-5

Petracca M, Camata G (2022) STKO Scientific ToolKit for OpenSees. In: https://asdea.eu/software/about-stko/. https://asdea.eu/software/about-stko/

Tian Y, Filiatrault A, Mosqueda G (2015) Seismic response of pressurized fire sprinkler piping systems I: Experimental study. J Earthq Eng 19:649–673. https://doi.org/10.1080/13632469.2014.994147

Vukobratović V, Fajfar P (2024) Direct floor response spectra for nonlinear nonstructural components. Bull Earthq Eng 22:1033–1053. https://doi.org/10.1007/s10518-023-01818-4

Experimental seismic response assessment of piping networks in industrial facilities: The Mitplant Project

Francesco Micelli[1], Daniele Perrone[1], Giammaria Gabbianelli[2], Chiara Miglietta[1], Bryan Chalarca[2], Emanuele Brunesi[3], Mariano Ciucci[4]

[1] University of Salento
Via per Monteroni, Lecce (Italy)
e-mail: {francesco.micelli,daniele.perrone,chiara.miglietta}@unisalento.it
[2] University of Pavia
Via Ferrata, Pavia (Italy)
e-mail: {giammaria.gabbianelli,bryan.chalarcaecheverri}@unipv.it
[3] Eucentre Foundation
Via Ferrata, Pavia (Italy)
e-mail: emanuele.brunesi@eucentre.it
[4] INAIL, Department of Technological Innovations
Via del Torraccio di Torrenova, Rome (Italy)
e-mail: m.ciucci@inail.it

Abstract. Natural events such as earthquakes and floods in past years caused major disasters in industrial areas, mainly because of indirect losses associated with industrial facilities' downtime. Seismic damage to non-structural mechanical systems in such facilities (e.g. piping systems for hazardous substances transportation) represents a threat to the local economy and, more importantly, to human health. Past disasters prompted public administrations to introduce specific directives (e.g., Seveso III), aimed at establishing risk assessment procedures, including seismic vulnerability analysis of critical mechanical components. In the framework of the MITPLANT Project funded by the Italian National Institute for Insurance against Accidents at Work, two experimental campaigns aimed at investigating the seismic response of piping networks installed in industrial facilities were carried out. The experimental campaigns consist of monotonic and cyclic quasi-static tests of pipe-to-tank connections, as well as shake table tests simulating the dynamic response of piping networks. The two experimental campaigns are described, and the main results are discussed to provide some insights into the more critical components. Then, the results of laboratory tests will be used to calibrate numerical models for future parametric analyses and to provide a useful tool for investigating the seismic vulnerability of different basic configurations of pipelines with different types of connections.

Keywords: Natech, piping systems, industrial plants, seismic vulnerability.

1. INTRODUCTION

Natural disasters, such as earthquakes and floods, have repeatedly caused significant disruptions and extensive damage in industrial areas worldwide. Following these events, a significant portion of the economic and social impact stems from indirect consequences, particularly the prolonged downtime and operational disruptions of industrial facilities. In seismic events, damage to non-structural mechanical systems, such as piping networks that transport hazardous substances, storage tanks, and processing equipment, has proven to be a critical issue. The failure of these components can lead to catastrophic outcomes, including chemical leaks, fires, explosions, and environmental contamination. These incidents not only affect the local economy but also pose serious threats to human health and safety.

Historical earthquakes provide several examples of the impact that seismic hazards can have on industrial facilities. For instance, the Kocaeli earthquake in 1999 [Girgin, 2011; Korkmaz *et al.*, 2011] caused significant damage to many industrial plants, particularly affecting non-structural elements such as piping systems, storage tanks, and process equipment. Similarly, the 2011 Great East Japan earthquake [Krausmann and Cruz, 2013] triggered damage in several industrial facilities processing hazardous substances along the affected coast, resulting in the release of toxic material with consequent fires and explosions. Closer to Europe, the May 2012 Emilia, Italy, earthquake [Brunesi *et al.*, 2011] caused damage to industrial sites in the area, consisting mainly of precast reinforced concrete structures and steel storage tanks. The industrial production interruption led to considerable economic losses.

In response to devastating events, better called "Na-tech" events [Campedel, 2008], regulatory bodies around the world have implemented stringent measures aimed at reducing seismic risks in industrial settings. For instance, the European Union's Seveso III Directive [2012], implemented in Italy with Legislative Decree No. 105 [2015], focuses on controlling major-hazard accidents associated with hazardous substances and specifically requires the assessment of seismic vulnerability for critical mechanical components [Marino and Quinci, 2019]. These regulations highlight the importance of extending beyond just structural integrity to consider non-structural elements essential for the safe operation of industrial plants. Despite progress in regulations, managing seismic risks in industrial facilities still presents significant challenges. The behaviour of piping networks and related equipment during seismic loading is influenced by several factors, including the properties of the materials, connection details, differences between the masses and stiffnesses of the various components, and interactions with surrounding and supporting structures [Gabbianelli *et al.*, 2024]. The most critical points of piping networks are typically located at discontinuities, such as flanged or welded joints between adjacent pipe segments or the interface connections between a pipe and the wall of a storage tank. Excessive relative displacements at these points may lead to joint failure or rupture at the pipe-to-tank connection (Figure 1), potentially resulting in the release of hazardous fluids and posing significant safety and environmental risks. In addition, structural failures in the supporting structures or anchorage systems could trigger cascading effects, compromising the integrity of the entire piping network. To accurately predict their response, it is essential to have experimental data and advanced numerical models that can capture non-linear behaviours and potential failure modes.



(a) (b)

Figure 1. Failure of a flanged joint from FEMA E-74 [2012] (a); failure of a pipe-to-tank connection from Jain et al. [2002] (b)

For these reasons, the MITPLANT Project, funded by the Italian National Institute for Insurance against Accidents at Work, has undertaken comprehensive experimental investigations focused on the seismic response of industrial piping systems. This paper presents the two main experimental campaigns: monotonic and cyclic quasi-static tests on pipe-to-tank connections, aimed at understanding the mechanical performance and failure mechanisms under different loading conditions, and shake table tests simulating dynamic seismic excitations on piping networks representative of those installed in industrial facilities. These campaigns will provide crucial data on the vulnerabilities of critical components of piping systems. Moreover, the experimental results will be used to calibrate sophisticated numerical models that simulate the seismic behaviour of basic piping layouts and of pipe-to-tank connections. By integrating experimental evidence with numerical analysis, this research aims to support the evolution of seismic risk management practices in industrial contexts, thereby protecting both economic assets and public health.

2. EXPERIMENTAL TESTS ON PIPE-TO-TANK CONNECTIONS

2.1 DESCRIPTION OF EXPERIMENTAL CAMPAIGN

Numerous research contributions have focused on the seismic performance of pipe-to-pipe and pipe-to-tank connections. Reza et al. [2014] and La Salandra et al [2016] studied the performance of non-standard bolted flange joints while pipe-to-tank connections were studied by Aiba et al. [2000] and Wieschollek et al. [2013]. The latter carried out six experimental tests on three representative configurations of shell–nozzle reinforcements.

In the framework of the MITPLANT Project a series of monotonic and cyclic quasi-static tests were performed at Seers Lab of the University of Salento on steel specimens simulating the connection between a storage tank and its outlet pipeline, which are considered critical components in industrial piping networks. In fact, if a break occurs near the tank wall, and safety valves are not installed, it could lead to the loss of hazardous substances stored within the tank. This leak has the potential to cause fires and explosions, posing significant threat to human safety, the environment, and plant operations. The purpose of the research was twofold: to describe the nonlinear cyclic response of the joint under the different loading conditions, and to determine the possible failure mechanisms governing its structural behaviour.

The design of the specimens adhered to the nozzle specifications outlined in the European Standard EN 14015 [2006]. Each specimen consisted of a P355N steel pipe (yield strength of 355 N/mm^2) welded into a perforated S235J0 steel plate (yield strength of 235 N/mm^2), which simulates the local tank shell area where the pipe connection is usually installed. Two types of loading conditions were investigated: axial and transverse directions. For each direction, one monotonic test and two cyclic tests were conducted. The geometric characteristics of specimens are reported in Figure 2. A DN100 commercial steel pipe, commonly utilised in storage facilities, was selected for this project. Its minimum wall thickness of 8.5 mm was chosen based on standard reference tables, taking into account the pipe's diameter and material properties. The dimensions of the plate were determined to ensure that any deformations occurring in the connection zone could be clearly identified and measured during testing. Additionally, the plate's thickness was established using standard design tables for carbon steel tanks with diameters of up to 15 meters. Specimen S1 in Figure 2a was tested under axial loading, while specimen S2 in Figure 2b was tested under transverse loading. The two specimens differ only in pipe length, because it was necessary to adapt each specimen to the universal testing machine, depending on the direction of the load. The test setups are represented in Figure 3.

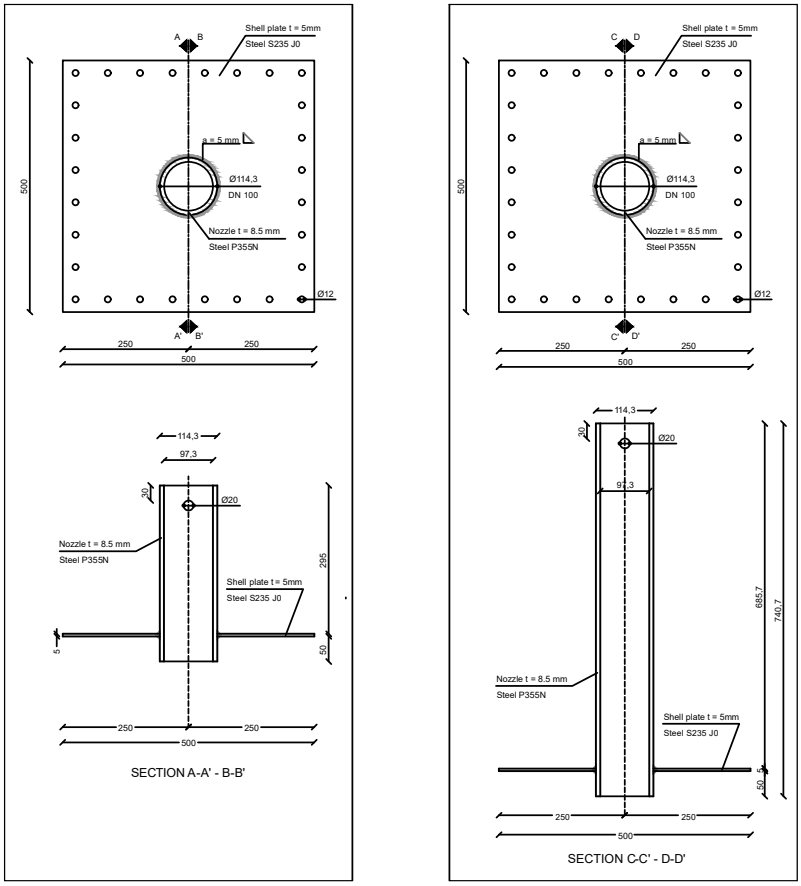


Figure 2. Geometric characteristics of S1 (a) and S2 (b)

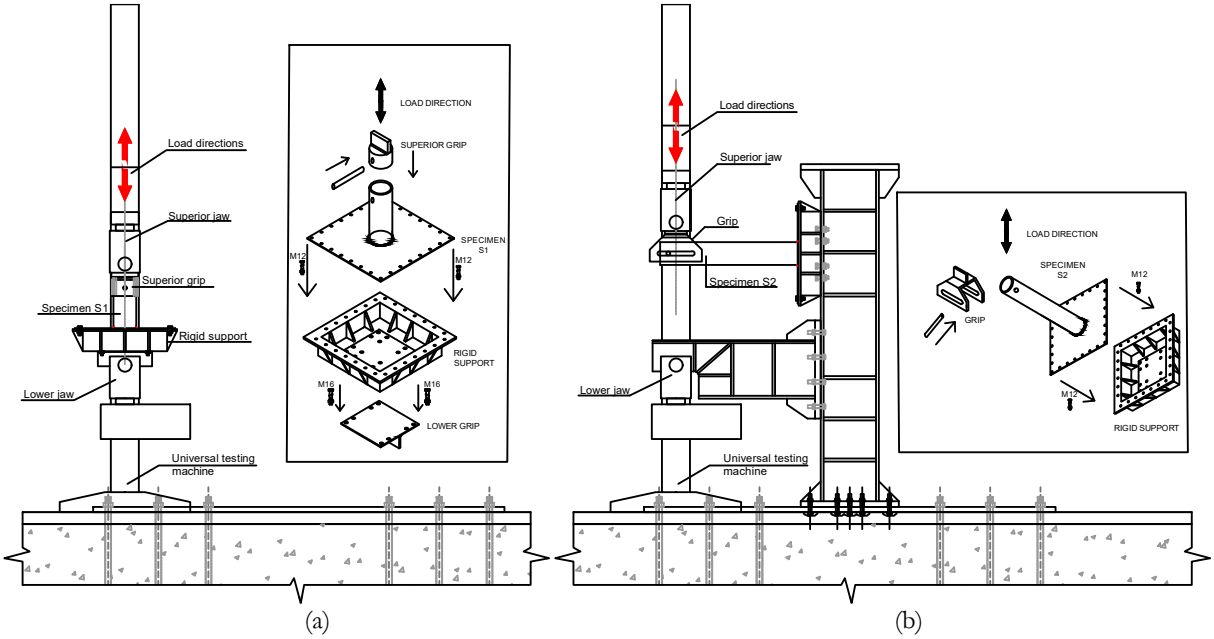


Figure 3. Test setups of S1 (a) and S2 (b)

Monotonic tests were performed with a loading rate of 2 mm/min; the different configurations of S1 and S2 result in different stresses: tension for S1 and pure shear for S2. Cyclic tests were performed under displacement control following the quasi-static loading protocol proposed by FEMA 461 [2007], which

applies load reversals at increasing displacement amplitude levels. Table 1 shows the complete experimental test program.

Table 1. Complete test ID program

Specimen ID	Test ID	Load direction	Test protocol
S1	T1_M_1	Axial	Monotonic
S1	T1_C_1 – T1_C_2	Axial	Cyclic
S2	T2_M_1	Transversal	Monotonic
S2	T2_C_1 – T2_C_2	Transversal	Cyclic

2.2 RESULTS OF EXPERIMENTAL TESTS

2.2.1 Experimental tests on S1

The setup for the monotonic test on S1 is illustrated in Figure 4a. The red arrow indicates the direction of the applied load. The opposite direction was not investigated with monotonic tests in this experimental campaign.

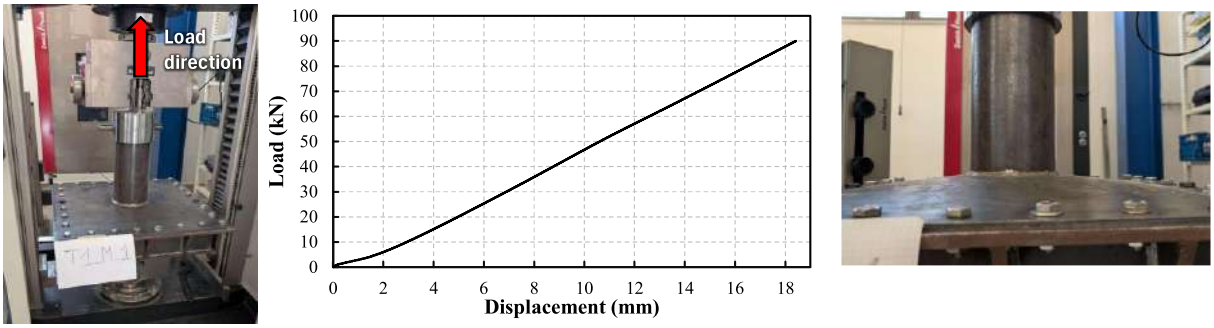


Figure 4. Test setup T1_M_1 (a); load-displacement curve of S1 (b); deformed configuration at final displacement (c)

The specimen, as illustrated in Figure 4b, demonstrated an initial elastic response up to a displacement of approximately 2-3 mm. Beyond this point, the load-displacement curve exhibited a change in slope, indicating the beginning of plastic deformation. When subjected to a maximum applied load of 90 kN from the universal testing machine, the specimen achieved a displacement of around 18 mm. The final deformed configuration, shown in Figure 4c, reveals a symmetrical upward bulging of the plate in the direction of the applied load. The cyclic testing protocol was calibrated according to FEMA 461 [2007]. A target displacement (Δ_m) of 10 mm was assumed and it is achieved through ten steps of progressively increasing amplitudes, each consisting of two cycles. Following the standard, it was decided to add three additional cycles, each with an increment of $0.3\Delta_m$. As a result, the final target displacement (Δ_m) reached 19 mm. The complete loading protocol for the two cyclic tests of S1 is reported in Figure 5.

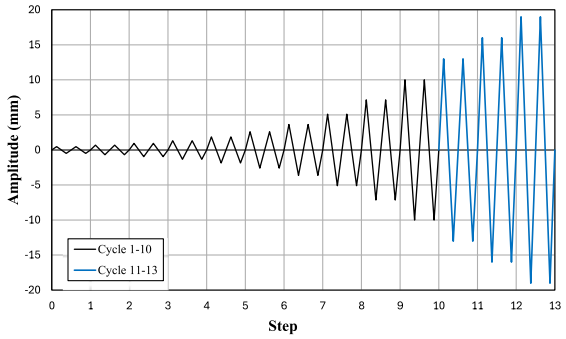


Figure 5. Cyclic loading protocol for S1

The first cyclic test (T1_C_1) was interrupted at step 10 when the displacement reached 10 mm due to a technical issue involving the misalignment of the specimen. Despite this interruption, the test results, in terms of the hysteretic load-displacement curve, are presented in Figure 6a, compared to the results of the monotonic test. The misalignment affected the test results, preventing correct overlap with the monotonic curve. Figure 6b illustrates the results of the second cyclic test on specimen S1, T1_C_2. In this case, the test reached the final step but was halted due to the achievement of the maximum load capacity of the testing machine. During the initial cycles, which involved small amplitude displacements, the slope of the branches closely resembled that of the monotonic curve, indicating that the overall elastic stiffness of the system was similar. However, as the amplitude increased, the cycles became wider, leading to greater energy dissipation. The peak loads observed in these cyclic tests were lower than those seen in the monotonic test, reflecting a loss of resistance due to the cyclic loads. At a displacement of 19 mm, a tensile load of about 80 kN was achieved. In contrast, the maximum load reached during compression at a displacement of 16 mm was higher (about 90 kN), demonstrating an asymmetrical response of the specimen depending on the load direction. The asymmetry in the specimen's behaviour under compression arose from the configuration of the rigid support. When the specimen was subjected to upward displacement, constraints were provided only by the bolts positioned 2.5 cm from the edge of the plate and support. In contrast, when the specimen was subjected to downward displacement, the entire 5 cm edge of the rigid support constrained it, resulting in slightly increased stiffness.

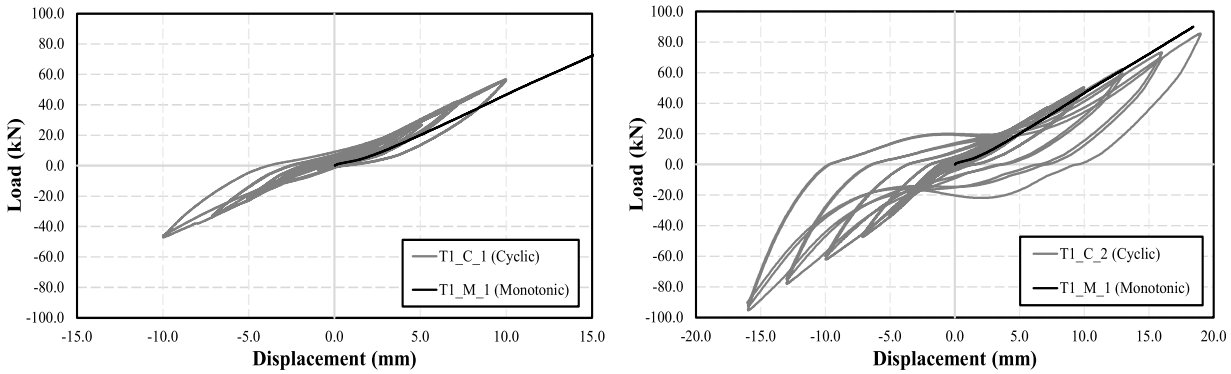


Figure 6. Hysteretic load-displacement curves of S1: T1_C_1 (a); T1_C_2 (b)

Figure 7a and 7b illustrate two examples of the deformed configuration of the sample under tension and compression. During upward displacements (tension), the area of the plate surrounding the weld deforms in alignment with the displacement of the pipe. In a mirrored manner, during downward displacements, the plate deformed inward. In both cases, the pipe, which is much stiffer than the plate, remained undeformed.

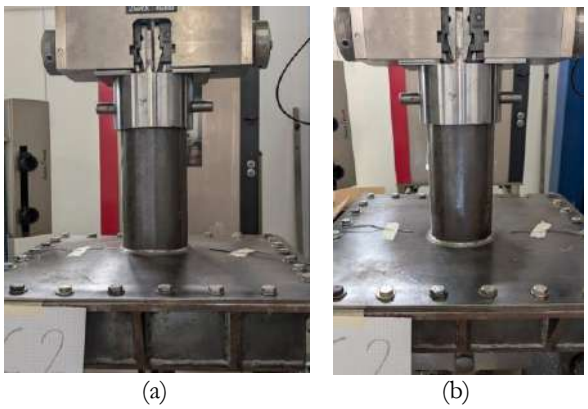
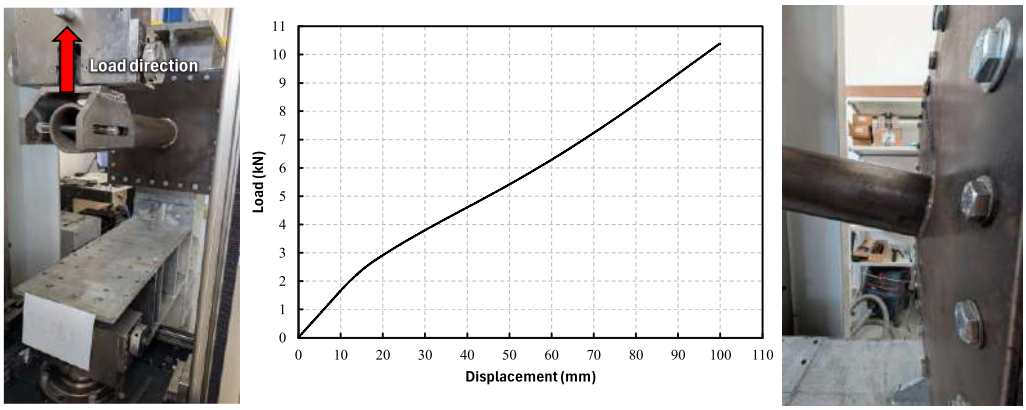


Figure 7. Deformed configuration during T1_C_2: 19 mm upward (a); 16 mm downward (b)

2.2.2 Experimental tests on S2

The setup for the S2 monotonic test is shown in Figure 8a, where the load direction is indicated by a red arrow. The test results are shown by the load-displacement curve depicted in Figure 8b. As illustrated, a hardening phenomenon occurred at a displacement of about 60 mm, when the applied load significantly loses its orthogonality with the pipe's longitudinal axis. The test ended at a load of approximately 10 kN, corresponding to a displacement of 100 mm. Figure 8c presents the deformed shape of specimen S2 at the maximum displacement imposed by the universal testing machine. It can be observed that the pipe remained completely undeformed, whereas the plate exhibited localised deformation around the weld. In particular, the plate bulged below the weld and buckled above it.



(a) (b) (c)

Figure 8. Test setup T2_M_1 (a); load-displacement curve of S2 (b); deformed configuration at final displacement (c)

The target displacement (Δ_m) for the cyclic loading protocol was defined immediately after the onset of plate yielding, corresponding to a displacement of 20 mm. According to FEMA 461 [2007], the target displacement was reached by ten steps of progressively increasing amplitudes. Each step includes two cycles at the same amplitude. The protocol was extended by ten additional cycles, each with a constant increment of $0.3\Delta_m$, because at a displacement of 20 mm, a degradation phase wasn't reached. The new final target displacement was equal to 80 mm. The complete loading protocol for the two cyclic tests is reported in Figure 9.

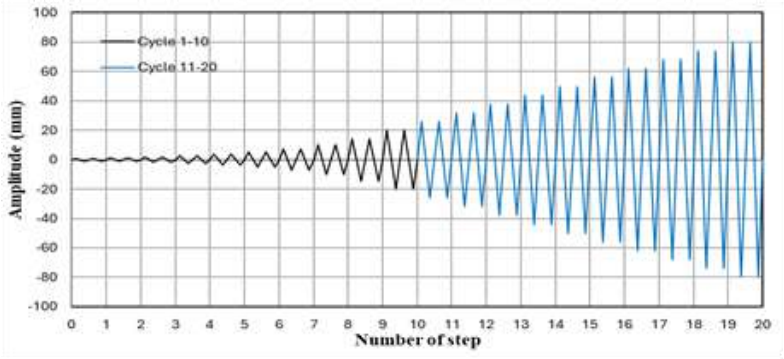
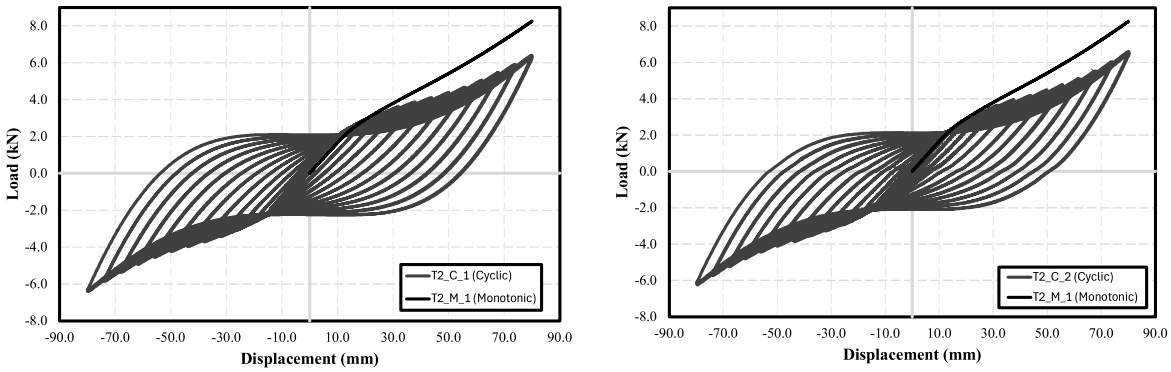


Figure 9. Cyclic loading protocol for S2

Two cyclic tests, T2_C_1 and T2_C_2, were performed on specimen S2. The hysteretic load-displacement responses of the two specimens are shown in Figure 10, together with the reference monotonic curve. In the first test, the maximum tensile and compressive loads were 6.2 kN and 6.3 kN, respectively, as illustrated in Figure 10a. For the second S2 specimen, peak loads of 6.5 kN in tension and 6.1 kN in compression were recorded, as shown in Figure 10b. In both cases, the maximum displacement prescribed by the loading protocol was 80 mm. The monotonic load-displacement curve coincided with the cyclic ones up to approximately 3.3 kN for the first test and 3.0 kN for the second. The hardening phenomenon observed

under cyclic conditions can be attributed to a partial misalignment between the load direction and the pipe's longitudinal axis. In both cyclic cases, the loads reached are lower than those achieved in the monotonic test for displacements greater than 30 mm. This observation indicates a loss of strength due to cyclic loading.



(a) (b)

Figure 10. Hysteretic load-displacement curves of S2: T2_C_1 (a); T2_C_2 (b)

The cyclic tests caused the plate to deform in an equal but mirrored manner depending on the direction of the applied displacement. As illustrated in Figure 11a, upward displacement caused the plate to bulge outwards below the weld and inwards above it. Conversely, downward displacement produced a mirrored deformation pattern, as shown in Figure 11b.



(a) (b)

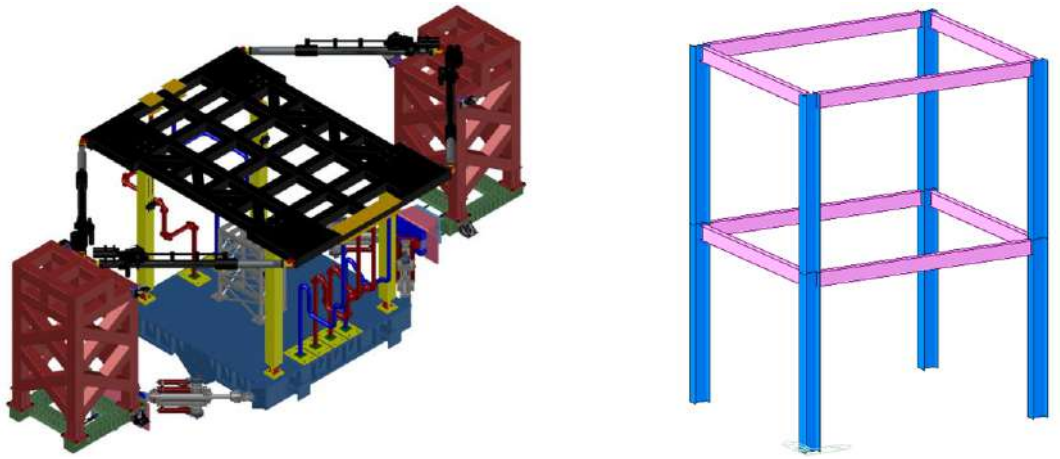
Figure 11. Deformed configuration after cyclic test at 80 mm: upward displacement (a); downward displacement (b)

3.EXPERIMENTAL SHAKE TABLE TESTS

3.1 DESCRIPTION OF THE SETUP

Three pipeline configurations, featuring different loop geometries and joint types, were tested under horizontal seismic excitations using the 9D shake-table facility at the Eucentre Foundation. This shake-table system consists of two independent platforms arranged vertically, with the upper one positioned 4060 mm above the lower, enabling the simultaneous reproduction of distinct floor accelerations representative of a multi-story structure (Figure 12a). To determine realistic seismic demands for industrial steel pipelines, a 3D two-story steel moment-resisting frame tower was designed and analysed through nonlinear time-history simulations using horizontal ground motions (Figure 12b). Based on these analyses, a representative accelerogram (record TK.0302.00.HNE.D.TK-1995) was selected as the input motion for the experimental

campaign. The pipelines were assumed to be anchored to the first and second floors of the frame; thus, the corresponding floor accelerations were applied to the bottom and top shake tables, respectively. Six pipeline specimens were tested: an Omega-shaped loop (1070 mm length, 761 mm height), a V-shaped loop (1125 mm length, 436 mm height), and a three-dimensional piping layout composed of straight segments and 90° elbow joints. Each specimen was subjected to the selected floor motions, scaled from 10% to 140% of their original intensity. The seismic response was recorded in terms of in-plane displacements, accelerations at the loop center, and strains at critical locations using Fiber Bragg Grating (FBG) sensors.



(a) (b)

Figure 12. Shake table test setup

3.2 RESULTS OF THE EXPERIMENTAL SHAKE TABLE TESTS

3.2.1 Acceleration response

The acceleration response of the pipeline specimens was recorded using 3D accelerometers installed at their midspan. Table 2 summarizes the maximum absolute accelerations measured for each configuration. The specimens with flanged joints showed higher peak absolute accelerations compared to those with welded connections. Furthermore, the out-of-plane direction generally exhibited greater acceleration amplitudes than the in-plane direction. Despite the absence of vertical input motions, the specimens also experienced noticeable vertical accelerations, attributed to their geometric configuration. This effect was particularly pronounced in the straight pipe specimens, whose irregular layout resulted in enhanced vertical acceleration responses.

Table 2. Peak absolute accelerations recorded at the center of each pipe specimen under the 100% shake intensity test

Pipe	Specimen	Peak absolute acceleration (g)		
		In-plane (x) axis	Out-of-plane (y) axis	Vertical (z) axis
Welded Omega loop	7	1.75	2.01	0.29
Flanged Omega loop	8	2.84	2.79	0.50
Welded V loop	9	1.41	1.72	0.33
Flanged V loop	10	1.82	2.25	0.47
Welded straight loop	11	2.00	1.50	1.02
Flanged straight loop	12	3.09	2.40	1.41

3.2.2 Displacement response

The relative in-plane displacement at mid-height of the pipe specimens was measured using LVDTs positioned at the central section. Table 3 presents the peak relative in-plane displacements recorded for each

specimen. It should be noted that a malfunction occurred in the displacement recording of specimen 7, which was only identified during post-processing. Consequently, although the corresponding values are included in the tables for completeness, they were excluded from the data interpretation. This issue was isolated and did not compromise the accuracy or integrity of the remaining measurements. Consistent with the acceleration results, the flanged specimens exhibited larger peak relative in-plane displacements, approximately 20% to 30% higher, than their welded counterparts. This increased displacement response may be attributed to greater dynamic amplification effects caused by the additional mass of the flanges. The displacement data also confirmed the stiffness trends observed in the acceleration measurements: specimens with Omega-shaped loops demonstrated higher flexibility than those with V-shaped loops, resulting in larger relative in-plane displacements. The straight-pipe specimens, characterized by their more irregular geometrical layout, showed the largest peak in-plane relative displacements among all configurations. Nevertheless, the peak in-plane relative displacements of all specimens remained within the same order of magnitude.

Table 3. Maximum relative in-plane displacement at the middle height span under the 100% shake intensity test

Pipe	Specimen	Peak relative in-plane displacement (mm)			
		10% intensity	50% intensity	100% intensity	140% intensity
Welded Omega loop	7	0.13	0.60	2.85	5.93
Flanged Omega loop	8	1.74	6.91	14.99	22.44
Welded V loop	9	0.99	5.22	11.20	16.14
Flanged V loop	10	1.46	7.10	13.66	19.97
Welded straight loop	11	1.75	7.04	13.90	19.10
Flanged straight loop	12	3.42	8.84	17.29	25.01

4. CONCLUSIONS

Piping systems are among the most seismically vulnerable non-structural components in industrial facilities due to their geometric complexity, distributed mass, and numerous joints and supports that may exhibit nonlinear behaviour under seismic excitation. In this study, monotonic and cyclic quasi-static tests of pipe-to-tank connections and shake table tests simulating the dynamic response of piping networks carried out within the MITPLANT Project were presented. The welded pipe-to-tank connections performed well under both axial and transverse loads; however, the experimental tests in the transverse direction involved lower loads than those in the axial direction. The shake table tests conducted on piping systems revealed that specimens with flanged joints exhibited higher peak accelerations and greater relative in-plane displacements compared to those with welded joints. Additionally, specimens featuring Omega-shaped loops displayed more flexibility than those with V-shaped loops. Finally, straight-pipe specimens experienced a greater relative in-plane displacement than all other types. The results of these two experimental campaigns will be essential for calibrating numerical models for future parametric analyses and for investigating the potential failure modes of piping systems during seismic events.

REFERENCES

Aiba, M., Grashi, K.I., Akiyama, H., Chiba, T. [2000] "Test of nozzles at wall of cylindrical tank for severe loads under earthquake," *Proceedings of 12th World Conference on Earthquake Engineering*, New Zealand.

Brunesi, E., Nascimbene, R., Pagani, M., Beilic, D. [2015] "Seismic performance of storage steel tanks during the May 2012 Emilia, Italy, earthquakes," *Journal of Performance of Constructed Facilities*, Vol. 29.

Campedel, M. [2008] "Analysis of major industrial accidents triggered by natural events reported in the principal available chemical accident databases," *JRC Scientific and Technical Reports*, JRC42281.

EN 14015 [2006] "Specification for the design and manufacture of site built, vertical, cylindrical, flat-bottomed, above-ground welded, steel tanks for the storage of liquids at ambient temperature and above".

EU, Directive 2012/18/EU on the control of major-accident hazards involving dangerous substances, amending and subsequently repealing Council Directive 96/82/EC. Offic. J. Eur. Union L 197/1.

FEMA E-74 [2012] "Reducing the risk of nonstructural earthquake damage – A practical guide," *National Earthquake Hazard Reduction Program (NEHRP)*, US.

FEMA 461 [2007] "Interim Testing Protocols for Determining the Seismic Characteristics of Structural and Nonstructural Components".

Gabbianelli, G., Perrone, D., Micelli, F., Ciucci, M. [2024] "Damage evaluation and mitigation in industrial facilities due to natech seismic events," *Proceedings of 18th World Conference on Earthquake Engineering*, Milan, Italy.

Girgin, S. [2011] "The natech events during the 17 August 1999 Kocaeli earthquake: aftermath and lessons learned," *Natural Hazards and Earth Systems Sciences*; Vol. 11, pp. 1129-1140.

Jain, S.K., Lettis, W.R., Murty, C.V.R., Bardet, J. P. [2002] "Bhuj, India Earthquake Reconnaissance Report," *Supplement to Earthquake Spectra*, Vol. 18(S1).

Korkmaz, K.A., Sari, A., Carhoglu, A.I. [2011] "Seismic risk assessment of storage tanks in Turkish industrial facilities," *Journal of Loss Prevention in the Process Industries*, Vol. 24, pp. 314-320.

Krausmann, E., Cruz, A.M. [2013] "Impact of the 11th March 2011, Great East Japan earthquake and tsunami on the chemical industry," *Natural Hazards*; Vol. 67, pp. 811-828.

Italian Legislative Decree of 2015/06/26 n. 105: Implementation of the Directive 2018/18/EU

La Salandra, V., Bursi, O.S., Alessandri, S., Di Filippo, R., Paolacci, F. [2016] "Cyclic response of enhanced bolted flanged joints for piping systems," *Proceedings of the ASME 2016 Pressure Vessels and Piping Conference*, Vancouver, British Columbia, Canada.

Marino, A., Ciucci, M., Barbieri Vita, L., Palermo, O., Quinci, G. [2019] "Valutazione e gestione del rischio sismico negli stabilimenti con pericolo di incidente rilevante," *XVIII Convegno Anidis*, Ascoli Piceno, Italy.

Reza, M.S., Bursi O.S., Paolacci, F., Kumar, A. [2014] "Enhanced seismic performance of non-standard bolted flanged joints for petrochemical piping systems," *Journal of Loss Prevention in the Process Industries*, Vol. 30, pp. 124-136.

Wieschollek, M., Hoffmeister, B., Feldmann, M. [2013] "Experimental and numerical investigations on nozzle reinforcements, *Proceedings of the ASME 2013 Pressure Vessels and Piping Conference*, Paris, France.

Seismic performance of a full-scale code-compliant fire sprinkler piping system in a six-storey building

Jitendra Bhatta[1], Prashanna Mishra[2], Dustin T. Cook[3], Siamak Sattar[4], John W. van de Lindt[5], and Andre R. Barbosa[6]

[1] Postdoctoral Fellow, Department of Civil and Environmental Engineering, University of Canterbury, Christchurch, New Zealand, jitendra.bhatta@canterbury.ac.nz

[2] Graduate Research Assistant, Department of Civil and Environmental Engineering, Colorado State University, Colorado, United States, prashanna.mishra@colostate.edu

[3] Research Structural Engineer, Earthquake Engineering Group, National Institute of Science and Technology, Gaithersburg, Maryland, United States, dustin.cook@nist.gov

[4] Acting Group Leader, Earthquake Engineering Group, National Institute of Science and Technology, Gaithersburg, Maryland, Unites Sates, siamak.sattar@nist.gov

[5] Harold H. Short Endowed Chair Professor, Department of Civil and Environmental Engineering, Colorado State University, Colorado, United States, john.van_de_lindt@colostate.edu

[6]Glenn Willis Holcomb Professor in Structural Engineering, School of Civil and Construction Engineering, Oregon State University, Corvallis, Oregon, United Sates, andre.barbosa@oregonstate.edu

Abstract. A braced fire sprinkler piping system was designed and installed, in accordance with the NFPA-13 (2022) standard, on the third and sixth floors of a six-storey mass timber building, which was tested on an outdoor shake table at the NHERI shared-use facility at the University of California, San Diego. A braced suspended ceiling was also installed on the sixth floor to examine its interaction with the sprinkler heads. The building was subjected to ground shaking during the testing, with horizontal peak floor accelerations reaching 2.05 g on the sixth floor. This study analyses the observed damage to the sprinkler piping system and compares the results with FEMA P-58 fragility functions. Overall, the piping system demonstrated strong seismic performance, sustaining minimal damage throughout the tests. A comparison of the FEMA P-58 fragility functions for leakage and breakage in sprinkler heads (dropping through braced ceiling tiles) and leakage in pipes with the experimental findings indicates that the FEMA P-58 fragility functions may be conservative, warranting further investigation. Meanwhile, the test results supported the FEMA P-58 fragility functions for pipe joint breakage. Moreover, component resonance ductility factors (C_{AR}) factors for sprinkler pipes recommended by ASCE/SEI 7-22 (2021) were found to be conservative for riser and distribution pipes but non-conservative for armover pipes.

Keywords: Full scale dynamic test, Fire sprinkler piping system, NFPA-13, FEMA P-58, six-storey building

1. INTRODUCTION

Fire sprinkler systems, among other non-structural elements, are specifically designed to detect, control, and suppress fire hazards from the outset. Maintaining the operational integrity of these systems after an earthquake is crucial for life safety and efficient recovery efforts. The fire sprinkler piping system consists of a network of pipes that deliver water to the fire sprinklers and control valves to regulate flow. Riser pipes serve as vertical conduits that transport water from the main supply to horizontal pipes on various building levels. The horizontal layout includes distribution pipes extending from the risers, branch pipes stemming from the distribution pipes, and armover pipes branching from the branch pipes. Sprinklers are located at the ends of droppers or sprigs that extend downward from armover pipes or upward from branch pipes, respectively. Due to their sensitivity to accelerations, these piping components require bracing to withstand seismic forces from the connected floors. Past seismic events, such as the 1994 Northridge earthquake, the 2010 and 2011 Christchurch earthquakes, the 2010 Chile earthquake, and the 2014 South Napa earthquake, have revealed poor seismic performance of fire sprinkler systems (Almufti et al., 2014; Baker et al., 2012; LeGrone, 2004; Miranda et al., 2012; NIST, 2017; Tian et al., 2013). Commonly reported damage includes broken sprinkler heads resulting from interactions with suspended ceilings or roof cross-bracing, leading to leaks and subsequent property damage from flooding, as well as failures in the bracing systems themselves.

Extensive experimental tests at the component level have been performed on various fire sprinkler piping connections, as well as hanger and bracing components, to document their failure mechanisms, strength, and deformation capacities, as well as to develop fragility functions for different observed damage states (Antaki, 2004; Blasi et al., 2018; Goodwin, 2005; Rashid, 2022; Tian et al., 2013; Wang et al., 2019). However, there are only a limited number of studies examining full-scale fire sprinkler piping systems subjected to dynamic loads on a shake table (Chen et al., 2016; Jenkins et al., 2017; Pantoli et al., 2016; Rashid, 2022; Tian et al., 2015). This knowledge gap limits the ability to produce comprehensive system-level fragility functions based on experimental findings. Consequently, FEMA P-58-3 (2018) developed fragility functions based on the insights and judgments of expert panels, focusing on pipe leakage and support failure for fire sprinkler piping systems, as well as for sprinkler drops that extend through various types of suspended ceilings.

In this study, full-scale pressurized fire sprinkler horizontal piping systems were installed on the third and sixth floors of a six-storey mass timber building, with the riser pipe extending from the ground level to the roof. The structure underwent multiple tests using different lateral force-resisting systems. A section of a back-braced suspended ceiling was added on the sixth floor to examine its interaction with the piping system. These tests were conducted as part of the Natural Hazards Engineering Research Infrastructure (NHERI) Converging Design project at the large high-performance outdoor shake table (LHPOST6) at the University of California, San Diego (NHERI, 2023). This research details the observed damage of the braced pressurized fire sprinkler piping system, compliant with the requirements of NFPA-13 (2022) subjected to applied ground motions. Additionally, it compares the types of damage experienced by the piping components in relation to peak floor accelerations with the heuristic fragility functions for sprinkler systems outlined in FEMA P-58-3 (2018).

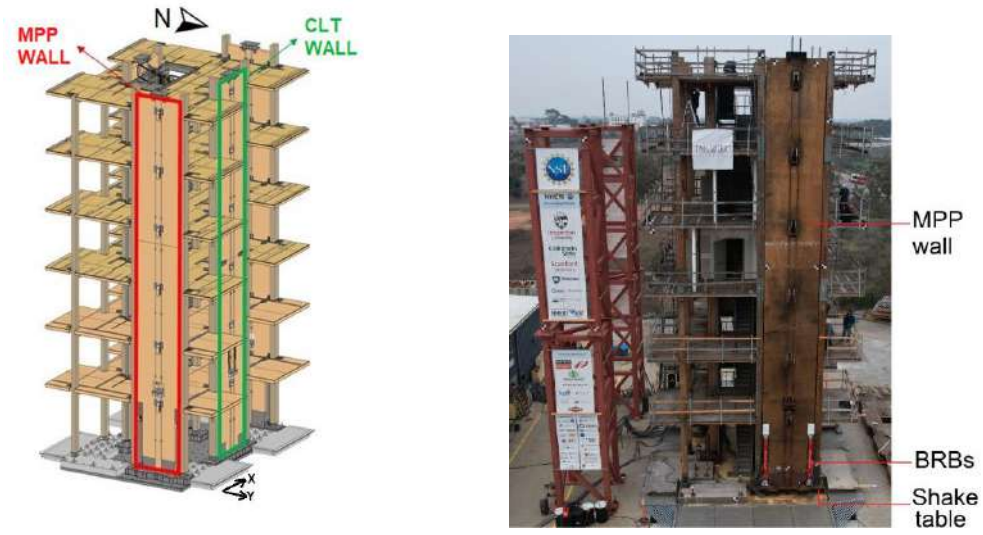
2.EXPERIMENTAL SETUP AND DATA ACQUISITION

The NHERI Converging Design project involved testing three different six-storey lateral force-resisting systems across three phases: Phase I, Phase II, and Phase III (NHERI, 2023; Barbosa et al., 2024). The braced sprinkler piping system was installed and tested during Phase II, which is the focus of this paper. While Barbosa et al. (2024; 2025) discussed the response and behaviour of the structural systems, this paper

offers an overview of these systems and the measured responses crucial for understanding the observed behaviour of the fire sprinkler piping systems.

2.1 OVERVIEW OF THE SIX-STOREY STRUCTURAL SYSTEMS

In Phase II of the NHERI Converging Design project, a six-storey mass timber structure built on the LHPOST6 platform featured two lateral force-resisting systems. In the East-West (EW) direction (hereafter as the X-direction), the structure incorporated two post-tensioned self-centring rocking walls (located on the north and south sides), which consisted of 9-ply cross-laminated timber (CLT) panels, laminated veneer lumber (LVL) columns as boundary elements, and U-shaped flexural plates (UFPs) connecting the LVL columns and CLT panels. In the North-South (NS) direction (hereafter as the Y-direction), the building utilized an alternative self-centring rocking wall system, which included post-tensioned mass ply panel (MPP) walls and buckling restrained boundary elements (BRBs) for energy dissipation, as shown in Figure 1. Barbosa et al. (2025) provide additional design details for this phase.



(a) 3D Schematic diagram of six-storey timber test structure (Barbosa et al. 2024)

(b) Six-storey timber test structure (East elevation), Photo Courtesy of Robert Beckley

Figure 1. Schematic views of six-storey timber test structure details (Bhatta et al., 2025)

2.2 FIRE SPRINKLER SYSTEM

During Phase II of the NHERI Converging Design project, a braced fire-sprinkler steel piping system was designed and installed by professional contractors in accordance with NFPA-13 (2022), which is typical of modern US construction. The sprinkler piping system was installed on the third and sixth floors of the building, as illustrated in Figure 2 and Figure 3. As shown in Figure 2a, a 100 mm diameter riser pipe extended from the ground level (Level 1) to a height of 915 mm above the roof level (Level 7). The riser pipe had flexible grooved connections above and below each floor to accommodate inter-storey displacements. Distribution pipes branched off from the riser on the third and sixth floors. Pressure gauges, without control valves, were installed at both the ground and roof levels on the riser pipe. At the junction where the distribution pipes connected to the riser, pressure gauges with control valves were used to maintain a pressure of approximately 0.89 MPa in the horizontal distribution pipes. Branch pipes then extended from the distribution pipes, and armover pipes extended off the branch pipes.

The sizes and plenum depths of the horizontal piping system are detailed in Table 1. Due to the increased plenum depth on the third floor, 300 mm-long sprigs extended from the branch pipes. The branch and armover pipes passed through structural beams via 90 mm holes on the sixth floor. Notably, fire-stopping

materials, such as mineral wool, were not used to seal the gaps between the riser pipes passing through the floors and the horizontal pipes passing through the beams. The absence of fire-stopping materials is not expected to impact the piping system's overall seismic performance. The joints in the branch and armover pipes were either welded or threaded. In addition, a section of a back-braced (or floating) "grid and tile" suspended ceiling was installed on the sixth floor to study the interaction between the sprinkler heads, connected to rigid and flexible hose droppers, and the ceiling, as shown in Figure 2c.

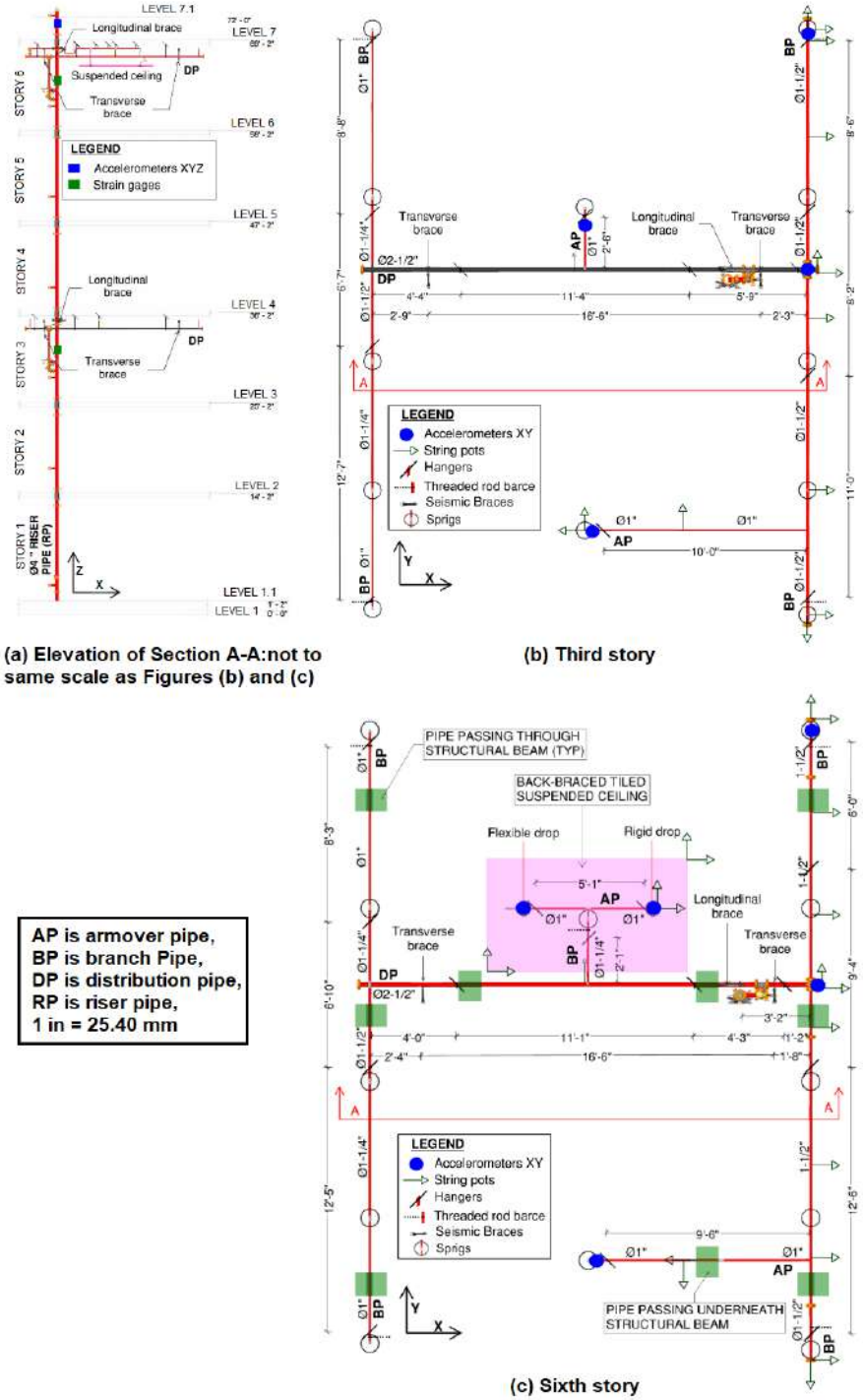


Figure 2. Fire sprinkler piping system schematic layout showing instrumentation (Bhatta et al., 2025)



(a) Sprinkler piping system on sixth storey **(b) Sprinkler piping system on third storey**

Figure 3. Photos of mass timber structure with fire sprinkler piping system (Bhatta et al., 2025)

Table 1: Properties of horizontal steel piping system

Pipe	Nominal pipe diameter	Schedule* and pipe thickness	Plenum depth
Distribution pipes	65 mm	Schedule 10: (3.05 mm)	457 mm
Branch pipes	25 mm to 40 mm	Schedule 10: (2.77 mm)	457 mm on third storey 152 mm on sixth storey
Armover pipes	25 mm	Schedule 40: (3.38 mm)	457 mm on third storey 152 mm on sixth storey

*The schedule number on pipe products corresponds to the wall thickness of the pipe: higher numbers indicate greater wall thickness.

The gravity load of the horizontal piping system was supported by 10 mm all-threaded hanger rods with surge restrainers. Longitudinal and transverse braces attached to the distribution pipes were designed in accordance with NFPA-13 (2022). The braces for the distribution pipes consisted of 25 mm diameter Schedule 40 steel pipes, with M12 through bolts used to secure the braces to the structure. Additionally, the ends of the branch pipes were braced with 10 mm threaded rods. The riser pipe, which terminated above the roof, was laterally braced in the Y-direction only using two steel pipes bolted to the riser pipe clamp.

The horizontal seismic force acting on the braces (F_{pw}) was calculated using the equation $F_{pw} = C_p W_p$ (Clause 18.5.9.3, NFPA-13 (2022), where C_p is the seismic coefficient, which depends on the short-period spectral response acceleration parameter (S_s). For the assumed value of S_s of 0.80 g, C_p was taken as 0.45, based on the seismic coefficient Table 18.5.9.3 in NFPA-13 (2022). The weight of the piping system, W_p, was 1.15 times that of the water-filled pipes. The calculated forces on the braces for the transverse and longitudinal directions relative to the distribution pipe were approximately 0.61 kN and 1.10 kN, respectively, considering all the pipes in the horizontal layout. Although NFPA-13 (2022) specifies that a maximum spacing of 12 m between transverse braces is sufficient to support this force, the actual spacing was reduced to 5 m due to spatial constraints in the layout (see Figure 2b and Figure 2c) resulting from the shake table footprint size. As a result, the transverse braces were not only "over-braced" in terms of the spacing by a factor of 12/5 = 2.4 (i.e., the ratio of maximum allowable spacing required by NFPA-13 (2022) to the spacing provided between the braces), but also had a capacity-to-demand ratio of 4.89, calculated from the values in Table 18.5.5.2 (a) of NFPA-13 (2022), with a capacity of 2.98 kN and a demand of 0.61 kN. The calculated forces for the transverse braces (0.61 kN) and longitudinal braces (1.10 kN) were compared to the maximum load capacity of 1.59 kN for the M12 through bolts used to secure the braces to the structure, resulting in factors of safety of approximately 2.60 and 1.44, respectively. Additionally, lateral restraints (see the threaded rod braces in Figure 2b and Figure 2c) were installed at the ends of the branch pipes at 8.5 m

intervals. This spacing is less than the maximum allowable spacing of 13 m for steel branch pipes with a 25 mm diameter and Cp ≤ 0.50 (as per NFPA-13 (2022)). As such, the branch pipes were "over-braced" in terms of the spacing by a factor of 13/8.5= 1.53.

2.3 TEST SCHEDULE

The mass timber test building was subjected to progressively increasing ground shaking intensities, ranging from 10 % to 100 % of the Risk-Targeted Maximum Considered Earthquake (MCE_R). The ground motions were scaled to minimize discrepancies between the target response spectra and spectral acceleration of the selected earthquake records across a period range from $0.2T_1$ to $1.5T_1$, where T_1 = 0.94 s was estimated as the structure's fundamental period from numerical models. These intensities were simulated using earthquake records from the 1994 Northridge, 2010 Maule Chile, 2010 Ferndale, and 1964 Niigata events, with scaling details provided in Table 2. Detailed information on the ground motion selection and their response spectra are available in Barbosa et al. (2025).

Table 2: Test matrix showing applied earthquake records during phase II (Barbosa et al., 2025)

Test Number	% MCE_R	Earthquake record	Applied Direction	Target Input PGA (g)		
				X	Y	Z
1*	10	1994 Northridge	XYZ	0.04	0.07	0.05
Inspection						
2	10	1994 Northridge	Y	-	0.07	-
3	30	1994 Northridge	Y	-	0.21	-
4	30	1994 Northridge	XY	0.13	0.21	-
5	30	1994 Northridge	XYZ	0.13	0.21	0.16
6	67	1994 Northridge	Y	-	0.48	-
Inspection						
7	67	1994 Northridge	XYZ	0.30	0.48	0.36
8	100	1994 Northridge	XYZ	0.44	0.71	0.54
Inspection						
9	30	1964 Niigata	XYZ	0.24	0.18	0.13
10	30	2010 Ferndale	XYZ	0.18	0.19	0.32
11	30	2010 Maule Chile	XYZ	0.13	0.15	0.11
Inspection						
12	67	2010 Ferndale	XYZ	0.40	0.42	0.71
13	67	2010 Maule Chile	XY	0.30	0.34	-
14	68.9	1964 Niigata	XYZ	0.55	0.42	0.30
15	100	2010 Ferndale	XYZ	0.60	0.62	1.06
Inspection						
16	100	2010 Maule Chile	XY	0.45	0.51	-
Inspection						
17	100	1964 Niigata	XYZ	0.79	0.61	0.44
Inspection						

* Test 1 is neglected due to the malfunctioning of several sensors that failed to record data accurately.

In addition, white noise tests were performed in the X and Y directions both before and after each earthquake simulation to monitor any changes in the modal frequencies and damping ratios of the structure.

Visual inspections of the fire-sprinkler system were carried out intermittently between tests, as outlined in Table 2. Any observed damage was photographed and documented manually.

2.4 INSTRUMENTATION AND DATA PROCESSING

The structure was equipped with string potentiometers to measure overall floor displacements in the X-direction, at floor levels 2 and 3, and in the Y-direction, across all floor levels. Accelerometers were used to capture horizontal floor accelerations in the X and Y directions, as well as vertical floor accelerations in the Z direction. Additionally, string potentiometers and accelerometers were installed on the symmetric half of the fire sprinkler piping system to record its horizontal displacements and accelerations relative to the structure, as illustrated in Figure 2. These results can be found in Bhatta et al. (2025). The recorded displacement and acceleration data were filtered to remove noise using a 4-node low-pass Butterworth filter (Butterworth, 1930) with a cutoff frequency of 50 Hz and a sampling frequency of 256 Hz.

3.EXPERIMENTAL RESULTS

3.1 PEAK SEISMIC RESPONSE OF THE STRUCTURE

The peak seismic response for the floor levels with the attached piping system showed that Level 7 experienced a resultant Peak Floor Acceleration (PFA) of 2.05 g during Test 15 and Level 4 recorded a lower resultant PFA of 1.43 g during Test 17. The peak inter-storey drift of the structure was 2 % during Test 8. Detailed information on the peak seismic response of the test structure is available in Barbosa et al. (2025).

3.2 COMPONENT RESONANCE DUCTILITY FACTORS (C_{AR})

The Component Resonance Ductility Factors (C_{AR}) for the fire sprinkler piping system were calculated by normalizing pipe accelerations (PCA) with floor accelerations (PFA). The results were compared to the ASCE/SEI 7-22 (2021) recommended value of 2.20 as shown in Figure 4. While the code was conservative for riser and distribution pipes (median C_{AR} ~3/5th of 2.20), it underestimated demands on armover pipes. Their median C_{AR} values for armover pipes exceeded the code value by a factor of 1.25, increasing to 1.60 for pipes interacting with a braced suspended ceiling. This suggests that dynamic excitations from connected pipes (Soroushian et al. 2016) and ceiling interactions can significantly elevate accelerations in armover pipes.

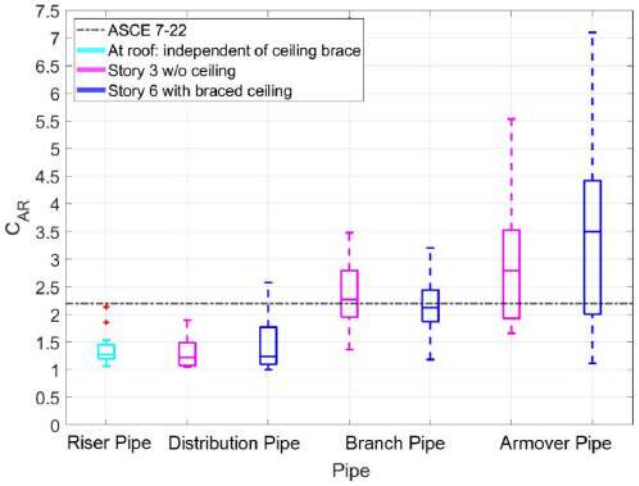


Figure 4. Box-plots showing statistical features of the calculated C_{AR} values compared to ASCE/SEI 7-22 (2021) requirements (Bhatta et al., 2025)

3.3 DAMAGE OBSERVATION

The inspection following Test 6, which involved a base shaking intensity scaled to 67 % of the MCE_R (i.e., the Design Earthquake intensity), revealed minor damage to the fire sprinkler piping system. The observed damage included buckling of the threaded rod braces, with small residual displacements, at the ends of the branch pipes on the third floor, loosening of the escutcheon plates between the sprinkler heads (connected to rigid droppers) and the suspended ceiling on the sixth floor, and yielding of the bolt connecting the riser clamp to the rod braces on the roof, as shown in Figure 5. The decision was made to leave the damage unrepaired and thoroughly evaluate the system's resilience under extreme seismic conditions. However, apart from the escutcheon plate connected to the rigid dropper falling off after Test 8 (a 100 % MCE_R intensity shake), no further damage was observed in subsequent tests, even under maximum PFAs and inter-storey drifts. Additionally, markings above and below the mass timber floors indicated some sliding of the riser-to-floor clamp during the applied ground motions. Despite this, no significant damage, such as leakage, joint failure, or issues with hangers and braces, was noted throughout the tests. Moreover, no damage was observed to the braced suspended ceilings on the sixth floor of the building.



(a) Sliding of riser-to-floor clamps (0.75 g - Test 6)



(b) Buckling of threaded rod brace (0.75 g - Test 6)



(c) Loosening of escutcheon plates (1.42 g - Test 6)



(d) Yielding of bolt between brace and riser (1.42 g - Test 6)



(e) Falling of escutcheon plates at rigid dropper (1.85 g - Test 8)

Figure 5. Damage was observed to the fire sprinkler piping system: the test number and measured resultant PFAs in the tests before the damage was observed are shown in parentheses (Bhatta et al., 2025)

3.4 DAMAGE ANALYSIS

FEMA P-58-3 (2018) developed heuristic fragility functions based on expert panel elucidation and judgment for (a) sprinkler drops that protrude through various types of suspended ceilings and (b) pipe leakage and support failure for fire-sprinkler piping systems. The fragility functions for sprinkler head leakage and breakage, with standard drops up to 1800 mm for "Braced laid-in tiles," are plotted in Figure 6, using the

median peak PFA and dispersion values provided in FEMA P-58-3 (2018). For the maximum resultant PFA of 2.05 g observed in all the tests, the fragility function for damage state DS1 (Leakage) suggests an approximately 84 % likelihood of leakage occurring in the sprinkler heads. Similarly, the fragility function for damage state DS2 (Breakage) estimates a 48 % probability of sprinkler head breakage. In the current experiment, no leakage (DS1) or breakage (DS2) of the sprinkler heads was observed for the specimen tested up to a 2.05 g resultant PFA. While the testing provided 16 data points for the fragility functions, these values are based on a single specimen. According to existing literature, Tian et al. (2015) reported that for fully braced piping under NFPA-13 (2010) conditions, branch pipes with braced or fully floating ceilings tested up to 0.65 g PFA showed no leakage or damage to sprinkler heads. Similarly, Soroushian et al. (2016), testing up to 1.22 g PFA, and Rahmanishamsi et al. (2014), testing up to 2.47 g PFA, observed damage only to ceiling tiles, with no damage to sprinkler heads. Based on these findings, the FEMA P-58-3 (2018) fragility functions appear conservative. However, the seismic performance of the fire-sprinkler piping system can be influenced by the design and layout of the horizontal pipes and braces/restraints. Therefore, additional experimental testing is necessary to draw more definitive conclusions.

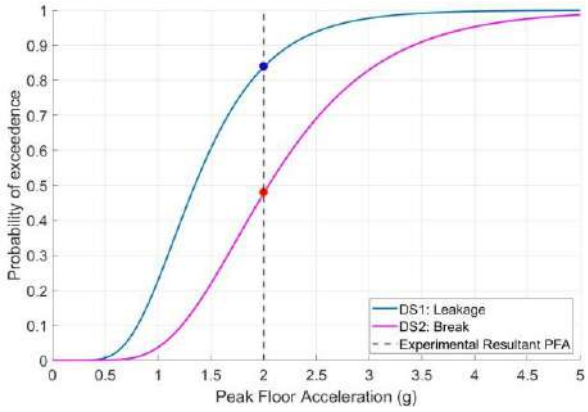


Figure 6. Fragility functions calculated for damage states of sprinkler heads for 'Braced laid-in tiles' using FEMA P-58-3 (2018)

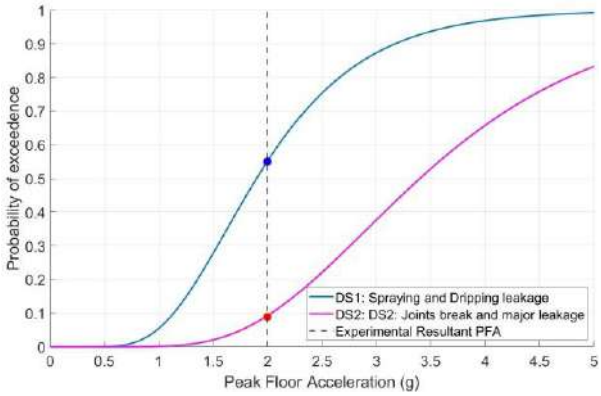


Figure 7. Fragility functions calculated for damage states for horizontal piping using FEMA P-58-3 (2018) recommendations: bracing according to OSHPD or similar criteria for SDC D/E/F

The fragility functions for leakage and breakage of fire-sprinkler pipes (Old style Victaulic, thin-walled steel), designed with bracing according to Office of Statewide Health Planning and Development (OSHPD), now known as Department of Health Care Access and Information (HCAI), or similar criteria for Seismic Design Categories (SDC) D/E/F, are plotted in Figure 7. These functions are based on the median peak PFA and dispersion values provided in FEMA P-58-3 (2018). For the resultant PFA of 2.05 g from all the tests, the fragility function for damage state DS1 (Spraying and Dripping Leakage) indicates approximately a 55 % likelihood of leakage occurring. Although the 55% likelihood of leakage does not guarantee it will happen consistently, but this probability appears inconsistent when compared to the experimental observations from full-scale fire sprinkler piping tests, complaint to NFPA-13 (2022) and NZS 4541 (2020), conducted by Jenkins et al. (2017), Chen et al. (2016), Rashid (2022), and Tian et al. (2015). In these tests, no leakage was observed in pipes subjected to PFAs within the range of 0.56 g to 2.47 g. The fragility function for damage state DS2 (Joints Break and Major Leakage) indicates an 8 % probability of damage. Current test results anecdotally support this, since no such damage was observed.

4.CONCLUSIONS

A braced fire sprinkler piping system, compliant with NFPA-13 (2022), which is typical in US design and construction, was tested under tri-axial full-scale shake table testing in a six-storey mass timber building as

part of the NHERI Converging Design project at the University of California, San Diego's large high-performance outdoor shake table. The systems were subjected to a peak floor acceleration of 2.05 g. The braced systems demonstrated excellent performance, sustaining no significant damage such as leaks or failure of braces, hangers, pipe joints, or anchors. This desired performance can be attributed to the transverse braces being "over-braced" in terms of spacing, with a factor of 2.4, and having a capacity-to-demand ratio of 4.89. Additionally, the transverse and longitudinal braces exceed the minimum requirements with a safety factor of 2.60 and 1.44, respectively. Minor damage included bending of threaded rod braces, yielding of bolt connections on riser clamps and braces, and the detachment of escutcheon plates covering gaps between sprinkler heads in the suspended ceilings. The use of flexible hose droppers successfully prevented damage to the escutcheon plates. Despite the minor damage, the operation of the fire sprinkler system was not impacted, and no repairs were deemed necessary, ensuring the building's functionality would remain unaffected post-earthquake.

A comparison of the current experimental results with the FEMA P-58-3 (2018) fragility functions for leakage and damage in sprinklers (passing through braced ceiling tiles) and minor leakage in pipes, the fragility functions being used in FEMA P-58-3 (2018) might be conservative. In contrast, the current test results supported the FEMA P-58-3 (2018) fragility functions for break in pipe joints. However, due to the limited number of tests conducted, further experimental research is needed to draw more conclusive results. Moreover, the component resonance ductility factors (C_{AR}) factors for sprinkler pipes recommended by ASCE/SEI 7-22 (2021) were found to be conservative for riser and distribution pipes but non-conservative for armover pipes.

ACKNOWLEDGMENT

We extend our appreciation and gratitude to team members of the NHERI Converging Design project and to all technical staff at UCSD for their invaluable assistance and support. Phase II of the NHERI Converging Design project was only possible with the support of many industry partners listed on the project website (NHERI 2023). This project was supported by the National Science Foundation award numbers 2120683, 2120684, and 2120692, with an important supplement provided by the National Institute of Standards and Technology under the NSF-NIST inter-agency agreement. Support from the TallWood Design Institute and USDA Agricultural Research Service Award #58-0204-9-165 are also acknowledged. The findings, opinions, recommendations, and conclusions in this presentation do not necessarily reflect the views of others, including the sponsors. Certain commercial or proprietary products may have been used in this study and discussed in the paper. This is not intended to imply recommendation or endorsement by NIST, nor to imply that such product is necessarily the best available for the purpose.

REFERENCES

Almufti I, Barbosa A, Bray J, Dawson T, Marrow J, Mieler M, et al. (2014). *"M 6.0 South Napa Earthquake of August 24, 2014. ".* https://learningfromearthquakes.org/2014-08-24-south-napa/images/2014_08_24_south_napa/pdfs/EERI_EQ_report/EERI-Special-Eq-Report-2014-South-Napa-versionOct19web.pdf.

Antaki G (2004). "Seismic capacity of threaded, brazed and grooved clamped joints". *ASME Pressure Vessels and Piping Conference,* 46814, 135–45. https://doi.org/10.1115/PVP2004-2915

ASCE/SEI:7-22. (2021). "*Minimum Design Loads and Associated Criteria for Buildings and Other Structures".* Reston, VA: ASCE: American Society of Civil Engineers.

Baker GB, Collier PC, Abu AK and Houston B (2012). "Post-earthquake structural design for fire-a New Zealand perspective".

Barbosa AR, Simpson B, van de Lindt J, Sinha A, Pryor S, Brown N, et al. (2024). "NHERI Converging Design Project: Overview of 6-Story Shake-Table Test Program. Presentation". 2024 EERI Annual Meeting, April 9–12. 2024, Sheraton Grand Seattle, 1400 6th Ave, Seattle, WA.

Barbosa AR, Simpson B, van de Lindt J, Sinha A, Field T, McBain M, Uarac P, Kontra S, Mishra P, Gioiella L et al. (2025). "Shake table testing program for mass timber and hybrid resilient structures datasets for the NHERI

Converging Design Project.", Report No. 24-03 V1.0, Oregon State University, https://doi.org/10.17603/ds2-rh8q-rn95
Bhatta, J., Mishra, P., Cook, D., Sattar, S., Barbosa, A. R., & van de Lindt, J. (2025). Seismic Response of Pressurized Full-Scale Fire Sprinkler Piping System in Six-Story Building. Journal of Earthquake Engineering, 1–27. https://doi.org/10.1080/13632469.2025.2470335
Blasi G, Aiello MA, Maddaloni G and Pecce MR (2018). "Seismic response evaluation of medical gas and fire-protection pipelines' Tee-Joints". *Engineering Structures,* **173**: 1039–1053. https://doi.org/10.1016/j.engstruct.2018.07.045
Butterworth S (1930). "On the theory of filter amplifiers". *Wireless Engineer,* **7**(6): 536–541.
Chen MC, Pantoli E, Wang X, Astroza R, Ebrahimian H, Hutchinson TC, et al. (2016). "Full-scale structural and nonstructural building system performance during earthquakes: Part I–specimen description, test protocol, and structural response". *Earthquake Spectra,* **32**(2): 737–770. https://doi.org/10.1193/012414eqs016m
FEMA P-58-3 (2018). *"Seismic Performance Assessment of Buildings, Volume 3 – Supporting Electronic Materials and Background Documentation, Third Edition".*
Goodwin ER (2005). *"Experimental Evaluation of the Seismic Performance of Hospital Piping Subassemblies".* University of Nevada, Reno.
Jenkins C, Soroushian S, Rahmanishamsi E and Maragakis E (2017). "Experimental fragility analysis of pressurized fire sprinkler piping systems". *Journal of Earthquake Engineering,* **21**(1): 62–86. https://doi.org/10.1080/13632469.2016.1157528
LeGrone PD (2004). "An analysis of fire sprinkler system failures during the Northridge earthquake and comparison with the seismic design standard for these systems". *13 WCEE: 13 Th World Conference on Earthquake Engineering Conference Proceedings.*
Miranda E, Mosqueda G, Retamales R and Pekcan G (2012). "Performance of nonstructural components during the 27 February 2010 Chile earthquake". *Earthquake Spectra,* **28**(1_suppl1): 453–471. https://doi.org/10.1193/1.4000032
NFPA-13 (2010). *"NFPA 13: Standard for the Installation of Sprinkler Systems*". National Fire Protection Association (NFPA), US
NFPA-13 (2022). *"NFPA 13: Standard for the Installation of Sprinkler Systems*". National Fire Protection Association (NFPA), US
NHERI. (2023). NHERI Converging Design. https://tallwoodinstitute.org/converging-design-home-5663/ (Accessed 05 November 2024)
NIST (2017). "NIST.GCR.17-917-44: Seismic analysis, design, and installation of nonstructural components and systems-background and recommendations for future work". https://nvlpubs.nist.gov/nistpubs/gcr/2017/NIST.GCR.17-917-44.pdf
Pantoli E, Chen MC, Wang X, Astroza R, Ebrahimian H, Hutchinson TC, et al. (2016). "Full-scale structural and nonstructural building system performance during earthquakes: Part II–NCS damage states". *Earthquake Spectra,* **32**(2): 771–794. https://doi.org/10.1193/012414eqs017m
Rashid M (2022). "Seismic assessment and design of fire sprinkler piping systems". PhD Thesis. University of Canterbury, Christchurch, New Zealand. http://dx.doi.org/10.26021/12872
Soroushian S, Maragakis E, Ryan KL, Sato E, Sasaki T, Okazaki T, et al. (2016). "Seismic simulation of an integrated ceiling-partition wall-piping system at E-Defense. II: Evaluation of nonstructural damage and fragilities". *Journal of Structural Engineering,* **142**(2): 04015131. https://doi.org/10.1061/(ASCE)ST.1943-541X.0001385
Tian Y, Filiatrault A and Mosqueda G (2015). "Seismic response of pressurized fire sprinkler piping systems I: experimental study". *Journal of Earthquake Engineering,* **19**(4): 649–673. https://doi.org/10.1080/13632469.2014.994147
Tian Y, Filiatrault A and Mosqueda G (2013). *" Experimental Seismic Study of Pressurized Fire Sprinkler Piping Systems".* MCEER. https://www.eng.buffalo.edu/mceer-reports/13/13-0001.pdf
Wang T, Shang Q, Chen X and Li J (2019). "Experiments and fragility analyses of piping systems connected by grooved fit joints with large deformability". *Frontiers in Built Environment,* **5**: 49. https://doi.org/10.3389/fbuil.2019.00049

Strength Evaluation of Inserts Hardware for Building Equipment under Deck Composite Slab

Ichiro Hirano[1] and Shoichi Kishiki[2]

[1] Specially Appointed Assistant Professor, IIR., Institute of Science Tokyo, Dr. Eng.
4259, Nagatsuta, Midori-ku, Yokohama, Japan
e-mail: hirano.i.219e@m.isct.ac.jp
[2] Professor, IIR., Institute of Science Tokyo, Dr. Eng.
4259, Nagatsuta, Midori-ku, Yokohama, Japan
e-mail: kishiki.s.02d9@m.isct.ac.jp

Abstract. Earthquake damage to building equipment, such as air conditioning units, often concentrates at the connections to the structural frame. Insert hardware embedded in ceiling slabs is subjected to tensile forces under normal conditions and to additional horizontal and axial forces during earthquakes. Furthermore, the use of deck plates creates unevenness on ceiling slab surfaces, and the structural behavior of insert hardware under these conditions has not been sufficiently clarified. In this study, experiments were conducted considering various insert types, differences in ceiling slab surface geometry due to deck plate configurations, and different loading conditions.

Through tensile, shear, and combined loading tests, we confirmed that each insert type exhibits distinct structural behavior. These differences are largely influenced by the embedment length, screw length, and whether the insert hardware protrudes beyond the ceiling slab surface. In tensile and shear tests focusing on the differences in slab surface shape, tensile strength was higher for concave surfaces and lower for convex surfaces. Similarly, shear strength was lower for convex surfaces, and different failure modes were observed. In the combined loading tests, it was also confirmed that greater tensile force sustained by multiple inserts led to a reduction in shear strength.

Keywords: Building equipment, Insert hardware, Combined loading, Composite deck slab.

1. INTRODUCTION

Past earthquakes have confirmed significant damage directly leading to building functional loss, such as suspended lightweight equipment falling due to fracture of suspension bolts at connection parts or the equipment detaching from the frame [AIJ, 2015; Earthquake Reconstruction Support Conference Equipment Damage Prevention Study Committee, 2013; Tohoku Air Conditioning and Sanitation Constructors Association, 2012]. In contrast, the Society of Heating, Air-Conditioning and Sanitary Engineers of Japan [2023] specifies in *Seismic Design and Construction Methods for Building Equipment (SHASE-S standard)* measures to prevent falling and lateral sway for suspended lightweight equipment weighing 1 kN or less, aiming to ensure equipment functionality after an earthquake. For example, the method shown in Figure 1, using full-threaded bolts to prevent lateral sway of suspended lightweight equipment, is cited. Furthermore, the Building Center of Japan [2014]'s *Guidelines for Seismic Design and Construction of Building Equipment* recommends using inserts as the primary method for connecting suspension bolts to the frame. Therefore, Inserts have an important part in the seismic support of these equipment.

Regarding inserts, SHASE [2004]'s *SHASE-S009-2004: Inserts for Building Equipment* specifies basic requirements such as insert types, shapes, and thread dimensions, serving as a standard for their use in supporting equipment and piping. However, three challenges exist in guaranteeing insert's seismic performance: First, inserts vary not only in shape but also in the position where suspension bolts are installed. The effect of these variations on the structural behavior of inserts has not been fully clarified. Second, the shape of the ceiling slab where inserts are installed varies. For example, when using deck plates, concave and convex parts are formed in the ceiling slab (Figure 1, right). Inserts are generally installed on the concave part to ensure their strength [SHASE, 2021]. Although previous studies have confirmed the effect of differences between concave and convex on their strength [Tsuchiya et al., 2020; Nakagawa et al., 2024], understanding the phenomena has not been achieved. Finally, inserts are subjected to horizontal forces and axial forces variations during earthquakes in addition to equipment weight. However, most studies have focused on tensile strength, and investigations under combined tensile and shear loading are insufficient. This study conducts experiments targeting inserts for building equipment, focusing on insert type, surrounding concrete geometry, and loading method. Furthermore, based on these results, it investigates the ultimate strength for tension and shear, as well as the allowable strength under combined tensile and shear loading.

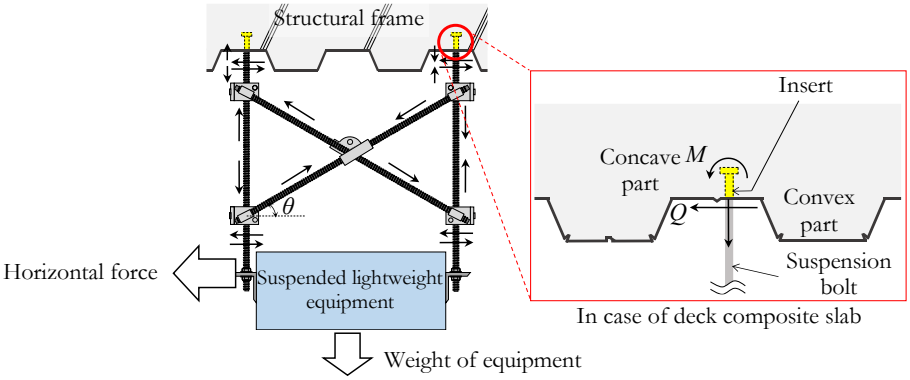


Figure 1. An example of general installation method for suspended lightweight equipment and the stress state of insert during earthquake

2.TEST OVERVIEW

2.1 OVERVIEW OF INSERTS

The inserts used in this experiment are shown in Figure 2. Generally, inserts are broadly categorized into those for plywood formwork and those for deck plates, with the latter further classified into embedded and

protruding types. In this paper, the plywood formwork insert is expressed as TC, while the embedded and protruding deck plate inserts are expressed as SHF and SH, respectively. The plywood formwork insert features a resin-coated insert section. Although its embedment length is shorter than the other inserts, it has a larger head diameter. The embedded type of deck plate insert was developed as a countermeasure against shear forces during earthquakes, allowing the suspension bolts to be inserted into the interior of the ceiling slab. In contrast, the protruding type allows the suspension bolts to be inserted externally, on the outer surface of the slab. Additionally, to confirm the effect of the insert's effective screw length S on the structural behaviour, one type with S =13mm for plywood formwork and two types with S =13mm and 25mm for deck plates were prepared for both the embedded and protruding types. The nominal size of the insert screws is W3/8 (diameter: approx. 9.5 mm), which is standard for building equipment suspension materials.

2.2 TEST PARAMETERS

The test specimens consist of an insert and surrounding concrete simulating a ceiling slab. The test parameters are insert type, surrounding concrete geometry, and the loading conditions. Five insert types (see previous section) were tested with flat geometry (0°). In addition to the flat case, concave and convex specimens were prepared using SHF-13, as shown in Figure. 3, varying the deck angle θ and insert position. The deck angle is defined as negative for convex and positive for concave, with flat (0°) as the reference. Four convex angles (-90° , -60° , -45°, -30°) and four concave angles (+90°, +60°, +45°, +30°) were prepared. Insert positions either symmetric and asymmetric. In deck-parallel sections, the edge clearance on one side was standardized to 40 mm, with 80 mm and 120 mm for symmetric and asymmetric configurations, respectively. In this paper, the surface corresponding to this section is referred to as the "surrounding concrete interface". The concrete compressive strength during testing was approximately σ_B = 24 N/mm². For each loading condition (tensile, shear, combined), multiple specimens were prepared with identical parameters. In combined loading, shear force was cyclically applied while maintaining tensile force. Four tensile force ratios, T/T_u = 0.20, 0.40, 0.70, and 0.85 were used, based on the ultimate tensile strength T_u.

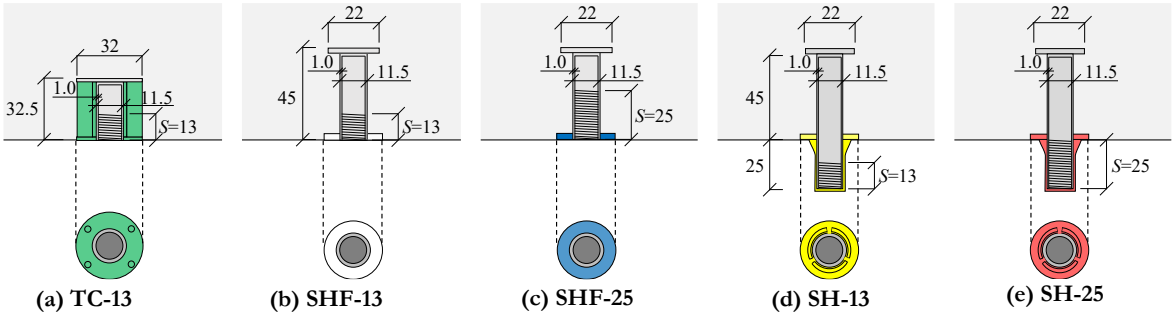


Figure 2. W3/8 inserts used in this experiment

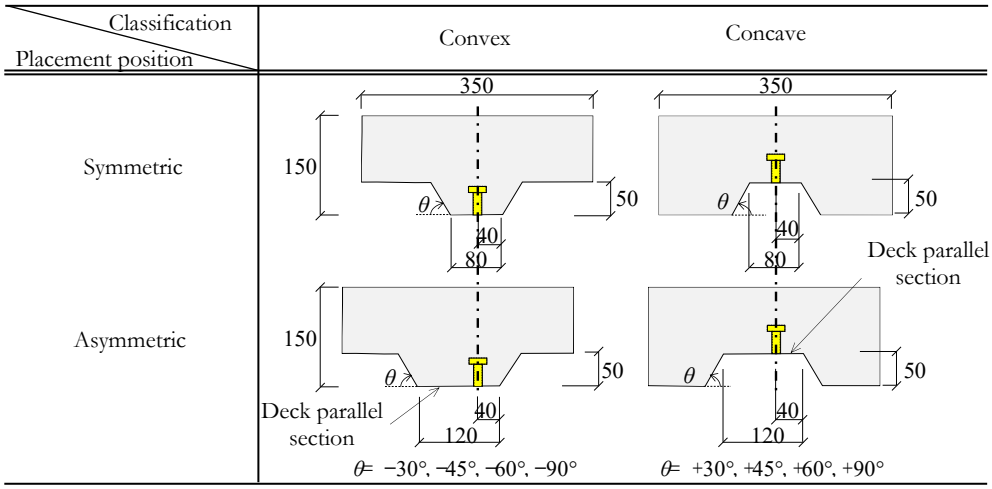


Figure 3. The geometry of surrounding concrete

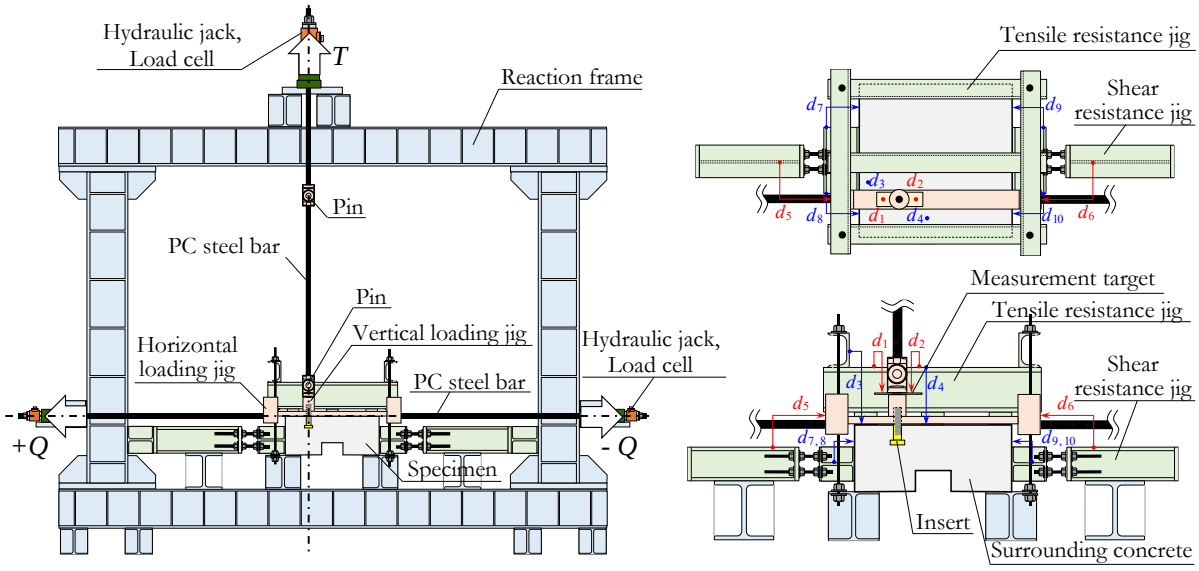
2.3 TEST SETUP AND MEASUREMENT METHOD

The setup is shown in Figure 4 (a), illustrating the combined loading test of inserts. The specimen is placed on the reaction frame, with tensile and shear resistance jigs positioned vertically and horizontally, respectively. The insert is connected vertically to the hydraulic jack on the upper beam side via the vertical loading jig, pin, and PC steel bar, and horizontally to the hydraulic jacks on the column side of the reaction frame via the horizontal loading jig and PC steel bar. The insert and vertical loading jig are connected by a full-thread bolt, inserted to the tip of the insert's threaded section.

The measurement method is shown in Figure 4 (b). Vertical deformation is obtained by subtracting the surrounding concrete's vertical displacement (d_3, d_4) from that of the target point below the pin (d_1, d_2). Horizontal deformation is obtained by subtracting the surrounding concrete's displacement (d_7 to d_{10}) from that of the horizontal loading jig (d_5, d_6). Loading is applied using hydraulic jacks on the column and upper beam sides of the reaction frame. Tensile and shear loads (T and Q) are obtained from load cell measurement.

2.4 LOADING METHOD

The loading methods are described below. For each loading condition, continue until specimen failure is confirmed, such as a sudden loss of strength. For tensile loading, use monotonic and unidirectional incremental cycles. For shear loading, use monotonic and alternating positive-negative incremental cycles. For combined loading, as described in Section 2.2, shear loading is applied while maintaining the tensile force. The yield shear strength Q_y is defined as the shear load at which the tangent to the hysteresis curve reaches a slope of 1/6 of the initial stiffness, as determined from prior monotonic loading test results.



(a) Test setup **(b) Measurement method**

Figure 4. Test setup and measurement method (Combined loading)

3.ULTIMATE TENSILE AND SHEAR STREGTH OF INSERTS

3.1 EFFECTS OF DIFFERENT INSERT TYPES

The load-deformation relationship comparing insert types is shown in Figure 5. The Figure shows the relationship between tensile load T and vertical deformation δ_T, and between shear load Q and horizontal deformation δ_S. It presents results for monotonic loading under tensile conditions and cyclic loading under shear conditions. For shear loading, the gray line represents the hysteresis curve obtained from experiments, while the black line shows the envelope curve extracted from the hysteresis curve. Among the positive and negative envelope curves, the side with the higher ultimate shear strength is shown in the first quadrant.

Examining the tensile loading (Figure 5(a)), the ultimate tensile strength for the shorter embedment length (TC-13) is lower than that for the longer embedment length (SHF, SH). Furthermore, the embedded type (SHF) exhibits a higher ultimate tensile strength than the protruding type (SH). Comparing inserts of the same type, the ultimate tensile strength increases slightly with longer effective screw length. Therefore, the ultimate tensile strength of inserts is influenced by embedment length, the protrusion from the surrounding concrete interface, and effective screw length. On the other hand, regarding shear loading (Figure 5(b)), the ultimate shear strength of the shorter embedment length (TC-13) is lower than that for the longer embedment length (SHF). Furthermore, the protruding type (SH) exhibits the lowest ultimate shear strength, being less than half that of the embedded type. Therefore, the ultimate shear strength of the insert is influenced by the embedment length and the protrusion from the surrounding concrete interface.

3.2 EFFECTS OF DIFFERENCE IN SURROUNDING CONCRETE GEOMETRY

Next, the load-deformation relationships comparing surrounding concrete geometry are shown in Figure 6. The representation is the same as in Figure 5. Note that the figures distinguish symmetrically and asymmetrically installed inserts using orange and blue lines, respectively. For shear loading, to compare the side with the shorter span length, the side with the lower ultimate shear strength is shown in the first quadrant.

Examining the load-deformation relationship under tensile loading (Figure 6(a)), the ultimate tensile strength of the concave specimens tends to increase as the deck angle increases. Conversely, the ultimate tensile strength of the convex specimens tends to decrease as the deck angle decreases. Comparing the insert installation positions, the ultimate tensile strength when installed symmetrically is lower than asymmetrically. On the other hand, regarding shear loading (Figure 6 (b)), the ultimate shear strength is nearly equal within the range of -60° to 0°, with a significant decrease observed only at -90°. Furthermore, within the scope of this experiment, no influence due to differences in the insert installation position was observed.

3.3 FAILURE MODE

Figure 7 shows the failure mode observed in this experiment. Under tensile loading, cone failure was observed in all specimens except for the +30° specimen (Figure 7(a)). In contrast, under shear loading, fracture of insert (Figure 7(b)) was the primary failure mode, and in some cases, fracture of the full-thread bolts connecting the vertical loading jig to the insert was also observed (Figure 7(c)). Furthermore, under shear loading tests focusing on surrounding concrete geometry, cracking was observed only at -90°, where the ultimate shear strength was significantly lower than elsewhere (Figure 7(d)). The cracking of the surrounding concrete was similar to concrete edge failure, occurring radially from the insert toward the edge.

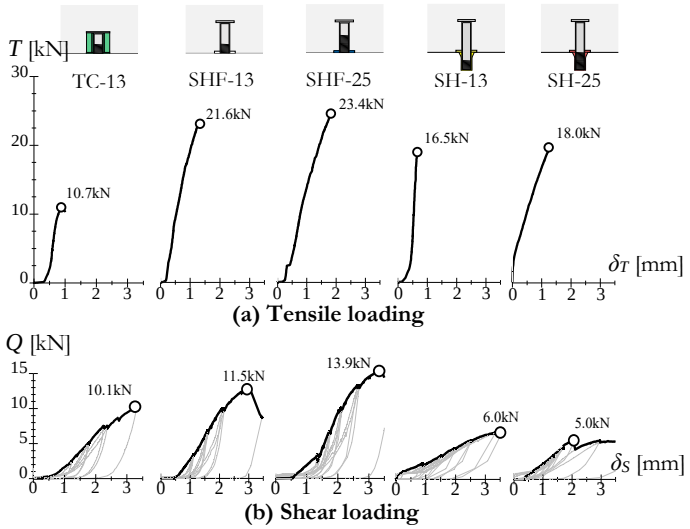
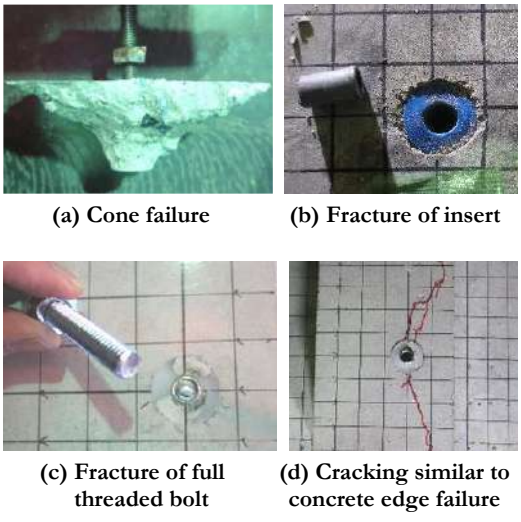


Figure 5. Load-deformation relationships comparing difference in insert type



(a) Cone failure **(b) Fracture of insert**

(c) Fracture of full threaded bolt **(d) Cracking similar to concrete edge failure**

Figure 7. Failure mode observed in this experiment

3.4 EVALUATION OF ULTIMATE TENSILE AND SHEAR STRENGTH

3.4.1 Effects of Different Insert Types

Focusing on the type of insert, we analyse the ultimate tensile strength T_u and ultimate shear strength Q_u. Here, representing the differences in insert types, we focus on the distance from the surrounding concrete interface to the tip of the insert's threaded portion (thread tip distance y) and show its relationship with T_u and Q_u in Figure 9. Note that the thread tip distance y is defined with the surrounding concrete interface as the origin, where the embedded type is positive and the protruding type is negative (Figure 8). Furthermore, for the ultimate tensile strength, the cone failure strength T_{cone} is obtained from the following equation, citing AIJ [2023]'s *Recommendation for Design of Composite Structures*, and is also shown in Figure 9.

$$T_{cone} = 0.31\sqrt{\sigma_B} \cdot A_c \tag{1}$$

In the equation, σ_B is the compressive strength of concrete (=24.1 N/mm²), and A_c is the effective horizontal projected area of the cone failure surface.

First, examining the ultimate tensile strength T_u (Figure 9(a)), the ultimate tensile strength for TC-13 is less than about 50% of that for SHF-13 with the same effective screw length, clearly showing the influence of embedment length. On the other hand, comparing deck plate applications, T_u and y show an almost

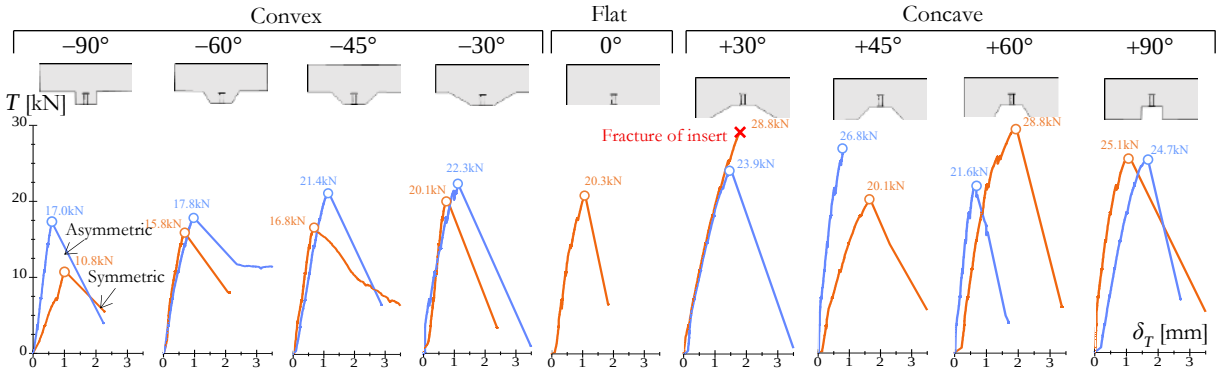


Figure 6. Load-deformation relationships comparing difference in surrounding concrete geometry

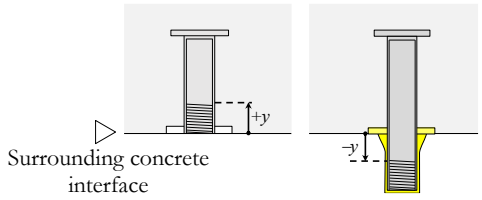


Figure 8. The definition of thread tips distance *y*

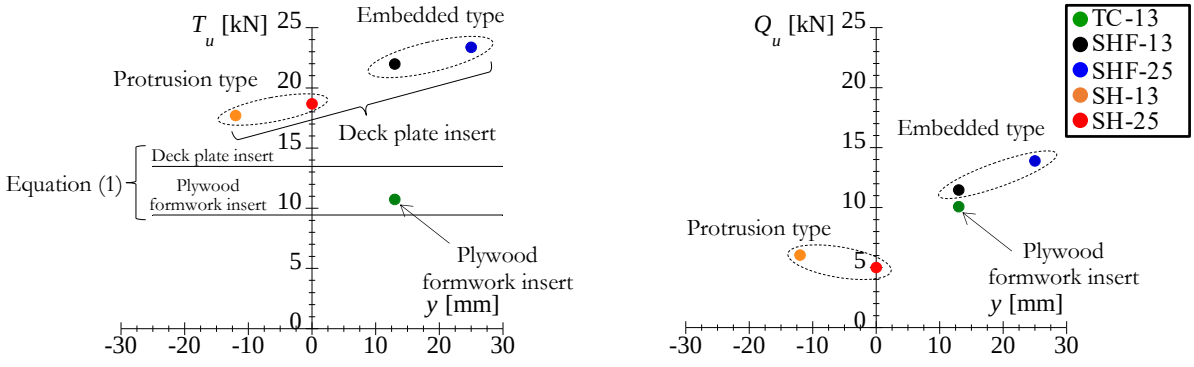


Figure 9. The relationships between ultimate strength and thread tip distance *y*

proportional relationship. Comparing the same effective screw lengths, the ultimate tensile strength of the protruding type is about 80% of the embedded type. The increase in ultimate tensile strength as the thread tip distance deeper into the concrete is thought to occur. Compared to the calculated cone failure strength, even for the insert with the smallest thread tip distance (SH-13), where the contribution of friction force is considered small, the ultimate tensile strength is safely evaluated. Next, examining the ultimate shear strength Q_u (Figure 9(b)), the ultimate shear strength increases as the thread tip distance y increases. The ultimate shear strength of the protruding type is approximately 36 to 60% of that for the embedded type and plywood formwork type. The ultimate shear strength is often determined by the fracture of the insert, with the fracture location occurring near the tip of the screw or the surrounding concrete interface.

3.4.2 Ultimate Tensile Strength When the Surrounding Concrete Geometry Differs

This study investigates a method to reflect deck shape difference into A_c based on the evaluation formula for cone failure strength (Equation (1)). In this experiment, the effective horizontal projection area of convex specimens is diagonally reduced from the edge, while that of concave specimens is increased (Figure 10). The surrounding concrete geometry are categorized as convex ($-90° \leq \theta < 0°$), flat ($\theta=0°$), and concave ($0° < \theta \leq +90°$). For flat (0°) case, a typical cone failure surface forms, A_c is given by the following equation.

$$A_c = \pi L(L+B) \tag{2}$$

Here, L is the embedment length, and B is the insert head diameter. For convenience in subsequent explanations, the effective horizontal projection area for the flat (0°) case is expressed as A_{c0}.

In the convex specimens ($-90° \leq \theta < 0°$), the cone failure surface intersects the deck slope section above the surrounding concrete interface. At $\theta = -90°$ (Figure 10(a)), A_c is smallest due to a right-angle notch. For

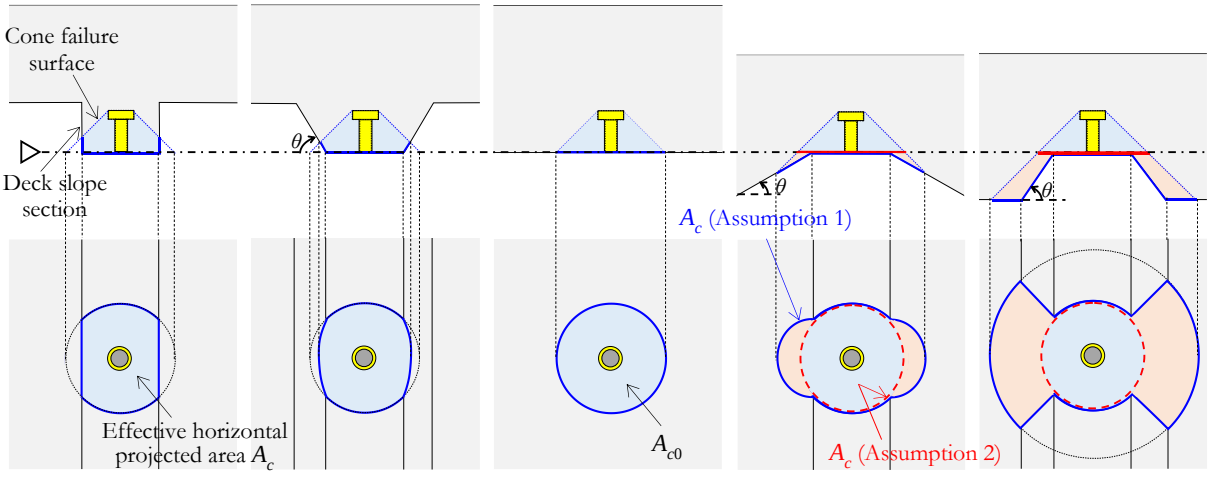


Figure 10. Concept of effective horizontal projection area A_c for deck shapes (Tensile loading)

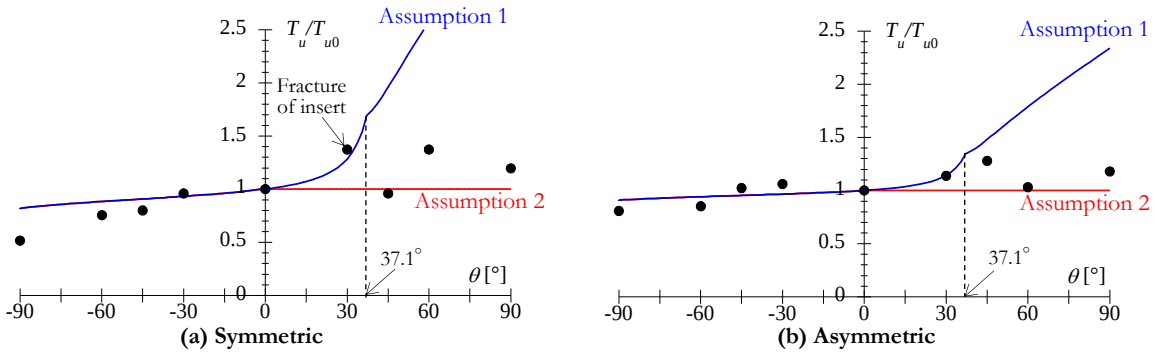


Figure 11. Ultimate tensile strength when surrounding concrete geometry differs

$-90° < \theta < 0°$ (Figure 10(b)), A_c is calculated by subtracting the notched portion from A_{c0}. In the concave specimens ($0° < \theta \leq +90°$), the cone failure surface intersects either the deck slope section or the bottom surface of the surrounding concrete. Two patterns are considered based on a boundary angle (37.1°) (Figure 10(d)(e)). In the first case, A_c is calculated by adding the projection area of the intersection (red portion in Figure 10(d)) to A_{c0} (blue solid line in Figure 10(d)). – This is "Assumption 1". In the second, A_c is defined based on continuity with the convex section. – "Assumption 2". In this case, A_{c0} equals that for the flat slab.

Figure 11 shows the ratio T_u/T_{u0} relative to the ultimate tensile strength T_{u0} at flat (0°) as the vertical axis and the deck angle θ as the horizontal axis. Experimental results are shown as ● plots; calculations based on Assumption 1 and 2 are shown by blue and red lines, respectively. In the convex section, T_u decreases almost linearly to −90°, and calculated values capture this trend, indicating that notching due to deck inclination is well reflected in A_c. On the other hand, in the concave section, experimental T_u values vary. Assumption 1 overestimates the experimental values beyond +37.1°, while Assumption 2 generally evaluates on the safe side. Therefore, areas where A_c increases due to slope should not be considered (red portion in Figure 10). Consequently, to ensure the ultimate tensile strength, inserts should be installed in concave part where strength is equal to or greater than that of the flat slab.

3.4.3 Ultimate Shear Strength When the Surrounding Concrete Geometry Differs

Next, the ultimate shear strength evaluated based on Q_{cone}, determined by concrete edge failure, using the AIJ [2023]'s *Recommendation for Design of Composite Structures*. Q_{cone} is expressed by the following equation.

$$Q_{cone} = 0.31\sqrt{\sigma_B} \cdot A_{qc} \tag{3}$$

Here, σ_B is the concrete compressive strength (=24.1 N/mm²), and A_{qc} is the effective horizontal projection area of the shear failure surface, generally $A_{qc} = 0.5\pi c^2$ (c: edge clearance). To account for deck shape effects on A_{qc}, a method is proposed as follows.

In the convex section, as the deck angle θ increases, the intersection between the cone failure surface and the deck slope moves outward from the insert central point, increasing Q_{cone}. Further increases in θ causes failure surface to no longer intersects the deck slope. Therefore, a pseudo-edge-clearance c_p is defined (Figure 12).

- For $-90° \leq \theta \leq -78.7°$ (Figure 12(a)), c_p is the horizontal distance to the intersection point.
- For $-78.7° < \theta \leq -24.4°$ (Figure 12(b)), c_p is the horizontal distance to the end of the deck slope.

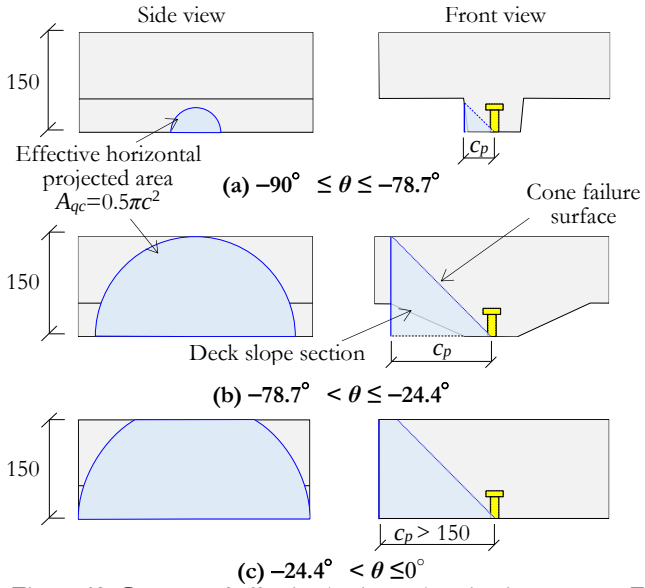


Figure 12. Concept of effective horizontal projection area A_{qc} for deck shapes (Shear loading)

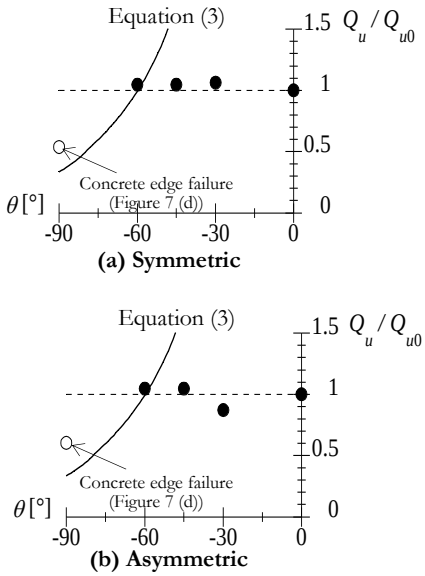


Figure 13. Ultimate shear strength when surrounding concrete geometry differs

These effective horizontal projection areas A_{qc} are expressed by the following equations.

$$A_{qc} = 0.5\pi c_p^2 \tag{4}$$

Furthermore, when the horizontal distance to the end of the deck slope exceeds the surrounding concrete thickness (150 mm, -24.4° < $\theta \leq$ 0°), the semicircle is notched by the top surface. In this case, the notched portion is subtracted from A_{qc} (Figure 12(c)). Figure 13 shows the ratio Q_u/Q_{u0} relative to the ultimate shear strength Q_{u0} at flat (0°) on the vertical axis and the deck angle θ on the horizontal axis. Experimental values (●, ○) reflect different failure modes; calculated values from equation (3) are shown as solid lines. As seen in Section 3.2, the experimental values remain nearly flat at $\theta \geq$ -60°, but drop significantly at -90°. Calculated values follow a similar trend, exceeding 1.0 at angles ≥ -60°, and dropping below 1.0 at -90°, capturing both strength and failure characteristics. However, the consideration of the downward trend from −60° to −90° remains a future study.

4. ALLOWABLE STRENGTH UNDER COMBINED LOADING

4.1 LOADING-DEFORMATION RELATIONSHIPS

The load-deformation relationship for each insert under combined loading is shown in Figure 14. The vertical axis represents the shear load Q, the horizontal axis represents the horizontal deformation δ_S, and the colors distinguish the magnitude of the tensile force T/T_u applied to the specimen. Note that among the positive and negative envelope curves, the side with the higher ultimate shear strength is shown in the first quadrant. Furthermore, the experimentally obtained elastic limit shear strength Q_e and ultimate shear strength Q_u are plotted as △ and ○, respectively. The elastic limit shear strength Q_e is defined as the shear load at which the tangent stiffness on the envelope curve decreases by approximately 10% from the initial stiffness. For TC-13, the difference in ultimate shear strength due to variations in tensile force magnitude is small, but the elastic limit shear strength tends to decrease as the tensile force increases. For SHF, SH, both the ultimate shear strength and elastic limit shear strength tend to decrease as tensile force increases, confirming the influence of combined loading.

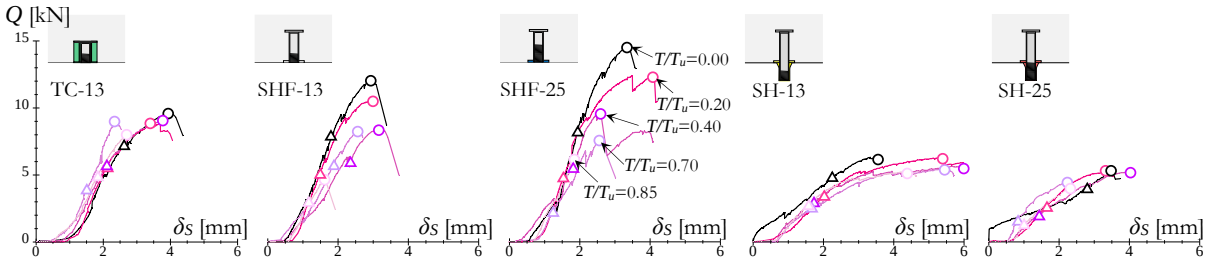


Figure 14. Load-deformation relationships (Combined loading)

4.2 EVALUATION OF STRENGTH UNDER COMBINED LOADING

4.2.1 Structural Model

This section evaluates the strength of inserts under combined tensile and shear loading based on the *M-N* interaction curve at the critical section. First, consider the structural model of the insert as shown in Figure 15. The insert is assumed to receive triangularly distributed reaction forces within the concrete. Let y_n be the distance from the surrounding concrete interface to the point where the reaction force direction changes, and let α be the slope of the reaction force distribution. From force equilibrium, the following equation holds:

$$Q - \frac{\alpha y_n^2}{2} + \frac{\alpha (L - y_n)^2}{2} = 0 \tag{5}$$

From the moment equilibrium around the surrounding concrete interface, the following equation holds:

$$\frac{\alpha y_n^2}{2} \cdot \frac{y_n}{3} - \frac{\alpha (L - y_n)^2}{2} \cdot \{ y_n + \frac{2}{3}(L - y_n) \} = 0 \tag{6}$$

Here, L is the embedment length of the insert, and Q is the elastic limit shear load or ultimate shear load from experiments. Furthermore, the bending moment $M(y)$ of the insert at an arbitrary position y from the surrounding concrete interface is expressed by the following equation.

$$M(y) = Q\left(\frac{y^3}{L^2} - \frac{2y^2}{L} + y\right) \tag{7}$$

From equation (7), the embedded type achieves its maximum bending moment, $4QL/27$, at $y = L/3$. Next, consider the maximum bending moment for the protruding type. Although fracture near the surrounding concrete interface has been observed in many cases, this corresponds to the inflection point. Thus, the experiments suggest a slight deviation between the inflection point and the structural model. The maximum moment is assumed to be $1.0D$ (D: insert outer diameter) from the surrounding concrete interface.

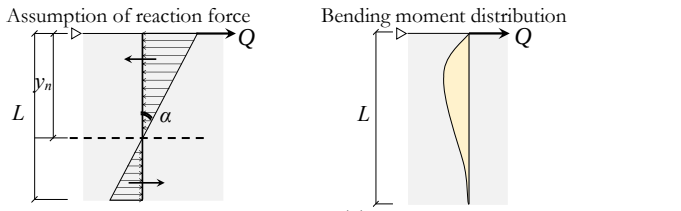
4.2.2 Evaluation Based on M-N Interaction Curve

The allowable strength of the insert is calculated as a circular hollow section, as shown in Figure 16. The yield moment M_{yc} and total plastic moment M_{pc} under tension are determined by the following equations, respectively, based on AIJ [2019]'s *Recommendations for Plastic Design of Steel Structures*.

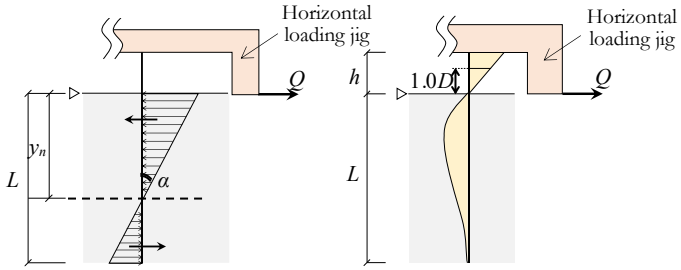
$$M_{yc} = \left(1 - \frac{T}{T_y}\right) M_y \tag{8}$$

$$M_{pc} = \cos\left(\frac{\pi}{2} \cdot \frac{T}{T_y}\right) M_p \tag{9}$$

Here, T_y is the yield tensile strength, calculated from the yield point σ_y and cross-sectional area. The T-Q interaction curve is obtained from the structural model in Section 4.2.1 and Equations (8) and (9). The allowable strength under combined loading is schematically illustrated in Figure 17, where the vertical axis is tensile load T and the horizontal axis is shear load Q. Equation (1), (8), and (9) are shown as solid lines;



(a) Embedded type (TC, SHF)



(b) Protrusion type (SH)

Figure 15. Structural model

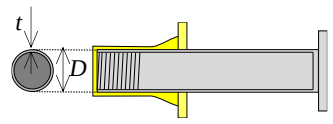


Figure 16. Assumption of cross-section

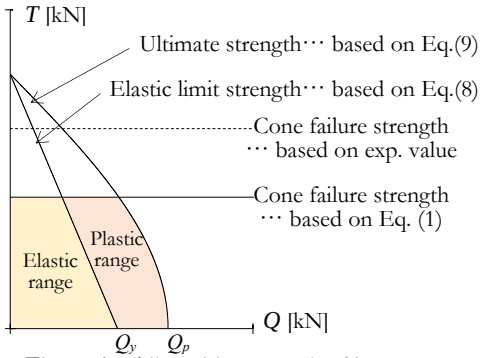


Figure 17. Allowable strength of inserts under combined loading

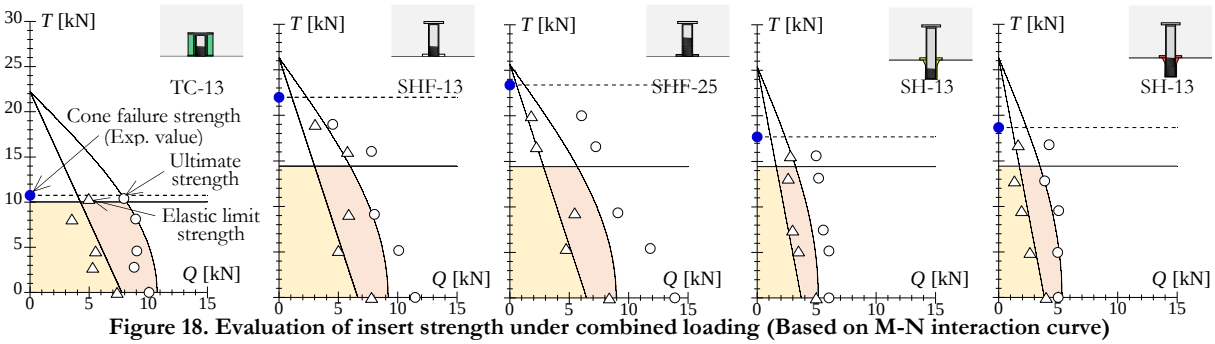


Figure 18. Evaluation of insert strength under combined loading (Based on M-N interaction curve)

experimental cone failure strength is shown as dashed lines. Given the insert's high yield ratio, the total plastic moment is taken as the ultimate strength. Thus, the range of allowable strength under combined loading, where neither yielding, fracture, nor cone failure occurs, is represented by the colored area. Figure 18 compares the allowable strength of tested inserts under combined loading with experimental results. In the figure, ●, △, and ○ indicate cone failure strength, elastic limit, and ultimate shear strength, respectively. For all inserts, the experimental elastic limit and ultimate shear strengths generally correspond to equations (8) and (9), respectively. Therefore, the allowable strength under combined loading can be evaluated using the *M-N* interaction curve at the critical section, and the tensile force upper limit is dominated by cone failure.

5. CONCLUSION

This study conducted experiments focusing on inserts for building equipment, examining insert type, surrounding concrete geometry, and loading conditions. The main findings are as follows.

1) For different insert types, ultimate tensile and shear strengths vary significantly, mainly due to embedment length and whether the insert protrudes from surrounding concrete. For different surrounding concrete geometries, tensile strength remained nearly constant in concave specimens, whereas it decreased in convex ones as deck angle decreased. To ensure strength greater than flat slabs, inserts should be installed in the concave section.

2) Ultimate shear strength showed a marked drop only at $\theta = -90°$, where edge-like cracking was observed. In contrast, incorporating deck shape differences into effective horizontal projected area resulted in agreement with experiments. However, the decreasing trend from $-60°$ to $-90°$ remains to be verified.

3) Shear strength under combined loading decreases with increasing tensile force. A method incorporating reaction force distribution and the M–N interaction curve at the critical section was developed. This enables evaluation of both elastic limit and ultimate shear strength under combined loading.

REFERENCES

AIJ [2023]: *Recommendations for Design of Composite Constructions*, Architectural Institute of Japan, Japan (in Japanese)

AIJ [2019]: *Recommendations for Plastic Design of Steel Structures*, Architectural Institute of Japan, Japan (in Japanese)

AIJ [2015]: Report on The Great East Japan Earthquake Disaster, Building Series Volume 8 Building Equipment and Environment, Architectural Institute of Japan, Japan (in Japanese)

BCJ [2014]: *Guidelines for Seismic Design and Construction of Building Equipment*, The Building Center of Japan, Japan (in Japanese)

Earthquake Reconstruction Support Conference Equipment Damage Prevention Study Committee [2013]: Report on Damage to Equipment and Seismic Countermeasures due to The Great East Japan Earthquake (in Japanese)

Nakagawa M., et al. [2024] "Experimental Study on Pull-out and Shear Strength of Ceiling Inserts Embedded in Composite Steel Deck Slab, Part1,2", *Summaries of Technical Papers of Annual Meeting, Architectural Institute of Japan*, pp.683-686 (in Japanese)

SHASE [2023]: *Seismic Design and Construction Methods for Building Equipment*, The Society of Heating, Air-Conditioning and Sanitary Engineers of Japan, Japan (in Japanese)

SHASE [2004]: *SHASE-S Standard, SHASE-S009-2004, Inserts for Mechanical and Electrical Equipment*, The Society of Heating, Air-Conditioning and Sanitary Engineers of Japan, Japan (in Japanese)

SHASE [2021]: *SHASE-S Standard, SHASE-S012-2021, Post Installen Anchor for Building Equipment*, The Society of Heating, Air-Conditioning and Sanitary Engineers of Japan, Japan (in Japanese)

Tsuchiya H., et al. [2020] "Experimental Study on Pull-out Strength of Composite Steel Deck Slab of Inserts for Building Equipment, Part1,2", *Technical Papers of Annual Meeting the Society of Heating, Air-conditioning and Sanitary Engineers of Japan*, pp.61-68 (in Japanese)

Tohoku Air Conditioning and Sanitation Constructors Association [2012] Report on Damage to Equipment Caused by The Great East Japan Earthquake (in Japanese)

Seismic Fragility Assessment of Industrial Pallet Racks in Italy

Marco Donà[123], Alberto Zonta[1], Marco Ceresara[1], and Francesca da Porto[1]

[1] Department of Geosciences, University of Padova, Via Gradenigo 6, 35131 Padova, Italy
e-mail: marco.dona.1@unipd.it; alberto.zonta@dicea.unipd.it; marco.ceresara@phd.unipd.it; francesca.daporto@unipd.it;
[2] Department of Cultural Heritage, University of Padova, Piazza Capitaniato 7, 35139 Padova, Italy
[3] Department of Information Engineering, University of Padova, Via Gradenigo 6/b, 35131 Padova, Italy

Abstract. Steel pallet racks are critical non-structural systems widely used in warehouses and production facilities. Despite their apparent simplicity, their seismic vulnerability can strongly influence the overall risk profile of industrial assets –especially in seismic-prone regions. Past earthquake events have shown that rack collapses not only endanger worker safety but can also trigger major economic losses due to damage to stored goods, prolonged production downtime, and supply chain disruptions. Yet, their seismic behaviour remains understudied, and quantitative tools for assessing their seismic fragility are still limited.

This study addresses this gap by proposing a robust and scalable methodology for seismic fragility assessment of industrial pallet racks. A stock of unbraced rack configurations, representative of the Italian context, was analysed through advanced 3D nonlinear finite element modelling and cloud-based time-history analysis. Fragility curves were derived with respect to multiple Engineering Demand Parameters (EDPs) and seismic Intensity Measures (IMs), considering both rigid and soft soil conditions. The results reveal the considerable seismic vulnerability of the investigated systems and identify global upright strain as the most reliable performance indicator for collapse. Specifically, rack failure is governed by the combined effects of axial–flexural deformation in the uprights, the nonlinear behaviour of beam-to-column joints, and the directionality of the seismic input. These findings, along with the proposed fragility models, can support the development of targeted seismic risk mitigation strategies, as well as more informed and effective industrial safety planning.

Keywords: Industrial pallet racks, Nonlinear finite element models, Time-history analysis, Cloud approach, Seismic fragility models.

1. INTRODUCTION

In recent years, the continuous growth of globalization and e-commerce has greatly increased the need for industrial storage solutions. Among these, standard adjustable steel pallet racks are the most used system in warehouses and logistics centres due to their modularity, versatility, and cost-effectiveness. These systems are typically composed of thin-walled cold-formed steel profiles, which are bolted or slotted together to create frame assemblies with multiple pallet levels. Their widespread adoption in Italy and many other countries is largely due to their ease of installation and adaptability to changing operational requirements.

However, pallet racks –especially unbraced configurations– exhibit significant seismic vulnerability. This is mainly due to several interacting features: high live loads even in service conditions, semi-rigid beam-to-column (*btc*) connections, the limited ductility of cold-formed open-section profiles, and the high slenderness of the vertical elements. Under seismic excitation, these characteristics lead to substantial lateral deformability, poor energy dissipation, and sensitivity to local or global instability mechanisms. In particular, the absence of longitudinal bracing –often omitted to facilitate forklift operations– drastically reduces the lateral stiffness in the down-aisle direction (X), making racks highly flexible and prone to global instability under seismic loads. In contrast, the cross-aisle direction (Y) is typically braced with diagonal and horizontal members, resulting in a significantly stiffer response. This directional asymmetry results in a complex seismic response: while the rack undergoes large deformations and potential instability along the unbraced direction, it is subjected to significant acceleration demands along the braced axis, as the greater stiffness in this direction tends to amplify the seismic input.

The damage observed after recent Italian earthquakes, including the 2012 Emilia-Romagna and 2016 Central Italy events, clearly demonstrated that pallet racks not only pose a risk to worker safety but also play a crucial role in the economic impact of seismic events [Perrone et al. 2019]. Their collapse can lead to both direct damage –e.g., loss of goods and equipment– and indirect losses –e.g., long business interruptions [Donà et al. 2019]. In several cases, rack failures caused prolonged downtime in entire industrial districts, aggravating the socio-economic consequences of the earthquake and severely affecting the regional supply chains.

The seismic performance of pallet racks has been the subject of several research initiatives at both the component and system level. Some experimental studies have investigated the buckling mechanisms and cyclic behaviour of cold-formed profiles under axial and flexural loading [e.g., Padilla-Llano et al. 2014]. Others have focused on the rotational response of *btc* connections, whose nonlinear and pinched hysteresis behaviour strongly influences the lateral response of racking systems and their dynamics [e.g., Bernuzzi and Castiglioni 2001]. Large-scale testing campaigns –such as SEISRACKS [Proença et al. 2009] and SEISRACKS2 [Drei et al. 2014]– have further advanced the understanding of rack behaviour through full-scale tests and provided data for the development of seismic design guidelines [e.g., CEN 2016]. Previous studies have consistently highlighted the high seismic vulnerability of pallet rack systems. In response, some technological solutions have been proposed to improve their performance, including base isolation systems [Simoncelli et al. 2020], energy-dissipating devices [Shaheen and Rasmussen 2022], and load-level isolation strategies [Donà et al. 2022, Bernardi et al. 2023]. However, only a few studies have specifically quantified the seismic fragility of these systems, despite its clear importance. Gabbianelli et al. [2020] derived fragility curves for two typical Italian rack types using 2D models and multiple-stripe analysis, while Nuñez et al. [2023] assessed four Chilean archetypes through 3D modelling and incremental dynamic analysis. These contributions, though valuable, underscore the lack of comprehensive fragility assessments for pallet racks and highlight the need for further research.

To address this gap, this study proposes a methodology for seismic fragility assessment of pallet racks, based on a cloud-type approach and 3D non-linear finite element modelling. A series of fragility models was developed for a stock of unbraced pallet racks used in Italy, considering ground motion sets representative of rigid and soft soils, and multiple engineering demand parameters (EDPs) and intensity measures (IMs).

2. SEISMIC FRAGILITY ASSESSMENT METHODOLOGY

2.1 PARAMETRIC TH ANALYSIS FRAMEWORK

The study focuses on a representative stock of 27 unbraced steel pallet rack configurations, commonly found in the Italian industrial sector. The rack systems are assumed to be designed for gravity loads only, with no consideration for seismic actions in their original design. All racks follow the same longitudinal and transverse plan geometry (Figure 1a): seven longitudinal bays of 2700 mm and two transverse frames of 1000 mm each, with a 300 mm gap. The 27 configurations (Figure 1b) are defined through the systematic combination of three parameters: upright cross-section type (U_1, U_2, U_3), load-level height (h_1=1.0 m, h_2=1.5 m, h_3=2.0 m), and total rack height (H_1=6 m, H_2=9 m, H_3=12 m).

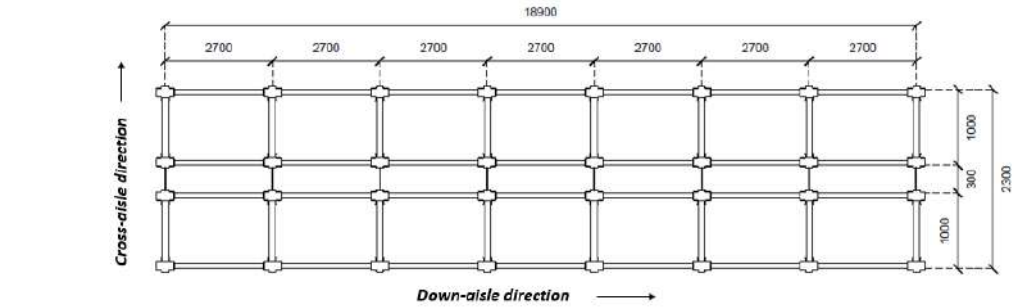
Each combination defines a unique configuration with specific vibration characteristics. The number of load levels per rack thus varies depending on the H/h ratio, from 3 to 12 levels. Importantly, the applied pallet loads (Figure 1b) were calculated based on the static bearing capacity of each transverse frame, which depends on the upright type and load-level height. This approach ensures comparable compressive stress conditions at the upright bases across racks, enabling consistent comparisons in fragility analysis.

For each configuration, the seismic analysis assumes a full-load condition, i.e., all pallet levels are occupied, which is considered the most demanding case for a comprehensive fragility evaluation. Therefore, load spatial variability is not considered in this study. Pallet loads are applied to a dummy pyramidal substructure that correctly locates each pallet's centre of gravity. A friction contact element beneath the pallets then models sliding in the cross-aisle direction once the friction force –calculated by using a friction coefficient μ_s=0.37 (for wood-to-steel contact, as per EN 16681 [CEN 2016])– is exceeded. Figure 2 shows the 3D FE model of the intermediate rack configuration alongside the cross sections of the main rack elements: pallet beams are Class 3 cold-formed profiles, while uprights and bracing elements fall into Class 4 (CEN 2005). Accordingly, local and distortional buckling effects in the Class 4 profiles were captured by reducing their stiffness and strength, whereas global buckling was explicitly modelled.

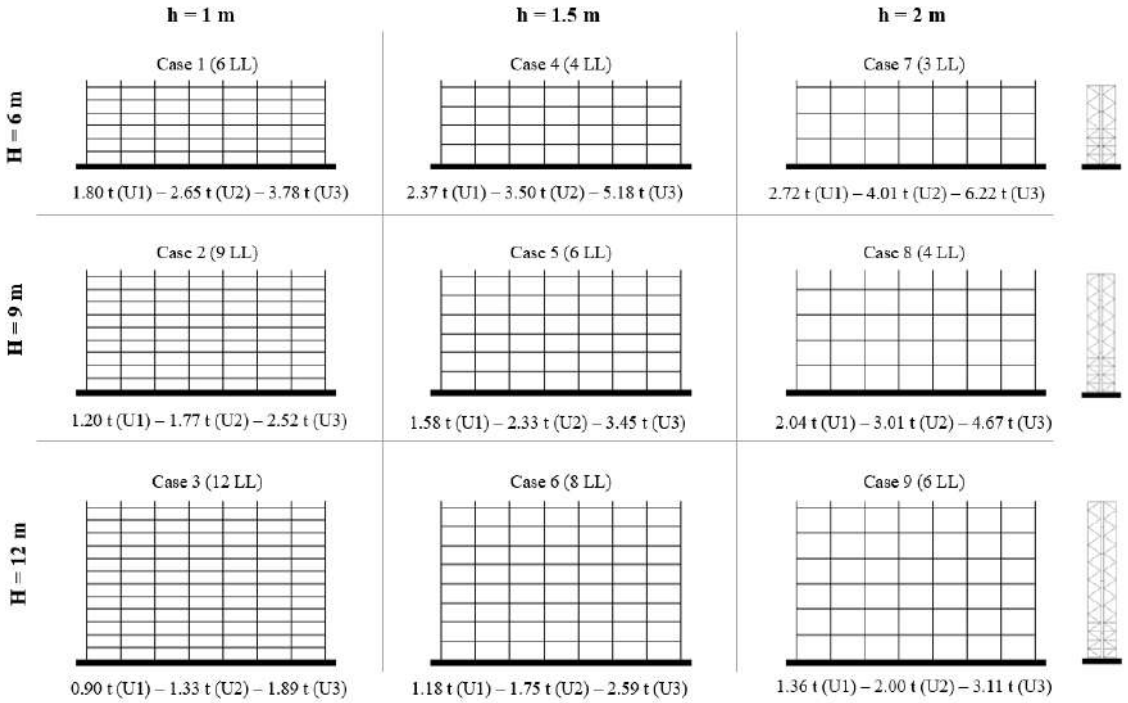
A customized parametric modelling framework was developed in MATLAB and OpenSees to automate the generation, analysis, and data extraction of the 3D models. The uprights were modelled using force-based beam-column elements with distributed plasticity, incorporating non-symmetric axial behaviour (tension vs. compression) and biaxial flexural response. Regarding the axial behaviour, reference was made to the experimental results of Padilla-Llano et al. [2014], while the flexural response was simulated through an elastoplastic model, which is an acceptable approximation –also adopted by other authors [e.g., Gabbianelli et al. 2020]– in favour of greater numerical stability.

Beam-to-column and base connections were represented using zero-length rotational elements with hysteretic response in the longitudinal plane of the rack (rotation around Y axis). The hysteretic law and pinching parameters were taken from Gabbianelli et al. [2020], whereas the yield and peak strengths of these connections were defined based on specific test results [Zonta 2023]. Pallet beams, horizontal and diagonal bracing elements, and spacers were modelled as linear elastic components, with their equivalent elastic stiffnesses. Table 1 summarizes the OpenSees elements employed to model the racks and outlines their section behaviours and material laws. The primary constitutive models are then illustrated in Figure 3.

To account for axial–bending interaction in upright sections modelled with separate response curves, their flexural capacity was scaled down according to the axial compression ratio. Since this ratio varies with load-level height (h), the corresponding flexural capacity reduction also varies: 40% at h = 1.0 m, 35% at h = 1.5 m, and 30% at h = 2.0 m. Furthermore, to capture the loss of frame stiffness due to joint clearances, the diagonal members' cross-sectional properties were reduced according to EN 15512 [CEN 2020]. Further details on the structural models of the pallet racks can be found in Donà et al. [2024]. Although the study does not introduce new modelling aspects, the overall modelling approach for these systems can be considered innovative compared to the state of the art.

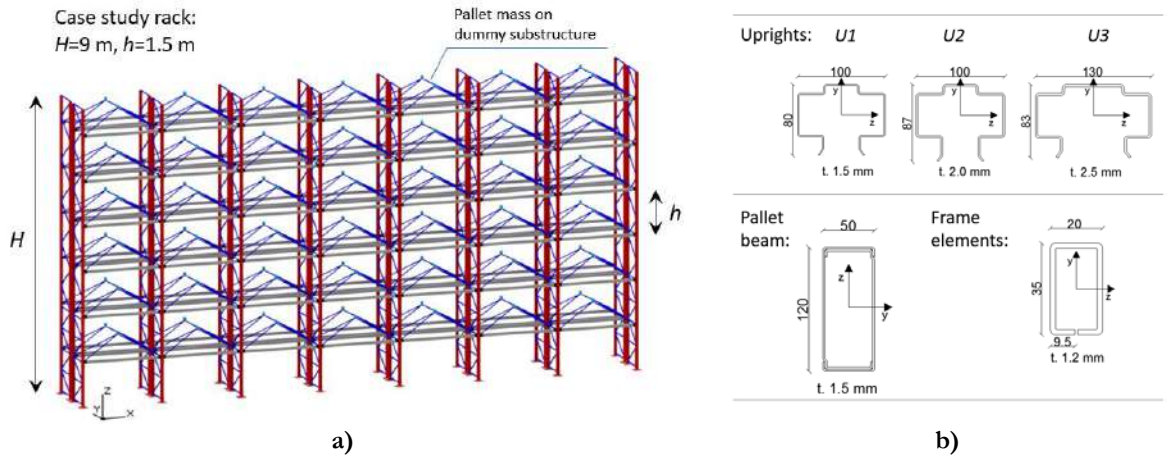


a)



b)

Figure 1. a) Common plan layout. b) Rack configurations showing pallet load per level, span, and frame.



a) b)

Figure 2. a) View of the 3D FE model for the intermediate case study rack. b) Main cross-sections.

Table 1. OpenSees objects and material laws employed in the pallet rack modelling.

Rack elements	OpenSees objects and material laws
Uprights	Force-Based Beam-Column Elements Hysteretic asymmetrical axial behaviour via "uniaxialMaterial Pinching4" (Figure 3), accounting for buckling. Elasto-plastic flexural behaviour. Five integration points per element.
Frame bracing elements	Beam With Hinges Elements Linear elastic beams with equivalent stiffnesses and end hinges to simulate truss-like behaviour.
Pallet beams/ Spacers	Elastic Beam Column Elements Linear elastic beams with equivalent stiffnesses.
Btc and base connections	Zero-Length Elements -Btc: hysteretic rotational behaviour around Y via "uniaxialMaterial Hysteretic" (Figure 3); linear elastic rotational behaviour around Z; rotation around X equal to that of the beam. -Base: hysteretic rotational behaviour around Y via "uniaxialMaterial Hysteretic" (Figure 3); released rotational stiffness around X; rotation around Z equal to that of the upright.
Mass substructures	Elastic Beam Column Elements Linear elastic beams simulating truss behaviour, without affecting modal results.
Pallet-beam contact	Zero-Length Element Equivalent friction model (Figure 3) with penalty stiffness and perfectly plastic behaviour.

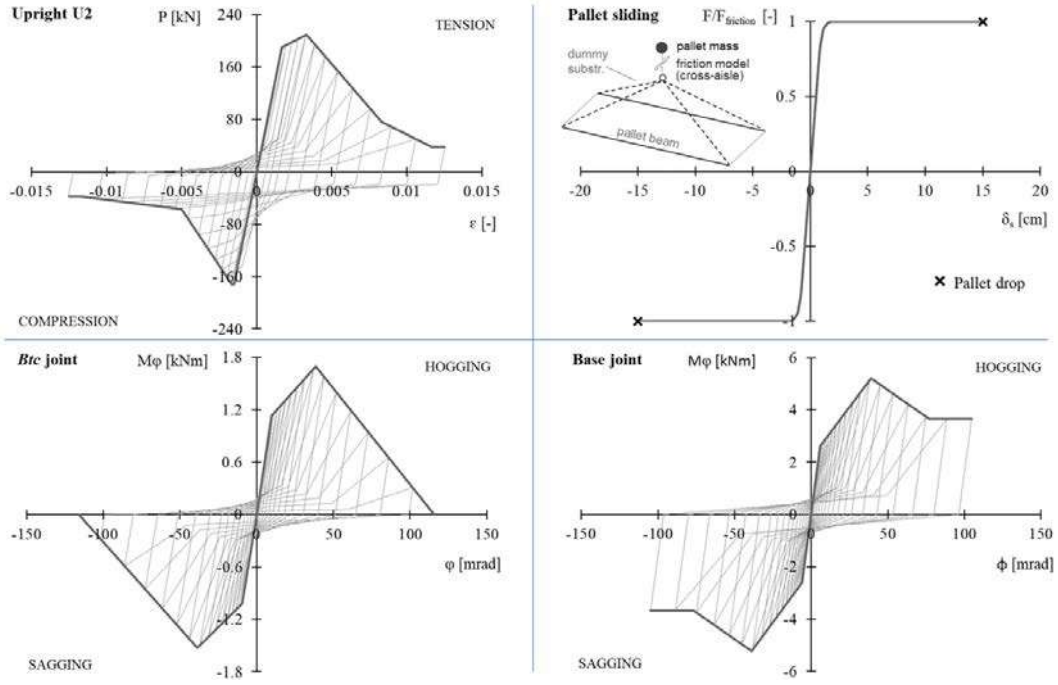


Figure 3. Main non-linear hysteretic laws used in the FE rack modelling

2.2 DEFINITION OF THE CLOUD APPROACH

To derive the rack fragility models from the time-history (TH) results, a cloud analysis approach was employed. The assessment was carried out using two distinct datasets of 134 unscaled bidirectional ground motion records each, both representative of Italian seismicity [Manfredi et al. 2022]: the first characterizing stiff soil conditions, and the second selected to reflect amplifying (soft) soil profiles. For each record, the peak ground acceleration (PGA) values of the two horizontal components (Hc_1 and Hc_2) are shown in Figure 4a. Two analyses were conducted per ground motion –applying Hc1 in the down-aisle (X) and then

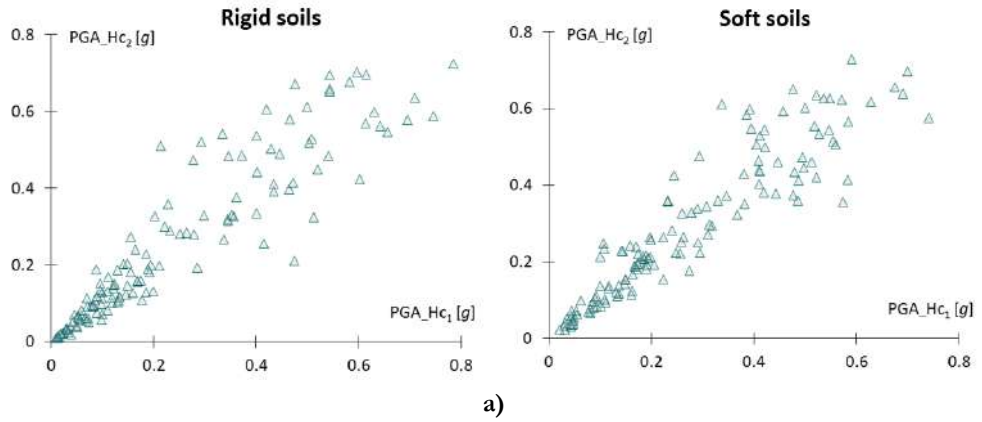
in the cross-aisle (Y) direction– resulting in 268 simulations per rack configuration and per dataset, for a total of 14,472 nonlinear dynamic analyses. Figure 4b shows the spectral acceleration (S_a) values corresponding to the fundamental periods of the racks in the two main directions ($T_{1,X}$ and $T_{2,Y}$).

Seismic fragility was conditioned to both PGA and S_a as intensity measures (IMs). While PGA is a structure-independent parameter widely used for large-scale risk assessments, S_a –evaluated at the fundamental periods of the rack system– is more effective in capturing the dynamic amplification effects and therefore the actual acceleration demand experienced by the structural system.

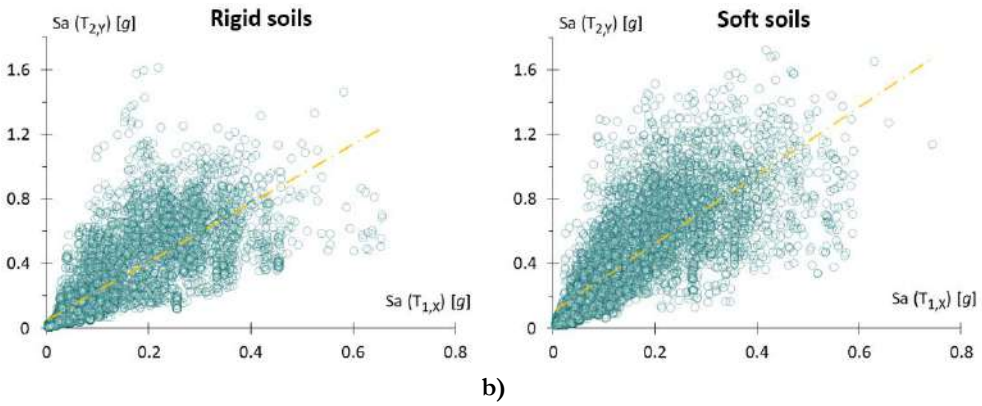
Fragility assessment was based on four Engineering Demand Parameters (EDPs) that capture key global and local deformation mechanisms: the normalized global strain of the uprights (ε^*), the down-aisle drift ratio (θ_X), and the maximum rotation of both beam-to-column (φ_{btc}) and base (φ_{base}) connections around the Y-axis. The ε^* parameter, defined in Equation (1), combines axial (ε_P) and flexural (χ_Y, χ_Z) demand components normalized by their respective yield thresholds, incorporating a buckling factor for the compressive behaviour (χ_P).

Each EDP was linked to three discrete damage states, labelled DS1, DS2, and DS3. DS1 corresponds to the onset of damage, where the system retains predominantly elastic behaviour. DS2 represents the initiation of yielding, still ensuring user safety and analogous to a Life Safety limit state. DS3 denotes a severe damage condition in which safety can no longer be guaranteed, and the likelihood of progressive failure –including partial or total collapse– is significant. The threshold values assigned to each damage state for the selected EDPs are reported in Table 2.

$$\varepsilon^* = \frac{\varepsilon_P}{\left(\varepsilon_{P,y} \cdot \chi_P\right)} + \frac{\chi_Y}{\chi_{Y,y}} + \frac{\chi_Z}{\chi_{Z,y}} \tag{1}$$



a)



b)

Figure 4. Information on ground motion dataset for rigid and soft soils: (a) PGA and (b) S_a values.

Table 2. Damage state thresholds associated with the adopted EDPs.

EDP	DS1	DS2	DS3
ε^*	[0.8, 1.0 [	[1.0, 1.5 [	[1.5, +∞ [
θ_X / $\theta_{X,y}$	[0.8, 1.0 [	[1.0, 1.5 [	[1.5, +∞ [
φ_{btc} / $\varphi_{btc,y}$	[0.8, 1.0 [	[1.0, 4.0 [	[4.0, +∞ [
φ_{base} / $\varphi_{base,y}$	[0.8, 1.0 [	[1.0, 6.5 [	[6.5, +∞ [
"▪,y" = yield value of specific EDP			

The median ($\mu_{DS,i}$) and logarithmic standard deviation ($\beta_{DS,i}$) of the assumed lognormal cumulative distribution function were estimated using the method of moments. To enhance the reliability of rack failure probability estimates, non-convergent analyses were also included in the fragility evaluation, as recommended by Jalayer et al. [2017]. Indeed, structural collapse was considered to occur under two distinct conditions: (i) the analysis converges and the global strain parameter ε* meets or exceeds its DS3 threshold; or (ii) the analysis does not converge (*NonC*), which is interpreted as an indication of potential collapse. Based on this dual criterion, the total collapse probability was computed using the total probability theorem (Equation 2). A conservative assumption was adopted by setting the conditional probability of collapse given non-convergence (P(D≥DS3 | IM, *NonC*)) equal to 1, while the probability of non-convergence as a function of seismic intensity (P(*NonC* | IM)) was determined through logistic regression, as detailed in Equation 3.

$$P\left(D \geq DS_3 \mid IM\right) = P\left(D \geq DS_3 \mid IM,\ Conv\right) \cdot \left(1 - P\left(NonC \mid IM\right)\right) + \\ + \ P\left(D \geq DS_3 \mid IM,\ NonC\right) \cdot P\left(NonC \mid IM\right) \tag{2}$$

$$P\left(NonC \mid IM\right) = \frac{1}{1 + e^{-\left(\alpha_0 + \alpha_1 \cdot \ln\left(IM\right)\right)}} \tag{3}$$

3. SEISMIC FRAGILITY MODELS

Given the use of bidirectional ground motion records, careful consideration was required when evaluating the correlation between EDPs and IMs. The parameters θ_X, φ_{btc}, and φ_{base} represent deformations occurring along the down-aisle direction and were therefore correlated with IM values in the X direction. On the other hand, ε^*, being a strain parameter influenced by axial force and biaxial bending, does not have an obvious directional association with a specific IM. However, due to the significantly greater stiffness of the analysed unbraced racks in the cross-aisle direction compared to the down-aisle direction –resulting in higher seismic accelerations and inertial forces along the Y axis– ε^* was associated with IM values in the Y direction.

For the entire rack stock under rigid soil conditions [Donà et al. 2024], Figures 5 and 6 present the developed fragility models with respect to the selected EDPs, using PGA and S_a as conditioning IMs, respectively. In addition to DS1, DS2, and DS3, the fragility curves representing the probabilities of non-convergence (*NonC*) and actual collapse (*Collapse*) are also displayed in the fragility model based on ε^*. For comparison, the Collapse curve –obtained by analysing ε^*– is also included in the fragility plots of the other EDPs. These fragility plots are accompanied by Table 3, which reports the corresponding median values (μ) and logarithmic standard deviations (β) of the lognormal distributions. The main considerations on these results are listed below.

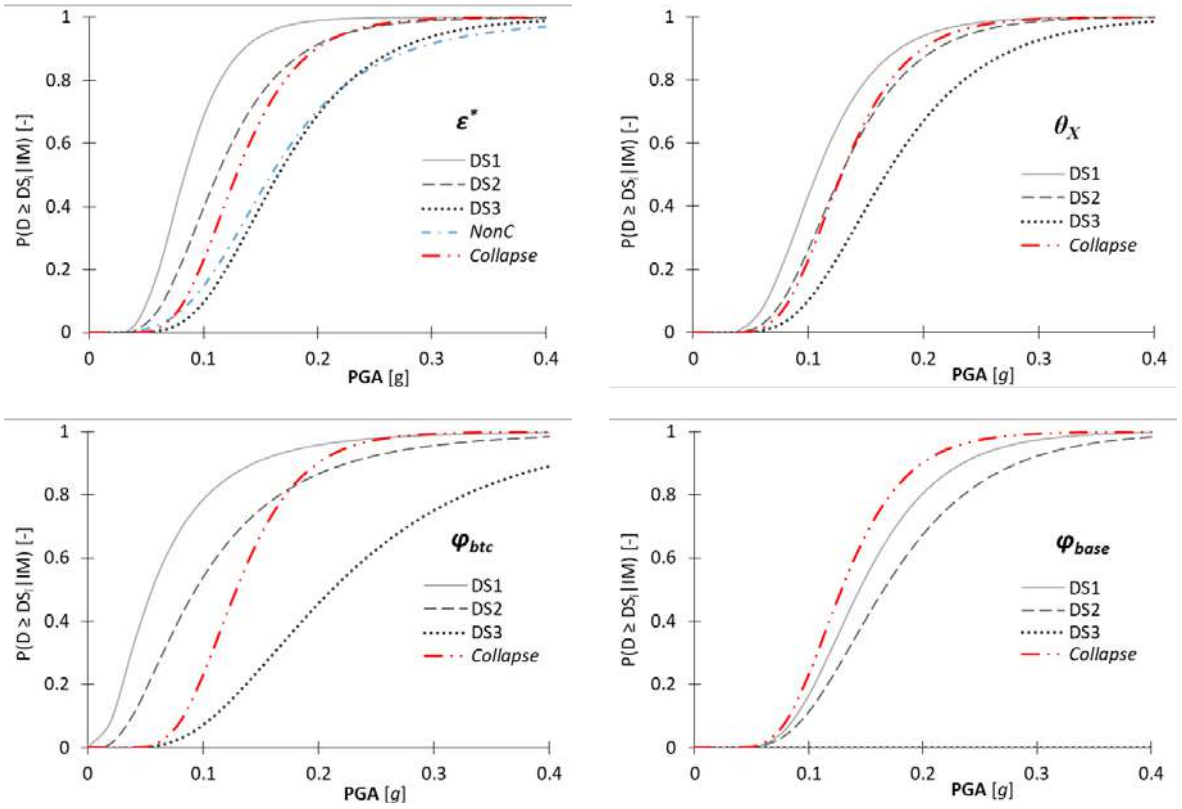


Figure 5. Fragility curves of the rack stock on rigid soils, in PGA: (a) ε*, (b) θ_X, (c) φ_{btc}, (d) φ_{base}.

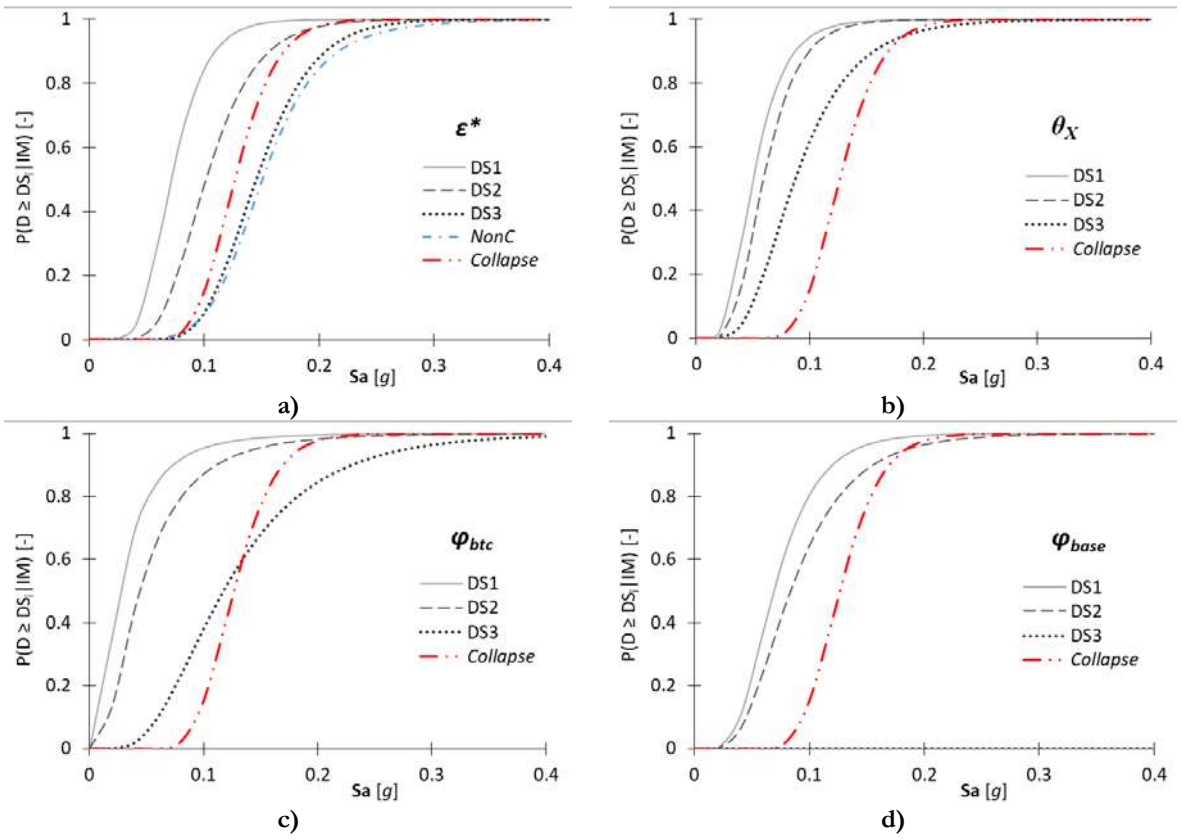


Figure 6. Fragility curves of the rack stock on rigid soils, in S_a: (a) ε*, (b) θ_X, (c) φ_{btc}, (d) φ_{base}.

Table 3. Median values (μ) and logarithmic standard deviations (β) for fragility models on rigid soils.

EDPs	**DS1**		**DS2**		***Collapse*** (ε*)/**DS3** (others)	
IM=PGA	μ_{PGA} (g)	β_{PGA} (-)	μ_{PGA} (g)	β_{PGA} (-)	μ_{PGA} (g)	β_{PGA} (-)
ε^*	0.083	0.378	0.112	0.427	0.129	0.340
φ_{btc}	0.055	0.748	0.093	0.689	0.211	0.517
θ_X	0.107	0.405	0.128	0.393	0.167	0.405
φ_{base}	0.144	0.380	0.165	0.420	-	-
IM=S_a	μ_{Sa} (g)	β_{Sa} (-)	μ_{Sa} (g)	β_{Sa} (-)	μ_{Sa} (g)	β_{Sa} (-)
ε^*	0.071	0.337	0.101	0.340	0.127	0.228
φ_{btc}	0.027	0.790	0.044	0.726	0.117	0.525
θ_X	0.050	0.406	0.059	0.406	0.087	0.457
φ_{base}	0.069	0.434	0.083	0.486	-	-

- The fragility based on ε^* –characterised by low median PGA values (μ_{PGA})– demonstrates the high seismic vulnerability of these structural systems. The narrow fragility interval between DS2 (μ_{PGA}=0.112 g) and *Collapse* (μ_{PGA}=0.129 g) demonstrates the limited redundancy and ductility capacity of these racks. The close overlap between DS3 (collapse with convergence) and *NonC* (non-convergence) suggests that non-convergence is mainly triggered by excessive upright strain.
- The *Collapse* curve (determined for ε^*) consistently precedes the DS3 curves of the other EDPs (θ_X, φ_{btc}, and φ_{base}), confirming that ε^* governs the collapse mechanism. Among the remaining EDPs, θ_X is the first to reach DS3, making it the most representative indicator of global rack deformation in the down-aisle direction.
- The *Collapse* curve is nearly coincident with DS2 of θ_X, indicating similar probabilities for upright failure and yielding along the X direction. Comparing φ_{btc} and θ_X, φ_{btc} exhibits lower μ_{PGA} values at DS1 and DS2, but higher values at DS3, reflecting a rapid loss of inter-storey stiffness once btc joints yield. Fragility for φ_{base} is the lowest: DS1 is reached after DS2 for θ_X and φ_{btc}, and DS3 is never attained, suggesting a hierarchical resistance among rack components.
- For ε^*, the acceleration ranges in PGA and S_a are comparable. For the other EDPs, however, the fragility ranges in S_a are significantly narrower than those in PGA, due to the long vibration periods in the down-aisle direction. Since the *Collapse* curve is derived from the analysis of ε^* –and is thus associated with IM values in the Y direction– it is no longer directly comparable with the fragility curves of θ_X, φ_{btc}, and φ_{base} when conditioned on S_a, although it still serves as a useful reference.

For the same rack stock under soft soil conditions [Donà et al. 2025], to maintain compactness, only Table 4 is reported, summarising the μ and β values of the associated fragility models. The general considerations that can be drawn are similar to those previously discussed for the fragility estimated under rigid soil conditions. Lastly, Figure 7 compares the median ($\mu_{DS,i}$) and logarithmic standard deviation ($\beta_{DS,i}$) values of the fragility curves based on ε^* across the two soil conditions, offering insight into the influence of local site effects on rack fragility estimates. Regarding this comparison, the main observations are as follows:

- The $\mu_{DS,i}$ values for PGA differ between rigid and soft soils: they are lower for soft soil, indicating higher fragility under amplifying conditions. This difference is reduced when S_a is used as seismic intensity measure. This proves that S_a is a more efficient IM to describe rack fragility. The latter observation is particularly relevant for spatial-scale risk assessments and may warrant further investigation (for instance, investigating alternative intensity measures, such as Housner intensity).
- The $\beta_{DS,i}$ values for PGA are higher for soft soil, which is consistent with the greater variability of seismic demand in amplifying conditions. In contrast, $\beta_{DS,i}$ values for S_a are similar across soil types, confirming the reduced sensitivity of rack fragility to soil condition when using this IM.

Table 4. Median values (μ) and logarithmic standard deviations (β) for fragility models on soft soils.

EDPs	**DS1**		**DS2**		***Collapse*** (ε*)/**DS3** (others)	
IM=PGA	μ_{PGA} (g)	β_{PGA} (-)	μ_{PGA} (g)	β_{PGA} (-)	μ_{PGA} (g)	β_{PGA} (-)
ε^*	0.049	0.412	0.088	0.524	0.097	0.336
φ_{btc}	0.048	0.424	0.083	0.604	0.204	0.313
θ_X	0.078	0.513	0.104	0.507	0.144	0.437
φ_{base}	0.119	0.458	0.143	0.431	-	-
IM=S_a	μ_{Sa} (g)	β_{Sa} (-)	μ_{Sa} (g)	β_{Sa} (-)	μ_{Sa} (g)	β_{Sa} (-)
ε^*	0.047	0.335	0.087	0.351	0.111	0.231
φ_{btc}	0.020	0.544	0.035	0.672	0.089	0.370
θ_X	0.033	0.564	0.043	0.546	0.065	0.483
φ_{base}	0.051	0.573	0.060	0.526	-	-

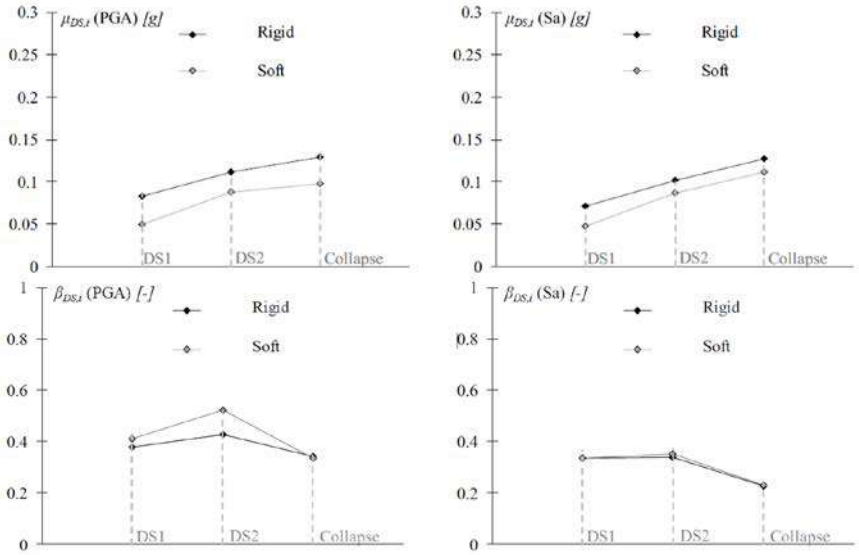


Figure 7. Comparison of $\mu_{DS,i}$ and $\beta_{DS,i}$ values of the fragility curves based on ε* for different soil conditions.

4. CONCLUSIONS

This study developed a methodology to quantify the seismic fragility of unbraced industrial pallet racks –non-structural systems whose failure can compromise safety, operations, and supply chain resilience in industrial settings. It addressed structural variability and soil effects by analysing 27 rack configurations –using 3D nonlinear FE modelling and a cloud approach– with two ground motion datasets representative of Italian seismicity in rigid and soft soils. Fragility models were derived using multiple EDPs, conditioned on PGA and S_a. Under full-load conditions, these racks exhibited marked seismic vulnerability. The narrow gap between yielding (DS2) and Collapse fragility curves, reflects a brittle seismic response, driven by low redundancy and limited energy dissipation. Among the EDPs, global upright strain (ε*) was the most effective collapse predictor, consistently governing failure across configurations and soil types. Other EDPs, down-aisle drift (θ_X) and joint rotations (φ_{btc}, φ_{base}), offered insight into local mechanisms but were less reliable for identifying collapse. While PGA is widely used in seismic risk mapping due to its simplicity and structural independence, PGA-based fragility curves proved sensitive to soil conditions. In contrast, S_a-based curves yielded more stable predictions across soil types, making them more suitable for consistent risk assessment at the regional scale. Overall, the proposed methodology represents a valuable tool for performance-based seismic risk assessment in industrial storage facilities. The derived fragility models support risk-informed decisions across scales and can be extended to assess alternative rack typologies or retrofit strategies, contributing to more resilient logistics infrastructure.

REFERENCES

Bernardi E., Donà M., Tan P., da Porto F. [2023] Optimal design method of the load-level isolation system for industrial steel racking. J Constr Steel Res; 210: 108096. https://doi.org/10.1016/j.jcsr.2023.108096

Bernuzzi, C., and Castiglioni, C. A. [2001]. "Experimental analysis on the cyclic behaviour of beam-to-column joints in steel storage pallet racks." Thin-Walled Structures, 39(10), 841-859.

CEN (European Committee for Standardization). [2005]. "EN 1993-1-1. Eurocode 3: Design of steel structures – Part 1-1: General rules and rules for buildings." Brussels: CEN.

CEN[2016]. "EN16681. Steel Static Storage Systems -Adjustable Pallet Racking Systems- Principles for seismic design." Brussels.

CEN[2020]. "EN15512. Steel Static Storage Systems -Adjustable Pallet Racking Systems- Principles for structural design." Brussels.

Donà, M., Bizzaro, L., Carturan, F., and da Porto, F. [2019]. "Effects of business recovery strategies on seismic risk and cost-effectiveness of structural retrofitting for business enterprises." Earthq. Spectra, 35(4):1795–1819.

Donà, M., Bernardi, E., Zonta, A., Ceresara, M. and da Porto, F. [2022]. Effectiveness of load-level isolation system for pallet racking systems. Frontiers in Built Environment, Volume 8 – 2022.

Donà, M., Piredda, G., Zonta, A., Bernardi, E., da Porto, F. [2024]. "Seismic fragility of unbraced industrial steel pallet racks." Structural Safety, 110, 102497. https://doi.org/10.1016/j.strusafe.2024.102497.

Donà, M., Zonta, A., Bernardi, E., Piredda, G., da Porto F. [2025], "Seismic fragility of a stock of unbraced pallet racks considering events on amplifying soils", in: M. Papadrakakis, M. Fragiadakis (eds.), Proc. of 10th ECCOMAS COMPDYN 2025, Rhodes, Greece, June 15-18.

Drei, A., Rovere, L., Vayas, I., et al. [2014]. "Seismic behaviour of steel storage pallet racking systems (SEISRACKS2): final report". European Commission, Directorate-General for Research and Innovation. Publications Office.

Gabbianelli, G., Francesco, C., and Nascimbene, R. [2020]. "Seismic vulnerability assessment of steel storage pallet racks." Ingegneria Sismica, 37(2)

Jalayer, F., Ebrahimian, H., Miano, A., Manfredi, G., Sezen, H. [2017]. "Analytical Fragility Assessment Using Unscaled Ground Motion Records." Earth Eng and Struct Dyn, 46 (15), 2639-63.

Manfredi, V., Masi, A., Özcebe, A. G., Paolucci, R., and Smerzini, C. [2022]. "Selection and spectral matching of recorded ground motions for seismic fragility analyses." Bull Earthq Eng, 1-27.

Nuñez, E., Aguayo C., and Mata, R. [2023]. "Incremental dynamic analysis of steel storage racks subjected to Chilean earthquakes." Thin-Walled Structures, 182, 110288.

Padilla-Llano, D. A., Moen, C. D., and Eatherton, M. R. [2014]. "Cyclic axial response and energy dissipation of cold-formed steel framing members." Thin-walled structures, 78, 95-107.

Perrone, D., Calvi, P. M., Nascimbene, R., Fischer, E. C., Magliulo, G. [2019]. "Seismic performance of non-structural elements during the 2016 Central Italy earthquake." Bull Earthq Eng, 17(10): 5655-77.

Proença, J., Rosin, I., and Calado, L. [2009]. "Storage racks in seismic areas". European Commission, Directorate-General for Research and Innovation. Publications Office.

Shaheen, M. S. A., and Rasmussen, K. J. R. [2022]. Development of friction damped seismic fuses for steel storage racks. J. Constr. Steel Res. 192, 107216. doi:10.1016/j.jcsr.2022.107216

Simoncelli, M., Tagliafierro, B., and Montuori, R. [2020]. Recent development on the seismic devices for steel storage structures. Thin-Walled Struct. 155, 106827. doi:10.1016/j.tws.2020.106827

Zonta, A. [2023]. "Seismic vulnerability of industrial steel pallet racks: development of fragility curves for existing and retrofitted configurations." Ph.D. Thesis, University of Padova, XXXV cycle

Design and testing of school furniture as life-saving non-structural building components: a case study

Alessandro Zona[1], Fabio Micozzi[2], Laura Gioiella[1], Fabrizio Scozzese[1], Michele Mirra[1], Michele Morici[1], Francesco Allegrezza[2], Graziano Leoni[1] and Andrea Dall'Asta[2]

[1] University of Camerino, School of Architecture and Design
Viale della Rimembranza 3, 63100 Ascoli Piceno, Italy
e-mail: {alessandro.zona, laura.gioiella, fabrizio.scozzese, michele.mirra, michele.morici, graziano.leoni}@unicam.it
[2] University of Camerino, School of Science and Technology
Via Gentile III da Varano 7, 62032 Camerino, Italy
e-mail: {fabio.micozzi, francesco.allegrezza, andrea.dallasta}@unicam.it

Abstract. This article presents the research developments involving an innovative coordinated system of school furniture designed to have life-saving functions in case of earthquakes, result of two multidisciplinary research projects that had expertise in structural and earthquake engineering interacting with designers and industrial producers of school furniture. The proposed furniture system includes school desks, shelving units, and prefabricated partitions intended as non-structural building components. The structural concepts behind each furniture element are summarized and the latest outcomes are illustrated through a selection of experimental results. Attention is given to the definition of an impact-testing methodology for school desks, conceived as an extension of current prescriptions for testing conventional school desk and that could be easily replicable in a structural engineering laboratory. The experimental outcomes were monitored using conventional contact sensors as well as computer-vision methodologies for displacement tracking, to gain insight into the structural response under impact loadings.

Keywords: Earthquake-resistant non-structural components, Life-saving furniture system, Impact-testing methodology, Seismic design, School safety.

1. INTRODUCTION

1.1 BACKGROUND

During emergency situations such as earthquakes, furniture and equipment inside a building can either become obstacles and barriers that increase the level of danger, especially for the elderly, children and people with reduced mobility, or, conversely, represent a possibility of protection in case of building damages or collapse. Within this framework, the authors of this study participated in an interdisciplinary research project ("Sustainable design of anti-seismic furniture as smart life-saving systems during an earthquake", acronym SAFE) funded by the Italian Ministry of University and Research (PON 2018-2021 Research and Innovation, Area of Design, Creativity, and Made in Italy). The project, carried out in close collaboration with designers and industrial producers of school furniture, aimed to create an innovative coordinated system of school furniture able to offer life-saving protection in case of earthquakes while remaining structurally efficient and economically competitive. The final goal was to have the mobile elements of everyday living or working spaces inside a building to act as protective shelters. Following the outcomes of the SAFE project, the research was further extended within a new funding by the European Union - NextGenerationEU, Mission 4, Component 2, under the Italian Ministry of University and Research within the 2022-2025 National Innovation Ecosystem VITALITY, Spoke 6, WP3 "Sustainable design of smart furniture system with life-saving function in conditions of emergency for community settings". In the VITALITY research project, revised and optimized versions of the school furniture were designed, produced and installed in two classrooms of a high school in Ascoli Piceno, Italy, in the area hit by the 2016 Central Italy Earthquakes, as a pilot demonstration and real-life assessment of their everyday use. A view of one of the two equipped classrooms is shown in Figure 1, illustrating the coordinated system including school desks, shelving units (equipped with an interactive board, lockers and hangers), and glass-aluminium partition walls.



Figure 1. Pilot installation of SAFE school furniture (desks, shelving units, partition walls) in a high school in Italy within the VITALITY research project.

1.2 SCHOOL DESKS WITH LIFE-SAVING FUNCTIONS

In seismic-prone areas around the world, children are instructed to hide under their school desks when an earthquake strikes. Such a recommendation implicitly assumes that the space below a school desk is a safe place to find protection in case the building hosting the classroom experiences some level of damage. Accordingly, school desks must be able to protect pupils from falling debris whose mass is highly uncertain, potentially ranging from plaster fragments, suspended ceilings, illumination, up to heavier non-structural or even structural elements from upper floors. A straightforward way to made school desks resistant to falling masses is through oversizing. Many examples can be found browsing the internet, although the engineering

and ergonomic quality of many designs is often questionable. Oversizing typically produces bulky, very heavy, and generally much more expensive desks than conventional commercial models, thus, making them impractical for everyday school use and unaffordable for public administrations managing schools.

During the SAFE project, the research brought to a different solution. A system of steel tubular members of diameter 22 mm and thickness of 1.5 mm (elements commonly used for school furniture) are arranged in an innovative shape able to emphasize structural performance (Figure 2). An external frame directly supports the tabletop, while an inner frame of similar geometry is connected to the outer frame at the four corners and at the basis, along the shorter sides of the desk. The outer and inner frames constitute a redundant structural system and collaborate with a bending progressive damage in case of severe overloading. To prevent penetration from falling objects, a 1 mm-thick steel sheet perforated to reduce its weight is welded to the top of the outer frame as a protective layer above the plywood tabletop. The proposed desk is significantly lighter and more cost-effective than existing earthquake-proof models, as it uses standard materials, sections, dimensions, and manufacturing processes already common in school furniture. It has no moving parts that could injure users and is designed with a bending-dominated failure mechanism under extreme loads, exploiting steel ductility to dissipate impact energy while preserving the protected volume. A view of the final prototype used in the pilot installation is shown in Figure 3.

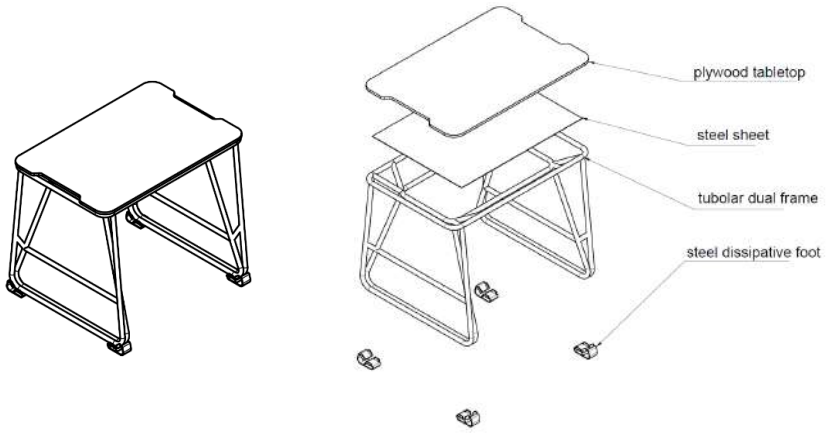


Figure 2. Dual-frame school desk proposed in the SAFE project.



Figure 3. Final version of the school desk used in the pilot installation.

The developed dual-frame configuration was patented (Italian Patent 202024000002719). In addition, the proposed school deck was equipped with dissipative steel feet at the interface between the bottom of the dual-frame and the floor, feet designed to yield for a force below the axial capacity of the desk legs, to further dissipate impact energy. The developed dissipative feet were also patented (Italian Patent 202022000003099).

1.3 SHELVING UNITS WITH LIFE-SAVING FUNCTIONS

Standard shelving units are typically installed against a partition wall and mechanically fastened to it. Beyond this basic measure, limited information is available regarding their seismic performance, as reviewed in Sciomenta et al. [2025]. A critical issue with these solutions is that if the supporting partition walls do not meet seismic standards, the anchored shelving unit follows the damage of the wall or could even be a worsening factor. To overcome these limitations, a self-supporting shelving was developed to act simultaneously as a functional storage solution and a safety device.

Figure 4 depicts the layout of the proposed self-supporting shelving unit whose uprights are the core structural elements. Each upright is composed of three parts, a central rectangular hollow profile, primarily resisting bending and axial forces, and two symmetric stiffening triangular profiles that host the central profile and carry axial force. The triangular profiles can be slid over the central one, allowing height adjustment and creating a versatile floor-to-ceiling structure that can fit different inter-storey height. Once reached the desired height, the triangular profiles are secured to the central profile using self-tapping metal screws. This configuration reduces the free length of deflection of the central profile, empowering simultaneously both the top and bottom restraints performance thanks to the compressive action developed. It also simplifies transportation and installation procedures. A prestress force is applied to the uprights to increase the efficiency of the restraints (higher friction resistance) and to maximize the effectiveness of a layer of elastomeric material located between the steel end support plates and the floor slab. The elastomeric layers provide a continuous contact surface and further increase the resistance against sliding. Adjacent uprights are connected by crossbeams, forming the complete shelving frame. A protective top panel can be installed to achieve the second objective of the life-saving shelving unit, that is providing protection against falling debris for students or people that cannot use school desks as a shelter. The developed shelving unit was patented (European Patent EP4194645B1).

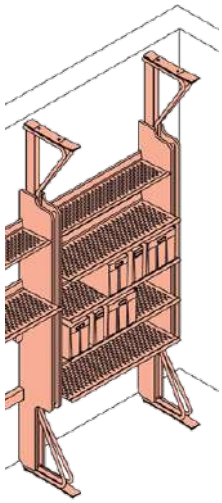


Figure 4. Shelving unit developed within the SAFE project.

Figure 5 shows some views of the shelving unit in the pilot installation. Under normal conditions, it works as a bookshelf hosting interactive whiteboards, teaching materials, and audiovisual equipment. In the event

of an earthquake, however, the unit is designed to protect nearby people by (i) preventing the collapse of the adjacent partition wall and (ii) shielding them from falling debris.

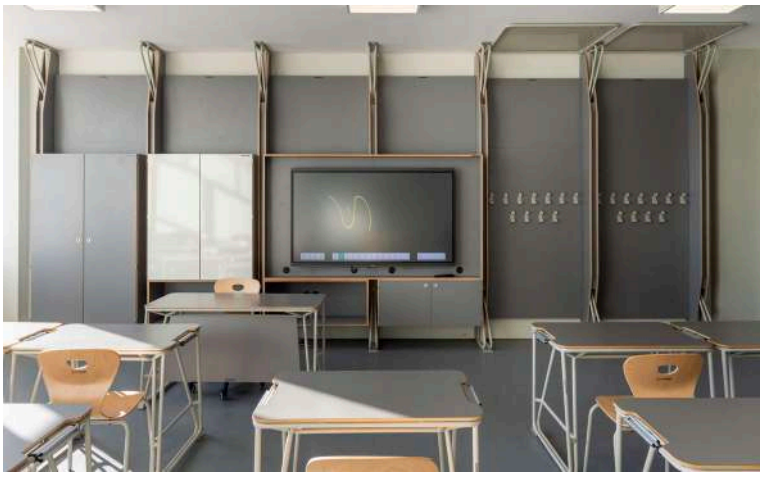


Figure 5. Final version of the shelving unit used in the pilot installation.

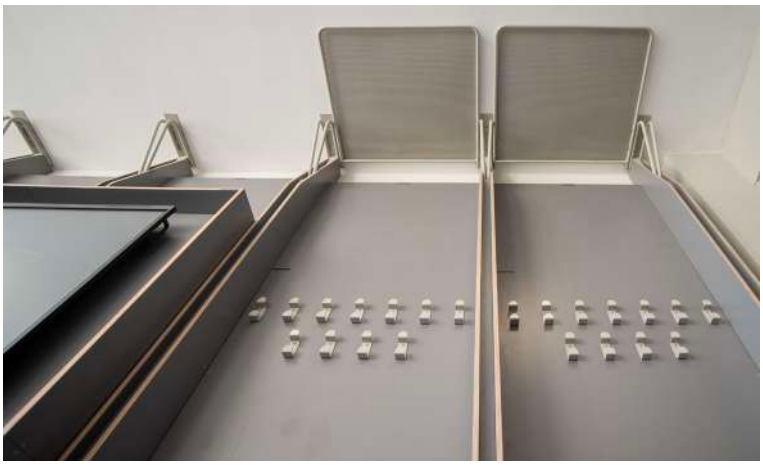


Figure 6. View of the upper connection of the shelving units at the ceiling with top protective panels.



Figure 7. View of the base connection of the shelving units at the floor.

1.4 PARTITION WALL WITH SEISMIC PROTECTIVE FEATURES

Glass partitions are appealing solutions for the subdivision of indoor spaces in buildings due to their architectural characteristics. However, the interaction between glass panels (usually thick, and hence, heavy, to meet acoustic isolation needs), their metallic frames, and the structural elements to which they are connected raises concerns in case of seismic events. Failure of these components might endanger life safety and result in high repair and downtime costs. Petrone et al. [2017] presented an experimental study on a prototype of a partition with glass panels with improved connections, able to avoid the unhooking of the panels from the supporting studs. A different approach was followed in Scozzese et al. [2024] where the seismic-resistant capacity of glass-aluminium partitions is obtained by exploiting a passive seismic protection concept inspired by dissipative seismic base isolation systems, scaled to the dimensions of a single module of the partition wall. Such function is assigned to elastomeric elements with viscoelastic properties made of high-damping rubber (HDR), capable of creating a dissipative coupling between each glass panel and the perimetral aluminium frame (Figure 8). The glass panels are transparent stratified glass, and adjacent panels are connected by transparent methacrylate joints attached to the glass through silicon adhesive, creating a continuous partition surface that prevents pounding between panels, and improves acoustic isolation. The developed partition wall was patented (European Patent EP4194632A1).

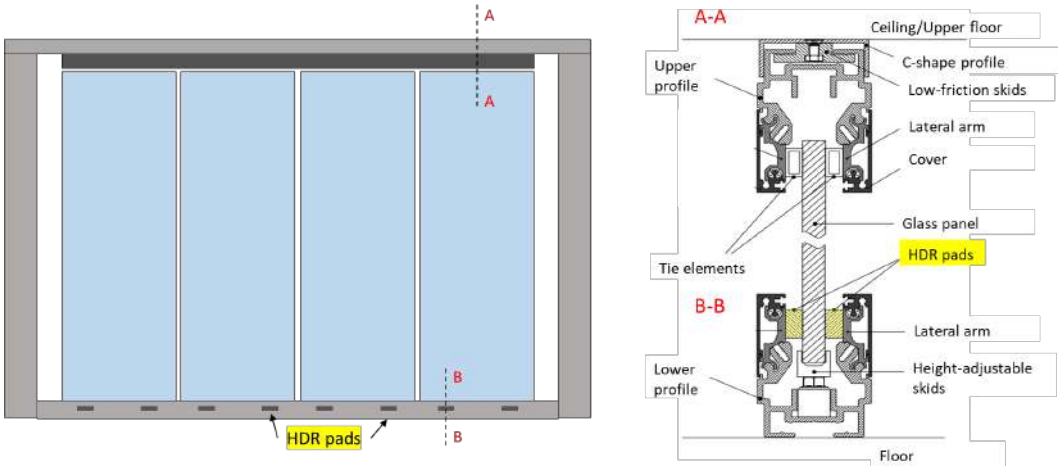


Figure 8. Partition wall with HDR dissipative pads.

2. STRUCTURAL ANALYSIS AND TESTING

2.1 SCHOOL DESK

2.1.1 Preliminary linear elastic analysis and first experimental campaign

The shape of the school desk was initially designed through linear elastic numerical simulations assessing the structural performance under vertically distributed and concentrated loads, applied both symmetric and non-symmetric. These analyses complemented ergonomic and functional considerations as well as production requirements. However, it was clear from the very beginning that these numerical simulations could only provide initial indications, and deeper insight could only be based on experimental validation. Accordingly, a large testing campaign including both static loading and impact tests were conducted during the SAFE project in the structural laboratory of the University of L'Aquila, as documented in Gioiella et al. [2022] and Sciomenta et al. [2025]. Impact tests were performed using assemblies of different sizes of clay bricks (total mass 300 kg, 450 kg, and 600 kg) tied together to form compact blocks with base dimensions approximately matching the tabletop footprint. These tests provided valuable information for refining the dual frame design of the proposed school desk. However, performing such tests was a complex and time-consuming task given that the mass once dropped was damaged and could not be used for additional tests,

with few exceptions, and it was difficult to achieve a controlled impact on the tabletop due to inevitable rotations and eccentricities during free fall.

2.1.2 Second experimental campaign

Given the limitations observed in the test methodology adopted in the SAFE project, namely the difficulty in controlling the impact location and the limited repeatability due to rotations and damage of the brick assemblies, a revised impact-test procedure was developed for the second experimental campaign. In addition, a uniform mass falling on the desk, although might sound impressive in terms of total amount, is not the most demanding loading condition, as a smaller footprint might generate much more damage due to higher localized pressure. Following these considerations and taking EN 1729-2 [CEN 2023] as reference for the loading condition, the new proposed impact test employs a spherical steel mass dropped along the symmetry plane perpendicular to the longer horizontal side at 100 mm from the edge, corresponding to the same loading point used in the static tests. The spherical geometry of the falling mass ensures much higher replicability of the tests, since any rotation during free fall does not affect the shape of the impact footprint. The second testing campaign was performed using a spherical steel mass of 100 kg (diameter about 29 cm) dropped from 150 cm above the tabletop. The instrumented school desk and the steel sphere before testing are shown in Figure 9, while Figure 10 illustrates the damaged condition of the school desk after the impact.



Figure 9. Instrumented school desk ready for the impact tests (the 100 kg steel sphere is on the left).



Figure 10. School desk after the impact test.

The sequence of the impact test, from the release of the steel sphere to the moment of its impact on the tabletop and subsequent bounces upwards, is summarized in Figure 11. Video recordings for computer-vision monitoring were made using an industrial global shutter monochrome camera (Teledyne FLIR BLACKFLY S BFS-U3-23S3M-C) equipped with a fixed-focal lens (Tamron 23FM50SP). Acquisition frequency was set at 200 frames per second. Fiducial markers were applied both on the steel sphere and on the steel tubes of the desk to track displacement through area-based template matching algorithms. The obtained vertical displacement of the upper front tube is shown in Figure 12. The interruptions of the experimental curve are a consequence of the steel ball moving in front of the monitored target after bouncing back, thus, temporarily interrupting its visualization.

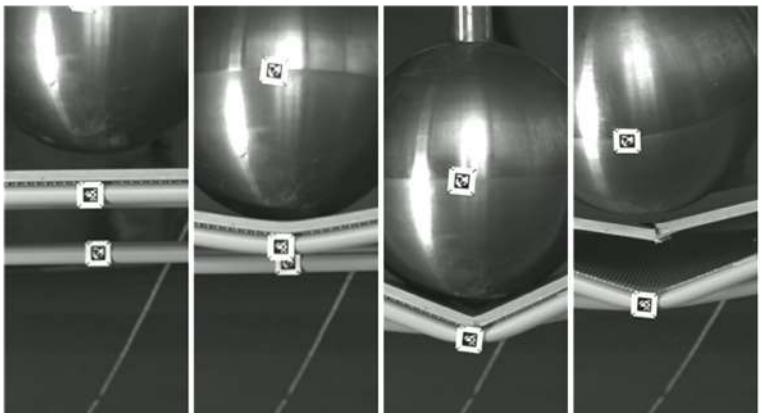


Figure 11. Video frames (from left to right) before impact, impact start, maximum deflection, bouncing back.

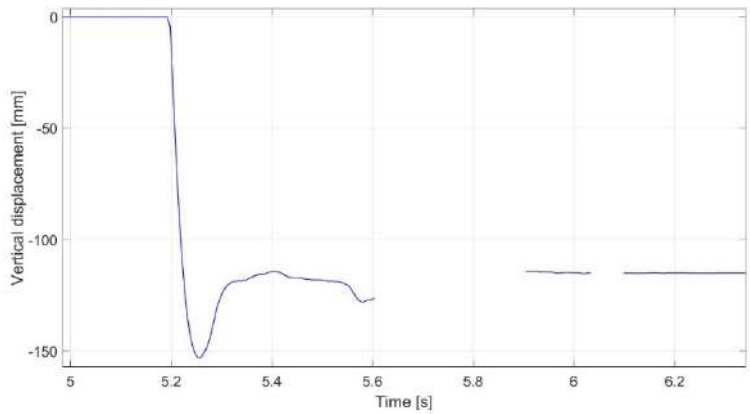


Figure 12. Vertical displacement of the upper front tube as extracted from the recorded video.

In addition to contactless vision-based monitoring, strain gauges were installed on the tubular elements of the school desk, and their signals were acquired during the test using a high-performance data logging system and its controlling software (Dewesoft Krypton and Dewsoft X). The acquisition frequency was set to 20000 samples/s. Results are here reported for six strain gauges, namely B3, B4, and B5 installed on a front leg of the external frame, as well as C1, C2, and C3 installed on the corresponding front leg of the internal frame, as illustrated in Figure 13. The results are reported in Figure 14 and Figure 15 where it is noted that the legs experienced a complex state of deformation with positive strains (elongation) and negative strains (shortening) determined by the combination of bending and axial force, and residual (permanent) plastic deformations clearly visible. Please note that the acquisition of the strain gauges and the acquisition of the video footage started at different times, hence the abscissa of Figure 12 has a different zero compared to the abscissa of Figure 14 and Figure 15.

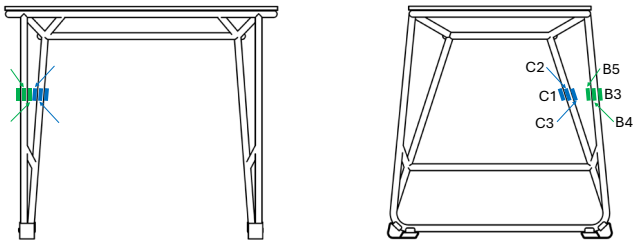


Figure 13. Position of the strain gauges considered in this study.

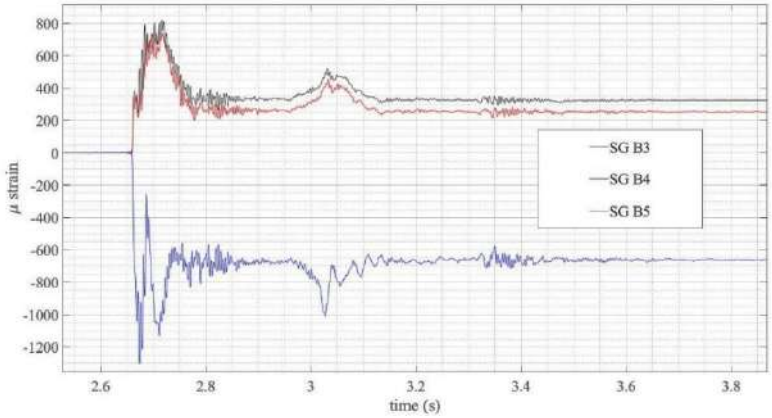


Figure 14. Strains in the leg of the external frame.

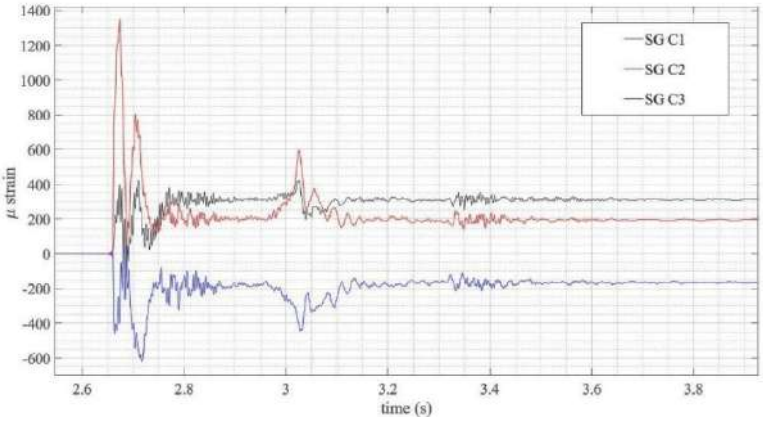


Figure 15. Strains in the leg of the internal frame.

2.1.3 Advanced nonlinear finite element model

The numerical model of the tested desk was developed and progressively refined using the finite element software SAP2000 (release 26 Ultimate). The steel frame is modelled with frame elements featuring distributed plasticity, to capture the nonlinear behaviour of the steel material. Each element was assigned a circular hollow cross section with external diameter 22 mm and thickness 1.5 mm. The legs of the desk are isostatically restrained, to enable their movement during the load application, as observed during testing. The 1-mm-thick perforated steel sheet is modelled with nonlinear shell elements, which use the same constitutive model as that of frames, but with yield strength and modulus of elasticity reduced by 30% to account for the presence of holes, also amounting to that percentage with respect to the total area of steel. The plywood tabletop above is modelled with nonlinear orthotropic shell elements. The nonlinear

constitutive law assigned to this user-defined material have a linear elastic branch up to the plywood's mean bending strength, followed by a softening phase representing the brittle failure and fracturing of the plate. The two layers of shell elements are connected to the links representing the contact between them, i.e. only the vertical degree of freedom was linked. Additionally, 13 links with shear stiffness are placed in the corresponding position of the screws joining the perforated steel plate with the plywood tabletop (four on the long sides, two on the short sides, and one at the centre of the tabletop). Finally, the bottom shell layer is connected to the frame by means of rigid links representing the welds, only in correspondence of the desk legs, and with links joining the vertical degree of freedom elsewhere. A schematic view of the finite element model is shown in Figure 16. Very encouraging results are being obtained, showing substantial agreement between numerical simulations and experimental measurements. However, at the moment of writing this article, no consolidated and verified results are available, they will be released and discussed in subsequent future articles.

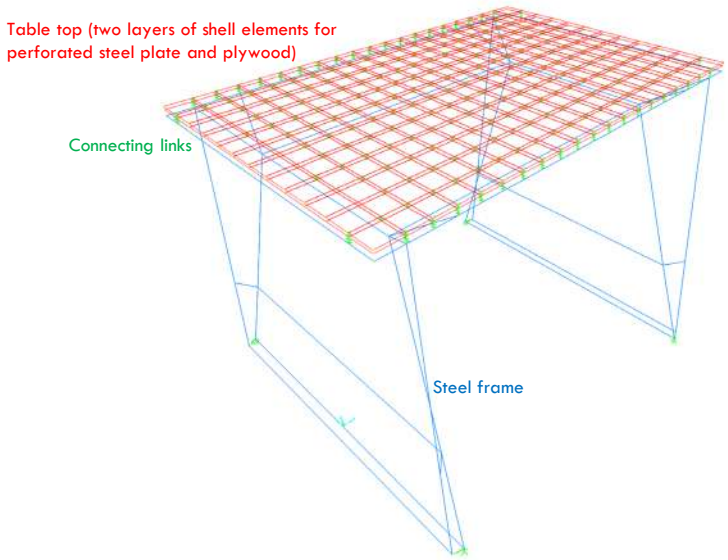


Figure 16. Three-dimensional view of the advanced finite element model of the school desk created in SAP2000.

2.2 SHELVING UNITS

The numerical analyses and full-scale experimental tests carried out on the shelving units with life-saving functions developed within the SAFE project are documented in Gioiella et al. [2022] as well as Sciomenta et al. [2025]. The experimental tests highlighted the crucial influence of the boundary connections at both the floor and at the ceiling in achieving the targeted structural performance.

2.3 PARTITION WALLS

The analysis and experimental testing (shake-table testing of downscaled and full-scale prototypes) of the developed shelving units with life-saving functions in case of earthquakes were developed under the SAFE project and the interested reader is referred to the articles by Ditommaso et al. [2022], Scozzese et al. [2024], and Ditommaso et al. [2025]. The experimental outcomes showed very good performances of the glass and aluminium partition wall with dissipative HDR pads above the design seismic input, with no signs of damages in both the partitions and in the dissipative devices. For a detailed analysis the interested reader is referenced to the article by Ditommaso et al. [2025].

REFERENCES

CEN [2023] EN 1729-2:2023 *European Standard for Furniture, Chairs and tables for educational institutions, Part 2: Safety requirements and test methods*, European Union, Bruxelles, Belgium.

Ditommaso, R., Scozzese, F., Mossucca, A., Auletta, G., Di Cesare, A., Nigro, D., Zona, A., Ponzo, F.C., Dall'Asta, A. [2022] "Preliminary results in the design and testing of earthquake-proof glass-aluminium partition walls", *Proceeding of the 17th World Conference on Seismic Isolation*, Turin, Italy.

Ditommaso, R., Scozzese, F., Zona, A., Dall'Asta, A. Ponzo, F.C. [2025] "Shake-table tests for seismic performance assessment of glass-aluminium partition walls with viscoelastic dissipative devices" *Journal of Earthquake Engineering*, 1-24.

Gioiella, L., Micozzi, F., Zona, A., Dall'Asta, A., Sciomenta, M., Tamagnone, G., Fragiacomo M. [2022] "Preliminary results in the design and testing of earthquake-resistant school furniture" *Proceeding of the 17th World Conference on Seismic Isolation*, Turin, Italy

Petrone, C., Magliulo, G., Manfredi, G. [2017] "Shake table tests on standard and innovative temporary partition walls" *Earthquake Engineering and Structural Dynamics*, Vol. 46, No. 10, pp. 1599–1624.

Sciomenta, M., Tamagnone, G., Gioiella, L., Micozzi, F., Zona, A., Dall'Asta, A., Fragiacomo, M. [2025] "Experimental testing of school furniture designed with life-saving functions in case of earthquakes" *Engineering Structures*, Vol. 336, No. 1, article 120389.

Scozzese, F., Zona, A., Dall'Asta, A. [2024] "Glass-aluminium partition walls with high-damping rubber devices: seismic design and numerical analyses" *Buildings*, Vol. 14, No. 8, article 2445.

Damage Behavior of Light Gauge Steel Partition Wall under In-plane and Out-of-plane External Forces

Yusuke Oki[1], Shoichi Kishiki[2] and Tadashi Ishihara[2]

[1] Building Research Institute
1, Tachihara, Tsukuba, Ibaraki,305-0802, Japan
e-mail: oki_y@kenken.go.jp
[2] Institute of Integrated Research, Institute of Science Tokyo
4259, Nagatsuta-cho, Midori-ku, Yokohama, Kanagawa, 226-8501, Japan
e-mail: kishiki.s.02d9@m.isct.ac.jp, ishihara.t.458a@m.isct.ac.jp

Abstract. To determine whether a building can continue to be used after a severe seismic event quickly, it is necessary to examine the damage to light gauge steel (LGS) partition walls caused by external forces. Particularly, to evaluate the buildings to keep operational level, immediate occupancy level or not, the damage mechanism is necessary for the LGS walls to be investigated under the actual load condition that simulates the seismic event. There have been many experimental studies focusing on the strength and damage patterns of partition walls under the in-plane or out-of-plane load, but few studies have fundamentally examined damage patterns under both loads applied at the same time. In this study, in-plane and out-of-plane simultaneous static loading experiments were conducted to simulate the damage behavior of the LGS partition walls. From the results of the experiment, the behavior that leads to serious damage under the simultaneous loads is investigated.

Keywords: Partition wall, Light gauge steel, Static loading test, Damage behavior, Simultaneous load

1. INTRODUCTION

A light gauge steel partition wall (LGS wall) is one of the non-structural elements used for fireproofing, sound insulation and separating rooms. In the case of Japan, there have been few cases of collapse or fall of structural frames in recent earthquakes, but damage to the LGS walls prevented occupancy as shelters and other facilities (reported by Kishiki et al.[2018]). To ensure operational or immediate occupancy level of the building, it is necessary to study the seismic performance of the LGS walls in detail.

LGS walls are seismically designed to resist inertial force and story drift of the floors, referencing guidelines such as "Recommendations for Aseismic Design and Construction of Nonstructural Elements" by the Architectural Institute of Japan (AIJ) [2003]. Systematic research on the seismic performance of non-structural components has also been conducted (for example by Zito et al. [2022]). In addition, there are much studies focusing on the load bearing capacity of the LGS walls under inertial forces or under story drift angles. For example, Tanaka et al [2012], Miyata et al. [2020], and Harayama et al [2018] focused on the strength or vibration characteristics for out-of-plane inertial force. Kato et al. [2007] and Yagi et al. [2021] were mainly focusing on the effect of the story drift, damage to the layer boards of the LGS walls due to interference between the boards and the structural frame has been observed.

On the other hand, the LGS wall is applied to both inertial force and the force due to the story drift during an earthquake, but the damage mechanism when both acts on the LGS wall has not been examined in previous studies. Furthermore, while case studies of composite damage have been identified through experimental investigations of LGS walls using full-scale vibration table tests, there have been few examples to date examining the effects of the balance between in-plane and out-of-plane external forces.

This paper investigates the effects of simultaneous in-plane story drift and out-of-plane load actions on the LGS walls using a proposed static experiment method to determine the seismic performance of non-structural elements by Oki Y. et al.[2024]. In this paper, we focus on "inertial force (simulated by the static out-of-plane middle height load)," and "in-plane story drift (i.e. deformation (or load) due to the story drift for in-plane direction)" as the external forces described in Figure 1.

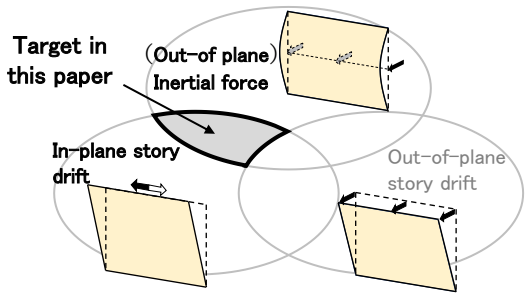


Figure 1. Target of external forces in this paper

2. EXPERIMENT METHOD

2.1 LOADING SYSTEM

Figure 2(a) - (e) show the overview of the loading frame motion. The loading frame proposed by Oki, et al. [2024] is composed of "in-plane part" (DI-1 - 6), "out-of-plane resistant part" (DO-1 - 6), "middle height loading part" (IF-1 - 6) and "resistant part" (FR-1, 2). Symbols such as IF-1 correspond to Oki, et al [2024]. Using the loading frame, it is possible to conduct not only a single loading but also simultaneous loading for the LGS wall.

In in-plane loading (to simulate the in-plane story drift), expansion and contraction of DI-6 cause DI-1 to move horizontally δ_{in} and the in-plane part to form a parallelogram shape. Resistant force is Q_{in}. At the same time when the in-plane part deforms δin at the top like Figure 2(a), out-of-plane resistant part also deforms as shown in Figure 2(c) and the middle height loading part moves $\delta_{in}/2$ laterally. In middle height loading, extension of IF-5 causes IF-1 - 3 to slide, IF-1 contacts with the specimen, and the out-of-plane middle height force P_{if} (simulating out-of-plane inertial force) is applied, causing an out-of-plane deflection δ_{if} in the specimen. As shown in Figure 2(b), experiments are conducted using in-plane story drift angle R_{in} and deflection angle θ_{if}, which are obtained by dividing δ_{in} and δ_{if} by H and h in Figure 2(a).

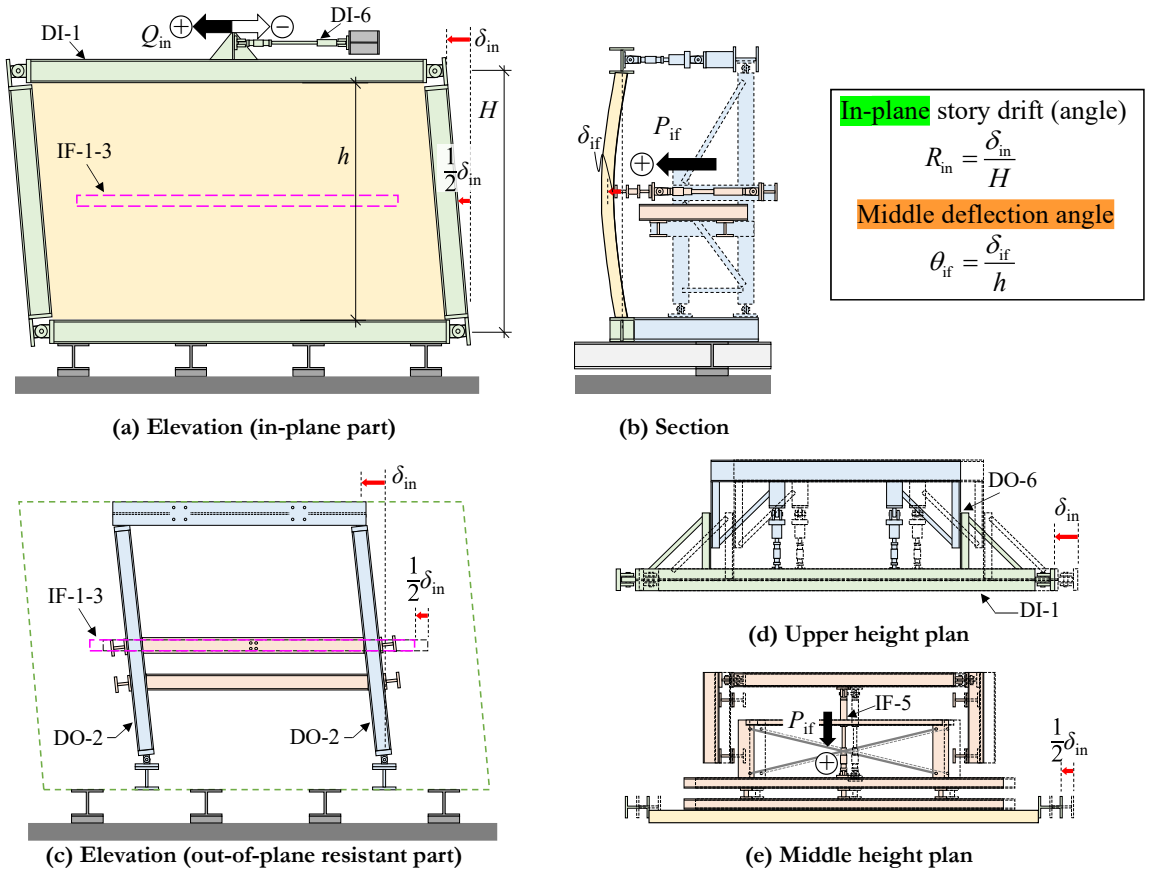
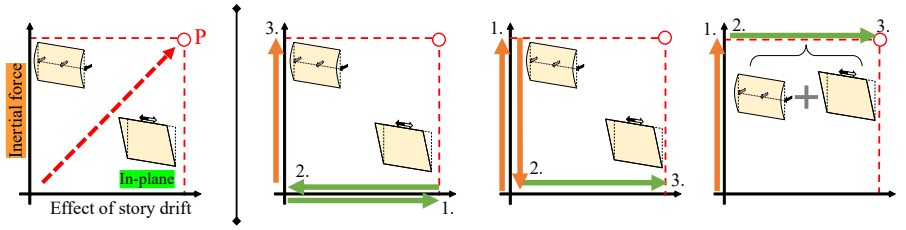


Figure 2. Overview of the loading frame motion

2.2 LOADING PROCEDURE

Consider a situation in which the LGS wall is simultaneously subjected to the load due to the story drift from the structural frame and the inertial force during an earthquake, then reaching at point P in Figure 3(a). To reproduce this situation in static experiments, we define [Condition A], [Condition B] and [Condition C] shown in Figure 3(b) - (d) as loading conditions. In each figure, the vertical axis shows the inertial force, and the horizontal axis shows the in-plane story drift. The arrows indicate the force transition acting on the specimen. Numbers (1., 2. and 3.) represent phases of load action. In [Condition A] shown in Figure 3(b), in-plane loading is conducted up to phase 1, in-plane part is returned to its original position (phase 2), and middle height load is applied up to phase 3. In [Condition B] shown in Figure 3(c), the middle height load is applied up to phase 1, IF-1 is moved away from the specimen (phase 2), and the in-plane loading is conducted up to phase 3. In [Condition C] shown in Figure 3(d), middle height load is applied up to phase 1, after that the in-plane loading is conducted up to phase 3 while maintaining the applied middle height

load (phase 2). [Condition C] is similar to [Condition B] in terms of applying the external force experience, but the final load state of the specimen is different.

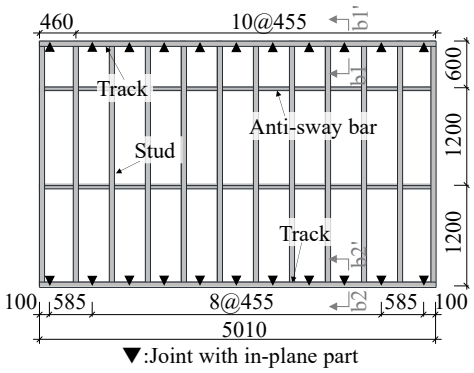


(a) Target condition (b) [Condition A] (c) [Condition B] (d) [Condition C]

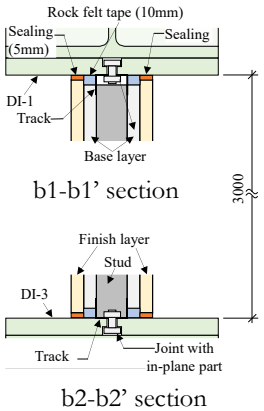
Figure 3. Simultaneous loading

2.3 LGS WALL SPECIMENS

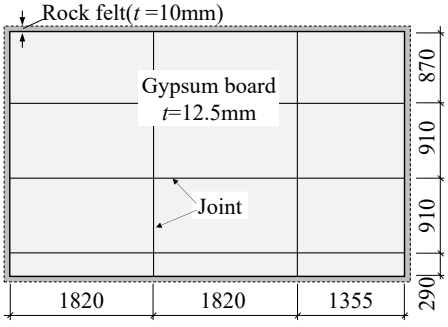
Figure 4(a) - (d) and Table 1 show the specimens. All specimens are the same specification. Figure 4(b) shows the details of the cross sections of parts b1-b1' and b2-b2' of Figure 4(a). The LGS wall specimen is the size of 5,010 mm width x 3,000 mm height, installed inside the in-plane part (DI-1 - 3 in Figure 2(a)). The light gauge steels are based on Japan Industrial Standard (JIS, 2010). The upper track is fastened to DI-1 and the lower track is fastened to DI-3 at intervals of 450 to 460 mm, respectively. The studs placed as shown in Figure 4(a). The wall is made of 12.5 mm fire-resistant gypsum boards for the base and the finish layers on the front and back sides of the studs. The base layers are screwed to the studs, and the finish layers are stapled and applied adhesive to each base layer. The space between the base layers and the in-plane part of the frame is filled with rock felt, and the space between the finish layers and the in-plane part is filled with the fire-resistant sealing, as shown in Figure 4(b). In the Table 1, the alphabet in the specimen names indicates the loading conditions, and the number indicates the final out-of-plane deflection angle due to the middle height load.



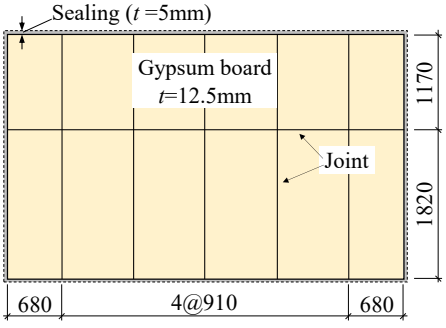
(a) Light gauge steel



(b) Details between the LGS wall and the loading frame



(c) Base layer



(d) Finish layer

Figure 4. Specimen of the experiment

Table 1. Specimen, loading condition and results

Specimen name	Loading Condition	Loading procedure	Target θ_{if}(%)	damage behavior of the gypsum board
A-2.0	A	In-plane loading, Middle height loading	0.00	Damage at the corners of the finish layers
B-2.0	B	Middle height loading, in-plane loading without middle height load	2.00	Out-of-plane detachment of the finish layer
B-1.0			1.00	Out-of-plane deformation of the base layer
B-0.5			0.50	Damage at the corners of the finish layers
C-1.0	C	Middle height loading, in-plane loading maintaining middle height load	1.00	Out-of-plane detachment of the finish layer
C-0.5			0.50	Out-of-plane detachment of the finish layer
C-0.41			0.41	Out-of-plane deformation of the base layer
C-0.25			0.25	Out-of-plane deformation of the base layer
C-0.16			0.16	Damage at the corners of the finish layers

2.4 LOADING CONDITIONS

The in-plane loading is controlled by the in-plane story drift (R_{in}) and is performed as positive-negative alternating incremental cyclic loading, two cycles for each amplitude. The middle height loading is performed as a positive incremental loading, one cycle for each amplitude. The deflection angle θ_{if} corresponding is used as the control amplitude, increasing up to the value named for each specimen (maximum +2.0%).

3. RESULTS AND DISCUSSIONS

3.1 EFFECT ON LOADING PROCESS

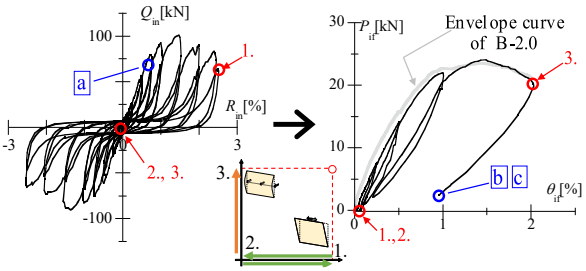
The force displacement relationships for specimen A-2.0 and B-2.0 are shown in Figure 5, 6, respectively. Figure 7 shows the typical damage. The vertical axis is Q_{in} and the horizontal axis is R_{in} in Figure 5(a) and 6(b). The vertical axis is P_{if} and the horizontal axis is θ_{if} in Figure 5(b) and 6(a). The red numbers "1." "2." and "3." refer to the loading process. The characters "a" - "g" in the figure correspond to Figure 7(a) - (g).

First, by comparing A-2.0 under [Condition A] (see Figure 5(a)) and B-2.0 under [Condition B] (see Figure 6(b)), the effects of the loading experience of inertial force on the damage of the LGS walls during in-plane loading are discussed. In both A-2.0 and B-2.0, the damage occurred at the four corners of the finish layers between $R_{in} \approx \pm 0.5$ - ± 0.75% (Figure 7(a)). Comparing the maximum strength of Q_{in}, it is +70.0 kN for B-2.0, which is about 70% of that of A-2.0 (=+101.1 kN). This is because the middle height load experience prior to in-plane loading causes the out-of-plane detachment of the finish layers (Figure 7(d)) and localized damage of the studs (similar to Figure 7(b)), as well as the reduced integrity between the light gauge steels and the layers. For A-2.0, which was not initially subjected to the middle height load, increasing in-plane story drift after reaching the maximum strength of Q_{in} only resulted in further damage development at the corners of the layers shown in Figure 7(a). On the other hand, in B-2.0, after reaching the maximum strength of Q_{in}, misalignment of the board joints was observed clearly (Figure 7(e)) in addition to the damage at the corners of the layers, after that the base layer was pulled out from the screws, resulting in significant out-of-plane deformation of the base layer (Figure 7(f)). Subsequently, the finish layer peeled off (Figure 7(g)).

Next, by comparing A-2.0 under [Condition A] (see Figure 5(b)) and B-2.0 under [Condition B] (see Figure 6(a)), the effects of the loading experience of in-plane story drift on the damage due to the middle height load are discussed. The gray line in Figure 6(a) shows the envelope curve of Figure 5(b). There is no significant difference in initial stiffness and maximum strength. After the experiment, the boards of A-2.0

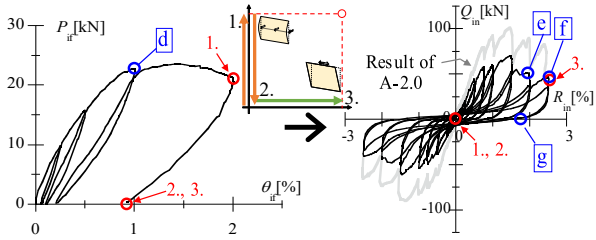
and B-2.0 were removed and the light gauge steels were observed. In A-2.0, local bending of the studs was observed at all of the studs in the middle height of the wall and at a height of approximately 300 mm from both outer edges to the second studs (Figure 7(b), (c)). In B-2.0, local bending of the studs was observed at all locations in the middle height of the wall, similar to Figure 7(b). According to the previous experiment by Miyata et al. [2019] and Kishiki et al. [2020] and other studies, the damage observed in Figure 7(b) is inferred to have been caused by middle height load. The envelope curves of the force displacement relationships are very similar because the damage at four corners of the layers when there was a loading experience of in-plane story drift did not affect the studs and other light gauge steel element for the resistance of the middle height load.

These results suggest that the behavior of the LGS walls may depend on the loading process of the in-plane story drift and the middle height load. Particularly, in the case the LGS wall is applied in the load due to the in-plane story drift after the damage by the middle height load, the damage will be more advanced and may not be the damage predicted by the result only for in-plane story drift.



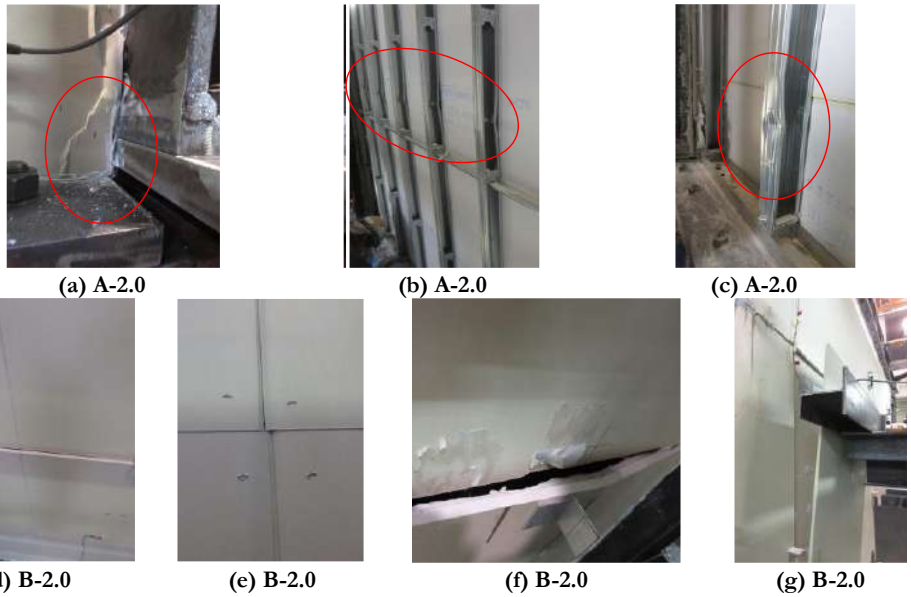
(a) In-plane story drift (b) Middle height load

Figure 5. Force displacement relationship of A-2.0 [Condition A]



(a) Middle height load (b) In-plane story drift

Figure 6. Force displacement relationship of B-2.0 [Condition B]



(a) A-2.0 (b) A-2.0 (c) A-2.0

(d) B-2.0 (e) B-2.0 (f) B-2.0 (g) B-2.0

Figure 7. Damage

3.2 Effect on Simultaneous Loading for In-plane Story Drift and Middle Height Load

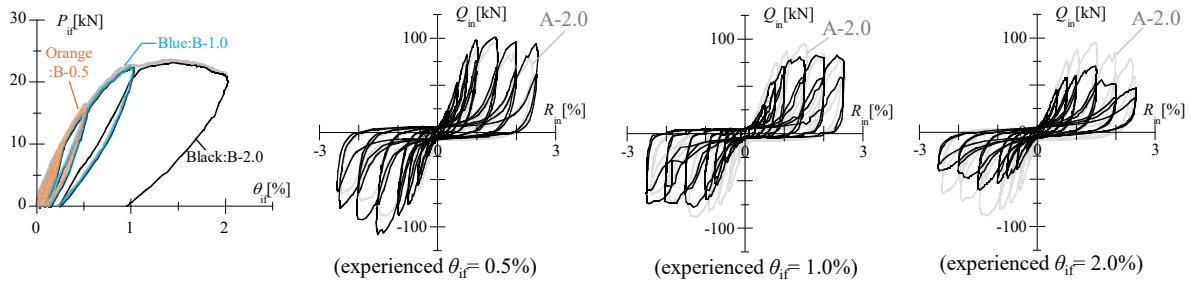
First, examine the effect on in-plane behavior under [Condition B] when the applied middle height force is unloaded. The force displacement relationship for out-of-plane middle height load in [Condition B] is shown

in Figure 8(a), the force displacement relationship for in-plane story drift are shown in Figure 8(b) - (d), respectively. In Figure 8(a), the maximum deflection angle experienced under the middle height load as the initial loading is referred to as the "experienced deflection angle." In each force-displacement relationship for in-plane story drift, the force-displacement relationship for in-plane story drift as an initial loading under [Condition A] is also shown in gray lines.

In the in-plane force displacement relationship, little difference is observed between the contact stiffness and unloading stiffness after contact between the in-plane frame column and gypsum board, even when the experienced deflection angle increases. On the other hand, focusing on the in-plane maximum strength, the B-2.0 and B-1.0 with experienced deflection angles of 2.0% and 1.0%, respectively, showed a reduction to approximately 70 – 80% of the strength of the A-2.0 without an experienced deflection angle. During in-plane loading of B-1.0 and B-0.5, damage of the corners of the gypsum boards was observed, but no out-of-plane damage occurred.

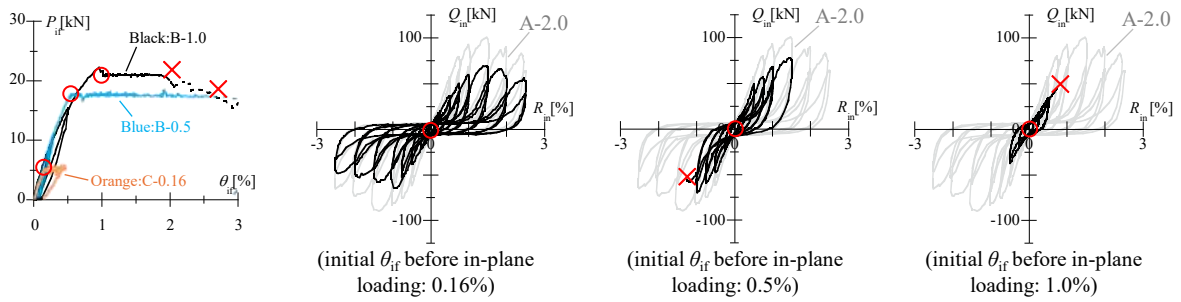
Second, examine the effect on in-plane behavior under [Condition B] when the applied middle height force is maintained. The force displacement relationship for middle height load in [Condition C] is shown in Figure 9(a), while the force displacement relationships for in-plane story drift are shown in Figure 9(b) - (d). In Figure 9(a) as the force displacement relationship for middle height load, the deflection angle when the middle height load maintenance begins is defined as the "maintenance starting deflection angle," and the maintaining middle height load during in-plane loading is called "the maintained inertial force." The circle in Figure 9(a) indicates the point at which the middle height loading began to be maintained, marking the start of in-plane loading. The cross (×) indicates the point at which the middle height load could not be maintained and finished the in-plane loading.

For all specimens, starting in-plane loading caused only the deflection angle to increase, and specimens C-1.0 and C-0.5 finally failed to maintain the maintained inertial force. That is, under inertial force maintenance, the resistance of the LGS wall to out-of-plane force decreases with in-plane loading. The maximum in-plane story drift angle at which inertial forces can be maintained during in-plane loading is 1.3% for C-0.5 (initial deflection angle 0.5%) and 0.7% for C-1.0 (initial deflection angle 1.0%). As the maintenance starting deflection angle increases, the maximum in-plane story drift angle at which inertial forces can be maintained decreases. Focusing on the maximum in-plane strength, it has decreased to approximately 50 to 70 percent of the value when middle height load are removed. C-0.4 and C-0.25, with maintenance starting deflection angles of 0.4% and 0.25% respectively, exhibited out-of-plane damage of the finish layer similar to Figure 7(d). C-1.0 and C-0.5, with maintenance starting deflection angles of 1.0% and 0.5%, respectively, exhibited out-of-plane delamination of the base layer similar to Figure 7(f).



(a) Middle height load **(b) In-plane story drift (B-0.5)** **(c) In-plane story drift (B-1.0)** **(d) In-plane story drift (B-2.0)**

Figure 8. Force displacement relationship [Condition B]



(initial θ_{if} before in-plane loading: 0.16%)

(initial θ_{if} before in-plane loading: 0.5%)

(initial θ_{if} before in-plane loading: 1.0%)

(a) Middle height load **(b) In-plane story drift (C-0.16)** **(c) In-plane story drift (C-0.5)** **(d) In-plane story drift (C-1.0)**

Figure 9. Force displacement relationship [Condition C]

4. CONCLUSION

In this paper, in-plane load (equivalent to the story drift) and out-of-plane load (equivalent to the inertial force) simultaneous static loading experiment were conducted on the capacity of the LGS walls, which are commonly used in Japanese interior construction. The conclusion obtained are presented below.

(1) When in-plane story drift and out-of-plane middle height load act on an LGS wall, the damage behavior of the wall differs depending on the loading process and the experience of the deflection angle. When the middle height force act first, damage incurred during inertial loading affects the maximum in-plane load capacity during in-plane deformation. Furthermore, the final damage state changed compared to when in-plane deformation acted first.

(2) When unloading the middle height load, the influence of the out-of-plane behavior can be negligible for in-plane behavior up to the experienced deflection angle of 0.5%. Beyond the 0.5%, behavior can be affected by damage due to the out-of-plane load.

(3) When maintaining the middle height load, the in-plane maximum strength is approximately 50–70% of the value when the out-of-plane middle height load was unloaded. In other words, applying the middle height load and in-plane story drift simultaneously results in a greater influence of the inertial force on the in-plane behavior of the LGS wall.

ACKNOWLEDGEMENT

We would like to thank Dr. Tatsumi (Lecturer, Aichi Institute of Technology), Dr. Kurosawa (Assistant Professor, Institute of Science Tokyo), Mr. Isoda (former graduate student, Tokyo Institute of Technology) and Ms. Kugimoto (former graduate student, Institute of Science Tokyo) for planning the loading frame and conducting the experiments. The research was supported by the Japan Iron and Steel Federation (JISF).

REFERENCES

AIJ. [2003] *Recommendations for Aseismic Design and Construction of Nonstructural Elements*, Architectural Institute of Japan, Japan. (in Japanese)

Harayama, K., Sakuraba, F., Suzuki, K., Seike T. [2018] "Development of Reduction Method for Seismic Damage to LGS Partition Wall Part 4. Out of Plane Vibration Tests on Vertical Installed LGS Partition Walls," *Summaries of Technical Papers of Annual Meeting*, AIJ, Materials and Construction: pp.1073-1074. (in Japanese)

Kato, M., Matsumiya, T., Suita, K., Matsuoka, Y., Nakashima, M. [2007] "Seismic Performance and Damage Evaluation of Drywall Partition," *Journal of Structural and Construction Engineering*, AIJ, (614): pp.139-146. (in Japanese)

Kishiki, S., Seike, T., Motoyui, S., Koshiishi, N. [2018] "Development of Reduction Method for Seismic Damage to LGS Partition Wall Part 1 research background and purpose of research," *Summaries of Technical Papers of Annual Meeting*, AIJ, Materials and Construction: pp.1073-1074. (in Japanese)

Miyata, H., Sakurada, S., Tatsumi, N., Kishiki, S., Nitta, W. [2020] "Development of Reduction Method for Seismic Damage to LGS Partition Wall Part 12 -14 Stiffness and Strength against out-of-plane Deformation (1) - (3)," *Summaries of Technical Papers of Annual Meeting*, AIJ, Materials and Construction: pp.1209-1214. (in Japanese)

Miyata, H., Sakurada, S., Tatsumi, N., Kishiki, S., Nitta, W., Oouchi, W., Someno, T., Sakuraba, F. [2019] "Development of Reduction Method for Seismic Damage to LGS Partition Wall Part 9-10," *Summaries of Technical Papers of Annual Meeting*, AIJ, Materials and Construction: pp.1425-1428. (in Japanese)

Oki, Y., Kishiki, S., Tatsumi, N., Ishihara, T. [2024] "Seismic Performance of Partition Walls Subjected to Story Drift and Inertial Force," *Proceedings of the 18th World Conference on Earthquake Engineering*, Milan, Italy

Tanaka, E., Terada, T., Sakuraba, F., Uchimoto, H., Ogawa, Y., Murota, F. [2012] "Anti-plane Static Loading Tests on Partition Walls with Light-gauge Steel," *AIJ journal of Technology and design*, 18(39): pp.575-578. (in Japanese)

Yagi, S., Iyama, J., Fukushima Y., Kishiki, S., Ishida, T., Seike, T., Yamada, S. [2021] "Damage Observation and Detection Using Accelerometer of Dry Partition Wall Installed in Steel Moment Frame under Large Story Drift," *Journal of Structural and Construction Engineering, AIJ*, 86(788): pp.1400-1411. (in Japanese)

Zito, M., Nascimbene, R., Dubini, P., D'Angela, D., Magliulo, G. [2022] "Experimental Seismic Assessment of Nonstructural Elements: Testing Protocols and Novel Perspectives," *Buildings 2022, 12, 1871*; https://doi.org/10.3390/buildings12111871.

Influence of in-plane damage on the out-of-plane seismic response of weak clay masonry infills through shaking table dynamic tests

Riccardo R. Milanesi[1], Maithree Kurukulasuriya[2], Igor Lanese[1], Guido Magenes[2], Paolo Morandi[1]

[1] Eucentre Foundation, via Ferrata 1, Pavia, Italy
e-mail: riccardo.milanesi@eucentre.it; igor.lanese@eucentre.it; paolo.morandi@eucentre.it
[2] Department of Civil Engineering and Architecture, via Ferrata 3, Pavia, Italy
e-mail: maithree.kurukulasuriya@unipv.it; guido.magenes@unipv.it

Abstract. Masonry infills, often treated as non-structural components within reinforced concrete and steel frames, have revealed significant vulnerability during recent earthquakes, prompting renewed investigation into their seismic performance. Although extensive research has been conducted, the impact of in-plane damage on out-of-plane behaviour remains insufficiently understood.
To address this gap, an experimental campaign is currently underway at the Eucentre Foundation, targeting horizontally hollow clay-masonry infills, which is a typology widely used in Mediterranean countries between the 1960s and 1980s. Full-scale, single-story, single-bay panels were constructed within steel-concrete composite frames and subjected to a range of boundary conditions: fully connected on all edges; with gaps at the top or sides; using both 12 cm and 8 cm thick masonry units; and in configurations both with and without openings. Each configuration underwent in-plane pseudo-static cyclic loading, dynamic out-of-plane shake-table testing, and sequential testing in which panels were first loaded in-plane to induce damage before being exposed to out-of-plane dynamic excitation until collapse.
This study aims to elucidate the interaction between in-plane and out-of-plane responses by taking into account the out-of-plane behaviour through shaking table dynamic tests, examine how damage progression and boundary conditions influence failure mechanisms, and assess the roles of infill thickness and openings. Key findings include detailed force–displacement relationships, damage propagation patterns, acceleration and displacement distributions, and observations of arching and bending behaviours. These insights contribute to more accurate seismic assessment and the safer design of masonry-infilled frames. The full experimental dataset is publicly available at https://experiments.builtenvdata.eu/datasets/43/.

Keywords: Weak masonry infill, Out-of-plane seismic response, Shake-table testing, Boundary conditions, In-plane Out-of-plane interaction.

1. INTRODUCTION

Masonry infills are widely used to enclose reinforced concrete and steel-framed buildings. In southern Europe, and many parts of the world, older pre-code constructions often feature thin (8–15 cm) single- or double-leaf infills made of highly perforated clay units. While some areas still employ this lightweight system, countries like Italy have moved toward thicker (minimum 20–25 cm) perforated or lightweight blocks, aiming to improve thermal and acoustic performance as well as construction efficiency. Thin panels are generally considered weak or slender, whereas thicker ones are classified as robust or strong.

Post-earthquake surveys in L'Aquila (2009), Lorca (2011), Emilia (2012), Central Italy (2016), Albania (2019), and most recently in Turkey and Syria (2023), consistently document severe damage or even collapse of slender infill walls under seismic action, leading to economic losses and risks to human life (Ricci 2011; De Luca 2014; Manfredi 2014; Masi 2019; Marinković 2022; Binici 2023). Such failures typically occur when in-plane cracking compromises out-of-plane stability, making it essential to understand how these mechanisms interact.

Although many static and pseudo-static studies have investigated infill behavior, relatively few have examined how prior in-plane damage influences subsequent out-of-plane resistance. Early research by Angel et al. (1994) and Calvi and Bolognini (2001) applied cyclic in-plane loading before out-of-plane testing, and later studies followed a similar approach (da Porto 2013; Morandi 2022). However, static out-of-plane tests, whether using line loads, point loads, or uniform pressure, cannot capture key seismic effects such as inertia, crack closure during motion reversals, or variable loading rates.

Dynamic shake-table experiments are therefore indispensable. While some campaigns have tested infilled frames or multi-storey models under bidirectional shaking (Hashemi 2006; Tu 2010; Baek 2023), very few have directly examined the out-of-plane response of single-bay, single-storey unreinforced masonry (URM) infills after in-plane damage. One notable exception is Milanesi et al. (2022), who studied innovative full-scale clay block infill panels with sliding joints, whereas the present study is focusing in traditional existing masonry infills.

To close this gap, the Eucentre Foundation has undertaken a large-scale experimental program on slender infills representative of Italian RC buildings from the 1960s–1980s. To date, 19 full-scale specimens have been tested. Steel–concrete composite frames (UPN400 grouted with high-strength concrete) were equipped with single-storey, single-bay infill panels and subjected to a variety of boundary and geometric conditions, including fully bonded perimeters, gaps at the top or sides, 12 cm or 8 cm units, and the presence or absence of openings. Each configuration was tested under in-plane pseudo-static cyclic loading, out-of-plane shake-table excitation, and combined sequences where panels were first damaged in-plane before being shaken out-of-plane to collapse.

This methodology enabled researchers to track how damage progresses under different boundary conditions, panel thicknesses, and opening configurations. It also provided data to construct charts of out-of-plane resistance versus in-plane drift, to map cracking and acceleration patterns, and to identify arching and bending failure modes.

The full dataset is openly available, and continuosly updated, at: experiments.builtenvdata.eu/datasets/43/

2. SPECIMEN DESIGN AND EXPERIMENTAL CAMPAIGN OVERVIEW

The full-scale masonry infills were constructed within structural frames composed of composite sections, combining UPN400 steel profiles (S355 grade) grouted with high-strength concrete. Further details on the frames and their in-plane response are reported in Morandi et al. (2025a). The frames were designed to replicate existing RC structures while ensuring that they remained undamaged throughout testing.

The infills represent a traditional unreinforced "weak" masonry typology, widely used in Italy during the 1960s–1980s, and built with horizontally hollowed clay blocks of 12 cm or 8 cm thickness. A general-purpose mortar type M2.5 (nominal compressive strength of 2.50 MPa) was used, consistent with construction practices of that era.

Each masonry panel measured 3.50 m in length and 2.75 m in height, with a thickness equal to the block thickness plus 1 cm of plaster applied on one face only. This specimen configuration was intended to reproduce a single wythe of a double-leaf infill, with plaster applied externally and not internally. The out-of-plane slenderness ratio λ (panel height over plastered thickness) was approximately 21.2 for 12 cm units and 30.6 for 8 cm units. Sixteen of the nineteen specimens were constructed fully bonded to the surrounding frame by mortaring the interface joints at the sides, while the remaining three specimens included a ~2.0 cm vertical gap between the infill and columns to create a vertical bending/arching mechanisms and avoid the horizontal or bidirectional effects. Four specimens were also built with deliberately poor boundary detailing to assess its influence. Mortar bed joints were ~1 cm thick, and head joints were left partially filled to reproduce typical workmanship of the period since the infills represent an existing solution.



Figure 1. Dimensions and details of the infill specimens.

The specimens were grouped into four batches (Table 1), each addressing a specific variable (Figure 1):

- Batch 1: Reference infills, 13 cm thick.
- Batch 2: Influence of poorly executed top boundary conditions.
- Batch 3: Effect of openings, tested with (3b) and without (3a) spandrel beams.
- Batch 4: Reduced-thickness infills (9 cm).

Table 1. Summary of specimen details and test program.

Specimen	Top Boundary condition	Thickness (masonry + plaster)	Lateral edges	Opening	In-Plane test	Max IP drift*	Out-of-Plane test	Max OOP PFA*	Batch (year)
T1	Filled	12+1=13 cm	Filled	No	Yes	1.00%	No	---	1 (2021)
T2	Filled	12+1=13 cm	Filled	No	Yes	0.30%	Yes	2.50g	
T3	Filled	12+1=13 cm	Filled	No	Yes	0.65%	Yes	1.50g	
T4	Filled	12+1=13 cm	Filled	No	No	---	Yes	2.75g	
T5	Filled	12+1=13 cm	Gap (about 2 cm)	No	No	---	Yes	1.00g	
T6	**Poorly executed**	12+1=13 cm	Filled	No	Yes	1.50%	No	---	2 (2022)
T7	**Poorly executed**	12+1=13 cm	Filled	No	Yes	0.65%	Yes	1.25g	
T8	**Poorly executed**	12+1=13 cm	Filled	No	No	---	Yes	1.75g	
T9	**Poorly executed**	12+1=13 cm	Gap (about 2 cm)	No	No	---	Yes	0.50g	
T10	Filled	12+1=13 cm	Filled	**Yes**	Yes	1.00%	No	---	3a (2023)
T11	Filled	12+1=13 cm	Filled	**Yes**	Yes	0.50%	Yes	1.50g	
T12	Filled	12+1=13 cm	Filled	**Yes**	No	---	Yes	2.00g	
T13	Filled	12+1=13 cm	Filled	**Yes**	Yes	1.00%	No	---	3b (2023)
T14	Filled	12+1=13 cm	Filled	**Yes**	Yes	0.50%	Yes	1.50g	
T15	Filled	12+1=13 cm	Filled	**Yes**	No	---	Yes	2.00g	
T16	Filled	**8+1=9 cm**	Filled	No	Yes	1.25%	No	---	4 (2024)
T17	Filled	**8+1=9 cm**	Filled	No	Yes	0.65%	Yes	0.20g	
T18	Filled	**8+1=9 cm**	Filled	No	No	---	Yes	1.80g	
T19	Filled	**8+1=9 cm**	Gap (about 2 cm)	No	No	---	Yes	0.50g	

** Nominal values*

Within each batch, the testing sequence consisted of:

- one specimen loaded in-plane only to collapse,
- one tested out-of-plane only to collapse,
- the remaining specimens subjected to combined loading, first in-plane up to a predefined drift level, then dynamically out-of-plane until failure.

For specimens restrained only along the top and bottom edges, testing was limited to out-of-plane loading. Table 1 reports the target in-plane drift levels and maximum nominal Peak Floor Accelerations (PFA) reached by each specimen.

2.1 MATERIAL CHARACTERIZATION

A comprehensive material testing program was performed for each batch. Clay block compressive strengths were measured under both vertical loading (perpendicular to perforations, f_b) and lateral loading (parallel to perforations, f_b'), according to EN 772-1 (CEN, 2015). Mortar flexural (f_f) and compressive (f_m) strengths were determined following EN 1015-11 (CEN, 2019). Masonry wallette tests (77 × 77 cm, 3 × 3 units) were conducted in accordance with EN 1052-1 (CEN, 2001) to obtain vertical (f_{vert}) and lateral (f_{lat}) compressive strengths, as well as elastic moduli (E_v, E_{lat}), evaluated at one-third of the corresponding peak stress. Diagonal compression tests, following ASTM E519-02 (ASTM, 2002), provided diagonal tensile strength (f_t) and shear modulus (G). Triplet tests in line with EN 1052-3 (CEN, 2007) yielded initial shear strength (f_{v0}) and friction coefficient (μ). Finally, four-point bending tests on wallettes, performed according to EN 1052-2 (CEN, 2016), gave flexural strengths parallel (f_{x1}) and perpendicular (f_{x2}) to the bed joints. For each direction, six specimens were tested under monotonic displacement control: three on the plastered face and three on the unplastered face, to capture plaster's influence on flexural behavior.

2.2 TEST SETUP AND INSTRUMENTATION

Figure 2 illustrates the test configuration. In-plane quasi-static cyclic loads were applied to the top beam of the frame by a servo-hydraulic actuator anchored to a rigid steel reaction frame. Out-of-plane displacements of the frame nodes were prevented by four inclined braces. During these tests, the shaking table was behaving as a rigid strong floor. For out-of-plane testing, the actuator was removed while the frame restraints remained in place, and seismic excitation was applied through the shake table. Specimens were rigidly anchored to the table to eliminate slip at the base.

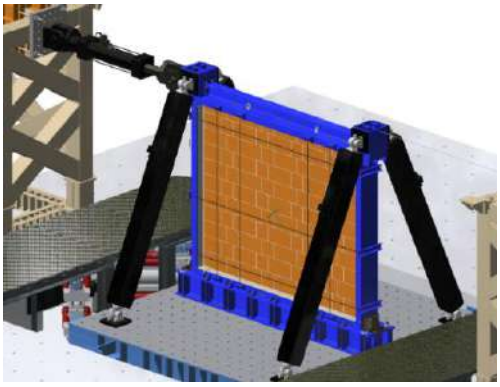


Figure 2. Sketch of experimental setup for the cyclic in-plane and dynamic out-of-plane tests (Morandi et al., 2025a).

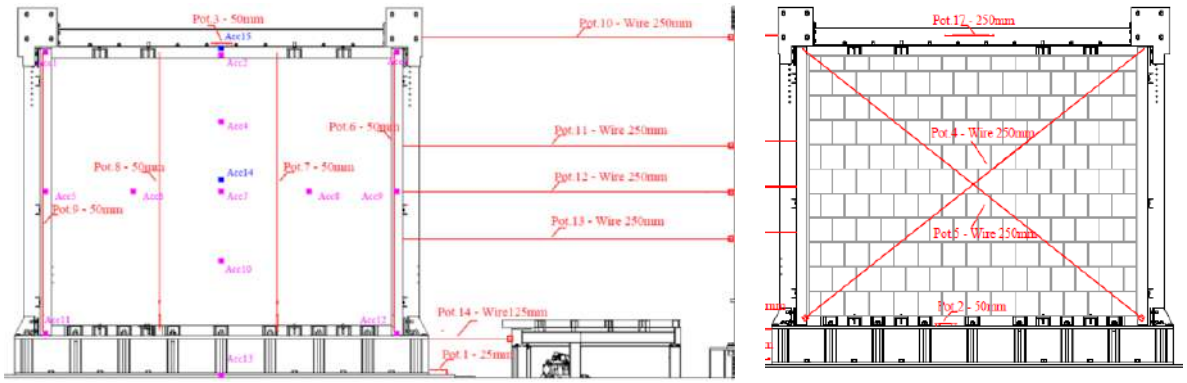


Figure 3. Instrumentation installed for in-plane cyclic pseudo-static tests (Morandi et al., 2025a).

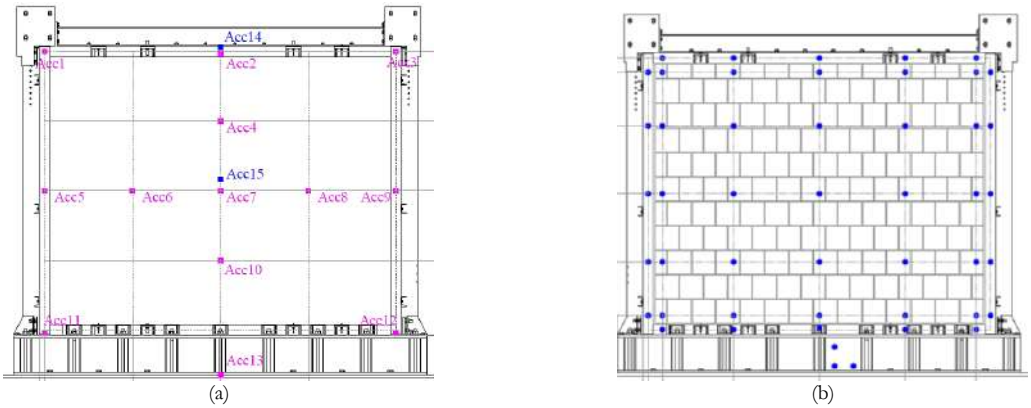


Figure 4. Instrumentation installed for out-of-plane dynamic shaking table tests: (a) accelerometers in the plastered side; (b) markers for displacement measurement in the unplastered side. (Morandi et al., 2025a).

Instrumentation differed slightly between in-plane and out-of-plane phases. Both employed accelerometers (Acc) and linear potentiometers (Pot), while out-of-plane tests also used optical tracking with markers and infrared cameras to capture detailed displacement fields. Sensors were arranged to record global specimen

behavior, both frame and infill, under acceleration and displacement demands. Figure 3 and Figure 4 show the layouts for cyclic in-plane and dynamic out-of-plane setups. Devices at risk of damage were removed once collapse was imminent.

2.3 LOADING PROTOCOLS

For in-plane quasi-static cyclic tests, specimens were subjected to three fully reversed, displacement-controlled cycles at increasing drift levels. Prior to infill installation, all bare frames were tested cyclically (Morandi et al., 2025a) to establish baseline force-displacement characteristics, allowing isolation of the infill contribution. Target drift levels were 0.05%, 0.10%, 0.20%, 0.30%, 0.40%, 0.50%, 0.65%, 0.75%, 1.00%, 1.25%, and 1.50% each repeated three times in both push and pull directions. The final drift level reached for each specimen is reported in Table 1.

For out-of-plane response, specimens were subjected to dynamic shake-table excitations until ultimate capacity was reached. Artificial ground motions were generated to match a horizontal Required Response Spectrum (RRS) based on ICC-ES AC156 (2020), with a spectral plateau from 1.3 to 10 Hz (Morandi et al., 2025a, Batch 1). Ground motions were applied incrementally: in 0.10g steps up to 0.50g, followed by 0.25g steps until collapse. Specimens with only vertical edge restraints were tested with a constant 0.10g increment. When collapse appeared imminent, the preceding motion was sometimes repeated without increasing acceleration. Prior to each seismic sequence, white-noise excitation was used to characterize dynamic properties and fine-tune shake-table control.

3. EXAMPLE OF EXPERIMENTAL RESULTS

3.1 IN-PLANE RESPONSE

The in-plane response of a fully bonded masonry infill is illustrated by specimen T1, tested under incremental drift levels until ultimate conditions were reached at a nominal drift of δ_n = 1.00%. While the same procedure was applied to all specimens, T1 is presented here as a representative example. Initial damage appeared at the frame–infill interfaces, where cracks developed along the mortar bed joints. These progressed into prominent diagonal step cracks that linked to a primary horizontal fissure. As drift increased, further cracking occurred along the mortar joints, progressively degrading the plaster and damaging the clay unit shells (Figure 6).

Cyclic tests on both bare and infilled frames were assessed by plotting applied force against the top-beam displacement at actuator level. For the infilled frames, hysteresis loops and peak envelope curves (Figure 5) are shown alongside the isolated infill contribution, obtained by subtracting the bare-frame response. The backbone curves for Batch 1 (T1, T2, T3) indicate comparable initial stiffness across specimens and a consistent onset of nonlinearity associated with degradation.

Specimen T1 reached maximum drifts of +0.91% (pull) and -0.95% (push). Strength and stiffness deterioration was evident, with force drops of 5-25% between the first and second cycles at a given drift. The bare frame itself remained elastic within the tested range. While identical analyses were performed for all specimens, results are detailed here for T1 as a representative example.

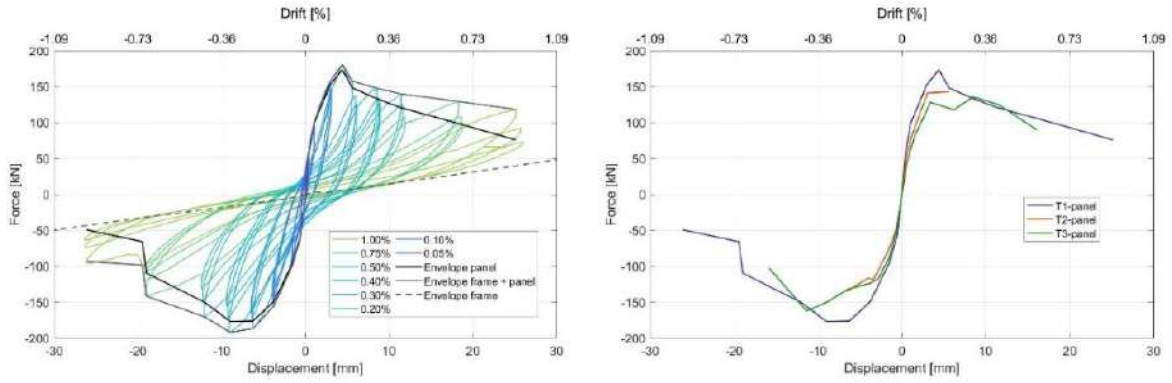


Figure 5. Force-displacement curve of T1 specimen (left) and comparison of the envelope curves of the infill only contribution of batch 1 specimens (T1, T2, T3) (right) (Morandi et al., 2025a).



Figure 6. Pictures of the damage state of infills T1 on unplastered (left) and plastered face (right) at the end of the in-plane tests.

3.2 OUT-OF-PLANE RESPONSE

Figure 7 illustrates the out-of-plane damage progression using sketches and video frames. Specimen T4, fully connected on all edges and not pre-damaged in-plane, demonstrated notable capacity: boundary cracks formed at PFA 0.1g, while the first panel crack (a horizontal fissure at mid-height) appeared only at PFA 1.0g. A second horizontal crack emerged above the 7th course at PFA 1.5g, followed by two diagonal cracks at PFA 1.8g. Limited additional cracking developed up to PFA 2.5g, after which plaster spalling, unit crushing at edges, and widespread joint opening accelerated. Collapse occurred at PFA 2.75g through overturning of an upper trapezoidal wedge that detached from the top beam. The same testing procedure was applied to T2, T3, and T5, but only T4 is reported here in detail (see Morandi et al., 2025a).



Figure 7. Sequence of pictures of the collapse mechanism of T4.

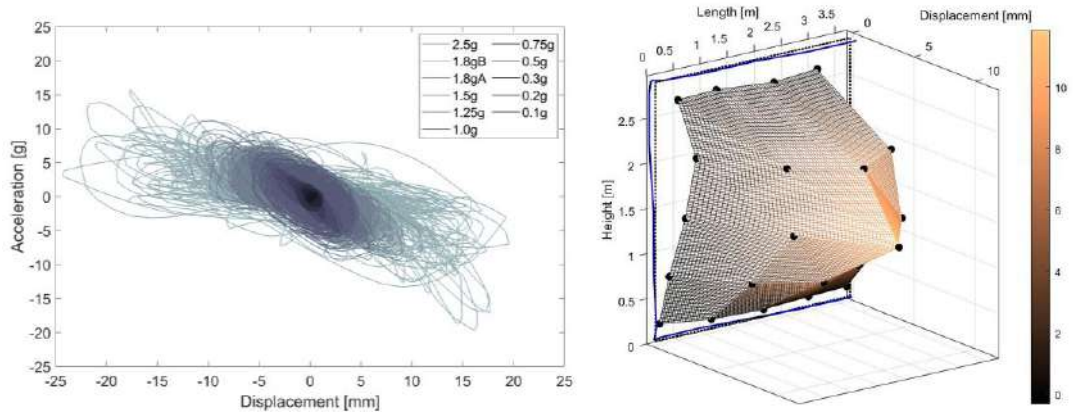


Figure 8. Out-of-plane hysteretic cyclic acceleration-displacement curves at the centre of the T4 (left) and 3D deformed shape of T4 (right). (Morandi et al., 2025).

3.3 DYNAMIC PROPERTIES

Dynamic characteristics were derived from accelerometers installed on one face of each infill (Figure 4a). During in-plane tests, controlled transverse impulses were applied before each drift increment, while out-of-plane tests used broadband white-noise excitations from the shaking table. Frequency content was extracted via FFT, and Operational Modal Analysis (Peeters et al., 2012) provided reliable frequency and damping estimates, even under high damping or noisy conditions.

In Batch 1, undamaged panels (T1, T4) had natural frequencies between 35.4-39.3 Hz, with differences reflecting material and construction variability. In-plane drift caused rapid stiffness loss, exceeding 20% frequency reduction by 0.30% nominal drift. Under subsequent out-of-plane loading, T2 and T3 showed additional degradation of more than 40% at just PFA 0.20g, whereas undamaged T4 reached the same level of degradation only at PFA 0.75g. The degradation of T1's fundamental frequency is presented in Figure 9a as an example. Further discussion of frequency tracking and innovative identification methods is given by Bolognini et al. (2024) (Figure 9b).

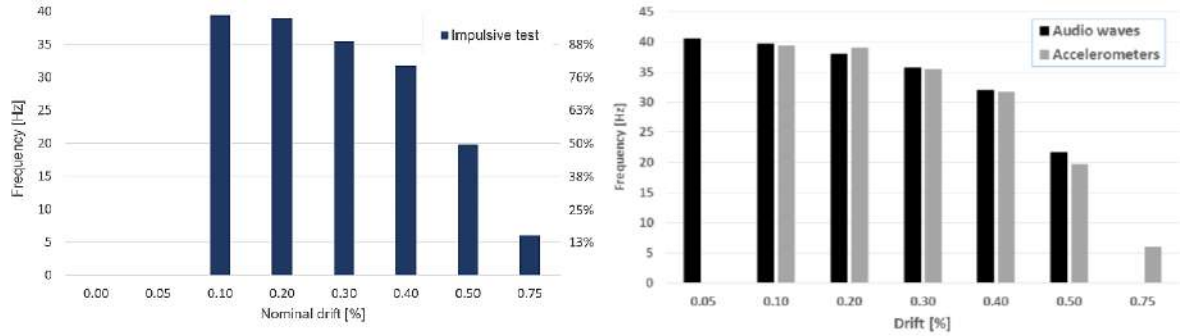


Figure 9. Influence of the in-plane drift damage on the fundamental frequency of the infill T1 (left) (Morandi et al., 2025a). Comparison of the innovative procedure presented by Bolognini et al. (2024) (right).

3.4 INTERACTION BETWEEN IN-PLANE AND OUT-OF-PLANE LOADING

By correlating measured in-plane drifts with peak out-of-plane forces at the panel centre, the interaction between cyclic in-plane displacement and dynamic transverse loading can be quantified. Figure 10 shows the maximum out-of-plane force versus the mean drift of the last three in-plane cycles (positive and negative), including the ultimate force for T5. Here, forces correspond to out-of-plane collapse for T2-T4, ultimate capacity for T5, and incipient in-plane collapse for T1. Although illustrated for Batch 1, the same methodology can be extended across all batches for comparative analysis.

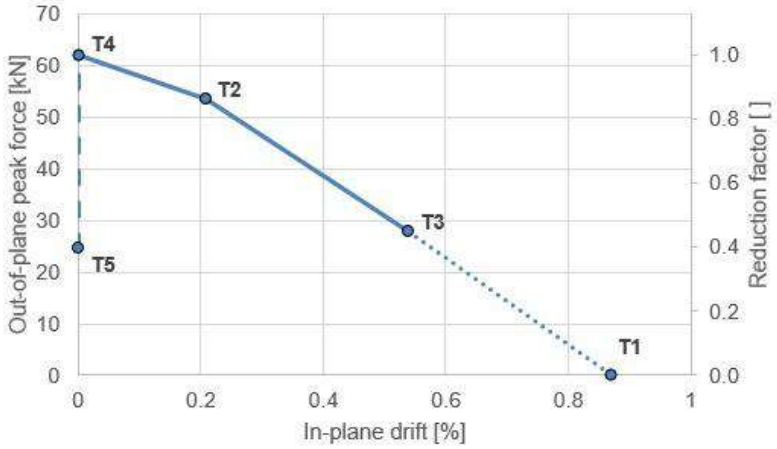


Figure 10. Influence of the in-plane drift damage on the out-of-plane force resistance of batch 1 (right). (Morandi et al., 2025a).

4.CONCLUSIONS, ONGOING AND FUTURE DEVELOPMENTS

Because the scientific literature on the dynamic testing of existing masonry infills is still limited, particularly studies that explicitly address their interaction with in-plane seismic demands, the Eucentre Foundation has undertaken an extensive program of nineteen full-scale experiments. These were organized into four homogeneous batches and focused on slender infills representative of Italian reinforced-concrete frames built between the 1960s and 1980s. The specimens, consisting of steel-concrete composite frames with single-story, single-bay masonry panels, were designed with different boundary conditions (either fully bonded perimeters or intentional edge gaps), two unit thicknesses (12 cm and 8 cm), and both solid and and with opening configurations.

The experimental program employed a combination of in-plane pseudo-static cyclic loading, dynamic out-of-plane shake-table tests, and sequential protocols where panels were first cycled in-plane and subsequently subjected to out-of-plane shaking up to failure. This approach made it possible to systematically investigate how boundary conditions, panel slenderness, and the presence of openings influence damage progression. It also allowed the development of force-drift relationships for out-of-plane loading, the mapping of cracking and acceleration patterns, and the identification of predominant arching and bending failure mechanisms.

For each batch, the research characterized the evolution of damage and limit states, quantified the in-plane force-displacement response, captured out-of-plane deformed shapes during shaking, measured fundamental frequencies, and evaluated the reduction of out-of-plane resistance as a function of the maximum in-plane drift sustained.

The project is still in progress. Current efforts are directed toward clarifying the influence of openings and panel thickness on both in-plane and out-of-plane seismic behavior, developing rapid assessment procedures based on acoustic interrogation techniques (Bolognini et al., 2024), and establishing protocols for simultaneous in-plane and out-of-plane loading. Ongoing studies are also exploring the effect of energy content under different loading histories (Gentile et al., 2025), refining design and assessment guidelines in line with the procedure proposed by Morandi et al. (2025b), and complementing the experimental work with numerical simulations (Kurukusaruriya et al., 2025).

ACKNOWLEDGEMENTS

The work presented in this paper was carried out within the framework of the DPC–Eucentre Research Programme 2019–2021, 2022–2023, and 2024–2026, specifically Work Packages 11 and 16, "Caratterizzazione della risposta sismica in piano e fuori piano di tamponamenti in muratura", funded by the Italian Department of Civil Protection. Additional support was provided through the DPC–ReLUIS Research Programme, Work Package 10, Subtask 10.1.2 (2022–2024) and Subtask 10.3 (2024–2026). The financial and technical contributions from these programs are gratefully acknowledged. The authors also wish to express their sincere thanks to Eng. Daniele Spina and Eng. Francesco Giordano of the Italian Department of Civil Protection for their valuable technical input throughout the various phases of the project.

REFERENCES

Angel, R., Abrams, D. P., Shapiro, D., Uzarski, J., Webster, M. (1994) "Behavior of reinforced concrete frames with masonry infills", *University of Illinois Engineering Experiment Station*, College of Engineering, University of Illinois at Urbana-Champaign.

ASTM E519-02 (2002) "Test Method for Diagonal Tension (Shear) in Masonry Assemblages", *ASTM International.*

Baek, E.R., Pohoryles, D.A., Bournas, D., (2023) "Seismic assessment of the in-plane/out-of-plane interaction of masonry infills in a two-storey RC building subjected to bi-directional shaking table tests", *Earthquake Engineering and Structural Dynamics*, 53, 2230-225, DOI: 10.1002/eqe.4109.

Binici, B., Yakut, A., Kadas, K., Demirel, O., Akpinar, U., Canbolat, A., Yurtseven, F., Oztaskin, O., Aktas, S., Canbay, E., (2023). "Performance of RC buildings after Kahramanmaraş Earthquakes: lessons toward performance based design". *Earthquake Engineering and Engineering Vibration*, 22(4), 883-894.

Bolognini, D., Dacarro, F., Grottoli, L., Milanesi, R.R., Morandi, P., (2024). "Development of A Method Based on Audio Waves for Fast In-Situ Out-of-Plane Dynamic Characterization of Masonry Infills". *Construction and Building Material*, 452, 138874.

Calvi, G.M., Bolognini, D., (2001) "Seismic response of reinforced concrete frames infilled with weakly reinforced masonry panels", *Journal of Earthquake Engineering*, 5(2), 153–185.

CEN (2001). "Methods of test for masonry - Determination of compressive strength. EN 1052-1:2001", Brussels, Belgium.

CEN (2007). "Methods of test for masonry - Determination of initial shear strength. EN 1052-3:2007", Brussels, Belgium.

CEN (2015). "Methods of test for masonry units - Determination of compressive strength. 772-1:2015", Brussels, Belgium.

CEN (2016). "Methods of test for masonry - Determination of flexural strength. EN 1052-2:2007", Brussels, Belgium.

CEN (2019). "Methods of test for mortar for masonry - Determination of flexural and compressive strength of hardened mortar. EN 1015-11:2019", Brussels, Belgium.

da Porto, F., Guidi, G., Dalla Benetta, M., Verlato, N. (2013) "Combined in-plane/out-of-plane experimental behaviour of reinforced and strengthened infill masonry walls", *Proc. 12th Canadian Masonry Symposium*, Vancouver, Canada.

De Luca, F., Verderame, G. M., Gómez-Martínez, F., Pérez-García, A. (2014). "The structural role played by masonry infills on RC building performances after the 2011 Lorca, Spain, earthquake", *Bulletin of Earthquake Engineering*, 12, 1999-2026.

Gentile, R., Angelucci, G., Wu, J., Di Benedetto, M., Di Trapani, F., Morandi, P., Milanesi, R.R., Mollaioli, F., O'Reilly, G.J., Freddi F., Jalayer, F., (2025). "State-dependent fragility via experimental validated energy-based approaches", *Proc. COMPDYN 2025*, 15-18 June 2025, Rhodes Island, Greece.

Hashemi, A., Mosalam, K.M. (2006). "Shake-table experiment on reinforced concrete structure containing masonry infill wall". *Earthquake Engineering and Structural Dynamics*, 35(14), 1827-1852.

ICC-ES AC156 (2000). "Acceptance criteria for seismic qualification by shake table testing of non-structural components and systems", *International Code Council Evaluation Service*.

Kurukulasuriya, M., Morandi, P., Magenes, G., (2025). "Numerical investigation of seismic-response of infills subjected to dynamic out-of-plane tests", *Proc. COMPDYN 2025*, 15-18 June 2025, Rhodes Island, Greece.

Manfredi, G., Prota, A., Verderame, G.M., De Luca, F., Ricci, P. (2014) "2012 Emilia earthquake, Italy: reinforced concrete buildings response". *Bull Earthq Eng* 12:2275-2298 https://doi.org/10.1007/s10518-013-9512-x

Marinković, M., Baballëku, M., Isufi, B., Blagojević, N., Milićević, I., Brzev, S., (2022). "Performance of RC cast-in-place buildings during the November 26, 2019 Albania earthquake". *Bull Earthq Eng* 20:5427-5480. https://doi.org/10.1007/s10518-022-01414-y

Masi, A., Chiauzzi, L., Santarsiero, G., Manfredi, V., Biondi, S., Spacone, E., DelGaudio, C., Ricci ,P. ,Manfredi, G., Verderame, G.M., (2019). "Seismic response of RC buildings during the Mw 6.0 August 24,2016 Central Italy earthquake: the Amatrice case study". *Bull Earthq Eng*,17(10),5631-5654.

Milanesi, R. R., Morandi, P., Manzini, C. F., Albanesi, L., Magenes, G. (2022) "Out-of-plane Response of an Innovative Masonry Infill with Sliding Joints from Shaking Table Tests", *Journal of Earthquake Engineering*, 26(4), 1789–1823.

Morandi, P., Ricci, P., Magenes, G., (2025b). "Guidelines for seismic design and verification of masonry infills in RC buildings", *Proc. XX ANIDIS Conference*, 7-11 September 2025, Assisi, Italy.

Morandi, P., Hak, S., Milanesi, R. R., Magenes, G. (2022) "In-plane/out-of-plane interaction of strong masonry infills: From cyclic tests to out-of-plane verifications", *Earthquake Engineering Structural Dynamics*, 51(3), 648‐672.

Morandi, P., Kurukulasuriya, M., Milanesi, R.R., Bolognini, D., Grottoli, L., Dacarro, F., Magenes, G.,(2025a). "Dynamic shaking table out-of-plane tests on weak masonry infills with and without previous in-plane loading". *J.Building Engineering*, 100, 111670. DOI 10.1016/j.jobe.2024.111670

Peeters, B., De Roeck, G. (2001). "Stochastic System Identification for Operational Modal Analysis: A Review". ASME. *J. Dyn. Sys., Meas.*, Control. 123(4): 659–667. https://doi.org/10.1115/1.1410370

Ricci, P., De Luca, F., Verderame, G.M. (2011). "6th April 2009 L'Aquila earthquake, Italy: reinforced concrete building performance". *Bull. Earthq Eng*, 9, 285-305.

Tu, Y.H., Chuang, T.H., Liu, P.M., Yang, Y.S. (2010). "Out-of-plane shaking table tests on unreinforced masonry panels in RC frames". *Engineering Structures*, 32(12), 3925-3935.

NHERI TallWood Project Part 1: Overview and Nonstructural Subassembly Details

Keri L. Ryan[1], Tara C. Hutchinson[2], Shokrullah Sorosh[2], William Roser[3], Yi-En Ji[1], Sir Lathan Wynn[1]

[1] University of Nevada, Reno
1664 N. Virginia St., Reno, NV 89557
e-mail: klryan@unr.edu; yji@unr.edu; sirlathanw@unr.edu
[2] UC San Diego
9500 Gilman Drive, La Jolla, CA 92093
e-mail: tahutchinson@ucsd.edu; ssorosh@ucsd.edu
[3] TY Lin International
1545 River Park Dr. #201, Sacramento CA 95815
e-mail: wf.roser@gmail.com

Abstract. Low damage structural systems for buildings promise to support resilience-based seismic design objectives, including the ability to avoid major disruption and facilitate quick restoration of functionality. However, the seismic response of the building's nonstructural systems must be addressed to achieve the resilience objective. Emerging solutions for vertically-distributed nonstructural components allow them to be isolated from interstory drift through movement joints. To this end, a variety of nonstructural subassemblies were erected in a 10-story mass timber building with a resilient rocking lateral system, as part of a recent large scale shake table experiment.

The nonstructural subassemblies and movement details are described in this paper. A variety of cold-formed steel (CFS) framed partition walls were installed, including fire-rated shaft walls. The partition walls included two types of horizontal slip joints (double slip tracks and horizontally slotted tracks) along with 3 different types of vertical expansion joints to accommodate incompatible movement at wall intersections. Three 3-story CFS-framed exterior corner subassemblies were installed, including platform-framed (with movement joints similar to interior walls), bypass-framed (with a sliding clip system and hinged expansion joints), and spandrel-ribbon (with movement accommodated generally across the window system). A two-story stick-built fire-rated curtain wall with steel mullions and solid glass occupied the 4th corner of the building. A 10-story stair tower utilizing a modular stair system (self-supporting stackable units) incorporated three types of movement joints across the stringer-to-landing: full multi-dimensional drift release, free sliding, and horizontally-slotted. The response of the building and subassemblies is described in the companion paper [Ryan et al. 2026].

Keywords: mass timber, shake table test, stairs, partition walls, exterior façade, curtain wall

1. INTRODUCTION

The NHERI TallWood Project represents a landmark effort to advance the seismic resilience of tall mass timber buildings through a full-scale, 10-story shake table test program. Conducted at the NHERI@UC San Diego outdoor facility, the project validated the performance of post-tensioned mass timber rocking walls as a low-damage lateral system and provided a unique opportunity to examine critical nonstructural systems under realistic 3D earthquake loading.

Resilience-based design objectives for the test building targeted no structural damage at the design-level earthquake and repairable damage under risk-targeted maximum considered earthquake (MCER) motions. Achieving these goals required careful attention to nonstructural systems, which strongly influence building functionality, safety, and recovery. To this end, the test building incorporated a diverse set of nonstructural subassemblies, including cold-formed steel (CFS) exterior façades, interior partition walls, a full-height stair tower, and a fire-rated curtain wall system. These assemblies were detailed with innovative drift-compatible connections developed through close collaboration with industry partners.

This, the first of companion papers, provides an overview of the building, test program, and nonstructural subassemblies. The second [Ryan et al., 2026] synthesizes the seismic response of both the building and the nonstructural assemblies, and summarizes the lessons learned to guide future design practice.

2. OVERVIEW OF TEST PROGRAM

2.1 MASS TIMBER BUILDING

The TallWood testbed was a 10-story, 34 m tall mass timber building constructed on the NHERI@UC San Diego outdoor shake table (Figure 1(a)). With a compact 10.5 m by 10.7 m footprint, it represented a realistic mixed-use prototype suitable for high-seismic regions. The lateral system consisted of four post-tensioned rocking walls: cross-laminated timber (CLT) walls oriented east–west and mass plywood panel (MPP) walls oriented north–south. These walls were anchored with unbonded post-tensioning rods to provide recentering (Figure 1(b)) and equipped with U-shaped flexural plates (UFPs) between the walls (Figure 1(c))

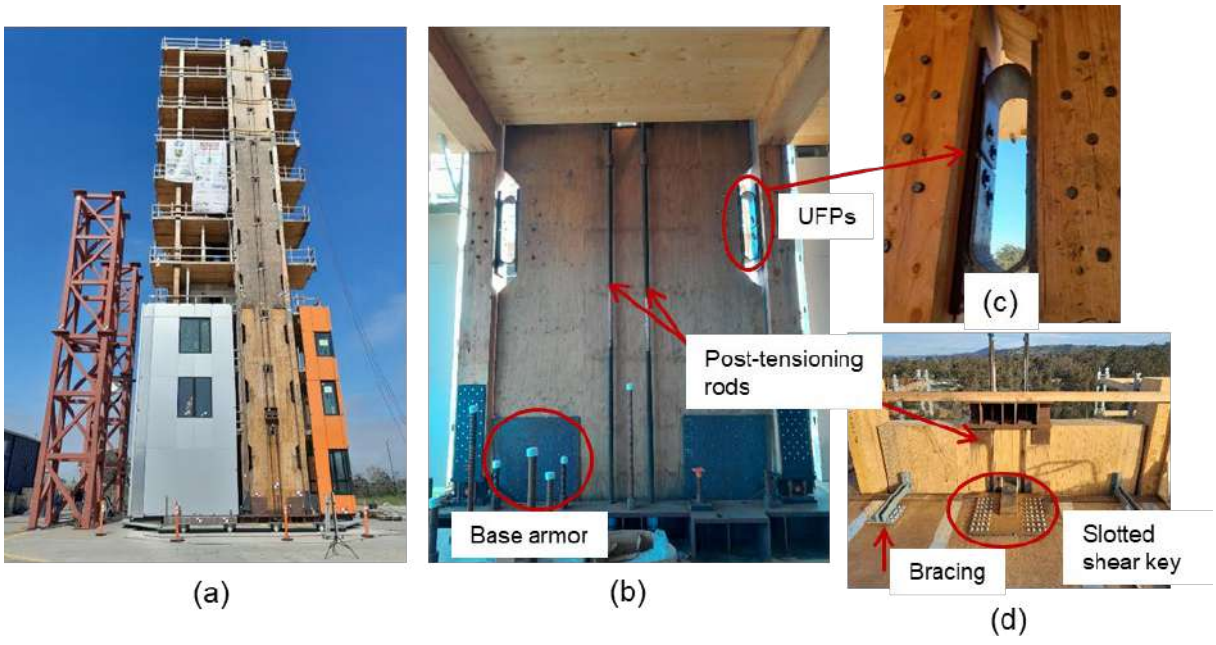


Figure 1. (a) 10-story building, (b) base of rocking wall, (c) UFP, (d) top of wall

and bounding columns for energy dissipation. The connection of the rocking wall to the floor diaphragms was through a slotted shear key (Figure 1(d)) to isolate the floors from the wall uplift motion.

Gravity framing used laminated veneer lumber (LVL) beams and columns, with column bases detailed as pinned and splices located at floor levels. Special beam hanger connections transferred vertical loads while permitting rotation, allowing the frame to remain elastic under large interstory drifts. Floor diaphragms incorporated multiple mass timber products, including CLT, glue-laminated, nail-laminated, dowel-laminated, and veneer-laminated timber.

The building was designed for seismic resilience, targeting no structural damage under design-level motions and repairable damage at the risk-targeted maximum considered earthquake (MCE_R). These performance limits were enforced through drift targets of approximately 0.5% at frequent seismic events, 1% at design-level shaking, and 2.5% at MCE_R intensity. The lateral system was validated through nonlinear response-history analyses prior to construction, and testing confirmed its ability to sustain repeated large motions without loss of gravity support, and no appreciable residual drift. Further details about the structural design and performance of the building are provided in Pei et al. [2024].

2.2 GROUND MOTIONS AND TESTING PROTOCOL

The TallWood building was designed for a representative West Coast seismic environment, with a site in Seattle, Washington, selected as the reference location. Seattle presents a unique hazard profile, combining contributions from shallow crustal faults, the Cascadia subduction interface, and intraslab events. Site-specific uniform hazard spectra were developed using the USGS 2014 seismic source model, and MCE_R values were established in accordance with ASCE 7-16. For design purposes, the target short-period and one-second MCE_R spectral accelerations were 1.65 g and 0.72 g, respectively.

To capture this hazard environment, nine ground motion records from past earthquakes were selected to represent the full range of source mechanisms. Selected events included the 1989 Loma Prieta, 1994 Northridge, 1999 Chi-Chi, 2004 Niigata, and 2011 Tohoku earthquakes. Records were amplitude-scaled to match the target hazard levels at desired return periods, with the following return periods represented: 43, 225, 475, 975, and 2475 years. Ground motions were applied in X-direction (E-W), Y-direction (N-S), XY, and XYZ (with vertical). In total, 88 earthquake simulations from 9 distinct records were applied over 16 active shake days; some records were repeated andcomplete data is only available from the final 59.

3. NONSTRUCTURAL SUBASSEMBLIES

Prior experimental research on nonstructural components has focused mostly on standard details to quantify existing practice and develop fragility functions to support life cycle analyses. This project aimed to expand to details specifically designed to accommodate movement, some of which have been used in practice but never validated, and others that are totally innovative. An industry working group was established in 2020 to guide the research team in this endeavor.

3.1 INTERIOR WALLS

The test plan was founded on a sizable body of literature on wood or cold-formed steel (CFS) framed interior partition walls. Interior walls have received much attention given early findings that they are vulnerable at low drift levels, with damage often initiating at drifts as low as 0.1%–0.2%. CFS-framed walls were chosen as they can more easily be detailed for deformation compatibility. These components are frequently found to be among the most damaged components in light to moderate earthquakes, and improving their response could greatly improve life cycle analysis. CFS-framed walls consist of vertical studs spaced 406 mm (16”) or 610 mm (24”) o.c. between top and bottom tracks, and sheathed with drywall on both sides. Commonly, the studs are connected to the tracks, and the tracks are fully connected to the floor

slabs above and below. With this stiff detailing, the partition wall is fully subjected to the interstory drift and sustains significant damage [Davies et al. 2011].

A slip track detail, sometimes referred to as a friction connection, has been proposed as a low damage detail. In basic slip track detailing, the studs are simply not connected to the top track, allowing for a movement joint at the top of the wall [Davies et al. 2011]. As the sliding studs may "pop out" from the top track at the ends of the wall, a double or nested top track has been investigated as a more robust alternative [Hasani and Ryan, 2021]. In general, the slip track detail has been found to work well until introducing intersecting or return walls, which create an incompatibility in the movement of the in-plane wall that slips and the out of plane wall that drifts. Thus, various solutions have been investigated to protect the intersecting walls [e.g., corner gap [Davies et al., 2011], flexible corner [Mulligan et al., 2022], distributed gap with thermal expansion joint [Hasani and Ryan, 2021], and two-way slip detail [Araya-Letelier et al., 2019]. Some of these solutions are only partially effective, while others are associated with significant build complexity and cost. Thus, a widely accepted solution has been elusive.

CFS-framed interior walls were installed on Stories 4 through 6 of the TallWood building to evaluate the seismic performance of both conventional partition walls and fire-rated shaft walls. The wall layouts on Stories 4 and 5 (Figure 2(a) and 2(b)) followed a simplified architect-inspired residential floor plan, including walls with door openings framed with reinforced jamb studs and headers. These floor plans combined conventional partition walls and fire-rated shaft walls. On the 5th story (3rd and 7th as well), traditional shaft walls were replaced with wall panels installed directly into the stair framing; the undersized wall panels were surrounded by a fire-rated filler material to allow the panels to rotate within the framing. While of interest, these wall panels were not instrumented or closely monitored by the research team and thus are not discussed further. Hollow metal doors with varied hardware were installed to assess the effect of drift on operability. On Story 6 (Figure 2(c)), isolated T-shaped and C-shaped wall segments were constructed specifically to study the interaction of drift with intersecting geometries and expansion joints.

Conventional partition walls used 362S162-33 studs at 406 mm spacing, framed into 362T125-33 tracks at the floor and ceiling. Each wall was sheathed with 15.9 mm gypsum board on both sides. To accommodate building drift, the walls incorporated top-of-wall slip joints at every story. Two slip track systems were applied: (1) double slip tracks with nested members (Figure 3(a)), where the inner track was fastened to studs and the outer track to the floor above, allowing relative movement between them; and (2) CEMCO CST slotted slip tracks (Figure 3(b)), where long horizontal slots allowed the top track to slide relative to the floor. Around the 4th story stair core, fire-rated shaft walls were constructed with 101.6 mm CH studs and fire-rated J-tracks (shown in green in Figure 2(a)). The shaft liner side used 25.4 mm gypsum shaft liner boards friction-fit into the studs, while the opposite side was sheathed with two layers of 15.9 mm gypsum. This detail allowed the liner boards to slip within the track under drift, preserving fire rating while reducing damage. Shaft walls were anchored to the timber diaphragms using heavy-duty connector screws at 406 mm spacing at the top and 203 mm at the base.

A variety of commercial expansion joint products were installed to isolate intersecting walls. On Stories 4 and 5, FWFC-600 gasketed joints (Figure 3(c)) were used to decouple perpendicular walls, accommodating up to 102 mm of movement. Where shaft walls intersected partition walls, RFX-4W fire barrier joints (Figure 3(d)) were applied to maintain fire separation while still permitting drift. On Story 6, AFWC-400 aluminum joint covers (Figure 3(e)) were applied at the corners/intersections of the C-shaped and T-shaped walls. These joint covers that slide within aluminum sleeves offer more aesthetic appeal than the gasketed joint cover, but were not designed for bidirectional slip, thus evaluating bidirectional slip capacity was an important objective of the research. For comparison, several wall intersections did not use expansion joints, but generally used flexible details (limited framing through the joint) to minimize damage. With interconnected wall layouts, walls may be affected by joint detailing throughout the plan, and protecting every wall would be very difficult.

The walls were erected by a local contractor who was inexperienced with the novel techniques utilized in this project. The erection of the walls was closely supervised by the research team and were built according to specification. As a result, a few challenges were observed during construction. (1) The nested tracks for the double slip detail fit together very tightly and sometimes had to be pounded together. (2) Two of the walls were placed adjacent to a structural beam, and thus were partially assembled on the floor and then slid into place. The double slip detail could not be used in this situation, because access is required to fasten the studs to the inner track once the wall is in place. (3) The fire barrier was a compressible material that should be compressed from 305 mm (12") down to 102 mm (4") for installation, which the contractor was unable to complete. With advice from another contractor, the research team managed to install it, but only after cutting off some of the layers. The material may have been exposed to weather-related moisture, causing it to expand and negatively impact its function. (4) Expansion joint installation was straightforward when adjacent to CFS framing. A couple of instances called for installation into wood or structural steel. An ad-hoc solution was developed, but in practice, a more robust detail would be required. Further details of the interior walls are provided in Ji [2025] and Roser et al. [2025].

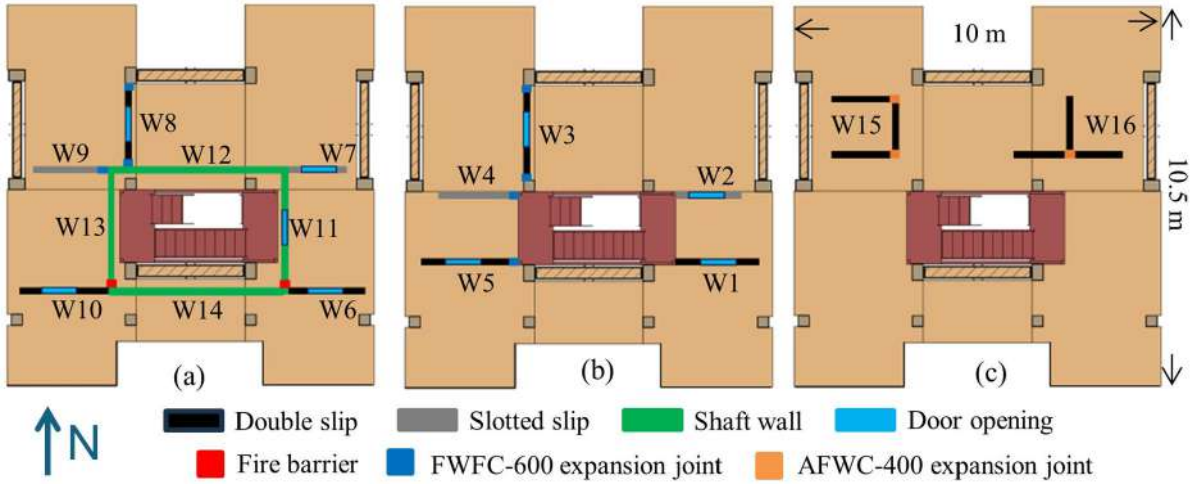


Figure 2. Interior wall plan: (a) Story 4, (b) Story 5, (c) Story 6

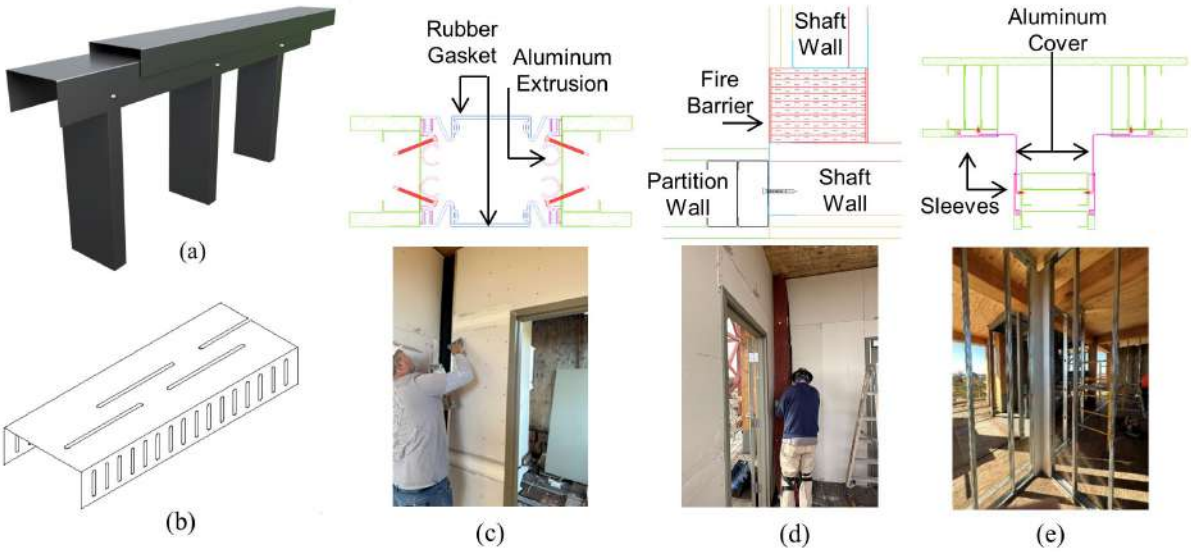


Figure 3. Interior wall details: (a) double slip track, (b) slotted slip track; commercial expansion joint covers by Construction Specialties [2025]: (c) FWFC gasketed joint, (d) RFX-4W fire barrier, (e) AFWC-400 aluminum joint

3.2 EXTERIOR WALL SUBASSEMBLIES

Four exterior wall subassemblies were installed at the base levels of the TallWood building, one at each corner. Three of these were 3-story cold-formed steel (CFS) framed and the fourth was a 2-story stick-built glass curtain wall. The CFS-framed assemblies (Figure 4) represented common façade framing paradigms: platform-framed, bypass-framed, and spandrel-ribbon, and utilized various drift-compatible details to accommodate interstory drift up to 2.5% without significant loss of enclosure performance. Common details of the CFS-framed assemblies are described next, before describing each of them in turn.

Each subassembly was constructed with 152 mm deep CFS studs (600S162-43) spaced at 406 mm on center, framed into matching track sections at the top and bottom. Where window framing was required, thicker 16-gauge members were substituted for jambs, sills, and headers to meet hardware installation requirements. Lateral stability of the studs was provided as needed with bridging channels attached through pre-punched holes. The interior face of the assembly was sheathed with 12.5 mm gypsum wallboard, while the exterior face was sheathed generally with fiberglass mat boards; CFS 2 required steel–gypsum composite panels for additional shear strength. Screw types were standardized across the assemblies, with #8 self-drilling screws used for attaching sheathing to studs, and heavier #10 or #14 screws used for stud-to-track, bridging, and clip connections. Powder-actuated fasteners (PAFs) or concrete screw anchors were used to attach bottom tracks to the reinforced-concrete foundations, while steel ledger connections were employed at locations cantilevered beyond the shake table.

Exterior finishes consisted of 4 mm aluminum composite material (ACM) cladding panels supported on extruded aluminum framing rails. ACM panels were connected with aluminum clips, installed either as single-edge clips or double clips between adjacent panels. To ensure drift compatibility, cladding panel seams were aligned with structural framing slip tracks so that no panel spanned across a joint in the framing. In

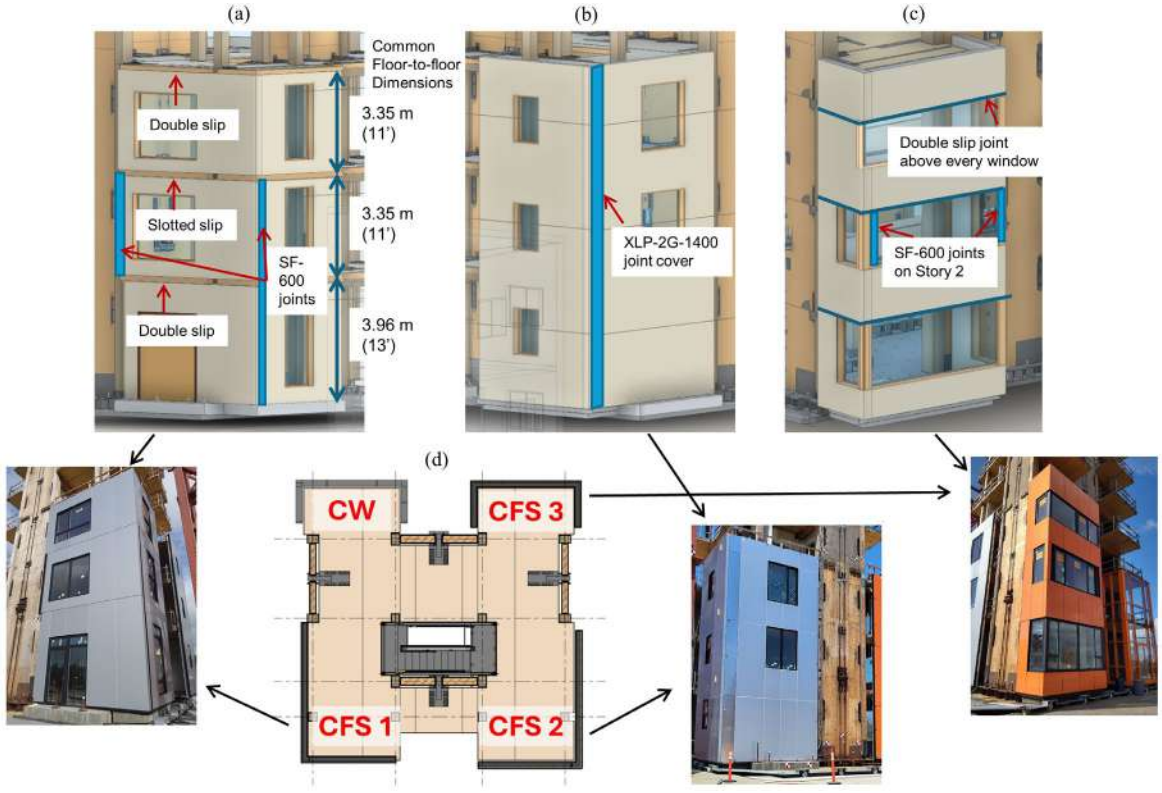


Figure 4. CFS exterior wall subassemblies: (a) CFS 1 platform-framed, (b) CFS 2 bypass-framed, (c) CFS 3 spandrels and ribbon windows; (d) location on floor plate

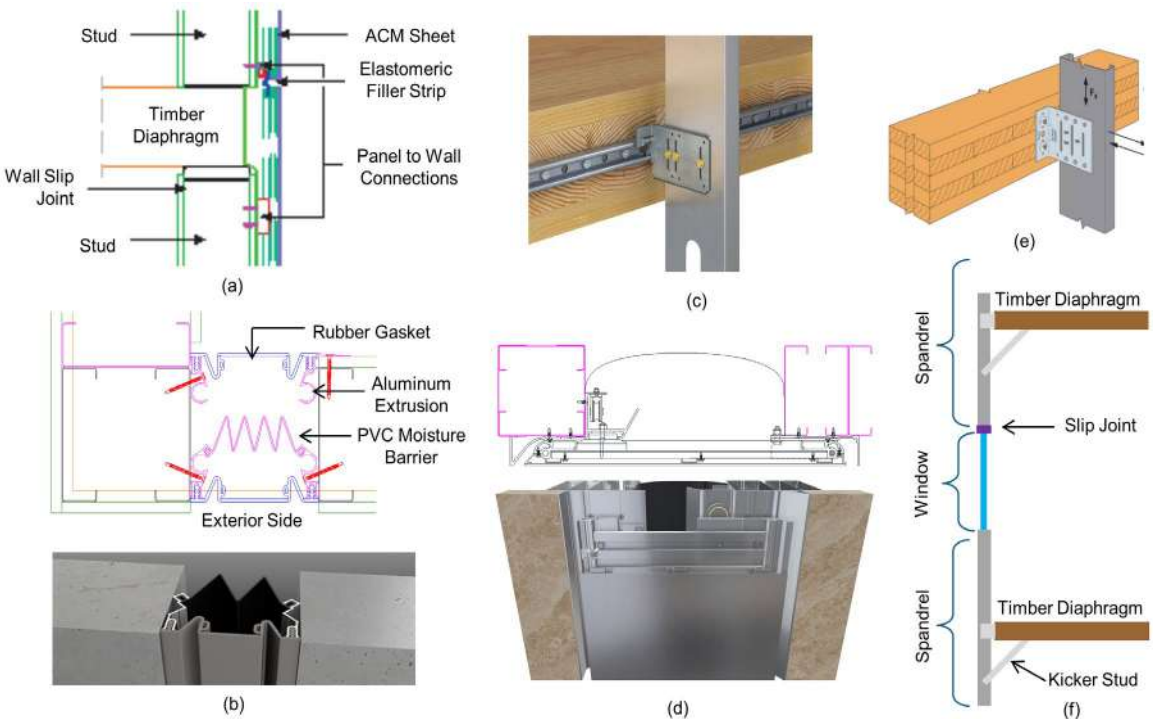


Figure 5. CFS exterior subassembly details: (a) ACM panel connection details, (b) SF-600 gasketed joint [Construction Specialties, 2025], (c) DSSCB sliding slip connection of stud to diaphragm [Simpson Strong-tie, 2025], (d) XLP joint cover [Construction Specialties, 2025], (e) rigid clip connection of stud to diaphragm, (f) spandrel-window details.

some locations, elastomeric filler strips were substituted for caulked seams, permitting horizontal sliding without tearing or binding.

Each subassembly incorporated commercial-grade windows provided by two industry partners. Manufacturer A windows employed a receptor head system: the window frame was set into a fixed receptor at the jambs and head, while the sash and frame were free to slide within the receptor slots. This provided approximately 19 mm of movement capacity in each direction. Manufacturer B windows, by contrast, used a strap anchor system, where steel straps were fastened to the surrounding framing while the window unit itself was shimmed within an oversized rough opening (≈12 mm clearance on all sides). This detail allowed the frame to move relative to the wall without transferring large forces to the glazing.

3.2.1 CFS 1: Platform-Framed Subassembly

The L-shaped platform-framed subassembly, denoted CFS 1, was constructed at the southwest corner of the building, spanning three stories (Figure 4(a)). In this configuration, studs extended from floor to floor, with the floor diaphragm interrupting the wall line at each level. To decouple wall drift from building drift, horizontal slip tracks were detailed at the top of each story. Double slip tracks as described earlier were applied on Stories 1 and 3, while slotted slip tracks were applied on Story 2. ACM panels were cantilevered above the slip joints to cover the floor diaphragms, and a sliding silicone elastomeric strip was applied in the panel-to-panel seam at the top of each story (Figure 5(a)).

A 152 mm gasketed expansion joint cover (Figure 5(b)) was installed at the intersecting wall corners on the first two stories to absorb incompatible movement between perpendicular walls (Figure 4(a)). This joint cover was also used where the wall abutted a gravity column on the second story. On the third story, the corner joint was omitted, creating a "crush zone" where localized gypsum damage was anticipated. The L-shaped ACM corner panel was hinged at both connection points to allow rotation through the building interstory drift.

3.2.2 CFS 2: Bypass-Framed Subassembly

The L-shaped bypass-framed façade (CFS 2), located at the southeast corner, followed a balloon-framing approach with continuous studs spanning three stories outside the structural frame (Figure 4(b)). To accommodate drift, the studs were connected to mass timber floor diaphragms using DSSCB drift clips seated within standard U-struts (Figure 5(c)). The clip-to-stud connections used vertical slotted holes with #14 shouldered screws, permitting both horizontal slip along the U-strut and limited vertical deflection. This system was designed to isolate the façade from in-plane story drifts while still transferring out-of-plane loads safely. To prevent drift clips from sliding out of U-struts at wall ends, the terminal studs were cantilevered off neighboring studs using deep track segments rather than directly connected to the diaphragm.

A large expansion joint was required at the corner between the two wall segments. Because the relative movement between the structure and the façade accumulates over the height, the joint was sized to allow 25 mm relative movement in each direction over the 3 stories. The chosen solution was an XLP-2G-1400 hinged expansion joint cover (Figure 5(d)), installed at the southeast corner where the perpendicular wall segments met (Figure 4(b)). The modular cover included an internal magnet and pulley system that kept the joint closed under normal conditions, but allowed it to open under drift demands and reclose afterward.

3.2.3 CFS 3: Spandrel-Ribbon Subassembly

The C-shaped spandrel-ribbon façade (CFS 3) was installed at the northeast corner of the building. CFS 3 used a spandrel-and-ribbon layout: short spandrel sections were attached to the floor, while ribbon zones between spandrels housed continuous windows and infill framing (Figure 4(c)). This configuration reflected a common architectural solution for mid- and high-rise façades. Spandrel studs were attached to the floor edge with fixed clips and braced with diagonal kicker studs (Figure 5(e) and 5(f)). At the ground level, a kneewall was built instead, fixed to the floor using heavy-duty connectors bolted to a steel ledger/angle along the foundation edge.

To accommodate drift, nested (double-track) slip joints were placed at the top of the window ribbon on every story (Figure 4(c)). Unlike CFS 1 and CFS 2, the slip in CFS 3 was intentionally between nonstructural elements: the upper track fastened to the underside of the spandrel above, and an inverted stud inside the lower track created a box section and flat bearing for the window head.

Corner treatment varied by story. On Stories 1 and 3, the windows wrapped the corners, necessitating that the windows would need to accommodate the incompatible movement. A resilient solution was attempted on Story 2 by separating the window units and installing the same SF-600 gasketed joint cover at each corner location (Figure 4(c)). Further details of the CFS exterior subassemblies are provided in Roser et al. [2025].

3.2.4 Stick-Built Glass Curtain Wall Subassembly

The final exterior subassembly was a C-shaped, stick-built glass curtain wall installed along the northeast corner, spanning stories 1 and 2 (Figure 6). Unlike conventional aluminum-framed systems, this 60-minute fire-rated assembly used S235JR steel mullions and transoms to achieve fire resistance, supporting 27 mm thick multilayer laminated glazing composed of thin sheets of annealed glass between intumescent layers for added fire protection. The curtain wall accommodated drift through racking of the framing, and rotation of glass panels within the framing. Glass panel layout included one panel at the maximum allowable area, another at the maximum height, and other smaller panels at various aspect ratios, enabling performance comparison across geometries (Figure 6(a)). A preassembled fire-rated door unit was also integrated.

The curtain wall subassembly was supported at the base of the structure on the steel ledger protruding from the edge of the concrete foundation slab using Nelson Weld Studs and slotted sill anchors. The curtain wall system was attached directly to the second and third floor diaphragms using vertically slotted wind-load and

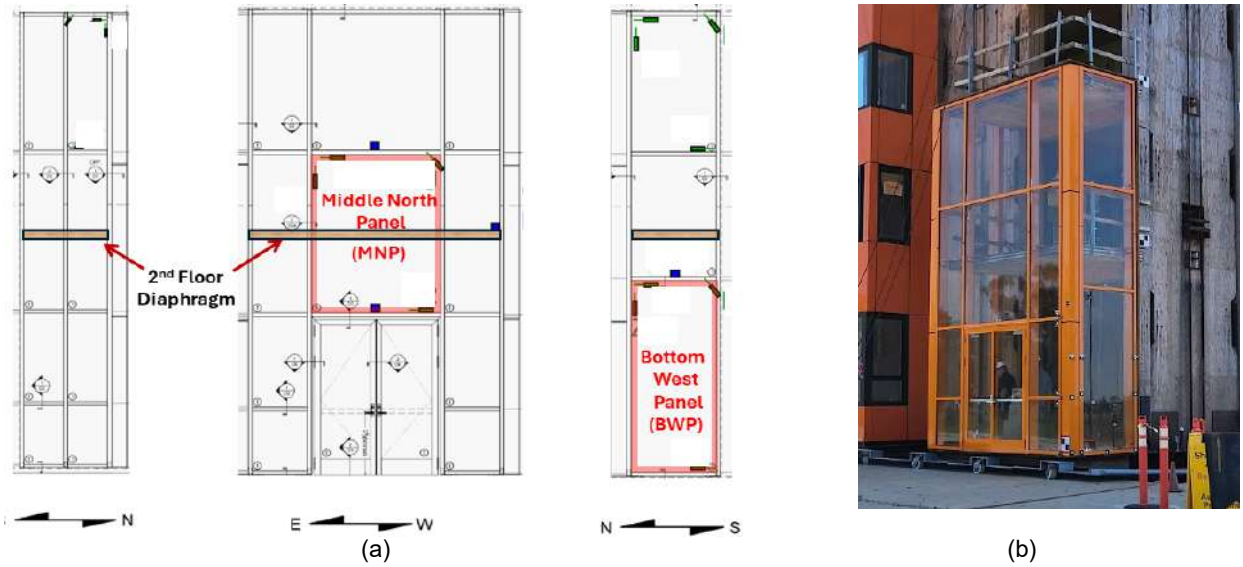


Figure 6. (a) Curtain wall drawings with largest panel (MNP) and tallest panel (BWP), (b) photo of finished assembly.

head anchors, respectively. The anchorage demands were calculated based on the design criteria for wind and seismic, considering MCE_R level shaking. All anchorage components were fabricated from ASTM A36 steel. The anchorage was governed by out-of-plane wind demands but detailed to permit in-plane drift by allowing the mullions to rack with the building rather than remain rigid.

Mechanically captured glazing was employed: the glazing panels were seated on calcium silicate setting blocks and held in place by gasketed pressure plates bolted through the glazing pocket. Prior to installation, glass panels were wrapped with intumescent tape to maintain fire protection at the edges. W-shaped anti-walk blocks were added to recenter the panels after racking. Extruded silicone corner transitions and mineral wool–stuffed perimeter seals completed the fire and weather barrier, while still accommodating drift.

3.3 TEN STORY STAIR TOWER

The TallWood project incorporated a full-height, 10-story prefabricated steel stair tower in a scissor configuration. The stair tower was located adjacent to the south rocking wall, occupying a 2032 mm by 4445 mm opening in the mass timber floor diaphragms. Stories 1-8 consisted of stacked modular stair system (MSS) units, each prefabricated and assembled as a complete story module with framing, landings, and stair stringers spanning floor-to-floor (Figure 7(a)). These stair systems, due to their freestanding and self-weight supporting capability, eliminate the need for scaffolding or other temporary support during construction, as they can be installed as a complete floor-to-floor unit. The MSS units contain corner gravity columns fixed to channel band framing at the top of the level. Stories 9-10 were constructed using traditional stick-built methods without modular gravity columns, providing a comparison in construction approaches. The modules were stacked vertically to form a continuous 10-story tower.

The horizontal seismic force due to the seismic weight in the MSSs (Levels 1 through 8) was transferred using two parallel tension straps and one perpendicular shear strap at each of the transverse ends of the stair channel band (i.e., through east and west edges). The top two stories of stair systems, which are absent gravity columns, transferred seismic force to the floor diaphragm using two tension straps and one steel angle at each end. The steel angle also transferred the landing gravity load to the floor diaphragm. In addition to the steel straps, the stair channel bands in the west, east, and north sides of the stair opening were fastened to the floor diaphragm using 152 mm (6”) self-drilling screws (SDS) at 305 mm (12”) o.c staggered. These connections were absent on the south side, which was adjacent to the rocking wall. The stair flights were fabricated from steel stringers with welded treads, connected to the landings via bolted end plates detailed per the selected connection type.

The stair flights (stringers) and landings are the most rigid part of the stair module and are susceptible to drift-related damage. To mitigate such damage, various details for accommodating movement through the stringer-to-landing connections were investigated. Each movement joint (one per stair flight) should be expected to accommodate about half of the anticipated interstory drift, which for the MCE_R target scaled test was about 84 mm (3.3") per story. At mid-landings of Stories 1-4 and 9-10, drift-compatible connections were used; these provided three degrees-of-movment, allowing stair flights to translate and rotate relative to the landing while maintaining gravity support (Figure 7(b)). Two different attachment strategies were used to attach the stair landing to the stringer via the drift compatible connection, a single attachment channel, and a dual attachment channel. The single attachment channel extended across the mid-landing and thus constrained the two stringers (from upper and lower flight) to move/rotate together relative to the mid-landing (Figure 7(c)). The dual attachment strategy, which attached each stringer's drift connection through a separate channel (Figure 7(d)) was only used in Story 4. In contrast, the remaining stories incorporated other connection strategies intended to comply with ASCE 7-16 [2016] guidelines for nonstructural stairs. Stories 5-6 incorporated a free-sliding connection, where the bottom of the flight rested on and could slide relative to the landing below (Figure 7(f)). Stories 7-8 used horizontally slotted connections with long horizontal slots (165 mm or 6.5") between the upper flight and mid-landing (Figure 7(e)). Other flight-to-landing connections were detailed with shorter transverse and longitudinal slots. Bolts across these slots were "snug" tightened to permit relatively unconstrained movement. The stair tower test objective was to evaluate the effectiveness of various movement joints to protect the stair components from damage. The configuration and details of the 10-story stair tower are described in Sorosh et al. [2025].

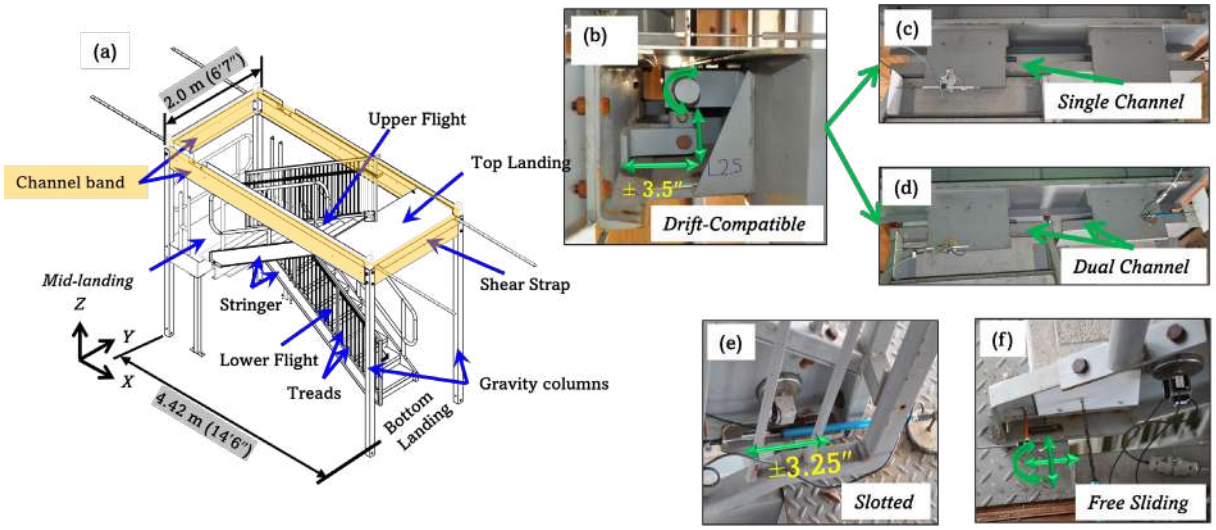


Figure 7. (a) Single story modular stair system; and various connections of stair stringer to landing (b) drift release with (c) single attachment channel and (d) dual attachment channel as seen from below, (e) horizontally slotted and (f) free sliding connection, which differ only by the bolt through the slot or lack thereof.

4.SUMMARY

The NHERI TallWood project provided the first opportunity to evaluate a full suite of drift-sensitive nonstructural systems within a 10-story mass timber building subjected to realistic earthquake ground motions. The testbed building, designed with post-tensioned rocking walls, could develop large interstory drifts without structural damage, allowing the focus to be on the resilience of nonstructural subassemblies.

Four major exterior wall subassemblies were included: three-story CFS platform-framed, bypass-framed, spandrel-and ribbon systems, and a two-story fire-rated glass curtain wall with steel mullions. Each incorporated slip tracks, drift clips, or expansion joints to isolate the assemblies from structural drift and prevent cladding or glazing damage. Interior CFS partitions and shaft walls employed slotted or double slip

tracks and commercial expansion joints, allowing the evaluation of advanced strategies to protect gypsum finishes, door openings, and fire separations. A 10-story prefabricated steel stair tower with multiple connection types provided an unprecedented system-level evaluation of egress functionality under seismic demands. The companion paper [Ryan et al., 2026] presents the results and lessons learned from the tests.

ACKNOWLEDGMENTS

See Ryan et al. [2026] for acknowledgments.

REFERENCES

Araya-Letelier, G., Miranda, E., and Deierlein, G. [2019]. "Development and testing of a friction/sliding connection to improve the seismic performance of gypsum partition walls", *Earthquake Spectra*, 35(2), 653-677.

ASCE7-16 [2016]. Minimum Design Loads and Associated Criteria for Buildings and Other Structures. Standard ASCE/SEI 7–16 (Structural Engineering Institute of American Society of Civil Engineers).

Construction Specialties [2025]. "Expansion Joint Solutions". https://www.c-sgroup.com/category/expansion-joint-solutions [Accessed 2025 July].

Davies, R. D., Saavedra, R. R., Mosqueda, G., and Filiatrault, A. [2011]. "Experimental Seismic Evaluation, Model Parameterization, and Effects of Cold-Formed Steel-Framed Gypsum Partition Walls on the Seismic Performance of an Essential Facility", *Report No. MCEER 11-0005*, University at Buffalo.

Hasani, H. and Ryan, K.L. [2021]. "Experimental cyclic test of reduced damage detailed drywall partition walls integrated with a timber rocking wall", *J. Earthquake Eng.,* 26(10), 5109-5129.

Ji, Y. [2025]. "Seismic Response of Nonstructural Platform framed Cold-formed Steel Walls Subassemblies Detailed for Drift Compatibility", *PhD Dissertation*, University of Nevada, Reno.

Mulligan, J., Sullivan, T. J., and Dhakal, R. P. [2022]. "Experimental seismic performance of partly-sliding partition walls", *J. Earthquake Eng.*, 26(3), 1630-1655.

Pei, S., Ryan, K. L., Berman, J. W., van de Lindt, J. W., Pryor, S., Huang, D., ... & Dolan, J. [2024]. "Shake-table testing of a full-scale 10-story resilient mass timber building", *J. Str. Eng.* (ASCE), *150*(12), 04024183.

Roser, W., Ryan, K. L., Ji, Y., Hutchinson, T. C., Wynn, S. L., ... & Pei, S. [2025]. "Seismic performance of cold-formed steel nonstructural exterior walls with drift-compatible details in full-scale shake table tests of a tall mass timber building", *J. Earthquake Eng.,* DOI:10.1080/13632469.2025.2492247.

Ryan, K. L., Hutchinson, T. C., Sorosh, S., Roser, W., Ji, Y-E., Wynn, S. L. [2026]. "NHERI TallWood Project part 2: Performance of building and nonstructural subassemblies", *Proceedings of Sixth International Workshop on the Seismic Performance of Non-Structural Elements (SPONSE 2026),* Tokyo, Japan.

Simpson Strong-tie [2025]. "DSSCB Bypass Framing Drift Strut Connector", https://www.strongtie.com/driftconnectors_coldformedsteelconstruction/dsscb_clip/p/dsscb [Accessed 2025 July].

Sorosh, S. Hutchinson, T.C., Ryan, K.L., Smith, K.W., Kovac, A., Zabet, S., Pei, S. [2025]. "Experimental characterization of a full-scale stair system detailed to achieve seismic resiliency", *Earthquake Eng. & Struct. Dyn.*, 54(14), 3519–3540. https://doi.org/10.1002/eqe.4376.

Sixth International Workshop on the Seismic Performance of Non-Structural Elements (SPONSE 2026)

NHERI TallWood Project Part 2: Performance of Building and Nonstructural Subassemblies

Keri L. Ryan[1], Tara C. Hutchinson[2], Shokrullah Sorosh[2], William Roser[3], Yi-En Ji[1], Sir Lathan Wynn[1]

[1] University of Nevada, Reno
1664 N. Virginia St., Reno, NV 89557
e-mail: klryan@unr.edu; yji@unr.edu; sirlathanw@unr.edu
[2] UC San Diego
9500 Gilman Drive, La Jolla, CA 92093
e-mail: tahutchinson@ucsd.edu; ssorosh@ucsd.edu
[3] TY Lin International
1545 River Park Dr. #201, Sacramento CA 95815
e-mail: wf.roser@gmail.com

Abstract. Low damage structural systems for buildings promise to support resilience-based seismic design objectives, including the ability to avoid major disruption and facilitate quick restoration of functionality. However, the seismic response of the building's nonstructural systems must be addressed to achieve the resilience objective. Emerging solutions for vertically-distributed nonstructural components allow them to be isolated from interstory drift through movement joints. To this end, a variety of nonstructural subassemblies were erected in a 10-story mass timber building with a resilient rocking lateral system, as part of a recent large scale shake table experiment.

This paper follows [Ryan et al. 2026] and presents the response of the building and its subassemblies. The building experienced peak interstory drift ratios approaching 2%, generally increasing with height. Drift reduction in interior walls ranged from 10% to 80%, which indicates a wide variation in activation of the slip joints. In the exterior cold-formed steel (CFS) framed platform subassembly, double slip joints did not slip at all, while slotted slip joints were effective in reducing drift to the wall. All vertical expansion joints accommodated the movement as expected. Significant drift reduction was observed in the CFS bypass-framed subassembly, but some clips were observed to bind and pull out after repeated shaking. Drift was accommodated in the spandrel-ribbon assembly through various mechanisms across the window units. The curtain wall demonstrated typical racking of the framing and glass movement, even with the more complex multi-directional dynamic input. Finally, all stair movement details accommodated sufficient seismic-induced movement such that damage to the stair system was minimal and assured continued functionality.

Keywords: mass timber, shake table test, stairs, partition walls, exterior façade, curtain wall

1. INTRODUCTION

The NHERI TallWood Project represents a landmark effort to advance the seismic resilience of tall mass timber buildings through a full-scale, 10-story shake table test program. Conducted at the NHERI@UC San Diego outdoor facility, the project validated the performance of post-tensioned mass timber rocking walls as a low-damage lateral system and provided a unique opportunity to examine critical nonstructural systems under realistic 3D earthquake loading.

Resilience-based design objectives for the test building targeted no structural damage at the design-level earthquake and repairable damage under risk-targeted maximum considered earthquake (MCE_R) motions. Achieving these goals required careful attention to nonstructural systems, which strongly influence building functionality, safety, and recovery. To this end, the test building incorporated a diverse set of nonstructural subassemblies, including cold-formed steel (CFS) exterior façades, interior partition walls, a full-height stair tower, and a fire-rated curtain wall system. These assemblies were detailed with innovative drift-compatible connections developed through close collaboration with industry partners. The building and its components were subjected to 88 three-dimensional ground motions, ranging from service-level shaking to maximum considered earthquake (MCE_R) intensity.

This paper is the second of companion papers and follows Ryan et al. [2026]. This paper synthesizes the seismic response of both the building and the nonstructural assemblies, and summarizes the lessons learned to guide future design practice.

2. STRUCTURAL RESPONSE OF TALLWOOD BUILDING

Recall that the building was subjected to 88 ground motions, scaled to hazard levels from service events to maximum considered earthquake (MCER). The structural response was recorded primarily by multiple tri-axial accelerometers located on every floor slab. The recorded acceleration was baseline corrected, zero padded, and filtered with a fourth-order Butterworth bandpass filter. The filtered acceleration was then integrated. The same steps were applied to the integrated signal (velocity) to obtain absolute floor displacements. Interstory drift histories were computed by subtracting the displacements of adjacent floors, and then normalized by story height to calculate interstory drift ratios. Displacements recorded from the shake table controller data, and string-pots attached inside the building diagonally between floors and horizontally between the building and fixed safety towers (available at lower floors only) were used to cross-check and verify the displacement results obtained through double integration. Roser [2025] presents a detailed treatment of the validation and optimization procedure to select the filter cutoff frequencies. Filter cutoff frequencies were selected as 0.18 Hz (lower cutoff frequency) and 25 Hz (upper cutoff frequency) to minimize the error between the integrated accelerations and displacements measured by string pots.

Figure 1 shows the peak interstory drift ratio (PIDR) profiles recorded during these tests in the X and Y-directions, color-coded by intensity level. The drift distribution was relatively uniform over height, with slightly larger demands concentrated in the upper stories, reflecting the inherent flexibility of the rocking wall system. At service-level shaking (43-year hazard), drift ratios remained below 0.2%. At the design-level event (475-year hazard), PIDRs approached 1%, and at MCE_R intensity, PIDRs reached approximately 2%. The PIDRs on the lower levels where most of the nonstructural walls are located were limited to about 1-1.5%. Various authors [Pei et al. 2024, Sorosh et al. 2025, Roser et al. 2025] have selected different optimized filter parameters depending on their objectives, and thus reported slight variations in derived drifts, which underscores the sensitivity to the drift processing algorithms. PIDR values were also less than projected during design, because the building was ultimately built without added mass that was included in the design,

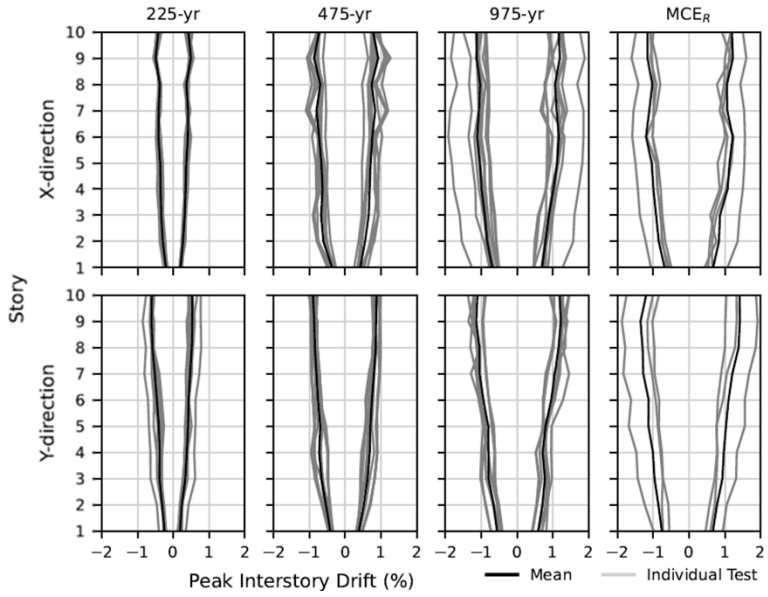


Figure 1. Absolute peak interstory drift ratio at each story in X- and Y-directions for individual ground motions (adapted from Roser et al. [2025]

and test motions were selected from suite means rather than extremes. The building's structural system remained undamaged with only slight visual wear on components (e.g., slight widening of structural bolt holes). These structural drift demands represent key input to the nonstructural systems.

3. RESPONSE OF NONSTRUCTURAL SUBASSEMBLIES

3.1 CFS PLATFORM-FRAMED WALLS (INTERIOR AND EXTERIOR, CFS 1 SYSTEM)

This section discusses the response of both the interior walls and CFS 1, which utilized floor-to-floor or platform framing with top of wall slip joints, as described in Ryan et al. [2026]. In the test program, slip was recorded across top of wall horizontal slip joints using displacement transducers or string pots and compared to interstory drift. Sample response histories for select walls are shown in Figure 2; in these plots, derived interstory drift, recorded slip, and derived wall drift (computed as interstory drift minus slip) are compared. The slip or movement joints are considered successful if the resultant wall drift is significantly reduced from the interstory drift. Figure 2(a) and 2(b) compare slip and resultant wall drift for representative Story 5 interior walls W4 with the slotted slip and W5 with the double slip joint detail, respectively, subjected to MCE$_R$ Ferndale XYZ. (Refer to Ryan et al. [2026] for floor plans.) In these cases, the slip joints were effective, and W4 recorded peak slip (depicted in green) that was slightly greater than the derived drift (depicted in blue), which was due to the uncertainty in the derived drift introduced by the processing algorithm. Regardless, the data shows that the W4 and W5 slip joints were highly effective. In general, drift reduction (percent of peak interstory drift not transmitted to walls) in interior walls under large shaking ranged from 10% to 80%, which indicates a wide variation in activation of the slip joints. That is, some walls slipped readily while others hardly moved.

Additional observations are as follows; see Ryan et al. [2026] for plan details. (1) As a whole, walls with the double slip detail performed better than walls with the slotted slip detail. Limited slip, classified as drift reduction of well less than 50% on average, was observed in double slip walls W1, W8, W15 and W16 (Y-direction), and in slotted slip walls W2 and W9. The slip performance was mostly independent of the expansion joints (i.e. expansion joints functioned as intended), but was affected in W1 and W2, which lacked proper expansion joints. In particular, W1 showed the ability for the wall to slip away from the joint due to the flexibility of the detailing, but not so much toward the joint. (2) Special detailing was applied to allow

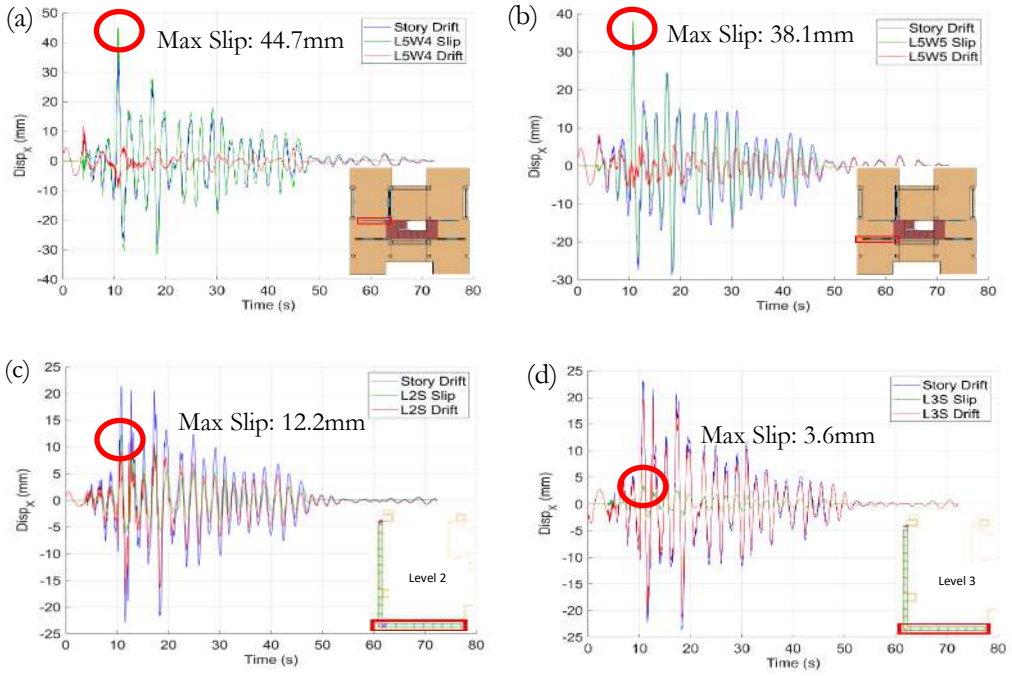


Figure 2. Interstory drift, slip, and wall drift in select walls under MCER Ferndale XYZ: (a) interior W4 with slotted slip track, (b) interior W5 with double slip track, (c) CFS 1 Story 2 south wall with slotted slip track, and (d) CFS 1 Story 3 south wall with double slip track (Adapted from Yi [2025]).

the connected south side partition walls and shaft wall (W10-W14-W6) to move together despite having different slip details. These walls were effectively separated from intersecting shaft wall segments W11 and W13. The detail worked as intended and W10-W14-W6 experienced unencumbered synchronized slip. (3) Partition wall W9 was separated by an expansion joint from intersecting shaft wall segments W12 and W13, which lacked a proper joint to accommodate their incompatible movement. In spite of this, W12 recorded significantly more slip than W9. The result was surprising, with the best explanation being that intersection of W12 and W13 were detailed to be as flexible as possible (e.g. leaving slight gaps at the ends of the gypsum wallboard. (4) All expansion joints at wall intersections were very effective except for, in some cases, the AFWC aluminum joint cover. The north and east adjacent segments of W15 experienced limited slip while the W16 experienced no slip for movement in the Y-direction. In several cases the bidirectional movement exerted a torque demand on the joint cover and caused the ends of the cover to pop out from their sleeves, which surely impacted their ability to move properly.

Even more than the interior partition walls, challenges were encountered with the slip joints in the exterior subassembly CFS 1, and in particular Stories 1 and 3 that were detailed with double slip track, measured almost no slip, while the slotted slip detail on Story 2 showed drift reductions of 30% on the south wall and 50–80% on the west wall. A comprehensive depiction of peak wall drift ratio (derived interstory drift – recorded slip) versus PIDR across the intensity range of the motions is shown in Figure 3(a) for the west walls of Stories 1-3. In this case, a one-to-one relation indicates ineffective slip and no reduction in wall drift. Explanations were sought as to why the slip in exterior walls was much less than the interior walls. For the double slip detail, the "fit" of the nested tracks was tighter than for interior partition walls due to thicker steel and only 3 mm (1/8") difference (oversize) in flange dimensions. Second, later inspections confirmed the presence of isolated screws across the slip joint; such screws were expected to shear off when the slip joints activated, but this was not observed. Third, the presence of exterior ACM panels, although also detailed for slip, added additional interfacing slip components that may have increased the overall resistance to slip. The lack of slip prevented the SF expansion joints on Stories 1 and 2 from being fully tested, but they appeared to work as intended. The control joint on Story 3 was effective under the limited

movement; no gypsum damage was observed at the interior wall and the hinged L-shaped ACM panel that wrapped the corner was able to rotate about its vertical axis to accommodate the differential movement of the two walls to which it was attached.

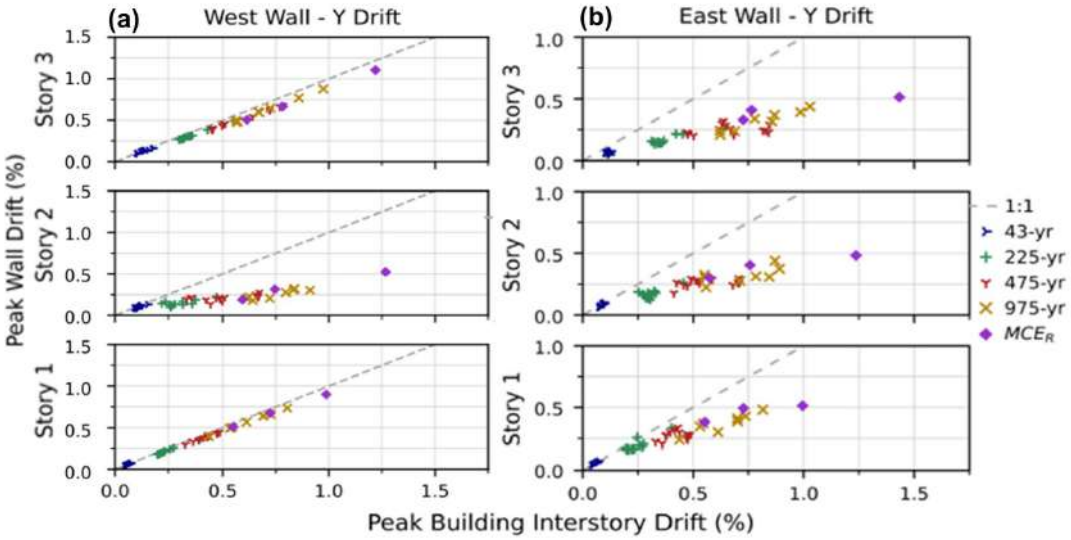


Figure 3. Peak interstory drift vs wall drift in Stories 1, 2 and 3 for (a) CFS 1 west wall, and (b) CFS 2 east wall (Adapted from Roser et al. [2025]).

Overall, the inability to reliably engage slip seems to be a departure from prior studies (mostly on isolated walls with displacement-based cyclic loading), of which the authors have not been able to explain. Many complexities were introduced by moving from the controlled laboratory setting to field installation on a real structure, such as multi-directional loading, tolerances and alignment of structural elements, multiple connected interacting walls, and lack of contractor inexperience. Analytical work by the authors has also shown that the observed slip response of these walls is not represented by a friction model; that is, the wall slip phenomenon seems to reflect increasing resistance (or hardening) even after the initiation of slip [Ji 2025], the source of which is unknown. While the lack of slip was disappointing, the walls—subjected to drift ratios of no more than 1.5%—showed only minimal damage. Since the walls were unfinished (interior walls lacked paint and the exterior walls lacked both mud/tape and paint), some minor damage states were not present that would have been present in fully finished walls. In particular, walls without tape between wall panels showed a slight capacity for panel rocking. Regardless, based on observations in this experiment, even the fully finished walls should be repairable with only minor patching. Importantly, the slip track detailing appeared to increase the walls' ability to move with the drift and provided some benefit even without the proper expansion joints. The responses of the platform-framed walls are further documented in Ji [2025] and Roser et al. [2025].

3.2 CFS 2: BYPASS-FRAMED SUBASSEMBLY

Recall that in bypass framing, studs are outboard and attached back to the floor studs using clips. In a prior full-scale building test with a bypass-framed system, rigid clips were employed, and drift demand was partially absorbed through yielding of the clips, leading to a large percentage of clip failure [Wang et al. 2015]. For this test's CFS 2 subassembly, rigid clips were replaced with sliding clips set into U-strut, and a large hinged "door" expansion joint was installed at the intersection walls [Ryan et al. 2026]. During the test program, the drift clips readily accommodated movement between the structure and the façade, and this approach was overall more effective than the top of wall slip joints in reducing the drift to the wall. As depicted for CFS 1, Figure 3(b) shows peak wall drift ratio against PIDR across the range of intensities for Story 1-3 east walls. Little drift reduction is observed for 43-year motions, however, as drift intensity

increased the relative wall drift decreased (i.e. improvement in drift reduction), and peak wall drift ratio seemed to level off at about 0.5%. The relative benefit also increased up the height from Story 1 to 3. To explain, the upper stories saw relatively more slip for the same level of drift since the movement between the building and the wall accumulated over the height. Figure 3(b) suggests that initial resistance to initiate sliding is overcome more readily as the height increases and the clips are subjected to increased slip demands.

While substantial (more than 50%) drift reduction in the wall was observed, the clips experienced some resistance to sliding within the U-strut. Figure 4 illustrates several of the damage modes that were observed throughout the test program. Issues first emerged after the first sequence of design level motions: at the uppermost story of the three-story subassembly, several clips experienced binding and partial screw pull-out (Figure 4(a) and 4(b)). After this damage was detected, the damaged clips were repaired with backing plates, extra screws, second clips on the back of the stud, etc. The repaired/reinforced clips demonstrated much greater resistance to screw pullout, but clip bending was observed (Figure 4(c)) and eventually, a few of the reinforced clips passed the damage along to the studs (e.g. Figure 4(d) shows stud buckling). Despite this, the system sustained many repeated large intensity motions. Since a significant portion of the clips slipped freely over the whole test program, the clip damage was unpredictable and localized failures did not propagate or compromise overall façade stability. Factors that may have prevented free slip include friction, poor installation/misalignment, lack of lubrication, and overtightening of vertical screws. The authors believe that the sliding issues did not manifest in earlier component tests of the clip conducted by the manufacturer. The hinged joint at the corner completely prevented damage by opening and closing as needed. Overall, the DSSCB clips successfully demonstrated the concept of isolating multi-story bypass framing from structural drift through controlled sliding connections; however, improvement in clip sliding mechanism and/or installation procedures is needed. The response of CFS 2 is further documented in Roser et al. [2025].



Figure 4. Damage modes: (a) incipient and (b) full pullout; (c) stud bending and (d) stud buckling

3.3 CFS 3: SPANDREL-RIBBON SUBASSEMBLY

Recall that CFS 3 alternated spandrel units rigidly attached to floor slabs between "ribbon" layers of windows. This configuration directed all interstory drift to the window units, and this configuration utilized double slip joints at the tops of the windows. Unfortunately, negligible movement was measured across the top of window slip joints. Nonetheless, no damage was observed in the walls, and it became apparent with further observation that the window framing was racking. Close-up video footage was captured to better understand the mechanisms of accommodating the racking, and video stills are shown in Figure 5. Manufacturer A's windows utilized a head receptor system, wherein an internal frame floats with respect to the exterior frame. Figure 5(a) and 5(b) illustrate the relative frame movement at the top and bottom of the window, respectively. With Manufacturer B's windows, the glass clearly moved and rotated within the framing, similar to the expected movement in a curtain wall. Figure 5(c) illustrates the glass moving away from the bottom corner as the framing racks to the right, while Figure 5(d) illustrates the glass moving toward the bottom corner as the framing racks to the left. In addition, initial separation of the framing units in the corner can be seen. Although these movements were observed, no noteworthy damage to the windows occurred, including at the corners where the incompatible movement was absorbed.

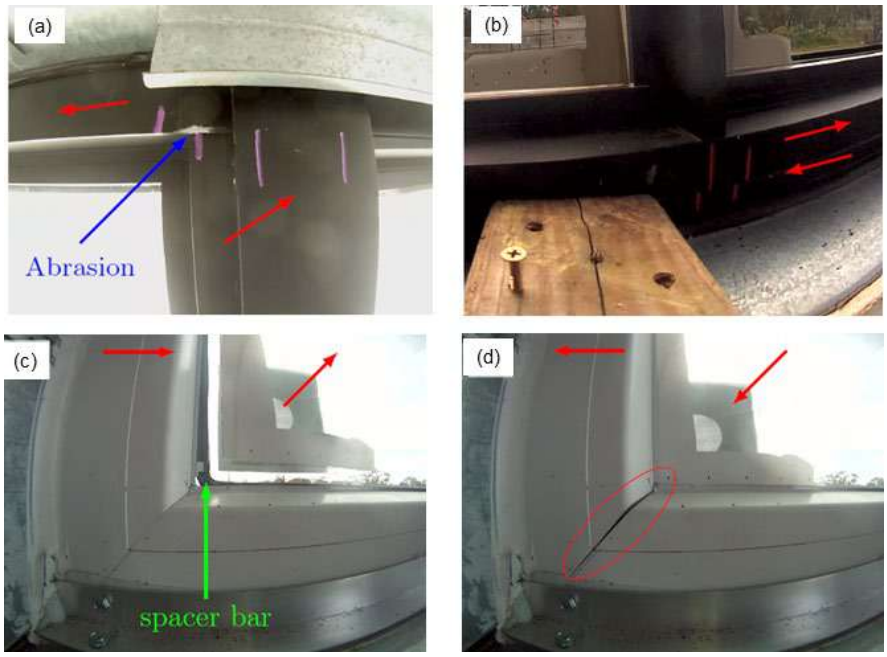


Figure 5. Relative frame movement observed in Manufacture A window (a) top, (b) bottom; glass movement observed in Manufacturer B window (c) away from corner, (d) toward corner. (Adapted from Roser et al. [2025])

The performance of the windows was remarkable; as the drifts imposed on the windows were roughly twice the interstory drifts due to the spandrel rigidity. Manufacturer A and B windows on Stories 1 and 3 absorbed equivalent to drift ratios exceeding 2% and 3%, respectively. Given the very different movement mechanisms exhibited by these two window samples, vast differences are expected industry-wide. The windows used in these experiments had not been seismically qualified through racking tests, a requirement for curtain walls but not for individual window manufacturers. Participants in this test expected their windows to have some capacity for movement, and were eager to challenge their systems. This suggests that all windows are not alike, and seismic qualification testing of windows would be valuable to pick resilient products. With the robust response of the window units, the spandrel-window paradigm was shown to be very effective. The response of CFS 3 is further documented in Roser et al. [2025].

3.4 STICK-BUILT GLASS CURTAIN WALL SUBASSEMBLY

The curtain wall accommodated the imposed interstory drifts, as expected primarily through racking of the steel mullion frame and rotation of the glass panels about their setting blocks**.** Several of the glass panels were instrumented with displacement transducers, and investigation is ongoing to explain the nature of the glass movement within the framing (relative amount of rocking versus sliding), how it is affected by size and aspect ratio of the panel, and whether it is affected by vertical ground shaking.

At low and moderate shaking intensities, the curtain wall moved elastically with the structure, showing no permanent deformation or distress. At higher drifts, the frame exhibited visible racking, but glazing remained seated within the mechanically captured pressure-plate system, and no glass fallout or seal failure occurred. The following minor damage mechanisms were observed. First, the top west panel exhibited permanent movement of the glass relative to the framing; over the sequence of motions, the glass panel ultimately moved about 12 mm toward the south (Figure 6), causing the tape around the edge of the glass to be exposed. Furthermore, the door attachment mechanism experienced such damage that it no longer closed properly and was observed to flap around during shaking. Damage to the latch mechanism is shown in Figure 7; in particular, the door latch rod was permanently bent (Figure 7(b)) and the rod insertion holes

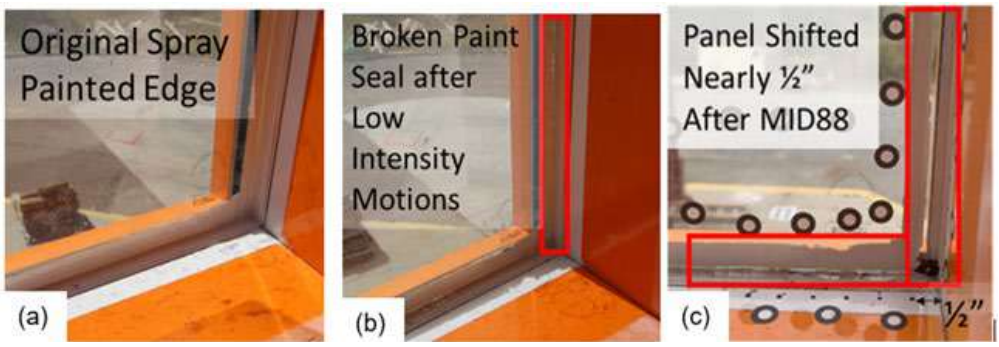


Figure 6. Migration of curtain wall top west panel over the course of testing; paint seal is broken, and panel shifts permanently by 12 mm (1/2")



Figure 7. (a) Door latch mechanism preventing closure, (b) and (c) opposite side views showing damage to door latch insertion hole

on the back side widened (Figure 7(c)). Both of these apparent damage mechanisms were likely caused by the unrealistic level of repeated shaking. However, they may compromise the fire resistance of the curtain wall, as full enclosure with no air gaps and a properly functioning door are essential to suppressing fire.

3.5 TEN STORY STAIR TOWER

The 10-story stair tower and the connections of the stair flights to the landings, which were the critical focus of the paper, are described in Sorosh et al. [2025], and Ryan et al. [2026]. Relative displacements between the stair flights and landings were measured using displacement transducers at Stories 2, 3, 4, 6, 8, and 10. Recall that each flight in a scissor-configured stair is subjected to approximately one-half of the interstory drift, and therefore a perfect flight-to-landing connection would experience this amount of relative displacement. Figure 8 shows 50% peak interstory drift vs peak connection displacement for select connections, one of each type. Peak responses to different ground motions are shown in a scatter plot format, color-coded by hazard level (correlated to intensity) of the input motion. A perfect one-to-one relation between 50% drift and connection displacement suggests that the connection perfectly accommodated the drift, although the peaks may not have occurred at the same time.

The drift-compatible (DC) connections had been developed and validated in prior tests of a single straight run stair configuration where the landing was mounted on a shake table while the flight was grounded [Black et al. 2020]. This was the first experiment incorporating drift-compatible connections into a realistic multi-story stair configuration with realistic boundaries and constraints. Theoretically, dual attachment style connections can accommodate the movement better because they allow for independent movement of the upper and lower stair flights relative to the mid-landing. Under inter-story, the stair flights are expected to be pulled in opposite directions with respect to the mid-landing, based on their respective attachments to the floor diaphragms above and below. However, the single attachment channel style was envisioned to be more favorable, satisfying practical constraints in design and construction.

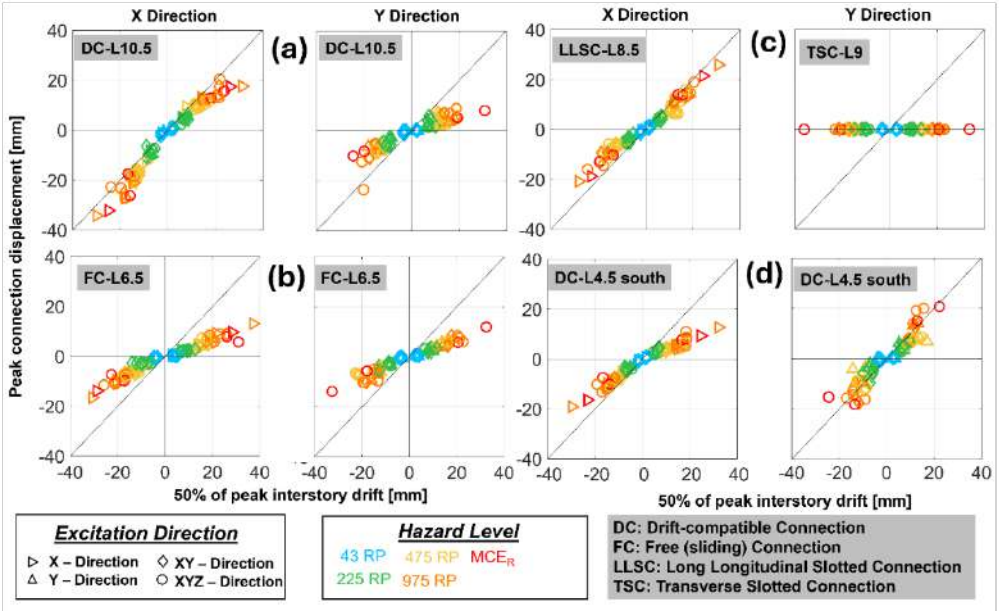


Figure 8. 50% of peak interstory drift vs. peak connection displacement in X and Y Direction for various connections (a) DR (single attachment channel) on Story 10, (b) longitudinal and transverse slotted on Story 8, free sliding on Story 6, and DR (dual attachment channel) on Story 4. (Figure adapted from Sorosh et al. [2025])

Figure 8(a) indicates that the single attachment DC connection on Story 10 accommodated most of the 50% interstory drift in the longitudinal (X) direction, and about half in the transverse (Y) direction. This level of connection movement was relatively larger than the other single attachment DC connections (which were measured on Stories 2 and 3). In particular, the DC connections on Story 3 recorded almost no movement. Differences in movement are due to the following. First, Story 3's modular stair system (MSS) unit was very stiff due to the presence of the shaft wall panels installed in the framing, which constrained its overall movement. (Of the stories containing the built-in stair shaft wall panels, only Story 3 was instrumented.) Second, Story 10 lacked the gravity framing of the MSS units, thus placing less constraint on the mid-landing and allowing flights to rotate (twist about their vertical axes) more freely to better accommodate the movement across the connection. Rotation was evident based on differences in movement measured on the two sides of the stair flight. The dual attachment DC connection on Story 4 (Figure 8(d)) also moved well, accommodating half or more of 50% interstory drift in the longitudinal direction and essentially all in the transverse direction without any significant rotation. Overall, the test data (albeit limited) seemed to validate the expectation that the dual attachment style could accommodate movement due to inter-story drift very well, but the single attachment style can also work if the rotation mechanism can be activated.

Prior research had raised concern that free sliding connections may be subject to a "whiplash effect", in which the stair unit vibrates independently of the building, causing the lower flight to move around excessively on its lower landing [Black et al. 2020]. Depending on space constraints, there are also practical limits to the amount of free sliding that can be accommodated. The free sliding connections on Story 6 (Figure 8(b)) accommodated about half of the 50% interstory drift in both directions, and thus did not seem to induce any independent vibration in the stairs. Such characteristics may depend on the relative stiffness and weight of the stair unit and the friction between the sliding interfaces. In this configuration, the stiffness of the MSS unit and the friction of the steel-on-steel interface may have helped to constrain the stairs from excessive sliding, and in such instances, the approach could be very cost effective. On Story 8, the longitudinally slotted connections demonstrated what appeared to be nearly perfect movement relative to the 50% interstory drift (Figure 8(c)), while no movement was recorded in the transversely slotted connections. The fact that the longitudinally slotted connections moved more than the free sliding connections is puzzling given that the configurations were essentially identical except for the bolts; however,

the lack of transverse constraint in the free sliding connection may have affected the overall sliding mechanism and engaged more friction during relative multi-directional movement. A more comprehensive presentation of the response of the stair tower can be found in Sorosh et al. [2025].

CONCLUSIONS

In surmising the outcomes of the test program, and the challenges encountered in ramping up to scale and complexity in a real building, the objective to develop seismic resilient details for vertically distributed nonstructural elements might be questioned. The authors argue the value in continuing this line of research and development. A comprehensive, proven set of solutions that are cost-effective, constructible and commonplace do not yet exist, but research will continue to move us toward this end. Effective and reliable solutions *are* available for some applications. For instance, for piping systems, flexible couplings and seismic separation assemblies are proven, accepted and often required by code. For other components, the details can be fine-tuned to be more reliable and "construction proof" to minimize added costs, coming closer to finding their niche in the market. The concepts that work well in one domain can be cross-pollinated to other classes of nonstructural elements, for example, functional slotted/sliding joint concepts. The authors have the following conclusions/recommendations specific to the components considered in this project.

Interior Partition Walls: Even in the absence of full activation, a slip track appears to provide a benefit if it can be built with modest additional expense. While double slip tracks exhibited slightly more slip in interior partition walls, they essentially did not slip in the exterior configuration. The slotted slip detail more closely resembles typical construction and requires only the use of a specialized horizontally slotted track. Component tests should be conducted to confirm the relation between screw tightness and slip resistance. Practically, for all but the simplest plan layouts, placing vertical expansion joints on every wall is architecturally challenging and likely to be cost prohibitive. The expansion joints provide reliable solutions for special cases, to protect a single wall or to serve dual purposes. However, for other situations, flexible detailing through the corner (i.e. corner gap or limited use of studs through the corner regions), can limit moderate drifts without excess damage.

Exterior Facades and Curtain Walls: Of the three different approaches investigated here, the platform-framed approach seems the most ready for implementation, noting the challenges with slotted slip connections. Although the bypass framing approach has some advantages (the reduction in slip joints greatly simplifies the ACM panel installation), its drawbacks are significant (height limitation, expansion joint requirements, and reliability of sliding clips which can be solved). The strip window system, which is a unique configuration conducive to certain architectural styles, also showed promise with the potential for drift to be accommodated entirely within the windows. More window products should be verified for movement by racking tests, and architects/engineers should specify products that have been verified. The glass curtain wall tested in this project, which had steel mullions and 27 mm thick glass, accommodated many cycles of complex multi-directional movement with minimal issues. However, typical curtain walls with aluminium mullions and insulated glass units should be validated independently.

Stair Systems. Several details for accommodating movement through the stair stringer-to-landing connections were tested, and all demonstrated the capacity to accommodate movement without loss of functionality. Technical and practical challenges of implementation in a compact scissor stair configuration emerged. The DC connection with dual attachment channels appeared to be most effective; however, the single attachment channel also accommodated movement through increased rotation of the stair flights about their vertical axes. The free sliding connection did not move as much as expected, and the relationship between the dynamic properties of the stair unit and the friction coefficients of the sliding interface should

be further explored. Horizontally slotted connections have also been shown to be effective, but can also bind (as with the transverse slotted connections considered in this project.)

ACKNOWLEDGMENTS

The authors are indebted to the many contributors that made this project possible. The structural system scope of NHERI TallWood Project was sponsored by NSF Grants No. 1636164, 1638363, 1634628, 1634204, and the use and operation of NHERI shake table facility was supported by National Science Foundation (NSF) through Grant No. 1520904. The nonstructural component scope of this project was sponsored by NSF Grant No. CMMI-1635363, USFS Grant No. 19-DG-11046000-16, Softwood Lumber Board, Computers and Structures Inc, the GAANN Fellowship Program. Materials and in-kind support were provided by many industry sponsors. Contributors to the wall subassemblies include CEMCO Steel, Construction Specialties, Ehmcke Sheet Metal, Innotech Windows and Doors, Simpson Strong-Tie, Winco Window, and USG. Installation support was provided by apprentices through the Southwest Carpenters Union Training Fund. Ehmcke Sheet Metal manufactured and installed exterior panels, along with the windows, through partial donation. The curtain wall was supplied by Allegion/Technical Glass Products. The stair system was supplied by Construction Specialties, with prefabricated MSS units delivered to the test site. The authors especially recognize the following individuals who contributed exceptionally to this project: the TallWood team (PI Shiling Pei, Jeffrey Berman, John van de Lindt, Steve Pryor), nonstructural industry collaborators Kevin Smith, Bill Taylor, Cliff Melcher, Robert Belvin, Ron Madeley, Lothar Erkens, George Nickel, and Fernando Sesma.

REFERENCES

Black, C., Aiken, I., Smith, K., Belvin, R., Peachey, A. [2020]. "Shake table testing of seismically resilient stair systems for buildings", *Proceedings of the 17th World Conference on Earthquake Engineering*, Sendai, Japan.

Ji, Y. [2025]. "Seismic Response of Nonstructural Platform framed Cold-formed Steel Walls Subassemblies Detailed for Drift Compatibility", *PhD Dissertation*, University of Nevada, Reno.

Pei, S., Ryan, K. L., Berman, J. W., van de Lindt, J. W., Pryor, S., Huang, D., ... & Dolan, J. [2024]. "Shake-table testing of a full-scale 10-story resilient mass timber building", *J. Str. Eng.* (ASCE), 150(12), 04024183.

Roser, W. [2025]. "Seismic Performance of Nonstructural Cold-Formed Steel Framed Exterior Walls with Drift Compatible Details in a 10-Story Mass Timber Building", *PhD Dissertation*, University of Nevada, Reno.

Roser, W., Ryan, K. L., Ji, Y., Hutchinson, T. C., Wynn, S. L., ... & Pei, S. [2025]. "Seismic performance of cold-formed steel nonstructural exterior walls with drift-compatible details in full-scale shake table tests of a tall mass timber building", *J. Earthquake Eng.,* DOI:10.1080/13632469.2025.2492247.

Ryan, K. L., Hutchinson, T. C., Sorosh, S., Roser, W., Ji, Y-E., Wynn, S. L. [2026]. "NHERI TallWood Project part 1: Overview and nonstructural subassembly details", *Proceedings of Sixth International Workshop on the Seismic Performance of Non-Structural Elements (SPONSE 2026),* Tokyo, Japan.

Sorosh, S. Hutchinson, T.C., Ryan, K.L., Smith, K.W., Kovac, A., Zabet, S., Pei, S. [2025]. "Experimental characterization of a full-scale stair system detailed to achieve seismic resiliency", *Earthquake Eng. & Struct. Dyn.*, 54, no. 14 (2025): 3519–3540. https://doi.org/10.1002/eqe.4376.

Wang, X., Pantoli, E., Hutchinson, T. C., Restrepo, J. I., Wood, R. L., Hoehler, M. S., ... & Sesma, F. H. [2015]. "Seismic performance of cold-formed steel wall systems in a full-scale building", *J. Str. Eng.* (ASCE), 141(10), 04015014.

Experimental shake table evaluation of non-structural elements in accordance with AC-156

Angela Poposka[1], Aleksandra Bogdanovic[1], Filip Manojlovski[1], Antonio Shoklarovski[1], Lidija Krstevska[1]

[1] Institute of Earthquake Engineering and Engineering Seismology, University "Ss. Cyril and Methodius" in Skopje, North Macedonia
e-mail: angela@iziis.ukim.edu.mk
[1] Institute of Earthquake Engineering and Engineering Seismology, University "Ss. Cyril and Methodius" in Skopje, Skopje, North Macedonia
e-mail: {saska, filipmanojlovski, antonio, lidija}@iziis.ukim.edu.mk

Abstract. With advancements in construction technologies and building typologies, non-structural components now represent a substantial portion of overall building value. Their damage during earthquakes can result in significant economic loss, functional disruption, and life safety risks. However, their seismic design is often inadequately addressed in building codes, leaving their performance and vulnerability insufficiently understood.

To address these challenges, full-scale experimental testing is essential for gaining insights into the behavior of non-structural components under seismic excitation. This paper presents the procedures and results of shake table testing conducted on various types of non-structural elements, including raised floor systems, ceiling systems, partition walls and cleanroom systems. These tests were performed at the Dynamic Testing Laboratory of the Institute of earthquake engineering and engineering seismology (IZIIS) in Skopje, Republic of North Macedonia. A custom-designed steel cube structure was used to simulate the seismic effects typical of a building story, enabling realistic testing conditions.

The seismic excitations applied during testing were generated following the guidelines of AC-156 standard for seismic qualification of non-structural components. Advanced instrumentation, including accelerometers, linear potentiometers, LVDTs, and strain gauges, ensured accurate data collection. Most of the tested components satisfied the AC-156 seismic acceptance criteria, offering valuable insights into their behavior and performance. These findings underscore the importance of rigorous seismic evaluation of non-structural components to enhance building safety and resilience.

Keywords: Non-structural components, seismic performance, shake table testing, AC-156

1. Introduction

Non-structural elements (NSE), including raised floors, ceilings and partition walls comprise an integral part of the buildings. Although they do not contribute to the load-bearing capacity of a structure, their damage during an earthquake can lead to serious economic losses or even risks of injuries [8, 19]. Recent earthquakes have repeatedly pointed out that non-structural component damage gives the largest contribution to the earthquake economic loss. Despite the significant economic and safety implications, the seismic performance of NS has long remained secondary to structural elements, especially in design practices [3], [6]. To address this critical oversight, the development of performance-based seismic design approaches suitable for non-structural structures has been frequently addressed in recent years. A 2018 American and Italian study [6] highlighted the necessity to integrate the seismic performance of non-structural components into building design. However, effectively designing for seismic resilience requires robust data. The limited data collected during past events are not sufficient to completely characterize the seismic behaviour of non-structural components and develop effective mitigation measures. The seismic vulnerability of suspended ceilings has been extensively documented by experimental studies, including shake table tests. Research conducted by working groups in China [11] and Turkey [12] reveal common damages such as tile dislodgement, hanger detachment, and perimeter loss. Furthermore, shake table testing carried out in China enabled a large-scale evaluation of ceiling behavior under different seismic simulations, including comparisons between fixed-base and isolated-base structures [13,14]. This research has effectively improved the understanding of the connections between ceilings and the supporting structure. In contrast, raised floors, commonly found in office buildings, data centers, and laboratories, have received comparatively less attention. Nevertheless, in 2024 a study conducted in Nottingham [2] addressed the structural behavior and sustainable design aspects of these systems, providing a basis for performance-based seismic design of NSEs. Given the complexity of various typologies of non-structural components subjected to seismic excitations, systematic experimental testing is necessary for a better understanding of their seismic behaviour [17,18]. To contribute to this necessary body of knowledge, a series of shake table seismic tests have been performed at the Institute of Earthquake Engineering and Engineering Seismology in Skopje, Republic of N. Macedonia [5]. These tests were conducted for the seismic qualification of specific types of raised floors, partition walls, ceilings and cleanroom systems, adhering to the AC-156 criteria. Analysis of dynamic behavior was performed, and results on seismic response of the considered elements have been obtained. Many different configurations of products were tested based on the most frequent installation scenarios. More in detail, the testing program included 32 different raised floor configurations (varying in height, constraints, etc.), 24 different types of partition walls, 6 different ceiling and 11 cleanroom configurations. All the elements were subjected to biaxial, artificially produced earthquake excitation time history. This paper presents a brief overview of the testing procedure and selected results obtained from this extensive experimental campaign.

2. Experimental configurations of non-structural elements

In this study, the testing and results of raised floor systems, partition walls, ceiling systems, and cleanroom systems are presented. To ensure compliance with testing requirements, the non-structural elements were mounted within a high-stiffness steel cube anchored to the shaking table. Steel frames were installed inside the cube at two levels, and the outer structure of the cube was welded on site.

2.1 RAISED FLOORS

Raised floor systems are non-structural assemblies designed to provide a walkable surface while accommodating various installations. In this study, three units were investigated, each consisting of vertical steel pedestals with heights of 0.5 m, 1.0 m, and 1.5 m. The pedestals were fixed at both ends and

interconnected by a grid of perpendicular steel beams. Their spacing in both directions was 0.6 m, corresponding to the dimensions of the floor panels. To control horizontal displacements, adjustable steel bracing was incorporated, with the type of bracing dependent on the specific system configuration. The dynamic properties of the 1.5 m-high system were evaluated by progressively increasing the number of panels. To assess seismic performance, two different loading conditions were applied: i) a uniform load of 3 kN/m² and ii) a combination of uniform load of 5 kN/m² and 15 kN concentrated load, for systems with heights of 0.5 m and 1.0 m, respectively (Figure 1).

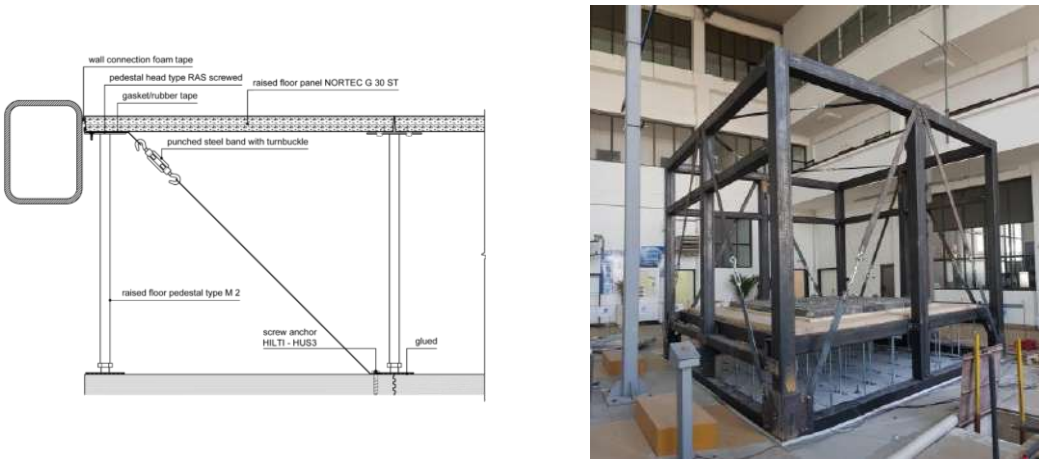


Figure 1. Raised floors – technical drawing and installation on the shake table

2.2 CEILING SYSTEMS

Ceiling systems are suspended non-structural elements designed to define architectural space while also providing accommodation for ventilation ducts and other installations. In this study, ten ceiling panel types were tested, organized into two layouts, each comprising five panel types supported by steel profiles within a basic steel cube. Both layouts were subjected to biaxial testing in the orthogonal Y–Z and X–Z directions (Figure 2). For layout 1, additional components such as seismic clips, screws, and stoppers were included, whereas layout 2 incorporated stoppers and ropes. To simulate service conditions, supplementary weights were applied to selected panels during testing.



Fig. 2 - Ceiling systems – technical drawing and installation on the shake table

2.3 PARTITION WALLS

Partition walls are non-structural elements intended to vertically subdivide interior spaces. A total of 24 wall panel types were examined, arranged in two layouts, 10 types in layout 1 and 14 types in layout 2 (Figure 3). All specimens were supported on steel profiles within a steel cube and subjected to biaxial excitation in the Y–Z and X–Z directions. Four configurations were tested, two for layout 1 and two for layout 2. The use of seismic clips was optional across all configurations and was applied only when walls without clips failed to meet AC156 performance requirements.

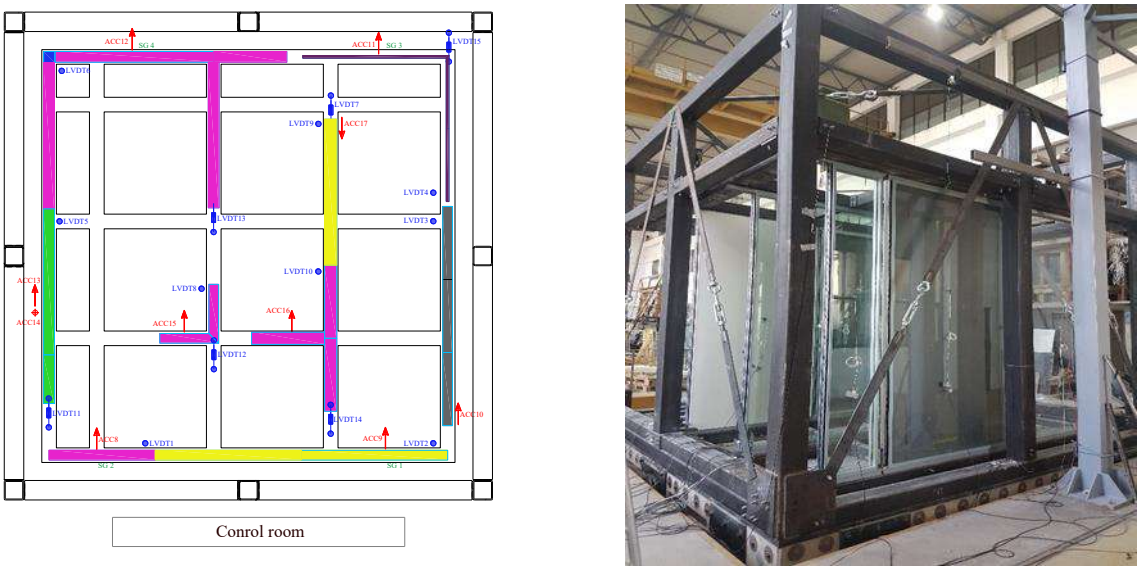


Fig. 3 - Partition walls - technical drawing and installation on the shake table

2.4 CLEANROOM SYSTEMS

Cleanroom systems are more complex non-structural assemblies than raised floors or ceilings, as they integrate multiple elements including ceilings, partitions, raised floors, and other installations. The tested specimens were organized into two layouts. Layout 1 included one ceiling type, 15 partition walls, two door types, and one installation, while layout 2 included one ceiling type, 20 partition walls, two door types, and one installation. Each layout incorporated additional or optional components, such as silicone walls or bracing systems. Testing applied either a uniform load of 150 kg/m² or a concentrated load of 4 × 150 kg. To account for horizontal asymmetry, specimens were rotated by 90° to test both directions. Considering the combinations of non-structural elements, optional components, load types, and specimen orientation, a total of eleven configurations were evaluated.

3. Instrumentation setup

The instrumentation schemes were designed to capture the most significant and reliable experimental data, considering the geometry of the specimens. The preparation of each scheme involved selecting appropriate measurement instruments, determining their optimal locations, and defining the number of measurement points on the specimens, based on the available instrumentation and data acquisition capacity at the IZIIS laboratory. Four types of transducers were employed: accelerometers (ACC), linear potentiometers (LP), linear variable differential transformers (LVDT), and strain gauges (SG), to measure acceleration, absolute and relative displacements, and strain. Figure 4 presents the instrumentation scheme for a representative configuration of the raised floor and ceiling systems.

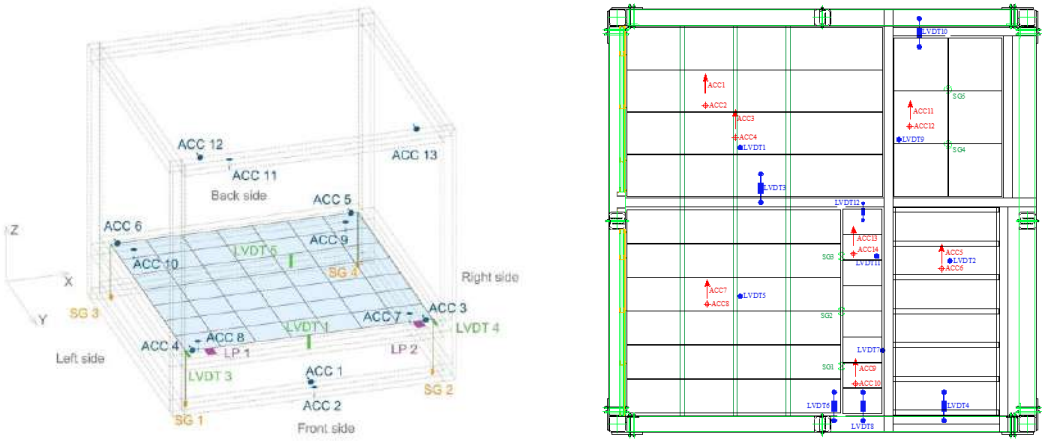
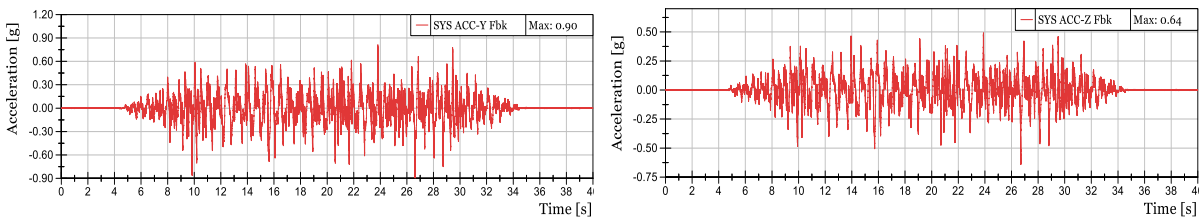


Fig. 4 - Instrumentation for the raised floor systems (left) and for the ceiling systems (right)

4. Testing methodology

The testing program was designed to comply with the seismic certification procedures outlined in Chapter 6 of AC156 – Acceptance Criteria for Seismic Certification by Shake Table Testing of Non-Structural Components. In accordance with these criteria, all specimens were tested simultaneously in both horizontal and vertical directions. Each specimen underwent two types of excitations: resonant frequency search tests to identify natural frequencies and time-history seismic excitations to evaluate the global dynamic response. All tests were conducted at the Laboratory for Dynamic Testing at IZIIS. The IZIIS shake table features a 5 m × 5 m platform supported by two lateral and four vertical actuators, providing five degrees of freedom.

For the resonant frequency search tests, random and sine-sweep excitations were applied independently in each direction—horizontal and vertical—at three stages: before testing (initial state), after selected biaxial tests, and after all tests (final state). The excitation frequency range was 1–35 Hz (up to 40 Hz in some cases) with a sweep rate of 2 octaves/min and peak acceleration levels of 0.01–0.05g. Additional sine-sweep tests were performed to determine the dynamic characteristics of raised floor systems with varying heights and sizes, using 0.02g input acceleration in the X–Z and Y–Z directions over frequency ranges of 1–40 Hz and 1–45 Hz, respectively. Biaxial time-history tests were performed in accordance with Section 6.5 of AC156, with simultaneous but independent horizontal and vertical inputs, each designed to produce the Required Response Spectrum (RRS) along the respective reference axis, calculated using 1/12-octave frequency bandwidth and 5% damping. Non-symmetric elements were rotated 90° to test both directions. The earthquake intensity was gradually increased, starting from 0.23g and 0.17g and reaching 0.9g and 0.64g in the Y and Z directions, respectively. Figure 5 presents the maximum input acceleration time histories in both directions along with the corresponding Test Response Spectra (TRS) matching the AC156 RRS.



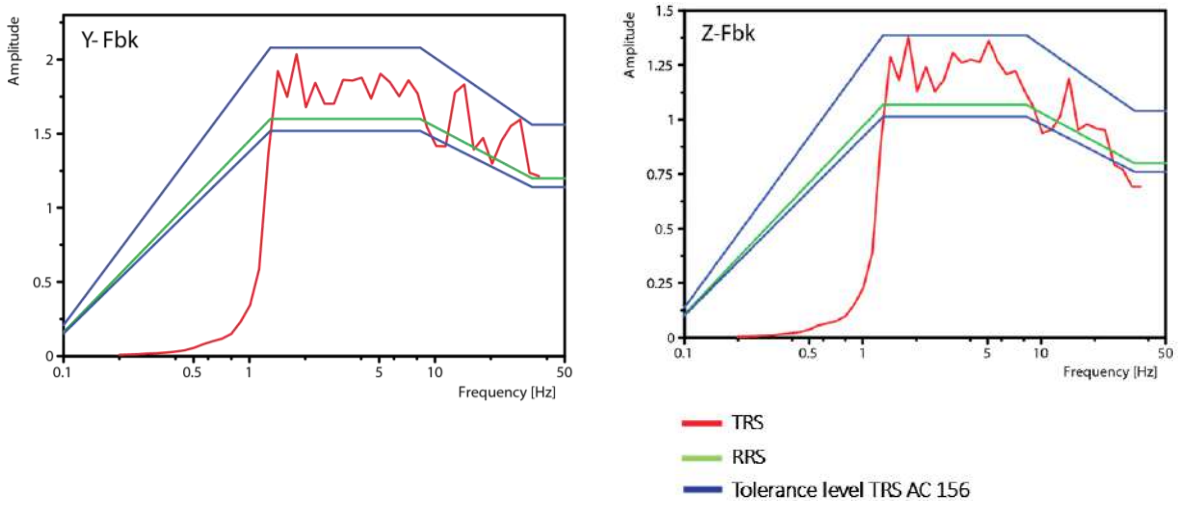


Fig. 5 - Input time histories of the test with the highest excitation and TRS vs RRS

5.Results and discussion

For the 1.0 m high raised floor systems, the horizontal-direction frequencies for bracing configurations with different numbers of panels were found to be 30.02 Hz, 11.35 Hz, 7.32 Hz, and 6.19 Hz for configurations 1×1, 3×3, 5×5, and 7×7 panels, respectively. It was observed that the increase of the number of panels led to a decrease of the value of the resonant frequency. The same tendency is visible for the panels without bracings where, in the same configurations, the measured respective frequencies of 6.36Hz, 4.25Hz, 3.81Hz, 4.67Hz are significantly lower compared to the previous ones (configurations with bracings) due to the lower stiffness. If the results obtained for the frequencies are compared, it is clear that the increased number of panels and the removal of bracings significantly reduce the value of the resonant frequency. The plot in figure 7 shows the input acceleration time history versus the acceleration time history at the level of floor panels. The maximum input acceleration is 0.85g and the top acceleration with certain amplification is 4.2g for the specific measured points. Related to the dynamic behaviour during the most intensive seismic tests, there was noticeable sliding and slight separation of the raised floors panels, but there was no damage of the elements of the system and no change in the stability of the tested configurations.

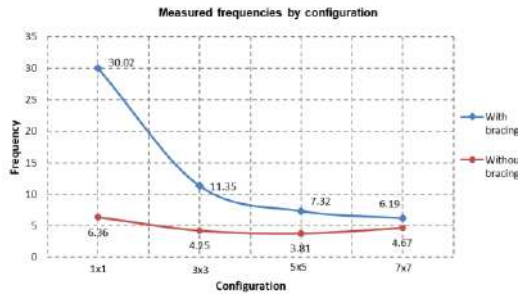


Fig. 6 - Change of dynamic characteristics of raised floors, 1.0m high

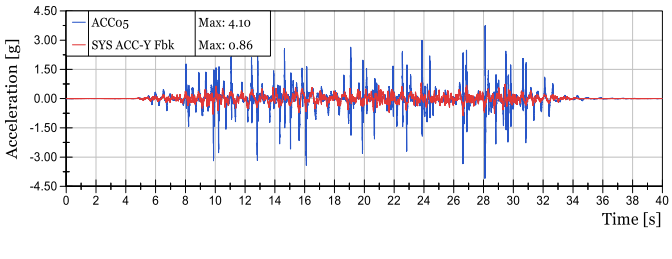


Fig. 7 - Input TH vs output TH of acceleration at point 5, braced raised floors with 1.0m high

Concerning the ceiling systems, the maximum relative horizontal displacement of the most flexible ceiling panel was 13.2 mm (Layout 1 – Configuration 1), while the maximum relative vertical displacement between the steel profile and the panel was 14.5mm (Layout 1 – Configuration 2), figure 8. The maximum measured acceleration in horizontal direction was 4.34g (ACC01) and the maximum measured acceleration in vertical direction was 3.31g (accelerometer ACC02), providing amplification factor or 4.7 and 5.1, respectively. The

selected time histories are shown in figure 9. During and after the seismic test, all units of the ceiling systems and their supporting structures showed neither damage nor loss of function, except two different types of panels, which fell during the strongest tests (figure 12 - left).

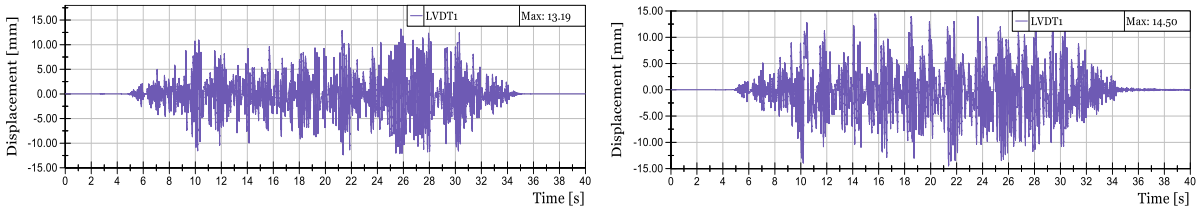


Fig. 8 - Time histories of maximum relative displacement for ceiling systems

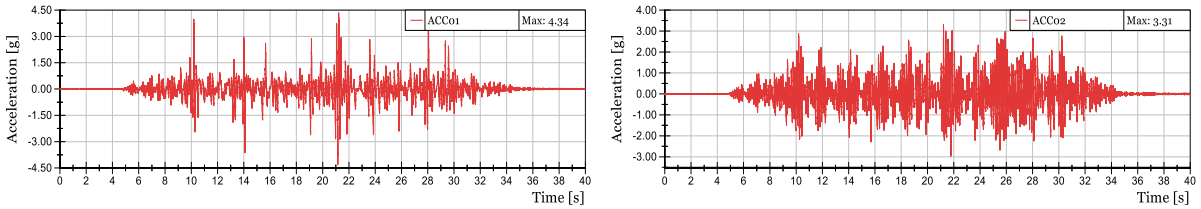


Fig. 9 - Time histories of maximum measured accelerations for ceiling systems

As for the cleanroom systems, maximum relative displacement of 19.6mm and maximum acceleration of 6.62g were measured during the intensive seismic tests. The corresponding time histories are presented in figure 10. After the test performed according to the test procedure, no visible damage nor loss of function was noticed in 9 configurations. In the remaining 2 configurations, slight bending of some panels and braces of the ceiling system was observed.

In respect of the partition walls, 24 different types of partition walls were tested of which only 2 types of partition walls did not pass the acceptance criteria for seismic certification by shake-table testing of non-structural components according to standard AC 156 (figure 12 - right). The first one was damaged for excitation of 50% of the RRS, with maximum measured displacement of 6.1 mm (figure 11 - left), whereas the second one was damaged for excitation of 100% of the RRS with maximum measured displacement of 13.8 mm (figure 11 - right).

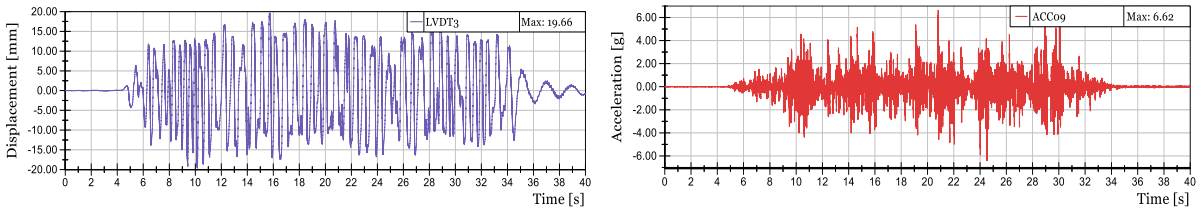


Fig. 10 – Time histories of max. rel. displacement and acceleration during the seismic tests for cleanroom systems

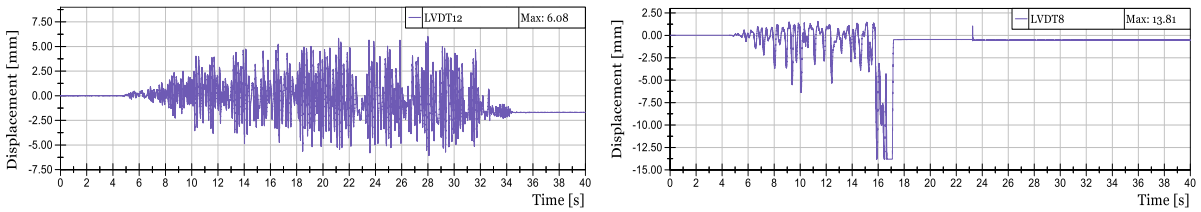


Fig. 11 – Time histories of maximum rel. displacement during the seismic tests for partition walls



Fig. 12 - Damages of the non-structural elements, ceiling systems (left) and partition walls (right)

6.Conclusions

During earthquakes, non-structural components can be seriously damaged, and their failure can result in loss of human lives and extensive repair costs. Their stability and seismic performance are necessary to be verified according to the acceptance criteria in the prescribed standards.

The presented testing of different configurations and layouts of raised floors, partitions, ceiling and cleanroom systems was performed according to the AC156 acceptance criteria for seismic qualification by shake table testing of non-structural components. Qualification by biaxial testing in horizontal and vertical direction was simultaneously performed with corresponding Test Response Spectra (TRS) that match the Required Response Spectra (RRS) given in AC156.

The obtained results of this complex experimental research showed that many of the tested systems successfully passed the seismic acceptance criteria for shake table testing of non-structural components and systems according to the applied standard wheraes several need further improvement.

REFERENCES

[1] Merino, R.J., Perrone, D., Filiatrault, A. [2020] "Consistent floor response spectra for performance-based seismic design of nonstructural elements," *Earthquake Engineering & Structural Dynamics*, Vol. 49, No. 3, pp. 261–284. https://doi.org/10.1002/eqe.3236.

[2] Peng, W., Su, D., Wang, S., Ianakiev, A. [2024] "Environmentally Sustainable Raised Access Flooring Product Development," *Buildings*, Vol. 14, No. 6, Art. 1849. https://doi.org/10.3390/buildings14061849. MDPI+1

[3] Devin (Austin) A., Fanning, P.J. [2019] "Non-structural elements and the dynamic response of buildings: A review," *Engineering Structures*, Vol. 187, pp. 242–250. https://doi.org/10.1016/j.engstruct.2019.02.044.

[4] Chalarca, B., Perrone, D., Filiatrault, A., Nascimbene, R., Blasi, G., Aiello, M.A. [2025] "Braceless seismic restraint for suspended nonstructural elements: Concept, design, and numerical and experimental assessment," *International Journal of Architectural Engineering & Design*. https://doi.org/10.1080/13632469.2025.2497955.

[5] Krstevska, L., Bogdanovic, A., Rimboeck, R., Poposka, A., Manojlovski, F., Shoklarovski, A., Naumovski, N., Markovski, I., Filipovski, D. [2021] "Shake table tests for seismic assessment of non-structural elements," *1st*

Croatian Conference on Earthquake Engineering – 1CroCEE, Institute of Earthquake Engineering and Engineering Seismology, Skopje, North Macedonia.
[6] Filiatrault, A., Perrone, D., Merino, R.J., Calvi, G.M. [2018] "Performance-based seismic design of nonstructural building elements," *International Journal of Architectural Engineering & Design*. https://doi.org/10.1080/13632469.2018.1512910.
[7] Perrone, D., Calvi, P.M., Nascimbene, R., Fischer, E.C., Magliulo, G. [2018] "Seismic performance of non-structural elements during the 2016 Central Italy earthquake," (report/paper), University School for Advanced Studies IUSS Pavia & collaborators.
[8] Dhakal, R.P. [2020] "Seismic performance of non-structural elements (SPONSE) and learning from earthquakes (LFE): New Zealand perspective," *Bulletin of the New Zealand Society for Earthquake Engineering*.
[9] Magliulo, G., Zito, M., D'Angela, D. [2024] "Dynamic identification and seismic capacity of an innovative cleanroom with walkable ceiling system," *Bulletin of Earthquake Engineering*. https://doi.org/10.1007/s10518-024-01895-z
[10] Dhakal, R.P., Rashid, M., Bhatta, J., Chen, C., Song, G.Q., Sullivan, T.J., MacRae, G.A., Clifton, G.C., Xiang, P., Jia, L.J. [2020] "Shake table testing plan for multiple non-structural elements and contents in a low-damage structural steel building," (report/paper), University of Canterbury; Tongji University; University of Auckland.
[11] Duozhi, W., Junwu, D., Zhe, Q., Xiaoqing, N. [—] "Shake table tests of suspended ceilings to simulate the observed damage in the Ms7.0 Lushan earthquake, China," Institute of Engineering Mechanics, Harbin, China.
[12] Ozcelik, O., Misir, I.S., Saridogan, S. [2016] "Performance evaluation of suspended ceiling systems using shake table tests," Dokuz Eylul University & General Directorate of State Hydraulic Works, Izmir, Turkey.
[13] Cao, Y., Qu, Z., Fu, H., Ji, X., Chakraborty, S. [2020] "A substructural shake table testing method for full-scale nonstructural elements," *Journal of Earthquake Engineering*.
[14] Fu, H., Cao, Y., Qu, Z. [2020] "Substructural shake table testing for nonstructural elements of various damage sensitivity in fixed-base and base-isolated buildings," *Earthquake Engineering and Structural Dynamics*.
[15] Perrone, D., Brunesi, E., Peloso, S. [2019] "Shake table testing for seismic performance evaluation of non-structural elements," University School for Advanced Studies IUSS Pavia.
[16] Dhakal, R.P., Rashid, M., Bhatta, J., Sullivan, T.J., MacRae, G.A., Clifton, G.C., Jia, L.J., Xiang, P. [2019] "Shake table testing for seismic performance evaluation of non-structural elements," *Journal of Earthquake Engineering*.
[17] D'Angela, D., Magliulo, G., Di Salvatore, C., Zito, M. **[2024]** "Seismic assessment and qualification of acceleration-sensitive nonstructural elements through shake table testing: Reliability of testing protocols and reliability-targeted safety factors," *Engineering Structures*, Vol. 301, Art. 117271. https://doi.org/10.1016/j.engstruct.2023.117271.
[18] Perrone, D., Brunesi, E., Dacarro, F., Peloso, S., Filiatrault, A. [2019] "Seismic Assessment and Qualification of Non-structural Elements in Europe: A Critical Review," *Proceedings of the 4th International Workshop on the Seismic Performance of Non-Structural Elements (SPONSE)*, International Association for the Seismic Performance of Non-Structural Elements, May 22–23, Pavia, Italy.
[19] CVR Murty CVR, Rupen Goswami, Vijaya Narayanan, Pradeep Kumar Ramancharla, Vipul Mehta. Introduction to earthquake protection to non-structural elements in buildings. Centre for Earthquake Engineering International Institute of Information Technology Hyderabad, India. 2013

A study on non-structural seismic damage of critical facilities in 0403 HuaLien earthquake in Taiwan

Fan-Ru Lin[1], Bai-Yi Huang[2], Wei-Hung Hsu[2], Min-Chi Ko[2], Wei-Chung Chen[2], Wen-Hsuan Huang[2] and Juin-Fu Chai[2]

1 National Center for Research on Earthquake Engineering, National Institutes of Applied Research
No. 200, Sec. 3, Xinhai Rd., Da'an Dist., Taipei City 106219, Taiwan
e-mail: frlin@niar.org.tw
2 National Center for Research on Earthquake Engineering, National Institutes of Applied Research
No. 200, Sec. 3, Xinhai Rd., Da'an Dist., Taipei City 106219, Taiwan
e-mail: {byhuang, mikehsu, mcko, wcchen, chai}@niar.org.tw

Abstract. Field investigations after the 2024 Hualien earthquake [Ou et al., 2024] revealed that while the structural systems of most critical facilities in Taiwan performed well, non-structural components such as ceilings, partition walls, parapets, water tanks, HVAC equipment, elevators, and storage racks suffered widespread damage. These damages caused functional interruptions and secondary hazards including water leakage and falling debris. The primary cause was the lack of detailed seismic provisions for non-structural components, particularly in anchorage, bracing, and displacement compatibility. Comparison with ASCE 7-22 [ASCE, 2022] showed that while Taiwan's design forces are often conservative, performance-based requirements remain limited. This paper documents observed damages, presents a case study on vibration-isolated equipment, and analyzes code gaps. Strategies for improvement include codification of requirements, anchorage enhancement, fall-prevention measures, and periodic audits. These measures are intended to ensure functionality and resilience of critical facilities after major earthquakes.

Keywords: 2024 Hwalien earthquake, seismic damage of critical buildings, MEP systems, vibration-isolated equipment

1. INTRODUCTION

Since the 1999 Chi-Chi earthquake, Taiwan has continuously revised seismic design code [MOI, 2024], significantly improving the seismic performance of structural systems. However, experiences from recent earthquakes such as Meinong and Hualien indicate that although structural damage has been reduced, non-structural components have emerged as the main source of earthquake-induced damage. Although such damages seldom cause immediate casualties, they lead to severe functional interruptions and economic losses, especially in critical facilities such as hospitals and high-tech factories. Therefore, seismic design of non-structural components is now a key issue in enhancing disaster resilience. Since 2005, Taiwan has incorporated seismic design forces for non-structural components into the 'Seismic Design Specifications and Commentary for Buildings'[MOI, 2024], with subsequent revisions in 2011 requiring non-structural checks in hospitals and critical facilities. Although the provisions adopt a conservative force equation compared with the International Building Code (IBC) [IBC, 2000], they still lack detailed requirements for suspended ceilings, fire protection piping, and vibration-isolated equipment. Current revisions aim to incorporate performance-based design concepts and evidence from shake-table experiments.

The 2024 Hualien earthquake (Mw 7.2) generated peak ground accelerations (PGA) exceeding 400 gal in eastern Taiwan. The National Center for Research on Earthquake Engineering (NCREE), in collaboration with Japanese and domestic universities, conducted field surveys in three hospitals and one university. The surveyed buildings are listed in Table 1, where the PGA values were estimated based on the building locations [NCREE, 2024]. A representative case of seismic damage occurred in a Taipei office building (Building E) during the 2024 Hualien earthquake. The building had a diesel emergency generator mounted on spring isolators to reduce vibration transmission. However, the isolators were designed only for vertical flexibility and lacked tensile resistance. When subjected to combined vertical and horizontal ground motions, the generator experienced uplift and lateral displacement. Several springs disengaged, and the generator frame shifted excessively, rendering the system inoperable and compromising the building's emergency power supply.

Table 1. Surveyed buildings with non-structural seismic damage

Building		Code	County/City	Structure	Above-ground Floors	Basement Floors	PGA (gal)
Hualien Hospital, Ministry of	Smart Building	A1	Hualien City, Hualien County	RC	4	1	417
	Kindness Building	A2		RC	6	1	417
	Dormitory	A3		RC	7	0	417
Tzu Chi Hospital	Xie Li Building	B1	Hualien City, Hualien County	SC	10	1	395
	He Xin Building	B2		SRC	10	1	395
Mennonite Christian Hospital Shoufeng Branch		C1	Shoufeng Township, Hualien County	RC	3	1	366
National Dong Hwa University	Library	D	Shoufeng Township, Hualien County	SRC	6	1	320
	Science Building I	D1		RC	4	0	315
	Science Building II	D2		RC	4	0	320
Office Building		E	Da'an District, Taipei City	RC/SC	13	1	84

2.Non-Structural Damage in the 2024 Hualien Earthquake

The major non-structural damages observed are summarized as follows. These findings highlight the vulnerability of non-structural systems to floor accelerations and displacement demands much higher than expected, reinforcing the need for proper seismic anchorage and design considerations.

2.1 CEILING SYSTEMS

Extensive collapses were observed in suspended ceilings due to insufficient frame strength in both main and secondary grids. Many installations lacked suspension wires within 20 cm of the perimeter, which caused frames to detach during shaking. Interaction with HVAC ducts also triggered failures, as some ceiling hangers were connected directly to vibrating air-conditioning units, leading to large-scale collapse. As shown in Figure 1**a**, the library suffered major non-structural damage, with suspended ceilings, ducts, and lights collapsing, especially on the fifth and sixth floors. Books fell and power outages further disrupted use. In the D2 building, Figure 1b shows weak ceiling grids and connectors in the auditorium causing partial collapse, while in severe cases Figure 1c illustrates ceiling fans and equipment falling with the ceiling, posing serious safety hazards.

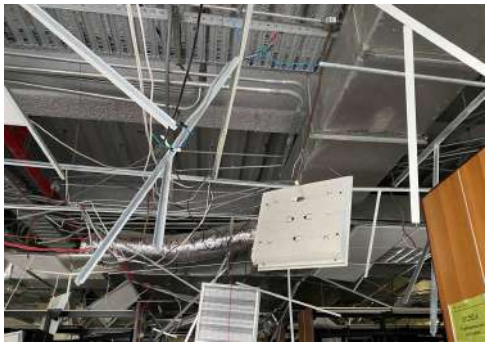
(a)  (b)  (c) 

Figure 1. Ceiling Systems: (a) Large-scale collapse at the library sixth floor; (b) Ceiling grid and connector failures in the D2 building auditorium; (c) Collapse of suspended ceiling with falling ceiling fans and electrical equipment. [Ou et al., 2024]

2.2 PARAPETS AND PARTITION WALLS

Parapet walls and decorative rooftop gables experienced significant earthquake damage. At University D, the rooftop windbreak walls of Building D2 collapsed out-of-plane, as shown in Figure 2a. These walls, built with C-channel steel frames and lightweight concrete, had corroded connections that reduced anchorage strength and contributed to the failure. Partition walls also showed extensive problems. Masonry infills in hospital wards developed diagonal shear cracks, while lightweight aggregate concrete (LWAC) partitions tilted or collapsed out-of-plane. In Building B1, LWAC walls enclosing a mechanical shaft fell on the sixth and eighth floors (Figure 2b), while the seventh-floor wall remained intact. The collapsed walls lacked proper boundary anchorage, which allowed them to overturn during shaking. Although the shaft and main ducts were not damaged, the adjacent offices suffered ceiling, lighting, and duct failures, leaving the spaces temporarily unusable.

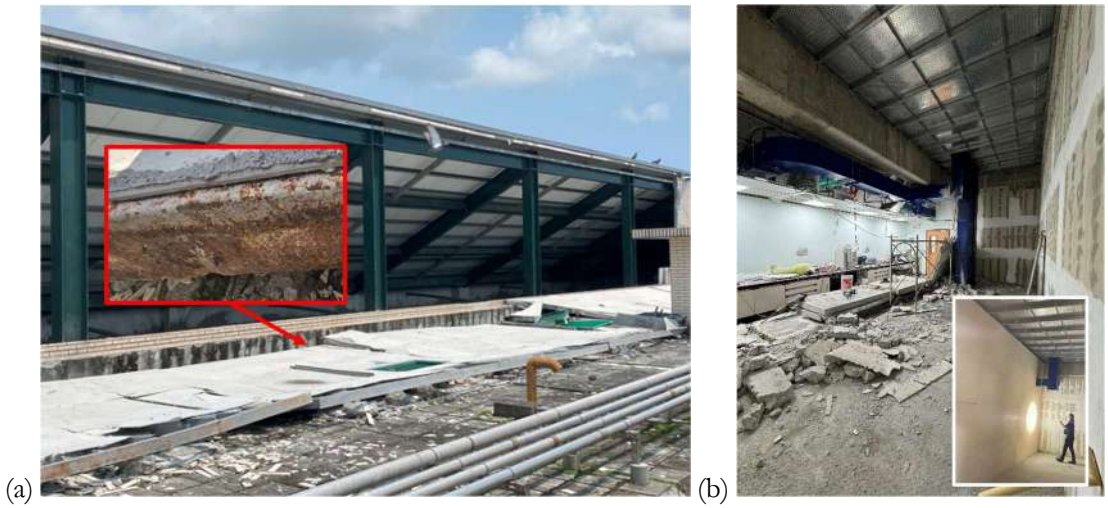


Figure 2. Parapets and Partition Walls: (a) Collapse of windbreak wall on the rooftop of Building D2; (b) Out-of-plane collapse of lightweight concrete partition wall on the eighth floor of Building B1. [Ou et al., 2024]

2.3 WATER SUPPLY SYSTEMS

Stainless steel rooftop tanks were deformed and support frames twisted under seismic inertial and hydrodynamic forces. An underground fiber-reinforced plastic (FRP) panel water tank ruptured due to poorly detailed vertical steel joints, leading to massive leakage. In another case, a reverse-osmosis (RO) water tank connection failed when an unrestrained tank swayed during shaking, pulling apart shared piping (Figure 3b).

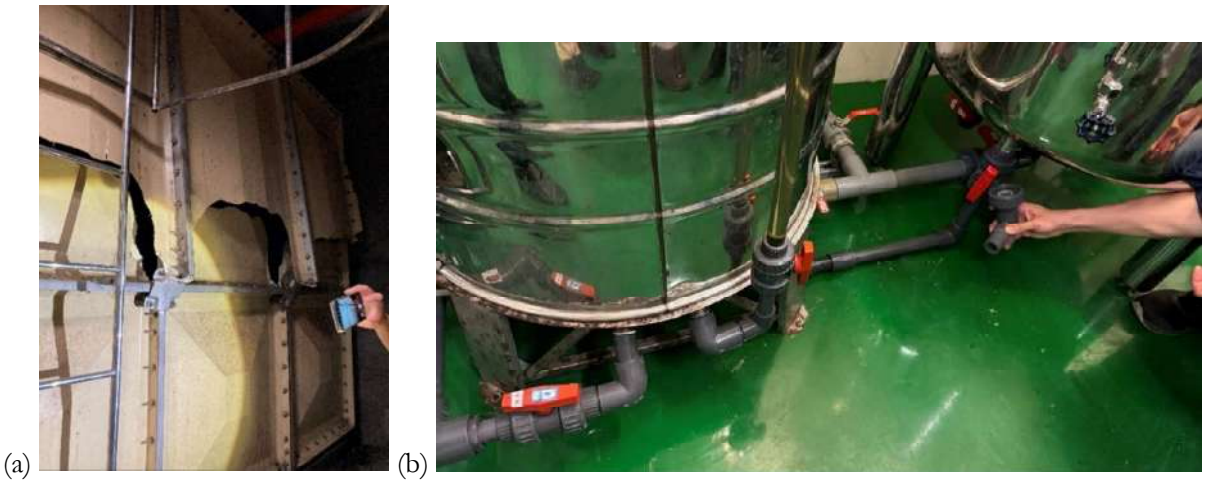


Figure 3. Water supply systems: (a) FRP water tank damage in Building B2; (b) Fractured PVC piping (repaired) in the RO water storage room at the basement of Building C1. [Ou et al., 2024]

2.4 HVAC SYSTEMS

Suspended Pre-Cooling Air Unit (PAU) anchored with spring isolators experienced excessive displacements, causing chilled water pipe ruptures. In the corridor of Building A2 on the fifth floor, PAUs struck adjacent sprinkler heads, breaking them and leading to extensive water leakage. In Hospital C, Small suspended fans also fell when short hanger rods fractured under shear. Rooftop FRP cooling towers suffered intake louver damage and base anchorage failures. On the roof floor of Building B1, anchorage bolts sheared, causing the tower to tilt dangerously, threatening loss of cooling capacity for the entire hospital (Figure 4b).

(a)  (b)  

Figure 4. HVAC systems: (a) PAU impact with fire sprinkler head; (b) Cooling tower damage on the roof of Building B1. [Ou et al., 2024]

2.5 ELEVATORS

Hospital C is equipped with four elevators. Among them, three were out of service due to displacement of hoisting machines, derailed cables, and counterweight blocks detaching from their frames. In two cases, the detached counterweight blocks struck the elevator car, rendering the system unusable.

(a)  (b) 

Figure 5. Counterweight blocks falling onto the tops of two elevator cars at: (a) Basement level; (b) First floor. [Ou et al., 2024]

2.6 CABINETS AND CONTENTS

At a university library, tall bookshelves and CD racks not anchored to floors toppled massively (Figure 6a). Nearly 90% of stored books fell, with some racks permanently deformed. Although many shelves were connected by horizontal bracing bars, some bars were buckled (Figure 6b) and some connections tore at bolt holes (Figure 6c), reducing effectiveness.

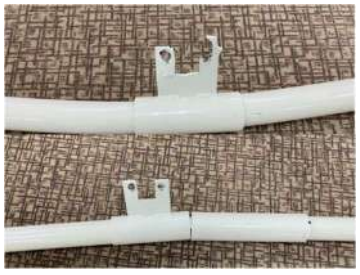
(a)  (b)  (c) 

Figure 6. Shelf and racks in the library: (a) Collapse of bookshelf rows on the 5th floor; (b) Buckling of connecting rods in 5th-floor bookshelves; (c) Deformation of rods and connector failure in 2nd floor CD racks. [Ou et al., 2024]

3.Finding and Analysis

Overall, structural systems in Taiwan demonstrated good seismic performance, but widespread non-structural damage occurred. The main contributing factors were:

1. Ceiling systems lacked proper edge fixing and suspension details.
2. Partition walls and parapets suffered from poor joint detailing.
3. Mechanical and electrical equipment lacked seismic anchorage or adequate bracing.
4. Large interior equipment and storage racks were not anchored.

These damages not only interrupted building operations but also triggered secondary hazards such as water leakage, fire, and explosion, threatening disaster response capacity.

3.1 COMPARISON OF NON-STRUCTURAL REQUIREMENTS BETWEEN TAIWANESE AND UNITED STATES CODES

Taiwanese seismic design provisions for non-structural components are based on NEHRP, UBC, and IBC, yet differences remain compared to the latest ASCE 7-22. For design seismic forces, both Taiwan and the U.S. consider amplification factors, importance coefficients, and resonance effects. Taiwanese coefficients are generally conservative, leading to higher design values for critical equipment. For displacement requirements, both countries demand verification of interstory drift compatibility, with the U.S. having adopted such requirements since NEHRP 1994. The global trend has shifted from 'life safety' towards 'performance-based design,' requiring critical equipment to remain functional after major earthquakes.

As shown in Table 2, according to the "Seismic Design Specifications and Commentary for Buildings" (MOI, 2024) in Taiwan, the minimum horizontal seismic force for nonstructural components is:

$$F_{ph} = 0.4\, S_{DS} \times I_p \times (a_p / R_{pa}) \times (1 + 2\, h_x/h_n) \times W_p \tag{1}$$

with both lower and upper bounds, i.e., not less than $0.3\, S_{DS}\, I_p\, W_p$ and not greater than $1.6\, S_{DS}\, I_p\, W_p$. This expression considers installation height amplification, resonance, and importance factor, and assumes roof-level accelerations can reach up to three times the ground peak acceleration. In the International Building Code (IBC), the design horizontal seismic force for nonstructural components is with similar minimum and maximum bounds as Taiwan. The main difference lies in the detailed classification of components and the adjustment of amplification factors.

On the other hand, ASCE/SEI 7-22 Section 13.3 provides a refined formula (Table 2):

$$F_p = 0.4\, S_{DS}\, I_p\, W_p \times (H_f / R_\mu) \times (C_{AR} / R_{po}) \tag{2}$$

where H_f is the floor amplification factor, $R\mu$ is the structural ductility reduction factor, C_{AR} is the component resonance ductility factor, and R_{po} is the component strength factor. This formulation requires explicit consideration of both horizontal and vertical seismic demands, and displacement compatibility with interstory drift.

While the Taiwanese and IBC equations are largely similar, Taiwan adopts more conservative coefficients, often leading to higher design values for critical components. However, ASCE 7-22 introduces a more performance-oriented philosophy, with detailed parameters for different categories of nonstructural systems. The international trend has clearly shifted from a "life-safety" focus toward "performance-based design," requiring critical facilities such as hospitals and high-tech factories to sustain post-earthquake operability.

Table 2 Comparative Summary of Taiwanese Codes and ASCE 7-22 for Non-Structural Components

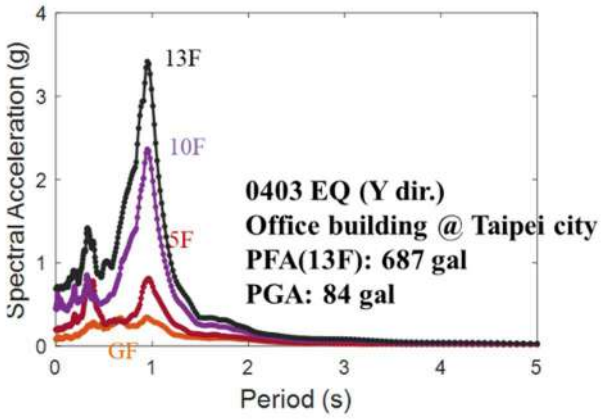
	Taiwan (Seismic Design Specifications, MOI 2024)	ASCE/SEI 7-22
Design philosophy	Predominantly prescriptive; focuses on force demand.	Performance-based; considers operability and functional recovery.
Horizontal force equation	$F_{ph} = 0.4\ S_{DS}\ I_p\ (a_p / R_{pa}) \times (1 + 2\ h_x/h_n)\ W_p$ with lower/upper bounds.	$F_p = 0.4\ S_{DS}\ I_p\ W_p\ (H_f / R_\mu) \times (C_{AR} / R_{po})$ with the same lower/upper bounds.
Roof acceleration assumption	Amplification up to 3× PGA; $PFA_R = 1.2\ S_{DS}$.	Floor amplification factor (H_f) determined by structural period and height.
Component resonance	Embedded indirectly via (a_p / R_{pa}).	Explicitly modeled through C_{AR} (Component Amplification and Resonance).
Ductility and overstrength	Addresses ductility qualitatively; limited overstrength provisions.	Explicitly includes a structural ductility reduction factor R_μ and component strength factor R_{po} in the nonstructural force equation, and further requires an overstrength factor Ω_{ap} for anchorage design.
Vertical acceleration effects	Not explicitly required for most components.	Explicit evaluation required for components sensitive to uplift or bearing compression.
Displacement compatibility	Required but general; limited component-specific rules.	Clear drift compatibility and deformation requirements for each system category.
Vibration-isolated equipment	Force-based; uplift resistance not clearly defined.	Requires bi-directional checks, uplift restraint, and strength amplification.
Ceilings & piping	Partially adopts ASTM E580 for ceiling; limited requirements for interaction.	Bracing, detailing, and drift limits following ASTM E580/NFPA 13 for ceiling and sprinkler piping.
Overall trend	Conservative in force estimation but lacks performance detail.	More refined, performance-oriented, and component-specific.

3.2 Case Study of Seismic Damage on Nonstructural Systems in Hualien Earthquake

During the Hualien Earthquake, Building E, which is located in Da'an District, Taipei, the rooftop diesel generator sustained severe seismic damage (Figure 7a). It is worth noting that the distance between this building and the epicenter is about 126.5 km. A site inspection was conducted by the user on April 9, 2024. The following assessment focuses on the generator, spring isolators, charger, and battery units, documenting the observed damage and providing improvement recommendations. The generator was a TECO diesel engine generator set with approximate dimensions of 3500 mm × 1250 mm × 2100 mm, a weight of 4000 kg, and a 600 L fuel tank. It was installed on multiple spring isolators inside the rooftop machine room to prevent operational vibration from transmitting into the building structure.

(a)





(b)

Figure 7. Spring-isolated equipment: (a) Emergency generator and damaged spring isolator (b) acceleration response spectrum of the roof-level floor

Field inspection revealed that most of the six spring isolators supporting the generator showed severe damage. Most of the spring isolators suffered severe damage, including anchor bolt pull-out, frame buckling, bolt loosening with concrete spalling, and excessive deformation due to insufficient tensile resistance. For auxiliary components, the battery rack was only anchored on one side of the floor. Although no visible damage occurred, reinforcement was recommended. The charger base was not anchored and displaced during the earthquake (Figure 7a).

According to the building's strong-motion records, the nearby ground-level peak ground acceleration (PGA) was about 84 gal. At the 13th floor, the peak floor acceleration (PFA) near the generator anchorage reached 687 gal (Figure 7b), approximately 8.2 times the PGA. At the building's fundamental period (around 1 second), the floor response spectrum (5% damping) reached approximately 3.5g, indicating that upper-story equipment can experience demands well above design assumptions. This indicates that equipment with longer fundamental periods at upper stories may experience inertial forces exceeding the expected demand prescribed by current seismic codes under the 475-year return period earthquake.

The building is located in Taipei seismic zone II, with design spectrum parameter S_{DS} = 0.6. According to Taiwanese Building Code regulations, the estimated rooftop acceleration was 0.72g (P_{FAR} = 1.2 × S_{DS}), which is slightly larger than the real floor response during the Hualien earthquake. Considering a clearance greater than 6 mm for the isolator and base, the design force was taken as 2Fp. The horizontal seismic demand for the generator anchorage was thus estimated as:

$$F_{ph} \approx 16.2 \text{ tonf } (\sim 2.7 W_p) \tag{3}$$

and the vertical demand was approximately 8.1 tonf. This required each anchor bolt to resist at least 1.41 tonf in shear and 2.45 tonf in tension. However, the original 1/2-inch expansion bolts used for the spring isolators had rated capacities of only 1.08 tonf in shear and 1.04 tonf in tension [SQUG, 2001], far below the required demand. The anchorage system was therefore critically deficient.

On the other hand, according to ASCE 7-22, the estimated design seismic force of the spring-isolated generator was also about 2.7 W_p (C_{AR}= 2.2, R_{po} =1.3, H_f=2.88, R_μ=1.3). The evaluated floor response is about 0.53 g, which is smaller than the evaluated value of current Taiwanese code and even real floor response during the Hualien earthquake. For the anchorage of the generator, the overstrength factor (Ω_{op}=1.75) should be used to amplify horizontal seismic effect then.

The April 3 Hualien earthquake revealed that the rooftop diesel generator's support system was inadequate, especially the spring isolators which lacked tensile resistance. Investigations identified two critical

deficiencies: (1) the absence of tie-down rods or tension-resistant devices to control uplift, and (2) insufficient anchorage of the generator base. Engineering analysis suggested that adding diagonal tie-down rods or adopting isolators with integrated tensile resistance, together with supplementary base anchorage, would have prevented the failure. This case demonstrates the danger of relying solely on vibration isolation while neglecting restraint against uplift and displacement.

Seismic demand calculations confirmed that the existing anchor bolts were far below the required strength. Meanwhile, the measured records show that the building response amplification exceeded code expectations. To improve performance, the generator requires stronger anchorage, isolators with uplift resistance or supplementary snubbers, and reinforced anchorage for auxiliary components such as the battery rack and charger. On the other hand, the overstrength requirement for anchorage at concrete in ASCE 7-22 could be referenced for Taiwanese code. These measures would help ensure the generator remains operational after future earthquakes.

3.3 STRATEGIES FOR ENHANCING SEISMIC PERFORMANCE OF NON-STRUCTURAL COMPONENTS

Based on observed failures and code comparison, several improvement strategies are proposed. The key lessons learned include:

1. Insufficient edge fixing and interaction control in ceiling systems.
   Many ceiling collapses were triggered by inadequate perimeter angles, lack of diagonal bracing, and unintended interaction with HVAC units. Heavy equipment suspended from ceilings further amplified the damage.
2. Inadequate boundary anchorage for partition walls and parapets.
   Failures in windbreak walls, masonry infills, and lightweight concrete partitions consistently involved poor anchorage details, corrosion of connectors, or missing boundary restraints.
3. Vibration-isolated equipment lacked uplift resistance.
   Numerous MEP components, especially generators, cooling towers, and PAUs, were mounted on spring isolators designed only for vertical flexibility. Without tensile restraint, isolators disengaged, leading to excessive displacement and secondary piping failures.
4. Storage racks and interior furnishings were rarely anchored.
   The collapse of bookshelves and deformation of connection elements in libraries demonstrated the lack of anchorage and inadequate design of connections under strong floor accelerations.
5. Floor response amplification at upper stories remains underestimated.
   Recorded PFAs exceeding 600 gal at the rooftop of a Taipei building—over eight times the ground PGA—illustrate that high-rise equipment may experience seismic demands far beyond prescriptive code predictions.

These lessons collectively indicate that while structural systems in Taiwan have reached high seismic reliability, non-structural components still lag in both design and enforcement, becoming the primary source of functional disruption after major earthquakes.

To supplement field observations, NCREE and collaborating universities have conducted full-scale shake-table tests on non-structural systems, providing valuable evidence for seismic design improvements. Combined with lessons from the Hualien earthquake and international codes, the following strategies are proposed:

1. Codification: Incorporate seismic requirements for non-structural components and MEP equipment into building permits and inspections, in line with NFPA 13 [NFPA, 2022], ASTM E580[ASTM, 2014], and related standards. In Taiwan, Appendix B of the current code already adopts excerpts from ASTM E580, and NCREE continues to update these provisions based on new research findings. Real damage cases of sprinkler piping revealed that systems without

transverse bracing were prone to joint separation, hanger failure, and rupture. Experimental studies have shown that introducing rigid bracing at adequate intervals effectively prevented instability and maintained water delivery capacity.

2. Anchorage enhancement: Cooling towers, elevators, and air-handling units should adopt seismic restraints and limiters in addition to vibration isolators. In the Hualien earthquake, the vibration-isolated equipment is especially focused. Rooftop cooling towers with poor anchorage exhibited base bolt shear and tilting. In addition, several cooling towers exhibited fractured FRP panels, broken louvers, and localized shell failures that were strongly associated with aging-induced brittleness rather than purely seismic demand. These deterioration mechanisms indicate that the seismic reliability of FRP-based cooling towers is closely linked to environmental durability. Periodic inspection and timely replacement of deteriorated FRP components are essential to prevent local failures and ensure overall system stability during future earthquakes. Air-handling units on spring isolators suffered excessive sway and secondary damage to piping; the addition of limit stops and tie rods successfully controlled displacement. In the case study mentioned above, it emphasizes that Taiwan's prescriptive design rules are inadequate when compared with dynamic experimental evidence. The observed seismic damage and related research are now being used to draft revisions of the national seismic design specifications, moving toward evidence-based codification. This research cycle—from testing to design recommendations—is expected to significantly improve resilience of non-structural systems in Taiwan. Adding anchorage points and using devices with both tensile and lateral restraints could ensure post-earthquake operation.
3. Fall prevention: Strengthen components in key spaces and evacuation routes (ceilings, shelves, parapets) to prevent falling hazards. Conventional suspended ceilings with only vertical hangers showed frequent collapse under strong accelerations, particularly at perimeter connections and where ducts interacted with frames. Adding diagonal bracing and improved perimeter fixing significantly increased stability.
4. Periodic audits: Critical facilities such as hospitals and universities should regularly assess and retrofit non-structural components. In addition, the U.S. NIST and ATC emphasize three critical aspects that Taiwan should adopt: (a) clear definition of performance objectives tailored to facility importance and earthquake levels, (b) establishment of design responsibility frameworks to ensure accountability across architects, engineers, and contractors, and (c) validation and education through shake-table tests and professional training programs. These measures will further transform Taiwan's current life-safety-oriented approach into a performance-based system.

4.Conclusion

The 2024 Hualien earthquake confirmed that although Taiwan's structural systems have achieved good seismic performance, non-structural components remain vulnerable and are the leading cause of functional disruption. Observed damages in ceilings, parapets, piping, HVAC systems, elevators, and storage units demonstrated the consequences of insufficient detailing and anchorage. The rooftop generator case study further illustrated the amplification of seismic demand at upper floors and the limitations of prescriptive anchorage rules. Comparisons with ASCE 7-22 show that although Taiwan's code is conservative in force estimation, it lacks detailed performance-based provisions. Moreover, despite the conservative force levels prescribed in Taiwan's code, non-structural components are seldom subjected to actual seismic design in practice, resulting in persistent vulnerabilities.

To address these gaps, the proposed strategies—codification, anchorage enhancement, fall prevention, and periodic audits—should be systematically implemented so that hospitals, emergency facilities, and critical infrastructure can maintain operability after major earthquakes. In addition, future research should critically evaluate whether parameter values in current seismic codes—many derived from empirical judgment or

broad component categories—are adequate for precision or mission-critical equipment. Full-scale testing and performance validation are needed to confirm their applicability and refine seismic demand parameters. Such evaluation will also help establish equipment-specific seismic design criteria.

REFERENCES

Y.-C. Ou, J.-L. Wu, C.-F. Chai, and C.-Z. Yao, *Report on the April 3, 2024 Hualien Earthquake*, NCREE Research Report, NCREE-2024-006, 2024 (in Chinese).

American Society of Civil Engineers, *Minimum Design Loads and Associated Criteria for Buildings and Other Structures* (ASCE/SEI 7-22), Reston, VA: ASCE, 2022.

Ministry of the Interior (MOI), *Seismic Design Specifications and Commentary for Buildings*, Taipei, Taiwan, 2024 (in Chinese).

International Code Council, *International Building Code* (IBC 2000). Falls Church, VA: ICC, 2000.
National Center for Research on Earthquake Engineering (NCREE), *Taiwan ShakeMap Assessment System*, 2024. [Online]. Available: https://seaport.ncree.org/smap/

Seismic Qualification Utility Group (SQUG). *Generic Implementation Procedure (GIP) for Seismic Verification of Nuclear Plant Equipment – Revision 3A*. Electric Power Research Institute (EPRI), Palo Alto, CA, USA; 2001. GIP-3A.

National Fire Protection Association, NFPA 13: *Standard for the Installation of Sprinkler Systems*, Quincy, MA: NFPA, 2022.

ASTM International, ASTM E580/E580M-14: Standard Practice for Installation of Ceiling Suspension Systems for Acoustical Tile and Lay-in Panels, West Conshohocken, PA, 2014.

Seismic resilience assessment of hospitals using dynamic bayesian network

Shuoguo Qiu[1] and Quincy Ma[2]

[1] PhD Candidate, Dept. of Civil & Environmental Engineering, The University of Auckland, NEW ZEALAND
e-mail: sqiu925@aucklanduni.ac.nz
[2] Associate Professor, Dept. of Civil & Environmental Engineering, The University of Auckland, NEW ZEALAND
e-mail: q.ma@auckland.ac.nz

Abstract. Resilient hospitals are essential in emergency response and community recovery following a major earthquake. The assessment and enhancement of the seismic resilience of hospitals are critical for improving the post-earthquake medical response capacity. Existing methodologies, such as indicator-based and simulation-based assessments, provide a broad and accurate evaluation but often require extensive data and specialised simulation knowledge, restricting their wider use in the engineering practice. To overcome these limitations, this study employs Dynamic Bayesian Networks (DBNs) to construct a unified framework for modelling hospital resilience. A generic DBN for essential hospital departments is developed based on a multilayered interdependency structure. The inference capability of DBNs is used to predict the functional states of hospital departments, while the repair process is modeled by transforming repair durations into transition probabilities that represent component repairing from damaged to fully functional states, thus capturing temporal dynamics. A case study is conducted to illustrate the effectiveness of the proposed framework. The results show the framework can trace critical components that drive hospital performance and has the potential to guide effective repair strategies.

Keywords: Hospital seismic resilience, Dynamic Bayesian networks, Post-earthquake recovery, Functional interdependencies, repair strategies

1. Introduction

Hospitals play a critical role in post-earthquake response by providing medical services to the injured, but past events show that they are vulnerable to non-structural components damage and lifeline failures, even when building structures remain safe (Achour et al. 2011, Santarsiero et al. 2019, Qu et al. 2023). To achieve a systematic performance assessment and improve emergency management capacity for hospitals after earthquakes, the concept of resilience has been adopted on hospital in recent years. It refers to a hospital's capacity to continue to render medical functions during a disruptive event, and its ability to efficiently recover to full operating capacity in the post-event phase (Bruneau et al. 2003, Bruneau and Reinhorn 2007).

Resilience is often presented as a resilience curve, which illustrates changes in system performance, as shown in Figure 1. The resilience index (R) is defined as the area under the resilience curve, mathematically in Equation (1) or graphically as the shaded area. $Q(t)$ represents a dimensionless measure of the system's functionality at any given time, and T_C refers to the control time for evaluating resilience.

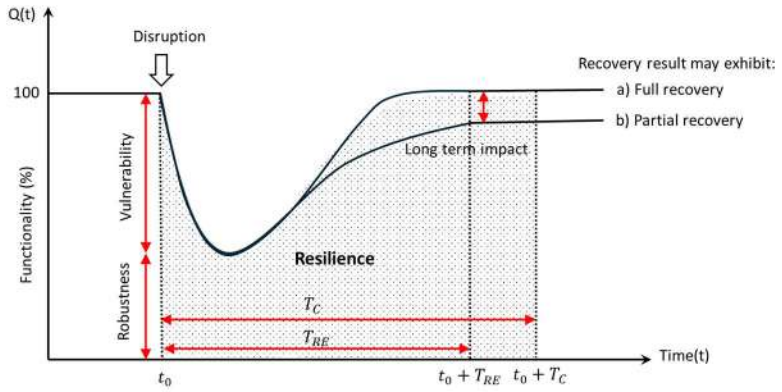


Figure 1. Definition of key parameters in a general resilience curve

$$R = \int_{t_o}^{t_o+T_C} Q(t)/T_C dt \quad (1)$$

Research studies have evaluated the seismic resilience of hospitals using either indicator-based or simulation-based methodologies (Yu et al. 2022). Indicator-based methods rely on expert judgment to assign subjective weights to influencing factors affecting resilience (Zhong et al. 2014, World Health Organization 2020), they provide comprehensive evaluations but cannot capture hospital recovery, which is important for effective emergency management and planning. Simulation-based approaches, such as Discrete Event Simulation (DES) and System Dynamics (SD), model hospital operations process under earthquake scenarios and can produce metrics like patient waiting time or treatment rate (Cimellaro et al. 2017, Li et al. 2020, Romani et al. 2023). Although simulation-based approaches can reproduce hospital operations and generate relevant performance indicators, they lack flexibility and require large amounts of data (Basaglia et al. 2022), which hinders their broader application.

Bayesian Networks (BNs) address these challenges by representing interdependencies and uncertainties through intuitive graphical structures. They allow predictions with limited data while preserving transparency in uncertainty representation. Dynamic Bayesian Networks (DBNs) extend BNs by incorporating temporal dependencies to model recovery. Prior studies have applied DBNs to mechanical structures (Zhang et al. 2021), process industries (Tong and Gernay 2023) and power systems (Caetano et al. 2024), but their application to hospitals remains limited.

This study advances hospital emergency management by employing a DBN framework that links component damage to post-earthquake functionality and recovery trajectories. It (a) develops a generic multilayer DBN model to predict hospital service performance, (b) introduces a method to simulate repair through transition probabilities between damaged and fully functional states, and (c) conducts a case study to illustrate its effectiveness.

2. Background

2.1 DYNAMIC BAYESIAN NETWORK

Before introducing the concept of Dynamic Bayesian Networks (DBNs), it is necessary to briefly explain Bayesian Networks (BNs). Bayesian network, also known as a belief network or causal network, is a probabilistic graphical model that represents a set of random variables and their probabilistic dependencies via a directed acyclic graph (DAG). It is a powerful tool used for reasoning under uncertainty, learning from data, and making predictions or decisions (Koller and Friedman 2009).

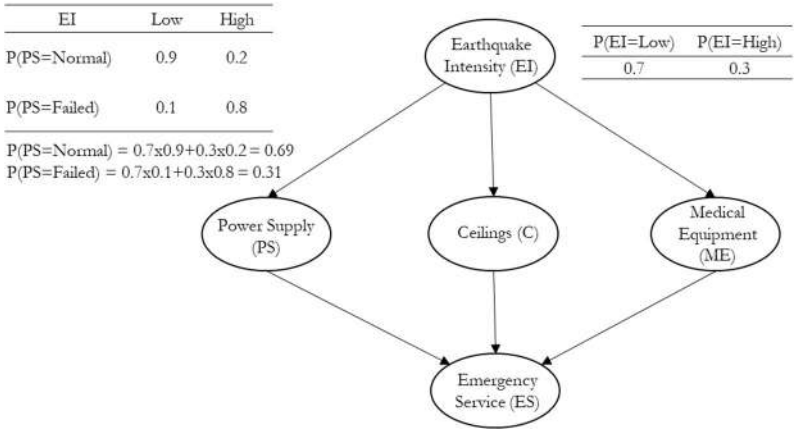


Figure 2. An example of BN and CPT of "Power Supply" node

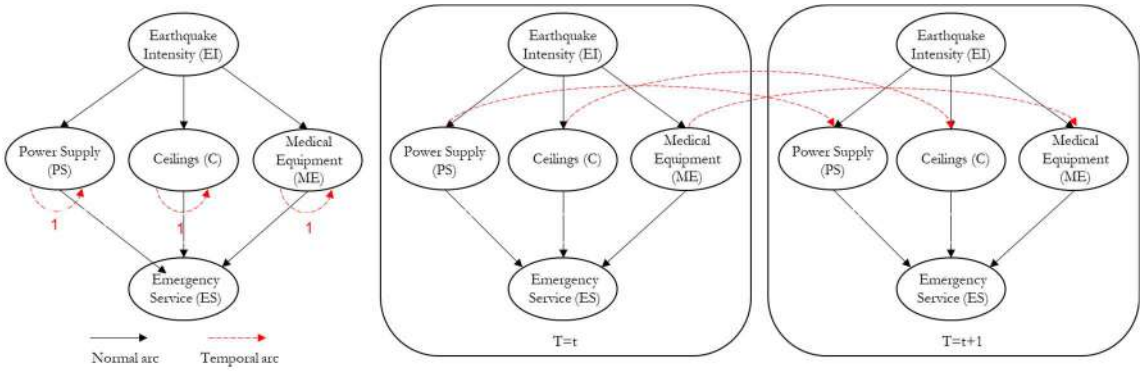
Figure 2 illustrates a simple example of a BN. It models how earthquake intensity can influence the emergency services capacity of hospitals through probabilistic relationships of its interdependent infrastructure. Each node in the BN represents a random variable that represents a physical or operational component, such as earthquake intensity, power supply, or emergency service functionality. Arcs originate from parent nodes and connect to child nodes, indicating a causal or probabilistic dependency the state of a child node depends on the condition of its parent node(s). For example, stronger ground shaking increases the likelihood of power supply disruption, which in turn may impair hospital emergency operations. These dependencies are quantified using Conditional Probability Tables (CPTs), which are a table of conditional probability usually derived from observational data or expert elicitation, following a process such as that described by Koller and Friedman (2009). Nodes without parents or children, such as "Earthquake Intensity" and "Emergency Service" in Figure 2 are termed root nodes and leaf nodes, respectively. The CPT of the "Power Supply" node, i.e. the conditional probability of the power system's operational state conditioned on different levels of earthquake intensity, is shown in the upper left of Figure 2. For the Earthquake Intensity root node, marginal probabilities are assigned and are as illustrated in the upper right of the figure.

The joint probability distribution of all nodes in the graph is expressed as the product of the conditional probabilities of each node given its parent nodes, as shown in Equation (2).

$$P(X_1, X_2, \dots, X_n) = \prod_{i=1}^{n} P\left(X_i \mid Pa(X_i)\right) \quad (2)$$

Where X_i represents the i-th node, $Pa(X_i)$ denotes its parent nodes

A Dynamic Bayesian Network (DBN) is an extension of Bayesian networks in order to model systems that evolve over time. It achieves temporal modelling by dividing time into discrete slices, where each slice corresponds to a specific point in a time series. In a DBN model, a node at time $t+1$ may be influenced by its parent nodes at time $t+1$ and its own node states from a preceding time slice t.



(a) Dynamic Bayesian network **(b) Unrolled form of DBN**

Figure 3. An example of DBN

Figure 3 presents a dynamic extension of the BN shown in Figure 2, which captures the dynamic recovery process of the network after earthquake causes damage to the components. The DBN incorporates temporal arcs, shown as red dashed lines, that establish probabilistic dependencies of nodes across different time slices. The numbers on temporal arcs indicate the time interval between two connected slices. In this example, the interval equals 1, meaning that nodes are updated at each time step. Consequently, the states of "Power Supply," "Ceilings," and "Medical Equipment" nodes at day $t+1$ depend directly on their conditions at day t. The transition probabilities between nodes connected by temporal arcs across different time slices are quantified using inter-slice CPTs, while intra-slice CPTs continue to represent static dependencites among nodes within the same time slice. The joint probability function for all variables in a DBN with a time interval of 1 can be mathematically expressed as Equation (3).

$$P(X_1^{t+1}, X_2^{t+1}, \dots, X_n^{t+1}) = \prod_{i=1}^{n} P\left(X_i^{t+1} \mid X_i^t, Pa(X_i^t), Pa(X_i^{t+1}) \right) \quad (3)$$

Parent nodes at previous time slice t and present time slice $t+1$ are represented by $Pa(X_i^t)$, $Pa(X_i^{t+1})$. X_i^t denotes the variables' states at previous time t.

3. Methodology

The framework proposed in this study for assessment of hospital seismic resilience is illustrated in Figure 4. It comprises the three following steps:

(1) Seismic analysis of hospital building - Begin by collecting engineering and functional information for the hospital, including geotechnical, structural characteristics and facility configuration. Based on this information, a specific ground shaking intensity defined by the response spectrum can be selected, and nonlinear time-history analysis is performed to obtain Engineering Demand Parameters (EDPs).

(2) DBN-Functionality and recovery analysis - A DBN is developed to evaluate the probability distribution of the various medical departments being in different functional states over time. EDPs are used as

inputs to evaluate the damage state probabilities for structural and non-structural components via fragility curves. Intra-slice CPTs are assumed to be constant for all time slices. Then, repair times for different damage states of each component are converted into inter-slice CPTs, enabling the DBN to capture the evolving recovery process. The approach is implemented using the GeNIe Python package ("SMILE Wrappers Programmer's Manual" 2024).

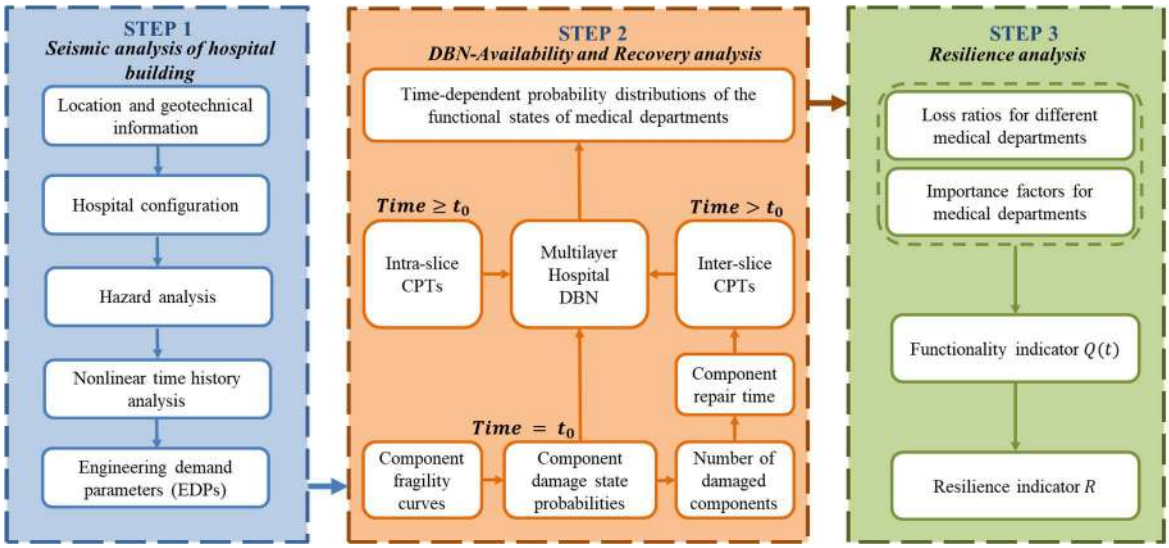


Figure 4. Flowchart of the DBN framework for hospital seismic resilience assessment

(3) Resilience assessment - Each functional state is assigned a corresponding functional loss ratio. By combining the loss ratios with the probability distribution of functional states obtained from the DBN at each time step, the expected functionality of each department can be derived. The overall hospital functionality indicator $Q(t)$ is calculated by aggregating departmental functionalities, weighted by their respective importance coefficients. Finally, the resilience index R is calculated according to Equation (1).

4. Functionality and recovery analisys

4.1 MULTILAYER DBN STRUCTURE AND CPTS

Hospitals are facilities where medical departments depend on both building-wide and floor-specific infrastructure. Critical services such as Power Supply (PS), Water Supply (WS), Medical Gas Supply (MGS), and Heating, Ventilation, and Air Conditioning (HVAC) originate from centralized sources but are distributed through floor-level systems, which may be damaged sporadically across different areas during earthquakes. To capture this variation, a multilayer BN is adopted, as shown in Figure 5. It consists of three hierarchical layers: (1) the building utility source layer, representing hospital-wide supplies; (2) the utility distribution layer, modeling the distribution of centralized services to components on a floor-by-floor basis; and (3) the medical system layer, modeling departmental functionality based on available utilities. This layered structure allows the framework to trace how localized failures propagate across systems and floors, providing a more realistic assessment of hospital resilience after earthquakes.

Binary or multi-level damage and functionality states are assigned to different nodes. At the whole-building level, binary states (e.g., "operational/failure") are used, while at the floor and departmental levels, multi-level states are introduced to reflect partial damage within a floor and to capture more detailed functional conditions.

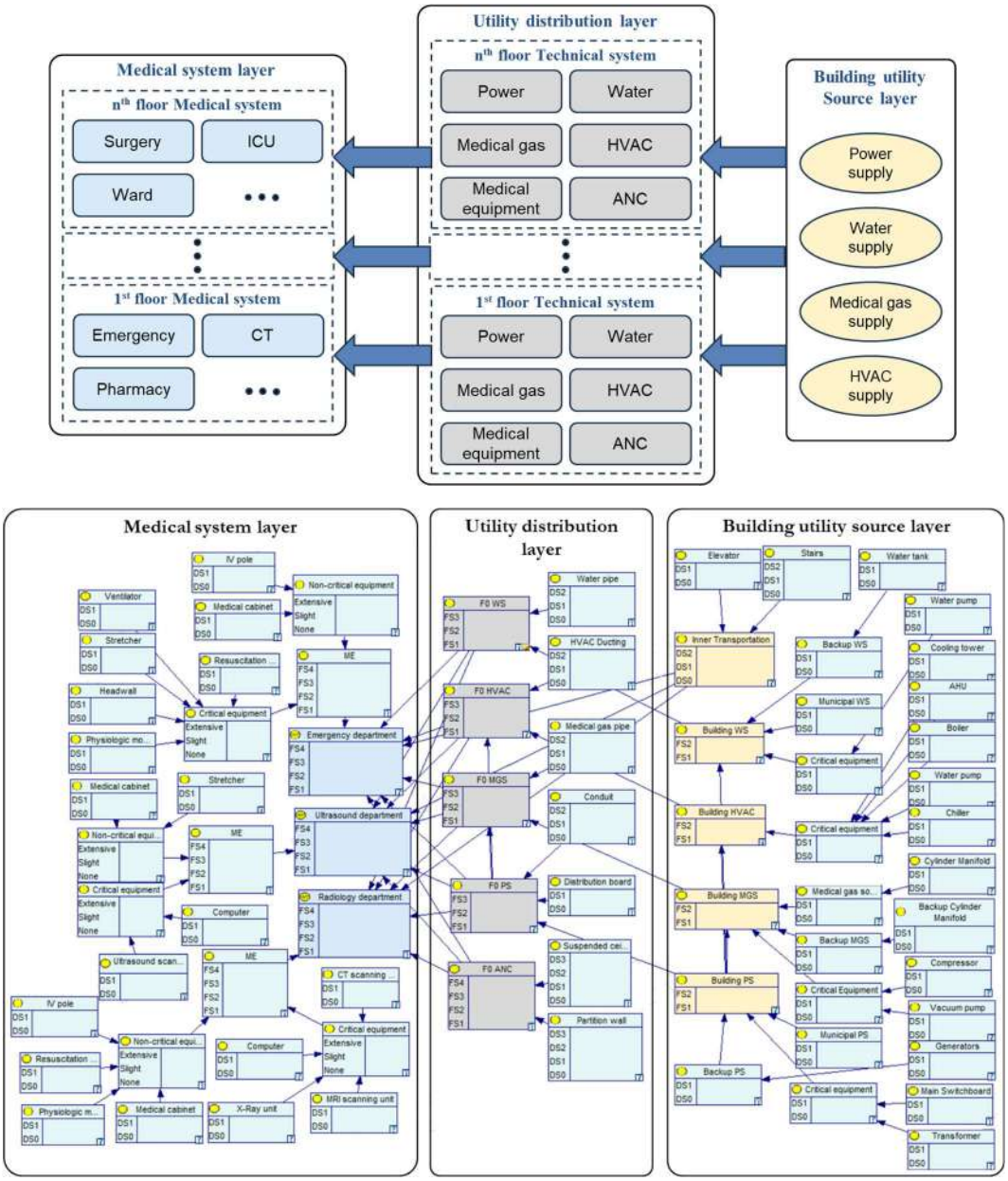


Figure 5. Overview of the multilayer Bayesian network structure (top) and a detailed example of the ground floor (bottom)

The functionality states, damage states and CPTs of nodes in the DBN follow the proposal detailed in Chavez et al. (2025) and Liu et al. (2022), but adapted to consider different type of critical utility service. Table 1 presents an example of the damage states and conditional probability table (CPT) for the architectural non-structural component (ANC) node. Its parent nodes include ceilings and partition walls, which are essential for providing the physical space of medical departments. The corresponding CPT is formulated according to the damage state's descriptions. Furthermore, Table 2 shows the functional states and associated loss ratios of medical departments. The functionality of each department is then calculated according to Equation (4), by combining the functional states with their assigned loss ratios.

$$\mathrm{F}_i = 1 - \sum_{i=1}^{n} P_i \cdot L_i \tag{4}$$

Where $\mathrm{F_i}$ is the functionality of department i, P_i is the probability of the department being in functional state i (FS_i), and L_i is the assigned loss ratio for functional state i.

Table 1. The damage states and CPT of ANC node (Liu et al. 2022)

Partition walls	DS_0				DS_1				DS_2				DS_3			
Suspended seilings	DS_0	DS_1	DS_2	DS_3	DS_0	DS_1	DS_2	DS_3	DS_0	DS_1	DS_2	DS_3	DS_0	DS_1	DS_2	DS_3
$DS_{ANC,1}$	1	0	0	0	0	0	0	0	0	0	0	0	0	0	0	0
$DS_{ANC,2}$	0	1	0	0	1	1	0	0	0	0	0	0	0	0	0	0
$DS_{ANC,3}$	0	0	1	0	0	0	1	0	1	1	1	0	0	0	0	0
$DS_{ANC,4}$	0	0	0	1	0	0	0	1	0	0	0	1	1	1	1	1

Note: (1) $DS_{ANC,1}$: represents no damage (DS_0) to partitions or suspended ceilings; (2) $DS_{ANC,2}$: represents slight damage (DS_1) to partitions or suspended ceilings; (3) $DS_{ANC,3}$: indicates moderate damage (DS_2) to partitions or suspended ceilings; (4)$DS_{ANC,4}$: means partitions or suspended ceilings are severely damaged (DS_3).

Table 2. Functional states of a medical department

Function states	Description	Loss ratio
FS_1	Full operational capability maintained, with no or negligible damage to utility systems.	0
FS_2	Minor reduction in system functionality resulting from limited damage to utility systems	0.33
FS_3	Severe degradation of operational capacity caused by moderate damage to key utility systems.	0.67
FS_4	Complete disruption of medical department functionality due to extensive damage across multiple utility systems.	1

4.2 FUNCTIONALITY FOR WHOLE HOSPITAL

The overall functionality of the hospital is quantified as a weighted sum of the functionality of individual departments, as expressed in Equation (5):

$$Q = \sum_{i=1}^{n} w_i \cdot F_i \tag{5}$$

Where F_i is the functionality of department i and w_i is its corresponding importance factor. The aggregated value Q reflects the hospital's total functionality. A Q value of 1 represents total function without disruption. The weighting/importantance factors represent the relative contribution of different departments to overall hospital function, are derived from the study of Shang et al. (2022) and are summarized in Table 3.

Table 3. Importance factors for each department

Department	Emergency department (ED)	Radiology department (RD)	Ultrasound department (UD)	Central sterile supply department (CSSD)	Clinical laboratory (CL)	Blood bank (BB)	Operating room (OR)	General ward (GW)	Intensive care unit (ICU)
Importance factor, w_i	0.177	0.075	0.072	0.085	0.074	0.085	0.177	0.113	0.142

This paper only considers the simple case, but in more realistic applications, medical departments with disproportionate or binary effects on overall hospital functionality can be included, and Equation (5) can be written in a piecewise form if needed.

4.3 RECOVERY ANALYSIS

The recovery process is modeled as a discrete Markov chain with daily step and constant transition probability. The time to repair completion is represented as a random variable following a geometric distribution, whose cumulative distribution function (CDF) is given in Equation (6). $P_{ij}(t)$ represents the probability that the repair of component i in damage state j is completed within t days, and p_{ij} denotes the constant per-day transition probability from damage states j (DS_{ij}) to the fully functional state (DS_{i0}).

$$P_{ij}(t) = 1 - \left(1 - p_{ij}\right)^{t} \tag{6}$$

The CDF of geomatric distribution $P_{ij}(t)$ asymptotically approaches 1 but never reaches it. In engineering applications, it is often desirable to define a practical completion threshold θ which represents the probability level at which the repair is considered effectively completed. By introducing the threshold θ, equation (6) becomes:

$$\theta_{ij} = 1 - (1 - pij)^{T_{ij}} \tag{7}$$

Where T_{ij} is the target repair duration of DS_{ij}. In practice, T_{ij} can be obtained from historical data, engineering guidelines or expert judgment. Solving Equation (7) for p_{ij} yields daily transition probability:

$$p_{ij} = 1 - \left(1 - \theta_{ij}\right)^{1/T_{ij}} \tag{8}$$

This study considered a maximum of three damage states. The resulting transition probability matrix is summarized in Table 4. For components with fewer damage states, the corresponding transition matrix is obtained by extracting the leading submatrix of Table 4 according to the number of damage states.

Table 4. Transition probability matrix

From\To	DSi0	DSi1	DSi2	DSi3
DSi0	1	0	0	0
DSi1	$\boldsymbol{p_{i1}}$	$\boldsymbol{1 - p_{i1}}$	0	0
DSi2	$\boldsymbol{p_{i2}}$	0	$\boldsymbol{1 - p_{i2}}$	0
DSi3	$\boldsymbol{p_{i3}}$	0	0	$\boldsymbol{1 - p_{i3}}$

5. Case study

5.1 HOSPITAL MODEL DESCRIPTION

The case study hospital is a five-story reinforced concrete frame building designed according to the Chinese seismic code, as reported in Liu et al. (2022) and Zhai et al. (2021). The building as shown in Figure 6 has a plan dimension of 60 × 15 m and an interstory height of 3.6 m. It is representative of a medium-sized

general-purpose secondary hospital in China. Different clinical services are distributed across the building as shown in Table 5.

Structural analyses are conducted under three seismic intensities defined in the Chinese code: service level earthquake (SLE, 63.2% probability of exceedance in 50 years), design basis earthquake (DBE, 10% probability of exceedance in 50 years), and maximum considered earthquake (MCE, 2% probability of exceedance in 50 years). The peak floor acceleration (PFA), peak floor velocity (PFV), peak inter-story drift ratio (PIDR) are calculated for each intensity（Figure 7).

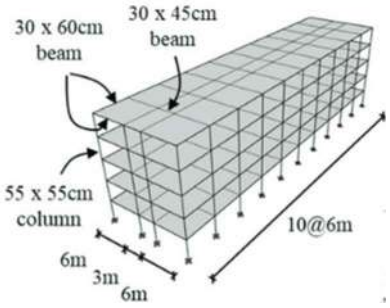


Figure 6. Structural layout of the hospital (Zhai et al. 2021)

Table 5. Hospital layout

Floor	Medical department
4	General Ward (GW4), Intensive care unit (ICU)
3	General Ward (GW3)
2	Operating room (OR)
1	Clinical labtory (CL), Central sterile supply department (CSSD), Blood bank (BB)
Ground	Radiology department (RD), Ultrasound department (UD), Emergency department (ED)

The data required in the framework, including (1) fragility functions, repair times, and inventories of non-structural components and medical equipment, and (2) the organization of repair tasks, as obtained from the Normative Quantity Estimation Tool (Federal Emergency Management Agency (FEMA) 2018), the Standard for Seismic Resilience Assessment of Buildings (National Standardization Administration Committee 2020), and relevant medical equipment studies (Shang 2021, Yu et al. 2023). Although the FEMA normative quantities are originally developed for U.S. building stock, they are employed here as a proxy due to the absence of comparable Chinese guidelines. With respect to the repair sequence, two strategies are considered: (1) serial repair, where components are restored floor by floor; and (2) parallel repair, where all components are repaired simultaneously. θ_{ij} is set to 0.995 to represent the completion of repair.

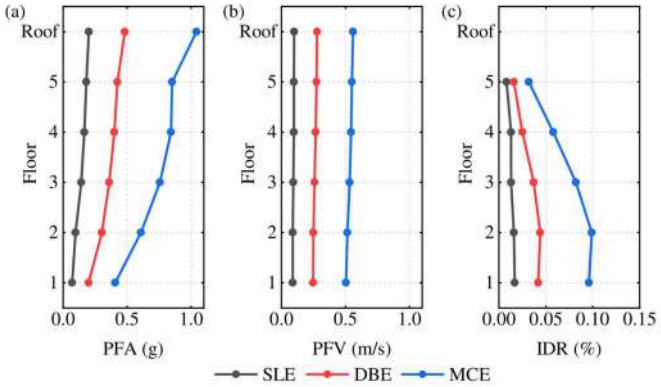


Figure 7. Structural response of case study hospital (Liu et al. 2022)

6. Results and discusion

Figure 8 presents the functionality of each medical demartment calculated according to Equation (4). As shown in the figure, medical department functionality decreases with increasing seismic shaking intensity. Under SLE, all departments maintain nearly full functionality, indicating slight disruption to hospital services. Under DBE, medical departments functionality declines to reduced levels (approximately 0.5-0.9), with more pronounced reductions in the OR, ICU and wards. Under MCE, the functionality of most departments falls below 0.5, with critical departments such as OR and ICU experiencing near-complete loss of function. This result highlights the vulnerability of life-saving departments during severe earthquakes. One advantage of the BN simulation is its traceability. When a department shows a significant reduction of functionality (e.g., ICU under MCE), the network can identify the key components that most contribute to the loss of function. For example, in the case of the OR under MCE, a sensitivity analysis was conducted with the OR node set to the lowest functional state (FS_4). The results as shown in Figure 9 as a tornado plot highlight the critical components whose failure drives the operational disruption of the OR. If the top five critical components are retrofitted to remain functional during an earthquake, the OR's functionality under MCE is projected to improve to approximately 50%. The proposed framework also enables engineers to obtain quantitative evidence to evaluate whether mitigation strategies, such as system decentralization or the addition of storage batteries, would effectively enhance the resilience of the facility.

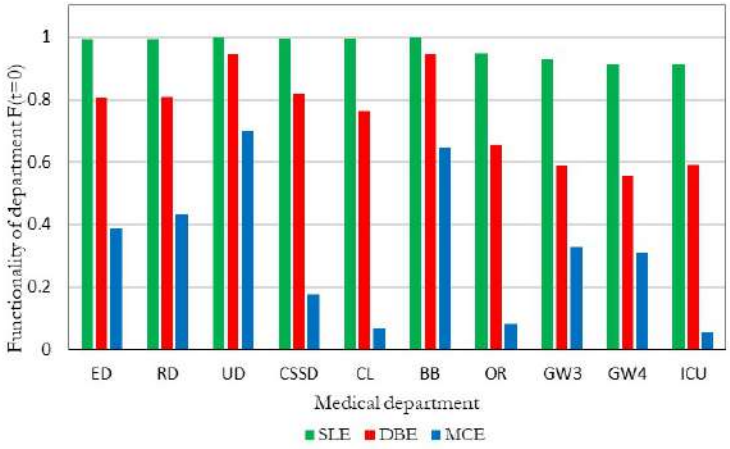


Figure 8. post-earthquake functionality of hospital departments under different seismic intensities: SLE, DBE, MCE

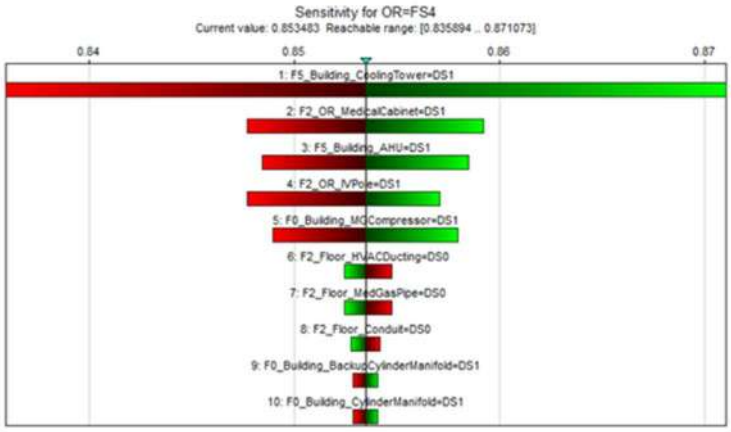
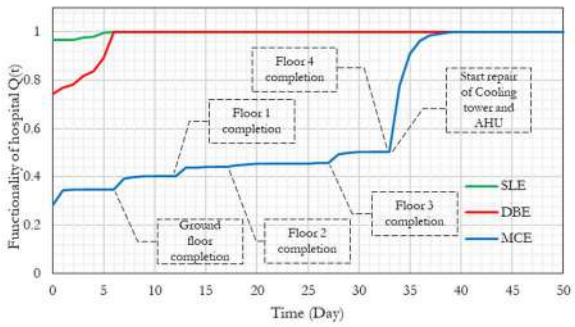
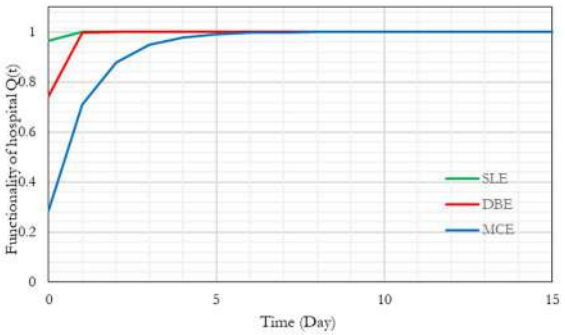


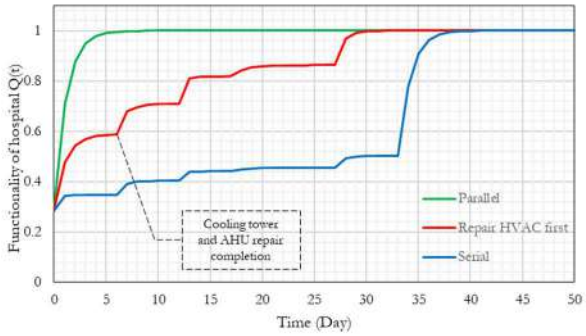
Figure 9. Tornado diagram of Operating departments (FS_4)



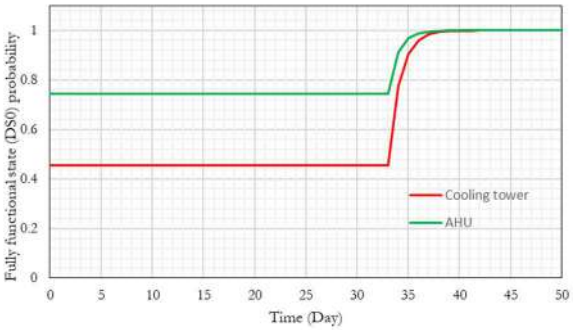
(a) Under serial repair strategy



(b) Under parallel repair strategy



(c) MCE event - Repair HVAC equipment first



(d) Probability of fully functional state for Cooling tower and AHU

Figure 10. Recovery curves – functionality over time

Figure 10(a)-(c) presents the recovery curves of the case study hospital assuming different repair strategies and earthquake intensities (SLE, DBE, and MCE). Figure 10(a) illustrates the serial repair strategy. Under SLE and DBE, although the initial functionality differs, the total recovery time is identical because the damage on each floor can be repaired within one day, making the recovery duration proportional to the number of floors. In contrast, under MCE, the hospital functionality increases gradually as each floor needs more time to repair. The small increases at the beginning of each floor repair are due to the initial restoration of certain components. The MCE recovery curve also exhibits an extended plateau with a sharp recovery occuring on day 33. This point corresponds to the repair of the rooftop cooling tower and air handling unit(AHU) (as shown in Figure 10(d)), which triggers the recovery of the building HVAC system and subsequently enhances the overall hospital functionality. Figure 10(b) shows the parallel repair strategy. In this case, the hospital can be fully restored within one day under SLE and DBE. Under MCE, a sharp

functionality increase occurs in the first two days, since most components can be repaired within a short time.

A third modified serial repair strategy is introduced. In this strategy, the rooftop HVAC equipment is repaired simultaneously with the first floor during the serial repair process, which represents a practical scenario where limited post-earthquake resources are prioritized for the most critical components. Figure 10(c) presents the recovery curve under this strategy and a comparison with the other two under MCE. The figure shows that hospital functionality can be substantially improved (due to rooftop HVAC equipment and ground floor repair) during the first six days compared with the serial strategy. Table 6 summarizes the resilience indices with different repair strategies under MCE. The parallel repair strategy achieves the highest resilience index. However, prioritizing the repair of rooftop HVAC equipment can enhance resilience within a comparable total recovery time compared with serial strategy. This demonstrates the potential of the DBN framework to inform effective recovery strategies.

Table 6. Resilience index and recovery time under different repair strategies

Repair strategy	Recovery time (days)	R
Serial	39	50.1%
Parallel	10	91.4%
Repair HVAC first	30	78.9%

7. Conclusion

This study proposed a dynamic Bayesian network for assessing the seismic resilience of hospital. A case study is conducted to illustrate the effectiveness of the framework. From this study the following conclusion can be drawn:

- The case study hospital functionality decreases with increasing earthquake intensity, with critical departments such as operating rooms (OR) and intensive care units (ICU) being the most vulnerable under MCE scenarios.

- The DBN provides traceability by identifying key components that drive functionality loss and shows targeted retrofit can substantially enhance resilience.

- The choice of repair strategy has a significant impact on recovery. The DBN can identify critical equipment that should be repaired first and has the potential to inform optimal recovery strategies.

8. REFERENCES

Achour, N., Miyajima, M., Kitaura, M., and Price, A. 2011. Earthquake-Induced Structural and Nonstructural Damage in Hospitals. Earthquake Spectra, **27**(3): 617–634. doi:10.1193/1.3604815.

Basaglia, A., Spacone, E., van de Lindt, J.W., and Kirsch, T.D. 2022. A Discrete-Event Simulation Model of Hospital Patient Flow Following Major Earthquakes. International Journal of Disaster Risk Reduction, **71**: 102825. doi:10.1016/j.ijdrr.2022.102825.

Bruneau, M., Chang, S.E., Eguchi, R.T., Lee, G.C., O'Rourke, T.D., Reinhorn, A.M., Shinozuka, M., Tierney, K., Wallace, W.A., and von Winterfeldt, D. 2003. A Framework to Quantitatively Assess and Enhance the Seismic Resilience of Communities. Earthquake Spectra, **19**(4): 733–752. doi:10.1193/1.1623497.

Bruneau, M., and Reinhorn, A. 2007. Exploring the Concept of Seismic Resilience for Acute Care Facilities. Earthquake Spectra, **23**(1): 41–62. doi:10.1193/1.2431396.

Caetano, H.O., Desuó N., L., Fogliatto, M.S.S., and Maciel, C.D. 2024. Resilience assessment of critical infrastructures using dynamic Bayesian networks and evidence propagation. Reliability Engineering & System Safety, **241**: 109691. doi:10.1016/j.ress.2023.109691.

Chavez, J.-P., Murcia-Delso, J., and López-Almansa, F. 2025. Probabilistic framework for post-earthquake functionality assessment of seismically isolated hospital buildings using Bayesian networks. Engineering Structures, **328**: 119633. doi:10.1016/j.engstruct.2025.119633.

Cimellaro, G.P., Malavisi, M., and Mahin, S. 2017. Using Discrete Event Simulation Models to Evaluate Resilience of an Emergency Department. Journal of Earthquake Engineering, **21**(2): 203–226. doi:10.1080/13632469.2016.1172373.

Federal Emergency Management Agency (FEMA). 2018. Seismic Performance Assessment of Buildings, Volume 2 -- Implementation Guide, Second Edition. FEMA, Washington, DC.

Koller, D., and Friedman, N. 2009. Probabilistic graphical models: principles and techniques. MIT Press, Cambridge, MA.

Li, Z., Li, N., Cimellaro, G.P., and Fang, D. 2020. System Dynamics Modeling-Based Approach for Assessing Seismic Resilience of Hospitals: Methodology and a Case in China. Journal of Management in Engineering, **36**(5): 04020050. doi:10.1061/(ASCE)ME.1943-5479.0000814.

Liu, J., Zhai, C., and Yu, P. 2022. A Probabilistic Framework to Evaluate Seismic Resilience of Hospital Buildings Using Bayesian Networks. Reliability Engineering & System Safety, **226**: 108644. doi:10.1016/j.ress.2022.108644.

National Standardization Administration Committee. 2020. Standard for Seismic Resilience Assessment of Buildings.

Qu, Z., Wang, F., Chen, X., Wang, X., and Zhou, Z. 2023. Rapid report of seismic damage to hospitals in the 2023 Turkey earthquake sequences. Earthquake Research Advances,: 100234. doi:10.1016/j.eqrea.2023.100234.

Romani, G.P., Blowes, K., and Molina Hutt, C. 2023. Evaluating post-earthquake functionality and surge capacity of hospital emergency departments using discrete event simulation. Earthquake Spectra, **39**(1): 402–433. SAGE Publications Ltd STM. doi:10.1177/87552930221128607.

Santarsiero, G., Di Sarno, L., Giovinazzi, S., Masi, A., Cosenza, E., and Biondi, S. 2019. Performance of the healthcare facilities during the 2016–2017 Central Italy seismic sequence. Bulletin of Earthquake Engineering, **17**(10): 5701–5727. doi:10.1007/s10518-018-0330-z.

Shang, Q. 2021. Research on seismic resilience assessment method of hospital systems. Doctoral Thesis, Institute of Engineering Mechanics, China

Shang, Q., Wang, T., and Li, J. 2022. A quantitative framework to evaluate the seismic resilience of hospital systems. Journal of Earthquake Engineering, **26**(7): 3364–3388. Taylor & Francis. doi:10.1080/13632469.2020.1802371.

SMILE Wrappers Programmer's Manual. 2024. BayeFusion, LLC.

Tong, Q., and Gernay, T. 2023. Resilience assessment of process industry facilities using dynamic Bayesian networks. Process Safety and Environmental Protection, **169**: 547–563. doi:10.1016/j.psep.2022.11.048.

World Health Organization. 2020. Hospital safety index guide for evaluators. World Health Organization, Geneva.

Yu, P., Zhai, C., Liu, J., Pei, S., Song, Z., and Xie, L. 2022. Resilience assessment methods for hospitals subjected to earthquakes: State of the art. Earthquake Engineering and Resilience, **1**(1): 40–59. doi:10.1002/eer2.6.

Yu, P., Zhai, C., Liu, J., and Wang, X. 2023. Shake table tests for the seismic performance assessment of desktop medical laboratory equipment considering the effect of adjacent walls and restrainers. Structures, **50**: 1922–1933. doi:10.1016/j.istruc.2023.02.093.

Zhai, C., Yu, P., and Wen, W. 2021. A Physical-organizational Method for the Functionality Assessment of A Hospital Subjected to Earthquakes. Journal of Earthquake Engineering,: 1–21. doi:10.1080/13632469.2021.1947419.

Zhang, Y., Cai, B., Liu, Y., Jiang, Q., Li, W., Feng, Q., Liu, Y., and Liu, G. 2021. Resilience assessment approach of mechanical structure combining finite element models and dynamic Bayesian networks. Reliability Engineering & System Safety, **216**: 108043. doi:10.1016/j.ress.2021.108043.

Zhong, S., Clark, M., Hou, X.-Y., Zang, Y., and FitzGerald, G. 2014. Validation of a Framework for Measuring Hospital Disaster Resilience Using Factor Analysis. International Journal of Environmental Research and Public Health, **11**(6): 6335–6353. doi:10.3390/ijerph110606335.

Performance of Non-Structural Components in a 5-Storey Shake-Table Test

Alex Shegay[1], Mojtaba Hosseini[1], Jitendra Bhatta[2], Rajesh Dhakal[2], Paul Kim[3], Scott Menegon[4], Glen Pring[5], Wei-Chung Chen[6], Min-Chi Ko[6]and Santiago Pujol[2]

[1] University of Auckland
e-mail: {alex.shegay, mhos245}@auckland.ac.nz
[2] University of Canterbury
e-mail: {jitendra.bhatta, rajesh.dhakal}@canterbury.ac.nz
[3] Rondo
e-mail: paul.kim@narlabs.org.tw
[4] Swinburne University
e-mail: s.menegon@swin.edu.au
[5] Flexitraxx
e-mail: glen@flexitraxx.com.au
[6] NCREE
e-mail: {chenwc, 2306027}@narlabs.org.tw

Abstract. Recent developments in structural engineering design philosophy—particularly in seismically active regions—have shifted from focusing solely on life safety to also prioritising post-earthquake functionality. To explore this broader performance objective, a joint research project between QuakeCoRE (New Zealand) and the National Center for Research on Earthquake Engineering (NCREE, Taiwan) conducted a shake-table test on a ¾-scale, 5-storey building with multiple non-structural components. The test aimed to evaluate whole-of-building performance and assess how typical New Zealand building systems might meet emerging functionality-based design goals.

Non-structural components were installed on the second and third storeys, including a sprinkler piping system, curtainwall façade, plasterboard partition walls with varying details, and both perimeter-fixed and fully-floating plasterboard ceilings. This paper presents initial observations of seismic response of the partitions, ceilings and sprinkler systems.

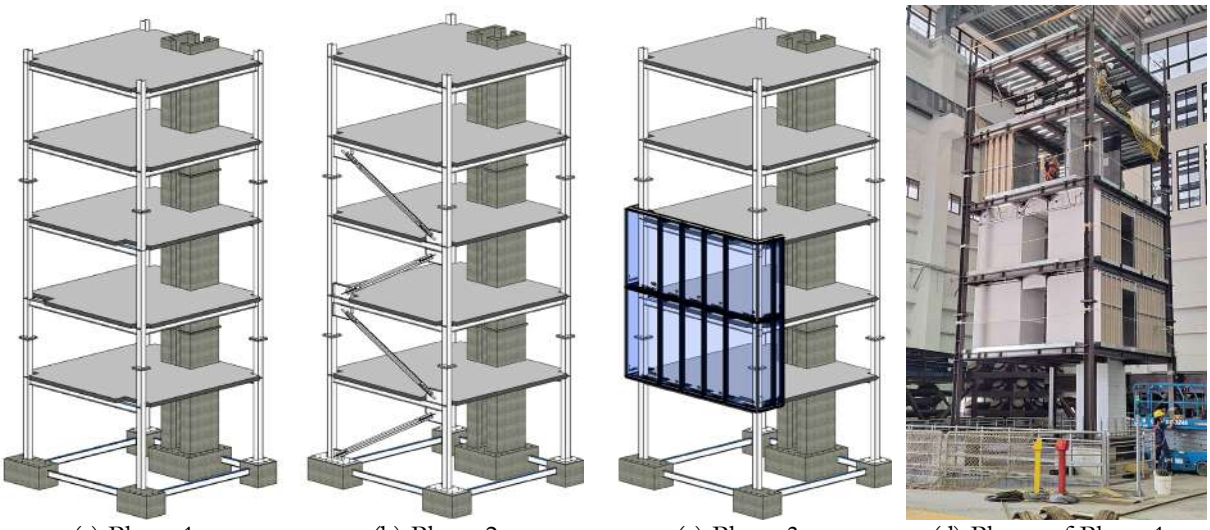
Keywords: Plasterboard ceiling, plasterboard partition, fire-sprinkler, shake-table

1. Introduction

Non-structural components (NSCs) account for a significant proportion of damage costs following earthquakes. Numerous research studies have focused on testing individual NSC; however, the primary cause of unexpected failure arises from the fact that these elements cannot be treated as independent entities (AWCINZ, 2018; Filiatrault & Sullivan, 2014). NSCs frequently share boundary conditions with other structural and non-structural elements, leading to potential incompatibilities in their seismic response. To explore this, a range of NSCs were installed on a ¾ scale 5-storey building dynamically tested as part of a joint research project between QuakeCoRE (New Zealand) and the National Center for Research on Earthquake Engineering (NCREE, Taiwan). The test structure, shown in Figure 1, was a 5-storey steel-RC wall hybrid building. The building had a 5 m x 5 m footprint. The experiment had several objectives including understanding (i) behaviour of hybrid reinforced concrete-steel structures, (ii) RC diaphragm to RC wall connections, (iii) torsional response of structures and (iv) effect of reduced design drifts on structural response. The structure was fitted with several NSCs including plasterboard partition walls, plasterboard perimeter fixed and fully floating ceilings, fire sprinkler pipe network and curtainwall façade. Additional components were also installed by the Taiwanese reserachers included bookshelves and stone veneer; however, these are outside the scope of this paper as they will be discussed in a separate publication.

The testing was conducted in three phases as depicted in Figure 1. In Phase 1, the structure was tested without buckling-restrainted braces (BRBs) and subjected to serviceability-level excitations. All the non-structural components were installed in the structure except for the curtainwall. In Phase 2, the BRBs were installed and the structure was subjected to maximum considered earthquake (MCE) level demands. Finally, in Phase 3, the BRBs were removed and curtainwall installed before repeating the excitation sequence of Phase 2.

In this paper, preliminary observations of the performance of the partition walls, ceilings and sprinkler pipes are presented. Comparisons in performance and effectiveness of various detailing in different systems are drawn.



(a) Phase 1 (b) Phase 2 (c) Phase 3 (d) Photo of Phase 1

Figure 1: Configuration of test specimen and photo

2.Outline of NSCs on the structure

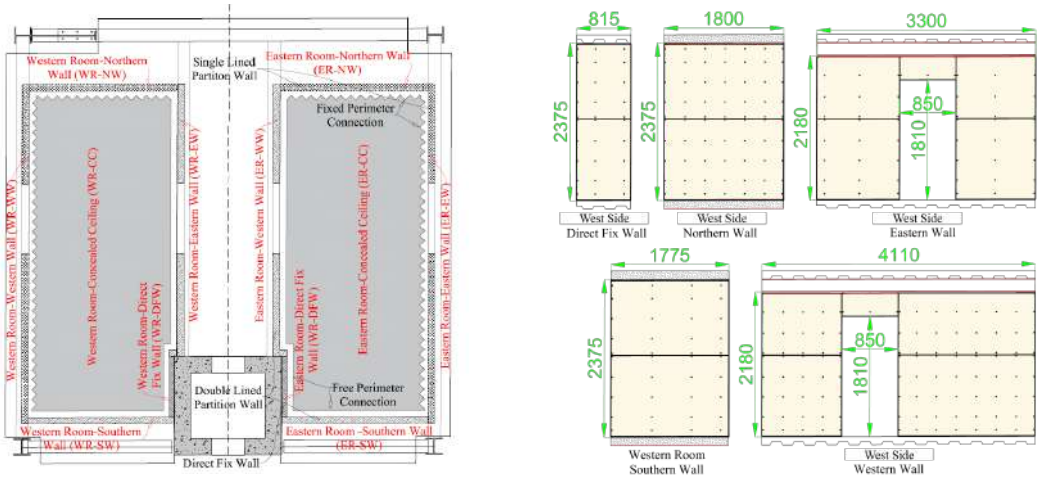
In this test, partition walls, ceilings, and unitized curtainwall glazing were installed on both the second and third floors of the building; also, sprinkler pipes were installed on the third floor. Further details associated with these NSCs will be provided in the following sections.

2.1 NON-STRUCTURAL PARTITIONS

A typical plan and elevation view of the partition walls and ceilings for Floors 2 and 3 is shown in Figure 2. On Floors 2 and 3, two rooms each were built using plasterboard partition walls and a plasterboard concealed ceiling. In the corridor between the rooms a fully floating (i.e., unbraced) ceiling was also installed. In all rooms, the plasterboard ceiling utilized typical boundary conditions used in practice, where a fixed connections was used along two adjacent walls and a free (sliding) connection was used on the opposing walls, as specified in Figure 2a. It is noted that all horizontal joints running between the ceiling and walls was set with tape and plaster, as would typically be done in practice. Each room contained five partition walls: two single-lined partition walls, two double-lined partition walls, and one direct-fix wall. In double-lined partition walls, plasterboard lining was attached on both sides of the steel studs, while in single-lined partition walls, plasterboard was attached only to the side of the studs facing the inside of the room. In direct-fix walls around the concrete core, plasterboard lining was screwed to furring channels, which are connected to the core walls using direct-fix clips (with exception of East-side room on Floor 2).

The elevation views and dimensions of the five partition walls and door openings in the west room are shown in Figure 2b. Owing to the symmetry of the plan layout, the dimensions of the walls in the east room were the same as those of the corresponding walls in the west room. As shown in Figure 2b, the height of the partition walls oriented in the NS direction (wall names ending in -EW or -WW), was smaller than that of the other walls because they are positioned beneath structural steel beams, and so were connected to the bottom flange of the beam, unlike the rest of the walls which were fixed to the steel deck of the floor above. All details mentioned regarding the dimensions apply to partition walls on both the second and third floors.

On both floors, the west-side room was designed using traditional partition wall detailing, while the east-side room utilized a low-damage system. All partition walls on floor 3 and in the east-side room on floor 2 were fire-rated, which means plasterboard lining spanned full-height, and the small gap between the lining and the soffit is filled with fire-rated sealant. Comparatively, for the partition walls located on floor 2 were non-fire rated walls.



(a) Plan View **(b) Elevation View**

Figure 2: Typical wall and ceiling layout.

Key differences between the partition walls in each room pertain to either the head track and base track connections to the soffit or wall joint detailing at room corners. The head track and base track connections of a representative wall in all four rooms is demonstrated in the Figure 3a, while the types of corner detailing used are shown in Figure 3b. In the floor 2 west-side room, the base track and the head track of each wall were fixed to floor slabs above and below using powder actuated nails. The wall studs were friction fitted between the base and head-tracks, and fixed using screws to the base-track only. The studs are not screw-fixed to the head-track to allow relative sliding and slab deflection – a common detail used in practice in NZ. The corner detailing shown in Figure 3b (also typical in practice) was used to connect two walls at their junction. The plasterboard lining spanned to 100 mm below floor soffit (i.e., partial-height lining). This is typically done for convenience of passing services between rooms where fire-rating is not a requirement. In the floor 3 west-side room, the detailing of the head track, base track, and corner junctions is identical to floor 2 west-side room, with the only difference being that lining spanned full-height of the floor height. A 20 mm gap was included between the lining and the soffit (to allow for vertical floor movement), which is filled with fire-rated sealant.

In the floor 2 east-side room, the low damage *Qubit 360* partition wall system was utilized. In this system, the partition walls are de-coupled from the movement of the floor above via a flexible bracket that is installed between the wall top track and the upper slab. When the top slab experiences storey displacement, the bracket flexes, thus preventing the top-track (and partition walls attached to it) from being dragged with the floor slab. The elevation and corner details of these walls is shown in Figures 3a and b, respectively. It can be seen in Figure 3b that no sealant gaps are required at the wall joints in this method of construction. Further details on this system can be found in (Menegon et al., 2023).

In the floor 3 east-side room, improved detailing designed to accommodate relative wall movements were adopted, roughly based on recommendations of the Association of Wall And Ceiling Industries of New Zealand (AWCINZ, 2018). As can be seen in Figure 3a, the head track and base track connections were the same as those in the floor 3 west-side room, except that the studs were also not screw-fixed to the base track, allowing them to slide freely inside the base and head tracks. The corner detailing of the partition walls (Figure 3a) in this room was designed with gaps at both ends of the walls oriented in EW direction, with the intention of accommodating relative movements at corners without crushing damage. The gaps were all filled with fire rated sealant.

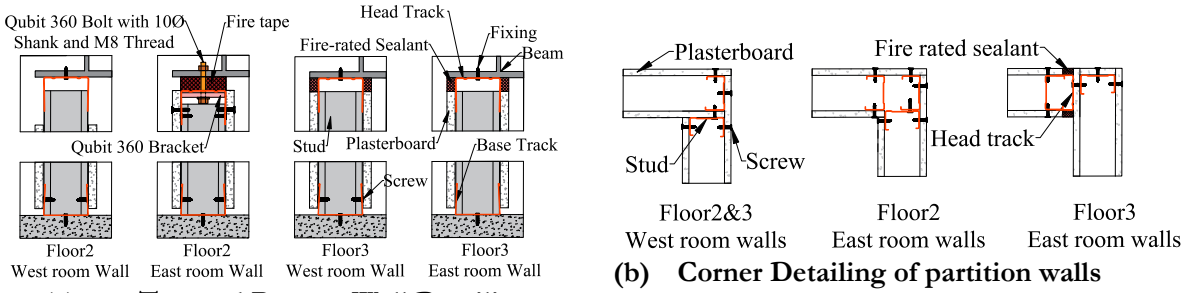


Figure 3: Wall construction detailing.

2.2 PLASTERBOARD CEILINGS

2.2.1 Concealed ceilings

In all rooms, the Key-Lock perimeter-fixed concealed ceiling system was used (with exception of easy-side room on Floor 2). Details of components are shown in Figure 4. In this type of ceiling, plasterboards were attached to furring channels using screws and the furring channels were fixed to the cross rails using interchange clips. The top cross rails were connected to suspension rods using suspension rod clips, and the suspension rods are connected to the slab using suspension rod brackets. Around the perimeter of the ceiling, furring channels and top cross rails were resting on angles that were fixed off to the partition wall studs. Where a 'fixed' connection of the ceiling was used, this perimeter connection was locked off with a

screw through the angle bracket while where the 'free' connection was utilized, no screws were used. For all ceilings, two layers of plasterboard were used to increase the seismic weight.

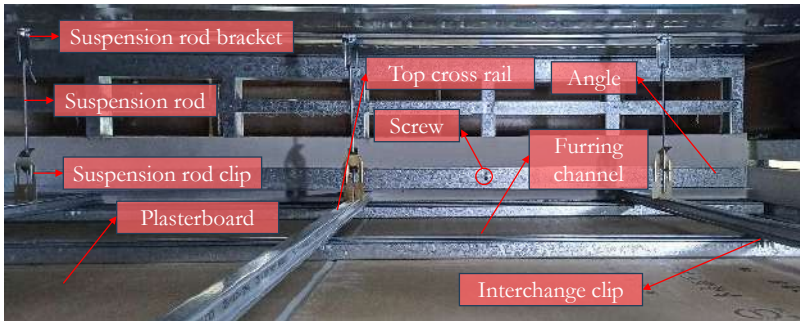
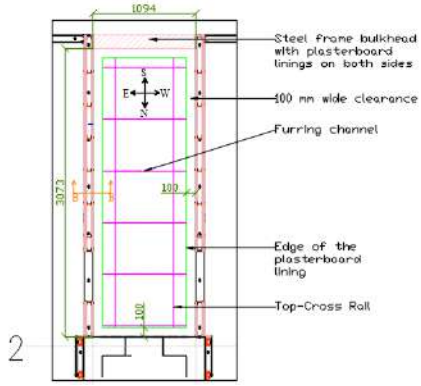


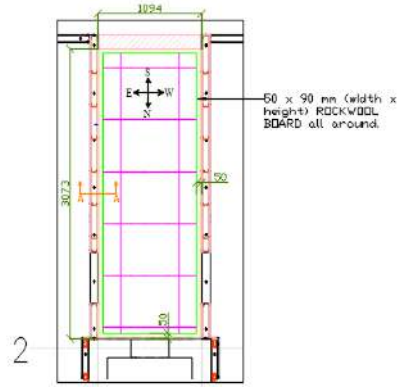
Figure 4: Configuration of the concealed ceiling components.

2.2.2 Fully floating ceilings

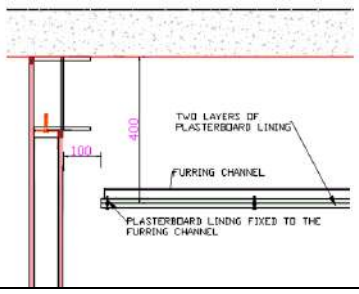
Fully floating ceilings (i.e., not fixed or braced to boundary elements Pourali et al. 2017) were installed in the corridor between the rooms on each floor. The plan view of the fully floating ceilings is shown in Figure 5. The ceilings were 1.09 m wide x 3.07 m long and comprised of two layers of 13 mm thick plasterboard linings, furring channels and top-cross rails having similar characteristics to the concealed ceilings. Two distinct installations were implemented in the corridor regions for these ceilings: floor 2 featured a ceiling with a 100 mm perimeter gap to all surrounding partition walls, bulkheads, and the core wall as shown in Figure 5a. In contrast, the ceiling on floor 3 utilized a continuous 50 mm wide x 90 mm deep rockwool strips around its perimeter, as shown in Figure 5b. This board acts as a buffer, preventing direct board-on-board impact (pounding) of the ceiling against adjacent elements and damping seismic response.



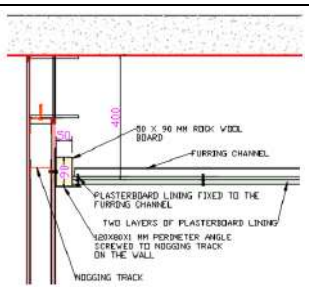
a) Fully floating ceiling on floor 2 (plan)



b) Fully floating ceiling on floor 3 (plan) – ceiling components similar to that of floor 2



c) Section B-B showing 100 mm wide gap all around fully floating ceiling on floor 2



d) Section A-A showing 90 x 50 mm wool isolation strips all around fully floating ceiling on floor 3

Figure 5: Fully floating ceiling plan and vertical sections (dimensions in mm)

2.3 SPRINKLER PIPE SYSTEM AND PENETRATIONS

In this test, a seismically designed fire sprinkler system, following NZS-4541:2020 (Standards New Zealand, 2020), was installed in the plenum of the third-story rooms, as shown in Figure 6. A main 50 mm pipe was placed outside the rooms in the EW direction. Four 25 mm diameter pipes (Schedule 40) branched out from the main pipe and penetrated walls through four different fitted HILTI® passive-fire protection details at the penetration points, including: (i) CP 606 Firestop acrylic sealant (applied only on inner wall), (ii) FS-ONE MAX Firestop intumescent sealant, (iii) CFS-CT B FS board, and (iv) CFS-BL firestop block (developed for sealing penetrations with cables). The fifth (central) pipe penetrated through the bulkhead in the corridor via a 30 mm diameter penetration, and did not utilize any fire protection. The branch pipes terminated with sprinkler heads that penetrated through the concealed ceilings into each room. The seismic performance was evaluated with a focus on two interactions: between the pipes and the fire-rated wall penetrations, and between the sprinkler heads and two types of plasterboard ceilings (fully floating and perimeter-fixed). The sprinkler heads were connected using both flexible hose and rigid pipes at different locations. The sprinkler piping system was also tested after removing the braces. Due to lab restrictions, the pipes could not be pressurized with water or other materials, resulting in reduced system mass and eliminated the potential for leakage assessment.

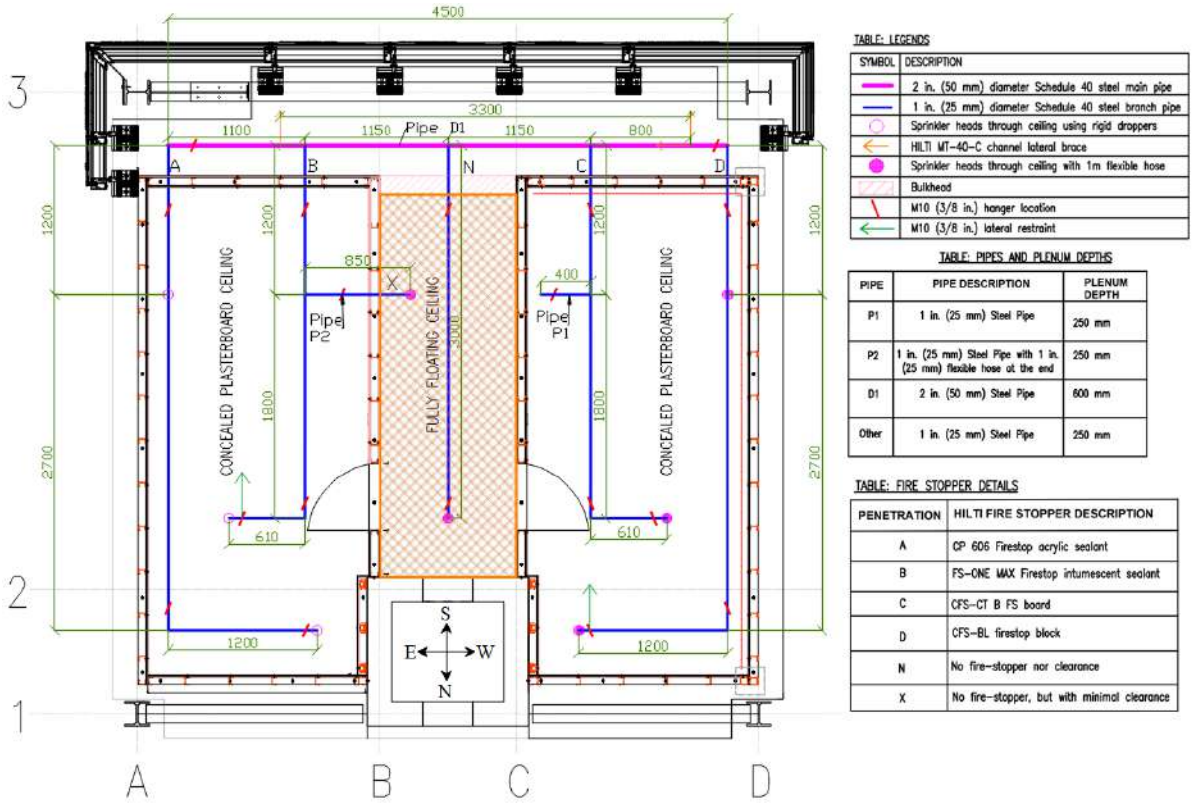


TABLE: LEGENDS

SYMBOL	DESCRIPTION
	2 in. (50 mm) diameter Schedule 40 steel main pipe
	1 in. (25 mm) diameter Schedule 40 steel branch pipe
	Sprinkler heads through ceiling using rigid droppers
	HILTI MT-40-C channel lateral brace
	Sprinkler heads through ceiling with 1m flexible hose
	Bulkhead
	M10 (3/8 in.) hanger location
	M10 (3/8 in.) lateral restraint

TABLE: PIPES AND PLENUM DEPTHS

PIPE	PIPE DESCRIPTION	PLENUM DEPTH
P1	1 in. (25 mm) Steel Pipe	250 mm
P2	1 in. (25 mm) Steel Pipe with 1 in. (25 mm) flexible hose at the end	250 mm
D1	2 in. (50 mm) Steel Pipe	600 mm
Other	1 in. (25 mm) Steel Pipe	250 mm

TABLE: FIRE STOPPER DETAILS

PENETRATION	HILTI FIRE STOPPER DESCRIPTION
A	CP 606 Firestop acrylic sealant
B	FS-ONE MAX Firestop intumescent sealant
C	CFS-CT B FS board
D	CFS-BL firestop block
N	No fire-stopper nor clearance
X	No fire-stopper, but with minimal clearance

Figure 6: Fire-sprinkler piping layout on storey 3 ceiling plenum space (dimensions in mm)

3.Performance of NSCs

The structure was subjected to a total of 42 simulated ground motions. The ground motion recorded during the 1940 El Centro, California earthquake was selected for most of the test runs. The amplitude of the applied ground motions was gradually scaled to represent different intensities ranging from 25 to 150% with 25% increments, where 100% corresponds to a ground motion with PGV of 40 cm/s and PGA of 0.4 g.

3.1 NON-STRUCTURAL PARTITIONS

In this study, wall damage was visually assessed using the damage state classification summarized in the Table 1. This classification is based largely on the repair effort required to restore them to their original state. Typical visual examples of each damage state in shown in Figure 7. This information was then used to develop damage state versus interstory drift curves for all partition walls, shown in Figure 8.

Table 1: Definition of damage states used to assess partition walls.

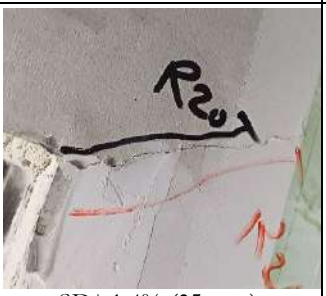
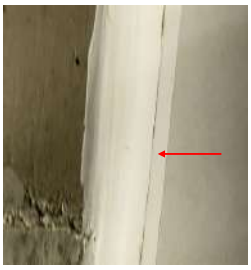
Damage State	Description of associated damage	Repair action
DS0	No Damage	No Repair
DS1	Minor cracks at joints, corners, and wall-to-ceiling interface	Repair Unlikely
DS2	A few screw impressions; separation in sealant	Replacing screws and the sealant, Patching, re-taping, sanding, and painting the gypsum wallboard
DS3	Extensive screw pull-out; plasterboard dislodging and crushing	Plasterboard replacement needed
DS4	Steel framing damage; significant residual wall displacement	Steel frame replacement needed

For partition walls in the floor 2 west room, DS1 was reached at about 0.9% storey drift (SD), characterized by hairline cracks around door openings and distortion of the joint tape at the corner joints and at the wall-to-ceiling interface. At 1.1% drift, the partition walls reached DS2, which included visible cracks in the corner joint sealant and a few screw impressions. Past 1.7% drift, the partition walls reached DS3, and included numerous screw impressions and localized crushing of plasterboard. At 2.1% drift, the walls reached DS4 due to damage to the framing, such as buckling of studs and bending of the head track flanges.

In the partition walls of the floor 2 east room DS1 was reached much later compared to the west room, at 1.4% drift. DS1 again manifested as minor cracks on the plasterboard at the door opening corners. At 2.1% drift, the partition walls reached DS2, where cracks on the plasterboard at their interfaces and screw impressions were observed. It is noted that 2.0% drift approximately corresponds to the displacement capacity associated Qubit360 bracket used to decouple of the partition wall from the slab (Figure 3a).

For the partition walls of the floor 3 west room, DS1 was observed at 0.6% drift – slightly earlier than for the floor 2 west room (only difference being the partial height lining). At 1.3% drift, the walls reached DS2, characterized by more pronounced separation in the corner joint sealant. At 2.2% drift, the walls reached DS3, with numerous screw impressions observed. Finally, at 2.6% drift, the walls reached DS4, where the corner studs exhibited local buckling and the plasterboard detached from the studs.

In the floor 3 east room, the EW walls differ from NS walls in terms of corner detailing - the EW walls in this room have low-damage corner detailing at both of their corner joints, which is not the case for the NS walls. Hence, they were presented separately in the figures and damage plots. Both the EW and NS walls of this room reached DS1 at 0.6% drift (characterized by minor separation of the corner joint sealants) and DS2 at 1.30% drift, (characterized by ~10 screw impressions each). The EW wall reached DS3 at 1.79% drift, as studs slid out of the base track and twisted during reverse motion. Damage progressed in the EW wall to DS4 by 2.6% drift and exhibited considerable residual displacement. The reason for the damaged studs/twisted and the residual displacement in the EW wall was the lack of a connection between the studs and the base track, and lack of connections at the corner joints. Comparatively, the NS wall did not exceed DS2, indicating that the low-damage decoupled corner detailing can be effective in reducing damage.

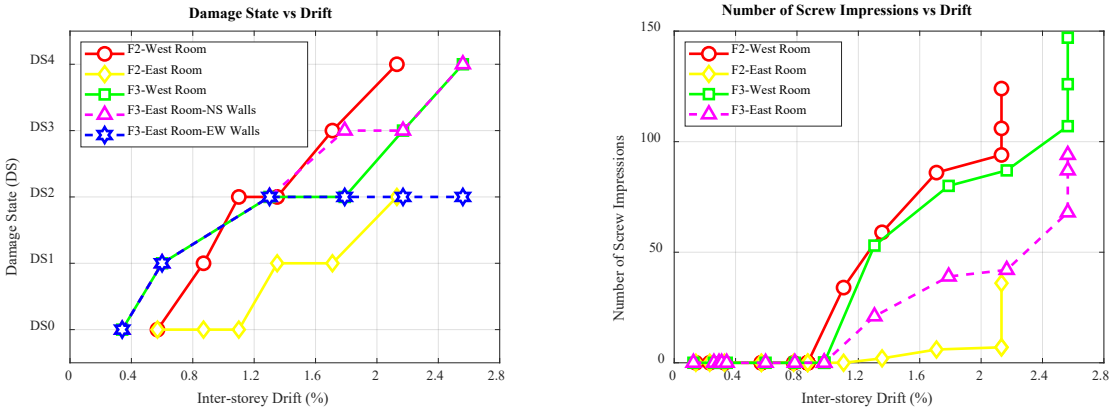
	DS1	DS2	DS3	DS4
Floor 2 West	 SD 0.9% (22.5 mm)	 SD 1.1% (27.5 mm)	 SD 1.7% (37.5 mm)	 SD 2.1% (52.5 mm)
Floor 2 East	 SD* 1.4% (35 mm)	 SD 2.1% (52.5 mm)	N/A	N/A
Floor 3 West	 SD 0.6% (15 mm)	 SD 1.3% (32.5 mm)	 SD 2.2% (55 mm)	 SD 2.6% (65 mm)
Floor 3 East (EW wall)	 SD 0.6% (15 mm)	 SD 1.3% (32.5 mm)	 SD 1.8% (45 mm)	 SD 2.6% (65 mm)
Floor 3 East (NS wall)	 SD 0.6% (15 mm)	 SD 1.3% (32.5 mm)		

*SD = Maximum storey drift after which damage was observed

Figure 7: Typical damage observed in each room at each damage state.

A graphical comparison of the progression of the 'overall' damage state for each room is shown in Figure 8a. The 'overall' damage state for the room is conservatively taken as highest damage state experienced by any partition wall in the room, and the inter-storey drift reported is taken as the higher value of the two planar directions. Here it can be seen that the floor 2 east room walls suffered the least damage compared to the others. This is due to the decoupling nature of the system described earlier, where the flexible bracket installed between the top track of the partition wall and the slab minimizes force transfer into the partition wall. As a result, the partitions experience greatly reduced inter-storey drift demands compared to the structure. The traditional partition walls in the west-side rooms on floors 2 and 3 performed almost the same; however, the partial-height lining walls in the floor 2 west room performed slightly better at lower drift levels. The two NS partition walls in the floor 2 east room performed nearly the same as the traditional walls in the floor 2 and floor 3 west rooms, but their failure mode was quite different, originating from differences in the connection between the studs and the base track. Meanwhile, the EW partition walls in the floor 2 east room performed much better than the NS walls, highlighting the effectiveness of low-damage corner detailing in reducing damage.

In addition to damage state, the number of screw impressions in each room (identified as screws that have visually impressed into the plasterboard and further confirmed drumming characteristics when knocking on the wall) was also counted after each run. The cumulative number of screw impressions for each room is plotted against interstory drift in Figure 8b. The curves are generally in agreement with the trends observed in Figure 8a, where the floor 2 east room partition walls exhibited the fewest screw impressions across different drift levels, followed by the floor 3 east room and then the traditional walls in the floor 2 and floor 3 west rooms. The plot further shows that the traditional partition walls in the floor 2 and floor 3 west rooms suffered almost the same rate of screw impressions despite different plasterboard lining heights.



(a) Damage States of Partion Walls

(b) Number of Screw Impressions in Walls

Figure 8: Progression of partition damage characteristics vs inter-storey drift.

3.2 PLASTERBOARD CEILINGS

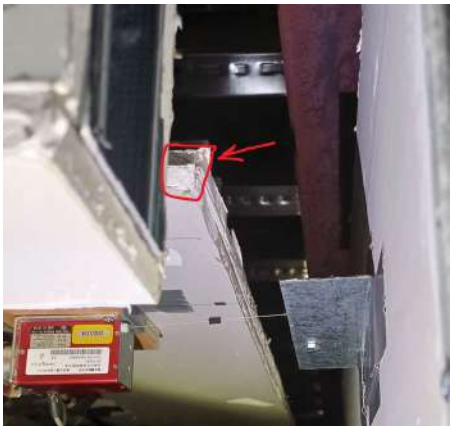
3.2.1 Concealed ceilings.

In general, no damage in the form of cracks, distortions or crushing were observed in the concealed ceilings in all the rooms. The exception was some minor separation cracking around the perimeter joints where ceiling met the partition walls. The limited damage is thought to be due to the stiff nature of the ceiling because of having reduced scale dimensions contrasting with unscaled plasterboards.

3.2.2 Fully Floating ceilings

Both fully floating ceilings on floor 2 and 3 experienced significant displacements resulting in contact with surrounding elements during testing. The fully floating ceiling on floor 3 sustained no damage over the full testing programme owing to the rockwool placed around the perimeter. In contrast, the ceiling on floor 2

exhibited localized crushing of edges due to collision with surrounding partition walls, as shown in Figure 9a. Subsequent shaking caused progressive damage to its plasterboard linings near the concrete core wall (Figure 9b), as well as crushing damage to the partition walls where contact occurred.



a) Sign of ceiling collision



b) Corner crushing observed

Figure 9: Impact damage to fully floating ceiling plasterboard on floor 2

3.3 FIRE SPRINKLER PIPE SYSTEM AND PENETRATIONS

The fire sprinkler piping system on floor 3, including its braces, hangers, joints, and sprinkler heads, sustained no damage throughout all test runs. This suggests that systems fabricated and designed to NZS-4541:2020 meet or exceed expected seismic performance. After the removal of braces on the main pipe, the system also remained undamaged. It is noted that reduced observed damage is also likely a consequence of the following conditions: (i) pipes being lighter than typically in service; (ii) short 250 mm hanger lengths resulting in reduced displacements.

3.4 WALL PENETRATIONS

3.4.1 FS-ONE MAX Firestop intumescent sealant

A hairline crack around the pipe, present since construction, gradually expanded, until a full crack had developed around the pipe within the sealant. By the end of the testing, a portion of the cracked sealant detached from the substrate, an event that likely compromised the assembly's fire-rating (Figure 10a).

3.4.2 CFS-BL firestop block

A progressive outward displacement of the firestop block from the wall, at penetration point D (Figure 6), was observed over the course of the test runs. By the end of the testing, the block had displaced such that about half of its depth was protruding beyond the wall line, as shown in Figure 10.

3.4.3 CFS-CT B FS board

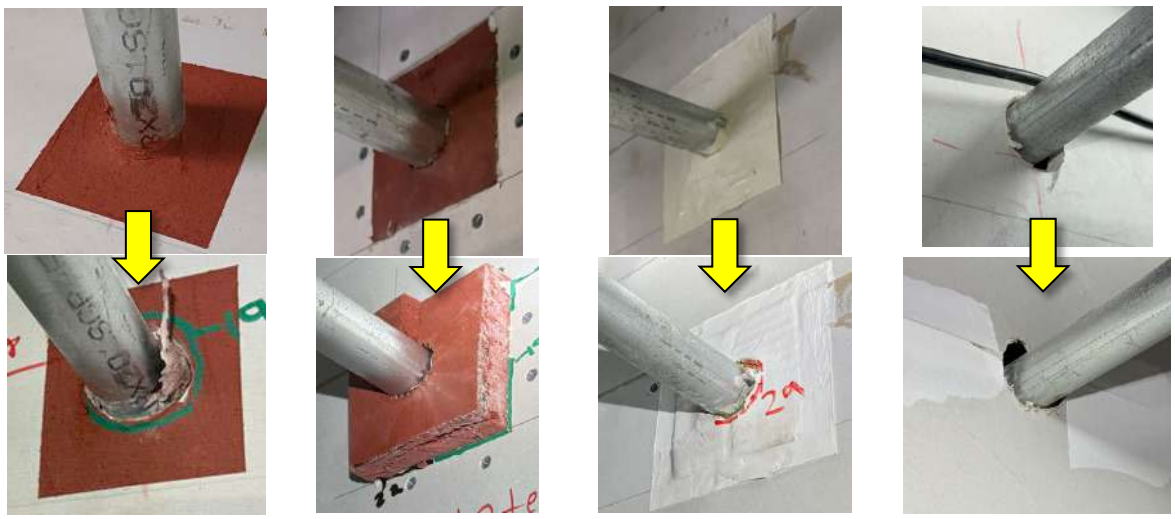
The board, at penetration point C (Figure 6) remained undamaged until storey drifts exceeded ~2.4%, during which a circumferential crack formed around the pipe penetration, as shown in Figure 10.

3.4.4 CP 606 Firestop acrylic sealant

The assessment of seismic performance of CP 606 sealant, at penetration point A (Figure 6) was not possible as it was above the concealed ceiling plenum inside the room. However, there was no damage to the plasterboard surrounding the pipe, without CP606, at this penetration when observed from outside.

3.4.5 Penetration without fire stoppers

The plasterboard lining surrounding the oversized penetration at point N (Figure 6), which was installed without a fire-stopper, sustained no observable damage, as shown in Figure 10. Conversely, the seismic performance of penetration point X (Figure 6) could not be evaluated due to its concealed location above the ceiling plenum.



(a) FS-ONE MAX sealant (b) CFS-BL firestop block (c) CFS-BL firestop block (d) No fire stopper

Figure 10: Damage to penetration sealants at start (top row) and end of testing (bottom row)

4.Summary

Testing was conducted on a suite of non-structural components installed on a 5-storey structure tested dynamically at the NCREE Tainan Laboratory. Initial observations of partition walls, ceiling and fire sprinkler systems demonstrated that their seismic performance strongly depends on detailing designed to accommodate interstorey movement. Traditional partition systems experienced onset of cracking earlier compared to low-damage partition systems that used flexible corner joints. Flexible joints could effectively delay onset of cracking and prevented stud damage; however, could result in other undesired and unexpected damage (such as large sealant separations and large residual drifts). Systems that decoupled the partitions from the rest of the structure showed superior performance within the range of the stroke of the components. Concealed ceilings remained largely undamaged, whereas fully floating ceilings without perimeter isolation sustained impact damage (perimeter rockwool buffers mitigated this damage). The fire-sprinkler system showed excellent performance, though some fire-stop sealants cracked or displaced under large drifts. Overall, flexible or decoupled connections and compliant fire-stopping materials are essential to preserving functionality and minimizing repair needs after strong earthquakes.

5.References

AWCINZ. (2018). *Code of Practice for the seismic design and installation of non-structural internal walls and partitions.* Association of Wall and Ceiling Industries of NZ.

Filiatrault, A., & Sullivan, T. (2014). Performance-based seismic design of nonstructural building components: The next frontier of earthquake engineering. *Earthquake Engineering and Engineering Vibration*, *13*(S1), 17–46. https://doi.org/10.1007/s11803-014-0238-9

Menegon, S. J., Hashemi, J., & Gad, E. F. (2023). *The next generation of drywall construction for low-damage design*.

Standards New Zealand. (2020). *NZS 4541:2020 Automatic fire sprinkler systems*.

6.Acknowledgements

The authors would like to acknowledge the National Center for Research in Earthquake Engineering (NCREE) and QuakeCoRE for the generous funding provided to make this test possible. Several companies have also donated materials for the non-structural components, including Rondo, Hilti, Intex and Thermosash. The authors would also like to greatly acknowledge the efforts of everyone involved in the testing, including NCREE technicians, NCREE staff, and students.

Issues in the fragility analysis of non-structural elements and the role of structural health monitoring

Gerard J. O'Reilly[1,2], and Masayoshi Nakashima[3,4]

[1]Centre for Training and Research on Reduction of Seismic Risk (ROSE Centre), Scuola Universitaria Superiore IUSS di Pavia, Pavia 27100, Italy

[2]European Centre for Training and Research in Earthquake Engineering (EUCENTRE), Pavia 27100, Italy

e-mail: gerard.oreilly@iusspavia.it

[3]Kobori Research Complex (KRC), Kajima Corporation, Tokyo 107-8502, Japan

[4]Disaster Prevention Research Institute, Kyoto University, Kyoto 611-0011, Japan

e-mail: nakashima@archi.kyoto-u.ac.jp

Abstract. Non-structural elements (NSEs) are critical to a building's seismic performance and often account for the largest share of repair and recovery costs when structural integrity remains intact. This paper examines data from commercial buildings equipped with structural health monitoring (SHM) systems, alongside insights from building manager interviews following the 2018 Osaka earthquake in Japan. The findings indicate that existing fragility models may underestimate NSE damage, as they fail to fully represent in-situ conditions. Several factors contributing to this discrepancy are identified, including installation variability, interactions with other building components, workmanship quality, and the effects of wear and ageing. SHM data are shown to provide a robust basis for refining fragility models, offering a more realistic alternative to laboratory-based experimental data. In addition, experiences and lessons drawn from past events highlight the potential of SHM-informed fragility analysis to advance future research and support the development of smarter, more resilient strategies for managing earthquake-induced damage.

Keywords: non-structural elements, fragility function, structural health monitoring, 2018 Osaka earthquake.

1. INTRODUCTION

Non-structural elements (NSEs), such as partitions, windows, furniture, and equipment, typically do not significantly contribute to a building's load-bearing system, but can suffer significant damage during earthquakes. While seismic codes have historically prioritised life safety, attention to NSEs has grown as their failures often impair building functionality, cause economic loss, and affect recovery. Early recognition of this issue dates back to Engle [1929], who stressed that neglecting NSEs was impractical given their high cost and impact on a building's functionality. Since then, guidelines and experimental studies [FEMA 2012; Filiatrault et al. 2001; NIST 2017; Taghavi and Miranda 2003] have highlighted their vulnerabilities. Japan's seismic design history illustrates this evolution. Initially focused on structural safety, limited consideration of NSEs led to repeated damage in major earthquakes, such as the 1978 Miyagiken-oki and 1995 Kobe events. Although structural performance improved, NSE damage, especially to equipment and machinery, exposed risks to business continuity, prompting the development of installation guidelines. However, standardisation remains difficult due to the proprietary and diverse nature of NSEs. The introduction of performance-based earthquake engineering (PBEE) and frameworks such as FEMA P-58 [2012] has enabled probabilistic assessment of building performance, extending beyond life safety to include repair costs, downtime, and functional losses. These concepts have also been extended to the seismic risk assessment and classification of NSEs also [Merino et al. 2023; O'Reilly and Calvi 2021]. These advances underline the critical role of NSEs in determining seismic resilience and post-earthquake recovery. This paper discusses some observed issues in the development of fragility functions for NSEs. It uses past observations and presented by O'Reilly et al. [2024] as its starting point to highlight some issues that are typically overlooked, especially when referring to experimental testing of NSEs in laboratory conditions. Additional discussion points surrounding the potential for structural health monitoring (SHM) solutions based on recent experiences in Japan by Fukutomi et al. [2025] are also presented.

2. ISSUES IN FRAGILITY FUNCTION DEVELOPMENT FOR NSES

To evaluate the risks linked to NSEs, researchers commonly use fragility functions. These functions express the probability of different damage states (DSs), such as window cracking, as a function of an engineering demand parameter (EDP), like storey drift. They are usually developed from experimental data, which remains the most widely used source despite being limited in availability, as highlighted by Bianchi and Pampanin [2022]. Still, laboratory testing does not always capture real-world conditions, and several such limitations are discussed here.

2.1 INSTALLATION CONDITIONS

The first issue concerns the difference between how NSEs are tested in laboratories and how they perform in real buildings. Bianchi and Pampanin [2022], in their review of previous studies, highlighted that fragility functions derived from experiments are strongly affected by connection details. This was evident for NSEs that are vulnerable to both storey drift and floor accelerations. For instance, Huang et al. [2022] showed through shake table tests on partition walls that boundary conditions can alter seismic fragility by as much as 42%. Similarly, Filiatrault et al. [2001] emphasised that while code-based force calculations for NSEs may be imperfect, their actual damage resistance often depends more on proper construction and detailing than on the intensity of shaking. Tasligedik et al. [2012] also observed that the poor seismic performance of drywall partitions during the 2010 and 2011 Canterbury earthquakes in New Zealand was largely due to inadequate protective technologies and construction details.[FEMA 2007]

Bianchi and Pampanin [2022] argued for improving detailing practices to achieve "low damage detailing" and enhance the overall resilience of NSEs, which raises an important consideration. Since most fragility

functions used in damage and loss assessments come from limited laboratory testing, and given that NSE behaviour is highly sensitive to connection details, one must ask: how accurately do these laboratory connection details represent reality? Laboratory experiments are often constrained by available setups, which may require compromises for both structural and non-structural components. While this may be less critical for structural elements, where key regions are typically away from test connections, it becomes a major concern for NSEs whose performance depends heavily on interface connections. As a result, the representativeness of some experimental fragility data, and the functions derived from them, may be questionable when compared to real-world conditions.

2.2 LOADING PROTOCOLS

The second issue concerns the loading protocols used in experimental testing and the way loads are applied to specimens. While loading protocols for structural elements have been widely studied and documented [Mergos and Beyer 2014; Richards and Uang 2006], guidance for NSEs has often relied on FEMA 461 [2007]. However, it is increasingly recognized that the number and amplitude of load cycles (Figure 1(c)) have a major influence on energy dissipation and damage accumulation. For instance, Gentile and Galasso [2021] highlighted the role of hysteretic energy in fragility assessments, Wilding et al. [Wilding et al. 2017] examined how loading protocols affect unreinforced masonry walls, whereas Gentile et al. [2025] has provided further insights into this topic through experimental testing with different energy inputs for a given level of drift demand to examine the damage induced in masonry infill panels. Although these studies focused on structural elements, the same principles apply to NSEs: loading protocols must realistically represent seismic demands.

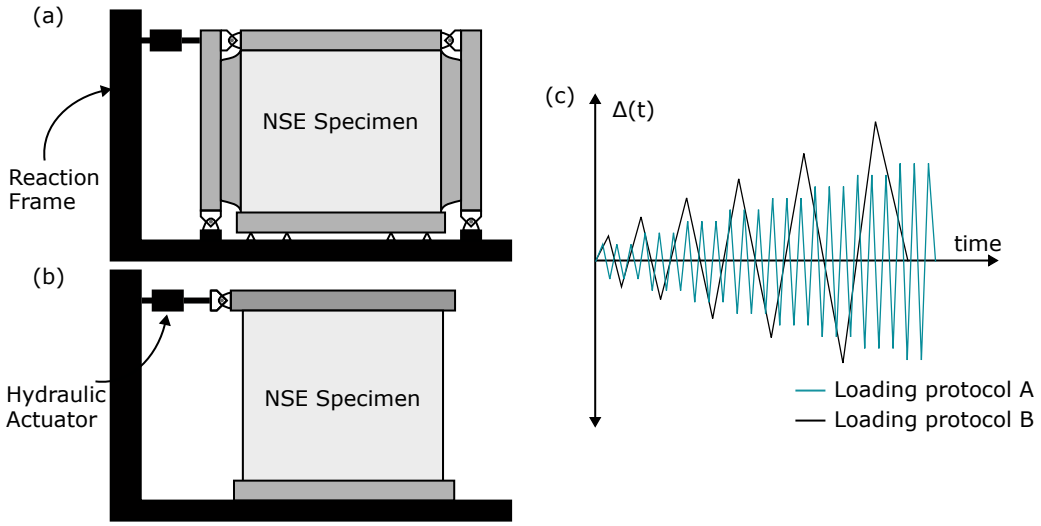


Figure 1. Illustration of (a)-(b) different experimental setup configurations to conduct a quasi-static test on an NSE specimen, and (c) the different loading protocols that may be applied

Beyond the choice of protocol itself, there is also the question of how loads are physically applied during testing. For example, Bianchi and Pampanin [2022] noted that early investigations into curtain wall performance in the 1960s [1961] considered only in-plane behaviour, whereas out-of-plane effects are now understood to be equally important. Moreover, cladding systems interact with the structural frame, meaning isolated tests may not capture their true response. Similarly, Lee et al. [2007] pointed out that many earlier studies on drywall partitions did not mount specimens within realistic frame systems. Figure 1(a) shows the setup they used for drywall partition testing, while Figure 1(b) depicts the quasi-static setup used by Retamales et al. [2013] for gypsum partitions with cold-formed steel frames. Although both setups targeted similar NSE types, they subjected specimens to different deformation and force conditions. Each approach may be valid in certain contexts, but combining their results risks inconsistency.

Ultimately, many experimental campaigns have been carried out using the best methods available at the time. Yet, as research evolves, it is becoming clear that older data may suffer from limitations. Nevertheless, these data remain embedded in available datasets and continue to inform many of the fragility functions currently in use for NSEs.

2.3 INTERACTION WITH OTHER NSES

Another limitation of fragility functions derived from single-specimen experimental tests is their inability to capture adverse interactions between different structural and non-structural elements within a building. This issue has been repeatedly observed in past earthquakes. For example, Baird and Ferner [2017] reported several cases during the 2016 Kaikōura earthquake in New Zealand where ceiling failures were triggered by interactions with services, partitions, and the main structure. Similarly, Chavez and Binder [1996] described extensive non-structural and contents damage at the Veteran Administration hospital in Sepulveda after the 1994 Northridge earthquake. In that case, most of the losses were due to leaking water pipes, which damaged underlying components and caused service interruptions—failures driven not by the pipes' own seismic fragility, but by the secondary effects of interaction. Comparable findings were noted by Miranda et al. [2012] for the Hospital de San Carlos and residential buildings in Santiago following the 2010 Chile earthquake, and by Yoshizawa et al. [2014], who reported that much of the NSE damage during the 2011 Tohoku earthquake in Japan resulted from interactions between equipment and surrounding elements, rather than from direct equipment failure.

These interactions have a major influence on both the extent of damage and the associated loss estimates. Relying solely on fragility functions that neglect such effects is unconservative and can lead to underestimation of economic losses and reduced accuracy in predicting post-earthquake functionality, as seen in the Northridge hospital case. Some of these limitations can be addressed through approaches such as the storey loss functions proposed by O'Reilly and Shahnazaryan [2024] , which account for inter-element damage-state dependencies. For instance, as Chavez and Binder [1996] highlighted, the loss of hospital furnishings may be triggered not by their direct fragility, but by damage to nearby water piping systems.

2.4 QUALITY OF WORKMANSHIP DURING INSTALLATION

Another concern is the difference in workmanship between laboratory-installed test specimens and those installed in real buildings. The representativeness of laboratory specimens is questionable, as contractors tasked with building a small number of NSE specimens for detailed scrutiny are likely to devote more care and precision than they would when installing dozens of similar elements in practice. This does not imply that real-world installations are of poor quality; rather, while construction standards are typically met, test specimens often reflect a much higher standard of workmanship. The PACT fragility function library partially acknowledges this issue by allowing users to specify installation quality for each NSE fragility function set, though no broad guidance is provided on how to apply such distinctions.

2.5 WEAR, TEAR AND UNANTICIPATED INTERVENTIONS

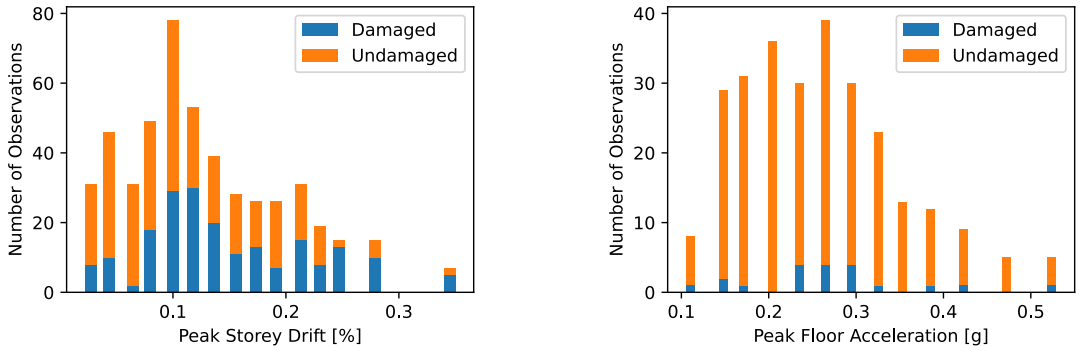
Another factor to consider is that NSEs are elements with which occupants regularly interact and use over time. A door or window that has been opened and closed for years is unlikely to behave the same as a pristine specimen tested in a laboratory. Continuous use can gradually wear down connections and moving parts, allowing for slightly more flexibility and potentially greater resilience to seismic demands. Similarly, piping systems that have been in service or subjected to maintenance may respond differently than new installations. Unplanned modifications can also alter performance—for instance, changes in pipe bracing, openings cut into partitions to accommodate other systems, or window glass replaced with more efficient types. In addition, cumulative effects from past minor earthquakes may cause subtle, unrepaired damage that alters behaviour without being classified as "damage". While these details may appear minor, previous studies have shown that such factors can meaningfully influence NSE performance, making them important to acknowledge in seismic damage assessments.

3. STRUCTURAL HEALTH MONITORING

The points discussed above highlight several ways in which laboratory-based experimental data for NSEs may fall short of accurately representing real conditions, largely due to inherent testing constraints. This does not diminish the value of experimental studies, but it does underscore that their limitations are widely recognised and contribute to overall uncertainty. An alternative approach to developing fragility functions, one that could address many of these challenges, is the collection of data directly from in-situ NSEs through structural health monitoring (SHM). In Japan, such a system has been under development for many years, which is termed q-NAVI has been discussed by Kanda et al. [2021].

3.1 IMPROVED FRAGILITY FUNCTIONS

A major challenge in developing fragility functions from SHM data combined with post-earthquake inspection reports lies in the format of the information obtained. In controlled experimental testing of NSEs (e.g., when applying a quasi-static protocol) multiple specimens can be tested, and the precise engineering demand parameter (EDP) at which each damage state (DS) occurs is recorded. With this data, fragility functions can be derived using the method of moments, known as Method A [Porter et al. 2007]. In contrast, SHM and post-earthquake inspections typically provide only the maximum observed EDPs alongside the final DSs of NSEs. This is a crucial difference, as the recorded EDP reflects the maximum experienced demand, not the actual value at which the DS was triggered. To handle such data, Porter et al. [2007] proposed an alternative "Method B", which relies on bounding information.



(a) Partition walls (b) Suspended ceilings

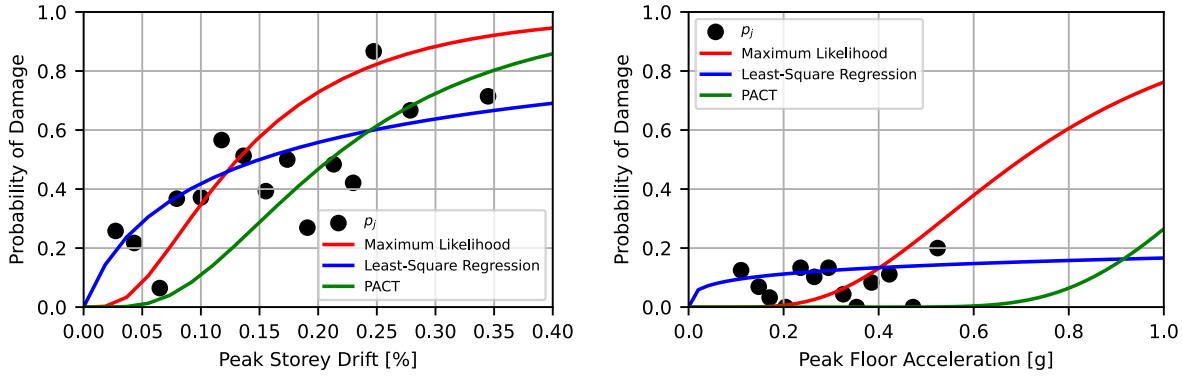
Figure 2: Binned distribution of damage observed following the 2018 Osaka earthquake

For illustration, Ogasawara et al. [2020] collected data from 26 office buildings (7–20 storeys, built between 1974 and 2009) surveyed after the 2018 Osaka earthquake, which was later used by O'Reilly et al. [2024] to develop fragility functions. None of the buildings experienced significant structural damage, but the q-NAVI system provided maximum demand data, while additional surveys assessed usability. Damage classification relied mainly on interviews with building managers about two months after the earthquake, supplemented by photographs taken immediately after the event to confirm early repairs. The dataset included eight NSE typologies, though detailed information was only available for partition walls and suspended ceilings, which showed the most severe damage. Importantly, survey data was recorded in binary form (damaged vs. not damaged). Future studies could improve on this approach by recording graded levels of damage (e.g., light, moderate, extensive), thereby providing a more refined basis for fragility function development.

For partition walls, damage data was collected in both orthogonal directions of the surveyed buildings, yielding a total of 494 observations. These results were grouped into bins and are shown in Figure 2(a). For suspended ceilings, 270 observations were recorded, with the corresponding binned data presented in Figure

2(b). The results clearly indicate that partition walls experienced significantly more cases of damage compared to ceilings.

Fragility functions were developed using both Method B from Porter et al. [2007] and the maximum likelihood estimation approach outlined by Baker [2015]. The results, shown in Figure 3, demonstrate that the Porter et al. [2007] method provided a poor fit to the data. Although the curve follows the available observations closely, it fails to account for data truncation, meaning that additional data would likely shift the trend toward more realistic behaviour. This shortcoming is reflected in the unrealistically high probability estimates at low demand levels. In contrast, the maximum likelihood approach of Baker [2015] produced a much better fit. Baker [2015] also critiqued Method B, noting that applying it in this context disregards the non-uniform variance of the dataset, thereby violating the assumptions of least-squares regression. As seen in Figure 3, this results in inflated probability estimates at very low demands, which is counterintuitive. The issue is particularly evident in the ceiling fragility function [Figure 3(b)], where the probability of damage is nearly constant across all demand levels. By comparison, maximum likelihood fitting captures the overall data trend far more reliably.



(a) Partition walls: fitted function $\{\eta = 0.13\%, \beta = 0.69\}$ and first DS for wall partition components (C3011.001a) in PACT

(b) Suspended ceilings: fitted function $\{\eta = 0.71\text{g}, \beta = 0.50\}$ and first DS for suspended ceilings (C3032.001a) in PACT

Figure 3: Illustration of fragility functions fit using the maximum likelihood method using data collected from the q-NAVI system during the 2018 Osaka earthquake compared with a corresponding fragility function from PACT

While the discussion has so far been limited to the fitting of the fragility functions to the SHM data, another important observation can be made. This is in relation to the previous discussion in Section 2, whereby many existing fragility functions developed based on experimental testing may not be entirely representative of the in-situ reality. To gauge this, comparable fragility functions for both partition walls and suspended ceilings were extracted from the PACT library and plotted in Figure 3. What is immediately clear is that both fragility functions from PACT have median values much higher (around 38% in both cases) than those derived using maximum likelihood fitting on actual data observed during earthquakes. The dispersion values tended to be quite similar, which is contrary to the general recommendations of FEMA P-58 to account for these issues in fragility function development.

Although these findings are preliminary, the relatively large dataset provides support for many of the earlier arguments when compared with actual field evidence. The conclusions draw not only on further analysis and interpretation of the SHM data, but also on the many small observations noted by researchers across numerous NSE experimental campaigns over the years. The key takeaway is that SHM systems such as q-NAVI can serve as a valuable complement to experimental testing, offering an improved basis for developing fragility functions for NSE damage.

3.2 REFLECTIONS BASED ON JAPANESE EXPERIENCE

Since the 2011 Tohoku earthquake, SHM for buildings has gained growing attention in Japan, especially in relation to business continuity and functional recovery. Most systems are market-driven, with building owners choosing to install SHM at their own expense to enable rapid post-earthquake condition assessments, typically classified with *Green*, *Yellow*, or *Red* tags. Fukutomi et al. [2025] report on experiences with SHM to date, including data use, monitoring practices, and engagement with building owners, highlighting three key insights, particularly concerning the advantages of the *Caution (Yellow)* tag.

The first opinion is that the damage criteria, namely the thresholds separating the three tags, should not be regarded as fixed but should instead be updated in light of experience and newly collected data. Immediately following noticeable shaking, one of the three statuses: *Green (Safe)* (i.e., minimal or no damage, continued occupancy ensured), *Caution (Yellow)* (i.e., some damage, no immediate evacuation required, detailed inspection recommended), or *Danger (Red)* (i.e., severe damage, evacuation advised) is provided by the SHM system to building managers and occupants. The *Green (Safe)* classification is based on conditions in which the stresses in primary structural members remain below their short-term allowable limits. A signal warning of potential non-structural damage is triggered when maximum floor acceleration reaches 0.1g. Default threshold values for maximum story drift ratios are set at 1/350 and 1/250 to define the boundaries among *Green*, *Yellow*, or *Red*. These thresholds are considerably smaller than the limits of 1/200 and 1/120 established in modern design codes, the difference reflecting the conservatism adopted to account for uncertainties. After past earthquakes, site visits were conducted, and building damage was observed. It was confirmed that the maximum story drift estimated by the SHM system was consistent with actual behaviour, though structural damage remained minor. This outcome reflected the conservatism of the threshold values. With the agreement of the building owners, the threshold values were subsequently relaxed for those buildings. The experience provided clear evidence that actual earthquake response data can be used to refine and adjust threshold values, thereby making the categorisation of damage states more appropriate.

The second opinion is that SHM represents one of the most effective approaches for characterising the damage and fragility of major non-structural elements, with the *Caution (Yellow)* tag being particularly relevant to non-structural damage in its early stages. Past earthquakes have provided numerous examples in which damage to manufacturing plants and the disruption of machinery severely impeded business continuity. Since the 2000s, when several large earthquakes affected Japan, increasing attention has also been directed toward non-structural damage in office buildings. Reports from these events indicated that the onset and progression of non-structural damage frequently preceded structural damage, with many cases observed where only non-structural elements were affected. Significant efforts have since been devoted to quantifying non-structural damage. However, this task has been constrained by certain characteristics unique to non-structural elements. In particular, their performance is strongly influenced by the manner in which they are connected to primary structural members. The quality of detailing, whether adequate or inadequate, can result in markedly different force transfer to these elements. Fragility functions are typically used to represent non-structural damage, requiring data that defines the relationship between external demands and the resulting level of damage. As previously noted, obtaining such data is far more challenging for non-structural elements than for primary structural members, making its accumulation difficult. In this context, SHM offers considerable value. As illustrated in the preceding subsection, SHM is capable of providing critical data on non-structural elements, thereby addressing a long-standing gap in fragility function development.

The third opinion is that the *Caution (Yellow)* status is a beneficial message for building owners and managers who have established contingency plans supported by readily available maintenance personnel and engineers. In contrast, when such plans are absent, the *Caution (Yellow)* message often generates concern or fear, which in turn discourages the adoption of SHM. From interactions with owners and managers of SHM-equipped buildings, it has been reconfirmed that large corporations managing multiple properties generally possess robust support systems for responding quickly to earthquakes and other hazards. In such

cases, maintenance staff are permanently stationed in each building, continuously monitoring the operation of structural, mechanical, and utility systems such as electricity, gas, and water. In addition, permanent contractual relationships are maintained with construction companies that can be dispatched immediately to address post-event problems, with priority given to the affected building. For owners without comparable support systems, however, the *Caution (Yellow)* status functions less as a useful warning and more as a source of frustration, since no effective action can be taken in response and effectively underscores the lack of adequate planning.

4. SUMMARY AND CONCLUSIONS

This paper has examined key challenges in estimating earthquake-induced damage to non-structural elements (NSEs) and the broader implications for building performance. Drawing on observations from commercial buildings affected by recent Japanese earthquakes, the discussion compared field evidence with developments in current research, particularly in relation to fragility functions and the emerging role of structural health monitoring (SHM). While SHM is often deployed to assess structural safety after major events, it also provides valuable data that can inform the development of more representative fragility functions for NSEs. From the discussions and examples presented, the following conclusions are drawn:

- Fragility functions are essential for estimating damage to both structural and non-structural components. However, those derived for NSEs often lack representativeness, due to factors such as installation conditions and loading protocols in laboratory testing, interactions with other elements, variability in workmanship, and wear or degradation over time. These issues were shown to significantly influence NSE performance and the reliability of associated fragility models.
- SHM offers a promising approach for deriving more representative fragility functions, particularly in cases where structural safety is not immediately at risk. Data collected from several Japanese buildings enabled the development of fragility functions for partition walls and suspended ceilings. Comparison with existing literature demonstrated that these elements may be more vulnerable than suggested by experimental fragility functions, underscoring the importance of real building demand data.
- SHM data combined with interviews with building owners and managers highlighted three key insights. First, the thresholds that define the *Green*, *Yellow*, and *Red* damage tags should not be considered fixed, but rather updated as new data and experience become available. Second, SHM provides one of the most effective means of characterising damage and fragility for major NSEs, with the *Yellow (Caution)* status being particularly relevant for identifying initial stages of non-structural damage. Third, while the *Yellow* status is beneficial for organisations with strong contingency plans and dedicated support systems, it can cause concern for those lacking such resources, discouraging SHM adoption in some cases.

Overall, the study underscores the limitations of experimental fragility models for NSEs and highlights SHM as a complementary and powerful tool for advancing more realistic fragility assessments.

ACKNOWLEDGEMENTS

The work presented here has been developed within the framework of the "Sensor-driven statistical tools to evaluate risks and manage safety in the built environment" (SONATA) project, which is a Starting Grant awarded by the Italian Science Fund (Fondo Italiano per la Scienza) at IUSS Pavia under grant number FIS2023-03215. This work is also supported by the Engineering Research Infrastructures for European

Synergies (ERIES) project (www.eries.eu), which has received funding from the European Union's Horizon Europe Framework Programme under Grant Agreement No. 101058684.

REFERENCES

Baird, A., and Ferner, H. [2017] "Damage to non-structural elements in the 2016 Kaikōura earthquake," *Bulletin of the New Zealand Society for Earthquake Engineering*, Vol. 50, No.2, pp. 187–193.

Baker, J. W. [2015] "Efficient Analytical Fragility Function Fitting Using Dynamic Structural Analysis," *Earthquake Spectra*, Vol. 31, No.1, pp. 579–599.

Bianchi, S., and Pampanin, S. [2022] "Fragility Functions for Architectural Nonstructural Components," *Journal of Structural Engineering*, Vol. 148, No.10.

Bouwkamp, J. G. [1961] "Behavior of window panels under in-plane forces," *Bulletin of the Seismological Society of America*, Vol. 51, No.1, pp. 85–109.

Chavez, C. W., and Binder, B. [1996] "A hospital as victim and responder: The Sepulveda VA Medical Center and the Northridge earthquake," *The Journal of Emergency Medicine*, Vol. 14, No.4, pp. 445–454.

Engle, H. M. [1929] "The earthquake resistance of buildings from the underwriters' point of view," *Bulletin of the Seismological Society of America*, Vol. 19, No.2, pp. 86–95.

Federal Emergency Management Agency. [2012] *Seismic Performance Assessment of Buildings - Volume 1 – Methodology FEMA P-58-1*, *Fema P-58-1*.

FEMA. [2007] *FEMA 461: Interim Testing Protocols for Determining the Seismic Performance Characteristics of Structural and Nonstructural Components*, Washington, DC.

FEMA. [2012] *FEMA E-74: Reducing the Risks of Nonstructural Earthquake Damage – A Practical Guide*, Washington, DC, USA.

Filiatrault, A., Christopoulos, C., and Stearns, S. [2001] "Guidelines, Specifications, and Seismic Performance of Nonstructural Building Components and Equipment," *PEER Report 2002/05*, Berkeley, California, USA.

Fukutomi, Y., O'Reilly, G., Nakashima, M., Kanda, K., Kusaka, A., and Ogasawara, S. [2025] "Three benefits of 'Caution (Yellow Tag)' in SHM-driven condition assessment of buildings: Eight years experience with market-based SHM," *Earthquake Spectra*, Vol. 41, No.1, pp. 979–994.

Gentile, R., Angelucci, G., Wu, J., Di Benedetto, M., Di Trapani, F., Morandi, P., Milanesi, R. R., Mollaioli, F., O'Reilly, G. J., Freddi, F., and Jalayer, F. [2025] "State-Dependent Fragility via Experimentally Validated Energy-Based Approaches," pp. 225–236.

Gentile, R., and Galasso, C. [2021] "Hysteretic energy-based state-dependent fragility for ground-motion sequences," *Earthquake Engineering & Structural Dynamics*, Vol. 50, No.4, pp. 1187–1203.

Huang, J., Kurata, M., Kawamata, Y., Kanao, I., Qi, L., and Takaoka, M. [2022] "In-Plane damage of partition walls with various boundaries during earthquakes," *Earthquake Engineering and Structural Dynamics*, John Wiley and Sons Ltd.

Kanda, K., Nakashima, M., Suzuki, Y., and Ogasawara, S. [2021] "'q-NAVI': A case of market-based implementation of structural health monitoring in Japan," *Earthquake Spectra*, Vol. 37, No.1, pp. 160–179.

Lee, T.-H., Kato, M., Matsumiya, T., Suita, K., and Nakashima, M. [2007] "Seismic performance evaluation of non-structural components: drywall partitions," *Earthquake Engineering & Structural Dynamics*, Vol. 36, No.3, pp. 367–382.

Mergos, P. E., and Beyer, K. [2014] "Loading protocols for European regions of low to moderate seismicity," *Bulletin of Earthquake Engineering*, Vol. 12, No.6, pp. 2507–2530.

Merino, R. J., Perrone, D., Nascimbene, R., and Filiatrault, A. [2023] "Performance-based seismic classification of acceleration-sensitive non-structural elements," *Earthquake Engineering & Structural Dynamics*, Vol. 52, No.13, pp. 4222–4244.

Miranda, E., Mosqueda, G., Retamales, R., and Pekcan, G. [2012] "Performance of Nonstructural Components during the 27 February 2010 Chile Earthquake," *Earthquake Spectra*, Vol. 28, No.S1, pp. S453–S471.

NIST. [2017] *Seismic analysis, design, and installation of nonstructural components and systems - background and recommendations for future work*, Gaithersburg, MD.

Ogasawara, S., Kanda, K., and Suzuki, Y. [2020] "Damage Investigation of Non-Structural Components in Buildings with SHM System in the 2018 Osaka Earthquake," *17th World Conference on Earthquake Engineering*, Sendai, Japan.

O'Reilly, G. J., and Calvi, G. M. [2021] "A seismic risk classification framework for non-structural elements," *Bulletin of Earthquake Engineering*, Vol. 19, No.13, pp. 5471–5494.

O'Reilly, G. J., Hasegawa, K., Shahnazaryan, D., Poveda, J., Fukutomi, Y., Kusaka, A., and Nakashima, M. [2024] "On the fragility of non-structural elements in loss and recovery: Field observations from Japan," *Earthquake Engineering & Structural Dynamics*, Vol. 53, No.3, pp. 1125–1144.

O'Reilly, G. J., and Shahnazaryan, D. [2024] "On the utility of story loss functions for regional seismic vulnerability modeling and risk assessment," *Earthquake Spectra*, Vol. 40, No.3, pp. 1933–1955.

Porter, K. A., Kennedy, R., and Bachman, R. E. [2007] "Creating Fragility Functions for Performance-Based Earthquake Engineering," *Earthquake Spectra*, Vol. 23, No.2, pp. 471–489.

Porter, K., Kennedy, R., and Bachman, R. [2007] "Creating fragility functions for performance-based earthquake engineering," *Earthquake Spectra*, Vol. 23, No.2, pp. 471–489.

Retamales, R., Davies, R., Mosqueda, G., and Filiatrault, A. [2013] "Experimental Seismic Fragility of Cold-Formed Steel Framed Gypsum Partition Walls," *Journal of Structural Engineering*, American Society of Civil Engineers (ASCE), Vol. 139, No.8, pp. 1285–1293.

Richards, P. W., and Uang, C. M. [2006] "Testing Protocol for Short Links in Eccentrically Braced Frames," *Journal of Structural Engineering*, American Society of Civil Engineers, Vol. 132, No.8, pp. 1183–1191.

Taghavi, S., and Miranda, E. [2003] "Response Assessment of Nonstructural Building Elements," *PEER Report 2003/05*, Berkeley, California.

Tasligedik, A. S., Pampanin, S., and Palermo, A. [2012] "Damage states and cyclic behaviour of drywalls infilled within RC frames," *Bulletin of the New Zealand Society for Earthquake Engineering*, Vol. 45, No.2, pp. 84–94.

Wilding, B. V., Dolatshahi, K. M., and Beyer, K. [2017] "Influence of load history on the force-displacement response of in-plane loaded unreinforced masonry walls," *Engineering Structures*, Vol. 152, pp. 671–682.

Yoshizawa, M., Nagae, T., Kajiwara, K., and Nakashima, M. [2014] "Analysis on earthquake damage to non-structural components and furniture sustained by low-rise RC-building and process of recovery from damage," *Journal of Structural Engineering (Japan Society of Civil Engineers)*, Vol. 60, pp. 521–528.

Proposed Ductility-Based Force Factors for Acceleration-sensitive Light Non-Structural Components

Majid Mehrjoo[1], Rola Assi[2]

[1] Department of construction engineering, École de technologie supérieure (ÉTS),
Montreal, Quebec, H3C 1K3, Canada
e-mail: majid.mehrjoo.1@ens.etsmtl.ca
[2] Department of construction engineering, École de technologie supérieure (ÉTS),
Montreal, Quebec, H3C 1K3, Canada
e-mail: rola.assi@etsmtl.ca

Abstract. This study examines the impact of the combined ductility of structural systems and non-structural components (NSCs) on the seismic demands placed on NSCs in moment-resisting frame buildings. The National Building Code of Canada (NBC 2020) estimates the NSC design forces based on elastic building response, using elastic spectral accelerations and a component force factor (S_P), which includes an empirical response modification factor (R_P) to account for NSC ductility. While recent proposed NBC provisions incorporate building period and structural ductility-related factors, both current and proposed approaches still do not explicitly account for the actual level of ductility of NSC attachment.

To address these limitations, nonlinear analyses were conducted on four moderately ductile frame buildings (3-, 6-, 9-, and 12-story) subjected to 24 ground motions matched to Montreal's Uniform Hazard Spectrum for very dense soil and soft rock. The NSCs were modelled with varying ductility capacities (μ_{comp} = 1.0, 1.25, 1.5, and 2.0) using elasto-plastic behavior, and their response was evaluated via time-history analyses with the Newmark integration method. The resulting component force factor (PSA/PGA) curves were validated against 12 detailed NSC models whose backbone parameters were identified in OpenSees with the IMK peak-oriented hysteretic model and implemented in the MATLAB time-history analyses.

The results indicate that structural nonlinearity substantially reduces seismic demands compared to elastic analyses, with reductions of 67–78% for components with elastic attachments and 9–64% for components with ductile attachments. The magnitude of the reduction generally diminishes as attachment ductility increases. The benefits of NSC attachment ductility are most evident when component periods are tuned to the building's fundamental period, where moderate ductility levels ($\mu_{comp} \approx 1.5$) achieve the best balance between performance and practical feasibility. These findings underscore the necessity of developing refined force modification models that capture both structural and non-structural nonlinear behavior.

Keywords: Nonstructural components, Ductility, Nonlinear response, Dynamic analysis, Elasto-plastic behavior.

1. INTRODUCTION

Non-structural components (NSCs) account for approximately 70% of building investment costs and play a crucial role in ensuring building functionality and occupant safety during seismic events [Miranda and Taghavi, 2005; Wang et al., 2021]. These components encompass architectural components (e.g., suspended ceilings, external cladding, and partition walls), building services components (e.g., mechanical, plumbing, electrical, and telecommunication devices), and building contents (e.g., furniture, office equipment) [CSA 2014a]. Post-earthquake reconnaissance has consistently documented NSC vulnerability across major seismic events, beginning with the systematically documented 1971 San Fernando earthquake and extending through the 1994 Northridge, 1995 Kobe, 2010 Maule, and 2023 Turkey-Syria earthquakes. These investigations have consistently demonstrated that NSCs sustain damage before the main structural system, creating life-safety hazards, blocking escape routes, and causing substantial economic losses [Lew et al., 1971; Esper and Tachibana, 1998; Naeim, 2004; Miranda et al., 2012; Perrone et al., 2019; Mehrjoo and Aval, 2024; Tapia-Hernández et al., 2025].

The seismic design of NSCs has evolved significantly, yet significant limitations persist in current code approaches. The National Building Code of Canada [NRC 2020] relies on simplified linear acceleration amplification based on elastic building response, while recent proposed provisions [CBHCC 2024] introduce more sophisticated formulations incorporating building dynamics. However, both approaches share a fundamental limitation: they fail to capture the combined actual nonlinear behavior of supporting structures and varying NSC attachment ductility levels under seismic conditions [Anajafi, 2018; ATC 2018].

Recent research has shown that the ductility of NSC attachments can substantially reduce seismic demands, particularly within the resonance range of a building's fundamental period, and lower repair costs compared to components with elastic attachments. Specifically, components with moderate to high attachment ductility can experience 40–60% less damage [Filiatrault et al., 2018; Obando and Lopez-Garcia, 2018; Mehrjoo and Assi, 2024, 2025a]. However, most of these findings are based on studies that assume elastic structural behavior, raising questions about their applicability when supporting structures undergo inelastic deformations. Previous research has established that inelastic structural responses can either amplify or attenuate floor accelerations compared to linear models, depending on factors such as building height, lateral system flexibility, and NSC period [Taghavi and Miranda, 2012; Ruggieri and Vukobratović, 2024]. The main shortcoming is that the combined effects of structural nonlinearity and component ductility on seismic demands remain insufficiently quantified for NSCs, particularly since the effectiveness of ductility varies with both the resonance ratio between component and structure and the extent of structural yielding.

Building upon the authors' previous work on elastic structural assumptions [Mehrjoo and Assi, 2024], this study investigates these limitations through nonlinear dynamic analysis of four archetype reinforced concrete moment-resisting frame buildings (3, 6, 9, and 12 stories) subjected to ground motions matched to Montreal's Uniform Hazard Spectrum for very dense soil and soft rock conditions. The analyses quantify how structural yielding modifies floor accelerations and, in turn, how NSC-attachment ductility affects the component force factor (S_P), which accounts for the in-structure amplification of ground motion and the component's dynamic properties. Based on these findings, the study proposes revised S_P values calibrated to performance-based design applications.

2. CASE STUDY BUILDINGS, GROUND MOTION SELECTION, AND MODELLING ASSUMPTIONS

This study examined four reinforced concrete moment-resisting frame structures (3, 6, 9, and 12 stories) with limited ductility, symmetric layouts, three 7 m bays in both directions, and uniform 3 m floor heights.

The buildings were designed following the NBC 2015 [NRC 2015] and CSA A23.3-14 [CSA, 2014] provisions, with full design details available in the study by Mazloom and Assi [2022]. The buildings were idealized as one-dimensional stick models with lumped mass and equivalent stiffness concentrated at each floor level, enabling the formulation of mass, damping, and stiffness matrices for the multi-degree-of-freedom (MDOF) systems. The equivalent floor stiffness was computed in ETABS software [CSI 2024] using the flexibility method, which involves applying unit forces to each degree of freedom and inverting the resulting flexibility matrix. Pushover analyses performed with discrete plastic hinge elements at beam-column interfaces per ASCE/SEI 41-23 standard [ASCE 2023], provided story-level yield displacements. The governing equations of motion for the MDOF system were then solved using the step-by-step Newmark integration method ($\gamma = 1/2$, $\beta = 1/6$) implemented in MATLAB [The MathWorks Inc., 2023], with story yield displacements incorporated to capture structural nonlinearity.

For the dynamic analysis, 24 ground motion records were used, comprising 12 historical accelerograms from the PEER NGA-East database [Goulet et al., 2021] and 12 synthetic records from Atkinson's database [Atkinson, 2009]. These motions were spectrally matched to the Montreal Uniform Hazard Spectrum (UHS) for very dense soil and soft rock conditions (NBC Site Class C), with return periods of 475 years and 2,475 years. Detailed selection methodology, spectral matching procedures, and complete modelling details are available in the studies by Mehrjoo and Assi [2024, 2025a].

3. DESCRIPTION OF THE NSCS AND THEIR MODELLING ASSUMPTIONS

Light NSCs with masses less than 0.1% of the supporting structures (303–3211 tonnes) were examined, enabling uncoupled analysis [Amin et al., 1971]. For the parametric study, the NSCs were modeled as single-degree-of-freedom (SDOF) systems positioned at the roof and intermediate floor levels with periods ranging from 0.01 to 2.0 s. Four distinct ductility levels were investigated to develop reliable component force factors: elastic behavior ($\mu_{comp} = 1.0$), low ductility ($\mu_{comp} = 1.25$), moderate ductility ($\mu_{comp} = 1.5$), and high ductility ($\mu_{comp}=2.0$). Ductility was defined as the ratio of maximum to yield displacement ($\mu_{comp} = u_m/u_y$). A bilinear elasto-plastic model was employed for computational efficiency in the parametric analyses while capturing essential nonlinear characteristics of NSCs.

To ensure the reliability of the proposed component force factors, 12 detailed NSC models with varying frequencies (1.0-9.0 Hz) and ductility ratios (μ_{comp} = 1.34-2.6) were adopted from the studies of D'Angela and Magliulo [2024 a; 2024 b; 2025]. These NSC models were used for comprehensive validation using advanced nonlinear models that incorporate realistic cyclic behavior. These advanced models include explicit deterioration mechanisms covering stiffness degradation (post-capping softening and cyclic degradation of unloading/reloading stiffness), strength deterioration, and rotation-capacity deterioration. These models represent cantilever-type NSCs with hollow square steel sections (S275 steel, Fy = 275 MPa), covering four frequency ranges and three ductility categories, as detailed in Table 1 and illustrated by their backbone curves in Fig. 1(d). These models were reproduced in OpenSees [McKenna et al., 2010] using the modified Ibarra–Medina–Krawinkler (IMK) peak-oriented hysteretic formulation to extract the backbone-curve parameters for the subsequent MATLAB-based uncoupled analysis (Fig. 1 (a-c)). Each NSC was modeled using zero-length rotational spring elements connected to elastic beam-column elements, with backbone curve parameters, initial stiffness (K_0), yield moment (M_γ), yield rotation (θ_γ), capping rotation (θ_c), residual rotation (θ_r), and ultimate rotation (θ_u).

A uniform modal damping ratio of 5% was adopted for all analyses, consistent with previous sensitivity studies that demonstrated minimal influence of damping variations on NSC seismic demands [Mehrjoo and Assi, 2024, 2025a].

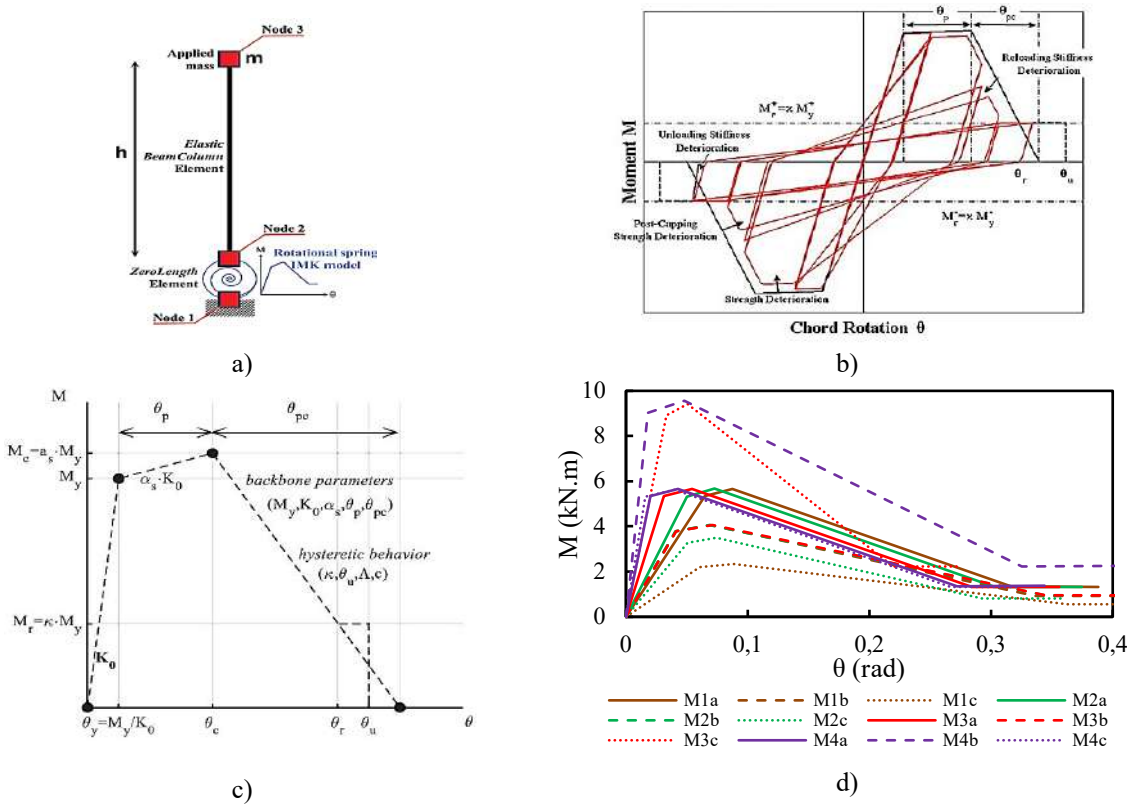


Fig. 1 The numerical model includes: (a) cantilever NSC modeling scheme; (b) the IMK hysteretic scheme, implemented in OpenSees, to capture cyclic behavior [Ibarra, 2004; Lignos and Krawinkler, 2013]; (c) an illustrative backbone curve [Magliulo and D'Angela, 2024]; and (d) backbone curves for all SDOF systems obtained from the OpenSees analyses [Mehrjoo and Assi, 2025b].

Table 1- Used NSC models: frequency and ductility parameters across four frequency ranges [Magliulo and D'Angela, 2024].

Frequency	Range I (~1.0 Hz)			Range II (~1.5 Hz)			Range III (~3.0 Hz)			Range IV (>3.0 Hz)		
Model	M1a	M1b	M1c	M2a	M2b	M2c	M3a	M3b	M3c	M4a	M4b	M4c
f (Hz)	1.02	1.03	1.13	1.48	1.52	1.52	2.97	3.04	3.06	5.86	7.34	9.02
μ_{comp} $=(\theta c/\theta y)$	1.34	1.67	1.41	1.46	1.66	1.46	1.76	1.67	1.54	2.15	2.42	2.6

Based on their natural-frequency characteristics, the 12 NSC models fall into two primary NBC [2020] categories: M1 and M3 groups correspond to suspended ceilings, light fixtures, and other ceiling attachments [McCormick et al., 2012], classified as NBC Category 7, while M2 and M4 groups represent machinery, fixtures, equipment, and tanks with contents [ASCE 2022], classified as NBC Category 12.

4. NSC SEISMIC DEMAND

This section presents the NSC seismic demands at the roof and intermediate floor levels, extending the elastic structural response analysis of Mehrjoo and Assi [2024] to incorporate structural nonlinearity effects. The intermediate floors considered are level 6 in the 12-storey building, levels 4 and 5 in the 9-storey building, level 3 in the 6-storey building, and level 2 in the 3-storey building. The analysis focuses on the mean response across all records and case studies and is organized into two parts. The first examines current

NBC provisions for calculating S_P factors, evaluating both the existing NBC 2020 method and the alternative formulation recommended for future editions. The second analysis focuses on the S_P force factor, examining how structural nonlinearity and component ductility influence the component force factor (PSA/PGA) across the entire period range considered. The computed mean response curves are validated against individual data points from 12 detailed NSC models (M1a -M4c), as illustrated in Fig. 2. The resulting analysis forms the basis for the proposed NSC force factors presented in Section 5.

4.1 ACCORDING TO THE NBC PROVISIONS

In the NBC, the seismic design force for NSCs is determined using a formula in which the S_P factor plays a central role in defining the peak seismic demand on the component. The S_P factor is expressed by Equation (1):

$$S_P = \frac{C_P A_r A_x}{R_P} \quad (1)$$

Where C_p (element/component factor), A_r (element/component force amplification factor), R_p (element/component response modification factor), and A_x (height factor) are as defined in the NBC, with C_p, A_r, and R_p values specified in Table 4.1.8.18.

For the machinery components (Category 12), the NBC specifies C_P = 1.50, A_r = 1.00, R_P = 1.25 for rigid connections, and C_P = 1.50, A_r = 2.50, R_P = 2.50 for flexible connections. For suspended ceiling components (Category 7), the NBC specifies C_P = 1.00, A_r = 1.00, and R_P = 2.50. The S_P factor is constrained to be not less than 0.7 and not greater than 4.0. The NBC offers two approaches for calculating the height factor A_X of the S_P formulation:

1. **NBC 2020 Method ($S_P(1)$):** The current code uses a simplified, linear amplification factor based on the component's relative height in the structure, as shown in Equation (2):

$$A_X = 1 + 2.5\frac{h_x}{h_n} \quad (2)$$

   This approach, designated as $S_P(1)$ in this study, assumes that the A_x factor increases linearly from the base to the roof, reaching a maximum value of 3.

2. **Alternative Code Method ($S_P(2)$):** A new, more detailed formulation has been recommended for future NBC editions [CBHCC 2024] to better capture the dynamic response of buildings, as shown in Equation (3):

$$A_X = \frac{1+\frac{1}{T_{ao}}\left(\frac{h_x}{h_n}\right)+\left(1-\left(\frac{0.4}{T_{ao}}\right)^2\right)\left(\frac{h_x}{h_n}\right)^{10}}{\sqrt{\frac{1.1R_{do}}{I_E}}} \quad (3)$$

   This method, designated as $S_P(2)$ in this study, incorporates the building's fundamental period (T_{ao}), structural ductility-related modification factor (R_{do}), and the importance factor for the building (I_E), aiming for a more realistic demand prediction. However, while $S_P(2)$ incorporates R_{do} to reduce demands based on structural ductility capacity, it relies on empirical fundamental period formulas (T_{ao}) that are calibrated to elastic structural behavior and do not capture the dynamic characteristic changes that occurs when structures respond nonlinearly under strong seismic loading.

To evaluate these code provisions against the proposed factors from this study (Section 5, Table 3), Table 2 compares the S_P values computed using both NBC methods across different building heights and component categories:

Table 2- Comparison of S_P values for NSC categories across building heights using two NBC calculation methods

			3 Storey		6 Storey		9 Storey		12 Storey	
Component Category	Specific Component	Specific Elevation	S_P (1)	S_P (2)	S_P (1)	S_P (2)	S_P (1)	S_P (2)	S_P (1)	S_P (2)
Suspended ceilings, light fixtures, and other attachments to ceilings		Intermediate level	0.7	0.7	0.7	0.7	0.7	0.7	0.7	0.7
		Roof level	1.4	1.41	1.4	1.16	1.4	1.04	1.4	0.97
Machinery, fixtures, equipment, and tanks (including contents)	Flexibly connected	Intermediate level	1.55	1.57	1.42	1.25	1.42	1.19	1.42	1.15
		Roof level	3.5	3.53	3.5	2.9	3.5	2.6	3.5	2.4
	Rigidly connected	Intermediate level	1.25	1.26	1.13	1.003	1.13	0.95	1.13	0.92
		Roof level	2.8	2.83	2.8	2.32	2.8	2.09	2.8	1.94

Analysis of Table 2 for the studied NSC categories (suspended ceilings and machinery components) reveals three key patterns. At intermediate floors, both NBC methods produce similar results: ceiling components reach the minimum S_P value of 0.7, while machinery components show only minor differences between $S_P(1)$ and $S_P(2)$, with $S_P(2)$ being slightly lower in most cases. At roof levels, $S_P(1)$ remains constant regardless of the building height (1.4 for ceilings, 3.5 for flexible machinery, 2.8 for rigid machinery), whereas $S_P(2)$ decreases as building height increases. The largest differences occur in tall buildings at the roof level: for the 12-storey building, $S_P(2)$ predicts substantially lower values than $S_P(1)$, with ceiling components dropping from 1.4 to 0.97, flexible machinery from 3.5 to 2.4, and rigid machinery from 2.8 to 1.94, representing approximately 31% reductions. These patterns establish the baseline for comparison with the nonlinear analysis results presented in Section 4.2.

4.2 COMPONENT FORCE FACTOR (S_P)

The results are presented as a function of the component-to-building period ratio (T_c/T_{b1}), where T_{b1} is the fundamental period of the building and T_C is the component period, as illustrated in Fig. 2.

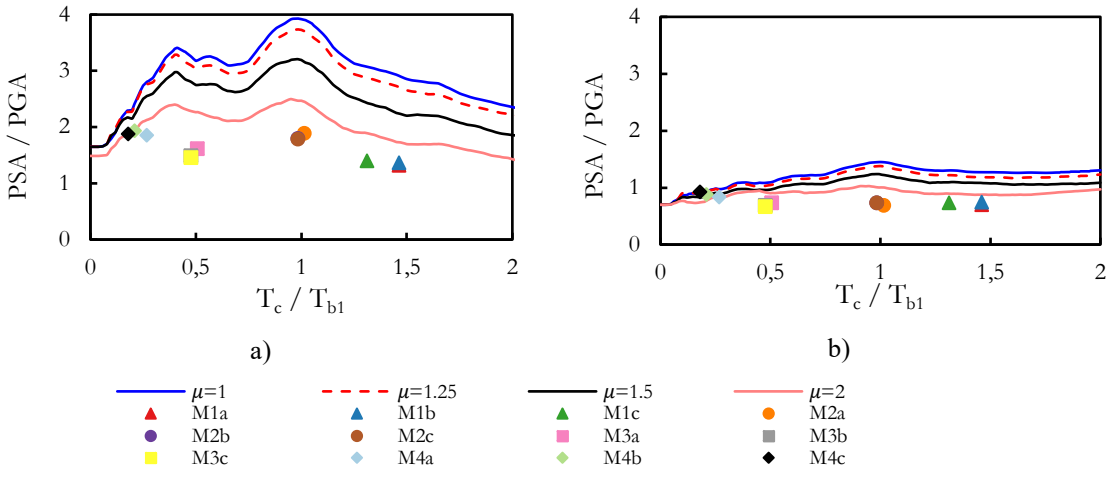


Fig. 2 Mean PSA/PGA values of archetype buildings at two building elevations: (a) roof, (b) Intermediate.

Fig. 2 reveals distinct elevation-dependent response patterns across all ductility levels, with roof-level NSCs experiencing significantly higher amplification than those at intermediate floors. At the roof level (Fig. 2a), the PSA/PGA spectra exhibit a distinct amplification, with PSA/PGA ratios of 3.5-4.0 in the resonant period range ($T_c/T_{b1} \approx 0.5$-1.5), showing a pronounced peak that gradually declines at longer periods. In contrast, intermediate floors (Fig. 2b) demonstrate markedly different behavior with significantly lower amplification (peak ratios of 1.5-2.0) and flatter response spectra that remain stable across the period range. Beyond $T_c/T_{b1} \approx 1.5$, intermediate floors responses converge toward ratios of approximately 0.95-1.2, while roof levels maintain higher amplification (1.4-2.2), indicating off-resonance dominance.

Another key finding is that the building nonlinearity substantially reduces seismic demands compared to elastic building assumptions [Mehrjoo and Assi, 2024], as summarized in Table 3. For elastic components ($\mu_{comp} = 1$), incorporating building nonlinearity reduces seismic demands by 67% at the roof level (from 11.9 to 3.92) and 78% at intermediate floors (from 6.46 to 1.45). This demonstrates that traditional elastic building assumptions noticeably overestimate NSC demands.

Beyond the effects of building nonlinearity, component ductility provides further reductions, primarily at the roof level. Increasing component ductility from elastic behavior ($\mu_{comp} = 1$) to moderate levels ($\mu_{comp} = 1.5$) decreased predicted S_P values at the roof by 15% (from 4.0 to 3.4), while high ductility ($\mu_{comp} = 2$) achieves an additional 21% reduction (from 3.4 to 2.7). In contrast, these ductility-related benefits are minimal at intermediate floors, where values remain relatively constant regardless of component behavior.

The analytical mean-response curves are validated by 12 NSC models (M1a-M4c), represented as individual data points distributed across the period ratio range ($T_c/T_{b1} \approx 0.2$ to 1.5) in Fig. 2. Most points fall below the mean analytical curves at both elevations, confirming the conservative nature of the mean-response curves. The greater vertical variation at the roof level (Fig. 2a) reflects a stronger influence of component characteristics such as attachment flexibility, mass distribution, and modal properties, while the reduced spread at intermediate floors (Fig. 2b) confirms their lower sensitivity.

Evaluation of the nonlinear analysis results against current NBC provisions in Table 2 reveals considerable shortcomings in the code formulations. For flexibly connected equipment at the roof of the 12-storey building, $S_P(1)$ yields 3.5, which is below the 3.92 obtained from nonlinear analysis for components with elastic behavior ($\mu_{comp} = 1$). The alternative method, $S_P(2)$, exhibits an even more pronounced underestimation, calculating an S_P of only 2.4 for the same configuration, nearly 39% below the nonlinear analysis value of 3.92. Similarly, for rigidly connected equipment, $S_P(2)$ predicts only 1.94 compared to 3.92 from the nonlinear analysis. The results demonstrate that current code provisions inadequately capture the nonlinear dynamic amplification effects observed in this study. This conclusion aligns with recent research showing that current code provisions, which rely on linear formulations, tend to underestimate NSC amplification factors and fail to reliably predict peak acceleration responses [Pürgstaller et al., 2020; Challagulla et al., 2023]. In particular, Fazileh et al. [2025] reached similar conclusions for Canadian RC moment-resisting frames when assessing the NBC 2025 equations against floor-response-spectrum demands.

5. PROPOSED FACTORS BASED ON OBTAINED RESULTS

This section presents the proposed S_P factors that incorporate both structural nonlinearity and component ductility effects, providing a realistic representation of seismic demands compared to traditional elastic assumptions. Table 3 presents both the computed mean and proposed S_P values, which are conservatively defined as the mean plus one standard deviation (Mean + STD). For comparison, the "Linear building" column shows S_P values from previous analysis assuming elastic building behavior [Mehrjoo and Assi, 2024].

Table 3- Computed mean S_P values for linear and nonlinear buildings with proposed design values for intermediate and roof levels.

μ_{comp}	Specific Elevation	Linear building	Nonlinear building	STD	Proposed Values
1	Intermediate level	6.46	1.45	0.39	1.9
	Roof level	11.9	3.92	0.18	4
1.25	Intermediate level	3.8	1.38	0.39	1.8
	Roof level	7.0	3.73	0.18	3.9
1.5	Intermediate level	2.4	1.23	0.3	1.5
	Roof level	4.5	3.2	0.21	3.4
2	Intermediate level	2.15	1.0	0.2	1.2
	Roof level	2.7	2.47	0.19	2.7

In Table 3, the small standard deviations (0.18-0.39) indicate high consistency across all building heights and ground motion records, confirming the reliability of the mean predictions. Consequently, the proposed values introduce only a minimal conservative margin, for instance, 4.0 versus 3.92 at the roof for elastic components, thereby ensuring safety without excessive conservatism.

For design purposes, Sp factors should be selected based on the attainable ductility of attachment0. For components with standard rigid connections, the values in the $\mu_{comp} = 1$ row are recommended ($S_P = 4.0$ at the roof, 1.9 at the intermediate floors). Where reliable ductile detailing can be implemented, the moderate ductility level ($\mu_{comp} = 1.5$) is recommended as the optimal design target, providing justified reductions ($S_P = 3.4$ at the roof) that translate directly to reduced installation and repair costs. Higher ductility levels ($\mu_{comp} = 2$) offer minimal additional benefit and are generally not recommended due to increased detailing complexity and uncertainty in nonlinear response.

6. CONCLUSION

This study investigates the influence of structural nonlinearity and component ductility on the component force factor (S_P) for acceleration-sensitive NSCs. The analysis, validated using the responses of 12 detailed NSC models, which showed excellent agreement with the computed mean response curves, yields key findings that provide quantitative evidence of substantial inaccuracies in current NBC provisions. These findings point toward more refined design approaches, particularly for taller buildings.

First, this study quantifies the combined effects of structural nonlinearity and component ductility on NSC demands, demonstrating reductions of 15-34% compared to traditional elastic analysis, depending on component ductility levels.

Second, a moderate component ductility of $\mu_{comp} \approx 1.5$ emerges as the optimal design target, reducing the roof-level S_P value substantially from 4.0 (elastic) to 3.4. This level of ductility offers considerable benefit while avoiding the complex and less predictable responses observed at higher ductility levels.

Third, component elevation is an important factor, with roof-level NSCs experiencing S_P demands that are 111-127% higher than those at intermediate floors. Moreover, the beneficial effects of component ductility are also most significant at the roof level.

Fourth, comparison with current NBC provisions indicates that both approaches are unconservative for mid- to high-rise buildings. The NBC 2020 approach ($S_P(1)$) is inaccurate because its assumed linear acceleration amplification profile does not represent the true dynamic response of nonlinear structures. The alternative NBC approach ($S_P(2)$) becomes particularly unconservative at the roof level, underestimating seismic demands by 39% in some cases, owing to its reliance on empirical fundamental period formulas that fail to capture structural nonlinear behavior under seismic loading. Furthermore, neither NBC approaches explicitly accounts for the level of ductility of NSC attachments (μ_{comp}) in the S_P calculation, overlooking the considerable potential for reducing seismic demands through controlled component nonlinearity.

Acknowledgments

The authors gratefully acknowledge the financial support from Le Centre d'études interuniversitaire des structures sous charges extrêmes (CEISCE). Special thanks to the research associate, Mr. Shahabaldin Mazloom, for carrying out the design of the case study buildings. The authors also wish to thank Dr. Gennaro Magliulo and Dr. Danilo D'Angela for their permission to reproduce their 12 NSC models and use Figure 1 from their paper "Seismic response and capacity of inelastic acceleration-sensitive nonstructural elements subjected to building floor motions" [D'Angela et al., 2024; Magliulo and D'Angela, 2024; D'Angela and Magliulo, 2025].

Data Availability Statement

Data generated or analyzed during this study are available from the corresponding author upon reasonable request.

Competing Interests

The authors declare there are no competing interests.

REFERENCES

American Society of Civil Engineers (ASCE), [2023] Seismic Evaluation and Retrofit of Existing Buildings. https://doi.org/10.1061/9780784416112

American Society of Civil Engineers (ASCE), [2022] Minimum Design Loads and Associated Criteria for Buildings and Other Structures.

Amin, M., Hall, W.J., Newmark, N.M., Kassawara, R.P., [1971] Earthquake Response of Multiply Connected Light Secondary Systems by Spectrum Methods, in: Proceedings of the 1st National Congress on Pressure Vessels and Piping, American Society of Mechanical Engineers, New York, NY. American Society of Mechanical Engineers, San Francisco, California, pp. 103–129.

Anajafi, H., [2018] Improved Seismic Design of Non-Structural Components (NSCs) and Development of Innovative Control Approaches to Enhance the Seismic Performance of Buildings and NSCs. University of New Hampshire.

Applied Technology Council (ATC), [2018] Recommendations for improved seismic performance of nonstructural components (No. NIST GCR 18-917-43). National Institute of Standards and Technology, Gaithersburg, MD. https://doi.org/10.6028/NIST.GCR.18-917-43

Atkinson, G., [2009] "Earthquake Time Histories Compatible with the 2005 National Building Code of Canada Uniform Hazard Spectrum." *Canadian Journal of Civil Engineering*, Vol. 36, pp. 991–1000. https://doi.org/10.1139/L09-044

Canadian Board for Harmonized Construction Codes (CBHCC), [2024] Proposed Change 1901: Modification of the Requirements for Determining the Specified Lateral Earthquake Force (Proposed Code Change). Ottawa, Canada.

Canadian Standards Association (CSA), [2014a] Seismic Risk Reduction of Operational and Functional Components (OFCs) of Buildings.

Canadian Standards Association (CSA), [2014b] *Design of concrete structures*, Sixth edition. ed. CSA A23.3-14 (2014a).

Challagulla, S.P., Kontoni, D.-P.N., Suluguru, A.K., Hossain, I., Ramakrishna, U., Jameel, M., [2023] "Assessing the Seismic Demands on Non-Structural Components Attached to Reinforced Concrete Frames." *Applied Sciences*, Vol. 13, No. 3, pp. 1817. https://doi.org/10.3390/app13031817

Computers and Structures Inc. (CSI), [2024] ETABS-Building Analysis and Design.

D'Angela, D., Magliulo, G., [2025] "Methodological Guidance and Quantitative Measures Regarding Seismic Capacity and Safety of Freestanding and Inelastic Anchored Nonstructural Elements Housed in Ordinary and Critical Facilities." *Reliability Engineering & System Safety*, Vol. 260, pp. 111029. https://doi.org/10.1016/j.ress.2025.111029

D'Angela, D., Magliulo, G., Zito, M., Calenzo, F., [2024] Seismic Fragility of Nonstructural Elements Modelled as Nonlinear Single-Degree-Of-Freedom Systems, in: Proceedings of the World Conference of Earthquake Engineering (WCEE), 1.

Esper, P., Tachibana, E., [1998] "Lessons from the Kobe Earthquake." *Geological Society, London, Engineering Geology Special Publications*, Vol. 15, No. 1, pp. 105–116. https://doi.org/10.1144/GSL.ENG.1998.015.01.11

Fazileh, F., Rodriguez, D., Cai, Z., [2025] "Evaluation of the seismic design equations for non-structural components specified in the National Building Code of Canada." *Journal of Building Engineering*, Vol. 114, pp. 114123. https://doi.org/10.1016/j.jobe.2025.114123

Filiatrault, A., Perrone, D., Merino, R.J., Calvi, G.M., [2018] "Performance-Based Seismic Design of Nonstructural Building Elements." *Journal of Earthquake Engineering*, Vol. 25, No. 2, pp. 237–269. https://doi.org/10.1080/13632469.2018.1512910

Goulet, C.A., Kishida, T., Ancheta, T.D., Cramer, C.H., Darragh, R.B., Silva, W.J., Hashash, Y.M., Harmon, J., Parker, G.A., Stewart, J.P., [2021] "PEER NGA-East Database." *Earthquake Spectra*, Vol. 37, No. 1_suppl, pp. 1331–1353.

Ibarra, L.F., [2004] *Global Collapse of Frame Structures Under Seismic Excitations*. Stanford University.

Lew, H.S., Leyendecker, E.V., Dikkers, R.D., [1971] *Engineering Aspects of the 1971 San Fernando Earthquake*. US National Bureau of Standards.

Lignos, D.G., Krawinkler, H., [2013] "Development and Utilization of Structural Component Databases for Performance-Based Earthquake Engineering." *Journal of Structural Engineering*, Vol. 139, No. 8, pp. 1382–1394. https://doi.org/10.1061/(ASCE)ST.1943-541X.0000646

Magliulo, G., D'Angela, D., [2024] "Seismic Response and Capacity of Inelastic Acceleration-Sensitive Nonstructural Elements Subjected to Building Floor Motions." *Earthquake Engineering & Structural Dynamics*, b, Vol. 53, No. 4, pp. 1421–1445. https://doi.org/10.1002/eqe.4080

Mazloom, S., Assi, R., [2022] "Estimate of V/H Spectral Acceleration Ratios for Firm Soil Sites in Eastern Canada." *Soil Dynamics and Earthquake Engineering*, Vol. 159, pp. 107350. https://doi.org/10.1016/j.soildyn.2022.107350

McCormick, J., Matsuoka, Y., Pan, P., Nakashima, M., [2012] "Evaluation of Non-Structural Partition Walls and Suspended Ceiling Systems Through a Shake Table Study," pp. 1–10. https://doi.org/10.1061/41016(314)223

McKenna, F., Fenves, G.L., Filippou, F., Mazzoni, S., Scott, M., Elgamal, A., Yang, Z., Lu, J., Arduino, P., McKenzie, P., [2010] "OpenSees." *University of California, Berkeley*.

Mehrjoo, M., Assi, R., [2025a] "Probabilistic Assessment of Seismic Acceleration Demands of Ductile Light NSCs in Moderately Ductile RC Frame Buildings." *Engineering Structures*, Vol. 335, pp. 120347. https://doi.org/10.1016/j.engstruct.2025.120347

Mehrjoo, M., Assi, R., [2025b] "Seismic Vulnerability Assessment of Ductile Light NSCs in Moderately Ductile RC Frame Buildings." *Journal of Urban Resilience and Earthquake Engineering (under review)*.

Mehrjoo, M., Assi, R., [2024] "Proposed Reliable Peak Component Factors for Ductile Light NSCs Subjected to Horizontal Ground Motions." *Bull Earthquake Eng.* https://doi.org/10.1007/s10518-024-02081-x

Mehrjoo, M., Aval, S.B.B., [2024] "Proposing New Design and Retrofitting Objectives for Seismic Design of Hospital Structures: A Case Study of Imam Khomeini Hospital in Eslamabad-E Gharb." *Bull Earthquake Eng.* https://doi.org/10.1007/s10518-024-01892-2

Miranda, E., Mosqueda, G., Retamales, R., Pekcan, G., [2012] "Performance of Nonstructural Components During the 27 February 2010 Chile Earthquake." *Earthquake Spectra*, Vol. 28, pp. 453–471. https://doi.org/10.1193/1.4000032

Miranda, E., Taghavi, S., [2005] "Approximate Floor Acceleration Demands in Multistory Buildings. I: Formulation." *J. Struct. Eng.*, Vol. 131, No. 2, pp. 203–211. https://doi.org/10.1061/(ASCE)0733-9445(2005)131:2(203)

Naeim, F., [2004] "Impact of the 1994 Northridge Earthquake on the Art and Practice of Structural Engineering." *The Structural Design of Tall and Special Buildings*, Vol. 13, No. 5, pp. 373–389. https://doi.org/10.1002/tal.280

National Research Council Canada (NRC), [2020] National Building Code of Canada (NBCC). https://doi.org/10.4224/W324-HV93

National Research Council Canada (NRC), [2015] National Building Code of Canada (NBCC).

Obando, J.C., Lopez-Garcia, D., [2018] "Inelastic Displacement Ratios for Nonstructural Components Subjected to Floor Accelerations." *Journal of Earthquake Engineering*, Vol. 22, No. 4, pp. 569–594. https://doi.org/10.1080/13632469.2016.1244131

Perrone, D., Calvi, P.M., Nascimbene, R., Fischer, E.C., Magliulo, G., [2019] "Seismic Performance of Non-Structural Elements During the 2016 Central Italy Earthquake." *Bull Earthquake Eng*, Vol. 17, No. 10, pp. 5655–5677. https://doi.org/10.1007/s10518-018-0361-5

Pürgstaller, A., Quintana Gallo, P., Pampanin, S., Bergmeister, K., [2020] "Seismic Demands on Nonstructural Components Anchored to Concrete Accounting for Structure-Fastener-Nonstructural Interaction (SFNI)." *Earthquake Engineering & Structural Dynamics*, Vol. 49, No. 6, pp. 589–606. https://doi.org/10.1002/eqe.3255

Ruggieri, S., Vukobratović, V., [2024] "The Influence of Torsion on Acceleration Demands in Low-Rise RC Buildings." *Bull Earthquake Eng*, Vol. 22, No. 5, pp. 2433–2468. https://doi.org/10.1007/s10518-024-01873-5

Taghavi, S., Miranda, E., [2012] Probabilistic Study of Peak Floor Acceleration Demands in Nonlinear Structures, in: Proceedings of the 15th World Conference on Earthquake Engineering (15WCEE), Lisbon, Portugal.

Tapia-Hernández, E., Geneş, M.C., Guerrero-Bobadilla, H., [2025] "Structural Behavior of Hospitals During the Kahramanmaraş Earthquake of February 6, 2023." *Earthquake Spectra*, Vol. 41, No. 2, pp. 1589–1615. https://doi.org/10.1177/87552930241298678

The MathWorks Inc., [2023] MATLAB.

Wang, T., Shang, Q., Li, J., [2021] "Seismic Force Demands on Acceleration-Sensitive Nonstructural Components: A State-of-the-Art Review." *Earthq. Eng. Eng. Vib.*, Vol. 20, No. 1, pp. 39–62. https://doi.org/10.1007/s11803-021-2004-0

Shake-table Tests on Full-Scale Non-Structural Elements in a Low-Damage 3-Story Steel Building: Key Results from the ROBUST Project

Rajesh P. Dhakal[1], Jitendra Bhatta[1], Rajesh Shrestha[2], Aasish Tiwari[2], Ping Xiang[3], Zhenduo Yan[4], Yu'ao Lin[3], Sixian Cao[3], Jiajun Yu[3], Yiqing Liu[3], Gregory A. MacRae[1], Geoffrey Rodgers[5], Shahab Ramhormozian[4], G. Charles Clifton[6], Liang-Jiu Jia[3] and Xianzhong Zhao[3]

[1] Department of Civil and Environmental Engineering, University of Canterbury, Christchurch, New Zealand, {rajesh.dhakal,jitendra.bhatta,gregory.macrae}@canterbury.ac.nz

[2] Department of Civil and Environmental Engineering, University of Canterbury, Christchurch, New Zealand, {rajesh.shrestha,aasish.tiwari}@pg.canterbury.ac.nz

[3] College of Civil Engineering, Tongji University, Shanghai, China, {p.xiang,2211319,2310458, 1952627, 2232509,lj_jia,x.zhao}@tongji.edu.cn

[4] Department of Built Environment Engineering, Auckland University of Technology, Auckland, New Zealand, {zhenduo.yan, shahab.ramhormozian}@aut.ac.nz

[5] Department of Mechanical Engineering, University of Canterbury, Christchurch, New Zealand, geoff.rodgers@canterbury.ac.nz

[6] Department of Civil Engineering, University of Auckland, Auckland, New Zealand, c.clifton@auckland.ac.nz

Abstract. The RObust BUilding SysTems (ROBUST) project aims to enhance the seismic resilience of buildings by introducing and validating low-damage concepts for structural and non-structural elements. A three-story, full-scale, structural steel building was tested at the International Joint Research Laboratory of Earthquake Engineering (ILEE) at Tongji University under unidirectional and bidirectional horizontal shakings. The test included multiple structural details and non-structural elements representative of typical New Zealand design and construction practices, alongside low-damage concepts.

The testing program focused on acceleration and drift-sensitive non-structural elements, encompassing five key elements: (1) suspended ceilings, (2) partition walls, (3) precast concrete cladding panels, (4) glazed curtain wall systems, and (5) fire sprinkler piping systems. Drift-sensitive partition walls were installed on the ground level, while acceleration-sensitive suspended ceilings and fire sprinkler piping systems were located on the upper two floor levels. Precast concrete cladding panels and glazing, sensitive to both drift and acceleration demands, were also attached to the upper stories. Each non-structural element was designed and configured to meet specific performance objectives critical to improving seismic performance. This paper presents the key results and demonstrates how each non-structural element performed under unidirectional and bidirectional seismic motions, offering valuable insights into improving the seismic resilience of buildings.

Keywords: Full-scale dynamic tests, three-storey building, non-structural elements, seismic resilience, low damage systems

1. INTRODUCTION

Non-structural/non-skeletal elements (NSEs) contribute a significant portion of the overall building cost (Khakurel et al., 2020; Taghavi and Miranda, 2003). Damage to NSEs like internal partition walls, suspended ceilings, and precast concrete cladding panels can also lead to significant repair costs and downtime of buildings after earthquakes. In some cases, cladding panel failures have also been found to result in fatalities. In response, innovative low-damage solutions have recently been developed for several NSEs. These include, (1) "rocking" dual-slot track systems for partition walls (Bhatta et al., 2023b, 2023c) , (2) "rocking" connection details of cladding panels to the structure (Bhatta et al., 2022, 2023a, 2023d), (3) Velcro-secured tiles in conventional grid-and-tile ceiling systems (Tiwari et al., 2025) and (4) fully floating suspended ceiling systems (Pourali et al., 2017). While these solutions showed promise in component and sub-assembly testing, comprehensive evaluation at full building scale had not been done because New Zealand did not have appropriate large-scale testing facilities. Recognizing this gap, New Zealand partnered with China's International Joint Research Laboratory of Earthquake Engineering (ILEE) at Tongji University, established in 2015 to foster global seismic research collaboration. This collaboration led to the launch of the RObust BUildings SysTem (ROBUST) Project- a landmark study involving full-scale shaking table tests of a three-story steel building equipped with both low-damage structural and NSE systems (Dhakal, 2019; MacRae et al., 2020). This ambitious initiative aimed to validate an entirely resilient building system capable of withstanding earthquakes with minimal damage to both structural and non-structural elements.

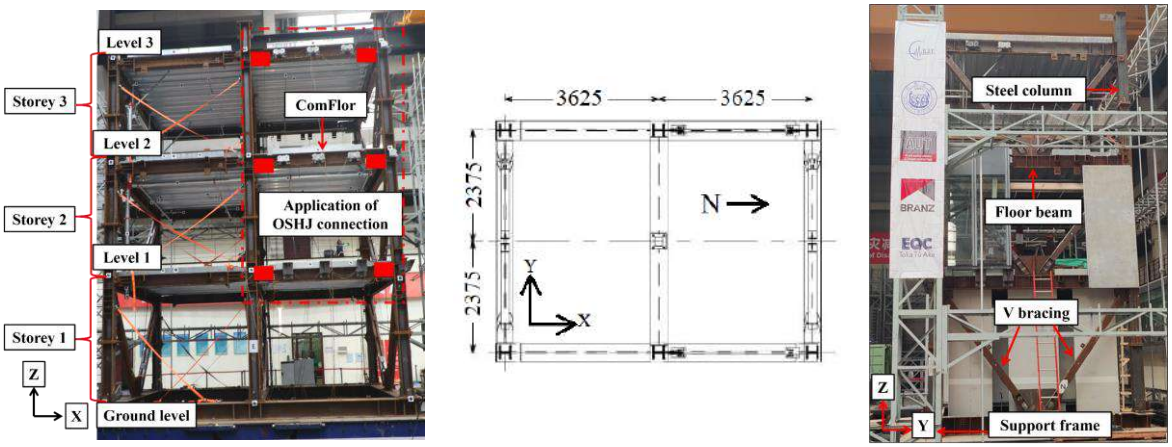
The focus of this paper is to provide an overview of the findings on the seismic performance of the NSEs tested as a part of the ROBUST project. The NSEs encompassed five key elements: (1) suspended ceilings, (2) partition walls, (3) cladding panels, (4) glazed curtain wall systems, and (5) fire sprinkler piping systems.

1.EXPERIMENTAL PROGRAMME

1.1 STRUCTURAL CONFIGURATIONS

The tested building was designed in accordance with NZS 1170.5:2004 (2004) as a three-storey office structure (importance level of 2.0) located in Wellington, New Zealand. It had plan dimensions of 7.25 m in the longitudinal direction (North-South or X) and 4.75 m in the lateral (East-West or Y) direction, with an inter-storey height of 3 m (Figure 1). The site was classified as shallow soil (subsoil class C) with a seismic zone factor of 0.4, and the building was designed for a ductility of 3 with the structural performance factor (Sp) of 0.7. Its primary energy dissipation mechanism was friction at structural connections. The structure was tested under nine different seismic-resisting configurations, all designed to dissipate energy solely through friction. These configurations included moment frames, braced frames, rocking frames, and rocking columns.

Non-structural elements (NSEs) were examined during the final configuration of the testing program. In this configuration, in the longitudinal (NS, X) direction of the structure, the lateral load-resisting system comprised of Bay 1 with pinned connections and Bay 2 as a Moment Resisting Steel Frame (MRSF) incorporating Optimized Sliding Hinge Joints (OSHJ) at the beam-to-column connections, referred to as the MRSF–OSHJ system (Figure 1a). In the transverse (EW, Y) direction, a Concentrically Braced Frame (CBF) with Symmetric Friction Connections using partially squashed Belleville Springs (SFCBeSs) at the brace-to-gusset plate connections, noted as CBF–V–SFCBeSs, provided seismic resistance (Figure 1c). The floor system consisted of ComFlor® 80 with a trapezoidal steel deck and concrete topping. Additional details about the structural system are provided in MacRae et al. (2024).



(a) NS-direction (X) with MRSF – OSHJ system, highlighted in red

(b) Plan view

(c) EW-direction (Y) with CBF– V– SFCBeSs system

Figure 1. Photographs of the final configuration of the three-storey steel test structure (Shrestha et al., 2025)

1.2 NON-STRUCTURAL ELEMENTS (NSES)

The testing program targeted acceleration- and drift-sensitive NSEs, covering five main components: (1) partition walls, (2) cladding panels, (3) suspended ceilings, (4) fire-sprinkler piping system, and (5) glazed curtain wall systems. Drift-sensitive partition walls were installed at ground level, while acceleration-sensitive suspended ceilings and sprinkler piping were positioned on the upper two floors. Precast cladding panels and glazing, being sensitive to both drift and acceleration, were fixed to the upper two storeys. The following section briefly describes the characteristics of these NSEs.

1.2.1 "Rocking" internal partition walls

Three configurations of rocking internal partition walls (L, T, and Planar) incorporating dual-slot tracks (DSTs) from (Bhatta et al., 2023b, 2023c) were installed on the ground floor (Figure 2).

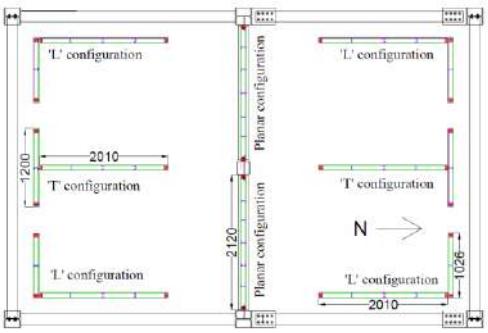


Figure 2. Partition wall layout plan on the ground floor

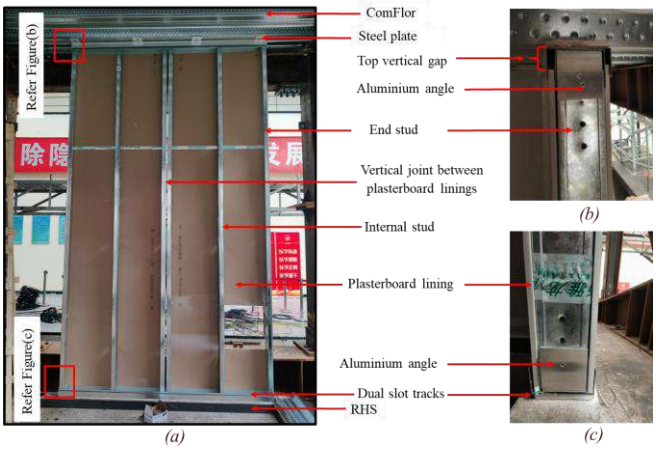


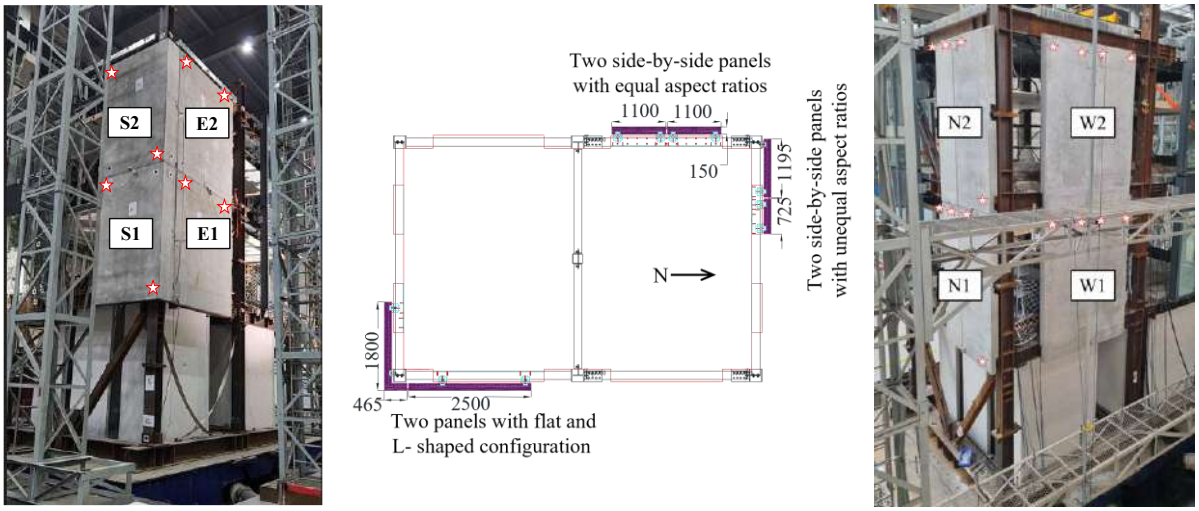
Figure 3. (a) Partition wall during construction; (b) top 'rocking' and (c) bottom 'rocking' connection details with dual-slot track (Shrestha et al., 2025)

The partition walls were 100 mm thick with plasterboard linings, varying in height by location. Bottom tracks of the L and T walls were fixed to Rectangular Hollow Sections (RHS) anchored to the shaking table, while the top tracks were attached beneath ComFlor decking using steel plates where needed. Planar walls were installed between RHS sections, and dual-slot tracks (DSTs) were formed using nested steel tracks with extended flanges for plasterboard insertion. Tracks were anchored with screws and concrete anchors,

and aluminium angles were installed at the ends and junctions for facilitating rocking. Studs at the extremes of all partition wall segment were boxed and their top and bottom ends were filled with timber planks to prevent localized deformation and damage, while intermediate studs were spaced at 500 mm. Studs and linings were free to move within the DSTs, allowing rotation and gap closure under drift, with a designed top gap for 2% in-plane movement. Vertical joints at T and L wall junctions were sealed with silicone and access panels (Luo et al., 2024) were installed at selected locations of the walls to facilitate inspection. Further details on these partition walls can be found in Shrestha et al. (2025).

1.2.2 "Rocking" Precast concrete cladding panels

Twelve full-height precast concrete cladding panels (150 mm thick, 3.05 m high, 40 MPa concrete) were installed on the second and third storeys, six per level, using rocking connections as described in (Bhatta et al., 2022) (Figure 4). Each panel had four vertically slotted steel embeds with vertical slots and two base weld plates. Weld plates supported the panels on welded RHS sections while rocking action takes place through sliding of bolts within vertically slotted steel embeds. Horizontal movement was restrained by tack-welding two (of the four) nuts at selected connections between each panel and the structure, while the remaining two nuts were left free to slide for rocking action (Figure 5). Joints between the panels were 20 to 30 mm wide and were sealed with silicone and cured for three days. Further details are provided in Shrestha et al. (2025).



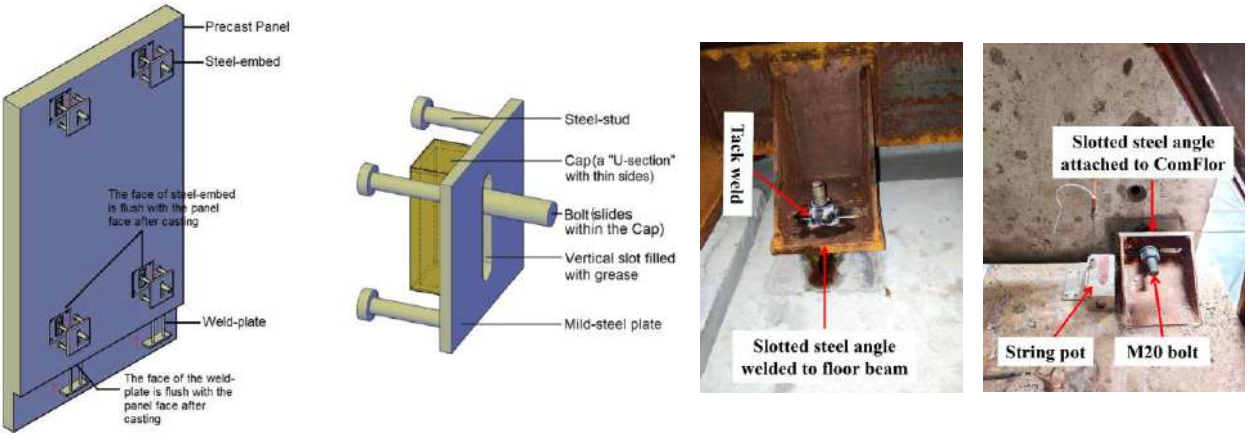
(a) Elevation view of south-east corner **(b) Plan view of layout of cladding panels on floors** **(a) Elevation view of north-west corner**

Figure 4. Arrangement of "rocking" cladding panels (Shrestha et al., 2025)

1.2.3 Velcro-secured lay-in tiles suspended ceilings

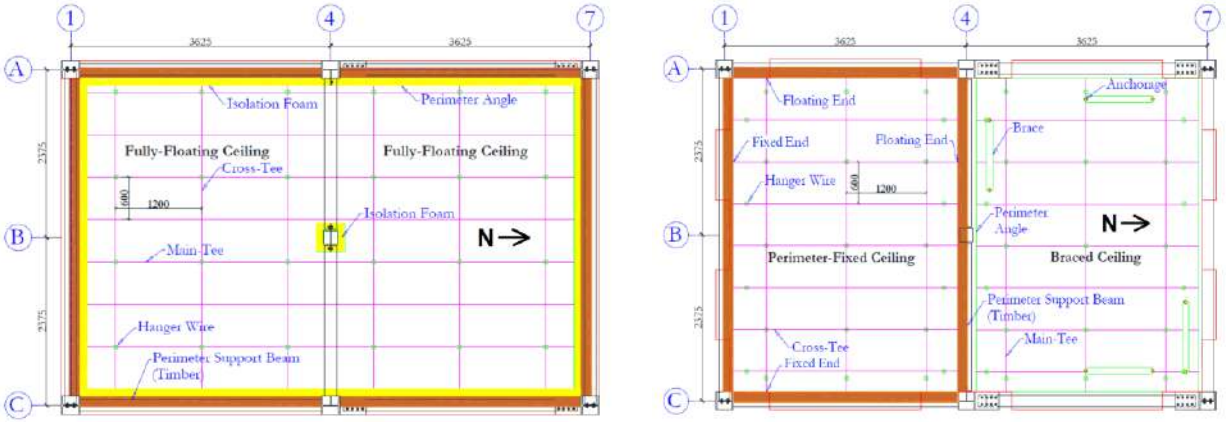
Three types of suspended ceiling systems: (1) perimeter-fixed, (2) braced, and (3) unbraced hung ceilings with isolation foam around the parameter (identified as "fully floating"), were installed on different floors of the test structure (Figure 6). The fully floating ceiling system was installed on floor level 2 of the test structure across its entire span, while perimeter-fixed ceiling system and braced ceiling system were installed on level 3 each type covering the half span.

All three ceiling systems were suspended from the floor slab using 2.68 mm hanger wires and constructed with main grids spaced at 1200 mm and cross grids at 600 mm. Ceiling tiles measured 1200 × 600 × 19 mm and were typically attached to grids with 10-100 mm long Velcrotape strips. Installation began with timber beams between columns, perimeter trims or channels, and suspension of grids from the slab.

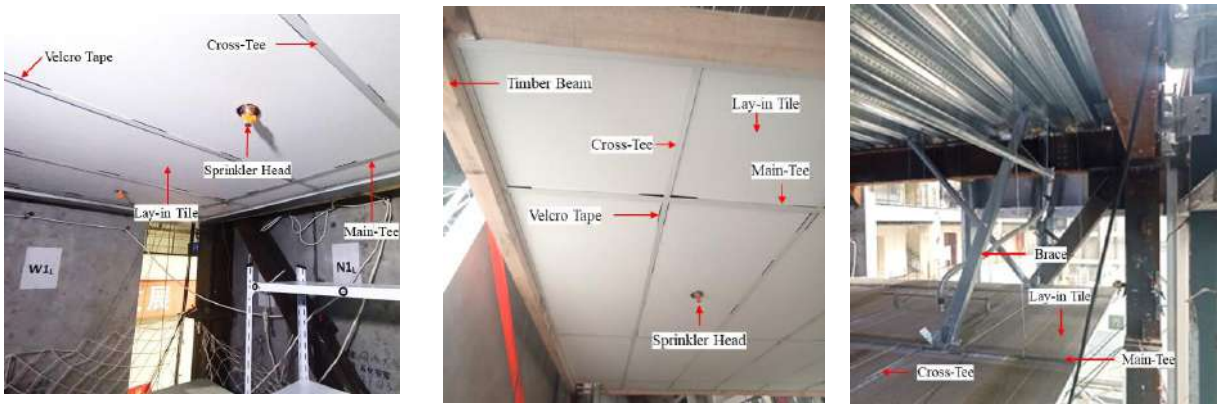


(a) Precast panel with steel-embeds and weld-plates **(b) Steel embed** **(b) Connnection with tack-weld** **(c) Connection without tack-weld**

Figure 5. Cladding panel components and connections to the structure (Bhatta et al., 2022; Shrestha et al., 2025)



(a) Fully floating ceiling installed at floor Level 2 **(b) Perimeter-fixed ceiling and braced ceiling installed at floor level 3**



(c) Fully floating ceiling **(d) Perimeter fixed ceiling** **(e) Braced ceiling**

Figure 6. Schematic plan views and photos of the ceiling systems (Rashid, 2022; Tiwari et al., 2025)

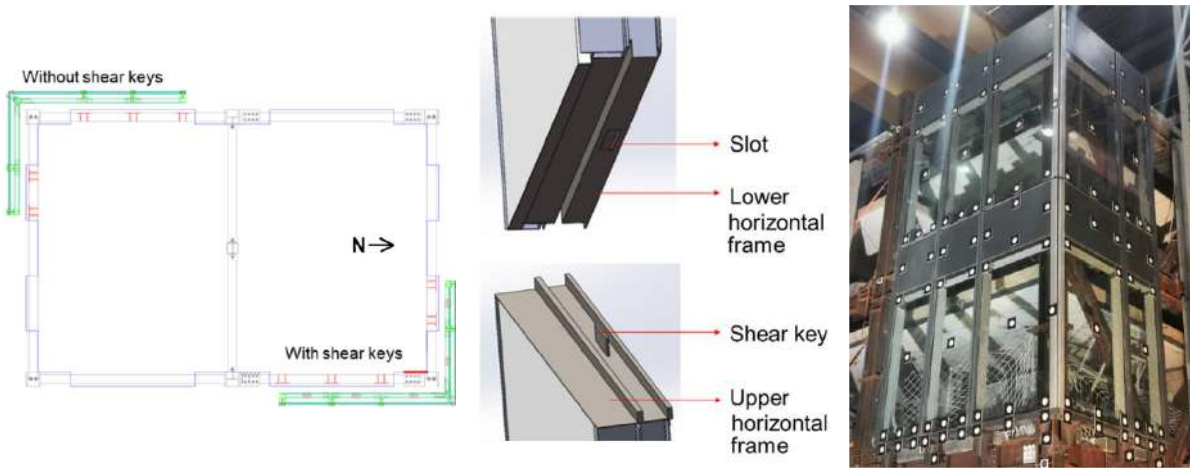
The key distinctions lay in their perimeter connections, bracing arrangements, and plenum depths which are shown in Table 1. Further details are available in Tiwari et al. (2025).

Table 1. Primary distinctions between the three ceiling systems installed in the test structure

Feature	Perimeter-Fixed	Braced	Fully-Floating
Plenum depth	1200 mm	1200 mm	700 mm
Perimeter connection	Double screws secured the tee ends to the perimeter trim, which was then attached to the timber beam on two adjacent sides of the ceiling.	All tee ends fixed to trims with double screws.	Tees were connected to seismic clips first using two screws, and then to the perimeter trim using two screws. Isolation foam was placed between the timber beam and wall angle on a perimeter channel.
Movement mechanism/ allowance	Floating mechanism via seismic clips on two adjacent sides	Gap between the ceiling and other elements around the perimeter	20 mm vertical gap + 10 mm horizontal gap (typical) at perimeter with isolation foam
Bracing	None	Four steel stud braces (no compression posts) in orthogonal directions at four different locations	None
Lateral load resistance	Perimeter connections	Braces	Perimeter gaps allow movement, therefore, no dedicated resistance except isolation foam

1.2.4 Unitized glazed curtain wall system

The unitized glazed curtain wall systems with and without shear keys were installed at the two upper stories of the structure are shown in Figure 7. Shear keys, installed at the middle of the upper horizontal frame and engaging slots in the lower frame of the unit above, were intended to help limit swing and reduce damage under large inter-storey deformations.



a) layout of curtain walls in the test structure **b) Isometric views of shear key and slot** **c) Photo of installed curtain wall system**

Figure 7. Arrangement and details of glazed curtain wall system installed in the test structure (Chen et al., 2020)

1.2.5 Code-compliant fire sprinkler piping system

In this test, fire sprinkler piping systems designed as per the seismic design provisions of (NZS-4541, 2013) were installed on the second and third levels of the building, connected by a riser pipe spanning through the floors (Figure 8). The piping layout differed between the two levels. One of the main objectives of the test was to evaluate the performance of a typical brace assembly (bracing element, pipe and floor attachments, and anchors) and investigate its failure hierarchy. A key limitation was the absence of

pressurized water in the piping system, which reduced the system mass and prevented assessment of leakage-related damage.

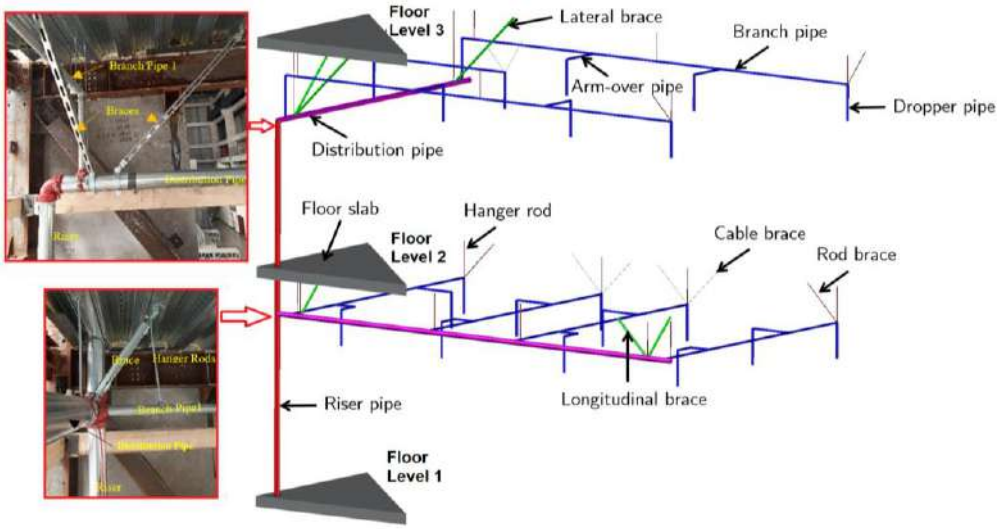


Figure 8. Three-dimensional layout of fire sprinkler piping system installed in the test structure (Rashid, 2022)

2.GROUND MOTIONS, TEST SCHEDULE AND DATA ACQUISTION

A loading sequence was prepared using the Imperial Valley earthquake record (El Centro, 1940, Array #9), scaled per (NZS 1170.5:2004, 2004) to match the target response spectrum for periods between 0.08 s and 1.97 s, covering all structural configurations (see (Bagheri, 2022) for details). The test included twenty-three shaking intensities ranging from 14% to 120% of the Maximum Considered Earthquake (MCE). Tests included unidirectional shaking in the NS/X and EW/Y directions (maximum PGA 0.60 g) and bidirectional shaking at each intensity (maximum PGA 0.88 g in both directions). Between successive shaking intensities, bidirectional white noise was applied to monitor changes in the building components' modal frequencies and damping. Both the structure and NSEs elements were instrumented with displacement transducers, accelerometers, and high-speed Digital Image Correlation (DIC) cameras to capture 3D coordinate changes at key locations.

3.EXPERIMENTAL RESULTS

3.1 PEAK STRUCTURAL RESPONSES

Table 2 summarizes the peak responses of the tested structure, which occurred during the shake with maximum targeted PGA of 0.88g in both directions. Prior to testing in this configuration, the first translational periods in the NS and EW directions were 0.67 s and 0.24 s, respectively. After subjecting the structure to the maximum bidirectional input motion, the periods remained unchanged, suggesting no significant structural (and non-structural) damage occurred that would alter the building's elastic stiffness.

3.1 PERFORMANCE OF NON-STRUCTURAL ELEMENTS

3.1.1 "Rocking" internal partition walls

Figure 10 illustrates typical damage to partition walls. The dual-slot track partition wall successfully resisted both in-plane and out-of-plane drifts, although the first observed damage was flange deformation in L-and

T-shaped walls' dual-slot tracks during 0.4 g PGA NS-direction shaking (causing 1.24% inter-storey drift). Subsequent 0.49 g PGA NS-direction shaking (producing 1.49% drift) led to sealant debonding and separation between the main and return walls of the L and T-shaped walls. Notably, the aluminium angles remained undeformed throughout the test.

Table 2. Peak structural responses of the tested structure during the bidirectional shake with maximum targeted PGA of 0.88g in both directions

Direction	MRSF-OSHJ (NS/X)				CBF-V-SFCBeSs (EW/Y)			
Peak floor acceleration (g)	**Ground Floor**	**Floor Level 1**	**Floor Level 2**	**Floor Level 3**	**Ground Floor**	**Floor Level 1**	**Floor Level 2**	**Floor Level 3**
	0.92	0.80 (0.84) *	0.60	0.90	0.97	0.95	0.60	0.82
Peak inter-storey drift ratios (%)	**Storey 1**	**Storey 2**	**Storey 3**		**Storey 1**	**Storey 2**	**Storey 3**	
	2.12	1.71	1.59		1.50	1.41	1.10	

* Measured during uni-directional shaking with maximum targeted PGA of 0.60 g.



a) Bending of lower dual-slot track (1.24 %) **b) Bending of upper dual-slot track (1.24 %)** **c) Sealant debonding and separation between the main and return wall (1.49 %)**

Figure 10. Damage to partition walls and peak inter-storey drifts at observed damage (Shrestha et al., 2025)

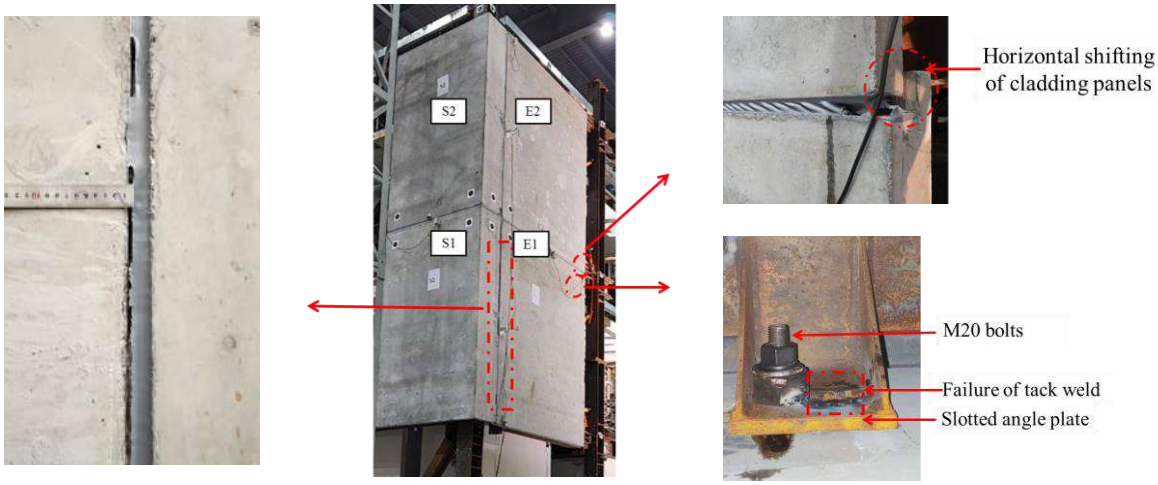
3.1.2 "Rocking" precast concrete cladding panels

The cladding panel system exhibited strong overall performance, with only two of the twelve cladding panels (panels E1 and E2) sustaining minor, easily repairable damage, as illustrated in Figure 11. The primary issues observed included adhesion failure of the sealant between the E1 panel and the adjacent corner panel (S1), as well as weld failure causing sliding of the nuts through the top horizontal slotted plates supporting panels E1 and E2. This weld failure allowed approximately 20-30 mm of horizontal panel displacement, which would necessitate realignment, weld repair, and joint resealing to restore full functionality. All other system components remained intact throughout testing, demonstrating the robustness of the recking cladding system.

3.1.3 Velcro-secured lay-in tiles suspended ceilings

The fully floating ceiling system (at floor level 2) remained undamaged throughout all loading sequences, as did the perimeter-fixed ceiling system at floor level 3, demonstrating high seismic resilience and making them suitable for critical areas where uninterrupted functionality is required (e.g., hospitals, emergency facilities). However, the braced ceiling system at floor level 3 showed signs of damage at different shaking intensities. Figure 12 shows the damage to the braced ceiling and corresponding resultant PFAs. The damage comprised of tearing of encasing material of the ceiling tiles, Tee grid distortion, lay-in tile uplifts (however,

Velcro tape effectively prevented the entire tile from being dislodged), and separation of the main-Tee at the installation joint.



a) Sealant detachment at the vertical joint between panels E1 and S1 (0.51 %)

b) Location of damage to cladding panels

c)Damage to panels E1 and E2 (1.41 %)

Figure 11. Damage to cladding panels and peak inter-storey drifts at observed damage (Shrestha et al., 2025)

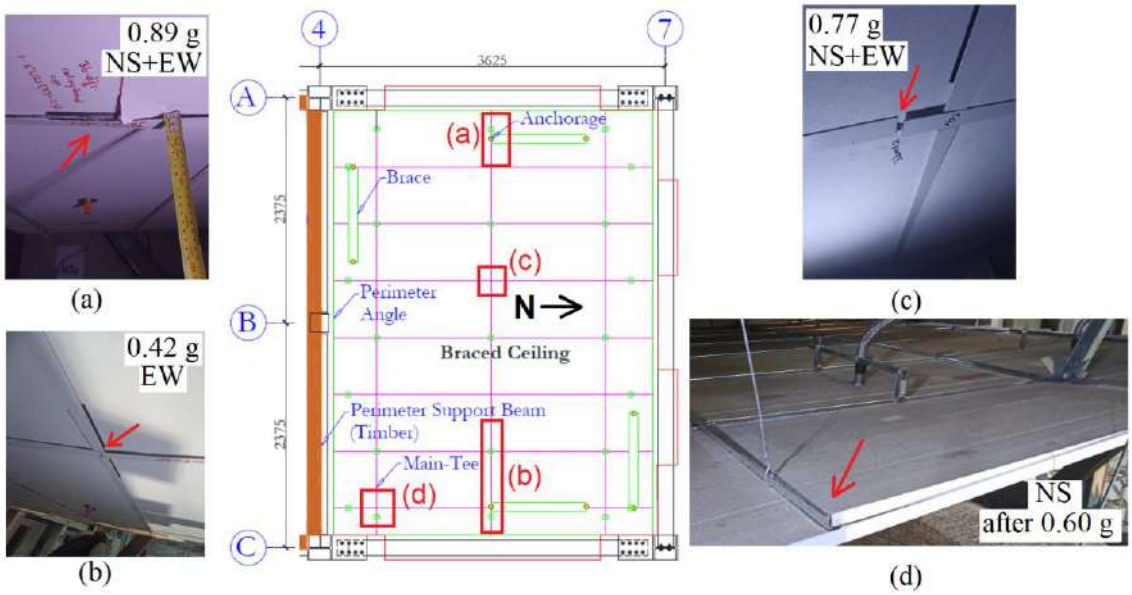


Figure 12. Damage to braced ceiling system and resultant peak floor accelerations and direction of shaking at observed damage: (a) Tearing of encasing material of the lay-in tile; (b) Distortion in one of the main-Tees in the vertical direction; (c) Separation of the main-Tee at the installation joint; (d) Uplift of lay-in tile due to punching shear from a brace at opposite end (Tiwari et al., 2025)

3.1.4 Unitized glazed curtain wall system

There was no significant damage to the curtain wall system, while minor damage was observed as shown in Figure 13. Following the bidirectional 0.88 g PGA shaking, the rubber strips at the end of the panels extruded (Figure 13a). The curtain wall with shear keys showed minimal vibration but developed collision marks at slot edges (Figure 13b). In contrast, the curtain wall panels without shear keys exhibited pronounced shaking, particularly in the NS-direction, while motion in the EW-direction and corner panels remained minimal. As such, the presence of shear keys is effective in controlling vibration and consequently

minimizing serviceability concerns. In the curtain wall panel without shear keys, under 0.1 g PGA NS-direction shaking (0.19 g PFA at floor level 3), permanent gaps formed between the adjacent panels and progressively widened in subsequent shakings (Figure 13c), indicating probable loss of weathertightness, potential water/air infiltration risk and higher maintenance requirements. Additionally, collision marks were also visible on several hooks and connectors (Figure 13d).



a) Extruded rubber strip **b) Collision marks on slots** **c) Widened gap in adjacent curtain wall panels in EW-direction** **d) Collision marks on connectors**

Figure 13. Damage to curtain wall system panels observed after bidirectional 0.88 g PGA shaking

3.1.5 Code-compliant fire sprinkler piping system

The fire sprinkler piping system on Levels 2 and 3 sustained no damage across all applied shakings, confirming that properly fabricated sprinkler systems (equipped with flexible droppers) designed to NZS-4541 (2013) satisfy (if not exceed) the expected performance.

4.CONCLUSIONS

The ROBUST project conducted shaking table tests of a 3-storey steel frame building equipped with low-damage innovative structural systems and multiple drift and acceleration sensitive non-structural elements (NSEs). The test revealed that all evaluated NSEs performed well, with only minor and repairable damage occurring at relatively large shaking intensities. The dual-slot track partition walls displayed a "rocking" behaviour, effectively accommodating both in-plane and out-of-plane drifts. Damage initiation was observed only after relatively high shaking intensities, with flange deformation and sealant debonding being the primary issues. The precast concrete cladding system showed similarly robust performance, with only two panels sustaining minor adhesion and weld failures that could be addressed with minor repairs. The fully floating and perimeter-fixed suspended ceilings demonstrated excellent seismic resilience, remaining undamaged even at high intensity levels. However, the braced ceiling system, though functional, experienced tile tearing, grid distortion, and main-Tee separation. The glazed curtain wall system showed minimal damage, with the inclusion of shear keys proving beneficial in limiting panel vibrations and maintaining serviceability. In contrast, panels without shear keys experienced progressive serviceability issues such as widening gaps and collision marks, indicating greater maintenance needs. Finally, the fire sprinkler piping system, being code-compliant, exhibited no damage or movement under all test scenarios, confirming its adequacy for seismic performance. The results emphasize that well-designed and detailed non-structural elements can achieve high seismic resilience, minimizing post-event downtime and repair costs.

5.ACKNOWLEDGEMENT

The work described was conducted as part of a joint NZ-China research programme with the International Laboratories on Earthquake Engineering (ILEE), Tongji University, Shanghai, China and directly with Tongji University, Shanghai, China. Direct NZ funding is kindly provided by the Building Research

Association of NZ (BRANZ) under the Building Research Levy, EQC Toka Tū Ake, the HERA Foundation (a charitable trust associated with the Heavy Engineering Research Association), the Building Innovation Partnership, the Tertiary Education Commission funded QuakeCoRE (the NZ ILEE partner through whom the NZ funding is also coordinated), and the University of Auckland (UA). Administrative and personnel support is also provided by Auckland University of Technology (AUT), University of Canterbury, and the NZ Ministry of Business, Innovation and Employment, Endeavour Programme on Sustainable Earthquake Resilient Buildings for a Better Future - PROP-83779-ENDRP-AUT). Donations of materials are provided by ComFlor, Hilti Corporation, Tracklok, Gripple, Lanyon & LeCompte Construction Ltd., and Alutech Doors & Windows Ltd. Expertise has been generously provided by several Chinese and NZ industry representatives. The authors gratefully acknowledge this support. We would like to sincerely thank the RObust BUilding SysTem Project team for their support. Opinions expressed are those of the authors alone. This is QuakeCore publication number 1087.

REFERENCES

Bagheri, H. (2022). *Seismic Performance of a Full-Scale Steel Structure Using Resilient Slip Friction Joints.* Auckland, New Zealand: ResearchSpace@ Auckland. https://hdl.handle.net/2292/60019

Bhatta, J., Dhakal, R. P., & Sullivan, T. J. (2023a). Cyclic Behaviour of two-story low-damage rocking precast concrete cladding panel system. *Journal of Earthquake Engineering, 27*(6), 1414–1439.

Bhatta, J., Dhakal, R. P., & Sullivan, T. J. (2023b). Seismic evaluation of rocking internal partition walls with dual-slot track under quasi-static cyclic drifts. *Journal of Earthquake Engineering, 27*(14), 4161–4181.

Bhatta, J., Dhakal, R. P., & Sullivan, T. J. (2023c). Seismic performance of 'rocking'dual-slot track internal partition walls with concealed joints under lateral cyclic drift demands. *Journal of Earthquake Engineering, 27*(8), 2198–2223.

Bhatta, J., Dhakal, R. P., & Sullivan, T. J. (2023d). Seismic performance of a rocking precast concrete cladding panel system under lateral cyclic displacement demands. *Journal of Earthquake Engineering, 27*(4), 929–958.

Bhatta, J., Dhakal, R. P., Sullivan, T. J., & Lanyon, M. (2022). Low-damage rocking precast concrete cladding panels: Design approach and experimental validation. *Journal of Earthquake Engineering, 26*(9), 4387–4420.

Chen, C., Xiang, P., Jia, L. J., Zhao, X., Dhakal, R., MacRae, G., Bhatta, J., Clifton, C., & Dhakal, R. (2020). Seismic behavior of unitized glazed curtain walls in a low-damage structural steel building.

Dhakal, R. (2019). Shake table tests of multiple non-structural elements in a low–damage structural steel building.

Khakurel, S., Dhakal, R. P., Yeow, T. Z., & Saha, S. K. (2020). Performance group weighting factors for rapid seismic loss estimation of buildings of different usage. *Earthquake Spectra, 36*(3), 1141–1165.

Luo, Z., MacRae, G., Xue, J., & Pettinga, D. (2024). Benefit of structural access panels (SAP) for post-earthquake structural health monitoring. *Bulletin of Earthquake Engineering, 22*(4), 1881–1907.

MacRae, G., Dhakal, R., Zhao, X., Jia, L. J., Xiang, P., Clifton, C., Rodgers, G., & Ramhormozian, S. (2020). ROBUST friction building shaking table testing overview.

MacRae, G. A., Jia, L., Yan, Z., Clifton, C., Quenneville, P., Rodgers, G., Dhakal, R., Xiang, P., Ramhormozian, S., & Zhao, X. (2024). The ROBUST steel building response. Paper presented at the *International Conference on the Behaviour of Steel Structures in Seismic Areas,* 562–578.

NZS 1170.5:2004. (2004). *NZS 1170.5:2004, Structural Design Actions Part 5: Earthquake actions*. New Zealand Standard.

NZS-4541. (2013). *NZS 4541: Automatic Fire Sprinkler Systems.* Wellington, NZ: Standards New Zealand.

Pourali, A., Dhakal, R. P., MacRae, G., & Tasligedik, A. S. (2017). Fully floating suspended ceiling system: experimental evaluation of structural feasibility and challenges. *Earthquake Spectra, 33*(4), 1627–1654.

Rashid, M. (2022). Seismic assessment and design of fire sprinkler piping systems.

Shrestha, R., Bhatta, J., Dhakal, R., Sullivan, T., Tiwari, A., Macrae, G. A., Rodgers, G., Xiang, P., Liu, Y., Jia, L., Zhao, X., Yan, Z., Ramhormozian, S., Clifton, G. C., & Quenneville, P. (2025). Seismic behaviour of 'rocking' precast cladding and partition wall assemblies in a full-scale three-storey steel building. Paper presented at the *2025 NZSEE Annual Technical Conference,*

Taghavi, S., & Miranda, M. M. (2003). *Response assessment of nonstructural building elements*. Pacific Earthquake Engineering Research Center.

Tiwari, A., Dhakal, R., Bhatta, J., Sullivan, T., Shrestha, R., Macrae, G., Rodgers, G., Clark, S., North, P., Yu, Z. J., Xiang, P., Jia, L., Zhao, X., Yan, Z., Ramhormozian, S., Clifton, G. C., & Quenneville, P. (2025). Seismic performance of suspended ceilings with Velcro-secured lay-in tiles via shake table tests. Paper presented at the *2025 NZSEE Annual Technical Conference,*

The benefits and advantages of using RC frames with isolated or decoupled infills in practice: INODIS connection

Marko M. Marinković[1] and Christoph H. Butenweg[2]

[1] Chair of Engineering Mechanics and Theory of Structures, Faculty of Civil Engineering, University of Belgrade
Bulevar kralja Aleksandra 73, 11000 Belgrade, Serbia
e-mail: mmarinkovic@grf.bg.ac.rs
[2] Center of Wind and Earthquake Engineering, RWTH Aachen University
Mies-van-der-Rohe-Str. 1, 52074 Aachen, Germany
e-mail: butenweg@lbb.rwth-aachen.de

Abstract. In seismically active regions, reinforced concrete frame buildings with masonry infills are frequently utilized. Infill walls are frequently damaged in the event of a fan earthquake and are subject to both in-plane and out-of-plane loads during seismic activity. According to recent research, the combination of these stresses puts both structures and masonry infills at serious risk. Under such circumstances, conventional mortar-based connections break down, increasing the shear stresses acting on the RC columns and causing the infills to collapse. A novel system called INODIS was created to solve this problem. It uses recycled rubber strips as the infill/frame connection to detach the infill from the frame. Full-scale specimens were used to evaluate this connection under quasi-static cyclic in-plane and out-of-plane loads. At drifts greater than 2%, the first cracks showed up, suggesting that the technique can reduce infill damage and repair expenses. A thorough experimental campaign demonstrates that INODIS provides a way to improve seismic resistance and case study example shows economic benefits by lowering the quantities of concrete and reinforcing required for structural elements. A straightforward design concept was created that makes practical use easy, therefore INODIS presents a significant step forward in improving seismic behaviour of infill walls as non-structural elements, but also of a structure as well.

Keywords: Seismic loading, In-plane load, Out-of-plane load, Non-interacting, INODIS.

1. INTRODUCTION

Reinforced concrete (RC) frame structures with load-bearing elements are commonly found across the globe. Once the RC frames are constructed, masonry walls are typically added as internal and external partitions, firmly bonded to the RC frame with stiff mortar. These walls, known as masonry infills, are often considered non-structural components during seismic design. As a result, the influence of masonry infills is usually accounted for only as an additional vertical load on the RC frame during the structural design process. However, under seismic forces, masonry infills interact with the RC frames, significantly influencing the in-plane behavior of the overall structure. This interaction raises concerns about the accuracy and safety of the structural design. Recent earthquakes in Albania (2019) [Marinković et al., 2022], Croatia (2020) [Marinković et al., 2021], and Turkey (2023) [Dilsiz et al., 2023] have highlighted the severe damage caused to both masonry infills and RC frames, demonstrating that overlooking the role of masonry infills is not a conservative approach. Such oversight can lead to devastating consequences for the safety of residents and the economic stability of impacted areas.

Masonry-infilled RC frames have been extensively studied over the past decades, with much of the research focusing on their in-plane behavior [Mehradi et al., 1994; Morandi et al., 2017; Di Trapani et al., 2024]. These studies have identified several factors, such as frame-to-infill interface conditions, brick thickness, height-to-length ratio, and the presence of openings, that significantly affect the in-plane response of infilled RC frames. With advancements in computational technology, research utilizing numerical models [Nasiri and Liu, 2017; Di Trapani et al., 2018; Kubalski, 2023] to analyze the behavior of infilled RC frames has grown substantially. Despite the wealth of experimental and numerical findings, straightforward and practical methods for incorporating masonry infills into engineering codes remain lacking.

In recent years, research efforts have increasingly focused on creating solutions to enhance the seismic performance of masonry-infilled RC frames. Among these, the concept of decoupling [Tsantilis and Triantafillou, 2018; Jin et al., 2023] has emerged as one of the most promising approaches. However, ensuring the out-of-plane stability of decoupled infills remains a significant challenge. This issue has been addressed with the development of an innovative infill isolation system known as INODIS [Marinković and Butenweg, 2019; Milijaš et al., 2024], which simultaneously offers in-plane decoupling and out-of-plane restraint, providing a comprehensive solution to this problem. In this paper main advantages and benefits of the use of INODIS connection in practice is presented. The efficiency of the system has already been proved in an extensive experimental [Milijaš et al., 2024] and numerical campaign [Marinković and Butenweg, 2022].

2.DESCRIPTION OF THE INODIS CONNECTION

The purpose of the decoupling connection is to enhance both the in-plane drift capacity and the out-of-plane load resistance under individual and combined in-plane and out-of-plane seismic forces. This connection utilizes a durable elastomeric material made from recycled rubber, offering a cost-effective and sustainable solution. Additionally, it is compatible with various brick types and can be easily installed on-site, making it a practical choice for improving the seismic performance of masonry-infilled RC frames.

The conceptual outlook of the INODIS connection for a fully infilled RC frame is illustrated in Fig. 1. The connection comprises three recycled rubber strips. The middle strips are bonded to the surrounding RC frame, while the outer strips are attached to the masonry bricks, using a thin layer mortar as adhesive. Thicker rubber strips with lower stiffness are placed between the masonry infill and the columns to absorb the in-plane deformations of the frame, thereby delaying the activation of the infill. At the top and bottom of the masonry infill, thinner rubber strips with higher compression and shear stiffness are installed. These

thinner strips play a crucial role in ensuring out-of-plane stability by providing stiff boundary conditions that enable strong vertical arching action. Additional strips along the sides of the masonry infill further support its resistance to out-of-plane loads. At the top of the wall, the rubber strips are covered with sliding surfaces. This design allows the RC beam above the infill wall to slide freely, minimizing the transfer of shear forces to the masonry infill through friction.

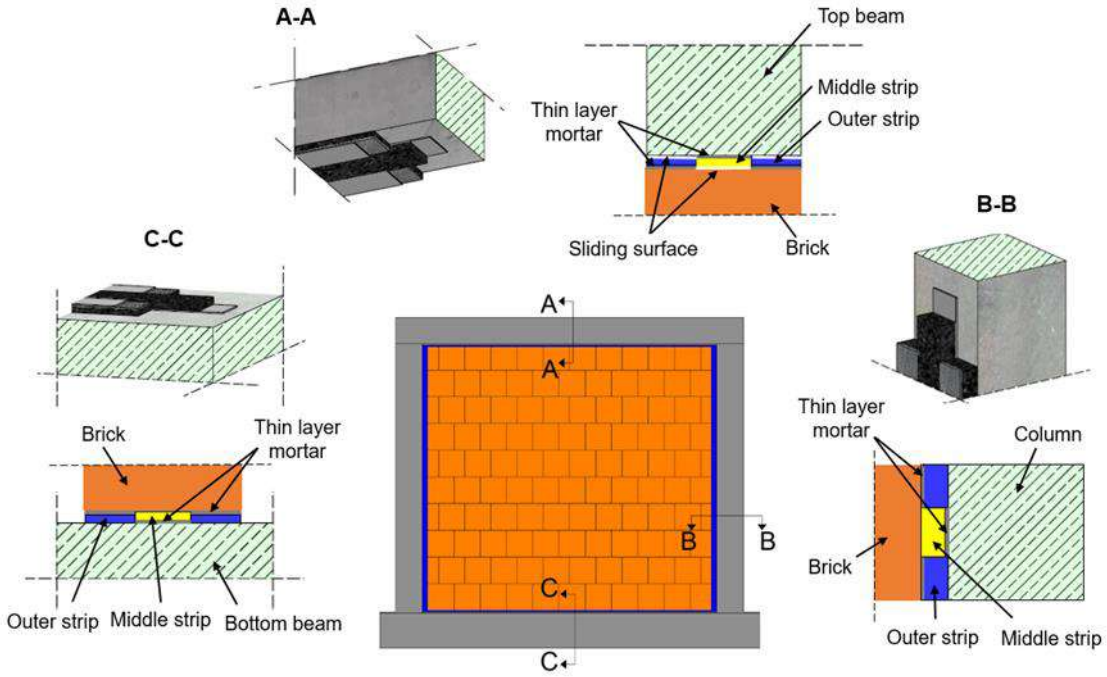


Figure 1. Outlook of the INODIS connection with cross section details [Milijaš et al., 2024]

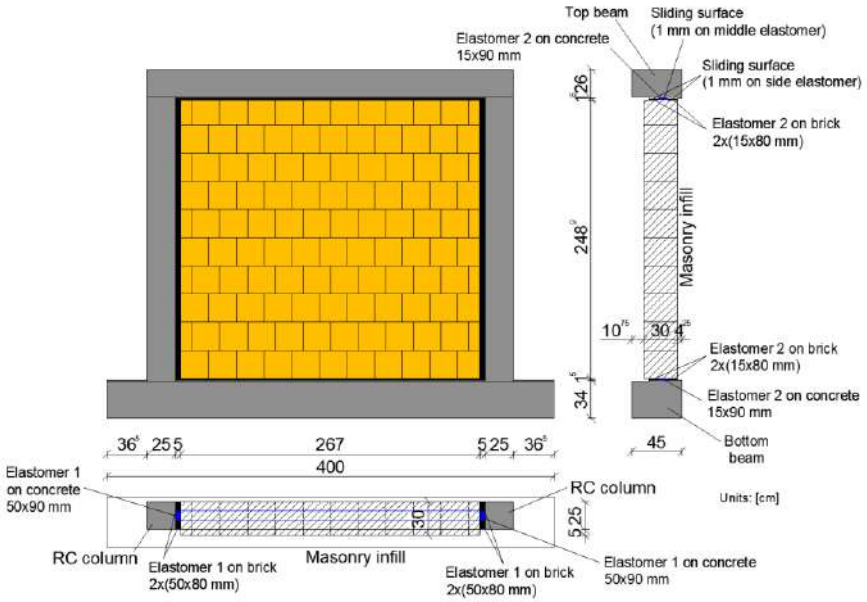


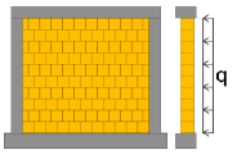
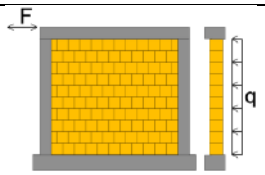
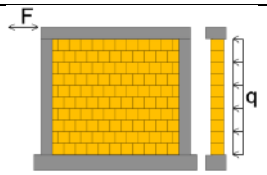
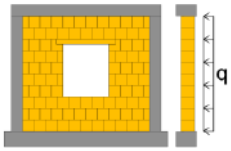
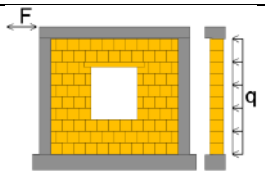
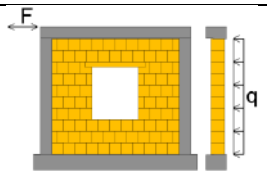
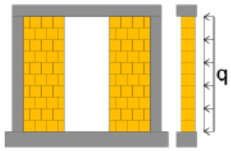
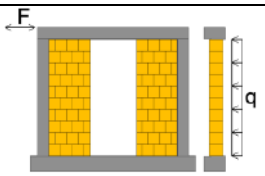
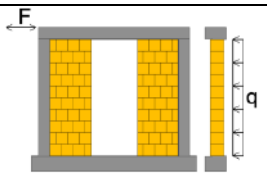
Figure 2. Details of the tested specimen with dimensions [Milijaš et al., 2024]

3.EXPERIMENTAL CAMPAIGN

Within the comprehensive experimental campaign in total 20 tests were conducted. Table 1 gives na overview about the tested specimens, whereas details of 9 tests on traditional infills are given in [Milijaš et

al., 2023] and detailed description of the 9 tests on infilled frames with INODIS connection are presented in [Milijaš et al., 2024]. Within this paper a brief summary of the results is given with the focus on the in-plane behaviour.

Table 1. Test programme with opening arrangements and loading types [Milijaš et al., 2023]

T1/D1: Solid infilled frame **OOP**	**T2/D2: Solid infilled frame** **IP – OOP**	**T3/D3: Solid infilled frame** **OOP + IP**
		
T4/D4: Infilled frame with window opening **OOP**	**T5/D5: Infilled frame with window opening** **IP – OOP - IP**	**T6/D6: Infilled frame with window opening** **OOP + IP**
		
T7/D7: Infilled frame with door opening **OOP**	**T8/D8: Infilled frame with door opening** **IP – OOP - IP**	**T9/D9: Infilled frame with door opening** **OOP + IP**
		

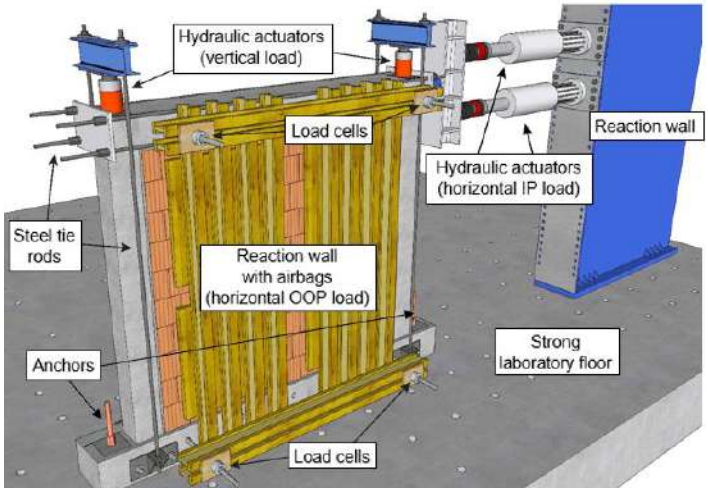


Figure 3. Test setup for the experimental campaign [Milijaš et al., 2023]

Fig. 2 illustrates and gives the dimenaions of an RC frame with a solid masonry infill and the decoupling system installed between the masonry and the RC frame. Fig. 3 shows the test setup. The RC frame used is designed as the exterior frame of a standard five-story building, following the specifications of Eurocode.

The frame and infill geometry, along with the percentage of openings in the infills, are identical to those described by [Milijaš et al., 2023]. This consistency ensures a direct comparison between the performance of traditional infill systems and those with the decoupling system. Details regarding the reinforcement distribution can also be found in the work of [Milijaš et al., 2023].

The important feature of the test set-up used in the experimental campaign is that it can apply in-plane and out-of-plane loads to the masonry infill separately and simultaneously.

Two servo-hydraulic actuators are used to apply cyclic in-plane loading to the RC frame. These actuators are attached to the frame via a rigid steel beam, which is connected at one end to a strong steel plate mounted on the top beam. Four steel tie rods link this steel plate to another identical plate at the opposite end of the top beam. This configuration enables the application of cyclic in-plane displacements in both positive (push) and negative (pull) directions. Due to the high torsional stiffness of the rectangular cross-section of the top beam, no additional restraints are necessary to counter potential torsional effects.

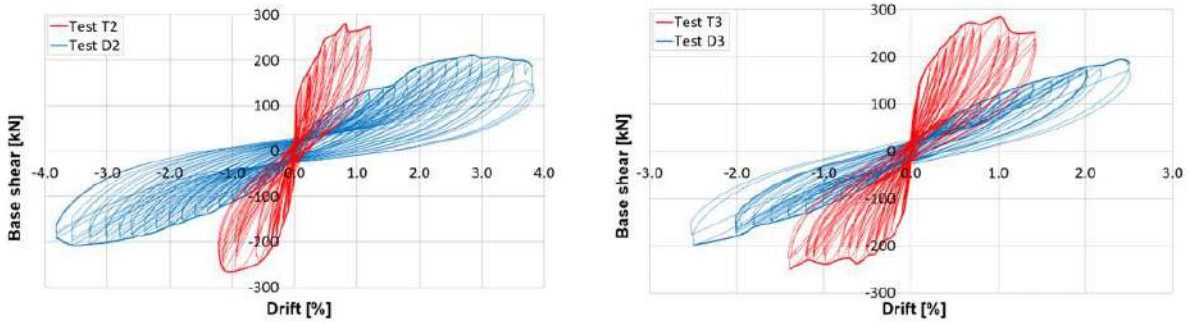


Figure 4. Force-drift hysteresis curves obtained from tests on fully infilled RC frames: sequential (left) and simultaneous (right) loading tests [Milijaš et al., 2024]

For applying out-of-plane loads, four airbags are placed between the back side of the masonry infill and a timber reaction wall. This reaction wall is secured to the top and bottom beams using four threaded rods. To accommodate simultaneous loading tests, the holes for the threaded rods are designed with enough clearance to allow free in-plane movement of the frame while still enabling the infill to be subjected to out-of-plane loads. The airbags are covered with a fleece layer that has a low friction coefficient, minimizing additional frictional forces on the actuators caused by the reaction wall. This setup ensures precise application of both in-plane and out-of-plane loads without interference.

The effect of the decoupling system on the in-plane behaviour of the specimens is assessed by direct comparison of the results obtained from the in-plane loading phases of the tests. Fig. 4 presents the hysteretic curves for solid infilled RC frames, both with and without the decoupling system. The hysteretic curves of RC frames with traditional masonry infills exhibit high initial stiffness and a pronounced pinching effect. In these cases, the maximum in-plane forces are observed at relatively low in-plane drifts, ranging between 0.8% and 1.0%, which coincide with significant damage to the infill walls. In contrast, the hysteretic curves of RC frames with decoupled infills are notably more stable and broader, with lower initial stiffness. The maximum in-plane load capacities are achieved at considerably higher in-plane drifts, exceeding 2.0%. Furthermore, thanks to the decoupling connection, the frames with decoupled infills can accommodate significantly larger in-plane drifts while sustaining minimal or no damage to the masonry infills, highlighting the effectiveness of the decoupling approach in improving seismic performance.

In Fig. 5a, the envelopes of all in-plane loading tests are compared with the envelope of the bare frame test (Test A). The results show that the in-plane response of RC frames with decoupled infills closely resembles that of the bare frame. Up to an in-plane drift of approximately 0.5%, there is no difference between the envelopes of the decoupled infills and the bare frame. This indicates that the initial stiffness and dynamic characteristics of RC frames remain unaffected when decoupling measures are applied. Conversely, RC

frames with traditional infills exhibit significantly increased initial stiffness, which varies depending on the percentage of openings in the infill. This variability complicates the estimation of the dynamic behavior of traditionally infilled frames, unlike the predictable response of frames with decoupled infills.

Fig. 5b presents infill contribution curves, obtained by subtracting the bare frame response from the responses of infilled frames. The curves reveal that decoupled infills are activated to a much lesser extent and only at higher in-plane drifts, compared to traditional infills. For instance:

- In Test T2 (full traditional infill), the maximum force of 192 kN occurs at 0.8% in-plane drift, with severe damage at 1.0%. In Test D2 (decoupled infill), at 1.0% drift, the contribution force is only 25.9 kN, with no infill damage.
- Similarly, in Test T3 (solid traditional infill), the maximum force of 195 kN is reached at 0.64% drift, and the test is terminated at 1.4% drift due to severe damage. In contrast, Test D3 (decoupled infill) shows only 35.8 kN of force at the same 1.4% drift, with minimal damage.

For infills with window openings:

- In Test T5, a maximum force of 115 kN is reached at 0.4% drift, while the decoupled infill in Test D5 remains barely activated at this drift.
- In Test T6, the maximum force of 125.8 kN occurs at 0.8% drift, while the contribution of the decoupled infill in Test D6 is only 16.7 kN at the same drift.
- For infills with door openings:
- In Tests D8 and D9 (decoupled infills), negligible contribution forces are observed, with activation starting only after 2.0% in-plane drift. Conversely, in Test T8 (traditional infill), severe damage occurs at 0.8% drift, and complete collapse follows at 1.6% drift under sequential loading. Under simultaneous in-plane and out-of-plane loading, traditional infill with a door collapses at just 1.0% drift.

The infill contribution curves confirm that traditional infills strongly interact with the RC frame at very low in-plane drifts ($\Delta \leq 0.3\%$). In contrast, significant interaction between the frame and decoupled infills occurs only at higher drifts, exceeding 2.0%. This highlights the effectiveness of the decoupling system in minimizing frame-infill interaction and reducing infill damage under seismic loading conditions.

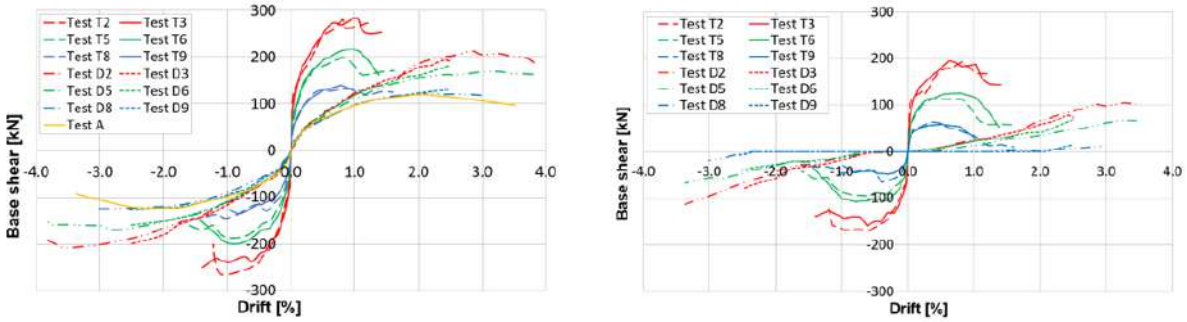


Figure 5. Comparison of force-drift in-plane envelopes from the sequential and simultaneous tests (left) and comparison of in-plane contribution curves from the sequential and simultaneous tests (right) [Milijaš et al., 2024]

4.DESIGN EXAMPLE ON CASE STUDY BUILDING

Parametric study presented in [Marinković and Butenweg, 2025] shows that infills with INODIS connection do not affect the dynamic characteristics of an RC structure, because the stiffness ratio of infilled frame with INODIS and bare frame is small whenever infill activation force is less than 30% of infill load capacity force. Thus, a straightforward design guideline may be to limit the amount of decoupled infill wall activation

to 30% of its load capacity ($H_{INF}<0.3V_{INF}$). This enables the contribution of the infill and effect to the RC structure (stiffness and shear force in columns) to be disregarded in all circumstances. This suggests that a decoupled infill wall does not require explicit simulation; rather, the thickness of the rubber (the gap's size) in the case of the INODIS connection must be sufficiently large to satisfy this requirement. This is made easy by calculating the compression force in rubber along the whole contact zone between the frame and infill. By applying the displacement from the structural model as interstory displacement at the level of the infill wall, the stress-strain curve of the rubber material can be utilized to determine the thickness of the rubber, which is equal to the infill activation force.

One of the primary benefits for the practical use is the RC structures' easy-to-understand design with infills that have an INODIS link. In order to assess the practical utility of the INODIS system in everyday structural engineering, a six-story structure was designed as an example. Eurocode 8 was followed over the entire design process. The two situations that are examined and contrasted are non-interacting (decoupled) and traditional (rigidly attached) masonry infills. For every arrangement, two models were created. The model was expanded to include diagonal struts with interacting infills. The analysis indicates that, in comparison to traditional infills, the INODIS technology permits a considerable reduction in the quantities of steel and concrete (Fig. 6). Significant cost efficiency is further achieved when one considers that the savings include the cost of the rubber INODIS connection and that investment expenses are still lower than in the traditional situation (Fig. 6). The cost has been computed using the current market prices in Serbia, accounting for RC walls, beams, columns, and infill walls. In conclusion, less money and material are needed to attain greater seismic safety. Furthermore, in the event of seismic activity, damage is avoided, saving money on repairs and downtime.

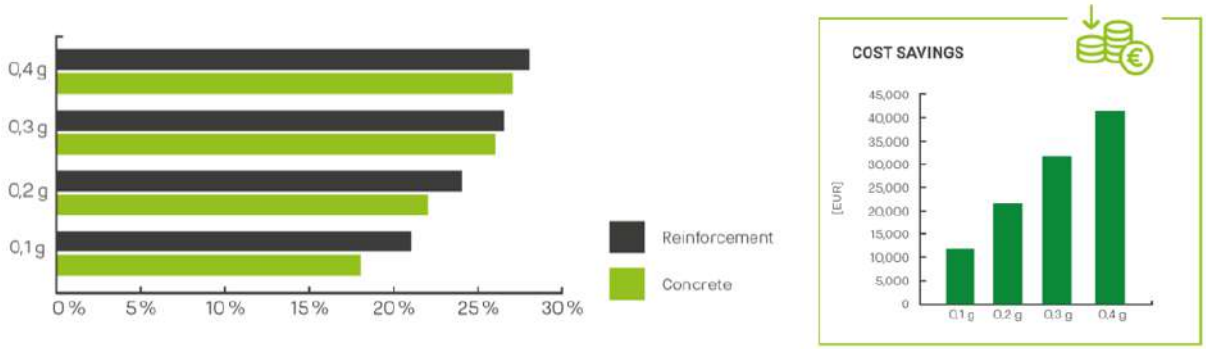


Figure 6. Less concrete and reinforcement (left) and Lower costs (right) when INODIS connection is used

5.ADVANTAGES AND BENEFITS OF THE INODIS CONNECTION

As evidenced by the experimental results, the INODIS decoupling system transforms masonry infill walls into true non-structural elements, effectively categorizing them as non-interacting infills. This approach protects the infill walls from damage during earthquakes. The low activation of the infills simplifies the design process, where only the RC structure is modeled, and the infill is treated as additional mass. The primary task is to select the appropriate rubber type in terms of thickness and stiffness. With the straightforward concept of infill isolation using soft materials, the infills are protected both in-plane and out-of-plane, thanks to the three-strip solution.

By isolating the infills, the surrounding RC structure is also safeguarded, as no additional forces from the infills act on the RC elements. This has several advantageous effects. First, the RC elements are not subjected to shear forces from the infills, allowing for reduced reinforcement and smaller concrete elements. This results in a more economical design and faster construction, saving time for the overall project. Second, this benefit is further amplified in the case of "short columns," which are avoided when INODIS is applied.

Moreover, the application of the INODIS connection enables flexible and irregular distribution of infill walls in both plan and height, without the need for repeated design and structural analysis. This flexibility is not possible with traditional (interacting) infills. The ability to change the position and type of infills (e.g., using different brick materials) during the building's use, without requiring a redesign or reanalysis, is another significant advantage of the INODIS connection.

When INODIS is installed, the "soft story" problem is also mitigated, as there is no abrupt change in stiffness between floors (which occurs with traditional infills). The connection's simple installation, using standard tools and conventional wall construction techniques, ensures quick on-site assembly with minimal manpower. This leads to faster construction compared to traditional infills, particularly due to the quick execution at the top of the wall. Additionally, INODIS can be applied to all types and sizes of brick units, with connections made using standard mortars commonly used in construction (e.g., general-purpose mortar, thin-layer mortar).

As INODIS is made from recycled rubber, it contributes to the circularity of the construction sector. It also supports more efficient building element design, leading to reductions in costs, time, energy, waste, and other resources.

Based on the described above, benefits of the INODIS system can be summarized in the following list:

- protection (both in-plane and out-of-plane) of infills from the damage during earthquakes
- non-interacting infills (with INODIS system) are real non-structural element, which force and stiffness activation is negligible, thus it does not influence the dynamic characteristics of the structure
- design of structure is simple and straightforward (infills are not modelled, only thickness and type of rubber is chosen based on the interstorey drift)
- protection of RC elements and structure, since infill/frame interaction is negligible resulting in lower amounts of reinforcement and size of RC elements
- reduced investments costs
- solving the problem of “soft story” when ground floor is open and upper floors have infill walls
- solving the problem of “short column”
- INODIS system allows random and irregular distribution of infill walls in plan and height, thus solving the potential torsional problems due to infills
- fast, simple and standardized installation
- applicable to all types and sizes of bricks/blocks
- reducing the repair time of the building after earthquake
- it contributes to the circular economy and reduction is costs, time, energy and waste.

6.SUMMARY

The visible effects of earthquakes on reinforced concrete (RC) structures with infill walls highlight the urgent need for a solution to address the substantial economic losses, delays in recovery, and threats to human safety caused by damage and failure of infills during seismic events. The analysis of field data supports previous research and reveals that factors such as detachment at the corners under non-loaded conditions, deterioration of connections between the frame and infill, and damage to the masonry infill itself, play a significant role in the failure of these structures. Often, the frame-infill connections are inadequate, particularly when the gap at the top is not sealed properly, which worsens the issue. Furthermore, the destructive effects of infill/frame interaction have led to the collapse of structures due to "soft story" and "short column" failures. While this problem has been studied for many years, it has become an urgent challenge that requires solutions to prevent future disasters.

To address this issue, a decoupling connection has been developed as a solution to improve the seismic resilience of masonry infills, with the goal of preventing interaction between the infill walls and the frame. The key concept is to isolate the infill walls from the frame, preventing any interaction during deflection. Notably, the system provides both in-plane decoupling and strong resistance to out-of-plane forces. Its effectiveness is confirmed through extensive full-scale experimental tests, including samples with and without window and door openings. The results, compared directly with conventional infills, highlight the superior seismic performance of the decoupling system. This innovative solution, made from recycled rubber material, offers a cost-effective method that can be applied to various brick types and sizes, easily integrated into construction procedures. In addition to protecting infill walls, it reduces stress concentrations in the frame, leading to minimal changes in the natural period of the RC structure. Its simplicity and reliability in design make it an attractive option for engineers in real-world applications. This breakthrough has the potential to significantly enhance the seismic resilience of masonry infills, ensuring their stability and resilience while having straightforward construction processes.

REFERENCES

Marinković, M., Baballëku, M., Isufi, B., Blagojević, N., Milićević, I., Brzev, S. (2022): Performance of RC cast-in-place buildings during the November 26, 2019 Albania earthquake. Bulletin of Earthquake Engineering, 20:5427-5480. https://doi.org/10.1007/s10518-022-01414-y

Marinković, M., Brzev, S., Baballëku, M., Isufi, B., Blagojević, N., Milićević, I., Žugić, Ž., Bursać, P. (2021): Out-of-plane behaviour of loadbearing and non-structural masonry walls during recent earthquakes. In Conference proceedings from 1st Croatian Conference on Earthquake Engineering-1CroCEE, 22nd to 24th March 2021, Zagreb, 2021 (Vol. 64, pp. 213-207). University of Zagreb, Faculty of Civil Engineering.

Dilsiz A. et al. (2023): "StEER: 2023 Mw 7.8 Kahramanmaras, Türkiye Earthquake Sequence Preliminary Virtual Reconnaissance Report (PVRR)", in StEER- February 6, 2023, Kahramanmaras, Türkiye, Mw 7.8 Earthquake. DesignSafe-CI. https://doi.org/10.17603/ds2-7ry2-gv66Mehrabi, A.B., Shing, P.B., Schuller, M.P., Noland, J.L. (1994): Performance of Masonry-Infilled R/C Frames under in-Plane Lateral Loads; Report No. CU/SR-94-6; Department of Civil, Environmental, and Architectural Engineering, University of Colorado: Denver, CO, USA

Morandi, P., Hak, S., Magenes, G. (2017): Experimental and numerical seismic performance of strong clay masonry infills. In Appendix: guideline proposal for seismic design of masonry infills. Research Report 2017a/02. EUCENTRE Foundation

Di Trapani, F., Khan, N. A., Zhou, L., Demartino, C., Monti, G. (2024): Cyclic response of infilled RC frames with window and door openings: Experimental results and damage interpretation. Earthquake Engineering & Structural Dynamics, 53(1), 43-67. https://doi.org/10.1002/eqe.4005

Nasiri, E., Liu, Y. (2017): Development of a detailed 3D FE model for analysis of the in-plane behaviour of masonry infilled concrete frames. Engineering Structures, 143, 603-616.

Di Trapani, F., Shing, P.B., Cavaleri, L. (2018): Macroelement Model for in-plane and out-of-plane responses of masonry infills in frame structures. Journal of Structural Engineering, 144(2):04017198. https:// doi. org/ 10. 1061/(ASCE) ST. 1943- 541X. 00019 26

Kubalski, T. (2023): Modellierung von seismisch beanspruchten Mauerwerksausfachungen in Stahlbetonrahmentragwerken (Doctoral dissertation, RWTH Aachen Univresity, 2022)

Tsantilis, A.V., Triantafillou, T.C. (2018): Innovative seismic isolation of masonry infills using cellular materials at the interface with the surrounding RC frames. Engineering Structure,s 155:279-297. https://doi.org/10.1016/j.engstruct.2017.11.025

Jin, W., Zhai, C., Zhang, M., Liu, W., Wei, Y., Xie, L. (2023): Experimental investigation on the in-plane and out-of-plane interaction of isolated infills in RC frames. Engineering Structures, 293, 116569. https://doi.org/10.1016/j.engstruct.2023.116569

Marinković, M., & Butenweg, C. (2019). Innovative decoupling system for the seismic protection of masonry infill walls in reinforced concrete frames. Engineering Structures, 197, 109435.

Milijaš, A., Marinković, M., Butenweg, C., Klinkel, S. (2024): Experimental investigation on the seismic performance of reinforced concrete frames with decoupled masonry infills: Considering in-plane and out-of-plane load interaction effects. Bulletin of Earthquake Engineering, 22, 7489-7546, https://doi.org/10.1007/s10518-024-02012-w

Marinković, M., Butenweg, C. (2022): Numerical analysis of the in-plane behaviour of decoupled masonry infilled RC frames. Engineering Structures, 272, 114959. https://doi.org/10.1016/j.engstruct.2022.114959

Milijaš, A., Marinković, M., Butenweg, C., Klinkel, S. (2023): Experimental results of reinforced concrete frames with masonry infills with and without openings under combined quasi-static in-plane and out-of-plane seismic loading, Bulletin of Earthquake Engineering, 21:3537-3579. https://doi.org/10.1007/s10518-023-01664-4

Marinković, M., Butenweg, C., (2025): Enhanced seismic safety of masonry infilled RC frame structures: INODIS connection, 21st MASE Conference, 24-27 September, Ohrid, North Macedonia.

Seismic Assessment of Concealed Grid Suspended Ceilings: Design of a Large-Scale Experimental Setup for Shaking-Table Testing

Alessandro Prota[1], Vito D'Addesa[1], Luigi Fiorino[1], Ghislain Rivron[2], Marco Garofalo[3],Dominik Herfurth[2], and Raffaele Landolfo[1]

[1] Department of Structures for Engineering and Architecture University of Naples "Federico II", Via Forno Vecchio 36, 80134 Naples, Italy
e-mail: {alessandro.prota, vito.daddesa, lfiorino, landolfo}@unina.it
[2] Knauf Gips KG, Am Bahnhof 7, 97346 Iphofen, Germany
e-mail: {ghislain.rivron, dominik.herfurth}@knauf.com
[3] Knauf di Knauf S.r.l S.a.s, Via Livornese 20, 56040, Castellina Marittima (PI), Italy
e-mail: marco.garofalo@knauf.com

Abstract. This study focuses on the experimental seismic assessment of concealed grid suspended ceiling systems, specifically in different configurations. These ceilings, which represent one of the most widespread non-structural elements in buildings, are particularly vulnerable to earthquake-induced damage, with failures often leading to economic losses, safety risks, and functional disruption. To realistically capture the dynamic behaviour of these systems, including full-system interaction, mode shapes, natural frequencies, and progressive failure mechanisms, testing on a sufficiently large ceiling area is essential. Large-scale testing also allows for the consideration of installation variability, which is a key factor influencing ceiling performance during earthquakes. While shaking table testing is the benchmark for simulating seismic demands, its use is often constrained by limited payload, platform size, and the high cost and effort required for large-scale mock-up construction and installation. To overcome these limitations, this work presents the design of a custom experimental setup specifically developed to enable testing of suspended ceilings with an area of up to 50 square meters, exceeding the dimensional constraints of small-to-medium-sized shaking tables. The proposed setup will support future dynamic testing aimed at observing global failure modes and capturing the complex seismic response of full-scale ceiling assemblies.

Keywords: dynamic testing, large-scale testing, shaking-table testing, suspended ceilings, test set-up.

1. INTRODUCTION

Non-structural components such as partitions, exterior finishes, and suspended ceilings are fundamental to the comfort, functionality, and architectural quality of buildings. Suspended ceilings, in particular, are a common choice in commercial, healthcare, and educational environments due to their acoustic performance, ease of installation, and ability to integrate lighting, ventilation, and other services. Although these systems are not part of the primary load-bearing structure, their behaviour during earthquakes can directly affect building safety and post-event operability. Earthquake damage to suspended ceilings has frequently been documented, with consequences ranging from blocked evacuation routes and injury from falling components to substantial repair costs [Dhakal et al., 2011].

The economic importance of protecting these systems is underscored by previous research showing that the cost of non-structural components and building contents can exceed that of the main structure [Taghavi and Miranda, 2003]. Among these, lightweight steel concealed grid and lay-in ceilings have proven particularly vulnerable, especially when not fitted with adequate seismic restraints. Despite gradual improvements in building codes and growing awareness of non-structural vulnerability, the seismic design of such ceilings was largely neglected for decades, leaving many existing installations at risk even under moderate ground shaking.

Evaluating the seismic behaviour of suspended ceilings is complicated by the geometric complexity of the systems and the non-linear interaction between their components—grids, hangers, boundary supports, and surrounding structural elements. Shaking table testing has become a valuable tool for capturing these interactions and for observing stiffness and strength degradation under cyclic loading. However, a persistent limitation in the available literature is the small size of tested specimens, dictated by the platform dimensions and payload capacity of most laboratory facilities. Real ceilings in large open spaces—such as airport concourses, shopping centres, or hospital wards—often cover tens of square metres, and their dynamic response can be influenced by large-area effects such as vibration wave propagation, full-perimeter interaction, and progressive damage patterns, none of which can be fully replicated in small-scale tests.

To address this limitation, the present paper introduces a large-scale experimental setup specifically designed to enable the seismic testing of concealed grid ceilings over areas of up to 50 m²—well beyond the capacity of conventional laboratory platforms. This solution not only makes it possible to reproduce realistic system-level behaviour and observe global failure mechanisms but also accommodates installation variability. While the larger scale offers significant advantages in terms of representativeness, it also poses challenges, including increased construction and dismantling costs and the need to work within the payload limits of the shaking table.

The paper begins with a description of suspended ceiling systems and their key components, followed by a review of previous experimental work on their seismic performance. It then details the design rationale, technical characteristics, and intended capabilities of the proposed large-scale setup, demonstrating how it overcomes the constraints of standard laboratory facilities to provide a more accurate assessment of real-world ceiling behaviour under earthquake loading.

2. LIGHTWEIGHT STEEL SUSPENDED CEILINGS

2.1 GENERAL FEATURES

In seismic performance considerations, non-structural components like suspended ceilings are generally classified as acceleration-sensitive elements. These systems are primarily affected by the inertial forces

generated by floor accelerations during an earthquake. Even in buildings that undergo limited lateral displacement, high accelerations at the floor level can induce significant forces on suspended ceilings, potentially causing damage such as panel dislodgement or failure of their support systems. This vulnerability is especially pronounced in stiff, low-drift structures, such as hospitals and airport terminals, where suspended ceilings often suffer due to abrupt inertial demands despite minimal building deformation.

2.2 TYPICAL CONFIGURATIONS

Two primary types of suspended ceiling systems are most commonly used in building construction: exposed grid and concealed grid ceiling systems. Both systems offer distinct installation methods, aesthetic appearances, and functional characteristics that influence their selection based on architectural preferences, maintenance needs, and seismic performance requirements [Qi et al., 2023].

Exposed grid ceilings, also known as "lay-in" ceilings, consist of a visible metal grid framework suspended from the structural slab or floor above. This grid typically comprises main tees and cross tees arranged in a regular pattern, supported by hanger wires and fasteners. Edge mouldings are installed along the perimeter walls to support the grid framework. Ceiling panels made from gypsum board, metal, wood, or mineral fibre are laid directly into the openings of the exposed grid. The visible grid creates a characteristic checkerboard pattern, providing ease of installation and allowing straightforward access to mechanical, electrical, and plumbing systems above the ceiling for maintenance. These systems are widely used in commercial spaces, educational institutions, healthcare facilities, and residential buildings due to their lightweight construction, design flexibility, acoustic performance, fire resistance, and ease of maintenance.

In contrast, concealed grid ceilings, often referred to as "continuous" ceilings, feature a supporting grid that is hidden from view to create a smooth, uninterrupted ceiling surface. The grid structure in these systems is generally composed of cold-formed steel (CFS) profiles shaped as C-sections, arranged in a bi-directional layout. The framework consists of main profiles, which are the primary load-bearing members suspended directly from the structural slab using hanger wires, and secondary profiles, attached to the main profiles, to which the ceiling panels are fixed on the underside. Edge mouldings are attached to the surrounding walls to provide perimeter support. Unlike exposed grid systems, the ceiling panels in concealed grid systems completely cover the supporting grid. In this case, it is important to highlight that in continuous ceilings, the panels or boards are screwed directly to the C-profiles, creating a flat surface with homogeneous characteristics.

2.3 LATERAL RESTRAINT FOR SEISMIC APPLICATIONS

When designing suspended ceilings to withstand seismic forces, engineers typically consider three main types of lateral restraint systems: perimeter-fixed, partially perimeter-fixed, and floating (or braced) systems (see Figure 1). Each approach has its own advantages and limitations, depending largely on the size of the ceiling and the expected seismic demands [Pourali et al., 2014].

Perimeter-fixed systems involve directly connecting the edges of the ceiling to the surrounding walls. This method is often recommended for small ceilings because it's straightforward and provides a simple way to stabilize the ceiling. However, during an earthquake, the walls themselves can move relative to one another, and this movement can transfer forces into the ceiling system. These forces, especially during dynamic shaking, may cause damage or detachment of the ceiling components.

To address this issue, a partially perimeter-fixed approach is often preferred. In this system, only two adjacent edges of the ceiling are fixed to the walls, while the other two edges remain free to move horizontally. This setup helps prevent unwanted force transfer caused by wall displacement. For the system to function effectively, there needs to be sufficient gaps on the free, or "floating," sides of the ceiling, ensuring that movement doesn't cause impact damage.

When ceilings are large, they often cannot resist the lateral forces induced by earthquakes if only connected to the walls. In such cases, a floating or fully separated system is used, where the ceiling isn't attached to the walls at all. Instead, it is braced to the structural floor or roof slab above through a properly detailed bracing system. This "back-bracing" allows the ceiling to absorb horizontal forces caused by floor accelerations. Like the partially fixed system, proper clearance between the ceiling and walls is crucial to prevent collision damage during seismic events.

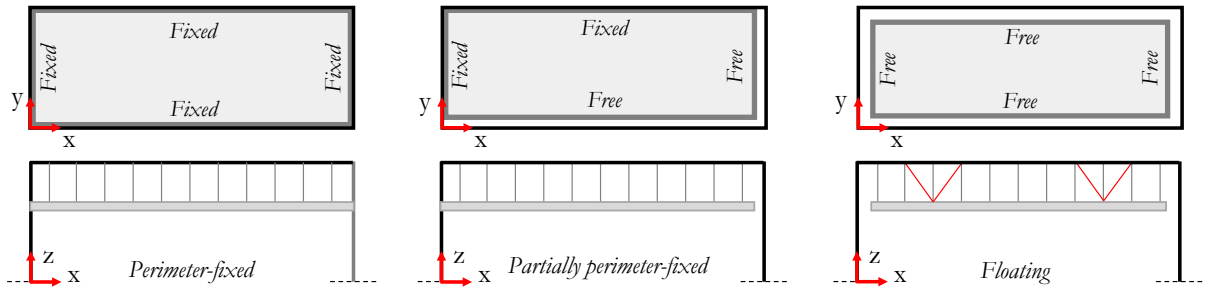


Figure 1. Suspended ceilings lateral restraint

Overall, the choice among these lateral restraint systems depends on the ceiling size, building dynamics, and the need to balance stability with flexibility to accommodate seismic movements safely.

3. PREVIOUS SHAKING TABLE EXPERIMENTAL ACTIVITIES ON SUSPENDED CEILINGS

Over the past decade, numerous experimental studies have explored the seismic behaviour of large-scale suspended ceilings using full-scale shake table tests. These investigations vary widely in terms of ceiling configurations, test setup geometries, instrumentation, and loading protocols. This section first presents an overview of the large-scale shake table tests, with a particular focus on the test setups employed in these experiments. It includes detailed descriptions of how the ceilings were arranged, supported, and instrumented to simulate realistic seismic conditions. Subsequently, research efforts aimed at designing innovative test setups that address and overcome common laboratory limitations are examined.

3.1 LARGE-AREA SUSPENDED CEILINGS

A large-area ceiling is generally defined as a suspended ceiling with a surface area of approximately 9 to 12 square meters or greater, extending up to 50 to 60 square meters or more. The primary aims of research involving tests on large-area suspended ceilings include:

- Capturing realistic dynamic behaviour, including full-system interaction, mode shapes, and natural frequencies.
- Observing global failure mechanisms and progressive damage under seismic loading.
- Incorporating variability related to installation practices and construction tolerances.
- Meeting seismic qualification requirements as mandated by relevant standards.

The work of Ryu & Reinhorn [2019] can be regarded as a pioneering contribution to the seismic performance assessment of exposed grid suspended ceilings, representing one of the most comprehensive and instrumentally refined studies in this domain. In the framework of large-area ceiling systems, this

research distinguished itself through a systematic investigation of boundary conditions and the unprecedented scale and realism of its experimental setup. In particular, perimeter-fixed, partially perimeter-fixed, and floating (braced) configurations were employed as lateral restraint systems for different ceiling prototypes having a wide range of panel unit weights (56–197 N/m²). The use of one or two synchronized shake tables to excite steel frame mock-ups—measuring 6.10 × 6.10 m and 6.10 × 15.24 m, respectively—enabled tests on prototypes with realistic ceiling areas ranging from 36 to 93 m², allowing for an unprecedented replication of in-situ conditions. Regarding the test setup, the bare steel frame exhibited natural frequencies of 12.2 Hz (X), 12.7 Hz (Y), and 22.0 Hz (Z) for the single shaking table configuration, and 13.5 Hz (X), 11.4 Hz (Y), and 21.9 Hz (Z) for the two synchronized shaking table configuration. The test setup design was based on prior foundational work conducted by Reinhorn et al. [2010], as documented in the MCEER-10-0004 report. This report presented a study aimed at analysing typical natural frequencies of floors and roofs in buildings to simulate realistic scenarios. It was recommended that the lateral load-resisting system of the test setup be designed to remain rigid relative to the floor and roof. Specifically, the suggested target frequencies for the setup were: vertical frequencies in the range of 8 to 10 Hz, and horizontal frequencies exceeding 20 Hz. From a methodological perspective, their adoption of multi-directional dynamic loading protocols—including uni-axial, bi-axial, and tri-axial excitations—combined with the ICC-AC156 standard [2000]. The extensive instrumentation network, with 12 tri-axial accelerometers, a uni-axial accelerometer, and 16 string potentiometers, provided a high-resolution understanding of both global and local ceiling responses.

In 2021, Jiang et al. conducted a comprehensive experimental investigation on very large-scale discontinuous suspended ceilings, with plan areas of up to 150 m² and a unit weight of 33 N/m². The study examined various boundary conditions—fixed, semi-free, and free—without the inclusion of bracing systems. The test rig, constructed from steel profiles, covered a plan area of 12.84 × 11.64 m with a height of 5.4 m, and was excited using two shake tables operating simultaneously. The bare frame exhibited natural frequencies of 8.9 Hz in the long-span direction and 8.4 Hz in the orthogonal horizontal direction. Instrumentation was extensive, comprising 30 uni-axial accelerometers, 17 displacement transducers, and 140 strain gauges for strain monitoring. Input motions included sweep waves, natural ground motions from the DGJ08-9-2013 standard [2013], and artificial waves from the Building Center of Japan (BCJ-L2), applied either simultaneously or separately in the two main horizontal directions.

In 2022, Jun et al. extended the experimental database by testing both discontinuous and concealed suspended ceilings with free boundary conditions on all sides. The tested ceiling areas ranged from 16 to 67 m², with hanger loads varying between 43.4 and 76.0 N, and no bracing systems were provided. Steel-profile frames were again adopted as the structural test rigs. Depending on the ceiling size, one or two shake tables were employed. The small-scale setup measured 4.1 × 4.1 m with a height of 3.2 m, while the large-scale setup measured 5.10 × 13.1 m with a height of 3.0 m. The corresponding natural frequencies were 23.0 Hz (long span) and 9.4 Hz (vertical) for the small-scale configuration, and 16.8 Hz (long span) for the large-scale configuration. Instrumentation consisted of up to four tri-axial accelerometers and five LVDTs for displacement measurements. Tests followed the ICC-AC156 protocol, with large-scale ceilings subjected to uni-axial excitation along the long span and small-scale ceilings tested under uni-axial or tri-axial inputs.

When compared to the recommendations outlined in the MCEER-10-0004 report by Reinhorn et al. (2010)—which suggested that the test setup should maintain vertical natural frequencies in the range of 8–10 Hz and horizontal natural frequencies exceeding 20 Hz—some differences can be observed. The large-scale setup of Jiang et al. met the vertical frequency recommendation but did not reach the horizontal target. Similarly, Jun et al.'s large-scale configuration, with a horizontal frequency of 16.8 Hz, fell slightly short of the recommended threshold, although it can be considered comparable to the 20 Hz benchmark. Conversely, Jun et al.'s small-scale frame largely satisfied the horizontal frequency criterion, while its vertical frequency was notably lower than the target range. These deviations from the prescribed dynamic characteristics suggest that the test setups in these more recent studies may have introduced dynamic

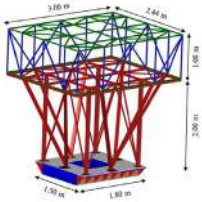
interactions not entirely representative of the rigid floor and roof conditions envisaged Reinhorn et al. [2010].

3.2 TEST SETUPS TO OVERCOME LABORATORY CONSTRAINTS

Several experimental studies have been devoted to characterizing the seismic performance of suspended ceilings, focusing on variations in ceiling configuration, boundary conditions, and test setup. Notably, these works have demonstrated the feasibility of testing ceiling specimens with plan areas larger than the available shaking table footprint through the design of appropriate supporting frames, a methodological achievement that allows for more representative seismic performance assessment at full-room scales (see Figure 2).

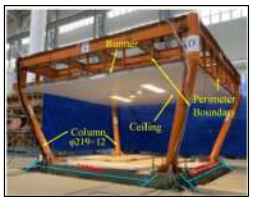
Matale et al. 2022





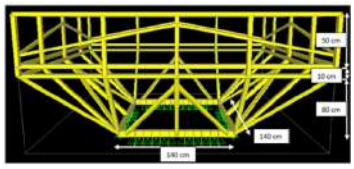
From **1.50 × 1.50 m** shake table to **3.00 × 2.44.**
Bare structure Fundamental frequencies:
20.0 Hz (short span)
22.7 Hz (long span)
15.6 Hz (vertical).

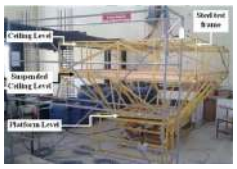
Zhou et al. 2021



From **3.50 × 3.50 m** shake table to **5.00 × 5.00.**
Fundamental frequencies :
9.3 Hz (Horizontal)

Ozcelik et al. 2016





From **1.40 × 1.40 m** shake table to **3.00 × 2.40.**
Bare structure fundamental frequencies :
20.0 Hz (Horizontal)

Figure 2. Steel testing frame designed in previous experimental activities

Ozcelik et al. [2016] carried out an experimental characterization of small-scale discontinuous suspended ceilings with fixed boundary conditions along the entire perimeter. The tested ceilings had a plan area of approximately 7 m², and the panel unit weights ranged from 16 to 71 N/m². No additional bracing systems were incorporated into the configuration. The test frame was fabricated from steel profiles, with top dimensions of 3.0 × 2.4 m and a height of 1.4 m. These dimensions exceeded the 1.4 × 1.4 m shaking table platform, meaning that the specimen overhung the table and was supported by a purposely designed frame to maintain the correct boundary conditions. The bare frame exhibited a natural frequency of 20 Hz in the horizontal direction. Instrumentation comprised four uniaxial accelerometers and four string potentiometers to monitor acceleration and displacement responses. The input motion was based on the ICC-AC156 standard [2000], with modifications necessitated by equipment limitations, while also considering recommendations from the IHBC standard [2008]. Motions were applied separately along the two principal horizontal directions. In this setup, the ceiling-to-table area ratio was 3.6, while the longest-side ratio was 2.1 (3.0 m test frame side vs. 1.4 m shaking table side).

The study by Zhou et al. (2021) represents a large-scale experimental program on a newly developed Discontinuous Suspended Ceiling (DSC) system, specifically designed for high-rigidity, high-frequency environments such as nuclear power plant control rooms. The tests were conducted on a six-degree-of-freedom shaking table with a platform size of 4.1 × 4.1 m. Notably, the ceiling plan measured 5.0 × 5.0 m (25 m²), exceeding the shaking table footprint. This was achieved by designing the steel frame to extend beyond the table edges, allowing for a representative full-room ceiling test without being constrained by the table dimensions. The bare steel frame exhibited fundamental horizontal frequencies of approximately 9–10 Hz, confirming its high stiffness and suitability as a test platform. Five boundary condition configurations were studied: i) no ceiling panels or angle steels installed; ii)ceiling panels without lateral restraints; iii) main and cross runners bolted to angle steels (effective lateral restraint); iv) cross runner restraints removed; v) all restraints removed, allowing free collision between runners and angle steels. The loading protocol comprised three types of ground motions—the 1940 El Centro record, the 1995 Kobe record, and an

artificial accelerogram generated according to the Chinese seismic code for a magnitude 8 event on site class II—applied in X, Y, and Z directions. In this case, the ceiling-to-table area ratio was 1.5, while the longest-side ratio was 1.2 (5.0 m ceiling side vs. 4.1 m shaking table side).

In 2022, Matale et al. [2022] investigated the seismic performance of concealed ceilings with free boundary conditions. The tested ceiling had a plan area of approximately 7 m² and a unit panel weight of 93.4 N/m². As in the previous study, no additional bracing was provided. The test frame measured 3.00 × 2.44 m at the top and was 3.00 m in height, supported on a 1.50 × 1.50 m shaking table. This configuration again required a frame extending beyond the table footprint, allowing for a ceiling larger than the table size to be tested under realistic boundary conditions. The bare frame exhibited fundamental frequencies of 20.0 Hz (short span), 22.7 Hz (long span), and 15.6 Hz (vertical). Instrumentation included nine uniaxial accelerometers, two LVDTs, and strain gauges to monitor local deformations. The seismic input was the N21E component of the 1952 Kern County earthquake (recorded at the Taft station), applied in two orthogonal horizontal directions. For this experimental campaign, the ceiling-to-table area ratio was 3.1, while the longest-side ratio was 2.0 (3.0 m test frame side vs. 1.5 m shaking table side).

4. PROPOSED TEST SET UP

4.1 SHAKING TABLE FEATURES AT THE DIST LABORATORY

The experimental campaign presented in this study will be conducted at the Laboratory of the Department of Structures for Engineering and Architecture, University of Naples "Federico II" (see Figure 3). The facility is equipped with two identical shaking tables having plan dimensions of 3.0 × 3.0 m, capable of supporting a maximum payload of 200 kN. They operate over a frequency range of 0–50 Hz, with a peak velocity of 1 m/s, a peak acceleration capacity of 1 g, and a maximum displacement of ±250 mm. The tables provide two degrees of freedom in the horizontal plane, with no vertical actuation. Although the laboratory hosts two identical shaking tables, only one will be used for the present testing program. To reproduce a ceiling with the desired plan area of about 50 m², a steel reaction frame has been designed to extend well beyond the shaking table footprint, thereby enabling the simulation of realistic boundary conditions for large-scale ceilings and ensuring both the experimental validity and the scalability of the results.



Figure 3. Shaking tables at the dist laboratory

4.2 DESIGNED TEST SETUP

The experimental setup has been designed to ensure sufficient lateral stiffness, targeting a natural frequency around 20 Hz as reported in Reinhorn et al. [2010], while also maintaining the total mass below the maximum payload capacity of the shaking table (200 kN). This allows for accurate dynamic testing without exceeding equipment limitations.

The base of the setup consists of a 3 m × 3 m vibrating table, on which a steel-framed reticular structure is mounted (see Figure 4). This structure serves both as a support system and as the boundary condition for the ceiling specimens under investigation. The maximum plan area available for ceiling installation is 7.7 × 6.5 m (≈50 m²), which significantly exceeds the 3.0 × 3.0 m table footprint (9 m²). This corresponds to a ceiling-to-table area ratio of approximately 5.6. Furthermore, the ratio between the largest setup dimension (7.7 m) and the shaking table side (3.0 m) is about 2.5.

The upper section of the structural frame is made up of steel reticular beams, to which secondary structural members are attached for connecting the ceiling hangers. These reticular beams incorporate L-shaped profiles for the vertical and diagonal elements and paired L-shaped profiles for the upper and lower chords. Each reticular beam has a total height of 0.8 m. Reticular beams are supported by lateral resisting systems constructed from paired UPN 300 profiles, resulting in a total column height of 1.7 m. The space between the lower chord of the reticular beam and the top of the lateral resisting system—referred to as the gap—defines the available area for positioning the suspended ceiling grid. This gap measures 0.6 m in height. To ensure sufficient in-plane stability, the setup includes two lateral resisting systems along each principal direction.

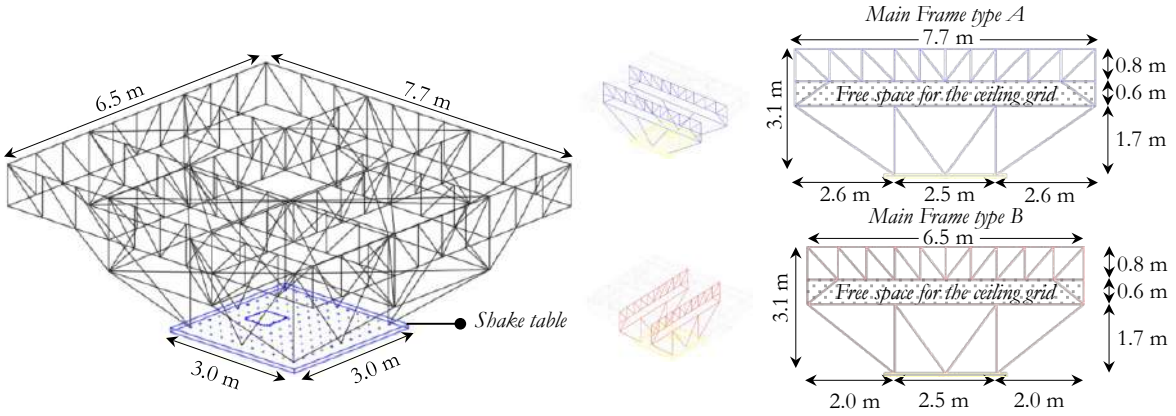


Figure 4. Geometrical features of the proposed test setup

Depending on the hanger positioning, the system accommodates suspended ceilings with overall heights ranging from 0.9 m to 1.3 m when hung from the upper chord, or from 0.1 m to 0.5 m when suspended from the lower chord of the reticular beam. The selection of structural profiles was primarily driven by stiffness considerations, while the choice of section types (L-shaped and paired UPN profiles) was made to facilitate ease of connection and assembly (see Figure 5).

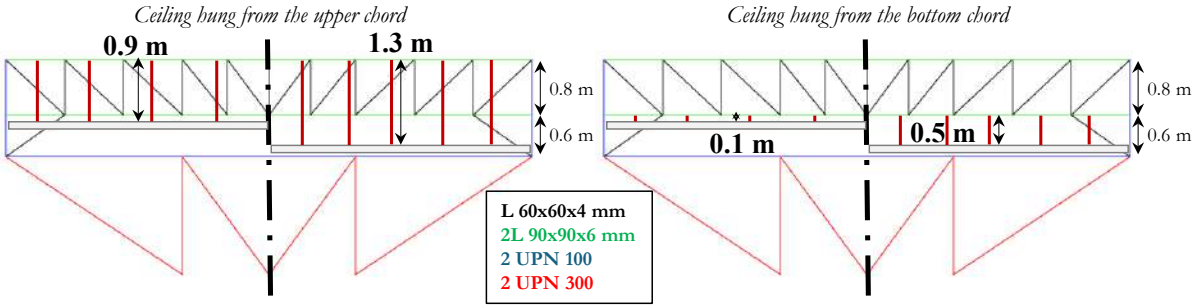


Figure 5. Suspended ceilings' heights of suspension range

The estimated self-weight of the entire structural setup, including secondary elements for connecting and suspending the ceiling, is approximately 95 kN. Assuming a typical heavy suspended ceiling system with a unit weight between 0.35 and 0.40 kN/m², the total weight of a 50 m² ceiling ranges from about 17.5 to

20.0 kN. Therefore, the combined weight of the setup and a heavy ceiling specimen is roughly 115 kN. Considering the shaking table's payload capacity of 20 kN, this setup allows for testing a broad spectrum of suspended ceiling configurations, from lighter systems such as mineral fiber or lightweight metal tiles to heavier assemblies like gypsum board or concrete-based panels, all within the permissible payload limits.

Table 1. Summary of test setup features

Parameter	Value / Description
Shaking table footprint	3.0 × 3.0 m (area = 9 m²), 2 DOF horizontal; max payload 200 kN; max displacement ±250 mm; frequency range 0–50 Hz
Platform/base system	Steel reticular frame mounted directly on the 3 × 3 m shaking table
Dimensional properties of the test frame	Overall ceiling installation area: 7.7 × 6.5 m (50 m²); Largest dimension: 7.7 m; Ceiling-to-table area ratio: 5.6; Largest-dimension-to-table ratio: 2.5; Reticular beams: height = 0.8 m; Lateral resisting system height: 1.7 m; Gap for ceiling installation: 0.6 m.
Ceiling plan	Maximum available ceiling area: 7.7 × 6.5 m (50 m²)
Ceiling suspension heights	From upper chord: 0.9–1.3 m; From lower chord: 0.1–0.5 m
Total mass of setup + heavy ceiling	≈115 kN (setup ≈95 kN + ceiling 17.5–20 kN)

4.3 BARE FRAME NUMERICAL MODAL ANALYSES

A numerical model of the test setup was developed in SAP2000, incorporating the cross-sectional properties defined during the design phase. Using this model, a preliminary modal analysis was conducted under bare-frame conditions, meaning without any suspended ceiling components installed. The analysis results indicate that the first two modes are primarily translational motions in the horizontal plane, while the third mode corresponds to a rotational motion around the vertical axis. The associated frequencies are summarized as follows: i) mode 1 (translational) with f_1 equal to 31.6Hz; mode 2 (translational) with f_2 equal to 31.9Hz; iii) mode 3 (rotational) with f_3 equal to 32.1Hz

These results highlight the high global stiffness of the supporting frame, aligning well with the design goal of achieving a dynamically rigid structure relative to the suspended ceiling components being tested. When compared to previously reported experimental setups in the literature, which typically exhibit fundamental frequencies ranging from 8.4 Hz to 23.0 Hz, the present setup is markedly stiffer. This increased stiffness ensures that the dynamic response of the frame remains effectively decoupled from that of the suspended ceiling system, thereby minimizing undesired interactions and allowing a more precise evaluation of the ceiling's seismic behaviour. The elevated natural frequencies confirm that the supporting structure functions as an almost rigid boundary condition, consistent with the design objectives.

5. CONCLUSION

This study presented the design and development of a large-scale experimental setup aimed at overcoming the traditional limitations of shaking table testing for suspended ceilings. By enabling the seismic testing of concealed grid systems with plan areas up to about 50 m²—well beyond the footprint of conventional laboratory platforms—the proposed configuration allows for a more representative reproduction of real in-situ behaviour of medium-to-large surface ceilings, including global failure mechanisms, full-perimeter interaction, and progressive damage patterns. The supporting steel frame was specifically designed to achieve high lateral stiffness, with fundamental frequencies above 30 Hz, exceeding the dynamic performance of many existing setups reported in the literature. This ensures that the frame behaves as a nearly rigid boundary condition, enabling a more accurate assessment of the suspended ceiling's seismic

response. With an estimated self-weight of 95 kN and a total payload capacity compatible with a wide range of ceiling types—from lightweight mineral fibre to heavy gypsum or concrete-based panels—the setup offers significant flexibility for future research. The use of modular structural elements also facilitates assembly, disassembly, and adaptation to different ceiling configurations and boundary conditions.

REFERENCES

AC156 [2000] "Acceptance Criteria for the Seismic Qualification of Nonstructural Components". *International Conference of Building Officials (ICBO)*, ICBO Evaluation Service, Inc., Whittier, California 2000.

DGJ08-9-2013 [2013] "Code for Seismic Design of Buildings", *Standards Press of China*, Shanghai, China, 2013.

Dhakal, R.P., MacRae, G.-A., Hogg, K. [2011] "Performance of ceilings in the february 2011 Christchurch earthquake", *Bulletin of the New Zealand National Society for Earthquake* 978 *Engineering,* Vol. 44, No. 4, pp. 379–89.

Istanbul Highrise Buildings Earthquake Code [2008]. "Istanbul Highrise Buildings Earthquake Code (in Turkish) – Draft Version", *The Kandilli Observatory and Earthquake Research Institute*, Bosphorus University, Cengelkoy, Istanbul 2008.

Jiang, H., Wang, Y., He, L. [2021] "Study of Seismic Performance of Chinese-Style Single-Layer Suspended Ceiling System by Shaking Table Tests" *Advances in Civil Engineering,* No. 9861722.

Jun, S.C., Lee, C-H., Bae, C-J. [2022] "Shake table testing of braced and Friction-Added suspended ceilings and associated numerical study" *Engineering Structures* Vol. 252, No.113724.

Matale, S.V., Kumar, M., Rai, D.C. [2022] "Experimental and Numerical Study of a Plasterboard Suspended Ceiling System with "Free" Perimeter Supports" *Journal of Structural Engineering* **Vol. 149**, No. 1.

Ozcelik, O, Misir, I.S., Saridogan, S. [2016] "Performance evaluation of suspended ceiling systems using shake table test." *Structural engineering and mechanics* Vol. **58**, No. 1, pp. 121-142

Pourali, A., Dhakal, R.P., MacRae, G. [2014] "Seismic performance of suspended ceilings: Critical review of current design practice". *NZSEE Annual Conference, Auckland, NZ.*

Qi, L., Luo, Z., Cao, Y., Xue, J. [2023] "Seismic damage mechanism and performance evaluation of suspended ceiling systems" *Journal of Building Engineering* Vol. 64, No. 6, pp. 1001–32.

Reinhorn, A.-M., Ryu, K.-P., Maddaloni, G. [2010] "Modeling and seismic evaluation of nonstructural component: testing frame for experimental evaluation of suspended ceiling systems", *Technical report MCEER-10-0004. University at Buffalo, State University of New York*, 2010.

Ryu, K.-P., and Reinhorn, A.-M. [2019] "Experimental study of large area suspended ceilings", *Journal of Earthquake Engineering* Vol. 23, No. 6, pp. 1001–32.

Taghavi, S., Miranda, E. [2003] "Response assessment of Nonstructural building elements," *Report no. PEER 2003/05. Berkeley: Pacific Earthquake Engineering Research Center, University of California,* 2003.

Zhou, T., Wang, X., Liu, W., Zhang, Z. Ma, B., Tan, W. [2021] "Shaking table tests on seismic 1066 response of discontinuous suspended ceilings". *Journal of Building Engineering* Vol. 43, No. 102916.

Experimental study on pounding response of suspended ceiling system with mineral wool board

Huanjun Jiang[1,*], Youlu Huang[2,3], and Xinyi He[4]

[1] State Key Laboratory of Disaster Reduction in Civil Engineering, Tongji University, Shanghai, e-mail: jhj73@tongji.edu.cn

[2] State Key Laboratory of Disaster Reduction in Civil Engineering, Tongji University, Shanghai, e-mail: 2010020@tongji.edu.cn

[3] Shanghai Research Institute of Building Sciences Co., Ltd., Shanghai, e-mail: 2010020@tongji.edu.cn

[4] State Key Laboratory of Disaster Reduction in Civil Engineering, Tongji University, Shanghai, e-mail: 2310480@tongji.edu.cn

Abstract. The pounding behavior occurring at the suspended ceiling (SC) boundary has been proved to have adverse effects on the seismic performance of the SC system with mineral wool boards during earthquakes. In this study pounding tests were conducted on four specimens of the SC with mineral wool boards. To achieve the unidirectional pounding between grid ends and wall angles, the sinusoidal excitation was input to ceiling specimens via a high-speed horizontal actuator. The influence of the type of grid members pounding with the wall angle, the boundary condition, and the frequency of sinusoidal input on pounding responses of the ceiling system was comprehensively investigated. The experimental results show that the damage patterns of the ceiling with different boundary conditions were roughly the same, except for the damage of the unseating of grid ends can be prevented by the seismic clip installed at the semi-free boundary. The grid connections were prone to damage under collision behavior. The grid members were mainly subjected to compressive force. In addition, the strain of gird members near the ceiling boundary was relatively large but much smaller than the yield strain of the steel. With the increase of input frequency, the pounding velocity increased accordingly. The pounding velocity had insignificant effects on the pounding stiffness of grid members. The pounding stiffness of different types of grid members was different. Specifically, the pounding stiffness of grid members rose with the increase of grid cross-sectional area. The influence of the boundary condition on the pounding stiffness of grid members was not evident. The linear model is adopted to simulate the pounding behavior, and the model parameters are identified using genetic algorithm based on test results. The numerical simulation results agree well with experimental results. The generic magnitudes for the pounding stiffness of grid members are provided, which can be used for numerical simulation of the SC system.

Keywords: Nonstructural component, Suspended ceiling, Collision response, Seismic clip, Genetic Algorithm.

1. INTRODUCTION

The damage to nonstructural components was reported to be serious during earthquakes. As a vital and widely used nonstructural components, the suspended ceiling (SC) system with mineral wool board was found to be easily damaged [Qi et al., 2023]. For example, during the 2011 Christchurch earthquake in New Zealand, the structural components of many buildings were slightly damaged, but the ceiling system were severely damaged [Dhakal et al., 2011]. It is found that the boundary condition has significant influences on the seismic performance of the SC system [Soroushian et al., 2019; Jiang et al., 2022]. Different from the explicit regulations in ASCE 7-16 [2016], there is no specification about the boundary condition of ceilings in Chinese standard JGJ 345 [2014]. The four boundaries of the ceiling are commonly set as free in practice. In general, there is a gap between grid members and wall angles at the free boundary, causing pounding happens between them under strong earthquakes. Similarly, the pounding behavior also occurs at the semi-free boundary when the seismic clip is used [Huang et al., 2024]. The experimental results show that the pounding behavior is detrimental to the seismic performance of the SC system [Jiang et al., 2022].

Accurately simulating the peripheral pounding behavior is very important to develop precise finite element model of the SC system. Some numerical models of the ceiling considered this type of pounding, while the model parameters used to simulate this pounding behavior lacked experimental verification [Jiang et al., 2022; Zaghi et al., 2016]. Currently, the studies on the behavior of the pounding between grid members and wall angles are limited. Li et al. [2025] performed a series of pounding tests on the SC system with mineral wool board, and the numerical model for simulating this behavior was developed correspondingly. However, the effects of the type of grid members occurring pounding and the boundary condition on pounding responses of the ceiling were not investigated.

To deeply study pounding responses of the SC system with mineral wool board, pounding tests on four ceiling specimens were conducted. To achieve the unidirectional pounding between grid members and wall angles, the specimens were excited by a high-speed horizontal actuator that can output sine wave. The design parameters included the type of grid members pounding with the wall angle, the boundary condition, and the frequency of input. The test results are discussed in detail with respect to damage patterns, the relationship between pounding force and displacement, pounding velocity, strain, and pounding stiffness. Then, the parameters for developed linear pounding model are identified via genetic algorithm based on test results. The identification results are compared with the experimental results to verify the accuracy of this model in simulating the collision behavior. Lastly, generic magnitudes for the pounding stiffness of grid members are proposed for numerical simulation of SC systems.

2. TEST PROGRAM

2.1 SPECIMEN DESIGN

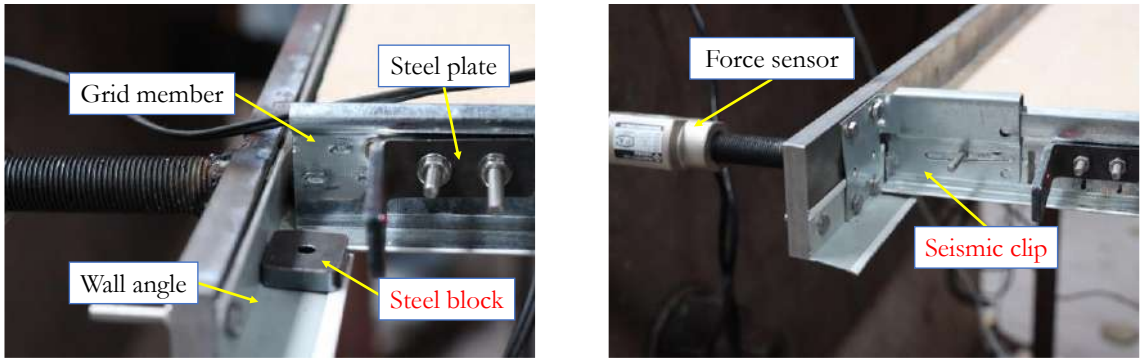
Four ceiling specimens with plan dimensions of 1.45 m × 1.40 m were designed and constructed in accordance with Chinese standard JGJ 345 [2014]. Each specimen mainly consisted of threaded rods, different types of grid members, and mineral wool boards. Cross tees were arranged with the spacing of 600 mm. Main tees and sub cross tees were alternatively arranged with the spacing of 1200 mm in the direction perpendicular to that of the cross tee. Wall angles providing vertical supports to the SC system were installed at the ceiling boundary. Threaded rods with the diameter of 8 mm and the length of 1000 mm were used to hang the entire ceiling system. Panels with the thickness of 16 mm are made by mineral wool, which were placed within ceiling grids without any attachments to surrounding grid members. There were two types of grid connections in the SC specimens, namely the connection between main tee and cross tee (MCT connection), and the connection between cross tee and sub cross tee (CST connection). The detailed

information of specimens is presented in Table 1. The specimens A1 and A2 were designed to evaluate the pounding behavior between cross tees and wall angles, the specimens B1 and B2 were designed to evaluate the pounding behavior between main tees and wall angles, and that between sub cross tees and wall angles.

Table 1. Detailed information of ceiling specimens

Specimen name	Grid members occurring pounding	Boundary condition
A1	Cross tee	Free
A2	Cross tee	Semi-free
B1	Main tee and sub cross tee	Free
B2	Main tee and sub cross tee	Semi-free

There were two kinds of boundary conditions in the ceiling specimens: namely free boundary and semi-free boundary, as depicted in Figure 1. In the free boundary, the grid end may not perpendicularly collide with the wall angle due to the lack of lateral constraints, which may cause the collision fail to occur. To solve this issue, two steel blocks were fixed on wall angles to restrict the movement direction of grid ends. In the semi-free boundary, the grid end can perpendicularly collide with the wall angle due to the constraints provided by the seismic clip.



(a) (b)

Figure 1. Boundary condition of ceiling specimen: (a) free, (b) semi-free

2.2 TEST LOADING

2.2.1 Loading scheme

Figure 2 illustrates the test setup. The whole SC system was mounted on the steel frame through threaded rods and connecting plates. The horizontal actuator was connected to the loading plate, which was then connected to grid members using angle steels. The entire SC specimen was excited by the loading plate when the actuator moved horizontally. Because of the small lateral stiffness of the ceiling system, the specimen was prone to significant offset and torsion during the test. To avoid this unfavourable movement, a slide rail was installed under the loading plate. Therefore, the loading plate can only move in the movement direction of the actuator.

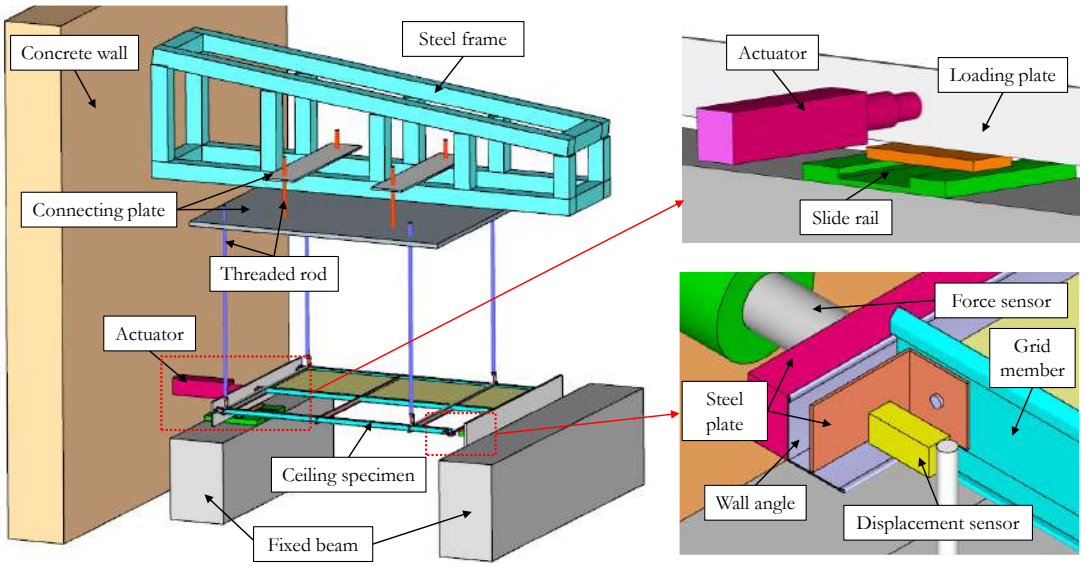


Figure 2. Test setup

2.2.2 Loading protocols

The sinusoidal excitation was input to the ceiling specimen via the loading plate by a hydraulic actuator. The displacement-controlled excitation was applied with 40 cycles in each loading case. The details of all loading cases are listed in Table 2. The width of gap between grid members and wall angles was set as 3 mm, which was the average width of the gaps in the previous shaking table tests [Jiang et al., 2022]. Obtained from this shaking table test [Jiang et al., 2022], the velocity of grid members ranged from 0.1 m/s ~0.4 m/s. To achieve these velocities in this pounding test, the amplitude of the sine wave was set as 6 mm considering the input frequency and the gap width. When the input frequency was greater than 8 Hz, there was an undesirable fluctuation in the actual amplitude of the excitation. To avoid the premature damage in the ceiling specimen caused by the accidental unseating of grid ends, the amplitude of sine wave was adjusted to 4 mm in the loading cases Nos. 5 to 7. This amplitude in the last loading case was set to be 8 mm to study the final failure patterns of SC specimens.

Table 2. Details of loading cases

Loading case No.	Input amplitude/mm	Input frequency/Hz
1	6	2
2	6	4
3	6	6
4	6	8
5	4	10
6	4	12
7	4	14
8	8	14

2.2.3 Instrumentation

Accelerometers, displacement transducers, force sensors, and strain gauges were installed to measure the collision responses of the SC specimens, as shown in Figure 3. Two accelerometers were installed on grid members to monitor the ceiling acceleration. Three S-type force sensors located behind the wall angle were used to record the pounding force. To accurately measure pounding force, the axis of force sensors was aligned with that of grid members. Three Keyence IL-065 series laser displacement sensors were applied to collect displacement data. In particular, the horizontal displacement of grid members was indirectly

measured by monitoring the displacement of the steel plate installed near the grid end. The strains of grid members at different positions were measured. There were two strain gauges attached at both sides of the flange of the T-shaped grid member. The DH8302 data acquisition system with sampling frequency of 20000 Hz was adopted to record the data of forces, displacements, and accelerations. Due to the limited channels of the above-mentioned acquisition instrument, the DH3816N data acquisition system was alternatively used to collect strain data.

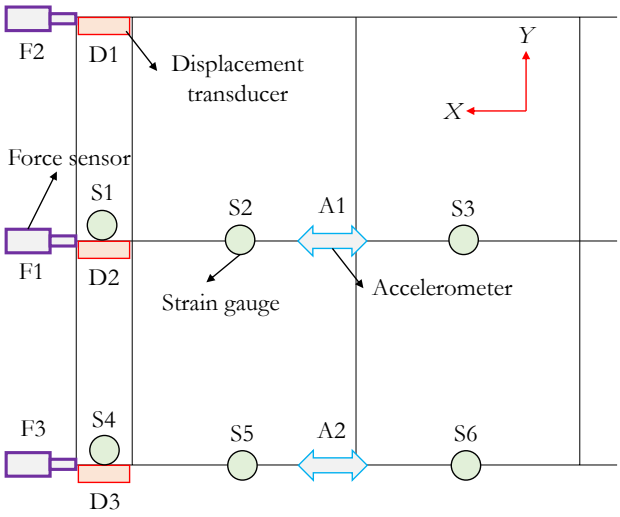


Figure 3. Instrumentation layout of the specimen

3.TEST RESULTS

3.1 DAMAGE PHENOMENON

In the test the damage evolution process of different ceiling specimens was roughly the same. As an example, the damage evolution process of the specimen A1 is shown in Figure 4. Resulted from the pounding between grid ends and wall angles, local buckling of grid ends section was first observed in the initial stages of the loading. This damage phenomenon was caused by the cross-sectional shape and axial stiffness of grid members. Specifically, the end of grid member with T-shaped cross-section protrudes from very thin metal sheets, leading to the low axial stiffness. All grid ends experienced local buckling under the loading case No. 2. Then, the MCT connections near the ceiling boundary began to buckle. Two panels were dislodged under loading case No. 6, and the number of buckling MCT connections increased as well. Under loading case No. 7, the damage to the ceiling specimen became heavier. Lastly, the specimen collapsed due to the failure of MCT connections. It is worth noting that the buckling degree of grid ends alleviated when grid ends were constrained by seismic clips, as shown in Figure 5(a) and (b). Moreover, the unseating of grid ends can be avoided when the seismic clips were used. All typical damage patterns of the ceiling specimens are shown in Figure 5.

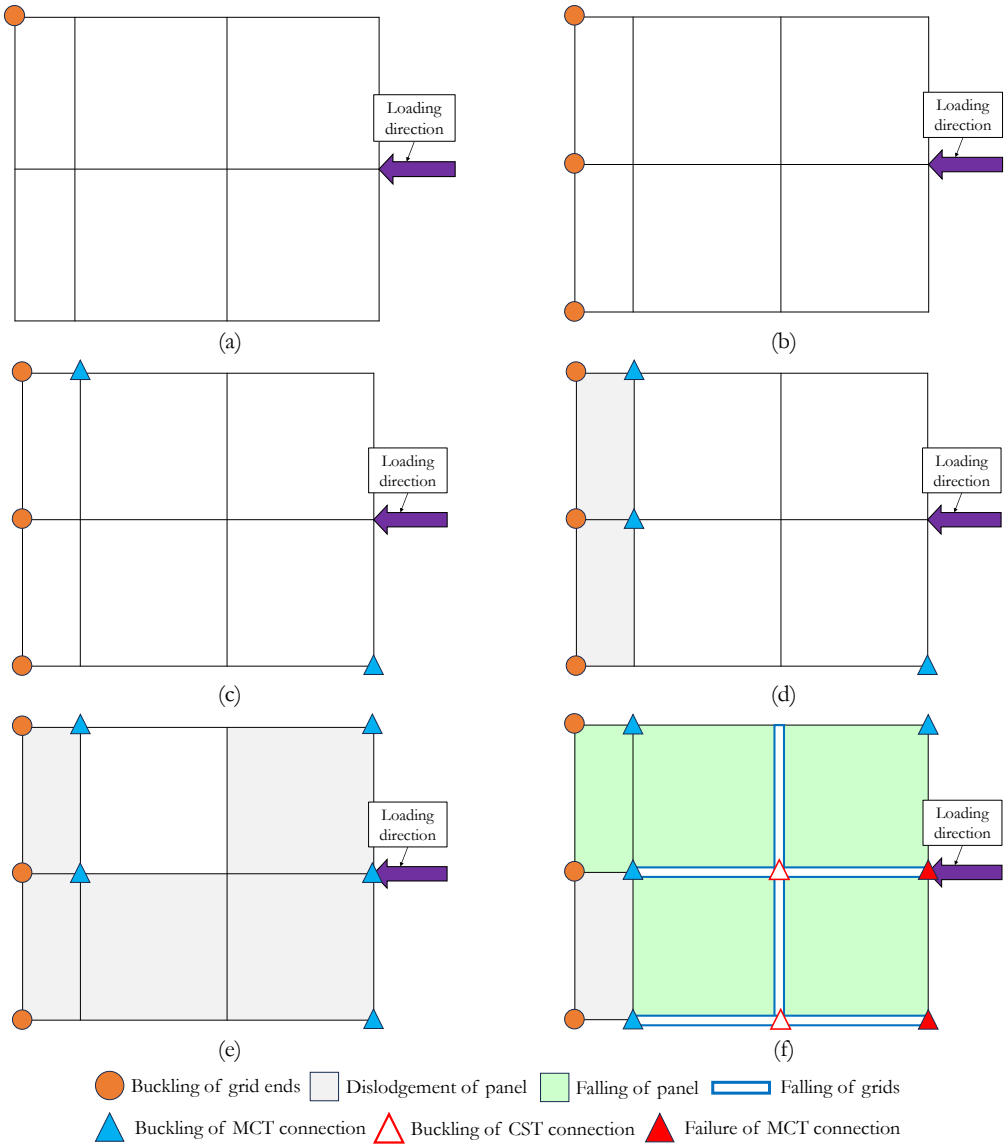


Figure 4. Damage evolution process of specimen A1: (a) loading case No. 1, (b) loading case No. 2, (c) loading case No. 4, (d) loading case No. 6, (e) loading case No. 7, (f) loading case No. 8

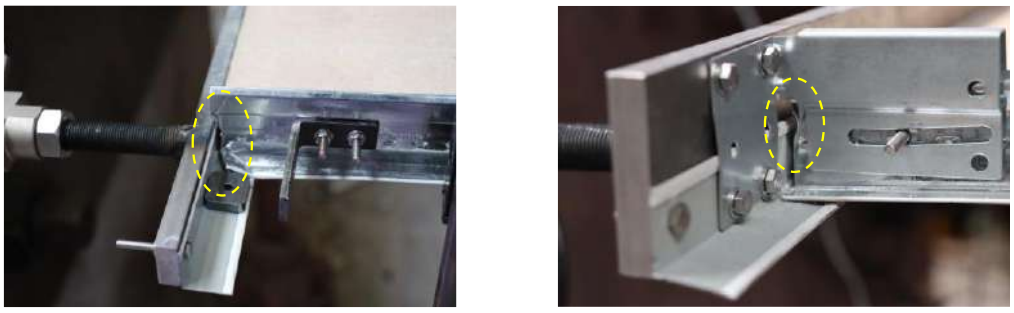




Figure 5. Photos of typical damage patterns: (a) local buckling of grid end section at free boundary, (b) local buckling of grid end section at semi-free boundary, (c) buckling of MCT connection, (d) separation of MCT connection, (e) buckling of CST connection, (f) panel dislodgement, (g) ceiling collapse

3.2 POUNDING FORCE-DISPLACEMENT RELATIONSHIP CURVE

When the pounding between grid members and wall angles happened, the pounding force sharply increased. There were some differences in the slope (i.e., pounding stiffness) of the pounding force-displacement relationship curves for different grid members, while the shapes of these curves were basically the same, as shown in Figure 6. The black lines in this figure represent the experimental results. More detailed analysis of the pounding stiffness is introduced in Section 4.2. It should be noted that there were some evident disturbance signals in the curves after the loading case No. 4. Taking the loading case Nos. 1 and 7 of the specimen A1 as an example, the pounding force-displacement curves for cross tees are shown in Figure 7. This may be caused by the fact that there were some differences between the gap widths at the gird ends. Accordingly, the data collected by force sensors was simultaneously affected by the collision between gird ends and wall angles occurring at different positions.

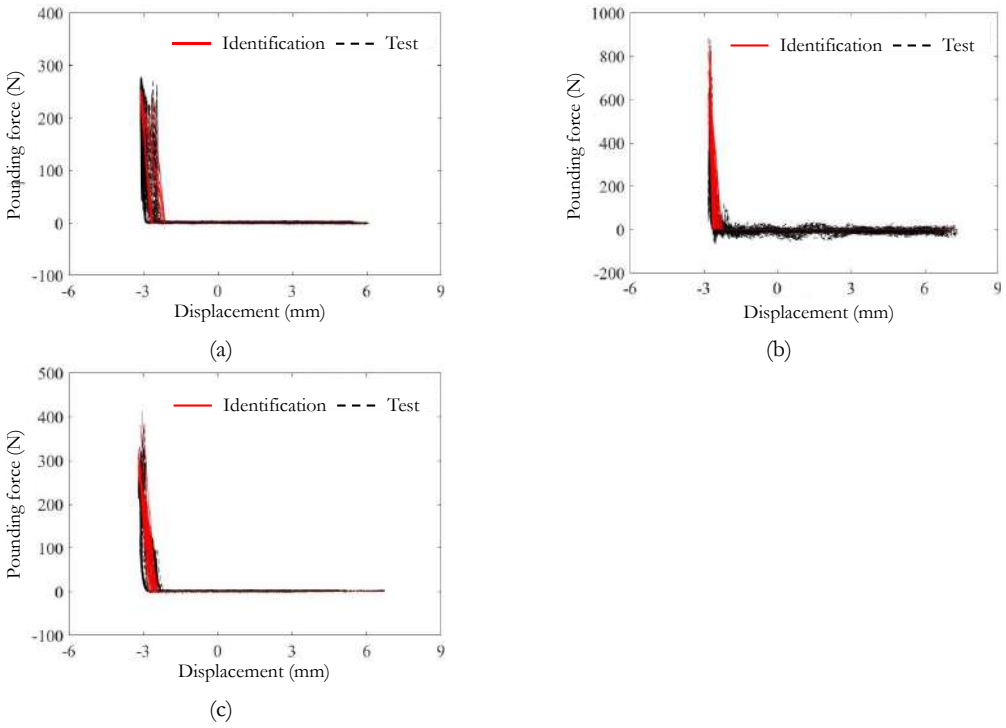


Figure 6. Comparison of the pounding force-displacement curves for typical grid members: (a) cross tee, (b) main tee, (c) sub cross tee

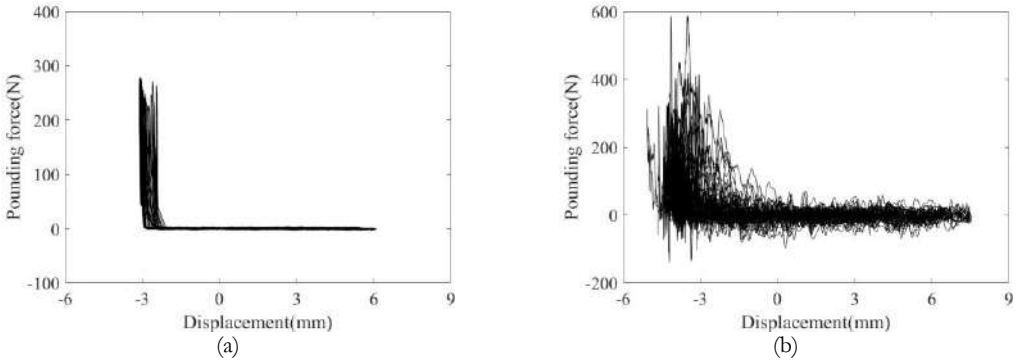


Figure 7. Pounding force-displacement curves for cross tees: (a) loading case No. 1, (b) loading case No. 7.

3.3 VELOCITY RESPONSE

The velocity of the pounding between grid members and wall angles can be obtained from the recorded acceleration responses. As described before, after loading case No. 4, controlling the width of gaps at various gird ends to be the same was difficult because of the severe local buckling of grid ends sections. Thus, the velocity of the pounding under loading case Nos. 1 to 3 (frequency ranged from 2 Hz to 6 Hz) is calculated and listed in Table 3. It is clear that the pounding velocity rose with the increase of input frequency. Some discrepancies of the pounding velocity in different specimens existed due to the unexpected differences of the gap width among grid ends.

Table 3. Velocity of the pounding between grid members and wall angles

Specimen name	Pounding velocity (m/s)		
	2 Hz	4 Hz	6 Hz
A1	0.10	0.13	0.15

B1	0.10	0.14	0.19
A2	0.08	0.14	0.18
B2	0.09	0.12	0.16

3.4 STRAIN RESPONSE

The maximum peak strains of grid members were between 100 $\mu\varepsilon$ and 200 $\mu\varepsilon$ before the collapse of ceiling, which was much lower than the nominal yield strain of the steel, indicating that the grid members remained elastic during the test. It is consistent with the damage phenomenon that grid connections suffered notable damage while grid members had no obvious damage except for local buckling at grid ends. Compared to the tensile strain, the compressive strains of grid members were significantly larger because of the severe pounding behavior. Similar to the test results introduced in the previous study [Jiang et al., 2022], the strain at the position near the ceiling boundary was greater.

4.IDENTIFICATION OF POUNDING PARAMETERS

4.1 DESCRIPTION OF LINEAR POUNDING MODEL

The linear model is widely applied to simulate the pounding behavior [Rajaram et al., 2014]. The main model parameters including the pounding stiffness (k) and the width of gap (g_p) need to be determined. Herein, the parameter identification is conducted via the genetic algorithm in the Matlab Global Optimization Toolbox. This process is transformed into an optimization problem to minimize the weighted error (using weight coefficient w_i) between the numerically predicted pounding force (F_{pred}) and the experimentally measured pounding force (F_{exp}). The genetic algorithm adopts 100 populations and 200 maximum generations, and the crossover function adopts "two points". The identification flowchart of the pounding parameters is depicted in Figure 8.

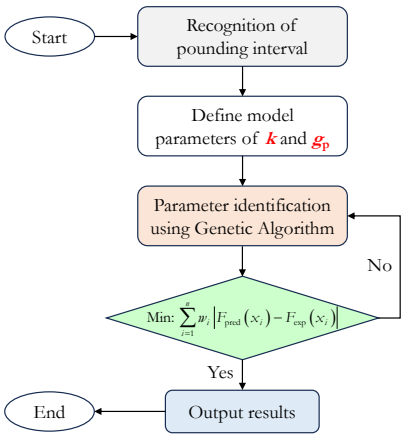


Figure 8. Identification flowchart of pounding parameters

4.2 IDENTIFICATION RESULTS

The comparison of pounding force-displacement relationship curves for typical grid members between identified results and experimental results is shown in Figure 6. Clearly, the two results have good agreement, indicating that the linear model can effectively simulate the pounding behavior between grid members and wall angles. The identified pounding stiffness and the corresponding gap width under loading case Nos. 1 to 3 are shown in Table 4. It can be found that the pounding stiffnesses of different types of grid members are significantly different. Besides, the width of gap at different grid ends has some discrepancies although it was designed as 3 mm originally. The cross-sectional areas for the main tee, the cross tee and the sub cross tee are 38 mm^2, 33 mm^2, and 28 mm^2, respectively. The pounding stiffness is greater for the grid member

with larger cross-sectional area. Because the pounding mechanism in different boundary conditions is basically the same, the boundary condition has slight effects on the pounding stiffness of grid members. The influence of pounding velocity on the pounding stiffness of grid members is not evident. The reason may be related to the local buckling of the grid end due to the pounding, which will reduce the effective contact area during the pounding. To facilitate establishing the finite element model for the SC system, the median value of the pounding stiffness under loading case Nos. 1 to 3 is deemed as the generic magnitudes for that type of grid members, as listed in Table 4.

Table 4. Identification results of pounding stiffness and gap width under different loading cases

Specimen No.	Grid member	Gap width (mm)			Pounding stiffness/(N/mm)			
		2 Hz	4 Hz	6 Hz	2 Hz	4 Hz	6 Hz	Suggested value
A1	Cross tee	2.7	3.4	3.6	556	558	426	558
B1	Main tee	3.0	3.2	3.5	2489	3777	2298	2489
B1	Sub cross tee	2.5	2.9	3.1	457	334	445	445
A2	Cross tee	2.6	2.7	2.9	659	529	812	659
B2	Main tee	3.4	3.5	3.2	2465	3256	2244	2465
B2	Sub cross tee	2.7	3.1	3.3	583	641	426	583

5. CONCLUSIONS

In this study the pounding behavior between grid members and wall angles was investigated by pounding tests, and the pounding stiffness of grid members is identified by genetic algorithm. The main findings are summarized as follows:

(1) The overall failure patterns of the ceiling specimens with free and semi-free boundary are basically the same, except that the unseating of grid ends can be successfully prevented by seismic clips installed at the semi-free boundary. When grid members collide with the wall angle, the cross-section of grid ends is prone to local buckling. The grid connections are the weak point of the ceiling, which are easy to be damaged and even cause the collapse of the ceiling system. The grid members are primarily subjected to compressive forces. The strain of grid members near the ceiling boundary is larger, which is significantly smaller than the yield strain of the steel.

(2) As the input frequency increases, the pounding velocity rises. The pounding velocity has insignificant effects on the pounding stiffness of grid members. There are significant differences in the pounding stiffness of different types of grid members. The pounding stiffness of grid members with larger cross-sectional area is greater. The influence of the boundary condition on the pounding stiffness of grid members is not evident.

(3) The identified results by adopting the linear pounding model agree well with test results, confirming that this model is suitable to simulate the pounding behavior existing at the ceiling boundary. The generic magnitudes for the pounding stiffness of grid members are proposed, which can be used for numerical analysis of the ceiling system.

ACKNOWLEDGMENT

The financial support from the National Natural Science Foundation of China under Grant No. 52478550 is gratefully acknowledged.

REFERENCES

ASCE 7-16. [2016] *Minimum Design Loads and Associated Criteria for Buildings and Other Structures*, American Society of Civil Engineers, Reston, VA.

Dhakal, R., MacRae, G. A., & Hogg, K. [2011] "Performance of ceilings in the February 2011 Christchurch earthquake," *Bulletin of the New Zealand Society for Earthquake Engineering*, Vol. 44, No. 4, pp. 379-389.

Huang, Y., Jiang, H., Wu, S., Wang, H., & Wang, Y. [2024] "Seismic behavior of discontinuous suspended ceiling system with boundary constraints," *Engineering Structures*, Vol. 305, 117780.

JGJ 345. [2014] *Technical Specification for Ceiling Engineering of Public Building*, China Architecture and Building Press, Beijing, China. (in Chinese)

Jiang, H., Wang, Y., & Huang, Y. [2022] "Shaking table tests and numerical modeling of discontinuous suspended ceiling system with free boundary condition," *Engineering Structures*, Vol. 273, 115069.

Jiang, H., Huang, Y., He, L., Wang, Y., & Wang, H. [2022] "Numerical modeling and experimental validation for suspended ceiling system with free boundary condition," *Journal of Building Engineering*, Vol. 61, 105285.

Li, M., Motoyui, S., Sato, D., and Chen, Y. [2025] "Numerical model for pounding phenomenon observed in CHN-US style ceiling tests," *Journal of Earthquake Engineering*, pp. 1-22.

Qi, L., Luo, Z., Cao, Y., & Xue, J. [2023] "Seismic damage mechanism and performance evaluation of suspended ceiling systems," *Journal of Building Engineering*, Vol. 64, 105595.

Rajaram, C., & Ramancharla, P. K. [2014] "Three dimensional analysis of pounding between adjacent buildings," *Journal of Structural Engineering*, Vol. 41, No. 2, pp. 1-11.

Soroushian, S., Rahmanishamsi, E., Jenkins, C., & Maragakis, E. M. [2019] "Fragility analysis of suspended ceiling systems in a full-scale experiment," *Journal of Structural Engineering*, Vol. 145, No. 4, 04019005.

Zaghi, A., Soroushian, S., Echevarria, H., Maragakis, M., & Bagtzoglou, A. [2016] "Development and validation of a numerical model for suspended-ceiling systems with acoustic tiles,". *Journal of Architectural Engineering*, Vol. 22, No. 3, 04016008.

Numerical Simulation of the Structural Test on a 2.5-Story Model Frame Representing Lower Stories of Existing High-Rise RC Buildings with Non-Structural Flat Walls

Peizhi Zhao[1], Rokhyun Yoon[1], and Yasushi Sanada[1]

[1] The University of Osaka
2-1 Yamadaoka, Suita, Osaka, Japan
e-mail: {zhao_peizhi, Yoon_rokhyun, sanada} @arch.eng.osaka-u.ac.jp

Abstract. Non-structural reinforced concrete (RC) flat walls, rigidly connected to RC moment-resisting frames, were widely employed in Japan until the 1990s. Although such walls have typically been excluded from structural design considerations, previous studies have indicated that these walls can significantly enhance the overall stiffness and strength of the structure, suggesting that their influence is not negligible in the seismic performance evaluation. However, due to the limited availability of detailed experimental data on the seismic behaviour/performance of multi-story frames, existing analytical models have not been thoroughly validated. Consequently, the interaction between non-structural flat walls and surrounding moment-resisting frames remains insufficiently understood. To address this gap, static lateral loading tests were conducted on a 2.5-story RC frame specimen designed to simulate the lower stories of a high-rise RC building incorporating flat walls. The test results demonstrated that the flat walls contributed notably to the shear strength of the frame. Based on these findings, a two-dimensional finite element analysis was performed to investigate the wall–frame interaction. The analytical model successfully reproduced the observed load–deformation behaviour and failure mechanisms, thereby confirming its validity and effectiveness.

Keywords: FEM analysis, Moment-resisting frame, Non-structural wall, Reinforced concrete, Structural performance.

1.INTRODUCTION

In recent earthquakes, such as the 2011 Great East Japan earthquake and the 2016 Kumamoto earthquake, severe damage to non-structural members, including reinforced concrete (RC) flat walls (hereafter referred to as flat walls) installed between wide openings in the exterior frames of RC residential buildings was observed, which in many cases hindered immediate building re-occupancy. Such earthquake-damaged walls have generally been excluded from Japanese structural design, as they have been regarded as non-structural members, and their influence on the performance of ductile RC moment-resisting frames has rarely been considered. However, previous research reported that the flat walls are subjected to high axial forces even at small deformation levels due to axial restraint from upper beams. It has also been shown that flat walls contribute significantly to lateral strength until shear failure occurs, thereby affecting the overall seismic performance of the buildings [Sanada et al., 2017].

Based on this background, the authors' group conducted a cyclic loading test on a scaled 2.5-story RC frame specimen, representing the lower stories of a high-rise building with flat walls, to experimentally clarify the interaction between flat walls and the surrounding moment frame [Zhao et al., 2025]. The tests successfully reproduced typical earthquake damage observed in recent events, namely the brittle failure of flat walls. Furthermore, the results confirmed that flat walls constructed monolithically with the main frame substantially affect the global structural performance, including contributing to the overall shear strength and reducing the shear margin of structural members.

In addition, uniaxial spring models and fibre models are commonly employed in numerical analyses of RC buildings. However, previous studies on RC shear walls have shown that these approaches cannot adequately capture the interaction among flexure, shear, and axial forces, often resulting in an overestimation of shear strength [Kolozvari et al., 2019]. Similar limitations are expected when analysing flat walls. To address this issue, the authors previously applied two-dimensional finite element (FEM) analysis to RC flat walls, which enabled a more explicit evaluation of their structural performance [Matsuo et al., 2022]. Nevertheless, a standardized analytical framework for RC moment frames incorporating flat walls has yet to be established, and the effectiveness of hybrid approaches—such as combining fibre models for beams and columns with FEM models for walls—remains insufficiently validated. Further refinement of modelling strategies is required, particularly for application to high-rise buildings where such damage has been repeatedly observed.

Accordingly, the objective of this study is twofold: (1) to investigate in greater detail the interaction between RC flat walls and the surrounding moment frame, and (2) to develop an analytical modelling approach capable of evaluating the structural performance of RC frames incorporating such walls. To achieve these objectives, two-dimensional FEM analyses were performed on the scaled specimens previously tested by the authors, and the accuracy of the analytical model in reproducing the experimental behaviour was examined.

2. SUMMARY OF EXPERIMENTAL TEST

To verify the validity of the analytical model discussed later, comparisons were made with previous test results of Zhao et al. [2025]. To avoid duplication while preserving the integrity of this article, a concise summary of the experiment is presented below.

2.1 TARGET FRAME

The target structure was a 12-story RC moment-resisting frame representative of a typical high-rise RC building, designed in a preliminary study by Yoshida et al. [2021]. The building had uniform spans of 7 m and 10 m in two orthogonal directions and a story height of 3.5 m, giving a total height of 42 m. Figure 1 shows the elevation of the target structure. For the experiment, a one-span, 2.5-story portion of the lower structure was extracted as the test specimen.

2.2 TEST SPECIMEN

The test specimen was a 30% scale partial frame model of the target structure (Figure 1). Its dimensions and reinforcement details are summarized in Table 1, and the reinforcement layout is illustrated in Figure 2. To measure the column shear and axial forces, load cells were installed at the centres of the 1F and 2F columns and below the pin supports of the 3F columns. Concrete casting was carried out in three phases. The details of the flat walls were determined with reference to walls that were damaged in the 2011 Great East Japan earthquake [Sanada et al., 2017]. The structural details of the wall are also presented in Table 1. To simulate the axial restraint exerted on the walls by upper beams, a fixed-end steel beam with equivalent stiffness was installed above the 2.5 story (Figure 2).

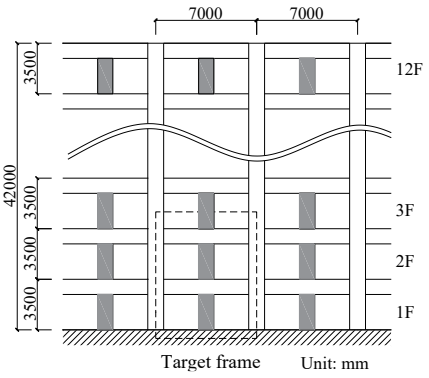


Figure 1. Elevation of the target structure

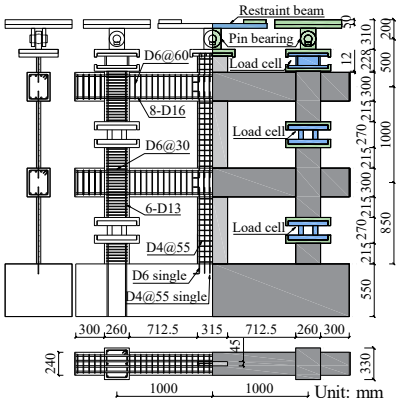


Figure 2. Dimension and reinforcement layout of the specimen

Table 1. Specifications of the specimen

	Width × Depth	Longitudinal/ Vertical rebar	Shear/ Horizontal rebar
Column	330 mm × 260 mm	6-D13	2-D6@30
Beam	240 mm × 300 mm	8-D16	2-D6@60
Wall	45 mm × 315 mm	D4@55 single (D6 single for edge)	D4@55 single

2.3 LOADING PROGRAM

The loading setup is shown in Figure 3. A 1000 kN horizontal hydraulic jack applied lateral force to the top of the specimen, corresponding to the contraflexure point of the 3F columns where pin supports were placed. Cyclic loading followed the loading history shown in Figure 4. The global drift ratio R was defined as the average displacement $\delta_{ave.}$ ($=(\delta_1+\delta_2+\delta_3+\delta_4)/4$, see Figure 3) of the 2.5F columns divided by the specimen height H = 2,350 mm. Before lateral loading, constant axial forces of 300 kN were applied to each column using two vertical hydraulic jacks (2,000 kN), corresponding to an axial load ratio of 0.06. During lateral loading, the total axial force acting on the both columns was kept constant at 600 kN. The mechanical properties of the concrete and reinforcement are listed in Table 2 and Table 3 respectively.

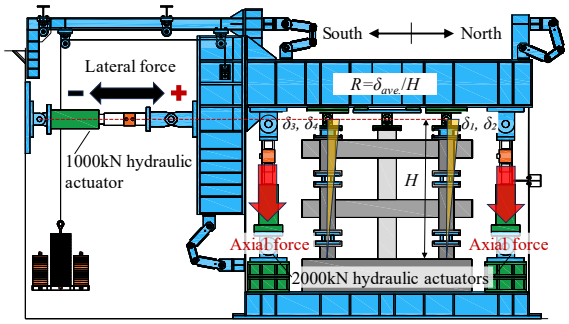


Figure 3. Experimental setup

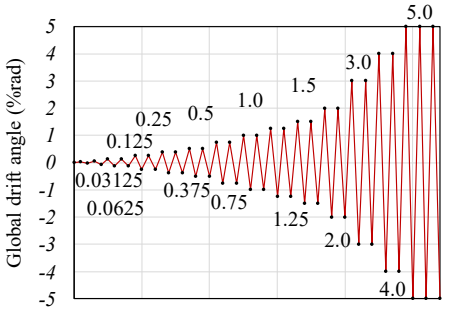


Figure 4. Loading History

Table 2. Mechanical properties of the concrete

Floor	Compressive strength	Elastic modulus
1	58.6 N/mm^2	30.9×10^3 N/mm^2
2	52.3 N/mm^2	27.1×10^3 N/mm^2
3	52.5 N/mm^2	29.9×10^3 N/mm^2

Table 3. Mechanical properties of the reinforcement

Type	Yield stress	Elastic modulus	Tensile strength
D16	388 N/mm^2	189×10^3 N/mm^2	551 N/mm^2
D13	393 N/mm^2	190×10^3 N/mm^2	542 N/mm^2
D6	433 N/mm^2	193×10^3 N/mm^2	550 N/mm^2
D4	380 N/mm^2	211×10^3 N/mm^2	529 N/mm^2

2.4 EXPERIMENTAL RESULTS

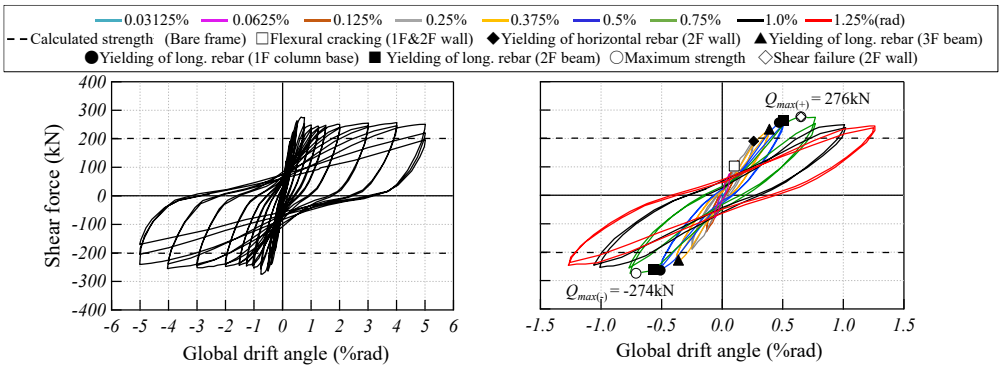
Figure 5 shows the lateral force–global drift hysteresis curves for the specimen, while Figure 6 illustrates the observed damage progression. For reference, Figure 5 also includes the theoretical lateral strength of the bare frame without walls [Zhao et al., 2025]. Figure 7 presents the shear force–rotation angle and axial force–rotation angle relationships (compression taken as positive) of the flat walls at each story. In this study, a story drift angle of 1/75 rad was defined as the safety limit drift in accordance with the Limit Strength Method [National Institute for Land and Infrastructure Management, 2020]. Thus, Figure 7 presents the results only up to a global drift angle of R =1.25% rad, at which point the maximum story drift angles of the second and third stories reached the safety limit of 1/75 rad. The vertical axes of Figure 7 represent the shear and axial forces of the flat walls, obtained by subtracting the forces measured in the columns (via load cells installed as described in Section 2.3) from the total applied horizontal and vertical forces. The horizontal axes indicate the wall rotation angles, defined as the inter-story displacement divided by the clear span of the flat wall.

Key findings are summarized as follows:

- The 2F flat wall experienced shear failure prior to the 1F wall because its drift angle was larger under the same loading cycle. Subsequently, the 1F and 3F flat walls, which experienced reduced axial restraint, failed primarily in flexure.

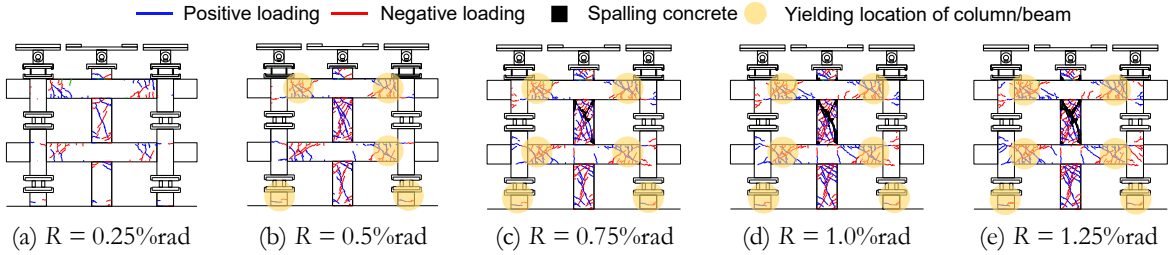
- At peak strength, the flat walls carried approximately 30% of the lateral resistance of the overall frame, indicating that their influence on global structural performance cannot be disregarded, despite their classification as nonstructural members.

- At the safety limit drift angle of 1/75 rad specified by the Limit Strength Method, damage to the structural members remained relatively minor. At the same time, the flat walls failed in a brittle manner, reproducing the characteristic seismic damage observed in recent earthquakes.



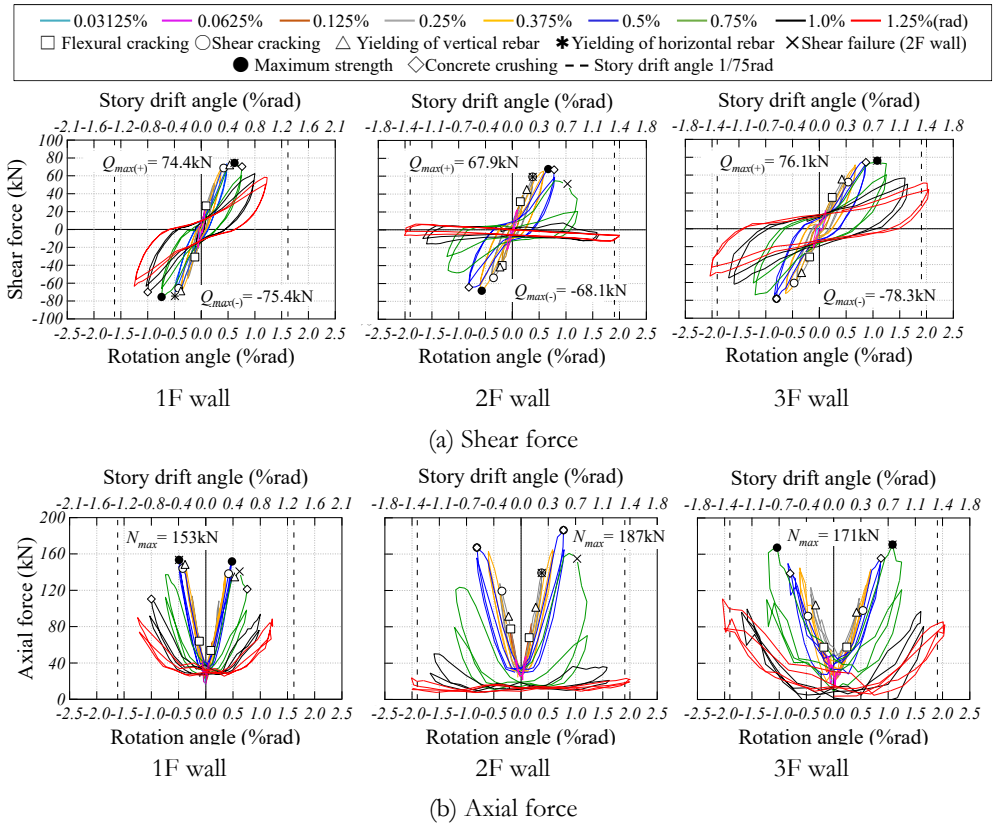
(a) All cycles (b) Up to R = 1.25%rad

Figure 5. Lateral force versus global drift angle relationships of the specimen



(a) R = 0.25%rad (b) R = 0.5%rad (c) R = 0.75%rad (d) R = 1.0%rad (e) R = 1.25%rad

Figure 6. Damage progression of the specimen



1F wall 2F wall 3F wall

(a) Shear force

1F wall 2F wall 3F wall

(b) Axial force

Figure 7. Internal forces versus rotation angle relationships for the flat walls (Up to R = 1.25%rad)

3.NUMERICAL MODELLING AND SIMULATION

3.1 MODELLING OF THE TEST SPECIMEN

The analytical model is shown in Figure 8. Two-dimensional finite element (FEM) analyses were performed under the plane stress assumption. Columns and beams were modelled using flexural-type fibre elements, whose computational efficiency and accuracy have been widely validated in previous studies [Ceresa et al., 2007]. In contrast, the flat walls were modelled using an FEM approach previously verified by Matsuo et al. [2022], as this method can explicitly capture the interaction among flexure, shear, and axial forces. The analyses were carried out using the commercial FEM program FINAL.

Figure 9 illustrates the divisions of the column and beam cross sections. Each element cross section was divided into 20 pieces or fibres i.e. reinforcement fibre and concrete fibre. Each discrete fibre follows its own nonlinear constitutive stress–strain relationships. The response of all fibres is added to obtain the cross-sectional level behaviour in the form of moment–curvature relationships. The rigid zones at beam–column connections were assumed to extend over one-quarter of the member depth from each joint (Figure 8).

In the fibre-based beam-column element, stiffness is generally overestimated because the additional rotation of the column and beam, which results from the slip of the longitudinal reinforcement from the anchorage in the joints, is not included. Thus, rotational springs were introduced at the beam and column ends to simulate the additional deformations, as illustrated in Figure 10. The rotational spring stiffness K_{slip} was assumed linear and calculated based on the model shown in Figure 11 using Equations (1)–(3). The development length L_b and average bond stress τ_{bond} were determined in accordance with the Standard Specifications for Concrete Structures-Design [JSCE, 2022] using Equations (4) and (5).

$$K_{slip} = \frac{M_y}{\theta_s} \tag{1}$$

$$\theta_s = \delta_y / d_n \tag{2}$$

$$\delta_y = \varepsilon_y L_b / 2 \tag{3}$$

$$L_b = \alpha \frac{\sigma_y d_b}{4\tau_{bond}} \geq 20 d_b \tag{4}$$

$$\tau_{bond} = 0.28 f_c'^{2/3} \leq 3.2\ N/mm^2 \tag{5}$$

where M_y is the yield moment (N·mm), θ_s is the yield rotation angle (rad), δ_y is the bond-slip displacement at yielding (mm), σ_y and ε_y are the yield stress (N/mm²) and strain of the longitudinal reinforcement respectively, d_n is the distance from the tensile reinforcement to the neutral axis (mm), d_b is the diameter of the reinforcement (mm), f_c' is the compression strength of concrete (N/mm²), and α is a factor of bond efficiency (taken as 0.6, when $2.5 < c/d_n + 15A_t/(sd_n)$). Here, c denotes the minimum of the cover thickness or half of the clear spacing between anchor bars (mm), A_t is the transverse reinforcement area perpendicular to the splitting crack surface (mm²), and s is the spacing of transverse reinforcement (mm).

The element layout of the flat walls is also shown in Figure 8. The concrete was modelled using quadrilateral plane stress elements; vertical reinforcement was represented with truss elements, and horizontal reinforcement with embedded reinforcement elements. The connection between the beam and the flat wall was assumed to be rigid and modelled using quadrilateral elements (Figure 8). The material properties of concrete and reinforcement were assigned according to the values provided in Tables 2 and 3.

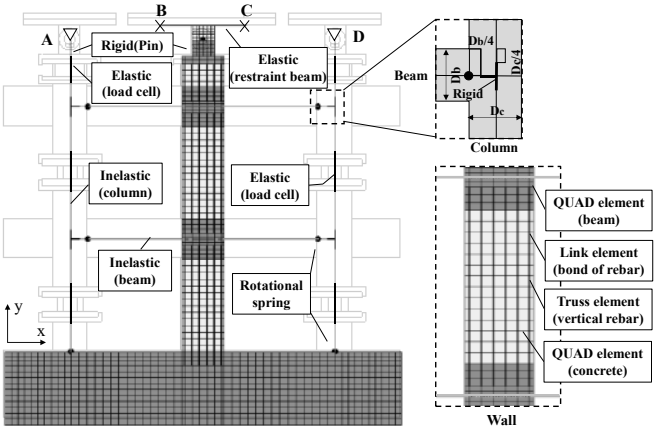


Figure 8. Analytical model and details

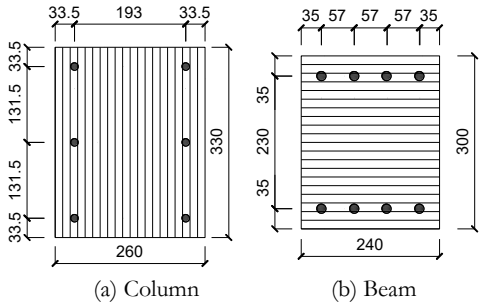


Figure 9. Cross-sectional modeling of members (Unit: mm)

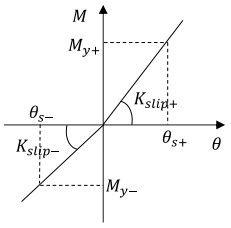


Figure 10. Rotational spring stiffness

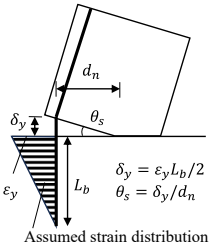


Figure 11. Assumptions of rotational spring

In the analytical model, the pin supports attached to the 3F columns were assumed rigid. The restraining steel beam installed above the 3F flat wall was modelled as a fibre element with equivalent stiffness. To reproduce the boundary conditions of the experiment, the bottom of the stub was completely fixed, the nodes at the tops of the 3F columns (nodes A and D) were modelled as pins, and the rotational degrees of freedom at the ends of the restraining steel beam (nodes B and C) were restrained. In addition, the loading points (nodes A, B, C, and D) kept the same displacement during loading. Constant axial loads of 300 kN were applied to nodes A and D, while cyclic horizontal displacements were imposed simultaneously on all four loading points.

3.2 MATERIAL MODELS

(1) Beam–Column Frame

The compressive stress–strain relationship of concrete was represented by the modified Ahmad model [Naganuma, 1995] up to the peak compressive strength, and beyond this point, strength degradation was modelled by a strain-softening relationship in which the stress decreases to $0.2\sigma_B$ at a strain of $5\varepsilon_c$ (Figure 12(a)). The constitutive law for concrete in tension used a linear model as the ascending branch and a the Izumo model [Izumo et al., 1987] with a parameter of c=0.4 as the descending branch (Figure 12(b)). Post-cracking shear transfer across cracks was modelled using the approach proposed by Naganuma [1991] (Figure 12(c)). The cyclic stress–strain behaviour of concrete was represented by the curve model [Naganuma and Ohkubo, 2000] shown in Figure 12(d). The stress–strain relationship of reinforcement was modelled using the modified Menegotto–Pinto model proposed by Ciampi et al. [1982] (Figure 13).

(2) Flat Wall

For the flat wall, the stress–strain relationships of both concrete and reinforcement were modelled in the same manner as those used for the fibre model. The bond–slip relationship between longitudinal

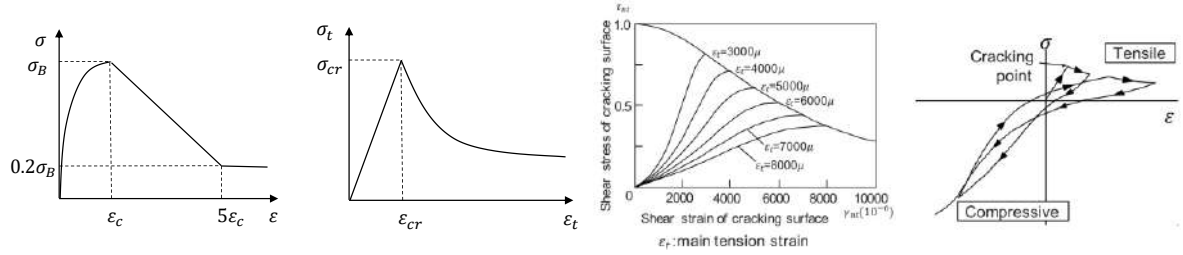
reinforcement and concrete was modelled using the approach proposed by Naganuma et al. [2004], as illustrated in Figure 14. The maximum bond stress was evaluated using the bond strength formula specified in the AIJ Standards [AIJ, 2010], with the corresponding slip at maximum bond stress assumed to be 1.0 mm.

4. COMPARISON OF ANALYTICAL AND EXPERIMENTAL RESULTS

4.1 SHEAR FORCE–DRIFT RELATIONSHIP AND DAMAGE PROCESS

Figure 15 compares the hysteretic responses from the analysis and the experiment up to the safety limit of 1/75 rad, as specified in the Limit Strength Method (corresponding to a global drift of R = 1.25% rad). The analytical model accurately reproduced the initial stiffness, peak strength, and subsequent strength degradation associated with the shear failure of the 2F flat wall. The progression of damage events also showed close agreement with the experimental observations.

Figures 16 and 17 further compare the observed and simulated damage patterns and yielding states of wall reinforcement up to R = 1.25% rad. The analysis successfully reproduced column base yielding, beam-end yielding, shear failure of the 2F wall, and flexural crushing of the 1F and 3F walls. Regarding the shear reinforcement, the extent of yielding in the 1F wall was slightly overestimated beyond R = 0.75% rad. However, when considered together with the minimum principal stress distributions shown later in Figure



(a)Compression model (b)Tension model (c)Shear transfer model (d)Hysteresis model

Figure 12. Constitutive Models for concrete

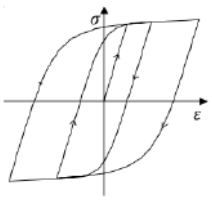


Figure 13. Hysteresis model for steel

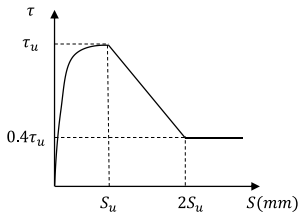


Figure 14. Bond-slip model

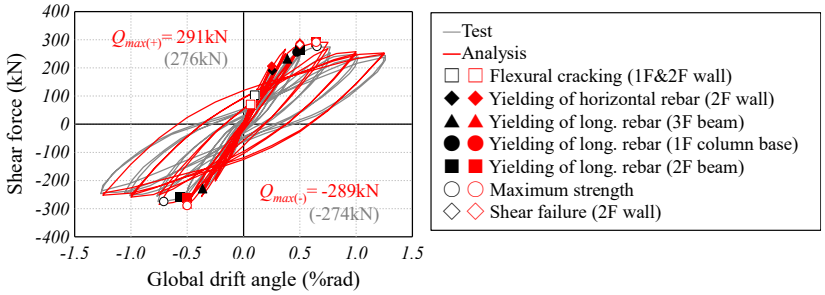


Figure 15. Comparison of the shear force versus drift angle relationships (Experimental and analytical)

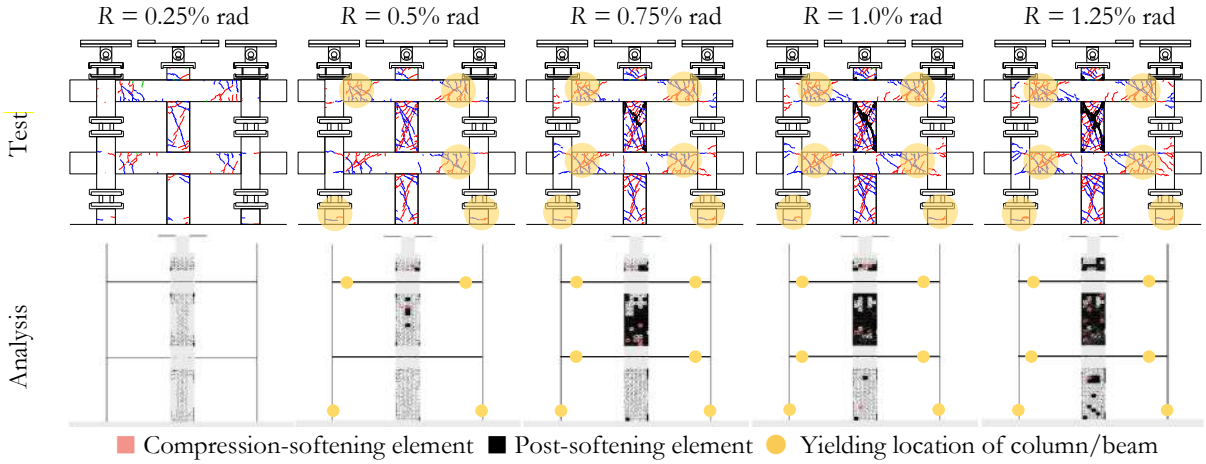


Figure 16. Comparison of the damage progression (Experimental and analytical)

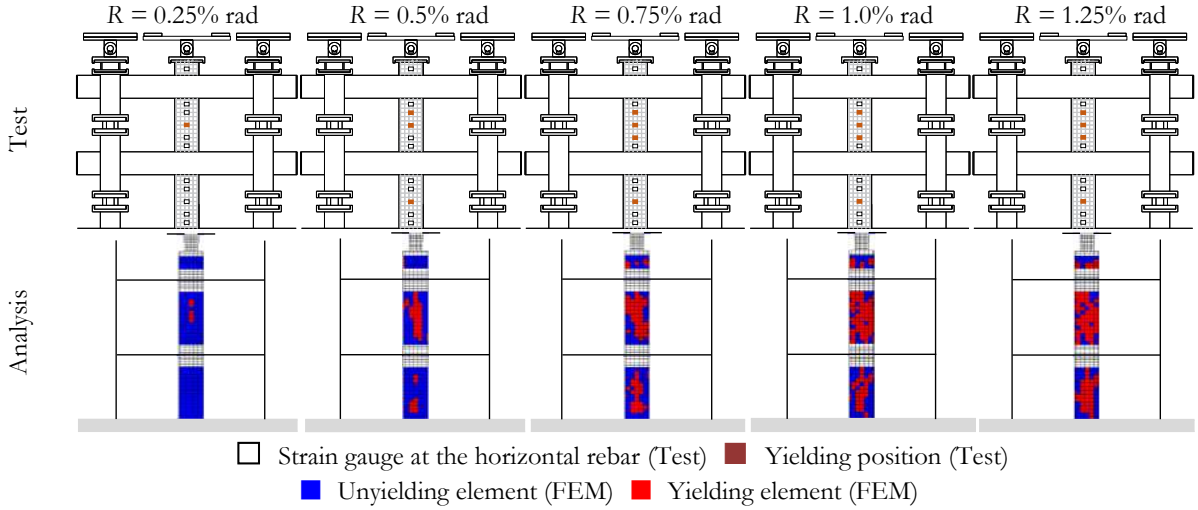
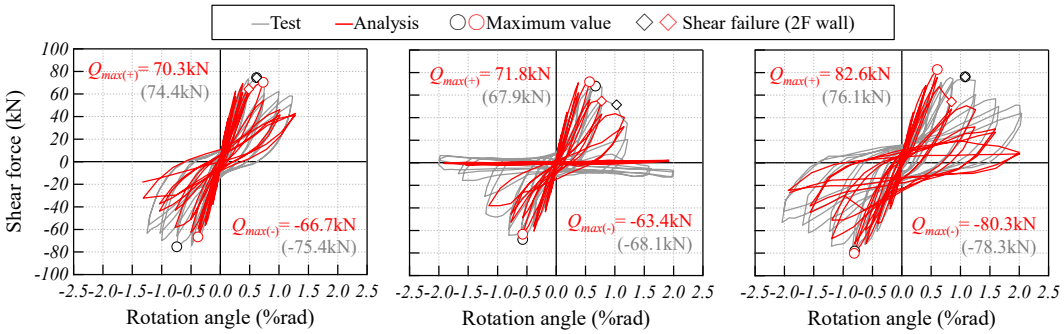


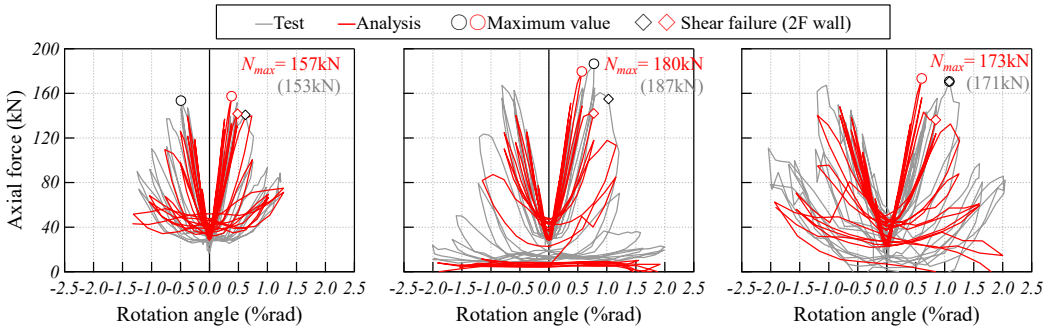
Figure 17. Comparison of the yielding of wall horizontal reinforcements (Experimental and analytical)



(a) 1F wall (b) 2F wall (c) 3F wall

Figure 18. Comparison of the shear force versus rotation angle relationships for walls (Experimental and analytical)

20, it is evident that the analysis accurately captured the reduction in shear resistance due to the diagonal strut failure in the 2F wall, consistent with the experimental results.



(a) 1F wall (b) 2F wall (c) 3F wall

Figure 19. Comparison of the axial force versus rotation angle relationships for walls (Experimental and analytical)

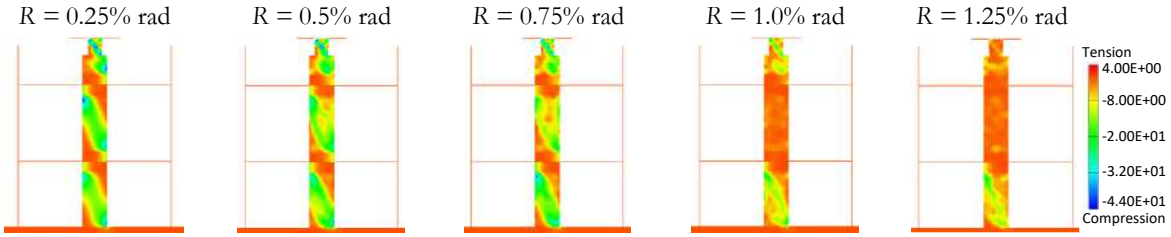


Figure 20. Distribution of minimum principal stresses for walls (Unit: MPa)

4.2 SHEAR FORCE –ROTATION ANGLE AND AXIAL FORCE –ROTATION ANGLE RELATIONSHIPS OF FLAT WALLS

Figures 18 and 19 compare the shear and axial force–rotation angle relationships of the flat walls obtained from the experiment and the analysis up to R = 1.25% rad. The analytical model reasonably reproduced the initial stiffness and maximum strength of the walls. In particular, it accurately simulated the strength degradation following shear failure of the 2F wall.

Figure 20 presents the minimum principal stress distributions obtained from the FEM analysis. Compression struts were clearly identified in all flat walls up to R = 0.5% rad, explaining the high shear resistance observed in Figure 18. At R = 0.75% rad, as shear damage progressed in the central region of the 2F wall, the strut mechanism was disrupted, leading to reduced shear transfer in subsequent cycles.

Overall, the analytical model successfully reproduced the experimental behaviour with reasonable accuracy, capturing the essential features of the observed seismic performance.

5.CONCLUSIONS

This study investigated the interaction between non-structural RC flat walls and the surrounding frame through two-dimensional finite element analyses of specimens previously tested by the authors. The analytical results were compared with the experimental observations to validate the proposed modelling approach. The analyses successfully reproduced the load–drift relationships, hysteretic behaviour, and damage progression observed in the tests. In particular, the structural performance of the flat walls at each story (including the shear force–rotation angle and axial force–rotation angle relationships) was reasonably captured, thereby demonstrating the effectiveness of the analytical model. Future research will extend this modelling approach to evaluate seismic performance and damage in high-rise buildings incorporating flat walls.

REFERENCES

AIJ [2010] *AIJ Standard for Structural Calculation for Reinforced Concrete Structures,* Architectural Institute of Japan, Japan.

Ceresa, P., Petrini, L. and Pinho, R. [2007] "Flexure-shear fiber beam-column elements for modeling frame structures under seismic loading—state of the art," *Journal of Earthquake Engineering*, Vol. 11(S1), pp. 46–88.

Ciampi, V., Eligehausen, R., Bertero, V. V. and Popov, E. P. [1982] "Analytical Model for Concrete Anchorages of Reinforcing Bars Under Generalized Excitations," *Report No. UCB/EERC-82/23*, Univ. of California, Berkeley.

Izumo, J., Shima, H. and Okamura, H. [1987] "Analytical model of reinforced concrete plate element subjected to in-plane force," *Concrete Journal*, Vol. 25, No. 9, pp: 107-120. [in Japanese]

JSCE [2022] *Standard specifications for concrete structures-Design*, Japan Society of Civil Engineers, Japan. [in Japanese]

Kolozvari, K., Biscombe, L., Dashti, F., Dhakal, R. P., Gogus, A., Gullu, M. F., Henry, R. S., Massone, L. M., Orakcal, K., Rojas, F. and Shegay, A. [2019] "State-of-the art in microscopic modeling of isolated planar reinforced concrete structural walls," *Engineering Structures*, Vol. 194, pp. 46–65.

Matsuo, K., Sanada, Y., Yoon, R. [2022] "Effects of conventional and damage control flat walls on the seismic performance of high-rise RC buildings," *Journal of Structural and Construction Engineering (Transactions of AIJ)*, Vol. 87, No. 791, pp: 128–138. [in Japanese]

Naganuma, K. [1995] "Stress-strain relationship for concrete under triaxial compression," *Journal of Structural and Construction Engineering (Transactions of AIJ)*, Vol. 60, No. 474, pp: 163-170. [in Japanese]

Naganuma, K. [1991] "Nonlinear Analytical Model for Reinforced Concrete Panels under In-plane Stresses: Study on nonlinear analytical method for reinforced concrete wall structures (Part 1)," *Journal of Structural and Construction Engineering (Transactions of AIJ)*, Vol. 421, No. 0, pp: 39-48. [in Japanese]

Naganuma, K. and Ohkubo, M. [2000] "An analytical model for reinforced concrete panels under cyclic stresses," *Journal of Structural and Construction Engineering (Transactions of AIJ)*, Volume 65, No. 536, pp: 135-142. [in Japanese]

Naganuma, K., Yonezawa, K., Kurimoto, O. and Eto, H. [2004] "Simulation of nonlinear dynamic response of reinforced concrete scaled model using three-dimensional finite element method," *Proceedings of 13th World Conference on Earthquake Engineering*, Vancouver, B.C., Canada.

National Institute for Land and Infrastructure Management [2020] *Commentary on Structural Regulations of the Building Standard Law of Japan*, Official Gazette Co-operation of Japan, Japan.

Sanada, Y., Yoon, R., Akahori, T., Ojio, Y., Kim, Y. [2017] "Softening effects of RC nonstructural flat walls on ductile concrete buildings," *Earthquake Engineering and Structural Dynamics,* Vol. 46, No. 10, pp: 1645–1665.

Yoshida, H., Sanada, Y., Awano, M. [2021] "Feasibility study on evaluating required seismic capacity for safety limit design of high-rise RC buildings in OS1 and OS2 regions and its estimation based on the equivalent linearization method," *Journal of Structural and Construction Engineering (Transactions of AIJ)*, Vol. 86, No. 780, pp: 235–245. [in Japanese].

Zhao, PZ., Sanada, Y., Yoon, R., Quan, CR., Uchida, B. [2025] "Experimental structural performance evaluation of a 2.5-story model frame representing lower stories of high-rise RC buildings with flat walls," *Japan Architectural Review*, Vol.8, No.1, e70035.

Shaking Table Test of Seismic-Resistant Ceiling Systems with Asymmetric Mass or Stiffness Distribution

Haruki Yamaguchi[1], Tadashi Ishihara[2], and Yusuke Oki[3]

[1] Graduate Student, Institute of Science Tokyo
4259 Nagatsuta-cho, Midori-ku, Yokohama, Kanagawa, 226-8501, Japan
e-mail: yamaguchi.h.3a08@m.isct.ac.jp
[2] Professor, Institute of Science Tokyo, Dr. Eng.
4259 Nagatsuta-cho, Midori-ku, Yokohama, Kanagawa, 226-8501, Japan
e-mail: ishihara.t.458a@m.isct.ac.jp
[3] Senior Research Engineer, Building Research Institute, Dr. Eng.
1 Tachihara, Tsukuba, Ibaraki, 305-0802, Japan
e-mail: oki_y@kenken.go.jp

Abstract. In this paper, seismic responses of earthquake-resistant ceilings with asymmetric mass or stiffness properties are investigated through shake table tests. The vibration excitation is horizontal along one axis. The test specimens have a plan dimension of approximately 2.8 m in the excitation direction and approximately 3.6 m in the orthogonal direction. Two sets of bracing are installed along both the excitation direction and orthogonal direction. A total of four specimens are tested. Three specimens have mass or stiffness eccentricity. The comparative test specimen has no eccentricity. A ground motion and floor response accelerations are used as inputs. All input motions are within the linear (elastic) response range of the test specimens. The differences in response for each input motion are examined. This paper presents the torsional response, comparisons of response waveforms for each input motion, peak displacement and peak acceleration for each test specimen and mode characteristics. The characteristics of each mode are presented by comparing the experimental results and theoretical ones. The contribution of each mode to the responses is examined.

Keywords: Japanese seismic-resistant ceiling, Torsional response, Shake table test, Eigenmode, Eccentricity

1. INTRODUCTION

Damage to non-structural components during earthquakes has been reported, and research to enhance the seismic resistance of non-structural components is being conducted in many countries and regions [Perrone, 2019; Ryu, 2019]. In Japan, braces are often installed to ceilings to enhance earthquake resistance. However, depending on the layout of equipment in the ceiling cavity, uneven bracing placement may cause stiffness eccentricity in the ceiling. Therefore, it is essential to examine the effects of torsion due to this eccentricity.

Regarding the torsional effects due to eccentricity in secondary systems, Ishihara analytically investigated the torsional vibration using a single-story, single-axis eccentric model, based on the modal analysis [Ishihara, 2024]. On the other hand, experimental studies have been conducted using conventional ceilings as test specimens, focusing on ceiling falling [Futatsugi, 2014], seismic reinforcement [Watakabe, 2012] and brace buckling [Kobayashi, 2020]. However, no studies have examined the effects of torsion. This paper investigates the effect of torsion on ceiling responses during earthquakes through shake table experiments.

2. TEST PROGRAM

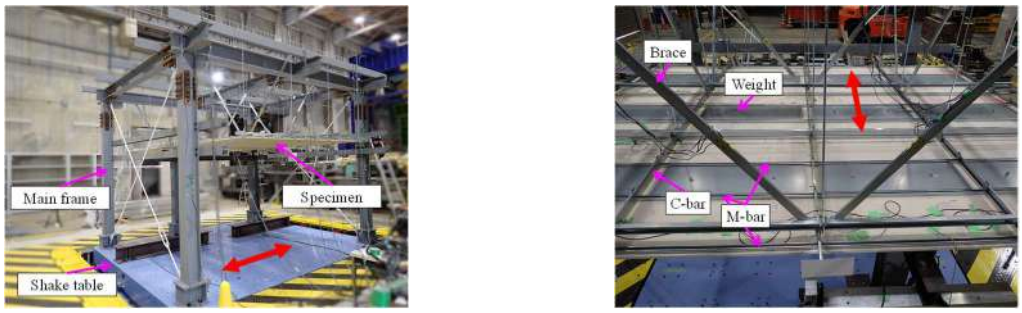
Figure 1 and Photo 1 show the test setup. This setup consists of a shake table, a frame and a test specimen.

2.1 SHAKE TABLE

The dimensions of the shake table are 4,500 mm (excitation direction) × 3,500 mm (orthogonal direction). Only uniaxial horizontal excitation can be generated. The arrow in Figure 1 shows the direction of excitation.

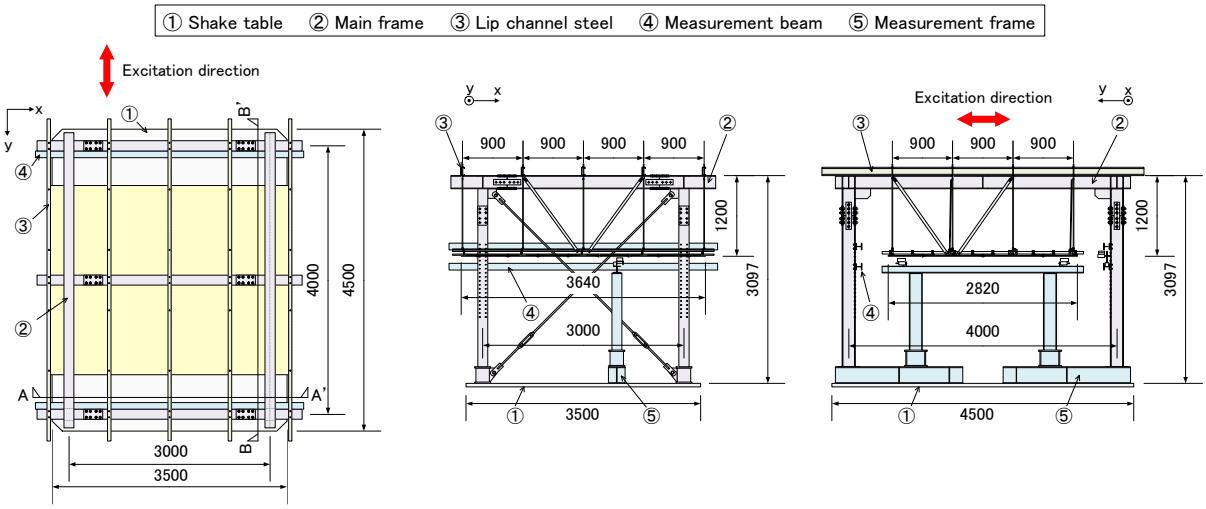
2.2 FRAME

The main frame used to suspend the test specimen is shown in Figure 1. It spans 4,000 mm in excitation direction and 3,000 mm in orthogonal direction, with a height of 3,097 mm. The main frame is supported by four columns mounted on the shake table, with column bases connected using high-strength bolts. Sections of columns and beams are both H-194×150×6×9. Columns and beams are rigidly connected, and splice joints are connected by high-strength bolts. The natural period of the main frame is 0.084 s. At the top of the main frame, lip channel members with cross-section C-125×50×20×3.2 are bolted to the beams. Holes for threaded suspension bar are provided in the lip channel members at 900 mm spacing. Turnbuckles with a diameter of 22 mm are attached in the orthogonal direction. Instrumentation is installed both on a measurement beam and on an independent measurement frame located on the shake table. The measurement beams (H-100×100×6×8) are arranged orthogonally to the excitation direction and bolted to the main frame's columns at heights of 1,740 mm and 1,950 mm.



(a) Overall **(b) Specimen**

Photo 1 Test set up



(b-1) Excitation direction (A-A') (b-2) Orthogonal direction (B-B')

(a) Plain (b) Section

Figure 1 Test set up

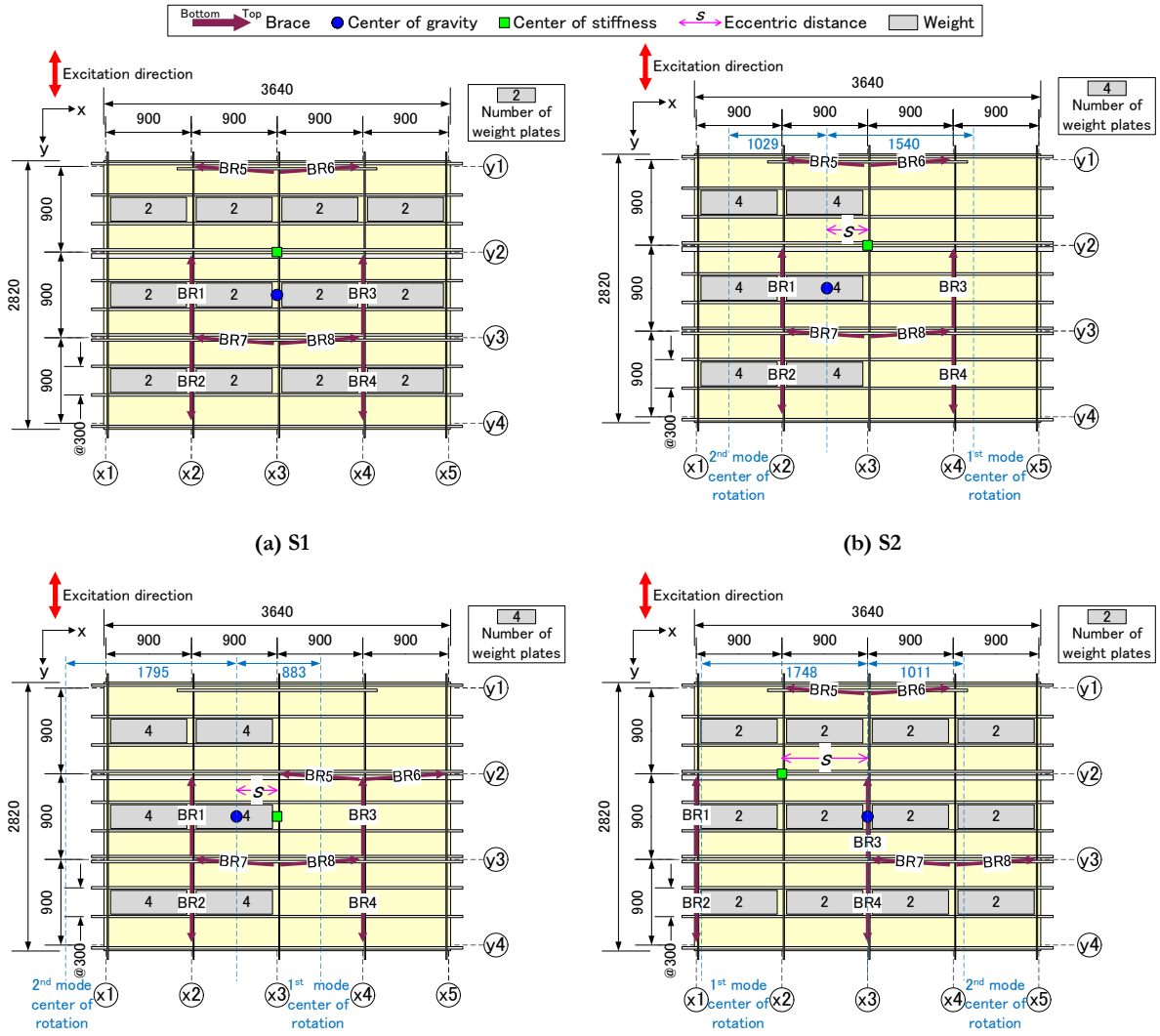
2.3 TEST SPECIMEN

Table 1 lists the test specimens, and Figure 2 shows them. They are the Japanese-style conventional seismic-resistant ceilings. The distance from the suspension point to the bottom surface of the ceiling is 1,200 mm. The plan dimensions are approximately 2,820 mm in the excitation direction and 3,640 mm in the orthogonal direction. The ceiling framework is composed of members with JIS (Japanese Industrial Standards) 19-type sections. M-bars are installed at approximately 300 mm pitch (Photo 1 (b)). To enhance seismic resistance, clips are fastened at the top with small bolts and connected to the M-bar and C-bar using screws (Photo 2 (b)). Hangers are similarly connected to the C-bar with screws (Photo 2 (c)). Two sets of braces ([-38×12×1.2) are installed in both excitation and orthogonal directions. The ceiling gypsum boards and M-bars are fastened with screws at 150 mm pitch. The ceiling boards are single-layer gypsum boards with a thickness of 12.5 mm. To increase the inertial force applied to the ceiling, steel weights (800 mm × 250 mm, thickness t=3.2 mm, approximately 5 kg per piece) are placed on the boards and fastened with bolts. The total weight of the specimen is approximately 260 kg.

Table 1 List of specimens

Specimen	Mass eccentricity	Stiffness eccentricity	Eccentricity ratio R_{ex}	Radius of gyration i [cm]	Elastic radius e [cm]	Eccentric distance s [cm]
S1	-	-	0	133	127	0
S2	○	-	0.34	122		43
S3	○	-	0.43		101	
S4	-	○	0.71	133	127	90

○: eccentricity, - : no eccentricity



(a) S1

(b) S2

(c) S3

(d) S4

Figure 2 Plan of specimens

For specimens with eccentricity, two types of eccentricity are considered: (1) stiffness eccentricity by offsetting the brace arrangement and (2) mass eccentricity by uneven distribution of weights. S1 has no eccentricity; S2 and S3 have mass eccentricity; S4 has stiffness eccentricity. S3 has smaller elastic radius e than that of S2 by reducing the spacing of the orthogonally oriented braces. All specimens are constructed with the same framework, with only the placement of braces and weights changed.

The eccentricity ratio R_{ex} is calculated using Equation (1). R_{ex} is an index used in Japanese structural design of buildings. This index is used to represent the magnitude of eccentricity in this paper. The radius of gyration i is calculated, assuming a uniform weight distribution across the entire specimen for S1 and S4, and across half the specimen for S2 and S3. The higher the numerical value of the specimen name, the larger the eccentricity ratio R_{ex}.

$$R_{ex} = s/e \tag{1}$$

Here, s is the eccentricity distance in the considered direction, and e is the elastic radius about the center of stiffness.

2.4 INSTRUMENTATION

Figure 3 shows the locations and directions of the measurement instruments. The relative displacements and the absolute accelerations of the ceiling surface are measured. Displacements are measured in excitation direction. Laser displacement sensors mounted on the measurement beam are used to track targets which are attached to the edges of the C-bars of the specimen. Measurement points for displacement consist of five locations in the excitation direction (D_{x1} to D_{x5}). Accelerations are measured in the excitation direction. Accelerometers are installed on the top surface of the ceiling. Measurement points for acceleration consist of five locations in the excitation direction (A_{x1} to A_{x5}).

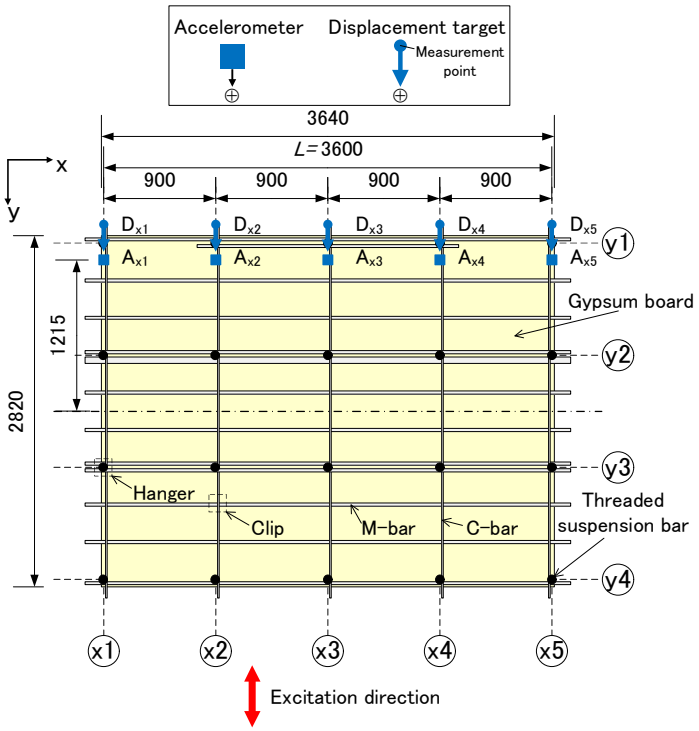
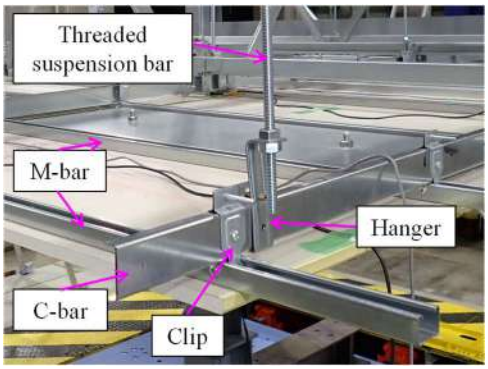


Figure 3 Measurement plan



(a) Joint



(b-1) Clip (Front)



(b-2) Clip (Side)



(c) Hanger

Photo 2 Ceiling framework

2.5 INPUT MOTION

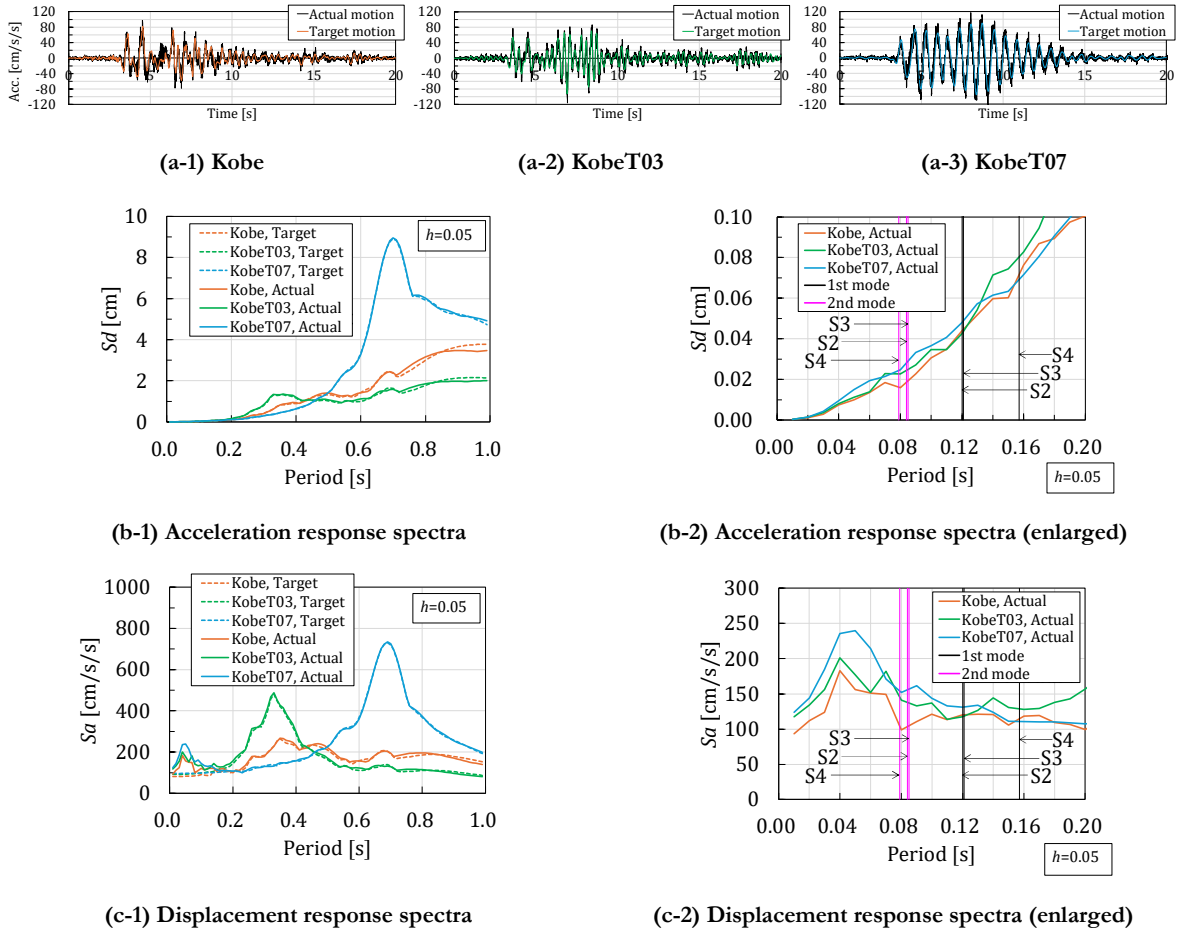
Table 2 lists the input motions. Figure 4 shows the corresponding time histories and response spectra (damping ratio h = 0.05) of the target and actual motions applied to the shake table. For secondary systems such as ceilings, the floor response acceleration (hereafter FRA) of the structural frame acts as an inertial force input. Therefore, two types of input motions are considered: (1) observed ground motion and (2) FRA of a single-degree-of-freedom (SDOF) system representing the structural frame subjected to the observed ground motion.

The observed ground motion used as the input motion is JMA Kobe NS component (hereafter Kobe). Kobe is used for FRA, and the floor responses are obtained by time-history analyses of an SDOF system with natural periods of 0.3 s and 0.7 s. These are hereafter referred to as KobeT03 and KobeT07, respectively.

The input scaling is set as follows: 0.1 times the original Kobe motion for Kobe and 0.05 times the obtained acceleration responses for KobeT03 and KobeT07. All input motions are within the linear (elastic) response range of the test specimens.

Table 2 Input motion

No.	Input motion	Scale (%)	PGA (Target) (cm/s/s)	Note
1	Kobe	10	82	Ground motion
2	KobeT03	5	92	Floor response acceleration (T=0.3 s, Kobe input)
3	KobeT07	5	96	Floor response acceleration (T=0.7 s, Kobe input)



(a-1) Kobe **(a-2) KobeT03** **(a-3) KobeT07**

(b-1) Acceleration response spectra **(b-2) Acceleration response spectra (enlarged)**

(c-1) Displacement response spectra **(c-2) Displacement response spectra (enlarged)**

Figure 4 Input motion

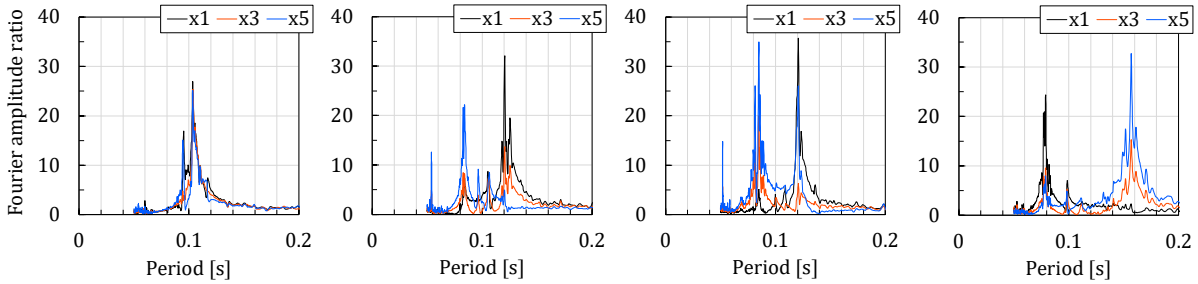
3. TEST RESULTS

3.1 NATURAL PERIOD OF CEILINGS AND EIGENMODE

Figure 5 shows the Fourier amplitude ratios under the Kobe input, which are the ratios of A_{x1} to A_{x5} to the measured acceleration at the top center of the main frame. The non-eccentric S1 shows its dominant mode at the period of 0.1 s. For the eccentric S2 to S4, two modes appear around 0.1 s due to the influence of torsion. For S2 and S3, the second mode is dominant on the side without the weight (x5). Additionally, for S3, amplitudes of the primary mode are relatively large at both x1 and x5. For S4, the second mode is dominant on the side where the brace is attached (x1).

Table 3 shows the measured ceiling natural periods under the Kobe input. Except for S3, the ratio of the second to first natural periods T_2/T_1 decreased as the eccentricity ratio R_{ex} increased. This trend is consistent with the theoretical relationship also described in reference [Ishihara, 2024]. The experimental natural period ratios capture the trend with theoretical values.

Figure 6 shows the Fourier amplitude ratio at each measurement position for each mode in S2, S3 and S4. The data is the same as in Figure 5. Each dashed line indicates the center of rotation (node) of each mode obtained from the theory, indicating that the amplitude of each mode decreases near it. For example, in Figure 6 (b), it can be confirmed that the plot for the second mode increases as the distance from the node at around x1 increases. Furthermore, the values are large at both ends (x1 and x5) of the first mode. In general, theoretical modes and the experimental ones agree well.

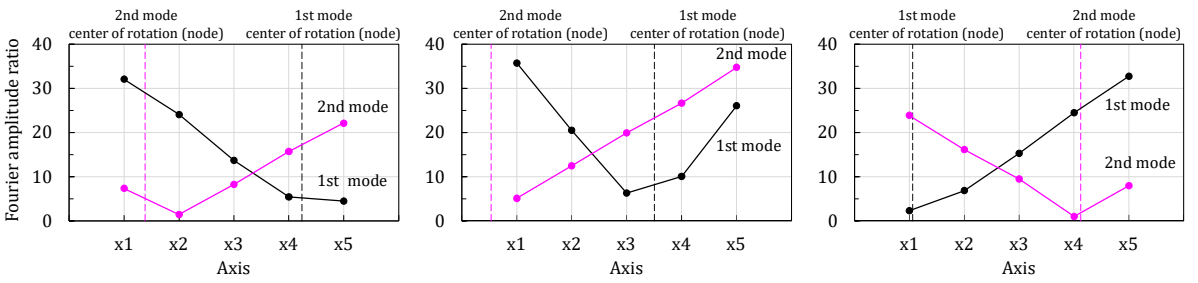


(a) S1 **(b) S2** **(c) S3** **(d) S4**

Figure 5 Fourier amplitude ratio, Kobe

Table 3 Natural period of ceilings

Specimen	Natural period		T_2/T_1 (Experiment)	T_2/T_1 (Theory)	Input motion
	T_1 [s]	T_2 [s]			
S1	0.103	-	-	-	Kobe
S2	0.120	0.084	0.700	0.715	
S3	0.121	0.085	0.702	0.646	
S4	0.157	0.079	0.503	0.507	



(a) S2 **(b) S3** **(c) S4**

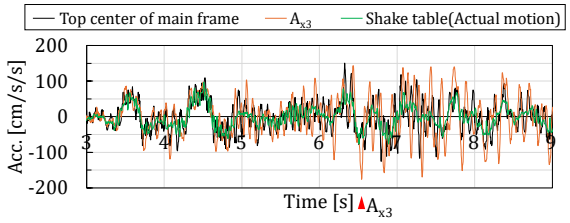
Figure 6 Fourier amplitude ratio at each measurement position for modes

3.2 TIME HISTORY

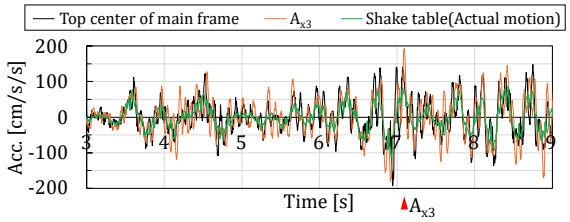
Figures 7 and 8 show the time histories of displacements and accelerations for S4. Each figure displays data from 3 s to 9 s. The red triangle marks in the figure indicate the peak values. Input motion is Kobe in (a), KobeT03 in (b) and KobeT07 in (c).

Figure 7 shows the acceleration response A_{x3} as the orange line, the acceleration measured at the top center of the main frame as the black line and the acceleration measured at the shake table (Actual motion) as the green line. Since the frame and ceiling test specimens have short periods, the three motions shown in Figure 7 are generally similar to one another. For Kobe, the A_{x3} component attached to the ceiling test specimen is the largest, but for KobeT03 and KobeT07 with FRA as the input, the frame and ceiling exhibit similar levels.

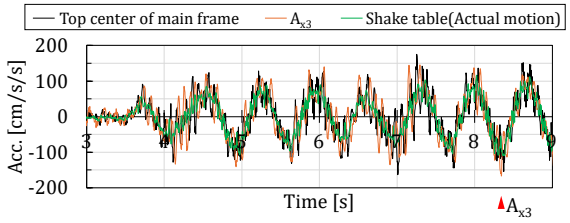
Figure 8 shows displacement responses D_{x1} (blue line) and D_{x5} (orange line) of S4. In Figures 8 (a), (b) and (c), the waveform amplitude differs depending on the measurement location.



(a) Kobe

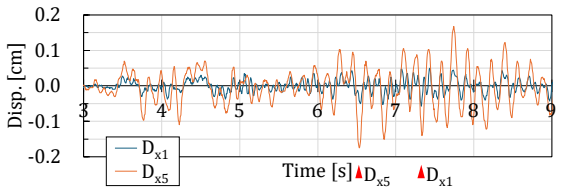


(b) KobeT03

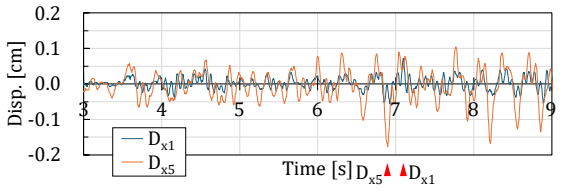


(c) KobeT07

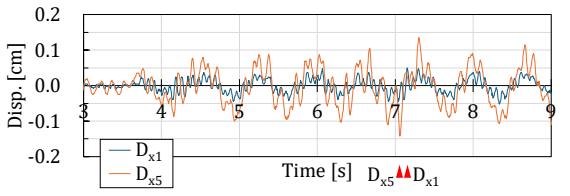
Figure 7 Acceleration time history at A_{x3} (S4)



(a) Kobe



(b) KobeT03



(c) KobeT07

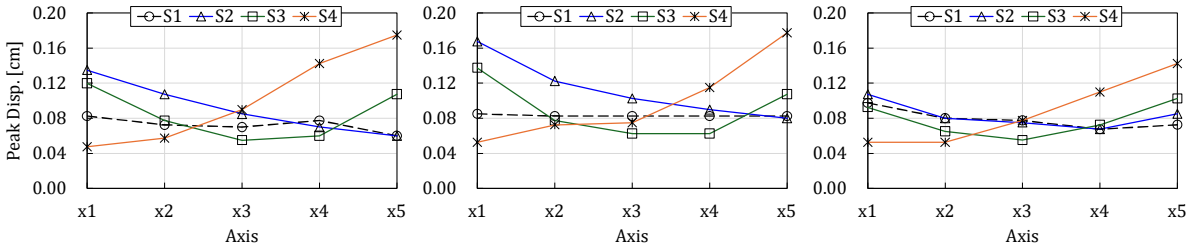
Figure 8 Displacement time history at D_{x1} and D_{x5} (S4)

3.3 PEAK TRANSLATIONAL RESPONSES

Figures 9 and 10 show the peak displacement and acceleration responses at each measurement point for each input motion. The horizontal axis represents positions x1 to x5, corresponding to the measurement locations in the excitation direction. The vertical axis represents the peak values of displacements or accelerations. Figures (a), (b) and (c) correspond to the Kobe, KobeT03 and KobeT07 input motions, respectively, showing results for all specimens. It should be noted that the times at which the peak responses occur do not necessarily coincide.

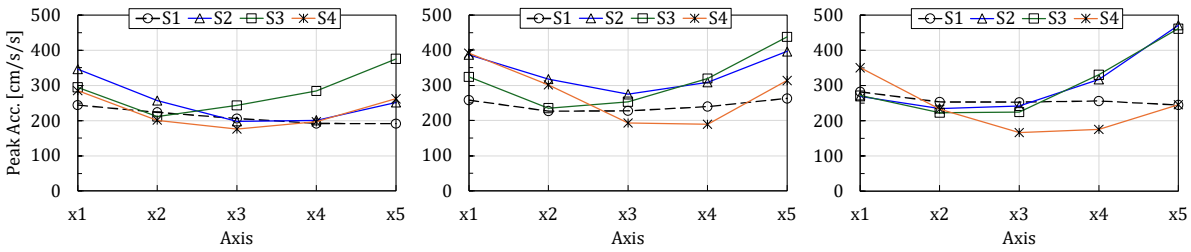
Focusing on displacements in Figure 9, the non-eccentric S1 exhibits uniform peak displacements. In S2, the side with concentrated weights experiences larger inertial forces, leading to increased displacement response at the corresponding end (x1). S3 shows a "U-shaped" pattern of peak displacements symmetric about x3. This is related to the position of the mode's center of rotation. S4 shows a larger displacement at x5. This tendency is consistent with the static theory, which states that the center of gravity displaces more than the center of stiffness if a static horizontal load acts. The response increases by up to about 2 times in S4, and up to 1.5 times in S2 and S3 compared to S1, which has no eccentricity. In Figure 9(c), the ratio of displacement responses of S2, S3 and S4 to S1 is smaller overall than in Figures 9(a) and 9(b). It seems that the increase in displacement due to eccentricity tends to be suppressed when exposed to FRA with relatively long natural period (KobeT07) rather than when exposed to direct ground motion (Kobe) or FRA with relatively short natural period (KobeT03).

Focusing on accelerations in Figure 10, the non-eccentric S1 exhibits uniform peak accelerations. For S2, S3 and S4, the plots show a "U-shaped" peak with a depression in the center of the excitation direction and increased response at the edges. For S2 and S3, the response is about twice as high as that of S1, which has no eccentricity. Regarding acceleration, no reduction in torsional response due to differences in the type of input motion is observed. As shown in Figure 4(b-2) and Figure 4(c-2), the displacement spectrum value is larger for the first mode than for the second mode, while the acceleration spectrum value is the same degree for the first and second modes. Therefore, the trends in the displacement and acceleration responses are different.



(a) Kobe **(b) KobeT03** **(c) KobeT07**

Figure 9 Peak displacement



(a) Kobe **(b) KobeT03** **(c) KobeT07**

Figure 10 Peak acceleration

3.4 PEAK TORSIONAL RESPONSES

Figures 11 and 12 show the peaks of the translational displacement of the center of gravity U_G and the rotational angle θ for each specimen. The rotational angle θ is calculated using Equation (2). The vertical axis represents the peak values of U_G and θ, respectively, while the horizontal axis corresponds to the input motions. The center-of-gravity position for S1 and S4 is on x3, while that for S2 and S3 is between x2 and x3.

$$\theta = (D_{x5} - D_{x1})/L \tag{2}$$

Here, D_{x1} and D_{x5} represent the measured displacements at both ends of the specimen in the excitation direction. L is the distance of the two displacement sensors, which is 3,600 mm.

In Figure 11, the peak U_G values of each input motion for each specimen are approximately in the order S2 > S4 > S1 > S3. In specimens with eccentricity, S2 has the smallest R_{ex} and S4 has the largest one. The peak U_G of S2 is higher than that of S4. In addition, S3 shows a smaller peak than non-eccentric S1. These observations indicate that the magnitude of R_{ex} does not directly correlate with the peak U_G.

In Figure 12, the peak θ values for each input motion show the order S4 ≈ S3 > S2 > S1, arranged in order of increasing R_{ex}.

Figure 13 shows the ratio of the peak rotational displacement $i\theta$ to the peak translational displacement of the center of gravity U_G (hereafter rotation ratio $i\theta/U_G$) for each specimen, representing the degree of torsion. The vertical axis represents the rotation ratio $i\theta/U_G$, and the horizontal axis corresponds to the input motions. A larger value of $i\theta/U_G$ indicates a greater contribution of torsional rotation.

Even when the input motion changes, $i\theta/U_G$ for each specimen does not change significantly. This trend differs from the numerical analysis results using artificial ground motion [Ishihara, 2024]. $i\theta/U_G$ is the largest for S3 and does not follow the order of R_{ex}. As pointed out in literature [Ishihara, 2024], R_{ex} is not necessarily enough index to represent dynamic torsional behavior, because it neglects mass distribution or radius of gyration i.

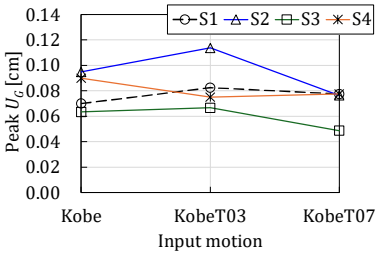


Figure 11 Peak U_G

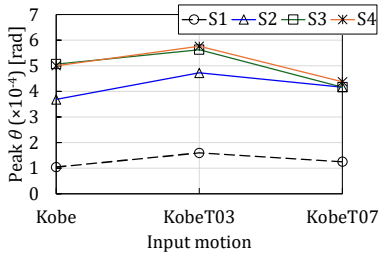


Figure 12 Peak θ

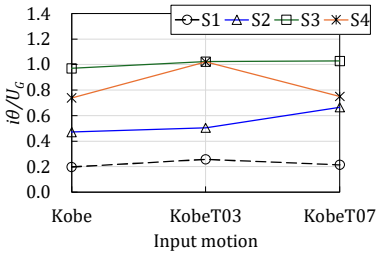


Figure 13 Rotation ratio $i\theta/U_G$

4. CONCLUSIONS

In this paper, the effects of non-uniform mass and stiffness distributions on the seismic response of Japanese-style conventional seismic-resistant ceilings are investigated through shake table tests using both ground motion and floor response accelerations as inputs. The results are summarized as follows.

1. When eccentricity is present, the first and second natural periods appear on both sides of that of the non-eccentric case.

2. The mode shapes obtained from the Fourier amplitude ratios correspond relatively well to the theoretical values.

3. Peak displacement and acceleration responses in specimens with eccentricity increase by up to about 2 times compared to non-eccentric one.

4. Whether the input is seismic ground motion or floor response, the rotation ratio $i\theta/U_G$ does not change significantly. This trend differs from the numerical analysis results [Ishihara, 2024], where an artificial ground motion is used.

ACKNOWLEDGEMENTS

This work is supported by JSPS KAKENHI Grant Number JP23K26244.

REFERENCES

Futatsugi, S., Minewaki, S., Okamoto, H., Takahashi, H., Yamamoto, M., Tomioka, H., Kamoshita, N., Aoi, A. [2014] "A study on falling down of suspended ceilings without seismic bracing," *AIJ J. Technol. Des.*, Vol. 20, No. 44, pp. 149-152. (In Japanese)

Ishihara, T. [2024] "Seismic torsional response of asymmetric secondary systems," *18th World conference on Earthquake Engineering*, Milan, Italy

Kobayashi, T., Arai, T. [2020] "Flexiural-torsional buckling capacity of brace for aseismic ceiling," *J. Struct. Constr. Eng.*, *AIJ*, Vol. 85, No. 770, pp. 629-637. (In Japanese)

Perrone, D., Calvi, P. M., Nascimbene, R., Fischer, E. C., Magliulo, G. [2019] "Seismic performance of non-structural elements during the 2016 Central Italy earthquake," *Bulletin of Earthquake Engineering*, Vol. 17, pp. 5655-5677.

Ryu, K. P., Reinhorn, A. M. [2019] "Analytical study of large-area suspended ceilings," *Journal of Earthquake Engineering*, Vol. 23, No. 4, pp. 592–624.

Watakabe, M., Iizuka, S., Inai, S., Ishioka, T., Takai, S., Kanagawa M. [2012] "Development of seismically engineered suspended ceiling of large space structures subjected to earthquake excitation," *AIJ J. Technol. Des.*, Vol. 18, No. 39, pp. 465-470. (In Japanese)

Preliminary observations on the effects of 2024-2025 bradyseism earthquakes on nonstructural elements in Campi Flegrei

G. Magliulo[1,2], C. R. Addeo[2], D. D'Angela[2], M. De Stefano[3], C. Di Salvatore[2] and F. Tuozzo[2]

[1] University of Naples Federico II, Department of Structures for Engineering and Architecture
Via Claudio 21, 80125 Naples, Italy
{gmagliul, carmenrosaria.addeo, danilo.dangela, chiara.disalvatore, federico.tuozzo} @unina.it

[2] National Research Council (CNR), Construction Technologies Institute (ITC)
Via Lombardia 49, 20098 San Giuliano Milanese, Italy

[3] University of Firenze, Department of Architecture
Via della Mattonaia 8, 50121 Florence, Italy
e-mail: mario.destefano@unifi.it

Abstract. This study presents a preliminary assessment of nonstructural damage observed in various buildings in the areas of Campi Flegrei, following the most intense seismic events induced by bradyseism that occurred between May 20, 2024, and June 30, 2025. Infill walls, partition walls, finishes, furnishings, and contents often experienced light to moderate damage. Furniture/object overturning and content displacement was often observed, also in public and commercial buildings. This highlights the importance of anchoring furnishings for safety purposes. In museums, damage was minimal thanks to mitigation measures already in place. On-site inspections and analyses revealed a non-uniform distribution of damage to infill and partition walls along the building height. This phenomenon is attributable to the dynamic structural characteristics of the buildings, particularly their stiffness and natural resonance frequency. The document recommends safety assessments in accordance with the NTC 2018 code, mitigation measures, and best practices for the management of furnishings. In conclusion, it emphasizes the need for an integrated seismic risk management approach to protect people, property, and cultural heritage.

Keywords: Bradyseism, Campi Flegrei, Nonstructural elements, Earthquake, Damage.

1. INTRODUCTION

In recent years, the increasing frequency of low-intensity to medium-intensity seismic events in volcanic areas such as the Campi Flegrei has highlighted the need to deepen the study of seismic response, not only of structurally significant buildings, but also of non-structural elements and interior contents, which are often of high historical, cultural, or economic value [Prota et al., 2022]. In this context, special attention must be given to buildings that house museums, art collections, or historical archives, where damage to non-load-bearing components can be equally critical. Non-structural elements include both fixed architectural components, such as infill walls, partitions, suspended ceilings, and window frames, and movable or semi-movable items, such as furniture, display cases, and artworks, which are often unanchored [D'Angela et al., 2024]. Although these elements do not contribute to the building's load-bearing capacity, they can sustain significant damage during a seismic event, compromising occupant safety, the usability of structures, and, in some cases, resulting in irreversible cultural losses [Magliulo and D'Angela, 2024]. Regarding the Phlegraean bradyseism, the predominant frequencies of ground motion tend to fall within a specific range, which may interact significantly with the natural vibration period of buildings. As a result, structures with dynamic characteristics similar to those of the ground may experience resonance phenomena, amplifying seismic effects and related damage, especially to the most vulnerable elements. Within this framework, it is fundamentally important to understand how a building's natural vibration period influences the damage level sustained by non-structural elements, in order to identify the categories of buildings and contents that are most at risk [Magliulo et al., 2014]. A systematic analysis of seismic response as a function of vibration period not only allows for a better interpretation of observed field damage, but also informs targeted risk prevention and mitigation strategies, through either local or global interventions on existing buildings or those under design. The present study fits into this context, offering a comparative numerical analysis of the seismic response of three buildings of different height and stiffness, representative of structures with short, medium, and long periods, subjected to real seismic recordings associated with bradyseismic events. The dynamic analyses aim to evaluate acting forces, floor accelerations, inter-story drifts, and potential amplification effects based on the buildings' dynamic properties, with particular focus on the impact on non-structural elements. The objective of this work is twofold: (a) to analyse the influence of a building's natural vibration period on the severity of damage observed following low-magnitude seismic events that may nonetheless be harmful to non-structural components, such as those recorded in the Campi Flegrei area in 2024 and 2025. As a complement to the numerical analyses, the results are compared with in-situ observations made after the seismic events of May 20, 2024, and March 13, 2025, in order to verify the consistency between the model-predicted response and the actual recorded damage. (b) to provide operational guidance for assessing the seismic capacity of buildings and for developing risk mitigation strategies, particularly for the existing architectural and cultural heritage. This integrated approach is essential for addressing, in a scientifically sound and informed manner, the challenges posed by the increasing seismicity of the Phlegraean area, with a view toward urban resilience and heritage preservation.

2.DATA AND SEISMIC CONTEXT

The Campi Flegrei area represents a complex volcanic system with high seismic and volcanic risk, characterized by bradyseismic episodes and micro-seismicity that can significantly impact the safety conditions of buildings and infrastructure across the territory. During the period under investigation, two significant seismic events were recorded: The first occurred on May 20, 2024, at 18:44 UTC, with a magnitude of 4.3, a hypocentral depth of 2.57 km, and an epicentre located at coordinates 40.8273°N, 14.13875°E. The second event, marking the peak of the seismic sequence, occurred on March 13, 2025, with a duration magnitude (M_d) of 4.6. This earthquake, the strongest recorded in the Campi Flegrei area since the beginning of instrumental seismic monitoring [Weekly Bulletin 10/03/2025 – 16/03/2025], had a hypocentral depth of 2.41 km, with an epicenter at 40.8188°N, 14.1575°E. Both events generated ground

motions with distinct characteristics in terms of intensity, duration, and spectral content, providing essential data for evaluating local seismic response and studying the effects induced on existing buildings. The seismic records used for the numerical analyses were collected from a network of accelerometric stations located at strategic points throughout the area, offering good spatial coverage that allowed for capturing significant variations in ground response [Cito et al., 2025]. In particular, the East-West (applied along the X direction) and North-South (Y direction) seismic components were selected, as they are considered representative of the main horizontal forces acting on buildings. For each station, recordings from both seismic events were considered, with special attention paid to time-domain and spectral characteristics that influence the dynamic response of structures, such as ground motion duration, dominant frequency, and energy content. These data served as the basis for the time-history numerical analyses performed on the model buildings, enabling a detailed assessment of the effects of seismic motion on both structural and non-structural elements, in terms of forces, deformations, and possible local amplifications depending on the building's natural vibration period. In this context, an in-depth understanding of the seismic setting and the availability of high-quality accelerometric data represent key factors for developing reliable predictive models and designing effective mitigation strategies to ensure the seismic safety of the built heritage.

3. FIELD OBSERVATIONS ON STRUCTURAL AND NON-STRUCTURAL DAMAGE

Following the seismic events of May 20, 2024, and March 13, 2025, an extensive on-site investigation campaign was carried out to document the damage sustained by buildings located in the Campi Flegrei area. The inspections, conducted between May 2024 and July 2025, involved both buildings of historical and cultural significance, such as the Archaeological Museum of the Baia Castle and the Church of Sant'Anna in Bagnoli, as well as strategic facilities like the ASL Napoli 2 Nord – District Health Center 35, and numerous residential buildings distributed throughout Pozzuoli, Bagnoli, and Naples. The survey included both reinforced concrete and masonry constructions, with the aim of identifying various structural and non-structural vulnerabilities based on construction characteristics, state of preservation, and dynamic response to the seismic events. Structural damage observed was generally limited and confined to pre-existing buildings already affected by degradation or previous construction deficiencies. At the Church of Sant'Anna, following the March 13, 2025 earthquake, cracks were observed on the main façade and the bell tower, accompanied by localized detachment of decorative friezes and external plaster. The most significant cracks appeared near the arches, indicating potential critical areas that should be closely monitored in anticipation of future seismic events. A residential building on Via Ilioneo, in Bagnoli, presented small cracks in the vaulted ceiling of the internal staircase, without however showing significant compromise of its load-bearing capacity. In contrast, non-structural damage proved to be much more widespread, with intensity ranging from slight to moderate. In the most severe cases, it led to the temporary evacuation of buildings. Interior partitions, infill walls, and vertical finishes were among the most vulnerable elements: superficial cracks were found in plaster coatings, while in moderate cases, the cracks reached a depth sufficient to affect the interface between infill and structure, especially at geometric discontinuities such as niches, corners, or openings (Figure 1). In some buildings, immediate action was necessary to prevent further deterioration, through temporary repairs or emergency stabilization measures. No evident damage was observed in suspended ceilings or lighting systems on lower floors; however, significant consequences were noted with respect to furnishings and internal contents, including in public-use buildings.



Figure 1. Cracks developed at geometric discontinuities along the building interface, as a result of stresses induced by seismic events.

In a supermarket in Pozzuoli, products were reported to have fallen from the shelves, resulting in broken bottles and widespread spillage of goods, which required immediate intervention to ensure safety. Similarly, in the museums inspected, such as the one at the Baia Castle, no significant damage was observed to the structure or to the display systems, although some small items, such as coins or loom weights, were found to have been displaced or fallen from their original positions, confirming the actual shaking experienced. Other minor damage was noted to window frames and fittings. In an apartment located on Via Ilioneo, some shutters were found completely open, presumably as a result of the vibrations; in several inspected apartments, the overturning of objects inside display cabinets was also observed (Figure 2).



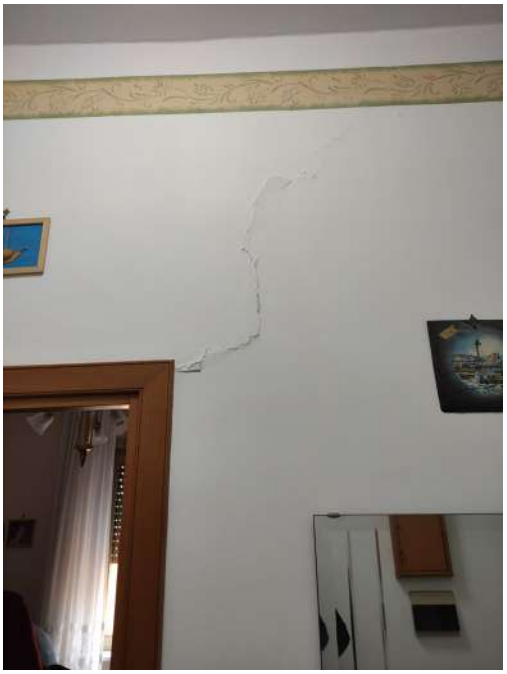
Figure 2. Overturning of objects inside a display cabinet in an inspected apartment.

In several residences located between Via Acate and Via Caio Asinio Pollione, in Bagnoli (Figure 3 and Figure 4), the most visible damage was concentrated on the ground floor. Buildings situated on slopes also exhibited partial detachment of infill walls and cracks in internal partition walls, although there was no evidence of compromised overall structural stability. While these damages are not critical from a structural standpoint, they contribute to increasing public concern and fuel the debate over the seismic adequacy of existing buildings.



Figure 3. Ground floor of a building located on Via Acate, Bagnoli.

(a)



(b)



Figure 4. Photographs showing the damage observed in reinforced concrete residential buildings located in Bagnoli, in (a) Via Acate and (b) Via Caio Asinio Pollione.

The results of the field observations showed good agreement with the outcomes of the numerical analyses, particularly regarding the higher seismic demand experienced by stiffer buildings (short-period structures), which were subjected to greater forces compared to more flexible ones. In multi-story buildings, a greater amplification of accelerations was recorded on intermediate or upper floors, consistent with modelling results that highlighted acceleration and inter-story drift peaks precisely at the central floors. These observations einforce the need for a thorough assessment of the behaviour of non-structural elements, which are often overlooked but may prove critical in terms of safety and post-earthquake functionality.

4.SEISMIC CAPACITY ASSESSMENT AND RISK MITIGATION FOR NON-STRUCTURAL ELEMENTS

4.1 CAPACITY

The seismic capacity of both structural and non-structural elements plays a fundamental role in risk assessment and in defining mitigation strategies for building safety, especially in historical and cultural contexts. Capacity refers to the strength, ductility, and deformability of elements when subjected to seismic loads and must be analysed considering specific construction characteristics, materials used, as well as degradation related to age and maintenance interventions [Celano et al., 2016]. For structural elements, capacity is commonly evaluated through experimental testing, detailed numerical modelling, and analyses based on technical codes, which set safety limits based on force, displacement, and deformation values. In particular, capacity must ensure that, even in the event of intense seismic events, the structure can dissipate energy without sustaining irreparable damage, preserving both global and local stability. For non-structural elements, often characterized by lower ductility and strength, capacity is strongly influenced by anchorage methods, their nature (rigid, flexible, fragile), and their position within the building. Verification of these elements' capacity therefore requires a thorough understanding of their mechanical properties and installation conditions. Product certifications, experimental tests at real scale or in laboratories (such as shaking table tests), and high-resolution numerical simulations are essential to estimate their response and resistance under seismic loads [Zito et al., 2023]. In capacity assessment, it is also important to consider possible interactions between structural and non-structural elements, which can amplify stresses or, conversely, dissipate energy, thus altering the overall behaviour of the building. In the context of cultural heritage, capacity takes on an even more delicate meaning: it is necessary to reconcile the preservation of historical and architectural features with the need to ensure an adequate level of seismic safety. This requires design solutions that improve seismic capacity without compromising the integrity and aesthetics of elements, often through minimally invasive interventions, advanced technologies, and materials compatible with the original ones. Finally, capacity must be periodically reassessed, especially in the presence of maintenance works, structural modifications, or deterioration over time, to ensure a dynamic and updated management of seismic risk.

4.2 SEISMIC SAFETY VERIFICATION

Current technical regulations, such as the Italian NTC 2018, govern the seismic safety verification of non-structural elements by requiring the assessment of both stability and functionality under seismic loads. The seismic demand, meaning the expected force or displacement, is calculated using recognized formulas and models, such as those provided by Eurocode 8 or the Italian Guidelines. This demand is then compared with the seismic capacity of the element, that is, its resistance or tolerance to seismic stress, certified by the manufacturer or determined through experimental tests (e.g., shaking table tests) or numerical simulations. In the case of elements anchored to the main structure, it is essential to verify the strength of the anchorage points, which is strongly influenced by the nature of the masonry support. In historic buildings, featuring non-standard masonry types, specific tension and shear tests are required, in compliance with European evaluation documents such as EAD 330076-00-0604 (Metal injection anchors for use in masonry). These

verifications can be performed during the design phase for new installations or retrospectively for existing elements, in order to identify vulnerabilities and define mitigation strategies.

4.3 SEISMIC RISK MITIGATION

If the verification results indicate insufficient safety levels, specific mitigation measures must be adopted, varying according to the characteristics and attachment method of the elements:

- Anchored elements: performance can be improved by reinforcing the support, enhancing the connection to the structure, introducing controlled sliding mechanisms, or using seismic isolation systems that decouple the element from ground motion.
- Self-supporting elements: for tall and slender elements, overturning movements can be limited by increasing the base area, adding mass, or using discrete anchoring systems that allow controlled movements but prevent overturning.

It is crucial to avoid seismic interaction between different elements, such as furniture, objects, and structures, as this can alter the overall seismic demand and capacity. Adequate spacing must therefore be maintained to prevent collisions during an earthquake. Base isolation is an effective solution for highly valuable and fragile elements, although its high cost limits its application. However, costs can be reduced by grouping multiple elements under a single isolation system, such as small objects displayed in cases or common shelving. General good practices include maintaining distance from masonry elements or systems to avoid contact, placing elements away from damaged structures or suspended components, lowering the center of gravity through weight redistribution, securely fixing internal components, and ensuring that the element behaves as a rigid or box-like structure during seismic events [Celano et al., 2016].

4.4 STORAGE AND HANDLING OF ELEMENTS

During storage and handling phases, specific precautions must be taken to reduce seismic risk. Loads should be evenly distributed along the perimeter walls, avoiding weight concentrations at the centre of floor slabs. Objects or crates should preferably be stored resting on their longest side, and when this is not possible, anti-overturning anchoring systems must be used. Storage and handling areas must be clearly identified in the design and located in undamaged parts of the building, free of fragile or suspended components, such as false ceilings, partition walls, or lighting systems, that could collapse during a seismic event.

5.FINAL SUMMARY AND CONCLUSIONS

The integrated analysis conducted in this study highlighted the complexity of the seismic response of buildings located in the Campi Flegrei area, a geological and urban context particularly vulnerable due to the combination of local seismicity, heterogeneous stratigraphic conditions [Vanorio et al., 2015, 2025], and a diverse building heritage that includes both historic structures and modern buildings. The accelerometric data recorded during the events of May 20, 2024, and March 13, 2025, provided an important experimental basis for understanding the temporal and spectral characteristics of the seismic motion, as well as local amplifications and the distribution of stresses on buildings. Field investigations showed a generally moderate extent of structural damage, with more significant phenomena concentrated on buildings with pre-existing construction deficiencies or situated in unfavourable geotechnical conditions. Conversely, non-structural damage was found to be widespread, even in buildings with adequate load-bearing structures, highlighting the critical role these elements play in determining the degree of safety and post-event functionality. This study further explored the influence of the dynamic characteristics of buildings, particularly the vibration period, on the level of damage observed during seismic events associated with bradyseism phenomena. Through three-dimensional numerical models developed in OpenSees, buildings with varying heights (from one to six stories) were analysed, evaluating the response in terms of base shear forces, floor accelerations,

and inter-story displacements. The results showed that buildings with shorter vibration periods (low-rise, stiff buildings) are subject to greater seismic forces, while taller buildings with longer periods tend to experience lower base shear forces but amplified accelerations at some intermediate floors. These observations were supported by the analysis of relative accelerations and damage indices recorded in the field, confirming the necessity of considering the specific dynamic response of each structure for an accurate assessment of seismic vulnerability. Attention then shifted to risk reduction strategies for non-structural elements (particularly for the safety and preservation of cultural and museum heritage), which include targeted reinforcements, improved anchoring systems, the introduction of isolation mechanisms, and careful management of spaces and distances between elements to prevent damage from interaction. Particular care must also be given to storage and handling phases to ensure optimal safety conditions. In conclusion, the combination of detailed numerical analyses, rigorous regulatory checks, and targeted mitigation strategies represents the most effective approach to seismic risk management, especially in contexts of high cultural value. Therefore, seismic risk mitigation cannot disregard the proper evaluation and management of non-structural elements, which are often responsible for significant damage even during moderate earthquakes. Targeted interventions on infill walls, suspended ceilings, systems, internal partitions, and fixed furnishings can drastically reduce the risk of injury to people and interruptions of essential services, improving the overall safety of buildings and their post-event functionality. Consequently, the protection of non-structural elements must be considered a priority component in seismic prevention strategies.

ACKNOWLEDGEMENTS

This study was supported by (1) the Italian Ministry of University and Research (MUR) through the PRIN 2020 project YKY7W4 ENRICH and (2) Italian Department of Civil Protection (DPC) in the framework of the National project DPC – ReLUIS 2024-2026 WP17: "Componenti non strutturali".

REFERENCES

British Standards Institution (BSI), CEN/TC250/SC8 [2005] "Eurocode 8 – Design of structures for earthquake resistance: Assessment and retrofitting of buildings," British Standards Institution.

Cito, P., Baraschino, R., Iervolino, I. [2025] "Ground motion, estimated shaking, and structural response at Campi Flegrei during bradyseism," Earthquake Engineering & Structural Dynamics, Vol. 54, No. 5, pp. 1313–1323. https://doi.org/10.1002/eqe.4303.

Celano, F., Cimmino, M., Coppola, O., Magliulo, G., Salzano, P. [2016] "Report dei danni registrati a seguito del terremoto del Centro Italia del 24 agosto 2016 (Release 1)," Network ReLUIS (Rete dei Laboratori Universitari di Ingegneria Sismica). Disponibile online: http://www.reluis.it/images/stories/Centre%20Italy%20earthquake%20damage%20report.

D'Angela, D., Magliulo, G., Di Salvatore, C., Zito, M. [2024] "Seismic assessment and qualification of acceleration-sensitive nonstructural elements through shake table testing: Reliability of testing protocols and reliability-targeted safety factors," *Engineering Structures*, Vol. 301, p. 117271. https://doi.org/10.1016/j.engstruct.2023.117271.

Istituto Nazionale di Geofisica e Vulcanologia (INGV) [2025] "Campi Flegrei – Bollettino settimanale 10/03/2025 – 16/03/2025," Osservatorio Vesuviano. Disponibile online: https://www.ov.ingv.it/index.php/monitoraggio-e-infrastrutture/bollettini-tutti/boll-sett-flegrei/anno-2025.

Istituto Nazionale di Geofisica e Vulcanologia (INGV) [2025] "Campi Flegrei – Bollettino settimanale 30/06/2025 – 06/07/2025," Osservatorio Vesuviano. Disponibile online: https://www.ov.ingv.it/index.php/monitoraggio-e-infrastrutture/bollettini-tutti/boll-sett-flegrei/anno-2025.

Magliulo, G., D'Angela, D. [2024] "Seismic response and capacity of inelastic acceleration-sensitive nonstructural elements subjected to building floor motions," Earthquake Engineering & Structural Dynamics, Vol. 53, No. 4, pp. 1421–1445. https://doi.org/10.1002/eqe.4080.

Magliulo, G., Ercolino, M., Petrone, C., Coppola, O., Manfredi, G. [2014] "The Emilia earthquake: seismic performance of precast reinforced concrete buildings," Earthquake Spectra, Vol. 30, No. 2, pp. 891–912.

Prota, A., et al. [2022] "Preliminary results of shake table tests of a typical museum display case containing an art object," Advances in Civil Engineering, Vol. 2022, No. 1, p. 3975958. https://doi.org/10.1155/2022/3975958.

Repubblica Italiana [2004] "Decreto Legislativo 22 gennaio 2004, n. 42. Codice dei beni culturali e del paesaggio," Gazzetta Ufficiale, n. 45 - Suppl. Ordinario n. 28.

Vanorio, T., Geremia, D., De Landro, G., Guo, T. [2025] "The recurrence of geophysical manifestations at the Campi Flegrei caldera," Science Advances, Vol. 11. https://doi.org/10.1126/sciadv.adt2067.

Vanorio, T., Kanitpanyacharoen, W. [2015] "Rock physics of fibrous rocks akin to Roman concrete explains uplifts at Campi Flegrei Caldera," Science, Vol. 349, pp. 617–621.

Zito, M., D'Angela, D., Maddaloni, G. and Magliulo, G. [2023] "A shake table protocol for seismic assessment and qualification of acceleration-sensitive nonstructural elements", Computer aided Civil Eng, vol. 38, no. 12, pp. 1699–1726, doi: 10.1111/mice.12951.

Optimising seismic retrofit design to reduce non-structural element losses using multiple objectives

Besim Yukselen[1], Gianrocco Mucedero[2], and Ricardo Monteiro[3, 4]

[1] PhD Student, University School for Advanced Studies IUSS, Pavia, Italy
[2] Research Fellow, University School for Advanced Studies IUSS, Pavia, Italy
[3] Associate Professor, University School for Advanced Studies IUSS, Pavia, Italy
[4] CONSTRUCT, Faculty of Engineering, University of Porto, Porto, Portugal
e-mail: {besim.yukselen, gianrocco.mucedero, ricardo.monteiro}@iusspavia.it

Abstract. Recent earthquakes have underscored the importance of considering, in seismic retrofit design, not only structural safety but also economic losses and downtime, which generally are significantly related to the performance of the non-structural elements (NSEs). In parallel, the interest in optimisation-based retrofit design has grown because of improved accessibility and efficiency of computational resources. This study investigates how structural seismic retrofitting optimisation might be targeted at reducing losses associated with structural components and NSEs. To do so, a residential reinforced concrete (RC) infilled building, built in the 1960s without specific seismic design provisions, was selected as a case study, while a recently proposed optimisation framework coupled with a stochastic iterative retrofitting algorithm (SIRA) was used. Two optimisation objective sets were examined: the first considers only the retrofitting installation costs, an approach believed to be aligned with current engineering practice, while the second includes multiple objectives: installation cost, expected annual losses and ratio of NSE losses to total ones. In both cases, the solution space is constrained by code compliance requirements. The results indicate that incorporating seismic risk–related objectives in the optimisation process leads to a significant reduction of NSE losses, highlighting the broader benefits of multi-objective structural retrofit optimisation in improving overall building performance.

Keywords: seismic retrofitting, downtime, seismic losses, multi-objective retrofit optimisation.

1. INTRODUCTION

Recent earthquakes have underscored the urgent need to address risks in the existing built environment, particularly in buildings constructed before the adoption of modern seismic code regulations. Research indicates that the majority of economic losses and recovery downtime are primarily driven by damage to non-structural components [Mucedero *et al.*, 2025]. Consequently, the reduction of losses associated with non-structural elements should be explicitly incorporated as an objective within the decision-making process during retrofitting design, alongside conventional considerations such as cost efficiency, overall loss reduction, and compliance with building code requirements. In parallel, the interest in optimisation-based retrofit design has grown due to the improved accessibility and efficiency of computational resources [Falcone, Lima and Martinelli, 2020]. Different studies have employed optimisation algorithms for seismic retrofitting design. For example, Seo et al. [2018] implemented Ant Colony Optimisation (ACO) to determine the optimal placement of retrofitted columns in a school building, to minimise the number of interventions. Mahdavi et al. [2019] compared Genetic Algorithms (GA) and Particle Swarm Optimisation (PSO) for retrofitting RC frames, targeting the minimisation of material quantities. Falcone et al. [2019] adopted GA to reduce the initial cost of retrofit designs in RC buildings, while Braga et al. (2019) employed a gradient-based Active-Set algorithm to minimise costs in dissipative bracing systems. Di Trapani et al. [2022] applied GA-based optimisation with additional constraints to limit the expected annual loss (EAL), integrating cost and risk aspects. Similarly, Minafò and Camarda [2022] utilised GA to optimise the placement of buckling-restrained braces (BRBs) for cost minimisation. More recently, Park et al. [2024] applied the Non-Dominated Sorting Genetic Algorithm III (NSGA-III) to FRP retrofitting of masonry-infilled RC frames, addressing three objectives simultaneously: minimising cost, maximising dissipated energy, and improving constructability. Yukselen et al. [2025a] introduced the Stochastic Iterative Retrofitting Algorithm (SIRA) to generate the initial population in optimisation-based retrofitting of masonry infilled RC buildings, and evaluated its integration with Genetic Algorithm (GA) and Particle Swarm Optimisation (PSO). The framework was firstly extended to a scalarised multi-objective problem with two objectives (installation cost and installation-related environmental impact) [Yükselen, Mucedero and Monteiro, 2025b], and later to a multi-objective formulation using the Non-Dominated Sorting Genetic Algorithm II (NSGA II), considering four objectives: installation cost, environmental impact, expected annual loss, and downtime [Yükselen, Mucedero and Monteiro, 2025c].

This study applies such a framework to the optimisation of seismic retrofitting in a residential RC building with masonry infills. Two formulations are examined: one reflecting current practice by minimising only installation costs using GA, and another that additionally considers expected annual losses and the ratio of non-structural element (NSE) losses to total losses, hereafter referred to as the NSE loss ratio, using NSGA-II. In both cases, code compliance is imposed as a constraint. Results show that explicitly including seismic risk-related objectives can substantially reduce NSE losses, underscoring the benefits of multi-objective retrofit optimisation for improving building resilience.

2. METHODOLOGY

2.1 PROBLEM FORMULATION AND OBJECTIVE EVALUATION

The overall goal of this study is to investigate how structural seismic retrofitting optimisation might be targeted at reducing losses associated with structural components and NSEs. To do so, a residential reinforced concrete (RC) building with unreinforced masonry (URM) infills, built in the 1960s in Portugal before the adoption of modern seismic design standards, was chosen as a case study. According to the blueprints, the concrete and reinforcement correspond to B225 and A40 grades, respectively. Although the drawings indicate varying infill wall thicknesses without specifying material properties, the weak masonry

typology experimentally characterised by Calvi and Bolognini [2001], typical in many southern European seismic-prone regions [Mucedero, Perrone and Monteiro, 2021], was adopted with an assumed 80 mm thickness. Further details on the structural model can be found in Yukselen et al. [2025a]. The optimisation framework recently proposed by Yukselen et al. [2025a], which initiates the optimisation process with the stochastic iterative retrofitting algorithm (SIRA), was utilised. Two distinct optimisation settings are considered to examine how seismic retrofitting of RC buildings can be directed towards reducing losses in both structural components and non-structural elements (NSEs), and to evaluate the extent to which incorporating these metrics alters the outcomes relative to a cost-only optimisation strategy. The first setting involves a single-objective optimisation problem, which is the minimisation of the installation cost, whereas the second setting incorporates multiple objectives, namely installation cost, expected annual losses, and the NSE loss ratio. The optimisation problem of the retrofitting scheme may be stated as a constrained optimisation problem. Depending on the objective set identified for the current study, the problem may be expressed as a single- or multi-objective optimisation problem through equations (1) and (2):

$$\text{Minimise: } f(\bar{x}), \text{ Subject to: } c_i = 0, \bar{x} \in \Omega \tag{1}$$

$$\text{Minimise: } \boldsymbol{f}(\bar{x}) = [f_1(\bar{x}), f_2(\bar{x}), f_3(\bar{x})], \text{ Subject to: } c_i = 0, \bar{x} \in \Omega \tag{2}$$

where $\bar{x}$ is the design vector representing the retrofitting configuration, $f(\bar{x})$ is the vector of objective functions, and Ω is the feasible solution space defined by code-compliance constraints. A solution is considered feasible only if all structural members satisfy Eurocode 8 performance criteria, such that $c_j(\bar{x})=0$. The design vector $\bar{x}$ encodes the presence or absence of steel jacketing for each beam and column, as well as the selected retrofitting parameters, including the lateral lengths of angle sections and the spacing of battens, all defined through a discrete set of feasible design alternatives. For columns, steel jacketing consists of four equal-angle sections connected by battens, while beams are jacketed using two equal-angle sections applied along the bottom, adopting a steel yield strength of 275 MPa. All jacketed members in a solution are assumed to use the same configuration of angle sections and battens. The angle sections have lateral lengths of 50 mm, 75 mm, or 100 mm, with a fixed thickness of 5 mm. In turn, the battens are rectangular plates with matching widths (50, 75, or 100 mm) and a thickness of 5 mm. Batten spacing is selected from seven discrete values, ranging from 100 to 400 mm in 50 mm increments. The material properties of the angle sections were updated in accordance with the recommendations of Campione et al. [2017], implementing configurations without end connections.

To solve the defined optimisation problems, the Genetic Algorithm (GA) is adopted for single-objective settings. In contrast, the Non-dominated Sorting Genetic Algorithm II (NSGA-II) is used to solve the multi-objective optimisation setting, offering a diverse set of Pareto-optimal solutions without requiring predefined weights for each objective. For both settings, infeasible solutions (non-compliant solutions) encountered during the evolutionary process are excluded from the population and not included in the parent selection for producing the offspring. Regardless of the optimisation settings, all objectives are evaluated for candidate solutions, and only those objectives specified in the optimisation settings are used within the optimisation process. The installation cost is obtained by summing the quantities and unit prices of all necessary actions. The unit costs of each action are summarised in Table 1.

Table 1. Adopted costs per action for steel jacketing

Action	Unit	Cost (€)
Cementitious mortar	kg	3.16
Structural steel	tonnes	3370
Intumescent coating	m2	10.8
Addition of plaster and paint	m2	32.6
Infill demolishing	m2	11.46
Concrete cover removal	m2	13.1
Cementitious mortar	kg	3.16

To estimate the Expected Annual Loss (EAL) and the losses attributed to the NSEs for each retrofitting design candidate, the nonlinear structural responses were obtained through a multiple-stripe analysis (MSA) approach. Ground motions were selected based on conditional spectra for twelve intensity levels corresponding to return periods ranging from 30 to 4000 years. Probabilistic seismic hazard analysis and disaggregation were performed using the ESHM20 [Danciu *et al.*, 2021] via the OpenQuake engine [Silva *et al.*, 2014], considering AvgSa in the 0.15–2.25 s period range. To reduce computational demands, nonlinear static pushover analyses were conducted in both principal directions, considering positive and negative loading in each case, using modal load patterns and scaled ground motions. The Capacity Spectrum Method (CSM) [Federal Emergency Management Agency, 2005] was used to identify performance points; in cases of multiple performance points, the one minimising the absolute difference between the geometric mean spectral displacement (AvgSdk) and the displacement at each performance point was selected, following Nettis et al. [2021]. Collapse fragility curves were modelled as lognormal distributions fitted via the maximum likelihood method [Baker, 2015], with total dispersion incorporating both record-to-record and epistemic uncertainties [Mucedero, Perrone and Monteiro, 2023]. Peak inter-storey drift (PID) values were obtained at the performance point. Peak floor accelerations (PFA) were estimated using the formulation by Merino et al. [2024], based on the derived drift. EAL was then computed using the FEMA P-58 component-based assessment framework via the Pelicun tool [FEMA, 2018b; Zsarnoczay *et al.*, 2025]. The building inventory was defined through structural and architectural layouts, supplemented by informed assumptions, while the most suitable component fragilities and consequence functions were adopted. The reconstruction cost was set at € 2,064,000, assuming a unit cost of € 1,720/m². In addition, the NSE loss ratio was calculated by estimating the expected annual non-structural losses. The building components inventory and the selected consequence models are provided in Table 2.

Table 2. Summary of the building components inventory and consequence functions source

Component	Category	Fragility Source / Reference
Beam–column joints	Structural	[Cardone, 2016]
Columns	Structural	[Cardone, 2016]
Masonry infills without openings	Non-structural	[Cardone and Perrone, 2015]
Masonry infills with openings	Non-structural	[Cardone and Perrone, 2015]
Acceleration-sensitive masonry infills	Non-structural	[Cardone and Perrone, 2015]
Doors	Non-structural	Associated with masonry collapse
Hot and cold-water piping	Non-structural	[FEMA, 2018a]
Energy control panel	Non-structural	[FEMA, 2018a]
Staircases	Non-structural	[FEMA, 2018a]
Elevator	Non-structural	[FEMA, 2018a]

2.2 ADOPTED OPTIMISATION ALGORITHMS

Gradient-free optimisation methods are essential in this study, as seismic retrofitting problems involve discrete variables, nonlinear and multi-modal objectives, and a search space constrained by code requirements and computationally expensive evaluations. As abovementioned, two algorithms are adopted depending on the optimisation setting: the Genetic Algorithm (GA) for the single-objective problem of minimising installation cost, and the Non-dominated Sorting Genetic Algorithm II (NSGA-II), a widely used multi-objective extension of GA, for the multi-objective setting addressing installation cost, expected annual losses (EAL), and the NSE loss ratio. In both algorithms, each candidate retrofit solution is encoded as a vector of design variables that correspond to the problem's dimensions. The algorithms (Figure 1) begin with the identification and evaluation of the initial population, which can be defined randomly using conventional statistical methods or through an informed (biased) initialisation technique that incorporates prior knowledge of feasible or near-feasible solutions for the optimisation task. At each iteration, candidate solutions are evaluated, parents are selected, and genetic operators, such as crossover to exchange information and mutation to preserve diversity, produce new offsprings. This evolutionary cycle continues

until termination criteria are met, typically a maximum number of generations. GA applies this evolutionary process in a single-objective context, targeting cost minimisation. NSGA-II extends the framework to multi-objective optimisation by introducing non-dominated sorting and crowding distance measures to maintain diversity and solution quality. Using binary tournament selection with a crowded comparison operator and an elitist strategy that retains the best solutions across generations, NSGA-II yields a diverse Pareto front that captures trade-offs among installation cost, EAL, and NSE loss ratio.

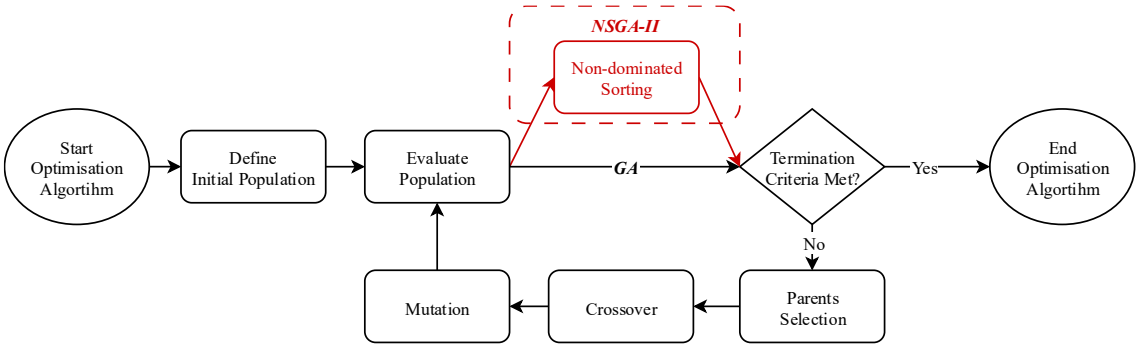


Figure 1. General workflow of genetic algorithm (GA) and non-dominated sorting genetic algorithm II (NSGA-II).

2.3 BIASED INITIALISATION WITH STOCHASTIC ITERATIVE RETROFITTING ALGORITHM

To efficiently identify the initial population while ensuring that the candidate solutions are feasible or nearly feasible, the Stochastic Iterative Retrofitting Algorithm (SIRA) (Figure 2) is adopted. SIRA ensures that the initial population used in the optimisation process includes retrofitting schemes that satisfy code requirements. The algorithm is based on how decisions are commonly made in practice throughout the retrofitting design process, which is typically guided by observed performance deficiencies and engineering judgment. A straightforward yet robust approach for the retrofitting design process can be described as an iterative procedure. The process begins by identifying structural members that fail to meet the code-specified performance criteria. It then applies a local intervention technique to all non-compliant members and repeats the cycle until all members achieve compliance. In practice, engineers rarely retrofit every non-compliant member at once. Instead, they choose a subset for intervention, guided by straightforward principles like preserving structural regularity. Although formalising this decision-making process with fixed rules is challenging, SIRA models the underlying logic using a stochastic approach. This method converts the uncertainty stemming from subjective engineering judgment, known as epistemic uncertainty, into randomness that the algorithm can handle, known as aleatory uncertainty. At the beginning of SIRA, a probability value P is defined, representing the likelihood that a failing member will be retrofitted. The algorithm evaluates the as-built structure, identifies non-compliant members, and considers each individually. For every member, a random number between 0 and 1 is generated; if the number is less than or equal to P, the member is retrofitted, otherwise it is left intact. Once all members are iterated, the retrofitted structure is re-evaluated, and the process repeats until all members meet local performance requirements. The algorithm does not enhance the design beyond feasibility and focuses solely on member-level compliance, without addressing global performance, consistent with national codes such as the Portuguese Annexe of EC8 [CEN, 2005; IPQ, 2009].

As the algorithm incorporates randomness, running it multiple times with the same input parameters can yield different feasible solutions. This is advantageous, as it enables SIRA to generate a variety of retrofitting designs to serve as initial candidates for optimisation. To control the computational effort, a maximum number of iterations can be set. In this study, 100 SIRA runs were conducted with a 30% probability value and a maximum of 25 iterations per run.

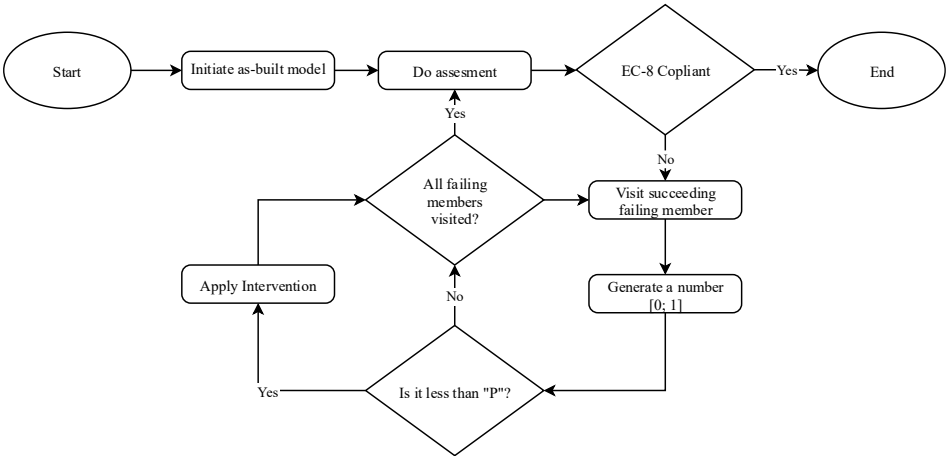


Figure 2. Workflow of stochastic iterative retrofitting algorithm (SIRA).

3. APPLICATION TO THE CASE STUDY BUILDING

A six-storey RC residential building with unreinforced masonry (URM) infills in Benfica, Lisbon, constructed in 1966 before modern seismic codes were enforced, was selected as the case study. The structure includes RC moment-resisting frames, weak URM panels, and in-plane irregularities. Geometric and reinforcement details were taken from the original blueprints, and the soil is assumed to be Type C. Numerical modelling of as-built and retrofitted candidates was conducted using OpenSees with the aid of CAD2Sees [Yükselen, Mucedero and Monteiro, 2025a]. Beam and column elements employed lumped plasticity with endpoint integration. Plastic hinge behaviour in each direction was defined through a multi-linear fit to the moment-curvature relationship and assigned to the Pinching4 material, then combined at each element's ends. Shear behaviour was considered elastic, with shear failure analysed by comparing demands to maximum capacity [Mucedero, Perrone and Monteiro, 2022, 2023]. Beam-column joints were modelled using a rotational spring link, as proposed by O'Reilly and Sullivan [2019]. The effects of URM infills, including openings, were represented by equivalent diagonal single-strut models, as described by Mucedero et al. [2020]. Code compliance was verified using the extended N2 method for infilled frames [Martinelli, Lima and De Stefano, 2015], with a 308-year return period (75% of the 475-year design PGA), suitable for Importance Class II buildings per the Portuguese Annexe of Eurocode 8 [CEN, 2005]. Among 300 structural members, 127 did not fulfil shear criteria (near-collapse), and 125 exceeded chord rotation limits (significant damage) in the as-built condition.

4. RESULTS

The optimisation procedures were carried out adopting steel jacketing as retrofitting technique, with initial populations identified through SIRA. The number of generations was limited to 50 for both GA and NSGA-II. All optimisation processes were implemented in the *pymoo* framework [Blank and Deb, 2020]. Table 3 summarises the performance of the as-built structure and the selected Pareto-optimal retrofit solutions obtained from the SIRA-only, SIRA+GA (single objective optimisation considering only cost minimisation), and SIRA+NSGA-II (multi-objective optimisation) frameworks. The presented solutions correspond to the configurations that achieve the minimum value for each of the three key objectives: installation cost, EAL and the NSE loss ratio. The results highlight the progressive improvement achieved through the different optimisation frameworks. The as-built structure exhibits expected annual loss (EAL)

of € 9,155 with NSE loss ratio 17%. The application of SIRA notably reduces EALs to around € 2,250–2,600, but retrofit costs remain high (up to € 165,000), and the contribution of NSE loss ratio increases to more than 75%. When optimisation is introduced, the single-objective GA (SIRA + GA) achieves a significant cost reduction of more than 50% compared to SIRA alone, reaching minimum costs of around € 67,000. However, this cost efficiency comes at the expense of slightly higher EALs (around € 2900) and comparable NSE loss ratios (around 80%), reflecting the expected trade-off in cost-driven optimisation. The multi-objective NSGA II (SIRA + NSGA II) approach delivers a more balanced outcome. The minimum EAL solution (€2080) is achieved at a moderate cost (€ 90,000) and a high NSE loss ratio (around 89%), whereas the solution minimising the NSE loss ratio (around 56%) incurs higher losses (€ 3200). This behaviour confirms that minimising NSE losses alone can lead the algorithm toward designs that are more fragile globally, while including both EAL and NSE loss ratio objectives encourages a balanced exploration of trade-offs. Overall, the multi-objective formulation yields a diverse and efficient Pareto set that more effectively captures the interplay between cost, damage, and non-structural performance.

Table 3. Performance metrics for the as-built and Pareto-optimal solutions from SIRA only, SIRA with GA, and SIRA with NSGA-II, based on minimum cost, EAL, and NSE loss ratio.

Objective	As Built	SIRA-Only Pareto			SIRA+GA Pareto			SIRA+NSGA-II Pareto		
		EAL Min	Cost Min	Ratio Min	EAL Min	Cost Min	Ratio Min	EAL Min	Cost Min	Ratio Min
EAL	9155	2257	2619	2391	2170	2932	3235	2081	2850	3200
NSE Ratio	17%	79%	80%	75%	84%	81%	62%	89%	84%	56%
Cost	-	165k	98k	126k	138.5k	67k	91k	90k	66k	80k

Figure 3 presents a parallel coordinate plot illustrating the trade-offs between installation cost, expected annual loss, and the NSE loss ratio for three settings: SIRA, SIRA+GA, and SIRA+NSGA-II. Each line in the plot represents a retrofit solution on the Pareto front of the corresponding setting. The SIRA-only solutions generally cluster around moderate EAL and NSE loss ratio values, but they span a relatively broad range of costs. The SIRA+GA (cost optimisation) solutions achieve lower costs overall, but this comes at the expense of higher EAL and NSE ratios, highlighting the trade-off inherent in single-objective cost-focused optimisation. In contrast, the SIRA+NSGA-II solutions exhibit a more balanced distribution, attaining competitive EAL and NSE performance at moderate cost levels.

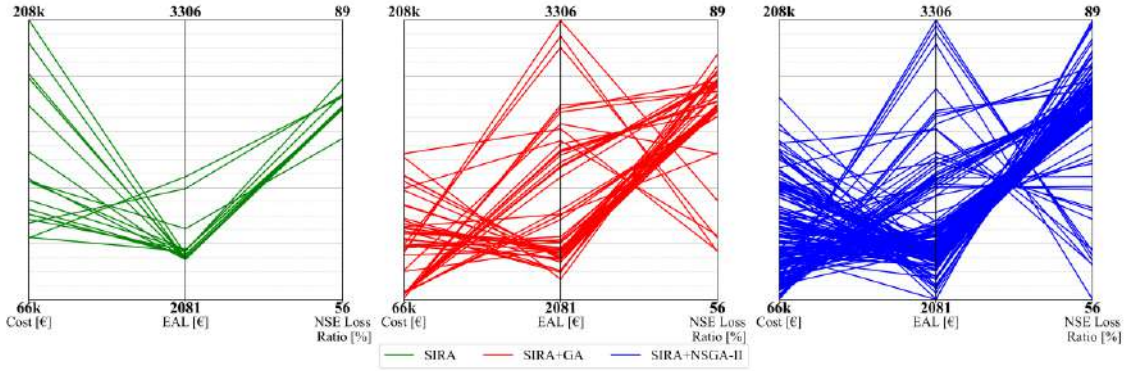


Figure 3. Parallel coordinate plot showing trade-offs among cost, expected annual loss (EAL), and NSE loss ratio for SIRA-only, SIRA + GA, and SIRA + NSGA-II.

Figure 4 presents partial two-dimensional Pareto plots illustrating all pairwise combinations among the three objectives: (1) EAL vs cost, (2) NSE Loss Ratio vs cost, and (3) NSE Loss Ratio vs EAL. The SIRA-only solutions (green) form a limited and concentrated Pareto front, generally achieving moderate EAL and NSE loss ratio values, although these solutions are associated with higher costs. The clustering of EAL and NSE ratio values indicates restricted Pareto coverage in this configuration. In contrast, the single-objective

optimisation solutions (SIRA + GA) (red) exhibit a more distributed Pareto front, demonstrating reductions in cost and NSE loss ratio, though with limited improvement in EAL. This approach yields a broader range of Pareto solutions compared to the SIRA-only case. Instead, the multi-objective optimisation (SIRA + NSGA-II) (blue) approach achieves simultaneous reductions in EAL, cost, and NSE loss ratio, resulting in a significantly wider Pareto front than both of the other settings.

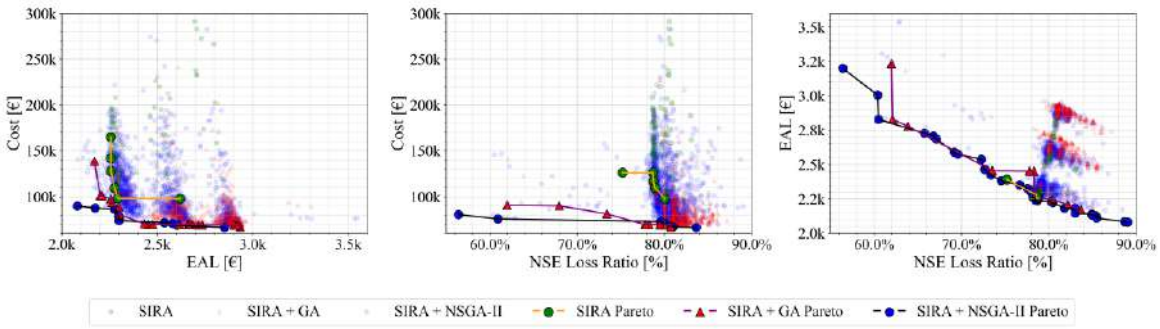


Figure 4. Partial two-dimensional Pareto plots showing pairwise relationships among installation cost, expected annual loss (EAL), and NSE loss ratio for SIRA-only (green), SIRA + GA (red), and SIRA + NSGA-II (blue) solutions.

5. CONCLUSIONS

This study explored how optimisation-based seismic retrofitting can be directed not only toward ensuring structural safety but also toward mitigating losses associated with non-structural elements (NSEs). A residential reinforced concrete (RC) building with unreinforced masonry infills, representative of pre-code Portuguese construction, was adopted as the case study. The framework integrated the Stochastic Iterative Retrofitting Algorithm (SIRA) with Genetic Algorithm (GA) and Non-Dominated Sorting Genetic Algorithm II (NSGA-II) to explore both single- and multi-objective optimisation formulations. Two optimisation strategies were examined: a cost-only minimisation reflecting current engineering practice, and a multi-objective formulation incorporating installation cost, expected annual loss (EAL), and the ratio of NSE-related losses to total losses, with the aim of assessing how explicitly accounting for seismic risk-related objectives together with NSE-related objectives influences retrofit design outcomes. The results showed that including NSE- and risk-related goals in the optimisation process significantly improves retrofit performance. Solutions using only SIRA provided feasible retrofits that were costly and offered limited trade-off options. On the other hand, the cost-focused single-objective optimisation (SIRA + GA) lowered installation costs while still achieving high NSE losses. Alternatively, the multi-objective approach (SIRA + NSGA-II) effectively reduced cost, EAL, and NSE losses simultaneously, creating a broader and more balanced Pareto front. These results confirm that explicitly considering NSE performance in retrofit design enhances seismic risk reduction, paving the way for more resilient and cost-effective retrofitting strategies.

ACKNOWLEDGEMENTS

This work was carried out within the activities of CONSTRUCT – Instituto de I&D em Estruturas e Construções (UID/04708) and the project 2022.08138.PTDC (SERENE) with DOI identifier: https://doi.org/10.54499/2022.08138.PTDC, all funded by Fundação para a Ciência e a Tecnologia, I.P./MCTES (PIDDAC). Additional support was provided by the project "ReLUIS 2024–2026 (WP5–WP13)", funded by the Italian Civil Protection Department. The simulations presented in this work were carried out on the High Performance Computing DataCenter at IUSS, co-funded by Regione Lombardia through the funding programme established by Regional Decree No. 3776 of November 3, 2020.

REFERENCES

Baker, J. W. [2015] 'Efficient Analytical Fragility Function Fitting Using Dynamic Structural Analysis', *Earthquake Spectra*, 311, pp. 579–599. doi: 10.1193/021113EQS025M.

Blank, J. and Deb, K. [2020] 'Pymoo: Multi-Objective Optimization in Python', *IEEE Access*, 8, pp. 89497–89509. doi: 10.1109/ACCESS.2020.2990567.

Braga, F., Gigliotti, R. and Laguardia, R. [2019] 'Intervention cost optimization of bracing systems with multiperformance criteria', *Engineering Structures*, 182, pp. 185–197. doi: 10.1016/j.engstruct.2018.12.034.

Calvi, G. M. and Bolognini, D. [2001] 'SEISMIC RESPONSE OF REINFORCED CONCRETE FRAMES INFILLED WITH WEAKLY REINFORCED MASONRY PANELS', *Journal of Earthquake Engineering*, 52, pp. 153–185. doi: 10.1080/13632460109350390.

Campione, G. *et al.* [2017] 'Frictional Effects in Structural Behavior of No-End-Connected Steel-Jacketed RC Columns: Experimental Results and New Approaches to Model Numerical and Analytical Response', *Journal of Structural Engineering*, 1438, p. 04017070. doi: 10.1061/(ASCE)ST.1943-541X.0001796.

Cardone, D. [2016] 'Fragility curves and loss functions for RC structural components with smooth rebars', *Earthquakes and Structures*, 105, pp. 1181–1212. doi: 10.12989/EAS.2016.10.5.1181.

Cardone, D. and Perrone, G. [2015] 'Developing fragility curves and loss functions for masonry infill walls', *Earthquakes and Structures*, 91, pp. 257–279. doi: 10.12989/EAS.2015.9.1.257.

CEN [2005] 'Eurocode 8: Design of structures for earthquake resistance - Part 3: Assessment and retrofitting of buildings'.

Danciu, L. *et al.* [2021] *The 2020 update of the European Seismic Hazard Model - ESHM20: Model Overview*. EFEHR European Facilities of Earthquake Hazard and Risk, p. 500Mb. doi: 10.12686/A15.

Di Trapani, F., Sberna, A. P. and Marano, G. C. [2022] 'A genetic algorithm-based framework for seismic retrofitting cost and expected annual loss optimization of non-conforming reinforced concrete frame structures', *Computers & Structures*, 271, p. 106855. doi: 10.1016/j.compstruc.2022.106855.

Falcone, R. *et al.* [2019] 'Seismic retrofitting of existing RC buildings: a rational selection procedure based on Genetic Algorithms', *Structures*, 22, pp. 310–326. doi: 10.1016/j.istruc.2019.08.006.

Falcone, R., Lima, C. and Martinelli, E. [2020] 'Soft computing techniques in structural and earthquake engineering: a literature review', *Engineering Structures*, 207, p. 110269. doi: 10.1016/j.engstruct.2020.110269.

Federal Emergency Management Agency [2005] *Improvement of Nonlinear Static Seismic Analysis Procedures*. FEMA 440. Federal Emergency Management Agency.

FEMA [2018a] *FEMA P-58-3: Seismic Performance Assessment of Buildings, Volume 3 – Supporting Electronic Materials and Background Documentation*. FEMA P-58-3. Federal Emergency Management Agency.

FEMA [2018b] *Seismic Performance Assessment of Buildings, Volume 1 -- Methodology, Second Edition*. FEMA P-58-1. Federal Emergency Management Agency.

IPQ [2009] 'Eurocódigo 8: Projecto de estruturas para resistência aos sismos'.

Mahdavi, G., Nasrollahzadeh, K. and Hariri-Ardebili, M. A. [2019] 'Optimal FRP Jacket Placement in RC Frame Structures Towards a Resilient Seismic Design', *Sustainability*, 1124, p. 6985. doi: 10.3390/su11246985.

Martinelli, E., Lima, C. and De Stefano, G. [2015] 'A simplified procedure for Nonlinear Static analysis of masonry infilled RC frames', *Engineering Structures*, 101, pp. 591–608. doi: 10.1016/j.engstruct.2015.07.023.

Merino, R. J. *et al.* [2024] 'Estimation of consistent absolute acceleration and relative displacement floor response spectra in existing masonry-infilled reinforced concrete buildings', *Bulletin of Earthquake Engineering*, 2210, pp. 5083–5118. doi: 10.1007/s10518-024-01961-6.

Minafò, G. and Camarda, G. [2022] 'An open-source GA framework for optimizing the seismic upgrading design of RC frames through BRBs', *Engineering Structures*, 251, p. 113508. doi: 10.1016/j.engstruct.2021.113508.

Mucedero, G. *et al.* [2020] 'Numerical Modelling and Validation of the Response of Masonry Infilled RC Frames Using Experimental Testing Results', *Buildings*, 1010, p. 182. doi: 10.3390/buildings10100182.

Mucedero, G. *et al.* [2025] 'Estimation of seismic downtime for building retrofitting decision-making', *Resilient Cities and Structures*, 43, pp. 15–29. doi: 10.1016/j.rcns.2025.07.001.

Mucedero, G., Perrone, D. and Monteiro, R. [2021] 'Nonlinear static characterisation of masonry-infilled RC building portfolios accounting for variability of infill properties', *Bulletin of Earthquake Engineering*, 196, pp. 2597–2641. doi: 10.1007/s10518-021-01068-2.

Mucedero, G., Perrone, D. and Monteiro, R. [2022] 'Infill Variability and Modelling Uncertainty Implications on the Seismic Loss Assessment of an Existing RC Italian School Building', *Applied Sciences*, 1223, p. 12002. doi: 10.3390/app122312002.

Mucedero, G., Perrone, D. and Monteiro, R. [2023] 'Seismic risk assessment of masonry-infilled RC building portfolios: impact of variability in the infill properties', *Bulletin of Earthquake Engineering*, 212, pp. 957–995. doi: 10.1007/s10518-022-01563-0.

Nettis, A. *et al.* [2021] 'Cloud Capacity Spectrum Method: Accounting for record-to-record variability in fragility analysis using nonlinear static procedures', *Soil Dynamics and Earthquake Engineering*, 150, p. 106829. doi: 10.1016/j.soildyn.2021.106829.

Park, S., Choi, S. W. and Choi, I. [2024] 'Seismic retrofitting optimization model using fiber-reinforced polymer jacketing and NSGA-III', *Developments in the Built Environment*, 19, p. 100508. doi: 10.1016/j.dibe.2024.100508.

Seo, H., Kim, J. and Kwon, M. [2018] 'Optimal seismic retrofitted RC column distribution for an existing school building', *Engineering Structures*, 168, pp. 399–404. doi: 10.1016/j.engstruct.2018.04.098.

Silva, V. *et al.* [2014] 'Development of the OpenQuake engine, the Global Earthquake Model's open-source software for seismic risk assessment', *Natural Hazards*,723, pp.1409–1427. doi:10.1007/s11069-013-0618-x.

Yükselen, B., Mucedero, G. and Monteiro, R. [2025a] 'Evaluation and Enhancement of Optimisation Algorithms for Automated Seismic Retrofitting of Existing Buildings', *Journal of Earthquake Engineering*, 2914, pp. 2959–2992. doi: 10.1080/13632469.2025.2541237.

Yükselen, B., Mucedero, G. and Monteiro, R. [2025b] 'Multi-variable Optimisation of Building Seismic Retrofitting', in. *COMPDYN 2025 10th ECCOMAS Thematic Conference on Computational Methods in Structural Dynamics and Earthquake Engineering*.

Yükselen, B., Mucedero, G. and Monteiro, R. [2025c] 'Enhancing Multi-Objective Seismic Retrofitting Design Through Optimisation', in. *XX ANIDIS Conference*.

Zsarnoczay, A. *et al.* [2025] 'NHERI-SimCenter/pelicun:v3.6'. Zenodo. doi: 10.5281/ZENODO.15446022.

Sixth International Workshop on the Seismic Performance of Non-Structural Elements (SPONSE 2026)

Interaction of Suspended Ceilings and Pressurized Piping in a Full-Scale 10-Story Cold-Formed Steel Building Shake Table Test Program

Amanpreet Singh[1], Fidence Cyizere Rukundo[1], Jason R. Ameen[2], Saeed Fathali[3], Jordan Jaramillo[3], Bob Torbin[3], Jereme Huntress[4], Geza Szakats[5], Dustin T. Cook[6], Matthew S. Speicher[6], Siamak Sattar[6], Tara C. Hutchinson[7], and Benjamin W. Schafer[1]

[1] Dept. of Civil and Systems Engineering, Johns Hopkins University, Baltimore, MD 21218
e-mail: {amanprs, fcyizer1, schafer}@jhu.edu
[2] Armstrong World Industries, Lancaster, Pennsylvania 17604
e-mail: jrameen@armstrongceilings.com
[3] Omega Flex, Inc., Exton, PA 19341
e-mail: sfathali@gmail.com, jordan.jaramillo@omegaflex.com, Bob.Torbin@omegaflex.net
[4] COSCO Fire Protection, San Diego, CA 92123
e-mail: jhuntress@coscofire.com
[5] Holmes, San Francisco, CA 94104
e-mail: Geza.Szakats@holmes.us
[6] National Institute of Standards and Technology, Gaithersburg, MD 20899
e-mail: {dustin.cook, matthew.speicher, siamak.sattar}@nist.gov
[7] Dept. of Structural Engineering, University of California San Diego, La Jolla, CA 92093
e-mail: tara@ucsd.edu

Abstract. A 10-story cold-formed steel (CFS) building, referred to as CFS10, was constructed and tested at the 6-DOF Large High Performance Outdoor Shake Table (LHPOST6) at UC San Diego (NHERI@UC San Diego). This unique building specimen was designed beyond current seismic provisions, notably exceeding the height limit as prescribed in ASCE 7-22 and employing shear wall detailing that is currently not available in the most recent AISI S400-20 design standard. The test specimen was additionally outfitted with a wide range of nonstructural components and systems, designed and installed at various levels of the building, to understand the evolution of damage in a real building system under multi-directional seismic excitation. Limiting damage to nonstructural components plays a key role in maintaining or regaining post-earthquake building functionality. To this end, an essential aspect of the test program is to improve upon the key gaps in the state of knowledge of nonstructural seismic performance and functional recovery of buildings, especially in CFS-framed buildings. This paper presents preliminary observations of damage and functionality correlated with the measured seismic response of select nonstructural systems, namely suspended ceilings, and pressurized fire sprinkler and gas piping systems, focusing on their performance and interactions at the ceiling of Story 10 in the building. Observations related to damage and functionality can inform the development of fragility functions for these nonstructural systems and support improved functional recovery design provisions.

Keywords: Nonstructural components, seismic performance, functional recovery, shake table tests.

1. INTRODUCTION

Nonstructural components and systems (NCSs) make up 70–80% of the original construction cost of a commercial building [FEMA (Federal Emergency Management Agency), 2012]. Furthermore, effective design strategies that minimize nonstructural damage are critical to the postearthquake functionality and operability of a building [ATC (Applied Technology Council), 2008]. Nonetheless, NCS damage and their disproportionate contribution to repair costs have been frequently cited in earthquake reconnaissance reports [Dhakal, 2010; Miranda *et al.*, 2012; Perrone *et al.*, 2019]. NCSs are particularly vulnerable to seismic damage and present a substantial risk to life safety. In response, recent research efforts have focused on investigating the seismic behaviour of various NCS, such as ceiling systems [Pourali *et al.*, 2017; Patnana and Rai, 2022], piping systems [Tian *et al.*, 2014], and mechanical equipment [Fathali and Filiatrault, 2008] through component-level experiments. Simultaneously, system-level full building experimental programs, such as Soroushian *et al.* [2016] and Pantoli *et al.* [2016], have aimed at characterizing the response of NCS and their interaction as installed in a building.

1.1 CFS10 EXPERIMENTAL PROGRAM

A 10-story cold-formed steel (CFS) building, referred to as CFS10, was tested at the 6-DOF Large High Performance Outdoor Shake Table (LHPOST6), part of the Natural Hazards Engineering Research Infrastructure at University of California San Diego (NHERI@UC San Diego) [McCartney *et al.*, 2025]. Figure 1 shows the test building which had a total building height of 31.6 m and plan dimensions of 11.58 m (X-direction, east-west) by 6.86 m (Y-direction, north-south). The layout consisted of two room-space compartments and two "balconies" with a 79.4 m^2 floor plan area, and emulated archetype designs developed by Torabian *et al.* [2016]. The lateral force resisting system used Type I shear walls [AISI (American Iron and Steel Institute), 2020] with single-sided steel sheet sheathing installed over CFS framing (or structural tubes) and ledger framing for floor diaphragm-to-wall connections. Interested readers are referred to Hutchinson *et al.* [2026] for an overview of the experimental program and Singh *et al.* [2022, 2024] for details regarding the structural design. The test specimen was subjected to increasing intensity multi-directional seismic excitation. Table 1 lists the 18 earthquake motions imposed on the specimen during the seismic test protocol, including 15 service-level earthquakes (SLE), one design earthquake (DE), and two risk-targeted maximum considered earthquakes (MCE_R). In between seismic tests, 37 low-amplitude unidirectional white noise tests were conducted. Following the seismic tests, Levels 6 and 9 of the building were subjected to fire tests for post-earthquake fire performance evaluation.

The test specimen was outfitted with a wide range of NCSs distributed across the different levels of the building, with the goal of understanding the seismic behavior of these systems as integrated into a full-scale building subjected to seismic loading. These included fire sprinkler and gas piping systems, suspended ceilings, a resilient stair system, windows, swing and roll-up doors, roof-mounted mechanical equipment, and architectural wall and ceiling finishes. Collectively, these systems captured a representative sample of critical NCSs that are common in modern mid-rise residential construction. Particularly at Story 10 of the building, pressurized fire sprinkler and gas piping systems were installed inside the suspended ceilings hung from the floor joists of Level 11 (i.e., the roof), creating a dense ceiling plenum space as shown in Figure 1. This location was chosen to evaluate the vulnerability of overhead services at upper stories, where seismic demands can be significantly amplified. Similar to an earlier study [Soroushian *et al.*, 2016] which considered the interactions in an integrated ceiling-partition wall-piping system installed in a 5-story steel building, the present study looks at the interactions between suspended ceilings and pressurized gas and fire sprinkler piping within the ceiling plenum space and confining structural walls as installed in a 10-story CFS building. This paper presents the physical damage observations and post-hazard functionality of these select NCS, with emphasis on their measured seismic performance. For this suite of NCSs, Level 11 serves as the reference level. Figure 2 shows the installed uniaxial MEMS (micro-electromechanical system) and tri-axial accelerometers, the latter provided by Community Seismic Network (CSN), at this level.



Figure 1. (a) Annotated photograph of the CFS10 test building (northeast view, photo courtesy of R. Ji, UC San Diego), (b) photographs of distributed NCS at ceiling of Story 10 before ceiling board installation: (left) view looking up and (right) field-of-view of the yellow cartoon denoted in left photographs.

Table 1: Earthquake test protocol imposed on the CFS10 building [Hutchinson *et al.*, 2026]

Hazard level	MID	Earthquake event				Input DOF	Components		PIA_x [g]	PIA_y [g]	PIA_z [g]
		Name, location	Year	M_w	Station		X	Y			
SLE	1	Loma Prieta, California	1989	6.9	Gilroy Array #3	XYZ	90°	0°	0.126	0.122	0.082
	2					XYZ	90°	0°	0.118	0.114	0.096
	3					X	90°		0.133	0.041	0.025
	4					Y		0°	0.042	0.109	0.024
	5	Northridge, California	1994	6.7	LA City Terrace	XYZ	90°	180°	0.125	0.121	0.081
	6					XYZ	180°	90°	0.184	0.094	0.084
	7					X	180°		0.168	0.027	0.023
	8					Y		90°	0.026	0.093	0.021
	9	Cape Mendocino, California	1992	7.0	Rio Dell Overpass	XYZ	270°	360°	0.084	0.109	0.099
	10					XYZ	360°	270°	0.078	0.122	0.151
	11	Kahramanmaras, Türkiye	2023	7.8	4611	XYZ	E	N	0.095	0.075	0.050
	12					XYZ	E	N	0.117	0.110	0.064
	13	Elbistan, Türkiye	2023	7.5	4611	XYZ	E	N	0.100	0.061	0.052
	14	Maule, Chile	2010	8.8	Curicó Hospital	XY	EW	NS	0.097	0.091	0.033
	15	Kahramanmaras, Türkiye	2023	7.8	4611	XYZ	E	N	0.119	0.089	0.063
DE	16	Loma Prieta, California	1989	6.9	Gilroy Array #3	XY	90°	0°	0.454	0.388	0.014
MCE_R	17	Loma Prieta, California	1989	6.9	Gilroy Array #3	XY	90°	0°	0.723	0.619	0.016
	18	Cape Mendocino, California	1992	7.0	Rio Dell Overpass	XY	360°	270°	0.782	0.336	0.025

MID = motion identification number, DOF = degree of freedom, SLE = service level earthquake, DE = design earthquake, MCE_R = risk-targeted maximum considered earthquake, PIA = (achieved) peak input acceleration

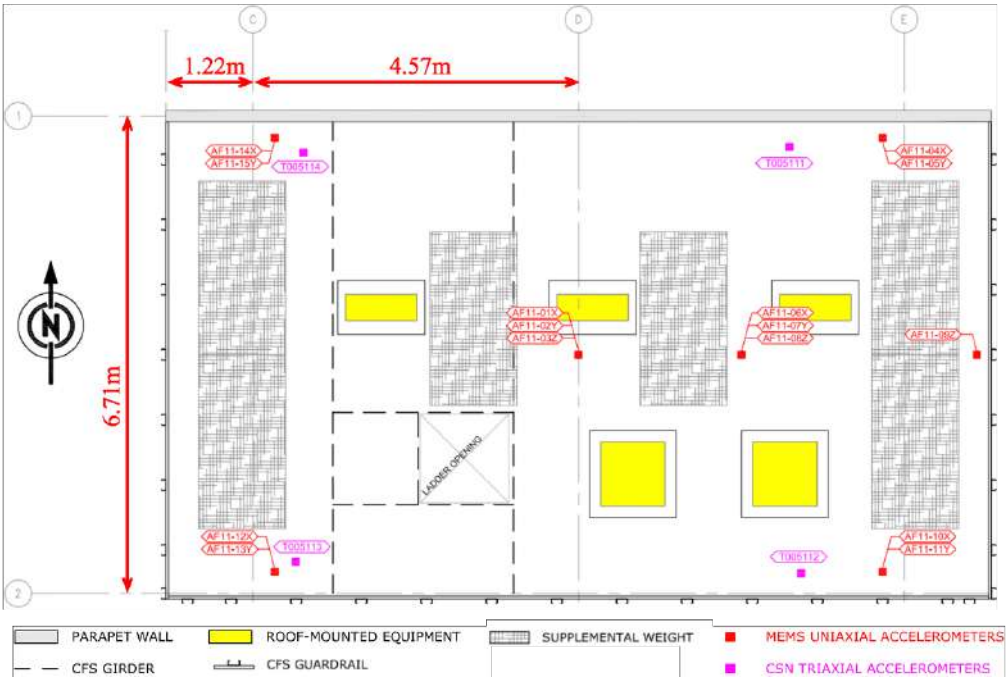


Figure 2. Level 11 (roof) plan and layout of installed accelerometers.
Note: Sensors installed on roof-mounted mechanical equipment not shown for clarity.

2.NCS WITHIN LEVEL 10 CEILING PLENUM SPACE

The ceiling plenum space of Story 10 was outfitted with a suspended (dropped) ceiling, horizontal fire sprinkler system and, in the east space, a horizontal gas piping system, see Figure 3. Several different types of analog sensors, such as accelerometers, displacement transducers and strain gauges, were installed in the test building and the various NCS. In total 730 seismic sensors from LHPOST6 inventory, 34 uni-directional and 75 tri-axial accelerometers courtesy of California Strong Motion Instrumentation Program (CSMIP) and CSN, respectively, and 47 synchronized high-definition cameras and 17 GoPro cameras were installed throughout the specimen. Sorosh *et al.* [2026] describes the features and configurations of the different sensor types deployed during the CFS10 project. The response from the 35 accelerometers installed on the NCS of interest is discussed in this paper. Design of all NCS met or exceeded the requirements set by ASCE 7-22 [ASCE (American Society of Civil Engineers), 2022] seismic provisions and building design criterion required for Seismic Design Category D. The installation details of each system are discussed next, with as-built photographs shown in Figures 1, 4, 5 illustrating the discussed details at various stages of construction.

2.1 SUSPENDED CEILINGS

In the CFS10 building, two different light-gage drywall grid suspended ceiling systems were installed in the west and east rooms at the ceiling of Story 10. The two tested ceilings were designed as: (1) an unbraced ceiling system in the west room with all edges fixed, and (2) a laterally braced ceiling system using splay wires and compression posts in the east room with two adjacent edges fixed and two edges floating. These are referred to as the fixed-fixed ceiling and fixed-floating ceiling, respectively. Each ceiling system measured 4.41 m by 6.55 m, hung from the floor joists of Level 11 using 3mm diameter vertical steel suspension (hanger) wires nominally spaced at 1.22 m. The main tees, spaced at 1.22 m, used 3.8 cm by 4.3 cm (cross-section face profile by height) heavy-duty drywall beams that ran along the east-west direction. The cross tees, spaced at 0.41 m, used 3.8 cm by 3.8 cm drywall tees that ran along the north-south direction. The fixed-fixed ceiling used 3.8 cm by 3.8 cm hemmed angle molding while the fixed-floating ceiling used 5.1 cm by 5.1 cm hemmed angle molding at the edges of the ceilings. The ceiling grids were assembled using #8

(4 mm shank diameter), 14.3 mm long Phillips screws. The west room ceiling had an opening of 1.22 m by 1.22 m to accommodate a ships ladder that provided access to the roof. The braced fixed-floating ceiling used (4) 0.8 mm thick compression posts fastened to the main runner and located 1.1-1.3 m away from the long edge and 1.4 m away from the short edge. The diagonal restraints used (4) 3mm diameter splay wires secured to the main runner and splayed 90° from each other and at an angle between 10° and 45° from the horizontal plane of the ceiling. Both ceiling systems used staggered 16 mm thick gypsum boards (9.0 kg/m²) screwed using #6 Phillips screws (3.5 mm shank diameter) at 0.3 m spacing on center. At the floating edges of the floating-fixed ceiling, the first gypsum board screw was installed at a distance of 76 mm from the face of the interior gypsum board installed on the wall. Both ceiling systems were hung at a distance of 0.36 m from the face of floor joists to the lower face of the ceiling drywall board. Though the details for the two ceiling systems are quite different, both satisfy the suspended drywall grid ceilings requirements per ASCE 7-22 and ASTM C1858 [ASTM (American Society for Testing and Materials), 2024].

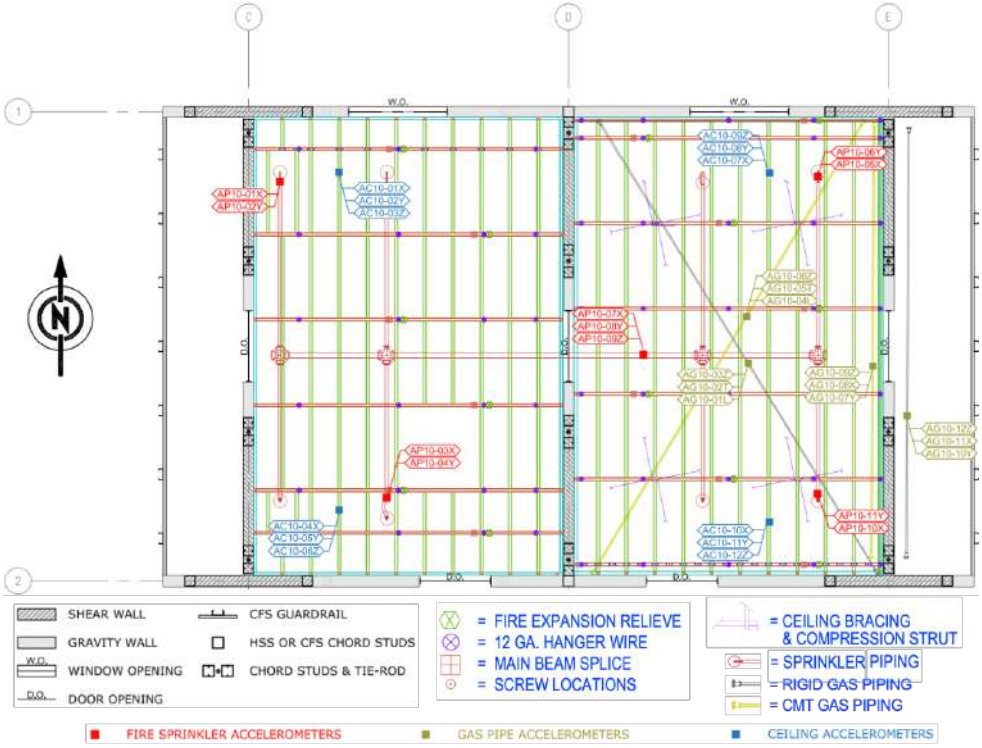


Figure 3. NCS within Level 10 ceiling plenum space and layout of installed accelerometers. Note: Ceiling board not shown for clarity.

2.2 FIRE SPRINKLER SYSTEM

A water-pressurized fire sprinkler piping system ran horizontally and was hung from the ceiling of Story 10. Designed per ASCE 7-22 and NFPA 13 [NFPA (National Fire Protection Association), 2022] standards, this isolated piping system consisted of a long main line and eight branch lines orthogonal to the main line. The main line pipe was aligned with the X-axis (east-west) of the test building. The main line was a 7.57 m long ASTM A135 [ASTM, 2021] Grade A steel pipe with 73 mm outer diameter and 3.05 mm wall thickness (schedule 10 pipe). Both ends of the main line pipe were seismically braced in the longitudinal and transverse directions using brace pipes with 33.4 mm outer diameter and 3.38 mm wall thickness. Similarly, the four branch lines off to the north side from the main line measured 2.74 m in length, while the four branch lines off to the south side measured 2.31 m in length. Branch lines used ASTM A135 Grade A steel pipes with 48.3 mm outer diameter and 3.68 mm wall thickness (schedule 40 pipe). Branch lines ends were provided with termination restraints using one vertical and one inclined 9.5 mm diameter all-thread rods. Vertical hangers along the pipes used the same all-thread rods. All main line to branch line joints used flexible pipe couplings. A pressure gauge was installed on one branch line, which read 760 kPa after water pressurization.

Each branch line had a sprinkler pendant which was detailed as either a flexible or rigid drop through the gypsum board. Appropriately sized escutcheon plates were provided to cover the cutouts in ceiling boards to allow for the required clearance around sprinkler heads per NFPA 13 and suspended ceiling designs.

The fire sprinkler system within the CFS10 building was similar to other recent system-level experiments, e.g. Bhatta *et al.* [2025], where a main riser pipe traversed the height of the building and spread out into horizontal layouts at different levels of the building. However, a key difference with the fire sprinkler piping system at Story 10, in particular, was that it was installed as an isolated system, i.e., it was not connected to the main vertical riser pipe. This decision was made to avoid having the riser pipe pass through the ceiling, which would have required extra cut-outs in the gypsum board and possible adjustments to the ceiling grid.

2.3 GAS PIPING SYSTEM

The gas piping system hung from the ceiling of Story 10 was designed per ASCE 7-22 and ASME B31.9 [ASME (American Society of Mechanical Engineers), 2025] standards, comprised of two 50.8 mm diameter rigid copper and two 66.7 mm diameter jacketed corrugated metal tubing (CMT) pipes. The CMT pipe test articles were assemblies with seismic qualification for medical gas service, installed in accordance with the manufacturer's instructions. Although used primarily in hospitals and medical facilities, their materials, corrugated geometry, fittings, and installation practices are representative of corrugated metal assemblies with seismic qualification that are also used in other gas or liquid services with comparable certification pathways. At Story 10 of the CFS10 building, one rigid and one CMT pipe were installed as isolated units, i.e. end-restrained runs with no continuity to a riser, aligned along the Y-axis (north-south) of the building. Only the CMT isolated pipe was situated inside the ceiling plenum space. The rigid isolated pipe was installed with same detailing from the floor joists of Level 11; however, since there was no suspended ceiling system in the "balconies" (see Figure 3), this horizontal pipe run was exposed. The main rigid and CMT pipe horizontal runs, originating from vertical pipes that traversed the height of the building, ran along the two diagonals of the east room inside the ceiling plenum space. Cutouts in the ceiling gypsum boards allowed the vertical runs into the plenum space and turned into horizontal runs. All four pipes were provided with one longitudinal and two transverse seismic braces using brace pipes with 33.4 mm outer diameter and 3.38 mm wall thickness. Additionally, all-thread rods were used as gravity hangers. All pipes were supplied with pressure gauges and were pressurized with air up to 380 kPa prior to testing. The gauges were monitored to detect any loss in pressure as a result of failure in any joint or fitting during seismic tests.

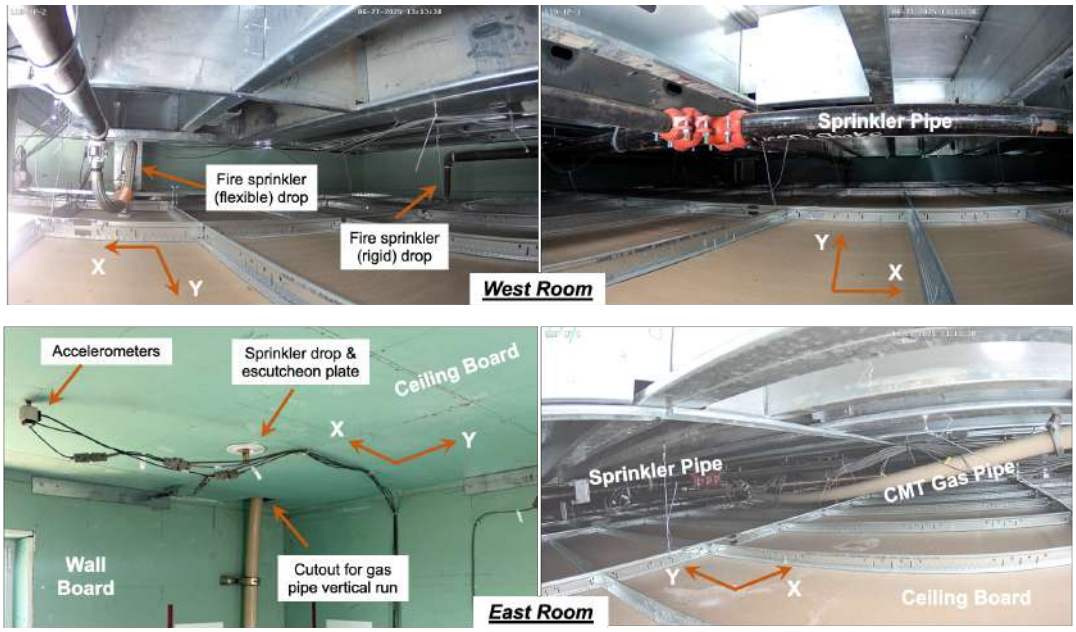


Figure 4. Photographs of distributed NCS after ceiling board installation.

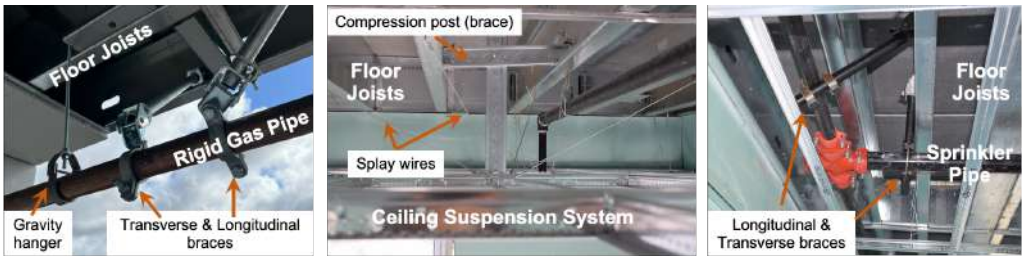


Figure 5. Photographs of seismic bracing for gas pipes (left), suspended ceiling (center) and fire sprinkler pipe (right).

3.EXPERIMENTAL RESPONSE AND DISCUSSION

3.1 PHYSICAL OBSERVATIONS

During the seismic test protocol, only minor physical damage was observed to the NCSs within the Story 10 ceiling plenum space. Noticeable items include minor tilting of screws at individual ceiling board edges. Additionally, minor board crushing was observed at the wall-ceiling interface due to small relative movement of the ceiling system at MCE_R level shaking (MID17). Post-testing, ceiling boards were removed to closely inspect for any damage to the ceiling grid or pipe components. Though the CMT pipes pounded against the ceiling grid during seismic tests, as noted from captured video footage, this interaction amongst the various NCSs did not cause noticeable physical damage to any main or cross-tees. Only minor movement of gravity hangers along gas pipes was observed. No pressure loss in any gas pipe or the fire sprinkler system was observed throughout the seismic test protocol. While comprehensive imaging solutions were employed to document the physical state of the building and its subsystems [Singh *et al.*, 2026], it is noted that differences in construction workmanship and physical damage were admittedly difficult to always consistently reconcile.

3.2 NONSTRUCTURAL RESPONSE AMPLIFICATION

Of particular interest in the present study is capturing an understanding of the amplified seismic response of various NCSs. The component resonance ductility factor, C_{AR}, is calculated using the data collected herein, as the ratio of the peak component acceleration (PCA) relative to the peak floor acceleration (PFA). Per ASCE 7-22 Chapter 13, the C_{AR} is prescribed as 1.0 for ceilings and 2.2 for pipes. For the analysis presented in this paper, PFA is determined in two different ways from the sensor measurements: Method 1 is based on accelerometers at the center of mass of the reference floor, see Figure 2, and Method 2 is based on interpolation from the known floor accelerations at the coordinates (in plan) of the NCS accelerometer, projected onto the reference floor, using the *scatteredInterpolant* function in MATLAB. Thus, Method 1 (floor COM PFA) is consistent with broad system level amplification, and Method 2 (interpolated local PFA) is relative to the actual location in the ceiling.

3.2.1 Suspended Ceiling Systems

The maximum measured acceleration across all seismic tests on the unbraced fixed-fixed ceiling was 1.97 *g*, 1.03 *g* and 1.86 *g* in the X-, Y-, and Z-directions, respectively (where $g = 9.81$ m/s^2). Similarly, the maximum measured acceleration on the braced fixed-floating ceiling was 1.90 *g*, 1.28 *g* and 1.15 *g* in the X-, Y-, and Z-directions, respectively. Figure 6 shows the acceleration amplification factor, which is the ratio of PCA to PFA for all seismic tests in the three orthogonal directions. PFA in this case for each test is calculated based on the two methods described earlier. Based on the scatter for each set of points, Method (2) (interpolated local PFA) results in lower variation in amplification results. For some tests, no data points are plotted, e.g. MID4 in the X-direction. This indicates that a particular motion did not have an input component in that direction; see Table 1 for input motion DOFs. ASCE 7-22 based C_{AR} factors are also plotted in the subplots pertaining to the in-plane directions of the suspended ceilings. It can be noted from Figure 6a-b that C_{AR} = 1.0 is a suitable criterion compared to the mean of PCA/PFA for X-direction (0.99) and Y-direction (1.01)

across all tests based on Method 2 (interpolated local PFA), with a COV (coefficient of variation) of 5.7% and 4.7% in the two directions. This shows that drywall ceilings developed in-plane stiffness, behaving as diaphragms capable of transferring lateral forces to the surrounding walls. This is consistent with the ASCE 7-22 (Commentary Section C13.5.6) assumption about suspended ceilings constructed with screw-attached gypsum boards. However, in the Z-direction, the braced fixed-floating ceiling has a lower component acceleration amplification ratio (3.3, COV = 33%) compared with the unbraced fixed-fixed ceiling (4.9, COV = 21%), on average across all tests; see Figure 6c. However, seismically bracing the ceiling system demonstrated smaller acceleration amplifications in the out-of-plane (Z) direction. ASCE 7-22 does not specify a C_{AR} factor for ceilings in Z-direction.

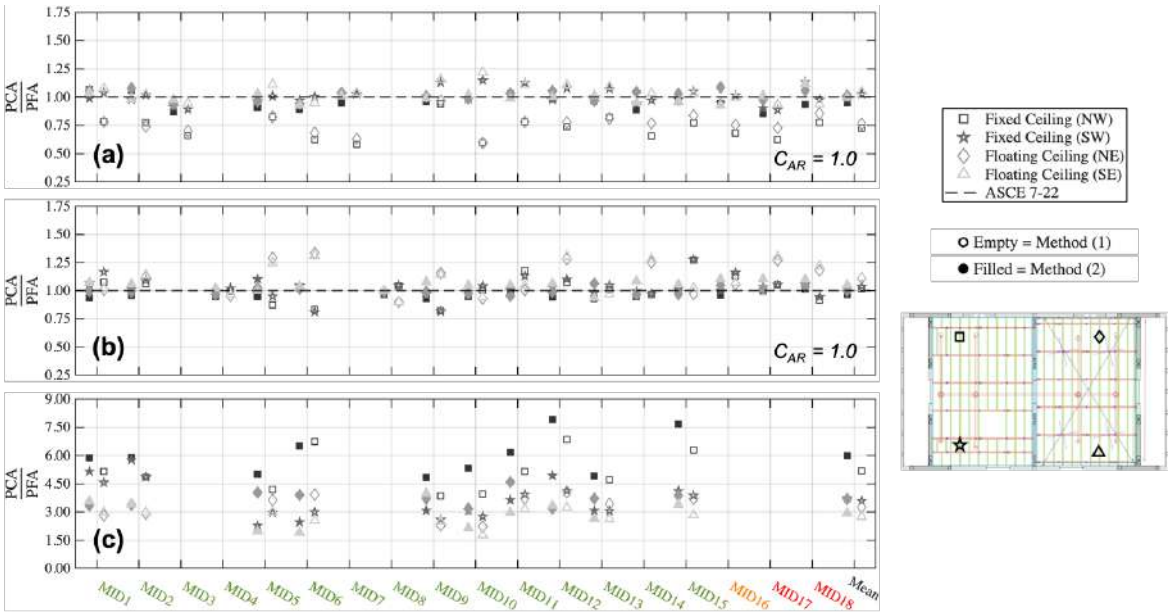


Figure 6. Acceleration amplification ratio for suspended ceiling in (a) X-direction, (b) Y-direction and (c) Z-direction. Note: X-axis label colors relate to hazard level of input motion; green = SLE, orange = DE, red = MCE_R.

3.2.2 Pressurized Piping Systems

The maximum measured accelerations, across all seismic tests, on the branch lines and main line in the local transverse direction of the pipe were 5.08 *g* and 1.82 *g*, respectively. Figure 7a shows the acceleration amplification ratios for all seismic tests in the local transverse direction. The ASCE 7-22 prescribed value of C_{AR} = 2.2 is a conservative estimate compared to the mean of PCA/PFA measured for all pipes of the isolated fire sprinkler system across all seismic tests. On average and based on Method 2 (interpolated local PFA), larger response amplification was measured for branch lines (1.85, COV = 30%) compared with the main line (1.53, COV = 16%); however significantly lower than 2.2. Among the branch lines, the largest average amplification was observed for the one with a flexible drop at its end, based on Method 1 (floor COM PFA). Branch lines with rigid drops have additional fixity provided through interaction with the suspended ceiling system. In the context of resilient design of fire sprinkler systems, flexible drops generally offer more robust performance. Yet, greater amplification in branch lines with flexible drops may render those pipe joints more vulnerable. Similarly for gas piping, the maximum measured accelerations on the main rigid, isolated rigid, main CMT and isolated CMT gas pipes in the transverse direction were 5.42 *g*, 4.22 *g*, 2.73 *g*, and 6.22 *g*, respectively. From Figure 7b, C_{AR} = 2.2 is observed to be conservative for the main and isolated CMT gas pipes based on amplification results (1.7, COV = 27% and 1.6, COV = 26%, respectively) on average. However, the acceleration amplification ratios are significantly larger than ASCE 7-22 prescribed value for main and isolated rigid gas pipes (4.8, COV = 43% and 2.7, COV = 21%, respectively); almost twice compared to CMT systems under identical boundary conditions. The relative amplification of CMT systems to ASME B31 rigid piping is consistently observed to be less than unity, reflecting higher ductility of CMT systems.

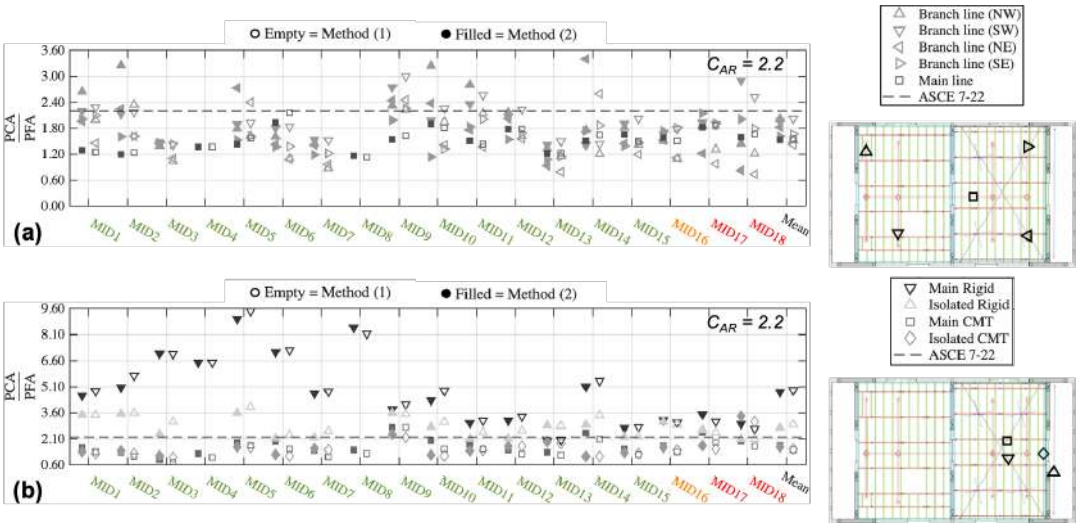


Figure 7. Acceleration amplification ratios for (a) fire sprinkler piping, and (b) gas piping in pipe transverse direction.

4.CONCLUSIONS

A 10-story cold-formed steel building, referred to as CFS10, was constructed and tested at the 6-DOF Large High Performance Outdoor Shake Table. The building was outfitted with an array of nonstructural components and systems, including a densely populated ceiling plenum space of Story 10, complete with a suspended ceiling, gas piping, and fire sprinkler piping systems. The present paper summarizes the observed response of these subsystems within this plenum space when the building was subjected to a series of increasing intensity multi-directional earthquake motions, up to and including risk-targeted maximum considered earthquakes. Throughout the seismic test protocol, all nonstructural components remained fully functional. Interaction between pipes with ceiling grid was observed without major damage. However, joint rotations and relative displacements were not directly measured and are identified as a limitation for future work. For the isolated fire sprinkler piping system at the ceiling of Level 10, larger acceleration amplification was measured for branch line with flexible sprinkler drop in the transverse direction, possibly rendering those pipe joints more vulnerable. Conversely, branch lines with rigid drops have additional fixity through interaction with the suspended ceiling system. Further attention should be given to the amount of rotation that pipe joints can accommodate. Eliminating joints is an alternative way of enhancing resiliency, as seen from the comparisons of the measured response of different gas pipes. Gas pipes with corrugated metal tubing system showed significantly lower acceleration amplification than their rigid gas pipe counterparts. In practice, adopting a lower C_{AR} with higher R_{p0} (component strength factor) as permitted, or an adjusted C_{AR}/R_{p0} ratio may be used to obtain design forces comparable with ASME B31 piping, as supported by experiments. While no functionality issues were observed during the CFS10 seismic tests, reconnaissance reports and previously conducted experiments have highlighted the vulnerability of such rigid pipe joints.

ACKNOWLEDGEMENTS AND DISCLAIMER

The CFS10 project is a collaborative research project, with support through the National Science Foundation (NSF) grants CMMI 1663569 and CMMI 1663348, project entitled: Collaborative Research: Seismic Resiliency of Repetitively Framed Mid-Rise Cold-Formed Steel Buildings and numerous other federal/state and industry partners. A complete list of all sponsors/partners to the CFS10 program may be found at: cfs10.ucsd.edu/sponsors-partners. The efforts of all undergraduate and graduate students, visiting scholars (cfs10.ucsd.edu/people) and LHPOST6 staff (nheri.ucsd.edu/about/personnel) are greatly

appreciated. Support for the first author through the NIST Professional Research Experience Program is gratefully acknowledged. Certain commercial or proprietary products may have been used in this study and discussed in the paper. This is not intended to imply recommendation or endorsement by National Institute of Standards and Technology or any other sponsor/partner, nor is it intended to imply that such product is necessarily the best available for the purpose. Findings, opinions, recommendations and conclusions are those of the authors and do not necessarily reflect those of the sponsoring organizations.

REFERENCES

AISI [2020] *AISI S400-20 North American standard for seismic design of cold-formed steel structural systems*, American Iron and Steel Institute, Washington, D.C., USA.

ASCE/SEI [2022] *ASCE/SEI 7-22 Minimum Design Loads and Associated Criteria for Buildings and Other Structures*, American Society of Civil Engineers/Structural Engineering Institute, Reston, VA, USA.

ASME [2025] *ASME B31.9 Standards of Pressure Piping – Building Services Piping*, American Society of Mechanical Engineers, New York, NY, USA.

ASTM [2021] *ASTM A135/A135M-21 Standard Specification for Electric-Resistance-Welded Steel Pipe*, American Society for Testing and Materials International, West Conshohocken, PA, USA.

ASTM [2024] *ASTM C1858/A1858M-24 Standard Practice for Design, Construction, and Material Requirements for Direct Hung Suspended T-bar Type Ceiling Systems Intended to Receive Gypsum Panel Products in Areas Subject to Earthquake Ground Motions*, American Society for Testing and Materials International, West Conshohocken, PA, USA.

ATC [2008] *Reducing the Risks of Nonstructural Earthquake Damage: State-of-the-Art and Practice Report*, ATC-69 Report, prepared by Applied Technology Council for Federal Emergency Management Agency, Washington, D.C., USA.

Bhatta, J., Mishra, P., Cook, D., Sattar, S., Barbosa, A.R., van de Lindt, J. [2025] "Seismic Response of Pressurized Full-Scale Fire Sprinkler Piping System in Six-Story Building," *Journal of Earthquake Engineering*, pp. 1–27. DOI: 10.1080/13632469.2025.2470335.

Dhakal, R.P. [2010] "Damage to non-structural components and contents in 2010 Darfield earthquake," *Bulletin of the New Zealand Society for Earthquake Engineering*, Vol. 43, No. 4, pp. 404-411. DOI: 10.5459/bnzsee.43.4.404-411.

Fathali, S., Filiatrault, A. [2008] "Experimental Seismic-Performance Evaluation of Integrated Isolation/Restraint Systems for Heavy HVAC Equipment," *ASHRAE Transactions*, Vol. 114, pp. 56-67.

FEMA E-74 [2012] *Reducing the Risks of Nonstructural Earthquake Damage – A Practical Guide*, Federal Emergency Management Agency, Washington, D.C., USA.

Hutchinson, T.C., Eladly, M., Ji, R., Rivera, D., Cyizere Rukundo, F., Singh, A., Sorosh, S., Zhang, J., Zhang, X., Padgett, L., Jones, H., Karns, J., Schafer, B.W. [2026] "Advancing use of cold-formed steel framing systems for mid-rise residential construction in seismic zones via full-scale shake table testing," *Proceedings of the 8th Residential Building Design & Construction Conference*, University Park, PA, USA. In press.

McCartney, J.S., Van Den Einde, L., Morrison, M., Palermo, A., Lotfizadeh, K., Lai, C-T., Conte, J.P. [2025] "Multi-degree of freedom shake table testing of large-scale structural and geotechnical systems with NHERI-UCSD LHPOST6," *Frontiers in Built Environment*, Vol. 11, pp. 1573390. DOI: 10.3389/fbuil.2025.1573390.

Miranda, E., Mosqueda, G., Retamales, R., Pekcan, G. [2012] "Performance of Nonstructural Components during the 27 February 2010 Chile Earthquake," *Earthquake Spectra*, Vol. 28, pp. 453-471. DOI: 10.1193/1.4000032.

NFPA [2022] *NFPA 13 Standard for the Installation of Sprinkler Systems*, National Fire Protection Association, Quincy, MA, USA.

Pantoli, E., Chen, M.C., Wang, X., Astroza, R., Ebrahimian, H., Hutchinson, T.C., Conte, J.P., Restrepo, J.I., Marin, C., Walsh, K.D., Bachman, R.E., Hoehler, M.S., Englekirk, R., Faghihi, M. [2016] "Full-scale structural and nonstructural building system performance during earthquakes: Part II–NCS damage states," *Earthquake Spectra*, Vol. 32, No. 2, pp. 771-794. DOI: 10.1193/012414eqs017m.

Patnana, V., Rai, D.C. [2022] "Experimental testing on nonstructural continuous plasterboard suspended ceiling systems under shake table-generated motions," *Earthquake Spectra*, Vol. 38, No. 3, pp. 1918-1945. DOI: 10.1177/87552930221085298.

Perrone, D., Calvi, P.M., Nascimbene, R., Fischer, E.C., Magliulo, G. [2019] "Seismic performance of non-structural elements during the 2016 Central Italy earthquake," *Bulletin of Earthquake Engineering*, Vol. 17, No. 10, pp. 5655-5677. DOI: 10.1007/s10518-018-0361-5.

Pourali, A., Dhakal, R.P., MacRae, G., Tasligedik, A.S. [2017] "Fully floating suspended ceiling system: experimental evaluation of structural feasibility and challenges," *Earthquake Spectra*, Vol. 33, No. 4, pp. 1627-1654. DOI: 10.1193/092916eqs163m.

Singh, A., Hutchinson, T.C., Torabian, S., Schafer, B.W., Peterman, K.D., Padgett, L., Jones, H. [2022] "Structural Design Narrative of the CFS-NHERI 10-Story Test Building for Multi-Dimensional Shake Table Testing," *Proceedings of the Cold-Formed Steel Research Consortium Colloquium 2022*, Baltimore, MD, USA.

Singh, A., Zhang, J., Rivera, D., Eladly, M., Jones, H., Kovac, A., Padgett, L., Rivera, D., Smith, K., Torabian, S., Peterman, K.D., Schafer, B.W., Hutchinson, T.C. [2024] "CFS-NHERI 10-Story Building Shake Table Test Specimen: Design Updates," *Proceedings of the 18th World Conference on Earthquake Engineering*, Milan, Italy.

Singh, A., Speicher, M.S., Cyizere Rukundo, F., Hutchinson, T.C., Schafer, B.W. [2026] "Application of 360 Degree Imaging and Construction Progress Documentation Platforms in Large-scale Experiments: a CFS10 Case Study," *Proceedings of the 13th National Conference on Earthquake Engineering*, Earthquake Engineering Research Institute, Portland, OR, USA. In review.

Sorosh, S., Zhang, J., Lotfizadeh, K., Haddadi, H., Swensen, D., Branum, D., Kohler, M.D., Guy, R., Skolnik, D., Saifullah, K.M., Schafer, B.W., Hutchinson, T.C. [2026] "Implementation Strategies and Utility of a Multi-sensor Suite Deployed in a Full-scale 10-story Building Shake Table Test Program," *Proceedings of the 13th National Conference on Earthquake Engineering*, Earthquake Engineering Research Institute, Portland, OR, USA. In review.

Soroushian, S., Maragakis, E.M., Ryan, K.L., Sato, E., Sasaki, T., Okazaki, T., Mosqueda, G. [2016] "Seismic simulation of an integrated ceiling-partition wall-piping system at E-Defense. II: Evaluation of nonstructural damage and fragilities," *Journal of Structural Engineering*, Vol. 142, No. 2, pp. 04015131. DOI: 10.1061/(ASCE)ST.1943-541X.0001385.

Tian, Y., Filiatrault, A., Mosqueda, G. [2014] "Experimental seismic fragility of pressurized fire suppression sprinkler piping joints," *Earthquake Spectra*, Vol. 30, No. 4, pp. 1733-1748. DOI: 10.1193/111011eqs278m.

Torabian, S., Nia, S.Z., Schafer, B.W. [2016] "An archetype mid-rise building for novel complete cold-formed steel buildings," *Proceedings of Wei-Wen Yu Int. Specialty Conf. on Cold-Formed Steel Structures*, Baltimore, MD, USA.

Study on the horizontal stiffness of single and double-layer CHN-US style ceiling

Minhui. LI[1], Daiki. SATO[2], and Shojiro. MOTOYUI[2]

[1] Doctoral Student, School of Environment and Society, Institute of Science Tokyo
4259 Nagatsuta, Midori-ku, Yokohama, Kanagawa 226-8502, Japan
li.m.ah@m.titech.ac.jp
[2] Associate Professor, School of Environment and Society, Institute of Science Tokyo
4259 Nagatsuta, Midori-ku, Yokohama, Kanagawa 226-8502, Japan
sato.d.7887@m.isct.ac.jp
[3] Emeritus Professor. School of Environment and Society, Tokyo Institute of Technology
4259 Nagatsuta, Midori-ku, Yokohama, Kanagawa 226-8502, Japan
smotoyui@gmail.com

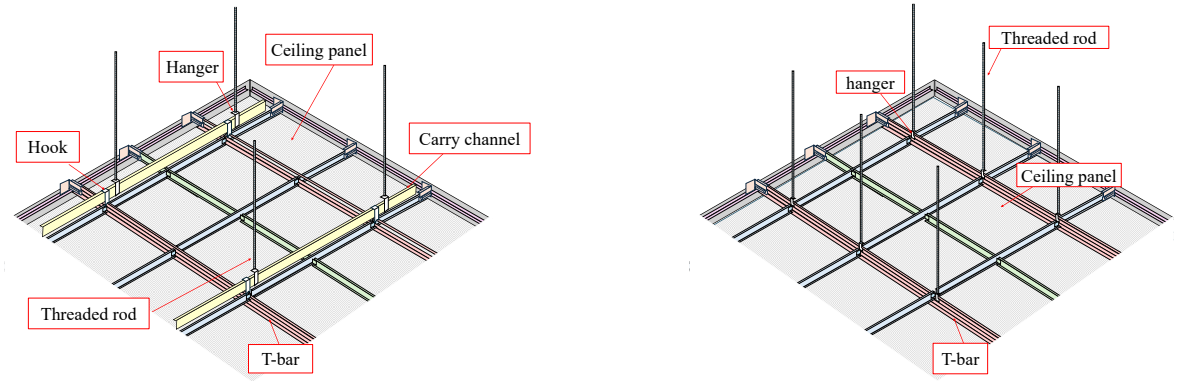
Abstract. CHN-US style suspended ceilings are developed from US-style ceilings, which are hung by threaded rods instead of hanging wires. There are mainly two types of bottom connection systems for the threaded rods used in the CHN-US style ceiling: the double-layer system and the single-layer system. In the double-layer system, the ceiling is connected to the threaded rod through hooks, C-channels, and hangers. On the other hand, in the single-layer system, the ceiling is connected to the threaded rod only by hangers. Due to the differences between the double-layer system and the single-layer system, the horizontal stiffness of both types of bottom connection systems in the CHN-US style ceiling needs to be investigated experimentally. This paper aims to clarify the horizontal stiffness of the double-layer system and single-layer system of the CHN-US style ceiling by a series of static loading tests.

Keywords: CHN-US style ceiling, Double-layer system, Single-layer system, Horizontal stiffness

1. INTRODUCTION

Chinese-style grid system ceilings (which we call CHN-US style ceilings in this paper) are developed from US-style ceilings, which consist of T-shaped galvanized steel beams (T-bar) and mineral wood boards (ceiling panels). In US-style ceilings, hanging wires are the primary method for suspending the ceiling grid[2], whereas in CHN-US style ceilings, threaded rods are the main method for suspending the ceiling[3]. Furthermore, there are mainly two types of bottom connection systems for the threaded rods used in the CHN-US style ceiling: [1] double-layer[4] system (DLS): the ceiling is connected to the threaded rods by a hanger – C-channel – hook system (HCH system) (Fig. 1(a)), [2] single-layer[5] system (SLS): the ceiling is directly connected to the threaded rods by hangers (Fig. 1(b)). In recent years, CHN-US style ceilings collapsing or sustaining damage during earthquakes have been reported, leading to human casualties and functional losses. Particularly, significant damage occurred on the CHN-US style ceiling of school classrooms and halls during the 2013 Ya'an earthquake in Sichuan[1], raising concerns about substantial damage in the future. However, the dynamic behavior of CHN-US style ceilings is not clear. Thus, we have to develop a numerical model for the CHN-US style ceiling, and the horizontal stiffness of the DLS and the SLS used in the CHN-US style ceiling is an especially important parameter for the numerical model, which needs to be clarified by experimental methods.

Due to the difference between the DLS and the SLS, the horizontal stiffness of both types of bottom connection systems in the CHN-US style ceiling needs to be investigated experimentally, respectively. Therefore, this paper aims to clarify the horizontal stiffness of the DLS and SLS of the CHN-US style ceiling by a series of static loading tests.



(a) Double-layer system (DLS) (b) Single-layer system (SLS)

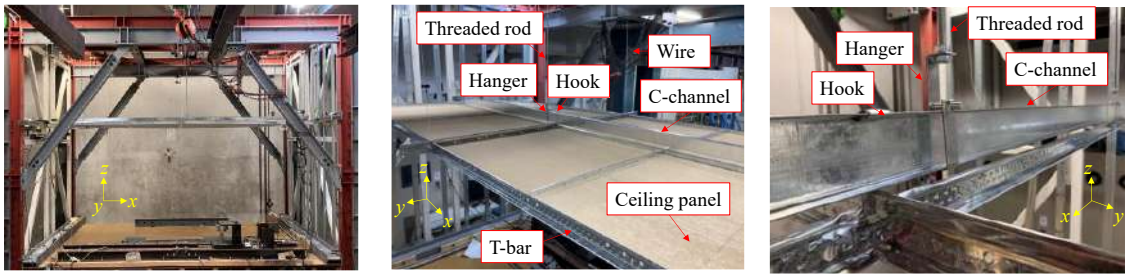
Fig.1 Two types of bottom connection systems for the threaded rods of the CHN-US style ceiling

2. TEST SPECIMEN

Section 2 describes the details of the test specimen used in the static loading test for DLS and SLS.

2.1 TEST SPECIMEN FOR THE DLS OF THE CHN-US STYLE CEILING

The overview of the loading test setup is shown in Fig. 2(a). The test specimen is assembled as a 4×2 grid ceiling unit. The test specimen was constructed using the T-bars (Fig. 2(b)), ceiling panels (600 mm × 600 mm mineral wood boards), HCH system (Fig. 2(c)), and M8 threaded rod. Only the central row of the specimen is equipped with three M8 threaded rods, and the test specimen was stabilized using wires to maintain overall balance. The boundary conditions of the test specimen were entirely free.

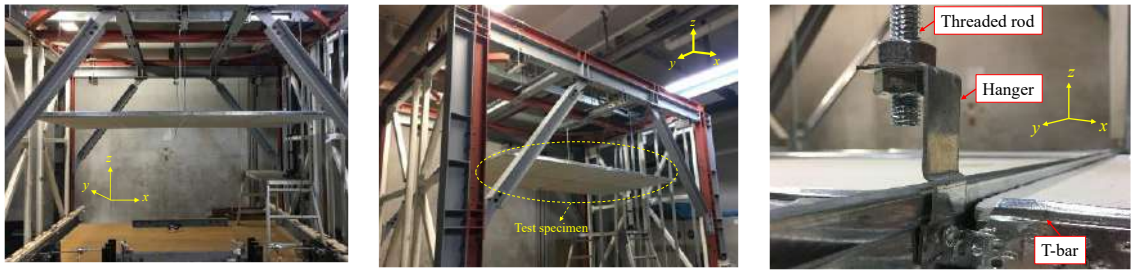


(a) Test setup (b) Test specimen (c) HCH system

Fig.2 Test photos for the DLS

2.2 TEST SPECIMEN FOR THE SLS OF THE CHN-US STYLE CEILING

A static loading test is also conducted to clarify the horizontal stiffness of the single-layer CHN-US style ceiling. The overview of the static loading test setup is shown in Fig. 3(a). The test specimen was constructed using the same T-bars and ceiling panels as the loading test described in Section 2. The suspension method is different from the ceiling specimen used in Section 2, where the ceiling is directly connected to the threaded rod by a hanger instead of the HCH system, as shown in Fig. 3(b).



(a) Test setup (b) Test specimen (c) Hanger part

Fig.3 Test photos for the SLS

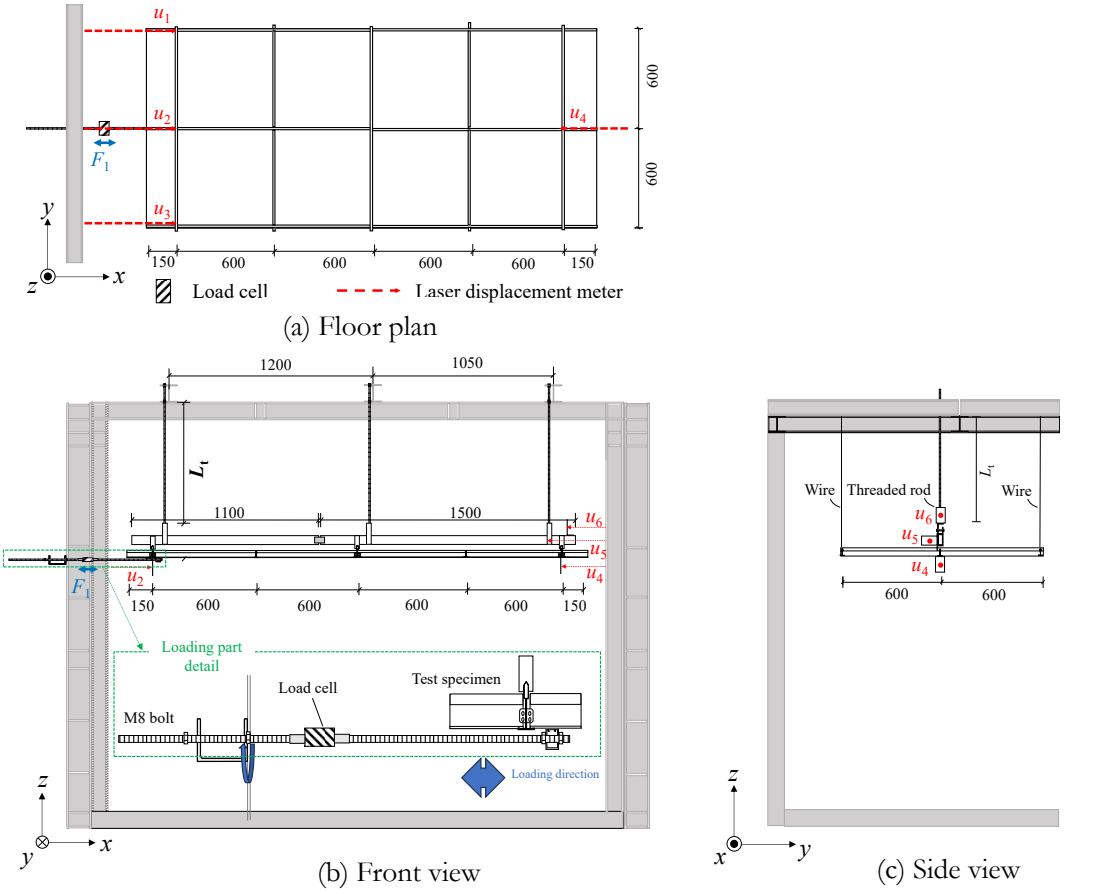
3. MEASUREMENT AND LOADING METHOD

Section 3 shows the measurement and loading method of the static loading test for DLS and SLS.

3.1 MEASUREMENT FOR THE DLS AND THE SLS

The measurement for the DLS includes the displacement and the loading force of the ceiling specimen. To confirm whether the deformation occurred at the test specimen, 6 laser displacement meters with a maximum measurement value of ± 20mm are installed at 6 locations in total, as shown in Fig. 4: (1) u_1: the displacement of the specimen at the left behind, (2) u_2: the displacement of the specimen at the left middle, (3) u_3: the displacement of the specimen at the left front, (4) u_4: the displacement of the specimen at the right middle, (5) u_5: the displacement of the specimen at the hanger, (6) u_6: the displacement of the specimen at the carry channel. To measure the loading force F_1 applied to the test specimen, a high-precision tensile-compressive load cell is used.

The measurement for the SLS includes a high-precision load cell, which is employed to apply the load to the specimen and measure the loading force as F'_1, as shown in Fig. 5, and the displacement of the test specimen u'_1 was recorded using a laser displacement meter.

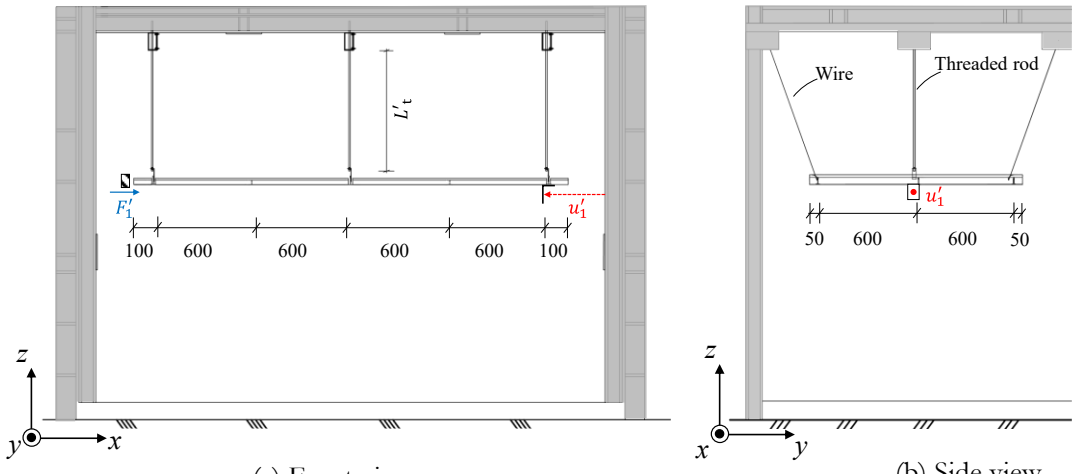


(a) Floor plan

(b) Front view

(c) Side view

Fig.4 Measurement for the DLS



(a) Front view

(b) Side view

Fig.5 Measurement for the SLS

3.2 LOADING METHOD

The loading method for the DLS applied a displacement-controlled loading cycle. In the DLS specimen, the loading displacement ranged from - 10 mm to 10 mm. Three threaded rods with varying lengths, L_t, (as shown in Table 1) are used to carry out the loading tests to establish a relationship between the lateral stiffness of the threaded rod with the HCH system and its length. It should be noted that L_t denotes the length of the threaded rod, defined as the vertical distance from the slab to the hanger level, as shown in Fig. 4(b).

In the SLS specimen, the loading displacement ranged from 0 mm to 30 mm. Three threaded rods with varying lengths, L'_t, (as shown in Table 2) are applied to conduct the loading tests.

Table 1. Test case for the DLS

Test case name	Length of the threaded rod L_t
L-850	850 mm
L-650	650 mm
L-450	450 mm

Table 2. Test case for the SLS

Test case name	Length of the threaded rod L_t
S-900	900 mm
S-700	700 mm
S-500	500 mm

4.TEST RESULT

Section 4 compares the test results between the DLS and the SLS used in the CHN-US style ceiling.

4.1 TEST RESULT OF THE DLS SPECIMEN

Fig. 6 illustrates the displacement result of u_1 to u_6 of the DLS specimen for the test L-850. It is confirmed that the displacement on the left and right sides (u_1, u_2, u_3, and – u_4) of the test specimen is the same (Fig. 6(a)). This implies that there is no internal deformation in the loading direction and no movement in the perpendicular direction. Furthermore, the displacements u_4, u_5, and u_6 are nearly identical (Fig. 6(b)), the relative displacement of approximately 0.5 mm between the hanger and C-channel (Fig.6(c)) occurs, but shows no direct relationship with the ceiling displacement u_4, which can be considered as noise.

Fig. 7 shows the loading force F_1 - displacement u_2 relationship of each test case. The total lateral stiffness of the test specimen $N_t k_l$ (N_t is the number of threaded rods in the test specimen, k_l is the lateral stiffness of each threaded rod), can be obtained as 0.43 N/mm (L-850), 0.7 N/mm (L-650), and 1.6 N/mm (L-450).

Generally, the threaded rod of the ceiling was modeled as a cantilever beam with a rotational spring of stiffness k_θ attached at the roller end, as shown in Fig. 8(a). The lateral stiffness $N_t k_l$ is calculated as

$$N_t k_l = N_t k_t + K_p \quad (1)$$

where

$$k_t = [\frac{1}{3} - \frac{1}{4} \cdot \frac{1}{1 + \frac{E_t I_t}{k_\theta L_t}}]^{-1} \frac{E_t I_t}{L_t^3} = \lambda \frac{E_t I_t}{L_t^3} \quad (2)$$

$$K_p = \frac{Mg}{L_t} \quad (3)$$

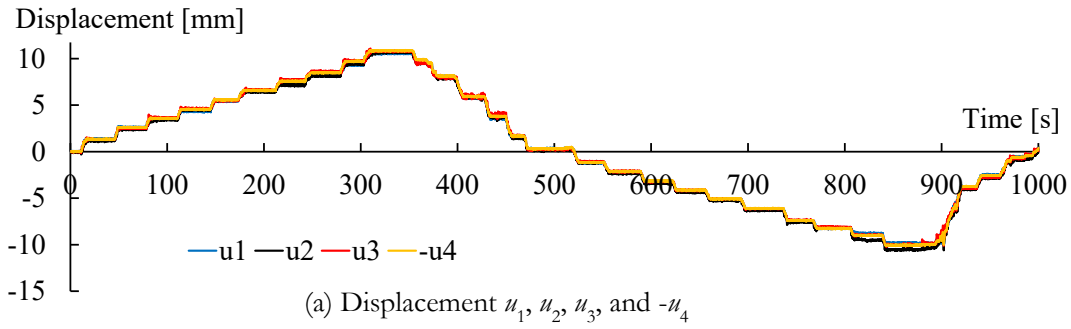
Here, k_t and K_p denote the equivalent stiffness of the theoretical threaded-rod model, shown in Fig. 8(a), and the pendulum stiffness of the ceiling specimen, respectively. The number of threaded rods N_t in the ceiling specimen is 3. k_θ is the stiffness of the rotational spring, and λ is the amplification factor for k_t. E_t is the Young's modulus of the threaded rod (205000 N/mm²). M is the total mass of the ceiling (20 kg). The moment of inertia I_t of the threaded rod is expressed as

$$I_t = \frac{\pi(\alpha_t d_t)^4}{64} \quad (4)$$

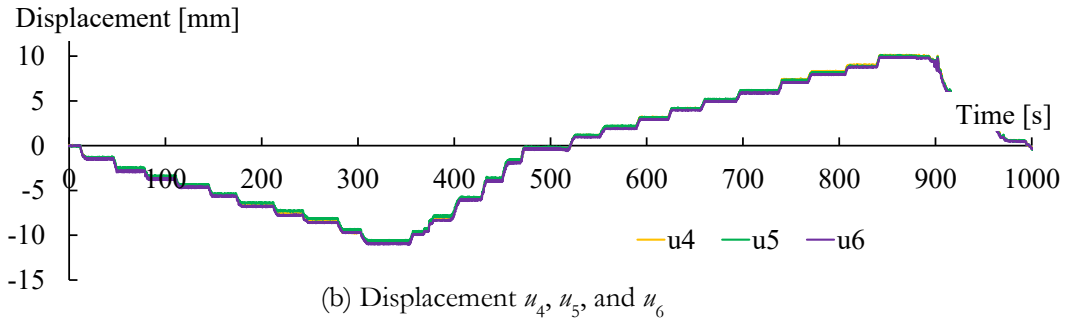
where α_t is the effective diameter ratio (taken as 0.7; see Appendix), and d_t is the diameter of the threaded rod (7.5 mm).

Fig. 8(b) compares the theoretical values of k_t, calculated using Eq. (2) with rotational spring stiffnesses k_θ = 1000, 12000, and 20000 N·mm/rad (broken lines), with the experimental results. The best agreement with the experiment is obtained for a rotational spring stiffness of 12000 N·mm/rad.

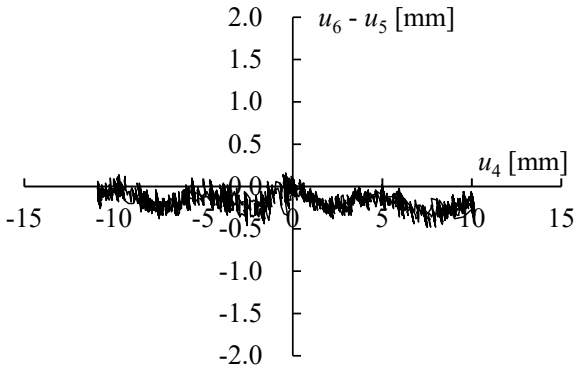
Fig. 9 further compares the experimental results with the theoretical curve of the amplification factor λ, calculated using Eq. (2) under k_θ = 12000 N·mm/rad. The experimental results show good consistency with the theoretical prediction.



(a) Displacement u_1, u_2, u_3, and $-u_4$

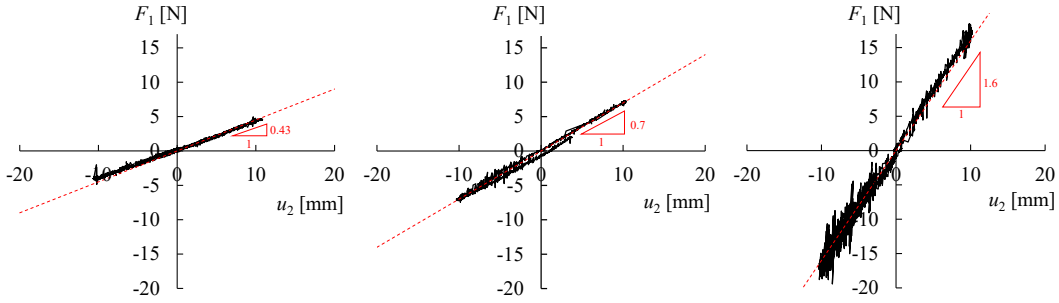


(b) Displacement u_4, u_5, and u_6



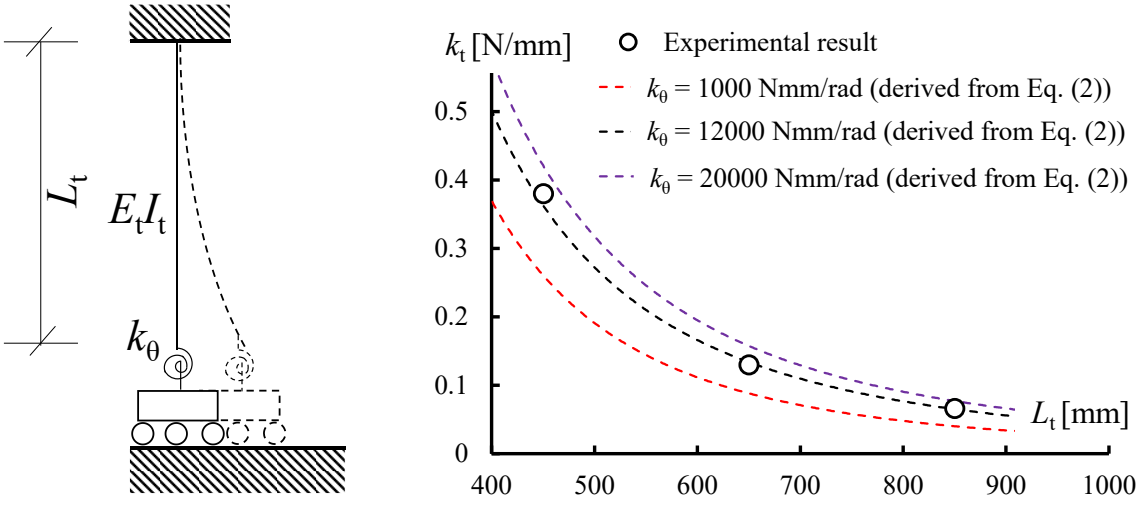
(c) Relationship between $u_6 - u_5$ and u_4

Fig.6 Displacement result of Test L-850 (DLS)



(a) L-850 (b) L-650 (c) L-450

Fig.7 Loading force F_1 - displacement u_2 relationship of the DLS



(a) Theoretical model for the threaded rod (b) Relationship between L_t and k_t with different k_θ

Fig.8 Evaluation on the k_t of the threaded rod used in the DLS

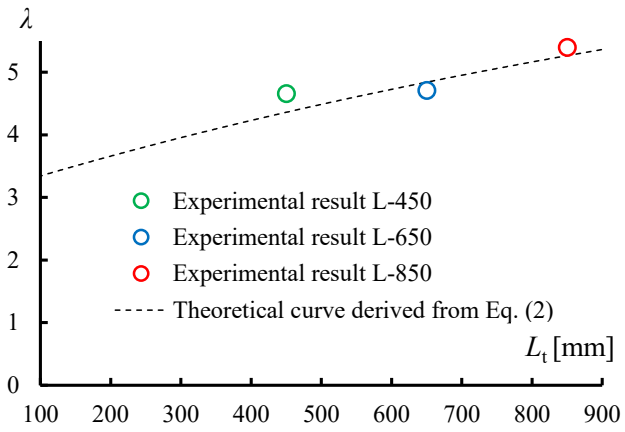
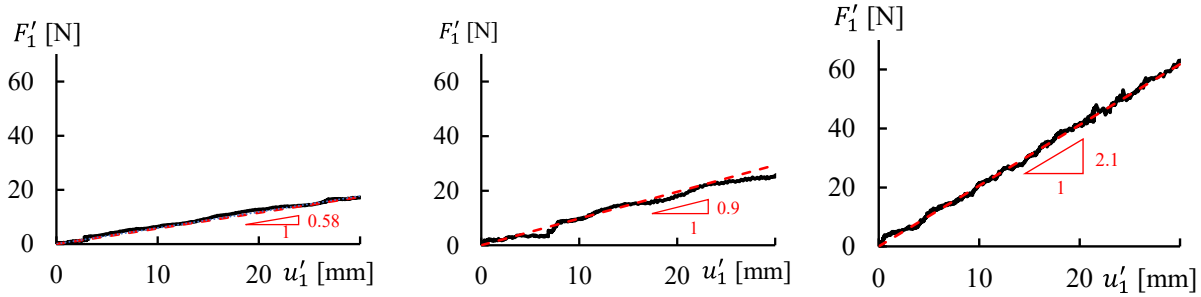


Fig.9 Relationship between L_t and λ

4.2 TEST RESULT OF THE SLS SPECIMEN

Fig. 10 shows the loading force F'_1 - displacement u'_1 relationship of each test case. The total lateral stiffness of the test specimen $N'_t k'_1$, can be obtained as 0.58 N/mm (L-900), 0.9 N/mm (L-700), and 2.1 N/mm (L-500). The same theoretical formulation presented in Eq. (2) is applied to the SLS specimen. In this section, the parameters associated with the SLS specimen are distinguished by a superscript " ′ ". Compared with the DLS specimen, the SLS specimen provides a significantly higher rotational stiffness. The identified rotational stiffness k'_θ is approximately ten times larger (120000 Nmm/rad) than that of the SLS specimen, as shown in Fig. 11, reflecting the enhanced rotational restraint.



(a) S-900 (b) S-700 (c) S-500

Fig.10 Loading force F'_1 - displacement u'_1 relationship of the SLS

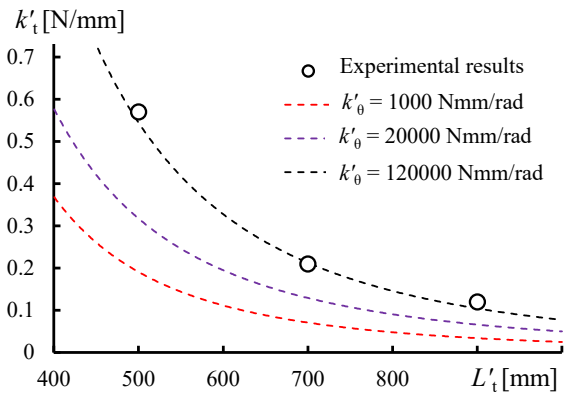


Fig.11 Evaluation on the k'_t of the threaded rod used in the SLS

4.3 DISCUSSION

This section compares the test results between the DLS and the SLS. Both the DLS and the SLS show that the horizontal stiffness is influenced by both the rotational stiffness and the pendulum stiffness of the ceiling.

However, the rotational stiffness of the threaded rod used in the SLS is approximately 10 times that of the threaded rod used in the DLS. This is because the threaded rod is directly connected to the ceiling by the hanger in the SLS, as shown in Fig. 12(a), and the hanger is attached to the ceiling by a screw with a nut. The boundary condition of the bottom of the threaded rod used in the SLS can be considered as a nearly rigid restraint.

On the other hand, in the DLS, there are more connections between the threaded rod and the ceiling, as shown in Fig. 12(b). Firstly, the threaded rod is connected to a C-channel by a hanger (the C-channel is under free condition). Then, the C-channel attaches to the ceiling by a hook. It should be noted that the hook is not fastened to the C-channel by any screws or bolts; its stability relies solely on the contact between the bent part of the hook and the C-channel. Therefore, there are more flexible joints between the threaded rod and the ceiling, which makes the rotational stiffness smaller than that of the SLS.

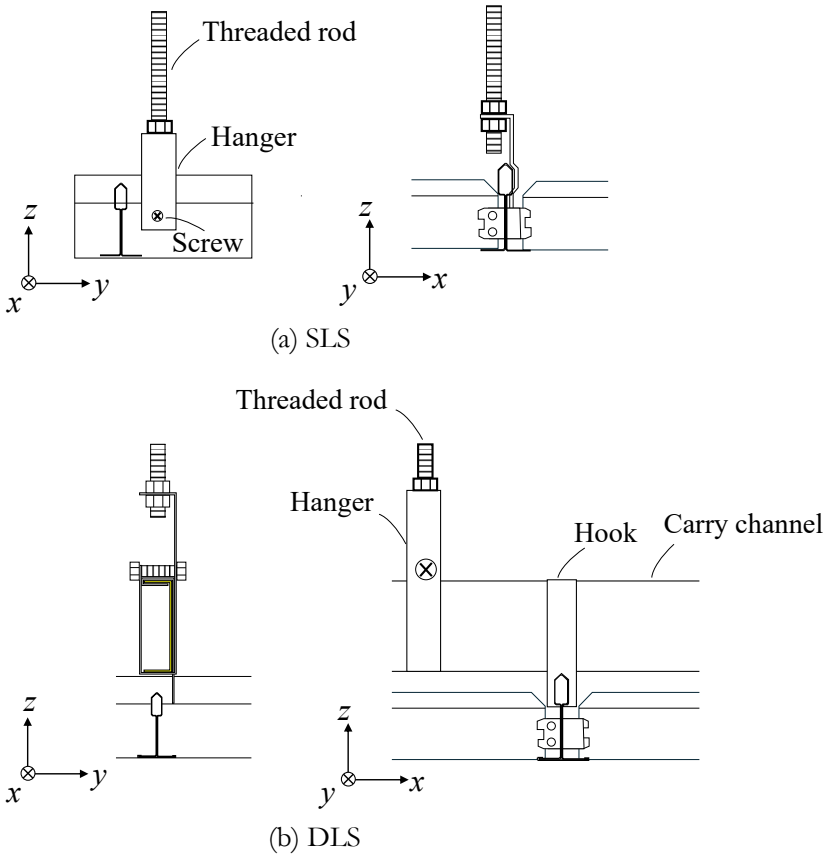


Fig.12 Details of the bottom connection of the threaded rod

5. CONCLUSION

This study aims to investigate the horizontal stiffness of the DLS and SLS of the CHN-US style ceiling by using a series of loading tests. In this research, the evaluation formula for the horizontal stiffness of the threaded rod was obtained experimentally. The rotational stiffness of the threaded rod used in the SLS is approximately 10 times that of the DLS, as the SLS has a more rigid bottom connection of the threaded rod.

REFERENCE

[1] .Q.LI, Z. Qu, Q. XIE, D. WANG, Seismic damage characteristics and fragility of suspended ceilings in chinese public buildings[j], *Engineering Mechanics* 36 (2019) 207–215. doi:doi:10.6052/j.issn.1000-4750.2018.10.0358.

[2] ASTM International, Standard Practice for Installation of Ceiling Suspension Systems for Acoustical Tile and Lay-in Panels in Areas Subject to Earthquake Ground Motions, *ASTM International*, 2022. URL https://www.astm.org/e0580_e0580m-22.html

[3] J502-2-2012, Indoor decoration: suspended ceiling inside (in Chinese), Beijing, China: *China Planning Press*, 2012.

[4] Y. Wang, H. Jiang, S. Motoyui, K. Kasai, Z. Qin, Y. Huang, Study on seismic performance of suspended ceiling system with semi-free boundary condition, *Engineering Structures* 275 (2023) 115208. doi:https://doi.org/10.1016/j.engstruct.2022.115208.

[5] H. Jiang, Y. Wang, & L. He (2021). Study of seismic performance of Chinese-style single-layer suspended ceiling system by shaking table tests. *Advances in Civil Engineering*, 2021(1), 9861722.

ACKNOWLEDGEMENT

This work was supported by the JST SPRING, Grant Number JPMJSP JPMJSP2180, and JST Program on Open Innovation Platform with Enterprises, Research Institute and Academia and JSPS KAKENHI Grant Number JP16H02375. The authors would like to express sincere gratitude to Mr. CHHAT Tola for sharing the research data from his master's thesis, which contributed to this work.

APPENDIX

This appendix summarizes the three-point bending test on M8 threaded rods used in the CHN-US style ceiling.

Fig. A1 shows the overall setup and boundary details of the test. In the test, both ends of the threaded rod were roller-supported, and a concentrated load was applied at the mid-span to obtain the bending stiffness. Five rod lengths were tested: 150 mm, 200 mm, 300 mm, 400 mm, and 580 mm. From the applied load P

and mid-span deflection w, the bending stiffness was calculated, and the load–deflection relationships are shown in Figure A2.

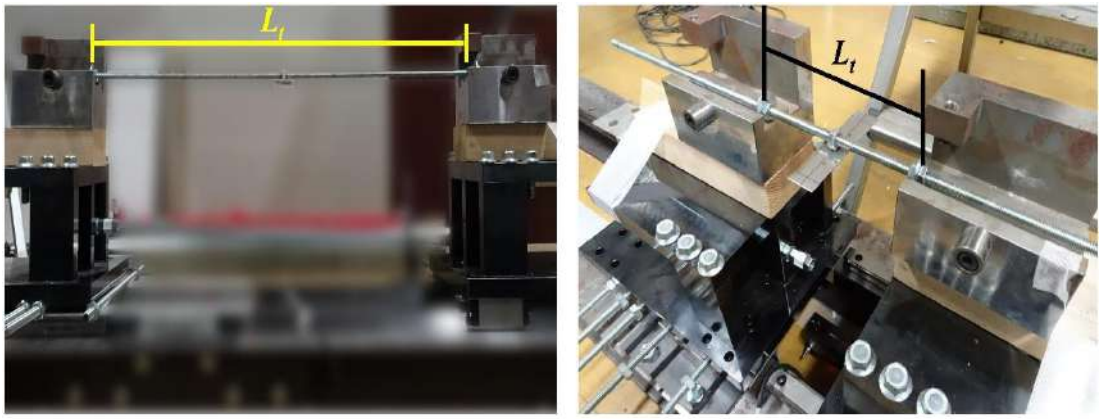
For a simply supported beam, the theoretical bending stiffness K_b is expressed as:

$$K_b = \frac{48E_tI_t}{L_t^3} \quad (A1)$$

where E_t = 205,000 N/mm² is the Young's modulus, I_t is the second moment of area, and L_t is the rod length. The effective diameter ratio α_t is obtained from:

$$I = \frac{\pi(\alpha_t d_t)^4}{64} \quad (A2)$$

The effective diameter ratio α_t was derived from the test results (d_t is the nominal value of the M8 threaded rod used in the CHN-US style ceiling which is taken as 7.5 mm) and is shown in Figure A3. The results confirm that the effective diameter ratio α_t of the threaded rod is approximately 0.7.



(a) Test setup (b) Boundary condition

Fig.A1 Test photos of the three point bending test

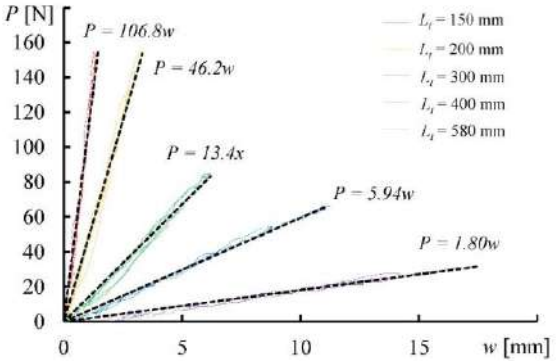


Fig.A2 Load P – deflection w relationship

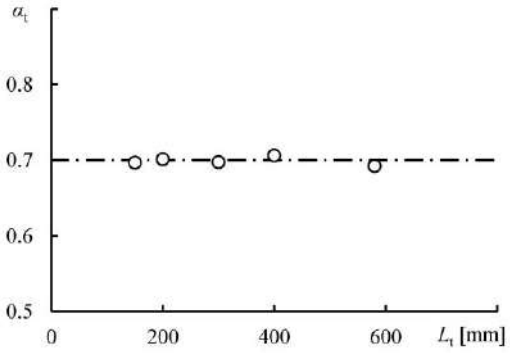


Fig.A3 Evaluation on effective diameter ratio

Estimation of Floor Response Spectra for Risk-Targeted Seismic Design of Non-Structural Elements

Roberto J. Merino[1], Roberto Gentile[2], and Carmine Galasso[1]

[1]Department of Civil, Environmental and Geomatic Engineering, University College London

Gower Street, London, WC1E 6BT; e-mails: r.merinovela@ucl.ac.uk, c.galasso@ucl.ac.uk

[2]Department of Risk and Disaster Reduction, University College London

Gower Street, London, WC1E 6BT; e-mail: r.gentile@ucl.ac.uk

Abstract. The seismic performance of buildings is heavily influenced by the seismic performance of non-structural elements. Seismic damage to non-structural elements can significantly contribute to economic losses, loss of functionality, and loss of life, influencing the overall seismic risk of the building they are installed in. To mitigate these consequences, simple risk-targeted seismic design methodologies have been proposed by various researchers. However, these methodologies currently consider damage to non-structural elements in a nonspecific manner using peak floor acceleration profiles and storey loss functions, not allowing for a detailed seismic design of critical non-structural elements. Floor response spectra play a crucial role in determining the seismic demand on many typologies of non-structural elements and are, therefore, required for a more detailed consideration of damage. This paper presents a simplified methodology to estimate absolute acceleration and relative displacement floor response spectra, consistent with the pseudo-spectral relationship, which can be directly integrated into risk-targeted design methodologies. The proposed methodology is based on the assumptions that the contribution of first mode response of the supporting structure to the floor response spectrum can be approximated using the bilinear force-displacement curve of the equivalent single-degree-of-freedom system representing the supporting structure, and that the higher mode contributions can be estimated using closed-form solutions of a continuous cantilever shear beam. The proposed methodology is benchmarked against the results from non-linear time history analyses of two reinforced concrete moment resisting frames, showing good agreement between the proposed methodology and the results from non-linear time history analyses.

Keywords: floor response spectra, non-structural elements, nonstructural components, seismic demand, risk-targeted seismic design.

1. INTRODUCTION

Non-structural elements (NSEs) play a crucial role in maintaining both the economic value and the post-earthquake functionality of buildings. Recent earthquakes have demonstrated that critical buildings such as hospitals, schools, universities, airports, and industrial plants can lose their functionality immediately after earthquake, hindering the post-disaster recovery of communities [Miranda et al., 2012; Perrone et al., 2019; Qu et al., 2023].

Contemporary seismic design guidelines prescribe simplified force-based seismic design methodologies for NSEs, based on a simplified equivalent static force procedure [NTC, 2018]. This approach has many limitations as discussed by Filiatrault et al. [2021]. Because of these limitations, Filiatrault et al. [2021] proposed a direct displacement-based seismic design (DDBD) procedure for acceleration-sensitive NSEs, with a single point of support in the structure and whose damage is due to excessive displacements relative to their point of support in the structure. This procedure requires that relative displacement floor response spectra (FRS) be estimated to represent the seismic demand on NSEs. Even though this procedure is a step forward for finding NSE design solutions that achieve a given performance level under a specified level of seismic intensity, it is still unclear what is its associated reduction of seismic economic losses and loss of functionality. Many recent research efforts have focused on developing risk-targeted seismic design methodologies for buildings [Gentile & Calvi, 2023; O'Reilly & Calvi, 2019]. These methodologies consider damage to acceleration-sensitive NSEs in simplified ways such as using building level fragility functions [Gentile & Calvi, 2023], or storey-loss functions [O'Reilly & Calvi, 2019], which do not allow for detailed consideration of damage for specific critical NSEs. This limitation of existing methodologies for the risk-targeted seismic design of buildings does not allow the structural engineer to consider the seismic design of some acceleration-sensitive NSEs that are critical for the safety and functionality of the building (e.g. fire-safety suspended piping systems, back-up power generators, suspended ceilings, etc). A simple procedure for estimating FRS that can fit into risk-targeted seismic design methodologies for buildings would be a valuable tool for achieving a risk-targeted seismic design of NSEs.

Calculating FRS from non-linear time history (NLTH) analyses is computationally demanding and time-consuming. Several methods have been proposed to estimate absolute acceleration and relative displacement FRS [Calvi, 2014; Calvi & Sullivan, 2014; Degli Abbati et al., 2018; Haymes et al., 2020; Merino et al., 2020, 2024; Vukobratović & Fajfar, 2017]. Many of these procedures require results from modal and pushover analysis of the supporting structure. In seismic design, the detailed properties of both the supporting structure and its NSEs are not generally known before the design has been completed. Additionally, seismic design usually requires various iterations before a final solution is achieved. Therefore, there is a need for FRS estimation methodologies that can seamlessly fit into such seismic design framework. Petrone et al. [2015] and Rodriguez et al. [2023] proposed simplified methodologies to estimate FRS without structural analyses as preparatory steps. However, these methodologies have many limitations since they are based on empirical relations that may give unsound results in some cases. This paper presents a simplified and computationally inexpensive methodology for estimating absolute acceleration and relative displacement FRS for RC frame buildings based on an existing procedure to estimate FRS [Merino et al., 2020, 2024], and that can be directly integrated into risk-targeted seismic design procedures for NSEs in RC frame buildings.

2. CASE STUDY BUILDINGS

This section introduces the two reinforced concrete (RC) frame supporting structure archetypes used to benchmark the proposed methodology to estimate FRS. The archetype RC frames were taken from a previous study by Gentile et al. [2021]. Figure 1 shows the geometrical configurations of both RC archetype frames. The two archetypes have 4 and 6 storeys respectively, and have identical bay lengths of 5.5 m and

identical inter-storey heights of 3.3 m. All the beams of both archetypes have a transverse cross-section of 30 cm by 60 cm, while the columns have transverse cross-sections of 60 cm by 60 cm. The RC frames are the longitudinal perimetral frames of two buildings with plan dimensions of 22 m long and 11 m wide. Internal gravity columns are provided in the building, and are not considered in the proceeding analyses. The concrete was assumed to have a compressive strength (f'_c) of 25 MPa, while the longitudinal reinforcing steel in the beams was assumed to have yield, f_y, and ultimate, f_u, strengths of 300 MPa and 390 MPa, respectively. The longitudinal reinforcement in the columns, as well as the transverse reinforcement in beams, columns, and beam-column joints were assumed to have f_y and f_u of 450 MPa and 585 MPa, respectively. The seismic weight of each storey is constant along the height and has a value of 2017 kN, which implies a total seismic weight on each of the two longitudinal frames of 1008 kN per storey. The strength of the archetype frames was determined using DDBD for a target inter-storey drift of 2.5% [Priestley et al., 2007], and a ground displacement spectrum consistent with the New Zealand Code [NZS, 2004], for a PGA of 0.25 g and a shallow subsoil. The reinforcement details of the frames can be found in Gentile et al. [2021].

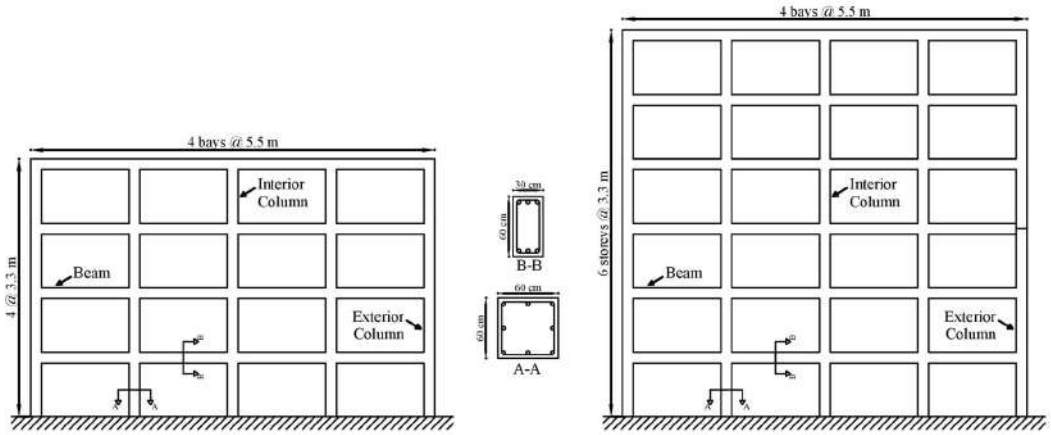


Figure 1. Geometrical configurations of both archetype frames.

The RC archetype frames were modelled using the structural analyses program Ruaumoko [Carr, 2016]. The moment-curvature relationships of the beams and columns were obtained using standard practice. The flange effect of the floor slabs on the negative moment capacity of the beams was accounted for by increasing their moment capacity by 30%. The ends of the base columns at the foundation were modelled as fixed. P-delta effects were neglected. The floor slabs were modelled as rigid diaphragms. The non-linear behaviour of the beams and columns was modelled using a lumped plasticity approach relying on the mono-dimensional Giberson elements. The hysteretic moment curvature response of beams and columns is modelled using the Takeda fat hysteresis model available in Ruaumoko. Rigid elements are used to model the beam and column ends framing into the beam-column joints, which are connected to lumped rotational springs that are used to model the non-linear behaviour of the beam-column joints. The fundamental periods of the two archetypes are 0.49 s and 0.74 s.

The RC archetype frames were analysed under the FEMA P695 far-field set [ATC, 2009]. This set consists of 22 ground motion pairs with a total of 44 individual horizontal ground motion records. The 44 individual horizontal ground motion records of the FEMA P695 set are scaled to three levels of seismic intensity. As such, each record is scaled so that the spectral acceleration at the fundamental period of each archetype frame, $S_a(T_1)$ matches a given multiple of the acceleration causing yielding of the supporting structure, S_{ay}, (commonly referred to as the seismic coefficient). These multiples are 0.75, 1.50, and 4.00, to capture a representative range of structural responses.

3. SUMMARY OF ESTIMATION PROCEDURE BY MERINO *ET AL.*

The proposed simplifications presented in this paper are focused on the methodology proposed by Merino et al. [2020] and extended by Merino et al. [2024]. The basic steps of the methodology are presented below.

1) Perform a modal analysis of the supporting structure to obtain the first four or five lateral modes of vibration of the supporting structure, including the modal periods, T_i, and mode shapes, $\phi_{i,j}$, where i is the mode number and j is the storey number. 2) Using the results of the modal analysis, along with a ground response spectrum compute the modal contributions to the peak floor acceleration, $a_{i,j}$, and peak floor relative displacement, $\Delta_{Ri,j}$, with Equations (1) and (2) respectively:

$$a_{i,j} = \Gamma_i \, \phi_{i,j} \, S_A\left(T_i, \xi_p\right) \tag{1}$$

$$\Delta_{R,i,j} = \Gamma_i \, \phi_{i,j} \, S_D\left(T_i, \xi_p\right) \tag{2}$$

where Γ_i is the modal participation factor for mode i, and S_A and S_D are the ground spectral ordinates evaluated at the i^{th} modal period of the supporting structure and for a supporting structure with a damping ratio equal to ξ_p. 3) Using the force-displacement curve of the supporting structure, verify if the supporting structure yields under the previously specified ground response spectrum. If the supporting structure is verified to yield at the specified seismic intensity, then, perform a non-linear static demand analysis such as the N2 method [Fajfar, 2000] or the capacity spectrum method, [Priestley et al., 2007], and compute the contributions to the peak floor acceleration, $a_{1,j}$, and peak floor relative displacement, $\Delta_{R1,j}$ of the fundamental mode of the supporting structure using Equations (3) and (4) respectively:

$$a_{1,j} = \Gamma_{\delta,1} \;\; \delta_j \, S_{ay} \tag{3}$$

$$\Delta_{R,1,j} = \Gamma_{\delta,1} \;\; \delta_j \, \Delta_d \tag{4}$$

where δ_j is the value of the first non-linear mode shape at floor j, $\Gamma_{\delta,1}$ is the modal participation factor related to the first non-linear mode shape, and Δ_d is the equivalent single-degree-of-freedom (SDOF) displacement demand of the supporting structure obtained through the application of the non-linear static procedure. 4) Estimate the dynamic amplification factor (DAF_i) for each of the modes i of the supporting structure. This can be done following the equations proposed by [Vukobratović & Fajfar, 2017]:

$$DAF_i = 2.5\sqrt{\frac{0.1}{(0.05+\xi_a)}} \quad \text{for } \frac{T_i}{T_C}=0 \tag{5}$$

$$DAF_i = \text{linear between } DAF_i\left(\frac{T_i}{T_C}=0\right) \text{ and } DAF_i\left(\frac{T_i}{T_C}>0.2\right) \quad \text{for } 0\leq\frac{T_i}{T_C}\leq 0.2 \tag{6}$$

$$DAF_i = \frac{1}{\sqrt{\xi_a}} \quad \text{for } \frac{T_i}{T_C}>0.2 \tag{7}$$

where T_C is the period marking the end of peak spectral acceleration plateau of the design ground acceleration spectrum. 5) Using the values of DAF_i computed in the previous step, estimate the peak floor spectral accelerations, $S_{AF,maxi,j}$, at each mode i at floor j with Equation (8):

$$S_{AF,max,i,j} = DAF_i \, a_{i,j} \tag{8}$$

$S_{DF,maxi,j}$ can be obtained by applying the pseudo-spectral relationship to the value of $S_{AF,maxi,j}$. 6) Estimate the effective periods, $T_{e,i}$, of the *i* modes of the supporting structure using the Equation (9) developed by Akiyama, [1985]:

$$T_{e,i} = T_i \sqrt{\frac{1+\sqrt{\mu}+\mu}{3}} \quad \text{for } i \leq 2 \tag{9}$$

where μ is the ductility demand in the supporting structure. For simplicity and to ease the application of the equations to estimate the modal contributions to the floor spectrum shown later, it is assumed that for values of i greater than 2 and when the supporting structure is elastic for all values of i, the value of $T_{e,i}$ is taken equal to T_i. 7) Using the values of $S_{AF,max1,j}$ and $T_{e,1}$ for the fundamental mode, compute the peak floor spectral relative displacement, $S_{DF,max1,j}$, and compare it to the peak ground spectral displacement, $S_{D,max}$, taken directly from the design ground response spectrum. If $S_{D,max} < S_{DF,maxi,j}$, then the movement of the supporting structure relative to the foundation dominates the spectral ordinates in the long-period range and, therefore, estimate the peak floor absolute displacement, $\Delta_{ab,i,j}$, using:

$$\Delta_{ab,1,j} = \sqrt{\Delta_{R,1,j}{}^2 + PGD^2} \tag{10}$$

$$\Delta_{ab,i,j} = \Delta_{R,i,j} \qquad \text{for } i>1 \tag{11}$$

where PGD is the peak ground displacement estimated as the ground spectral displacement ordinate at 10 s. Otherwise, if $S_{D,max} > S_{DF,maxi,j}$, then the ground motion dominates the floor spectral ordinate in the long-period range and special considerations are required for estimating the contribution of the fundamental mode of the supporting structure to the FRS, as shown in step 8. 8) Estimate the modal contributions to the total relative displacement FRS. For the cases of i = 1 and $S_{D,max} < S_{DF,maxi,j}$, or i >1 for $S_{D,max} < S_{DF,maxi,j}$ and $S_{D,max} > S_{DF,maxi,j}$, use the following equations:

$$S_{DF,i,j}(T_a) = \frac{1}{4\pi^2}\left(\frac{T_a^2}{T_i}\right)^2 \left(S_{AF,max,i,j} - a_{i,j}\right) + \frac{T_a^2}{4\pi^2} a_{i,j} \qquad \text{if } T_a \le T_i \tag{12}$$

$$S_{DF,i,j}(T_a) = \frac{T_a^2}{4\pi^2} S_{AF,max,i,j} \qquad \text{if } T_i < T_a \le T_{e,i} \tag{13}$$

$$S_{DF,i,j}(T_a) = \Delta_{R,i,j} + \left(\frac{T_{e,i}}{T_a}\right)\left(S_{DF,max,i,j} - \Delta_{R,i,j}\right) \qquad \text{if } T_a > T_{e,i} \tag{14}$$

For the special case that i = 1 and $S_{D,max} > S_{DF,maxi,j}$, use the following equations instead:

$$S_{DF,1,j}(T_a) = \frac{1}{4\pi^2}\left(\frac{T_a^2}{T_1}\right)^2 \left(S_{AF,max,1,j} - a_{1,j}\right) + \frac{T_a^2}{4\pi^2} a_{1,j} \qquad \text{if } T_a \le T_1 \tag{15}$$

$$S_{DF,1,j}(T_a) = \frac{T_a^2}{4\pi^2} S_{AF,max,1,j} \qquad \text{if } T_1 < T_a \le T_{e,1} \tag{16}$$

$$S_{DF,1,j}(T_a) = \Delta_{R,1,j} + \left(\frac{T_{e,1}}{T_a}\right)\left(S_{DF,max,1,j} - \Delta_{R,1,j}\right) \qquad \text{if } T_a > T_{e,1} \text{ and } \mu \le 1 \tag{17}$$

$$S_{DF,1,j}(T_a) = S_{DFmax\,1,j} + \frac{\left(S_{D,max} - S_{DFmax\,1,j}\right)}{\left(T_{e,1} - T_D\right)}\left(T_a - T_{e,1}\right) \qquad \text{if } T_{e,1} < T_a < T_D \text{ and } \mu > 1 \tag{18}$$

$$S_{DF,1,j}(T_a) = S_{D,max} \qquad \text{if } T_a > T_D \text{ and } \mu > 1 \tag{19}$$

where T_D is the period marking the beginning of the constant displacement plateau in the design ground response spectrum. The absolute acceleration FRS can be estimated with the estimate of the relative displacement FRS and Equation 20.

$$S_{AF} = \frac{4\pi^2}{T_a^2} S_{DF} \tag{20}$$

9) The modal contributions are then combined through SRSS and enveloped with the design ground response spectrum for floors in the lower half of the supporting structure and for non-structural periods longer than $T_{e,1}$ to account for the influence of the rigid motion of the supporting structure on the FRS.

4. PROPOSED SIMPLIFICATIONS

The proposed procedure to estimate FRS requires as input the mass distribution up the height of the supporting structure, a ground response spectrum, and the bilinear force-displacement curve of an equivalent SDOF system representing the supporting structure. The main required parameters of this curve are the yield displacement, Δ_y, and the yielding acceleration (or seismic coefficient), S_{ay}. Both parameters are readily available from the seismic design of the supporting structure [Gentile & Calvi, 2023; Priestley et al., 2007]. In alternative, these parameters can be estimated using the simple lateral mechanicm analysis (SLaMA) [Gentile et al. 2021].

4.1 ESTIMATION OF MODAL PERIODS OF THE SUPPORTING STRUCTURE

The fundamental period of a RC frame structure could be directly estimated from the force-displacement curve of the equivalent SDOF system using Equation (21).

$$T_y = 2\pi \sqrt{\frac{\Delta_y}{S_{ay} g}} \tag{21}$$

Where Δ_y is the yield displacement of the bilinear approximation to the force-displacement curve of the equivalent SDOF system, S_{ay} is the yielding acceleration in units of gravity, and g is the acceleration of gravity. T_y is the period of the equivalent SDOF system. However, analysis of the two archetype frames of Section 2, where the values from Equation (21) were compared with the values of fundamental period obtained from modal analyses, revealed that the following relationship can better capture the location of the fundamental period, T_1, for FRS estimation:

$$T_1 = 0.84\, T_y \tag{22}$$

This relationship between T_y and T_1 accounts for the period elongation of the supporting structure in the elastic range because of cracking in tension of the concrete sections. In the elastic range of response, the fundamental period of the supporting structure transitions from T_1 (uncracked section stiffnesses) to T_y (secant-to-yielding stiffness), as the seismic intensity increases. Even though Equation (22) is used to find the location of the peak related to the fundamental mode in the FRS, T_y needs to be used for the response spectrum and the non-linear static analyses as per usual practice [Fajfar, 2000].

It is difficult to estimate the higher mode periods of the supporting structure exactly without performing a modal analysis. However, the ranges of periods on which the higher mode periods of the supporting structure are likely to be can be estimated using the results presented by Miranda & Reyes [2002]. These ranges are expressed with the ratio between the higher mode period to the fundamental mode period, T_i/T_1, where i is the mode number. Accoring to Miranda & Reyes [2002] the second mode period is between 1/4 and 1/3, the third mode period is between 1/7 and 1/5, and the fourth mode period is between 1/9 and 1/7. It is proposed here that these ranges can define constant acceleration plateaus in the absolute acceleration FRS. The response spectrum analysis is conservatively performed with the lower bounds of these ranges.

4.2 ESTIMATION OF MODE SHAPES OF THE SUPPORTING STRUCTURE

Like the periods of the supporting structure, the mode shapes of the supporting structure can also be estimated for FRS estimation without performing modal analysis. Gentile et al. [2021] proposed Equation (23) to estimate the non-linear mode shape, δ, of RC frame supporting structures for frames with more than two storeys.

$$\delta_j = \frac{4}{3}\left(\frac{H_j}{H_n}\right)\left(1 - \frac{H_j}{4H_n}\right) \tag{23}$$

where δ_j is the value of the non-linear displaced shape at storey j, H_j is the height of storey j above the foundation, and H_n is the total height of the building structure. Figure 2a presents the comparison between the mode shapes obtained from modal analyses of the two archetype RC frames and Equation (23). A good match can be observed between the results from modal analyses and Equation 23. Equation (23) is therefore recommended for estimation of FRS.

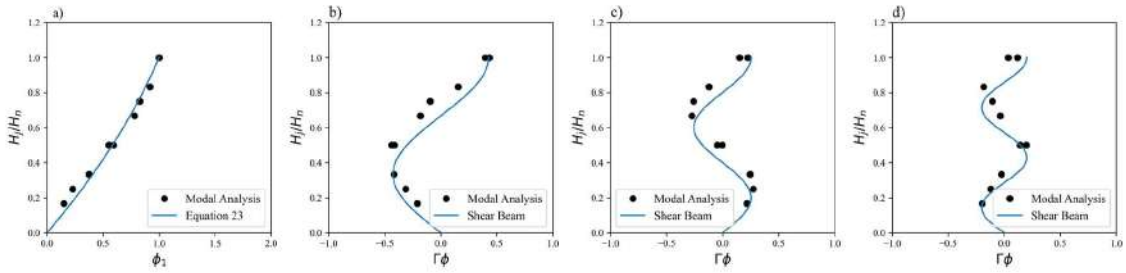


Figure 2 Comparison of results from modal analyses with proposed closed-form equations: a) first mode; b) second mode; c) third mode; and d) fourth mode.

It is proposed here that the product of the participation factor, Γ, and the corresponding higher mode shapes, ϕ, for RC frames can be estimated using the closed-form solutions for the mode shapes of a continuous cantilever Timoshenko shear beam [Wiebe & Christopoulos, 2015] for FRS estimation:

$$\Gamma_i \phi_i(z) = \Gamma_i \sin(\beta_i z) \tag{28}$$

Where $z = H_j/H_n$, and Γ_i and β_i are taken from the vectors: Γ_i = [0.426, 0.254, 0.202] and β_i = [4.71, 7.85, 10.99], where each entry corresponds to the second, third, and fourth modes respectively. Figure 2 b, c, and d show the comparisons between Equation (28) and the results from modal analyses for the two archetype RC frames. A close match is observed between the two quantities from Figure 2 b, c, and d. Equation (28) is recomeded for estimation of FRS.

4.3 QUANTIFICATION OF ERROR BETWEEN NUMERICAL AND BILINEAR FORCE-DISPLACEMENT CURVES

Figure 3a presents the numerical force-displacement curve of the 4-storey archetype RC frame obtained from numerical pushover analysis. The bilinear approximation of the force-displacement curve, obtained using the software SLaMA [Gentile et al., 2021], is also presented in Figure 3a. The bilinear curve gives higher values of force for the same value of displacement than the numerical curve around the yield point of the supporting structure. This error affects the estimates of the first mode contribution to FRS.

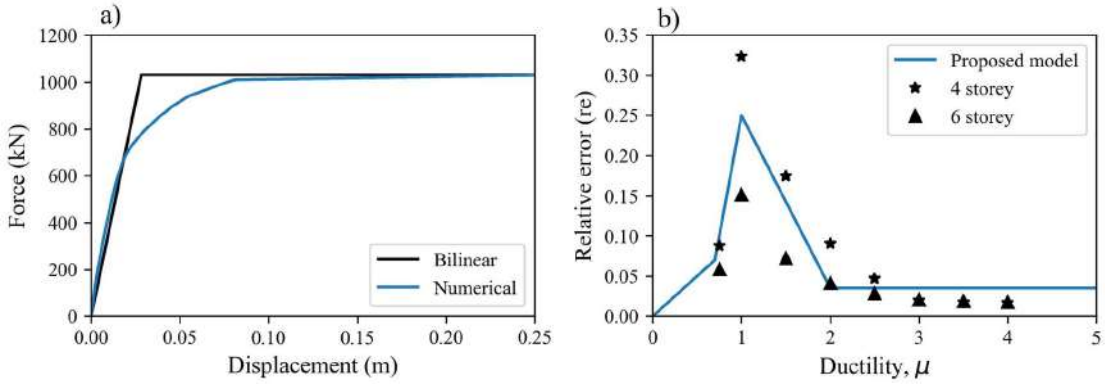


Figure 3. a) Bilinear and numerical force-displacement curves of the 4-storey RC archetype frame; b) variation of relative error between bilinear and numerical force-displacement curves for both archetype frames.

The relative errors, re, between the numerical and bilinear force-displacement curves for the two archetype RC frames were calculated. The relative errors, re, were computed for ductility values of 0.75, 1.00, 1.50, 2.00, 2.50, 3.00, 3.50, and 4.00, and are shown in Figure 3b. A simplified model is fitted to the error data in Figure 3b to account for this error in FRS estimation. The average values of the values of re ate ductility levels of 0.75, 1.00, and greater than 2.00 were calculated from both archetypes. A piecewise linear model was fitted to the data using these average values. The model increases linearly from 0 to 0.075 for ductility ratios from 0 to 0.75. Then, the model increases linearly from 0.075 to 0.25 for ductility ratios from 0.75 to 1.00. Next, the model decreases linearly from 0.25 to 0.03 for ductility ratios between 1.00 and 2.00. Finally, the model is constant at 0.03 for values of ductility greater than 2.00. This model is used to correct the values of $S_A(T_1,\xi_p)$ and S_{ay} in Equations (1) and (3) respectively when estimating FRS.

5. BENCHMARKING WITH NLTH ANALYSES

This section shows the benchmarking of the proposed methodology with NLTH analyses of the two archetype RC frames presented in Section 2. The comparisons are made for the top storey of both archetypes and for a 5.00% non-structural damping ratio, ξ_a, considering only the median from NLTH analyses from the 44 ground motions used to analyse the archetypes. The comparisons are also made for the three seismic intensities presented in Section 2, which are 0.75, 1.50, and 4.00 times the value of S_{ay} of each supporting structure. Figure 4 presents the comparisons between the absolute acceleration and relative displacement FRS for the 4-storey archetype RC frame, while Figure 5 shows the same comparisons for the 6-storey archetype RC frame.

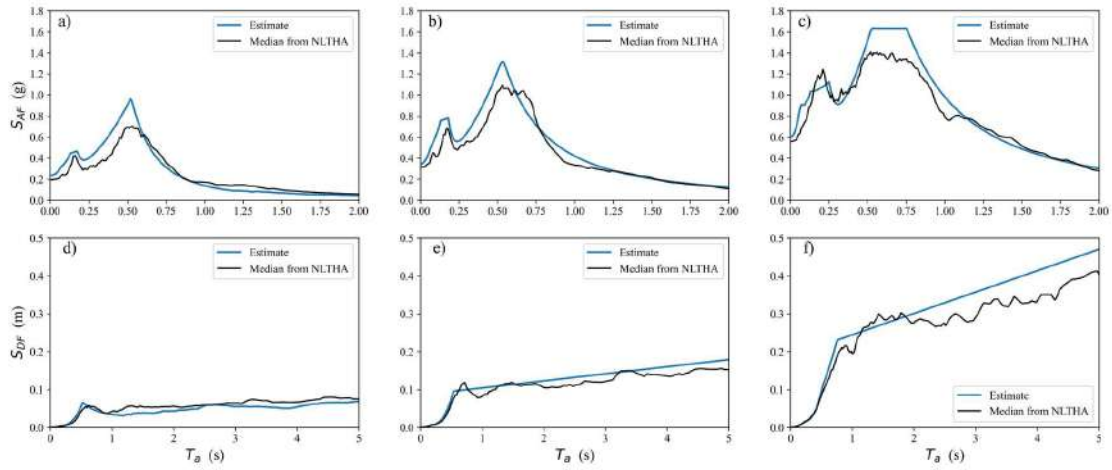


Figure 4. Comparisons of the FRS obtained from NLTH analyses and the predictions of the proposed methodology for the 4-storey archetype RC frame: a) absolute acceleration FRS for 0.75 S_{ay}; b) absolute acceleration FRS for 1.50 S_{ay}; c) absolute acceleration FRS for 4.00 S_{ay}; d) relative displacement FRS for 0.75 S_{ay}; e) relative displacement FRS for 1.50 S_{ay}; f) relative displacement FRS for 4.00 S_{ay}.

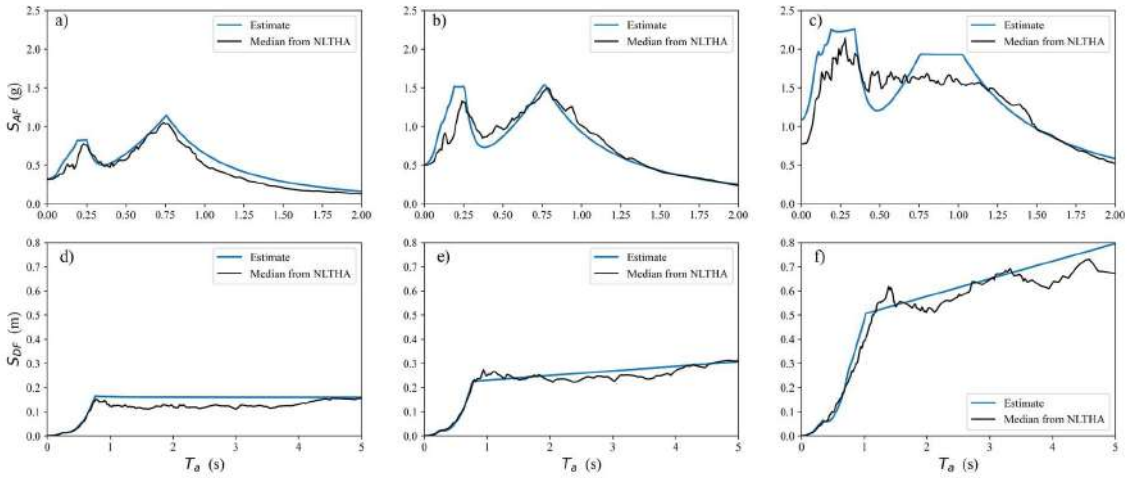


Figure 5. Comparisons of the FRS obtained from NLTH analyses and the predictions of the proposed methodology for the 6-storey archetype RC frame: a) absolute acceleration FRS for 0.75 S_{ay}; b) absolute acceleration FRS for 1.50 S_{ay}; c) absolute acceleration FRS for 4.00 S_{ay}; d) relative displacement FRS for 0.75 S_{ay}; e) relative displacement FRS for 1.50 S_{ay}; f) relative displacement FRS for 4.00 S_{ay}.

Figure 4 and Figure 5 show a general good agreement between the median FRS from NLTH analyses and the predictions from the proposed methodology. The location and amplitude of the peak of the FRS related to the fundamental mode of the supporting structure are well captured by the proposed procedure. The mean relative errors for the region $0.5T_1 – 1.5T_1$ are all approximately 10% except for the 4-storey frame at $0.75S_{ay,}$ which is 28%, although this error is conservative. The locations and amplitudes of the peaks of the FRS related to the higher mode periods of the supporting structure are conservatively captured using the plateaus proposed in Section 4.1 with mean relative errors for the period range 0 - $0.5T_1$ being between 8% and 30%, with the excessive errors of 30% being on the conservative side. In general, all the higher mode peaks tend to fall within the proposed limits. To quantify the error between the median from NLTH analyses and the predictions from the proposed methodology for the entire period range, the mean relative errors between the two curves were calculated for a non-structural period range between 0 s and 5 s. These errors are approximately between 19% and 22% for the seismic intensity of 0.75 S_{ay} for both frames and for both absolute acceleration and relative displacement FRS. For the other two seismic intensities, where the supporting structure responds in the non-linear range, the errors are approximately 10% for both frames and for both absolute accelerations and relative displacement FRS. These values confirm that the proposed methodology can give relatively accurate predictions of FRS for a wide range of seismic intensities. However, the procedure is more accurate in the non-linear range than in the linear elastic range. This difference is because of the error between the numerical and bilinear force-displacement curves of the supporting structure presented in Section 4.3. Even though the relative error model presented in Section 4.3 helps in reducing the errors between the predictions of the proposed model and the results from NLTH analyses, it cannot fully eliminate this error, causing the proposed procedure to give slightly conservative FRS estimates in the elastic range.

6. CONCLUSIONS

This paper proposed a simplified methodology to estimate floor response spectra in reinforced concrete frames without the need of numerical analyses of the supporting structure as preparatory steps. Especifically, the proposed methodology relies on the estimation of the fundamental period of the supporting structure using a bilinear force-displacement curve of an equivalent single-degree-of-freedom system representing the

supporting structure. The fundamental mode shape of the supporting structure is estimated using a closed-form equation to estimate the non-linear shape of the supporting structure. Constant absolute acceleration plateaus are proposed to account for the locations of floor spectral peaks related to higher modes in floor response spectra estimation. Finally, the higher mode shapes are estimated using the closed-form solutions to the differential equations of a cantilever shear beam. The proposed procedure was benchmarked against the results from non-linear time history analyses of two reinforced concrete frame archetypes. A general good agreement was found between the floor spectral estimates of the proposed procedure with the median from non-linear time history analyses. Mean relative errors of 20% and 10% were found for the elastic and non-linear ranges respectively. The proposed methodology to estimate floor response spectra requires further verifications with more archetype frames. The proposed methodology should also be extended to reinforced concrete wall buildings and steel frames. Many of the simplifications proposed in this paper could also be extended to other existing methodologies to estimate floor response spectra, if validations with non-linear time history analyses are performed. Finally, the simplicity and low computational cost of the proposed procedure make it ideal for risk-targeted seismic design procedures for non-structural elements, where critical non-structural elements could be designed in parallel to the supporting structure. Future research is needed in this topic.

ACKNOWLEDGEMENTS

This work was funded by UK Research and Innovation (UKRI) under the UK government's Horizon Europe funding guarantee, grant agreement No. EP/Z002842/1 (UKRI Postdoctoral Fellowships Guarantee, HORIZON-MSCA-2023-PF-01: Improving Seismic resilience of Critical Facilities by Enhanced Assessment of Non-structural Elements - ISCREANE) for Roberto J. Merino.

REFERENCES

Akiyama, H. [1985]. *Earthquake-resistant Limit-state Design for Buildings*.

ATC. [2009]. *Quantification of Building Seismic Performance Factors. FEMA P695*.

Carr, A. J. [2016]. *Ruaumoko Manual: User Manual for the 2:Dimensional Version, Ruaumoko 2D* (Vol. 2). University of Canterbury.

Degli Abbati, S., Cattari, S., & Lagomarsino, S. [2018]. Theoretically-based and practice-oriented formulations for the floor spectra evaluation. *Earthquake and Structures*, *15*(5), 565–581. https://doi.org/10.12989/eas.2018.15.5.565

Fajfar, P. [2000]. A Nonlinear Analysis Method for Performance Based Seismic Design. *Earthquake Spectra*, *16*(3), 573–592.

Filiatrault, A., Perrone, D., Merino, R. J., & Calvi, G. M. [2021]. Performance-Based Seismic Design of Nonstructural Building Elements. *Journal of Earthquake Engineering*, *25*(2), 237–269. https://doi.org/10.1080/13632469.2018.1512910

Gentile, R., & Calvi, G. M. [2023]. Direct loss-based seismic design of reinforced concrete frame and wall structures. *Earthquake Engineering and Structural Dynamics*, *52*(14), 4395–4415. https://doi.org/10.1002/eqe.3955

Gentile, R., del Vecchio, C., Pampanin, S., Raffaele, D., & Uva, G. [2021]. Refinement and Validation of the Simple Lateral Mechanism Analysis (SLaMA) Procedure for RC Frames. *Journal of Earthquake Engineering*, *25*(7), 1227–1255. https://doi.org/10.1080/13632469.2018.1560377

Haymes, K., Sullivan, T. J., & Chandramohan, R. [2020]. A PRACTICE-ORIENTED METHOD FOR ESTIMATING ELASTIC FLOOR RESPONSE SPECTRA. *Bulletin of the New Zealand Society for Earthquake Engineering*, *53*(3).

Merino, R. J., Mucedero, G., Perrone, D., Monteiro, R., Aiello, M. A., & Nascimbene, R. [2024]. Estimation of consistent absolute acceleration and relative displacement floor response spectra in existing masonry-infilled reinforced concrete buildings. *Bulletin of Earthquake Engineering*, *22*(10), 5083–5118. https://doi.org/10.1007/s10518-024-01961-6

Merino, R. J., Perrone, D., & Filiatrault, A. [2020]. Consistent floor response spectra for performance-based seismic design of nonstructural elements. *Earthquake Engineering and Structural Dynamics*, *49*(3), 261–284. https://doi.org/10.1002/eqe.3236

Miranda, E., Mosqueda, G., Retamales, R., & Pekcan, G. [2012]. Performance of nonstructural components during the 27 February 2010 Chile earthquake. *Earthquake Spectra*, *28*(SUPPL.1). https://doi.org/10.1193/1.4000032

Miranda, E., & Reyes, C. J. [2002]. Approximate Lateral Drift Demands in Multistory Buildings with Nonuniform Stiffness. *Journal of Structural Engineering*, *128*(7), 840–849. https://doi.org/10.1061/[ASCE)0733-9445(2002)128:7(840)

NTC. [2018]. Aggiornamento delle Norme tecniche per le costruzioni. In *Ministero delle Infrastrutture e dei Trasporti*.

NZS. [2004]. *NZS1170.5. Structural Design Actions*.

O'Reilly, G. J., & Calvi, G. M. [2019]. Conceptual seismic design in performance-based earthquake engineering. *Earthquake Engineering and Structural Dynamics*, *48*(4), 389–411. https://doi.org/10.1002/eqe.3141

Perrone, D., Calvi, P. M., Nascimbene, R., Fischer, E. C., & Magliulo, G. [2019]. Seismic performance of non-structural elements during the 2016 Central Italy earthquake. *Bulletin of Earthquake Engineering*, *17*(10), 5655–5677. https://doi.org/10.1007/s10518-018-0361-5

Petrone, C., Magliulo, G., & Manfredi, G. [2015]. Seismic demand on light acceleration-sensitive nonstructural components in European reinforced concrete buildings. *Earthquake Engineering and Structural Dynamics*, *44*(8), 1203–1217. https://doi.org/10.1002/eqe.2508

Priestley, M. J. N., Calvi, G. M., & Kowalsky, M. J. [2007]. *Displacement-Based Seismic Design of Structures*. IUSS Press.

Qu, Z., Wang, F., Chen, X., Wang, X., & Zhou, Z. [2023]. Rapid report of seismic damage to hospitals in the 2023 Turkey earthquake sequences. *Earthquake Research Advances*, *3*(4). https://doi.org/10.1016/j.eqrea.2023.100234

Rodriguez, D., Perrone, D., & Filiatrault, A. [2023]. Seismic demand on non-structural elements for quantifying seismic performance factors. *Earthquake Engineering and Structural Dynamics*, *52*(4), 1016–1039. https://doi.org/10.1002/eqe.3799

Vukobratović, V., & Fajfar, P. [2017]. Code-oriented floor acceleration spectra for building structures. *Bulletin of Earthquake Engineering*, *15*(7), 3013–3026. https://doi.org/10.1007/s10518-016-0076-4

Wiebe, L., & Christopoulos, C. [2015]. A cantilever beam analogy for quantifying higher mode effects in multistorey buildings. *Earthquake Engineering and Structural Dynamics* , *44*(11), 1697–1716. https://doi.org/10.1002/eqe.254

Evaluation of component amplification factor considering structure-NSC interaction and NSC-clustering

Chang-Jun Bae[1], Cheol-Ho Lee[2], and Su-Chan Jun[3*]

[1] School of Architecture & Architectural Engineering, Hanyang University ERICA
Ansan-si, Gyeonggi-do 15588, Republic of Korea
e-mail: changjun0125@hanyang.ac.kr
[2] Dept. of Architecture and Architectural Engineering, Seoul National University
Seoul 08826, Republic of Korea
e-mail: ceholee@snu.ac.kr
[3] Dept. of Architectural Engineering, Dankook University
Gyeonggi-do, 16890, Republic of Korea
e-mail: scjun@dankook.ac.kr (corresponding author)

Abstract. This study analyzed the seismic demand on nonstructural components (NSCs) using structural–nonstructural coupled systems to incorporate coupling effects arising from the dynamic interaction between the supporting structure and NSCs. In the first part, a two-degree-of-freedom (2-DOF) coupled system was analyzed, and it was observed that peak component acceleration (PCA) and component amplification factors (C_{AR}) are significantly reduced due to coupling effects, particularly when resonance occurs between the structure and the NSC. These effects were found to be most sensitive to the NSC-to-structure mass ratio. Notably, as the mass ratio increases, the influence of component damping ratio on C_{AR} diminishes, and the values tend to converge for each ductility level. Based on these results, a more rational C_{AR} factor was proposed for moderate- to heavy-weight NSCs compared to the ASCE 7-22 provisions. The study was further extended to a coupled (N+1)-DOF system to evaluate the clustering effects of multiple NSCs. Numerical simulations revealed that the degree of structure–NSC coupling experienced by each component varies depending on the period differences within the cluster. To quantify the coupling effect of individual NSCs within a cluster, an equivalent coupling mass was introduced, which accounts for the relative period ratios among clustered NSCs.

Keywords: Component amplification factor, Structure-NSC coupling effect, NSC-to-structure mass ratio, NSC-clustering.

1. INTRODUCTION

Recent earthquake events have revealed significant damage to nonstructural components (NSCs), underscoring the importance of their seismic design [Perrone *et al.*, 2019]. However, excessive conservatism in design can lead to unnecessary cost and inefficiency. To achieve a more practical design, it is essential to understand the dynamic behavior of NSCs. This study investigates the seismic demand on acceleration-sensitive components.

NSCs are known to experience seismic forces much greater than the ground motion due to successive amplification processes [Bachman *et al.*, 2004; NIST, 2018]. The ground motion at the surface, represented by the peak ground acceleration (PGA), is amplified to the peak floor acceleration (PFA) through the dynamic characteristics of the supporting structure—its period, damping, and nonlinearity—known as in-structure amplification. The dynamic behavior of the components further amplifies the motion from PFA to peak component acceleration (PCA), referred to as component amplification, with the largest amplification occurring when the component and structural frequencies are closely tuned.

Extensive studies have examined the relationships among PGA, PFA, and PCA using the floor response spectrum (FRS) method [Sankaranarayanan and Medina, 2007; Anajafi *et al.*, 2020] and recorded acceleration histories from instrumented buildings [Anajafi and Medina, 2019; Magliulo and D'Angela, 2024]. Among these, the FRS method is widely regarded as the most practical tool, as it captures key factors influencing the amplification process using reliable floor acceleration histories obtained from analyses, tests, or measurements. Building on this approach, several studies [Petrone *et al.*, 2015; Abbati *et al.*, 2018; Zito *et al.*, 2023; Vukobratović and Fajfar, 2024] have proposed simplified equations to estimate the seismic demands of acceleration-sensitive components and to refine code provisions.

However, the FRS method treats the structure and NSCs separately and therefore does not account for their coupled behavior. Although the coupling effect is negligible for components with very small mass ratios ($m_{nsc}/m_s < 0.1\%$) [Singh and Suarez, 1987], it should be considered since major design codes, such as ASCE 7-22 [ASCE, 2021], allow NSCs to have masses up to 25% of the supporting structure. Hadjian and Ellison [1986] reported that, even within this limit, the response error between coupled and decoupled systems can reach 100%, indicating excessive conservatism. Moreover, as illustrated in Figure 1, acceleration-sensitive components are often densely clustered, which can further amplify coupling with the supporting structure. Therefore, incorporating the coupling effect is essential for more accurate and rational estimation of seismic demands on NSCs.



Figure 1. Clustered NSC scenario in telecommunication buildings

This study investigates the seismic demand on NSCs using structural–nonstructural coupled models that account for dynamic interaction effects. First, a two-degree-of-freedom (2-DOF) model, in which both the supporting structure and the NSC are represented as single-degree-of-freedom systems, is analyzed to

examine the influence of structure–NSC coupling on PCA and the component amplification factor. The analysis is then extended to a coupled (N+1)-DOF model to evaluate the clustering effects of multiple NSCs. Based on these findings, a more rational component amplification factor explicitly incorporating the structure–NSC coupling effect and a refined method for considering NSC clustering are proposed.

2. SEISMIC DEMANDS FOR ACCELERATION-SENSITIVE NONSTRUCTURAL COMPONENTS

Seismic design codes such as ASCE 7-22 and Eurocode 8 [Cen, 2004] provide equations for estimating seismic forces on NSCs, reflecting the successive amplification from PGA to PFA and PCA. Although their formulations differ, two factors are consistently emphasized: the in-structure amplification factor and the component amplification factor. This section briefly summarizes the equivalent static seismic design force for NSCs in ASCE 7-22, applicable when the NSC-to-structure mass ratio is less than 25%. The horizontal seismic design force (F_p) is given by Eq. (1):

$$F_p = 0.4 S_{DS} I_p W_p \left[\frac{H_f}{R_\mu} \right] \left[\frac{C_{AR}}{R_{po}} \right] \tag{1}$$

where S_{DS} = short period spectral acceleration, W_p = component operating weight, I_p = component importance factor, H_f = factor for force amplification as a function of height in the structure, R_μ = structure ductility reduction factor, C_{AR} = component resonance ductility factor, and R_{po} = component strength factor. Rearranging Eq. (1) clarifies the relationship among PGA, PFA, and PCA, as shown in Eq. (2):

$$\begin{aligned} F_p &= \text{PCA} \times W_p I_p \\ &= \text{PGA} \times \frac{\text{PFA}}{\text{PGA}} \times \frac{\text{PCA}}{\text{PFA}} \times W_p I_p \\ &= 0.4 S_{DS} \times \frac{H_f}{R_\mu} \times \frac{C_{AR}}{R_{po}} \times W_p I_p \end{aligned} \tag{2}$$

The base acceleration ($0.4S_{DS}$) represents the design ground acceleration, while in-structure amplification (PFA/PGA) is expressed as H_f/R_μ, with H_f increasing PFA with height and R_μ reducing it due to inelastic behavior. Since this study does not focus on in-structure amplification, formulas for H_f and R_μ are omitted.

Amplification from PFA to PCA is represented by C_{AR}, which accounts for tuning with the structure and reductions from NSC nonlinearity. As shown in Table 1, ASCE 7-22 specifies C_{AR} = 4.0 for elastic components, decreasing with higher ductility. These values apply to components with period ratios between 0.5 and 1.5, while C_{AR} = 1.0 is used outside this range, as noted in the ASCE 7-22 Commentary. When the period ratio is unknown, C_{AR} values for various component types can be taken from Tables 13.5-1 and 13.6-1 of ASCE 7-22. The component strength factor (R_{po}) serves as an overstrength factor and reduces the design force and is also listed in Tables 13.5-1 and 13.6-1. This study modeled NSCs as elasto-perfectly-plastic systems (see Chapter 3); thus, R_{po} was set to 1.0 and omitted.

Table 1. Component ductility categories and corresponding C_{AR} factors in ASCE 7-22

Ductility category	Assumed component ductility	C_{AR} (=PCA/PFA)
Elastic	1.00	4.0
Low	1.25	2.8
Modertate	1.50	2.2
High	≥ 2.00	1.4

Many studies have proposed refined component amplification factors considering key parameters such as tuning with the supporting structure. Singh *et al.* [2006] and Calvi and Sullivan [2014] derived improved formulations using the floor response spectrum method based on numerically obtained floor accelerations, while Fathali and Lizundia [2011] and Kazantzi et al. [2020] evaluated actual amplification using recorded floor acceleration data from instrumented buildings. Based on these studies, the ATC-120 project [NIST, 2018] proposed ductility-dependent amplification factors, which form the basis of the C_{AR} in ASCE 7-22.

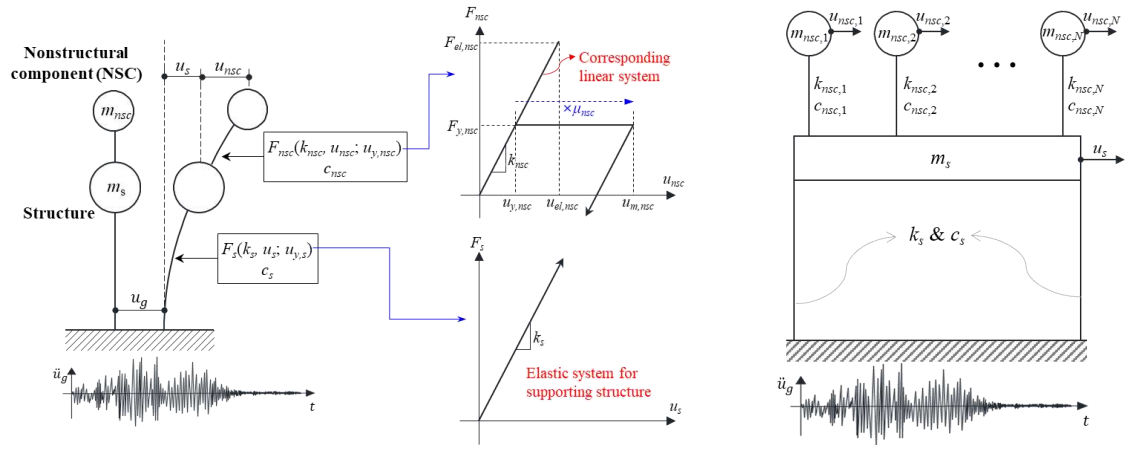
Despite these advances, two main limitations remain: (1) most numerical studies neglect structural–nonstructural interaction by generating floor motions without internal NSCs; and (2) due to the lack of sufficient information on instrumented buildings, studies using recorded data—including those underlying ASCE 7-22—cannot fully capture the effect of structure–NSC coupling. Therefore, this study performs linear and nonlinear time-history analyses on idealized structural–nonstructural coupled systems to explicitly consider coupling effects and the dynamic properties of the combined system.

3. GOVERNING PARAMETERS AND NUMERICAL ANALYSIS OF COUPLED STRUCTURE-NSC SYSTEMS

3.1 GOVERNING EQUATIONS FOR STRUCTURE-NSC COUPLED SYSTEMS

In this study, the coupling effects of the supporting structure–NSC system were analyzed using idealized two-degree-of-freedom (2-DOF) and (N+1)-DOF models (see Figure 2). In general, a combined structure–NSC system possesses a large number of degrees of freedom, making numerical integration computationally demanding, particularly when nonlinear behavior is considered. However, 2-DOF and (N+1)-DOF models, in which the supporting structure is idealized as a single-degree-of-freedom (SDOF) system, remain computationally efficient while capturing key dynamic characteristics, including nonlinearities, and are therefore well suited for investigating coupling effects.

This modeling approach does not capture variations in PGA-to-PFA amplification along the building height or higher-mode effects in actual buildings. However, since an SDOF system effectively represents the fundamental-mode response of a structure, it is sufficient for describing the primary acceleration amplification mechanisms. Therefore, although there remain a few limitations, the idealized coupled models provide a valid and efficient basis for analyzing the seismic demand on NSCs.



(a) 2-DOF coupled system (b) (N+1)-DOF coupled system

Figure 2. Schematics of idealized structural-nonstructural coupled systems in this study

The equation of motion (EOM) for the coupled 2-DOF system can be seen as follows:

$$\begin{cases} m_s\ddot{u}_s + c_s\dot{u}_s + F_s\left(u_s;k_s,u_{y,s}\right) - c_{nsc}\dot{u}_{nsc} - F_{nsc}\left(u_{nsc};k_{nsc},u_{y,nsc}\right) = -m_s\ddot{u}_g \\ m_{nsc}\left(\ddot{u}_s + \ddot{u}_{nsc}\right) + c_{nsc}\dot{u}_{nsc} + F_{nsc}\left(u_{nsc};k_{nsc},u_{y,nsc}\right) = -m_{nsc}\ddot{u}_g \end{cases} \tag{3}$$

where m_s, c_s, F_s, k_s = mass, damping coefficient, restoring force, and initial stiffness of the supporting structure; m_{nsc}, c_{nsc}, F_{nsc}, k_{nsc} = those of the NSC; u_s = displacement of the structure relative to the ground; u_{nsc} = displacement of the NSC relative to the structure; and $\ddot{u}_g$ = ground acceleration. Using the definitions of floor and component accelerations ($\ddot{u}_{floor}$, $\ddot{u}_{comp}$), Eq. (3) can be rewritten as:

$$\ddot{u}_{floor} = \ddot{u}_s + \ddot{u}_g, \qquad \ddot{u}_{comp} = \ddot{u}_{nsc} + \ddot{u}_s + \ddot{u}_g \tag{4}$$

$$\begin{cases} m_s\ddot{u}_s + c_s\dot{u}_s + F_s\left(u_s;k_s,u_{y,s}\right) = -m_s\left[\ddot{u}_g + \dfrac{m_{nsc}}{m_s}\ddot{u}_{comp}\right] \\ m_{nsc}\ddot{u}_{nsc} + c_{nsc}\dot{u}_{nsc} + F_{nsc}\left(u_{nsc};k_{nsc},u_{y,nsc}\right) = -m_{nsc}\ddot{u}_{floor} \end{cases} \tag{5}$$

When N NSCs are clustered on the same floor and the structure has a rigid diaphragm with little torsional irregularity, such that all NSCs experience identical floor acceleration ($\ddot{u}_{floor}$), the EOM of the coupled system can be formulated as Eq. (6), in the same manner as Eq. (5):

$$\begin{cases} m_s\ddot{u}_s + c_s\dot{u}_s + F_s\left(u_s;k_s,u_{y,s}\right) = -m_s\left[\ddot{u}_g + \dfrac{1}{m_s}\displaystyle\sum_{r=1}^{N} m_{nsc,r}\ddot{u}_{comp,r}\right] \\ m_{nsc,1}\ddot{u}_{nsc,1} + c_{nsc,1}\dot{u}_{nsc,1} + F_{nsc,1}\left(u_{nsc,1};k_{nsc,1},u_{y,nsc,1}\right) = -m_{nsc,1}\ddot{u}_{floor} \\ \vdots \\ m_{nsc,N}\ddot{u}_{nsc,N} + c_{nsc,N}\dot{u}_{nsc,N} + F_{nsc,N}\left(u_{nsc,N};k_{nsc,N},u_{y,nsc,N}\right) = -m_{nsc,N}\ddot{u}_{floor} \end{cases} \tag{6}$$

In the first equations of Eqs. (5) and (6), neglecting the term associated with the NSC response ($\ddot{u}_{comp}$) yields the conventional floor response spectrum (FRS) method, representing a decoupled system. That is, the coupled system includes the feedback from the NSC response ($\ddot{u}_{comp}$), which gives rise to the coupling effect. This effect becomes more pronounced as the NSC-to-structure mass ratio (m_{nsc}/m_s) increases, highlighting a key limitation of the FRS method, which is valid only when NSCs are much lighter than the structure.

Although individual NSCs are typically lightweight, making the FRS method applicable in most cases, they are often installed in clusters of similar equipment (Figure 1). In such configurations, the collective influence of multiple NSCs on the structure increases with their number, as described by Eq. (6). Therefore, even multiple medium- to lightweight NSCs on the same floor can produce noticeable coupling effects with the supporting structure.

Accordingly, this study first evaluates the influence of single NSC–structure coupling on the seismic demand of NSCs and then investigates how NSC clustering modifies this coupling effect.

3.2 NONLINEAR MODEL AND OUTLINE FOR NUMERICAL ANALYSES

To evaluate the component amplification factor consistent with the ductility concept in ASCE 7-22, NSCs were modeled as elasto-perfectly-plastic systems, with the yield threshold defined by dividing the maximum elastic demand from the corresponding linear system by the seismic reduction factor (R_{nsc}). The supporting structure was assumed to remain elastic, as it generally sustains little or no damage even when NSCs experience high seismic demands due to amplification effects.

$$u_{y,s} \text{ or } F_{y,s} \to \infty, \quad u_{y,nsc} \text{ or } F_{y,nsc} = u_{el,nsc}/R_{nsc} = F_{el,nsc}/R_{nsc} \tag{7}$$

The nonlinearity of NSCs was characterized by the ductility parameter (μ_{nsc}), defined as the ratio of the maximum inelastic deformation to the yield deformation (see Figure 2a). Three ductility levels were considered following ASCE 7-22 (Table 1): low (μ_{nsc} = 1.25), moderate (μ_{nsc} = 1.50), and high (μ_{nsc} = 2.00). The corresponding seismic reduction factor (R_{nsc}) for each ductility level was determined iteratively using the procedure outlined by Chopra [2012].

The nonlinearity of NSCs was characterized by the ductility parameter (μ_{nsc}), defined as the ratio of the maximum inelastic deformation to the yield deformation (Figure 2a). Three ductility levels were considered following ASCE 7-22: low (μ_{nsc} = 1.25), moderate (μ_{nsc} = 1.50), and high (μ_{nsc} = 2.00). The corresponding reduction factors (R_{nsc}) were obtained iteratively using the procedure outlined by Chopra [2012].

The bilinear hysteretic behavior was described by the following differential equations [Thyagarajan, 1990]:

$$\begin{aligned} F_i\left(u_i;k_i,u_{y,i}\right) &= \alpha_i k_i u_i + \left(1-\alpha_i\right)k_i z_i \\ \dot{z}_i &= \dot{u}_i\left[1-H\left(\dot{u}_i\right)H\left(z_i-u_{y,i}\right)-H\left(-\dot{u}_i\right)H\left(-z_i-u_{y,i}\right)\right] \end{aligned} \tag{8}$$

where, a_i = post-yield stiffness ratio (= 0 for elasto-perfectly plastic model), $H(\cdot)$ = Heaviside step function, and z_i = auxiliary variable that represents inelastic behavior that depends on the history of u_i. The EOMs (Eqs. (5) and (6)) and Eq. (8) were solved simultaneously using the 4th-order Runge–Kutta method.

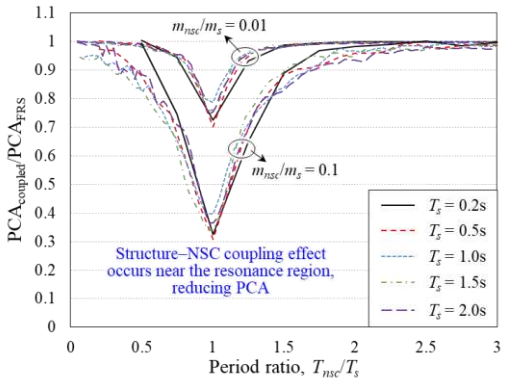
Twenty DBE-level ground motion records (LA01–LA20) from the Los Angeles area were used, with details in Somerville *et al.* [1997]. As the analyses focused on nondimensional responses such as acceleration amplification and ductility, the records were used with their original PGAs specified in Somerville *et al.* [1997], without additional scaling. All results discussed herein are based on ensemble averages of the responses from these 20 records.

As indicated in Eqs. (5) and (6), the dynamic behavior of the coupled systems depends on the NSC-to-structure mass ratio (m_{nsc}/m_s), natural periods (T_s, T_{nsc}), damping ratios (ξ_s, ξ_{nsc}), and NSC ductility (μ_{nsc}). The structural damping ratio (ξ_s) was fixed at 5%, while NSC properties were varied in the analyses.

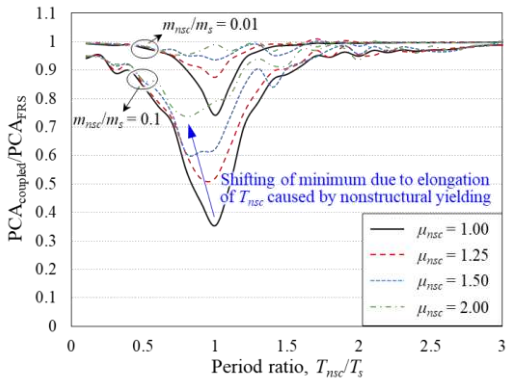
4. EVALUATION OF STRUCTURE-NSC COUPLING EFFECT ON PCA AND COMPONENT AMPLIFICATION (PCA/PFA)

4.1 INFLUENCE OF COUPLING EFFECT ON PCA

This section investigates how the seismic demand on nonstructural components, represented by the peak component acceleration (PCA), is influenced by the structure–NSC coupling effect. The coupling effect was quantified by normalizing the PCA from the 2-DOF coupled system ($PCA_{coupled}$) with that obtained from the FRS method (PCA_{FRS}), as shown in Figure 3. The coupling effect becomes pronounced when NSCs are closely tuned with the supporting structure, where $PCA_{coupled}/PCA_{FRS}$ falls below 1.0, indicating that the seismic demand of coupled NSCs tends to be lower than that predicted by the FRS method. In consistent with Eq. (5), the coupling effect intensifies as the mass ratio (m_{nsc}/m_s) increases.

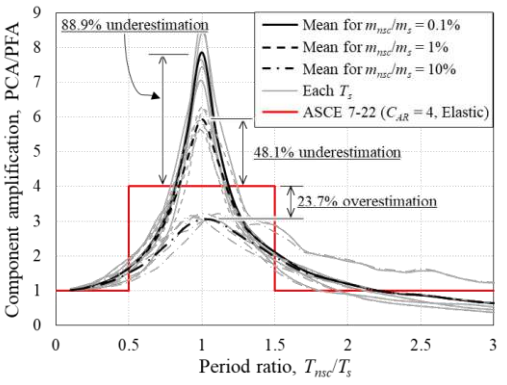


(a) $PCA_{coupled}/PCA_{FRS}$ spectra varying structural period

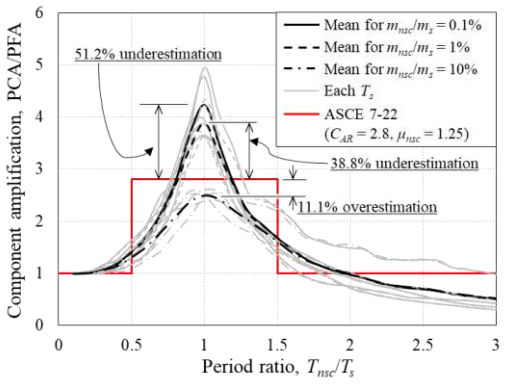


(b) $PCA_{coupled}/PCA_{FRS}$ spectra varying component ductility

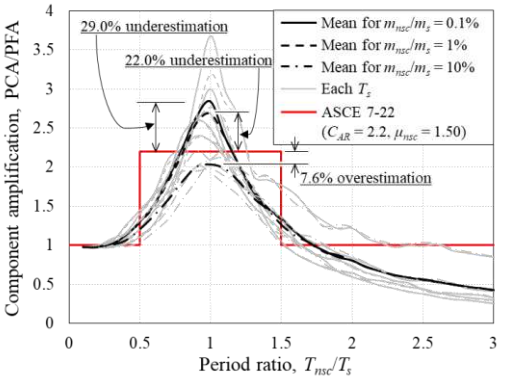
Figure 3. Effects of structure-NSC coupling on PCA (ξ_{nsc} = 2%)



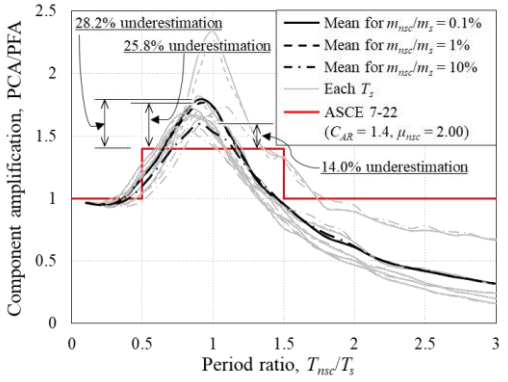
(a) Elastic components (μ_{nsc} = 1.0)



(b) Low-ductile components (μ_{nsc} = 1.25)



(c) Moderately-ductile components (μ_{nsc} = 1.50)



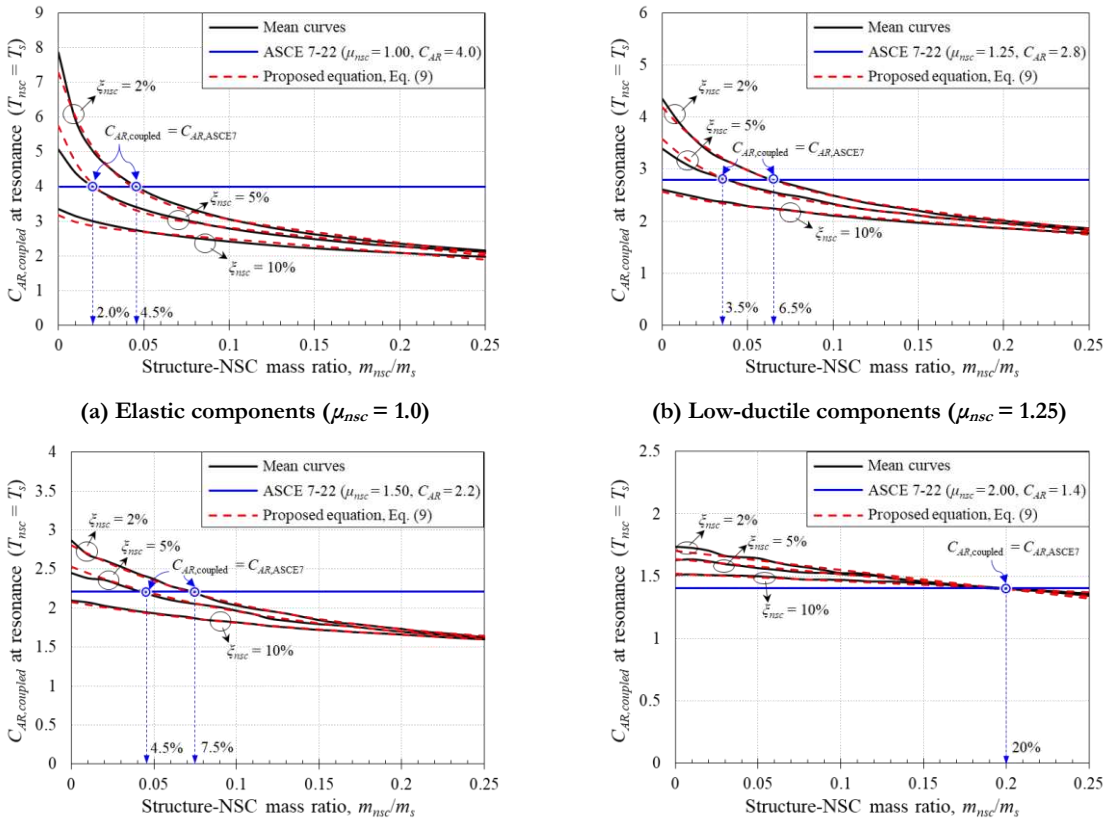
(d) Highly-ductile components (μ_{nsc} = 2.00)

Figure 4. Component amplification spectra incorporating structure-NSC coupling effect (ξ_{nsc} = 2%)

4.2 COMPONENT AMPLIFICATION SPECTRA INCORPORATING COUPLING EFFECT

The component amplification factor (C_{AR} = PCA/PFA) defined in ASCE 7-22 was evaluated considering the structure–NSC coupling effects, as illustrated in Figure 4. For components with a damping ratio of 2% and a negligible mass ratio (m_{nsc}/m_s = 0.1%), ASCE 7-22 significantly underestimates C_{AR} by approximately 88.9%, 51.2%, 29.0%, and 28.2% for elastic, low-, moderate-, and highly ductile components, respectively. This underestimation diminishes as the mass ratio increases, and for m_{nsc}/m_s = 10%, the calculated C_{AR} becomes lower than the code value for all ductility levels except the high-ductility case. Given that ASCE 7-22 allows a structure-to-NSC mass ratio of up to 25%, a reduced C_{AR} may be appropriate for moderate- to heavy-weight components.

4.3 PROPOSAL OF COMPONENT AMPLIFICATION FACTOR INCORPORATING COUPLING EFFECT



(a) Elastic components (μ_{nsc} = 1.0) **(b) Low-ductile components (μ_{nsc} = 1.25)**

(c) Moderately-ductile components (μ_{nsc} = 1.50) **(d) Highly-ductile components (μ_{nsc} = 2.00)**

Figure 5. Comparison of C_{AR} from 2-DOF coupled system, ASCE 7-22, and the proposed equation (Eq. (9))

Further analysis of the coupled component amplification under tuned conditions was extended up to a mass ratio of 25%, the upper limit specified in ASCE 7-22. Figure 5 presents the relationship between C_{AR} and the structure–NSC mass ratio across four ductility levels. The black lines denote the ensemble-averaged resonant C_{AR} ($C_{AR,coupled}$) from coupled systems with five structural periods (T_s = 0.2–2.0 s) subjected to 20 ground motions, while the blue horizontal lines indicate the code-specified values ($C_{AR,ASCE7}$).

For lightweight NSCs (m_{nsc}/m_s < 2%), $C_{AR,coupled}$ is sensitive to damping and exceeds the code value at low damping. As the mass ratio increases, $C_{AR,coupled}$ decreases and rapidly approaches the code values, implying that the ASCE 7-22 provision is reasonable for small mass increases. The damping effect becomes negligible for heavier NSCs, and $C_{AR,coupled}$ converges to approximately 2.07, 1.82, 1.61, and 1.35 for elastic, low-, moderate-, and high-ductility components—about 0.52, 0.65, 0.73, and 0.96 times $C_{AR,ASCE7}$, respectively.

Based on these findings, a lower amplification factor is suggested for moderate- to heavyweight NSCs to achieve a more rational and economical design. Accordingly, Eq. (9) proposes a regression-based expression for $C_{AR,coupled}$ as a function of the mass ratio (m_{nsc}/m_s) and damping ratio (ξ_{nsc}), with coefficients listed in Table 2. As shown in Figure 5, the proposed equation (red dashed lines) accurately predicts the mean $C_{AR,coupled}$ up to the 25% mass ratio limit. When the m_{nsc}/m_s is unknown, the converged values of 2.1, 1.8, 1.6, and 1.4 for components with mass ratios above 6% can be reasonably adopted, where 6% corresponds to the average threshold at which 2%-damped elastic-to-moderate ductile components fall below the code-specified C_{AR}.

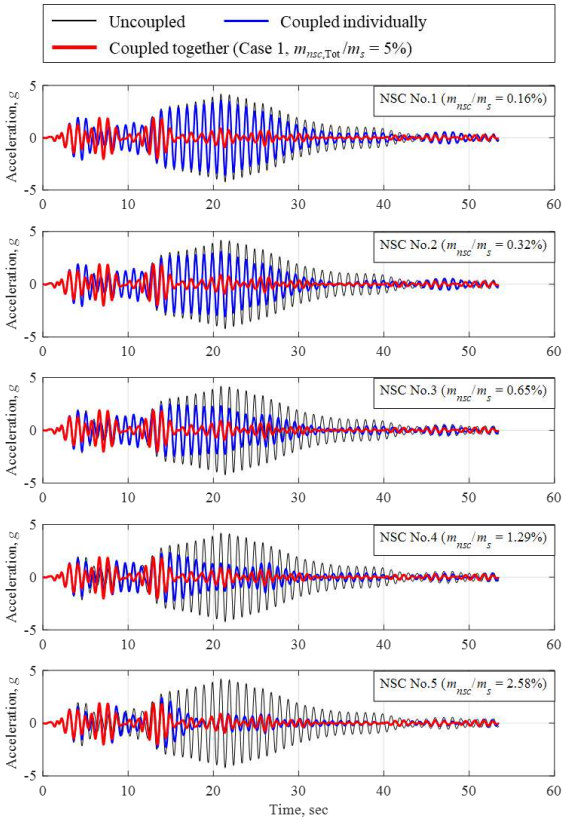
$$C_{AR,coupled} = (a \cdot \xi_{nsc} + b) \cdot \exp\left(-(c \cdot \xi_{nsc} + d)\frac{m_{nsc}}{m_s}\right) + (e \cdot \xi_{nsc} + f)\frac{m_{nsc}}{m_s} + (g \cdot \xi_{nsc} + h) \quad (9)$$

Table 2. Coefficients evaluated for the regression Eq. (9) of $C_{AR,coupled}$

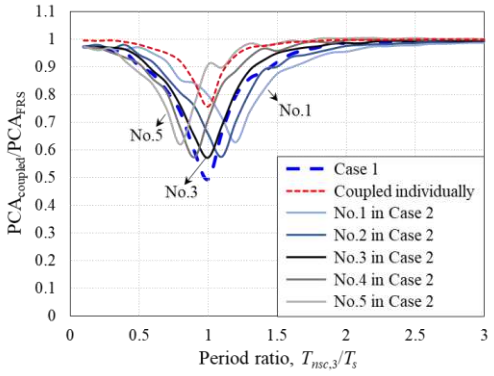
Component ductility (μ_{nsc})	Coefficients							
	a	***b***	***c***	***d***	***e***	***f***	***g***	***h***
Elastic (μ_{nsc} = 1.00)	-42.45	4.54	423.64	30.96	26.54	-6.57	-8.99	3.77
Low (μ_{nsc} = 1.25)	-16.58	1.85	148.27	20.62	9.41	-3.51	-3.62	2.74
Modertate (μ_{nsc} = 1.50)	-11.98	1.50	8.96	8.51	-8.30	0	2.99	1.48
High (μ_{nsc} = 2.00)	0	0	0	0	11.81	-1.77	-2.31	1.75

5. EVALUATION OF STRUCTURE-NSC COUPLING EFFECT ON CLUSTERED NSCS

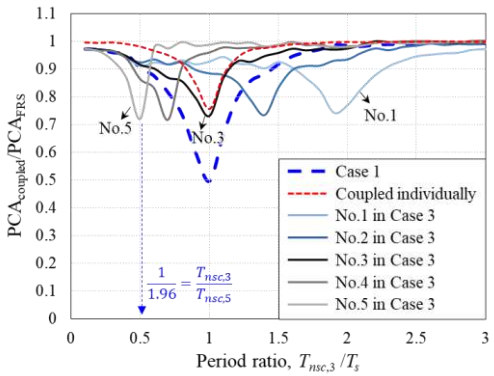
As shown in Eq. (6), when multiple NSCs are installed in a cluster, their coupling effects with the supporting structure are superimposed. If all components share identical dynamic characteristics, the responses of individual NSCs ($\ddot{u}_{comp}$) coincide, producing a coupling effect equivalent to that of the total NSC mass. In practice, however, clustered NSCs vary in dynamic properties and mass distribution. Accordingly, this section investigates the interaction level between individual NSCs and the supporting structure through several case studies.



(a) Comparison of acceleration histories for uncoupled, individually coupled, and clustered-coupled scenarios (Case 1)



(b) $PCA_{coupled}/PCA_{FRS}$ spectra for Case 2 scenario



(c) $PCA_{coupled}/PCA_{FRS}$ spectra for Case 3 scenario

Figure 6. Influence of NSC-clustering effects on PCA (T_s = 1.0 sec, ξ_{nsc} = 2%)

5.1 EFFECTS OF NSC-CLUSTERING ON COUPLED PCA

Table 3 summarizes the mass and period distributions of NSCs for the clustering scenarios analyzed. To examine the structure–NSC coupling effects acting on individual NSCs within a cluster, the analyses were

performed under elastic conditions for both the supporting structure and the NSCs, with T_s = 1.0 s and ξ_{nsc} = 2% for all components. Case 1 assumes identical natural periods (T_{nsc}) with varying masses, while Cases 2 and 3 assign equal masses but increasing period spacing among individual NSCs.

Table 3. Mass and period distributions for clustering scenarios considered for the case study

Case No.	$m_{nsc,1}/m_s$ ($T_{nsc,1}/T_{nsc,3}$[b])	$m_{nsc,2}/m_s$ ($T_{nsc,2}/T_{nsc,3}$[b])	$m_{nsc,3}/m_s$ ($T_{nsc,3}/T_{nsc,3}$[b])	$m_{nsc,4}/m_s$ ($T_{nsc,4}/T_{nsc,3}$[b])	$m_{nsc,5}/m_s$ ($T_{nsc,5}/T_{nsc,3}$[b])	$m_{nsc,\mathrm{Tot}}/m_s$[a]
1	0.16 % (1.00)	0.32 % (1.00)	0.65 % (1.00)	1.29 % (1.00)	2.58 % (1.00)	5.00 %
2	1.00 % (0.83)	1.00 % (0.91)	1.00 % (1.00)	1.00 % (1.10)	1.00 % (1.21)	5.00 %
3	1.00 % (0.51)	1.00 % (0.71)	1.00 % (1.00)	1.00 % (1.40)	1.00 % (1.96)	5.00 %

[a] $m_{nsc,\mathrm{Tot}}/m_s$ = total mass ratio of NSCs to the structure for each case
[b] Period ratios are expressed as values normalized by the period of No. 3 NSC.

Figure 6 presents the PCA of individual NSCs in clustered configurations obtained from the (N+1)-DOF coupled analyses. In Case 1, where all NSCs have identical dynamic properties, even very lightweight NSCs exhibit pronounced structure–NSC coupling effects due to clustering, resulting in a notable reduction in PCA and identical acceleration time histories among all components (Figure 6a). This confirms the validity of the $C_{AR,coupled}$ proposed in Section 4.3. Figure 6b and 6c show the $\mathrm{PCA}_{\mathrm{coupled}}/\mathrm{PCA}_{\mathrm{FRS}}$ spectra for individual NSCs in Cases 2 and 3, where components have different natural periods, compared with the individually coupled case (red line) and Case 1 with identical periods (blue line). Because all NSCs in Case 1 share the same natural period, they produce identical acceleration responses ($\ddot{u}_{comp}$) and thus identical spectra. In contrast, NSCs in Cases 2 and 3 display distinct spectral minima at different period ratios, since only one component resonates with the structure at a time while the others remain off-resonance. For instance, in Case 3, NSC No. 5 resonates with the structure at $T_{nsc,3}/T_s = 1/1.96$ (Figure 6c). As the period differences among NSCs increase, their resonant responses gradually diminish from the identical level observed in Case 1 and converge toward those of the individually coupled case.

5.2 PROPOSAL OF EQUIVALENT COUPLING MASS AND COUPLING PARTICIPATION FACTOR

Since the clustering configuration affects the coupling behavior of individual nonstructural components, as discussed in Section 5.1, it is essential to determine how clustering modifies the coupling response of each component. Accordingly, this study introduces an equivalent coupling mass concept, enabling the coupling level of individual NSCs in a cluster to be represented by that of a single NSC–structure coupling case.

The equivalent coupling mass of the j-th component ($m_{nsc,j,eq}$) is defined as the sum of the individual masses of the NSCs in the cluster, each weighted by a coupling participation factor ($p_{co,ij}$):

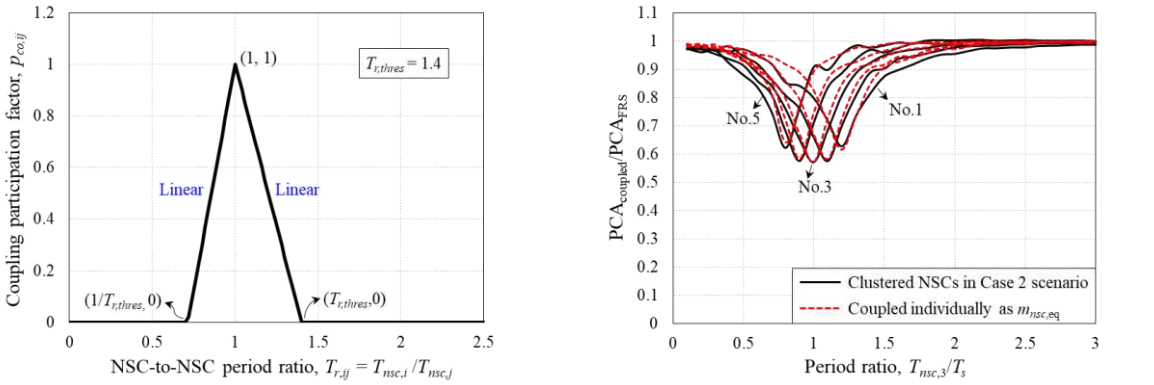
$$m_{nsc,\,j,eq} = \sum_{i=1}^{N} p_{co,ij}\left(T_{r,ij}\right) \times m_{nsc,i} \tag{10}$$

where $m_{nsc,j,eq}$ = equivalent coupling mass for the j-th NSC, $m_{nsc,i}$ = mass of the i-th NSC, $p_{co,ij}$ = coupling participation factor representing the extent to which the i-th NSC contributes to the structure-NSC coupling effect of the j-th NSC, and $T_{r,ij}$ = period ratio between the i-th and j-th NSCs.

As shown in Section 5.1, the influence between components weakens as their period difference increases; thus, $p_{co,ij}$ is expressed as a function of $T_{r,ij}$. In this study, for simplicity, it was modeled as a piecewise linear function connecting ($1/T_{r,thres}$, 0), (1, 1), and ($T_{r,thres}$, 0), as illustrated in Figure 7a:

$$p_{co,ij}\left(T_{r,ij}\right) = \begin{cases} aT_{r,ij} + b & (1 \le T_{r,ij} \le T_{r,thres}) \\ bT_{r,ij} + a & (1/T_{r,thres} < T_{r,ij} \le 1) \\ 0 & \text{otherwise} \end{cases} \quad \text{where} \quad a = -\frac{1}{T_{r,thres}-1},\ \ b = \frac{T_{r,thres}}{T_{r,thres}-1} \tag{11}$$

Here, $T_{r,thres}$ is the threshold period ratio used to determine whether a component should be included in the equivalent coupling mass calculation. A threshold period ratio of $T_{r,thres}$ = 1.4 was adopted, based on case studies of various clustering scenarios. The detailed derivation process is omitted due to space limitations.



(a) Coupling participation factor, $p_{co,ij}$

(b) $PCA_{coupled}/PCA_{FRS}$ spectra using equivalent coupling mass for Case 2 scenario

Figure 7. Coupling participation factor and validation of the equivalent coupling mass concept

Figure 7b demonstrates the validity of this concept. The black lines show $PCA_{coupled}/PCA_{FRS}$ spectra of individual NSCs from (N+1)-DOF coupled analyses for Case 2, while the red lines show the results from 2-DOF coupled analyses in which each component is modeled as a single NSC with its equivalent coupling mass. Although minor discrepancies exist outside the resonance range, the 2-DOF analyses using the equivalent coupling mass accurately predict the resonant responses observed in the (N+1)-DOF results.

These results confirm that the equivalent coupling mass is an effective parameter for estimating the coupling level of individual NSCs within a cluster. By incorporating this concept into the $C_{AR,coupled}$ proposed in Section 4.3, the seismic demand of clustered NSCs can be rationally estimated.

6. SUMMARY AND CONCLUSIONS

In this study, numerical analyses of idealized structural–nonstructural coupled systems were conducted to investigate the influence of the structure–NSC coupling effect on the seismic demand of acceleration-sensitive components, represented by the peak component acceleration (PCA). From the 2-DOF coupled analyses, it was confirmed that PCA decreases as the NSC-to-structure mass ratio increases due to the coupling effect, and a more reasonable component amplification factor, $C_{AR,coupled}$, was proposed as a function of the mass ratio. Furthermore, based on (N+1)-DOF coupled analyses, the coupling levels of individual components within a cluster were examined, and an equivalent coupling mass concept was introduced to estimate these levels. The validity of this concept was verified by 2-DOF coupled analyses using the equivalent coupling mass. By incorporating this concept into the $C_{AR,coupled}$, the seismic demand of individual NSCs within a cluster can be reasonably estimated.

ACKNOWLEDGEMENT

This research was supported by the National Research Foundation of Korea funded by the Ministry of Education (RS-2023-00247620).

REFERENCES

Sankaranarayanan, R., Medina, R.A. [2007] "Acceleration Response Modification Factors for Nonstructural Components Attached to Inelastic Moment-Resisting Frame Structures," *Earthquake Engineering & Structural Dynamics*, Vol. 36, No. 14, pp. 2189–2210.

Abbati, S.D., Cattari, S., Lagomarsino, S. [2018] "Theoretically-Based and Practice-Oriented Formulations for the Floor Spectra Evaluation," *Earthquake Spectra*, Vol. 15, pp. 565–581.

Anajafi, H., Medina, R.A., Santini-Bell, E. [2020] "Inelastic Floor Spectra for Designing Anchored Acceleration-Sensitive Nonstructural Components," *Bulletin of Earthquake Engineering*, Vol. 18, pp. 2115–2147.

Anajafi, H., Medina, R.A. [2019] "Lessons Learned From Evaluating the Responses of Instrumented Buildings in the United States: the Effects of Supporting Building Characteristics on Floor Response Spectra," *Earthquake Spectra*, Vol. 35, No. 1, pp. 159–191.

ASCE/SEI, 7-22 [2022] *Minimum design loads and associated criteria for buildings and other structures*, Reston, VA: American Society of Civil Engineering.

Bachman, R., Bonowitz, D., Caldwell, P.J. [2004] "Engineering Demand Parameters for Nonstructural Components," *Report No. ATC-58*, Applied Technology Council.

Calvi, P.M., Sullivan, T.J. [2014] "Estimating Floor Spectra in Multiple Degree of Freedom Systems," *Earthquake and Structures*, Vol. 7, pp. 17–38.

CEN. [2004] *Eurocode8: Design of Structure for Earthquake Resistance, Part 1.1: General Rules, Seismic Actions and Rules for Buildings*. EN 1998-1, European Committee for Standardization.

Chopra, A.K. [2012] Dynamics of Structures. 4th ed. Pearson Prentice Hall.

Fathali, S.F., Lizundia, B. [2011] "Evaluation of Current Seismic Design Equations for Nonstructural Components in Tall Buildings Using Strong Motion Records," *The Structural Design of Tall and Special Buildings*, Vol. 20, pp. 30–46.

Hadjian, A.H., Ellison, B. [1986] "Decoupling of Secondary Systems for Seismic Analysis," *Journal of Pressure Vessel Technology*, Vol. 108, pp. 78-85.

Kazantzi, A.K., Vamvatsikos, D., Miranda, E. [2020] "Evaluation of Seismic Demands on Building Nonstructural Elements," *Journal of Structural Engineering*, Vol. 146, 04020118.

Magliulo, G., D'Angela, D. [2024] "Seismic Response and Capacity of Inelastic Acceleration-Sensitive Nonstructural Elements Subjected to Building Floor Motions," *Earthquake Engineering & Structural Dynamics*, Vol. 53, No. 4, pp. 1421–1445.

NIST [2018] "Recommendations for Improved Seismic Performance of Nonstructural Components," *NIST GCR 18-917-43*, National Institute of Standards and Technology.

Petrone, C., Magliulo, G., Manfredi, G. [2015] "Seismic Demand on Light Acceleration-Sensitive Nonstructural Components in European Reinforced Concrete Buildings," *Earthquake Engineering & Structural Dynamics*, Vol. 44, No. 8, pp. 1203–1217.

Perrone, D., Calvi, P.M., Nascimbene, R., Fischer, E.C., Magliulo, G. [2019] "Seismic Performance of Non-Structural Elements During the 2016 Central Italy Earthquake," *Bulletin of Earthquake Engineering*, Vol. 17, pp. 5655–5677.

Singh, M.P., Suarez, L.E. [1987] "Seismic Response Analysis of Structure Equipment Systems With Non-Classical Damping Effects," *Earthquake Engineering & Structural Dynamics*, Vol. 15, pp. 871–888.

Singh, M.P., Moreschi, L.M., Suárez, L.E., Matheu, E.E. [2006] "Seismic Design Forces. II: Flexible Nonstructural Components," *Journal of Structural Engineering*, Vol. 132, pp. 1533–1542.

Somerville, P., Smith, N., Punyamurthula, S., Sun., J. [1997] "Development of Ground Motion Time Histories for Phase 2 of the FEMA/SAC Steel Project".

Thyagarajan, R.S. [1990] "Modeling and Analysis of Hysteretic Structural Behavior", *Ph.D. Dissertation*, California Institute of Technology, USA.

Vukobratović, V., Fajfar, P. [2024] "Direct Floor Response Spectra for Nonlinear Nonstructural Components," *Bulletin of Earthquake Engineering*, Vol. 22, pp. 1033–1053.

Zito, M., D'Angela, D., Maddaloni, G., Magliulo, G. [2023] "A Shake Table Protocol for Seismic Assessment and Qualification of Acceleration Sensitive Nonstructural Elements," *Computer–Aided Civil and Infrastructure*, Vol. 38, pp. 1699–1726.

Experimental and Field Investigations of Suspended Air Handling Units

W.C. Chen [1], M.C. Ko[2], W.H. Huang [2], J.F. Chai [3], and F.R. Lin [3]

[1] National Center for Research on Earthquake Engineering, National Institutes of Applied Research
No. 2001, Sec. 1, Zhongzheng S. Rd., Guiren Dist., Tainan City 711015, Taiwan
e-mail: 2006023@niar.org.tw

[2] National Center for Research on Earthquake Engineering, National Institutes of Applied Research
No. 2001, Sec. 1, Zhongzheng S. Rd., Guiren Dist., Tainan City 711015, Taiwan
e-mail: 2306023@ niar.org.tw, 2206027@ niar.org.tw

[3] National Center for Research on Earthquake Engineering, National Institutes of Applied Research
No. 200, Sec. 3, Xinhai Rd., Da'an Dist., Taipei City 106219, Taiwan
e-mail: chai@ niar.org.tw, frlin@ niar.org.tw

Abstract. Following the major earthquake that struck Hualien, Taiwan, on April 3, 2024, the National Center for Research on Earthquake Engineering (NCREE) promptly conducted field investigations in the affected areas. The investigations revealed widespread damage to suspended air handling units, particularly in hospitals and schools, resulting in substantial financial losses and significant disruption to building functionality.

Recognizing the critical importance of improving the seismic resilience of suspended air handling units, NCREE initiated a comprehensive research program to investigate the seismic performance of the equipment. As part of this project, a series of full-scale shaking table tests were carried out at the NCREE Tainan Laboratory. These tests were designed to replicate realistic seismic conditions in order to identify structural vulnerabilities, evaluate the effectiveness of current installation practices, and enhance domestic seismic construction methodologies.

This paper presents the cases of damage to suspended air handling units observed during the Hualien earthquake and introduces preliminary findings from the aforementioned shaking table tests. The study provides insights into the failure modes and proposes seismic strategies for suspended air handling units.

Keywords: 0403 Hualien Earthquake, Suspended air handling unit, Shaking table test, Nonstructural component.

1. INTRODUCTION

On April 3, 2024, a major earthquake with magnitude of 7.2 struck the Hualien region of Taiwan, with a focal depth of 22.5 kilometers. It was the most powerful earthquake experienced in Taiwan since the 1999 Chi-Chi Earthquake. Following the event, the National Center for Research on Earthquake Engineering (NCREE) promptly investigated the affected areas. Extensive damage to suspended air handling units (AHUs) and associated pipilines in hospitals and schools was observed, resulting in significant financial losses and impairing the functionality of these critical facilities, as shown as Figure 1.



Figure 1. Failure of the AHUs caused indoor flooding



Figure 2. Spring isolator

Reconnaissance observations revealed that suspended AHUs damaged during the earthquake generally lacked seismic protection measures. The problem is closely associated with the suspension method employed for the AHUs. As illustrated in Figure 2, the AHUs were suspended beneath the floor slab using spring isolators. These spring isolators are primarily intended to prevent mechanical vibrations generated by the fan motors inside the AHU from being transmitted through the suspension rods to the floor slab above, thereby maintaining occupant comfort. However, due to the absence of standardized seismic design guidelines or retrofit strategies, suspended AHUs in Taiwan are typically not equipped with seismic protection measures, making them vulnerable to damage during earthquakes.

This paper is divided into two parts. The first part presents cases of seismic damage to suspended AHUs observed in the Hualien earthquake, along with an analysis of the failure characteristics and the potential causes. The second part introduces a shaking table test conducted to evaluate the seismic performance of suspended AHUs. This study aims to provide practical guidance for enhancing the seismic resilience of such equipment. Based on the experimental results, critical factors affecting seismic performance are identified, and seismic strategies are proposed to improve the safety of suspended AHUs.

2. SEISMIC INVESTIGATION OF SUSPENDED AHUs

After the Hualien earthquake, NCREE, together with research teams from Taiwan and Japan, conducted investigations on critical facilities that experienced severe damage to nonstructural component. This section presents the observed seismic damage to suspended AHUs in two hospitals and one university.

2.1 HL HOSPITAL

HL Hospital is located approximately 130 meters from the Meilun Fault and consists of multiple buildings constructed in different periods. One of these buildings, completed in 1995, is a reinforced concrete (RC) structure with a basement and eight stories above ground. Significant seismic damage to suspended AHUs

was observed in the corridors on the 2nd, 3rd, 4th, and 5th floors of this building. Ruptures were found in the chilled water pipes connected to the suspended AHUs, as well as in the PVC drainage pipes. The failure locations of the AHUs are indicated as points A, B, and C in Figure 3. In some cases, the suspended AHUs also collided with nearby fire sprinkler heads, leading to severe water leakage, as illustrated in Figure 4.

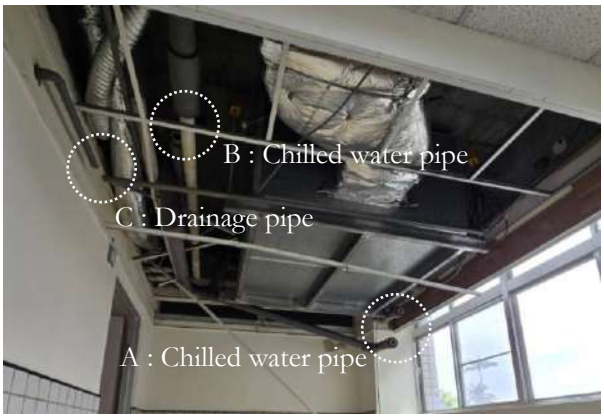


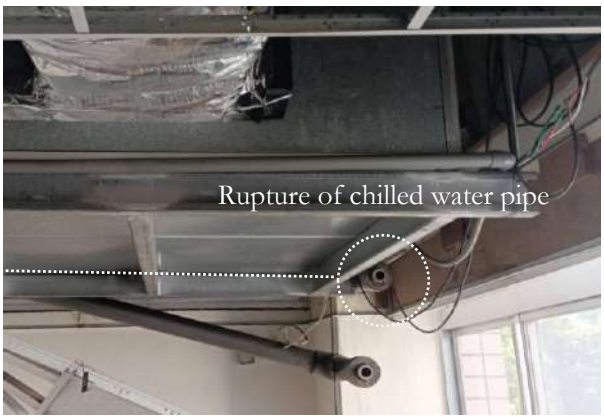
Figure 3. Failure of the AHUs and associated pipilines



Figure 4. Failure to fire sprinkler heads



(a)



(b)

Figure 5. (a) Impact marks on the wooden bulkhead; (b) Rupture of chilled water pipe.



Figure 6. Facture of drainage pipe



Figure 7. Rupture of sprinkler head

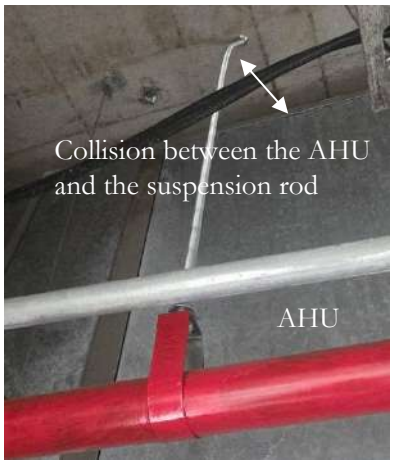


Figure 8. Suspension rod

The failure mechanisms of the damaged pipelins can be reasonably inferred based on on-site observations. As shown in Figure 5(a), visible impact marks were found on a nearby wooden bulkhead adjacent to the damaged chilled water pipe. This suggests that the suspended AHUs experienced significant displacement

during the earthquake, causing a direct collision between the chilled water pipe and the wooden bulkhead, which eventually led to the pipe's rupture, as illustrated in Figure 5(b). The failure of the PVC drainage pipe can slao be attributed to the displacement of the suspended AHUs during seismic shaking. While the pipe moved along with the AHUs, its motion was constrained on the patient room side by a partition wall, leading to stress concentration at the pipe's bend and causing it to fracture, as shown as Figure 6.

In addition, several fractured fire sprinkler heads were observed, as illustrated in Figure 7. The suspension rods supporting the AHUs in the figure exhibit significant deformation, likely caused by impact with the fire sprinkler system. Figure 8 shows noticeable deformation in the suspension rods of the fire sprinkler system near the AHUs, providing additional evidence of a strong collision between the suspended AHUs and the fire sprinkler system.

2.2 TC HOSPITAL

TC Hospital is located approximately 1,800 meters from the Meilun Fault and consists of four main buildings. Significant seismic damage to suspended AHUs was observed in one of the buildings, a steel reinforced concrete (SRC) structure with a basement and ten stories above ground. The AHUs are primarily installed in a catwalk-level space beneath the roof, suspended at a height of 1.9 meters, and are not equipped with any seismic protection measures. Following the earthquake, many chilled water pipes connected to the suspended AHUs were found to have ruptured, as shown in Figure 9. Reconnaissance observations revealed significant deformation of the suspension rods, likely caused by impact from the AHU equipment (Figure 10). It is concluded that the suspended AHUs experienced substantial displacement during the earthquake, exceeding the tolerance limits of the chilled water pipes and resulting in fractures at the elbow joints.



Figure 9. Rupture of chilled water pipes



Figure 10. Deformation of suspension rods



Figure 11. Rupture of chilled water pipes



Figure 12. Deformation of suspension rods

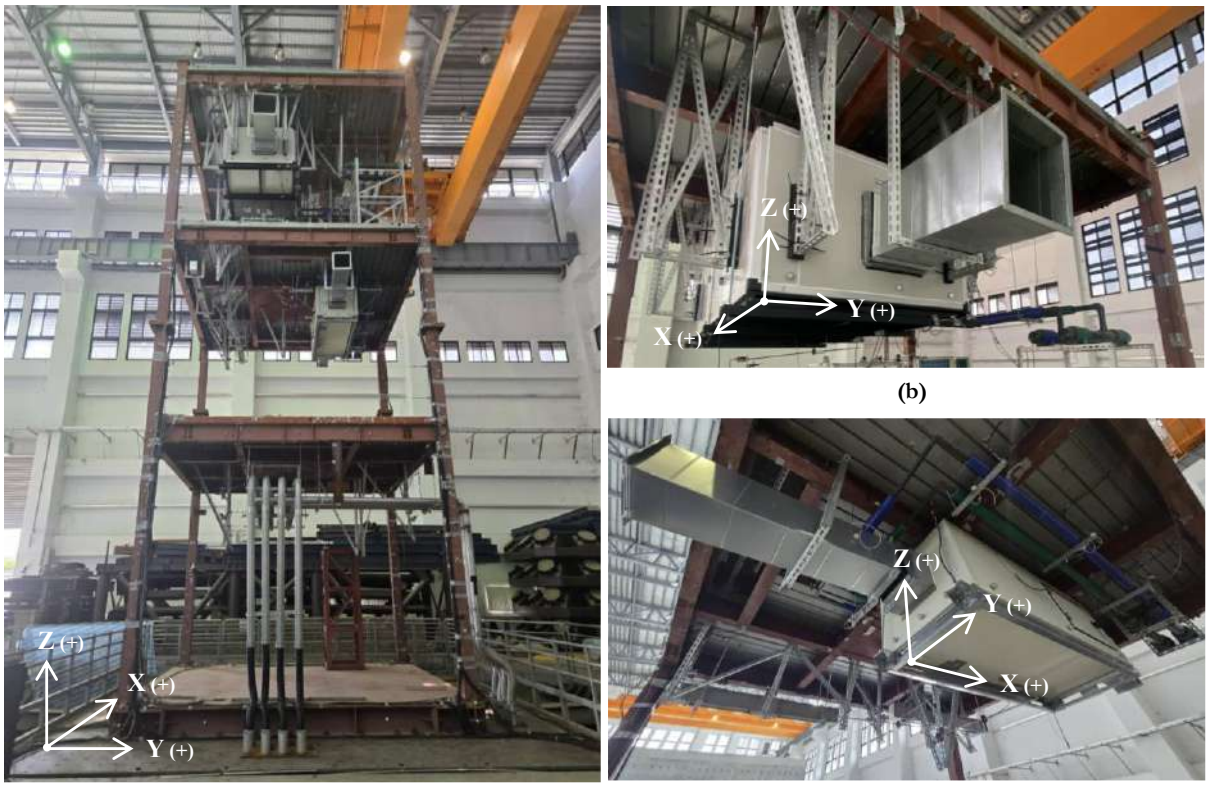
2.3 DW UNIVERSITY

The administration building located inside the DW University campus is a reinforced concrete (RC) structure with a basement and six stories above ground. It was observed multiple suspended AHUs and associated piping within the building sustained significant damage, resulting not only in substantial economic loss but also had a direct impact on the functional use of the building's interior spaces.

As shown in Figure 11, the suspension rods supporting the suspended AHUs were damaged, placing the equipment at risk of falling. Additionally, on-site observations revealed that the nearby partition walls were also severely damaged, as illustrated in Figure 12. This damage is believed to have been caused by impacts from the suspended AHUs, indicating that the equipment experienced considerable displacement during the earthquake.

3. SHAKING TABLE TEST OF SUSPENDED AHUs

To thoroughly investigate the seismic performance and dynamic behavior of suspended AHUs in Taiwan, full-scale shaking table tests were conducted at the NCREE Tainan Laboratory. A three-story test frame (Figure 13(a), with the coordinate system as shown in the figure), measuring 5 m × 5 m in plan and 12.7 m in height, was mounted on the shaking table. Two air handling units, along with the required piping, were installed on the second and third floors of the test frame, as shown in Figure 13(b) and Figure 13(c).



(a) (b) (c)

Figure 13. (a) The three-story test frame; (b) specimen on the third floor; (c) specimen on the second floor

To ensure that the test specimen is subjected to seismic conditions representative of actual damage scenarios, this study selected the previously described building from TC Hospital as the simulation model. The main

reason for this selection is that the hospital is equipped with strong-motion instruments, enabling the use of ground motions recorded from Hualien earthquak as input for the shaking table tests

According to on-site measurement results (Figure 14), the natural frequencies of the selected building in the two horizontal directions are 1.4 Hz and 1.1 Hz, respectively. Additionally, the first-mode natural frequency of the test frame was identified as 1.25 Hz, as also shown in Figure 15. The close alignment between these structural frequencies further supports the validity of the test results and provides a solid basis for evaluating the seismic performance of the suspended AHUs.

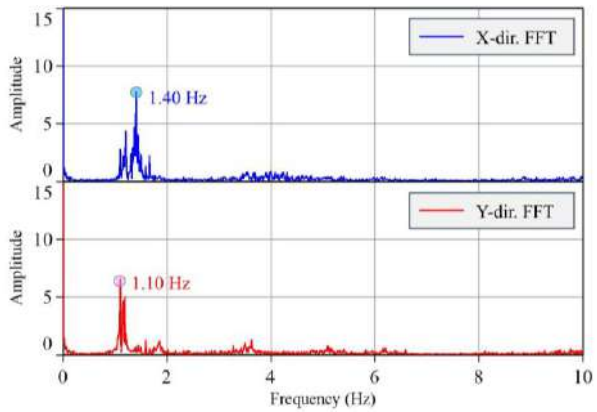


Figure 14. Natural frequency of the TC Hospital building

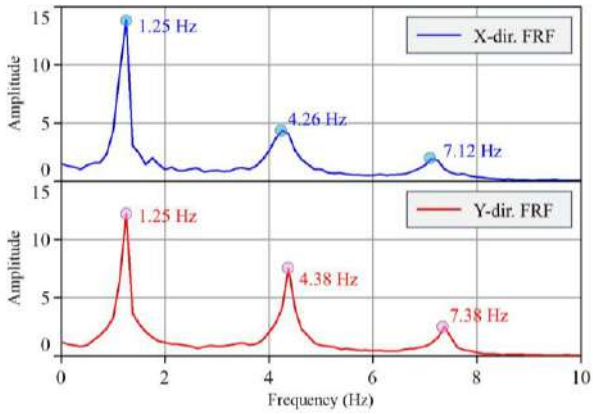


Figure 15. Natural frequency of the test frame

3.1 TEST SETUP

This test simulates two installation scenarios of suspended AHUs. The first scenario replicates the actual configuration of suspended AHUs observed in the building at TC Hospital. The second scenario is based on the configurations found in the buildings within HL Hospital as well as the administration building at DW University. The primary differences between the two setups lie in the AHU dimensions, weight, and suspension length. These variations are intended to evaluate the seismic performance of AHUs under different installation conditions and to further understand the damage mechanisms of suspended AHUs during seismic events.

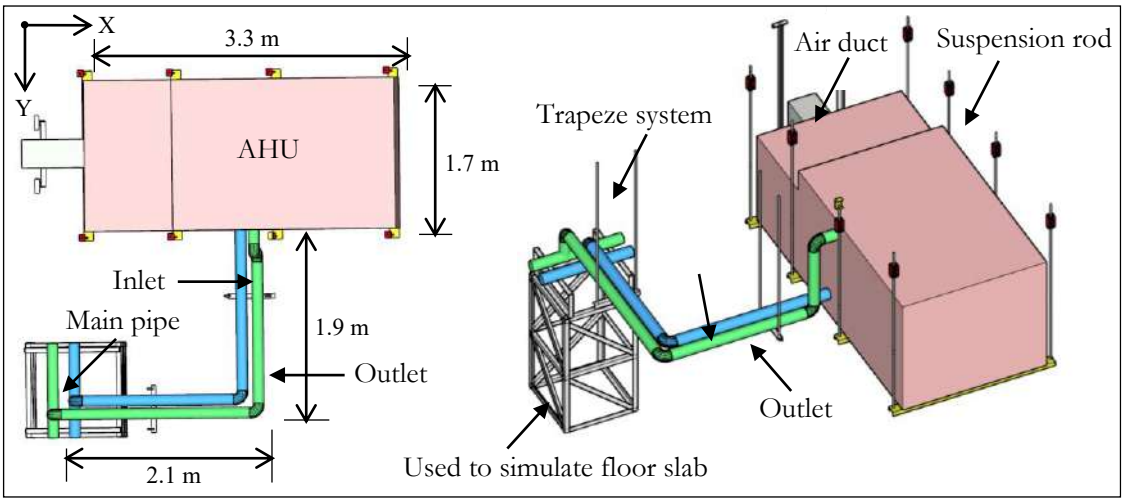


Figure 16. Test specimen of AHU on the third floor

Figure 16 shows the AHU test specimen installed on the third floor of the test framework. The specimen measures 3.3 m in length, 1.7 m in width, and 1.1 m in height, with a weight of 670 kgf. It is designed to

simulate the AHU installed in the catwalk level of TC Hospital. The floor height of this level is approximately 2.5 m. As this area is not a primary zone for human activity, there are no concerns regarding interference with personnel movement due to the presence of the suspended AHUs. Therefore, to enhance operational and maintenance accessibility, the suspension length of the test specimen was designed to be 1.9 m, positioning the equipment at an optimal working height. The construction details of the test specimen were identical to the actual site conditions in the hospital, ensuring the experimental results are practically relevant and applicable.

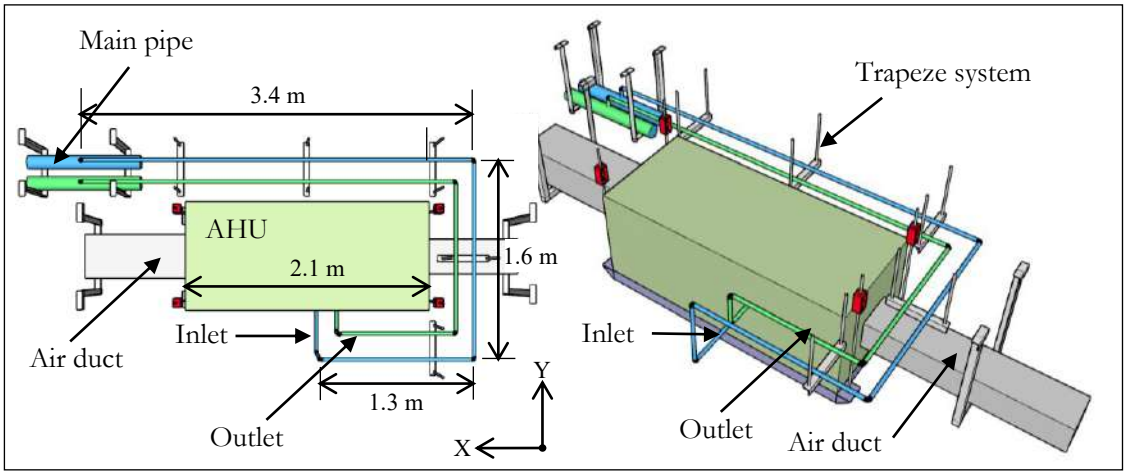


Figure 17. Test specimen of AHU on the second floor

Figure 17 shows the AHU test specimen installed on the second floor of the test framework. The specimen measures 2.1 m in length, 0.9 m in width, and 0.8 m in height, with a weight of 230 kgf. This specimen is used to simulate the suspended AHUs installed in building corridors at HL Hospital and DW University. To maximize usable interior space, suspended AHUs are typically installed as close as possible to the overhead slab. Accordingly, in alignment with actual site conditions, the suspension length of this specimen was designed to be 1.0 m for this test.

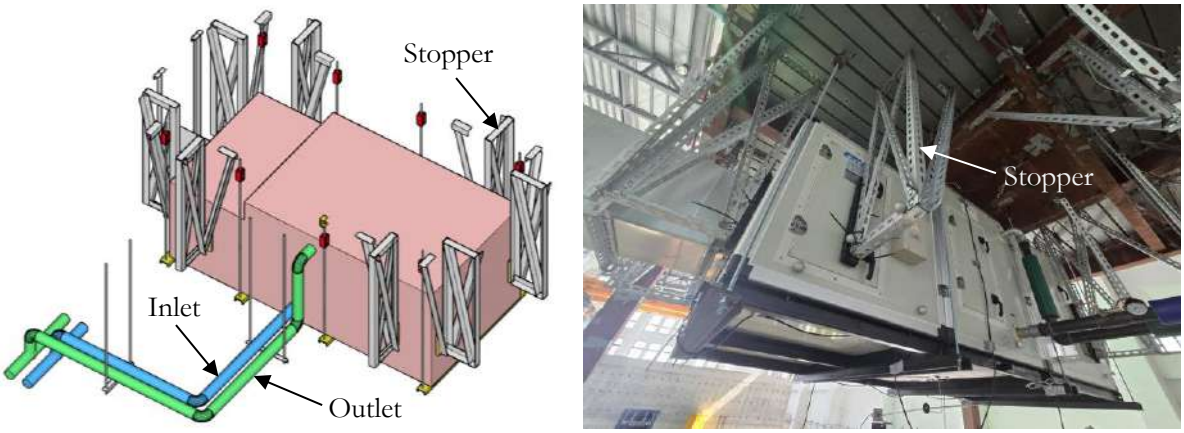


Figure 28. Test specimen of third-floor AHU with seismic stoppers

The test comprised two phases. The first phase tested the suspended AHUs equipped with seismic reinforcement measures, while the second phase excluded seismic protection to simulate the seismic response of the suspended AHUs under current practices. By comparing the results from both phases, this test aims to identify critical seismic damage characteristics and propose appropriate seismic strategies. Based on the reconnaissance survey, limiting the displacement of suspended AHUs is considered a rational approach for seismic strategy. For the AHU test specimen on the third floor, eight stoppers were installed

around the specimen, as shown in Figure 18. Each stopper measures 0.4 m in width and 1.6 m in height. The stoppers were constructed from L-shaped steel angles (50 mm × 50 mm × 5 mm) and were reinforced with diagonal bracing in both the in-plane and out-of-plane directions. A small clearance was intentionally maintained between the stoppers and the test specimen to avoid direct contact, thereby preventing the transmission of operational vibrations from the AHU to the floor above.

On the second floor, two diagonal cable wires were installed at each of the four corners of the test specimen for reinforcement, as illustrated in Figure 19. The cables, composed of 7×7 strands with an overall diameter of 3.2 mm, were arranged orthogonally and inclined at a 45° angle to the horizontal plane. During installation, no preload was applied. The cable wires were pulled taut just enough to eliminate any sagging, without inducing significant tension.

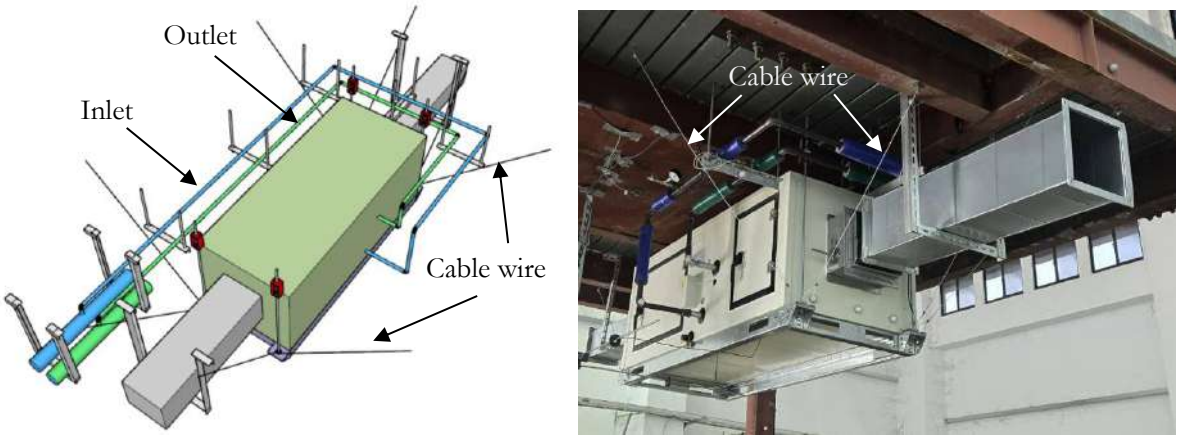


Figure 39. Test specimen of second-floor AHU with cable wires

3.2 INPUT MOTION

In this study, two ground motion records from the Hualien earthquake were selected as input motions for the shaking table tests. The first input motion was the ground acceleration time history recorded at ground level at TC Hospital (designated as HWA BA). Figure 20 illustrates the actual output signal of the shaking table corresponding to the HWA BA record. Tests were conducted sequentially at 25%, 50%, 75%, and 100% of the input motion intensity.

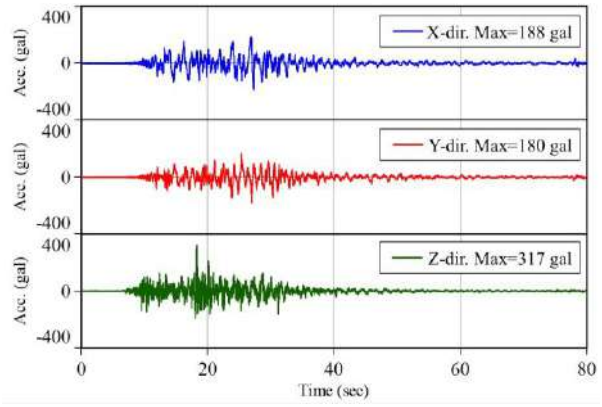


Figure 20. Output signal of 100% HWA BA

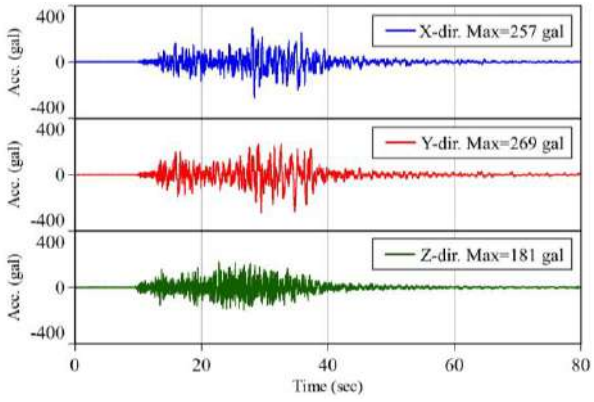


Figure 21. Output signal of 100% HWA 068

The second input motion was the ground acceleration time history recorded near DW University during the Hualien earthquake (designated as HWA 068). Figure 21 presents the actual output signal of the shaking table corresponding to the HWA 068 record. Tests were conducted sequentially at 33%, 66%, and 100% of the input motion intensity.

3.3 TEST RESULTS

The test results indicate that the suspended AHUs without seismic reinforcement experienced substantial displacement during testing, which led to various types of damage. These damage patterns closely corresponded with those observed in reconnaissance investigations. In contrast, while the suspended AHUs equipped with seismic reinforcements initially exhibited enhanced performance, the reinforcement measures progressively accumulated damage as the input motion intensity increased, ultimately resulting in a loss of seismic effectiveness.

During the tests, the AHU without seismic reinforcement experienced impacts against the suspension rods even at the lowest intensity level. As the input motion intensity progressively increased, the impacts became more frequent and severe, causing damage to the spring isolators (Figure 22), deformation of the suspension rods (Figure 23), and in some cases, complete shearing of the suspension rods, as illustrated in Figure 24.

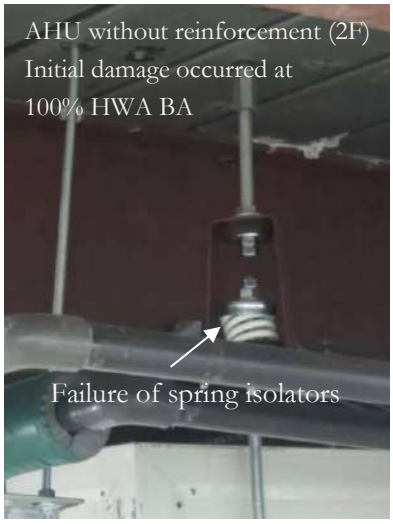


Figure 22. Failure of spring isolators

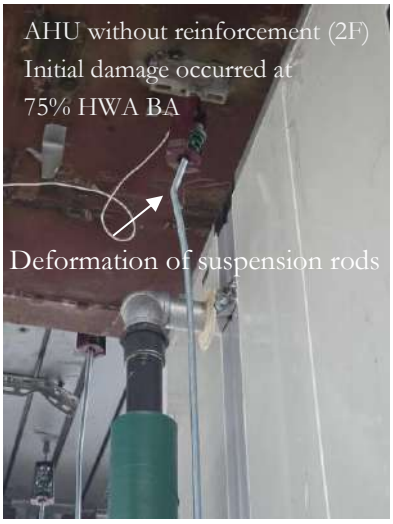


Figure 23. Deformation of rods



Figure 24. Failure of suspension rods

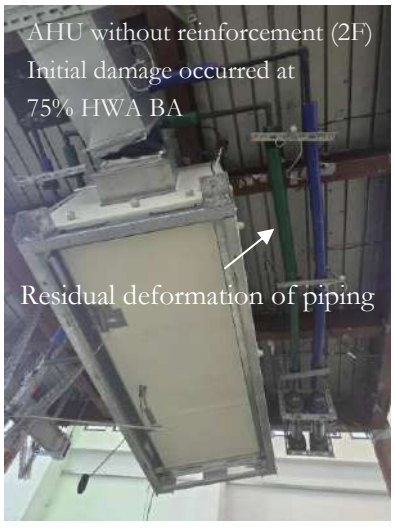


Figure 25. Deformation of piping

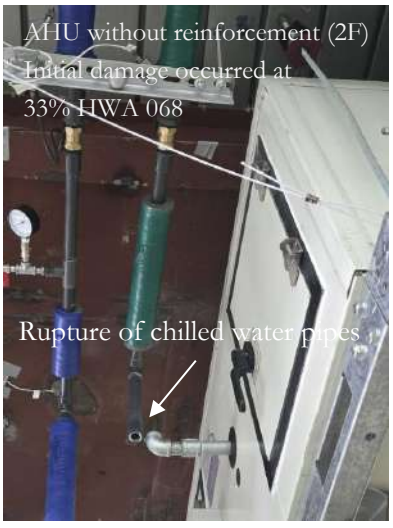


Figure 26. Rupture of water pipes



Figure 27. Rupture of water pipes

In addition to damage to the suspension rods, another major failure mode observed was damage to the chilled water pipes. When the AHU specimen experienced significant displacement, it collided directly with the chilled water pipes and the trapeze systems, resulting in large residual deformation of the piping, as

shown in Figure 25. In more severe cases, the connection between the chilled water pipe and the AHU completely fractured, as illustrated in Figure 26 and Figure 27.

The test results indicate that the seismic reinforcement measures evaluated in this study were effective during the lower-intensity stages of shaking table tests. However, as the input motion intensity increased, the reinforcement measures sustained progressive damage and ultimately led to a loss of seismic effectiveness.

For the AHU specimen on the third floor, the stoppers failed to fully achieve the intended strength and stiffness, primarily due to the connection design. The stoppers were constructed from L-shaped steel angles, secured with M12 bolts, and reinforced with in-plane and out-of-plane diagonal bracing to enhance stiffness and stability. However, the slotted hole connection between the in-plane bracing and the vertical members allowed the bolts to slip under lateral loads, as shown in Figure 28. This situation significantly reduced the in-plane shear resistance of the stoppers, leading to deformation into a parallelogram shape (Figure 29). As a result, gaps developed between the stoppers and the AHU, causing more frequent and forceful impacts. The increasing gap amplified the impact forces, ultimately causing severe damage to the stoppers, including anchor bolt pullout, as illustrated in Figure 30.



Figure 28. Slippage of bolts



Figure 29. Deformation of stoppers

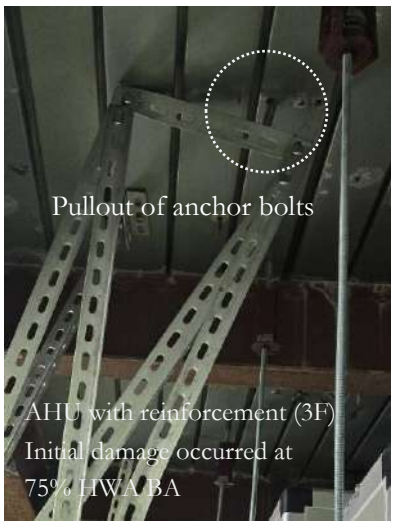


Figure 30. Pullout of anchor bolts



(a) **(b)**

Figure 31. (a) Cable wires before the tests; (b) Cable wires were found to be slack after the tests

For the AHU specimen on the second floor, the cable wires were not fully tensioned during installation, allowing slight displacement of th the AHU during low-intensity tests and resulting in minor impacts with

the suspension rods. As the input motion intensity increased, the cables gradually slackened and sagged, leading to more frequent collisions between the AHU, suspension rods, and chilled water pipes. As shown in Figure 31, by the end of the high-intensity test stage, the cable wires had become completely slack. This led to severe impacts between the AHU, suspension rods, and chilled water pipes, causing deformation of the rods and fracture of the chilled water pipes.

4. CONCLUSIONS

The test results demonstrate that excessive displacement leading to impact is the primary cause of seismic damage. During the tests, the suspended AHUs initially collided with the suspension rods. As the displacement increased, the AHU eventually struck the chilled water pipes, resulting in pipe rupture. Displacement data analysis revealed that the suspended AHUs experienced movements exceeding 500 mm.

Traditional seismic reinforcement methods that increase system stiffness are unsuitable for suspended AHUs because mechanical vibrations from the equipment can be transmitted directly to the floor above. This study confirms the effectiveness of both stoppers and cable wires as seismic reinforcement measures. However, stopper designs must carefully account for impact forces to ensure proper functionality. Additionally, cable wires should be regularly inspected, especially after significant seismic events, to prevent loss of effectiveness caused by excessive slackening.

REFERENCES

Construction and Planning Agency Ministry of the Interior [2022] *Seismic Design Specifications and Commentary of Buildings*, Construction and Planning Agency Ministry of the Interior, Taipei, Taiwan.

Wang, R. T., Wang, H. H. et al. [2018] *Reconnaissance report of seismic damages caused by the 6 February 2018 Earthquake, Hualien, Taiwan*, NCREE-18-005, National Center for Research on Earthquake Engineering, Taipei, Taiwan.

Sung, Y. C., Li, C. H. et al. [2010] *Reconnaissance Report on Jiaxian Earthquake in Kaohsiung on March 4, 2010*, NCREE-10-010, National Center for Research on Earthquake Engineering, Taipei, Taiwan.

Luo, J. X. et al. [1999] *Streamlined Reconnaissance Report of 921 Chi-Chi Earthquake (First Draft)*, NCREE-99-033, National Center for Research on Earthquake Engineering, Taipei, Taiwan.

Todd, D. R., Carino, N. J., Chung, R. M., Lew, H. S., Taylor, A. W., & Walton, W. D. [1994] *1994 Northridge Earthquake: Performance of Structures, Lifelines and Fire Protection Systems*, NISTIR 5396, National Institute of Standards and Technology, USA.

Innovative seismic isolation strategies for equipment and non-structural components: Experimental investigation and analytical modeling of systems isolated with spring-viscoelastic mounts (SPONSE 2026)

Ahmed Awad[1], Marco Simoncelli[1], and Claudio Bernuzzi[1]

[1]Politecnico di Milano, Department of Architecture, Built Environment and Construction Engineering
Milano, Italy
e-mail: {ahmed.awad,marco.simoncelli,claudio.bernuzzi}@polimi.it

Abstract. Seismic events pose major challenges to the integrity and safety of critical infrastructure. Ensuring the uninterrupted functionality of lifeline facilities, such as hospitals, data centers, and industrial plants, requires safeguarding essential systems during and after earthquakes. In this context, the protection of non-structural components, including HVAC equipment, generators, and UPS systems, is fundamental to operational continuity. As shown by Taghavi and Miranda [2003], non-structural damage can dominate earthquake-induced economic losses, reaching 82% in office buildings, 87% in hotels, and 92% in hospitals. Reducing these vulnerabilities is therefore central to both resilience and service continuity.

In the previous study, Awad et al. [2024] investigated the seismic performance of an industrial chiller equipped with spring anti-vibration mounts through triaxial shaking table tests. Displacement, acceleration, and frequency response were measured in accordance with established seismic qualification standards, namely ICC-ES AC156 [2010], IEEE Std 693 [2018], and IEC 60068-3-3 [2019], and complementary analytical models were developed to reproduce the behavior of vibration-isolated equipment with flexible connections.

Building on this evidence, a novel seismic isolation system is proposed, combining induced tilting mechanisms with viscoelastic fluid dampers. Spring-viscoelastic anti-vibration mounts, traditionally applied to heavy machinery, are adapted here for lighter equipment (<10 tons). Unlike ball bearings or PTFE sliders, the system provides vertical restraint while preserving isolation efficiency under high deflections. The use of polyisobutylene fluid ensures effective low-frequency damping, thereby improving vibration control and reducing seismic demands.

Keywords: Seismic isolation, Non-structural Elements, Spring-viscoelastic mounts, Seismic qualification, Infrastructure resilience

1. INTRODUCTION

Seismic events pose a major threat to the operational continuity of lifeline facilities such as hospitals, data centers, and industrial plants. Beyond structural safety, the functionality of non-structural systems such as heating, ventilation and air conditioning (HVAC) units, generators, and uninterruptible power supply (UPS) systems is essential during and after earthquakes. As shown by Taghavi and Miranda [2003], failures in these components often cause severe disruptions and economic losses, with surveys indicating that non-structural damage accounts for up to 92% of costs in hospitals, while structural repairs represent only a minor share. Despite advances in seismic qualification and standards such as IEEE Std 693-2018 [IEEE, 2018], ICC-ES AC156 [ICC-ES, 2010], and IEC 60068-3-3 [IEC, 2019], current solutions remain limited in addressing vertical constraints and ensuring both vibration and seismic isolation. In a previous study, Awad et al. (2024) evaluated the seismic response of an industrial chiller with spring anti-vibration mounts through triaxial shaking table tests. Based on the research outcomes, this paper introduces a novel isolation strategy that combines spring viscoelastic mounts with induced tilting mechanisms and polyisobutylene dampers, adapted for lighter equipment (<10 tons). The objective is to enhance the seismic protection of vibration-isolated equipment through combined experimental and analytical investigations within international standards, and to propose a scalable solution for improving the resilience of non-structural components in critical facilities. To frame this new strategy, it is first necessary to discuss the state of the art of spring–viscoelastic anti-vibration mounts, since they represent the technological foundation of the proposed system and provide the background for their adaptation into seismic isolators for light equipment.

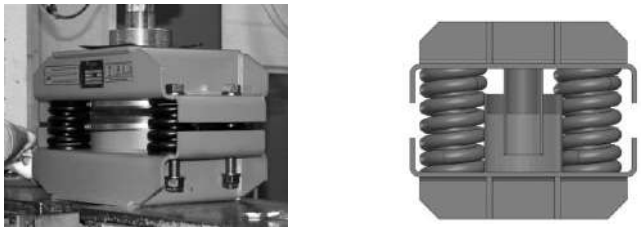


a) b)

Figure 1. Experimental setup: (a) tested equipment; (b) triaxial shake table [EUCENTRE Laboratories, n.d.].

Spring-viscoelastic anti-vibration mounts are widely used in industrial settings to mitigate vibrations in heavy machinery, such as presses, nuclear turbines, and heavy piping systems. These mounts effectively absorb and dissipate intense vibrational forces, thereby ensuring operational stability and extending the lifespan of machinery. While their benefits in seismic applications are well recognized, their primary application is in industrial environments where accurate vibration control is crucial for maintaining machine alignment and performance. Additionally, spring-viscoelastic anti-vibration mounts are utilized to protect civil structures from train-induced vibrations. This study specifically explores their adaptation as seismic isolators for light equipment, assessing both their potential and the design requirements for an economical and scalable solution.

A spring–viscoelastic anti-vibration mount combines steel spring elements with a viscous damping mechanism. The structural steel housings, designed in accordance with EN 1993-1-1 [CEN, 2005], contain helical compression springs arranged according to the required load capacity. Positional stability and shear transfer are ensured by spring guides welded to the housing, with springs placed individually or in nested rows. The damping system consists of a cylindrical piston moving within a fluid-filled pot. As the piston displaces, the viscous medium, typically bituminous or polymeric, undergoes shear deformation and produces velocity-dependent damping forces. A distinctive property of this isolator is its frequency-dependent response: the damping coefficient is relatively high at low frequencies, improving seismic energy dissipation, but decreases significantly above 10 Hz as shown by Makris and Constantinou [1992], thus minimizing its influence on operational vibration isolation.



a) b)

Figure 2. Spring viscous damper: (a) product by LISEGA [Vicoda Lisega, n.d.]; (b) simplified sectional drawing

Currently, there is no unified standard for spring anti-vibration mounts with viscoelastic dampers. However, UNI EN 15129 [UNI, 2018] serves as a valuable reference for characterizing their damping properties. Spring anti-vibration mounts can be evaluated using the test protocols outlined for fluid viscous dampers (FSD). Another relevant standard for dynamic testing is UNI 11059 [UNI, 2003]. This standard provides comprehensive guidelines for elastomeric mats used in railway and tramway tracks. It outlines procedures for dynamic testing, focusing on the control of force and displacement. The standard serves as a crucial reference for assessing the dynamic properties and damping properties. Table 1 reports the reference standards used to assess the mechanical properties of spring anti-vibration mounts.

Table 1. Reference standard of spring anti-vibration mounts with viscoelastic damping

No	Mechanical properties	standard
1	Vertical stiffness	EN 13906-1 [CEN, 2013]
2	Vertical load-bearing capacity	EN 13906-1 [CEN, 2013]
3	Horizontal stiffness	EN 13906-1 [CEN, 2013]
4	Horizontal load-bearing capacity	EN 13906-1 [CEN, 2013]
5	Vertical and horizontal damping parameters	-

Viscoelastic spring dampers typically use three classes of media, each with characteristic thermal and rheological behavior:

- Bituminous viscoelastic compounds provide high loss factors within a practical service window of about 10–40 °C; specialized grades can remain effective up to about 80 °C.
- Polyisobutylene oils deliver intermediate loss with tunable viscosity and a broad operating range from roughly −10 to 180 °C; they exhibit low volatility and good compatibility with elastomeric seals.
- Silicone oils offer lower loss but excellent thermal stability and a very wide operating range from about −45 to 200 °C, together with relatively modest viscosity–temperature sensitivity.

For the proposed isolator, a polyisobutylene-based medium was selected to achieve the target damping, to ensure viscosity stability across service temperatures, and to maintain long-term material compatibility. Effective damping depends on both viscosity and damper geometry. It must balance vibration isolation with seismic protection. High damping improves behavior near resonance but reduces isolation efficiency at higher frequencies; therefore, it is desirable to have low damping when $fd/fn > \sqrt{2}/2$, where f_d is the operating (driving) frequency of the unit and f_n is the natural frequency of the isolated system. The damping medium should therefore provide low coefficients at operating frequencies and higher ones at seismic frequencies to limit displacements and enhance seismic safety. In summary, this paper presents and validates a novel seismic isolation system that addresses a key deficiency: conventional anti-vibration solutions for light and medium-weight equipment ensure vibration control but lack sufficient seismic protection. The proposed approach combines spring–viscoelastic mounts with induced tilting mechanisms and

polyisobutylene dampers. After introducing the strategy and applying it to a representative case study, the paper outlines the design principles, describes the prototype and its testing, and validates the results through dynamic simulations. The research outcomes confirm the effectiveness of the method and its potential as a cost-effective and scalable solution to improve the seismic resilience of critical vibration-isolated equipment.

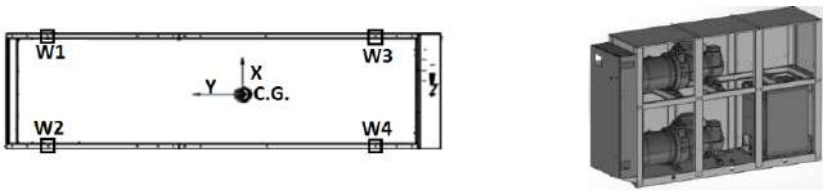
2. NOVEL SEISMIC ISOLATION METHOD FOR EQUIPMENT

2.1 CASE STUDY: DYNAMIC RESPONSE OF SPRING-ISOLATED EQUIPMENT

In the aforementioned study, the authors tested an industrial chiller on the EUCENTRE triaxial shake table [EUCENTRE Laboratories, n.d.] in accordance with ICC-ES AC156 [ICC-ES, 2010]. The main characteristics of the unit are summarized in Table 2 and Table 3

Table 2. Geometric and mass properties of the tested chiller specimen.

Mass m [kg]	Length L [mm]	Width b [mm]	Height H [mm]	CG Height H_g [mm]
3350	3401	808	2118	1215



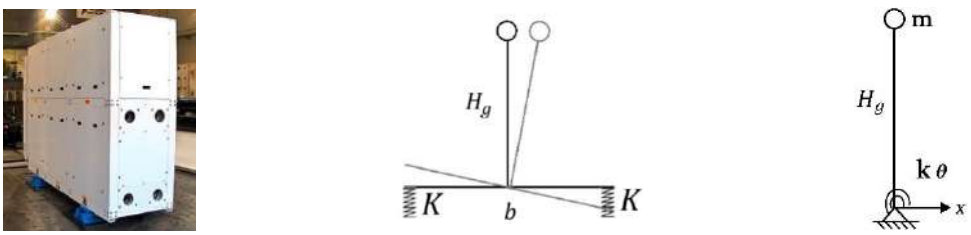
a) b)

Figure 3. (a) Top view of the unit with reference axes highlighted (b) tested chiller 3d model

Table 3. Static load distribution, vertical stiffness, and spring static deflection of the chiller supports.

	W1	W2	W3	W4	Total
Static Load [kg]	626	626	1049	1049	3350
Vertical Stiffness [N/mm]	525	525	883	883	2816
Static Spring Deflection [mm]	11.7	11.7	11.6	11.6	

During testing, differential compression of the isolation springs induced a rotational tilt of the unit along its longitudinal axis. This behavior was attributed to the combined influence of the high flexibility of the vibration mounts and the elongated geometry of the unit along the y-axis. Consequently, the system was modeled as a beam with a concentrated mass supported by two axial springs (Fig. 4b).



a) b) c)

Figure 4. (a) tested chiller (b) beam with axial springs (c) beam with rotational spring

The model was further simplified as a pinned beam with a concentrated mass and a base rotational spring (Fig. 4c). A dynamic analysis in SAP2000 [CSI, 2024] used the shake table time-history in the x-direction. The mechanical model consists of a simply supported rigid beam with a rotational spring and a concentrated mass representing the chiller, assumed rigid relative to the mounts. Accelerations at the center of gravity were extracted from the FEM model. Comparison with accelerometer data showed good agreement, confirming that the simplified model can reproduce the experiments and provide reliable predictions of the amplification factor for equipment isolated with flexible mounts.

2.2 CONCEPT AND DESIGN PRINCIPLES

Building on the findings reported in Awad et al. [2024], a novel methodology is proposed to isolate mechanical vibrating units through controlled tilting along their most vulnerable axis. This increases the vibration period and reduces seismic demand. Tilt amplitudes are controlled, and overturning is prevented, by a viscoelastic damping medium. The approach, intended for HVAC equipment, transformers, and generators, employs specially developed spring viscoelastic anti-vibration mounts with containment structures, tested in accordance with ANSI/ASHRAE 171-17 [ASHRAE, 2017].

The implementation follows three main phases:

- **Dynamic Analysis:** Determine the most critical tilt direction; reduce the natural frequency by adjusting spring stiffness; evaluate tilt and deflection under seismic loading; estimate critical and target damping; select a viscoelastic damper (tuned via pipe diameter to achieve the required damping coefficient); and perform seismic analysis with restraints modeled as links of suitable constant stiffness and frequency-dependent damping;
- **Vibration Analysis:** Assess vibration isolation using the combined spring stiffness and viscoelastic damping at the main excitation frequency. A one-degree-of-freedom (1DOF) mass–spring–damper model is employed to provide an effective approximation of isolation performance;
- **Static Analysis:** Apply equivalent seismic forces at the center of gravity to compute restraint loads. Design or select the structural components and bolts of the anti-vibration mounts in compliance with ANSI/ASHRAE 171-2017 [ASHRAE, 2017] to ensure adequate strength under seismic actions.

2.3 APPLICATION OF THE NOVEL METHODOLOGY FOR THE CASE STUDY

To enable a comparison of simulation results with the triaxial seismic test performed, the Test Response Spectrum (TRS) of the test was utilized. This TRS was derived by applying Fourier Transform directly to the accelerograms recorded at the center of the seismic table.

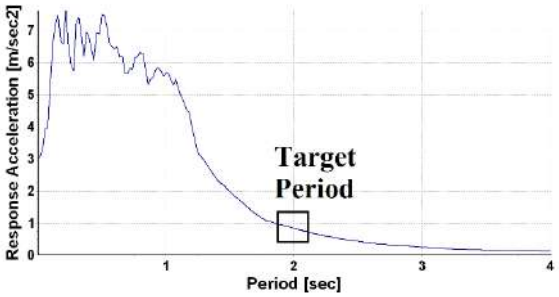


Figure 5. X-direction Test Response Spectrum (TRS)

The most vulnerable direction for the unit is the tilting along the y-axis. This motion is attributed to the high flexibility of the mounts and the unit's predominant dimensions along the y-axis. The first step of the

proposed methodology is to identify a target stiffness to reduce the acceleration zone of the required response spectrum. The target period of 2 s is selected because, as shown in Figure 5, the spectral acceleration decreases to 0.8 m/s² instead of the 7 m/s² plateau at shorter periods. Lower periods would impose much higher acceleration demand, while higher periods would lead to large displacements and require impractically tall springs. Thus, 2 s provides the most balanced design choice. The target stiffness K is calculated by combining the following equations derived from the simplified beam model with a rotational spring.

$$\omega_n = \sqrt{\frac{k_\theta}{\left(m * {H_g}^2\right)}} \tag{1}$$

$$\omega_n = \frac{2\pi}{T} \tag{2}$$

$$k_\theta = \frac{K*b^2}{2} \tag{3}$$

Where: m: Mass of the unit
b: Distance between the anti-vibration mounts in the x direction
k_θ: Equivalent rotational stiffness of the simplified model presented in figure 4
K: Target Total stiffness of the mounts on one side
T: Target period of the isolated unit (2s)
H_g: Height of center of gravity, Hg=1.5 m (1.215 m+design mount height)

It is therefore possible to obtain the following equation:

$$K = \frac{8 * m * {H_g}^2 \pi^2}{b^2 T^2} \tag{4}$$

In the case study, the target stiffness was defined as 227 kN/m for the pair of anti-vibration mounts, corresponding to 113 N/mm for each mount. The first three vibration modes of the unit, when isolated with this target stiffness, are reported in Table 4.

Table 4. Data on the three vibration modes of the chiller with the proposed seismic isolation mounts.

Mode	Frequency [Hz]	Description
1	0.6	Primary tilting frequency
2	1.3	Secondary tilting frequency
3	1.8	Vertical anti-vibration motion

A fundamental step in this methodology is the evaluation of the critical damping c_{crit}. For the first vibration mode, it can be expressed as:

$$c_{crit,1} = 2 * m * \omega_{n,1} = 25.3\ kNs/m \tag{5}$$

A target damping of 60% of the critical value is adopted to avoid overdamping while ensuring sufficient motion to fully activate the energy dissipation capacity of the isolators. Damping ratios approaching the critical level would increase the energy dissipated per cycle but simultaneously amplify transmitted forces. As the stiffness of the tested dampers is significantly lower than that of the external spring, the damping is expressed as a frequency-dependent modal parameter.

$$c_{target,1} = \frac{0.6 * c_{crit}}{4} = 3.8 \ kNs/m \quad (6)$$

3. PROTOTYPE TESTING OF VISCOELASTIC FLUID DAMPERS

The design and experimental evaluation of a prototype viscoelastic fluid spring damper are herein described, which has been developed according to the target parameters defined in the previous analysis.

3.1 PROTOTYPE DESIGN

The spring has been designed to meet the following specifications:

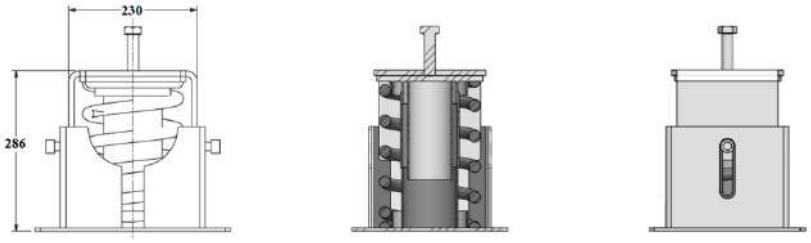
- An internal diameter of 140 mm to accommodate the installation of the viscoelastic fluid damper.
- A solid spring deflection of 140 mm to allow additional travel during seismic forces
- A stiffness of 103 N/mm.

Table 5 presents the main data on the prototype spring, manufactured by Soleco Engineering [Soleco Engineering, n.d.] and designed according to EN 13906-1:2013 [BSI, 2013].

Table 5. Prototype spring parameters

Stiffness [N/mm]	Internal Diameter [mm]	Working Deflection [mm]	Free Length [mm]	Solid Spring Deflection [mm]	Horizontal Stiffness [mm]
103	140	80	260	147	96

The prototype structure was designed according to the requirements of the previous section. The main function of the external structure is to be able to withstand the static seismic force and to accommodate the spring and the internal damper. The anti-vibration mount is designed to allow rotation of the lid around the axis obtained connecting the 2 lateral bolts. Drawings for all components were prepared using SolidWorks.



a) b) c)

Figure 6. Proposed anti-seismic viscoelastic fluid damper: (a) front view; (b) sectional view; (c) lateral view

The internal Viscoelastic damper was designed for a spring with 80 mm static deflection and an additional dynamic deflection of ±15 mm. A 3D-printed prototype was prepared for a test campaign, featuring internal cylinders constructed from cut plexiglass tubes.

3.2 EXPERIMENTAL SETUP

The proposed internal damper for the seismic isolator was tested using a HUD030-11 [STEP Lab, n.d.] electrodynamic testing machine.



a (b) c)

Figure 7. (a) HUD030 [STEP Lab, n.d.] (b) prototype structure of the viscoelastic fluid damper (c) prototype testing

The 3D-printed prototype was filled with polyisobutylene. To facilitate the filling process, a heating band was applied, since at room temperature the compound's viscosity was difficult to manage.

3.3 EVALUATION OF THE DAMPING COEFFICIENT

Tests were performed under displacement control, imposing a sinusoidal function $x(t) = A\sin(\omega t)$ with prescribed amplitude A at a predefined frequency. Assuming a linear viscous model $F_d(t) = c\,\dot{x}(t)$, the energy dissipated per cycle E is

$$\mathrm{E} = \oint F_d \,\mathrm{dx} = \int_0^{\mathrm{T}} c\,\dot{x}^2 \,\mathrm{dt} = \frac{1}{2}\,\mathrm{c\,A^2\omega^2\,T} = \pi\,\mathrm{c\,A^2\omega} \tag{7}$$

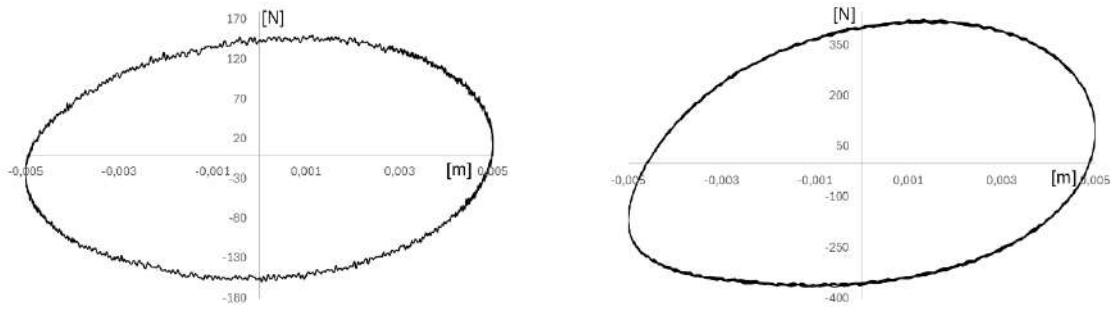
The (equivalent) viscous damping coefficient, c, is therefore determined as:

$$c = \frac{E}{\pi A^2\,\omega} \tag{8}$$

Where E is the energy dissipated over one cycle corresponding to the area of the hysteretic loop

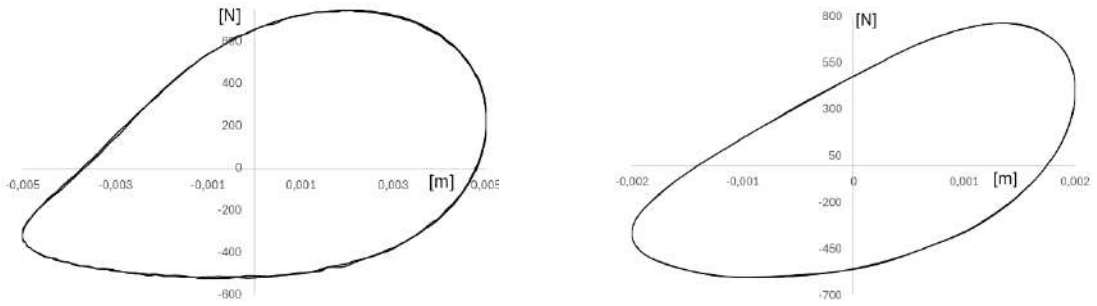
3.4 RESULTS AND DISCUSSION

Dynamic tests were carried out on the 3D-printed prototype under displacement control, with amplitudes of ±5 mm at frequencies near the natural modes identified by the modal analysis, and with a reduced amplitude of ±2 mm at the operating frequency of 15 Hz, representative of the unit's service conditions.



a) b)

Figure 8. Hysteretic Loop (a) 0.5 Hz applied displacement ±5 mm (b) 1.5 Hz applied displacement ±5 mm



a) b)

Figure 9. Hysteretic Loop (a) 3 Hz applied displacement ±5 mm (b) 15 Hz applied displacement ±2 mm

Table 6. Frequency-dependent damping coefficients from experimental results

	0.5 Hz	1.5 Hz	3 Hz	15 Hz
Damping coefficients [Ns/m]	9533	8116	5716	2260

This assessment showed that the damping coefficient at 15 Hz is markedly lower than at seismic frequencies. Consequently, the damping medium has only a limited effect on vibration isolation at the operating frequency, thereby ensuring seismic protection while maintaining effective operational isolation. The experimentally derived values in Table 6 were reduced by a factor of three in the analytical model to prevent overdamping. These values were then interpolated to evaluate the damping contribution of each vibration mode. Future work will address geometric adjustments of the damper diameter to achieve the target values, which the experimental preliminary campaign has confirmed to be attainable with the selected medium.

Table 7. Damping coefficients adopted in the dynamic analysis

Mode	Frequency [Hz]	Damping per Isolator [kNs/m]	Total Damping (4 Isolators) [kNs/m]	Critical Damping [kNs/m]	Modal Damping [%]
1	0.6	3.1	12.5	25.2	50
2	1.3	2.8	11.2	54.7	20
3	1.8	2.6	10.4	75.7	13

4. DYNAMIC SEISMIC SIMULATION AND VIBRATION ANALYSIS

4.1 DYNAMIC SIMULATION

A simplified three-dimensional model of the chiller was reconstructed in SAP2000 [CSI, 2024], with the anti-vibration mounts modeled as link elements. The total mass of the chiller was applied at the center of gravity, and a modal linear time-history analysis was performed using the three accelerometer records from the experimental setup. In this approach the natural vibration modes of the system are first determined, the earthquake records are applied in the time domain to each mode, and the resulting modal responses are superimposed to obtain the overall structural behavior.

The analysis was performed for both mounting configurations: the proposed isolation system and the standard mounts previously tested on the triaxial seismic table, with stiffness properties summarized in Table 3. For the standard mounts, a uniform modal damping ratio of 3% was adopted, consistent with the behavior of steel spring isolators with minimal elastomeric components integrated into the mount. For the proposed mounts, mode-dependent damping ratios were considered, as reported in Table 7.

Table 8 compares the accelerations measured at the unit's center of gravity with the corresponding SAP2000 [CSI, 2024] results at the same location.

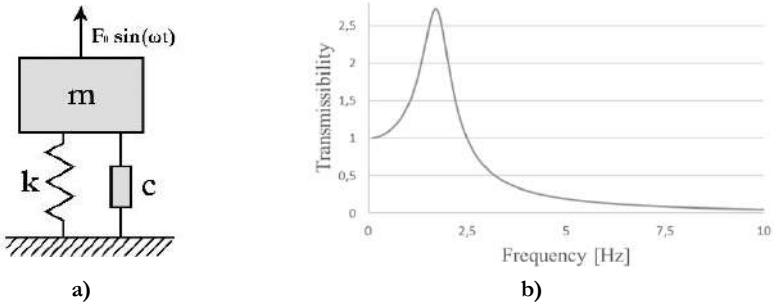
Table 8. Peak C.O.G. accelerations: measured and analytical (standard mounts) and analytical (improved mounts)

	x [m/s²]	y [m/s²]	z [m/s²]
Seismic test with standard vibration mounts (measured)	7.4	4.7	3.9
Time-history analysis with standard anti-vibration mounts	8.1	4.9	3.5
Time-history analysis with improved anti-vibration mounts	1.1	2.5	1.8

The dynamic vertical deflection of the prototype spring remained within ±30 mm in all seismic time-history analyses, safely inside the operating range defined by the solid-height deflection in Table 5, thereby ensuring full functionality and operability of the isolator.

4.2 VIBRATION ANALYSIS

In standard operating conditions, the unit exhibits a dominant forcing frequency of 15 Hz. Figure 10 shows the vertical transmissibility function of the forced spring mass damper system, evaluated using the spring stiffness reported in Table 5 and the damping ratio evaluated at 15 Hz. The analysis indicates that the system achieves an isolation efficiency of approximately 98% at the operating frequency. Therefore, the introduced damping medium does not compromise the isolation performance.



a) b)

Figure 10. (a) Schematic of the forced spring–mass system; (b) theoretical transmissibility curve for the case study

5. CONCLUDING REMARKS AND FUTURE DEVELOPMENTS

Dynamic tests and numerical simulations validated the proposed methodology, showing that its correct implementation improves both vibration control and seismic isolation of equipment supported on spring anti-vibration mounts. The results demonstrated substantial reductions in peak accelerations, ranging from about 50% to 85% compared with conventional supports. These outcomes also emphasize the need for a dynamic analysis for spring-isolated equipment, as the equivalent lateral force procedure prescribed by most building codes fails to capture their true seismic response. Future work will address improved damper modeling through an exponential Maxwell formulation for direct-integration analysis, capable of capturing the variation of damping with the dynamic deflection of the spring. In this study, the modal time-history analysis represented the damper by a fixed damping ratio at each vibration mode evaluated at a reference deflection, an assumption that does not reflect the wide range of deflections occurring in actual operation. Additionally, further developments will include a dedicated experimental campaign on a triaxial shake table to validate the proposed methodology, thereby advancing the seismic protection of vibration-isolated equipment.

ACKNOWLEDGMENT

The authors gratefully acknowledge the financial support of Soleco Engineering [Soleco Engineering, n.d.], which contributed to the PhD research activities and the execution of the experimental test campaign.

REFERENCES

ASHRAE [2017] *ASHRAE 171-17 – Test Method for Seismic Restraint Devices for HVAC&R Equipment*, American Society of Heating, Refrigerating and Air-Conditioning Engineers, Atlanta, GA, USA.

Awad, A., Bernuzzi, C., Simoncelli, M. [2024] "Seismic characterization of chillers with vibration isolation systems," *Proceedings of the XXIX Congresso CTA*, Milan, 26–28 September 2024, pp. 421–428.

CEN [2013] EN 13906-1:2013 Cylindrical helical springs made from round wire and bar – Calculation and design – Part 1: Compression springs, European Committee for Standardization (CEN), Brussels, Belgium.

CEN [2005] EN 1993-1-1 Eurocode 3: Design of steel structures – Part 1-1: General rules and rules for buildings, European Committee for Standardization (CEN), Brussels, Belgium.

CSI [2024] SAP2000, Computers and Structures Inc., Version 23.3.1.

EUCENTRE Laboratories [n.d.] Official website. Available at: https://www.eucentre.it/laboratori-eucentre/

ICC-ES [2010, editorial revision 2012] *AC 156: Acceptance Criteria for Seismic Certification by Shake-Table Testing of Nonstructural Components*, International Code Council Evaluation Service, USA.

IEEE [2018] IEEE Std 693-2018 – *Seismic Design of Substations*, Institute of Electrical and Electronics Engineers, New York, USA.

IEC [2019] IEC 60068-3-3: Seismic Test Methods for Equipment, International Electrotechnical Commission.

Makris, N., Constantinou, M.C. [1992] Experimental study and analytical prediction of response of spring viscous damper isolation system, *Proceedings of the 10th World Conference on Earthquake Engineering*, SUNY, USA.

Soleco Engineering, official website, available at: www.solecosrl.com

SolidWorks [2024] SolidWorks, Dassault Systèmes, Version 2024, available at: https://www.solidworks.com

STEP Lab -HUD030 – High Dynamic Testing System. Available at: www.step-lab.com

Taghavi, S., Miranda, E. [2003] *Response assessment of nonstructural building elements*, PEER Report 2003/05, University of California, Berkeley, USA.

UNI [2003] UNI 11059: *Antivibrating elements – Elastomeric mats for railway/tramway tracks – Qualification and check tests to determine their mechanical characteristics and performance parameters*, Ente Italiano di Normazione (UNI), Italy.

UNI [2018] UNI EN 15129: *Anti-seismic devices*, Ente Italiano di Normazione (UNI), Italy.

Vicoda Lisega, official website, available at: www.lisega.de

Low-Carbon Resilient Curtain Walls: Experimental Study of Timber-Glass Unitized Systems

Simona Bianchi [1], Guido Lori [2], Jonathan Ciurlanti[3], Giovanni Milan[3], Nebojša Buljan[2]

[1] Delft University of Technology, Delft, The Netherlands
s.bianchi@tudelft.nl

[2] Permasteelisa S.p.A., Vittorio Veneto, Italy
{g.lori, n.buljan}@permasteelisagroup.com

[3] Arup, Amsterdam, The Netherlands
{jonathan.ciurlanti, giovanni.milan}@arup.com

Abstract. Unitized curtain walls typically cover most of the building façade, accounting for a large portion of both construction costs and embodied carbon emissions. In these systems, replacing malfunctioning glazing units can substantially increase the cumulative embodied energy and carbon footprint of the façade. Preventing functional loss and damage to these components is therefore critical, especially in seismic-prone regions. This requires the development of low-carbon resilient systems that reduce post-earthquake monetary losses, safeguard public safety and meet broader sustainability goals.

This research investigates the potential of structural sealant-glazed systems with timber framing for seismic applications. Full-scale mock-ups were subjected to quasi-static cyclic and dynamic loading to assess their seismic performance at both serviceability and ultimate limit states, including the analysis of damage progression up to failure. The results demonstrate the high seismic resilience of the tested façade units, further validated by numerical simulations used to derive fragility curves for risk assessment. The study also compares the structural, energy and environmental performance of the timber-glass configuration with a conventional aluminium-glass solution, confirming engineered timber as a viable and sustainable alternative for high-performance curtain wall applications.

Keywords: Curtain Wall, Seismic Resilience, Timber-Glass, Experimental Testing, Damage.

1. INTRODUCTION

Curtain walls contribute significantly to the environmental impacts of buildings, primarily due to their reliance on energy-intensive materials such as aluminium, high-performance glass, insulation and sealants. These systems can account for up to 30% of a building's total embodied carbon emissions [Hartwell *et al.*, 2021]. Growing awareness of energy efficiency and sustainability has recently led to the exploration of wood as an alternative framing material for building envelopes. Currently, the market remains dominated by aluminium-framed curtain wall systems. Hybrid solutions that combine structural timber with aluminium profiles have been introduced; however, these often limit the structural potential of timber. In such systems, aluminium profiles are used to anchor the curtain wall and shield timber from exterior exposure, reducing the role of timber to a secondary material. An emerging alternative is the use of timber-glass composite profiles, where glass panes are adhesively bonded to timber structures without aluminium carrier. These unitized timber envelope systems have demonstrated the potential to reduce embodied carbon by up to around 50% compared to conventional unitized curtain walls, primarily due to timber's biogenic carbon storage [Alabdulrazzaq *et al.*, 2025].

In addition to its environmental benefits, timber offers an excellent strength- and stiffness-to-weight ratio, making it a reliable option for load-bearing applications and particularly advantageous in seismic environments. Its tensile, compressive and bending strengths, combined with its relatively low weight, provide clear structural benefits. Furthermore, as a lightweight material with low thermal conductivity, timber delivers superior thermal performance compared to aluminium, while also enhancing interior spaces through its natural warmth and aesthetic appeal [Georgoulopoulou, 2022]. Building on these properties, the timber-glass system has been proposed as an innovative structurally glazed curtain wall concept, entirely composed of glued-laminated timber profiles within a fully prefabricated unitized design. By eliminating aluminium elements, the system preserves high levels of weathertightness while leveraging timber's inherent advantages, thus achieving environmental, structural and aesthetic performance that equals (or even exceeds) that of conventional aluminium curtain wall systems [Buljan *et al.*, 2015; Buljan *et al.*, 2017].

Throughout the service life of curtain walls, the replacement of malfunctioning glazing units has a significant impact on the cumulative embodied energy and carbon of the façade. It is therefore crucial to prevent functional loss and damage to these components, particularly in seismic-prone regions. Over the past decade, research has increasingly focused on understanding the seismic behavior of curtain walls through analytical, experimental and numerical studies, as discussed in Huang *et al.* [2017]; Bianchi and Pampanin [2022]; Momeni and Beton [2024]. Recent works have also investigated the expected damage patterns of unitized systems, which are affected by inter-story drift ratios and inertial forces during seismic movements. These studies consistently demonstrate that structural sealant glazing systems outperform dry-glazed systems with mechanical restraints, as they can accommodate larger drift levels before reaching equivalent damage states [Bianchi *et al.*, 2024]. However, existing research has focused primarily on conventional aluminium-glass facades, leaving the seismic performance of timber-glass solutions largely unexplored. In particular, no seismic studies have been conducted on the newly proposed timber-glass unitized walls designed without an intermediate aluminium carrier.

This study contributes by examining the seismic behaviour of such solution and comparing its performance with conventional aluminium-glass systems. Experimental seismic tests were carried out at the Permasteelisa facility in Vittorio Veneto, Italy, to evaluate the response of full-scale façade specimens, with focus on post-earthquake serviceability under low-intensity motions and damage progression up to collapse. A comprehensive testing protocol was defined, including water-resistance tests, quasi-static and dynamic experiments. This paper presents an overview of the test setup and summarizes the key findings obtained from data analysis and damage observations. The experimental findings were benchmarked against numerical simulations, used to estimate the probability of reaching or exceeding a certain damage state given a specific drift ratio (i.e, to derive fragility curves). These results were also compared with previously reported

outcomes for conventional aluminium-glass curtain walls, enabling an initial assessment of structural, thermal and carbon-related trade-offs between the two façade concepts.

2. PERFORMANCE ASSESSMENT

2.1 SPECIMEN DETAILS

A timber-glass curtain wall, with 1500 mm x 3600 mm unit dimensions, was used for the full-scale mock-up (Figure 1). The façade, a 10-year-old system stored at the Permasteelisa factory, had originally been developed as part of a research project [Buljan *et al.*, 2015; Buljan *et al.*, 2017]. The project goal was to design a fully unitized curtain wall system with 0% aluminium content, while maintaining the same frame width as an equivalent aluminium system. It was required to achieve structural properties and load bearing capacity equal to or greater than aluminium, provide equal or improved weather tightness, superior energy performance and adequate durability.

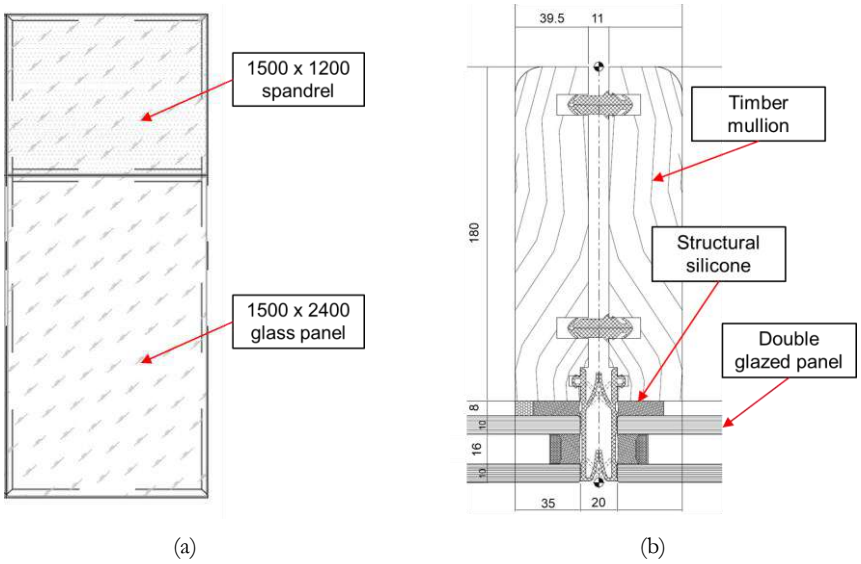


Figure 1. (a) Unit and (b) section detailing, with dimensions in mm

The units employ split mullions, which in conventional aluminium framing are designed to be slim, ensuring aesthetically narrow sight lines. The system was designed to withstand a wind pressure of 2 kPa. The allowable lateral deflection under design load was considered in accordance with EN 13830 [2003], and the timber frame elements were engineered to match the stiffness of an equivalent aluminium system. This required an increase in system depth of approximately 30% to achieve comparable structural performance. Further improvements in the mechanical properties of the timber profiles were achieved through spatial lamination [Turkulin, 2013]. The glass panels were bonded to the timber frame using a two-component structural silicone (Sikasil SG500, 25mm bite). For the connection detailing, the façade design allows horizontal reactions from upper units to be transferred to lower units through the stack joint using bespoke corner spigots in stainless steel 1.4404 [Buljan *et al.*, 2015].

2.2 TEST SETUP

The experiments were carried out at the Permasteelisa facility in Vittorio Veneto, Italy, where façade prototypes were mounted on an existing steel support frame consisting of upper and lower fixed beams and an intermediate moving beam, as described in Bianchi *et al.* [2025]. Three testing phases were conducted,

each involving units with identical properties but different layouts (one- or two-storey configurations), as illustrated in Figure 2. Phase 1 investigated the in-plane seismic performance of a two-storey façade (with units U1-U4), focusing on the behaviour of the vertical units' connection and the post-earthquake serviceability (weather tightness) following low-intensity motions. Phase 2 examined the behaviour of three units (U1-U3) arranged in a row, with particular attention to the movement of the middle unit under low- to moderate-intensity seismic motions. Phase 3 aimed at reaching the collapse of a façade unit (U5) in order to identify the various system failure modes.

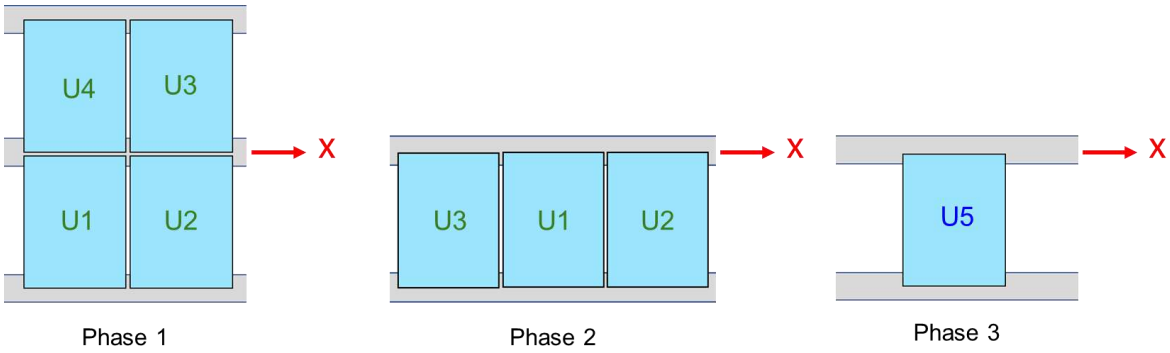


Figure 2. Testing phases

2.2.1 Testing protocol

Different load types were simulated during the experimental campaign (Table 1). Crescendo tests consisted of a series of sinusoidal cycles, with four ramp-up intervals followed by four constant-amplitude intervals, in accordance with AAMA 501.6 [2009]. These tests were conducted at low-to-moderate intensity levels, considering selected drift ratios based on the performance criteria of JASS14 [1996], i.e., H/300 (no damage to internal or external components), H/200 (external components must not exceed allowable stress and sealing must be repairable), H/100 (no glass damage or component dropout is allowed). These corresponded to maximum in-plane drifts of 12mm, 24mm and 36mm, respectively. To simulate realistic earthquake sequences and investigate their impact on façade damage, two ground motion records were selected from a set of spectrum-compatible earthquakes: one far-field record (Friuli 1976 earthquake, PGA = 0.11 g, Soil Type C, Station ST33) and one near-fault record (Christchurch 2011 earthquake, PGA = 0.17 g, Soil Type D, Station CCCC). As in Bianchi *et al.* [2025], the testing protocol involved applying inter story drift time series generated through non-linear dynamic analysis of a multi-story reinforced concrete building. Additionally, monotonic tests were performed on the U5 façade unit to identify ultimate failure modes and mechanisms. These involved imposing drift levels up to a maximum displacement of 250 mm (7% drift) at a loading rate of 0.5 mm/s, corresponding to the maximum capacity of the testing facility. After each loading step (every 50 mm), the tests were temporarily halted to allow for visual inspection of the façade. Phase 1 (Figure 3a) also included water leakage tests, carried out before and after the seismic tests to evaluate the post-earthquake serviceability of the façade. These tests were performed in the same test chamber by assessing the watertightness at the central joint between the four units, using sprayed water in accordance with the procedures outlined in CWCT Technical Note 41 [1980].

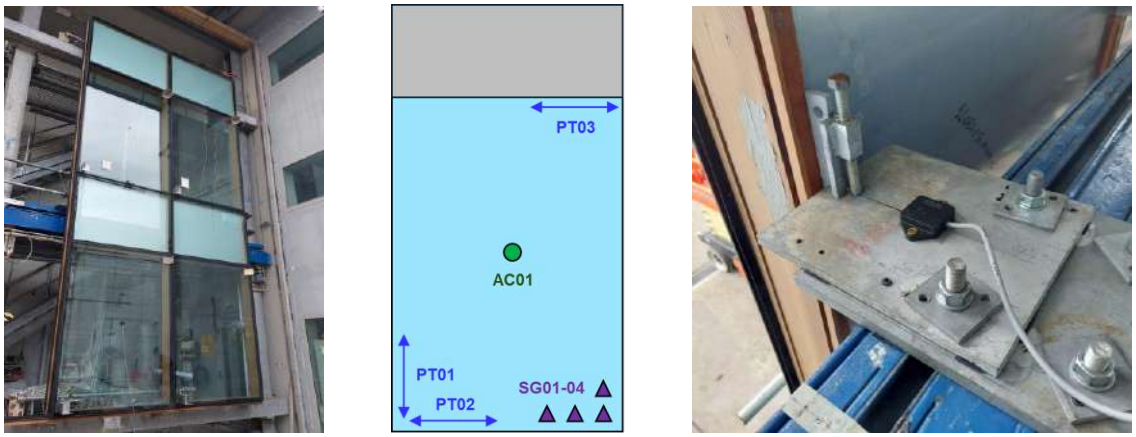
Table 1. Test protocol drift levels

Type	Phase 1	Phase 2	Phase 3
Crescendo test	0.33% 0.67%	0.33% 0.67% 1.00%	0.33% 0.67% 1.00%

			1.33%
Earthquake record (Friuli and Christchurch)	0.33% 0.67%	0.33% 0.67% 1.00%	0.33% 0.67% 1.00% 1.33%
Monotonic test	-	-	Up to 7.00%

2.2.2 Monitoring plan

Following the scheme discussed in Bianchi *et al.* [2024, 2025], an instrumentation layout was designed for each configuration to capture the movements of the glass, frame and unit connections during seismic loading. The monitoring system comprised 34 displacement sensors, including potentiometers (PT) and LVDT transducers with strokes of 50, 100 and 200 mm, and 3 laser sensors with detection ranges of 200 and 500 mm. These sensors measured vertical and horizontal (absolute) displacements of the glass panels (Figure 3b) and timber frame. Two draw wires with a 50 mm measurement range monitored diagonal and corner elongations of the frame. Five accelerometers (AC, ±6 g) recorded accelerations on the glass panels and bracket connections (Figure 3c), while strain gauges (SG) measured strains on one glass panel and a bracket connection to the seismic beam. Video recordings from GoPro and other digital cameras captured both front views and local joint behaviour. All measurements were acquired using a single data acquisition system with calibrated factors to ensure accuracy. Data were collected at a sampling frequency of 200-1000 Hz to provide sufficient resolution for post-processing. A Butterworth low-pass filter was applied to all recorded acceleration data to remove noise outside the range of interest.



(a) (b) (c)

Figure 3. Specimen in Phase 1 (a) and example sensors (b - scheme for a glass panel; c - accelerometer on the bracket)

2.3 TEST RESULTS

2.3.1 Seismic demand

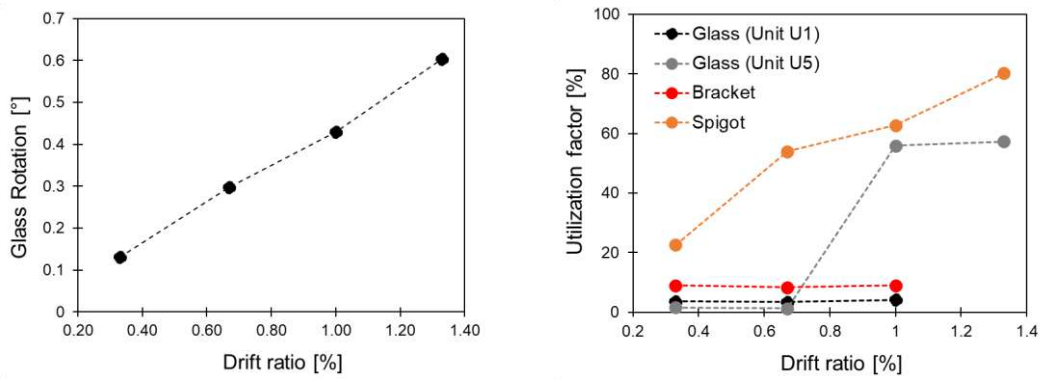
A first post-processing of all experimental data was conducted to derive seismic displacements and accelerations experienced by the main façade components, namely the glass panels, timber frame and hook-to-bracket upper connections. The façade behaved in line with a typical unitized curtain wall system. When subjected to in-plane movements driven by drift amplitudes, a combined racking and rocking response was activated, characterized by a rigid-body translation and rotation of the façade units.

When focusing on the overall system behaviour, it was observed that the glass and frame exhibited similar displacements in the positive and negative X-directions during the Crescendo tests, due to the symmetrical constraint system at the base and the stabilizing effect of the corner connections. The maximum recorded Crescendo responses aligned closely with the time-history responses across the different drift intensity levels (e.g., Table 2), with the main difference related to the frequency content of two earthquake inputs, Near-Fault (Christchurch) vs Far-Field (Friuli), which resulted in comparatively lower or higher vertical excitation of the façade components. Differences were also evident between the first- and second- floor units. The first-floor specimens were intentionally disconnected at their base, which allowed the sill beam to move and better replicate real building behaviour. This "inverse configuration" ensured that seismic demand was transferred predominantly to the second floor and prevented the introduction of unrealistic stress concentrations at the base.

Table 2. Displacement responses (max) recorded during Phase 2 for unit U1

Type	Drift amplitude [mm]	Glass Top X displ. [mm]	Glass Bottom X displ. [mm]	Glass Bottom Y displ. [mm]	Frame Top X displ. [mm]	Frame Bottom X displ. [mm]	Frame Top Y displ. [mm]	Frame Bottom Y displ. [mm]
Crescendo	12	6.33	0.65	3.08	11.70	0.89	2.31	3.07
	24	14.94	1.06	8.10	24.04	1.45	6.43	8.01
	36	24.33	1.47	13.77	38.57	2.09	11.76	13.37
Christchurch	12	6.08	0.60	0.86	10.18	0.88	3.11	0.87
	24	14.29	1.01	3.22	22.92	1.56	6.70	3.39
	36	23.62	1.43	5.75	37.01	2.08	11.12	5.74
Friuli	12	7.92	0.52	3.89	12.87	0.86	2.88	3.69
	24	16.35	1.04	8.56	24.49	1.59	6.01	8.52
	36	23.83	1.27	13.17	36.68	2.17	9.69	13.05

For the glass panels, the measured displacements were used to derive rotations relative to the panel diagonals, which linearly increased reaching values up to 0.5% during the 48 mm drift level in Phase 3 (Figure 4a). Accelerations were found to be higher on the first-floor units, where the sill beam was free to move. Peak values of 0.51 g were measured during Phase 3, with the external glazing recording higher accelerations than the internal panes, on the order of 0.1 g, being less constrained and experiencing lower damping. These accelerations show significant amplification compared to the peak value of 0.15 g recorded at the bracket on the seismic beam, corresponding to an amplification factor of more than 3 relative to the floor. Focusing on the timber frame, displacements increased nearly linearly with seismic intensity in both the X- and Y- directions, indicating that the system retained an essentially elastic response throughout the test range. Elongations measured at the corners and along the diagonals reached a maximum of 0.48 mm at the highest intensity levels, and no visible damage was detected in the timber members. This confirms that the frame provided good performance under the considered low-to-moderate seismic demands, accommodating drift without degradation.



(a) (b)

Figure 4. (a) Glass rotations at increasing drift level; (b) Utilization factors recorded for different unit components

Strain data were also obtained by means of strain gauges, which were applied to one glass unit and the brackets during Phases 1 and 2, and to one corner spigot of the frame during Phase 3. By assuming characteristic strength values of 40 MPa for glass, 270 MPa for stainless steel and 355 MPa for bracket steel, the recorded strains were converted into stresses using Hooke's law ($\sigma = E \cdot \varepsilon$). In Phases 1 and 2, the utilization factors remained well below critical thresholds, with the glass operating at less than 5% and the brackets below 10% of their strength capacity. In Phase 3, the strain gauges were repositioned to unit U5, where a pre-existing crack had been identified during storage, and to a bottom spigot of the frame. Here, significantly higher utilization levels were recorded: the cracked glass unit reached up to 60% of its capacity, while the spigot achieved 65% due to the rocking motion concentrated at the joints (Figure 4b). These local stress amplifications, however, did not compromise the overall seismic integrity of the system.

2.3.2 Damage patterns

The experimental campaign demonstrated that the timber-glass façade system responded in a controlled and largely elastic manner under increasing drift demands, up to a 1.33% drift ratio during both Crescendo and time-history inputs. To further evaluate post-earthquake serviceability, Phase 1 also included water-tightness tests at the central façade joint, which confirmed that the system remained functional up to a drift level of 0.67%. To investigate collapse-level damage states, quasi-static loading tests were carried out in Phase 3 on unit U5, and the observed damage mechanisms are summarized in Table 3.

Table 3. Observed damage states

Drift ratio	Damage	Description	Façade design
2.14%.		Cracks in the timber mullion close to the upper bracket connection	*Modified*: limited unit rotation capacity (bottom transom constrained to the starter sill)

4.61%		Displodgment of the unit from the corner spigots during rotations	*Original*: high unit rotation capacity (bottom transom free to move)

In its original configuration, collapse was due to the dislodgement of the unit from the corner spigots during unit rotations. This represents a severe damage state, as it can potentially endanger pedestrians at street level, and was recorded at 4.61% drift (77 mm vertical displacement at the base). A second configuration was also tested, in which the base fixing of the bottom transom was constrained to the starter sill, thereby limiting deformation capacity to simulate an alternative design scenario. Under this configuration, the monotonic test revealed the formation of a crack in the timber mullion, near the upper bracket connection, at a drift ratio of 2.14%. These results highlight how design choices directly influence both the damage mechanisms and the severity of failure.

2.4 NUMERICAL VS. EXPERIMENTAL STUDY

As part of the research, a numerical model was developed in LS-DYNA to study the in-plane seismic performance of the timber-glass façade and to derive fragility functions for risk assessment, as detailed described in Milan *et al.* [2025]. To verify its accuracy, experimental data at the H/150 displacement level were used to compare numerical vs. experimental displacements of both frame and glass components. A sensitivity analysis was also conducted to identify the parameters most influencing the overall behaviour. The results showed that unit disengagement exhibited high sensitivity to drift, whereas the silicone utilization factor had a comparatively lower influence. The frame utilization factor, which was not monitored during the experiments, was found to be less than 0.1. This low value reflects the moment-resisting connection between the transom and mullion, which caused the unit response to be dominated by rigid-body rotation.

Fragility functions were derived using inter-story drift ratio as a proxy for seismic intensity. With regard to response, the maximum utilization factor from each mechanism (unit disengagement, silicone failure) was considered. The probability of reaching or exceeding a utilization factor of 1, when governed by silicone response, was interpreted as the probability of glass fallout from a design perspective. This approach is conservative as the utilization factor is calculated based on design stress rather than actual failure stress, and it reflects the maximum observed stress at any location within the silicone joint. When comparing numerical and experimental results in terms of damage state, very good agreement was observed. For the tested specimen with 25mm silicone bite, the numerical model predicted failure due to unit dislodgement from the spigot at a drift ratio of 4.8%, which aligns closely with the experimentally observed 4.61% drift level (original design configuration).

3. TIMBER VS. ALUMINIUM GLASS SYSTEMS

The tested façade was compared with an equivalent aluminium-glass system (series 180, Galli [2011]) in terms of seismic, energy and environmental performance. Both systems share similar dimensions (3600 mm x 1500 mm for the timber-glass unit, while 3800 mm × 1500 mm for the aluminium-glass unit) and frame

width (90 mm sight line). As discussed above, due to wood's lower modulus of elasticity and limiting bending stress, the timber frame depth was increased by ~30% (180 mm vs. 140 mm) to match the aluminium system's lateral stiffness. Both façades employ structural silicone glazing (Sikasil SG500) with wet connections, similar bracket hook connections to beams and shear-key-supported bottom transoms.

3.1 STRUCTURAL PERFORMANCE

The experimental results on the timber-glass façade system can be compared with those recorded in 2011 for the aluminium-glass counterpart [Galli, 2011]. Focusing on the cyclic tests performed at three seismic intensity levels (H/300, H/200, H/100) (as the monotonic and higher intensity-level testing were conducted only on the timber-glass units), both systems demonstrated very good seismic performance. Nevertheless, the timber-glass system exhibited larger rotations (up to 0.45°) compared with the aluminium-glass system (up to 0.32°) under H/100 loading. This difference is primarily attributed to the rigid-body dominated rotation of the timber configuration, whereas the aluminium façade, which relies on pin connections between mullions and transoms, displayed higher frame distortion.

Additional insights are provided by numerical simulations calibrated on both experimental campaigns [Ciurlanti *et al.*, 2023; Milan *et al.*, 2025]. When considering identical silicone bite dimensions (15 mm), sensitivity analyses showed that the silicone experienced greater stress in the timber configuration, with a utilization factor approaching 50% at 1% drift compared with 30% for the aluminium-glass system. Both systems exhibited low glass and frame utilization factors, although the aluminium system showed slightly higher values for the glass (≈10%) compared with <5% in the timber case. Comparison of fragility curves shows that the timber-glass system reaches severe damage earlier, with a 50% probability of unit dislodgment from the corner spigots at a drift ratio of 4%. In contrast, the aluminium-glass system demonstrates much higher capacity, with less than 5% probability of dislodgment at the same drift level, where failure is governed instead by uplifting at the hook-bracket connection (which only occurs at larger vertical displacements, exceeding 100 mm compared to the 77 mm spigot height).

3.2 ENERGY AND ENVIRONMENTAL PERFORMANCE

For the two systems, a comparison in terms of energy performance is provided by Buljan *et al.* [2015, 2017]. The authors demonstrated that the wood-based framing system outperforms the equivalent aluminium curtain walling, achieving approximately 35-41% lower thermal transmittance of the frame alone (when using warm-edge glass technology) and up to 20% lower overall thermal transmittance of the building envelope. The thermal transmittance was calculated including the influence of fixing screws, with simulations performed using Bisco software under boundary conditions of 0 °C external temperature and +20 °C internal temperature (Figure 5). However, the authors also observed that the risk of condensation is higher for the timber system compared to aluminium, and this is primarily due to the way heat flux is distributed. In timber frames, the high thermal resistance of wood tends to concentrate heat transfer at the glass-gasket contact points, creating colder surface zones where condensation is more likely to occur.

Beyond thermal performance, the environmental impact of the timber-glass system is significantly lower. The absence of aluminium content reduces both the embodied energy and the overall carbon footprint of the façade, while also lowering operational energy demand and associated energy costs when compared to prefabricated aluminium elements. Life-cycle assessments confirm these benefits, indicating that, when production and construction stages are considered together, the timber system achieves an 11-17% reduction in global warming potential, with savings depending on geographic context and the location of the glass manufacturer [Hens *et al.*, 2022]. These findings highlight the role of timber curtain walling as a viable low-carbon alternative in façade design.

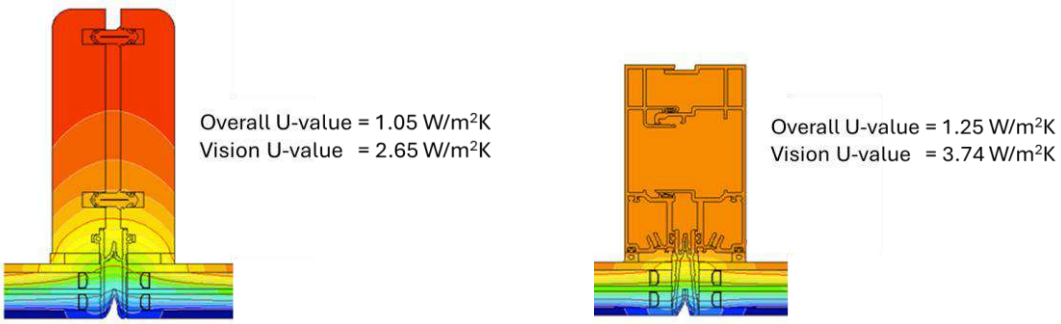


Figure 5. Thermal simulation for the (a) timber vs. (b) alluminium glass system, including thermal transmittance values (U) for a double glazed unit (10/16/10) coated and with plastic spacer [modified after Buljan *et al.*, 2015]

4.CONCLUSIONS

This study investigated the seismic performance of timber-glass unitized curtain walls through an experimental campaign involving in-plane dynamic and quasi-static loading. The results showed that the timber-glass façade exhibited a controlled, predominantly elastic response up to a 1.33% drift ratio. Units were characterized by rigid body rotation, with the frame accommodating drift without damage. Strain measurements confirmed that most components remained well below material limits, although pre-existing cracks caused local amplifications up to 60-65% of capacity for the glass. Collapse was governed by unit dislodgement from corner spigots at 4.6% drift, while base-constrained configurations (characterized by limited rotation capacity) exhibited timber cracking at 2.1% drift. Overall, the system maintained functionality, including water-tightness, under low-to-moderate seismic loads.

Comparison with an equivalent aluminium-glass unit (series 180) showed that the timber-glass façade provides comparable structural performance under the same seismic demand. The timber system, however, exhibited larger rigid-body rotations and higher stresses on silicone joints, reaching severe damage earlier. In contrast, the timber façade demonstrated superior thermal performance, and the absence of aluminium reduces embodied energy and carbon footprint, while also lowering operational energy demand and costs. Overall, timber-glass systems represent a viable low-carbon alternative to conventional aluminium curtain walls. Future research should focus on improving system detailing, particularly corner spigots, to preserve structural and thermal performance while mitigating moisture-related risks. Additionally, extending the analysis to multi-hazard scenarios (including fire, heat and seismic events) and life-cycle aspects (e.g. material degradation) will enable a more comprehensive comparison of aluminium and timber options and support trade-off decisions for optimized holistic designs.

REFERENCES

AAMA501.6-09 [2009] *Recommended Dynamic Test Method for Determining the Seismic Drift Causing Glass Fallout From a Wall System*, American Architectural Manufacturers Association.

Alabdulrazzaq, H., Brambilla, A., Chen, T., Gasparri, E. [2025] "Comparative study of unitised curtain wall and unitised timber envelope systems: pathways to reducing embodied carbon and enhancing circularity in facade design," *Proceedings of World Conference on Timber Engineering,* Brisbane, Australia.

Bianchi, S., Lori, G., Hayez, V., Manara, G., Schipper, R., Pampanin, S., Overend, M. [2025] "Seismic Testing and Performance Evaluation of Unitized Curtain Walls," *Earthquake Engineering and Structural Dynamics*.

Bianchi, S., Lori, G., Hayez, V., Overend, M., Manara, G. [2024] "Influence of Design Variables on Seismic Performance of Unitized Curtain Walls: A Parametric Experimental Study," *Glass Structures & Engineering*, Vol. 9, No. 2, pp. 165–184.

Bianchi, S., Pampanin, S. [2022] "Fragility Functions for Architectural Nonstructural Components," *ASCE Journal of Structural Engineering*, Vol. 148, No. 10.

Buljan, N., Bjelanovic, A., Turkulin, H. [2017] "Structurally glazed timber curtain wall," *Proceedings of 1st International Conference on Construction Materials for Sustainable Future*, Zadar, Croatia.

Buljan, N., Bjelanovic, A., Turkulin, H., Zobec, M. [2015] "TimberCW – structurally glazed laminated wood façade," *Proceedings of International Conference on Advanced Building Skins,* Münich, Germany.

Ciurlanti, J., Milan, G., Dennis, J., *et al.* [2023] "Sensitivity Analysis and Risk Assessment of Unitised Glass Curtain Walls," *Proceedings of SECED 2023 Conference*, Cambridge, United Kingdom.

CWCT 41 [1980] *Technical Note 41: Site testing for watertightness*, Centre for Window and Cladding Technology.

EN 13830:2003 [2003] *Curtain Walling – Product Standard*, European Standard.

Galli, U. [2011] "Seismic Behaviour of Curtain Wall Facades—a Compari son Between Experimental Mock-Up Test and Finite Element Method Analysis," *MSc thesis*, Technical University of Milan, Italy.

Georgoulopoulou, M., [2022] "Timber-Glass Curtain Wall," *Master Thesis*, Delft University of Technology, Delft, The Netherlands.

Hartwell, R., Macmillan, S., Overend, M. [2021] "Circular Economy of Façades: Real-World Challenges and Opportunities," *Resources, Conservation and Recycling*, Vol. l, No. 175.

Hens, I., Pennetier, S., Schleicher, S. [2022] "Embodied Carbon Of Timber Unitized Curtain Wall," *Proceedings of Facade Tectonics 2022 World Congress*, Los Angeles, United States.

Huang, B., Chen, S., Lu, W., Mosalam, K. M. [2017] "Seismic Demand and Experimental Evaluation of the Nonstructural Building Curtain Wall: A Review," *Soil Dynamics and Earthquake Engineering*, Vol. 100, pp. 16–33.

JASS14 [1996] *Japanese Architectural Standard Specification Curtain Wall*, Architectural Institute of Japan.

Milan, G., Ciurlanti, J., Bond, D., Bianchi, S., Bujan, N., Lori, G., Dennis, J. [2025] "Probabilistic seismic assessment of unitised glass curtain walls with timber framing," *Proceedings of 10th ECCOMAS Thematic Conference on Computational Methods in Structural Dynamics and Earthquake Engineering,* Rhodes Island, Greece.

Momeni, M., Bedon, C. [2024] "Review on Glass Curtain Walls Under Different Dynamic Mechanical Loads: Regulations, Experimental Methods and Numerical Tools," *Façade Design Challenges and Future Perspective*, Intech Open.

Turkulin, H. [2013] "Technical Design of the Wooden Prototype Members of The Curtain Walling System," *Technical Report*, Laboratory for Wood in Construction of the Faculty of Forestry, Zagreb, Croatia.

In-Plane Loading Experiments on Seismic Damage and Functional Retention Performance of LGS Partition Walls with Opening

Zeyu SUN[1], Miku KUROSAWA[1], Shoichi KISHIKI[1],

Yusuke OKI[2], Shinichi HONDA[3], and Takayuki SATOU[4]

[1] Institute of Science Tokyo
J3-1, 4259 Nagatsuta Midori, Yokohama, 226-8503, Japan
e-mail: sun.z.8b11@m.isct.ac.jp
e-mail: {kurosawa.m.776a, kishiki.s.02d9}@m.isct.ac.jp
[2] Building Research Institute
1 Tachihara, Tsukuba, Ibaraki, 305-0802, Japan
e-mail: oki_y@kenken.go.jp
[3] OKUJU Co., Ltd
1-19-1, Kanda Nishikicho, Chiyoda, Tokyo, 101-0054, Japan
e-mail: s.honda@okuju.co.jp
[4] FUJISASH Co., Ltd
4-32-1, Nishigotanda, Shinagawa, Tokyo, 141-0031, Japan
e-mail: takayuki-satou@fujisash.net

Abstract. This study aims to investigate the seismic behaviour and the functional performance of light-gauge steel dry partition walls (LGS walls) with openings. Full-scale in-plane static cyclic loading experiments have been conducted on LGS partition walls attached to a steel frame. The test parameters include the gypsum board specifications (two 12.5 mm gypsum boards on one side, two 12.5 mm gypsum boards on both sides, and two 21 mm gypsum boards on one side), the presence or absence of a steel door (SD), and the loading protocol. A total of ten specimens combining these parameters were prepared. An increase in the total thickness of the gypsum boards led to earlier damage initiation in the LGS walls. In addition, for specimens with gypsum boards on one side, the SD became inoperable at a story drift angle of 1/67 rad. In contrast, for specimens with gypsum boards on both sides, SD operability was lost earlier, starting from a story drift angle of 1/100 rad.

Keywords: Light-gauge steel, Partition wall, Opening, Steel door, In-plane deformation.

1. INTRODUCTION

In recent decades, improvements in structural design and the revision of the Building Standards Act in 1981 have contributed to enhanced seismic performance of structural members. As a result, during the 2011 Great East Japan Earthquake, the extent of structural damage was reported by the Joint Editorial Committee for the Report on the Great East Japan Earthquake Disaster [2019] to be relatively limited compared with the scale of the event. However, damage to non-structural components—such as ceilings and interior and exterior walls—has still been frequently observed and has led to casualties from falling elements, as well as economic losses from interruptions to building functions. Such cases were also documented in the 2016 Kumamoto Earthquake by the National Institute for Land and Infrastructure Management [2016]. Therefore, evaluating the seismic performance of non-structural components and establishing methods to mitigate their damage are becoming increasingly important.

This study focuses on light-gauge steel dry partition walls (LGS walls). The configuration of the LGS wall and deformations is shown in Figure 1. LGS walls are composed of the light-gauge steel backing frame (LGS backing frame), lower reinforcing gypsum boards (lower boards), and upper reinforcing gypsum boards (upper boards). During an earthquake, the LGS walls experience inter-story deformation caused by in-plane and out-of-plane deformations transmitted from the structural frame. In addition, out-of-plane inertial deformation due to the wall's self-weight (inertial force) occurs in response to the acceleration of each story.

Previous studies have investigated the in-plane and out-of-plane behaviour of flat LGS walls under combined loading by Isoda [2021] and Kugimoto [2025], and in-plane loading experiments with variable LGS wall arrangements by Lee [2007] and Seike [2019]. Partition walls, however, serve a functional role in dividing spaces and typically require openings to allow access between rooms. The presence and location of openings can significantly affect the wall's seismic behaviour and damage patterns, as well as the operability of doors, which is critical for safe evacuation. Regarding LGS walls with openings, Lyu [2023] and Kawamura [2025] studied techniques to reduce damage around openings using quasi-static loading tests. Regarding door operability, Yagi [2022] conducted a static loading test on an LGS wall with a steel door installed in an RC frame, and Ito [1986] conducted a static loading test on a full-scale six-story steel-framed building with concrete block walls and steel doors. However, the interaction between different LGS wall specifications and door position during seismic loading, as well as the door operability, has not yet been clarified.

In this study, static in-plane loading tests were conducted on LGS walls with center-located openings to simulate seismic conditions. The experiments aimed to investigate damage patterns and the operability of steel doors (SD) for different LGS wall specifications when openings are fixed at the center of the wall.

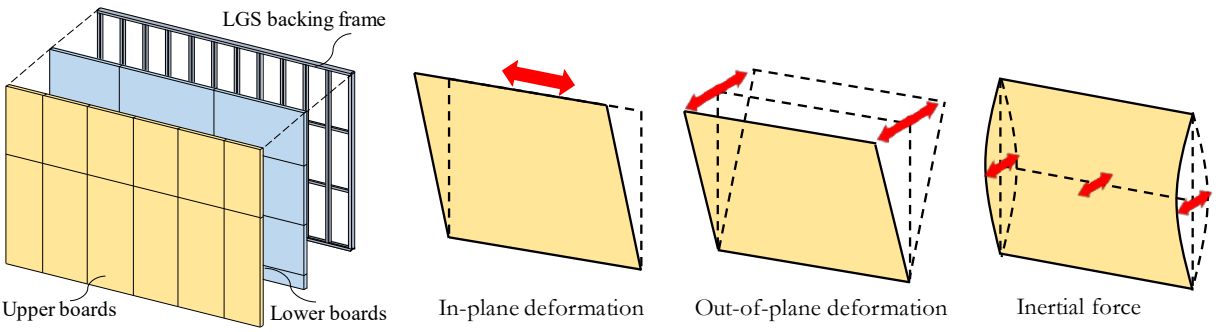


Figure 1. Configuration of the LGS wall and deformations

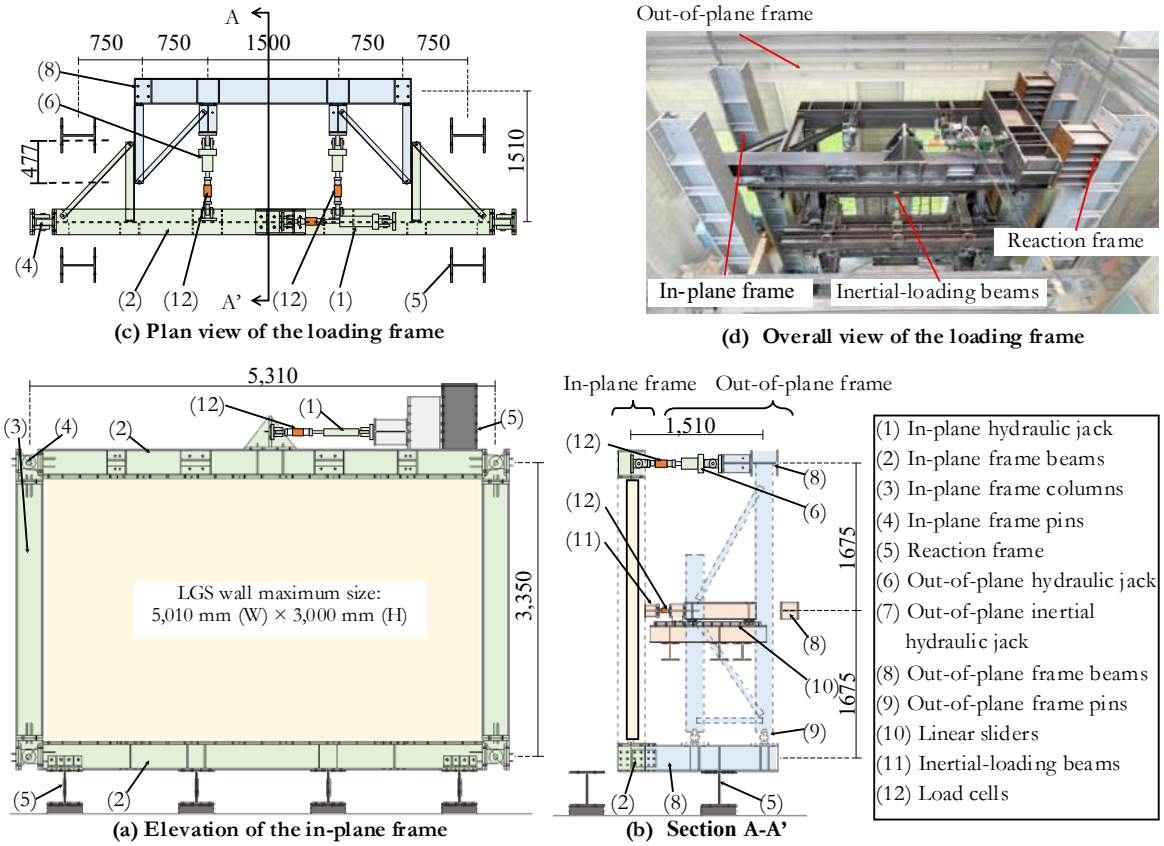
2. TEST PROGRAM

2.1 LOADING FRAME

Firstly, loading frame components are shown in Figure 2. The loading frame is capable of applying combined loads, including in-plane deformation, out-of-plane deformation, and out-of-plane inertial forces. In this study, only in-plane loading was used; therefore, the description below focuses on the in-plane frame.

The in-plane frame was configured as a rectangular frame, with in-plane frame columns and beams connected via four in-plane frame pins. The LGS wall specimens were installed within this frame. Static lateral forces were applied to the LGS wall using a hydraulic jack attached to the upper beam of the in-plane frame, inducing in-plane deformation.

The maximum specimen dimensions accommodated by the frame were 5,010 mm × 3,000 mm. It was confirmed that, at an inter-story drift angle less than ± 1/40 rad, no contact occurred between the in-plane frame columns and beams, and the frame provided no lateral resistance; only the *P-Δ* effects associated with the self-weight were present.



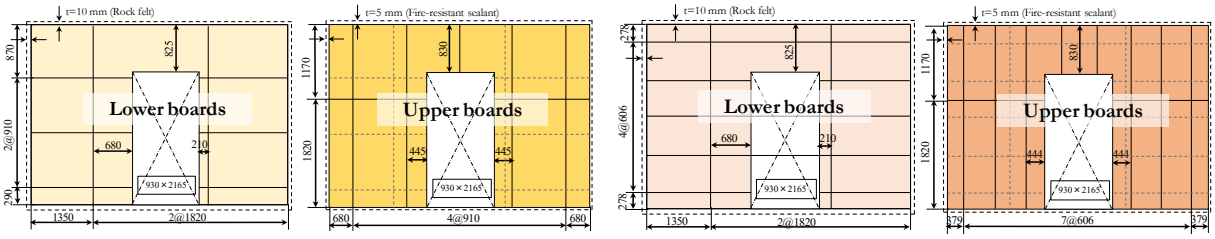
(c) Plan view of the loading frame

(d) Overall view of the loading frame

(a) Elevation of the in-plane frame

(b) Section A-A'

Figure 2. Loading frame



(a) 12.5 mm gypsum boards

(b) 21 mm gypsum boards

Figure 3. Gypsum board layout

2.2 SPECIMENS AND TEST PARAMETERS

The configuration of the test specimens, including the gypsum board layout, is shown in Figure 3. Each LGS wall specimen has dimensions of 5010 mm (width) by 3000 mm (height). This study used Japan Industrial Standard (JIS) 65 series; for track, WR-65; for stud, WS-65. And C-65×30×10×2.3 sections were adopted as opening reinforcements. The details of the LGS backing frame are shown in Figure 4. The tracks were anchored to the in-plane loading frame with bolts via track-connected jigs, and the studs were spaced at 455 mm spacing without connecting to the tracks. The reinforcing channels connecting each stud are generally spaced at 1,200 mm from the floor end. The details of the opening will be shown in section 2.3.

The gypsum boards, with dimensions of 910 mm × 1820 mm and 12.5 mm thickness, or 606 mm × 1820 mm and 21 mm thickness, were used. The lower boards were screwed to the LGS backing frame, and the upper boards were attached to the lower boards with adhesive. Clearances of 10 mm and 5 mm were provided between the lower/upper boards and the in-plane loading frame, respectively, using rock felt and fire-resistant sealant. The opening dimension is 930 mm × 2165 mm, located approximately at the center of the LGS wall. In the second phase of the experiment, the opening position is planned to be considered as a test parameter.

Test parameters and a list of specimens are shown in Table 1. Test parameters are: (1) Gypsum board specification – three types were prepared (two 12.5 mm gypsum boards on one side, two 12.5 mm gypsum boards on both sides, and two 21 mm gypsum boards on one side). (2) Presence of opening and SD – three conditions were prepared: without opening, opening without SD, and opening with SD. Even in cases opening without SD, the opening reinforcements and jamb were installed, enabling the effect of the presence of SD or not to be examined. In addition, (3) Loading protocol – details are provided in Section 2.4, is also set as a test parameter. Therefore, in this experiment, 10 specimens were prepared by combining the above test parameters.

2.3 CONFIGURATION OF THE OPENINGS

The details of the LGS backing frame components used in all specimens are shown in Figure 4. The LGS backing frame consisted of (1) upper and lower tracks, into which (2) studs were inserted and laterally restrained with (3) reinforcing channels. For the opening, (4) lip channel steels were employed as the opening reinforcements. Inside the reinforcement, (5) a jamb composed of light-gauge steel members with variable cross-sections was installed, along with (6) a threshold at the bottom. The jamb was fastened to the opening reinforcements using screws, while the reinforcement itself was connected to the tracks and in-plane loading frame through L-shaped fittings with bolts. The threshold was welded to the jamb and further bolted to the in-plane loading frame through L-shaped fittings. An SD, 830mm × 2,100 mm, was mounted onto the jamb

Table 1. List of specimens

No.	LGS backing frame	Gypsum board	Opening	Loading protocol
1	Track: WR-65 Stud: WS-65	GB-F 12.5 mm–on side	Without opening	Standard
2		GB-F 12.5 mm–both sides	Without opening	Standard
3		GB-F 21 mm–on side	Without opening	Standard
4		GB-F 12.5 mm–on side	Opening without SD	Standard
5		GB-F 12.5 mm–both sides	Opening without SD	Standard
6		GB-F 21 mm–on side	Opening without SD	Standard
7		GB-F 12.5 mm–on side	Opening with SD	Standard
8		GB-F 12.5 mm–both sides	Opening with SD	Standard
9		GB-F 21 mm–on side	Opening with SD	Standard
10		GB-F 12.5 mm–both sides	Opening with SD	Reverse

via hinges and a door closer. Clearances were provided between the SD and the jamb and threshold: 5 mm on the left jamb, 4 mm on the right jamb, 3 mm at the head jamb, and 6 mm at the threshold.

Finally, the attachment details between the gypsum boards and the jamb are shown in Figure 5. For both one side and both sides gypsum board specifications, the gypsum boards were installed in direct contact with the opening reinforcement. To accommodate this, the jamb was designed with an irregular cruciform cross-section, resulting in depths of 129 mm, 137 mm, and 146 mm, respectively.

2.4 LOADING PROTOCOL

The experimental setup is using the in-plane loading frame described in Section 2.1; loading was displacement-controlled based on the inter-story drift angle R, defined as the in-plane displacement δ_{in} divided by the wall height H (= 3,350 mm).

The loading protocol in this experiment is indicated in Figure 6. The pushing direction of the hydraulic jack was defined as positive, while the pulling direction was defined as negative. In this experiment, positive and negative alternating cyclic loading was applied, starting from an inter-story drift angle of 1/1000 rad and incrementally increasing up to 1/40 rad. The loading was repeated for two cycles at each amplitude. As one of the experimental parameters ((3) loading protocol), the asymmetry of the SD was taken into account. While the standard protocol began with loading in the positive direction, one specimen was additionally tested with negative direction loading initiated first.

2.5 STEEL DOOR OPERATION TESTS

During the cyclic loading tests described in section 2.4, supplementary SD operation tests were conducted. The timing of these tests is indicated in Figure 6 by ● and ○ marks. At each cycle, the operability test was performed both at the positive and negative peak deformations and during unloading.

The procedure for the SD operation test consisted of two steps: (1) checking the operability of the lever handle, and (2) checking the operability of the SD. The lever handle was operated by a manual winch attached to the door with bolts, while the SD opening was performed either manually or with an electric winch. In manual operations, the same operator was used throughout the experiments to ensure consistency. The operational forces required for steps (1) and (2) were measured using load cells.

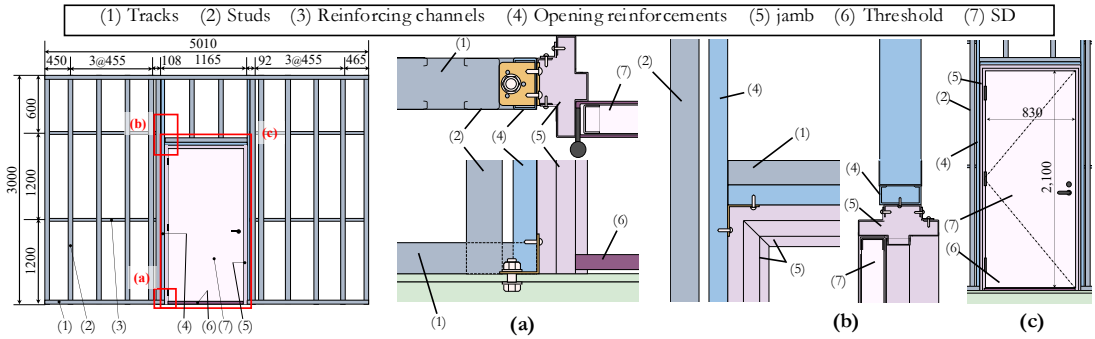
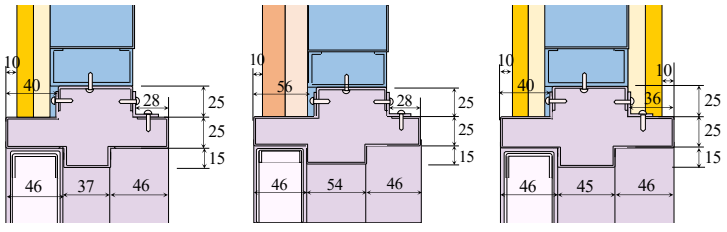


Figure 4. Details of the LGS backing frame



(a) 12.5 mm one side (b) 21 mm one side (c) 12.5 mm both sides

Figure 5. Section of jambs with gypsum boards

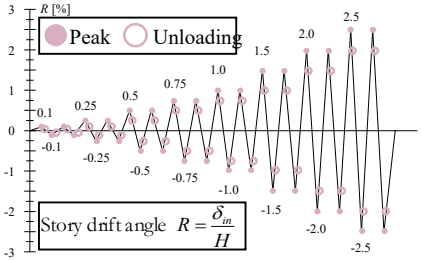


Figure 6. Loading Protocol

The results of the SD operation tests were classified into three categories: (a) Easily operable – the door could be opened manually without difficulty. (b) Poorly operable – the door could be opened manually with considerable effort, or by using the electric winch. (c) Inoperable – the door could not be opened even with the electric winch. Here, the rated capacity of the electric winch was 980 N.

3.TEST RESULTS AND DISCUSSION

3.1 RESULTS OF THE LGS WALL

Figure 7 shows the load–deformation relationships for specimens with gypsum boards of 12.5 mm and 21 mm thickness, tested under loading starting in the positive direction. A summary of the observed damages during loading is presented in Figure 8. In Figure 7, the vertical axis indicates the shear force Q obtained from the load cell attached to the in-plane jack, and the horizontal axis indicates the story drift angle R, which is measured by displacement transducers. Damage (a)~(f) in Figure 7 corresponds to those shown in Figure 8.

For all specimens, crushing at the board corners was observed at story drift angles approximately 1/200~1/100 rad. The shear force under previously unexperienced displacement amplitudes decreased significantly from the second cycle onward, and the difference became more pronounced as the amplitude increased. In terms of cyclic behaviour, the specimens exhibited slip behaviour with nearly constant resistance. No significant strength degradation was observed for specimens with an opening due to the stroke limit of 1/40 rad drift angle.

Compared with the 12.5 mm one side specimens (Figure 7 (a), (d), (g)), the maximum load increased by approximately 1.2~1.5 times for the 21 mm one side specimens (Figure 7 (b), (e), (h)) and by approximately 1.5~2.0 times for the 12.5 mm both side specimens (Figure 7 (c), (f), (i)).

Regarding parameter (2), the presence of opening and SD, the specimens with opening reduced the maximum load by approximately 0.6~0.8 times for all specifications of gypsum boards. In terms of the SD effect, the 12.5 mm one side specimens (Figure 7 (d) vs. (g)) exhibited almost identical load–deformation relationships, whereas for the 21 mm one side specimens (Figure 7 (e) vs. (h)) and 12.5 mm both sides specimens (Figure 7 (f) vs. (i)), with SD were increased the maximum load in the negative direction by approximately 1.2 times. The detailed mechanisms causing this load difference due to the SD will be analysed in future studies.

Next, the significant damage observed during the tests and their occurrence sequence are summarized. Six identified damage were: (a) cracking at the opening corner, (b) crushing at the board corner, (c) vertical cracking, (d) hinge detachment, (e) deformation of stud, and (f) screw pull-out. For specimens without an opening, only (b) crushing at the board corner, (e) deformation of stud, and (f) screw pull-out were observed. However, (d) hinge detachment was observed only under negative loading, whereas other damages first appeared under positive loading and subsequently occurred at the symmetric timing during the following negative loading cycle. The story drift angles at which these damages were first observed are shown in Figure 8.

Damage (a), cracking at the opening corner, was the earliest to occur. It was observed at a story drift angle of 1/200 rad for all 12.5 mm specimens and at 1/133 rad for the 21 mm specimens. This indicates that thicker gypsum boards tend to delay crack initiation. The cracks are considered to result from stress strut at the opening corners due to diagonal compression forces within the LGS walls during deformation. For one side specimens, such cracks were also observed in the lower boards.

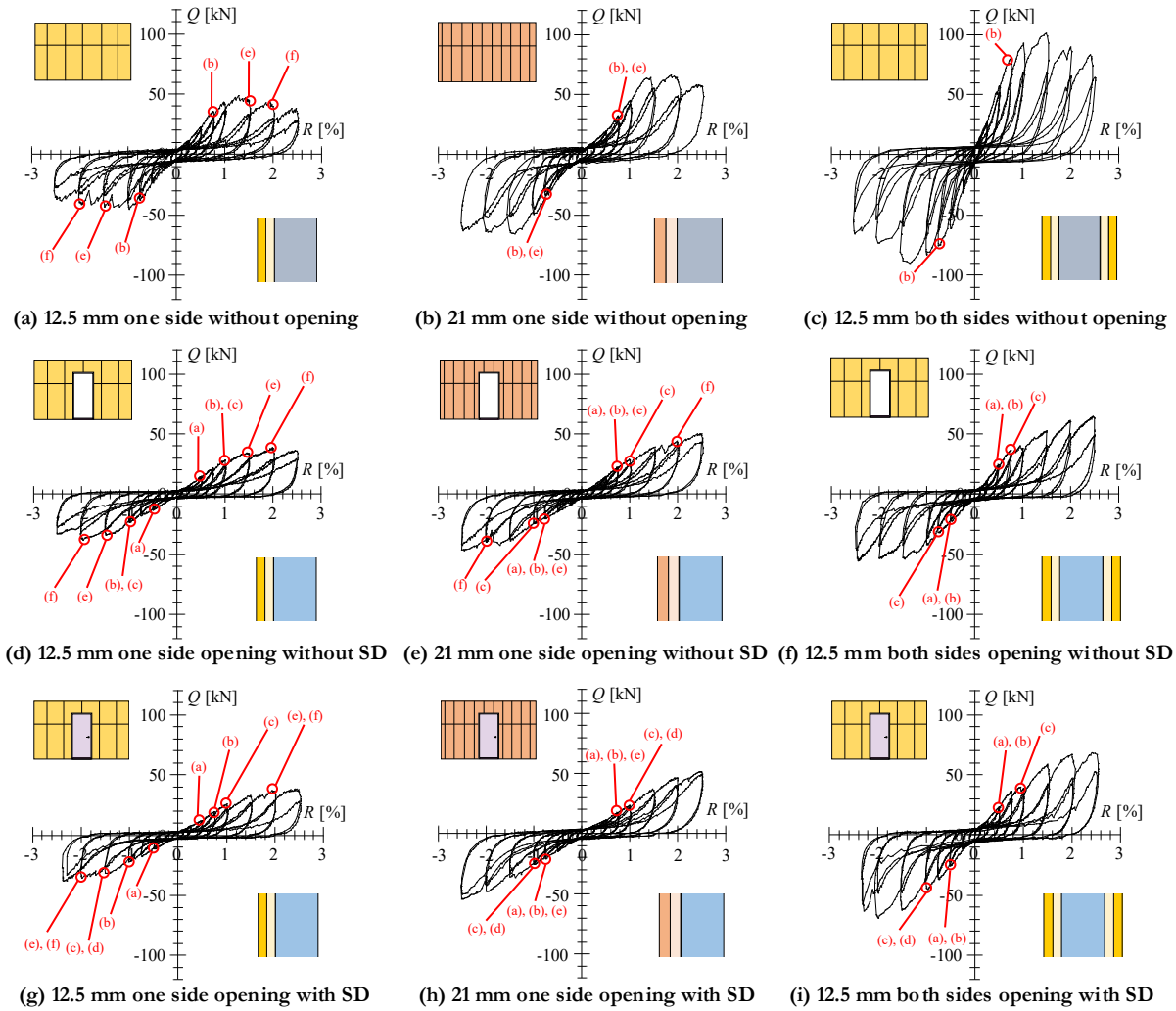


Figure 7. Load-deformation relationships

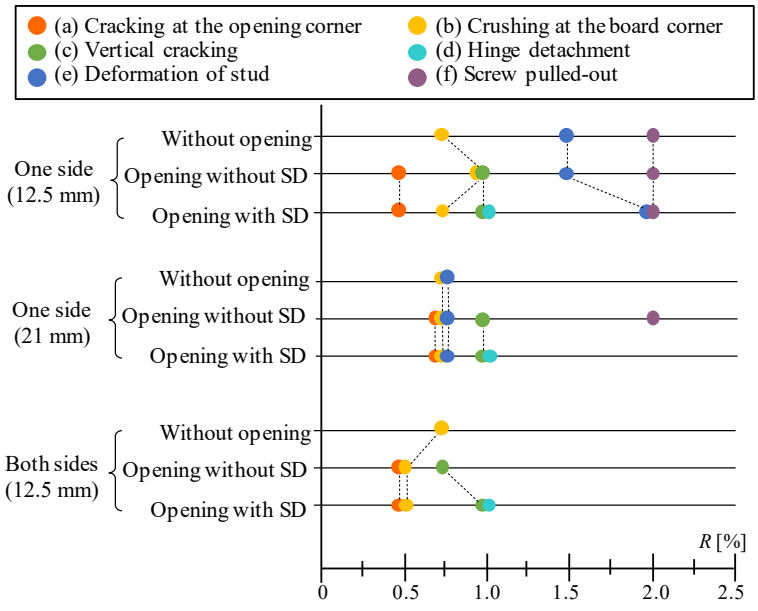


Figure 8. Observed damage corresponded to the story drift angles



Photo 1. observed damage

Damage (b), crushing at the board corners, tended to occur earlier as the total gypsum board thickness increased. This is attributed to the fact that as the total thickness of the gypsum boards increases, their tendency to rock decreases, which leads to earlier contact with the in-plane frame.

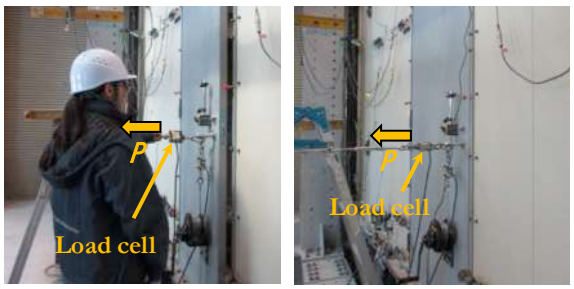
Damage (c), vertical cracking, is considered to have developed due to the relative deformation between the left and right portions of the LGS wall around the opening. Once vertical cracks occurred, the two sides of the wall tended to deform independently with rotational displacement.

Damage (d), hinge detachment, is thought to have resulted from contact between the SD and the threshold, causing the SD to rotate around the contact point and lift the hinge side.

Damage (e), deformation of stud, and (f), screw pull-out, were observed only in the one side specimens. In contrast, post-test inspection of the both sides specimens revealed local buckling of the studs.

3.2 Results of Steel Door Operation Tests

The SD operation tests were evaluated using the opening force P (Photo 2) and the door displacement δ_{SD}, as defined in Section 2.5. An example of test result is shown in Figure 9. In addition, the load–deformation relationships from Figure 7 were replotted in Figure 10, with different markers indicating the SD's operability status. Furthermore, the lower part of Figure 10 also shows the same relationships with the vertical axis replaced by the opening force P. Note that the lever handle always appropriately functioned; therefore, its results are omitted.



(a) Manual (b) Electric winch

Photo 2. Door opening in the test

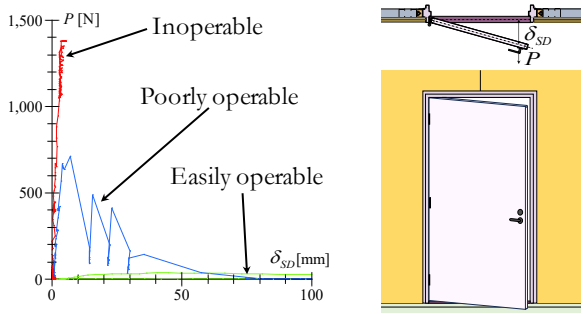
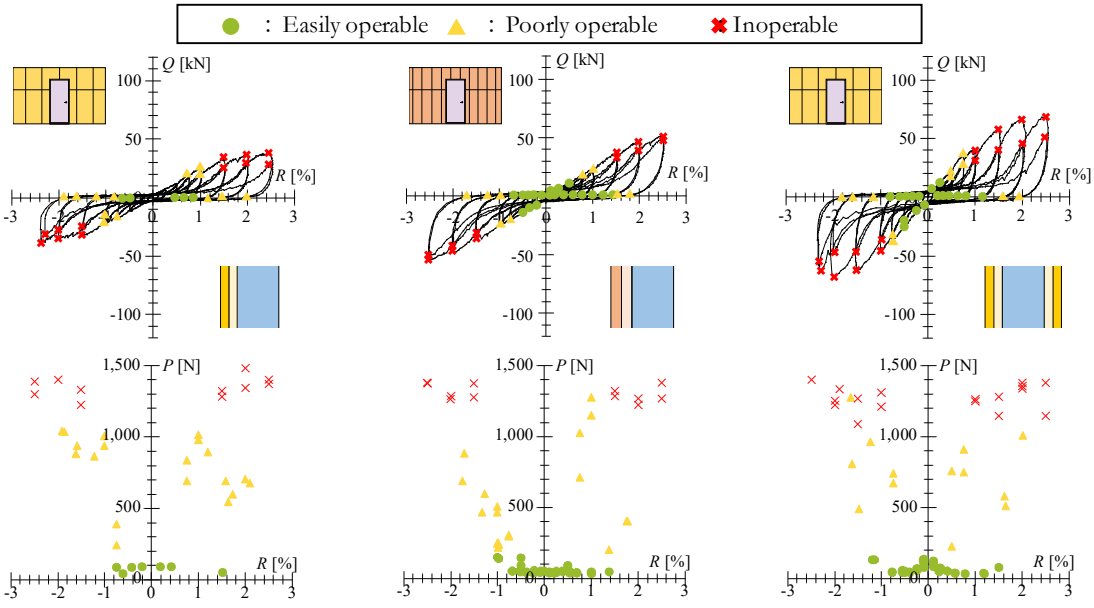


Figure 9. Load–displacement relationship of SD opening



(a) 12.5 mm one side (b) 21 mm one side (c) 12.5 mm both sides

Figure 10. Operability of the SDs

As shown in Figure 9, doors classified as "easily operable" required an opening force P of less than 100 N, whereas those classified as "poorly operable" exhibited a distinct peak load and required substantially greater forces. However, in the "inoperable" case, the load is increased linearly until it reaches the electric winch's rated capacity, at which point the test is terminated.

Figure 10 shows that, for one side specimens (Figure 10 (a), (b)), the SD became inoperable at a story drift angle of approximately ±1/67 rad, whereas for both sides specimens (Figure 10 (c)), inoperability occurred earlier, at approximately ±1/100 rad. This earlier loss of operability is attributed to both sides of the boards being in uniform contact with the jamb cross-section, which caused the jamb to deform earlier and engage with the SD. Furthermore, regardless of gypsum board specification, inoperability consistently occurred earlier during positive loading cycles than during negative loading cycles. This asymmetry is attributed to the different clearance between the SD and the jamb (3 mm at the head jamb and 6 mm at the threshold). As the SD inclines together with the hinge-side jamb, earlier contact occurs at the head jamb under positive loading due to its smaller clearance, whereas under negative loading contact occurs at the threshold.

Finally, examining the relationship with the opening force *P* (lower part of Figure 10), SD was classified as "easily operable" when P<100 N, corresponding to peak story drift angle below 1/200 rad for one side specimens and 1/400 rad for both sides specimens. SD required an opening force of 100~1000 N was classified as "poorly operable" with corresponding peak story drift angles below 1/100 rad for one side specimens and 1/133 rad for both sides specimens. When the opening force exceeded 1000 N, the SD were classified as "inoperable," which occurred at drift angles above 1/100 for one side specimens and above 1/133 rad for both sides specimens.

Since both studies conducted SD operation tests installed in LGS walls, the results of this study are compared with those of Yagi [2022]. In the study, an LGS wall (2640 mm × 2040 mm) with WS-65 studs spaced at 303 mm and 21 mm gypsum boards on one side was installed on an RC frame, with an SD placed at the center of the wall. The results showed that the SD started poorly operable when the story drift angle exceeded 1/200 rad, and became inoperable when the story drift angle exceeded 1/100 rad. For the present specimen with 21 mm one side, the story drift angle at poorly operable was nearly identical. However, inoperable occurred at a slightly smaller story drift angle in the test. This is because the study defined inoperable as a required opening force exceeding 300 N. When this force criterion is taken into account, the results of the two studies are essentially consistent.

4.CONCLUSIONS

In this study, static in-plane loading tests were conducted on LGS walls with a center-opening, aiming to clarify damage patterns and SD operability for various LGS wall specifications. The main findings are summarized as follows:

(1) LGS walls with an opening reduced the lateral load-bearing capacity, while the presence of SD had little effect.

(2) LGS walls with an opening accelerated the initiation of wall damage.

(3) Regarding damage patterns, specimens with 12.5 mm gypsum boards on one or both sides exhibited earlier damage initiation. In contrast, specimens with 21 mm gypsum boards on one side showed a tendency for delayed damage initiation.

(4) With respect to SD operability, on one side gypsum board specimens, the SD became inoperable at story drift angles of approximately ±1/67 rad. In contrast, on both sides gypsum board specimens, inoperability occurred earlier, at approximately ±1/100 rad.

Future studies will focus on the gypsum board specifications associated with early inoperability of the SD (12.5 mm on both sides) and early damage of the LGS walls (12.5 mm on one side). In particular, the influence of the opening position will be examined to clarify how different opening locations affect both LGS wall damage and SD operability.

REFERENCES

Isoda, M., Oki, Y., Tatsumi, N., Kishiki, S., Ishihara, T., [2021] "Behaviour of LGS walls against in-plane relative displacements and out-of-plane inertial force," *Proceeding of Constructional Steel*, Vol. 29, pp. 366-373.

Ito, H., Nishida, K., Sakamoto, I., Yamanouchi, H., [1986] "-U.S. -Japan cooperative research program utilizing large-scale testing facilities-full-scale seismic test of nonstructural elements," *Summaries of Technical Papers of Annual Meeting, Architectural Institute of Japan,* pp.309-312.

Joint Editorial Committee for the Report on the Great East Japan Earthquake Disaster [2019] *Report on the Great East Japan Earthquake Disaster, Building Series Volume 6, Non-Structural Elements*, AIJ Press, Japan.

Kawamura, Y., Huang, J., Kurata, M., Takaoka, M., Lyu, Z., [2025] "A study on damage mitigation measures for lightweight steel framed partition walls with doors," *Kinki Chapter, Architectural Institute of Japan*, pp. 321-324.

Kugimoto, M., Kishiki, S., Kurosawa, M., Oki, Y., [2025] "Experiments on combined in-plane and out-of-plane behaviour of LGS partition walls with various specifications," *Kanto Chapter, Architectural Institute of Japan*, pp. 173-176.

Lee, T., Kato, M., Matsumiya, T., Suita, K., Nakashima, M. [2007] "Seismic performance evaluation of non-structural components: Drywall partitions," *Earthquake Engineering & Structural Dynamics*, Vol. 36, pp.367-382.

Lyu, Z., Takaoka, M., Kurata, M., Huang, J., Kawamura, Y., [2023] "Studies on effects of door openings on cold-formed framed gypsum partition walls for reducing damage," *Summaries of Technical Papers of Annual Meeting, Architectural Institute of Japan,* pp.915-916.

National Institute for Land and Infrastructure Management [2016] "Quick Report of the Field Survey and the Building Damage by the 2016 Kumamoto Earthquake," *Technical Note of National Institute for Land and Infrastructure Management No.929, Building Research Data No.173*, National Institute for Land and Infrastructure Management, Building Research Institute, Japan.

Seike, T., Yamada, S., Kishiki, S., Ishida, T., Iyama, J., Tatsumi, N., [2019] "Cyclic loading test of dry partition wall within steel frame," *Summaries of Technical Papers of Annual Meeting, Architectural Institute of Japan,* pp.1431-1440.

Yagi, S., Tatsumi, N., Isoda, M., Kishiki, S., Honda, S., Seike, T., Maeda, M., Nishimura, K., [2022] "Experimental evaluation of LGS partition wall and steel door installed in RC frame," *AIJ Journal of Technology and Design,* Vol. 28, No. 70, pp.1125-1130

Hysteretic behavior, stiffness degradation, and energy dissipation in screw connections of cold-formed steel framed plasterboard partitions

D. D'Angela[1], A. Bonati[2], O. Coppola[2], and G. Magliulo[1,2]

[1] University of Naples Federico II, Department of Structures for Engineering and Architecture
Via Claudio 21, 80125 Naples, Italy
{danilo.dangela, gmagliul}@unina.it
[2] National Research Council (CNR), Construction Technologies Institute (ITC)
Via Lombardia 49, 20098 San Giuliano Milanese, Italy
{antonio.bonati, orsola.coppola}@itc.cnr.it

Abstract. The paper investigates the hysteretic behavior of screw connections in cold-formed steel framed plasterboard partitions by means of quasi-static cyclic tests, up to failure. The focus is on the hysteretic curves and on the quantification of stiffness degradation and energy dissipation measures, as a function of the different partition characteristics and arrangement, along the mechanical degradation. The investigated partition characteristics include number of board layers, thickness of the board, type of screw connection, and stud cross-section; three different loading schemes and testing configurations were considered. The evolution of stiffness degradation and energy dissipation along the cyclic response is quantified, and clear trends are identified. In particular, statistical-based closed-form expressions are developed, referring to the number of cycles. These expressions represent quantitative tools to estimate hysteresis behavior of screw connection in various plasterboard partition systems, for expeditious assessment and development of accurate numerical models.

Keywords: Seismic risk, Functional adaptability, Resilience, Non-structural elements, Healthcare facilities.

1. INTRODUCTION

Light internal partitions typically consist of vertical board panels attached to timber or cold-formed steel frames, often including internal insulation. Plasterboards are commonly used for their cost-effectiveness, ease of installation, and fire resistance, and are generally fastened to the frame using self-drilling screw connections.

These nonstructural elements are highly vulnerable during earthquakes, as confirmed by post-event surveys (Baird et al., 2011 and seismic loss assessments [Magliulo et al., 2021]. Even moderate seismic events can cause significant damage to plasterboard partitions, leading to operational disruptions [Tokas, 2011], economic losses [Magliulo et al., 2021], and, in severe cases, risks to human safety [Perrone et al., 2021], particularly in critical facilities such as hospitals [Di Sarno et al., 2019].

In the framework of Performance-Based Earthquake Engineering (PBEE) [Bertero et al., 2002], plasterboard partitions are classified as inter-story drift-sensitive in-plane components, as cyclic deformations of the main structure can damage partitions without an edge gap. Out-of-plane collapse is also possible, influenced by the acceleration at the centre of mass and the partition's mass. In-plane deformations may further trigger out-of-plane failure through buckling of the internal steel frame [Petrone et al., 2015], highlighting the dual sensitivity of these partitions to both displacements and accelerations.

Over the past decade, analytical and numerical models have been developed to simulate the seismic response of partitions efficiently. While early studies on plasterboard partitions date back to the 1980s [Agbabian, 1981; Anicic et al., 1980], the literature has expanded rapidly with numerous experimental campaigns [Fiorino et al., 2019; Retamales et al., 2013] and modelling efforts [Davies et al., 2011; Kanvinde et al., 2006]. However, the element most critical to seismic response, the screw connection between board and frame, remains relatively underexplored. Most previous research focused on overall partition behaviour rather than generalizable findings on connection performance. Only a few studies have specifically addressed screw connections, performing experimental tests [Magliulo et al., 2025; Rahmanishamsi et al., 2016a] and combining experimental characterization with numerical modelling [Abeysiriwardena et al., 2020; Rahmanishamsi et al., 2016b; Saifullah et al., 2022; Tawfik and Abu-Hamd, 2024] to capture hysteretic behaviour.

The study reports further elaborations and technical insights associated with experimental tests carried out by the authors at the Department of Structures for Engineering and Architecture, University of Naples Federico II ([Magliulo et al., 2025]. The experimentation consists in cyclic shear assessment of panel-to-stud screw connections in steel-framed plasterboard partitions. Hysteretic curves are assessed, and secant stiffness and dissipated energy measures are expressed as a function of cyclic degradation behavior.

2.METHODOLOGY

Cyclic quasi-static mechanical tests were carried out on a wide range of panel-to-stud screw connections to characterize their hysteretic behaviour. These connections were representative of realistic cold-formed steel framed plasterboard partitions, accounting for several uncertainty sources associated with loading condition and specimen features. Hysteretic force-deformation curves were assessed, and stiffness degradation and energy dissipation were estimated as a function of the cyclic loading. The experimental campaign is described in detail in [Magliulo et al., 2025], and the present paper provides further elaborations and discussion remarks, aiming at providing useful behaviour insights into the seismic response and capacity of screw connections in plasterboard partitions.

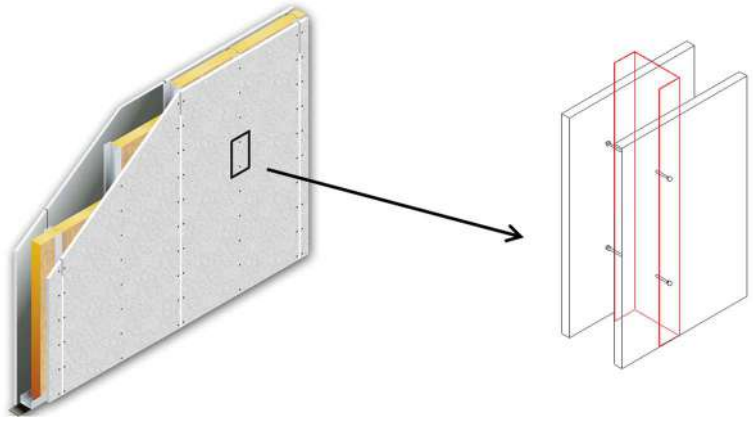
2.1 SPECIMENS AND TEST CONFIGURATIONS

Various panel-to-stud screw connection specimens were tested, and these represented a portion of partition panels. An example of plasterboard partition and related screw connection specimen is depicted in Figure 1, considering a single board layer partition panel.

Each specimen consisted of a steel stud with one or two plasterboard panels fastened to each side of the stud flange using screws. The specimens vary in terms of stud cross-section, plasterboard thickness, and the number of boards applied per side of the partition. The studs are cold-formed steel members with a C-shaped profile. Table 1 reports the tested specimens, and they are identified by the letter C, followed by the web depth (90 or 60 mm), flange width (38 mm), stiffener length (6 mm), and profile thickness (0.5, 0.6, or 0.85 mm). The mean tensile yield strength was 301.0 N/mm², while the average Young's modulus was 210,000 N/mm², both values determined experimentally. The plasterboards were attached to the studs with self-drilling screws, 3.5 mm in diameter, with lengths of 19, 25, 35, or 45 mm depending on the number and thickness of the board layers. The screw strength was assessed through Rockwell hardness testing, yielding a value of about 44.

Three loading configurations were examined for each specimen to comprehensively assess the seismic behaviour (shear response) of the screw connections, as detailed below. Further details and drawings could be found in [Magliulo et al., 2025].

- Configuration 1 (C1): the stud is attached to the plasterboards with two screws spaced 300 mm apart, protruding 18 mm from the edge of the panels. Vertically, the screws are positioned 10 mm from the panel edge. This setup reproduces the interface conditions between the stud and adjacent boards.
- Configuration 2 (C2): the stud is fixed to the plasterboards with two screws spaced 300 mm apart, aligned with the panel edges. In this case, the screws are placed 22 mm from the vertical edge of the panels. This configuration represents the condition of an internal stud, away from the board edges.
- Configuration 3 (C3): the stud is connected to each plasterboard panel by a single screw.



(a) (b)

Figure 1. (a) Example of steel framed plasterboard partition and detail of panel-to-stud screw connection (single board layer partition panel).

2.2 TEST SETUP AND LOADING PROTOCOLS

The testing setup was designed considering the specific loading scheme and condition, reproducing realistic shear loading configurations on the screw specimens. Figure 2 illustrates the testing machine and setup during a representative test on a double board layered specimen.

Table 1. Specimen configuration, screw connection type, and testing configuration. Screw connection types refer to implementation of (A) internal and (B) external screws, which cross double panels and single panels, respectively.

Specimen configuration				Screw connection type	Testing configuration
ID	**Type of studs**	**Board thickness [mm]**	**Number of board layers [-]**		
SC01	C 90x38x6x0.85	15	1	A	C1,C2,C3
SC02	C 90x38x6x0.85	15	2	A	C1,C2,C3
				B	C1,C2,C3
SC03	C 90x38x6x0.85	12.5	2	A	C1,C2,C3
				B	C1,C2,C3
SC04	C 90x38x6x0.85	12.5	2	A	C1,C2,C3
				B	C1,C2,C3
SC05	C 90x38x6x0.85	12.5	1	A	C1,C2,C3
SC06*	C 90x38x6x0.85	12.5	2	A	C1,C2,C3
				B	C1,C2,C3
SC07	C 90x38x6x0.85	10	1	A	C1,C2,C3
SC08	C 90x38x6x0.85	15	1	A	C1,C2,C3
SC09	C 60x38x6x0.50	15	1	A	C1,C2,C3
SC10	C 60x38x6x0.60	15	2	A	C1,C2,C3
				B	C1,C2,C3
SC11	C 60x38x6x0.60	10	2	A	C1,C2,C3
SC12	C 90x38x6x0.85	12.5 & 15**	2	A	C1,C2,C3
				B	C1,C2,C3
SC13	C 60x38x6x0.50	12.5	1	A	C1,C2,C3
SC14*	C 90x38x6x0.85	12.5	2	A	C1,C2,C3
				B	C1,C2,C3
SC15	C 60x38x6x0.50	12.5	2	A	C1,C2,C3
				B	C1,C2,C3
SC16	C 90x38x6x0.85	15	2	A	C1,C2,C3
				B	C1,C2,C3
SC17	C 60x38x6x0.50	15	2	A	C1,C2,C3
				B	C1,C2,C3

* plasterboards are made by different materials; ** each side has one layer 12.5 mm thick and the second one 15 mm thick.

The tests under displacement control following the quasi-static FEMA 461-I protocol [FEMA, 2007]. Specifically, twenty incremental loading steps were applied, each consisting of two loading cycles with the same peak displacement amplitude (a_i), considering an incremental factor (c parameter) equal to 1.4. The initial displacement amplitude was selected to be sufficiently smaller than the threshold at which the first damage state had been identified in previous reference tests. In particular, the initial (final) displacement amplitude was set equal to 0.04 (22.00) mm, and the loading rate (v) during the steps regularly increased from 0.01 mm/s to 0.50 mm/s, according to reference applications. Further detail regarding the loading protocol is provided in Figure 3, where a_i and v are depicted for all loading steps.

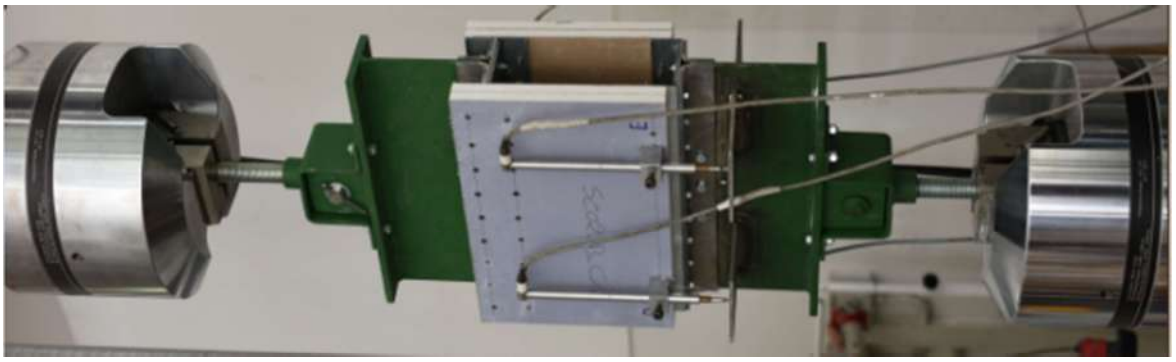


Figure 2. Testing machine and setup with specimen under loading (90° rotated view).

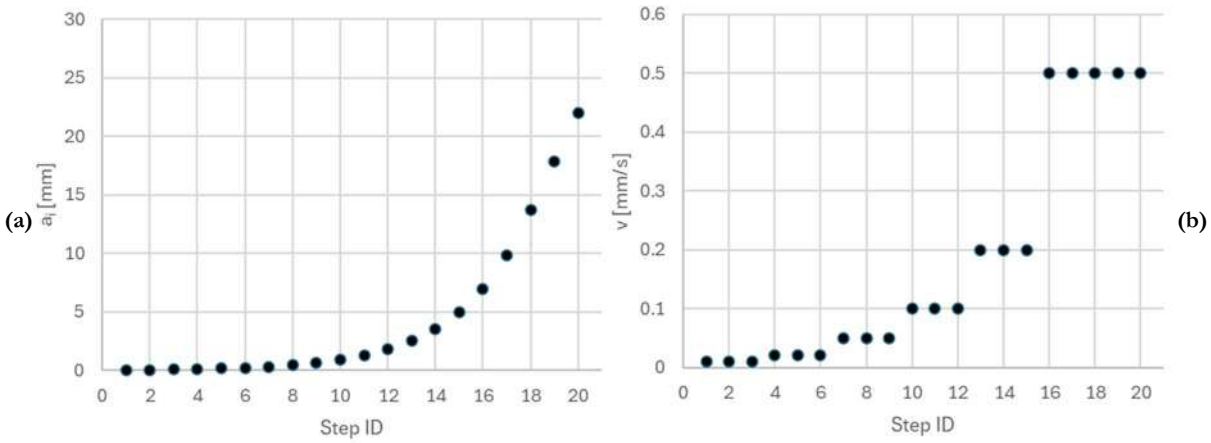


Figure 3. Loading protocol features: (a) displacement peak amplitude (a_i) and (b) loading rate (v) as a function of testing Step ID.

3.RESULTS AND DISCUSSION

3.1 GENERAL BEHAVIOUR

Figure 4 shows representative force (F) vs. displacement (d_m) curves for each screw connection configuration, with displacements obtained as the average of LVDT readings. The hysteretic curves refer to single screw behaviour, and they were derived by dividing the total specimen shear force by the number of screws.

Configurations C1 (Figure 4a) and C2 (Figure 4b) display asymmetric behaviour: peak strength in positive shear (tension loading direction) is reached at smaller displacements than in negative shear (compression loading direction), and this latter strength is generally higher. This asymmetric behaviour is due to the different resisting and damage mechanisms that are exhibited along the positive and negative shear directions, which are associated with a higher ductility along negative direction. Failure progresses through screw tilting in the stud flange (yielding, green markers), edge breakage of the board near the screw (post-peak drop, yellow markers), and eventual screw pull-out. In C3 (Figure 4c), the response is more stable and relatively symmetric along the positive and negative directions; this is due to favourable screw positioning; damage involves tilting (yielding, green marker) followed by pull-through at maximum strength in both directions.

3.2 HYSTERETIC RESPONSE: COMPARISON ANALYSIS

A comparison analysis was carried out to identify the quantitative influence of the investigated specimen and loading features (e.g., see Rahmanishamsi et al., 2016). The behaviour of the screw connections was evaluated with respect to the following main variables: (1) test configuration, (2) connection type, (3) board thickness, (4) number of board layers, and (5) additional influencing factors.

The analysis highlights that tensile F_{max} in C2 is on average 22% higher than C1, while C3 exhibits about 32% higher tensile strength than C1–C2, with only minor reduction in compression. Tensile displacements at maximum strength d_{max} are 46% higher in C2 than C1 and 53% higher in C3 than C2, whereas compression results are less regular. Additional parameters also affect response: type B connections show higher strength (+20% along tension +25% along compression) but lower deformability than type A; double-layer boards increase strength by 10–50%; board thickness has a variable influence; and stud cross-section is negligible.

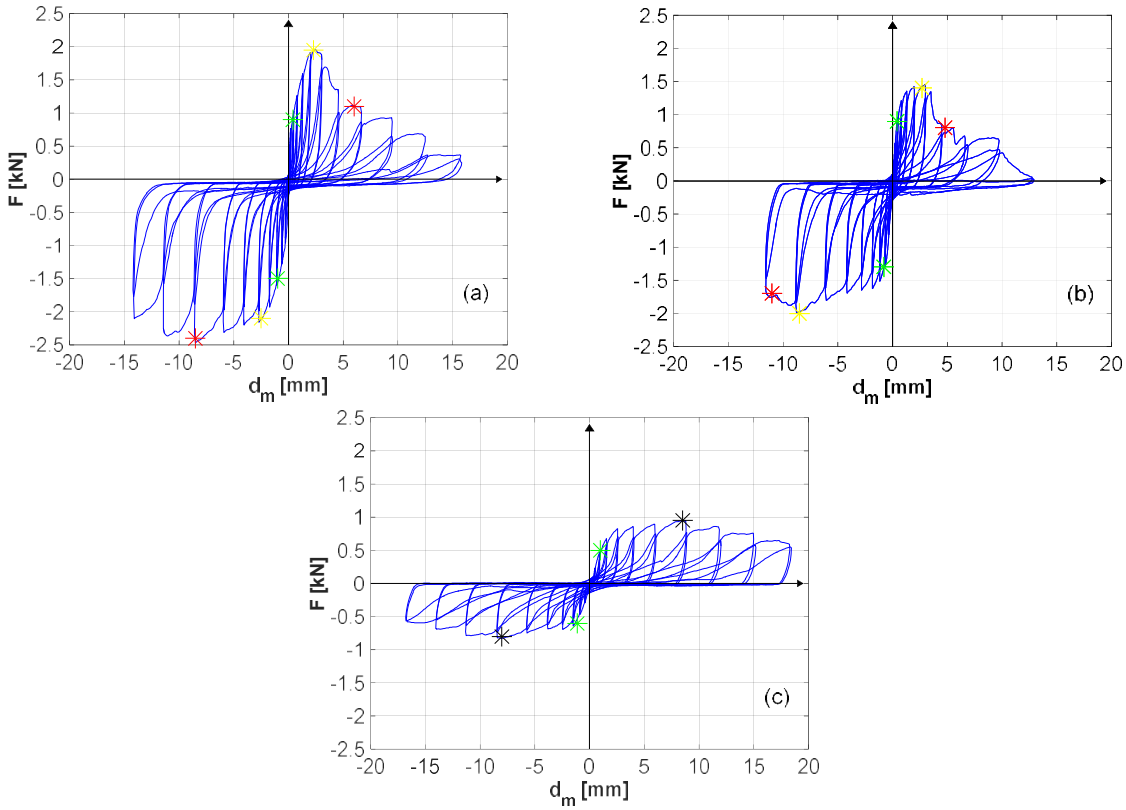


Figure 4. Force (F) vs. displacement (d_m) curves associated with representative test results: (a) C1, (b) C2, and (c) C3 configuration.

3.3 STIFFNESS DEGRADATION

Statistical models were developed for these parameters in relation to the cyclic secant stiffness and dissipated energy, and models for secant stiffness degradation are estimated. Cyclic secant stiffness (K_{Si}) was evaluated to capture the influence of hysteretic response on loading stiffness and to serve as an indicator of damage. For each positive cycle and for both first and second fixed-amplitude cycles, K_{Si} was calculated using Equation (1), where $F_{max,i}$ and $F_{min,i}$ ($d_{max,i}$ and $d_{min,i}$) denote the maximum and minimum force (displacement) of the ith cycle, respectively.

$$K_{Si} = \frac{F_{max,i} - F_{min,i}}{d_{max,i} - d_{min,i}} \quad (1)$$

Figure 5 shows the cyclic response and secant stiffness for a representative case. $K_{S1,i}$ and $K_{S2,i}$ denote the ith secant stiffness along the positive displacement cycles for the first and second curves, respectively. Stiffness remains nearly constant up to the 6th cycle, then decreases sharply, halving by the 8th cycle, and dropping below 15% of the initial value by the 12th cycle. Similar trends were observed in other specimens, with differences mainly in the cycle and displacement at which degradation begins, while the overall reduction pattern remains comparable. Initial stiffness values were determined for all cases as a reference for the elastic response, and statistical models, including dimensionless degradation laws.

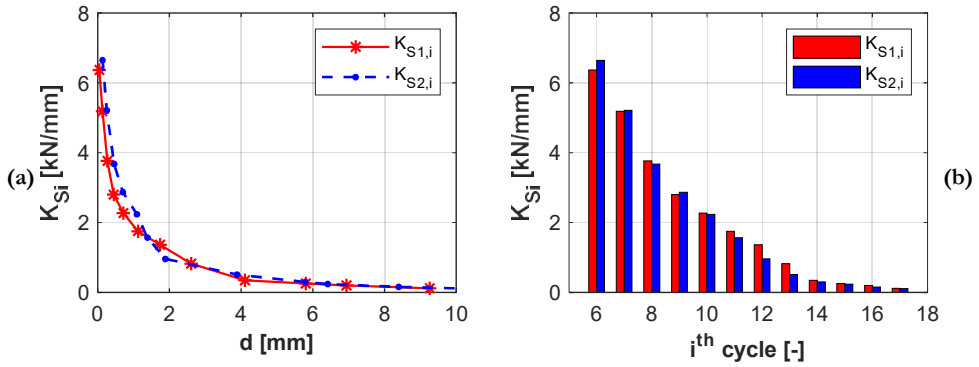


Figure 5. Secant stiffness results associated with SC07_A_C1 case: (a) secant stiffness values ($K_{S1,i}$ and $K_{S2,i}$) plotted against positive *i*th semicycle displacement d and (b) $K_{S1,i}$ and $K_{S2,i}$ plotted as a function of the *i*th cycle. S1 and S2 refer to first and second fixed-amplitude cycles, respectively.

3.4 Energy Dissipation

For each cycle, energy dissipation was determined by integrating the hysteretic force–displacement loops, considering both first- and second-cycle curves. Figure 6 illustrates the cyclic response and the corresponding dissipated energy for a representative specimen. $E_{D1,i}$ and $E_{D2,I}$ indicate the energy dissipated during the ith cycle, calculated as the sum of positive and negative semicycles, although the plots refer to positive displacements. In this case, dissipation starts at the 8th cycle (Figure 6c), when the positive peak displacement reaches approximately 2 mm (Figure 6b). Up to the 13th cycle, energy dissipation in the first and second cycles is almost identical; beyond this point, dissipation during the second cycle grows significantly larger than in the first, reaching very high values by the final cycle. Statistical models associated with the total energy dissipated are estimated across all cycles and links dissipation to the specimen properties and loading characteristics.

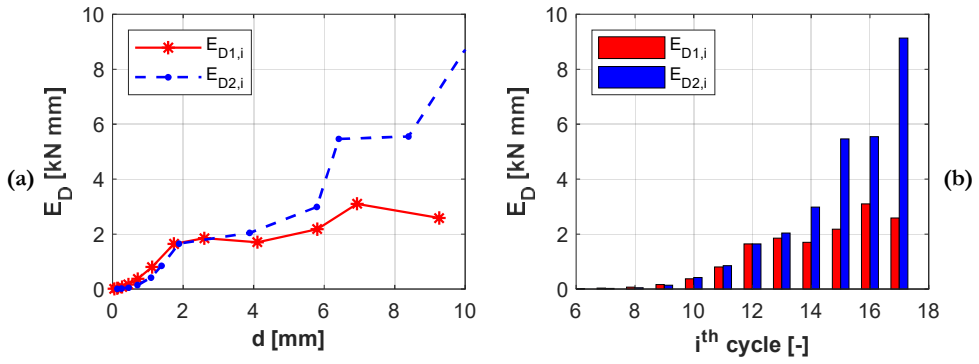


Figure 6. Dissipated energy results associated with SC07_A_C1 case, (a) dissipated energy valyes ($E_{D1,i}$ and $E_{D2,i}$) plotted against positive *i*th semicycle displacement d and (b) $E_{D1,i}$ and $E_{D2,i}$ plotted as a function of the *i*th cycle. ED_1 and ED_2 refer to first and second fixed-amplitude cycles, respectively.

The response in the second cycle dissipates substantially more energy than that of the first cycle, with measurable differences observed through both direct comparisons and statistical analyses. Other specimen and testing parameters also strongly influence energy dissipation: for instance, specimens with thicker

boards exhibit greater dissipation, while testing configuration and connection type can further impact the dissipation behaviour.

4. CONCLUSIONS

This study investigates the hysteretic behaviour of screw connections in cold-formed framed plasterboard partitions through cyclic quasi-static tests, aiming to understand the influence of specimen and testing parameters on energy dissipation, stiffness degradation, and damage evolution. Tests considered variations in testing configuration, screw type, board thickness, number of layers, and stud cross-section width. The main stages of the hysteretic response were identified and linked to observed damage conditions.

The effects of key parameters were quantified, and statistical-based capacity curves were produced to account for representative uncertainties associated with the investigated features. The results provide insights into the influence of specimen and loading features on mechanical behaviour, support optimized partition design, and serve as a basis for rapid assessment and calibration of numerical models. Ongoing work extends these findings to additional panel and screw types.

ACKNOWLEDGEMENTS

This study was supported by (1) Etex Building Performance International under the project agreement ETEX-DIST 2016–2018, and (2) the Italian Ministry of University and Research (MUR] through the PRIN 2020 project YKY7W4 ENRICH. The authors gratefully acknowledge Eng. Pauline Lopez for her assistance with the experimental tests and Eng. Maurizio Martino for his support in both the experimental tests and data processing.

REFERENCES

Abeysiriwardena T, Peiris M, Mahendran M. Local in-plane strength and stiffness of stud-to-sheathing fastener connections in LSF wall panels. Thin-Walled Structures 2021;160:107383. https://doi.org/10.1016/j.tws.2020.107383.

Agbabian MS. Seismic resistance of interior partitions. Proceedings of the Seminar on Repair and Retrofit of Structures, Univ of Michigan, Dep of Civil Engineering; 1981, p. 109–25.

Anicic D, Zamolo M, Soric Z. Experiments on non-structural partition walls exposed to seismic forces. Proceedings of the 7th World Conference on Earthquake Engineering, vol. 6, Istanbul, Turkey: World Conference on Earthquake Engineering; 1980, p. 144–50.

Baird A, Tasligedik AS, Palermo A, Pampanin S. Seismic Performance of Vertical Nonstructural Components in the 22 February 2011 Christchurch Earthquake. Earthquake Spectra 2014;30:401–25. https://doi.org/10.1193/031013EQS067M.

Bertero RD, Bertero VV. Performance - based seismic engineering: the need for a reliable conceptual comprehensive approach. Earthq Engng Struct Dyn 2002;31:627-52. https://doi.org/10.1002/eqe.146.

Davies R, Retamales G, Mosqueda G, Filiatrault A. Experimental Seismic Evaluation, Model Parameterization, and Effects of Cold-Formed Steel-Framed Gypsum Partition Walls on the Seismic Performance of an Essential Facility. Technical Report MCEER-11-0005. State University of New York: University at Buffalo; 2011.

Davies R, Retamales G, Mosqueda G, Filiatrault A. Experimental Seismic Evaluation, Model Parameterization, and Effects of Cold-Formed Steel-Framed Gypsum Partition Walls on the Seismic Performance of an Essential Facility. Technical Report MCEER-11-0005. State University of New York: University at Buffalo; 2011.

Di Sarno L, Magliulo G, D'Angela D, Cosenza E. Experimental assessment of the seismic performance of hospital cabinets using shake table testing. Earthquake Engng Struct Dyn. 2019; 48: 103–123. https://doi.org/10.1002/eqe.3127

Federal Emergency Management Agency (FEMA]. Interim protocols for determining seismic performance characteristics of structural and nonstructural components through laboratory testing. Report No. FEMA 461. Washington D.C., USA: 2007.

Fiorino L, Bucciero B, Landolfo R. Evaluation of seismic dynamic behaviour of drywall partitions, façades and ceilings through shake table testing. Engineering Structures 2019;180:103–23. https://doi.org/10.1016/j.engstruct.2018.11.028.

Kanvinde AM, Deierlein GG. Analytical Models for the Seismic Performance of Gypsum Drywall Partitions. Earthquake Spectra 2006;22:391–411. https://doi.org/10.1193/1.2191927.

Kyprianou C, Kyvelou P, Gardner L, Nethercot DA. Characterisation of material and connection behaviour in sheathed cold-formed steel wall systems – Part 2: Analytical modelling. Structures 2021;30:1184–99. https://doi.org/10.1016/j.istruc.2020.12.052.

Magliulo, G., D'Angela, D., Bonati, A., Coppola, O., 2025. Cyclic behavior of screw connections in plasterboard partitions. Construction and Building Materials 484, 141780. https://doi.org/10.1016/j.conbuildmat.2025.141780

Magliulo G, D'Angela D, Lopez P, Manfredi G. Nonstructural Seismic Loss Analysis of Traditional and Innovative Partition Systems Housed in Code-conforming RC Frame Buildings. Journal of Earthquake Engineering 2021:1–28. https://doi.org/10.1080/13632469.2021.1983488.

Perrone D, Filiatrault A, Peloso S, Brunesi E, Beiter C, Piccinin R. Experimental seismic response evaluation of suspended piping restraint installations. Bull Earthquake Eng 2020;18:1499–524. https://doi.org/10.1007/s10518-019-00755-5.

Petrone C, Magliulo G, Lopez P, Manfredi G. Seismic fragility of plasterboard partitions via in-plane quasi-static tests. Earthquake Engng Struct Dyn 2015;44:2589–606. https://doi.org/10.1002/eqe.2600.

Price HJ, De Sortis A, Schotanus M. Performance of the San Salvatore Regional Hospital in the 2009 L'Aquila Earthquake. Earthquake Spectra 2012;28:239–56. https://doi.org/10.1193/1.3673595.

Rahmanishamsi, E., Soroushian, S., & Maragakis, M. Cyclic shear behavior of gypsum board-to-steel stud screw connections in nonstructural walls. Earthquake Spectra 2016a, 32(1), 415-439. https://doi.org/10.1193/062714EQS091M

Rahmanishamsi, E., Soroushian, S., and Maragakis, M. Analytical model for the in ‐ plane seismic performance of cold ‐ formed steel ‐ framed gypsum partition walls. Earthquake Engineering & Structural Dynamics 45.4 (2016b): 619-634. https://doi.org/10.1002/eqe.2676

Rahmanishamsi, E., Soroushian, S., and Maragakis, M. Capacity evaluation of typical stud-track screw connections in nonstructural walls. Journal of Earthquake Engineering 2016c, 20(6), 931-953.

Retamales R, Davies R, Mosqueda G, Filiatrault A. Experimental Seismic Fragility of Cold-Formed Steel Framed Gypsum Partition Walls. J Struct Eng 2013;139:1285–93. https://doi.org/10.1061/(ASCE]ST.1943-541X.0000657.

Saifullah I, Gad E, Shahi R, Wilson J, Lam N, Watson K. Shear behaviour of screw connections in plasterboard sheathed cold-formed steel-framed ceiling diaphragms: experimental and comparative study. Australian Journal of Civil Engineering 2022;20:326–44. https://doi.org/10.1080/14488353.2021.1974659.

Tawfik, N.M., Abu-Hamd, M., 2024. Numerical modeling of sheathed screw connections in CFS shear walls. Structures 63, 106311. https://doi.org/10.1016/j.istruc.2024.106311

Tokas, C.V., 2011. Nonstructural Components and Systems-Designing Hospitals for Post-Earthquake Functionality, in: AEI 2011. Presented at the Architectural Engineering Conference (AEI) 2011, American Society of Civil Engineers, Oakland, California, United States, pp. 378–389. https://doi.org/10.1061/41168(399)45

Sixth International Workshop on the Seismic Performance of Non-Structural Elements (SPONSE 2026)

Experimental Analysis of the Seismic In-Plane Performance of Cold-Formed Steel Gypsum Drywall Systems: Glued vs. Screwed Connections

Catalina M. Nigro[1] and Ghislain Rivron[2]

[1] Universidad Tecnologica Nacional Facultad Regional Concepcion del Uruguay
Ingeniero Pereyra 676, 3260 Concepción del Uruguay, Argentina
e-mail: catalinamnigro@gmail.com
[2] Knauf
Knauf Gips KG, Am Bahnhof 7, 97346 Iphofen, Germany
e-mail: ghislain.rivron@knauf.com

Abstract. Over the past years, the spotlight has increasingly turned to non-structural seismic-resistant partitions. Research and real-world experience have proven their significant impact on the overall seismic safety of buildings. Among these, cold-formed steel (CFS) gypsum drywalls stand out as a key element for improving seismic performance by reducing structural weight, minimizing hazards during failure, and facilitating post-event repair and reconstruction, without compromising sustainability, health, or comfort.

In the pursuit of enhanced drywall partitions in the face of seismic events, innovations in board-to-frame connections have emerged as an important area of study. Glued connections are an alternative to the traditional screwed connections, offering the potential to improve stiffness and overall mechanical performance.

This study aims to investigate the seismic behaviour of single-layer drywall systems with screwed and glued connections through a comparative analysis. One in-plane test for each type of board-to-frame connection was conducted following the loading protocol described in FEMA 461. The results, presented as force versus inter-storey drift curves and their correlation with damage states, suggest that glued connections minimise damage at low inter-story drift ratio (IDR) levels and eliminate the effects that often initiate damage mechanisms, such as screw tilting.

These findings mark a step forward in the development of more seismic resilient and cost-effective drywall systems and collaborates in the improvement of life safety and reduced post-seismic repair costs, offering a practical solution to the challenges of seismic design.

Keywords: Non-structural elements, drywall partitions, in-plane testing, glued connections, damage states.

1. INTRODUCTION

Learnings from previous earthquakes have shown that non-structural elements (NSEs) can also sustain significant damage during these natural events. Particularly, in low to moderate intensity earthquakes where structural risk is low, properly designing NSEs increases building safety and enables them to remain operational after an earthquake, while also reducing repair costs (Zito, et al., 2022).

As a widely used architectural NSE, cold-formed steel (CFS) gypsum drywalls are of high interest due to their light weight, ease of repair, and contribution to the seismic performance of buildings. When exploring the potential system improvements, innovations in board-to-frame connections emerge as a promising area of study. Researchers (Yazdi, et al., 2022) (Guzman, et al., 2025) (Komara, et al., 2017) have proposed the use of adhesive connections. Connect board to frame by using adhesive implies the total, or almost total, replacement of screws and the development of a continuous bonding leading to a full composite behaviour.

Traditional screw-based connections, while effective, introduce discontinuities in the system that may act as stress concentrators, potentially leading to localized damage. As explained in past studies (Shin & Kim, 2020), damage to partitions normally begins at the edges of the gypsum boards due to tilting of the screws when approximately 75% of the maximum load is reached. This then tends to evolve into joint loosening and screw head pull-through, followed by the appearance of damage in the board with increasingly larger cracks and deformation in the studs resulting in loss of functionality or risk to life.

In contrast, adhesive connections offer the potential for a continuous bond between the board and frame, which decreases concentration of stresses and could enhance desirable properties such as stiffness and strength (Guzman, et al., 2025). However, this approach also introduces new challenges, such as behaviour at higher inter-storey drift ratios (IDR) and fire resistance, where the presence of adhesive and the continuity of the bond may lead to unintended failure modes or performance trade-offs.

Regarding seismic behaviour, FEMA 461 (Applied Technology Council, 2007) and FEMA P-58 Background Document 3.9 (Miranda & Mosqueda, 2011) propose a protocol to test partitions under in-plane quasi-static cyclic loads and analyse their behaviour across three damage states (DS) related to drywall reparability.

The main objective of this research is to examine the influence of board-to-frame connections on the seismic behaviour of drywall partitions, with particular focus on the interaction and failure mechanisms between the deformable metal frame and the less ductile gypsum board when adhesive is used as the bonding method. Understanding this interaction is crucial for developing design strategies that minimise damage and enhance the seismic resilience, the overall performance of drywall partitions and the reduction of post-event repair demand.

To this end, experimental research was conducted on two full-scale specimens: one with screwed connections and one with glued connections. A one-to-one comparison is presented, focusing on Force vs. IDR curves and the correlation between IDR and DS.

2. EXPERIMENTAL WORK

Experimental testing is considered the most reliable and robust option when assessing NSEs. In this sense the following describes the methodology carried out and the process to obtain the stated results.

2.1 DESCRIPTION OF TESTS SPECIMENS AND MATERIALS

The experimental campaign consists of two real-scale, single-layer specimens, each 4.0 m high and 3.75 m long. One specimen has traditional screwed board-to-frame connections (W-01), while the other has glued connections (W-02). Details of the materials used for the drywalls are listed in Table 1.

Table 1: Material details

	Track	Stud	Board	Connection	Joint tape	Joint filler
W-01	UW 75 - 0.6 mm	CW 75 - 0.6 mm s/625 mm	GKB - 12.5 x 2500 mm	TN 25 s/250 mm	Knauf Kurt Tape	Knauf Uniflott
W-02	UW 75 - 0.6 mm	CW 75 - 0.6 mm s/625 mm	GKB - 12.5 x 2500 mm	Glue - Knauf Power Kleber	Knauf Kurt Tape	Knauf Uniflott

Figure 1 explains how the boards were attached to the frame using glue on the vertical studs and screws in the upper corners of each board to prevent them from sliding. Also, it shows the final aspect of the test specimen.



Figure 1: Test specimen with glued board-to-stud connections.

2.2 TEST SET-UP AND INSTRUMENTATION

The drywall partitions were tested at Knauf's facilities using a monotonic in-plane cyclic testing method based on the FEMA 461 protocol "Interim Testing Protocols for Determining the Seismic Performance Characteristics of Structural and Non-structural Components". This protocol was specifically developed to evaluate and quantify the seismic behaviour of non-structural elements (NSEs).

In accordance with these guidelines, the specimens were mounted in a testing rack. Horizontal cyclic loading with increasing displacement was then applied to the top corner of the rack to investigate the effect of the IDR on the specimens. During the tests, relative displacements and resisted loads were continuously

recorded with sensors. Eight linear potentiometers (WT01 to WT08) were installed in pairs at each corner to measure relative displacement between the wall and concrete surroundings in both horizontal and vertical directions, while two wire potentiometers (WP01 and WP02) were placed along the diagonals to capture deformation in that direction. The layout of the instrumentation is shown in Figure 2.

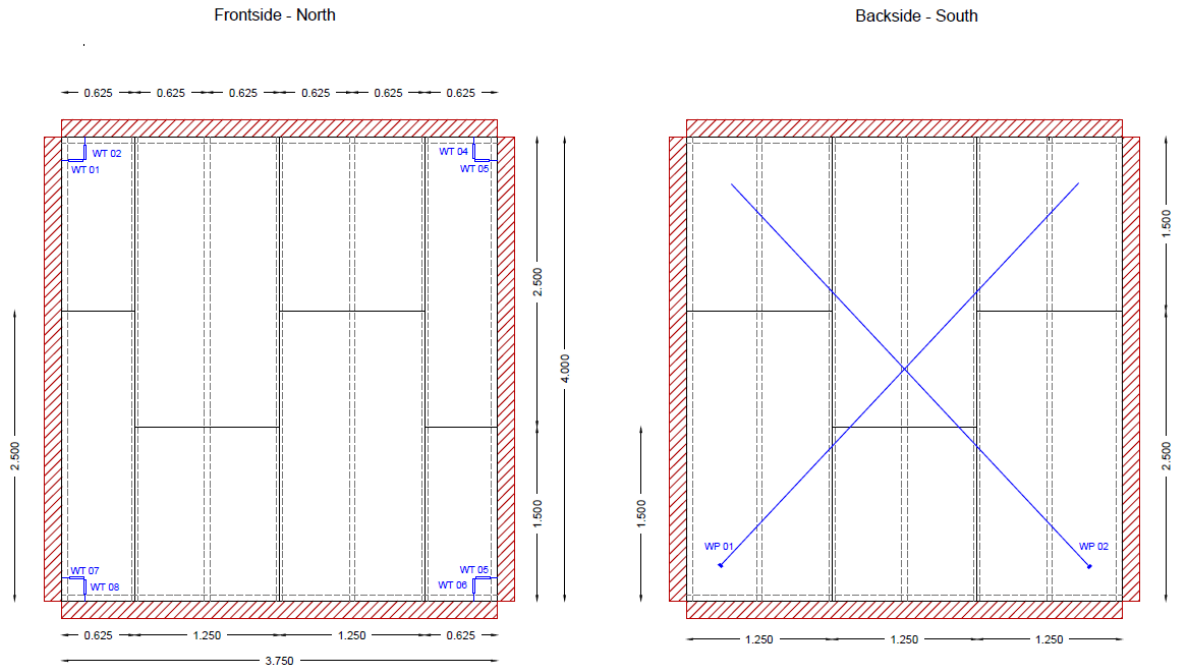


Figure 2: sensors layout

To complement this quantitative evaluation, the qualitative assessment of the wall behaviour followed the guidance and recommendations of FEMA P-58 Background Documentation 3.9.2: "Seismic Fragility of Building Interior Cold-Formed Steel Framed Gypsum Partition Walls". This document serves as a technical reference for analysing non-structural components and for identifying damage states (DS), particularly in relation to their reparability.

By combining the quantitative results of the testing protocol with the qualitative classification of damage, the seismic performance of each specimen was characterized in terms of deformation and load capacity, as well as typical damage patterns such as origin, size, length, and surface markings, which give indications regarding the damage mechanism involved.

2.3 LOADING HISTORY

Specimens were tested according to FEMA 461 protocol. This document provides for in-plane quasi-static cyclic tests a loading history with two cycles per drift level and stepwise increasing displacement amplitudes given by the relation in Equation 1:

$$a_{i+1} = 1{,}4\ a_i \tag{1}$$

The initial amplitude a_1 must be equal to the targeted smallest deformation Δ_0 set here as 0,15% of the wall height. The last amplitude of the cyclic protocol must be the targeted maximum deformation Δ_m set here as 3% of the wall height. From that point and up to the load capabilities of the set-up, the loading history continues in increments of $0{,}3\ \Delta_m$.

3. EXPERIMENTAL RESULTS

In the following lines, results of the experimental campaign are presented and discussed.

3.1 FORCE VS. IDR CURVES

The measurement of force and deformation through the actuator and sensors, combined with the post-processing of the collected data, enables the plotting of a Force vs. IDR curve for each wall, as seen in Figure 3. The IDR is calculated by dividing the measured displacement by the wall height and expressing the result as a percentage.

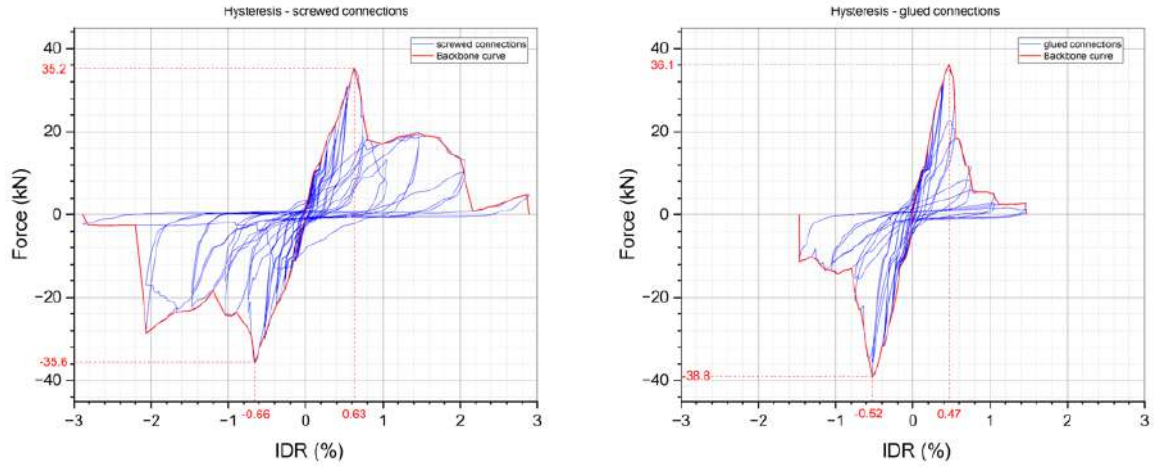


Figure 3: Hysteretic curves resulting of the in-plane tests performed with, on the left, the test specimen with screwed connections and, on the right, with glued connections.

Traditional drywall partitions with screwed connections exhibit a certain ductile behaviour, characterized by their capacity to absorb forces and deform without immediate failure. This is reflected in a relatively low force-to-displacement ratio during the initial loading cycles. In the tested wall, the maximum force resisted was 35.2 kN for an IDR of 0.63% in the positive direction and 35.6 kN for an IDR of 0.66% in the negative direction. Observations during the test suggest that the drop in peak force is likely due to increased screw tilting, which causes detachment from the outer frame. After this point, the wall experiences a significant reduction in strength and an incremental deformation, ultimately reaching an IDR of 2.89%, at which the partition loses functionality.

In contrast, the glued drywall partition demonstrates less ductile behaviour, with limited deformation under high forces before damage occurs. This partition achieved a slightly higher peak force of 36.1 kN for an IDR of 0.47% in the positive direction and 38.8 kN for an IDR of 0.52% in the negative direction. However, the force begins to decline even before visible damage is observed, likely due to gypsum core cohesive failure at board-to-stud connection areas with glue.

Quantitatively, screwed connections exhibit 5.5% less strength but at a displacement 30% higher compared than for glued connections. For deformation-sensitive NSEs, the capacity to accommodate deformations is more critical than achieving higher strength. Furthermore, higher load-bearing capacities can be problematic due to the unintended and unaccounted interaction with structural components. This minimal loss in strength observed in screwed connections suggests that the load-bearing capacity in the plane of CFS gypsum partition walls is not primarily determined by the type of board-to-frame connection. Instead, it is

likely influenced by other factors, such as the thickness, the number of board layers, as well as the thickness and size of the studs.

3.2 DS TO IDR CORRELATION

When discussing Damage States (DS), the primary definition is provided in FEMA P-58, BD 3.9.2, where each level is associated with the wall's repairability.

To accurately identify and classify damage, a detailed DS table, showed as Table 2, provides indicators for each state, ensuring consistency and clarity in the assessment process.

Table 2: Damage States description

DS1 Repair requires plaster, tape and paint	DS2 Repair requires replacement of boards	DS3 Repair requires replacement of wall
1. Minor curved cracks and minor crushing	5. Cracks in corners	11. Horizontal cracks
2. Cracks in joints	6. Vertical cracks	12. Wide cracks
3. Detachment of joint to outer frame	7. Diagonal cracks	13. Plastic deformation of the frame
4. Screw tilting	8. Screw head pulls through the board	14. Wall to surrounding connection failure
	9. Screw thread pulls out of the metal profiles	15. Wall out of plane failure
	10. Gypsum core cohesive failure	

For the glue connected wall, an additional DS2 signal, labelled as number 10, was introduced. In this way the risk of failure in the gypsum core caused by the high strength of the adhesive, typical in this connection, is considered in the possible damage.

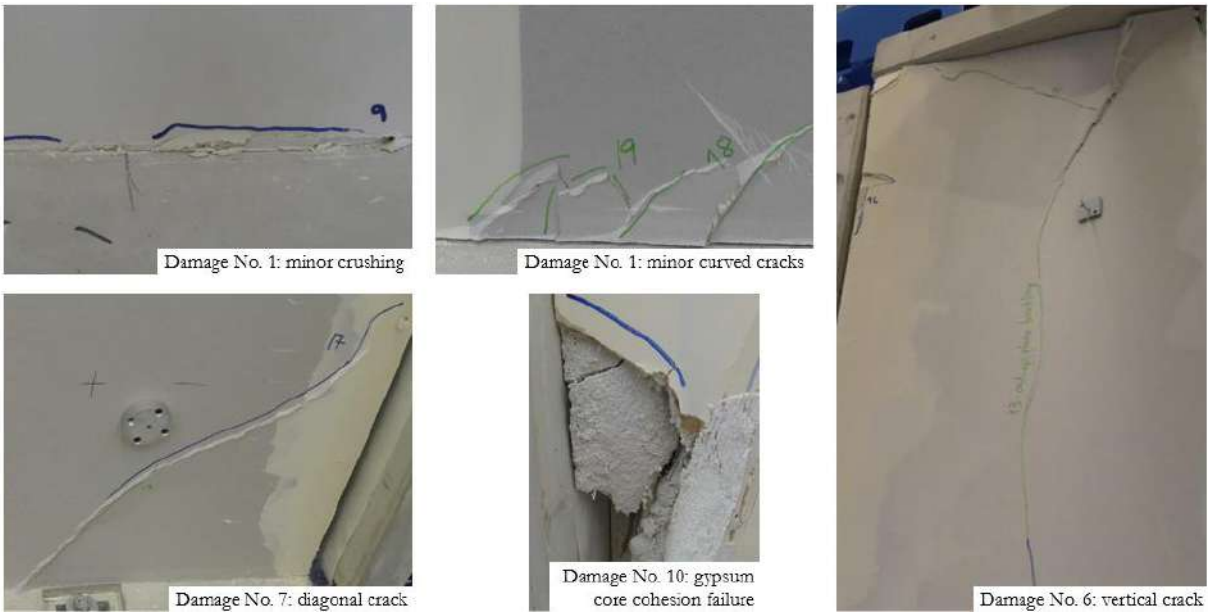


Figure 4: Examples of damage observe during the test. The number in the bottom right of each picture refers to the type of damage in Table 2.

With this outlined, it was possible during the test to classify each damage seen into a category and under a specific name. This information processing allowed for the determination of the minimum value of IDR at which a certain level of damage occurs. Understanding the walls through their capacity to tolerate deformations with varying levels of damage enables a straightforward comparison of their seismic behaviour and the assessment of the corresponding seismic risk.

Table 3 shows the minimum IDR in which each DS happens for traditional screwed connections and the proposed glued one.

Table 3: IDR values for screwed drywall

Description		*Screwed drywall*		*Glued drywall*	
		IDR	**IDR min.**	**IDR**	**IDR min.**
DS1	1. Minor curved cracks and minor crushing	0.38%	0.20%	0.54%	0.54%
	2. Cracks in joints	0.75%		-	
	3. Detachment of joint to outer frame	0.75%		-	
	4. Screw tilting	0.20%		-	
DS2	5. Cracks in corners	1.48%	0.75%	2.07%	0.54%
	6. Vertical cracks	1.05%		0.54%	
	7. Diagonal cracks	0.75%		0.75%	
	8. Screws pull out or through the board	1.48%		-	
	9. Screws pull out or through the frame	2.89%		-	
	10. gypsum core cohesive failure	-		0.75%	
DS3	11. Horizontal cracks	2.07%	2.07%	0.75%	1.48%
	12. Wide cracks	2.07%		1.48%	
	13. Plastic deformation of the frame	2.89%		2.07%	
	14.Wall to surrounding connection failure	-		2.07%	
	15. Wall out of plane failure	2.89%		-	

This analysis highlights the distinct damage mechanisms between wall configurations, particularly in how failure is initiated. For screwed connections, the primary issue is screw tilting, which triggers damage early in the process. However, this damage mechanism spans a relatively wide range of IDRs before progressing to DS2. This indicates that during low-intensity seismic events, damage may remain confined to DS1, which is relatively minor and can be easily repaired through simple measures like painting or retaping.

In contrast, DS1 is not relevant for glued connections. Typical failure modes such as edge crushing, local deformation, or joint cracks are not observed in this configuration. Instead, damage corresponding to DS2 begins earlier compared to screwed systems. This behaviour is attributed to the continuous bond created by the adhesive, which facilitates a monolithic interaction between the board and the frame, unlike the discretised connection provided by screws. Consequently, each wall configuration offers unique advantages and is better suited to specific scenarios, depending on the required performance and anticipated loading conditions.

4. CONCLUSION

This experimental research focused on studying board-to-frame connections in cold-formed steel (CFS) gypsum drywall systems. To achieve this, two full-scale specimens (3.75 m by 4 m) were tested under in-plane quasi-static cyclic loading history: one featuring traditional screwed connections and the other utilizing glued connections. The tests were conducted in accordance with FEMA 461, and the results were analysed following the guidelines of FEMA P-58/BD 3.9.2.

The achieved objective was to clarify the role of glue in the connections and to deepen current knowledge regarding the seismic behaviour of screwed connections and drywall systems in general.

Based on the findings, the following conclusions can be drawn:

- Screwed connections, being the typical bonding method with good mechanical properties and easy installation, are both well-established and actively studied in current research. This allows for the identification of weak points and performance predictions.
- In contrast, as a less common and less studied option, damage mechanisms and performance patterns in glued connections are harder to predict.
- Screws create a discretized system with stress concentration points, allowing greater deformation with a ductile behaviour, resulting in a high capacity of dissipating energy. In contrast, glued connections provide a continuous bond with minimal relative movement between board and frame and uniform force distribution, that causes damage to occur in the boards rather than at the connection.
- Damage in screwed walls initiates early (DS1 at 0.20% IDR) but extends across a wide range of IDRs (up to 0,75% IDR), allowing for manageable repairs after low-to-moderate intensity earthquakes. In contrast, glued walls exhibit no DS1 damage, making them well-suited for low-intensity seismic events. However, the transition to DS2 occurs earlier (0,54% IDR), with damage primarily concentrated on the board surface rather than at the edges or joints.
- Screwed connections exhibit slightly lower strength (–5.5%) but substantially higher displacement capacity (+30%) compared to glued connections. This indicates that the in-plane strength of the specimens is primarily influenced by factors such as the type of sheathing rather than by the type of connection.
- The strength of glue eliminates screws as weak points but increases the likelihood of gypsum core failure, which cannot be repaired and requires replacement of the gypsum board.

This study showed that CFS gypsum drywalls with glued board-to-stud connections made it possible to identify damage mechanisms—such as gypsum core cohesion failure—that had not been observed in specimens with screwed connections. These findings highlight the potential of further investigations involving alternative types of gypsum boards and adhesives, which may offer opportunities to enhance the seismic performance of CFS gypsum drywalls with glued connections. Moreover, glued connections appear to be a suitable option in scenarios where the seismic risk is of low intensity. Overall, this research contributes to advancing the knowledge and understanding of the seismic behaviour of drywall partitions.

5. REFERENCES

Applied Technology Council, 2007. *FEMA 461: Interim Testing Protocols for Determining the Seismic Performance Characteristics of Structural and Nonstructural Components,* s.l.: s.n.

Guzman, C., Araya-Letelier, G., Miranda, E. & Gallegos, M., 2025. Out-of-plane monotonic testing and fragility function development of screw and adhesive connections of steel-framed gypsum-board panels. *ELSEVIER.*

Komara, I., Taskin, K., Wahyuni, E. & Suprobo, P., 2017. Experiment on Cold-Formed Steel C-Section Joint with Screw and Adhesive Material. *International Journal of Sience and Technology.*

Miranda, E. & Mosqueda, G., 2011. *FEMA P-58/BD-3.9.2: Seismic Fragility of Building Interior Cold-Formed Steel Framed Gypsum Partition Walls,* s.l.: s.n.

Shin, D. H. & Kim, H. J., 2020. Macro-Modelling Approach for the In-Plane Cyclic Response of Cold-Formed Steel Partition Walls. *Applied Science MDPI.*

Yazdi, H., Hashemi, J. & Gad, E., 2022. Seismic fragility assessment of non-structural drywall partitions with screw and adhesive fixing through multi-axis cyclic testing. *ELSEVIER.*

Zito, M. et al., 2022. Experimental Seismic Assessment of nonstructural elements: Testing Protocols and Novel Perspectives. *Buildings MDPI.*

SPONSE 2026
EARLY CAREER BEST PAPER AWARD

EARLY CAREER BEST PAPER AWARD

Paper ID	Presenting Author	Title
26019	Wei-Chung Chen	Experimental and field investigations of suspended air handling units
26056	Simona Bianchi	Low-carbon resilient curtain walls: experimental study of timber-glass unitized systems
26059	Zeyu Sun	In-plane loading experiments on seismic damage and functional retention performance of LGS partition walls with opening

NOMINEE FOR EARLY CAREER BEST PAPER AWARD

Paper ID	Presenting Author
26004	Roberto J. Merino
26006	Amanpreet Singh
26009	Minhui Li
26019	Wei-Chung Chen
26053	Chang-Jun Bae
26056	Simona Bianchi
26059	Zeyu Sun
26067	Danilo D'Angela
26078	Ghislain Rivron
26101	Ahmed Awad

The candidates for the EARLY CAREER BEST PAPER AWARD were selected based on the following criteria:

- Currently a **student or employed with less than ten years** of experience as of the start of 2026.
- The author must have **applied for the award** at the time of abstract submission.
- From the applicants who meet the above criteria, the top **10 papers with the highest review scores** were selected.

The final award recipients were determined through **voting by the award session attendees**.